20th International Conference on Sustainable Energy Technologies

15th to 17th August 2023, Nottingham, UK

Sustainable Energy Technologies 2023

Conference Proceedings: Volume 1

Proceedings of the 20th International Conference on Sustainable Energy Technologies

SET 2023

15th – 17th August 2023, Nottingham, UK

Edited by
Professor Saffa Riffat

SET 2023 Admin Support
Department of Architecture and the Built Environment
Faculty of Engineering, University of Nottingham

Supported by the Conference Organising Committee:

Chair: Professor Saffa Riffat
Professor Yuehong Su
Dr Emmanuel Tapia-Brito
Dr Ziwei Chen

© 2023 Copyright University of Nottingham & WSSET

The contents of each paper are the sole responsibility of its author(s); authors were responsible to ensure that permissions were obtained as appropriate for the material presented in their articles, and that they complied with antiplagiarism policies.

Reference to a conference paper:

To cite a paper published in these conference proceedings, please substitute the highlighted sections of the reference below with the details of the article you are referring to:

Author(s) Surname, Author(s) Initial(s), 2023. 'Title of paper'. In: Riffat, Su,. ed., **Sustainable Energy Technologies**: Proceedings of the 20th International Conference on Sustainable Energy Technologies, 15th – 17th August 2023, Nottingham, UK. University of Nottingham: Buildings, Energy & Environment Research Group. Pp XX-XX. Available from: nottingham-repository.worktribe.com/ [Last access date].

ISBN-13: 978 085358 357 8

Version: 15.12.2023

Foreword

SET2023 in Nottingham, UK, continued the tradition of this esteemed annual conference, building upon the momentum regained in 2022 after a 2-year hiatus due to COVID-19.

The 20th International Conference on Sustainable Energy Technologies was a pivotal international academic conference in the realm of global sustainable energy. The conference served as a platform for the exchange of the most recent technical insights, the dissemination of current research findings, and the discussion of major challenges that could influence the future trajectories of human society, such as sustainable energy technology research, its applications, and energy security.

Held from August 15th to 17th, 2023, in Nottingham, UK, the conference was a collaborative effort between the World Society of Sustainable Energy Technologies (WSSET) and the University of Nottingham. Distinguished experts and scholars in the field, as well as representatives from eminent enterprises and universities, convened to deliberate on new advancements and accomplishments in the sector, whilst fostering academic exchange, the practical application of scientific discoveries, and collaborations between universities and industries, as well as between governments and industries.

The papers included in these proceedings concentrated on the same key topics as the previous year, such as Energy Storage for the Age of Renewables; Research, Innovation and Commercialisation in Sustainable Energy Technologies; Integrating Planning & Policy, Architecture, Engineering & Economics; Energy and Environment; Engineering Thermo-physics; and Systemic Change for Cities.

Over 200 delegates attended SET2023, with nearly 350 abstracts received. Although the number of papers presented and posters displayed is yet to be confirmed, the conference was a rich forum for academic and practical discourse.

We extend our gratitude to all participating authors for their invaluable contributions to both the conference and the publishing of this book. Our international scientific committee deserves special mention for their advisory role and their meticulous review of papers. We also express our unreserved thanks to Zeny Amante-Roberts and Celia Berry for their relentless efforts in making SET2023 a successful event. A special acknowledgement goes to our sponsors PCM Products Ltd., Terry Payne, and the newly added Stormsaver Ltd, for their generous support.

Professor Saffa Riffat
Chair in Sustainable Energy Technologies
President of the World Society of Sustainable Energy Technologies
SET 2023 Chair

CONTENTS

Paper Reference #	Title of Paper	Page Number
#2	A disruptive approach to improving energy efficiency of air conditioning chillers	1
#4	Integrated IEC+MVC air conditioning system for future sustainability	9
#6	Experimental and numerical investigation on thermal heterogeneity of a novel zoning air conditioner	16
#9	Solar cooking experiments with a finned heat storage cooking pot	27
#10	Design and techno-economic analysis for electric vehicle charging station	34
#13	A multi-directional flap fin louver windcatcher	44
#14	Deep learning-based vision for real-time building occupancy and window status detection	55
#15	Continual learning-based adaptive data-driven model for building energy prediction	62
#17	Harvesting with self-cleaning features: examining the role of wetting state in dust removal	71
#18	Remote monitoring unit for solar home systems	82
#19	Classification of climate zone using degree-day method	92
#21	Using system intrinsic thermal storage to enhance chiller plant efficiency – on-site proof of concept test	102
#22	A spectrally selective metal mesh coating for photovoltaic/thermal applications	112
#23	Solar control devices on glazed facades	121
#24	BIM-based building circularity assessment: conceptual framework	130
#27	Toward zero-carbon HVAC for temperate regions: cooling using thermoelectric heat exchanger	138
#30	A field study on occupants' thermal sensation vote in a test room equipped with trombe wall	148
#31	Minimizing the performance gap using longitudinal monitoring of environmental measurements: a case of a residential building	158
#33	The intermittency and flexibility of heating systems with different terminal types in buildings	169
#34	Investigation on heat transfer and flow organization characteristics of porous medium in quick freezer based on entransy analysis model	179
#35	A novel hybrid multi-layer CDTE based PV ventilated window system integrated with phase change material: concept, construction and experimental investigation	192
#39	Evaluation of photovoltaic/thermal radiative cooling (PVT-RC) system for closed-loop hydronic cooling of PV panels in the hot and arid region	202
#42	Comparison of spray characteristics for diesel and its blends with diethyl ether: an experimental study	212
#43	Concept of net-zero-ready residential buildings in hot-humid region	221
#44	Exploring vernacular courtyard strategies to improve thermal performance of modern housing in Dhaka	232
#47	Machine learning applications in data centre cooling performance optimisation and forecasting: a review	239
#48	Rapid evaluation of buildings thermal performance using infrared thermography and artificial intelligence	249
#51	Electricity distribution networks for multi-technology residential communities: a sufficiency assessment	261
#53	A novel modelling approach for performance analysis of a concentrated radiative cooling system using the compound parabolic concentrator	271
#54	Simulation of thermal performance and thermal interference of horizontal slinky-loop ground heat exchangers	281
#55	A novel PCM cooling system for building applications	291
#56	Performance of CO_2 air-to-water heat pumps for small domestic buildings in the UK	302
#57	Design, production and thermodynamic analysis of solar energy supported, nanofluid integrated thermoelectric vaccine cabinet	313
#58	Design, production, and performance analysis of a pyramid-type solar desalination system: an experimental study	318
#62	Experimental researches on the operation modes for a water source heat pump system to expand heating operation range	323
#63	Sustainable cooling solutions for rural communities: solar PV-driven DC vapour compression with low cost PCM storage	331
#66	Assessing the economic viability of a proposed DSM program utilizing heat pump driven thermochemical heat storage	338
#67	Graph neural network-based spatio-temporal methodology for hydraulic-thermal modelling of district cooling systems	345
#68	Rotary desiccant wheel systems: a review	354
#69	Thermal insulation performance assessment of UK dwellings through co-heating test methodology: a critical review	361
#72	Experimental and numerical analysis of a wind tower with run around heat exchanger	365
#73	Rural energy accessibility profiling to enable effective energy decarbonisation research	376
#74	A BIM-based conceptual framework for embodied carbon assessment	387
#75	Forecasting PV generation for a community energy scheme	395
#83	Feasibility study of machine learning in solar energy storage systems optimisation	401
#86	Enhancing energy efficiency in hospital buildings	412
#93	Splitting the exergy destruction into avoidable and unavoidable parts for integrated biomethane liquefaction process and liquid air energy storage system	423
#96	A comparison of photovoltaic sun tracking methods	432
#97	sSudy on the effect of inter-cellular gaps on the thermal profile of solar photovoltaic systems	442
#98	Exploring the relationship between investor profiles and sustainable investment drivers: a systematic review	450

#2: A disruptive approach to improving energy efficiency of air conditioning chillers

Kim Choon NG[1], Muhammad BURHAN[1], M. KUMJA[1], Doskhan YBYRAIMKUL[1], Qian CHEN[2], Faheem AKHTAR[3], Muhammad Wakil SHAHZAD[4]

[1]King Abdullah University of Science and Technology, Saudi Arabia, kimchoon.ng@kaust.edu.sa, muhammad.w.shahzad@northumbria.ac.uk
[2]Institute of Ocean Engineering, Shenzhen, International Graduate School, Tsinghua University, Shenzhen 518055, China.
[3]Department of Chemistry and Chemical Engineering, SBA School of Science & Engineering, DHA, Lahore 54792, Pakistan,
[4]Mechanical and Construction Engineering Department, Northumbria University NE1 8ST, UK

Abstract: In 1902, Willie H. Carrier invented the first electrically driven chiller for air conditioning (AC). Since then, assorted figures of merits (FOMs) were used for energy efficiency evaluation, assuming parity between all types of derived energy consumed. Such practices of interpreting FOM expressions are deemed thermodynamically incomplete, as the units of energy conveyed merely the quantitative aspects, ignoring its embedded qualitative potential. The quality exclusion in derived energy has plagued the chiller industry since its inception with a numerical oddity, i.e., the useful output (kWh cooling) of chillers is found greater than the input (kWh electricity or thermal). Pedagogically, the incongruity defies the Laws of Thermodynamics of any cycle because all real chillers incurred much dissipation. Rationally, the energy efficiency must always be less than unity unless there exists a fundamental abnormality.

At this juncture, a standard primary energy (QSPE) platform is proposed for all FOM expressions of chillers. Invoking the classical heat engines and the Carnot work associated with the derived energy, its equivalent QSPE at a common primary energy platform can be correlated via the corollary of the Laws of thermodynamics. By assigning the QSPE to both the input and output expressions of chiller FOM, namely the Coefficient of Performance (CoP), an accurate universal efficiency is formulated, resolving the said misconception and ensuring the laws of energy conservation within a cycle are observed. Henceforth, the chillers' efficacy expression returns to its normalcy where its ratio always less than unity. In addition, the causal efficacy development enables designers and users to intuitively improve the aspects of design and optimal rating regimes of chillers. The methodology ensures a better understanding of chillers' performance needed of AC towards a sustainable cooling future.

Keywords: Air conditioning, hybrid cooler, sustainable cooling future.

1. INTRODUCTION

Over the past three decades, the world electricity consumption by cooling or air conditioning (AC) has been increasing rapidly at CAGR rates ranging from 4% to 6% annually (Shahzad, Burhan, Ybyraiymkul, Oh, et al. 2019). Such a trend in electricity demand can be attributed to three factors, namely (i) the desire for better work environment, (ii) the increasing GDP per capita of many countries and (iii) the exponential growth in world's population. For example, the AC electricity consumption in 1990 was a miniscule 550 TWh/y. However, by 2020 electricity consumption for AC increased by 4-fold to 2199 TWh/y whilst its projected electricity demand by 2050 is 6205 TWh/yr, shown graphically in Figure 1 (Birol 2018; Kian Jon et al. 2021). Furthermore, such an insatiable appetite for electricity consumption by AC can be partly attributed to the phenomena of energy efficacy levelling of mechanical vapor chillers (MVCs) over the same period. The intrinsic dual roles of evaporator coils for sensible and latent cooling and the finite size of condenser needed in cycle heat rejection, have fixed the operational thermal lift of compressor, i.e., its specific work input.

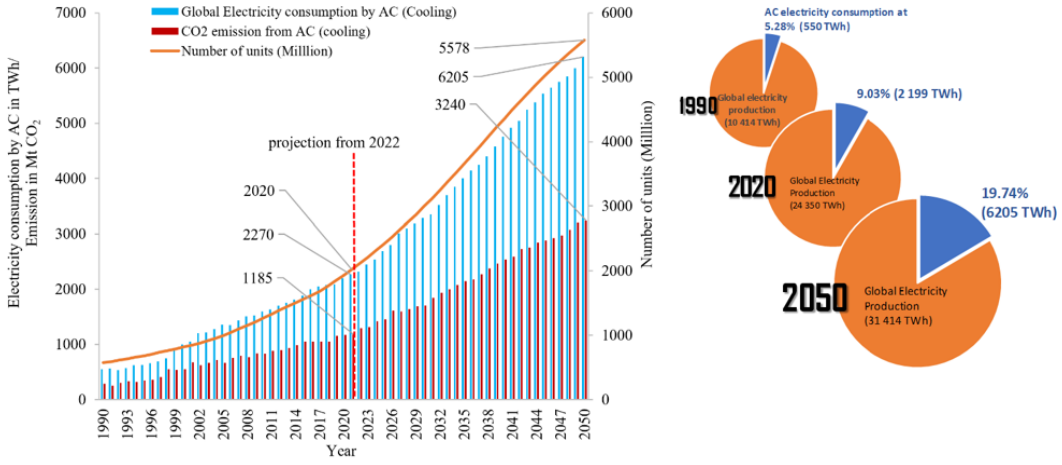

Figure 1 Air conditioning stock and energy consumption trend.

At King Abdullah University of Science & Technology (KAUST), a cooling Initiative (KCI) grew from an urgent need for highly efficient sustainable cooling technologies to counter the looming global increase in electricity demand from AC. Within KSA, air conditioning (AC) systems are not only energy (electricity) intensive, they are responsible for the majority of peak power demand and over 66% of annual building related electricity consumption (Alshehri et al. 2020; Howarth et al. 2020; Krarti and Howarth 2020). Although air conditioning industry is deemed as a mature technology, yet, its annual global market turnover is still increasing, amounting to more than 150 billion USD. Thus, the shear market size of cooling industry has provided much motivation for innovative cooling research at KAUST.

In general, there are two approaches to improving energy efficiency(EE) of cooling devices: Firstly, an improvement over the existing efficacy level by decoupling of sensible and latent processes within an evaporator for the treatment of supply air (Duan et al. 2012; Jradi and Riffat 2014; K.C. Ng et al. 2019). It allows the best available cooling methods to be designed separately and later, re-combined or hybridized to achieve better overall performances. Nevertheless, the dehumidification process of supply air yet follows a condensation process path along its dew points as the local air temperatures are continuously lowered at saturation states. In such designs, across the moist air and the refrigerant of evaporator, it incurs several heat and mass transfer resistances. Across the condenser, it has similar heat transfer resistances except the absence of condensation. Constrained by these temperature limits, the thermal lift across cooling cycle (representing compressor work) of MVC is somewhat fixed due to the dual requirements of supply air treatment. Table 1 tabulates the anticipated heat and mass transfer resistances along with the pressure drop of air flow incurred by air treatment via the evaporator and condenser.

Table 1: A comparison of heat and mass transfer resistances between the supply air (SA) and the heat exchangers of conventional MVC and the proposed DC-MVC cycles.

Types of cooling processes in the heat exchangers of chillers	Chiller designed with dehumidification via lowering fin surfaces lower than dew point of air (conventional MVC)	Proposed disruptive cooling cycle:- The desiccant-coated coil MVC designed with sensible cooling & dehumidification.
Evaporator (Tube-fin type) 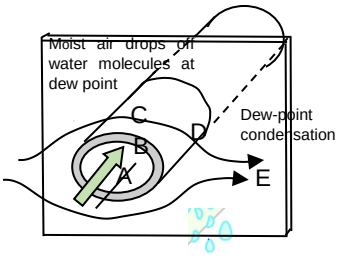 	(A) Refrigerant heat transfer resistance (HTR)- {1/(Ap hC)}, (B) Tube wall material HTR { ln(ro/ri)}/(2πLk) } (C) Convective air flow over the tube-fin area –{1/(Af hConv)} (D) Water molecules transfer at dew points, {1/(Af hD)} (E) Pressure drop (ΔP) of air flowing across exchanger.	(A) Refrigerant HTR (-1/(A_p h_C)}, (B) Tube wall material HTR { ln(r_o/r_i)}/(2πLk) }, (C) Convective air flow over the tube-fin– {1/(A_f h_{Conv})} (D) Direct water vapor capture (sorption) by adsorbent. Temperature gradient to refrigerant of evaporator favors uptake of water molecules. (E) Pressure drop (ΔP) of air flowing across exchanger.
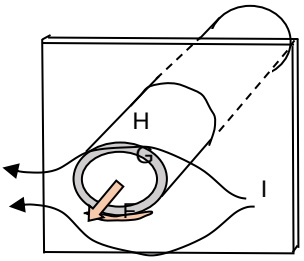 Condenser (Tube-fin exchanger)	(F) Refrigerant HTR-{1/(Ap h_C)}, (G) Tube wall material HTR { ln(ro/ri)}/(2πLk) } (H) Convective air flow over the tube-fin area –{1/(Af h_{Conv})} (I) Pressure drop (ΔP) of air flowing across exchanger.	(F) Refrigerant HTR-{1/(Ap h_C)}, (G) Tube wall material HTR { ln(ro/ri)}/(2πLk)} (H) Convective air flow over the tube-fin area –{1/(Af h_{Conv})} (I) Pressure drop (ΔP) of air flowing across exchanger. (J) Desorption of water molecules from desiccant due to high fin surface temperatures from the condensation heat of refrigerant.

2. BARRIER TO ENERGY EFFICIENCY(EE) IMPROVEMENT

Figure 2(a) depicts the typical mechanical vapor compressor (MVC) cycle in the treatment of supply air (SA). The flowing air is cooled at constant humidity ratio (ω) until its thermodynamic state reaches the local dew points, and this is followed by both sensible and latent cooling along the saturation states until its desired humidity ratio is achieved. The air leaving the evaporator is then mixed with the untreated return air (RA) to achieve the suitable temperature (T_{SA}) and ω of SA to the space or room. Obviously, given the above-mentioned operational temperature limits of heat exchangers, the energy efficiency of MVC has reached an asymptotic behaviour, typically hovering around 0.85±0.05 kW/*Rton* (tropical rating "A" conditions of ARI). Such a MVC efficacy behaviour is unlikely to achieve a further quantum reduction from the existing rating unless there is a paradigm shift in the cooling cycle or process design.

3. DISRUPTIVE COOLING CYCLE

Since the first invention of vapor compression chillers, the design and performance of major components within a cooling cycle, hitherto, have been greatly studied and improved upon by the vibrant chiller industry. Despite continued attempts to improve EE of chillers, any further EE improvement over the existing MVC levels were deemed marginal at best. AS mentioned in the introduction, two plausible methods were attempted at the laboratory of KAUST Cooling Initiative (KCI): Firstly, the de-coupling of sensible and latent treatment of SA, enabling the best practical cooling and dehumidification processes to be implemented in the design. These separate processes are then re-combined to form a hybrid cooling cycle for better EE vis-à-vis over existing chillers. From our recent publications, such hybrid chillers could achieve up to 35% increase in chiller COPs over the conventional MVC (Chen et al. 2020, 2021a, 2021b, 2022; Shahzad et al. 2021). Secondly, a disruptive moist air treatment that avoids any dew-point condensation at evaporator. Water vapor molecules are captured directly via a high performance adsorbent, called adsorption by composite-salt porous cage (CSPC) (Akhtar et al. 2021; Wang et al. 2022). A thin CSPC desiccant layer (100-120μm) that has high affinity to water molecules. The coated coils (evaporator and condenser of MVC) operate in batch *tandem:* An adsorption (vapor uptake at 12-18^{o}C) process is affected by the cooled evaporator in a half-cycle, whilst the condenser (over 50^{o}C) undergoes the desorption of water vapor (discharged from desiccant) over the same period. Note that the cycle waste heat is reused for the regeneration of desiccant. Direct dehumidification by supply air (SA) via evaporator offers a seemingly "disruptive" path between the outdoor air (OA) and the SA. This paradigm shift in dehumidification has two advantages towards reducing the compressor

work: Firstly, the MVC thermal lift of compressor is now reduced significantly. Secondly, the higher vapor density of refrigerant at inlet of compressor increases the refrigerant flow, as observed in the psychrometric chart of Figure 2(b).

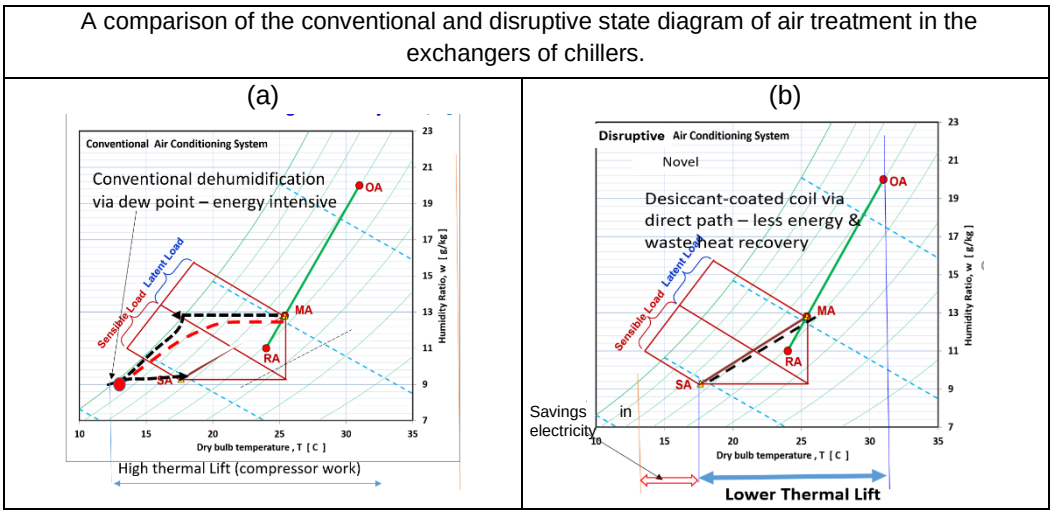

Figure 2 A comparison of the conventional and disruptive state diagram of air treatment in the exchangers of chillers

Figure 3(a) shows a conventional silica cage of 8-20µm diameters where its internal is hollow by design. As composite salts is impregnated into the hollow cages, the salts tend to leak out of the cage at relative humidity(rh) > 90%. To avoid the deliquescent problem at high rh, we filled the cage with aerogels or air sacs and "pillar walls" where the inter-connecting walls remain highly porous, as shown in Figure 3(b). The presence of these inter-connecting walls provided the surface tension forces between the softened salts and the porous walls, holding back the composite salts even at 100% rh. The reliability of CSPC was found to remain unchanged with hundreds of water uptake cycling tests. Our proprietary composite-salts porous cage (CSPC) depicts the highest vapor uptake over all other desiccants available hitherto, as shown in Figure 4(a). It is observed that the maximum uptake at 95% rh for impregnated CSPC at 37%/50%/62% by mass were found to be 220%, 410% and 520%, respectively. Note that the CSPC has performed several folds better than the MOF family of desiccant. Furthermore, the cost of CSPC is 3 order lower as compared with the MOF desiccants (Akhtar et al. 2021).

(a) Conventional silica cage	(b) The activated silica cage impregnated with $LiCl_2$
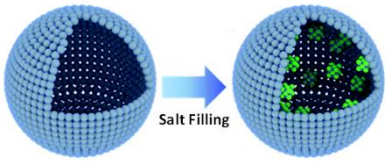	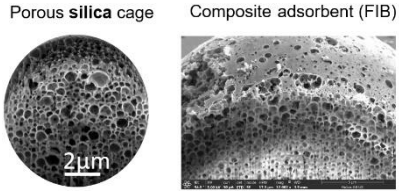
Hollow silica cage tends to leak the softened salts at high relative humidity.	Activated silica cage with air sacs can prevent deliquescent problem at 100% rh. The internal walls (FIB photo) provided porous "pillars" for surface tension effects that hold back the salts.

Figure 3 The comparison between hollow silica cage and the activated silica cage with filled air sacs and porous "pillars"

The CSPC desiccant is coated onto the conventional MVC system using a suitable binder where the coating thickness is about 75-110µm. An electrostatically charged spray gun is used to deliver the CSPC powder onto the gap in between tube-fin exchangers, as shown in Figure 4(b). During operation, the coated coils of MVC would alternate their roles as evaporator and condenser, switching the operation over intervals of 3 to 7 minutes for optimal cooling. The compressor operates continuously where the refrigerant flow could be switched by a 4-way valve, directing the refrigerant flow of compressor from evaporator to suction port and from discharge port of compressor to the condenser.

Figure 4(a) (Akhtar et al. 2021)A comparison of the water vapor uptake by assorted desicants over a range of relative humidity (rh).	Figure 4(b). Example of CSPC adsorbent coated on the tube-fin aluminum coil. The coating is performed with a binder and electrostatic spraying technique.
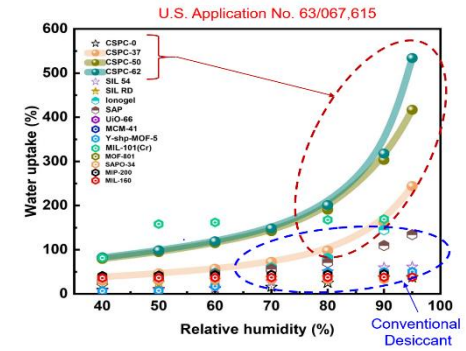 **(a)**	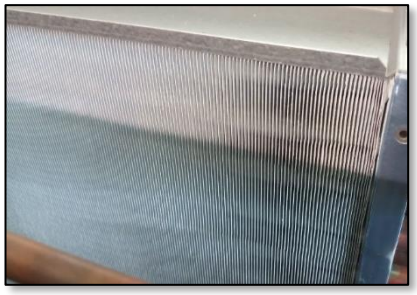 **(b)**

Figure 4 Comparison of water uptake and adsorbent coating on heat exchanger

4. EXPERIMENTAL RESULTS

The coated-coil MVC or DC-MVC was evaluated under the outdoor weather conditions of Jeddah, a city with distinct seasons of wide range of air temperature and humidity(Figure 5(a)(Krarti et al. 2023)). As per ASHRAE standards-55, the thermal comfort zone for human comfort (at 0.5 cloth factor) straddled across temperatures of 21^{o}C to 24^{o}C and humidity ratios of 10-11.5 g/kg of air. As a consequence of direct water molecules capture, the desired states of SA leaving the evaporator could be raised higher to 18±1^{o}C for optimal operation whilst the humidity ratios around 9±0.5 g/kg of air. Typical traces of the temperatures and humidity ratios of key components of DC-MVC are depicted in Figures (b,c,d) and the COP could reach more than two times of the conventional MVC. Owing to the disruptive path, the higher evaporator temperature operation favors (i) an increase in density of refrigerant entering the suction port of compressor and (ii) the sorption isotherms of water molecules by coated desiccant is enhanced by its positive temperature gradient of pore surfaces. At the condenser, desorption of water vapor resulted in mass transfer from the pores of adsorbent, effecting a drop in the saturation temperature of condenser from >50^{o}C to 45^{o}C ot 5K. On comparison to the conventional MVC, the savings in electricity consumption is reduction in the thermal lift of compressor is shown in Figure 5(e). The alternating roles of evaporator-condenser operation must also be complemented by the switching air flow circuits, namely (i) RA of room to evaporator, (ii) OA air to condenser prior to discharging into ambient. These processes were accomplished succinctly with a 4-way valve (in refrigerant circuits) and a pair of 2-way valves with fans for moving treated air (SA) to the room or space as well as purging of condenser air continuously. A universal efficiency parameter has been developed to evaluate the performance of all chillers at common energy platform (Kim Choon Ng et al. 2021; Shahzad et al. 2022; Shahzad, Burhan, Ybyraiymkul, and Ng 2019; Shahzad, Burhan, and Ng 2019).

Sample of experimental results of DC-MVC tests under the meteorological data of Jeddah area.

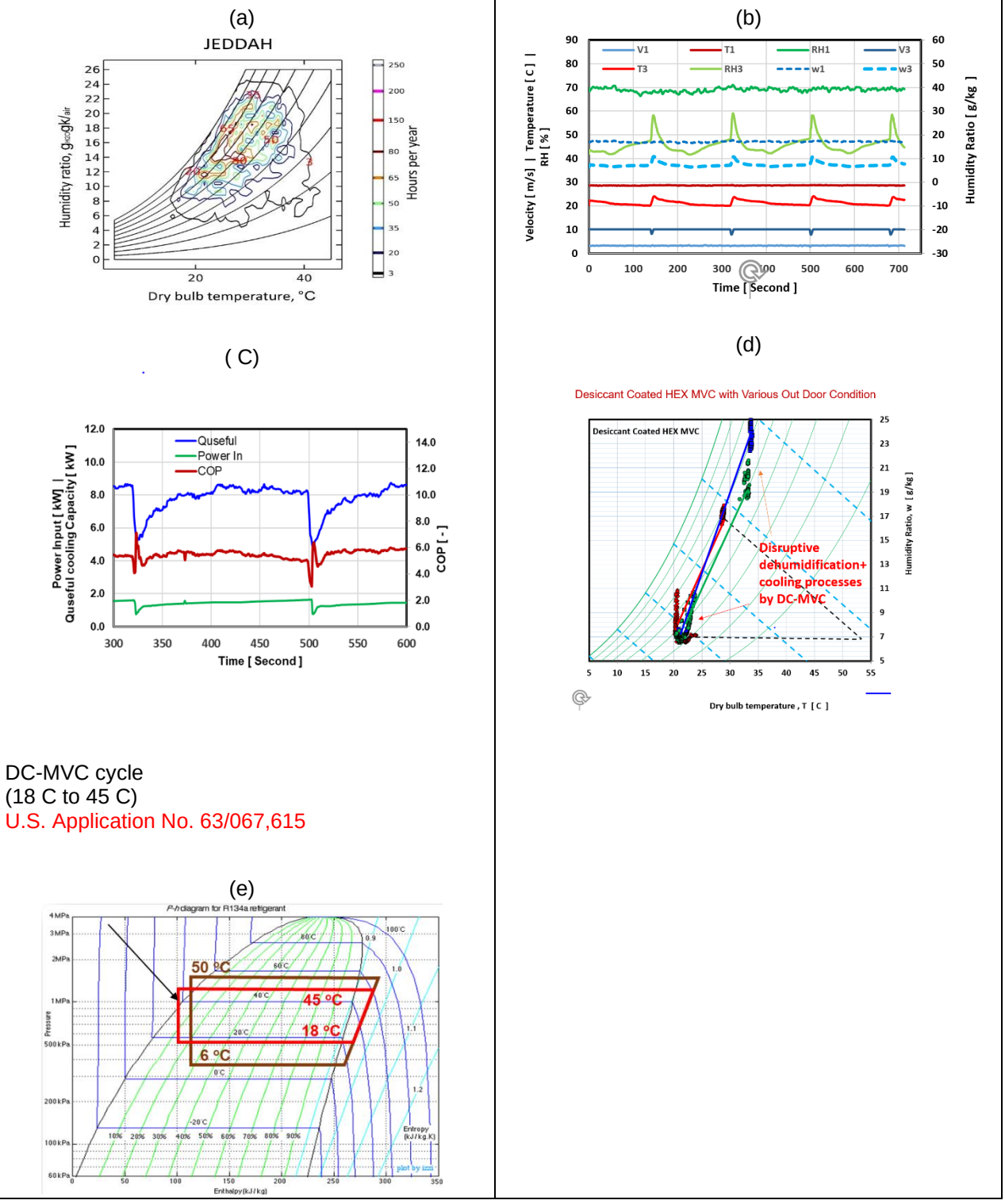

Figure 5 Sample of experimental results of DC-MVC tests under the meteorological data of Jeddah area

5. CONCLUSION

The coated-coil MVC (DC-MVC) has been successfully developed and tested for the treatment of supply air(SA) in an air conditioning system. The dual latent and sensible cooling in evaporator offers a disruptive cooling path, differs totally from the conventional dew-point cooling path of existing MVC. At the same cooling load, the direct treatment of SA reduces the compressor work up to 2 folds, increasing its COP significantly vis-à-vis of the conventional MVC. In addition, the cooling path is dry (no condensation) and avoided the

inherent bio-fouling on the evaprator with less maintenance. Furthermore, the DC-MVC cycle can be hybridized with the IEC to give the IEC-DC-MVC cycle, achieving higher electricity savings by the evaporative power of IEC. We opine that the design of disruptive chiller, i.e., IEC-DC-MVC, is inexpensive as it utilizes the robust speed-controlled MVC as the anchoring device for active control of the SA conditions for cooling comfort. Given these quantum advantages, the IEC-DC-MVC design could meet the sustainable development goals of chiller industry for its cooling future.

6. ACKNOWLEDGEMENT

The authors are grateful for the funding of KAUST Cooling Initiative (KCI), REP/3988/01-01, 2019-2023. Author also would like to thank to Northern Accelerator for grant NACCF - 232 (Shahzad)

7. REFERENCES

Akhtar, Faheem Hassan et al. 2021. "Defining Sulfonation Limits of Poly(Ether-Ether-Ketone) for Energy-Efficient Dehumidification." *Journal of Materials Chemistry A* 9(33): 17740–48.

Alshehri, Thamir, Nicholas Howarth, Rolando Fuentes, and Natalia Odnoletkova. 2020. "The Future of Cooling in Saudi Arabia: Technology, Market and Policy Options." (August). files/167/Alshehri et al. - 2020 - The Future of Cooling in Saudi Arabia Technology,.pdf%0Ahttps://www.researchgate.net/publication/344285392_The_Future_of_Cooling_in_Saudi_Arabia_Technology_Market_and_Policy_Options.

Birol, Fatih. 2018. International Energy Agency *The Future of Cooling*. https://www.iea.org/reports/the-future-of-cooling (January 2, 2022).

Chen, Qian et al. 2020. "Simultaneous Production of Cooling and Freshwater by an Integrated Indirect Evaporative Cooling and Humidification-Dehumidification Desalination Cycle." *Energy Conversion and Management* 221(July): 113169. https://doi.org/10.1016/j.enconman.2020.113169.

———. 2021a. "A Hybrid Indirect Evaporative Cooling-Mechanical Vapor Compression Process for Energy-Efficient Air Conditioning." *Energy Conversion and Management* 248(September): 114798. https://doi.org/10.1016/j.enconman.2021.114798.

———. 2021b. "A Hybrid Indirect Evaporative Cooling-Mechanical Vapor Compression Process for Energy-Efficient Air Conditioning." *Energy Conversion and Management* 248(July): 114798. https://doi.org/10.1016/j.enconman.2021.114798.

———. 2022. "Experimental Study of a Sustainable Cooling Process Hybridizing Indirect Evaporative Cooling and Mechanical Vapor Compression." *Energy Reports* 8: 7945–56. https://doi.org/10.1016/j.egyr.2022.06.019.

Duan, Zhiyin et al. 2012. "Indirect Evaporative Cooling: Past, Present and Future Potentials." *Renewable and Sustainable Energy Reviews* 16(9): 6823–50.

Howarth, Nicholas et al. 2020. "Staying Cool in a Warming Climate: Temperature, Electricity and Air Conditioning in Saudi Arabia." *Climate* 8(1).

Jradi, M., and S. Riffat. 2014. "Experimental and Numerical Investigation of a Dew-Point Cooling System for Thermal Comfort in Buildings." *Applied Energy* 132: 524–35. http://dx.doi.org/10.1016/j.apenergy.2014.07.040.

Kian Jon, Chua, Md Raisul Islam, Ng Kim Choon, and Muhammad Wakil Shahzad. 2021. Green Energy and Technology *Advances in Air Conditioning Technologies*. Springer Nature Singapore Pte Ltd. http://link.springer.com/10.1007/978-981-15-8477-0.

Krarti, M. et al. 2023. "Energy Performance of Hybrid Evaporative-Vapor Compression Air Conditioning Systems for Saudi Residential Building Stocks." *Journal of Building Engineering* 69(January).

Krarti, M., and Nicholas Howarth. 2020. "Transitioning to High Efficiency Air Conditioning in Saudi Arabia: A Benefit Cost Analysis for Residential Buildings." *Journal of Building Engineering* 31(April): 101457. https://doi.org/10.1016/j.jobe.2020.101457.

Ng, K.C., M.W. Shahzad, M. Burhan, and S.J. Oh. 2019. "Approaches to Energy Efficiency in Air Conditioning: Innovative Processes and Thermodynamics." In *Energy Procedia*,.

Ng, Kim Choon et al. 2021. "A Thermodynamic Platform for Evaluating the Energy Efficiency of Combined Power Generation and Desalination Plants." *npj Clean Water* 4(1): 1–10. http://dx.doi.org/10.1038/s41545-021-00114-5.

Shahzad, Muhammad Wakil, Muhammad Burhan, Doskhan Ybyraiymkul, Seung Jin Oh, et al. 2019. “An Improved Indirect Evaporative Cooler Experimental Investigation.” *Applied Energy* 256(March): 113934. https://doi.org/10.1016/j.apenergy.2019.113934.

Shahzad, Muhammad Wakil et al. 2021. “A Spatiotemporal Indirect Evaporative Cooler Enabled by Transiently Interceding Water Mist.” *Energy* 217: 119352. https://doi.org/10.1016/j.energy.2020.119352.

———. 2022. “Demystifying Integrated Power and Desalination Processes Evaluation Based on Standard Primary Energy Approach.” *Thermal Science and Engineering Progress* 27(October 2021): 101153. https://doi.org/10.1016/j.tsep.2021.101153.

Shahzad, Muhammad Wakil, Muhammad Burhan, and Kim Choom Ng. 2019. “A Standard Primary Energy Approach for Comparing Desalination Processes.” *npj Clean Water* 2(1): 1–7. http://dx.doi.org/10.1038/s41545-018-0028-4.

Shahzad, Muhammad Wakil, Muhammad Burhan, Doskhan Ybyraiymkul, and Kim Choon Ng. 2019. “Desalination Processes’ Efficiency and Future Roadmap.” *Entropy* 21(1).

Wang, Shunli et al. 2022. “Recent Advances in Developing Mixed Matrix Membranes Based on Covalent Organic Frameworks.” *Separation and Purification Technology* 301(June): 122004. https://doi.org/10.1016/j.seppur.2022.122004.

#4: Integrated IEC+MVC air conditioning system for future sustainability

Muhammad Wakil SHAHZAD[1], Kim Choon NG[2], Qian CHEN[2], Nida IMTIAZ[1,3], Muhammad Ahmad JAMIL[1], Muhammad BURHAN[2], M. KUMJA[2], Doskhan YBYRAIMKUL[2], Ben Bin XU[1]

[1] Mechanical and Construction Engineering Department, Northumbria University NE1 8ST, UK, muhammad.w.shahzad@northumbria.ac.uk
[2] King Abdullah University of Science and Technology, Saudi Arabia
[3] Universiti Teknologi Malaysia, Johor Bahru, Malaysia

Abstract: The global air conditioning (AC) demand have increased significantly, from a mere 800 TWh/yr in 2002 to 2200 TWh/yr in 2022, growing annually at a CAGR of 4.8%. Over this period, the increase in global warming effect is marked by a 16% increase in cooling-degree days (CDD) and almost 96 % increase in the European Union countries. The unusually high ambient temperatures recorded in many countries have affected the regional climatic weather patterns where severe draughts, stronger heatwaves and cyclones or hurricanes are increasingly occurring. In a business-as-usual (BAU) report on global cooling demand, it predicted by 2050 the AC electricity consumption could reach a massive 6300 TWh/yr or about 19% of global electricity production. Without major breakthrough in technology innovation and adequate green-house gases (GHG) emission guidelines from AC, the World Economic Forum predicted that the cooling industry alone could worsen the ambient temperatures rise by as much as 0.5-degree Celsius. In addition to the global warming effects from AC electricity, the continued usage and production of refrigerants for compressors, such as the hydro-chloro-fluorocarbon (HCFC) and hydro-fluorocarbons (HFC), have damaging effects on weather patterns from their high specific GWP potentials, typically 1500 times than CO2. However, the International Energy Agency (IEA) predicted a likely reduction of refrigerants use in AC and this reduction may lessen global warming gradually till then. The adoption of Montreal Protocol (1987) by all countries was an excellent example in limiting the production, consumption and trade of HCFCs and CFCs refrigerants. Similar concern in the continued production of HFC-32 and HFC-125 refrigerants for AC had similar bad effects to the environment, but the policy to curtailed their production could reduce emissions to the ambient by 50% and 100%, respectively. Despite the zero-ozone potential of HFCs, their usage as alternative to HCFCs could still harm the environment due to their high GWPs. The high energy consumption and GWP effect from AC refrigerants could be attributed partially to the low performance conventional chillers.

We proposed innovative hybrid cooling system for future sustainability. In proposed system, indirect evaporative cooler (IEC) is hybridized with mechanical vapor compression (MVC) chiller to improve overall performance, effective temperature and humidity control and reduced water consumption. Hybrid IEC+MVC system is designed, fabricated and tested as assorted outdoor air conditions. In schematic, partial air from room return is utilized as a working air in IEC and accordingly outdoor air is introduced to makeup the cooling requirement. The IEC handles 33-45 of the total cooling load, and the energy consumption can be reduced by 20-40% as compared to conventional MVC. Moreover, the condensate collected from the evaporator can compensate for >75% of water consumption in IEC, making the system applicable in arid regions. We also proposed a simplified empirical model for hybrid system performance evaluation based on experimental results.

Keywords: Air conditioning, hybrid cooler, sustainable cooling

1. INTRODUCTION

In 2019, the average number of cooling degree days was 16% higher than in 2000 due to record-high temperatures in most countries of the world. These frequent and extreme heatwaves coupled with rising living standards are expected to accelerate unprecedented cooling demand in next decade. Currently, over 2 billion air conditioners (AC) units are in operation and it is expected to grow to 3.5 billion by 2030 (as shown in Figure 1), making it the fastest-growing end use in buildings (Elizabeth O'Grady and Saarthak Narsipur, 2018).

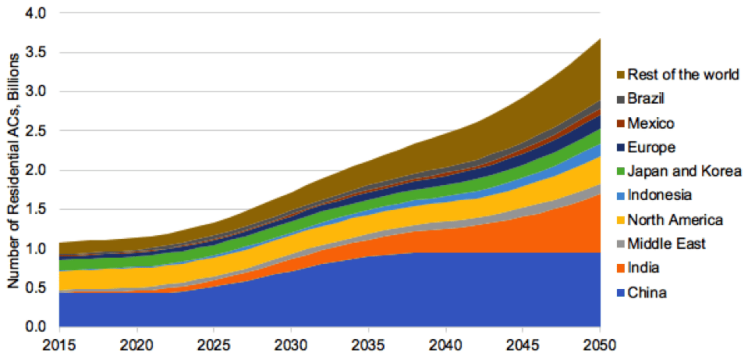

Figure 1 Global air-conditioning stock 2015-2050

By 2050, over 2/3 of global household will have AC and half of stock will be installed in India, Indonesia and China. The energy demand for space cooling has been tripled to 2199 TWh since 1990 and it is projected to grow to 6000 TWh by 2050 with business-as-usual operation (*Global air conditioner stock, 1990-2050 – Charts – Data & Statistics - IEA*, no date). This increase in AC demand and corresponding energy consumption will cause potentially a massive problem for the world in terms of carbon and refrigerant pollution. Therefore, reducing the energy consumption for AC is the one of the most critical ways to alleviate global energy stress and cut CO2 emissions.

The indirect evaporative cooler (IEC) is emerged as an alternative approach due to its energy efficiency (Shahzad *et al.*, 2021). It utilizes the water evaporative potential (>2200 kJ/kg & 1 kJ/kg-℃) to extract heat from outdoor air. It only utilizes electricity for fan and water pump. Therefore, IEC coefficient of performance (COP) is several times higher than conventional AC systems (Jradi and Riffat, 2014; Kian Jon *et al.*, 2021). Despite higher COP of IEC systems, its commercial applications were not witnessed due to several intrinsic limitations. Firstly, they are unable to maintain supply air temperature due to passive operation. Secondly, they can only handle sensible load. Lastly, complex construction and high maintenance requirements.

To overcome these limitations, we proposed hybridization of IEC with mechanical vapor compressor (MVC) chillers to improve overall system performance. With this integration, IEC will work as a pre-cooler for outdoor air temperature and MVC will help to control set temperature and humidity. The proposed hybrid system achieved over up to 45% performance improvement as compared to conventional MVC systems.

2. PROPOSED HYBRID COOLER

In proposed hybrid system, IEC is used as a precooler for MVC system. Since IEC can perform better at higher outdoor air temperature (Lin, Shahzad, *et al.*, 2021; Lin, Thu, *et al.*, 2021), so we exploit this potential to precool outdoor air temperature before introducing to MVC system as shown in Figure 2.

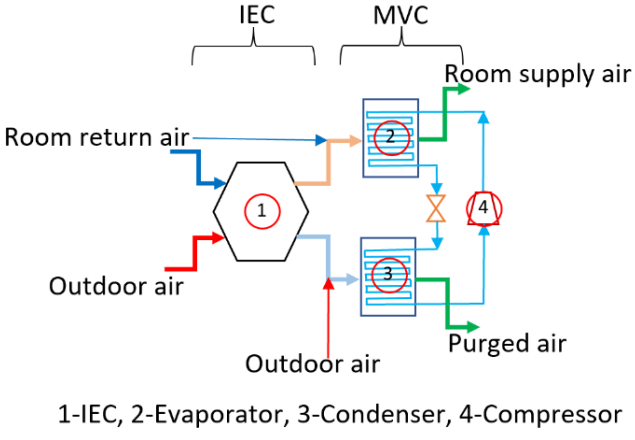

Figure 2 Schematic of hybrid IEC+MVC system

In wet channel of IEC, part (20-30%) of room return air is used as a working air. Humid air after wet channel is purged through condenser to reject refrigerant heat. High moisture in purged air help to maintain lower condenser temperature and hence lower thermal lift across compressor.

Outdoor air is passed through dry channel to transfer heat to working air in wet channel. Cold air after dry channel exit is mixed with room return air and passed through the MVC evaporator to achieve set temperature and humidity. It can be noticed that only same percentage as bleed air for wet channel is introduced from outdoor to maintain air flow rate to room

3. HYBRID COOLER PILOT

A pilot of proposed hybrid MVC+IEC cooler is designed, fabricated and commissioned at King Abdullah University of Science and Technology (KAUST) Saudi Arabia under KAUST Cooling Initiative project. Hybrid system 3D model is presented in Figure 3 and pilot is shown in Figure 4.

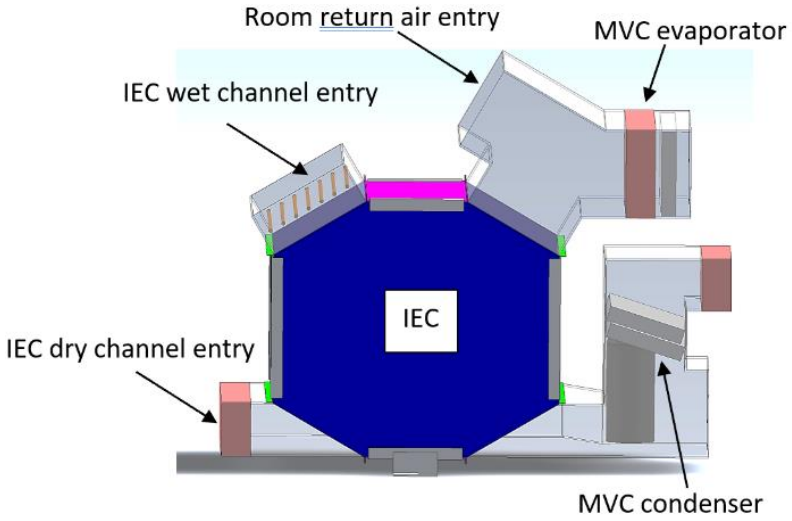

Figure 3 Hybrid MEV+IEC system 3D model

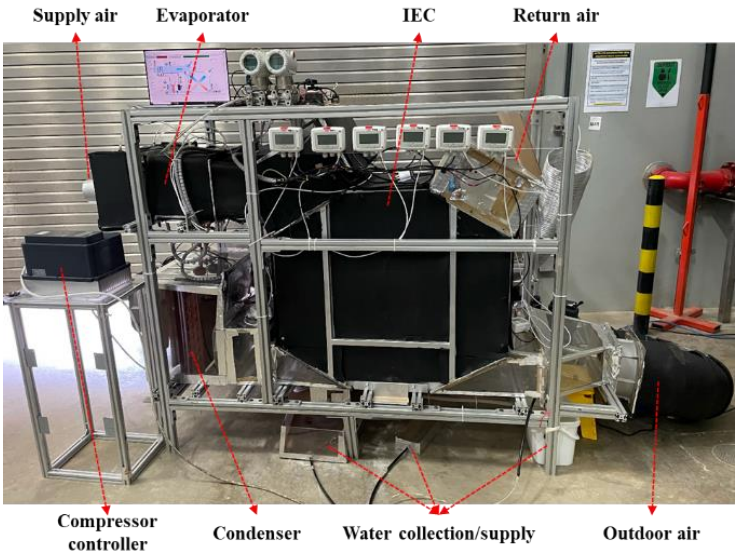

Figure 4 Hybrid MEV+IEC pilot at KAUST

The IEC pilot consists of 100 dry and wet channels separated by aluminium foil of 300 µm (Chen *et al.*, 2021). Similarly, MVC system consists of a commercial scroll compressor (Copeland™ ZR36K3E-TF5-522), throttling valve and fin tube heat exchanger evaporator and condenser. It is operating with R134a refringent due to distinctive advantages over other commercial refrigerants.

Hybrid pilot is equipped with all necessary instrumentation to log all possible trends. Instrumentation detail is provided in Table 1.

Table 1: Hybrid pilot instrumentation detail

Parameter	Manufacturer and type	Range	Accuracy
Temperature	OMEGA (thermistor)	0-60 °C	±0.1 °C
Relative humidity	Degree Controls Inc. (FH400)	10-90%	±2%
Pressure transmitter	ABB (2600T Series Pressure Transmitter)	0-400 Pa	± 5 Pa
Power	SCHNEIDER ELECTRIC (PowerLogic PM5100)	-	±0.5%

4. EXPERIMENTATION

Experiments were conducted at assorted OA temperature and humidity to evaluate the performance of hybrid pilot. Figure 5 shows experimental results at OA humidity 16.5g/kg. It can be noticed that IEC was able to achieve 18-20 ℃ temperature at all OA temperatures in contrast to conventional IECs whose performance varies with OA temperature. This is because of working air temperature which was bled from room return air and its flow rate. Therefore, IEC was able to cool down the OA to almost same temperature at assorted OA conditions. After the IEC, the MVC evaporator coils further cool down the supply air to 8-10 ℃.

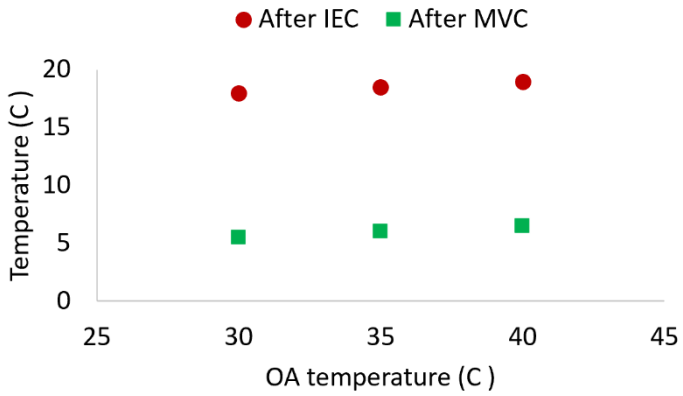

Figure 5 Temperatures of air from IEC and MVC

Coefficient of performance (COP) was calculated based on data logged via instrumentation and presented in Figure 6. Hybrid pilot improved COP 30-45% as compared to conventional MVC system.

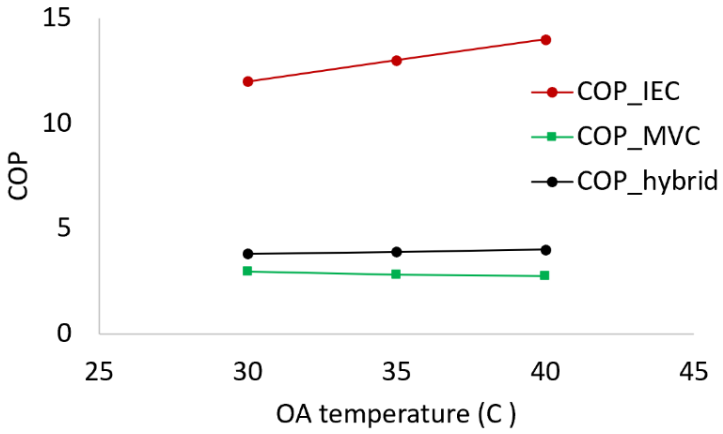

Figure 6 COP of IEC and MVC at assorted OA temperatures

It can be clearly noticed that hybrid IEC+MVC system benefits from the high energy efficiency of IEC and has a higher COP than conventional MVC systems. The operation on psychrometric chart is presented in Figure 7.

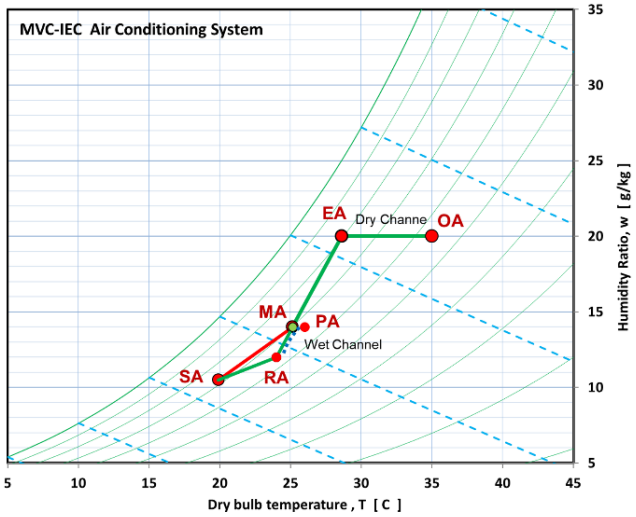

Figure 7 IEC+MVC operation on psychrometric chart

Experiments were repeated at assorted OA humidity and summary of temperatures is provided in Table 2 and COP in Table 3.

Table 2: Temperatures summary of IEC and MVC

OA temperature	After IEC	After MVC
OA humidity 10g/kg		
30	18.5	5.7
35	17.8	5.3
40	18.2	5.6
OA humidity 16g/kg		
30	19.1	8.5
35	18.8	8.7
40	19.5	9.1

Table 3: COP summary of IEC and MVC

OA temperature	COP_IEC	COP_MVC	COP_hybrid	% improvement
OA humidity 10g/kg				
30	7.9	3.5	3.8	8.6%
35	9.1	3.2	3.85	20.3%
40	10.5	2.9	3.9	34.5%
OA humidity 16g/kg				
30	12	2.97	3.8	27.9%
35	13	2.8	3.9	39.3%
40	14	2.75	4	45.5%

It can be clearly noticed that hybrid IEC+MVC have clear advantages over conventional MVC systems in terms of energy savings.

We also tested system at assorted locations in Saudi Arabia and results are presented in Figure 8. The percentage load handled by IEC varies depending on humidity at location. It can be seen in dry regions such as Riyadh, IEC can handle upto 85% load (sensible cooling) and overall 60% energy savings were calculated with IEC+MVC hybrid system. Even in high humid locations, 30-35% energy savings were noted.

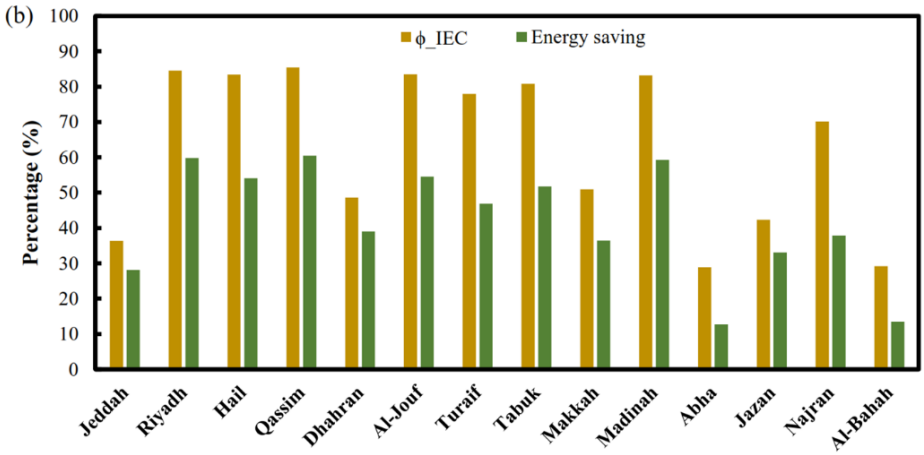

Figure 8 IEC+MVC hybrid testing at assorted locations in Saudi Arabia

5. PERFORMANCE MODEL DEVELOPMENT

Finally, we developed IEC effectiveness model presented in Equation 1. We also developed COP model for IEC and MVC systems as presented in Equation 2 & 3. COP of IEC is a linear function of the enthalpy change. These models will help for quick evaluation of performance of IEC and MVC systems.

$$\varepsilon = 0.416 - 5.81 \times 10^{-3} T_{oa} + 4.65 \times 10^{-3} \omega_{oa} + 1.42 \times 10^{-3} T_{ra} - 5.65 \times 10^{-3} \omega_{ra} + 7.49 \times 10^{-4} \frac{\dot{m}_{oa}}{\dot{m}_{ra}}$$

$$COP_{IEC} = 0.4892 \times \Delta h + 1.4254$$

$$COP_{MVC} = 0.0304 \times T_{sa} - 0.0761 \times T_{oa} + 4.992$$

Overall 5-8% error has been recorded in experimental data regression. The equations were developed using excel add-in for data regression.

6. CONCLUSION

A hybrid IEC+MVC cooler unit is designed, fabricated, and tested at assorted outdoor air conditions and performance improvements is evaluated. Major concluding remarks are:

- The improved IEC configuration can pre-cool the outdoor air to 18-20 ℃ at all outdoor air conditions by utilizing room return air as a working air.
- The MVC coil maintain 8-10C supply air temperature and around 10g/kg humidity.
- The hybrid IEC+MVC improved performance 30-45% as compared to conventional MVC units.
- The proposed model allows quick performance evaluation of IEC and MVC units.

7. ACKNOWLEDGEMENT

Author would like to thank to Northern Accelerator for grant NACCF - 232 (Shahzad) - Advance Cooling System for Data Centre and Space (AC4DCs) and KAUST cooling initiative (REP/1/3988-01-01).

Copyrights: Some of contents of this research also submitted to HEFAT2022 conference that might appear in proceedings. We reproduced here with authors permission.

8. REFERENCES

Chen, Q. *et al.* (2021) 'A hybrid indirect evaporative cooling-mechanical vapor compression process for energy-efficient air conditioning', *Energy Conversion and Management*, 248(September), p. 114798. doi: 10.1016/j.enconman.2021.114798.

Elizabeth O'Grady and Saarthak Narsipur (2018) *The AC Industry Conundrum: Cooling Is Warming the Planet, but Market Failures Are Preventing the AC Industry from Innovating*, *RMI*. Available at: https://rmi.org/ac-industry-conundrum/.

Global air conditioner stock, 1990-2050 – Charts – Data & Statistics - IEA (no date). Available at: https://www.iea.org/data-and-statistics/charts/global-air-conditioner-stock-1990-2050 (Accessed: 2 January 2022).

Jradi, M. and Riffat, S. (2014) 'Experimental and numerical investigation of a dew-point cooling system for thermal comfort in buildings', *Applied Energy*, 132, pp. 524–535. doi: 10.1016/j.apenergy.2014.07.040.

Kian Jon, C. *et al.* (2021) *Advances in Air Conditioning Technologies*, *Green Energy and Technology*. Springer Nature Singapore Pte Ltd. Available at: http://link.springer.com/10.1007/978-981-15-8477-0.

Lin, J., Shahzad, M. W., *et al.* (2021) 'A robust physics-based model framework of the dew point evaporative cooler: From fundamentals to applications', *Energy Conversion and Management*, 233, p. 113925. doi: 10.1016/j.enconman.2021.113925.

Lin, J., Thu, K., *et al.* (2021) 'Understanding the transient behavior of the dew point evaporative cooler from the first and second law of thermodynamics', *Energy Conversion and Management*, 244(July), p. 114471. doi: 10.1016/j.enconman.2021.114471.

Shahzad, M. W. *et al.* (2021) 'A spatiotemporal indirect evaporative cooler enabled by transiently interceding water mist', *Energy*, 217, p. 119352. doi: 10.1016/j.energy.2020.119352.

#6: Experimental and numerical investigation on thermal heterogeneity of a novel zoning air conditioner

Yunqin FAN[1], Mamoru HAMADA[1], Shogo TAMAKI[1], Makoto WADA[2]

[1] *Living environment systems laboratory, Mitsubishi Electric Corporation, Kamakura, Japan*
[2] *Shizuoka works, Mitsubishi Electric Corporation, Shizuoka, Japan*

Abstract: Thermal heterogeneity in indoor environment is not only critical for the thermal comfort with high indoor environment quality, but also contributes to the complexities of ZEB energy saving solutions. There is a growing consensus that variability in indoor conditions can be acceptable to occupants, reduce the energy consumption of buildings without compromising on the thermal comfort perception in occupied spaces. The contribution of this study is to create a novel indoor unit for the zoning air conditioning system and to reveal its thermal heterogeneity in an open-plan office in terms of temperature non-uniformities in the zoning thermal environment.

The novel zoning air conditioning system is consisted of multiple supply air openings mounted on zone border separately and one central return air opening. Those supply air (SA) openings, central return air (RA) opening and indoor unit are connected by ducts, the return air is directly conditioned through the central RA and supplied to the border SA openings. Hence in each zone, circulating airflow form from border to the centre, which reduce the air convection between neighbouring zones and improve the thermal efficiency.

In this study, the impact of various control strategies on zoning thermal environment are investigated by using computational fluid dynamics (CFD) numerical analysis which are validated through the full-scale field experiments. The CFD simulation prediction result is highly comparable to the experimental findings with an average temperature difference of approximately 0.4K.

This research aims to investigate and evaluate the thermal heterogeneity of the novel zoning air conditioning system under varier control strategies. Cases studies under different operating schedules are successful in providing the acceptable temperature difference between neighbouring zones through the CFD numerical analysis. The mechanisms of zoning thermal heterogeneity for circulating airflow application are evaluated, the finding shows that the maximum temperature difference between the neighbouring zone can reach up to 2.8K.

Keywords: Zoning air conditioning system, CFD, field measurement, thermal heterogeneity, temperature non-uniformity

1. INTRODUCTION

According to Japanese Ministry of Economy, greenhouse gas (GHG) emissions was obligatory to reduce by 26% from 2013 levels by 2030 and to promote the development of innovative technologies 2050, in the third step to achieve net zero GHG emissions by 2050 (Japan's Roadmap to "Beyond-Zero" Carbon). A total of 40%-50% primary energy and 30% CO_2 emissions used by buildings (Shibuya and Croxford 2016), in additionally, heating, ventilation, and air conditioning (HVAC) systems account for 18%-73% according to Ürge-Vorsatz and Cabeza (2015)'s investigation. Nearly/net Zero energy building (ZEB) remain as promising solution to the increasing indoor environmental problems. To reduce the energy consumption of buildings without compromising on the thermal comfort perception in occupied spaces has become a major concern, since people spent 90% of their time in indoor environment on average. The standard EN 15232 regulated the use of control systems including thermal zoning as a fundamental condition in the energy efficiency in buildings. Fan and ITO (2012), Cao (2014) also pointed out that thermal heterogeneity causse by air distributions is responsible for the indoor thermal comfort and air environmental quality, which significantly affect the health and productivity of occupants. Frontczak and Wargocki (2011) showed that thermal comfort was an Indoor Environment Quality (IEQ) measure that was directly affected by the performance of the Air-conditioning and Mechanical Ventilation system. In addition, Newsham and Brand et al (2009) conducted a survey in open-plan office building in USA and indicating that overall satisfaction with Indoor environmental quality (IEQ) was correlated with job satisfaction and satisfaction with management. Thermal heterogeneity in indoor environment is not only critical for the thermal comfort with high indoor environment quality, but also contributes to the complexities of ZEB energy saving solutions.

Karimipanah and Awbi (2002) indicated that impinging confluent jet (ICJ) effectively overcoming the thermal buoyancy effect, had slightly better thermal comfort and air quality compared with displacement system. Tian and Lin (2011) pointed out Stratum ventilation (SV) directly deliver the treated air to the occupied zone, was proposed to decrease the percentage dissatisfied caused by the draft from 34% to 8% compared with the constant air supply. Along with the optimization of control strategy, Fan and Toyoshima (2018) presented a novel indoor fan control algorithm, to generate intermittent jet flow by applying fan cycles on-off intermittently instead of compressor on–off cycling. Results find that intermittent air jet can reduce system energy consumption and create a satisfactory environment in occupied zone. In addition, Li and Wang (2022) developed the Interactive cascade ventilation (ICV) with a pulsating air supply also indicate that ICV reduce draught rate by 72% compared to the stratum ventilation. Assaad et al (2018) explored that the intermittent personalized ventilation (IPV) achieved 7.52% and 15.04% energy savings compared to a steady system and standalone chilled ceiling respectively under similar comfort conditions. Fan (2020) investigated thermal performance of oscillating air jet from a cassette type air conditioner and indicated the oscillating airflow provided uniform thermal environment with 0–35% draught rates on the face range also shorten the pre-cooling time by 20%.

The contribution of this study is to present a novel zoning air conditioning system and to reveal its thermal heterogeneity in an open-plan office in terms of temperature non-uniformities. A CFD validation study is conducted to compare with the full-scale experimental measurement based on selected control mode on the steady state condition. Cases studies under various operating schedules are successful in providing the acceptable temperature difference between neighbouring zones though the CFD numerical analysis.

2. METHODOLOGY

2.1. Experimental setups and testing apparatus

The experiment for the subject study of zoning air conditioning system took place in an open-plan office. This field test target area was divided as 6 air conditioning sub-zones, and total size of the demonstration space was 28 m(L) x13 m (W) x 2.7 m (H) as shown in Figure 1 .

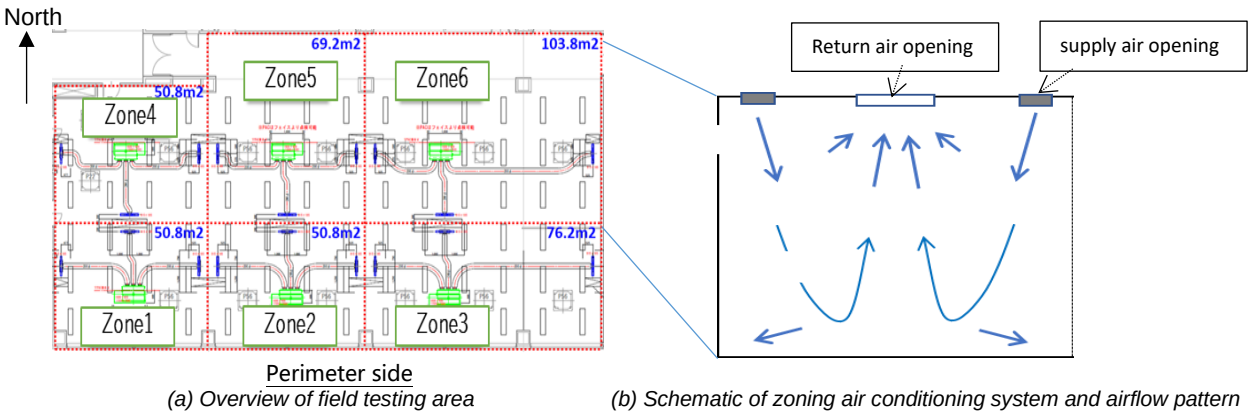

(a) Overview of field testing area *(b) Schematic of zoning air conditioning system and airflow pattern*

Figure 1 Experimental setup (a)Field testing area, (b) Airflow pattern of the zoning air conditioning system

Glass windows were installed on the exterior of the South-facing 2/3-height of perimeter wall. Sun shading cover whole windows to minimize solar radiation heat gain (Figure1 a). The indoor unit for the zoning air conditioning system is consisted of multiple supply air openings mounted on zone border separately and one central return air opening (Figure1 b). Those supply air (SA) openings, central return air (RA) opening and indoor unit are connected by ducts, the return air is directly conditioned through the RA opening and supplied to the border SA openings.

Thermocouple array were set throughout the office at the height of 0.1m, 0.6m, 2.1m and 2.6m above the ground level (Figure 2), supply air temperature and return air temperature of indoor units respectively to capture and log the data of indoor air temperature. The measurement range of sensors were within the operating conditions of the experiment with industry grade accuracy (Table 1). The data acquisition and storage system for the measurement instrument was created on a centralized workstation with direct LAN cabling from the data logger as well as supporting data-logging software that were also installed. Data from independent loggers were exported directly to the workstation. The collection of measured data was fixed at an interval of 1 minute.

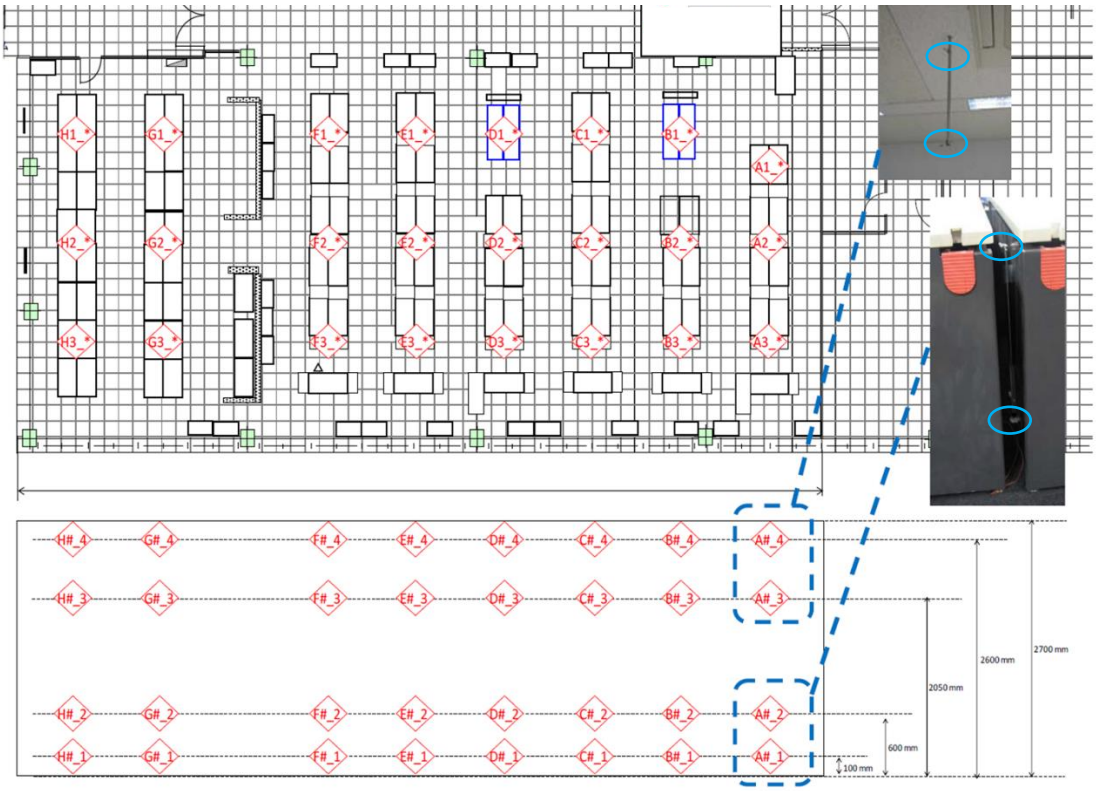

Figure 2 Thermocouple displaying in the target open-plan office

Table 1: Summary of instrument utilized in the experiment with the relevant specification

Measuring instruments	Measure parameters	Range	Accuracy
Type-T thermocouple	Air temperature [℃] Wall surface temperature [℃]	-270℃~370℃	±0.5℃
Heat flux sensor	Wall, ceiling, floor [W/m²]	(-10 ~ 10) x 10³ W/m²	± 5 %
Thermometer (T&D)	ıdoor, outdoor air temperature [℃] / Humidity [%] AC Supply air, Return air temperature [℃] / Humidity [%]	-20℃~70℃ 1%-100% RH at -40~75℃	±0.5℃ ±2%

2.2. Numerical model

In this study, FlowDesigner was applied as commercial CFD tool to construct the physical model, generate the mesh and calculate the thermal environment. Figure 3 displays the open-plan office model which was consist of 6 air conditioning zones respectively. In each zone, three supply air openings were mounted on zone border separately and one return air opening was in the centre. Field testing data included surface temperature of wall, floor and ceiling temperature were adopted as the boundary conditions.

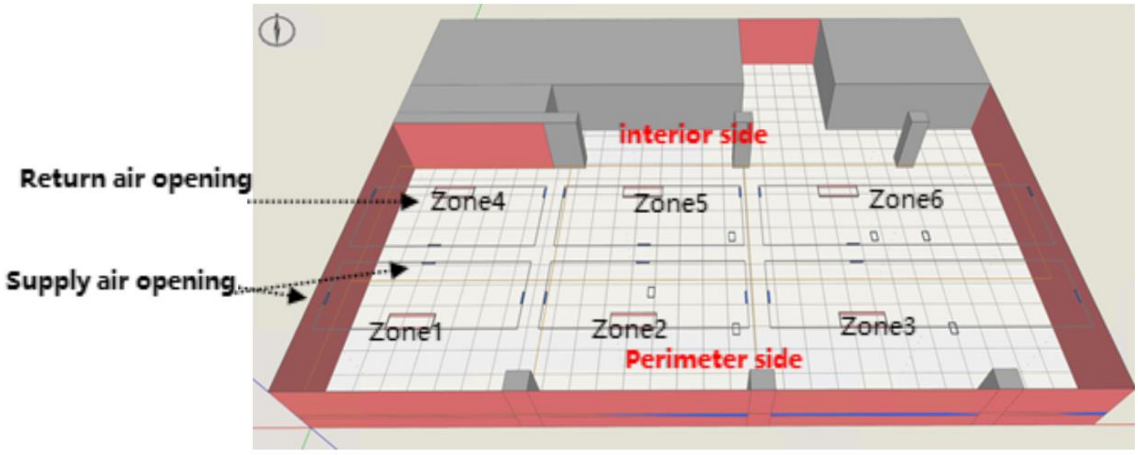

Figure 3 Computational geometry displaying

The airflow pattern in the target space was investigated using a RNG k-ε turbulence model with a generalized logarithmic type of wall function. Zhang and Chen (2007) pointed out the Reynolds averaged Navier-Stokes (RANS) modelling performs well in indoor environmental prediction. Ito K (2015) found that RANS model provides reasonable results with the least amount of computing time compared with large eddy simulation and direct numerical simulation. The RNG k-ε turbulence model was employed to simulate the indoor turbulent flow, based on literature review.

Equation 1: The transport equations for turbulent kinetic energy

$$\frac{\partial k}{\partial t}+\frac{\partial kU_j}{\partial x_j}=\frac{\partial}{\partial x_j}\left[\left(\nu+\frac{\nu_t}{\sigma_k}\right)\frac{\partial k}{\partial x_j}\right]+P_k+G_k-\varepsilon$$

Equation 2: The transport equations for dissipation rate

$$\frac{\partial \varepsilon}{\partial t}+\frac{\partial \varepsilon U_j}{\partial x_j}=\frac{\partial}{\partial x_j}\left[\left(\nu+\frac{\nu_t}{\sigma_\varepsilon}\right)\frac{\partial \varepsilon}{\partial x_j}\right]+\frac{\varepsilon}{k}\cdot\left[C_{\varepsilon 1}\cdot\left(P_k+C_{\varepsilon 3}G_k\right)-C_{\varepsilon_2}\cdot\varepsilon\right]$$

Equation 3: Production term P for turbulent kinetic energy

$$P_k=-\overline{u_i u_j}\frac{\partial U_j}{\partial x_j}\approx 2\nu_t S_{ij}S_{ij}$$

Equation 4: Buoyancy production term for turbulent kinetic energy

$$G_k=-\beta g_i\overline{u_i\theta}\approx\beta g_i\frac{\nu_t}{\sigma_\Theta}\frac{\partial\Theta}{\partial x_i}$$

Equation 5: The transport equation of the relevant parameters, e.g., temperature, humidity et al.

$$\frac{\partial\Phi}{\partial t}+\frac{\partial\overline{U}_i\Phi}{\partial x_i}=\frac{\partial}{\partial x_i}\cdot\left(\left(\Gamma+\frac{\mu_t}{\sigma_t}\right)\frac{\partial\Phi}{\partial x_j}\right)+S_\Phi$$

Where,

- $\overline{U}_i$ = ensemble averaged air velocity vector (m/s)
- Φ = target scalar
- Γ = molecular diffusion coefficient of the scalar in air (m/s)
- μ_t = turbulent viscosity (m²/s)
- σ_t = Turbulent Schmidt number
- S_Φ = source term

The SIMPLE (Semi-Implicit method for pressure linked equation) algorithm was applied to couple the pressure and velocity coupling terms. The standard interpolation scheme was adopted for pressure, and the second-order upwind scheme was used to discretize the convection and diffusion-convection terms in all governing equations. The buoyancy model which employed the Boussinesq approximation was integrated. The turbulent dissipation is resolved by the second-order upwind scheme to attain better numerical convergence. The conservation governing equations were discretized by a finite volume method. Convergence is obtained when residuals for x, y and z momentum, k, ε and continuity are stably below 1e-3.5 and the residual for energy is below 1e-6.

In this study, grid-independent check using 3 types (15 million 7milion 1million size) of grid design was carefully conducted prior to the final calculation, and the cell quality was precisely controlled. Boundary conditions of CFD numerical prediction are shown in Table2.

Table 2: Boundary condition of CFD simulation

Analysis Condition		Steady state
Turbulence model		RNG k-ε turbulent model
Total mesh number		7milion (structured)
Algorithm		SIMPLE
scheme		2nd order
AC	SA	Q_{inAC} = 19m³/min T_{inac}=18°C/21°C k_{in} = 3/2×(0.1U_{in})², ε_{in} = ($C_{\mu}^{3/4}k_{in}^{3/2}$)/$l_{in}$, l_{in} = 0.1L_0
	RA	Q_{inAC} = 19m³/min U_{out} = k_{out} = ε_{out} = link with SA
Wall surface		Velocity: generalized log law
Heat load	wall	0.32 W/m²k
	window	4.3 W/ m²K
	ceiling	4.04 W/ m²K
	floor	0.24 W/ m²K
	Infiltration	T_{out}=35°C Q_{inf}=0.001 m³/min
Heat recovery ventilation		T_{hev}=27.8°C Q_{hev}=16.15 m³/min

Where,

- Q_{inAC} = airflow rate through air conditioning system (m³/min)
- Q_{hev} = airflow rate through heat recovery ventilation (m³/min)
- T_{inac} = supply air temperature of AC(°C)
- T_{hev} = supply air temperature of Heat recovery ventilation (°C)
- Q_{inf} = airflow rate through Infiltration (m³/min)
- k_{in}/ k_{out} = turbulent kinetic energy (J/kg)
- ε_{in} /ε_{out} = turbulent dissipation rate (m²/s³)
- L_0 = turbulent length scale (m)

2.3. Modelling the zoning control system

Heterogeneous distribution of indoor environmental quality was known as significant impact on the human comfort and productivity. As described in Figure 4, to realize the thermal heterogeneity between the occupied and un-occupied zone, the control system model acts at two modes: cooling mode and fan mode. In fan mode, an air conditioner only operated the indoor fan blower to circulate air. The compressor was not operated in fan mode. While, in cooling mode, inverter compressor was adjusting automatically to cool the indoor air based on the evaporate temperature. Figure 4 presents the control system model flowchart that resumes the proposed algorithm. Table 3 describes the operating scenarios.

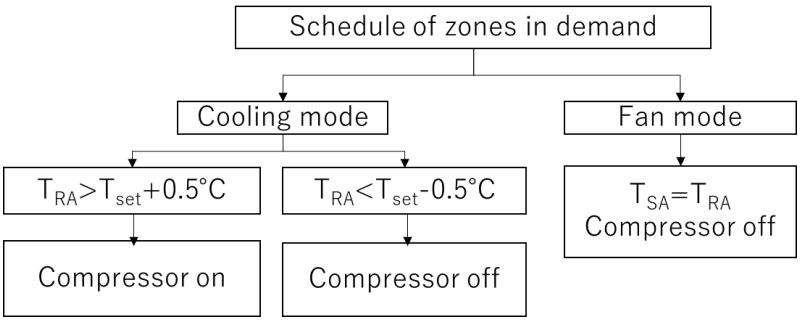

Figure 4 Flowchart of control system model

Where,

- T_{RA} = return air temperature (°C)
- T_{SA} = supply air temperature (°C)
- T_{set} = setting temperature (°C)

Table 3: Scenarios of operating strategies

Scenario	Cooling mode	fan mode
Case 1	Zone1、Zone2、Zone3	Zone4、Zone5、Zone6
Case 2	Zone4、Zone5、Zone6	Zone1、Zone2、Zone3
Case 3	Zone4、Zone6、Zone1、Zone3	Zone5、Zone2
Case 4	Zone4、Zone5、Zone1、Zone2	Zone6、Zone3
Case 5	Zone5、Zone6、Zone2、Zone3	Zone4、Zone1

3. RESULTS AND DISCUSSIONS

3.1. Validation of the CFD model

A CFD validation study was conducted to compare with the full-scale experimental measurement on the steady state condition. The control system model was set as case2 (interior side Zone4, Zone5, Zone6 for cooling and perimeter side Zone1, Zone2, Zone3 for air blowing), which was assigned as a boundary condition in the CFD simulation. We compared the vertical calculated air temperature profiles at 0.1m, 0.6m, 2.1m and 2.6m above the ground level at A, C, H, F sensor lines (Figure 5) with the corresponding experimental data.

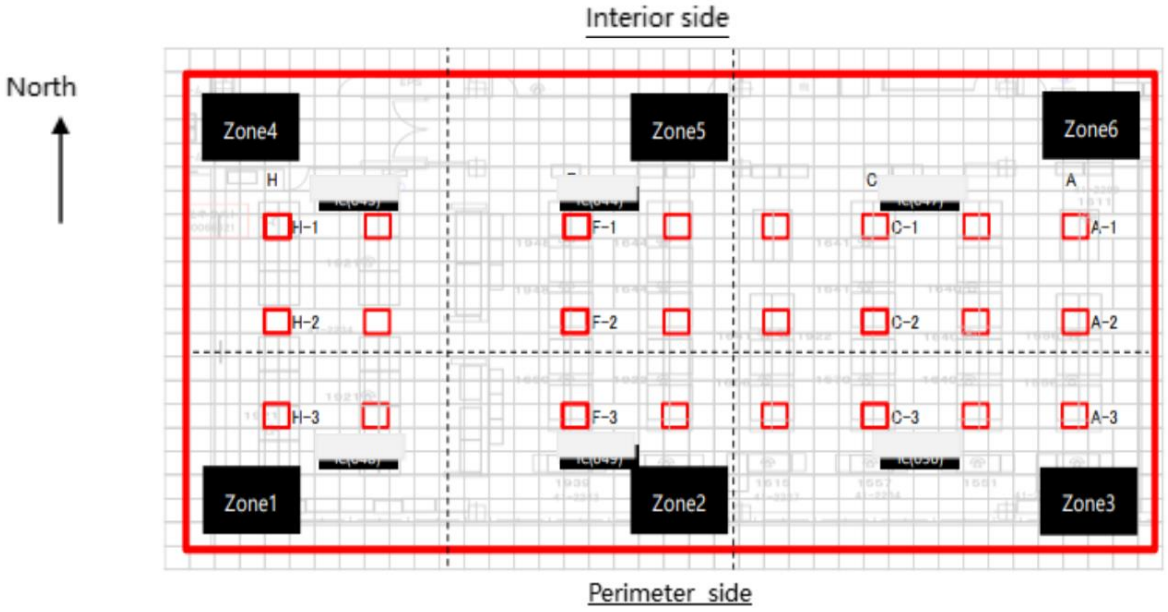

Figure 5 Layout of thermocouple placement

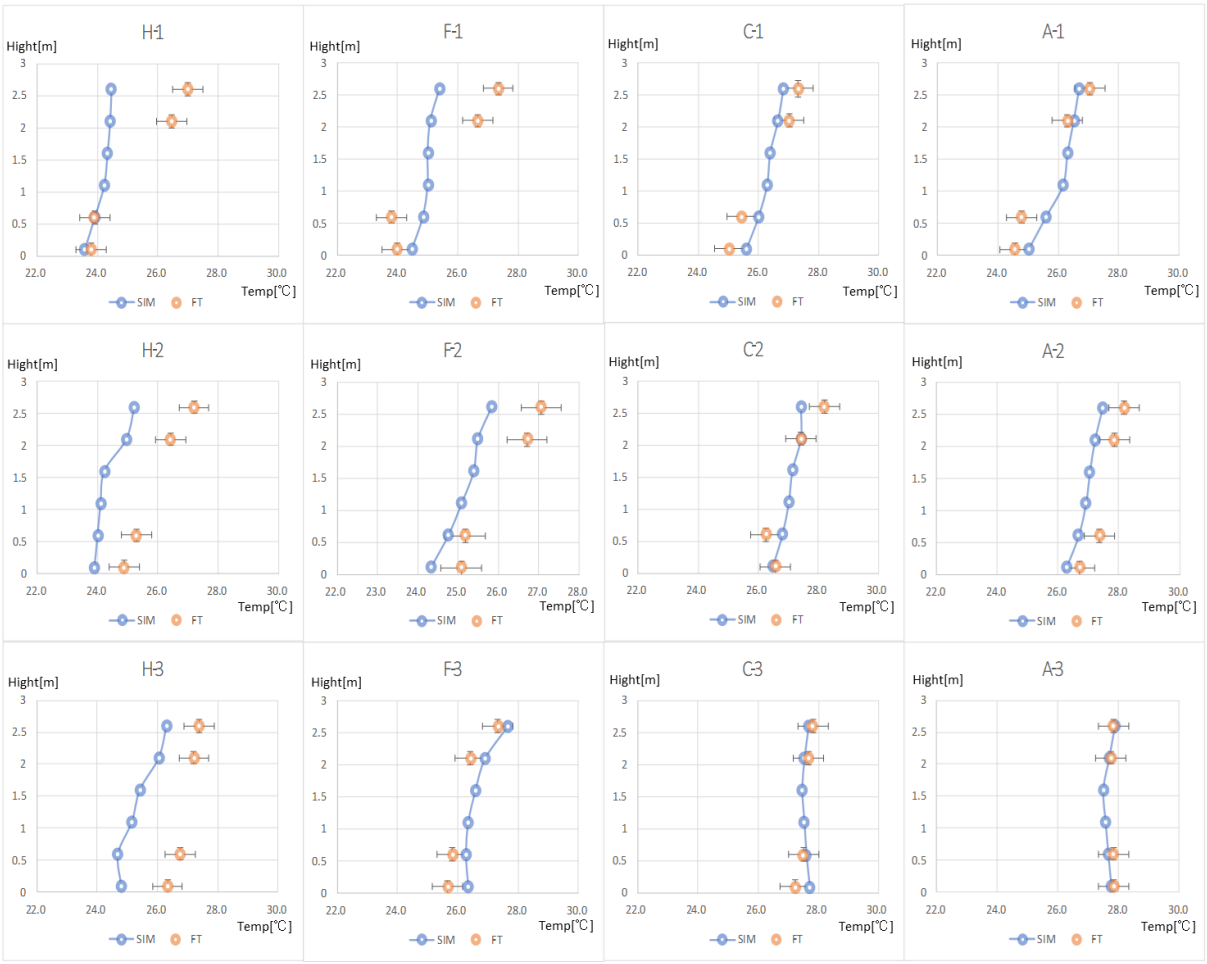

Figure 6 CFD validation of experiment (based on case 2)

Figure 6 shows the comparison between simulated and measured temperature profiles of each selected representative sensor lines among the demonstrate area. In general, the predicted temperature distribution profiles present similar variation patterns as those of the experimental measurements data. As illustrated in Figure 6, the result depicted that the air temperature of all sensor lines at the cooling zones (H-1,F-1,C-1,A-1) are around the setting temperature 26 degree Celsius (degC) with relatively larger about 2~3K vertical temperature distribution, while the air temperature at the air blowing zones (H-3,F-3,C-3,A-3) close to 28 degC with less than 0.5K vertical temperature distribution. In addition, as shown in figure 6, the simulated vertical temperature distribution is smaller than FT, especially close to the celling area in cooling zones.

Large temperature bias (about 1.5K) between the simulation prediction result and field measurement occurred in zone1 and Zone4, which indicates that thermal load penetrated from the west wall was underestimated in simulation prediction comparing to the filed measurement.

The simulated vertical temperature distribution is smaller which is cause by a constant 28 degC ceiling boundary condition (Neumann and Dirichlet boundary). Additionally, indoor air around the ceiling in the filed measurement is effect by the ceiling light and heat flux distribution around the ceiling, therefore, stagnant high temperature air realizes relatively lager vertical temperature difference.

Figure 7 shows the air temperature mapping by using field measurement testing array at 3 different view sections.

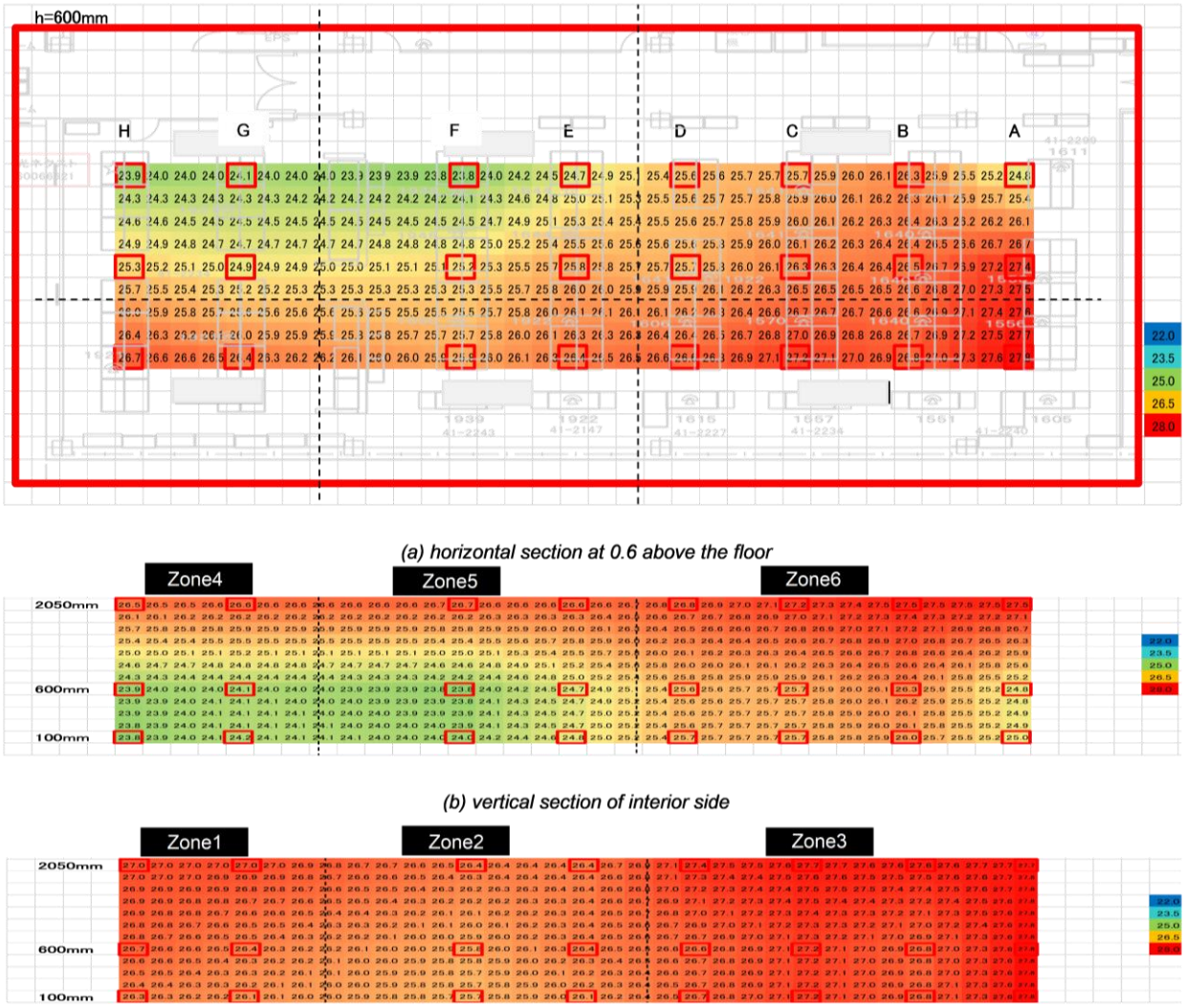

Figure 7 Air temperature mapping by using field measurement testing data (a)horizontal section at 0.6m above the floor (b)vertical section of interior side (c) vertical section of perimeter side (based on case 2)

Table 4 displays the differences between simulation prediction results and field measurement data for the average temperature of selected sensor lines. The simulation prediction result (SIM) has highly consistency to the filed measurement (FT) data with the average temperature bias of approximately 0.4K as shown in Table 4.

Table 4: Differences between simulation prediction and field measurement

	SIM [° C]	FT [° C]	FT-SIM [K]		SIM [° C]	FT [° C]	FT-SIM [K]		SIM [° C]	FT [° C]	FT-SIM [K]		SIM [° C]	FT [° C]	FT-SIM [K]
H1	24.2	25.3	1.1	F1	25.0	25.4	0.5	C1	26.3	26.2	-0.1	A1	26.0	25.9	-0.1
H2	24.4	26.0	1.5	F2	25.1	26.0	0.9	C2	27.1	27.1	0.1	A2	26.9	27.5	0.6
H3	25.4	26.9	1.5	F3	26.7	26.3	-0.4	C3	27.6	27.6	0.0	A3	27.7	27.8	0.1

3.2. Comparison of thermal zoning effect

The thermal heterogeneity between the sub-zone in the open-plan office are investigated by comparing varier operating schedules of cooling mode and fan mode. (Figure 8)

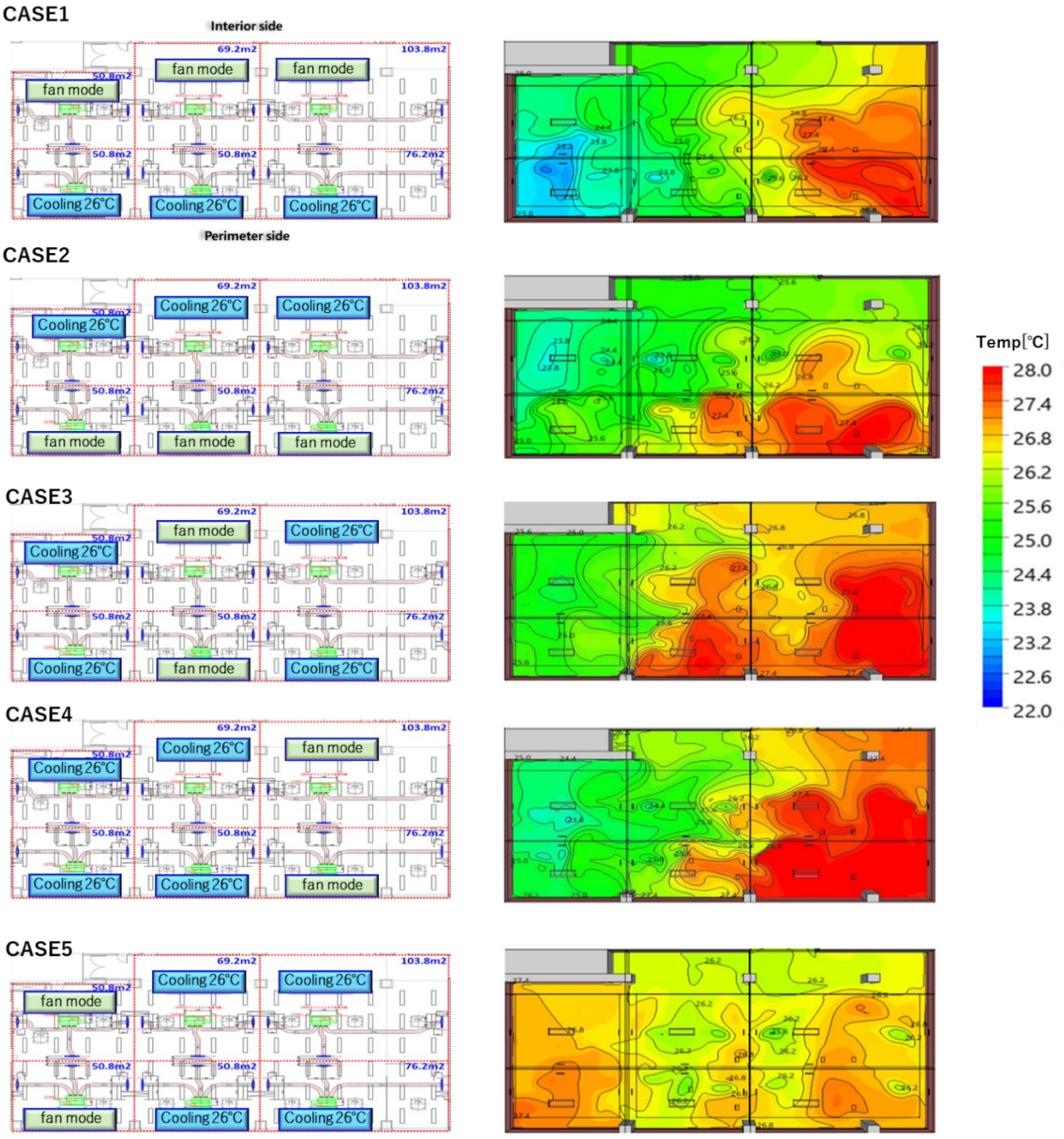

Figure 8 Temperature distribution among different scenarios of operating strategies (0.6m above floor level)

The mechanisms of zoning thermal heterogeneity for circulating airflow application are evaluated, as the average temperature difference between cooling zone (occupied zone) and air blowing zone (un-occupied zone) are summarized in Table5, the finding shows that the maximum temperature difference between the neighbouring zone can reach up to 2.8K. As illustrated in table 5, the maximum temperature differences by each case are underlined. It is believed that the thermal heterogeneity between the sub-zone in terms of temperature non-uniformities contributes to a reasonable energy saving without sacrificing indoor environment quality.

Table 5: Average temperature difference between cooling zone and air blowing zone

Scenario	Cooling mode - fan mode	average temperature difference [K]
Case 1	Zone1-Zone4	<u>0.8</u>
	Zone2-Zone5	0.7
	Zone3-Zone6	0.2
Case 2	Zone1-Zone4	1.3
	Zone2-Zone5	2.2
	Zone3-Zone6	<u>2.3</u>

Case 3	Zone1-Zone2	1.3
	Zone4-Zone5	1.9
	Zone2-Zone3	0.4
	Zone5-Zone6	0.6
Case 4	Zone2-Zone3	2.1
	Zone5-Zone6	1.4
	Zone1-Zone3	2.8
	Zone4-Zone6	1.9
Case 5	Zone1-Zone2	1.1
	Zone4-Zone5	0.7
	Zone1-Zone3	0.4
	Zone4-Zone6	0.6

4. CONCLUSION

In this study, thermal heterogeneity between the sub-zone in the open-plan office are investigated by comparing varier operating strategies of cooling mode and fan mode to simulate the occupied and un-occupied zones. This research aims to investigate and evaluate the thermal heterogeneity of the novel zoning air conditioning system. The investigation was divided in two main parts: (1) A CFD validation study was conducted to compare with the full-scale experimental measurement based on selected control mode on the steady state condition. (2) The CFD prediction results are then applied to investigate the thermal heterogeneity of the novel zoning air conditioning system under varier operating strategies.

The experiment investigated the heterometal performance of the novel zoning air conditioning system in an actual indoor environment. The temperature array was measured at different heights in the test cell. The results indicated that CFD numerical prediction are successful in providing the acceptable temperature difference between neighbouring zones compared with full-scale filed testing results.

The mechanisms of zoning thermal heterogeneity for circulating airflow application are evaluated, the finding shows that the maximum temperature difference between the neighbouring zone can reach up to 2.8K. It is observed that heterogeneity between the sub-zone can be varied according to operating strategies. Thermal heterogeneity trends displayed that thermal heterogeneity between neighbouring zone for all scenario corresponded with the optimization of control strategy the indoor environment.

5. REFERENCES

Japan's Roadmap to "Beyond-Zero" Carbon.
https://www.meti.go.jp/english/policy/energy_environment/global_warming/roadmap/

Shibuya T, Croxford B, 2016. The effect of climate change on office building energy consumption in Japan. *Energy and Buildings.* 117,1-11.

Ürge-Vorsatz D, Cabeza LF, Serrano S, Barreneche C, et al. 2015. Heating and cooling energy trends and drivers in buildings. *Renewable and sustainable energy reviews*, 41, 85-98.

Cao G, Awbi HB, Yao R, Fan YQ, et al. 2014. A review of the performance of different ventilation and airflow distribution systems in buildings. *Building and environment*, 73,171-186.

Fan YQ, Ito K, 2012. Energy consumption analysis intended for real office space with energy recovery ventilator by integrating BES and CFD approaches. *Building and Environment,* 52, 57-67.

Frontczak M and Wargocki P, 2011. Literature survey on how different factors influence human comfort in indoor environments. *Building and Environment*. 46, (4), 922-937.

Newsham G., Brand J., Donnelly C., Veitch J, et al. 2009. Linking indoor environment conditions to job satisfaction: a field study. *Build Research and Information*, 37 (2) 129-147.

Karimipanah T, Awbi HB, 2002. Theoretical and experimental investigation of impinging jet ventilation and comparison with wall displacement ventilation. *Building and Environment* 37(12),1329-1342.

Tian L, Lin Z, Wang Q, 2011. Experimental investigation of thermal and ventilation performances of stratum ventilation. *Building Environment* 46 (6),1309-1320.

Fan YQ, Toyashima M, Saito M, 2018. Energy conservation and thermal environment analysis of room air conditioner with intermittent supply airflow. *International Journal of Low-Carbon Technologies*.13 (1), 84-91.

Fan YQ. 2019.Performance evaluation of different air distraction system on thermal uniformity and energy saving: A Case study of a Japanese detached house. *Indoor and Built Environment.* 28 (2), 186-194.

Li H, Wang ZY, Li JC, Wang L, et al. 2022.Study on thermal comfort of interactive cascade ventilation based on body multi-node thermal demand. *Energy and buildings*, 273 (15),112404.

D. Al Assaad, K. Ghali, N. Ghaddar, 2018.Effectiveness of intermittent personalized ventilation assisting a chilled ceiling for enhanced thermal comfort and acceptable indoor air quality. *Building and Environment*. 144 (2), pp. 9-22.

Fan YQ. 2020. Mathematical and experimental analysis of the thermal effectiveness of an oscillating jet with side-to-side swing louvers in a cassette split type air conditioner. *Indoor and Built Environment.* 29(2), 240-254.

Zhang Z, Zhang W, Zhai ZJ, Chen Q, 2007.Evaluation of various turbulence models in predicting airflow and turbulence in enclosed environments by CFD: Part 2 —comparison with experimental data from literature. *HVAC & R Research*; 13(6):871-886.

Ito K, Inthavong K, Kurabuchi T, Ueda T, et al. 2015.CFD Benchmark Tests for Indoor Environmental Problems: Part 1 Isothermal/non-isothermal flow in 2D and 3D room model. *International Journal of Architectural Engineering Technology*. 2 (1), 01-22.

#9: Solar cooking experiments with a finned heat storage cooking pot

Ashmore MAWIRE[1], Oyirwoth P. ABEDIGAMBA[2], Atul A. SAGADE[3]

[1]North-West University, Material Science, Innovation and Modelling (MaSIM) Research Focus Area, Department of Physics, Private Bag X2046, Mmabatho 2745, Mahikeng, South Africa, email address: ashmore.mawire@nwu.ac.za
[2]Department of Physics, Kyambogo University, P.O Box 1, Kyambogo, Uganda, email address: oyigamba@kyu.ac.ug
[3]Departamento de Ingeniería Mecánica, Universidad de Tarapacá, Arica, Chile, email address: asagade@academicos.uta.cl

Abstract: Solar storage cooking pots can use stored heat for cooking during non-sunshine periods to enhance their usefulness during non-sunshine hours. A finned-type solar cooking storage pot is designed and evaluated experimentally. The storage cooking pot is designed with a finned storage cavity to store heat during sunshine cooking periods. Sunflower oil is used as the storage medium inside the cavity with a capacity of 4 litres. The solar cooking pot is heated up during solar cooking periods with a 1.8 m parabolic dish concentrator. During storage cooking periods, the pot is placed in a wonderbag insulating cooker to investigate the storage performance. Sunflower oil and water are used as the cooking loads. For both solar and storage cooking periods, 1 kg of water/sunflower oil is used as the load. The solar and storage cooking periods are both 3 hours. 1 kg of water is boiled in 30 minutes, and all the water in the pot is fully evaporated after around 2.5 hours. The maximum temperature achieved by sunflower oil in the storage cavity is about 134 °C during the solar cooking period using water as the load. For sunflower oil as the load during the solar cooking period, the maximum temperatures achieved in the pot and storage cavity are around 188 °C and 190 °C, respectively, at the end of 3 hours. For the storage cooking period, fresh water poured into the pot achieves a maximum temperature of around 85 °C in about 30 minutes. The load temperature is around 70 °C at the end of the storage cooking period. For the oil heating test, fresh sunflower oil in the pot achieves a maximum temperature of 150 °C in about 20 mins. The cooking temperature drops to around 120 °C at the end of the storage cooking period. Higher temperatures are achieved with sunflower oil as the load compared to water. The pot is also evaluated with chicken, and it can fry chicken during both solar and storage cooking periods.

Keywords: Experimental thermal performance; Finned storage cooking pot; Solar and storage cooking

1. INTRODUCTION

Solar cookers are devices that use energy from the sun to cook food. Unlike traditional biomass used in developing countries to cook food, solar cookers do not emit any greenhouse gases that are detrimental to both the environment and people (Aramesh et al., 2019). Greenhouse gas emissions particularly cause lung diseases and premature deaths in developing countries which could be reduced with the use of solar cookers (Sharma et al., 2023). The concentrating type of solar cookers offer the advantages of higher operating temperatures for multiple cooking processes such as baking, frying, and roasting and faster cooking times compared to other types of solar cookers such as panel and box type of solar cookers (Lentswe et al., 2021). Parabolic dish-concentrating solar cookers are more versatile and popular compared to parabolic trough solar cookers in terms of cooking temperature and speed (Lentswe et al., 2021). As a result of these faster cooking times and higher operating temperatures of parabolic dish cockers, recent work has focussed on improving their thermal performance (Kumar et al., 2018; Sagade et al., 2018; Ahmed et al., 2020; Mekonnen et al., 2020; Sagade et al., 2021). As with other types of solar cookers, parabolic dish solar cookers perform very poorly during cloudy periods and cannot be operated at night unless some type of thermal energy storage (TES) is employed. It is thus essential to incorporate TES for non-sunshine periods.

A significant amount of recent work has focussed on the incorporation of TES in the cooking vessel to improve the off-sunshine capabilities of parabolic dish solar cookers (Lecuona et al., 2013; Rekha & Sukchai, 2018; Bhave & Thakare, 2018; Mawire et al., 2020; Mawire et al., 2022). Even with the incorporation of TES, the heat transfer rate of solar cooking pots is still not optimized thus heat transfer fins can be used to improve heat transfer as carried out in limited recent endeavours (Harmin et al., 2008; Harmin et al., 2010; Bhave & Kale, 2020; Vengadesan & Senthil, 2021; Goyal & Eswaramoorthy, 2023). To further demonstrate heat transfer enhancement in a solar cooking storage pot, a novel storage pot is designed and experimentally evaluated using sunflower oil as the storage material in the storage cavity of the pot. The main novel aspect investigated is employing horizontal fins radially around the pot and vertical fins at the base of the pot to improve heat transfer in the storage cavity during solar cooking and storage off-sunshine cooking periods. The solar cooking tests are performed in sunny conditions for 3 hrs with the finned pot exposed to direct concentrated solar energy from a 1.8 m parabolic dish solar cooker. Off-sunshine tests are conducted by placing the finned storage cooking in a wonderbag insulating cooker (Mawire et al., 2020) for 3 hrs after the solar period. One litre of water and oil are used as the heating loads to evaluate the effectiveness of the finned storage cooking pot in separate tests. The objective of the study is to evaluate the performance of the finned storage cooking pot during solar and storage cooking periods to add to the limited body of knowledge of finned solar storage cooking pots.

2. EXPERIMENTAL SETUP AND METHOD

A schematic diagram showing the details and dimensions of the finned aluminium storage cooking pot is shown in Figure 1. The diameter of the base of the pot is 26 cm and its height is around 22 cm. The pot has three layers of horizontal fins fabricated around its height which are circularly distributed on the walls of the pot. A total of 20 horizontal fins are disturbed radially, and the radial spacing between each fin is around 4 cm. Each horizontal fin has a length of 1.5 cm and a thickness of 2 mm. The first horizontal layer is around 7 cm from the top of the pot, and the subsequent horizontal fin layers are located at 5 cm and 10 cm below the top layer. The pot lid has a hole at the top to place a K-type thermocouple to measure the temperature of the load during cooking experiments. There is also a screw cap hole on the cavity of the pot to allow thermal expansion during of the storage material. About 4 litres of sunflower is poured into the cavity of the storage cooking pot through the hole for the screw cap. Screw K-type thermocouples to measure the temperature distribution of sunflower oil in the storage cavity are placed at 7, 14 and, 21 cm, respectively from the top of the pot. All thermocouples measure the temperature with an accuracy of ±2.0 °C. The are also four vertical fins (thickness 2 mm, width 1.5 cm and length 22 cm) at the bottom on the interior walls of the pot. All the finned layers are enclosed in a fabricated cylindrical housing which creates the inner cooking walls of the storage cooking pot.

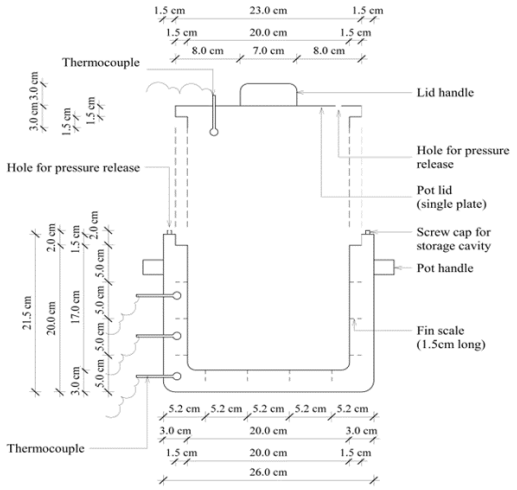

Figure 1 Schematic diagram of the finned storage cooking pot

A photograph of the finned solar storage cooking pot is shown in Figure 2 with a slivered test cooking pot. It is painted black to improve its absorption of solar radiation. The screw cap hole to pour sunflower oil for storing thermal energy in the cavity is also shown together with the hole in the lid to place a K-type thermocouple that measures the cooking load temperature. The three holes for screw K-type of thermocouples to measure the sunflower storage temperatures are also shown in the photograph. This finned storage cooking was placed on the focal region of a 1.8 m parabolic dish solar cooker during solar cooking experiments. For storage cooking experiments, the pot was placed in an insulated wonderbag slow cooker. A photograph of the parabolic dish solar cooker with a diameter of 1.8 m is shown in Figure 2. It is made up of 6 bolted triangular stainless-steel petals that are covered with high-quality aluminium foil strips of varied sizes (7 per petal). The parabolic dish solar cooker was purchased from Sunfire Solutions (Sunfire Solutions, 2023), and its assembly size is 80 x 72 x 10 cm with a focal point of around 70 mm. Its weight is 21 kg, and its rated power is around 1600 W. The solar cooker uses a manual tracking mechanism to focus solar energy onto the cooking pot during the solar cooking period. The solar cooker is a scaled-up version of our previously reported work (Mawire et al. 2020; Mawire et al., 2021). The insulated wonderbag slow cooker where the finned storage cooking pot is placed for off-sunshine storage cooking is shown in Figure 4, and more technical details of this wonderbag have been presented in our previous work (Mawire et al., 2020; Mawire et al., 2021).

Figure 2 A photograph of the finned storage cooking pot

Figure 3 A photograph of the 1.8 m parabolic dish solar cooker with a silvered cooking pot containing water as the test load

For the solar cooking period, the finned storage cooking pot is placed on the solar cooker, and sunlight is focused on the pot using the manual tracking mechanism. 1 kg of water or oil placed inside the pot is heated during the solar cooking period for 3 hrs (11:00-14:00 h). Temperature profiles inside the storage medium and the cooking pot are monitored by four K-type thermocouples connected to an Agilent 34970 A data-logger that is connected to a data-logging computer. The data-logging computer records the temperature at 10 s intervals. The solar radiation during the solar cooking period with a Kipp & Zonen CHP1 pyrheliometer that was placed on a Kipp & Zonen SOLYS 2 Solar tracker. Immediately after the solar cooking period, fresh samples of 1 kg of water or oil are poured into the storage cooking pot. The storage cooking pot is then placed inside the wonderbag and the top cover of the wonderbag is closed to start the storage cooking process. Data are also recorded every 10 s during the storage cooking period which begins just after 14:00 h and ends at 17:00 h (3 hrs in total).

Figure 4 A photograph of the insulated wonderbag slow cooker used for off-sunshine storage cooking periods. The finned storage cooking pot was placed inside the wonderbag solar cooker

3. RESULTS AND DISCUSSION

Figure 5 shows the experimental results of heating 1 kg of water in the finned cooking storage pot. The solar cooking period was from 11:00-14:00 h, while the storage cooking period was from 14:00-17:00 h immediately after the solar cooking period. The direct solar radiation was recorded from 11:00-17:00 h even though solar radiation was only utilised from 11:00 -14:00 h. Solar radiation values range from a maximum of around 950 W/m^2 attained between 11:00-13:00h to a minimum of around 570 W/m^2 at 17:00 h. Heated water boils within the first 30 mins of the solar cooking period (11:30 h), and the water in the pot is fully evaporated at around 13:20 h. Fresh water is added to the finned storage cooking pot which explains the very rapid temperature at around 13:20 h to the achieving boiling within 10 mins at 13:30 h. At 14:00 h, 1 kg of fresh water was added to the finned storage pot that was placed in the wonderbag, and it took 30 mins to achieve a maximum temperature of 85 °C which is sufficient to slow cook some foods requiring lower cooking temperatures like noodles and potatoes. The load temperature drops from the maximum value to become around 70 °C at the end of the storage cooking period. There is still enough thermal energy in the finned storage cooking pot to warm food at the end of the 3 hrs of storage cooking. The storage temperatures fluctuate slightly up and down due to manual tracking of the parabolic dish solar cooker. The middle and bottom sections of the storage cavity show higher temperatures than the top section since solar radiation to heat the pot is concentrated at the bottom, and the middle section shows the highest temperature of around 134 °C before adding fresh water at around 13:20 h. At the end of the solar cooking period, the highest storage temperature is around 125 °C. For the storage cooking period, the storage temperatures for the middle and top sections are almost identical to the profile of the heated water. The bottom shows slightly lower temperatures than the other sections during the storage cooking period. The ambient temperature ranges between 22-28 °C during the experimental testing period.

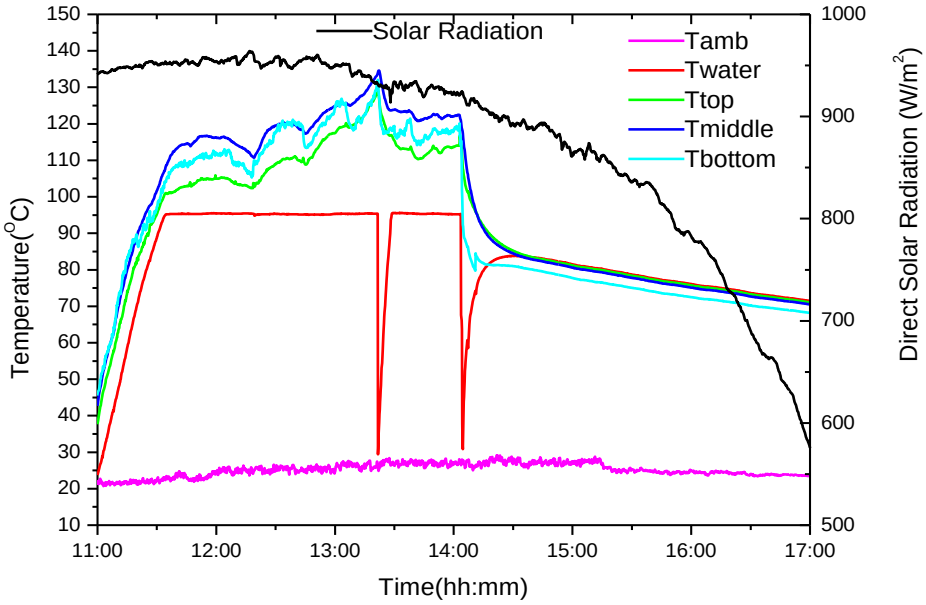

Figure 5 Experimental results for a 1 kg water heating test using a finned storage cooking pot

The temperature profiles in the finned storage cooking period for solar and storage cooking periods using 1 kg of sunflower oil as the load is shown in Figure 6. The solar radiation varies from a maximum of around 995 W/m^2 to a minimum of around 640 W/m^2 during the experimental period. As in the test with water, the solar radiation was only used during the first 3 hrs or so during the solar cooking period. Sunflower oil with a lower thermal mass compared to water shows a higher

maximum cooking temperature of around 188 °C at the end of the solar cooking period. The bottom and middle sections of the storage cavity show higher temperatures compared to the top sections like the water heating test. The maximum temperature attained in the storage cavity of around 190 °C is very close to that of the heating oil in the pot. These higher cooking and storage temperatures are high enough for most cooking processes such as frying, roasting, and baking. For the storage cooking period, the heated oil reaches a maximum temperature of around 150 °C within the first 25 mins of the storage cooking period. The temperature in the pot drops to around 120 °C at the end of the storage cooking period. The top storage temperature is noisy fluctuating up and down during the initial stages of storage cooking indicating some erratic behaviour of the measuring thermocouple at the top. The middle and bottom sections do not show such a behaviour, the thermal behaviour of the middle section is almost identical to the heated sunflower oil in the pot. The middle storage section shows higher temperature cooking period other storage sections for the whole duration of the storage cooking period. The bottom and top sections show identical thermal profiles from around 14:40 h to the end of the storage cooking period. The final middle section storage temperature is around 120 °C at the end of the storage cooking period whereas the top and bottom sections show temperatures close to 114 °C at the end of the storage period. These final storage cooking temperatures indicate that is possible to cook food after 17:00 h using the stored heat. The ambient temperature ranges between 28-34 °C during the experimental test period as a result of the slightly higher solar radiation conditions for the sunflower oil heating test compared to the water heating test.

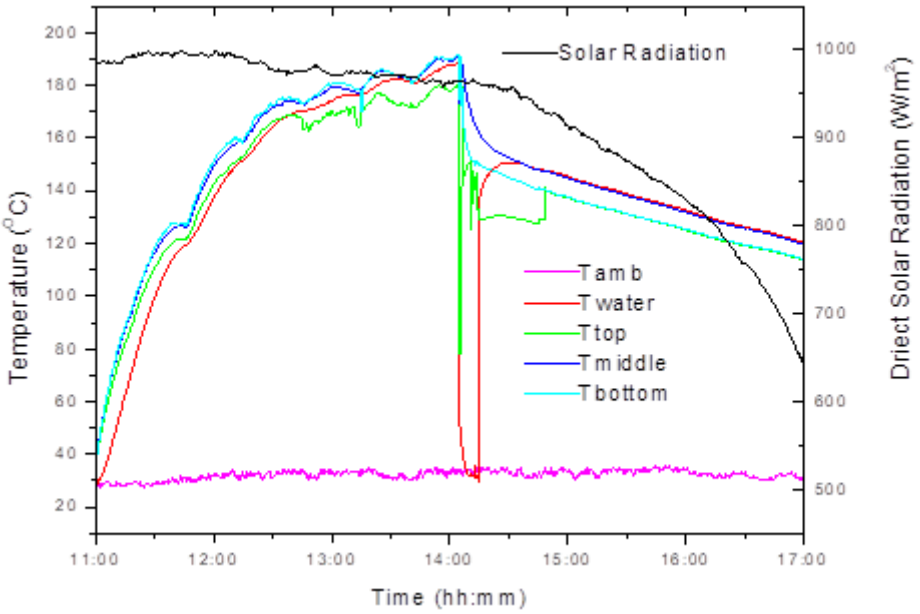

Figure 6 Experimental results for a 1 kg sunflower oil heating test using a finned storage cooking pot

Figure 7 shows photographs of chicken that was fried during the solar and storage cooking periods using the finned storage cooking pot. The chicken was fried in the bot cases, but the storage cooking case shows more crisper chicken pieces indicating better frying.

Figure 7 Photographs of fried chicken using (a) the parabolic dish solar cooker during the solar cooking period, and (b) the wonderbag slow cooker during the storage cooking period

4. CONCLUSION

An experimental evaluation of a finned storage cooking pot was presented for both solar and storage cooking periods. Sunflower oil was used as the storage medium inside the cavity with a capacity of 4 litres. The solar cooking pot was heated during solar cooking periods with a 1.8 m parabolic dish concentrator. During storage cooking periods, the pot was placed in a wonderbag insulating cooker to investigate the storage performance. Sunflower oil (1 kg) and water (1 kg) were used as the cooking loads. 1 kg of water was boiled in 30 minutes with all the water in the cooking pot being evaporated after around 2.5 hours of heating. Sunflower oil in the storage cavity achieved a maximum temperature of around 134 °C during the solar cooking period using water as the load. For sunflower oil as the load during the solar cooking period, the maximum temperatures achieved in the pot and storage cavity were around 188 °C and 190 °C, respectively, at the end of 3 hours. For the storage cooking period, fresh water poured into the pot achieved a maximum temperature of around 85 °C in about 30 minutes. The load temperature was round 70 °C at the end of the storage cooking period. For the oil heating test, fresh sunflower oil in the pot achieved a maximum temperature of 150 °C in about 20 mins. At the end of the storage cooking period, the cooking temperature dropped to around 120 °C. Higher temperatures were achieved with sunflower oil as the load compared to water. The pot was also evaluated with chicken, and it fried chicken during both solar and storage cooking periods.

5. ACKNOWLEDGEMENT

The authors would like to acknowledge the National Research Foundation (NRF) and SASOL for funding to carry out the work under the Sasol-NRF Research Grant (138608)-Development of low-cost standalone solar cookers with thermal energy storage for decentralized communities. We acknowledge that opinions, findings and conclusions or recommendations expressed in any publication generated by the NRF supported research are our own, and that the NRF accepts no liability whatsoever in this regard. The authors also acknowledge the Instruments Making Department of the North-West University for fabricating the experimental setup particularly, the head of the Department, Mr Thys Taljaard.

6. REFERENCES

Ahmed S.M.M., Rahmatullah M., Al-Amin M.R., Ahammed S., Ahmed F., Saleque A.M., Rahman M.A. (2020). Design, construction and testing of parabolic solar cooker for rural households and refugee camp. Solar Energy 205, 230-240.

Aramesh M., Ghalebani M., Kasaeian A., Zamani H., Lorenzini G., Mahian O., Wongwises S. (2019). A review of recent advances in solar cooking technology. Renewable Energy 140, 419-435.

Bhave A.G., Thakare K.A. (2018). Development of a solar thermal storage cum cooking device using salt hydrate. Solar Energy 171, 784-789.

Bhave A.G., Kale C.K. (2020). Development of a thermal storage type solar cooker for high temperature cooking using solar salt. Solar Energy Materials & Solar Cells 208, 110394.

Goyal R.K., Eswaramoorthy M. (2023). Thermal performance enhancement on a box-type solar cooker using a triangular fin over a conventional cooking pot. Solar Energy 258, 339-350.

Harmim A., Boukar M., Amar M. (2008). Experimental study of a double exposure solar cooker with finned cooking vessel. Solar Energy 82, 287-289.

Harmim A., Belhamel M., Boukar M., Amar M. (2010). Experimental investigation of a box-type solar cooker with a finned absorber plate. Energy 35, 3799-3082.

Kumar A., Shukla S.K., Kumar A., (2018). Heat loss analysis: An approach toward the revival of parabolic dish type solar cooker. International Journal of Green Energy.15, 96-105.

Lecuona A., Nogueira J.I., Ventas R., Rodríguez-Hidalgo M.., Legrand M. (2013). Solar cooker of the portable parabolic type incorporating heat storage based on PCM. Applied Energy 111, 1136-1146.

Lentswe, K., Mawire, A., Owusu, P., Shobo, A., 2021. A review of parabolic solar cookers with thermal energy storage. Heliyon 7 (10), e08226.

Mawire A., Lentswe K., Owusu P., Shobo A., Darkwa J., Calautit J., Mark Worall, M. (2020). Performance comparison of two solar cooking storage pots combined with wonderbag slow cookers for off-sunshine cooking. Solar Energy 208, 1166-1180.

Mawire A., Lentswe K., Owusu P. (2022). Performance of two solar cooking storage pots using parabolic dish solar concentrators during solar and storage cooking periods with different heating loads. Results in Engineering 13, 100336.08226.

Mekonnen B.A., Liyew K.W., Tigabu M.T. (2020). Solar cooking in Ethiopia: Experimental testing and performance evaluation of SK14 solar cooker. Case Studies in Thermal Engineering 22, 100766.

Rekha S.M.S., Sukchai S. (2018). Design of Phase Change Material Based Domestic Solar Cooking System for Both Indoor and Outdoor Cooking Applications. Journal of Solar Energy Engineering140, 041010.

Sagade A.A., Samdarshi, S.K., Panja P.S. (2018). Enabling rating of intermediate temperature solar cookers using different working fluids as test loads and its validation through a design change. Solar Energy 171, 354-365.

Sagade A.A., Samdarshi S.K., Sagade N.A., Panja P.S. (2021). Enabling open sun cooling method-based estimation of effective concentration factor/ratio for concentrating type solar cookers. Solar Energy 227, 568-576.

Sharma B., Sarkar S., Bau S. (2023). Understanding population exposure to size-segregated aerosol and associated trace elements during residential cooking in northeastern India: Implications for disease burden and health risk. Science of the Total Environment 875, 62539.

SunFire Solutions (2023). SunFire 18 Parabolic Solar Cooker: https://www.sunfire.co.za/product-category/solar-cooking/ website accessed 30 June 2023.

Vengadesan E., Senthil R. (2021). Experimental investigation of the thermal performance of a box typesolar cooker using a finned cooking vessel. Renewable Energy 171, 431-446.

#10: Design and techno-economic analysis for electric vehicle charging station

Hisham ALGHAMDI[1]

[1]*Electrical Engineering Department, College of Engineering, Najran University, Najran, Saudi Arabia*

Abstract: Fossil fuel utilization has increased considerably over the last few decades, which has increased global warming. Developing nations face multiple challenges, and it becomes necessary to grow their economy by satisfying sustainable development goals by establishing a green energy sector. Integrated Renewable Energy Systems (IRES) are a promising solution for conventional electricity generation. The transport sector is one of the main contributors to rising emissions worldwide. Introducing electric vehicles makes developing an environmentally friendly, alternative transport sector. Infrastructure development requires significant investment and the latest technologies, a major obstacle to adopting electric vehicles. This paper proposes a standalone Integrated renewable energy system-based charging station development for electric vehicles (EV). To design, optimize and techno-economic analysis of multiple combinations of standalone integrated renewable energy systems considered. The HOMER software performs the simulations of considered systems. The optimized, integrated scheme is obtained according to economic, technical and environmental parameters for EV charging stations. The present analysis demonstrates that the optimized, integrated system provides low-cost and reliable power to fulfil the charging capacity of estimated Electric Vehicles' energy demand with the proper renewable fractions. The optimal integrated system is obtained as the combination of Solar PV, Wind Energy system, Battery Energy Storage and Diesel Generator Units for Najran City's considered location in the Kingdom of Saudi Arabia. The optimal integrated energy system for electric vehicle charging stations positively achieves sustainable electricity generation in this study, which may be a suitable future model for electric vehicle charging projects.

Keywords: Electric Vehicle,Integrated Systems, Renewable Energy,Charging Station, Najran City

1. INTRODUCTION

Due to rising global populations and industrial expansion, energy consumption and requirements are anticipated to grow multiple times (Turkdogan, 2021). Many global leaders have agreed and signed agreements to find a permanent solution for reducing emissions and protecting the environment. Most nations, including developing countries, are shifting their power generation capacity from conventional fossil fuels toward alternative or renewable energy resources. Introducing renewable energy resources creates a new perspective focused on countering the growing energy demands by reducing conventional fossil fuel-based generation by improving renewable energy resources (Wogan et al., 2019). According to ECRA (2017), the expansion of the economy and the population in Saudi Arabia has increased the demand for electricity over the past few years. In Saudi Arabia, most power plants utilize heavy fuel oil, crude oil, diesel, and natural gas for electricity generation. Saudi Arabia's total electricity consumption is expected to rise in multiple dimensions, mostly depending on the country's oil production (EIA report, 2013). According to IEA reports (Luomi, 2021), electricity and heat production account for 40% of the Kingdom's total CO2 emissions. According to Ekren, O et al. (2000), "Transportation" accounts for 24% of global energy consumption and is one of the most heavily reliant on conventional energy sources. As indicated by (Wogan et al., 2019), Between 1996 and 2014, Saudi Arabia's total CO2 emissions rose from 200 million to 600 million tons, with transportation accounting for 20% of the increase. One option that can significantly reduce emissions from the transportation system is the use of electric vehicles (EVs). Dominguez et al.,2019) mentioned that electric vehicles produce zero carbon emissions directly. In the future, EVs can benefit the environment, air quality and public health.

Saudi Arabia is consistently improving the utilization of sustainable power for the country's growing energy utilization which primarily depends on fossil fuels and produces higher carbon emissions. Electric vehicles would be very helpful for reducing the climate-affecting carbon emissions produced by the transportation sector and improving public health. The nation has started numerous schemes and initiatives for encouraging alternative renewable resources and switching towards clean energy generation for future growing energy demand. As a result, the most effective approach towards the green energy-based environment is the introduction of Electric vehicles. Moreover, the development of an optimal charging system that can satisfy energy requirements and reduce negative environmental impacts by utilizing renewable energy resources to meet the demands of electric vehicles. However, enabling alternative resources for electricity generation and electric vehicle charging facilities can play an important role in achieving the environmental and economic goals of Saudi Vision 2030 (Elshurafa et al., 2020). The incorporation of the technologies mentioned earlier into the electric grid may result in a decrease in oil consumption and dependence. However, gradually introducing electric vehicles charging in plug-in mode into the conventional power grid may increase peak requirements. Therefore, the direct accommodation of EV charging requires the advancement of the electrical system to manage the additional demand for electric charging, which may create a huge financial and technical burden on the existing system. Electric vehicle penetration also results in transformer overloads and distribution feeder congestion. It is essential to minimize the impact of electric vehicle loading on a distribution network. Therefore, the best choice is a standalone renewable energy charging facility (Aljanad et al., 2015).

Implementing an integrated renewable energy system with energy storage support has been the subject of numerous studies in various aspects and different functioning modes, either standalone or grid-connected. Wang et al., 2020 proposed an integrated charging station design using multiple renewable resources and storage devices as backup being. The research problem of integrated charging stations can be resolved by multi-objective optimization schemes satisfying reliability and environmental profit. In contrast, many studies optimized the techno-economic parameters with a single-objective approach. A cost-benefit analysis of an electric vehicle charging system was performed by Abronzini et al. (2015). The study focused on sizing and maintaining the power flow control in a grid-connected multisource integrated EV charging system. The charging system worked better, and the output was at its best. Nizam et al. (2018) looked into the best size of Integrated renewable power for Electric Vehicle charging facilities in Indonesia. They found the integrated systems with the best results for optimization parameters for EV charging stations like initial capital cost, net present cost, and operating cost included in the economic analysis. Caruso et al. (2016) consider the two Integrated renewable source arrangements with storage systems. They studied the effects on the energy cost concerning the panel orientation and energy storage capacity and tried to lessen the impact of Electric Vehicle charging on university campuses. An optimized system design capable of adapting to changing requirements and minimizing electricity costs for electric vehicle charging was presented by Zhou et al. (2019). An innovative smart techno-economic operation of an aggregator-controlled EVCS in Egypt based on a hierarchical model was proposed by Peter M. et al. in 2023. Makeen P et al.2022 presented a higher stage of the model to balance the station's generated and used power and flatten the excess electricity delivered to the utility grid in the EVs' deterministic charging scheduling.

The charging process, efficiency, and longevity are major barriers to the widespread adoption of electric vehicles (EVs). Due to its high energy density and extended lifespan, lithium-ion batteries have replaced other types of batteries as the main power source for EVs. Khan MW et al. (2022) provide a multi-agents-based optimal energy scheduling technique at the microgrid level to reduce overall expenses associated with residential energy consumption, the charge of electric vehicles at a given market price, and degrading battery costs. At the microgrid level, Khan MW et al. (2022) provide a multi-agents-based optimal energy scheduling technique to reduce overall expenses associated with residential energy consumption, the charge of electric vehicles at a given market price, and degrading battery costs. In their study from 2022, Firouzjah KG. et al. (2022) assess the impact of electric vehicle charging practices in parking lots on distribution networks. The analysis is provided using a three-stage process. Based on a multivariate statistical distribution in the historical database, the first step is generating random data on electric vehicles in the parking lot. As the market share of electric

vehicles keeps expanding, the interdependencies between electric power networks and transportation systems are getting tighter. Therefore, it becomes crucial to improve the performance of the electricity and transportation systems as an integrated system (Thangaraj A. et al., 2022). According to Rahman MM et al. (2023), employing an electric car as an energy storage system (ESS) can supply electricity to the grid when needed. Numerous studies have compared the economic efficiency of various stationary ESSs; however, investigations on the viability of V2G technology in cold climes are few and far between. This work created a techno-economic model based on engineering principles to calculate the levelized cost of storage (LCOS) of V2G technology for frequency control and energy arbitrage.

The primary contribution of this study is that it connects supplementary systems, such as utility grids and batteries, with renewable energy sources, such as Solar Photovoltaic and wind energy systems for EVs charging. After reviewing and comparing many similar studies and assessing their shortcomings, more environmental analyses should be conducted. This study's main contribution is connecting the multiple domains of optimization sizing analysis in the present scenario. The study aims to investigate various Integrated renewable energy arrangements for electric vehicle charging near Najran City, Saudi Arabia. In order to identify the issue and investigate previous methods of charging electric vehicles, a comprehensive study was carried out. Utilizing HOMER (Hybrid Optimization of Multiple Energy Resources) software, a techno-economic analysis was conducted to meet the energy input and load profiles. In this paper, the optimal size of a hybrid system is first described, and then the economic and technical aspects of hybrid systems are examined. Additionally, a renewable fraction study and an environmental analysis were presented.

2. METHOD AND APPROACH OF OPTIMIZATION SCHEME

The operational plan for techno-financial measuring and demonstrating the Integrated sustainable power framework is discussed here. The HOMER software carried out the economic, technical and environmental analyses. A case study, its input data, and the equations that were considered concerning the HOMER software are presented in this section. The HOMER software is used to perform the entire scheme successively, beginning with the study location, load estimation, and evaluation of the available renewable resources. Hence, the Sizing and techno-economic analysis of different IRES systems are performed to obtain the best feasible arrangement within the context of a detailed methodological structure.

2.1 Study Location

The proposed study considered the outskirts of Najran city (18°50' 19.75" N, 44° 14'21.11" E) located in the Southern Region of Saudi Arabia to analyse the Integral design for EV charging as shown in Figure 1 (Location, 2023). The locations' overview, geographical arrangement, and coordinates are shown in Table 1. It is simple to get the charging station location because there is less population in this region, and this area has been chosen as the location for the charging stations.

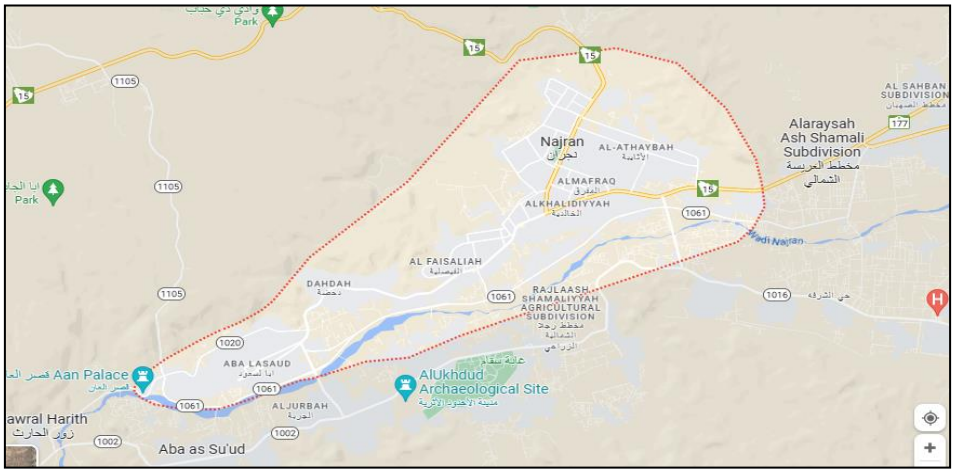

Figure 1 Considered location of Najran city

2.2 Meteorological Resources

The considered site of the present study has high renewable resources potential because of the sunny climate. Figure 2 depicts the lowest daily radiation (3.78 kWh/m2/day) in December, while May observed the highest daily radiation (6.38 kWh/m2/day). The wind speed at the considered location was recorded as maximum in July (6.54 m/s), whereas the lowest wind speed was observed in April (4.2 m/s), as shown in Figure 2(Najran Climate, 2023; NREL Database, 2022). The renewable resources data in HOMER software are interlinked with the NREL website (HOMER, 2022).

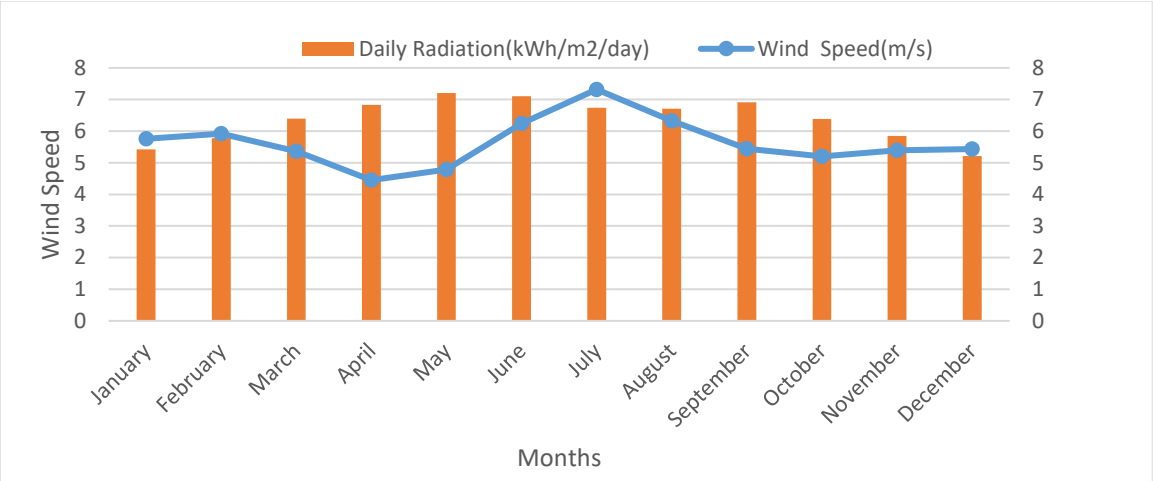

Figure 2 Wind Speed (m/s), and Solar Radiation (kWh/m^2/day) at Najran

Table 1: Profile of location chosen for the study

S.N	Name	Values
1	Location	Najran City
2	Region	Southern Region, Kingdom of Saudi Arabia
3	Wind Energy Average (m/s)	5.67 m/s
4	Solar Radiation (kWh/m2)	6.38 kWh/m2
5	Clearness Index	0.65
6	Temperature Average (°C)	23.53°C

3. LOAD ESTIMATION FOR ELECTRIC VEHICLE CHARGING STATION

The battery capacity and vehicle characteristics determine the required energy for EVs' charging. In this context, the electric vehicle chosen for this study has a battery storage capacity of 60 kWh, a range of 425 kilometres, and emits zero carbon (Kane,2022). It is assumed that the EV will be fully charged, and the maximum number of EVs will arrive in the morning and midday during working hours. Therefore, an average arrival of 2 Electric Vehicles per hour in peak duration (12 hours) and 1 Electric vehicle (6 hours) at the charging station is assumed. In contrast, the charging station operation hour is 6:00 AM to midnight. An additional consumption of 30kWh/day is also utilized for other daily basic charging station needs. Therefore, electricity demand for EV charging is estimated at 1470 kWh/day, with a 129.7 kW peak. The technical information regarding the load profile is summarized in Table 2. The charging station's daily load profiles are depicted in Figure 4.

Table 2: Summarized Load profile of Electric Vehicle Charging Station chosen for the study

SN	Parameter	Specific Values
1	Load Average (kWh/Day)	1470
2	Peak Load (kW)	129.98
3	Average Load (kW)	61.25
4	Load Factor Considered	0.47
5	Monthly Energy Average (kWh)	44100

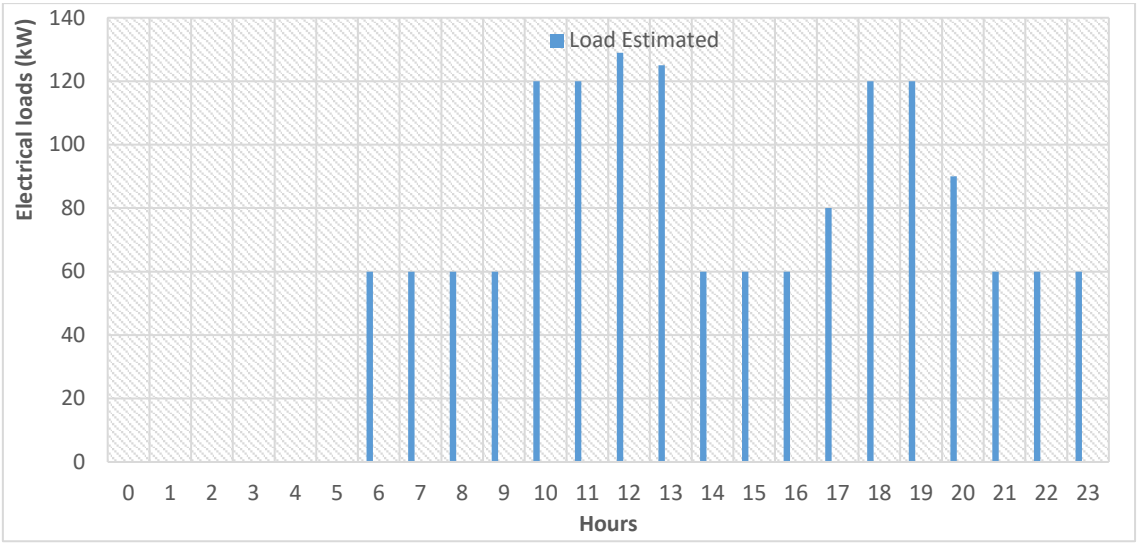

Figure 3 Hourly Load Profile for Electric Vehicle Charging Station

4. DESCRIPTION OF INTEGRETED SYSTEM COMPONETS

4.1. Solar photovoltaic system (SPV)

The power generation by SPV arrangement is given in terms of solar radiation, temperature and derating factor by Equation 1. The generic SPV panel with a rated capacity of 1kW is considered in this work (Taghavifar et al., 2021). The efficiency and derating factor of the SPV array is 18% and 88%. The optimization parameters connected with the chosen SPV system are introduced in Table 3.

Equation 1: power generation by SPV system

$$P_{pv} = P_n \times f_{dpv} \times (\frac{S_{gi}}{S_{std}}) \times \left(1 + \alpha_{tc}(\theta_{ct} - \theta_{cst})\right)$$

Where,
P_n= Nominal capacity in kW,
f_{dpv}=Derating factor
S_{gi}= Solar incident radiation
S_{std}= Standard temperature conditions,
θ_{ct}= Cell temperature °C,
α_{tc} = Temperature coefficient (%/°C) and
θ_{cst}= PV cell temperature at STC (25ºC).

4.2. Wind Energy System (WES)

Depending on wind speed, wind turbines, also known as wind energy systems, generate electrical energy from wind-generated mechanical energy. According to Taghavifar et al. (2021), the wind turbine's power at standard conditions can be calculated as equation 3. In this study, a rated capacity of a generic wind energy system of 10 kW is used for analysis with a Life span is 20 years.

Equation 3: Power Generation by Wind Energy System

$$P_{w_{STP}}(t) = \frac{1}{2}\rho A v_h^3(t) C_p(\lambda, \theta)$$

Where,

ρ = Air density
A = Area of the blades
v_h= speed of wind
Cp= Power coefficient
λ =Tip speed ration (TSR)
θ= Pitch angle

4.3. Converter System (CON)

A suitable converter framework is required for the power transformation between DC to AC supply, furthermore, giving interfacing among both AC and DC systems (Das, B.K,2021). Equation 4 provides a power change connection. The rated capacity of 5 kW is considered for IRES system with an efficiency of 90% and a lifespan of 15 years.

Equation 4: Power equation for the Converter System $$P_{con} = \frac{P_{peak}}{\eta_{con}}$$

Where,
P_{peak} = Peak rating
η_{con}= converter efficiency.

4.4. Battery Energy System (BES)

An Energy Storage System is an important choice for the standalone Integrated energy system, which overcomes the unreliability of renewable resources. This work chooses the Lead Acid Flooded type battery for system design. (Alotaibi et al, 2021). The rated parameters of the battery storage unit are, Nominal voltage is 12V, Maximum capacity is 83.4Ah, and Nominal capacity is 1kWh. The operation of battery storage is supervised and preserved by State of Charge (SC) and Depth of Discharge (DD). Both parameters are calculated by using the following formula given in Equations 5 & 6.

Equation 5: State of Charge for Battery Storage $$SC = SC(\tau_o) - \frac{1}{q(\int_{\tau_o}^{0} i(\tau)d\tau}$$

Equation 6: Depth of Charge for Battery Storage $$DD(\%) = 100[\frac{1}{q}\int_{\tau_o}^{0} i(\tau)d\tau]$$

Where,
SC =State of Charge
DD = Depth of Discharge
τ = Discharge time (h)
$i(\tau)$= Extracted capacity (Ah),
q = Maximum battery capacity (Ah)

Table 3: Optimization Specification of Components (Das, B.K,2021, WES, SPV, DGU, Converter details)

Components	Capital Cost	Replacement Cost	O&M Cost	Life Span
SPV	$550/kW	$450/kW	$10/kW-yr	25 years
WES	$10250/Unit	$8000/Unit	$200/Unit-yr	20 years
BES	$225/Unit	$180/Unit	$10/Unit	10 years
CON	$712/Unit	$712/Unit	$10 /year	15 years

5. INTEGRATED ENERGY SYSTEM DESIGN FOR EV CHARGING STATION

The designing of optimal integrated energy framework is executed by considering five most likely arrangement for estimated electric vehicle charging load. These systems are designated asS1:SPV/DGU, S2:SPV/WES/BES, S3:SPV/DGU/BES, S4:WES/DGU/BES, and S5:SPV/WES/BES/DGU. The typical integrated system S1 and S5 are demonstrated in Figure 4. The SPV module, Wind Energy Framework, and battery schemes are associated with the DC Bus, while the DG units, and load demand are associated with the AC bus in these arrangements. Through a bi-directional converter, the energy moves from the DC bus to the AC bus to charge the battery or meet the demand load.

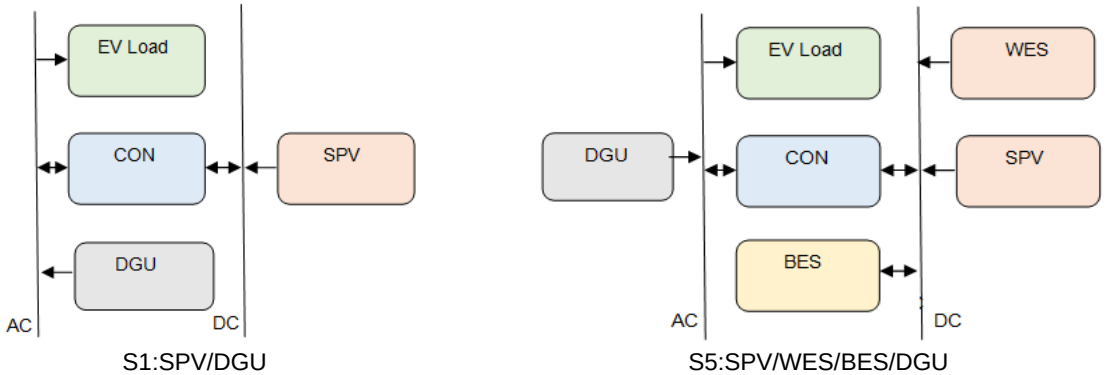

Figure 4 Schematic Arrangement of Integrated Energy System of Electric Vehicle charging

5.1 Simulation Results and Optimization Analysis

In this work, five different integrated arrangements are considered for analysis. Parameters of system design optimization and Analysis belong to the Economic, technical and Environmental domains like Net Present Cost, Cost of Energy, Capital cost, Fuel Cost, fuel consumption, Energy Generation, Unmet Load, Capacity Shortage Factor, Renewable Fraction, Life Cycle Emission (Samikannu,2019; Sriboon, 2016)As discussed and simulated, the load estimated for the EV charging

station at Najran City can meet by many renewable energy combinations. The simulation results are summarized in Tables 4, 5, and 6 according to economic, technical and environmental parameters.

Economic Analysis

The economic analysis of the chosen integrated system combinations using the HOMER software is discussed in this section and summarized in Table 4. The equations presented above serve as the foundation for the HOMER software's optimization of the critical economic factors, NPC and COE. For the lifetime investigation of the different economic costs, factors like the initial capital expense, Operation & maintenance, and upkeep (O&M) costs are also mentioned here, considering fuel cost and the salvage value as other important economic factors. Table 4 indicates the economic assessment of each scenario of the considered five integrated systems (S1 to S5). System S2 has the highest COE value (0.273 $/kWh), whereas the proposed S5 system has the lowest COE value (0.104 $/kWh). Systems S3 and S1 show proximity to S5 regarding COE; a similar pattern is followed for Net present Cost from S1 to S5. The initial cost of a project is one of the important factors for the investors; system S5 requires the minimum initial capital cost, while system S4 shows the maximum initial capital cost. The system S3 needed the lowest maintenance cost following the S4.Diesel-based generation is utilized for urgently required peak demand or abnormal conditions of renewable energy generation. The fuel cost reflects the support obtained by the DG system. System S3 gives the minimum fuel cost among all the DG-based integrated systems. System S5 and S4 reflect very closer values of the lowest fuel cost related to System S3. The proposed power framework was described by a high beginning cost yet low working and maintenance costs. Systems S4 and S2 show the maximum and minimum salvage. The system S3 and S5 shows closer values of salvage, lying among the highest and lowest values.

Table 4: Optimaleconomic parameters of consideredintegrated systems

System	COE($)	NPC($)	O&M($)	Initial Capital($)	Fuel Cost($)	Salvage($)
S1:SPV/DGU	0.193	l1,99,216	71,440	3,71,918	2,07,272	-6905
S2:SPV/WES/BES	0.273	l6,93,430	68,959	8,94,861	00.00	-69,817
S3:SPV/DGU/BES	0.124	7,67,499	33,545	3,79,039	91,440	-39,363
S4:WES/DGU/BES	0.251	l5,58,738	53,703	9,36,837	1,25,547	-2203
S5:SPV/WES/BES/DGU	0.104	6,45,116	107863	3,48,313	1,05,957	-41967

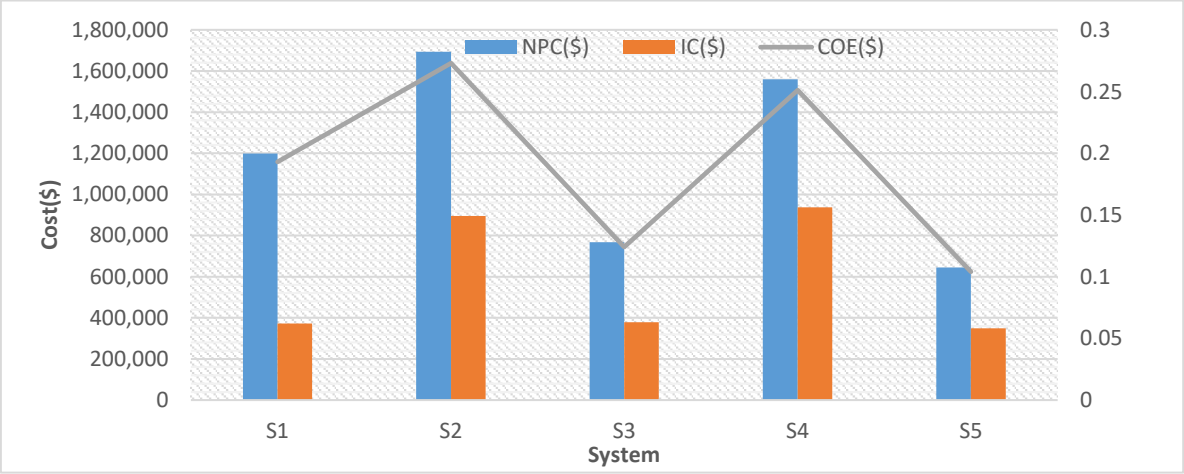

Figure 5 Economic ParametersRepresentationof Integrated Energy System for EV charging

Technical & Environmental Analysis

The optimal sizes of different systems in Table 5 were obtained from the HOMER simulation. The simulated systems are combinations of multiple arrangements of renewable components. System S2 shows the maximum number of SPV panels (722 kW), Battery storage sizes (989 Strings), including the highest size of converters (165kW). Another most increased size of renewable components wind energy system (55 Nos.) is shown by System S4 with the second largest size of the Battery storage sizes (761Strings), including the highest size of converters (165kW). System S1 is the only system having a single energy source (SPV) integrated with DG Unit as supplementary resources. This system simulation estimated the highest values of DG Units. The HOMER simulation estimated the system S5 as the most optimised size of renewable energy components consisting of 318kW SPV,2 Numbers of the wind energy system and the least amount of battery storage (270 strings). The DG and Converters are showing fair values in the system S5. System S3 shows closer values of the renewable energy system to system S5, except for the unavailability of a wind energy system. This system cannot generate energy at night; therefore, it requires high support from the DG unit and large battery storage.

Table 5: Optimal Configuration of system considered

System	SPV (kW))	WES (No)	DGU(kW)	BES (String)	Converter(kW)
S1:SPV/DGU	590	NA	150	NA	89
S2:SPV/WES/BES	722	2	NA	989	165
S3:SPV/DGU/BES	345	NA	50	355	100
S4:WES/DGU/BES	NA	55	50	761	105
S5:SPV/WES/BES/DGU	318	2	65	270	94

HOMER optimizes the system by cycle charging and Load flow dispatch strategies. Table 6 displays the technical parameters of the simulated scenarios. A good electrical generation system design symbolizes satisfying load demand without capacity shortage and null unmet load conditions. The minimum excess energy generation with the least fossil fuel consumption and a maximum renewable fraction is considered the best attribute of the best energy system designed. System S1 has a generation capacity of 14,67,826 kWh/year to supply the estimated load demand following the CC dispatch strategy. The S1 has a maximum share of excess energy (63%) and a minimum renewable fraction of 24% due to fuel consumption. The system S2 improves capacity generation by 13,19,589 kWh/year, a renewable fraction (100%), and excess energy generation (52.7%) compared to the previous system. System S2 shows the unmet load condition (224 kWh/year) and capacity shortage (0.10%), which are unsuitable for a hybrid energy system.

Similarly, using the LF dispatch strategy, system S3 reveals the 8,07,283 kWh/year energy generated. Despite of least excess energy generation (29%) and the highest renewable fraction (64.80) for less amount of fuel consumption, it shows unmet load (329 kWh/year) conditions and capacity shortage (0.10%) that do not make it to consider as suitable generating system. The average generation capacity of 9,62,586 kWh/year is obtained in system S4 using the CC dispatch strategy with higher excess power (40.8%). The hybrid generation system displays the top unmet load condition (329 kWh/year) and capacity shortage (0.11%) with 49.90% of the renewable fraction. The system has the flexibility to respond to load demands because it uses multiple primary energy sources. In addition, using wind energy systems increased the renewable energy generation capacity, as shown in system S5. All four apparatuses (SPV/WES/BES/DGU) are integrated to meet the same energy demand. The output of the system S5 is equivalent to 8,98,217 kWh/year. The SPV/WES/BES/DGU system increased the renewable capacity and fraction (60.20%). Moreover, this system does not show the unmet load condition (00.00 kWh/year) and capacity shortage (0.00%) and presents Integrated systems' strong power generation profiles. The diverse arrangement of power sources (Solar et al. Energy Systems, Batteries and Diesel generators) also satisfies the good level of the renewable fraction.

Table 6: Optimized economic parameters of system considered

System	Dispatch	Energy Generated (kWh/yr)	Energy Consumption (kWh/yr)	Excess Energy (kWh/yr)	UL (kWh/yr)	CS (%)	RF (%)	Fuel Cons. (L/yr)
S1:SPV/DGU	CC	14,67,826	5,36,550	9,22,570	00.0	00.0	23.6	1,37,682
S2:SPV/WES/BES	CC	13,19,589	5,36,326	6,95,922	224	0.10	100	NA
S3:SPV/DGU/BES	LF	8,07,283	5,36,397	2,33,653	153	0.10	64.8	60,740
S4:WES/DGU/BES	CC	9,62,586	5,36,221	3,96,756	329	0.11	49.9	83,396
S5:SPV/WES/BES/DGU	LF	8,09,217	5,36,550	2,45,634	00.0	00.0	60.2	70,383

Optimized System Architecture

The economic, technical, and environmental analyses for every integrated system considered for the design of an EV charging station are presented in this section. This examination is valuable since it financially determines how the costs of the innovations can be diminished to make them more reasonable and introduce them in integrated frameworks. Even though there was a compromise among cost and other framework factors, from the investors' point of view, the economic parameters are considered for primary selection; later on, techno-environmental properties are selected. From the financial analysis, all five systems are primarily compared for NPC and COE. In the case of both parameters system, S5 gives the best values among all the considered scenarios. System S3 competitively relates the S5 for NPC and COE, while other systems fall after both. Irrespective of different parameters, Initial cost, Fuel cost and operation and maintenance cost system S5 is found at the suitable position or winning position in terms of economic analysis from a cumulative and comprehensive approach. The above section presents all the integrated systems' technical and environmental analyses in Tables 5 & 6. The basic parameter for the technical analysis is energy generation without unmet load conditions and capacity shortage. The minimum excess energy generation and the least amount of component sizes are also desirable for a suitable technical energy system. The system S5 generated sufficient energy, 8,09,217kWh/year, without unmet load conditions (00.00kWh/year) and capacity shortage (0.00%). The SPV/WES/BES/DGU system increased the renewable capacity and fraction (60.20%). Moreover, this system shows strong power generation profiles among all the considered Integrated systems. The diverse arrangement of power sources (Solar PV, Wind Energy Systems, Batteries and Diesel generators) also satisfies the good level of a renewable fraction. Therefore, from techno–an economic perspective, systemS5 was established as a comparatively wining system to meet the energy demand of EV charging stations. The proposed system was eco-friendly and exhibited the best performance from an environmental perspective. Moreover, the integrated arrangement of Solar PV, Wind Energy Systems, Batteries and Diesel generators also satisfies the good level of renewable fraction (60.20%), the second highest among the five studied integrated combinations indicating its good

environmental performance and generating the lesser electricity excess. Also, it was the most productive framework for conveying the necessary capacity to deliver the required power to the load, framework adaptability and improving the environmental execution.

6. CONCLUSION

The primary topics of this paper are the feasibility and techno-economic analysis of hybrid energy systems with renewable energy technology for electric vehicle charging stations. It comprises a diesel generator, battery storage, PV and wind power sources, and more. A technical and economic plan is developed to discuss the proposed method using available resources. This plan identifies the initial requirements and conditions for the feasibility of PV/wind/diesel/battery hybrid energy system EV charging stations that lead to the growth of this hybrid system. The review investigated the necessary size space, the produced speculation cost and an appraisal of the foundation's natural and innovative person. This study examined the economics and technical viability of using multiple hybrid systems, with or without batteries, for electric vehicle charging stations in Saudi Arabia's southern region. The main outcomes are as follows: Under a combined dispatch (CC) strategy, the ideal outcome for an optimized system is a COE of 0.104/kWh, an operating cost of 107863, a total NPC of 6,45,116, and an initial capital of 3,48,313. The setup relates to the PV/DG/BT framework, which contains an318 kW PV, 20 kW WES, 65 kW DG and 270 strings batteries.

7. REFERENCES

Abronzini, U.; Attaianese, C.; D'Arpino, M.; Di Monaco, M.; Genovese, A.; Pede, G.; Tomasso, G 2015. Multi-source power converter system for EV charging station with integrated ESS. In Proceedings of the 2015 IEEE 1st International Forum on Research and Technologies for Society and Industry Leveraging a better tomorrow (RTSI), Torino, Italy,

Aljanad, A.; Mohamed, A.; Shareef, H. 2015. Impact study of plug-in electric vehicles on electric power distribution system. In Proceedings of the 2015 IEEE Student Conference on Research and Development (SCOReD), Kuala Lumpur, Malaysia, pp. 339–344

Alotaibi, M.A.; Eltamaly, A.M. 2021. A Smart Strategy for Sizing of Hybrid Renewable Energy System to Supply Remote Loads in Saudi Arabia. Energies, 14, 7069.

Annual Statistical Booklet for Electricity and Seawater Desalination Industries. 2019. Available online: www.ecra.gov.sa/en-us/ MediaCenter/doclib2/Pages/SubCategoryList.aspx?categoryID=5 (accessed on 22 February 2020).

Caruso, M.; Di Tommaso, A.O.; Imburgia, A.; Longo, M.; Miceli, R.; Romano, P.; Salvo, G.; Schettino, G.; Spataro, C.; Viola, F 2016. Economic Evaluation of PV System for EV Charging Stations: Comparison between matching Maximum Orientation and Storage System Employment. In Proceedings of the 5th International Conference on Renewable Energy Research and Applications (ICRERA), Birmingham, UK.

Das, B.K.; Alotaibi, M.A.; Das, P.; Islam, M.S.; Das, S.K.; Hossain, M.A 2021. Feasibility and techno-economic analysis of stand-alone and grid-connected PV/Wind/Diesel/Batt hybrid energy system: A case study. Energy Strat. Rev., 37, 100673.

Dominguez-Navarro, J.A.; Dufo-Lopez, R.; Yusta-Loyo, J.M.; Artal-Sevil, J.S.; Bernal-Agustin, J.L 2019. Design of an electric vehicle fastcharging station with integration of renewable energy and storage systems. Int. J. Electr. Power Energy Syst. 105, 46–58.

ECRA, 2017. Annual Statistical Booklet for Electricity and Seawater Desalination Industries. Electricity and Cogeneration Regulatory Authority, Riyadh.

Ekren, O.; Canbaz, C.H.; Guvel, C.B 2021. Sizing of a solar-wind hybrid electric vehicle charging station by using HOMER software. J. Clean. Prod., 279, 123615.

Elshurafa, A.M.; Peerbocus, N 2020. Electric vehicle deployment and carbon emissions in Saudi Arabia: A power system perspective. Electr. J., 33, 106774.

Firouzjah KG. 2022. Profit-based electric vehicle charging scheduling: comparison with different strategies and impact assessment on distribution networks. IntJ Electr Power Energy Syst,138,107977.DGU Details Available online:KIBOUR Diesel Generator Model SW10DES 950x530x700mm : Buy Online at Best Price in KSA - Souq is now Amazon.sa: Patio, Lawn & Garden

Converterdetails, Available online:Hybrid Inverter,48V 5500W 120V/230V Split Phase Solar Inverter with 80A MPPT Solar Charge Controller, for Off-Grid Areas, Home, Office : Buy Online at Best Price in KSA - Souq is now Amazon.sa: Automotive (Accessed on 27 March 2023).

Himabindu, N.; Hampannavar, S.; Deepa, B.; Swapna, M 2021. Analysis of microgrid integrated Photovoltaic (PV) Powered Electric Vehicle Charging Stations (EVCS) under different solar irradiation conditions in India: A way towards sustainable development and growth. Energy Rep. 7, 8534–8547

Kane, M. Compare Electric Cars: EV Range, Specs, Pricing & More. Available online:https://insideevs.com/reviews/344001 /compare-evs/ (accessed on 23 December 2022).

Khan MW, Wang J. 2022. Multi-agents based optimal energy scheduling technique for electric vehicles aggregator in microgrids. Int J Electr Power Energy Syst,134, 107346.Location of Najran City on Google map, Available online: https://goo.gl/maps/aEPSmeGQWAZFu29u7(Accessed on 24 March 2023).

Luomi, T.A.S.M.; Howarth, N. Measuring to Manage 2021.: The Case for Improving CO2 Monitoring and Reporting in Saudi Arabia; King Abdullah Petroleum Studies and Research Center: Riyadh, Saudi Arabia.

Makeen P, Ghali HA, Memon S2022. A review of various fast charging power and thermal protocols for electric vehicles represented by lithium-ion battery systems. Future Trans, 2(1),281–301.

NREL database National renewable energy laboratory data linked: https://admin.homerenergy.com/

Najran Climatic conditions, Available online: Najran climate: Temperature Najran& Weather By Month - Climate-Data.org(Accessed on 24 March 2023).

Nizam, M.; Wicaksono, F.X. R 2018. Design and Optimization of Solar, Wind, and Distributed Energy Resource (DER) Hybrid Power Plant for Electric Vehicle (EV) Charging Station in Rural Area. In Proceedings of the 2018 5th International Conference on Electric Vehicular Technology (ICEVT), Surakarta, Indonesia,

Peter M, Hani AG, Saim M, Fang D, 2023. Smart techno-economic operation of electric vehicle charging station in Egypt. Energy, 264,126151.

EIA report on Saudi Arabia. 2013. Available online: https://www.eia.gov/international/analysis/country/SAU (accessed on 22 March 2021).

Rahman MM, Eskinder G, Abayomi O, Amit K, 2023.The development of a techno-economic model for assessment of cost of energy storage for vehicle-to-grid applications in a cold climate Energy,262 (A), 125398

Sriboon, T.; Sangsritorn, S.; Tuohy, P.G.; Sharma, M.K.; Leeprechanon, N 2016. Simulation and analysis of renewable energy resource integration for electric vehicle charging stations in Thailand. In Proceedings of the 2016 International Conference on Cogeneration, Small Power Plants and District Energy (ICUE), Bangkok, Thailand.

Samikannu, R.; Kumar, V.S.; Diarra, B.; Ravi, R. 2019. Cost Optimization and Development of Hybrid Energy Systems for Rural Areas in Ethiopia with a Balance of Their Energy Need and Resources Availability (A Case Study-On Tuludimtu). J. Test Eval., 47, 4141–4160.

SPV details, Available online: Longi Solar Panels: The Complete Review - Solaris (solaris-shop.com)(Accessed on 25 March 2023).

Thangaraj A, Xavier SAE, Pandian R2022. Optimal coordinated operation scheduling for electric vehicle aggregator and charging stations in integrated electricity transportation system using hybrid technique. Sustain Cities Soc, 80, 103768.

Turkdogan, S 2021. Design and optimization of a solely renewable based hybrid energy system for residential electrical load and fuel cell electric vehicle. Eng.Sci. Technol. Int. J., 24, 397–404.

Taghavifar, H.; Zomorodian, Z.S 2021. Techno-economic viability of on grid micro-hybrid PV/wind/Gen system for an educational building in Iran. Renew. Sustain. Energy Rev., 143, 110877.

WES details, Available online: 10KW Horizontal Wind Turbine 96v 220v 380v10000w Wind Generator High Efficiency Free Power (96V, 10000W) (96v) : Buy Online at Best Price in KSA - Souq is now Amazon.sa: Patio, Lawn & Garden(Accessed on 26 March 2023).

Wogan, D.; Carey, E.; Cooke, D 2019. Policy Pathways to Meet Saudi Arabia's Contribution to the Paris Agreement; Climate Change Governance: Washington, DC, USA,

Pearre, N.S.; Kempton, W.; Guensler, R.L.; Elango, V.V 2011. Electric vehicles: How much range is required for a day's driving? Transp. Res. Part C Emerg. Technol., 19, 1171–1184.

Wang, D.; Locment, F.; Sechilariu, M 2020. Modelling, Simulation, and Management Strategy of an Electric Vehicle Charging Station Based on a DC Microgrid. Appl. Sci., 10, 2053.

Zhou, Y.; Kumar, R.; Tang, S 2019. Incentive-Based Distributed Scheduling of Electric Vehicle Charging Under Uncertainty. IEEE Trans. Power Syst., 34, 3–11.

#13: A multi-directional flap fin louver windcatcher

Experiment, numerical and field test investigations

Jiaxiang LI [1], John CALAUTIT [1], Carlos JIMENEZ-BESCOS [2]

[1] *Department of Architecture and Built Environment, University of Nottingham, UK*
[2] *School of Built and Natural Environment, University of Derby*

Abstract: Windcatchers, as natural ventilation apparatuses, are integrated into architectural designs to facilitate fresh air circulation, minimize energy expenditure, and occasionally, enhance indoor thermal comfort. However, their operational efficacy is often compromised by adverse meteorological conditions. To circumvent this limitation, researchers have been exploring the amalgamation of passive and low-energy heating, cooling, and dehumidification technologies. Despite these advancements, the majority of existing studies have not adequately addressed the impact of fluctuating wind conditions, which can potentially render windcatchers ineffective. In response to this gap, we propose an innovative windcatcher design equipped with flap fins at the inlet openings. This design ensures a consistent supply of fresh air, irrespective of wind direction, and facilitates the integration of passive and low-energy technologies. Drawing inspiration from the check valve mechanism, the flap fin design permits unidirectional wind flow into the windcatcher's supply channel, thereby ensuring that changes in wind direction do not affect the ventilation rate or the positioning of the supply and return channels. This, in turn, allows for the effective application of passive technologies. The flap fin, which operates via gravity and leverages wind pressure around the openings to regulate airflow, is lightweight. We developed an open wind tunnel and test room to experimentally assess the ventilation performance of the proposed windcatcher prototype. Additionally, a validated Computational Fluid Dynamics (CFD) model was constructed. Preliminary findings indicate that the ventilation performance of the flap fin louver windcatcher is independent of wind direction, as observed in both field tests and wind tunnel experiments. Furthermore, the use of lighter and longer fins appears to enhance the ventilation rate.

Keywords: buildings; CFD; natural ventilation, windcatcher, wind tunnel

1. INTRODUCTION

Researchers are exploring sustainable, cost-effective strategies to improve indoor thermal comfort and air quality while reducing air-conditioner use (Jomehzadeh, Hussen et al. 2020, Tien, Wei et al. 2022). This becomes even more crucial considering the COVID-19 pandemic highlighted the importance of indoor air quality and ventilation in mitigating the spread of airborne diseases (Yong and Calautit 2023). The construction and built environment sectors account for over 40% of global carbon emissions (He, Yang et al. 2014), with more than half of building energy consumption coming from HVAC systems (Pérez-Lombard, Ortiz et al. 2008, Liu, Justo Alonso et al. 2022). Natural ventilation, which uses wind and thermal buoyancy to supply fresh air and remove heat, moisture, and pollutants, is a promising solution (Ghalam, Farrokhzad et al. 2021). However, it often fails to provide adequate thermal comfort in extremely hot and cold climates, especially in hot and humid climates where high outdoor temperatures and humidity can cause discomfort (Bay, Martinez-Molina et al. 2022, Nasrollahi and Ghobadi 2022).

Windcatcher is a rooftop natural ventilation device to force natural ventilation by the wind from higher levels (Sangdeh and Nasrollahi 2022, Jomehzadeh, Nejat et al., 2017). Some traditional windcatchers only have one opening (Montazeri and Azizian 2008), but displacement ventilation with multiple-opening windcatchers is more efficient (Pan, Liu et al. 2019, Nejat, Hussen et al. 2020). The positive pressure at the windward side of the windcatcher drives the supply airflow. While the negative pressure at the leeward side and sides of the windcatcher extracts the polluted air out of the building (Jomehzadeh, Hussen et al. 2020, Nejat, Calautit et al. 2016a). With the integration of passive technologies, the thermal performance can be enhanced such as evaporative cooling in arid regions (Noroozi and Veneris 2018, Ghoulem, El Moueddeb et al. 2020, Jafari and Kalantar 2022), heat transfer coil (Pelletier and Calautit 2022) and earth-air heat exchanger (EAHE) (Gilvaei, Poshtiri et al. 2022). Like any natural ventilation device, windcatchers' ventilation and thermal performance largely depend on the outdoor wind and climate conditions. In the field, the wind speed and direction frequently change, unlike the stable wind conditions simulated in wind tunnels and steady-state CFD in many windcatcher studies (Jiang and Chen 2002, Nejat, Calautit et al. 2016b). The wind direction will not always be the same as the design wind direction, and hence, it must be considered when evaluating the ventilation technology. In a multi-opening/sided windcatcher, the supply and return airflow direction within its channels will vary as the wind direction changes and could influence the ventilation rate and the performance of the integrated low-energy or passive technologies (Kumar, Bardhan et al. 2022, Sangdeh and Nasrollahi 2022).

As an example, as shown in Figure 1, the efficiency of passive cooling in the conventional four-sided windcatcher will be impacted by changing wind directions or even working against it. For example, adding the cooling device in the windcatcher's windward side channel would be beneficial when the wind flow is from the same side. However, once the wind direction changes, the cooling devices (now in the leeward channel) may not be as effective, or if the wind is in the opposite direction, it will cool the exhaust air instead. Adding the cooling device in all channels will cool the supply airflow but also the exhaust airflow, which will lead to wastage. The same issue would also occur in applying the passive technology in the windcatcher with a separate inlet and outlet. For example, using a windcatcher with evaporative cooling in regions with limited water resources should consider the potential wastage of water caused by inefficient operation (Calautit, Tien et al. 2020).

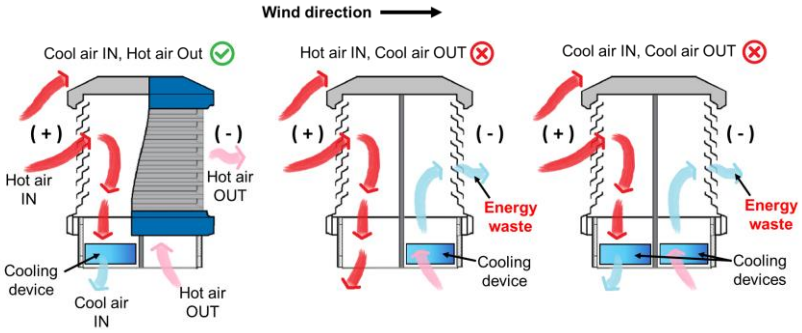

Figure 1 Conventional windcatcher with the cooling device in the windward channel, leeward channel and both channels (from left to right).

Currently, the research about integrating windcatchers and passive cooling or heating technologies to satisfy the thermal comfort, fresh air requirements and low carbon emissions for the building sector is insufficient, and an appropriate windcatcher needs to be developed (Li, Calautit et al. 2022). The impact of the changing wind direction was not always taken into account in previous research (Nejat, Salim Ferwati et al. 2021). The ventilation performance of the traditional windcatcher would also be decreased by a slight change in the wind direction, and the effectiveness of passive technologies would also be affected (Mahon, Friedrich et al. 2022, Li, Calautit et al. 2023).

To address this issue, this research aims to develop and evaluate a novel dual-channel windcatcher with inlet openings equipped with flap fins and central stack exhaust for passive or low-energy technology integration with several functions; (1) the airflow direction and ventilation rate inside the system are fixed regardless of wind direction, (2) the supply and return airflow channels are adjacent to allow heat transfer between them for example, for heat recovery, (3) the polluted

air from the outlet would not contaminate the supply air, and (4) there will be no air-short circuiting. This will be achieved by the following objectives; (1) development of a scaled windcatcher prototype and evaluation of the ventilation performance in an open wind tunnel and field test experiment, (2) development of a CFD model and validation of the model with the experiment results, and (3) parametric analysis of the proposed windcatcher design including thickness, length and layout of the flap fins.

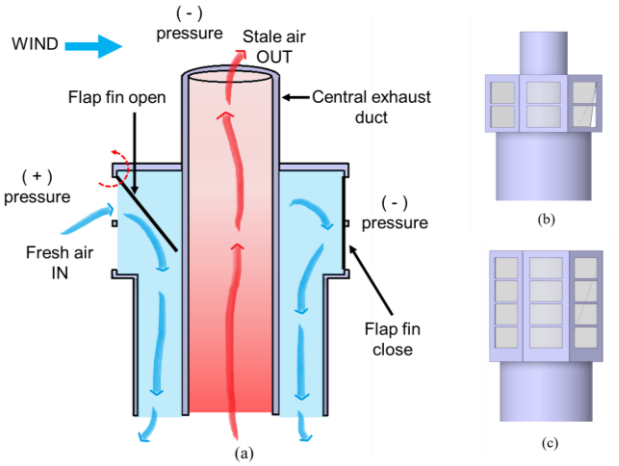

Figure 2 Flap fin louver windcatcher concept (a) airflow diagram (b) single height model (c) double height model

The flap fin louver windcatcher, as shown in Figure 2, was designed based on the conventional 8-side windcatcher, and the flap fins were applied at each opening to control the airflow supply based on the check valve strategy. A circular tube duct located centrally extracts the stale air out to the top of the windcatcher. The lightweight fins, which allow for a self-opening and -closing mechanism, use the pressure differential at the openings to control the opening and closing of the flap fin automatically. As the wind blows from the windward side, the flap fin on this side will open, allowing the air to enter the windcatcher into the room below. If the pressure outside of the openings were lower than the inside, the pressure difference would force the flap fins to be attached to the windcatcher wall and block the opening, which is slightly smaller than the flap fin, to avoid air leaving the windcatcher. This effectively shuts the flap fins on the leeward side openings of the windcatcher, which are in the negative pressure region. The dynamic process of opening and closing the flap fins at different sides works similarly to a wind scoop without the rotary components, which always have the opening facing the wind. The flap fin design creates a low-cost alternative to the rotary wind scoop and eliminates the rotating mechanism. In the proposed design, the air would always enter the supply channel from the windward side openings without leaving the windcatcher channel on the leeward side as the flap fins will be closed. The stale air is extracted via the central return duct, which works as a chimney and prevents the mixing of the supply and exhaust air channels. With the combination of chimney and flap fin design, the airflow supply and exhaust direction inside the natural ventilation system will be fixed regardless of the wind direction.

2. METHODOLOGY

The wind tunnel tests, CFD simulations and field tests of the flap fin louver windcatcher were explored in this research.

2.1. Experiment test

The experiment was carried out with a scaled test room with a size of 1.2m cube using a simplified wind tunnel and the details of the experiment measurement points were presented in Figure 3. In the experiment section, the speeds of airflow at different points were measured and the data were recorded to validate the simulation model. In the evaluation of the rotary scoop windcatcher and flap fin louver windcatcher, the wind speed measurement points were identical. The wind measurement points and the wind speeds measured from the experiment and CFD simulation at these three different points in the test room were measured for the CFD model validation, as shown in Figure 3.

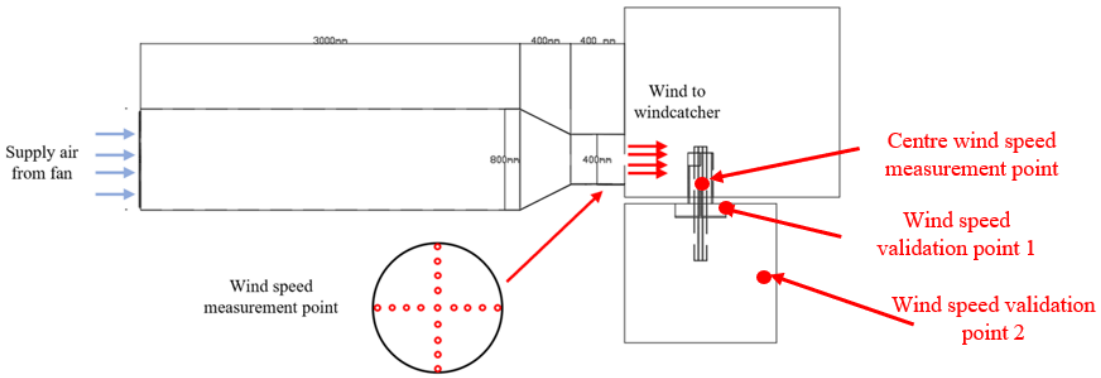

Figure 3 Open wind tunnel specification and windcatcher setup

2.2. CFD simulation

In this research, the Computational Fluid Dynamic (CFD) simulation of the proposed windcatcher was investigated by the commercial software FLUENT. The mass and momentum equations are solved for the airflow in this model. The energy governing equation was not applied as the heat transfer was not investigated in the present study to simplify the CFD simulation process. The Reynolds-averaged Navier-Stokes (RANS) model was employed with the k-epsilon, re-normalization group (RNG), turbulence model, which is capable of performing accurate simulations of airflow in similar natural ventilation systems, as highlighted in the literature including (Blocken, van Hooff et al. 2011). The SIMPLE algorithm was applied in the simulations (Kobayashi, Sandberg et al. 2022). In turbulent airflow simulations, the semi-implicit method is typically used, and a solver using pressure-linked equations segregated pressure-based algorithm is applied due to its robustness and computational efficiency. A second-order upwind scheme is employed to discretize all the transport equations. The governing equations for the mass (eqn.1), momentum (eqn.2), and k and epsilon (eqn.3 and 4) (Hughes, Calautit et al. 2012) are detailed below:

Equation 1: Governing equations for the mass

$$\frac{\partial \rho}{\partial t} + \nabla \times (\rho u) = 0$$

Equation 2: Governing equations for the momentum

$$\frac{\partial \rho}{\partial t} + \nabla \times (\rho u \nabla u) = -\nabla p + \rho g + \nabla \times (u \nabla u) - \nabla \times \tau_t$$

Equation 3: Governing equations for the k

$$\frac{\Delta}{\delta t}(\rho k) + \frac{\delta}{\delta x_i}(\rho k u_i) = \frac{\delta}{\delta x_i}\left(a_k \mu_{eff} \frac{\delta k}{\delta x_j}\right) + G_k + G_b - \rho\varepsilon - Y_M + S_k$$

Equation 4: Governing equations for the epsilon

$$\frac{\Delta}{\delta t}(\rho \varepsilon) + \frac{\delta}{\delta x_i}(\rho \varepsilon u_i) = \frac{\delta}{\delta x_j}\left(a_k \mu_{eff} \frac{\delta \varepsilon}{\delta x_j}\right) + C_{1\varepsilon}\frac{\varepsilon}{k}(G_k + C_{3\varepsilon}G_b) - C_{2\varepsilon}\rho\frac{\varepsilon^2}{k} - R_\varepsilon + S_\varepsilon$$

Where:

- u = fluid velocity vector (m/s)
- t = time (s)
- ρ =density (kg/m^3)
- p = pressure (Pa)
- g = gravitational acceleration (m/s^2)
- τt = divergence of the turbulence stresses
- μ = dynamic molecular viscosity (Pa*s)
- Gb = generation of turbulence kinetic energy due to buoyancy
- Gk = generation of turbulence kinetic energy due to mean velocity gradients
- Y_M = overall dissipation rate
- α_k = inverse effective Prandtl numbers for k
- α_ε = inverse effective Prandtl numbers for ε
- S_k/S_ε = user-defined source terms

It should be noted that the validation CFD model was based on the open wind tunnel experiment. The CFD settings are detailed in Table 2.

Table 1: CFD settings and boundary conditions

Term	Value and settings
Inlet	
Velocity (m/s)	0-3 (wind profile based on the wind tunnel)
Initial Gauge Pressure (Pa)	0
Turbulence Model	K-epsilon RNG
Turbulence Kinetic Energy (m^2/s^2)	1
Outlet	
Gauge Pressure (Pa)	0 (atmospheric)
Wall (domain and windcatcher)	
Shear Condition	No slip
Roughness Model	Standard
Roughness Height	0
Roughness Constant	0.5
Converged residuals	
Continuity / k / Epsilon	0.001
X/Y/Z velocity	0.0001

The supply and return duct section areas were not perfectly balanced, which resulted in a higher airflow velocity in the return duct and a higher-pressure loss than in balanced supply and return channels. As shown in Figure 4a, the return duct was extended into the room, by 350mm, to increase the distance between the wind speed measurement point and the inlet of the return duct to reduce the airflow velocity difference between the middle and the side. This extension was necessary for better experiment measurement accuracy with a lower wind speed difference between the middle and edge, as the airflow in the return duct got more uniform after entering the return duct for a longer distance. However, the extension is not necessary for the real application which takes the space in the room and increases the system pressure loss.

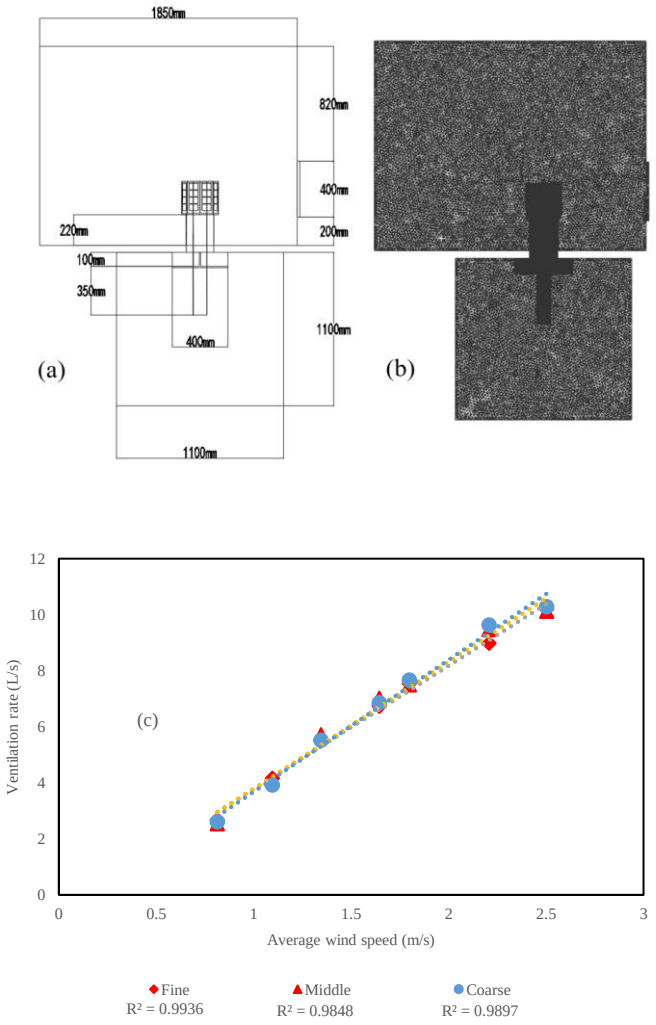

Figure 4 (a) CFD simulation domain and dimensions in mm (b) mesh of the simulation model (c) mesh independence analysis result

In the CFD simulation model in Figure 4b, the full wind tunnel geometry was not included in the simulation, and instead, a circular inlet was modelled to simulate the outlet of the open wind tunnel by using the wind speed profile at the outlet of the open wind tunnel measured from the experiment. The element number of the fine, medium and coarse mesh in the independence analysis was 3.2 million, 1.2 million and 0.3 million, respectively. The ventilation rates predicted by the model with different mesh sizes were compared for the mesh independence analysis to support the model verification. In the model with different mesh qualities, the maximum ventilation rate gap reached 0.5 L/s but most of the results were identical, and the trend lines of the ventilation rate to the outdoor wind speed matched well. Thus, for the ventilation rate evaluation in this research, the simulation model was independent of the mesh quality. The fine mesh quality with about 3.2 million mesh elements, in Figure 4c, was selected for the final simulation validation, with the highest R^2 value in the research.

A conventional 8-sided windcatcher with similar geometry to this research was selected for ventilation performance comparison as the ventilation rate of the 8-sided windcatcher was almost independent of the wind direction. A fixed 8-sided windcatcher model with the same opening size as the flap fin louver windcatcher in this research was made. The simulation settings and outdoor wind speeds in the 8-sided windcatcher simulation were identical to the previous validation model.

2.3. Field test

Even though the ventilation rate of the flap fins windcatcher to the environment wind speed was evaluated under different windcatcher directions, the performance of the flap fins windcatcher needs to be proved in a field test to evaluate the performance under the real conditions with varying wind directions which kept changing all the time. And the wind tunnel could only generate wind speed of up to 3m/s which was not large enough to simulate the entire flow region. Thus, an experimental field test was conducted to investigate the performance of the windcatcher under real outdoor conditions. Two sets of tests were conducted during a typical winter period in the UK. During the tests, the outdoor wind speeds range between 0 - 8m/s. The field study was carried out at the Jubilee campus at the University of Nottingham in the UK on a large open field. The outdoor temperature ranged between 16-19° C in test 1 and 17-21° C in test 2, and both the outdoor wind direction and speed fluctuated during the test.

Figure 5 Field test model in the University of Nottingham

3. RESULT

3.1. Ventilation rate measurement and validations

The ventilation rate of the windcatcher model with double height and single long fins was also validated. The trendline of the ventilation rate in the model with all the fins differed from the model without the windward fins. As shown in Figure 6, a linear relationship was achieved after 1 m/s wind speed. The poor ventilation rate of the flap fin louver windcatcher was caused by the energy loss on pushing up the plastic sheet. Under the low outdoor wind speed conditions, the wind was not able to blow the fin up, and the small opening angle of the fin resulted in a block of airflow. The average gap between the ventilation rate in the experiment and simulation was 0.16L/s with an average error of 4.5% in the condition with wind from the edge direction (22.5° wind). And the average difference between the ventilation rate in the experiment and simulation was 0.09L/s with an average error of 2.3% in the condition with wind from the face direction (0° wind). The trendlines of the simulation and experiment results almost overlapped, and the error was within the accuracy range of the anemometer.

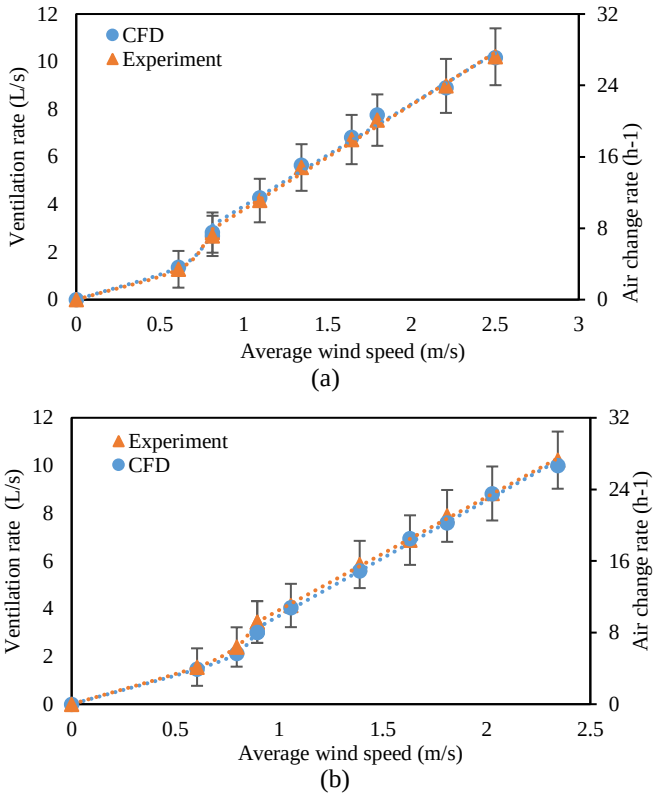

Figure 6 Ventilation rate validation of the windcatcher with all fins (a) 0° wind (b) 22.5° Wind

In Figure 7, in the single-height model, the wind from the windcatcher face direction (0° wind) could generate a slightly higher ventilation rate than the wind from the edge direction (22.5° wind), but the difference was ignorable compared to the performance of the traditional multiple-opening windcatchers. In the double-height model, the impact of wind direction was almost zero, and the ventilation rate in the two conditions was almost the same. In an eight-sided windcatcher, if the ventilation performance was stable in the range between 0° to 22.5°, the ventilation performance in the other directions would also be stable. Thus, if the fin length was long enough, which is about 20cm in this research, the windcatcher could provide a stable fresh air supply no matter how the wind directions were changed.

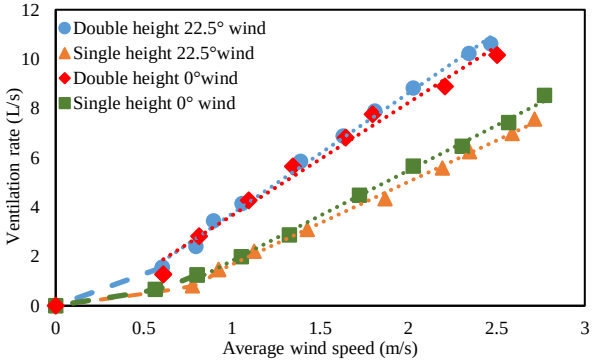

Figure 7 Comparison of ventilation rate under different wind directions

3.2. CFD simulation result

The airflow velocity is shown in Figure 8a. The wind speed started decreasing before arriving at the windcatcher because of the size of the wind tunnel. The air was diffused by the anti-short circuit device and the velocity of air at the occupancy level in the room was lower than 0.2m/s at 2.5m/s environment wind speed which would not cause discomfort and air draught. Even though the velocity of air inside the room was low, the air was well circulated and the fresh air from the windcatcher can be supplied to the level of occupants. The average wind speed at the plane with a height of 0.5m was 0.03m/s and the circulation of air would not cause discomfort. In the current test room, a slow but well-circulated airflow was achieved in the experiment. However, in order to circulate the air in a large room, the size of the supply opening inside

the room can be decreased and the supply air velocity could be increased to circulate in a large region. The ventilation rate would be slightly decreased by the higher system friction but better air circulation is more beneficial for the application.

In Figure 8b, the pressure at the inlet was higher than the room to force the air entering the environment into the room. And the pressure at the outlet was lower than the room to extract the air leaving the room from the chimney. A low-pressure zone was created above the windcatcher around the outlet opening because of the sharp edge in the front. Thus, placing the opening on the top of the windcatcher could increase the ventilation rate with a larger negative pressure around the outlet. The overall replacement ventilation was achieved by the appropriate airflow direction created by the pressure differences between the inlet, room and outlet.

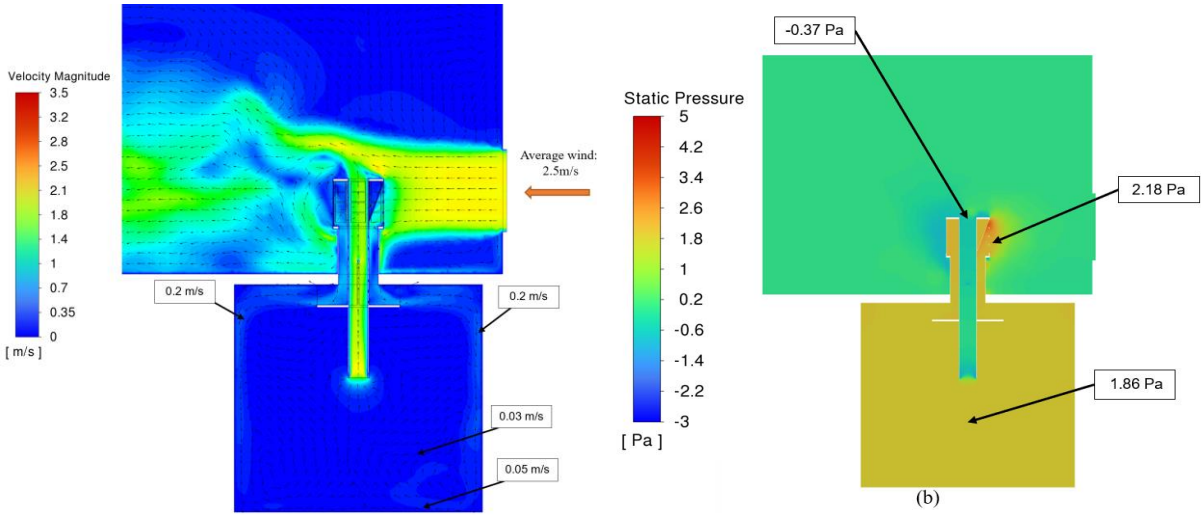

Figure 8 (a)Wind speed contour and vector (in-plane) (b) Static pressure contour

3.3. Comparison to conventional 8-sided windcatcher

The conventional 8-sided windcatcher and the comparison result is shown in Figure 9. At wind speed higher than 1m/s, even though the ventilation performance of the flap fin louver windcatcher was affected by the flap fin, the ventilation performance of the flap fin louver windcatcher was still higher than the 8-sided windcatcher. In the 8-sided windcatcher, most of the air would enter the room through the two or three openings in the front, which resulted in a higher wind speed at the supply channels and a higher total pressure loss than the windcatcher with balanced supply and return channels area. Moreover, the low-pressure zone at the top of the flap fin louver windcatcher had a larger negative pressure than the back and the side of the 8-sided windcatcher and extracted more air from the outlet openings.

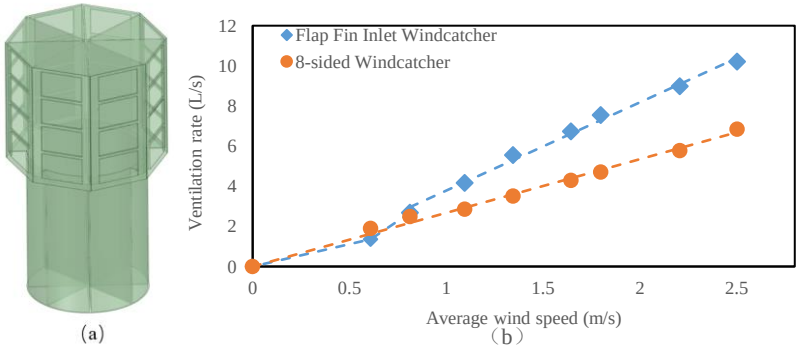

Figure 9 (a) Conventional 8-sided windcatcher and (b) Ventilation rate comparison at 0° wind

3.4. Field test results

A good linear relationship between the average ventilation rate in each minute and the outdoor wind speed was achieved during the test, even though the wind conditions kept changing during the test in Figure 10. The results of the two field tests with high and low outdoor wind speeds were compared. The trend lines of the two tests were almost the same, with R^2 higher than 0.99. The stable performance of the flap fin louver windcatcher was verified by the different tests with different environment wind speeds and directions. As the wind speed generated by the wind tunnel was different to the natural wind because of the atmospheric boundary layer profile and the edge of the test room, achieving an identical

performance in the field study was impossible. Thus, the average ventilation rate of the field test was slightly lower than the experiment. However, a similar ventilation performance was achieved in the field test compared to the findings of the open wind tunnel test. At low environmental wind conditions, the ventilation rate in the experiment was slightly higher than the field study results.

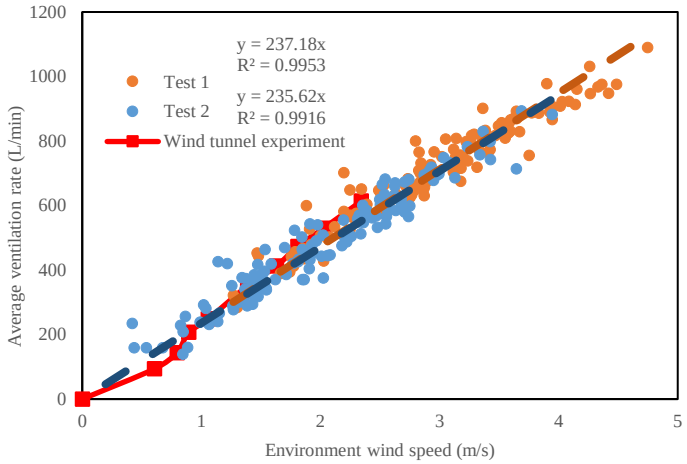

Figure 10 Field test results of average ventilation rate against the outdoor wind speed and the open wind tunnel experimental result

4. DISCUSSIONS

In practice, the dimensions of the windcatcher can be determined based on the area/volume and ventilation demand of the building, similar to our earlier works (Calautit and Hughes 2014, Calautit and Hughes 2014). The current system is not sized based on an actual building or installation, as the current research is still in the initial stages of development. Future works can focus on evaluating how the flow rate scale on the dimensions of the windcatcher.

Regarding the materials of the windcatcher employed in the experiment, the frame in the prototype was the wood panel and the flap fin was made of 0.1mm-0.25mm polyvinyl chloride. Clearly, this prototype was not designed for actual or real building installations and more work is required to develop a close-to-market prototype, which can withstand various weather conditions. The selected materials in the experiment were due to various factors including the prototyping capabilities and cost restrictions. The ventilation performance of the windcatcher was strongly affected by the opening angle of the fins, especially at low wind speed conditions. The connection at the joint and the mass of the fin had a large impact on the fin's open angle. In the current prototype, the fin mass was minimized by using a light and thin PVC material, but other materials like metal foil/film could be considered. Balancing the mass of the fin to reduce the impact of fin mass and decrease the friction at the hinge joint is necessary for optimizing performance.

An open exhaust or chimney was used in this windcatcher design. However, an open chimney without any protection was not practical for real applications because of the entry of rain, snow and insects. The exhaust outlet needs to be integrated with a chimney cap or cowl to protect the outlet from the rain or be combined with a rotary turbine ventilator or a flap fin outlet design.

Finally, the current research tests the ventilation performance of the flap windcatcher and the windcatcher integrated with the passive technologies needs to be investigated further, including solar heating using the windcatcher tube or roof, evaporate cooling, heat pipe heat recovery, earth-air heat exchanger or phase change materials. The internal duct could be further extended above the top of the windcatcher and painted black to generate a solar chimney effect and increase the ventilation rate. The water spray system could also be placed in the supply channel to cool the supply air. The heat recovery can be achieved with metal fins, tubes or heat pipes between the supply and return channels as the channels were adjacent and the airflow direction would not be changed during the operation.

5. CONCLUSION

A flap fin louver windcatcher design was proposed with the function of; (1) the airflow direction and ventilation rate inside the system are fixed regardless of wind direction, (2) the supply and return airflow channels are adjacent to allow heat transfer between them for example, for heat recovery, (3) the polluted air from the outlet would not contaminate the supply air, and (4) there will be no air-short circuiting. This windcatcher addresses the issue of the incorporation of passive/low-energy heating and cooling technologies in conventional windcatchers. With the fixed and adjacent supply and return channels not affected by the changing wind direction, passive/low-energy technologies can be applied in this windcatcher, such as solar heating and heat transfer devices.

Wind tunnel tests and field tests were provided to evaluate the ventilation performance of the flap fin louver windcatcher with an average wind speed between 0-3m/s in the wind tunnel test and 0-5m/s in the field test. The relationship between the average ventilation rate and environment wind speed in the field test was similar to the results in the experiment and the ventilation rate of the windcatcher was independent of the environment wind directions. The validation of the CFD model and experiment model was done in this research using the wind speeds at different locations in the model and the ventilation rate to environment wind speeds in different models and wind directions. The ventilation rate of the flap fin louver windcatcher was higher than the traditional 8-sided windcatcher with the same opening size under an environment wind speed higher than 1m/s, because of a higher-pressure difference between the inlet and the outlet and a lower system pressure loss. The current scaled experiment model with a diameter of 20cm could provide about 10L/s fresh air supply at 2m/s environment wind speed with an air change rate over 27 h-1. The full-scale model investigation and ventilation rate optimization need to be tested in further research.

In future research, the geometry of the windcatcher needs to be further optimized, such as adjusting the surface of the windcatcher faces and using deformable fins. And passive heating, cooling, and energy recovery technologies need to be applied in the fixed supply duct. Passive heating using solar thermal and passive cooling using evaporative or absorption cooling should be investigated by experiment and field study, and the possible passive dehumidification method should be evaluated. The ventilation performance of a larger windcatcher with an appropriate flap fin design should be evaluated in a larger wind tunnel in further research. The flap fin design was applied in this research to create a controlled inlet, and a similar flap fin design could also be used in an extract chimney as an outlet with reversed fin direction, which can avoid the reverse flow of pollutants.

6. REFERENCES

Bay E, Martinez-Molina A, Dupont WA, 2022. Assessment of natural ventilation strategies in historical buildings in a hot and humid climate using energy and CFD simulations. Journal of Building Engineering, 51, 104287.

Blocken B, van Hooff T, Aanen L, Bronsema B, 2011. Computational analysis of the performance of a venturi-shaped roof for natural ventilation: Venturi-effect versus wind-blocking effect. Computers & Fluids, 48(1), 202-213.

Calautit JK, Hughes BR, 2014. Measurement and prediction of the indoor airflow in a room ventilated with a commercial wind tower. Energy and Buildings, 84, 367-377.

Calautit JK, Hughes BR, 2014. Wind tunnel and CFD study of the natural ventilation performance of a commercial multi-directional wind tower. Building and Environment, 80, 71-83.

Calautit JK, Tien PW, Wei S, Calautit K, Hughes B, 2020. Numerical and experimental investigation of the indoor air quality and thermal comfort performance of a low energy cooling windcatcher with heat pipes and extended surfaces. Renewable Energy, 145, 744-756.

Ghalam NZ, Farrokhzad M, Nazif H, 2021. Investigation of optimal natural ventilation in residential complexes design for temperate and humid climates. Sustainable Energy, Grids and Networks, 27, 100500.

Ghoulem M, El Moueddeb K, Nehdi E, Zhong F, Calautit J, 2020. Analysis of passive downdraught evaporative cooling windcatcher for greenhouses in hot climatic conditions: Parametric study and impact of neighbouring structures. Biosystems Engineering, 197, 105-121.

Gilvaei ZM, Poshtiri AH, Akbarpoor AM, 2022. A novel passive system for providing natural ventilation and passive cooling: Evaluating thermal comfort and building energy. Renewable Energy.

He B-j, Yang L, Ye M, Mou B, Zhou Y, 2014. Overview of rural building energy efficiency in China. Energy Policy, 69, 385-396.

Hughes BR, Calautit JK, Ghani SA, 2012. The development of commercial wind towers for natural ventilation: A review. Applied Energy, 92, 606-627.

Jafari S, Kalantar V, 2022. Numerical simulation of natural ventilation with passive cooling by diagonal solar chimneys and windcatcher and water spray system in a hot and dry climate. Energy and Buildings, 256, 111714.

Jiang Y, Chen Q, 2002. Effect of fluctuating wind direction on cross natural ventilation in buildings from large eddy simulation. Building and Environment, 37(4), 379-386.

Jomehzadeh, F., Nejat, P., Calautit, J.K., Yusof, M.B.M., Zaki, S.A., Hughes, B.R., & Yazid, M.N.A.W., 2017. A review on windcatcher for passive cooling and natural ventilation in buildings, Part 1: Indoor air quality and thermal comfort assessment. Renewable and Sustainable Energy Reviews, 70, 736-756.

Jomehzadeh F, Hussen HM, Calautit JK, Nejat P, Ferwati MS, 2020. Natural ventilation by windcatcher (Badgir): A review on the impacts of geometry, microclimate and macroclimate. Energy and Buildings, 226, 110396.

Kobayashi T, Sandberg M, Fujita T, Lim E, Umemiya N, 2022. Numerical analysis of wind-induced natural ventilation for an isolated cubic room with two openings under small mean wind pressure difference. Building and Environment, 109694.

Kumar N, Bardhan R, Kubota T, Tominaga Y, Shirzadi M, 2022. Parametric study on vertical void configurations for improving ventilation performance in the mid-rise apartment building. Building and Environment, 215, 108969.

Li J, Calautit J, Jimenez-Bescos C, Riffat S, 2023. Experimental and numerical evaluation of a novel dual-channel windcatcher with a rotary scoop for energy-saving technology integration. Building and Environment, 110018.

Liu, M., Jimenez-Bescos, C., & Calautit, J., 2022. CFD investigation of a natural ventilation wind tower system with solid tube banks heat recovery for mild-cold climate. Journal of Building Engineering, 45, 103570.

Liu P, Justo Alonso M, Mathisen HM, 2022. Heat recovery ventilation design limitations due to LHC for different ventilation strategies in ZEB. Building and Environment, 224, 109542.

Mahon H, Friedrich D, Hughes B, 2022. Wind tunnel test and numerical study of a multi-sided wind tower with horizontal heat pipes. Energy, 260, 125118.

Montazeri H, Azizian R, 2008. Experimental study on natural ventilation performance of one-sided wind catcher. Building and Environment, 43(12), 2193-2202.

Nasrollahi N, Ghobadi P, 2022. Field measurement and numerical investigation of natural cross-ventilation in high-rise buildings; Thermal comfort analysis. Applied Thermal Engineering, 211, 118500.

Nejat, P., Calautit, J.K., Majid, M.Z.A., Hughes, B.R., & Jomehzadeh, F., 2016a. Anti-short-circuit device: A new solution for short-circuiting in windcatcher and improvement of natural ventilation performance. Building and Environment, 105, 24-39.

Nejat, P., Calautit, J.K., Majid, M.Z.A., Hughes, B.R., & Zeynali, I. & Jomehzadeh, F., 2016b. Evaluation of a two-sided windcatcher integrated with wing wall (as a new design) and comparison with a conventional windcatcher. Energy and Buildings, 126, 287-300.

Nejat, P., Hussen, H.M., Fadli, F., Chaudhry, H.N., Calautit, J., & Jomehzadeh, F., 2020. Indoor Environmental Quality (IEQ) Analysis of a Two-Sided Windcatcher Integrated with Anti-Short-Circuit Device for Low Wind Conditions. Processes, 8, 840.

Nejat P, Ferwati MS, Calautit J, Ghahramani A, Sheikhshahrokhdehkordi M, 2021. Passive cooling and natural ventilation by the windcatcher (Badgir): An experimental and simulation study of indoor air quality, thermal comfort and passive cooling power. Journal of Building Engineering, 41, 102436.

Noroozi A, Veneris Y, 2018. Thermal Assessment of a Novel Combine Evaporative Cooling Wind Catcher. Energies, 11, 442.

Pan W, Liu S, Li S, Cheng X, Zhang H, Long Z, Zhang T, Chen Q, 2019. A model for calculating single-sided natural ventilation rate in an urban residential apartment. Building and Environment, 147, 372-381.

Pelletier K, Calautit J, 2022. Analysis of the performance of an integrated multistage helical coil heat transfer device and passive cooling windcatcher for buildings in hot climates. Journal of Building

Tien PW, Wei S, Darkwa J, Wood C, Calautit JK, 2022. Machine Learning and Deep Learning Methods for Enhancing Building Energy Efficiency and Indoor Environmental Quality – A Review. Energy and AI, 10, 100198.

Yong, L.X. & Calautit, J.K., 2023. A Comprehensive Review on the Integration of Antimicrobial Technologies onto Various Surfaces of the Built Environment. Sustainability, 15, 3394.

#14: Deep Learning-based vision for real-time building occupancy and window status detection

Enhancing Energy Efficiency and Indoor Comfort

Paige TIEN [1], Wuxia ZHANG[2], Shuangyu WEI[3], John CALAUTIT[4]

[1] *Department of Architecture and Built Environment, University of Nottingham, UK, paige.tien@ nottingham.ac.uk*
[2] Department of Architecture and Built Environment, University of Nottingham, UK, *wuxia.zhang@nottingham.ac.uk*
[3] Department of Architecture and Built Environment, University of Nottingham, UK, *shuangyu.wei@nottingham.ac.uk*
[4] Department of Architecture and Built Environment, University of Nottingham, UK, *john.calautit1@nottingham.ac.uk*

Abstract: This study introduces a vision-based deep learning approach aimed at enhancing the control of Heating, Ventilation, and Air-Conditioning (HVAC) systems by detecting and recognizing occupant activities and window opening behaviour in real-time. Traditional HVAC control methods often fall short in responding to the dynamic behaviours of occupants, leading to energy inefficiencies and compromised indoor air quality. The motivation behind this research arises from the pressing need for energy-efficient buildings and sustainable practices. Leveraging deep learning and computer vision techniques, the proposed methodology involves the development and training of a specialized convolutional neural network (CNN) model using diverse video data capturing occupant actions and window operations. Rigorous experimental evaluations conducted within a case study building demonstrate impressive detection accuracies of 92.72% for occupant activities and 87.74% for window operations, validating the model's ability to accurately identify a wide range of occupant behaviours, including subtle window-opening actions. By utilizing real-time detection, Deep Learning Influenced Profiles (DLIP) are generated, allowing for building energy simulations to assess the approach's impact on energy demand and indoor air quality. The implications of this vision-based deep learning approach are far-reaching, as it holds promise in predicting indoor air quality, enhancing thermal comfort, and optimizing HVAC and natural ventilation systems based on real-time occupant behaviour, thereby contributing to energy conservation and fostering a more sustainable and comfortable indoor environment.

Keywords: buildings, computer vision, energy, HVAC, occupancy

1. INTRODUCTION

Occupancy behavior within buildings plays a significant role in influencing the energy performance and operation of heating, ventilation, and air-conditioning (HVAC) systems (Kallio et al., 2021; Zhang et al., 2022). Conventional HVAC control strategies, relying on fixed setpoint schedules, often fail to adapt to the actual requirements of conditioned spaces, resulting in either over-conditioning or under-conditioning of the building (ASHRAE 2017; ASHRAE 2019). Additionally, unintended window openings can lead to considerable heat loss, leading to increased energy consumption (de Rubeis, 2020). To optimize building operations, it becomes imperative to implement demand-driven controls capable of monitoring indoor space utilization and providing occupants with their specific thermal comfort requirements (Wang et al., 2022; Wang et al., 2023; Wei et al., 2022). Several studies, including (Tien et al., 2021; Tien et al., 2020a), have explored the potential impact of vision-based detection and recognition approaches on building energy demand and thermal comfort (Tien et al., 2022a). Early research focused on developing detection methods for occupancy activities, equipment usage, and window operations (Tien et al., 2022b), which can aid in estimating internal heat gains and ventilation heat loss. One of the notable advantages of this approach lies in its ability to perform multiple types of detection within a space using a single sensor or camera. However, the integration of these methods has yet to be fully explored. Furthermore, only limited studies (Tien et al., 2020b; Wei et al., 2020) have employed such solutions to detect and recognize occupants' activities and predict the heat emitted by occupants (sensible and latent heat gains) and equipment usage. Moreover, the overall impact of implementing this approach on energy consumption and its practical feasibility warrants further investigation.

2. METHOD

The current research advances the innovative methodologies presented in (Tien et al., 2020b) by formulating and assessing a comprehensive framework facilitating real-time detection and recognition of occupancy activities and the status of windows (open/close) within a building space, as initiated by its occupants. This proposed approach not only enables instantaneous prediction of internal heat gains but also provides valuable insights for building control systems. The framework (Figure 1) comprises two distinct parts: Part 1 revolves around the development and practical implementation of the proposed deep learning model, while Part 2 delves into a detailed analysis of the model's utilization in real-time detection scenarios derived from experimental testing. Furthermore, the framework's efficacy is examined under various scenario-based situations, employing building energy simulation (BES) to gauge its potential impact. This comprehensive investigation aims to showcase the potential practicality and efficiency of the proposed deep learning approach in dynamically responding to and managing building conditions based on real-time occupancy patterns and window states.

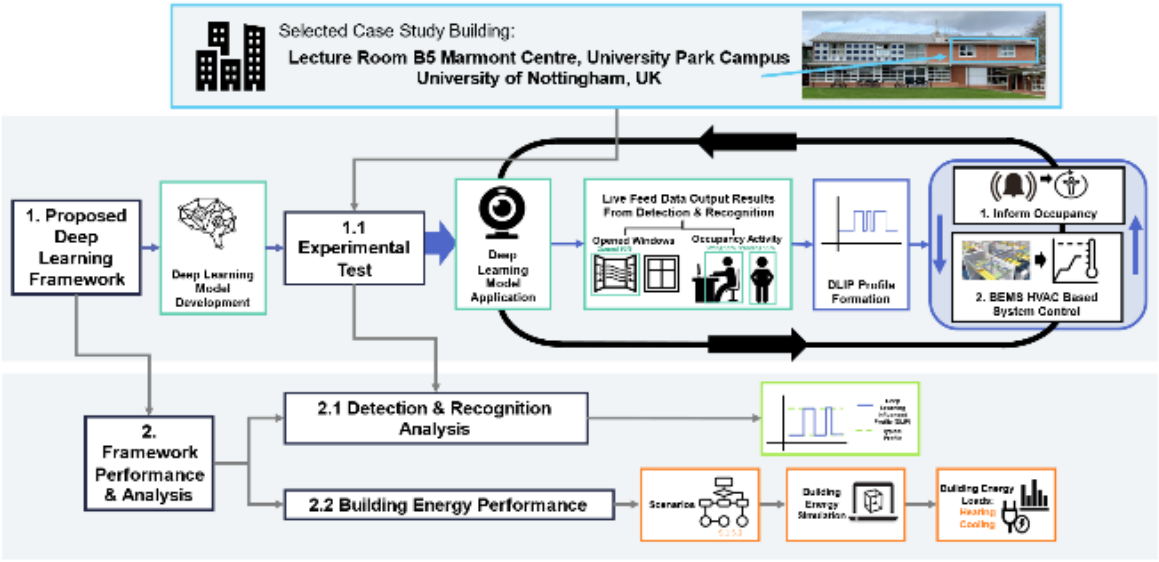

Figure 1 Overview of the research method

2.1. Deep learning method for detection

In this research, a Faster Region-Based Convolutional Neural Network (Faster R-CNN) was harnessed to develop and train an AI-based multi-detector capable of detecting and recognizing occupancy activities and window status through camera inputs. A dataset of images was meticulously collected and labelled to serve as the training input, adhering to the desired format. To illustrate the labelling process, Figure 2 exemplifies the types of images gathered and the manual labelling process applied to highlight specific regions of interest within each image. As previously indicated in [6], numerical labels were assigned to each image based solely on its content. In most cases, multiple labels were assigned by delineating bounding boxes around each occupant and the gaps on all sides of the windows.

Figure 2 Example images gathered from Google Images to form the image datasets (training and testing) for both categories of occupancy activities and windows, along with the examples of how images were manually labelled to highlight the specific region of interest.

For the present study, a suitable model was selected from the TensorFlow detection model zoo to configure the desired detector's pipeline. The TensorFlow Detection Model Zoo encompasses a collection of detection models pre-trained on diverse image-based datasets. Specifically, the COCO-trained model of Faster R-CNN (With Inception V2) was chosen [5-8]. Subsequently, two separate models, Model A for occupancy activity detection and Model B for window detection, were configured and individually trained. Once the successful training of these models was achieved, they were combined and deployed within a single AI-powered camera setup.

To validate the trained models, testing data were utilized, and the accuracy and suitability of real-time detection capabilities were evaluated. The robustness and effectiveness of the AI-based multi-detector in identifying occupancy activities and window status were thoroughly assessed to ascertain its potential for practical implementation.

2.2. Application of deep learning method

For the evaluation of the proposed deep learning vision-based approach, a lecture room situated on the first floor of the Marmont Centre at the University of Nottingham (University Park Campus, Nottingham, UK) was selected as the testbed (see Figure 3). A comprehensive field experiment was conducted in this designated building space to assess the capabilities and performance of the proposed approach in terms of detection and recognition. To ensure focused detection, the positioning of the detection camera was directed towards a specific section of the room, namely, the 'South Facing Windows 1'. The camera employed for this experiment was a standard 1080p camera, possessing a wide 90-degree field of view. It was strategically positioned at a height near the room's ceiling to simulate the typical installation of a room ceiling sensor.

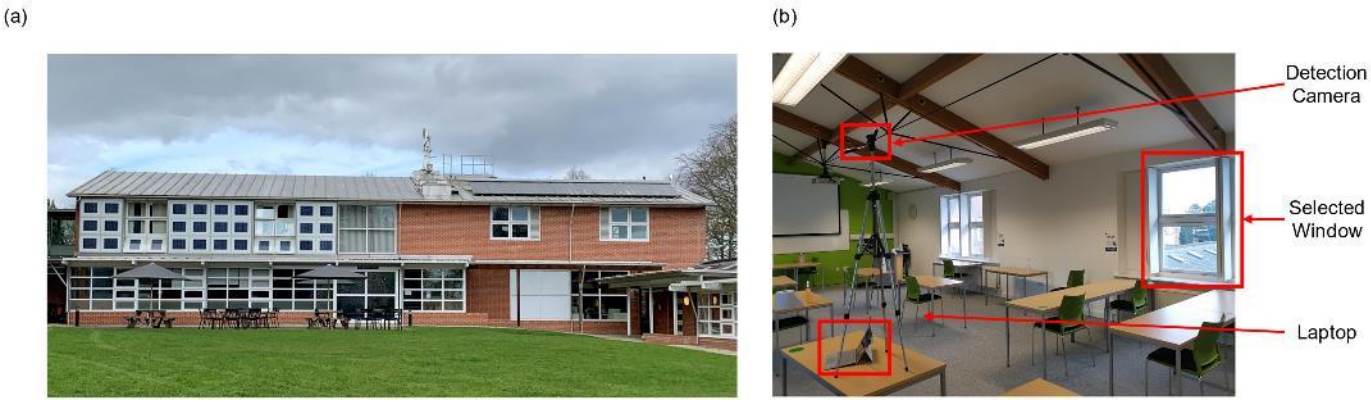

Figure 3 (a) Marmont Centre at the University of Nottingham, UK. (b). Set up for the experimental test

The chosen building features natural ventilation and is equipped with a central heating system. The lecture room itself boasts a spacious floor area of 96.9m2, with dimensions measuring 12.75m x 7.6m and a floor-to-ceiling height of 2.5m. For the simulation, weather data from Nottingham, UK was utilized. The heating profiles were adjusted to maintain an indoor temperature of 21°C during occupied hours [2,3]. Additionally, the infiltration rate was assumed to be constant, with 0.5 air changes per hour accounting for air exchanges. The windows in the room were considered to have a top hung window opening, allowing for an openable area of 50% and a maximum openable angle of 45°.

This experimental setup serves as a crucial testing ground, providing valuable insights into the proposed vision-based approach's functionality and its potential impact on optimizing indoor climate control and energy management in real-world settings.

2.3. Scenario-based building energy simulation (BES)

To comprehensively evaluate the potential of the framework and the method's impact on building energy loads, building energy simulation (BES) was conducted. This simulation allowed for the investigation of various scenario-based operation profiles, aiming to assess indoor air quality and potential energy savings achievable through the proposed approach. For this purpose, a 4-day test scenario was designed. To gain insights into diverse system responses that can aid the HVAC control system in providing optimal indoor thermal comfort and air quality, while simultaneously enhancing building energy performance, five distinct cases were established (see Figure 4b).

Case A represented the conditions where building systems and HVAC systems operated based on predefined or fixed schedules. In contrast, Cases B, C, D, and E demonstrated alternative ways in which the deep learning-based framework could be effectively utilized to support HVAC system operations. Through this comprehensive analysis, the study sought to shed light on the capabilities of the vision-based approach and its potential to revolutionize HVAC control strategies, paving the way for improved indoor environmental conditions and energy efficiency.

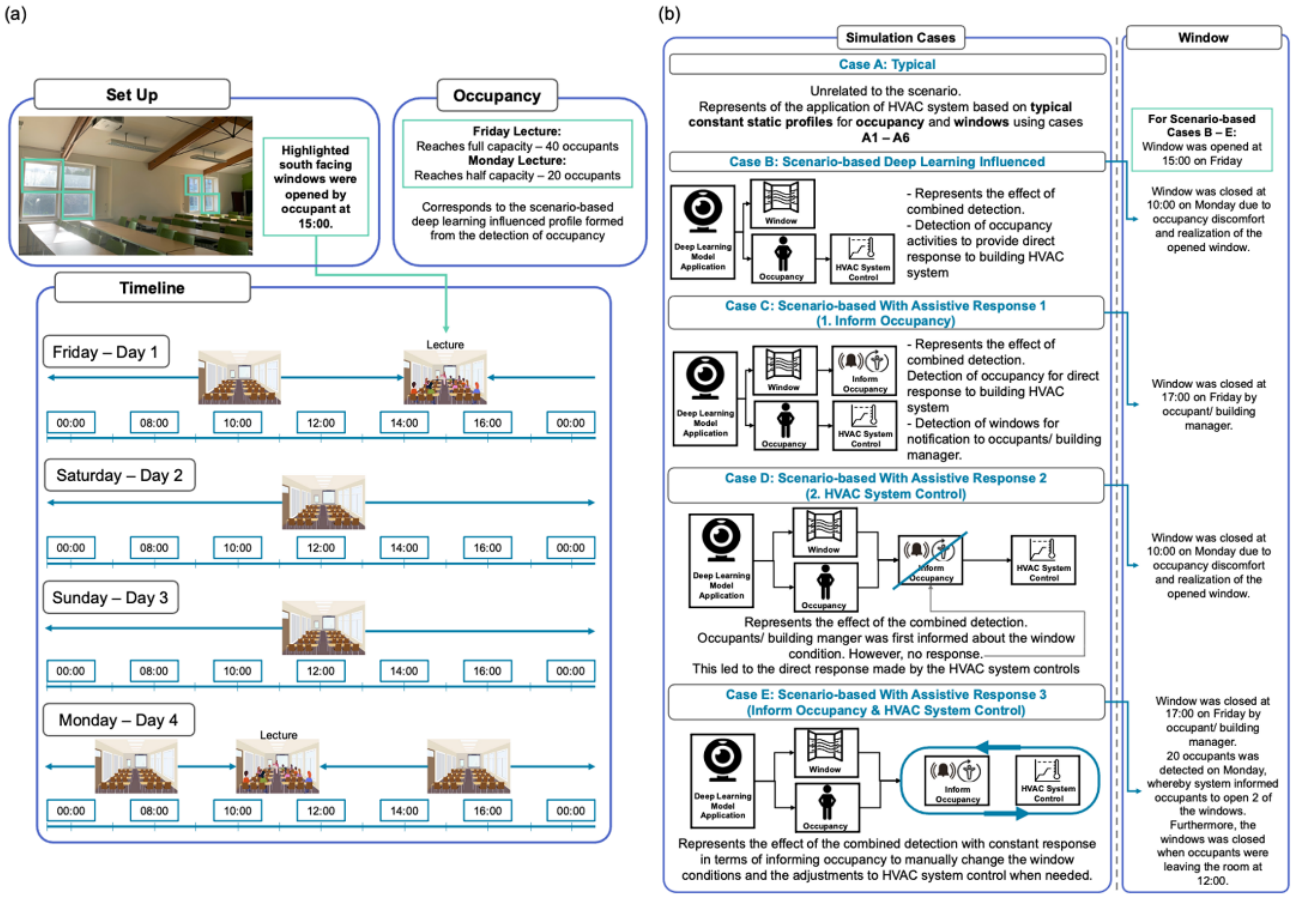

Figure 4 (a). Timeline of activities in the selected lecture room during a typical week. (b). Description of the different simulation cases based on the different system responses

3. RESULTS AND DISCUSSION

Prior to deploying both models to create an AI-based detector for real-time detection, a comprehensive model performance evaluation was carried out using still images from the test dataset. The evaluation revealed encouraging results, with an average accuracy of 94.04% for detecting sitting activities, 91.43% for standing activities, 92.70% for walking activities, and 87.74% for detecting opened windows. Figure 5 provides a glimpse of the real-time detection and recognition process, showcasing the integrated vision-based detection approach in action within the case study lecture room. During real-time detection, bounding boxes were applied to indicate the recognized objects for each instance, and detection accuracy was assessed based on the Intersection over Union (IoU) value. It is worth noting that the images of the detection process are not retained, and they are solely included in Figure 5 for illustrative purposes.

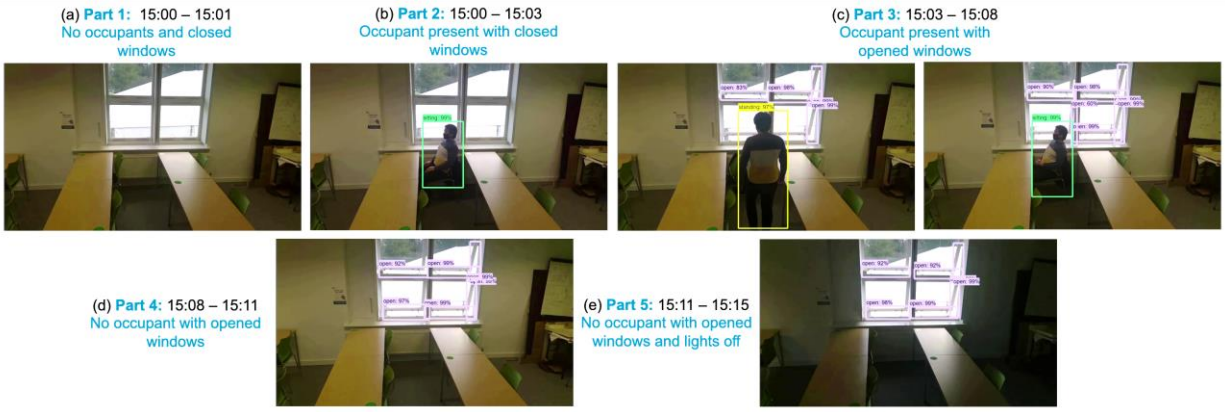

Figure 5 Key stages of the occupancy activity and window detection during the experimental test

Figure 6 illustrates the generated Deep Learning Influenced Profiles (DLIP) for occupancy activities and window conditions during the experimental test. These profiles offer a detailed record of the number of occupants involved in each selected activity and the count of opened windows. The envisioned utilization of this data is to inform and optimize the operations of HVAC controls and building energy simulation (BES) modeling. Considering the scenario cases, Figure 7 showcases the predicted occupancy sensible and latent heat gains. To provide benchmarks representing conventional systems within office buildings, the results for Typical Office 1 and 2 are included, showing predicted heat gains of 165.6kWh and 208.8kWh, respectively. Notably, the lecture room, with its limited occupancy for only a few hours, demonstrated a significantly lower total occupancy heat gain of 16.6kWh, as captured by the DLIP. This underscores the importance of the proposed approach in discerning whether a room is occupied or unoccupied, as well as understanding the specific activities performed by occupants at any given time. Such insights hold promise for optimizing building energy consumption and enhancing indoor environmental quality.

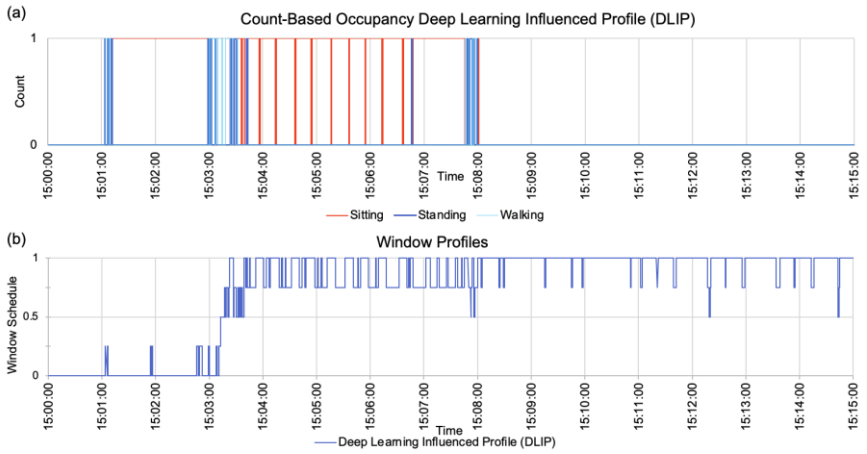

Figure 6 Generated (a) count-based occupancy deep learning influenced profile (DLIP) and (b) window DLIP during the experimental test

Prior to deploying both models to create an AI-based detector for real-time detection, a rigorous model performance evaluation was undertaken, assessing their detection and recognition abilities on still images from the test dataset. The evaluation yielded promising results, with an average accuracy of 94.04% for detecting sitting activities, 91.43% for standing activities, 92.70% for walking activities, and 87.74% for identifying opened windows. Figure 6 provides a preview of the real-time detection and recognition process, showcasing the integrated vision-based detection approach in action within the case study lecture room. During real-time detection, bounding boxes were applied to pinpoint the recognized objects for each instance, and the detection accuracy was assessed based on the Intersection over Union (IoU) value. It is worth noting that the images of the detection process are only displayed for illustrative purposes and are not stored.

In Figure 6, the generated Deep Learning Influenced Profiles (DLIP) present a comprehensive record of occupancy activities and window conditions during the experimental test. The data obtained holds the potential to inform and support the operations of HVAC controls and building energy simulation (BES) modelling. Moving on to Figure 7, the predicted occupancy sensible and latent heat gains are displayed, with benchmark values for Typical Office 1 and 2 serving as references for conventional office building occupancy profiles, showing predicted heat gains of 165.6kWh and 208.8kWh, respectively. Remarkably, in the lecture room, which remained unoccupied for most of the time and hosted only a small number of occupants for limited hours, the DLIP accurately predicted a significantly lower total occupancy heat gain of

16.6kWh. This underscores the importance of the proposed approach in accurately discerning the occupancy status and understanding the specific activities performed by occupants at any given time.

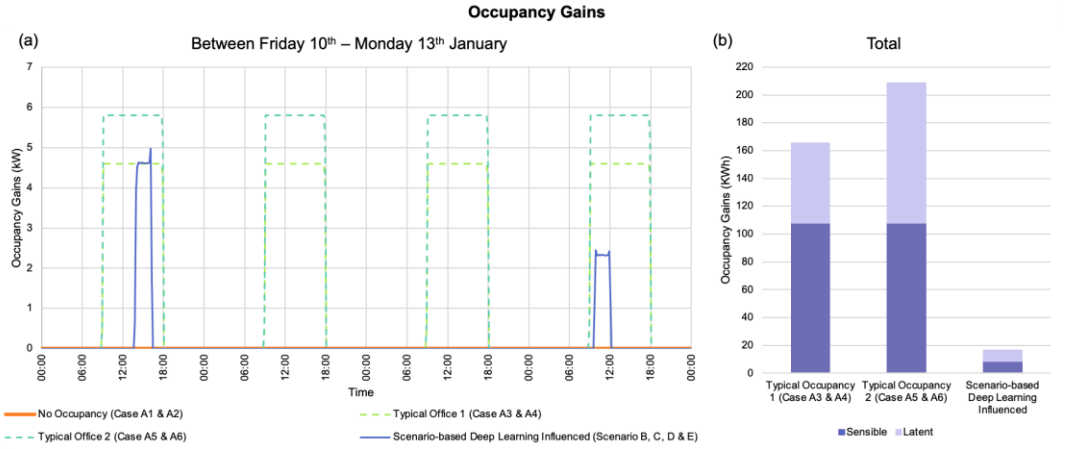

Figure 7 Comparison of the (a) occupancy heat gains across time and (b) the predicted total sensible and latent occupancy heat gains based on the scheduled profiles and scenario based DLIP

Figure 8 further demonstrates the impact of indoor-outdoor conditions and the number of opened windows on the amount of ventilation heat losses achieved. The results for Case B, C, D, and E were significantly influenced by the window profiles generated from detections based on occupancy behavior. Hence, this highlights the critical role of ascertaining whether windows are opened or closed, as it profoundly affects the ventilation conditions within the indoor environment. These findings emphasize the effectiveness and practical significance of the vision-based approach in enabling accurate real-time detection and recognition, thereby contributing to the optimization of indoor environmental quality and energy management strategies.

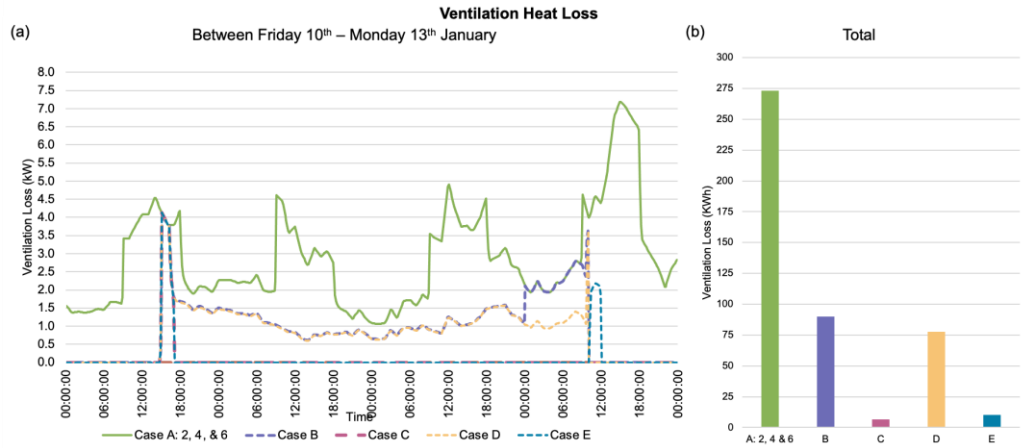

Figure 8 Total building ventilation heat loss prediction for all simulated cases with (a) presenting heat losses for all cases under the 4-day scenario across time and (b) with the total losses

4. CONCLUSION AND FUTURE WORKS

In this study, we propose a data-driven deep learning framework designed to detect and recognize occupancy activity and window status. To assess its effectiveness, we conducted an experimental test within a lecture room at the University of Nottingham. The real-time detection process generated valuable data, including the number of occupants engaged in specific activities and the status of open windows, which was subsequently utilized to construct a deep learning influenced profile (DLIP). Building energy simulation was then performed using scenario-based cases, allowing us to evaluate the deep learning approach and gain insights into how this detection method can empower HVAC systems to adapt and respond to dynamic changes in occupancy. This, in turn, enables the system to make informed decisions, such as instructing occupants to open or close windows or enabling demand-controlled heating and ventilation systems to fulfil the precise requirements while minimizing unnecessary energy loads. Looking ahead, our future research endeavours involve developing a streamlined framework-based solution that defines the requisite HVAC control system conditions based on real-time detection data responses. This includes identifying the most appropriate indoor/room setpoint temperature to be assigned to HVAC systems, ensuring adequate thermal conditions based on the real-time understanding of space utilization by occupants. By leveraging the potential of this data-driven deep learning framework, we aim to optimize HVAC system performance, enhance energy efficiency, and create a more comfortable and sustainable indoor environment.

5. ACKNOWLEDGEMENT

This work was supported by the Department of Architecture and Built Environment, University of Nottingham and the PhD studentship from EPSRC, Project References: 2100822 (EP/R513283/1).

6. REFERENCE

ASHRAE, 2017. Standard 55 - Thermal environmental conditions for human occupancy.

ASHRAE, 2019. ANSI/ASHRAE/IES Standard 90.1-2019 -- Energy Standard for Buildings Except Low-Rise Residential Buildings.

de Rubeis T, Falasca S, Curci G, Paoletti D, Ambrosini D, 2020. Sensitivity of heating performance of an energy self-sufficient building to climate zone, climate change and HVAC system solutions. Sustainable Cities and Society, 61, 102300.

Kallio J, Tervonen J, Räsänen P, Mäkynen R, Koivusaari J, Peltola J, 2021. Forecasting office indoor CO2 concentration using machine learning with a one-year dataset. Building and Environment, 187, 107409.

Tien PW, Wei S, Calautit JK, 2020a. A computer vision-based occupancy and equipment usage detection approach for reducing building energy demand. Energies, 14, 156.

Tien PW, Wei S, Calautit JK, Darkwa J, Wood C, 2020b. A vision-based deep learning approach for the detection and prediction of occupancy heat emissions for demand-driven control solutions. Energy and Buildings, 226, 110386.

Tien PW, Wei S, Calautit JK, Darkwa J, Wood C, 2021. A deep learning approach towards the detection and recognition of opening of windows for effective management of building ventilation heat losses and reducing space heating demand. Renewable Energy, 177, 603-625.

Tien PW, Wei S, Darkwa J, Wood C, Calautit JK, 2022a. Machine Learning and Deep Learning Methods for Enhancing Building Energy Efficiency and Indoor Environmental Quality – A Review. Energy and AI, 10, 100198.

Tien PW, Wei S, Calautit JK, Darkwa J, Wood C, 2022b. Real-time monitoring of occupancy activities and window opening within buildings using an integrated deep learning-based approach for reducing energy demand. Applied Energy, 308, 118336.

Wang Z, Calautit JK, Wei S, Tien PW, Xia L, 2022. Real-time building heat gains prediction and optimization of HVAC setpoint: An integrated framework. Journal of Building Engineering, 49, 104103.

Wang Z, Calautit JK, Tien PW, Wei S, Zhang W, Wu Y, Xia L, 2023. An occupant-centric control strategy for indoor thermal comfort, air quality and energy management. Energy and Buildings, 285, 112899.

Wei S, Tien PW, Calautit JK, Wu Y, Boukhanouf R, 2020. Vision-based detection and prediction of equipment heat gains in commercial office buildings using a deep learning method. Applied Energy, 227, 115506.

Wei S, Tien PW, Chow TW, Wu Y, Calautit JK, 2022. Deep learning and computer vision based occupancy CO2 level prediction for demand-controlled ventilation (DCV). Journal of Building Engineering, 56, 104715.

Zhang W, Wu Y, Calautit JK, 2022. A review on occupancy prediction through machine learning for enhancing energy efficiency, air quality and thermal comfort in the built environment. Renewable and Sustainable Energy Reviews, 167, 112704.

#15: Continual learning-based adaptive data-driven model for building energy prediction

Ao LI[1], Fu XIAO[1,2]

[1] *Department of Building Environment and Energy Engineering, The Hong Kong Polytechnic University, Hong Kong, China*
[2] *Research Institute for Smart Energy, The Hong Kong Polytechnic University, Hong Kong, China*

Abstract: Data-driven models have been increasingly employed in smart building energy management due to their superior performance. To avoid performance degradation, the data-driven models should be continuously updated to adapt to the changes of building operation characteristics. During the continual model update process, the knowledge of previous learned task(s) can be lost as information relevant to the current task is incorporated (i.e., catastrophic forgetting issue). Conventional model update methods cannot address concept drift and catastrophic forgetting issues in an efficient and effective way. Continual learning focuses on learning a model from a continuous data stream which can originate from changing input domains or be associated with different tasks. This paper conducted a comparison study on the performance of two advanced continual learning methods (i.e., Elastic weight consolidation, Gradient episodic memory) and three conventional update methods (i.e., accumulative learning, incremental learning, and ensemble learning) for adaptive building energy prediction. The case study on a large open-source dataset demonstrated that, the CV-RMSE of Elastic weight consolidation and Gradient episodic memory decreased by around 14% and 8% on average compared with static model and accumulative learning. The research insights could facilitate the wide deployment of advanced machine learning techniques in the building energy sector.

Keywords: Building energy prediction, Model update, Continual learning, Accumulative learning, Incremental learning

1. INTRODUCTION

Machine learning, a rapidly growing data-driven technical domain, is situated at the intersection of computer science and statistics and serves as the foundation of Artificial Intelligence and data science (Jordan, 2015). Machine learning has been utilized in various aspects of smart building energy management applications (Hong, 2020), such as building design optimization, building energy prediction, fault detection and diagnosis, and building retrofit analysis. Research has shown that machine learning models can achieve comparable, or even superior, performance while requiring less expert knowledge and building physical information than white-box and grey-box models (Fan, 2021). The adoption of data-intensive machine learning methods in smart building management leads to more evidence-based decision-making (Zhang, 2021).

Deploying machine learning models in smart buildings is an ongoing process. Due to changes in working conditions and varying system characteristics, the relationship between input and output may change over time, leading to inaccurate predictions on new datasets (Liang, 2019; Deng, 2022). This phenomenon, known as concept drift or data drift, is a common cause of performance degradation in data-driven models (Lu, 2018). Concept drift can be classified into several categories, including sudden drift where the data changes suddenly (e.g., sudden machine failures), incremental and gradual drift (e.g., change of occupancy behaviour), and reoccurring drift (e.g., seasonality of meteorological conditions and working patterns) (Deng, 2022). To capture the changes of system characteristics and prevent performance degradation, continual model update (or retraining) is proposed. Two widely-used model update methods are accumulative learning and incremental learning, which update the model parameters based on the gradient descent algorithm (or its variants) as new data become available without altering the model architecture (Fekri, 2021). In this paper, the preceding and following data are referred to as the historical dataset and the incoming dataset, respectively, with the most recent model update acting as the dividing line. In contrast to incremental learning, which solely employs the latter, accumulative learning refines or retrains a data-driven model utilizing integrated datasets of historical and incoming datasets. A typical drawback of accumulative learning is that it usually cannot quickly adapt to the changes in system characteristics, which leads to significant model performance degradation. Moreover, accumulative learning requires high computation resources as the data used for model update accumulates substantially over time. Another challenging issue with updating data-driven models is catastrophic forgetting, i.e., the knowledge learnt from the historical dataset may be forgotten after the model is updated on newly collected data (Kirkpatrick, 2017; Parisi, 2019). For instance, Deng's study shown that a model that was trained using data from the first year's spring may perform poorly in the second year's spring since it had been updated with data from the first year's summer to winter (Deng, 2022). As a lightweight approach, incremental learning cannot address the catastrophic forgetting issue in principle. As the distribution of subsequent subsets can be very different, the model parameters before and after fine-tuning on the incoming dataset may be dramatically altered.

In general, conventional model update methods cannot address the concept drift and catastrophic forgetting issues in an effective manner. As a new subfield of machine learning, continual learning (also referred to as lifelong learning) concentrates on learning from a continuous data stream which “can stem from changing input domains or can be associated with different tasks” (De Lange, 2021). Continual learning has recently drawn increasing attention as a promising solution for concept drift and catastrophic forgetting issues (Parisi, 2019; Khan 2019). For instance, by preserving the model parameters that are crucial for past prediction tasks during the model update process, regularization-based continual learning methods maintain learnt knowledge when obtaining new knowledge. As opposed to accumulative learning, this approach is more effective and requires fewer resources because it just needs to recall the key model parameters for earlier tasks. An adaptive building load prediction model based on elastic weight consolidation and continuous learning was proposed by Zhou et al. (Zhou, 2022). The continuous learning-based model beat the incremental learning and static models and exhibited equal accuracy to the accumulative learning-based one with significantly decreased computation time and data storage. Continuous learning has promise for accelerating building transformation in the era of pervasive artificial intelligence (Zhou, 2022; Lee, 2020).

The primary goal of model update is to strike a balance between acquiring new knowledge and memorizing prior knowledge. Therefore, the performance of model update method/strategy is highly influenced by the building-specific concept drift types (e.g., gradual drift, seasonal drift), which vary with buildings. However, the data used in previous research are usually limited to a single building. The research results cannot comprehensively reflect the performance of various model update methods under different conditions (i.e., concept drift type). To this end, this study comprehensively investigates different online update methods for adaptive short-term building energy prediction. Three conventional methods (i.e., accumulative learning, incremental learning, ensemble learning) and two advanced continual learning methods (i.e., elastic weight consolidation and gradient episodic memory) are tested and compared. The model update methods are compared in terms of both prediction accuracy and computation resources required. Considering the diversity of buildings, the comparison study is conducted on one hundred buildings taken from an open-source dataset for comprehensive and generalizable results. The impact of model update frequency is also investigated by adopting different frequencies to update the model.

The findings and conclusions obtained from this study can facilitate the selection of proper model update method for smart building energy management. The remaining part of the paper is constructed as follows. Section 2 introduces the research methodology. The comparison study results are elaborated in Section 3. Section 4 concludes the paper.

2. RESEARCH METHODOLOGY

2.1. Research outline

This research aims to comprehensively investigate different continual learning methods for adaptive data-driven building hourly electricity consumption prediction. The overall research methodology is shown in Figure 1, which mainly consists of three steps, i.e., data preprocessing, performance evaluation of model update methods, and post-analysis on building-specific concept drift differences. All the data used for the case study are extracted from a public-available benchmarking building dataset. Data preprocessing consists of data cleaning (e.g., filling in missing values, outlier detection) and feature selection. The entire dataset is segmented into several subsets based on the model update setting (i.e., length of the historical dataset, and update frequency). Then, a baseline neural network model is developed for building energy prediction. The model performance under a continuous data stream using different model update methods is evaluated regarding prediction accuracy and computation resources (required for model update).

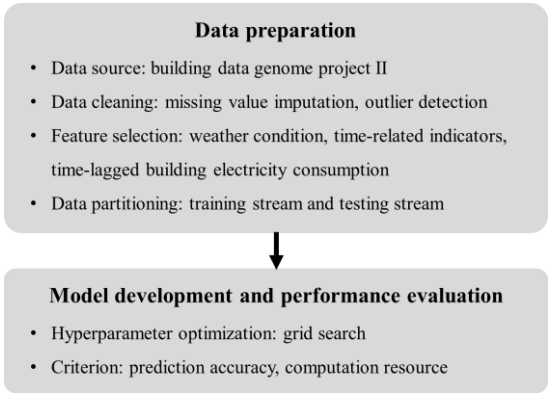

Figure 1 Research outline

2.2. Data preparation

The data used in this study are extracted from Building Data Genome Project 2 (BDGP2) (Miller, 2020). BDGP2 is an open source building dataset, consisting of more than one thousand non-residential buildings with a range of two years (2016 and 2017) at an hourly frequency. In this dataset, the parameters for each building mainly include building information (e.g., area, size, usage, year of construction), energy usage (e.g., electricity consumption, hot water) and climate conditions (e.g., temperature, humidity, wind speed and direction). To comprehensively evaluate the model update methods under various circumstances, one hundred buildings' data are randomly selected from this BDGP2. Some characteristics of the tested buildings are summarized in Figure 2.

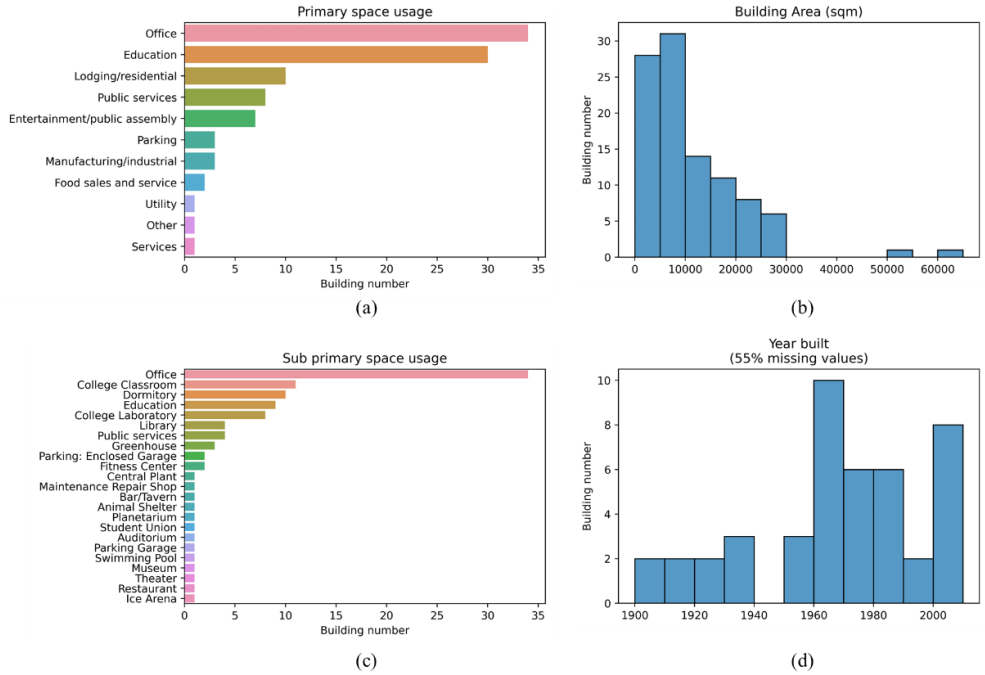

Figure 2 Building characteristics of all tested buildings (a) primary space usage; (b) building area; (c) sub primary space usage; (d) year built.

The selected buildings represent a relatively wide distribution on these dimensions, which lead to representative research results. Data cleaning is performed to improve data quality, including filling in missing values and outlier detection based on statistical criteria. In this study, three main categories of features are selected as the input of the building energy prediction model, including weather features, time-related indicators, and time-lagged electricity consumption. Min-max normalization is conducted for each feature to improve the numerical stability of the prediction model.

2.3. Model update methods and performance evaluation criterion

Five online model update methods are tested, including three conventional methods (i.e., accumulative learning, incremental learning, and ensemble learning) and two continual learning methods (i.e., elastic weight consolidation, and gradient episodic memory). The static model, which is trained on the historical dataset and never updated, serves as the baseline case. Figure shows typical update processes for data-driven models on a continuous data stream. Depending on the timesteps at which the model is updated, the continuous data stream can be divided into a number of subsets, i.e., historical dataset and incoming datasets. As illustrated in Section 1, the conventional gradient descent-based update methods (i.e., accumulative learning and incremental learning) have their limitations in tackling the concept drift issue. Accumulative learning is time-consuming and necessitates large data storage, while incremental learning cannot prevent catastrophic forgetting issue. Ensemble learning is another option which trains a separate model for each subset and then ensemble them together (Krawczyk, 2017; Sagi, 2018). The model update time is much reduced compared with accumulative learning as only the incoming dataset is used, and storing previous models typically takes less memory than storing all historical data. The weights associated with each model can be set equally or updated based on the global prediction error (Kolter, 2005). The drawback of the ensemble learning strategy is also obvious, i.e., the ensemble model will grow in size over time. This is unacceptable for online optimization tasks that require fast model inference.

To address concept drift and catastrophic forgetting simultaneously, the data-driven models must have the capacity to acquire new knowledge and refine existing knowledge on the basis of continuous input (i.e., plasticity), while preventing the new input from significantly interfering with existing knowledge (i.e., stability) (Awasthi, 2019). For instance, the neural weights of an artificial neural network can be regarded as a type of knowledge learnt from training dataset. The stability-plasticity dilemma is a well-known constraint for artificial neural systems (Awasthi, 2019; Qi, 2018). Continual learning is a subfield of machine learning which aims to strike a balance between stability and plasticity. Based on the working principle, continual learning methods can be mainly divided into three categories: regularization-based, memory replay, and neural resource allocation (Awasthi, 2019).

Elastic weight consolidation (EWC), proposed by DeepMind, is one of the most widely used continual learning methods (Kirkpatrick, 2017). EWC adds a quadratic penalty on the difference between the parameters of previous and new models in the loss function, which inhibits the finetuning for task-relevant weights coding for previously learned knowledge. The loss function of EWC can be expressed by $L'(\theta) = L(\theta) + \lambda \sum_i b_i (\theta_i - \theta_i^b)^2$, where $L(\theta)$ represents the mismatch between predicted values and actual labels; θ_i are the updated model parameters; and θ_i^b are the model parameters learned from previous task. b_i represents the importance degree of parameter i on previous task(s), which is calculated based on Fisher information matrix. λ is a hyperparameter that indicates the relative importance of historical knowledge and new knowledge.

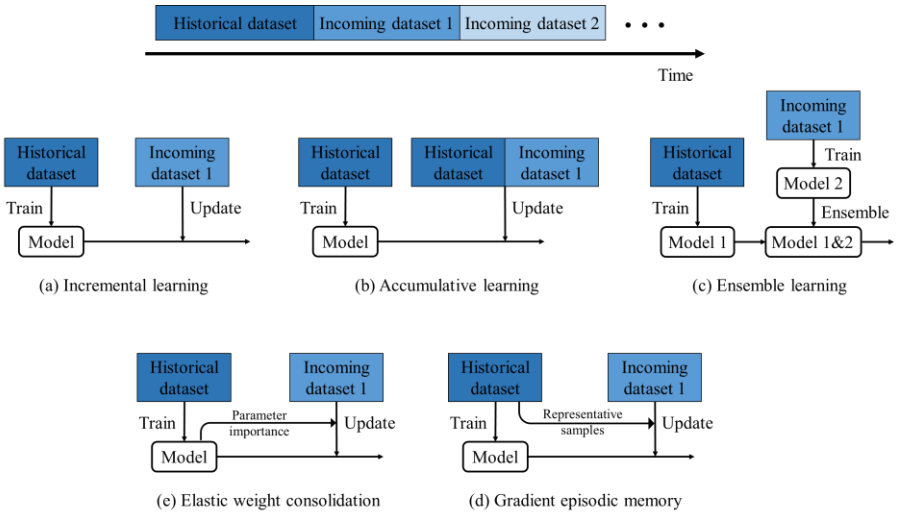

Figure 3 Diagram of data-driven model update methods tested in this study

Gradient episodic memory (GEM) is a special method in the memory replay branch, which yields beneficial transfer of knowledge to previous tasks when updating the model (Lopez-Paz, 2017). The main feature of GEM is an episodic memory M_i, which stores a subset of the observed examples from task i (to calculate the loss gradient). GEM seeks to reduce the loss of the current task without increasing the loss of the previous task(s). While minimizing the loss on current task t, GEM

treats the losses on the episodic memories of tasks $k < t$ as inequality constraints, avoiding their increase but allowing their decrease. Lee et al. (Lee, 2020) adopted GEM to improve and accelerate the learning performance of a multi-client power consumption prediction model deployed on an edge-cloud system and reduce computation resources and alleviate hardware loads. The proposed method was robust to dynamically changed data features and time-variant stream data.

The most straightforward Artificial neural network, i.e., multilayer perceptron (MLP), is adopted as the prediction model. Based on grid-search in preliminary test, the number of hidden layers, neuron number and activation function of each hidden layer are determined as 2, 30 and ReLU (Nair, 2010), respectively. This comparison study adopts the straightforward periodic update strategy, which updates the model on a regular basis. The whole data stream can be separated into chronological sequences of subsets $D_{All} = \{D_1, D_2, \dots, D_i\}$. D_1 is the historical dataset utilized for training the static model, and D_i $(i \geq 2)$ is the continual in-coming datasets. The update frequency is the length of subsets D_i .

In this study, the length of the entire data stream from each building is two years. The length of the historical dataset D_1 is set as two months. Two update frequencies, i.e., one month and two months, are tested. The hyperparameters of each model update method are determined based on preliminary grid-search tests on one example building and used for all other buildings. The settings and results of the grid search are shown in the Appendix. All the models and methods are tested using Python programming language, as well as PyTorch (Paszke, 2019) and Avalanche (Lomonaco, 2021) packages.

Data permutation experiment is widely adopted to compare different model update methods in regression tasks including data-driven time-series prediction modeling, i.e., training a model with a dataset along with a permuted version of the same dataset (Kemker, 2018). However, it is not applicable to building energy prediction, as the building dataset is in chronological order and should not be rearranged due to the inherent temporal correlation of the building operations. Therefore, this study increases the variety of data streams by testing on multiple buildings.

An accuracy matrix $R \in \mathbb{R}^{T \times T}$ is constructed, where $R_{i,j}$ represents the model prediction accuracy (i.e., RMSE and CV-RMSE on subset D_j after update on subset D_i, $i, j \in [1, T]$). The overall accuracy of static model and adaptive models on the whole data stream can be calculated by the following equations:

$$R_{static} = \frac{1}{T-1} \sum_{i=1}^{T-1} R_{1,i+1} \tag{1}$$

$$R_{adaptive} = \frac{1}{T-1} \sum_{i=1}^{T-1} R_{i,i+1} \tag{2}$$

A relative ratio indicating the effect of model update method x can be derived by xxx. Two criteria metrics are adopted to assess the model prediction accuracy and construct the accuracy matrix R, i.e., the root mean squared error (RMSE), and the coefficient of variation of the root mean squared error (CV-RMSE):

$$RMSE = \sqrt{\sum_{i=1}^{n} \frac{(y_i - \hat{y}_i)^2}{n}} \tag{3}$$

$$CV - RMSE = \frac{\sqrt{\sum_{i=1}^{n} \frac{(y_i - \hat{y}_i)^2}{n}}}{\frac{\sum_{i=1}^{n} y_i}{n}} \tag{4}$$

Where y_i is the actual value, $\hat{y}_i$ is the model predicted value (i.e., building hourly electricity consumption).

3. RESULTS ANALYSIS

Results on all tested buildings

Table 1 provides the statistical results on all tested buildings (under two update frequency settings). A scale-independent indicator $CV_{average}$ is calculated by averaging the CV-RMSE prediction accuracy of each method on all tested buildings. The static model is regarded as the baseline in the comparison study. The prediction performance of adaptive models is normalized based on the static model, obtaining R_{Norm}. That is, a R_{Norm} less than one indicates that the update method achieves a performance improvement (over the static model). The improving ratio represents the proportion of buildings on which the update method achieves better prediction performance over the static model. For each indicator, the best results are highlighted in bold.

The results showed that, with the same prediction model architecture, all update methods improved the model performance to a pretty large extent. Compared with the static model, the two continual learning methods not only greatly improves the upper limit (i.e., min value of R_{Norm}), but also ensure the lower limit (i.e., max value of R_{Norm}). This reflects the reliability

and robustness of continual learning methods. Increased update frequency further strengthened the performance of incremental learning and all continual learning methods, while this beneficial effect was less clear for accumulative learning and ensemble learning. Changing the update frequency from two months to one month can further reduce the $CV_{average}$ and increase the improving ratio.

The static model achieved an average CV-RMSE of 36.6% on all tested buildings. It can be observed from the statistical results of R_{Norm} that, EWC and GEM outperform other methods overall. In setting 2, GEM improved the static model from 36.6% to 33.1% in terms of $CV_{average}$. In setting 1, EWC improved the model performance from 36.6% to 31.6% in terms of $CV_{average}$. The performance of accumulative learning and ensemble learning are similarly mediocre. The low standard deviation of R_{Norm} indicates that these two methods perform stably with different buildings. Among the traditional methods, incremental learning is the most effective. It has achieved top overall performance under both settings. It is worth mentioning that incremental learning obtained the smallest R_{Norm} value in both settings, which indicates the maximum amount by which the update method can outperform the static model.

Table 1: Statistical summary of model performance on all tested buildings

Update frequency: one month							
Update method		Static	AL	IL	EL	EWC	GEM
$CV_{average}$		36.6%	34.4%	31.7%	34.0%	**31.6%**	31.8%
R_{Norm}	Average	1	0.942	0.875	0.935	**0.868**	0.869
	Median	1	0.984	0.946	0.978	0.932	**0.923**
	Max	1	1.23	1.03	1.26	1.02	**1.01**
	Min	1	0.557	**0.257**	0.521	0.33	0.459
	Std	0	**0.114**	0.157	0.115	0.147	0.140
Improving ratio			76%	91%	87%	**98%**	93%
Update frequency: two months							
Update method		Static	AL	IL	EL	EWC	GEM
$CV_{average}$		36.6%	34.7%	33.8%	34.6%	33.6%	**33.1%**
R_{Norm}	Average	1	0.948	0.928	0.945	0.918	**0.906**
	Median	1	0.981	0.979	0.976	0.967	**0.948**
	Max	1	1.27	1.2	1.28	1.32	1.22
	Min	1	0.548	**0.33**	0.548	0.459	0.466
	Std	0	**0.114**	0.144	0.111	0.141	0.134
Improving ratio			71%	71%	75%	78%	**79%**

3.1. Results on one example building

This section provides a detailed elaboration on the model performance on an example building under the continuous data stream. A college classroom (building identity: Fox_education_Rosie) is selected from the benchmark dataset as an example building. This building is located in Phoenix, America. Figure shows the monthly-average electricity consumption profile of this building and the local climate condition (i.e., dry-bulb temperature and dew temperature) throughout the whole period (from 2016 to 2017). The solid line and shaded area represent the average value and standard deviation, respectively. The local climate exhibits obvious seasonal patterns, i.e., hot summers and mild winters. The building's energy usage is relatively steady most of the time, with a significant increase during the winter months.

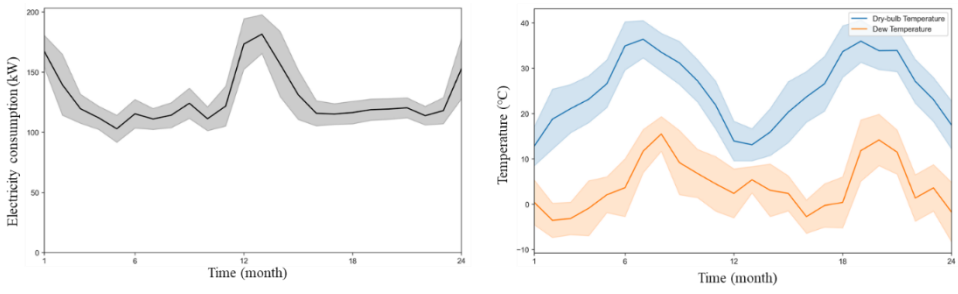

(a) Building electricity consumption (b) Climate condition

Figure 4 The (a) monthly average electricity consumption and (b) climate condition of the example building throughout the whole time period (from 2016 to 2017)

Figure 5 depicts the monthly-average model accuracy in terms of RMSE for different update methods. The performance profile of the static model clearly exhibits the concept drift phenomenon, i.e., its accuracy declines dramatically in the second half of both years. The most likely causes are the large discrepancies between the training and testing periods in terms of building electricity consumption patterns and climate conditions. In comparison, the continuously-updated models, no matter the update methods, perform better as they can adapt to the change of building electricity consumption pattern. However, for many adaptive models, the catastrophic forgetting phenomenon can be observed on the 13th and 14th months (i.e., the 7th testing subset). In these two months, the static model performs well while many continuously-updated models clearly forget the knowledge learned from the historical dataset (when acquiring new knowledge). It can be observed from Figure 5 that, EWC and GEM can efficiently alleviate the catastrophic forgetting problem. Particularly, the prediction model updated using GEM demonstrates excellent and consistent performance during the entire period. The CV-RMSE is 0.134, showing a 62% improvement over the static model.

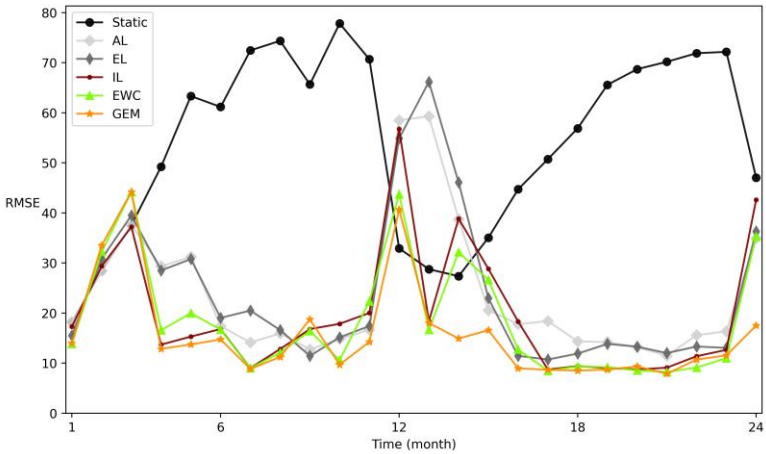

Figure 5 The monthly average RMSE of building energy predictions using different update methods in the whole time period. (Update frequency: one month).

Figure 6 presents the accuracy matrix R of incremental learning and gradient episodic memory (update frequency: two months). The length of each training/testing subset is 2 months. The results of the first row (i.e., $R_{1,j},\ j \in [1,2,\dots,12]$) represent the model performance after training on the historical dataset D_1 (i.e., the static model). The results marked with white boxes represent the model performance ($R_{i,i+1}, i \in [1,2,\dots,11]$) during the entire period. The variation in model performance on the same testing subset (e.g., D_1) reflects how effectively the model retains previously learned knowledge. For instance, it can be observed from the seventh column that (i.e., $R_{i,7}, i \in [1,2,3,4]$) of Figure 6(a) that the model initially performs well on subset D_7 after training on the historical dataset D_1 (i.e., $R_{1,7} = 28.5$), but the error increased fast due to the finetuning of model parameters on subsequent subsets. This indicates a catastrophic forgetting occurrence. On the other hand, as an effective continual learning method, GEM can help the prediction model retain the previously learned knowledge and perform well when encountering similar task(s), as shown in Figure 6(b). However, maintaining a strong anti-forgetting capability (over a long period) sacrifices the model 'plasticity', which may occasionally result in a net loss.

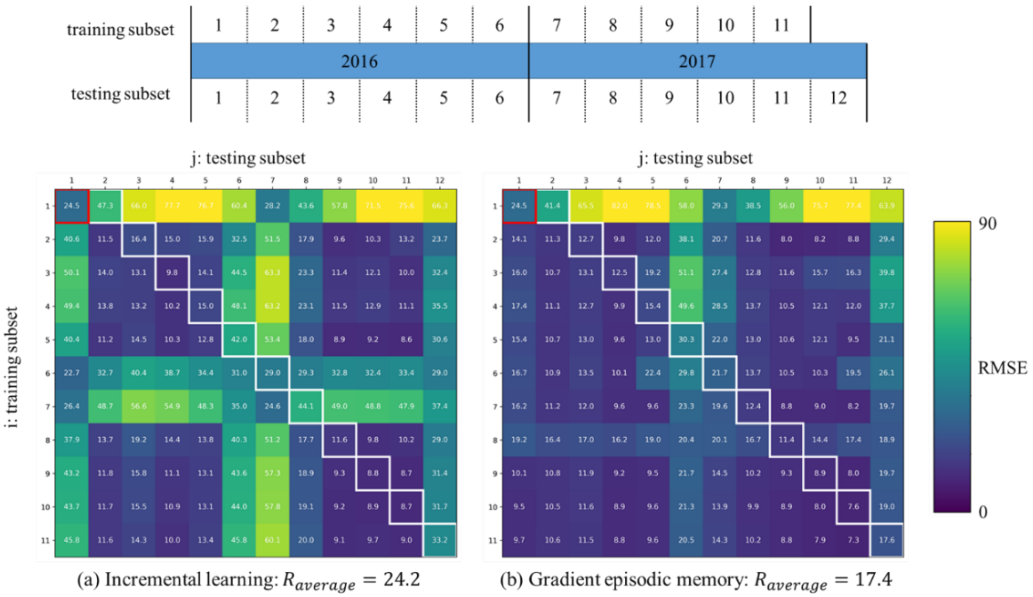

Figure 6 Accuracy matrix R_{ij} (RMSE) of (a) Incremental learning; and (b) Gradient episodic memory. The results marked with white boxes represent the adaptive model performance ($R_{i,i+1}, i \in [1,2,\dots,T-1]$).

4. CONCLUSION

During model deployment, continuous model update is essential to adapt to the changes of building characteristics and alleviate performance decline. This research conducts a comprehensive comparison between eight update methods for building energy prediction, including three conventional methods and two continual learning methods (i.e., Gradient episodic memory and Elastic weight consolidation). The case study on one hundred buildings from an open-source dataset evaluates these methods in terms of prediction accuracy and computation time. The results reveal that the continual learning methods can significantly improve the prediction accuracy and reduce the model training time compared with the widely-used accumulative learning method. The research insights can guide and facilitate the application and deployment of advanced machine learning algorithms in the building management sector.

5. ACKNOWLEDGEMENT

The authors gratefully acknowledge the support of this research by National Key Research and Development Program of China (2021YFE0107400), the Research Grants Council (C5018-20GF) and Innovation and Technology Fund (ITP/002/22LP) of the Hong Kong SAR, China.

6. REFERENCES

Awasthi, A., & Sarawagi, S. (2019, January). Continual learning with neural networks: A review. In Proceedings of the ACM India Joint International Conference on Data Science and Management of Data (pp. 362-365).

De Lange, M., Aljundi, R., Masana, M., Parisot, S., Jia, X., Leonardis, A., ... & Tuytelaars, T. (2021). A continual learning survey: Defying forgetting in classification tasks. IEEE transactions on pattern analysis and machine intelligence, 44(7), 3366-3385.

Deng, Y., Fan, J., Jiang, H., He, F., Wang, D., Li, A., & Xiao, F. (2022, June). Behavior testing of load forecasting models using BuildChecks. In Proceedings of the Thirteenth ACM International Conference on Future Energy Systems (pp. 76-80).

Fan, C., Yan, D., Xiao, F., Li, A., An, J., & Kang, X. (2021, February). Advanced data analytics for enhancing building performances: From data-driven to big data-driven approaches. In Building Simulation (Vol. 14, No. 1, pp. 3-24). Tsinghua University Press.

Fekri, M. N., Patel, H., Grolinger, K., & Sharma, V. (2021). Deep learning for load forecasting with smart meter data: Online Adaptive Recurrent Neural Network. Applied Energy, 282, 116177.

Hong, T., Wang, Z., Luo, X., & Zhang, W. (2020). State-of-the-art on research and applications of machine learning in the building life cycle. Energy and Buildings, 212, 109831.

Jordan, M. I., & Mitchell, T. M. (2015). Machine learning: Trends, perspectives, and prospects. Science, 349(6245), 255-260.

Kemker, R., McClure, M., Abitino, A., Hayes, T., & Kanan, C. (2018, April). Measuring catastrophic forgetting in neural networks. In Proceedings of the AAAI Conference on Artificial Intelligence (Vol. 32, No. 1).

Khan, I. A., Akber, A., & Xu, Y. (2019, May). Sliding window regression based short-term load forecasting of a multi-area power system. In 2019 IEEE Canadian Conference of Electrical and Computer Engineering (CCECE) (pp. 1-5). IEEE.

Kirkpatrick, J., Pascanu, R., Rabinowitz, N., Veness, J., Desjardins, G., Rusu, A. A., ... & Hadsell, R. (2017). Overcoming catastrophic forgetting in neural networks. Proceedings of the national academy of sciences, 114(13), 3521-3526.

Kolter, J. Z., & Maloof, M. A. (2005, August). Using additive expert ensembles to cope with concept drift. In Proceedings of the 22nd international conference on Machine learning (pp. 449-456).

Krawczyk, B., Minku, L. L., Gama, J., Stefanowski, J., & Woźniak, M. (2017). Ensemble learning for data stream analysis: A survey. Information Fusion, 37, 132-156.

Lee, C., Kim, S. H., & Youn, C. H. (2020, November). An Accelerated Continual Learning with Demand Prediction based Scheduling in Edge-Cloud Computing. In 2020 International Conference on Data Mining Workshops (ICDMW) (pp. 717-722). IEEE.

Liang, F., Hatcher, W. G., Xu, G., Nguyen, J., Liao, W., & Yu, W. (2019, July). Towards online deep learning-based energy forecasting. In 2019 28th International Conference on Computer Communication and Networks (ICCCN) (pp. 1-9). IEEE.

Lomonaco, V., Pellegrini, L., Cossu, A., Carta, A., Graffieti, G., Hayes, T. L., ... & Maltoni, D. (2021). Avalanche: an end-to-end library for continual learning. In Proceedings of the IEEE/CVF Conference on Computer Vision and Pattern Recognition (pp. 3600-3610).

Lopez-Paz, D., & Ranzato, M. A. (2017). Gradient episodic memory for continual learning. Advances in neural information processing systems, 30.

Lu, J., Liu, A., Dong, F., Gu, F., Gama, J., & Zhang, G. (2018). Learning under concept drift: A review. IEEE Transactions on Knowledge and Data Engineering, 31(12), 2346-2363.

Miller, C., Kathirgamanathan, A., Picchetti, B., Arjunan, P., Park, J. Y., Nagy, Z., ... & Meggers, F. (2020). The building data genome project 2, energy meter data from the ASHRAE great energy predictor III competition. Scientific data, 7(1), 1-13.

Nair, V., & Hinton, G. E. (2010, January). Rectified linear units improve restricted boltzmann machines. In Icml.

Qi, X., & Liu, C. (2018, October). Enabling deep learning on iot edge: Approaches and evaluation. In 2018 IEEE/ACM Symposium on Edge Computing (SEC) (pp. 367-372). IEEE.

Parisi, G. I., Kemker, R., Part, J. L., Kanan, C., & Wermter, S. (2019). Continual lifelong learning with neural networks: A review. Neural Networks, 113, 54-71.

Paszke, A., Gross, S., Massa, F., Lerer, A., Bradbury, J., Chanan, G., ... & Chintala, S. (2019). Pytorch: An imperative style, high-performance deep learning library. Advances in neural information processing systems, 32.

Sagi, O., & Rokach, L. (2018). Ensemble learning: A survey. Wiley Interdisciplinary Reviews: Data Mining and Knowledge Discovery, 8(4), e1249.

Zhang, L., Wen, J., Li, Y., Chen, J., Ye, Y., Fu, Y., & Livingood, W. (2021). A review of machine learning in building load prediction. Applied Energy, 285, 116452.

Zhou, Y., Tian, X., Zhang, C., Zhao, Y., & Li, T. (2022). Elastic weight consolidation-based adaptive neural networks for dynamic building energy load prediction modeling. Energy and Buildings, 265, 112098.

#17: Harvesting with self-cleaning features: examining the role of wetting state in dust removal

GHASSAN HASSAN[1, 4], BEKIR SAMI YILBAS[1, 2, 3, 4]

[1]*Mechanical Engineering Department, King Fahd University of Petroleum and Minerals (KFUPM), Dhahran 31261, Saudi Arabia.*
[2]*Turkish Japanese University of Science and Technology, Istanbul, Turkey.*
[3]*IRC for Renewable Energy and Power, King Fahd University of Petroleum and Minerals (KFUPM), Dhahran 31261, Saudi Arabia.*
[4]*K.A.CARE Energy Research & Innovation Center, Dhahran 31261, Saudi Arabia. ghassan.abdelmajid@kfupm.edu.sa*

Abstract: The optical properties of protective surfaces used for solar photovoltaic (PV) are crucial for efficient solar energy harvesting. These surfaces must have high transmittance and low absorption to achieve maximum performance. However, environmental factors such as temperature, humidity, and dust settlement can cause severe damage and lower system efficiency for solar thermal and solar PV systems. When the dust settles on protective covers, it scatters and diffuses incident solar radiation, negatively impacting solar receiver performance. Despite efforts to mitigate the effects of dust particles on protective covers and reflective surfaces, the cost-effective removal or self-cleaning of these surfaces remains challenging. Dust particles in humid air collect water vapour and produce mud on solid surfaces, creating a chemically active fluid layer through condensation. This layer can dissolve alkaline (K, Na) and alkaline earth metal (Ca) compounds, causing selective surfaces to lose optical transparency. Therefore, dust must be removed before chemically active layer development. Creating a hydrophobic state on a surface is one method for facilitating the removal of dust particles. Nano/micropillars can trap air and reduce surface dust particle interaction. Therefore, the wetting state of a surface plays a significant role in the self-cleaning application of surfaces, with droplet dynamics being the preferred method for dust particle removal. Experimental evaluations have been conducted on the optical properties of self-cleaning surfaces and the influence of dust on water droplets. Water droplets remove the accumulated dust from the hydrophobic surface; however, the primary mechanism for environmental dust cleaning is the fluid cloaking over the particles.

Keywords: Solar Energy, Energy Harvesting, Self-cleaning, Environmental Dust, Water Droplet

1. INTRODUCTION

The optical characteristics of protective surfaces, such as high transmittance and low absorption, for photovoltaic (PV) modules are critical for effective solar energy harvesting. Numerous environmental factors, including air temperature, rainfall, wind speed, humidity, and dust accumulation, impact the power production of solar energy systems (Hasan et al., 2022). Syed et al. (2018) reported that dust build-up could considerably affect the PV output power. This loss depends on the environmental dust's size, density, and chemical composition. The dust accumulation on the protective cover has similar influences on the performance of the solar thermal receiver due to the scattering and diffusion of incident solar radiation by the settled dust on the protective surface. Yu et al. (2018) analyzed the dust removal process from PV modules using wind cleaning. The wind cleaning process was estimated using particle resuspension theory. This theory includes effects of hydrodynamic force, adhesion, and torque detachment. The results show that the required wind velocity as shear velocity was 0.2 m/s to 58 m/s and 0.8 to 2210 m/s for dust particles of around 0.1 - 100 µm in diameter, respectively. The experimental investigation revealed that the wind from the surfaces could effectively pick up particles with relatively large diameters (more than one µm). However, it was ineffective in cleaning small particles by wind due to the large shear force required for detachment. Different methods have been carried out to remove the accumulated dust particles, including water cleaning, mechanical brushing, mechanical excitation, and air jet blowing (Vedulla et al., 2023). Many dust removal techniques require additional efforts and external forces; therefore, self-cleaning technologies can reduce the required external energy and effectively remove dust. Several treatment approaches were conducted to mitigate the effect of environmental dust particles on the optical characteristics of solar reflective surfaces and protective covers. However, cost-effective removal and self-cleaning of environmental dust from protective covers remain challenging (Conceicao et al., 2022). Superhydrophobic surfaces with reduced particle contact area and low free surface energy will utilize self-cleaning because of air gaps generated between the surface textures.

Under humid environments, the water vapor condenses on the environmental dust particle's top surface, which accumulated dust particles have absorbed to form a mud layer on top of solid protective covers. The mud layer dries because of incident solar radiation that adheres to the protective covers. Therefore, removing dry mud from protective surfaces becomes hard; consequently, extra energy is needed because of the massive adhesion between the surface and dried mud. Different researchers have investigated dust particles' nature and their influences on reflective surfaces and protective glass covers. In this regard, Sand et al. (2012) have investigated the influence of dust accumulation, humid air grade, and wind speed on the performance of PV modules. It was revealed that the accumulation of dust particles, wind speed, and humidity had influenced the efficiency of PV panels to an almost similar magnitude. In addition, Rajput and Sudhakar (2013) have investigated the effect of dust accumulation on the power output efficiency of selected PV panels (monocrystalline modules). It was observed that dust settlement lowered the device's efficiency by 90%. Several researchers have reviewed the dust accumulation effect on protective covers in the Middle East and North Africa region (MENA). Ghazi, Ali, and Kenneth (2014) observed that MENA exhibited the highest storms of environmental dust around the globe. Benghanem et al. (2018) have reported the influence of temperature and dust settlement on PV modules in Madinah, KSA. It was reported that after 60 days of exposure, the power output has reduced by 28%, and the short circuit reached 27% due to dust accumulation. In addition, they proposed a new parameter called dust deposition coefficient (%/mg.cm-2). Alnaser et al. (2018) compared the cleaning process between natural and Man-made cleaning of PV modules in Bahrain. It was reported that dusty PV panels without Man-made cleaning would reduce the performance by 10% for one month of exposure. This present can reach up to 100% on some dusty days. Due to water availability, it was also recommended that PV panels be cleaned once a month to avoid solar-generated electricity losses. In addition, they recommend using PV panels with self-cleaning features through Nano-technology.

Researchers have considered the chemistry of dust accumulation and its relation to PV systems performance. Yilbas et al. (2015) have reported that settled dust consists of various elements and compounds. In addition, it was found that environmental dust has alkaline earth/metallic compounds, which dissolve in the water before condensation on the top surfaces of PV's protective covers in humid environments. Therefore, a mud solution with chemically active behaviour will form and flow through accumulated dust due to gravity reaching the solid substrate where dust has settled. In addition, a chemically active fluid film forms due to the condensation of water vapour onto the environmental dust particles. Therefore, this modifies the optical transparency properties of the selective surfaces because of the dissolution of earth metal alkaline (Ca) and alkaline (K, Na) compounds. Therefore, removing dust particles preceding the formation of this chemically active layer on the surface must be accomplished. One of the techniques for facilitating dust particle removal from the surfaces is creating a hydrophobic state on the surface. This can be obtained by producing Nano/micro-size pillars in which air can trap in these gaps while lowering the contact area of the dust on surfaces. Moreover, surface energy reduction contributes to a hydrophobic wetting state and further lessens the dust adhesion on surfaces.

The surface wetting state refers to the interaction between a liquid and a solid surface, determining how the liquid spreads on that surface. It is primarily characterized by the contact angle formed at the three-phase boundary where the liquid, solid, and vapor phases meet. The wetting state is crucial for surface cleaning via water droplet sliding/rolling in self-cleaning applications. Many studies have focused on generating a hydrophobic surface to obtain a self-cleaning effect (Ding et al., 2017 and Lomga et al., 2017). In addition, Liu et al. (2017) developed superhydrophobic surface efficient emulsion separation for self-cleaning applications using one-step spray coating. The produced coating was observed to have good water droplet impact and sand abrasion stability. Moreover, the superhydrophobic film was visible and

translucent through the coated substrate. Many researchers have investigated the droplet motion, impact, and rolling on inclined hydrophobic surfaces (Mahadevan and Pomeau, 1999, and Stephane et al., 2008). The spreading coefficient of the droplet on superhydrophobic substrates was influenced by static and rolling contact angles. In addition, a water droplet's rebounding coefficient depended on the rolling inclination angle; in this case, a higher inclination angle revealed a smaller coefficient of rebounding of the water droplet (Yeong et al., 2014). The adhesion energy is essential in determining how water droplets roll on superhydrophobic flat substrates. As the contact area between the hydrophobic surface and the water droplet changes, so does the three-phase contact line. However, the use of adhesion in predicting droplet mobility on inclined superhydrophobic surfaces is limited. Even though there is a significant difference in water droplets' receding and advancing profile on hydrophobic surfaces, superhydrophobic substrates behave differently (iMcHale ,2004). The force required to roll water droplets on hydrophobic surfaces is higher than on superhydrophobic surfaces. Despite this, droplet sliding occurs along with rolling, which affects the rolling dynamics iMcHale, 2004). Therefore, a control system for sliding direction is necessary for self-cleaning applications (iMiwa, 2000). This study analyzes the dynamics of droplets on surfaces for self-cleaning applications using analytical and experimental methods. The study evaluates the influence of environmental dust on water droplet dynamics and the amount of dust particles collected by the water droplet on inclined hydrophobic surfaces. The collected dust particles are analyzed using analytical tools before the experiments. The high-speed camera assesses droplet sliding and rolling motions on superhydrophobic surfaces.

2. EXPERIMENTAL PROCEDURE

Environmental dust that settled on the top surfaces of PV panels was collected manually using soft brushes from the Laboratory of renewable energy near the Arabian Gulf in Dhahran City. Using analytical tools, environmental dust particles were analysed based on elemental composition, shape, size, and weight. These analytical tools include X-ray Diffraction (XRD), Energy Dispersive Spectroscopy (EDS), and Scan Electron Microscopy (SEM). 70 mm $\times$ 25 mm $\times$ 2.5 mm polycarbonate sheet was used as the substrate. The sheet was cleaned ultrasonically and crystallized by acetone (immersing for three minutes) to generate a hierarchical structure on the surface. After several examinations, a 60% acetone concentration (by volume) has been selected in line with published work (Yilbas et al., 2016). In addition, the contact angle hysteresis is reduced by depositing silica nanoparticles on the top of the crystallized substrate, generating a louts effect on the hydrophobic substrate. Ammonium hydroxide, isobutyltrimethoxysilane (OTES), tetraethyl orthosilicate (TEOS), and ethanol have been used for silica synthetization. The crystallized hydrophobic surface was cleaned with distilled water and piranha solution before depositing silica Nanoparticles. The solvent casting method has been used for the deposition process. After solvent evaporation under vacuum, the produced surface has a dynamic water contact angle of around 160° and 2° hysteresis.

Analytical tools were utilized to characterize the hydrophobic surface. FESEM, EDS, AFM, and XRD were used to examine environmental dust and the modified hydrophobic cover. An auto-dispensing device with a 0.1 µL step controls the droplet volume. The collected dust particles were uniformly distributed on the polycarbonate superhydrophobic surface. A metallic stand was designed with a protractor to control the inclination angle of the hydrophobic substrate. In addition, a high-speed camera (Dantec Dynamic- Model: Spd-Sns-9040) was incorporated to track the water droplet dynamic on the clean/dusty hydrophobic surface in slow motion mode (up to 1000 frames/sec). The optical properties (transmittance and absorbance) were evaluated using a UV spectrophotometer (Jenway, UK).

3. RESULTS AND DISCUSSION

Water droplet dynamics with different volumes and inclination angles with and without settled dust particles were examined for self-cleaning applications.

3.1. Surface Texture and Dust Mechanics

Figure 1 shows the scanning microscope image of a polycarbonate with a hierarchical structure. A crystallized polycarbonate surface with a hierarchical microstructure was produced, and the red arrows show a whisker-like structure on the surface. The modified silica nanoparticles are placed on top of the crystallized polycarbonate to decrease the hysteresis of the contact angle. Condensation on the silica surface and some side reactions result in agglomeration of the modified silica nanoparticles, as shown in Figure 2.

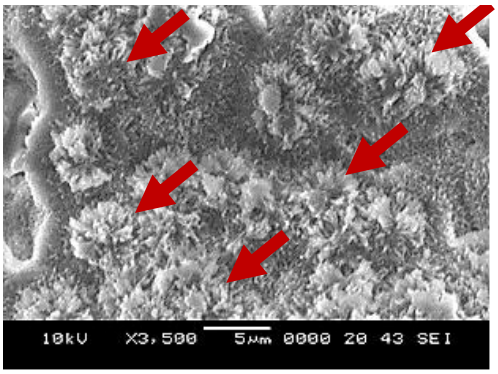

Figure 1 A crystallized polycarbonate surface with a hierarchical micro-structure on SEM. Red arrows show a whisker-like structure on the surface

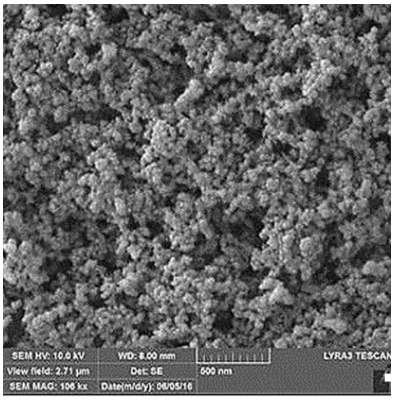

Figure 2 The polycarbonate surface with silica nanoparticles

Figure (3) shows the various sizes and shapes of the settled dust particles. In addition, the dust particles were collected manually in the Dhahran region, Saudi Arabia. Due to the electrostatic charges, small dust adheres to the large particles, as shown in the SEM micrograph (Figure (3)). The long-time exposure of the dust particle to solar radiation will increase its static charging (Wagner et al. 2009). The present study is conducted close to Arabian Gulf in the Kingdom's eastern region, where the relative humidity and temperature remain high. Therefore, these conditions facilitate the formation of natural mud that sticks to the panel surface and becomes difficult to remove. The dust's geometric features can be evaluated by aspect ratio (Equation 1) and shape factor (Equation 2). Hence, the aspect ratio and shape factor representations can be written as:

Equation 2: Aspect ratio

$$A_{Aspect} = \frac{\pi\left(L_{proj}\right)^2}{4A}$$

Equation 2: Shape factor

$$R_{Shape} = \frac{P^2}{4\pi A}$$

Where:

- L_{proj} = extended projection length (m)
- A = cross-sectional area (m^2)
- P = the perimeter of a dust particle (m)

A mathematical relationship was formulated between the aspect ratio and shape factor. The aspect ratio represents the particle roundness, while the shape factor represents the axes ratio of an ellipsoid that fits the dust particle. Therefore, the particle's shape factor increase as the aspect ratio decrease. However, the shape factor of relatively small dust particles less than 2 µm approaches unity while larger particles more than 10 µm approach 3.

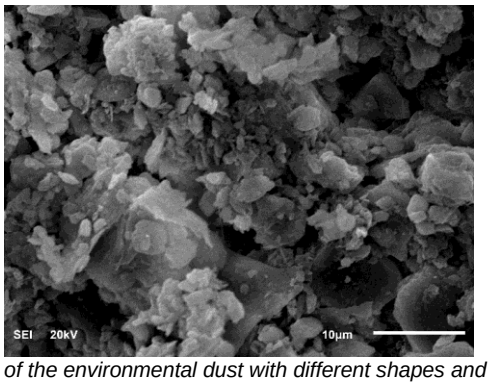

Figure 3 Image of the environmental dust with different shapes and sizes on SEM

Analytical tools characterize the settled dust particles and the formed mud layer. The EDS data presented in Table 1 shows different elements that are contained by dust particles, such as Mg, Si, Na, Ca, K, S, Cl, O, and Fe. The presence of Cl reveals that environmental dust particles include some salt compounds while the oxygen presence indicates the presence of oxide compounds. In addition, XRD analysis is conducted to dust and formed mud layers. The results shown in Figure 4 revealed the presence of salt compounds because of peaks corresponding to Na, K, Fe, and Cl.

Table 1: The elemental composition data for the settled environmental dust particles

Element	C	Na	Mg	Al	Ca	Si	K	O
Wt%	16.7	7	2.1	1.4	8.2	24.9	2.5	BAL

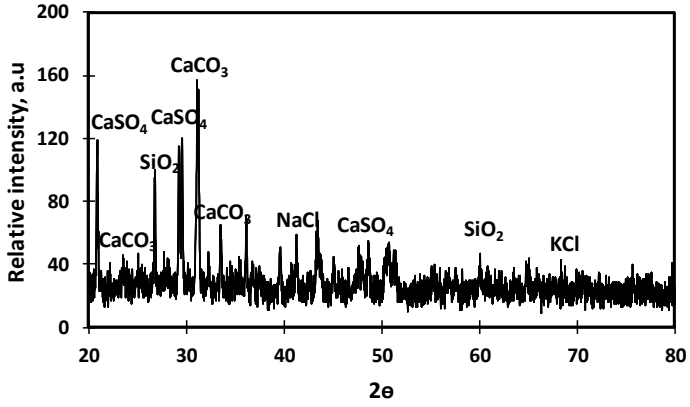

Figure 4 XRD diffractogram of the collected environmental dust

3.2. Droplet dynamics

The inclination angle and hysteresis of the contact angle of superhydrophobic surfaces affect the water droplet contact line dynamics. Higher hysteresis of the contact angle revealed higher attachment into the superhydrophobic surface because of the high adhesion force (Tuck and Schwartz, 1991). In addition, when the frictional and adhesion force becomes lesser than the gravity, the water droplet can slide/roll on the inclined superhydrophobic surfaces. Droplet size and inclination angle are critical in determining the droplet geometrical changes and bulging. Therefore, the droplet can roll and slide with a spherical shape for a relatively low capillarity length. The capillarity length (Equation 3) is the scaling factor between surface tension and gravity that can be written as:

Equation 3: capillarity length of the water droplet.

$$\kappa^{-1} = \sqrt{\frac{\sigma}{\rho g}}$$

Where:

- κ^{-1} = capillary constant (m)
- g = gravity (m/s^2)
- σ = surface tension (N/m)
- ρ = fluid density (kg/m^3)

The net force defines the acceleration of the water droplet (Equation 4). The droplet can roll/slide with continuous changing on the droplet centre of mass for a more considerable capillarity length due to high adhesion force. On the other hand, the

droplet undergoes elastic deformation during the motion on the inclined superhydrophobic substrate. The diagram force balance for droplets on the inclined superhydrophobic flat surface is shown in Figure (5).

Equation 4: The net force balance for water droplet dynamic. $$mg\ sin\ \delta - F_{ad} - F_{\tau} - F_f - D_a = \frac{2}{5}mR\omega^2$$

Where:

- δ = inclination angle (degree)
- g = gravity (m/s^2)
- m = mass of droplet (kg)
- R = radius of rotation (m)
- ω = rotation velocity (rad/s^2)
- D_a = air drag force(N)
- F_f = frictional force(N)
- F_{τ} = shear force (N)
- F_{ad} adhesion force

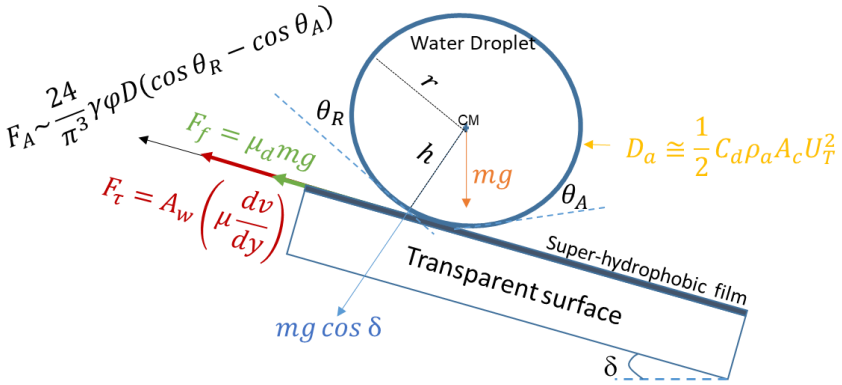

Figure 5 The force balance diagram for a droplet of water on the inclined superhydrophobic surface

The formulation of these forces is summarized in Table 2. The frictional force is explained in terms of the friction coefficient and normal force of the surface. The friction coefficient (μ_f) is obtained from AFM frictional mode and was around 0.03. The adhesion force was formulated early by Pilat et al. (2012). The three-phase contact line position established a polynomial function based on experimental data. Later, a roughness parameter was added to the polynomial function to express the effect of surface texture. In addition, the shear force is estimated based on the fluid strain rate developed at the interface between the superhydrophobic substrate and the water droplet. Where A_w represents the area of contact, (is the fluid's viscosity, and V is flow velocity. While rolling water droplets, the air resistance causes a drag force. A simplified model of the drag force was reported by Mccormick (1995).

Table 2: The forces influencing the water droplet during steady rolling

Definition	Equation
Frictional force	$F_f = \mu_d mg$
Adhesion force	$F_A \sim \frac{24}{\pi^3}\gamma\varphi D(cos\ \theta_R - cos\ \theta_A)$
Shear force	$F_\tau = A_w\left(\mu\frac{dv}{dy}\right)$
Air drag force	$D_a \cong \frac{1}{2}C_d\rho_a A_c U_T^2$
Total force	$F_{tot} = F_f + F_{ad} + F_\tau + D_a$

In this case, the energy balance of the water droplet on an inclined superhydrophobic substrate allows the water droplet velocity formulation to be (Equation 5):

Equation 5: the water droplet velocity formulation. $$V = \sqrt{2g\left[\begin{array}{c}\Delta L\sin\delta - \mu_f \Delta L - \frac{24}{\pi^3 mg}\Upsilon_L D f \Delta L(\cos\theta_R - \cos\theta_A) \\ -\frac{4\gamma_L}{\rho g \Delta L}\left(\frac{D_{h_1}-D_{h_2}}{D_{h_1}D_{h_2}}\right) - \frac{1}{mg}A_w\left(\mu_t\frac{dV_f}{dy}\right)\Delta L - \frac{1}{2g}K_L U_T^2\end{array}\right]}$$

Where:

- V= translational velocity of flow (m/s)
- ΔL = translational distance (m)
- μ_f = coefficient of friction (N/m^2)
- γ_{LV} = surface tension (N/m)
- f = solid substrate fraction
- D= droplet diameter (m)
- θ_R, θ_A = receding and advancing angle (degree)
- D_h = instant hydraulic diameter (m)
- Aw= area of contact (m^2)
- μ_t= viscosity of droplet (N/m^2)
- V_f = droplet velocity (m/s)
- K_L= drag loss coefficient
- y= position from the contact surface (m)
- U_T= tangential velocity (m/s)

The predicted translational velocity obtained from the above equation and the measured translational obtained from the experiment of 40µL water droplet on 1^{o} inclined hydrophobic surface are presented in Figure 6. A drastic increase is observed at the beginning of droplet motion then the increasing rate reduces gradually. This can be attributed to energy dissipation due to wobbling, air drag, and adhesion of water droplets. Figure 6 provides a good agreement between the measured and predicted translational velocities. However, minor discrepancies are observed due to the sizeable wobbling scale, which results in more droplet deformation and high energy dissipation. It should be noted that uncertainty analyses were carried out, and the experiments were repeated ten times to ensure a 95% confidence level in line with the early work (Coleman and Steele, 1989). The uncertainty (U) is determined from the precision (U_p) and bias (U_B) uncertainties through $U = \sqrt{U_p^2 + U_B^2}$. The calculations reveal that the experimental uncertainty is about 5%.

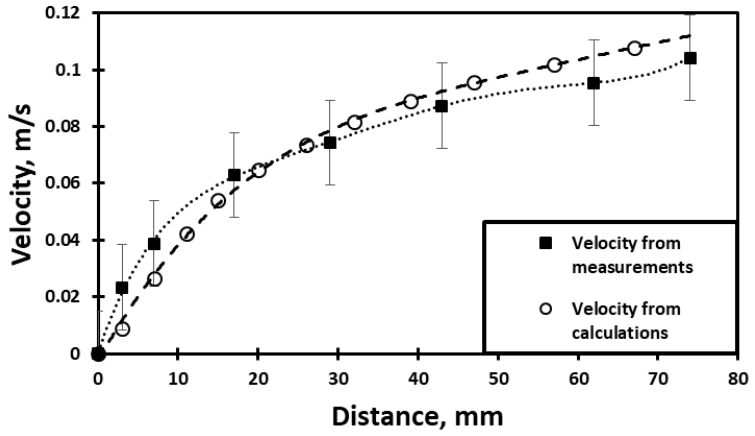

Figure 6 The predicted and measured translational velocity for 40µL and 1˚ inclination angle.

Figure 7 shows the Froude number relation with the droplet position along an inclined superhydrophobic surface. Hence, the Froude number (Fr) (Equation 6) is the ratio between the inertia and the gravitational force.

Equation 6: Froude number. $$\mathrm{Fr} = \frac{\mathrm{V}}{\sqrt{\mathrm{gL}}}$$

Where:

- V= translational velocity (m/s)
- L =distance (m)
- g= gravity (m/s^2)

The Froude number decreases with increasing the distance on the inclined superhydrophobic surface due to the gravity influence from Figure (7a). Despite the adverse effects of the droplet weight on the Froude number, the Froude number increases with larger droplet sizes and inclination angles due to the higher droplet inertial force. Therefore, the influence of droplet acceleration is more significant than gravitational acceleration in determining the dynamics of a droplet on a hydrophobic surface. In addition, the Weber number is presented in Figure (7b). Weber number (We) is the ratio of the fluid's inertia over its surface tension (Equation 7).

Equation 7: Froude number.

$$\mathrm{We} = \frac{\rho \mathrm{L} \mathrm{V}^2}{\gamma}$$

Where:

- γ air to liquid surface tension(N/m)
- ρ fluid density (kg/m^3)

The Weber number shows an increase with the inclination angle and droplet volume along the inclined hydrophobic surface due to the low surface free energy of the surface. However, the Weber number does not exceed the maximum critical value to cause droplet breaking on the inclined surface (Tarnogrodzki, 1993).

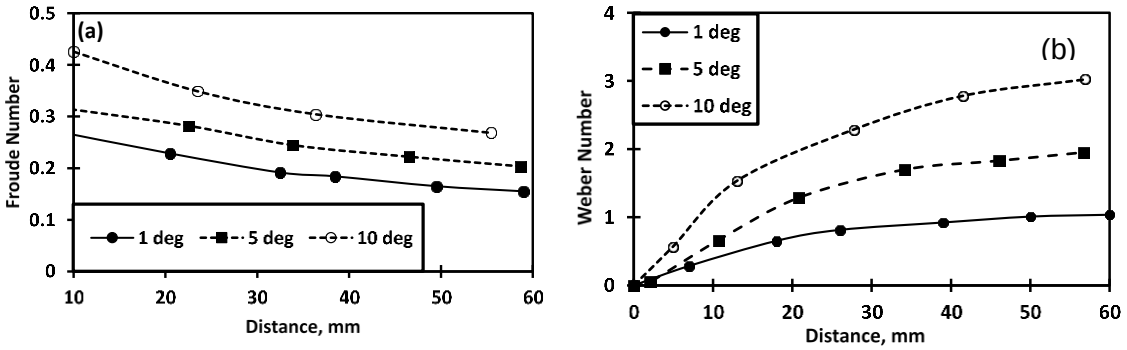

Figure 7 a) Froude number and b) Weber number for droplets on superhydrophobic

3.3. Removal of Dust from a superhydrophobic surface

The optical transmittance of the clean and dusty surface is shown in Figure 8. The transmittance reduction ratio for the clean and dusty hydrophobic surface is also provided in Figure 8. The ratio is determined from the transmittance profile of as received surface over the dusty surface. The significant difference in optical properties between the clean and dusty surfaces indicates the energy recovery obtained by self-cleaning for such solar energy applications.

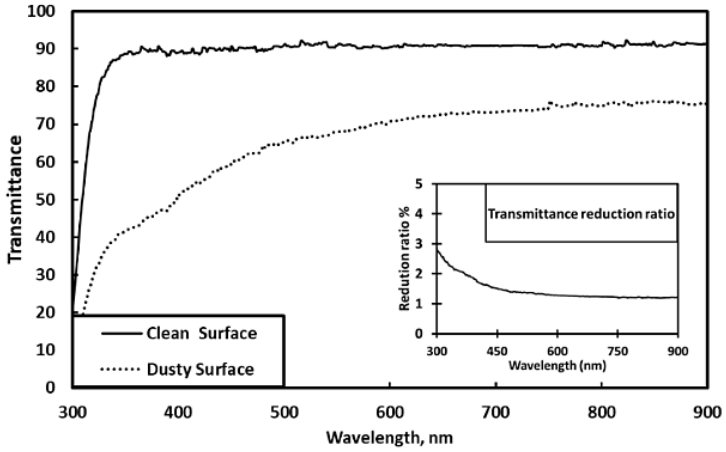

Figure 8 The optical transmittance of the clean and dusty surface

Figure 9 shows the behaviour of droplet translational velocity with different droplet volumes and inclination angles on dusty hydrophobic surfaces. The data in the figure are obtained from slow-motion recording using a high-speed camera. The water droplet motion for clean surface data is plotted for comparison. It can be observed that droplet velocity reduces in the dusty region compared with the clean region due to the adhesion and friction on the inclined hydrophobic surface. Therefore, environmental dust creates frictional resistance and increases the water droplet's weight. Moreover, the hydrophobic surface properties change in dust particles' presence and influence the wetting

state. Generally, it is observed that the water droplet velocity is more sensitive toward the inclination angle than the droplet volume.

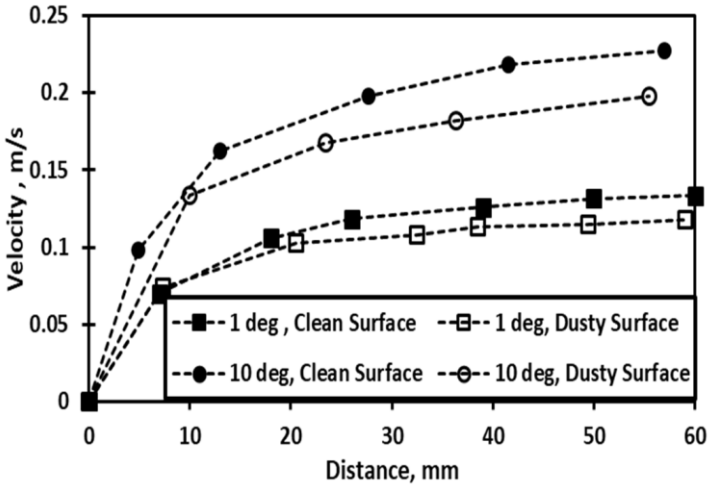

Figure 9 The water droplet velocity on dusty/clean surfaces for different inclination angles

Figure 10 shows a 3-D optical of a water droplet track on the dusty inclined superhydrophobic surface. A 3D image has been taken before (dusty) and after (clean) the droplet movement. Image J's image processing software estimates the cleaned area on the droplet path. It is observed that around 95% of dust particles have been removed from the top surface by the droplet. It should be noted that the percentage of the dust particles removed was based on the area cleaned (removed from the surface) by the droplet after examining the 3D optical images of the droplet path. Hence, 95% cleaning represents where the droplet removes dust particles. The oscillatory appearance along the water droplet track can be attributed to the wobbling during droplet motion. Some dust residuals are observed by closely examining the droplet's 3-dimensional path. The observed dust residuals are lighter than the original dust particles. The SEM examination revealed that dust residuals consist of relatively small particles (≤ 2 µm); therefore, they become difficult to pick by the droplet due to high adhesion. The optical 3D images of water droplets before and after the cleaning process are shown in Figure 11. It was observed that the droplet of water cloaks the accumulated environmental dust while rolling/sliding on the inclined superhydrophobic substrate. The environmental dust picked up by the droplet has been wetted and clocked before the rolling cycle. Therefore, the primary dust removal mechanism is the water-cloaking of the dust particles (Hassan, 2019).

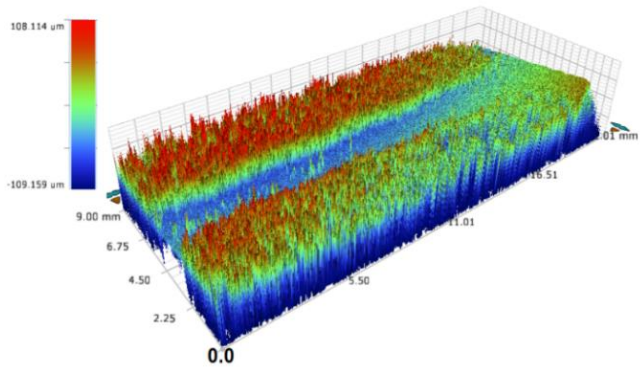

Figure 10 3D image of the droplet track on the dusty superhydrophobic substrate

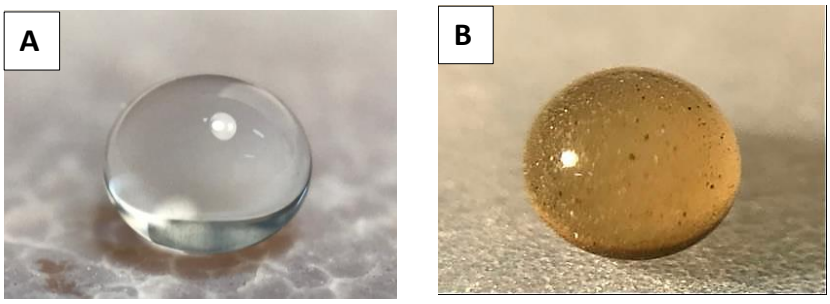

Figure 11 Optical images of water droplets: a) clean and b) dusty

4. CONCLUSION

Environmental dust was collected locally in Dhahran, KSA. The collected dust contains several elements: Mg, Si, Ca, K, Na, S, O, Cl, and Fe. A polycarbonate flat sheet is used as the substrate to examine the water droplet dynamic. Acetone crystallization and functionalized silica nanoparticle deposition are applied to modify the surface characteristics toward the hydrophobicity effect. An improved droplet contact angle around (160o ± 2º) and 2º hysteresis of the contact angle is observed on the crystallized hydrophobic substrate. The optical characteristics of the produced hydrophobic surface are evaluated using the optical UV transmittance. It was observed that the optical transmittance was reduced by 30% on the dusty surface. Water droplet dynamics with different volumes and inclination angles with/without dust particles are compared concerning self-cleaning applications. The translational velocity is predicted numerically and measured experimentally for dusty and clean surfaces. The results revealed good agreement between the predicted and measured results. The translational velocity of the water droplet increases with increasing the inclination angle and droplet volume due to the force balance. Gravitational, frictional, adhesion and air drag forces influence the transverse velocity. The accumulated dust has significantly influenced the hydrophobicity and the optical properties of protective surfaces. Thus, the presence of dust particles influences the water droplet mobility. However, few dust particle residuals settled on the droplet path due to its size and chemical nature. In addition, the cloaking of the droplet of environmental dust is the primary mechanism associated with removing environmental dust, which is faster than the water droplet's resident time on the inclined superhydrophobic substrate across the wetting length.

5. ACKNOWLEDGEMENT

The authors acknowledge the financial support of IRC Renewable Energy and Power System at King Fahd University of Petroleum and Minerals (KFUPM) through Projects # INRE2115 and King Abdullah City for Atomic and Renewable Energy (K.A. CARE) to accomplish this work.

6. REFERENCES

Alnaser,W., Al Othman,M., Dakhel, A., Batarseh, L., Najma, S., Alothman, A., Al Shawaikh, and Alnaser. W. (2018) 'Comparison between performance of man-made and naturally cleaned PV panels in a middle of a desert' Renewable and Sustainable Energy Reviews,82, pp.1048-1055.

Benghanem, M., Almohammedi, A., Taukeer K., and Al-Mashraqi. A. (2018) 'Effect of Dust Accumulation on the Performance of Photovoltaic Panels in Desert Countries: A Case Study for Madinah, Saudi Arabia', International Journal of Power Electronics and Drive Systems, 2088 (8694), pp. 1357.

Coleman, H. and Steele, W. (1989) 'Experimentation and Uncertainty Analysis for Engineers', John Wiley and Sons, New York.

Conceicao, R., Gonzalez-Aguilar, J., Merrouni, A.A. and Romero, M., (2022) 'Soiling effect in solar energy conversion systems: A review', *Renewable and Sustainable Energy Reviews*, *162*, p.112434.

Ding, S., Xiang, T., Li, C., Zheng, S., Wang, J., Zhang,M., Dong, C. and Chan, W. (2017) 'Fabrication of self-cleaning superhydrophobic nickel/graphene hybrid film with improved corrosion resistance on mild steel', Materials and Design, 117, pp. 280-288.

Ghazi, S., Ali, S., and Kenneth, I. (2014) 'Dust effect on flat surfaces – A review paper', Renewable and Sustainable Energy Reviews,33, pp. 742–751.

Hasan, K., Yousuf, S.B., Tushar, M.S.H.K., Das, B.K., Das, P. and Islam, M.S., (2022) 'Effects of different environmental and operational factors on the PV performance: A comprehensive review', *Energy Science & Engineering*, *10*(2), pp.656-675.

Hassan, G., Yilbas, B., Al-Sharafi, A. and Al-Qahtani, H. (2019) ' Self-cleaning of a hydrophobic surface by a rolling water droplet', Nature: Scientific Report, 9, pp. 5744.

Jiang, Y., Lin, L., Andrea, R., and Goodarz, A. (2018) 'Analyzing wind cleaning process on the accumulated dust on solar photovoltaic (PV) modules on flat surfaces', Solar Energy, 159, pp. 1031-1036.

Liu, H., Huang, J., Chen, Z., Chen, G., Zhang, K., Al-Deyab, S. and Lai, Y. (2017) ' Robust translucent superhydrophobic PDMS/PMMA film by facile one-step spray for self-cleaning and efficient emulsion separation', Chemical Engineering Journal, 330,pp. 26-35.

Lomga, J., Varshney, P., Nanda, D., Satapathy, M., Mohapatra, S. and Kumar, A. (2017) 'Fabrication of durable and regenerable superhydrophobic coatings with excellent self-cleaning and anti-fogging properties for aluminium surfaces', Journal of Alloys and Compounds,702, pp. 161-170.

Mahadevan, L. and Pomeau, Y. (1999) ' Rolling droplets', Physics of Fluids,11, pp. 2449-2453.

McCormick, B. (1995) ' Aerodynamics, aeronautics, and flight mechanics', John Wiley and Sons Inc.

McHale, G., Neil, S., and Newton, M.(2004) 'Contact-angle hysteresis on superhydrophobic surfaces', Langmuir, 20(23), pp. 10146–10149.

Mekhilef, S., Rahman, S., and Kamalisarvestani, M. (2012) 'Effect of dust, humidity and air velocity on efficiency of photovoltaic cells',Renewable and Sustainable Energy Reviews, 16 (5), pp. 2920–2925.

Miwa, M., Akira, N., Akira, F., Kazuhito,H., and Toshiya, W. (2000) 'Effects of the surface roughness on sliding angles of water droplets on superhydrophobic surfaces', Langmuir, 16(13), pp. 5754-5760.

Pilat, D., Papadopoulos, P., Schaffel, D., Vollmer, B. and Butt, H. (2012) 'Dynamic measurement of the force required to move a liquid drop on a solid surface', Langmuir, 28(49), ,pp. 16812-16820.

Rajput, D. and Sudhakar, K. (2013) 'Effect of dust on the performance of solar PV panel', International Journal of ChemTech Research, 5(2), pp. 1083–1086.

Said, S., Hassan, G., Walwil, H. and Al-Aqeeli, N. (2018) 'The effect of environmental factors and dust accumulation on photovoltaic modules and dust-accumulation mitigation strategies', Renewable and Sustainable Energy Reviews, 82(1), pp. 743-760.

Stephane, D., Terwagne, D., Vandewalle, N. and Gilet, T. (2008) 'Resonant and rolling droplet', New Journal of Physics,10(11), pp. 113021 – 113030.

Tarnogrodzki (1993) 'Theoretical prediction of the critical Weber number', International journal of multiphase flow, 19 (2).32

Tuck, E., Schwartz, L. (1991) 'Thin static drops with a free attachment boundary', Journal of Fluid Mechanics, 223, pp. 313-324.

Vedulla, G., Geetha, A. and Senthil, R., (2023) 'Review of Strategies to Mitigate Dust Deposition on Solar Photovoltaic Systems', *Energies*, *16*(1), p.109.

Wagner, F., Daniele, B., Sergio, P., Maria, J., Costa, A., Maria, S., Bernadett, W. and Michael, E. (2009) 'Properties of dust aerosol particles transported to Portugal from Sahara desert', Tellus B: Chemical and Physical Meteorology, 61(1), pp. 297–306.

Yeong, Y., James, B., Eric, L., and Ilker, S. (2014) 'Drop impact and rebound dynamics on an inclined superhydrophobic surface' Langmuir, 30(40), pp. 12027–12038.

Yilbas, B., Ali, H., Al-aqeeli, N., Khaked, M., Abu-Dheir, N. and Varanasi, K. (2016) 'Solvent Induced Crystallization of a Polycarbonate Surface and Texture Copying by PDMS towards Improved Surface Hydrophobicity', Journal of Applied Polymer Science, 133(22), pp. 43467.

Yilbas, B., Ali, H., Khaled, M., Al-Aqeeli, N., Abu-Dheir, N. and Varanasi, K. (2015) 'Influence of dust and mud on the optical, chemical, and mechanical properties of a pv protective glass' Scientific reports, 5, pp. 15833.

#18: Remote monitoring unit for solar home systems

A Field Trial

Matthew LITTLE[1], Richard BLANCHARD[2]

[1] CREST, Loughborough University, UK, M.E.Little@lboro.ac.uk
[2] CREST, Loughborough University, UK, R.E.Blanchard@lboro.ac.uk

Abstract: Solar home systems (SHS) can be utilised for electrification of areas for the 770 million people worldwide which do not have connection to a national electricity grid. SHS, comprised of a solar photovoltaic panel, charge controller, battery, and appliances, provide small amounts of power for household items such as charging phones, LED lights, radios, and televisions.

The practical implementation of SHS in, typically, remote rural locations make asset monitoring, operation and maintenance of these systems difficult. For example, in one programme over 30 % of SHS implemented had some form of fault reported within the first 12 months of operation. This impacts the economics and reputation of the SHS supplier and is highly inconvenient to the user. However, the faults were difficult to analyse, as their symptoms were reported verbally in varying levels of detail.

The ability to remotely monitor these systems in real time could help to improve their long-term performance and allow pre-emptive maintenance to be performed. Knowledge of the actual solar power generation and load provision on these systems helps a SHS supplier manage their assets and could help with the future development of lower cost and more efficient SHS.

This paper introduces the design of a low-cost low-power data-logging device for remote monitoring of SHS. The logging unit monitors voltage, current, power and temperature sensors, stores this data locally and sends it to a cloud-based store, either using Wi-Fi or General Packet Radio Service (GPRS). The system can be installed in any area with GPRS reception or Wi-Fi and monitored from anywhere with an internet connection. The data is presented in interactive graphs and maps via an Internet of Things (IoT) web dashboard.

Data from field trials of the remote monitoring unit on solar power systems in Zambia, Malawi and the UK is presented. This shows key issues, such as low battery state of charge, that can be used to inform customers when to reduce their loads and charge the battery.

Keywords: Monitoring, Remote Data-logging, Solar Home Systems, Solar Photovoltaics.

1. INTRODUCTION

This paper presents the design of a data-logging unit for monitoring solar home systems in remote areas, along with field trail data from prototype implementation. The aim of the data-logging unit is to monitor solar home systems for both usage profiles and for long-term operation and maintenance.

Solar home systems (SHS) can be utilised for electrification of areas which do not have connection to a national grid. At present around 770 million people worldwide do not have access to electricity, around 10% of the world's population, with 550 million of those without access located in sub-saharan Africa (International Energy Agency, 2021). SHS, comprised of a solar photovoltaic panel, charge controller, battery, and appliances, provide small amounts of power for household items such as charging phones, LED lights, radios, and televisions. Larger solar power systems can be used for providing productive uses of energy (PUE), such as refrigeration, water pumping, or supplying power to any economic activity.

In one implementation programme, over 300 SHS were installed in Tanzania with a "PayAs You Go" (PAYGo) repayment scheme. Over 30 % of these systems had some form of fault reported within the first 12 months of operation, which impacts the economics and reputation of the installation organisation and SHS supplier and is a great inconvenience to the user. The faults were difficult to analyse, as their symptoms were reported verbally in varying levels of detail. An overview of the faults from the verbal log from this SHS implementation programme is given in Figure 1. 95 of the 144 reported faults were related to the technical operation of the system, rather than human-related (such as payment) or physical issues (such as broken fixings) (Africa Power Ltd, Fault Log, Personal Communication, 29/11/2019). This highlights that long-term device monitoring would give essential information relating to the operation and maintenance of these systems. Finding the source of these problems requires knowledge of system parameters prior to the fault occurring. Knowing the battery voltage and temperature would help show if the battery is performing as per the specifications. Knowing the currents within the system would help understand issues relating to the solar input, charge controller and output loads. If these parameters are out of the normal operating range, pre-emptive maintenance can be performed.

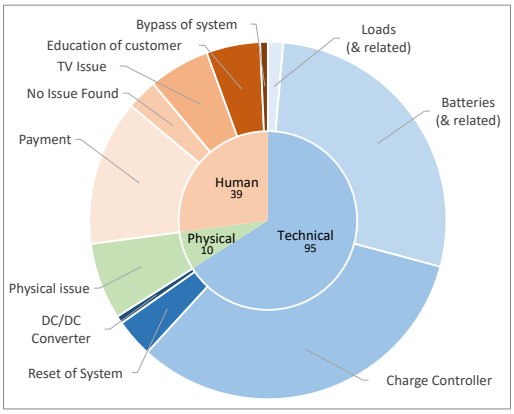

Figure 1 Analysis of 144 verbally reported faults

Load profiles show how much power is required by the load at a particular time. Load requirements on SHS vary on daily, monthly, and seasonal cycles. Load profiles are used to calculate the energy required by the system and hence size power supply systems, both for the solar photovoltaic panel size and any energy storage system. When designing a power supply system, accurate load profiles are required as they will affect either the system reliability if too small, or the system economics if too large. Finding load profile information for SHS and PUE systems in remote rural locations is difficult, as few systems are monitored or, if they are monitored, the data is not readily available. The monitor presented here will provide the time of use and power level throughout the year, so real-world load profiles can be analysed, and provide peak currents and temperatures for future SHS design improvements.

To monitor SHS in the field, this remote monitoring system has been developed both for operation and maintenance, for the organisation supplying the equipment, and to obtain data on typical real-world load profiles for SHS, for future research and development. This monitoring system can also be used to monitor prototype solar power systems supplying productive uses of energy (PUE), such as refrigerators and water pumping systems, and can provide data relating to their real-world operation. The primary initial application of this unit was to monitor solar home systems (SHS) in Zambia.

2. EXISTING SOLUTIONS

SHS are difficult to monitor as they are typically low power and used in remote areas without grid electricity or internet connectivity, although in most areas mobile phone reception is available. The main requirements for this application are low cost, low power, good accuracy, simple to install & configure, easy access to the data and, if possible, open-source design files and firmware. With regards to the best practice standards for monitoring photovoltaic system performance, the main reference is BS EN IEC 61724.

There are many stand-alone data loggers available, with a small sample given in Alphatemp Tech (2021), Comark (2021), DATAQ Instruments (2021), & Measurement Computing (2021). These units are typically relatively high cost ($250 to $4,000) and would require additional sensors for logging the DC current and voltage, and bespoke enclosures for implementation in the field. Their designs are usually not open source, so their design cannot easily be adjusted for different applications and data download may require proprietary services.

Many solar home system providers are including remote monitoring systems within their products. This helps to them analyse use and hence payment for the system, and it also helps investigate faults and potentially highlight maintenance issues. Bboxx have the 'Pulse' remote monitoring system (Bboxx, 2022), Connected Energy provide 'last mile ICT', which includes a cloud-connected solar charge controller (Connected Energy, 2023). These systems are proprietary, they are usually built into specific products and the data obtained is commercially sensitive, so is not typically shared in detail.

Many non-commercial monitoring units have been designed for use on off-grid solar power systems, with a review of some of these designs given in Kumar, Prajapati and Tiwari (2020). Gupta (2018) covers the considerations and design of a low-cost ESP32-based data logger for pico-solar systems, although their unit only connects to Wi-Fi and is only designed to measure one current and voltage. Fanourakis et al. (2017); Hadi et al.(2018) and Singh and Thakur (2019) all present low-cost data acquisition devices to measure current, voltage & temperature based on the ATMega328P microcontroller, although these units only store to an SD card and are not remotely connected. Singh and Thakur (2019) does have a Bluetooth connection for accessing the data via a mobile device, but that must be within range of only a few meters. The design presented by Shuvo et al. (2019) uses the Arduino Mega, based on the ATMega2560 microcontroller, and measures three sets of current and voltages, but again, does not have any remote connectivity options. Lopez-Vargas et al. (2019) present a remote area data-logging system using hall-effect current sensors, an Arduino UNO with ethernet connections. Remote data logging is provided using a 3G SIM-card based Wi-Fi router. This unit does cover most of the monitoring requirements, but the power consumption is high – running the router requires in the region of 5 - 10 W constantly and the hall effect sensors also have relatively high current requirements, in the region of 20 mA each. This would not be viable for measuring smaller SHS, which would be quickly discharged by the data-logging system load. Jiang and Iqbal, (2019) measures isolated PV systems with a radio connected weather station, although their system connects to a PC, so needs additional equipment and power. The monitoring unit presented by Wolfe (2015) re-uses older mobile phone technology but is not easily repeatable. Gupta et al. (2018) propose a remote metering system based on the Raspberry Pi low-cost computer, along with an analogue-to-digital converter (ADC) and using Wi-Fi for data connectivity. Due to the energy consumption of the Raspberry Pi and requirement for Wi-Fi, this is not suitable for smaller SHS. Saravanan and Lingeshwaran (2019) propose a solar PV monitoring system using an Arduino and Raspberry Pi, although it only monitors system voltages and does not specify the remote communications system. Kodali and John (2020) propose a design with an ESP8266 microcontroller and hall-effect current sensors. This system connects via MQTT to Amazon Web Services for data collection via Wi-Fi but does not have mobile phone network connectivity.

A previous data logging unit had been developed by the authors (Blanchard and Little, 2016), but it was developed for higher power systems (> 1 kW_p) and used hall-effect sensors for DC currents, which have high power consumption requirements. The online database for data storage from this unit is now obsolete. Learning from the design and implementation of the previous logger has help shape the design of the version presented here.

The designs reviewed here highlight the main features of a SHS datalogging system: measurement of battery voltage, current and temperature, as per BS EN IEC 61724, and storage of this data typically using a real time clock to an SD card. These systems are not commercially available, so they would need to be designed and built for each project and none cover the exact specifications required for this field trial, and the majority do not have the remote connectivity options required.

Recently low-cost, high-specification microcontrollers have dropped in price and improved in specification. For example, the ESP32 microcontroller from Espressif costs in the region of $4 - 6 (2023 price) and has an ultra-low power 32-bit processor with Wi-Fi and Bluetooth low energy and 384 kB of RAM & 384 kB of SRAM. Alongside this, free or low cost and open-source tools and libraries are readily available. The Arduino integrated development environment (IDE) is free to download and provides a simple environment to develop code applications, with many active developers providing open-source libraries and example code.

As none of the off-the-shelf options were suitable, a bespoke, data-logging unit for specific application to solar home systems was produced, with a brief design review given here. It is designed to provide accurate data for analysis of SHS use and operation, along with fault and condition monitoring, potentially providing pre-emptive maintenance. The design is highly configurable and can be readily adapted for other applications.

3. DEVICE OVERVIEW

An overview of the typical solar home systems to be monitored and the key sensors to include is given in Figure 2.

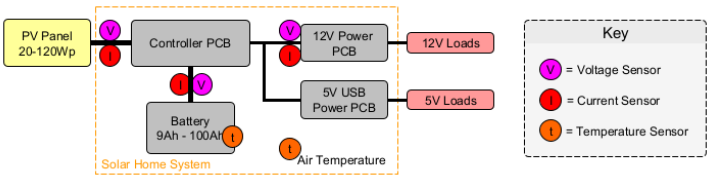

Figure 2 Overview of the solar home system and key sensor locations

The main functions of the logging device are to read the various sensors, average and convert the sensor values, record the values to a removable memory device with a timestamp, and send the data to an online cloud data store at regular intervals. To complete these tasks and ensure low power operation, the design was broken into two sections: a “sensor unit”, to handle regular reading and averaging of the sensor data, and an “upload unit” which ‘wakes up’ at regular intervals and records the data to an SD card and uploads the data to online cloud storage. These sections act independently but have a serial data communication connection. This means the data can still be monitored by the sensor unit while the upload unit sends data up to the cloud. The sensor unit can be swapped for different applications, without the additional expense of changing the upload unit. A block diagram overview of the monitoring unit is given in Figure 3 and the circuit boards shown in Figure 4.

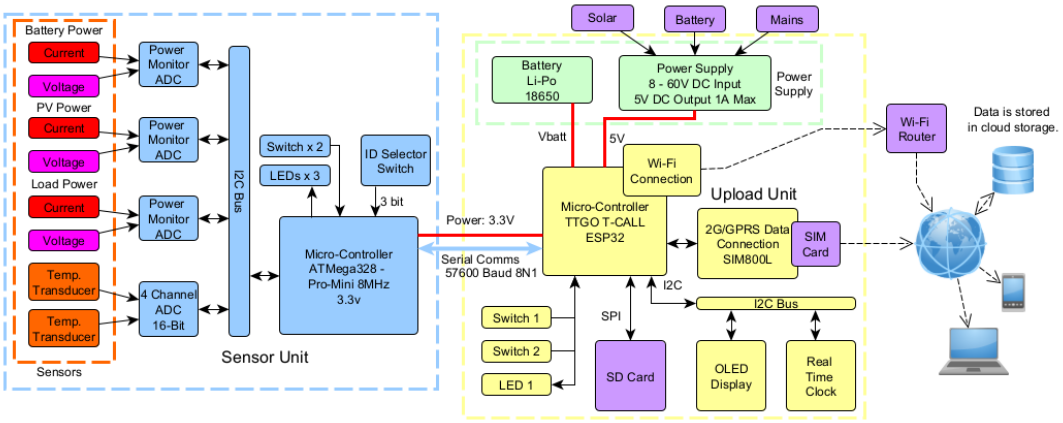

Figure 3 Overview of the monitoring units

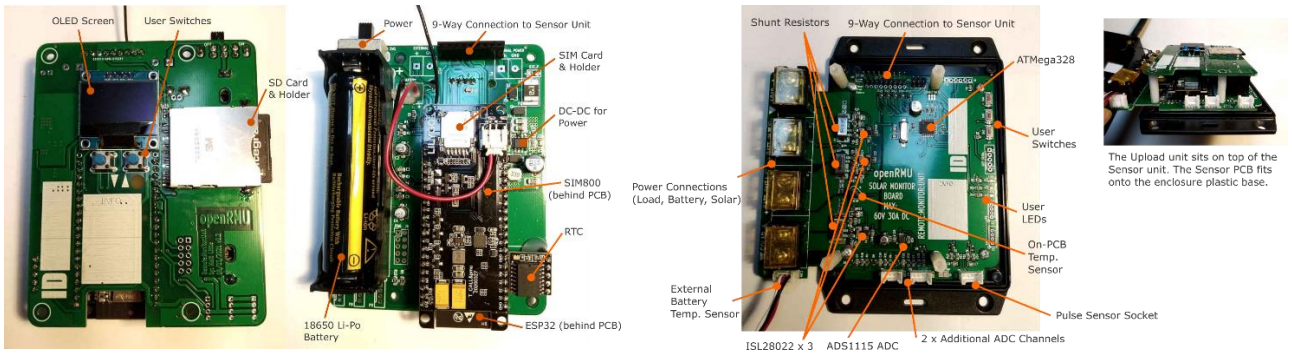

Figure 4 The upload unit (far left & left) and sensor unit (right & far right) with main features highlighted

The upload unit is the main controller for the system. It is mainly in ‘sleep’ mode, which conserves energy, and will only ‘wake up’ to store data to a .csv file on the SD card, upload data via Wi-Fi or General Packet Radio Service (GPRS) or display data when a button is pressed. The data stored includes the average value, along with the maximum and minimum values within the time interval. This can help with fault finding, for example highlighting if there was an over-current condition, when the average value would not have shown this. The upload unit is based upon an ESP32 micro-controller and a SIM800L GPRS module. Time is regulated with a DS3231 real time clock which is maintained at Universal Coordinated Time (UTC) either through connection to a time server on Wi-Fi or through the GPRS connection. A small OLED display and two user interface buttons are available to show information.

The control and operation of the upload unit is determined by a settings text file stored on the root of the SD card. When the upload unit wakes up it reads this settings file and bases the unit’s operation on those settings. The datalogger application logs data from several channels. For the upload unit firmware to convert raw data readings (e.g., analogue value or pulse counts) to physical values (e.g., voltage or temperature), each channel must be configured and converted. This configuration is done by writing a channels file, again a text file on the root of the SD card. The channels file allows the user to adjust the name of the channels and the order in which they are recorded. Each channel also has conversion factors that can be applied to calibrate the data. A full-size SD card is used to store the recorded data, along with the settings and channels information files.

The sensor unit is designed to be replaceable so different sensor units could be attached, but still communicate with the upload unit. The sensor unit was designed for this field trial to monitor the SHS, which included the solar PV information, the battery information, and any load information, along with some temperatures, as per Figure. The sensor unit is based on an ATMega328 microcontroller. This unit runs at 3.3V and utilises a serial connection at 57600 baud between the sensor unit and the upload unit. Each sensor board has a microcontroller and additional firmware. The initial sensor unit design includes three ISL8022 power monitoring ICs with shunt resistors to monitor power, voltage and current for three channels.

A 16-bit analogue to digital converter (ADC), the ADS1115, is used to measure two temperature sensors, with room for two more. The sensor unit firmware has been kept very simple, reading any attached sensors at regular intervals. It reports back the sensor values averaged over different time periods via the serial interface. The maximum and minimum values are also recorded. The max and min values are kept until they are read from the serial port, at which point they are reset. The sensor unit will sleep as much as it can between the tasks to conserve power but will wake up and respond to serial requests for the data as required.

The firmware for the upload and sensors units was written in C++, using the Arduino IDE to upload to the units. The PCB design has been produced using KiCAD, which is a fully open-source electronics design suite.

3.1. Data flow

This unit connects via Wi-Fi or a GPRS connection to upload data for cloud storage. For the initial deployment of devices, Microsoft Azure was chosen as the IoT device data cloud storage platform, although other data storage platforms can be used by altering the firmware on the upload unit. Within Azure, the 'IoT Central' application is used to control and display the data. Graphs can be displayed, and data downloaded for all the parameters recorded. A bespoke Azure function has been written to take the data from the GPRS connection and move it into IoT Central. This can also include adding custom timestamps, so data can be monitored and then batch uploaded. Data is stored into a 'cold' long term data store at very low cost. When new data arrives at IoT Central it is also added to a data 'stream' within Microsoft Power BI. Power BI allows visual data reports to be created for different clients and applications. These reports can be public facing, viewable on any browser, and can easily be included onto a website. An overview of the flow of data is given in Figure 5.

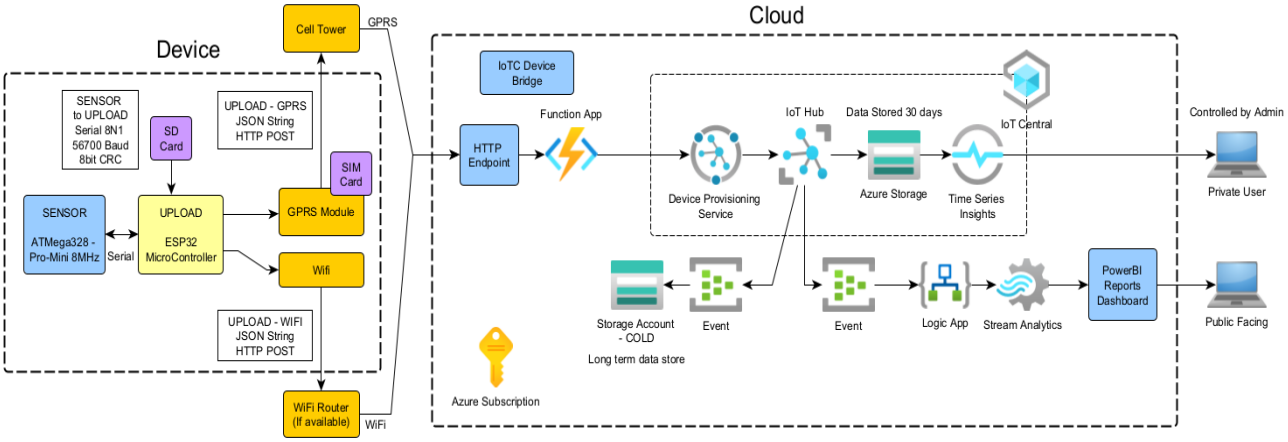

Figure 5 Data flow from monitoring unit to public and private facing online data access

3.2. Calibration & Validation

To calibrate and validate the data being recorded, each unit was powered with a BK 9205 power supply and was monitored using a GW Instek GPM8213 digital power meter and a LD400P programmable DC electronic load. Each logger unit was calibrated by comparing the logger value with the power meter value and adjusting the calibration settings on the logger SD card. Displayed data within 10 mA or 0.1 V of the measured data was regarded as a calibration pass. Once calibrated, sample units were validated with the logged data on the SD card was compared to the recorded data from the calibrated power meter. A current ramp was used to check the current readings. This was performed from 0 – 10 A for all three inputs (battery, load and solar). The current measured by this monitoring unit closely follows the calibrated power meter current. The difference between the monitored current and the lab test equipment was, on average, less than 9 mA, which is better than 0.1 % accuracy for a 10 A device. A voltage ramp was also performed, with no load applied, to see the accuracy of the voltage measurements, shown in Figure 6. The voltage measurements closely align with the calibrated test rig data, with an average difference of 2 mV, which is better than 0.01 % accuracy for a 30 V range.

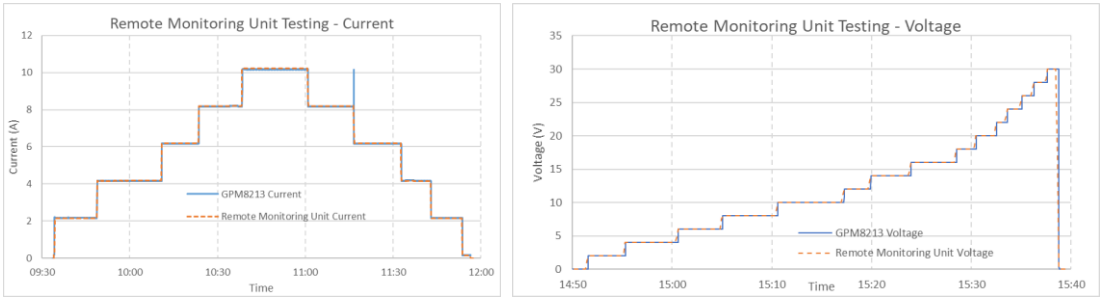

Figure 6 Comparison with calibrated test rig for current and voltage accuracy

SHS are designed to provide relatively small amounts of energy with battery banks in the range of 9 to 40 Ah, so high efficiency and low power is a requirement for any logging unit. Even small load currents may deplete the SHS battery quickly. The average current consumption of the logging unit presented here is 13.7 mA when writing data to the SD card every 10 seconds and sending data every hour. This is in a similar range to the current consumed by the controller board within the SHS, which used from 6 to 20mA continuously depending upon the SHS state. This could be reduced further by reducing the number of SD writes and reducing the display updates.

3.3. Device Cost

There are two costs associated with implementing these devices: the equipment cost and the ongoing monthly costs.

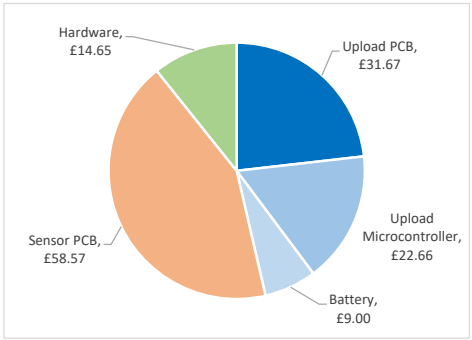

Figure 2 Logging unit equipment cost breakdown

The average equipment cost for the initial batch of 50 units was £136.55, although this did not include any construction costs. The PCB with surface mount components added was sourced from a manufacturer in China, with other items sourced or manufactured in the UK. Figure 7 shows a breakdown of the parts cost for the logger.

The ongoing monthly costs include the SIM card connection and data costs, the cost for Microsoft Azure services and the cost for the Power BI subscription. These costs will be highly dependent upon the amount of data recorded and the number of units installed. For the field trial implementation of 50 units with global SIM cards including 10 Mb data per month and a data upload rate of once per hour per unit, the total monthly cost was £2.81 per device.

If the SHS cost is greater than $600 and failure rates are higher than 15 % then the cost of this monitoring system is lower than the average equipment replacement costs and it would make economic sense to implement monitoring within these higher priced systems. For lower cost, smaller SHS, the monitoring equipment cost would be a large percentage of the total system cost and not economically viable.

4. FIELD TRIAL DATA

An initial batch of 50 units was manufactured for field trial installation. 42 monitoring units were shipped to Zambia in January 2023 for installation within SHS being supplied by a partner organisation, Africa Power Ltd (APL). These were installed within their Kua range of SHS, which has three different sizes: 20, 40 and 80 W_p solar modules with 9, 20 and 40 Ah lead-acid batteries, respectively. The logging unit required extension cables for the solar, battery and load connections to the logging unit. A battery temperature sensor was taped to the side of the battery. An additional metal enclosure section was manufactured to fit the logging unit into the SHS, with the aerial fitted through the top of the enclosure, as shown in Figure 8. These sections were then painted to match the SHS colour. The logging units use small internal lithium-ion batteries, which could not be air-freighted, so were obtained locally. A training session for four staff in Zambia was organised to explain the logger features and correct installation. A detailed installation manual was also provided.

When tested in location in Zambia only 27 of these units' sent data via the GPRS network. The reason for this is still unknown and the 15 'faulty' units worked when returned to the UK. This meant that only 27 monitoring units were available for the field trial.

Figure 8 Installation of the logging equipment into the Kua SHS in Zambia

These logging units were installed into Kua SHS that were gradually sold to customers in Zambia. Monitoring units were only supplied to SHS customers who were interested in being part of the field trial. No personal data was recorded as part of this field trial, and the monitoring units' names are anonymised. As of May 2023, only one Kua SHS unit with monitoring systems has been sold, so field trial data is limited.

Within the period of 7/4/2023 to 7/5/2023, data reliability from a monitoring system installed in Zambia, but not yet sold to a customer, was 98.5%. The reliability of data sent from the unit sold to a customer in the same period was only 64.4 %. The reason for this is unknown at present but may be due to the lack of reception in the area where the SHS is installed, or the customer may be moving the unit between work and home.

Example fault capture

Data from one unit failure was captured. The normal system operation can be observed in Figure 9 on the left, with the 80 W_p solar module recharging the battery. The battery voltage rises, with a short higher voltage peak due to the control algorithm of the SHS controller. A fault occurred on this system when a large load was applied to the unit, and it was drained until the low voltage disconnect occurred. This caused the SHS controller to fail, after which the battery is not recharged, and the battery voltage drops critically. This was highlighted back to the SHS O&M team for rectification.

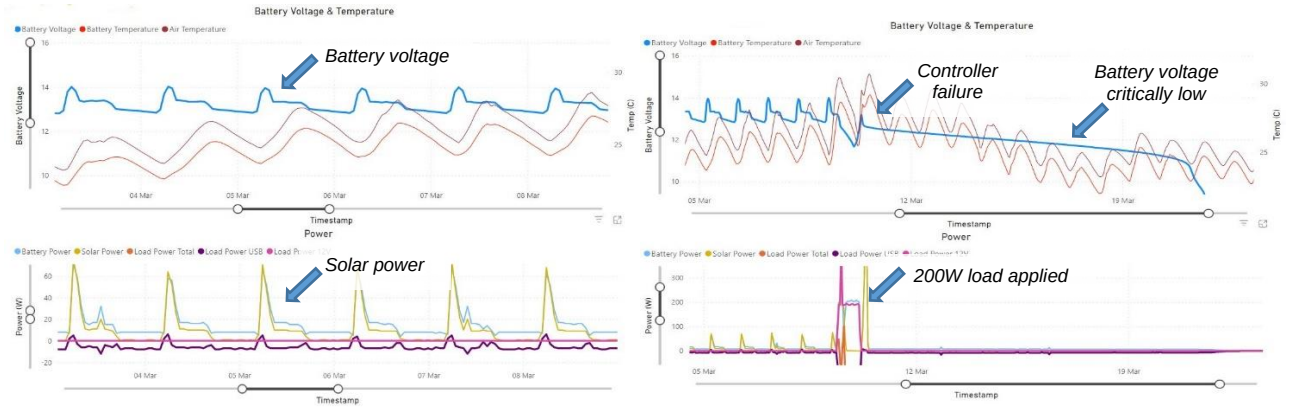

Figure 3 SHS normal operation (left) and fault condition (right)

Example load profile

Data from one real-world SHS has been captured, showing the day-to-day use of the system. Due to the limited installation time, this data has been taken over four weeks from 7/4/2023 to 7/5/2023, but data logging is on-going, and this data set will increase. Figure 10 shows the average daily load profile, along with the minimum and maximum loads to highlight the potential variability. Overnight there is a constant load every night of around 3W, this is the supply for the 2 x 1.5W LED security lights which are supplied with the SHS. A TV, radio and fan are also supplied with the SHS. The average consumption is highest in the evening, correlating with use of the TV. Lowest average use is in the morning, after the sun has risen. It is interesting to note that the maximum load on the unit is in the region of 30W which probably relates to powering the TV, the lights and running the fan, and that this could happen at almost any time, apart from the early hours of the morning. The average daily energy consumption is 247 Wh, but this can vary from 57 to 563 Wh.

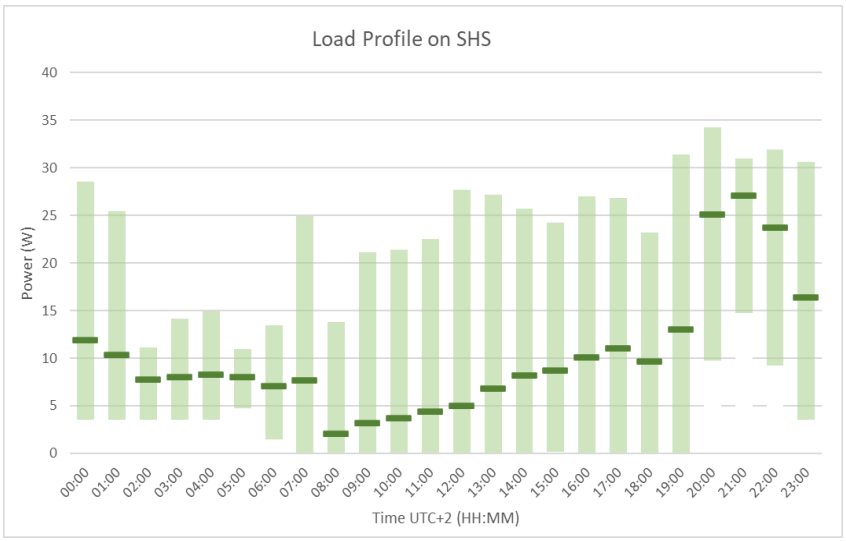

Figure 10 Load profile for solar home system in Zambia

Two logging units were also installed in Malawi for monitoring mini grids designed and implemented by University of Strathclyde. These units monitor battery and air temperatures for large lithium-ion battery banks (Figure 11). The battery banks provide storage for solar PV based mini grid systems providing electricity to communities of around 60 households. These units did not use GPRS but connected via a locally available Wi-Fi connection. This reduces power requirements and data costs, as SIM cards are not required.

Figure 11 Logger installation in Malawi (left), temperature sensor on battery pack (centre), external air temperature sensor (right)

Data from one of the Malawi mini-grid installations is given in Figure 12. Errors introduced on the serial data connection between the upload and the sensor board creates some spurious data points, seen where the data drops to zero. This has now been rectified by including a cyclic redundancy check (CRC) on the serial data. The battery temperature is an important parameter as higher temperatures greatly reduce the battery lifetime. An air conditioning (AC) unit was installed to cool the battery bank, but the data highlighted that the AC system failed, and the battery temperature rose to above 35 °C. This was observed remotely and reported back to the local engineer for rectification.

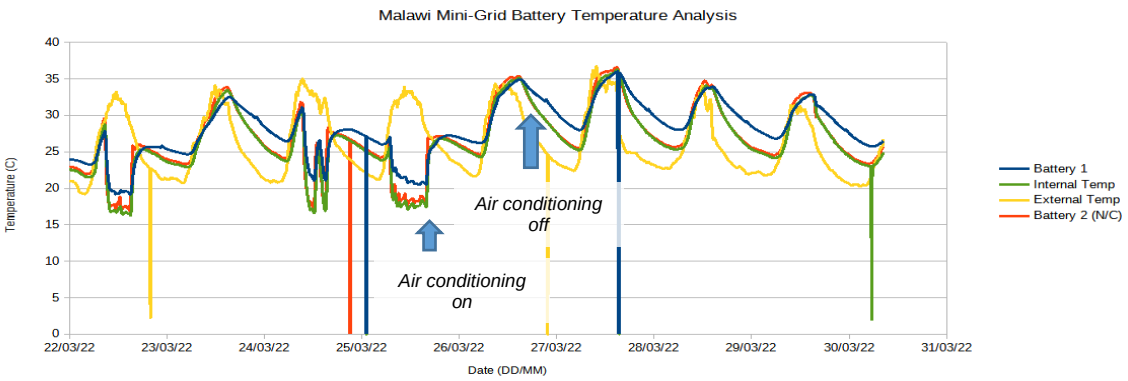

Figure 12 Temperature data from Malawi mini-grid system (A.Eales, Personal Communication, 18/7/2022)

5. CONCLUSION

The authors have presented a low-cost and low-power data-logging system for implementation on SHS. Prototypes have been built and tested within a laboratory environment. These have low power consumption, 13.7 mA on average when sending one upload per hour, and good accuracy, measuring voltage within 0.83 % for a 12 V nominal battery and current within 0.1 % of a 10 A range. Data is stored locally and uploaded to the cloud either using Wi-Fi or GPRS connection.

The parts cost of a hand-built small-batch production of 50 units of the data-logger unit was £140 per unit. This does not include any labour costs, which are significant with the present design. The upload unit (including the parts, PCB, microcontroller, and battery) is just under 50 % of this cost, with the sensor unit just over 40 % of this cost and the enclosure around 10 %.

A batch of 50 units was manufactured for field trails, 42 for installation within SHS in Zambia by Africa Power Ltd., a partner organisation, and two for monitoring mini-grid systems in Malawi, implemented by the University of Strathclyde. Of the 42 units supplied for monitoring SHS in Zambia, fifteen had an issue with GPRS connection and only one has been supplied to a customer. As more of these units will be sold, more data will be recorded which will improve the initial field trial results presented here.

Even within this small set of monitored systems, two faults were remotely observed and details regarding these faults were quickly reported back to the local installation companies and rectified. The first related to an overload of a SHS in Zambia which had a high current load applied with damaged the SHS controller board. The second fault related to an air conditioner failure for the battery bank of a mini grid installed in Malawi. If this failure had not been observed, the battery bank unit could have been permanently damaged and may have needed replacing.

Real world load profile data has been obtained for SHS in Zambia and it is hoped that this data set will improve as more monitoring systems are implemented. The load profile data will help inform the design of future SHS to make them more efficient and economic through optimisation of the solar and storage components.

Data from the monitoring units is stored in cloud-based data storage using IoT Central within Microsoft Azure. The full data can be accessed remotely with administrator access. Public facing reports can easily be created to show high-level system data, such as the overall load energy supplied and number of systems online. Reports showing more detailed data can also be created for any locally based operation and maintenance team.

6. FUTURE WORK

Monitoring of these systems is on-going and the data set for both fault analysis and load profiles will increase. More detailed analysis of this dataset is required, including applying machine learning algorithms to the data to highlight pre-emptive maintenance.

Reducing the cost of this monitoring equipment is required. A minimum viable product has been designed and the authors aim to manufacture this unit at reduced cost to improve the economic viability. Reducing the physical size of the logging unit will also improve the ease of installation within smaller SHS systems.

Additional sensor units for monitoring different types of installations and environmental parameters are in development. This includes a meteorological monitoring system for measuring solar and wind resource and AC power monitoring for off-grid systems. A wider range of DC monitoring boards will be investigated, including lower and higher power ratings.

7. ACKNOWLEDGEMENT

This work has been funded through Innovate UK Energy Catalyst Round 6: Project Number 10528, “Productive Use of DC Solar Power in Africa to Improve Quality of Rural Life”, and by the Enterprise Project Group (EPG), Loughborough University for the project “Solar Remote Monitoring Unit: Providing remote sensing monitoring services for solar power systems.”

The authors would like to thank the partner organisation, Africa Power Ltd, for their invaluable input into this work and help implementing logging systems in Zambia, and Aran Eales, from the University of Strathclyde, for help implementing logging systems in Malawi.

8. REFERENCES

Alphatemp Tech (2021) *Stand Alone Data Loggers*. Available at: https://alphatemptech.co.uk/stand-alone-data-loggers/ (Accessed: 7 June 2021).

Bboxx (2022) *Bboxx*. Available at: https://www.bboxx.com/technology/ (Accessed: 7 December 2022).

Blanchard, R. and Little, M. (2016) 'Developing an open access monitoring device for off-grid renewables', in *ICDRET 2016 - 4th International Conference on the Developments in Renewable Energy Technology*. Institute of Electrical and Electronics Engineers Inc. Available at: https://doi.org/10.1109/ICDRET.2016.7421511.

Comark (2021) *Standalone Data Loggers*. Available at: https://www.comarkinstruments.net/product-category/products/data-loggers/standalone-data-loggers/ (Accessed: 7 June 2021).

Connected Energy (2023) *Connected Energy*. Available at: https://connectedenergy.net/home-1 (Accessed: 4 May 2023).

DATAQ Instruments (2021) *Stand-alone Data Acquisition and Data Logger Systems*. Available at: https://www.dataq.com/data-logger/stand-alone/ (Accessed: 7 June 2021).

Fanourakis, S. *et al.* (2017) 'Low-cost data acquisition systems for photovoltaic system monitoring and usage statistics', in *IOP Conference Series: Earth and Environmental Science*. Institute of Physics Publishing. Available at: https://doi.org/10.1088/1755-1315/93/1/012048.

Grant Instruments (2021) *Data Loggers*. Available at: https://grantinstruments.com/support/support/daq-products/datataker-data-loggers (Accessed: 7 June 2021).

Gupta, A. *et al.* (2018) 'Real time remote solar monitoring system', in *Proceedings - 2017 3rd International Conference on Advances in Computing, Communication and Automation (Fall), ICACCA 2017*. Institute of Electrical and Electronics Engineers Inc., pp. 1–5. Available at: https://doi.org/10.1109/ICACCAF.2017.8344723.

Gupta, D. (2018) *Low Cost Data Logger and Monitoring System for a Small Solar PV Energy System*. Memorial University of Newfoundland.

Hadi, M.S. *et al.* (2018) 'Stand-Alone Data Logger for Solar Panel Energy System with RTC and SD Card', in *Journal of Physics: Conference Series*. Institute of Physics Publishing. Available at: https://doi.org/10.1088/1742-6596/1028/1/012065.

International Energy Agency (2021) *Access to electricity – SDG7: Data and Projections*. Available at: https://www.iea.org/reports/sdg7-data-and-projections/access-to-electricity (Accessed: 22 December 2020).

Jiang, B. and Iqbal, M.T. (2019) 'Open source data logging and data visualization for an isolated PV system', *Electronics (Switzerland)*, 8(4). Available at: https://doi.org/10.3390/electronics8040424.

Kodali, R.K. and John, J. (2020) 'Smart Monitoring of Solar Panels Using AWS', in *2020 International Conference on Power Electronics and IoT Applications in Renewable Energy and its Control, PARC 2020*. Institute of Electrical and Electronics Engineers Inc., pp. 422–427. Available at: https://doi.org/10.1109/PARC49193.2020.236645.

Kumar Prajapati, A. and Tiwari, P. (2020) 'A Review on Photo Voltaic Monitoring and Data Logging System', *International Research Journal of Engineering and Technology* [Preprint]. Available at: https://doi.org/10.3390/electronics8040424.

Lopez-Vargas, A., Fuentes, M. and Vivar, M. (2019) 'IoT Application for Real-Time Monitoring of Solar Home Systems Based on Arduino™ with 3G Connectivity', *IEEE Sensors Journal*, 19(2), pp. 679–691. Available at: https://doi.org/10.1109/JSEN.2018.2876635.

Measurement Computing (2021) *Data Loggers & Measurement Computing*. Available at: https://www.mccdaq.com/data-loggers (Accessed: 7 June 2021).

Saravanan, D. and Lingeshwaran, T. (2019) 'Monitoring of solar panel based on IOT', in *2019 IEEE International Conference on System, Computation, Automation and Networking, ICSCAN 2019*. Institute of Electrical and Electronics Engineers Inc. Available at: https://doi.org/10.1109/ICSCAN.2019.8878814.

Shuvo, A.M. *et al.* (2019) 'Design & Implementation of a Low Cost Data Logger for Solar Home System', *International Journal of Engineering and Management Research*, 9(1). Available at: https://doi.org/10.31033/ijemr.9.1.4.

Singh, T. and Thakur, R. (2019) 'Design and Development of PV Solar Panel Data Logger', *International Journal of Computer Sciences and Engineering*, 7(4), pp. 364–369. Available at: https://doi.org/10.26438/ijcse/v7i4.364369.

Wolfe, N. (2015) *An Open-Source Monitoring System for Remote Solar Power Applications*. Cornell University.

#19: Classification of climate zone using degree-day method

A Case Study of Saudi Arabia

Fahad MOHAMMED ALREFAI[1,3], Siddig ADAM OMER[2]

1 Department of Architecture and Built Environment, Faculty of Engineering, University of Nottingham, NG7 2RD, University Park, Nottingham, United Kingdom, fahad.alrefai@nottingham.ac.uk
2 Department of Architecture and Built Environment, Faculty of Engineering, University of Nottingham, NG7 2RD, University Park, Nottingham, United Kingdom, siddig.omer@nottingham.ac.uk
3 Department of Architectural Engineering, College of Engineering at Yanbu, Taibah University, 46421, Yanbu Al-Bahr, Kingdom of Saudi Arabia, frefai@taibahu.edu.sa

Abstract: Understanding the local climate specification is vital for designing and operating low-carbon buildings. This is particularly important in countries with a fast, hot and arid climate, such as the Kingdom of Saudi Arabia (KSA), where the meteorological data may be available only in specific locations. However, there is a lack of literature on the impact of the local climate on the behaviour of buildings with little local classification or zoning. The literature assessment of the building performance in the Saudi environment is based mainly on a general climate zone based on the hot, cold, and moderate classifications. In this paper, the authors used the degree-day method to address the gap in Saudi Arabia's hot and arid climate classification, currently adopted by the Saudi building codes and specifications. The cooling degree days (CDD) and heating degree days (HDD) for 21 cities in Saudi Arabia were calculated using recent meteorological data from Saudi weather stations over five years (2017-2021) that included cities from all 13 Saudi regions. In this study, the authors used DegreeDays.net software to compute the CDD and HDD for these cities, using an integrated approach. Multiple base temperatures were used to calculate the cooling and heating degree days, and then the results were categorised accordingly. Saudi Arabia's climate classification using this approach has produced a climatic zoning map more specific and accurate than previous hot and arid-based classifications. This will improve building design and thermal comfort for particular parts of the Kingdom. In addition, the proposed category will support energy and building research that can be applied to all Saudi buildings. In particular, the researchers provide valuable insights into sustainable building design and construction in KSA, with implications for policy and practice.

Keywords: Saudi Arabia; Climate Classification; Cooling Degree Days; Heating Degree Days

1. INTRODUCTION

The local climate substantially impacts the design and functioning of buildings. The land area of the Kingdom of Saudi Arabia (KSA) is 2,215,000 square kilometres (GOV.SA Platform, 2023). The KSA's land elevation varies between 0 and 3000 meters above mean sea level (Alrashed and Asif, 2015). As shown in Table 1, Saudi Arabia is divided into 13 regions, the most populated of which are Ar Riyadh, Makkah Al Mukarramah, Eastern Province, Al Madinah Al Munawwarah, and Aseer, respectively; also those regions have the most housing units. In particular, 67.6% of Saudi Arabia's population resides in Makkah Al Mukarramah, Ar Riyadh, and the Eastern region (General Authority for Statistics, 2023b). While Aseer is the highest region at 22,228 metres above sea level, Eastern Province is only 10 metres above sea level. According to the Saudi Census 2022, the total resident population of Saudi Arabia is 32,175,224, of which Saudi citizens comprise 18.8 million, counted as 58.4% of the total (General Authority for Statistics, 2023b). In 2022, the population of Saudi Arabia has increased by 34.2%, 8.2 million, since the last census in 2010 (GASTAT, 2023). Moreover, Ar Riyadh is the most populous region in Saudi Arabia, with 8,591,748 residents, which is 26.7% of the total population (General Authority for Statistics, 2023b). 14 per Km2 is the population density in Saudi Arabia. Table 1 indicates that 12,414,696 dwellings are in Saudi Arabia. There are 8,174,674 total residential households in Saudi Arabia, which is 65.8% of the total housing units (General Authority for Statistics, 2023a).

Table 1: Regions of Saudi Arabia

No	Region Name	Capital City	Elevation (m)	Region Population	Housing Units
1	Ar Riyadh	Riyadh	612	8,591,748	3,123,246
2	Makkah Al Mukarramah	Mecca	333	8,021,463	3,260,806
3	Eastern Province	Dammam	10	5,125,254	1,902,754
4	Al Madinah Al Munawwarah	Medina	603	2,137,983	843,660
5	Aseer	Abha	22,228	2,024,285	893,307
6	Jazan	Jizan	19	1,404,997	481,663
7	Al Qaseem	Buraydah	606	1,336,179	538,133
8	Tabuk	Tabuk	768	886,036	352,464
9	Hail	Hail	1,002	746,406	302,895
10	Al Jawf	Sakaka	689	595,822	190,336
11	Najran	Najran	1,310	592,300	217,768
12	Northern Borders	Arar	555	373,577	108,485
13	Al Bahah	Al Baha	2,176	339,174	199,179
	Total			32,175,224	12,414,696

**Data sources: The Saudi Census 2022 and meteoblue*

Similar house designs can be spotted in Saudi mountain cities such as Abha and Al Taif. An identical dwelling is also built in the middle of the desert, such as in Riyadh. Figure 1 is a map of Saudi Arabia depicting the variety of the country's elevations and the Saudi region's border. In addition, the map includes major Saudi cities such as Riyadh, Dammam, Madinah, Makkah, and Abha.

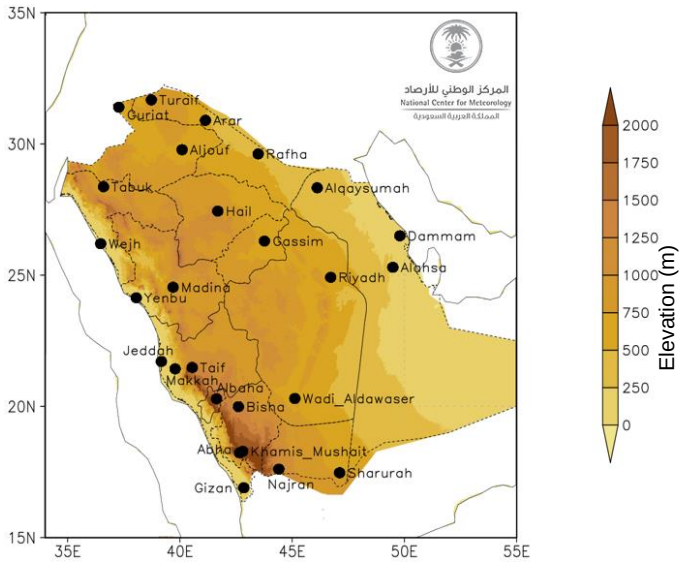

Figure 1 Elevation of Saudi Arabia and Weather Stations Map source: (National Center for Meteorology, 2023)

2. CLIMATIC LITERATURE REVIEW

The Kingdom of Saudi Arabia has been classed separately, as part of the Gulf Cooperation Council (GCC) Countries, as a member of the Arab World, and as a member of the Middle East and North Africa (MENA) region by scientific and administrative entities over the years (Alrashed and Asif, 2014). The Köppen climate classification represents one of the most broadly used climate zone classification systems. The system was created by the climatologist Wladimir Köppen in 1884; it has undergone various revisions and modifications over the years but has been used by scholars worldwide (Met Office, 2022). The Köppen-Geiger system categorises climate into five main classes and thirty sub-types (Buresova, 2022). The classification is based on seasonality, monthly air temperature, and precipitation threshold levels (Beck et al., 2018). According to the Köppen climate classification, Saudi Arabia is classified as a desert or arid climate, which comes under the hot desert climate (BWH) (Hasanean and Almazroui, 2015). Indeed, the system lacks categorising the country as one zone. Saudi Arabia's climate has been classified in various ways by researchers and Saudi authorities, such as (SBC 602, 2018), (Alrashed and Asif, 2014), (Said et al., 2003), and (Al-Hadhrami, 2013).

The Saudi Building Code (SBC) is a set of comprehensive codes and standards for building design, construction, and operation in Saudi Arabia. The primary purpose of the SBC is to establish minimum requirements, investigate public health and safety through the stability of buildings and facilities, and safeguard life and property from building-related dangers. The Saudi Building Code (SBC 206) divided the Kingdom of Saudi Arabia into three climate zones, and the categories of the three zones are based on the International Energy Conservation Code (IECC). The IECC code specifies best practices for energy efficiency. Zone 1 encompasses the majority of Saudi Arabia, while Zone 3 is the smallest and coldest. ASHRAE recommended 18.3 °C for a typical uninsulated building, which was confirmed by numerous tests (Indraganti and Boussaa, 2017). The SBC 206 lists selected Saudi cities subdivided by zone as calculated using CCD at 18.3 °C, including each town's locations and elevations.

Researchers have contributed to the development of a Saudi climatic zoning map produced by (Alrashed and Asif, 2014), who used the primary climate zone data introduced by (Said et al., 2003), which the zoning category proposed originally in (Said et al., 1996). Meanwhile, (Alrashed and Asif, 2014) categorised the climatic data for five different zones of Saudi Arabia compared to five similar climates cities worldwide. The comparison focuses on four climate aspects to show accurate analysis: annual temperature, relative humidity, annual wind speed, and annual mean global solar radiation. According to the study, Dahran is the hottest city, Guriat is the coldest, with 45.7 and -3.3 degrees Celsius, respectively, while Jeddah has the most significant humidity at 64.7 per cent. On the other hand, (Al-Hadhrami, 2013) reviewed Cooling Degree Days (CDDs) and Heating Degree Days (HDDs) in Saudi Arabia. The paper included suggested zones based on CDDs value for Saudi Arabia that range between 3400 and 7400. I will create a map using updated data. The zones have two fundamentals: first, they have a weather station, and second, they are categorised by similar annual CDDs. Zone 1 is the hottest area which demands more cooling; however, Zone 4 is the coldest zone which requires heating rather than cooling. Indeed, the discrepancy in the previous climate zoning studies and standards lead to the need for more deeply research.

3. MATERIALS AND METHODS

3.1. Climatic Zoning Parameters

Climate zoning is crucial when analysing energy demand and using computer simulations. In Saudi Arabia, climate zoning is vital for several key elements: accurate energy analysis, optimal building design and operation, energy efficiency measurement, informed policymakers and decision-makers, and understanding the impact on energy consumption patterns. There are several methods to develop climate zoning for a country, which apply to Saudi Arabia. A recent paper provided a comprehensive review of climatic zoning methodologies used for building energy efficiency programmes in 54 countries, with 80% of these countries defining their climatic zoning using only up to three techniques and variables (Walsh et al., 2017). Furthermore, degree days, temperature, altitude, lative humidity, and administrative divisions are the most common of the 19 parameters found to be utilised in climatic zoning (Walsh et al., 2017). In a study by (Büyükalaca et al., 2001), long-term and recently-measured data are used to calculate Turkey's heating and cooling degree days. In Oman, for instance, research estimated the CDD and HDD for 31 weather stations in the country to generate a map of Oman-specific climate classification (Al-Saadi et al., 2022). In this study, the researchers chose three methods to develop a climate classification zoning for Saudi Arabia, which included mainly the degree days method and modified the zoning borders using temperature and relative humidity. Indeed, the paper analyses climate parameters of temperature and humidity data to determine the feasibility of better classifying zoning in Saudi Arabia.

3.2. Degree Days Method

The degree day method is a technique used to estimate the heating or cooling required to maintain a comfortable indoor temperature in a building. The technique involves comparing the average daily outdoor temperature to a base temperature, which depends on the location. 'The balance temperature for a building is the outdoor temperature at which neither heating nor cooling is required.' (Al-Homoud, 1998). For instance, 18.3 °C (65 °F) is typically the base temperature in the USA (Lee

et al., 2014). Degree days are reported monthly for 18 regions in the United Kingdom, using a standard base temperature of 15.5 °C (CIBSE, 2006). However, the base temperature also differs between heating degree days and gets higher temperatures for cooling degree days. The difference between the base temperature and the average daily temperature is known as the degree day value. The degree-day approach is frequently used in calculating building energy consumption. Cooling Degree Day (CDD) is a measurement for calculating the energy needed to cool buildings. In addition, Heating Degree Day (HDD) determines the energy required to heat a building. In hot weather, Cooling Degree Days indicate the energy consumed for cooling; Heating Degree Days indicate the energy consumed for heating in cold weather. The calculation of CDD and HDD with the necessary equations is explained in the literature review provided by (Büyükalaca et al., 2001) and (Al-Saadi et al., 2022). In 2006, The Chartered Institution of Building Services Engineers, UK, published the updated TM 41 Degree-days: Theory and Application (CIBSE, 2006).

3.3. Software and Weather Data

The researchers utilised high-quality and accurate climate data obtained from local weather stations operated and monitored by the National Center of Meteorology in Saudi Arabia. Notably, the collected data has only 0.3% of the maximum annual estimated data to fill any gaps in the dataset. Indeed, the most detailed temperature records available were used in this paper.

Moreover, several weather stations are spread over the country, so only stations with the best-completed data recording are chosen to ensure the result is more accurate and valid. For instance, Riyadh has two metrological stations, OERK and OERK. The OERK station at King Khaled International Airport has only 0.02% of estimated recorded data annually. In contrast, OERY station data has up to 3% estimated climate data. As a result, recent climatic data for 2017 through 2021 have been utilised. Table 2 shows displays the selected meteorological stations from 21 Saudi Arabian cities.

Table 2: Selected Weather Stations in Saudi Arabia

No.	Station ID	Region	Station Location	latitude	longitude
1	OEGT	Al Jouf	Guriat	31.41N	37.28E
2	OERR	Northern Border	Arar	30.91N	41.14E
3	OESK	Al Jouf	Sakaka	29.79N	40.10E
4	OETB	Tabuk	Tabuk	28.38N	36.60E
5	OEHL	Hail	Hail	27.44N	41.69E
6	OEDF	Eastern Province	Dammam (KFIA)	26.43N	49.80E
7	OEGS	Al Gassim	Buraidah	26.30N	43.77E
8	OEWJ	Tabuk	Al Wejh	26.20N	36.48E
9	OERK	Al Riyadh	Riyadh (KKIA)	24.71N	46.73E
10	OEWD	Al Riyadh	Wadi Al Dawasser	24.71N	46.73E
11	OEMA	Al Madinah	Madinah	24.55N	39.71E
12	OEYN	Al Madinah	Yanbu	24.14N	38.06E
13	OEJN	Makkah	Jeddah	21.70N	39.18E
14	OETF	Makkah	Al Taif	21.48N	40.54E
15	OEBA	Al Baha	Al Baha	20.30N	41.63E
16	OEBH	Aseer	Bisha	19.98N	42.62E
17	OEKM	Aseer	Khamis Mushait	18.30N	42.80E
18	OEAB	Aseer	Abha	18.24N	42.66E
19	OENG	Najran	Najran	17.61N	44.42E
20	OESH	Najran	Sharurah	17.47N	47.12E
21	OEGN	Jazan	Jizan	16.90N	42.59E

Based on the integration method, the CDD and HDD were calculated in this paper using the DegreeDays.net website. There is also desktop application software available for this purpose. The Integration Method accounts appropriately for temperature fluctuations within each day and between days (BizEE Software, 2022). BizEE Software Limited is a company

based in the United Kingdom that develops software to assist businesses and other organisations in saving energy. In 2008, the company created DegreeDays.net to help energy-saving professionals better use degree days (BizEE Software, 2022). According to the developer company, Degree Days.net is an online application that calculates degree days using temperature data from many weather stations worldwide (BizEE Software, 2022). BizEE Software is one of the well-developed programs used in various academic publications. For instance, two researchers at Michigan Technological University in the USA did a recent study using the BizEE Software (Warty and Mehendale, 2021). Indeed, Degree Days.net was utilised in this research to determine CDD and HDD for the targeted cities in Saudi Arabia.

Figure 2 and Figure 4 illustrate the average degree days of cooling and heating (CDD & HDD) from 2017 to 2021, with a varying base temperature. The base temperatures tested included for CDD were 18 °C, 20 °C, 22 °C, and 24 °C. However, the base temperature for the HDD ranged between 12.5 °C and 24 °C, with a one Celsius temperature step.

3.4. Cooling Degree Days

Cooling Degree Days (CDD) are measured in (degree-days) or (°C-days). Cooling Degree Days indicate the cooling required to maintain a comfortable indoor temperature for a given period. CDD is calculated by subtracting a reference temperature from the average daily temperature for that particular day. When the average daily temperature exceeds the base temperature, such as 20 degrees Celsius, it is called a Cooling Degree Day. CDD is used in energy demand analysis, particularly for air conditioning and cooling systems. Tracking cumulative Cooling Degree Days over time assists in determining energy use and the effects of temperature on cooling requirements. This is particularly significant in countries with hot and arid climates like Saudi Arabia.

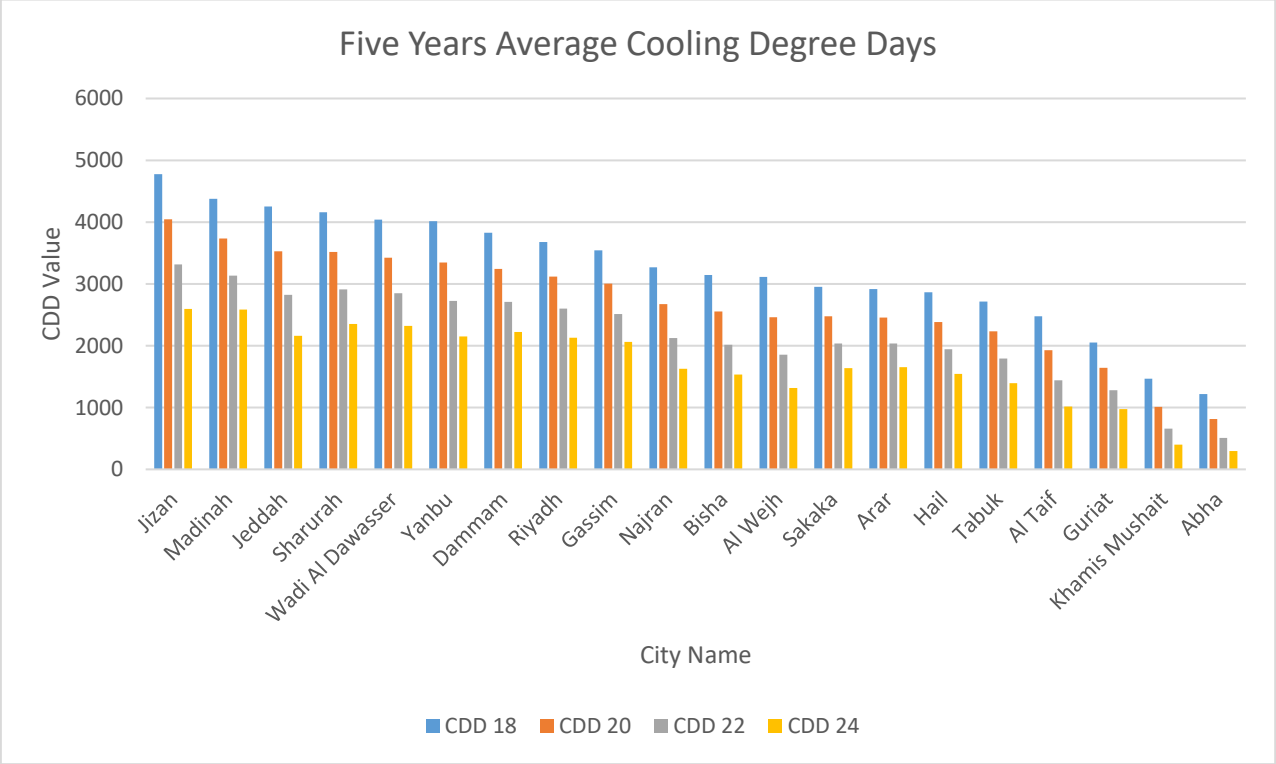

Figure 2 Average Cooling Degree Days from 2017 to 2021 with a varying base temperature

Cooling Degree Day (CDD) is used to understand the cooling demand and energy consumption patterns in a specific location, and it is commonly used by architects, engineers, and energy efficiency experts. CDD is a valuable tool for understanding energy consumption patterns and making energy-efficient decisions, especially in hot and arid countries with high air conditioning usage. There are several methods for calculating CDD, but the values shown in Figure are computed using DegreeDays.net based on the integration method with Celsius (°C) base temperatures. The integrated approach provides a more accurate calculation of CDD using a detailed temperature data record. The CDDs demonstrated in Figure 2 are listed from highest to lowest for better visual comparisons. The base temperature for CDD calculation is set differently depending on the country, and it is considered a balance between energy consumption for heating and cooling. The authors used 20°C as a base temperature in this study. Figure 2 shows that Jizan, Madinah, and Jeddah are the hottest cities in the country, with CDD values of 4045, 3734, and 3530, respectively. Meanwhile, Abha requires less cooling, with a CDD value of only 815, while Khamis Mushait has 1014 CDD. To conclude, the higher the CDD value, the greater the cooling demand and energy consumption.

Figure 3 depicts the Cooling Degree Day (CDD) values for seventeen cities in Saudi Arabia. The CDD values, which quantify the quantity of energy required to cool a building, range between 500 and 4000. The highest value, approximately 4000, is observed in Jazan, indicating the city's elevated cooling demand. On the other hand, Abha has the lowest CDD value of roughly 750, indicating a relatively milder climate than other cities. The average CDD value across all cities is approximately 2500, revealing the general cooling needs in Saudi Arabia. This graphic illustrates the varying cooling demands of cities nationwide, providing valuable insight into climate patterns and energy consumption associated with cooling systems.

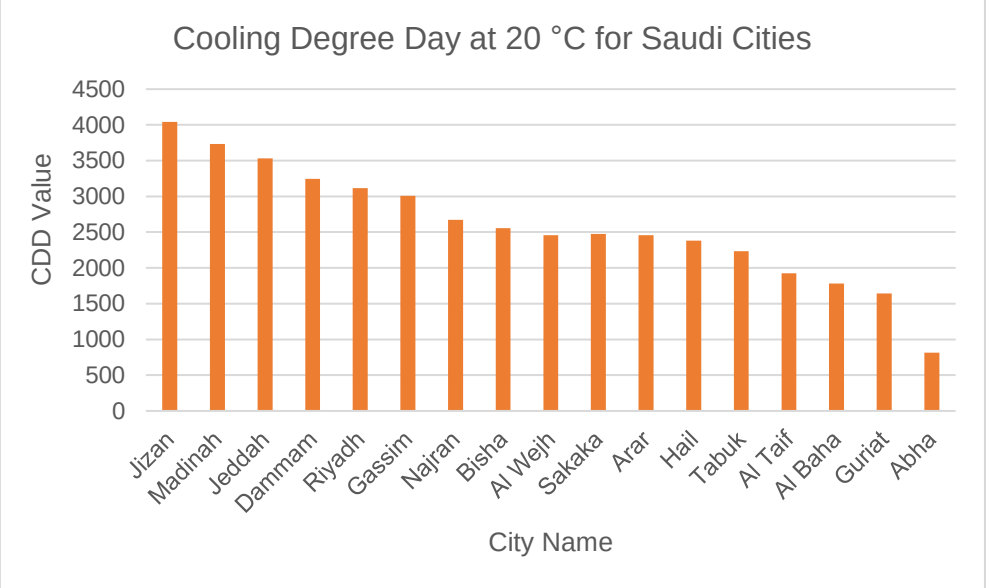

Figure 4 CDD for Saudi Cities with a base temperature of 20 °C

3.5. Heating Degree Days

Using local weather data, Figure 4 demonstrates the Heating Degree Days (HDD) value for Saudi Arabia from 2017 to 202. HDD was generated by the DegreeDays.net software, and the analysis focused on the base temperature of 15.5°C. In Figure 4, it is clear that most cities do not necessitate a significant amount of heating. Indeed, the north side of Saudi Arabia is the coldest spot.

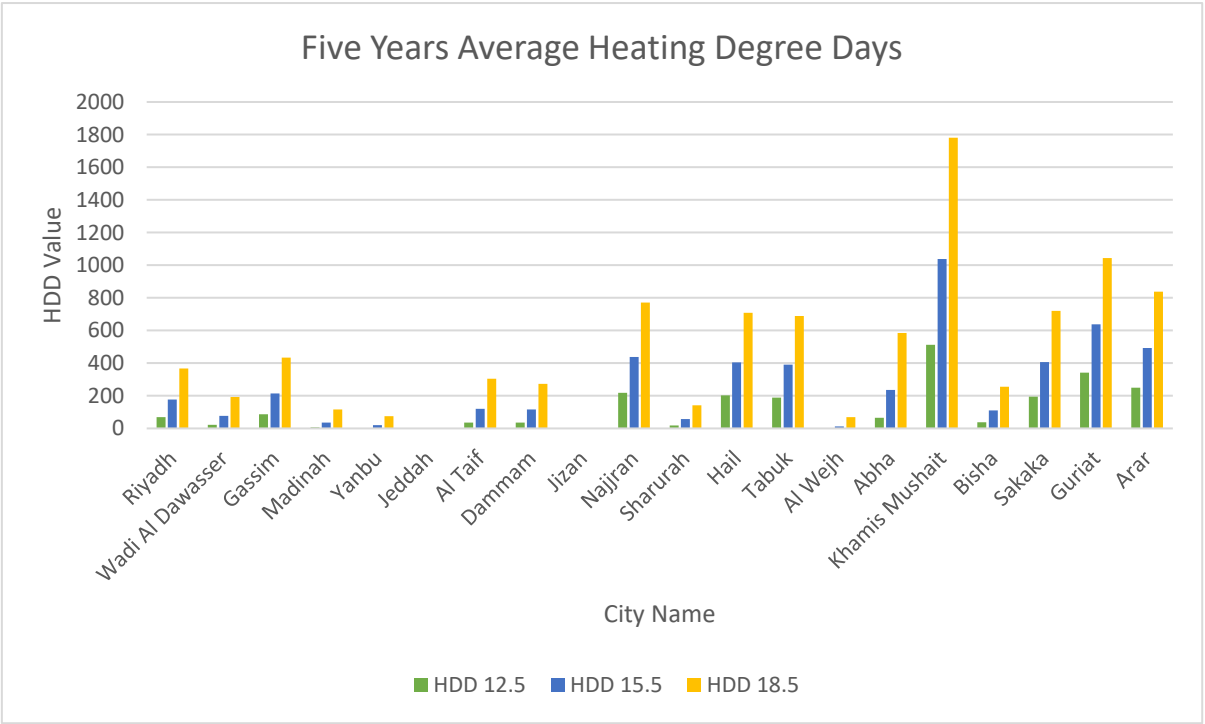

Figure 4 Average Heating Degree Days from 2017 to 2021 with a varying Celsius base temperature

4. RESULTS

In this research, the authors classified Saudi Arabia's climate based on the cooling degree days due to the need for cooling and then produced a climatic zone map. Figure 5 shows the Saudi regions reflecting the CDD values at 20 °C, using the Excel software mapping tools. It helps to define the general boundaries of each zone.

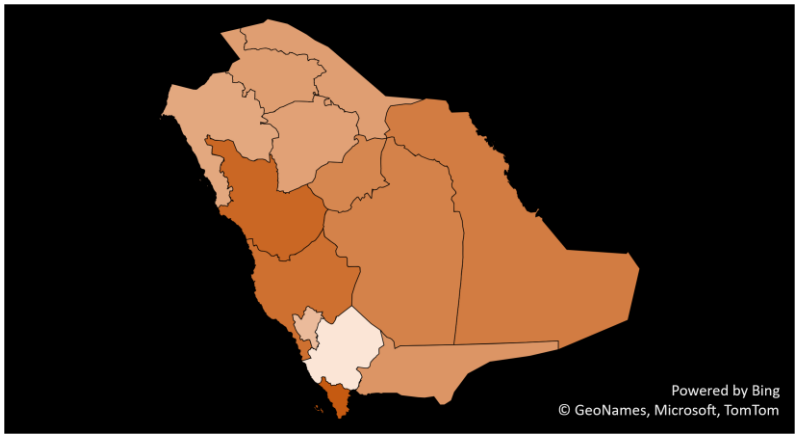

Figure 55 Saudi Regions Average CDD Values for Five Years at 20 °C (2017-2021)

The methodology consisted of four components: (1) using local climate data from weather stations for the Saudi cities shown in Table 2, (2) calculating CDD and HDD using the integration method with various base temperatures included in Figure 2 and Figure 4, (3) categorising SA climates using the calculated CDD of the base temperature of 20 °C into five groups as shown in Table 3, and finally (4) generating the Saudi classification climate map, as illustrated in Figure 6, with modified boundaries regarding the temperature and humidity. Alula, for instance, matches zone 4 while officially under Madinah governance.

Table 3 demonstrates the recommended climatic zones of Saudi Arabia, which the classification has five zones. At 20 °C, the maximum CDD value of 4044 was recorded in Jizan, while the lowest 814 was recorded in Abha.

Table 3 Categorising of Average CDD Values from 2017 to 2021

Zone No.	City Name	CDD	CDD Classified
1	Jizan	4044	3251 - 4500
	Madinah	3734	
	Jeddah	3530	
	Sharurah	3516	
	Wadi Al Dawasser	3423	
	Yanbu	3348	
2	Dammam	3243	3151 - 3250
	Al Qaysumah	3200	
3	Riyadh	3117	2501 - 3150
	Gassim	3006	
	Najran	2672	
	Bisha	2555	
4	Sakaka	2475	2001 - 2500
	Al Wejh	2460	
	Arar	2459	
	Hail	2383	
	Tabuk	2232	
5	Al Taif	1927	10 - 2000
	Al Baha	1780	
	Guriat	1641	
	Turaif	1602	
	Khamis Mushait	1014	
	Abha	814	

* Base temperature based is 20 °C

Figure 6 demonstrates the suggested climate zones for The Kingdom of Saudi Arabia, which have five different habited zoning. Al-Rub' Al-Khali (Empty Quarter) is a sandy, uninhabited desert region illustrated in the grey zone. The climate zones of Saudi Arabia are classified as follows: hot-dry climate, hot-humid climate, warm-humid climate, cold-dry climate, and high-altitude climate. The created climate classification is applicable and can be used in building codes and energy efficiency standards. The five climate zone categories in Saudi Arabia illustrate the diverse climatic conditions throughout the country, each having distinct characteristics and impact on the cooling and air conditioning needs of various regions.

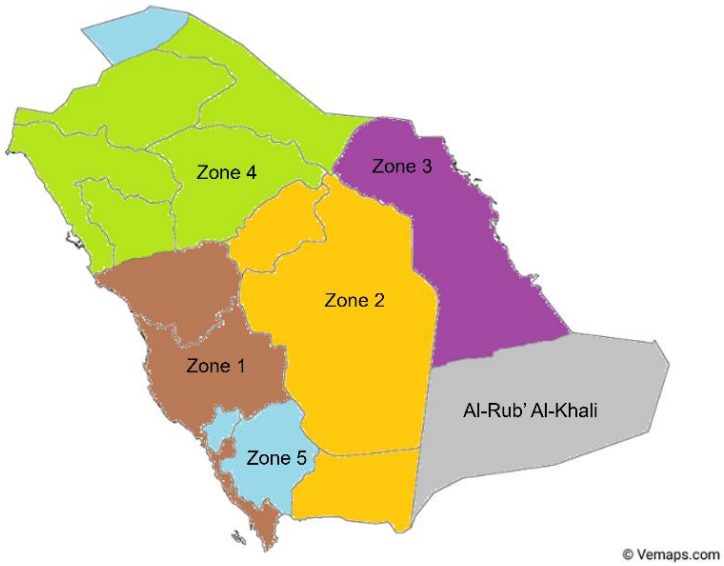

Figure 6 Saudi Arabia Recommended Climatic Zoning. Base map: vemaps.com

The suggested climate zones can be presented by cities such as Madinah, Riyadh, Dammam, Tabuk, and Abha, which are respectively categorised as:

1. Zone one, presented by Madinah, is a semi-arid climate with a subzone of a coastal environment. The summers are long, sweltering, and arid; the winters are short, comfortable, dry, and windy; and it is primarily clear year-round (Weather Spark). This zone experiences relatively moderate temperatures throughout the year due to the influence of the Red Sea. The average annual temperature ranges from 12°C to 43°C but rarely falls below 9°C or rises above 46°C.
2. The desert climate presented by Riyadh covers zone number two. The summers are lengthy, sweltering, and arid; the winters are cool and dry, and the weather is generally clear throughout the year. The average annual temperature ranges from 9°C to 43°C, rarely falling below 5°C or rising above 45°C. The zone is characterised by extremely high temperatures, minimal rainfall, and arid conditions. This climate zone experiences scorching summers and mild winters.
3. A Mediterranean climate prevails on the eastern coast of Saudi Arabia, including cities like Dammam and Zone Three. The summers are long, sweltering, humid, and arid; the winters are cool, dry, and windy; and the weather is predominantly clear throughout the year. The average annual temperature ranges from 11°C to 43°C, rarely falling below 7°C or rising above 46°C. This climate zone features hot, dry summers and relatively mild, wet winters, with more rainfall than other regions.
4. Zone four is a primary category in the northern regions of SA, and Tabuk is the central city presenting it. The zone has hot and arid climates, with extremely hot summers and cold winters.
5. Zone five is a highland climate that covers two areas in the country. A highland climate is present in the southwestern highlands, including the Asir region. Also, the top north of Saudi Arabia included Guria and Turaif. This zone is characterised by cooler temperatures, relatively high humidity, and more significant precipitation than the surrounding areas. These cities represent a mix of climatic conditions in Saudi Arabia, providing a glimpse into the diverse climate zones across the country.

The paper utilises a four-step process to categorise Saudi Arabia's climates into five zones. The methodology comprises (1) employing local meteorological data, (2) calculating Cooling Degree Days (CDD) and Heating Degree Days (HDD) using an integrated method with different base temperatures, (3) classifying SA climates into five groups based on the calculated CDD using a base temperature of 20 °C, and (4) creating the Saudi classification climate map.

5. CONCLUSION

This paper proposes a climatic division of Saudi Arabia into five zones based on the cooling degree days. This classification is based on the climate conditions determining the cooling degree days, such as monthly temperature, humidity,

topography, rainfall, and wind speed. Figure 2 and Figure 4 illustrate the average degree days of cooling and heating from 2017 to 2021, which had varying base temperatures. In particular, different base temperatures for CDD and HDD were tested in this study, ranging between 12.5 °C and 24 °C. Further, it delves into finding the country's appropriate base temperature. The recommended Saudi classification utilised high-accuracy weather data to enhance the quality of findings. In addition, it simplifies climate zoning based on relevant meteorological aspects such as relative humidity, wind speed, and average monthly temperatures. This climate classification ensures that each Saudi city is categorised according to its ideal weather conditions.

6. REFERENCES

Al-Hadhrami, L. 2013. Comprehensive Review of Cooling and Heating Degree Days Characteristics Over Kingdom of Saudi Arabia. Renewable And Sustainable Energy Reviews, 27, 305-314.

Al-Homoud, M. S. 1998. Variable-Base Heating and Cooling Degree-Day Data For 24 Saudi Arabian Cities. Ashrae Transactions, 104, 320.

Al-Saadi, S., Al-Rawas, G., Gunawardhana, L., Al-Farsi, N. & Al-Kalbani, H. 2022. Developing Climate Classification for Oman Using Degree-Days Method. Arabian Journal for Science and Engineering, 1-15.

Alrashed, F. & Asif, M. 2014. Analysis Of Critical Climate Related Factors for The Application of Zero-Energy Homes In Saudi Arabia. Renewable And Sustainable Energy Reviews, 41, 1395-1403.

Alrashed, F. & Asif, M. 2015. Climatic Classifications of Saudi Arabia for Building Energy Modelling. Energy Procedia, 75, 1425-1430.

Beck, H. E., Zimmermann, N. E., Mcvicar, T. R., Vergopolan, N., Berg, A. & Wood, E. F. 2018. Present And Future Köppen-Geiger Climate Classification Maps At 1-Km Resolution. Scientific Data, 5, 180214.

Bizee Software. 2022. Degree Days Calculated Accurately for Locations Worldwide [Online]. Available: Https://Www.Degreedays.Net/ [Accessed 04/23/2022].

Buresova, K. Vernacular Architectural Elements. Mitigating Climate Conditions In The Category Cfa. 11th Acau 2022: Proceedings Of 11th International Phd Students Conference, 2022-01-01 2022. Vut V Brne, Fakulta Architektury.

Büyükalaca, O., Bulut, H. & Yılmaz, T. 2001. Analysis Of Variable-Base Heating and Cooling Degree-Days for Turkey. Applied Energy, 69, 269-283.

Cibse, T. 2006. Degree-Days: Theory And Application. London: The Chartered Institution of Building Services Engineers, 16.

Gastat 2023. Saudi Census 2022. Riyadh: Ministry Of Economy & Planning.

General Authority for Statistics 2023a. Household Summary Report. Riyadh, Saudi Arabia: Ministry of Economy & Planning.

General Authority for Statistics 2023b. Population Summary Report. Riyadh, Saudi Arabia: Ministry of Economy & Planning.

Gov.Sa Platform. 2023. Know About Kingdom [Online]. Riyadh, Saudi Arabia: Ministry of Communications and Information Technology. Available: Https://Www.My.Gov.Sa/Wps/Portal/Snp/Aboutksa [Accessed 09/07/2023].

Hasanean, H. & Almazroui, M. 2015. Rainfall: Features And Variations Over Saudi Arabia, A Review. Climate, 3, 578-626.

Indraganti, M. & Boussaa, D. 2017. A Method to Estimate the Heating and Cooling Degree-Days for Different Climatic Zones of Saudi Arabia. Building Services Engineering Research and Technology, 38, 327-350.

Lee, K., Baek, H.-J. & Cho, C. 2014. The Estimation of Base Temperature for Heating and Cooling Degree-Days for South Korea. Journal Of Applied Meteorology and Climatology, 53, 300-309.

Met Office. 2022. Climate Zones [Online]. Exeter, United Kingdom. Available: Https://Www.Metoffice.Gov.Uk/ [Accessed 14/02/2022].

National Center for Meteorology. 2023. The Climate of Saudi Arabia [Online]. Riyadh, Saudi Arabia: Ministry of Environment Water & Agriculture. Available: Https://Ncm.Gov.Sa/Ar/Climate/Ksaclimate/Pages/Default.Aspx [Accessed 12/07/2023].

Said, S.-A. M., Kadry, H. M. & Ismail, B. I. Climatic Conditions for Saudi Arabia. Ashrae Winter Meeting, 1996. 37-44.

Said, S. A. M., Habib, M. A. & Iqbal, M. O. 2003. Database For Building Energy Prediction in Saudi Arabia. Energy Conversion and Management, 44, 191-201.

Sbc 602 2018. 602 Residential Buildings - Energy Conservation Code. Saudi Building Code National Committee.

Walsh, A., Cóstola, D. & Labaki, L. C. 2017. Review Of Methods for Climatic Zoning for Building Energy Efficiency Programs. Building And Environment, 112, 337-350.

Warty, A. & Mehendale, S. 2021. Energy Modelling and Energy Efficiency Opportunities for A Public Library Building In The Upper Peninsula Of Michigan.

#21: Using system intrinsic thermal storage to enhance chiller plant efficiency – on-site proof of concept test

Kui SHAN[1], Xiaoyu LIN[2], Shengwei WANG[3]

[1] *Department of Building Environment and Energy Engineering / Research Institute for Smart Energy, The Hong Kong Polytechnic University, Hong Kong, kui.shan@polyu.edu.hk*
[2] *Department of Building Environment and Energy Engineering, The Hong Kong Polytechnic University, Hong Kong, andyu.lin@connect.polyu.hk*
[3] *Department of Building Environment and Energy Engineering / Research Institute for Smart Energy, The Hong Kong Polytechnic University, Hong Kong, beswwang@polyu.edu.hk*

Abstract: Previous studies have proofed that the use of thermal energy storage can significantly improve the energy efficiency of a chiller plant via proper control. However, thermal energy storage systems are not commonly available in building cooling system. This study proposes an optimal control strategy to enhance chiller plant efficiency by utilizing the intrinsic thermal energy storage effect of the chilled water delivery system in a building. The fundamental idea of the proposed strategy is to maintain a high Part Load Ratio (PLR) of operating chillers so that they can produce cooling with high efficiency. The strategy also keeps the supply chilled water temperature within the allowed range, so that the building thermal comfort is not compromised. The proposed control strategy consists of two modes applicable for two different scenarios. Mode A is applicable during the end of office hours. It can bring forward the shutdown of chillers at the end of office hours and utilize the stored cooling energy to cool the building for a short period of time. Mode B is appliable for extreme low cooling load conditions (e.g., night mode operation), particularly when the actual cooling load is much lower than the rated capacity of a single chiller.

The concept of the optimal control strategy has been validated on-site in a high-rise commercial building served by a large and complex cooling system whose chilled water delivery system has a thermal capacitance of around 3,312,600 kJ/K. On-site validation of Control Mode A shown the efficiency of chiller plant was improved by14% during the tested period, and the electricity consumption was reduced by 998 kWh. On-site validation of Control Mode B shown that the chiller efficiency could be improved by 43.3% during the tested hours and the electricity consumption was reduced by 2508 kWh.

Keywords: optimal control, chiller efficiency, thermal energy storage, air-conditioning, building energy

1. INTRODUCTION

Buildings take up 39%, 37%, and 25% of energy use in the UK, EU and China, respectively (Klein et al. 2012). In Hong Kong, the commercial and residential sectors consume about 93% of total electricity consumption. Air-conditioning alone used 31% of total electricity (EMSD, 2017). Enhancing the energy efficiency of building cooling systems is always in high demand, particularly in cooling dominated regions.

For decades, optimal control of chiller plants has been widely and comprehensively studied by researchers from various disciplines. For instance, Liao et al. (2018) developed a method to enhance chiller sequencing control under uncertainty. Advanced control methods were developed to optimize chiller load distribution (Chan et al. 2005). Data driven models were adopted for chiller sequencing control (Shan et al. 2016).

One of the major problems in chiller operation is that chillers often operate at low part load ratio (PLR) due to overestimation of building load profile at design stage. Variable speed chillers are an effective solution to this problem. Variable speed drivers often consume 4%-8% of the energy converted. Also, they require higher initial and maintenance costs than constant speed chillers. An alternative solution is to use thermal storage techniques to enhance chiller efficiency during low part load conditions (Shan et al. 2019).

However, common HVAC systems are not equipped with a thermal storage system. This study proposes a control strategy to shift building load by using the thermal storage effect of chilled water delivery system, so that the chiller is either operating in high PLR or fully stopped. The concept of the strategy has been proved via on-site tests.

2. THE PROPOSED CHILLER PLANT CONTROL STRATEGY

2.1. The fundamental idea

It is well known that chiller efficiency is highly affected by part load ratio (PLR). Figure 1 demonstrates the chiller COP increases with the increase of PLR. The PLR in this study is defined as the actual chiller load divided by its rated capacity for easy calculation, as shown by Equation 1. A more rigorous definition is presented in Equation 2, where PLR is the actual chiller load divided by its maximum capacity at the same working condition. Because the actual chiller maximum capacity may exceed its rated capacity in real operation (e.g., when the chilled water temperature is higher than that in rated condition), the PLR calculated by Equation 1 could exceed 1.0.

Equation 1: part load ratio used in this study.

$$PLR = \frac{CL}{Q_N}$$

Equation 2: a more rigorous definition of part load ratio.

$$PLR' = \frac{CL}{Q_{max}}$$

Where:

- CL = chiller cooling load (kW)
- Q_N = rated capacity of chiller (kW)
- Q_{max} = maximum cooling capacity of chiller when operating at the same working condition (kW)

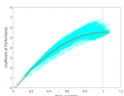

Figure 6 COP of a constant speed centrifugal chiller and its polynomial fit

It is proposed to utilize the thermal energy storage effect of the chilled water delivery system to improve chiller efficiency. The fundamental idea of the proposed strategy is to maintain a high PLR of operating chillers while keeping the supply chilled water temperature within the allowed range. The high PLR is achieved by postponing the start of an idling chiller,

bringing forward the stop of a running chiller, and adjusting the supply chilled water temperature set-point. Energy saving is achieved in two ways: increased overall chiller efficiency and less running time of the associated cooling water pumps and primary chilled water pumps.

The overall control strategy consists of two modes for different scenarios. Control Mode A is applicable during the end of office hours. Control Mode B is appliable for extreme low cooling load conditions, particularly when the actual cooling load is much lower than the predicted value at design stage.

2.2. Framework of Control Mode A (applicable during the end of office hours)

Figure 2 shows the scheme of the proposed Control Mode A. Outputs of the strategy consists of chiller on/off command and supply chilled water temperature reset command. The main routine consists of two parts, one for staging off a chiller, the other for staging on a chiller.

Deduction of an operating chiller

The chiller stage off criteria is redeveloped based on a previous control strategy which utilizes the real time chiller inlet guide vane opening as a reliable index of chiller efficiency for sequencing control and has been running on-site for several years (Shan et al. 2016). As shown in Figure 2, when chiller inlet guide vane opening is less than 60%, the deduction of an operating chiller will be considered. The maximum capacity of remaining chillers needs to be predicted if one chiller is switched off. If the predicted maximum capacity is higher than the present cooling load, the process to stage off a chiller will be triggered. Prior to switching off a chiller, a charging process is activated. The supply chilled water temperature set-point is reset to a relatively lower value (i.e., 5.5 °C). Once the supply chilled water temperature reaches 5.5 °C and return chilled water temperature reaches 8.5 °C, it is considered that the chilled water in the pipelines is fully charged, and one of the running chillers will be turned off. Ten minutes later, the associated cooling water pump and primary chilled water pump will also be shut down. The time delay of 10 minutes is to ensure the safe operation of chillers.

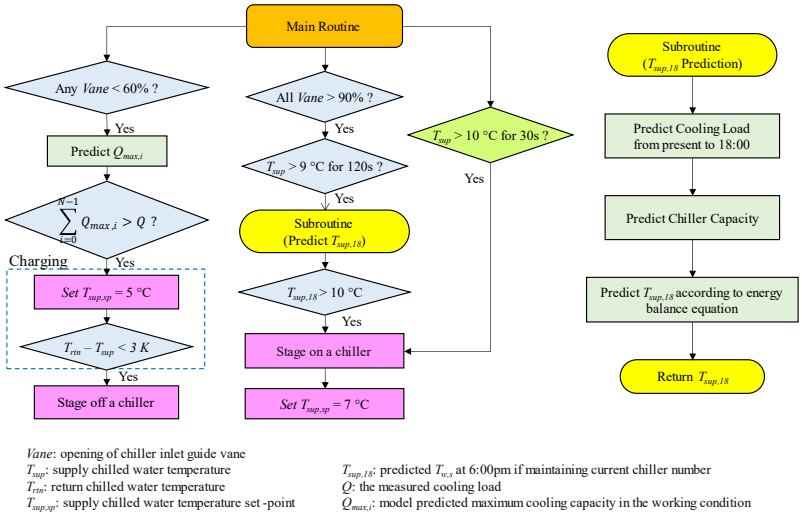

Figure 2 Framework of the proposed chiller control strategy during office hour

Addition of an idling chiller

The addition of a chiller will be considered if the inlet guide vane opening of all running chillers are higher than 90% and the supply chilled water temperature is higher than 9 °C for more than 2 minutes. A subroutine shown on the right side of Figure 2 is used to predict the supply chilled water temperature at the end of office hour (i.e., 18:00) if a chiller is not added into operation. If the predicted temperature ($T_{sup,18}$) is higher than 10 °C, an idling chiller will be put into operation, otherwise the present chiller status will be retained. A separate logic is adopted to guarantee building thermal comfort in case the prediction is not success. When the measured chiller supply water temperature is higher than the upper limit (i.e., 10 °C) for 30 seconds, an idling chiller is immediately put into operation. The supply chilled water temperature of all running chillers is also reset to normal value (i.e., 7 °C).

The part regarding the prediction of $T_{sup,18}$ shown in Figure 2 involves the prediction of cooling load and the prediction of the maximum chiller capacity. A data-driven model is adopted to predict the cooling load in the remaining working hours of the day. The average hourly cooling load is predicted based on the cooling load at present, forecasted weather condition, and time of the day.

Due to its simplicity in model structure, applicability for online calculation and good interpretability, a Multiple Linear Regression (MLR) model is adopted for the prediction of the maximum chiller capacity. As shown in Equation 3, the

maximum capacity is estimated based on the entering chilled water temperature and entering cooling water temperature. The model should be trained using selected real chiller operation data. In this study, the data with chiller inlet guide vane opening higher than 95% was selected for the model training. Considering the impact of deviation in chiller performance and sensor accuracy, each chiller will get its own set of model parameters for the prediction. With the predicted cooling load profile and maximum chiller capacity, the supply chilled water temperature at the end of office hours could be predicted using the energy balance equation shown in Equation 4.

Equation 3: prediction of maximum chiller capacity

$$Q_{max,i} \sim lm(T_{ev,in}, T_{cd,in})$$

Equation 4: supply chilled water temperature at the end of office hour

$$T_{sup,18} = \frac{3600 \cdot \sum CL_{\tau} - \sum Q_{max}}{C_{TES}} + T_0$$

Where:

- Q_{max} is the predicted maximum cooling capacity of the chiller (kW)
- $T_{ev,in}$ = the temperatures of water entering evaporator (°C)
- $T_{cd,in}$ = the temperatures of water entering condenser (°C)
- lm(·) = the MLR model.
- $\sum CL_{\tau}$ = predicted cooling load from present until the end of office hour (kWh)
- $\sum Q_{max}$ = the predicted maximum cooling capacity of running chillers from present until the end of office hour (kJ)
- C_{TES} = thermal capacitance of the virtual thermal mass representing the thermal storage effect of the chilled water delivery system (kJ/K)
- T_0 = the measured supply chilled water temperature at present (°C)

2.3. Framework of Control Mode B (applicable for extreme low cooling load conditions)

In some conditions, particularly in cool seasons, the *PLR* of the sole running chiller is still too low, resulting low chiller efficiency. With the proposed Control Mode B, the chiller efficiency could be improved significantly because it is either fully stopped or operating at high *PLR*. When in operation, the chiller produces more cooling than needed, and the extra cooling is stored in the chilled water system. The only operating chiller is turned off when the chilled water temperature is low enough. And the building is cooled by the cooling energy stored in the chilled water system.

Figure 7 demonstrates the framework of this Control Mode B. If there is only one chiller in operation and its *PLR* is lower than 80%, the control strategy will predict the period of which the building thermal comfort can be maintained if all chillers are turned off and the cooling is solely provided by the stored cooling energy. The prediction of such period is based on the energy balance equation presented by Equation 5.

Equation 5: energy balance equation for predicting stop period.

$$3600 \cdot \int_0^{T_{off}} CL(t)\, d_t = C_{TES} \cdot \Delta T$$

Where:

- T_{off} = the time period to be predicted (hour)
- $CL(t)$ = the building cooling load profile predicted previously (kW)
- C_{TES} = thermal capacitance of the virtual thermal mass representing the thermal storage effect of the chilled water delivery system (kJ/K)
- ΔT = the allowed temperature increase of the virtual thermal mass after discharging (K)

If the T_{off} is longer than a threshold (e.g., 1 hour), The charging process will be activated. Supply chilled water temperature will be set to 5.5 °C, and the secondary chilled water pump will be controlled to achieve a lower temperature difference ($\Delta T = T_{rtn} - T_{sup}$) between return and supply chilled water temperature. Once the supply chilled water temperature reaches its set-point and the ΔT is lower than 3 K, the only running chiller will be turned off. Its associated primary pump and condenser water pump will also be turned off in 10 minutes. The secondary pumps will remain in operation to keep the recirculation of chilled water. It should be noticed that the chilled water will flow through the bypass line in the reverse direction of that in normal operation, as demonstrated in Figure 4. When the supply chilled water temperature is higher than 10 °C for 30 seconds, it is considered that the stored cooling energy has been used up and a chiller need to be put into operation to avoid compromising building thermal comfort.

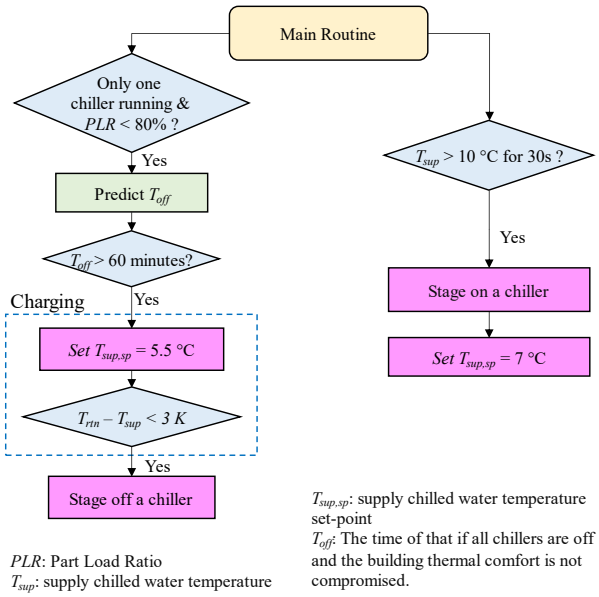

Figure 7 Framework of the proposed chiller control strategy during low load conditions.

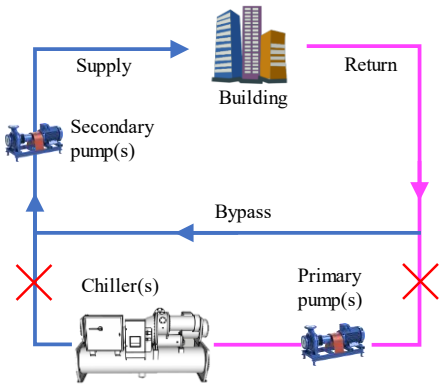

Figure 4 Chilled water flows in reverse direction through the bypass line when discharging.

3. THE BUILDING AIR-CONDITIONING SYSTEM AND SIMULATION PLATFORM

3.1. The building air-conditioning system

The proposed strategy is validated in the air-conditioning system for a high-rise commercial building in Hong Kong. The building has a height of 490 m and consists of 108 floors. It is divided into three sections: a car park (24,000 m^2) on the ground floor; shopping arcades (67,000 m^2) between the ground floor and the fifth floor; and the building tower (230,000 m^2) which consists of commercial offices and a hotel above the 100th floor.

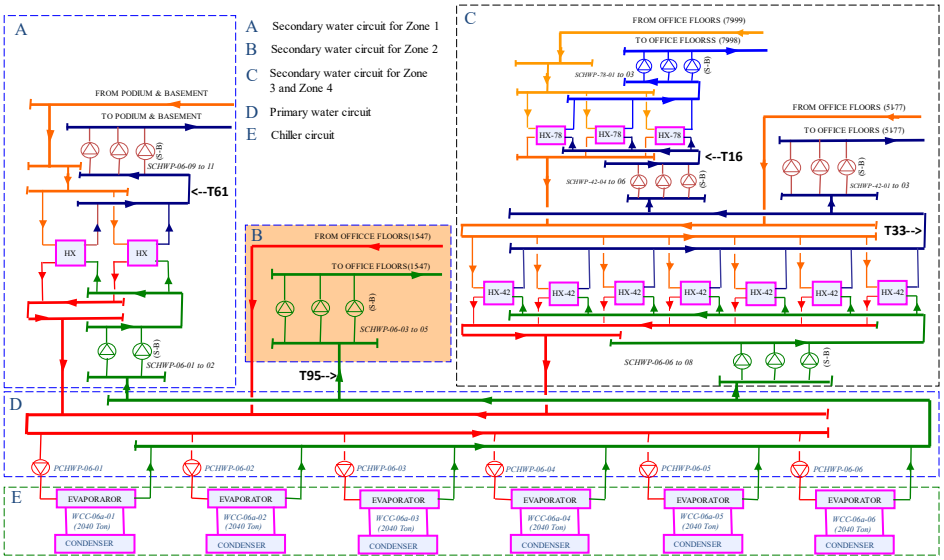

Figure 8 The chilled water production and delivery system

The large and complex air-conditioning system serves all floors except the hotel above the 100th floor. Figure 5 demonstrates the chilled water production and delivery system. The main equipment of the air-conditioning system is located in three mechanical zones: M1 (four floors in total, between 11th and 12th floor), M2 (two floors in total, between 47th and 48th floor) and M3 (two floors in total, between 77th and 78th floor). M2 and M3 mainly consist of the heat exchangers and chilled water pumps serving upper floors, while M1 consists of other major equipment, including the chillers, primary water pumps, cooling water pumps and cooling towers. Table 1 shows a summary of the specifications of the main equipment.

The system consists of six identical high voltage (11,000 volts) constant speed centrifugal chillers. Each chiller is associated with a primary chilled water pump and a cooling water pump, both are constant speed. Eleven cooling towers

of two groups provide chillers with cooling water. The fan speed of all cooling towers is modulated by a local controller to achieve the required cooling water temperature. Each office floor consists of two AHUs, and the chilled water is delivered to each floor via two sets of reverse return risers. Plate heat exchangers are used to isolate chilled water for individual zones to avoid high pressure in water pipes from gravity.

Table 1: Specifications of main equipment in the system

Chillers	N	$M_{w,ev}$ (L/s)	$M_{w,cd}$ (L/s)	CAP (kW)	W (kW)
WCC-06-01 to 06	6	345.0	410.1	7,230	1,346
Cooling Towers	N	M_w (L/s)	M_a (m^3/s)	Q_{rej} (kW)	W (kW)
CTA-06-01 to 06	6	250.0	157.2	5,234	152
CTB-06-01 to 05	5	194.0	127.0	4,061	120
Pumps	N	M_w (L/s)	Head (m)	η (%)	W (kW)
CDWP-06-01 to 06	6	410.1	41.60	83.6	202
PCHWP-06-01 to 06	6	345.0	31.60	84.5	126
SCHWP-06-01 to 02	1(1) *	345.0	24.60	82.2	101
SCHWP-06-03 to 05	2(1) *	345.0	41.40	85.7	163
SCHWP-06-06 to 08	2(1) *	345.0	30.30	84.2	122
SCHWP-42-01 to 03	2(1) *	294.0	36.50	87.8	120
SCHWP-42-04 to 06	2(1) *	227.0	26.20	84.3	69.1
SCHWP-78-01 to 03	2(1) *	227.0	39.20	85.8	102

* Values in round brackets indicate number of standby pumps.

3.2. Dynamic platform for real time test and validation

The thermal storage capacitance of the chilled water delivery system is estimated based on its design, including lengths, diameters, and wall thicknesses of the pipes. Equation 6 shows the equation for the estimation, in which thermal capacitance of water and steel pipes are considered.

Equation 6: Estimation of thermal capacitance of chilled water delivery system.

$$C_{TES} = c_p \cdot \rho_w \cdot S_w \cdot L + c_{p,s} \cdot \rho_s \cdot S_s \cdot L$$

Where:

- C_{TES} = the estimated thermal capacitance of the virtual thermal storage (kJ/kg)
- c_p = specific heat capacity of water
- $c_{p,s}$ = specific heat capacity of steel
- $S_w = \frac{\pi \cdot D^2}{4}$, the cross-sectional area of chilled water (m^2)
- $S_s = \pi \cdot D \cdot d$, the cross-sectional area of steel pipe (m^2)
- D = internal diameter thickness of the pipe (m)
- d = wall thickness of the pipe (m)
- L is the length of the pipes (including the main supply and reverse return water pipes) (m)

Table 2 provides a summary on the length and diameters of pipes in the real system. The estimated total thermal capacitance of the water and pipe steel are 3,100,000 kJ/K and 212,600 kJ/K, respectively. As a result, the thermal capacitance of the virtual energy storage is estimated to be around 3,312,600 kJ/K. It should be noticed that the actual capacitance of the system should be higher because the thermal capacitance of those branches and AHU cooling coils is ignored in the estimation.

Table 2: The length and diameters of the chilled water delivery system

Pipelines	Length (m)	Number of Pipes	Total Length (m)	Diameter (mm)
Risers: M1 to Zone 1 floors	63.03	6	378.18	500
Risers: M1 to Zone 2 floors	127.47	6	764.82	500
Risers: M2 to Zone 3 floors	120.42	6	722.52	500
Risers: M3 to Zone 4 floors	106.89	6	641.34	400
Risers: M1 to M2	139.65	2	279.3	800
Risers: M2 to M3	120.42	2	240.84	600
Main pipes inside M1	60	2	120	800
Branch pipes to AHUs	10	2	1280	150

4. ON-SITE PROOF OF CONCEPT TEST RESULTS

On-site tests were conducted to proof the concept of utilizing the system intrinsic thermal storage for enhanced system efficiency. Since the control strategy has not yet been programmed into the building management system (BMS), the tests were conducted by manually overriding the control command for the chillers, pumps, and cooling towers.

4.1. On-site test of Control Mode A

The control strategy was tested in May 2022 (a normal working day). Figure 6 shows the chiller supply temperature set-point (T_{sp}), supply chilled water temperature to different zones, and the operating chiller number. *T95*, *T33* and *T16* are the supply chilled water temperature to Zone 2, Zone 3 and Zone 4, respectively. *T95* also represents the chiller supply chilled water temperature. The chiller supply chilled water temperature was reset from 7 °C to 5.5 °C at 16:30 when there were two chillers in operation. After the resetting, the temperatures of supply chilled water to all zones began to decrease gradually. One of the two running chillers was switched off one hour later (at 17:28). The number of operating chillers remained unchanged during the rest of the day.

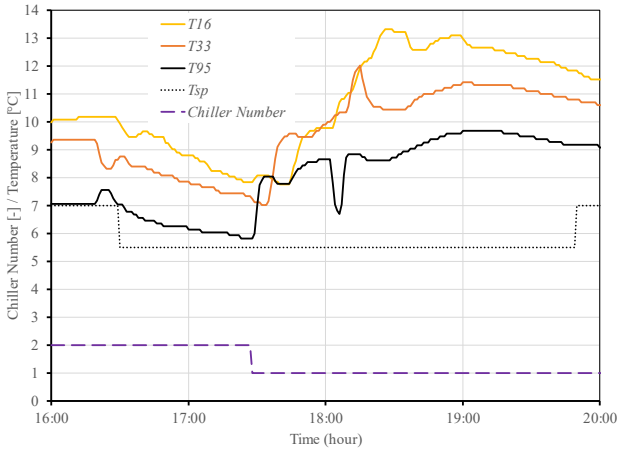

Figure 6 Supply chilled water temperature to different zones, chiller supply temperature set-point and operating chiller number

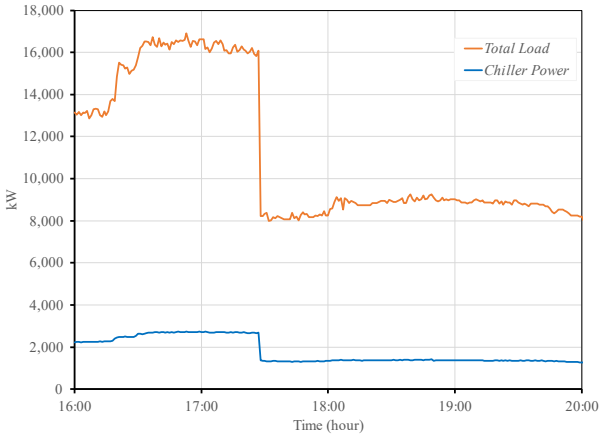

Figure 9 Total chiller load and total chiller power

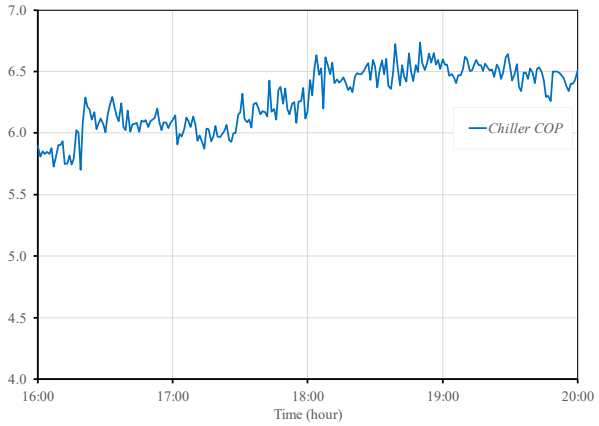

Figure 8 Overall chiller COP

Because the cooling load was still higher than the maximum capacity of the remaining operating chillers when one chiller was turned off, the temperature of supply chilled water temperature to the three zones began to increase immediately. The only operating chiller was pushed to its maximum capacity. As shown in Figure 6, there is a short drop in *T95* because some of the AHUs were automatically closed at 18:00 and the reduced cooling load. But the cooling load in the upper zones did not drop. *T95* soon returned to its original level because of the heat transferred via plate heat exchangers among the three zones. The trend continued until 19:00 when most of the office workers were off duty. Though the supply chilled water temperature was higher during the on-site test, the operation team received no complaints from occupants during the test, indicating that the building thermal comfort was not compromised.

Figure 7 shows the total chiller loading during the test. The charging process began at 16:30 and ended at 17:28. The total load increased significantly at around 16:30 due to the set-point resetting of supply chilled water temperature. Both chillers were running at their maximum capacity at the condition until one of them was turned off at 17:28. It is noticeable that the total chiller power increased slightly after the set-point reset of chiller supply chilled water temperature and dropped dramatically after the shutdown of one chiller.

Figure 8 shows the total chiller COP in the on-site test. It increased slightly due to higher *PLR* after 16:30 when the chiller supply chilled water temperature was reset lower. After one chiller was turned off at 17:28, it further increased from around 6.0 to around 6.5.

4.2. Energy saving of Control Mode A

The energy saving analysis was conducted by investigating the period between 16:00 and 19:00 when the charging and discharging process were conducted. The total chiller load and electricity consumption during the three hours were 35979 kWh and 5844 kWh, respectively. The mean chiller COP was 6.15 during the on-site test.

To estimate the energy saving of the control strategy, the test was compared with a virtual scenario where the total building cooling load was assumed to be maintained at the average value (11993kW) of the investigated three hours during the test. The chiller number was 2 during the three hours in the virtual scenario, and the COP was estimated to be 5.7 according to chiller operation data. The energy saving in chiller power consumption of the proposed control strategy was therefore estimated to be 468 kWh. Because the chiller was shutdown 1.5 hours earlier in the test, the estimated energy savings due to the shutdown of the associated primary chilled water pump and condensing water pump were 189 kWh and 303 kWh, respectively. The estimated saving from the cooling tower was 38 kWh. The total energy saving was therefore estimated to be 998 kWh. During the analysed three hours, the saving rate in chiller energy consumption was 8% and the total energy saving rate in the chiller plant was 14%.

4.3. On-site test of Control Mode B

The on-site test of Control Mode B was conducted in the night of April 14th, 2022, a working day with mild weather condition. Though the total occupancy number in the high-rise commercial building reduced from around 8000 to around 3000 during the home office period due to pandemic, mechanical cooling was still always needed by all floors and all zones.

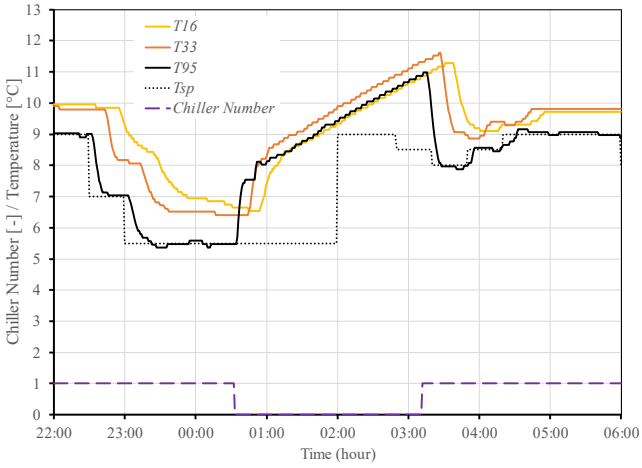

Figure 10 Supply chilled water temperature to different zones, chiller supply temperature set-point and operating chiller number.

Figure 9 shows the supply chilled water temperature and the operating chiller number during the on-site test. The supply chilled water temperature set-point was set to 5.5 °C at 23:00. It took 26 minutes for the actual supply chilled water temperature to reach its set-point (at 23:26). The only running chiller was turned off 1.5 hours later at 00:33am, and no chiller was in operation from 00:33am until 3:11am. The whole time period was 2 hours and 38 minutes when no chiller was running. The supply chilled water temperature was reset to 8 °C when a chiller was put into operation at 3:11am.

It can be seen that *T95*, *T33* and *T16* increased rapidly after the shutdown of the only running chiller at 00:33am. They increased around 2 K within 10 minutes. But the increasing speed became lower later, they gradually increased to around 11 °C during the period when no chiller was in operation. It should be noticed that when cooling was supplied by chillers, supply chilled water temperature to lower zone should be lower than that to upper zone, i.e., *T95* < *T33* < *T16*. This may change when the building is using the stored cooling energy in the chilled water delivery system. Though the three temperatures still have the same trend due to the interconnection, lower zone water temperature could be higher than that in upper zone.

4.4. Energy saving of Control Mode B

Energy saving analysis was conducted by comparing with the next day data between 22:00 and 6:00, when the building load profile was similar. Figure 10 (a) and (b) shows the measured chiller load and chiller power during the Test Day and the Reference Day, respectively. As can be seen from Figure 10(a), the total chiller load increased sharply at 22:30 and

23:00. That was because the chiller supply chilled water temperature was reset lower, and the chiller was charging cooling energy into the chilled water system. Despite of the increase in chiller loading after the reset of chiller supply chilled water temperature, chiller power consumption almost remained the same. The increase of chiller load happened again after the start of chiller at 3:11am, because the chiller was controlled to pull down the chilled water temperature to all zones. As comparison, the chiller load and power consumption varied slightly around a constant value. The chiller load was around 2000 kW, and chiller power was slightly lower than 1000 kW during the whole studied period.

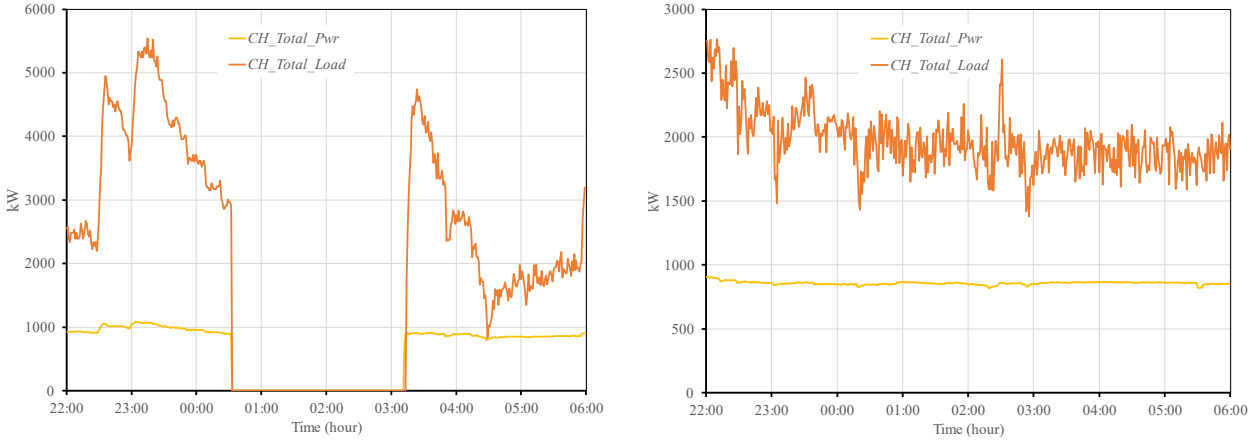

(a) Test Day *(b) Reference Day*

Figure 10 Comparison of measured chiller load and chiller power during the Test Day and the Reference Day

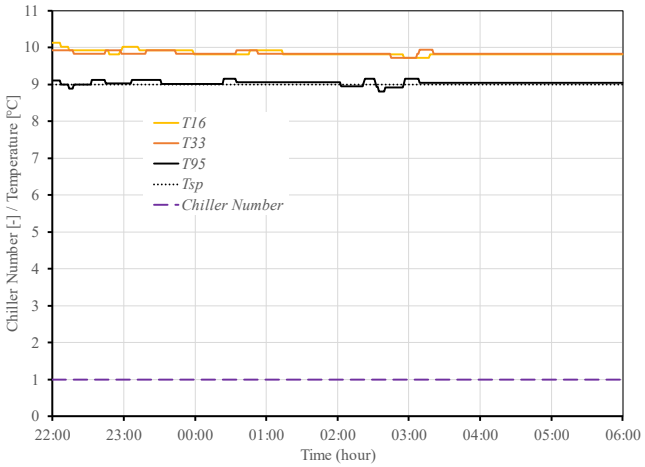

Figure 11 Supply chilled water temperature to different zones, chiller supply temperature set-point and operating chiller number (Reference Day).

Figure 11 shows the temperature in the Reference Day. The supply chilled water temperature was set to 9 °C, and the temperatures of chilled water supplied to all three zones almost remained unchanged. The recorded *T95*, *T33* and *T16* was 9°C, 10°C, and 10°C, respectively.

Table 3 shows the summarized data of chiller efficiency during the two days. Comparing with the Reference Day, although the total cooling load was 2.9% higher in the trial test, the total chiller power consumption was 28.1% lower. The chiller COP increased by 43.3%. The saved chiller power consumption was 1931 kWh. During the period when all chillers were turned off, the cooling towers, primary chilled water pumps and condenser water pumps were all turned off. The saved energy consumption of cooling towers and pumps was estimated based on their rated power consumption. The savings in primary pumps and condenser water pumps was 206 kWh and 330 kWh, respectively. The energy saving in cooling tower fan was about 41 kWh. Therefore, the total saving was around 2508 kWh.

Table 3: Comparison of Chiller Efficiency in the test day and the reference day

	Total load (kWh)	Total chiller power (kWh)	Total chiller COP
Test Day	16226	4929	3.292
Reference Day	15765	6860	2.298
Difference	461 / 2.9%	-1931 / -28.1%	0.994 / 43.3%

5. CONCLUSION

An optimal control strategy is proposed to enhance the chiller efficiency by utilizing thermal storage effect of chilled water delivery system. The proposed strategy maintains a high Part Load Ratio (PLR) of operating chillers so that they can produce cooling with high efficiency. A mechanism is adopted to guarantee building thermal comfort. The strategy has been validated on-site in a high-rise commercial building served by a large and complex cooling system. In one scenario during the end of office hours, the energy efficiency was improved by 14% (988 kWh reduction in electricity use). In another scenario at night, the energy efficiency was improved by 43.3% (2508 kWh reduction in electricity use).

6. FUNDING

The work described in this paper was fully supported by a grant from the Research Grants Council of the Hong Kong Special Administrative Region, China (Project No. PolyU 15205321).

7. REFERENCES

Chang, Y.-C., J.-K. Lin and M.-H. Chuang (2005). "Optimal chiller loading by genetic algorithm for reducing energy consumption." Energy and Buildings 37(2): 147-155.

EMSD, 2017. https://www.emsd.gov.hk/filemanager/en/content_762/HKEEUD2017.pdf [accessed 29 Mar. 2023].

Klein, L., Kwak, J.-y., Kavulya, G., Jazizadeh, F., Becerik-Gerber, B., Varakantham, P., & Tambe, M. (2012). Coordinating occupant behavior for building energy and comfort management using multi-agent systems. Automation in Construction, 22, 525-536.

Liao, Y., G. Huang, Y. Ding, H. Wu and Z. Feng (2018). "Robustness enhancement for chiller sequencing control under uncertainty." Applied Thermal Engineering 141: 811-818.

Shan K, Wang S, Gao D-c, Xiao F, 2016. Development and validation of an effective and robust chiller sequence control strategy using data-driven models. *Automation in Construction*, 65:78-85.

Shan, K., C. Fan, J. Wang, 2019. Model predictive control for thermal energy storage assisted large central cooling systems. *Energy*, 179: 916-927.

#22: A spectrally selective metal mesh coating for photovoltaic/thermal applications

Ken CHEN[1], Kongfu HU[2], Bin ZHAO[3], Gang PEI[4]

[1] Department of Thermal Science and Energy Engineering, University of Science and Technology of China, Hefei 230027, China, chenken@mail.ustc.edu.cn
[2] Department of Thermal Science and Energy Engineering, University of Science and Technology of China, Hefei 230027, China, gbhkf@mail.ustc.edu.cn
[3] Department of Thermal Science and Energy Engineering, University of Science and Technology of China, Hefei 230027, China, zb630@ustc.edu.cn
[4] Department of Thermal Science and Energy Engineering, University of Science and Technology of China, Hefei 230027, China, peigang@ustc.edu.cn

Abstract: In this work, a nano-scale metal (silver) mesh coating was proposed for the photovoltaic/thermal applications (PV/T), it has high transmittance in the solar radiation band (0.3-2.5 μm) and high reflectivity in the infrared band (2.5-25 μm). When combined with PV/T absorber that has high absorption/emission in the full band (0.3-25 μm), it can guarantee the spectral selection characteristics of high absorptivity in the solar band and low emissivity in the infrared band, which can significantly reduce the radiation heat loss of PV/T. Based on the finite-difference time domain method, the effects of mesh period, width and height of metal mesh coatings on the spectral characteristics were simulated and analyzed. The results show that when the period of the nano-metal mesh is 500nm, the height is 50 nm, and the width is 30 nm, the transmittance in the solar band reaches 0.90, and the mid-infrared reflectance reaches 0.88. Compared with the existing ITO coating, the solar radiation transmittance of the metal mesh coating is increased by 20%, the infrared reflectance is increased by 24%, and the sheet resistance (5.3 Ω Sq-1) is reduced 47%.

Keywords: Solar energy； metal mesh； thermal energy； photovoltaic/thermal applications； low emissivity coating

1. INTRODUCTION

The solar radiation band is mainly concentrated in 0.3~2.5 μm, and only part of the band can be used by conventional photovoltaic cells for photoelectric conversion. For example, crystalline silicon cells can only convert radiation in the 0.3~1.1 μm band, while solar radiation in the 1.1~2.5 μm band can only be dissipated and wasted (Huang, 2021). Photovoltaic/thermal (PV/T) technology, which couples the two processes of photoelectric conversion (PV) and photothermal conversion (PT), can provide both electric and thermal energy and greatly improve the comprehensive utilization efficiency of solar energy. In the past 20 years, PV/T has been one of the hottest research directions of solar energy comprehensive utilization (Chow, 2010). However, the spectral requirements of photoelectric and photothermal utilization are significantly different. The spectral requirements of photovoltaic cells only consider the absorption of photons above the band gap, while the infrared emissivity of photothermal films needs to be suppressed for lower radiation heat loss. Unfortunately, present PV/T absorbers generally refer to conventional photovoltaic cell materials and processes, causing high infrared thermal emissivity (~0.9) (Mellor, 2018). As the operating temperature increases, the non-negligible radiative heat loss makes the photothermal performance of PV/T significantly lower than that of individual photothermal conversion devices, limiting its large-scale application. For example, PV/T cannot meet the temperature requirements of most industrial heat; In terms of building energy supply, PV/T cannot meet the heating demand of buildings in winter, nor can it meet the temperature requirements of other building energy (such as absorption refrigeration) when heating is not needed in summer.

To solve the problem of PV/T's high radiation loss, the spectral selection characteristics of PV/T can be optimized. A typical idea is to add a kind of coating with high transmittance in the solar radiation band (0.3~2.5 μm) and high reflection in the infrared band (5~25 μm) to the PV/T absorber. Various theoretical and experimental works on the application of this coating to improve the thermal performance of PV/T systems have been carried out. For example, CH Cox Lii et al. (Cox, 1985) simulated the influence of spectral selectivity on monocrystalline silicon PV/T photoelectric and photothermal properties. The results showed that the low emissivity coating needs to have more than 0.85 solar radiation transmittance and less than 0.25 infrared emissivity to improve the solar energy comprehensive utilization efficiency in the case of photoelectric efficiency loss. Hu et al. (Hu, 2021) simulated the effect of infrared emissivity on the evacuated vacuum plate PV/T thermal efficiency. The results showed that the photothermal efficiency increased from 16.9 % to 54.4 % as the infrared emissivity decreased from 0.95 to 0.05. Lämmle et al. (Lämmle,2016) developed a silver-based six-layer dielectric low emissivity coating with a solar radiation transmittance of 0.79 and an infrared reflectance of 0.87. Alonso-Álvarez et al. (Alonso-Álvarez, 2017) studied indium tin oxide (ITO) as a low-emissivity coating, and the solar radiation transmittance and infrared reflectance were both 0.79. The solar radiation (0.3~2.5 μm) transmittance and infrared (5~25 μm) emissivity of the above low emissivity coatings are mutually restricted, the transmittance decreases with the decrease of emissivity. Therefore, the design of coatings with high solar transmittance and high infrared reflectivity is a potential problem for PV/T utilization.

In this work, a nano-scale metal silver mesh coating was proposed, which has high solar transmittance and high infrared reflectivity. Combined with the high infrared emission PV/T absorber, the overall low infrared emissivity characteristics can be achieved. The novel coating can not only be applied to the laminated on packaging materials of photovoltaic cells (such as glass, and PET), but also be directly applied to the photovoltaic cells, integrated with the top electrode of the photovoltaic cell to form a photovoltaic cell with spectral selectivity as the PV/T absorber because of its excellent electrical conductivity. By combining this coating with a full-band (0.3~25 μm) high absorption/emission PV/T absorber, spectral characteristics with high solar absorption and low infrared emission can be obtained. Huge radiation heat loss caused by PV/T operation temperature increases is reduced and photothermal efficiency is improved. Therefore, the coating has great application prospects in efficient PV/T systems. The finite-difference time-domain method was used to optimize the design of the nano-metal mesh coating, and the spectral and surface resistance calculation models were established to simulate the optical and electronic properties of the metal mesh coating.

2. THEROETICAL MODEL

2.1. Optical model

The electromagnetic field of the nano-scale silver mesh was calculated based on the finite difference time domain (FDTD) method by solving the Maxwell equation. As shown in Figure 1, the optical model of a nano-scale metal mesh was constructed. The plane wave was used as the light source to transmit through the nano-metal mesh. The transmittance (T) and reflectivity (R) were defined as the ratio of the Poynting vector (power flux) before and after the metal mesh, and the mesh size was set to 3 nm. Perfectly matched layer (PML) boundary conditions were used in the vertical direction. The plane direction was set as a periodic boundary condition to simulate an infinitely large area metal mesh. The optical constants of silver were derived from the Palik material optical database.

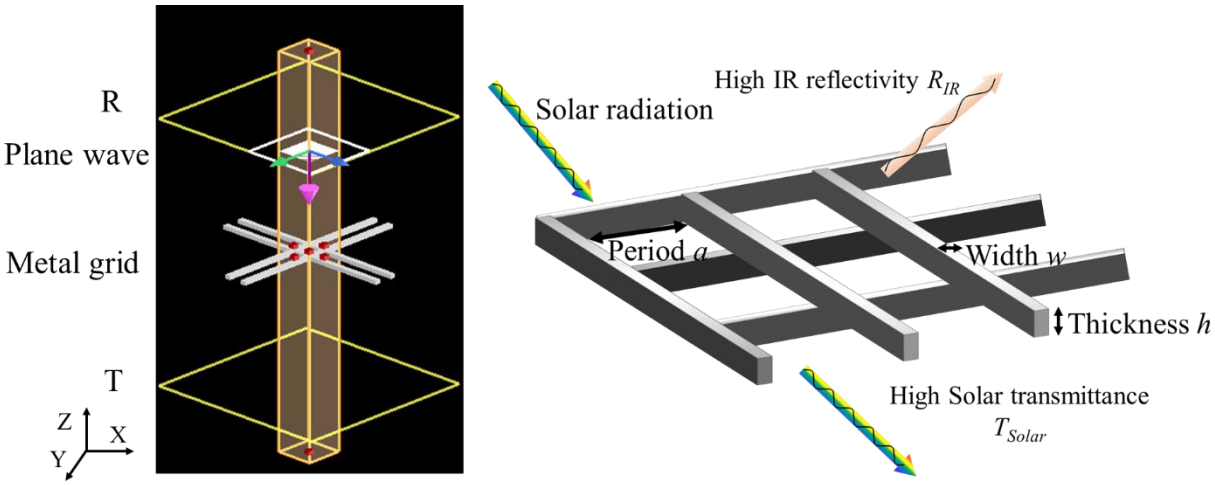

Figure 1 Schematic diagram of metal mesh optical model

The parameters of the nano-scale silver mesh model were set as shown in Table 1. The periods were set to 100,300,500,1000,3000 and 5000 nm (numbered 1-6), and the width (numbered 7-12) and thickness (numbered 13-18) were set to 10,30,50,100,300 and 500 nm, respectively.

Table 1: Parameters setting of the model

Parameter	Number	Period a/nm	Width w/nm	Thickness h/nm
Period a/nm	1	100	30	30
	2	300	30	30
	3	500	30	30
	4	1000	30	30
	5	3000	30	30
	6	5000	30	30
Width w/nm	7	500	10	30
	8	500	30	30
	9	500	50	30
	10	500	100	30
	11	500	300	30
	12	500	500	30
Thickness h/nm	13	500	30	10
	14	500	30	30
	15	500	30	50
	16	500	30	100
	17	500	30	300
	18	500	30	500

Formula (1): *The solar weighted transmittance* $T_{Solar.}$

$$T_{Solar} = \frac{\int_0^\infty T(\lambda) \times \mathrm{AM1.5g}(\lambda) d\lambda}{\int_0^\infty \mathrm{AM1.5g}(\lambda) d\lambda}$$

Formula (2): *The infrared weighted reflectivity* $R_{IR.}$

$$R_{IR} = \frac{\int_0^\infty R(\lambda) \times \mathrm{BB(298K)}(\lambda) d\lambda}{\int_0^\infty \mathrm{BB(298K)}(\lambda) d\lambda}$$

Where:

AM1.5g = the global solar radiation spectrum of atmospheric mass 1.5

λ = wavelength (nm)

T(λ) = Spectral transmittance at wavelength λ

R(λ) = Spectral reflectance at wavelength λ

BB(298K) = Blackbody radiation intensity at 298K ($W \cdot m^{-2} \cdot nm^{-1}$).

2.2. Optical model validation

The optical calculation model was verified by the data of (Catrysse, 2010). As shown in Figure 2, the solar radiation transmittance of 400~1000 nm calculated in this work is consistent, which can verify the accuracy of the model.

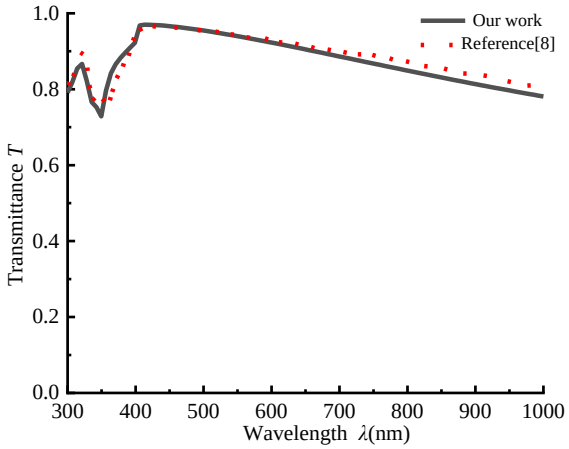

Figure 2 Diagram of metal mesh optical model verification

2.3. Surface resistance calculation

The sheet resistance of the nano-scale metal silver mesh is related to geometric parameters. The sheet resistance R_S of the thin film conductive material is related to the thickness.

Formula (3): The sheet resistance R_s of the nano-scale metal silver mesh (Van De Groe,2012).

$$R_s = \frac{\rho a}{wh}$$

Formula (4): The sheet resistance R_s of ITO thin film.

$$R_s = \frac{\rho}{h}$$

Where:

R_S = sheet resistance (Ω Sq^{-1})

a = Metal silver mesh period (nm)

w = Metal silver mesh width (nm)

h = Metal silver mesh or ITO layer thickness (nm)

ρ = Resistivity of Ag and ITO material ($\Omega \cdot m$) ($1.59 \times 10^{-8} \Omega \cdot m$ for Ag and $5 \times 10^{-5} \Omega \cdot m$ for ITO).

3. RESULTS AND DISCUSSION

The influence of different geometric parameters on the spectral characteristics of silver metal meshes were shown and discussed. In addition, the optical and electrical properties of the silver metal mesh were compared with the transparent conductive material ITO.

3.1. Spectral characteristic

In this section, the solar transmittance and infrared reflectivity of the nano-scale metal silver mesh with different periods, widths and thicknesses were discussed.

Metal mesh period

The nano-mesh period described in this work is the spacing between adjacent silver meshes. As shown in Figure 3, when the width and thickness of the nano-scale silver meshes are fixed at 30 nm, the calculation results of solar transmittance and infrared reflectance are as follows. The numbers 1-6 in the legend correspond to the numbers in Table 1. When the width and thickness of the metal mesh are determined, the period significantly affects the solar transmittance and infrared reflectance. When the metal mesh period is increased from 500 nm to 5000 nm, the solar transmittance is significantly improved (Figure 3a) and the infrared reflectivity is significantly reduced (Figure 3b). Specifically, the transmission peak of the metal mesh is related to the period. For example, when the period of the metal mesh is 300 nm, the transmission peak is about 300 nm, and then the transmittance decreases rapidly with the increase of the wavelength. The transmission peak of the metal mesh with a period of 500 nm is about 500 nm, and the transmittance begins to decrease after the wavelength of 500 nm. As the transmittance increases to 3000 nm, almost all bands of solar radiation can pass through the metal mesh. The phenomenon can be attributed to the plasmonic effect of the silver metal mesh. The absorption peak of silver metal is in the ultraviolet band. Due to the plasmon effect, part of the visible light band is absorbed, while there is no absorption effect in the infrared band after 2500 nm. Some infrared light can pass through the silver metal mesh with a period of more than 1000 nm. The reflectivity of the metal mesh with a period of more than 1000 nm in the infrared band is reduced to less than 0.5. The weighted solar transmittance and infrared reflectance of silver metal meshes with different periods are shown in Table 2. By comparison, the 500 nm periodic silver metal mesh was selected for further analysis due to its T_{Solar} = 0.93 and R_{IR} = 0.81.

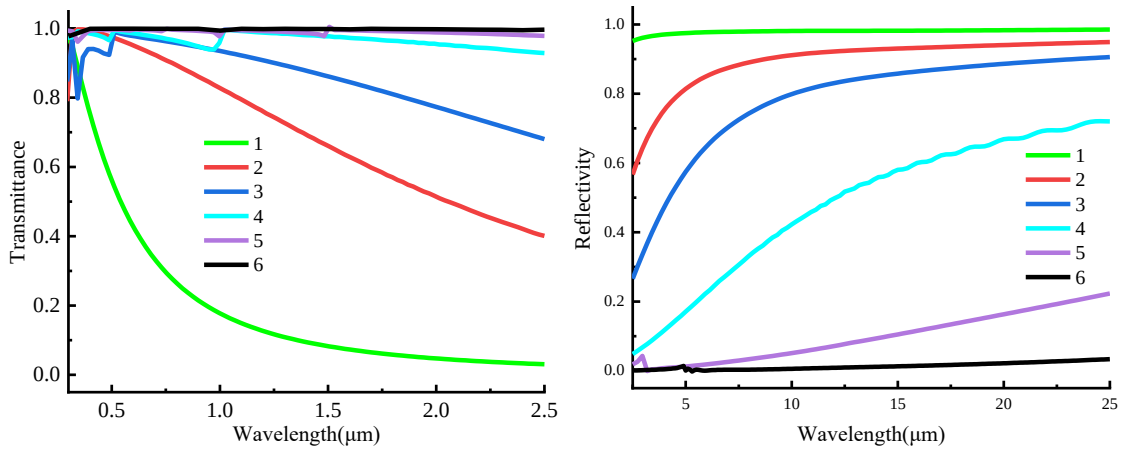

Figure 3 Solar transmission (left) and infrared reflection (right) spectrum of metal meshes with different periods

Table 2: Weighted transmittance in the solar band and weighted reflectance in the infrared band of metal meshs with different periods

Period a/nm	100	300	500	1000	3000	5000
T_{Solar}	0.35	0.87	0.93	0.99	0.99	0.99
R_{IR}	0.98	0.91	0.81	0.49	0.09	0.01

Metal mesh width

The width of the metal mesh represents the filling ratio of the metal silver in a period. Taking the metal mesh with a period of 500 nm and a thickness of 30 nm as an example, when the width of the metal mesh is 500, the metal mesh is a metal silver layer with a thickness of 30 nm. Figure 4 shows the simulation results of solar radiation transmittance and infrared reflectance of the silver mesh with different widths. The period and thickness are set to 500 nm and 30 nm, respectively. The numbers 7-12 in the legend correspond to the numbers in Table 1. As shown in Figure 4a, when the metal mesh width is 10,30,50 nm, the peak solar transmittance is about 500 nm, which is consistent with the 500 nm periodic metal mesh. As the width increases, the transmittance of the visible light band at 500 nm gradually decreases. When the width increases to 100 and 300 nm, the wavelength corresponding to the transmission peak is red-shifted, and the transmittance decreases rapidly at ~750 nm. Finally, when the width is 500 nm, the period and width are the same, which is equivalent to the silver thin metal layer structure with a thickness of 30 nm. The transmittance decreases at 300 nm, which matches the absorption peak of the metal silver. As shown in Figure 4b, due to the fixed period of the infrared band, the metal meshs show high infrared reflectivity (>0.5), and the increase in infrared reflectivity is less than the decrease in solar radiation transmittance. The calculated values of solar weighted transmittance and infrared weighted reflectance are shown in Table 2. Considering that the coating required for PV/T needs to maintain high solar band transmittance while meeting high infrared reflectance, a silver metal mesh with a width of 30 nm (T_{Solar}=0.93, R_{IR}=0.81) is considered to further analysis.

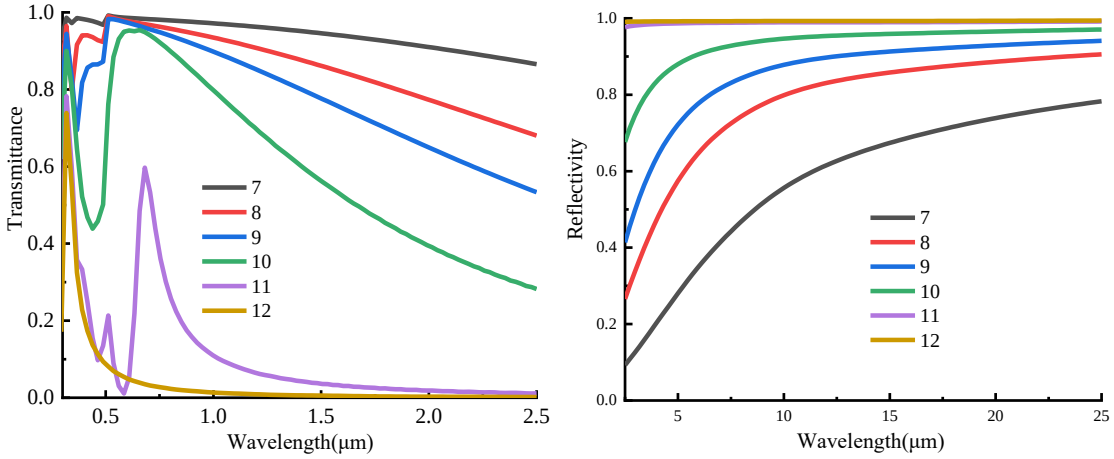

Figure 4 Solar transmission (left) and infrared reflection (right) spectrum of metal meshs with different widths

Table 3: Weighted transmittance in the solar band and weighted reflectance in the infrared band of metal meshes with different widths

Width w/nm	10	30	50	100	300	500
T_{Solar}	0.97	0.93	0.89	0.76	0.19	0.06
R_{IR}	0.60	0.81	0.88	0.95	0.99	0.99

Metal mesh thickness

The thickness of the metal mesh represents its length in the z-axis direction. The period and width of the metal mesh are set to 500 nm and 30 nm, respectively. Figure 5 shows the simulation results of solar radiation transmittance and infrared reflectance of silver metal with different thicknesses. The thickness increases from 10nm to 500nm. The numbers 13 ~ 18 in the legend correspond to the numbers in Table 1. As shown in Figure 5a, under the same period and width, the transmittance peaks of the metal mesh are basically the same. As the thickness increases from 10 nm to 300 nm, the transmittance of the metal mesh in the visible band of 300-550 nm gradually decreases, and the transmittance in the near-infrared band after ~750 nm gradually decreases. As the thickness increases from 300 to 500 nm, the metal mesh is basically not transparent after 1000 nm. As shown in Figure 5b, in the infrared band of 2.5-25 μ m, the reflectivity increases with the increase of thickness. Table 3 shows the weighted solar transmittance and infrared reflectivity. The metal mesh with a thickness of 50 nm is the optimal metal mesh parameter, which T_{Solar}=0.90 and R_{IR}=0.88.

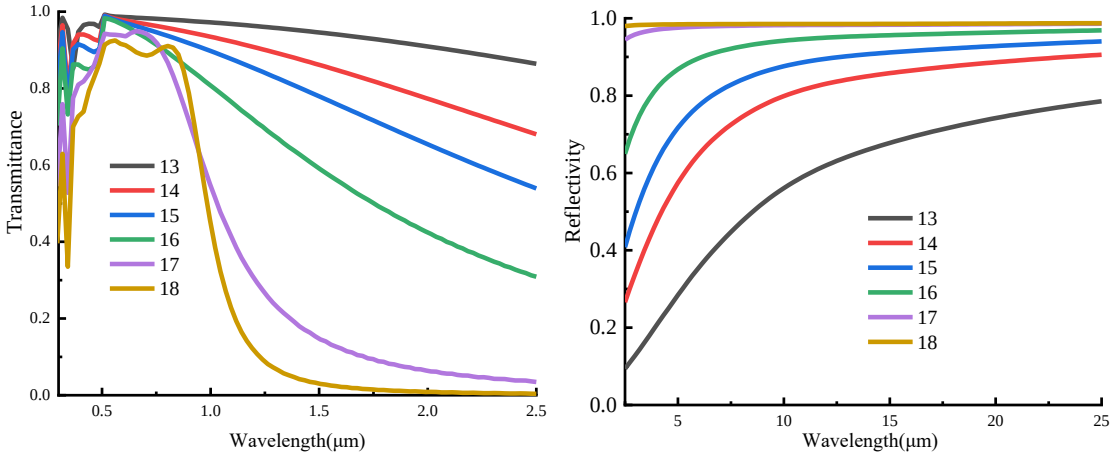

Figure 5 Solar transmission (left) and infrared reflection (right) spectrum of metal meshs with different thicknesses

Table 4: Weighted transmittance in the solar band and weighted reflectance in the infrared band of metal meshs with different thicknesses

Thickness w/nm	10	30	50	100	300	500
T_{Solar}	0.97	0.93	0.90	0.84	0.71	0.66
R_{IR}	0.61	0.81	0.88	0.94	0.98	0.99

Electric field strength analysis

According to the above simulation results, the silver metal mesh with a period of 500 nm, a width of 30 nm, and a thickness of 50 nm has an optimized solar transmittance and infrared reflectivity. Therefore, the electric field intensity distribution under such geometric parameters in the incident light plane was analysed. Two typical incident wavelength conditions

were used to analyse the electric field intensity distribution. The wavelength 550 nm represents the typical wavelength of the solar radiation band, and the wavelength 5 μm represents the mid-infrared thermal emission band. As shown in Figures 6 and 7, the illustration is the relative electric field intensity E1:E (E1 is the electric field intensity, E is the incident electric field intensity), indicating the multiple of the electric field intensity and the incident electric field intensity. The silver metal mesh is located at z=0, the plane wave light source is located at $z=7.5\times10^{-7}$ m and is incident from top to bottom.

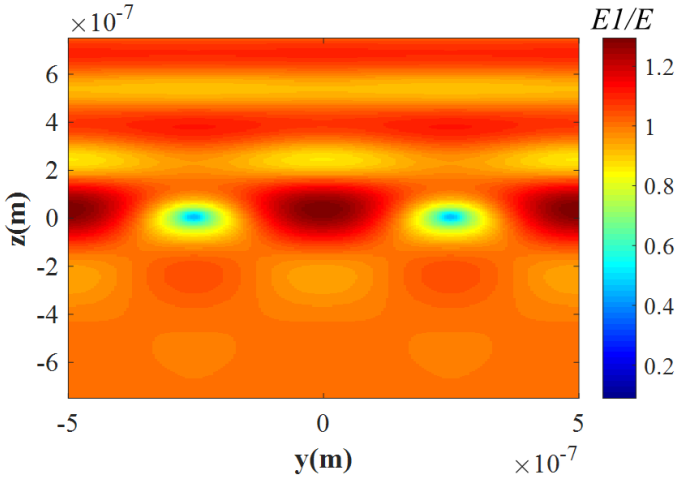

Figure 6 Distribution of relative electric field intensity around the metal mesh under the incident wavelength of 550 nm

When the 550 nm incident plane wave is incident on the surface of the metal mesh, the electric field intensity is the incident electric field intensity E. The electric field intensity in the area between adjacent silver metals is greatly enhanced because of the local plasmon effect is generated between the silver metal meshs. The ratio of the electric field intensity to the incident electric field intensity E is 0.97 after the plane wave light source passes through the silver metal mesh (Figure 6), indicating that the 550 nm wavelength incident light basically passes through the silver nano-metal mesh. When the wavelength of the incident light is 5 μm, the relative electric field intensity distribution has obvious regional changes (Figure 7). In the region below the silver metal mesh (z>0), the electric field intensity is basically 1.4 ~ 1.6 times the incident electric field, indicating that most of the infrared light is reflected, resulting in high infrared reflectivity.

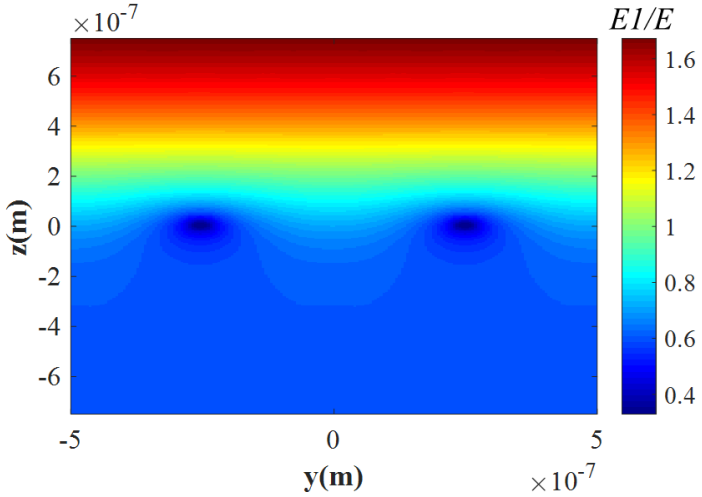

Figure 7 Distribution of relative electric field intensity around the metal mesh under the incident wavelength of 5 μm

From the results of the relative electric field intensity distribution shown in Figure 6 and Figure 7, it can be seen that:

(1) The area enclosed by the metal mesh generates a surface local electric field at the incident light of 550 nm, which improves the light absorption in this part of the area;

(2) The metallic silver mesh with a period of 500 nm, a width of 30 nm and a thickness of 30 nm can transmit most of the visible light and reflect most of the infrared light, resulting in spectral characteristics of high solar band transmittance and high infrared reflectance.

3.2. Performance comparison analysis

In this section, the spectral characteristics and sheet resistance characteristics of the proposed nano-scale metal silver mesh (period of 500 nm, width of 30 nm, variable thickness) and the commonly used low-emissivity coating indium tin oxide (ITO) material were compared.

Spectral characteristics comparison

ITO material is usually used as low-emissivity coating because of its high solar radiation transmittance (T_{Solar}) and high infrared reflectance (R_{IR}). Both T_{Solar} and R_{IR} are related to the thickness of the ITO layer. The solar radiation transmittance and infrared reflectance of the metal silver mesh and ITO layer with the same thickness were compared. The thickness range is 10,30,50,100,300,500 nm. As shown in Figure 8, when the thickness of ITO material is less than 100 nm, the transmittance is higher (T_{Solar}>0.7), while the infrared reflectivity is only below 0.4. When the thickness increases to 300 nm, the transmittance and infrared reflectivity of the solar band reach equilibrium, and T_{Solar} = 0.75, R_{IR} = 0.71. When the thickness further increases, the solar band transmittance decreases more. When the thickness of the metal mesh is less than 100 nm, the solar band has a high transmittance (T_{Solar}>0.85), while the infrared reflectivity still maintains a high level (R_{IR}>0.8). As the thickness increases to more than 100 nm, the transmittance gradually decreases. When the thickness is 50 nm, T_{Solar} reaches 0.90 and R_{IR} reaches 0.88. Compared with ITO material, the solar band transmittance increases by 20%, and the infrared reflectivity increases by 24%. Therefore, silver metal mesh is a better low emissivity coating material than ITO.

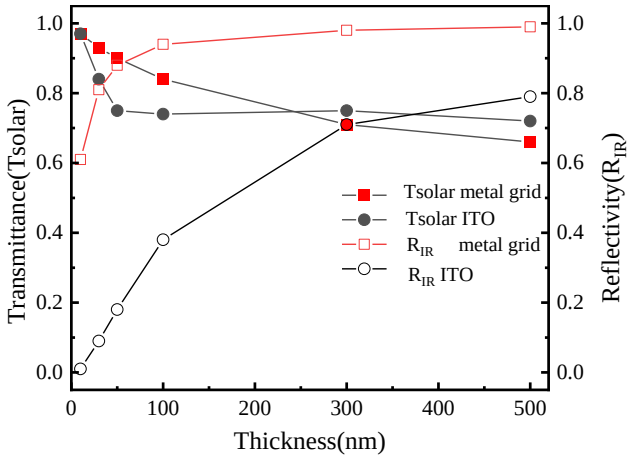

Figure 8 Spectral characteristics comparison of metal mesh and ITO material

Sheet resistance comparison

ITO material can also be used as transparent conductive electrode on the top electrode of PV/T photoelectric photothermal absorption layer because of its high conductivity. The conductivity of thin film can be compared by sheet resistance. The sheet resistance of silver metal mesh and ITO layer with different thickness are calculated and compared. As shown in Figure 9, the sheet resistance of metal mesh with the same thickness is lower than that of ITO material. According to formula (3) and (4), the lower sheetr resistance of silver metal mesh is due to the lower resistivity of silver relative to ITO material.

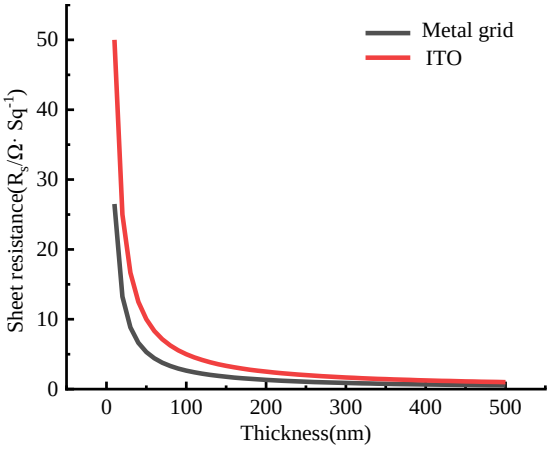

Figure 9 Sheet resistance comparison of metal meshs and ITO material

4. CONCLUSION

Aiming at the problems of high infrared thermal emissivity and high radiative heat loss of PV/T absorbers, a nano-scale metallic silver mesh structure was proposed in this work. It has high transmittance in the solar radiation band (0.3~2.5 μm) and high reflectivity in the infrared thermal radiation band (5~25 μm), which can significantly reduce the radiative heat loss caused by the increase in collector temperature. Based on the finite difference time domain method, the effects of the width, thickness and period of the nano-metal mesh on the solar transmittance and infrared reflection characteristics were analysed. Through the simulation results, the main conclusions are as follows:

(1) With the increase of nano metal mesh period, the transmittance of the solar band increases and the infrared reflectivity decreases; As the width of the nano-metal mesh increases, the transmittance decreases and the infrared reflectivity increases; With the increase of nano metal mesh thickness, the solar transmittance decreases and the infrared emissivity increases.

(2) The optimized nano-scale metal mesh has a period of 500 nm, a width of 30 nm, and a thickness of 50 nm. The solar radiation transmittance can reach 0.90, and the infrared reflectivity is 0.88. Compared with ITO material, the solar band transmittance is increased by 20 %, and the infrared reflectivity is increased by 24%.

(3) The surface resistance of nano-scale metal silver mesh is determined by the period, width and thickness of the metal mesh. Under the same thickness as ITO, the surface resistance is reduced by 47%, which has the potential as a transparent conductive electrode for PV/T photoelectric photothermal absorption layer.

5. ACKNOWLEDGEMENT

This work was supported by the National Natural Science Foundation of China (NSFC 52130601 and 52106276) and Xiaomi Young Scholars project.

6. REFERENCES

Alonso-Álvarez D, Llin L F, Mellor A, et al. ITO and AZO films for low emissivity coatings in hybrid photovoltaic-thermal applications[J]. Solar Energy, 2017, 155: 82-92.

Catrysse P B, Fan S. Nanopatterned metallic films for use as transparent conductive electrodes in optoelectronic devices[J]. Nano letters, 2010, 10(8): 2944-2949.

Chow T T. A review on photovoltaic/thermal hybrid solar technology[J]. Applied energy, 2010, 87(2): 365-379.

Cox Iii C H, Raghuraman P. Design considerations for flat-plate-photovoltaic/thermal collectors[J]. Solar energy, 1985, 35(3): 227-241.

Hu M, Guo C, Zhao B, et al. A parametric study on the performance characteristics of an evacuated flat-plate photovoltaic/thermal (PV/T) collector[J]. Renewable Energy, 2021, 167: 884-898.M. Lämmle, Development and modelling of highly-efficient PVT collectors with low-emissivity coatings, Solar Energy, 2016,130 :161-173.

Huang G, Wang K, Markides C N. Efficiency limits of concentrating spectral-splitting hybrid photovoltaic-thermal (PV-T) solar collectors and systems[J]. Light: Science & Applications, 2021, 10(1): 28.

Lämmle M, Kroyer T, Fortuin S, et al. Development and modelling of highly-efficient PVT collectors with low-emissivity coatings[J]. Solar Energy, 2016, 130: 161-173.

Mellor A, Alvarez D A, Guarracino I, et al. Roadmap for the next-generation of hybrid photovoltaic-thermal solar energy collectors[J]. Solar Energy, 2018, 174: 386-398.

Van De Groep J, Spinelli P, Polman A. Transparent conducting silver nanowire networks[J]. Nano letters, 2012, 12(6): 3138-3144.

#23: Solar control devices on glazed facades

Optimizing the Shape of an outer Slat Array as function of latitude, climate and solar control strategy

Antonio CARBONARI[1]

[1] *University IUAV of Venice, Dorsoduro 2206, 30123 Venezia, Italy, carbonar@iuav.it*

Abstract: The arrays of external movable slats are one of the most effective solar control devices on transparent building envelope elements. Furthermore, they significantly affect the image of the building. For a south facing glazed façade it is normally assumed that slats with the major axis horizontal are convenient, while for the east and west orientations it is better to arrange their major axis vertically. Therefore, intermediate inclinations should be appropriate for intermediate orientations of the façade. The optimal shape of a slat array depends on a number of factors such as: visible solar paths, which are defined by the Latitude and orientation of the façade, local climate and building's energy balance; the latter determines the relative weight of energy demand for heating, cooling and artificial lighting. If the slats are equipped with PV cells, the energy balance of the building must also take into account their electricity production. If the slats are movable and/or combined with other devices, such as internal curtains, any solar control strategy reduces the incoming luminous flux, and this increases the period of use of the lamps, with the necessary consequences on energy demand and comfort. Therefore, the part of the sky that the façade sees through the slats become important, and this depends on the inclination of slats longitudinal axis. In reference to a typical office room with a fully glazed exterior wall, in a northern Italian climate, in this work is proposed a computer method for finding the optimal slope of the slats longitudinal axis as a function of: local climate, façade orientation and various solar control strategies. The analysis was performed only by means of computer simulations. With regard to the case study in the examined climate the results show that the optimal arrangement of the slats major axis varies significantly depending on the solar control strategy adopted.

Keywords: Building Energy, Solar Control, comfort

1. INTRODUCTION

External movable slat arrays are one of the most effective solar control devices on transparent building envelope surfaces, particularly on a fully glazed façade. Their shape significantly affects the aesthetics of the building (Figure 1).

If the façade is oriented to the south It is normally assumed that slats with the major axis horizontal are convenient from an energy and comfort point of view, while in the case of the east and west orientations it is better to arrange their major axis vertically. Therefore, intermediate inclinations should be appropriate for intermediate orientations of the façade. Actually the optimal shape of a slat array depends on a number of factors such as:

visible solar paths, defined by latitude and façade orientation,

local climate, in particular: temperatures and intensity of solar radiation,

building's energy balance, which is a function of its intended use (time profile of use, internal gains, required Illuminance) and construction technologies of its envelope (which means U-values and thermal capacity),

weight of energy demand for artificial lighting compared to that for heating, ventilation and air conditioning.

if the slats are equipped with photovoltaic cells (PV cells), the energy balance of the building must also take into account their electricity production.

If the slats are mobile and/or combined with other devices, such as internal curtains, any solar control strategy reduces the incoming luminous flux, and this increases the period of use of the lamps, with the necessary consequences on energy demand and comfort. Therefore, it becomes important which part of the sky and the external luminous surfaces the façade sees through the slats, and this depends on the inclination of the slats longitudinal axis (their lateral slope).

Figure 1 Example of an office building equipped with an external slat array, in this case, with a horizontal major axis and built-in PV cells, the façade is oriented approximately to the south (building headquarters of the "Citadel of Construction" in Venice, photo by the author)

In reference to a typical office room with an entirely glazed exterior wall in a northern Italian climate, that of Venice (45.5° N, 20 °C-base heating degree-days equal to 2345), in this work is proposed a computer method to find the optimal inclination of the slats longitudinal axis as a function of: local climate, façade orientation and various solar control strategies. The analysis was performed only by means of computer simulations, the results of which are reported here.

The various solutions were evaluated in relation to the total primary energy demand, and their effects on general indoor comfort conditions. The primary energy demand considered is that for heating, ventilation, air conditioning (HVAC) and artificial lighting, since solar control strategies influence these end uses of energy. Furthermore, these end uses of energy are linked to each other; and analyzing them separately can lead to misleading results. For this reason the computer simulations were performed by using a specifically homemade software (Ener_Lux), which simulates the dynamic thermal and luminous behaviour of the room at hourly time steps, and allows simultaneous analysis of energy and comfort issues. The peculiarity of this software, already presented in a previous SET conference (Carbonari, 2017; Carbonari, 2023), is that, within each calculation time step, it calculates thermal and luminous comfort indexes values, on the base of these, it simulates the feedback on the solar control devices and/or on the set-point temperatures.

Various possible solar control strategies, aimed at minimizing the energy demand and avoiding glare phenomena, were simulated. One is based only on the use of the slats minor axis slope; another uses in addition to it an internal diffusing curtain. A strategy was also simulated aimed at maximizing the electrical production of photovoltaic cells positioned on the slats, while maintaining visual comfort conditions.

The results of the simulations show that for the case study in the examined climate the optimal arrangement of the slats major axis varies significantly depending on the solar control strategy adopted.

2. THE CASE STUDY

The case study consists in an office room of medium size located in a building with typical structure and glazing. The room dimensions are as follows: 5.88 m wide along the façade, 5.22 m deep orthogonally to it, with internal height equal to 2.70 m (Figure 2). The only external wall of the room is one of the longer, it is entirely glazed with a triple glazing with 0.004, 0.006 and 0.004 m thick glass layers. The air gaps are 0.018 m thick. The inner air gap as a low emissive layer in the external side of the internal glass (overall U_{value}: 1 $W \cdot m^{-2} \cdot K^{-1}$). It is hypothesized that the building has a point structure in beams-pillars in reinforced concrete, with floors in brick concrete 0.3 m thick. The inner walls are in hollow bricks 0.08 m thick with plaster in both sides.
In the energy balance of the room, all the five internal enclosing surfaces have been considered as adiabatic. The thermal capacity relative to a thickness corresponding to half of their total thermal resistance was attributed to each building element bordering the room. In this study, the shading effect of surrounding buildings has not been taken into account.

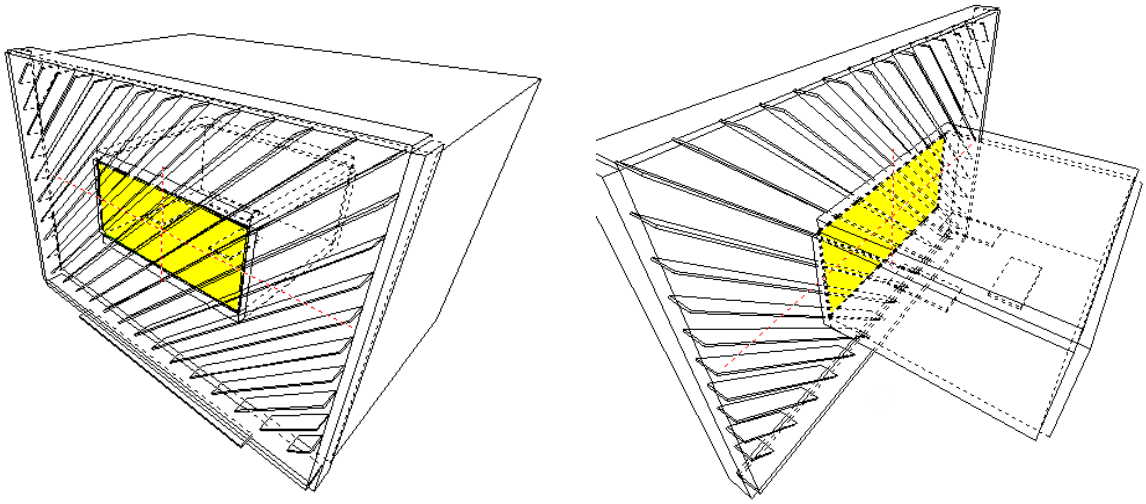

Figure 2 The geometric model of the examined room, in the figure the lateral slope of the slat array is +45 °. The increased extension of the slats and the other shielding elements serve to avoid edge effects

In the office room, the presence of three occupants with the relative equipment has been assumed. Therefore, the internal gains of the room consist of sensible and latent heat flows from occupants (3 people · 65 W of sensible thermal power and 65 W latent), office devices (3 computers and 1 printer for a time average total power equal to 150 W) and a light system consisting of fluorescent lamps (luminous efficacy: 91 lm/W, total power: 250 W). The lighting system is divided into two zones along two bands parallel to the glazed wall. There are no dimmers. The light system is sized to ensure the required illuminance of at least 500 lx, in harmony with Italian regulations for schools and offices. A daily occupation period equal to eleven hours was supposed: from eight in the morning to seven in the afternoon. With these assumptions the thermal load of the room is almost always negative.

The evaluation of the light comfort was carried out only in the hours of complete daylighting with both areas of the lamp set off. Two types of glare were considered here: the disability glare from direct radiation on the visual task, and discomfort glare due to exceeding luminance contrast inside the field of view (Hopkinson, 1963). This last is assessed by means of the Daylighting Glare Index (DGI), in case of extended light sources (Chauvel et al., 1982; UNI, 2000), or Unified Glare Rating (UGR) in case of smaller sources (CIE, 1995). In this study, the first type of glare is considered excessive when the luminance of the task or its irradiated parts exceeds 580 cd/m^2 (Robbins, 1986). It has been assumed that the presence of glare of any kind in one occupant's position entails solar control actions. For the purposes of visual comfort assessments, two lines of sight were considered for each occupant: one towards a visual task placed on the desk, therefore inclined downwards, the other, more critical, is horizontal and directed towards the center of the glass wall.

The glass wall is protected by a system of external slats whose reflection coefficient is equal to 0.6 on both sides, both in the thermal and light range. The slats are 0.6 m wide in the perpendicular direction to the façade (their minor axis) and vertically spaced 0.6 m apart. If the slats are equipped with PV cells, the reflection coefficient of their upper face is assumed to be equal to 0.2. The slats can be tilted around their longitudinal axis and the following solar control logic has been simulated:

- a "seasonal" control logic, according to which the slats are inclined at first in order to minimize the thermal load, but guaranteeing the required level of illuminance even in the most disadvantaged position, after which, if glare problems are detected, an internal diffusing curtain is lowered (its transparency coefficient is 0.5),
- the same seasonal control logic but without internal curtain; in this case the slats, after being inclined so as to minimize the thermal load, can be further inclined to avoid possible glare phenomena,
- if the slats are equipped with PV cells, two control logics has been simulated: one is aimed only at maximizing photovoltaic electricity generation and the other is aimed at doing this while maintaining as much as possible the daylighting in the room; in both cases, if glare phenomena are found, the internal curtain is used.

To calculate the primary energy demand related to HVAC, it is assumed that the building is equipped with a full air centralized loop, the room is used from 8 a.m. to 7 p.m. but the plant is activated at 07 a.m.. In the HVAC system, electrically driven chillers (vapor compression chiller) provide the fluid for the cooling coils, while the fluid for the heating coil is primarily provided by the condensers of the chillers, and an additional gas-boiler intervenes when necessary. The chillers have a nominal Coefficient of Performance (COP) equal to 4.5, while boilers have an efficiency of 0.9. In each calculation step, these values are modified according to the actual load. Internal set-point air temperatures are assumed to be 20°C in winter and 26°C in summer, as prescribed by the Italian law, while in half-seasons they have been assumed equal to the average daytime external temperature, since the clothing of the occupants is adapted to it. The relative humidity set-point is assumed equal to 50% all over the year. The following conversion factors were used to quantify primary energy demand: 1.05 and 2.77 for gas and electricity respectively, in accordance with Italian standards. The second coefficient is the inverse of the efficiency of the national electricity system (i.e. 0.36), the same coefficient was also used to estimate the primary energy equivalent to the possible electricity production of PV cells.

3. RESULTS

3.1. Room's primary energy demand

Given the assumptions made regarding the intended use and the construction technologies, room's thermal load is usually negative. Therefore, the annual primary energy demand for heating is minimal, that for cooling is the dominant item followed by that for artificial lighting, which generally is slightly lower.

In the following, the lateral inclination angles that rotate the slats major axis counterclockwise for an observer who looks at them from the outside are defined as positive, negative those that rotate it clockwise.

Since solar control strategies can significantly reduce the incoming luminous flux by significantly influencing energy demand for lamps and consequently for cooling, with a first series of simulations the energy demand of the room was analysed in the absence of any type of solar control, therefore with fixed slats, with minor axis orthogonal to the façade, and without internal curtain.

First, it has been observed that deviating from the south orientation of the glazed surface the total primary energy demand increases going eastwards, and decreases going westwards. This is mainly due to the time of use of the room, which is more extended in the afternoon; therefore, the south-west and west orientations result in lower consumption for artificial lighting and cooling (Figure 3).

While for the south orientation of the façade the horizontal arrangement of the slats is the most convenient, for the other orientations examined it is more convenient a lateral inclination of the slats of about ten sexagesimal degrees, in a positive direction going towards the east and negative going towards the west. In general, positive lateral inclinations are more convenient going eastwards while negative ones are more convenient in a westerly direction. These inclinations, in fact, reduce the incoming solar radiation, in particular its direct component and consequently that reflected by the slats, while there are no significant differences in the sky diffuse component. This reduces the energy demand for cooling, which is the most influential. In fact, in the absence of solar control actions, that can cause the lamps to turn on, there are no significant differences in the energy demand for artificial lighting.

Always in the absence of glare control, fixed slats but with a downward inclination of their outermost edge of thirty degrees were analysed. Understandably, with such inclination the differences between positive and negative lateral inclinations increase.

With the same hypotheses, similar results were found for locations at lower latitudes, i.e. Trapani and Marrakech, or higher, i.e. Berlin. But the differences described above are much less marked for locations further north, where the energy demand for cooling is lower.

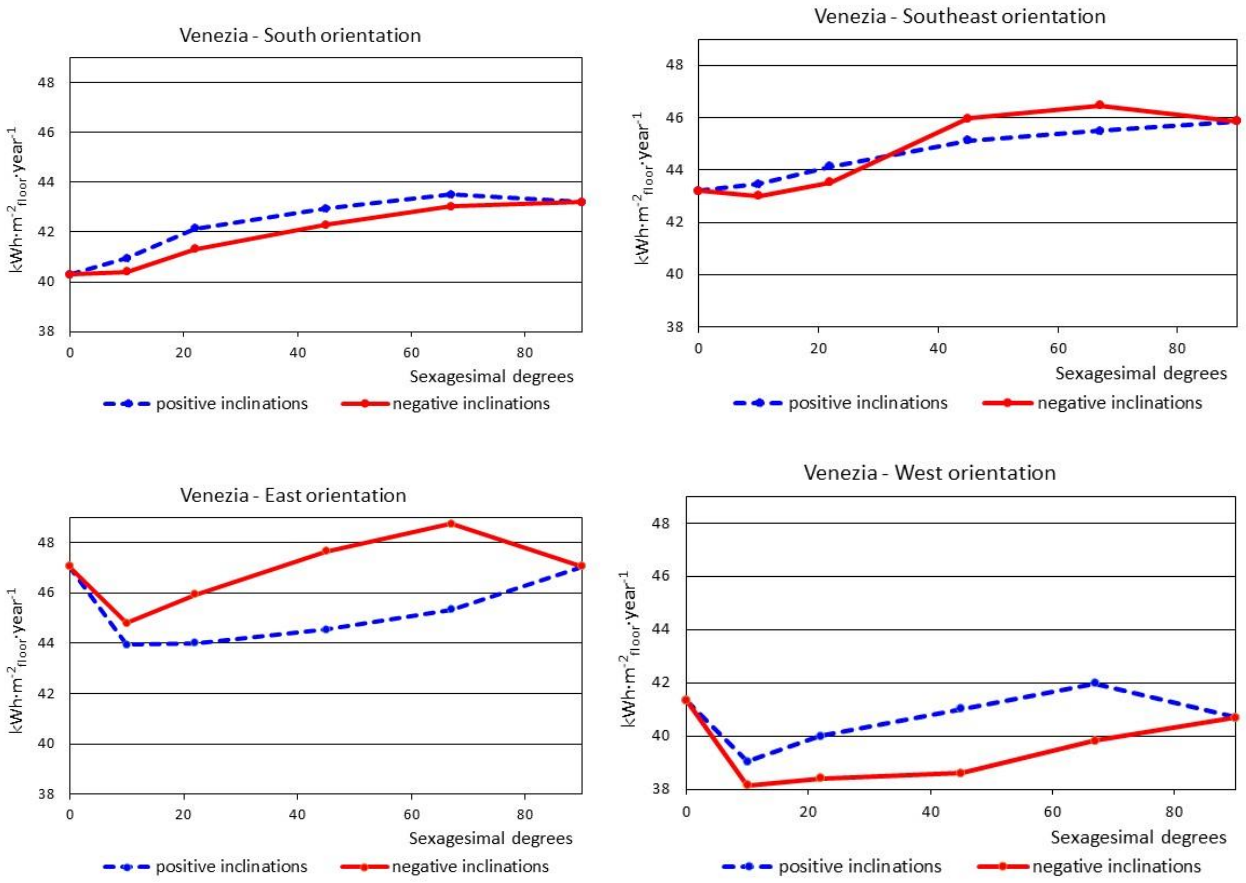

Figure 3 Array of fixed slats with minor axis orthogonal to the façade, total annual primary energy demand as a function of the lateral slope in the absence of glare control

By introducing solar control aimed at visual comfort through an internal curtain things change. Still examining fixed slats with the minor axis perpendicular to the facade, in general for all orientations examined the vertical arrangement of the slats major axis becomes the most convenient. This is due to the greater frequency of excessive values of the DGI that are found with the arrangements close to the horizontal one. Visual discomfort causes the curtain to be lowered, therefore a lower internal illuminance and greater energy consumption due to the lamps. The excessive values of the DGI are primarily due to the position occupied in the visual field by the upper part of the slats directly radiated by the Sun and not to the visible sky. This makes the lateral inclinations of the slats vertical or close to verticality more convenient with all the orientations of the façade (Figure 4). The differences in total energy demand between positive and negative inclinations are therefore due to a different number of cases of visual discomfort.

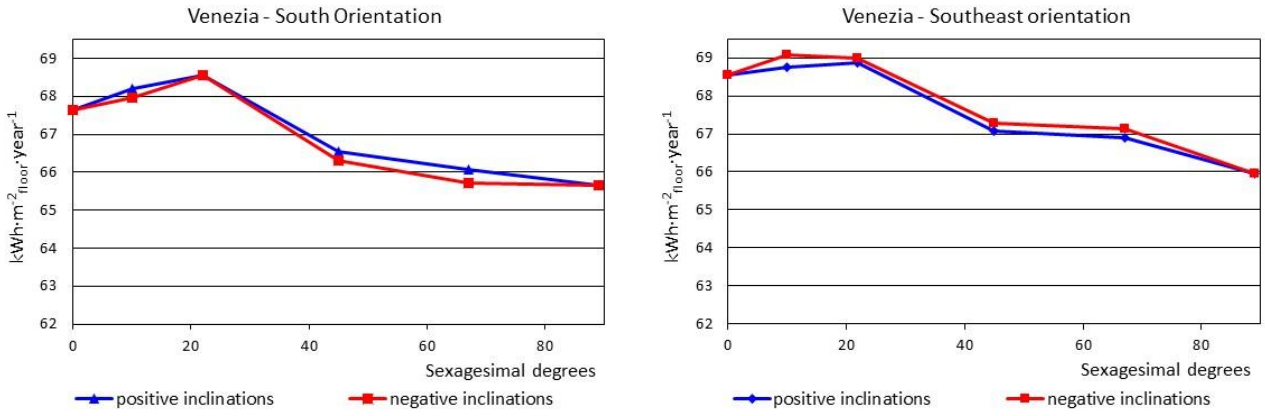

Figure 4 (a) Array of fixed slats with minor axis orthogonal to the façade, total annual primary energy demand as a function of the lateral slope in the presence of glare control operated by means of an internal blind

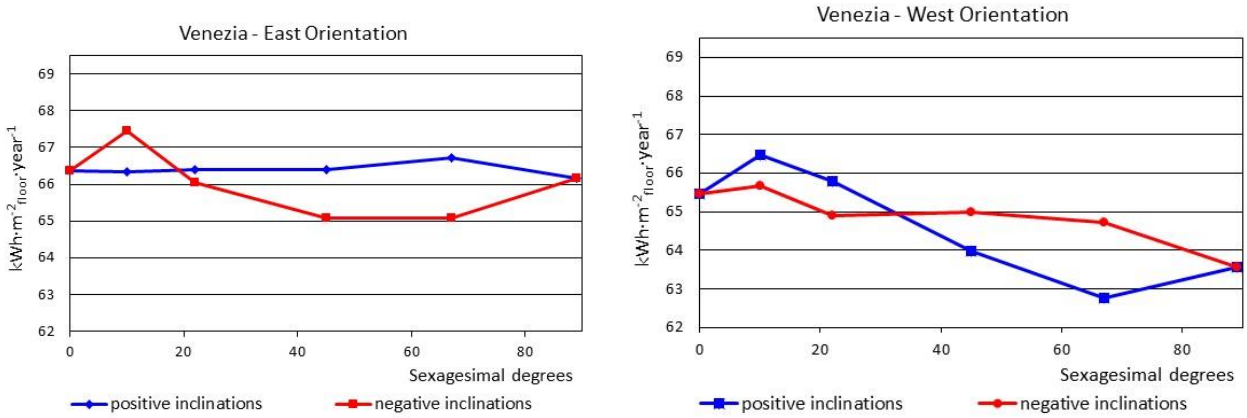

Figure 4 (b) Array of fixed slats with minor axis orthogonal to the façade, total annual primary energy demand as a function of the lateral slope in the presence of glare control operated by means of an internal blind

If the slats are fixed but with a downward inclination of their outermost edge of thirty degrees, the cases of glare due to the excessive luminance of their upper part are reduced, therefore, the differences between the various lateral inclinations are drastically reduced. Even more so if the slats are tilting in the direction perpendicular to the façade, the downward inclination of their outermost edge reduces the cases of glare due to the excessive luminance of their upper part in more cases, therefore there are significant energy savings compared to fixed slats. This is especially true when the slats longitudinal axis is horizontal. Therefore, the trend of energy demand as a function of the lateral slats inclination becomes that represented in the Figure 5. Variations in energy demand are almost exclusively due to artificial lighting. The advantages of the slats horizontal arrangement are greater with the south orientation of the glazed façade. The differences between the east and west orientations are always due to the effect of the time of use, which is longer in the afternoon.

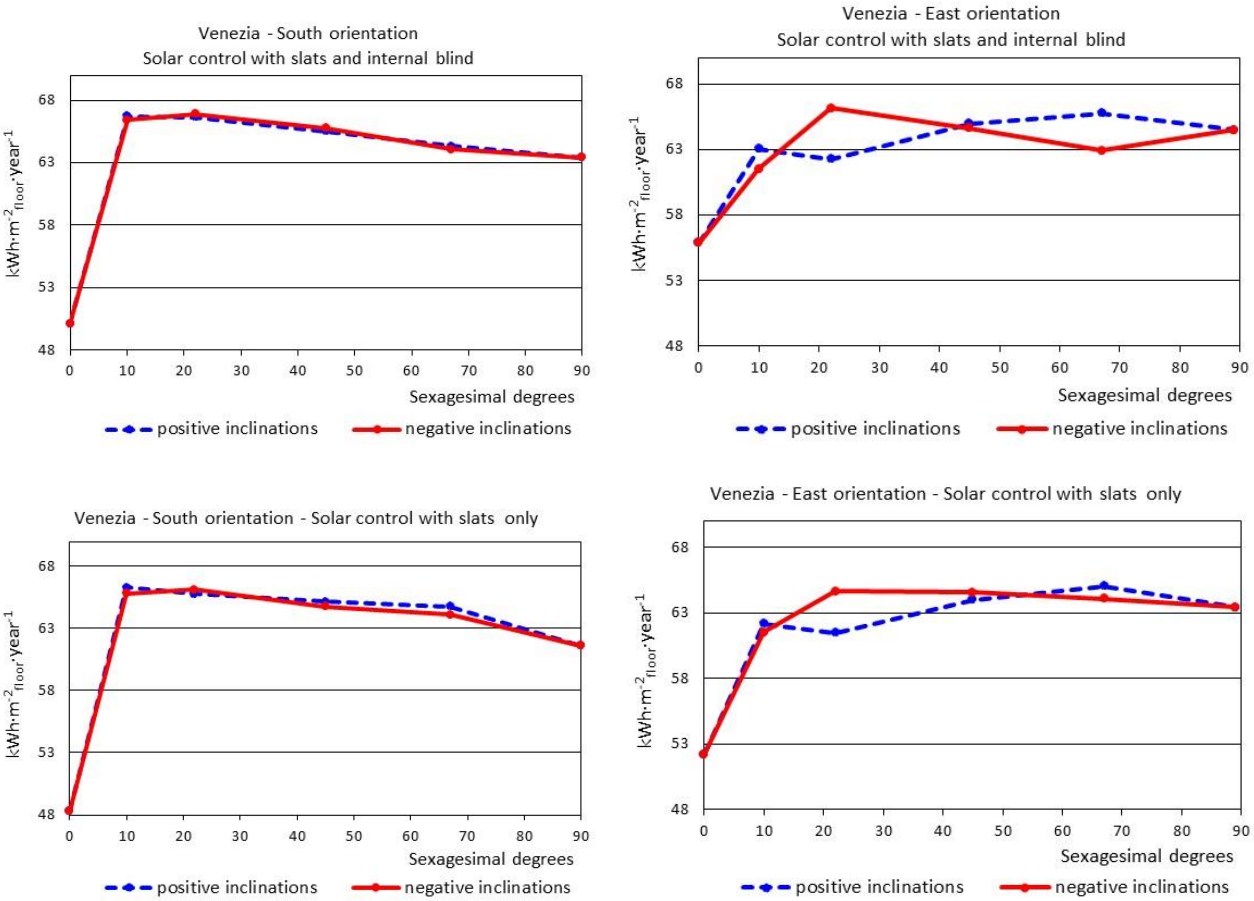

Figure 5 Array of movable slats, total annual primary energy demand as a function of the lateral slope in the presence of glare control operated by means of slats inclination and an internal blind (above) and by means of slats inclination alone (down).

In the case study, discomfort glare due to extensive light sources is the most frequent, it is evaluated by means of the DGI index (Figure 6).

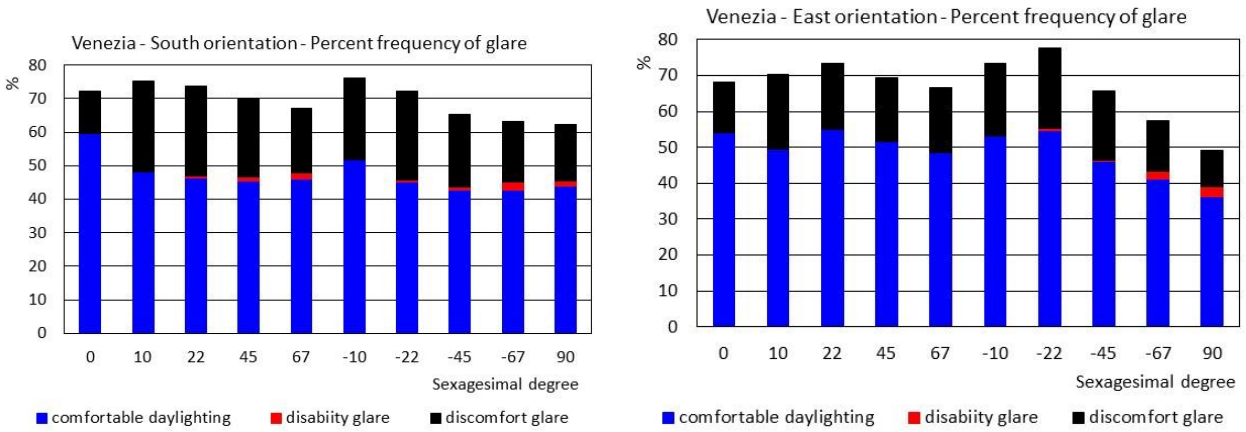

Figure 6 Solar control performed with movable slats, for each slats lateral slope percentage frequency of hours-occupant in visual comfort and discomfort conditions on the total hours-occupant, that are detected after the thermal load control actions, and before the glare control actions of various types, for south orientation (left) and east orientation of the facade (right)

The fact that the cases of discomfort detected do not always translate into increases in the energy demand from artificial lighting is because subsequent glare control actions do not always reduce the internal illuminance below the minimum value.

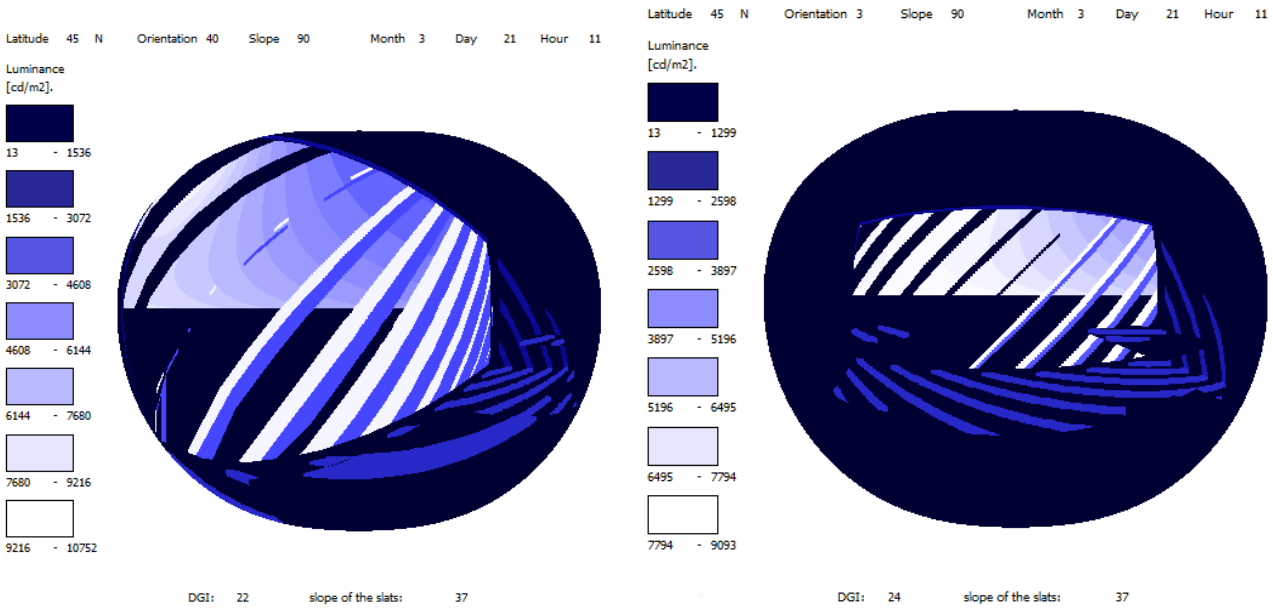

Figure 7 Examples of occupant visual field simulations, used by Ener_Lux software to calculate the DGI and UGR indices

The solar control strategy based on the use of slats alone is slightly more advantageous than the one that also involves the use of the internal curtain, particularly when the slats longitudinal axis is horizontal. This is because, with the same cases of visual discomfort detected, this strategy reduces less the incoming luminous flux (the transparency coefficient of the curtain is assumed to be equal to 0.5); therefore, it leads to less use of artificial lighting.

3.2. Slats equipped with PV cells

Two strategies for handling movable slats equipped with PV cells were compared: one is aimed only at maximizing photovoltaic electricity generation and the other is aimed at doing this while guaranteeing natural lighting in the room as much as possible. In both cases, to avoid glare, the internal curtain is used. Understandably, only positive inclinations of slats major axis were explored in the case of eastward orientations and only negative inclinations in the case of westward orientations.

The histograms shown in Figure 8 compare the various items of the energy balance of the room related to the first strategy and two orientations of the façade. The second strategy, which allows as much as possible natural lighting in the room,

slightly penalizes PV production with east and west orientations, and penalizes it to a greater extent for the south orientation (Figure 9).

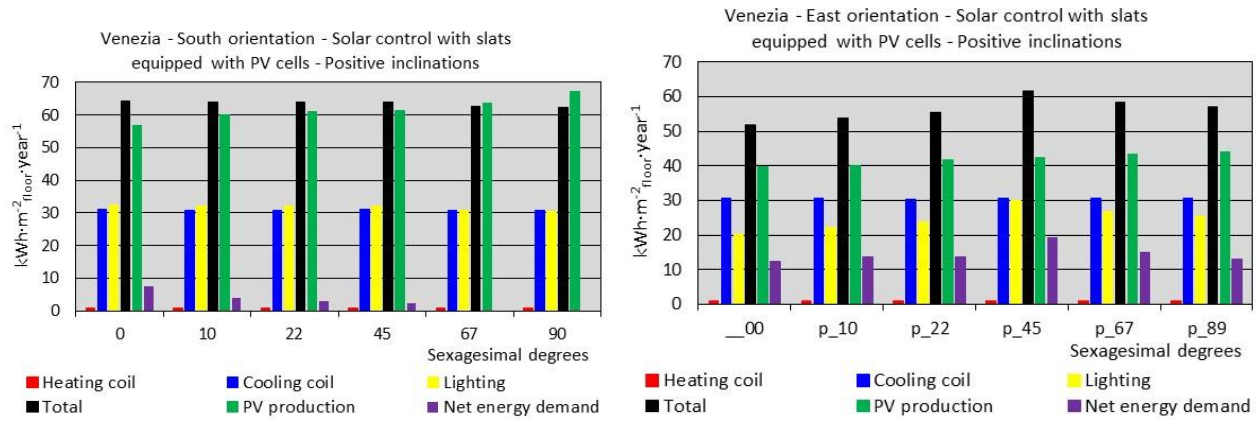

Figure 8 Examples of the values assumed by the annual primary energy demand for different uses and the production of photovoltaic electricity (always expressed in terms of primary energy) with the strategy aimed only to maximise the PV generation for two different orientations

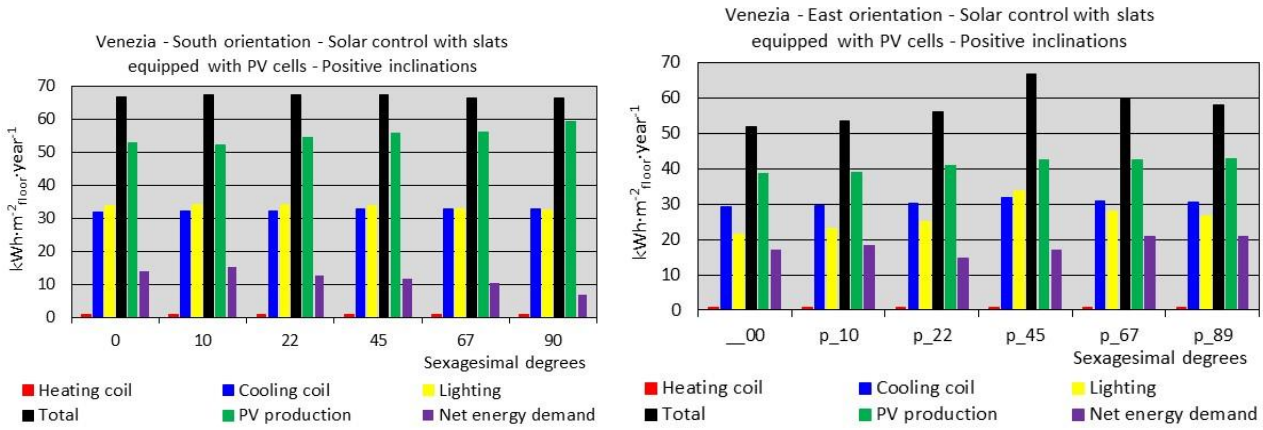

Figure 9 Examples of the values assumed by the annual primary energy demand for different uses and the production of photovoltaic electricity (always expressed in terms of primary energy) with the strategy aimed to guarantee the daylighting in the room as longer as possible for two different orientations

Of particular interest is the net primary energy demand, which is obtained by subtracting from the total room's energy demand the primary energy equivalent of photovoltaic electricity production (Figure 10). With both strategies, in the case of the east and west orientations of the façade it is not convenient to tilt the slats laterally, while in the case of the south orientation it is convenient a lateral slope as much as possible tending to verticality. Indeed, it allows to better exploit the solar radiation throughout the day, minimizing the angle of incidence of direct radiation on the slats.

Although PV production always tends to increase with the slats lateral slope, in the case of the east and west orientations the net demand does not always decrease as a result, because at the same time the energy demand for artificial lighting increases. The thing is more accentuated in the case of the west orientation, due to the time of use of the room that is more extended in the afternoon. With this orientation in fact the daylighting in the afternoon is often penalized by the use of the curtain to avoid the phenomena of glare.

The solar radiation data used are symmetrical with respect to noon, so, in the case of the first strategy and the southern orientation, the daily photovoltaic electricity generation of slats with the same lateral inclination, both positive and negative, is the same, but daylighting is required longer in the afternoon. Therefore, the slight differences that are found in the net energy demand are also due in this case to the energy demand for artificial lighting which is lower in the afternoon if the lateral inclinations of the slats are positive, with these inclinations in fact the upper face of the slats sees the brightest part of the sky and the incoming luminous flux is greater. For the same reason, the second strategy guarantees daylighting for longer with positive lateral inclinations, but this penalizes photovoltaic generation more, therefore the net primary energy demand is higher.

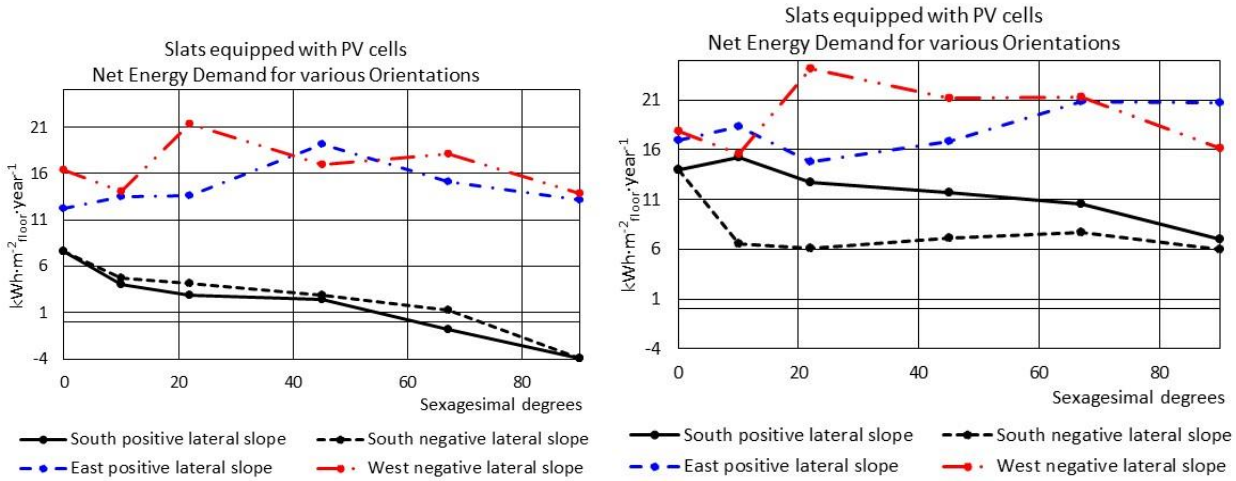

Figure 10 Net annual primary energy demand with slats equipped with PV cells. The diagram on the left is relative to a strategy aimed only to maximise the PV generation, the other to a strategy that seeks to guarantee the daylighting in the room as longer as possible

4. CONCLUSION

Simulations results show that for the case study, in the examined climate, the optimal arrangement of the slats major axis varies significantly depending on the solar control strategy adopted. In particular, the strategies based on the optimal inclination of the minor axis of movable slats, with or without the use of an internal curtain, turn out to be the most convenient and make the horizontal arrangement of the slats major axis more advantageous for any orientation of the façade, except in the case that the slats are equipped with photovoltaic cells. In this case, in fact, when the façade is oriented towards the east or west it is not convenient to tilt the slats laterally, while in the case of the southern orientation it is convenient a lateral slope vertical. Indeed, it allows to better exploit the solar radiation throughout the day, minimizing the angle of incidence of direct radiation on the slats.

The assumptions made regarding the intended use of the room and its construction technologies, mean that artificial lighting significantly influences the total energy demand. The period of use of the lamps is conditioned by glare control strategies, which can significantly reduce the internal illuminance. In this study it was assumed a spatially uniform artificial lighting system consisting of fluorescent lamps, but a more localised and less powerful lighting system would lead to lower overall energy demand and fewer differences between the various configurations of the slats.

5. REFERENCES

Carbonari, A. (2017) 'Solar control of extensively glazed facades: a computer method for predicting the effects of various devices and building's thermal inertia', *SET 2017 – 16TH International Conference on Sustainable Energy Technologies. Bologna, 17-20 Luglio 2017*. Bologna: WSSET and Alma Mater Studiorum Università di Bologna.

Carbonari, A. (2023) 'Retrofit of Massive Buildings in Different Mediterranean Climates. Interactions Between Mass, Additional Insulations and Solar Control Strategies'. *Future Cities and Environment,* 9(1): 7, pp. 1–16.

Chauvel, P., Collins, J.B., Dogniaux, R., and J. Longmore (1982) 'Glare from Windows: current views of the problem', *Lighting Research & Technology*, 14(1), pp.31-46.

Commission Internationale de l'Eclairage - CIE (1995) *Discomfort Glare in interior lighting. Technical report 117*. Vienna: CIE.

Deutsches Institut für Normung - DIN (1979) *DIN 5035 Innenraumbeleuchtung mit künstlichem licht*. Deutsches Institut für Normung.

Ente Nazionale Italiano di Unificazione – UNI (1997) *UNI EN ISO 7730: Moderate thermal environments - Determination of the PMV and PPD indices and specification of the conditions for thermal comfort*. Milano: UNI.

Ente Nazionale Italiano di Unificazione – UNI (2000). *UNI/TS 10840: Luce e illuminazione Locali scolastici: criteri generali per l'illuminazione naturale e artificiale*. Milano: UNI.

Fanger, P.O. (1970) *Thermal Comfort*. New York: Mc Graw-Hill.

Hopkinson, R.G., Petherbridge, P. and Longmore, J. (1963) *Daylighting*. London: Heinemann

Robbins, C. L. (1986) *Daylighting, design and analysis*. New York: Van Nostrand Reinhold Company.

#24: BIM-based building circularity assessment: conceptual framework

Ihab AL-QAZZAZ*, Carlos OSORIO-SANDOVAL, Serik TOKBOLAT, Georgia THERMOU

Department of Civil Engineering, The University of Nottingham, University Park NG7 2RD, ihab.al-qazzaz@nottingham.ac.uk

Abstract: The construction sector contributes substantially to the consumption of raw materials and the production of waste. Traditional building design strategies are based on an unsustainable economic linear model. Transition to the circular economy (CE) paradigm aims to reduce the consumption of raw materials and minimise waste. To achieve the promises of CE, it is crucial to assess sustainability aspects early. In the final design decision-making process, both technical circularity and sustainability strategies must be implemented. However, the existing building circularity assessment (BCA) models and tools are not comprehensive and fail to cover all the critical factors that affect circularity and sustainability in the built environment. Technical circularity and sustainability assessments are often conducted in isolation. There is a need for practical comprehensive assessment tools for use during the early design stage of construction projects, where crucial decisions are made as opposed to the late design stages, in which changes are more costly and complex. Since BCA requires a large amount of data, it requires the use of a supplementary tool to conduct the assessment effectively. Building information modelling (BIM) can serve as a useful tool to facilitate BCA. This paper proposes a framework that integrates technical circularity and sustainability aspects, such as environmental impact by life cycle assessment (LCA) and economic aspect by life cycle costing (LCC) within the BIM environment to achieve a sustainable circular-built environment. The framework is a promising step toward developing a prototype tool that assesses circularity and sustainability aspects simultaneously and helps decision-making for designers in the context of building design and material selection and trade-offs between the different aspects and selects more circular and sustainable alternatives. The proposed framework aims to contribute positively to reducing global warming and decarbonization in the building sector and the shift toward a sustainable circular-built environment.

Keywords: Building Circularity Assessment, Sustainability, Building Information Modelling, Circular Economy, Sustainable Construction

1. INTRODUCTION

The construction industry consumes 30% of raw materials and generates 25% of waste globally (Benachio et al., 2020). Traditional design strategies are based on the linear model of consuming the resources, in other words, “take-make-dispose” which is a cradle-to-grave approach. On the other hand, the new sustainability paradigm of a circular economy (CE) is based on the closed-loop of consumption and regeneration with materials efficiency through reuse and recycling, which is a “make–use – reuse/recycle” and it is considered the cradle-to-cradle approach. The shift toward a circular building and assessing the building’s circularity is not limited to the technical aspect of circularity. Pomponi & Moncaster, (2017) defined six research aspects within the built environment that relate to the concept of CE. The study states that there is a need for a holistic approach and research studies in each of these aspects it is essential to integrate the utilization of different disciplines to successfully meet the sustainability research goals. However, in practice, not all research aspects may be required, some of them such as two or three aspects may be included such as environmental, economic, and technological.

Building circularity indicators should measure the building’s impact on the environment and economy (Rahla et al., 2019). Zhang et al., 2021 define Building Circularity (BC) as “a building property that describes the circular capability, including its construction activities to create environmental quality, economic prosperity, and social equity” by R strategies such as reuse and recycling. Both the methods for building circularity assessment (BCA) and life cycle sustainability assessment depend on the life cycle perspective and advocate life cycle thinking. Despite the sustainability and circular economy terms becoming popular, the differences and similarities between both remain unclear. The relationship between them is not clearly outlined in the literature (Geissdoerfer et al., 2017). Each of them (i.e., sustainability and circularity) is considered complementary to the other as they do not have the same meaning (Blum et al., 2020). The new Level(s) framework for the building sustainability assessment includes six macro- and objective 2 linked to circularity by 4 indicators (Dodd & Donatello, 2021). Therefore, the final design decision-making process depends on implementing both circularity and sustainability. Thus, there is a need for the utilization of decision support systems (DSS) to select the most appropriate design option that aligns with the set objectives among different alternatives. Moreover, various researchers have suggested integrating circularity with sustainability when assessing building design (Pomponi & Moncaster, 2017) (Akanbi et al., 2018) (Blum et al., 2020) (Zhai, 2020) (Zhang, et al., 2021) (Zhang, Han, et al., 2021). However, Rahla et al., (2019) addressed the main obstacles and barriers that could influence the progress of creating an assessment tool for a building’s circularity such as assessing circularity versus sustainability and data collection/management.

BCA requires a large amount of information to conduct its assessments, and BIM can facilitate this (Rahla et al., 2019). Several studies state the need to leverage technology and digitalization to improve CE (Verberne, 2016) (Braakman et al., 2021) (Khadim et al., 2022). Due to the increased complexity and volume of data at a building level, a BIM-based tool should be developed to automate the building circularity assessment calculation. Data required for circularity assessment may be extracted from the BIM model. The BIM-LCA integration is used in building sustainability studies which could be expanded to circular assessment research (Feng et al., 2022). Such as analyzing LCA and LCC within the BIM environment as a data repository (Santos et al, 2019). The BIM-based end-of-life research theme is a connection between three trending issues in the building industry: digitalization, circular economy, and sustainability (Akbarieh et al., 2020). This research aims to integrate these three existing trends by proposing a framework for assessing building circularity and sustainability using BIM.

After the Introduction in Section 1, this paper is outlined as follows: Section 2 discusses current efforts and approaches to integrate BIM and circularity and sustainability assessment; Section 3 outlines the research methodology; Section 4 Overview of the proposed framework; Section 4 Conclusion and future work.

2. RELATED WORKS

Over the past few years, several researchers have tried to use BIM in BCA. There are three main streams or approaches of integrating BCA with BIM: 1) External Online platform; 2) Link BIM and external database; 3) Creating custom parameters. In the first approach, processing an exchange file such as Industry Class Foundation (IFC) and uploaded to an external platform and processed in the external platform for assessment. This approach is used by Building as Material Banks (BAMB), Madaster, and One Click LCA. The limitation of these external online platforms is requiring manual procedures to upload to the online platform. These manual steps decrease the efficiency of work and are time-consuming, particularly in the design phases which may require multiple assessments (Zhai, 2020); (Zhang et al., 2021). Hence, designers need a simplified approach that enables continuous assessment throughout the entire design phase instead of the end of the design phase that works within the BIM environment and enables a quick and real-time assessment of the building's circularity.

The second integration approach establishes a link between the BIM model and external databases that include data required for the assessment. Some studies used this integration approach (Zhai, 2020); (Zhang et al., 2021). However, the limitations of these two tools are not considered the sustainability aspects. Christian et al. (2021) and Heisel and Nelson (2020) proposed a BIM tool for building circularity indicator assessment based on the circularity indicator (CI) proposed by

Madaster and embodied carbon. However, it does not consider the economic aspect. In the third approach, users are required to create shared parameters for each building element and material-specific data containing the required information to conduct the assessment. Akanbi et al., (2018) developed a BWPE add-in for the parameters influencing recycling and reusability using Revit and C#. The limitation of BWPE it does not consider the sustainability aspects. However, this integration approach is time-consuming as users are required to manually create parameters for each necessary information and subsequently input the data into those parameters. Di Biccari et al. (2019) designed a tool to assess the circularity of the building level only based on a circular indicator proposed and the LCC. However, it is a semi-quantitative method and includes the environmental impact inside the calculation of their proposed indicator to assess circularity.

However, in previous studies, BIM tools are related to the fact that they do not cover all aspects of building circularity and sustainability. There is an essential need to explore BIM to assess building circularity considering the sustainability aspects and improving the decision-making in a simplified approach. Thus, integrating circularity with sustainability aspects within the BIM environment will establish a robust system for assessing the sustainability of building materials selection and design options (Akanbi et al., 2018). However, to the knowledge of the authors, this integration within the BIM environment as a data repository is still missing from the literature. Therefore, additional research and development in this field are required. Our proposed framework leverages BIM as a data repository to model the technical circularity, environmental, and economic sustainability aspects to assess buildings and inform design decisions.

3. METHODOLOGY

The research methodology comprises two steps: i) identifying the technical circularity and sustainability indicators by literature review, and ii) adopting the design science research methodology for developing the proposed conceptual framework for BIM-based building circularity assessment based on identified indicators.

4. IDENTIFYING THE INDICATORS

The proposed framework will integrate the technical circularity aspect with sustainability aspects, i.e., the environmental impact by using LCA, and the economic aspect by using LCC to conduct a comprehensive assessment.

4.1 Technical circularity indicators

Creating a new circularity assessment method is considered challenging (Jiang et al., 2022). WBCSD, (2018) recommended building upon existing frameworks. Moreover, academia also recommended that the improvements in the future must be standardized and aligned with previous literature (Khadim et al., 2022). However, the Material Circularity Indicator (MCI) for product level (Ellen MacArthur Foundation & Granta, 2015) and the Building Circularity Indicator (BCI) proposed by Verberne, (2016) are the most popular indicators. Many researchers and companies built their indicators on MCI and BCI. Therefore, they will be adopted in this research to develop the circularity assessment model. However, they should be adapted to be a form of life cycle perspective because they do not consider materials required for the use phase, and material wastage during the construction (Khadim et al., 2023).

4.2 Environmental impact indicators

The Life Cycle Assessment (LCA) method is widely utilized within the building and construction sector for environmental impact assessment (Lu et al., 2021) based on ISO 14040 & 14044:2006 series (ISO, 2006). These standards provide general guidelines for LCA. BS EN 15978 is a specific LCA standard for construction projects and buildings (BS EN, 2011). LCA covers different environmental impacts, and the global warming potential (GWP) is considered the biggest environmental impact contributor to climate change. GWP is caused due to emissions of greenhouse gases and carbon dioxide (CO_2) represents the largest percentage of GHGs that are released into the atmosphere, and the GWP of all other greenhouse gases over 100 years is calculated using the carbon dioxide equivalent unit (CO_2e) (RICS, 2017). Among LCA indicators, the most common environmental impact assessment of buildings is carbon emissions, and embodied carbon is the main factor that assesses the overall environmental impact of a building (Lu et al., 2021) (Fregonara et al., 2017).

4.3 Economic indicators

The economic factor is crucial in promoting circularity (Braakman et al., 2021). One of the key goals of circular buildings should be to generate economic value (Pomponi and Moncaster, 2017). The correlation between an increase in product circularity and the potential business benefits is not a straightforward one (Ellen MacArthur Foundation & Granta, 2019). Unknown relationship between circularity and life cycle costing (LCC) (Braakman et al., 2021). LCC is the most widely accepted technique for economic sustainability assessment, and it is one of the indicators of the new Level(s) framework

for building sustainability assessment. Life-cycle costing includes construction cost, operation and maintenance cost, and end-of-life cost (ISO 15686-5, 2017).

5. A PROPOSED CONCEPTUAL FRAMEWORK

The proposed conceptual framework aims to reflect the technical circularity and sustainability aspects of buildings. In this research, technical circularity will be integrated with environmental sustainability and economic sustainability within the BIM environment as a data repository. The proposed framework is based on a modified version of the circularity assessment model BCI (Verberne, 2016) to assess the technical circularity, LCA to assess environmental sustainability and use LCC to assess economic sustainability. The proposed conceptual framework uses BIM for integrating technical circularity, LCA, and LCC by benefitting from BIM-LCA/LCC integration frameworks (Lu et al., 2021), as illustrated in Figure 1, the proposed framework involves four steps, described below.

5.1. Define the goal and scope of the assessment

In the first step, the goal and scope of the assessment need to be clarified for each aspect. The indicators (technical circularity, environmental impact categories, and economic), the scope of life-cycle stage (A, B, C, D) modules and building components should be defined. The determination of the order of importance for the three aspects.

5.2. Inventory analysis and define the basic assumption

Step 2 includes analysing the material flows and building design information. Establishing the basic assumptions such as lifespan or the study period, inflation, and discount rate. Defining the calculation standard and formula. Creating a semantic enrichment of the BIM model that takes into account the level of details (LOD) and information including disassembly potential. To perform the BCA, LCA, and LCC it is essential to identify the information required for the assessment.

5.3. Conduct the assessment

In the third step, start conducting the assessment within the BIM environment. The circularity for each product will be calculated, and then they will be grouped according to building Brand, (1994) layers to calculate the SCI. Then, BCI will be calculated. For LCA/LCC, assessing the environmental impact and costs for each stage, and then accumulating these results to obtain the whole life cycle.

5.4. Interpretation and analysis of the results

In the last step, it is essential to perform an uncertainty analysis for both LCA and LCC due to various factors such as the uncertainty of the database, potential risks, and parameter settings (Lu et al., 2021). Moreover, due to the life span of buildings that may reach 50 years, uncertainties in the scenarios of the end of life could pose a risk of unsatisfactory CE performance (Lei et al., 2022). Defining the percentage of unrecoverable waste from the many materials used in building construction is hard because of the uncertainties surrounding the treatment of these materials at their end of life (Lei et al., 2021). Hence, uncertainty analysis is required. On the other hand, there is no simple correlation between technical circularity, LCA, and LCC. Therefore, it is essential to consider their trade-offs by developing a decision support system based on technical circularity and sustainability criteria by adopting optimization methods to enable the selection of optimal materials and design alternatives.

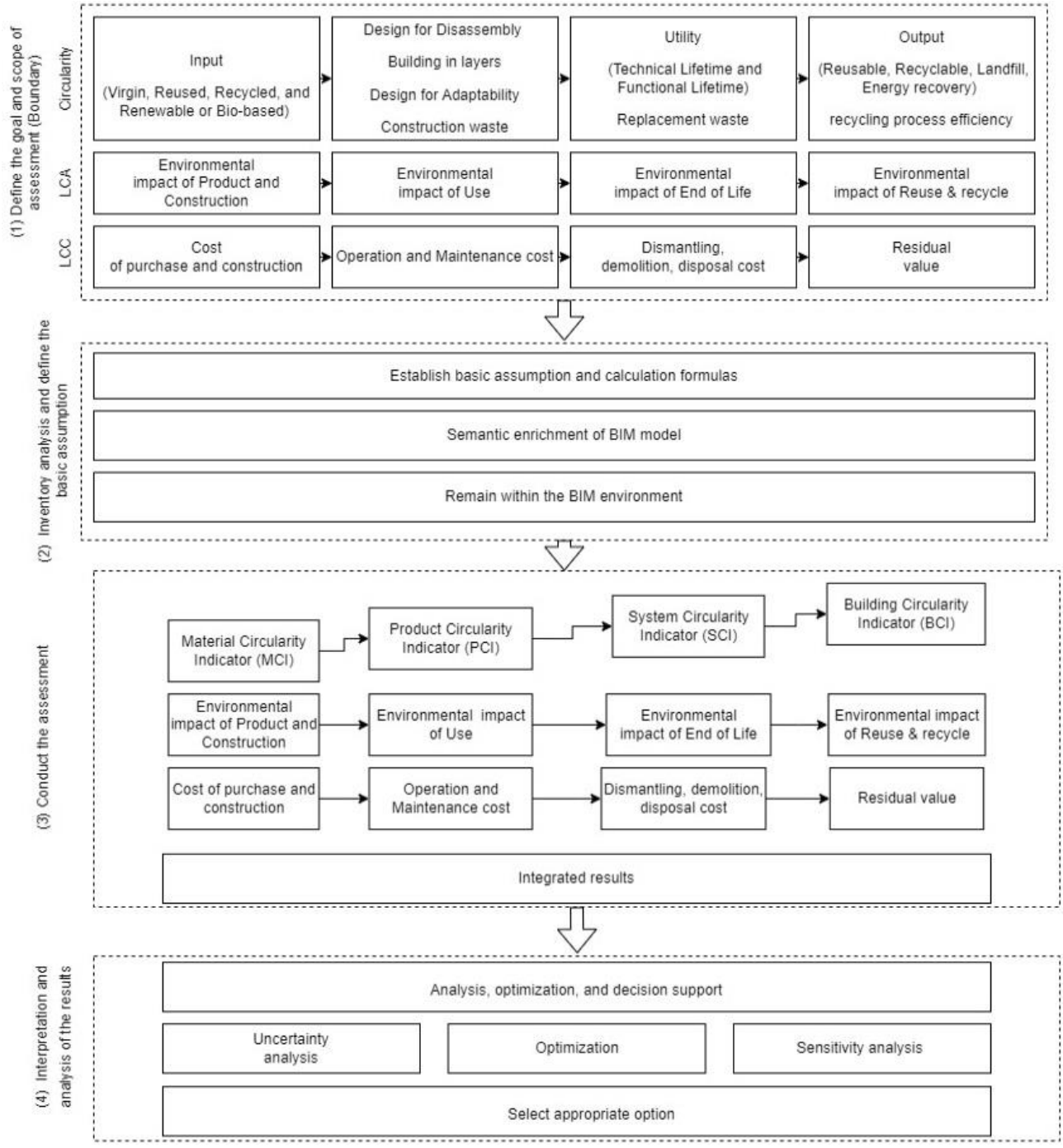

Figure 1 Proposed conceptual framework

6. THE PROTOTYPE DESIGN

A prototype tool will be developed based on the developed conceptual framework following the preliminary proposed system architecture to demonstrate the framework's functionality. The preliminary architecture is divided into three parts: input, process, and output as shown in Figure 2. The system takes inputs from the enriched BIM model including the information required for the assessment and the project data such as disassembly potential. The integrated assessment model embedded in BIM software calculates BCA, LCA, and LCC considering the uncertainty. The expected outcomes from the calculation and the optimization methods are to determine the best material and design alternatives for achieving a sustainable circular-built environment. In addition, the system outputs the results in a visualisation model.

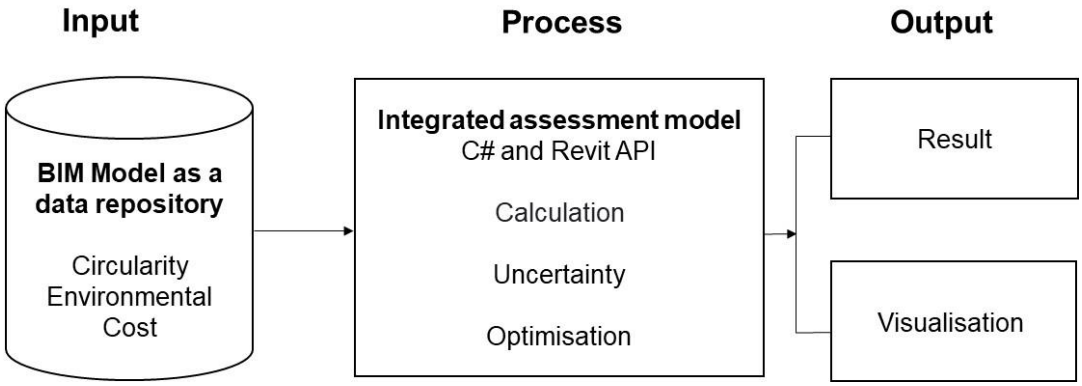

Figure 2 Proposed system architecture

7. CONCLUSION AND FUTURE WORK

An integrated framework to assess the circularity and sustainability of the building within the BIM environment at the early design stage is proposed in this research. It integrates the assessment of three key indicators: circularity, LCA, and LCC measures. The first indicator accounts for technical circularity while the other two give a measure of environmental impact and economic sustainability. Concepts of these indicators and aspects have been presented in this paper. The directions for the implementation of the BIM-integrated framework in the form of a prototype tool have been stated. The next step of this research will be implementing the developed conceptual framework in a BIM-based prototype tool and the framework will pave the way to develop a plugin within Autodesk Revit. To shift toward a circular and sustainable built environment, this paper presented a proposed BIM-based framework for assessing technical circularity with sustainability and using it to inform design decisions of buildings and serve as a decision support system and design tool.

8. ACKNOWLEDGEMENT

This project is part of an ongoing PhD research. The first author acknowledges the Higher Committee of Education Development in Iraq (HCED) for funding the PhD scholarship.

9. REFERENCES

Akanbi, L. A., Oyedele, L. O., Akinade, O. O., Ajayi, A. O., Davila Delgado, M., Bilal, M., & Bello, S. A. (2018). Salvaging building materials in a circular economy: A BIM-based whole-life performance estimator. *Resources, Conservation and Recycling*, *129*, 175–186. https://doi.org/10.1016/j.resconrec.2017.10.026

Akbarieh, A., Jayasinghe, L. B., Waldmann, D., & Teferle, F. N. (2020). BIM-based end-of-lifecycle decision making and digital deconstruction: Literature review. In *Sustainability (Switzerland)* (Vol. 12, Issue 7). MDPI. https://doi.org/10.3390/su12072670

Benachio, G. L. F., Freitas, M. do C. D., & Tavares, S. F. (2020). Circular economy in the construction industry: A systematic literature review. In *Journal of Cleaner Production* (Vol. 260). Elsevier Ltd. https://doi.org/10.1016/j.jclepro.2020.121046

Blum, N. U., Haupt, M., & Bening, C. R. (2020). Why "Circular" doesn't always mean "Sustainable." In *Resources, Conservation and Recycling* (Vol. 162). Elsevier B.V. https://doi.org/10.1016/j.resconrec.2020.105042

Braakman, L., Bhochhibhoya, S., & de Graaf, R. (2021). Exploring the relationship between the level of circularity and the life cycle costs of a one-family house. *Resources, Conservation and Recycling*, *164*. https://doi.org/10.1016/j.resconrec.2020.105149

Brand. (1994). *How Buildings Learn: What Happens After They're Built*. Penguin Publishing.

BS EN. (2011). *BS EN 15987:2011 Sustainability of construction works: assessment of environmental performance of buildings: calculation method.*

Christian, Yun-Tsui Chang, & Shang-Hsien Hsieh. (2021). BIM-based assessment of building circularity and embodied carbon for a circular built environment. *Conference on Computer Applications in Civil and Hydraulic Engineering, August 30-31, 2021 at National Central University, Taiwan*.

di Biccari, C., Abualdenien, J., Borrmann, A., & Corallo, A. (2019). A BIM-Based Framework to Visually Evaluate Circularity and Life Cycle Cost of buildings. *IOP Conference Series: Earth and Environmental Science*, *290*(1). https://doi.org/10.1088/1755-1315/290/1/012043

Dodd, N., & Donatello, S. (2021). *Level(s)-A common EU framework of core sustainability indicators for office and residential buildings User Manual 1: Introduction to the Level(s) common framework (Publication version 1.1)*. https://ec.europa.eu/jrc

Ellen MacArthur Foundation & Granta. (2015). *Circularity indicators - An approach to measuring circularity - Methodology*. Ellen MacArthur Foundation.

Ellen MacArthur Foundation & Granta. (2019). *Circularity indicators - An approach to measuring circularity - Methodology*. http://www.ellenmacarthurfoundation.org/circularity-indicators/.

Feng, H., Chen, Q., de Soto, B. G., & Arashpour, M. (2022). Using BIM and LCA to evaluate material circularity: Contributions to building design improvements. *Proceedings of the International Symposium on Automation and Robotics in Construction*, *2022-July*, 9–16. https://doi.org/10.22260/isarc2022/0004

Fregonara, E., Giordano, R., Ferrando, D. G., & Pattono, S. (2017). Economic-environmental indicators to support investment decisions: A focus on the buildings' end-of-life stage. *Buildings*, *7*(3). https://doi.org/10.3390/buildings7030065

Geissdoerfer, M., Savaget, P., Bocken, N. M. P., & Hultink, E. J. (2017). The Circular Economy – A new sustainability paradigm? In *Journal of Cleaner Production* (Vol. 143, pp. 757–768). Elsevier Ltd. https://doi.org/10.1016/j.jclepro.2016.12.048

Heisel, F., & Nelson, C. (2020). *RhinoCircular: Development and Testing of a Circularity Indicator Tool for Application in Early Design Phases and Architectural Education*. https://www.researchgate.net/publication/346678011

ISO. (2006). *ISO14040 Environmental management-Life cycle assessment-Principles and framework Management environnemental-Analyse du cycle de vie-Principes et cadre*.

ISO. (2017). *ISO 15686-5 Buildings and constructed assets — Service life planning — Part 5: Life-cycle costing*.

Jiang, L., Bhochhibhoya, S., Slot, N., & de Graaf, R. (2022). Measuring product-level circularity performance: An economic value-based metric with the indicator of residual value. *Resources, Conservation and Recycling*, *186*. https://doi.org/10.1016/j.resconrec.2022.106541

Khadim, N., Agliata, R., Marino, A., Thaheem, M. J., & Mollo, L. (2022). Critical review of nano and micro-level building circularity indicators and frameworks. In *Journal of Cleaner Production* (Vol. 357). Elsevier Ltd. https://doi.org/10.1016/j.jclepro.2022.131859

Khadim, N., Agliata, R., Thaheem, M. J., & Mollo, L. (2023). Whole building circularity indicator: A circular economy assessment framework for promoting circularity and sustainability in buildings and construction. *Building and Environment*, *241*, 110498. https://doi.org/10.1016/j.buildenv.2023.110498

Lei, H., Li, L., Yang, W., Bian, Y., & Li, C. Q. (2021). An analytical review on application of life cycle assessment in circular economy for built environment. In *Journal of Building Engineering* (Vol. 44). Elsevier Ltd. https://doi.org/10.1016/j.jobe.2021.103374

Lei, H., Yang, W., Wang, W., & Li, C. Q. (2022). A new method for probabilistic circular economy assessment of buildings. *Journal of Building Engineering*, *57*. https://doi.org/10.1016/j.jobe.2022.104875

Lu, K., Jiang, X., Yu, J., Tam, V. W. Y., & Skitmore, M. (2021). Integration of life cycle assessment and life cycle cost using building information modeling: A critical review. In *Journal of Cleaner Production* (Vol. 285). Elsevier Ltd. https://doi.org/10.1016/j.jclepro.2020.125438

Pomponi, F., & Moncaster, A. (2017). Circular economy for the built environment: A research framework. *Journal of Cleaner Production*, *143*, 710–718. https://doi.org/10.1016/j.jclepro.2016.12.055

Rahla, K. M., Bragança, L., & Mateus, R. (2019). Obstacles and barriers for measuring building's circularity. *IOP Conference Series: Earth and Environmental Science*, *225*(1). https://doi.org/10.1088/1755-1315/225/1/012058

RICS. (2017). *Whole life carbon assessment for the built environment* (1st edition). the Royal Institution of Chartered Surveyors (RICS).

Santos R., A.A. Costa, J.D. Silvestre, L. Pyl, Integration of LCA and LCC analysis within a BIM-based environment: a systematic approach, Autom. ConStruct. 103 (2019) 127–149, https://doi.org/10.1016/J.AUTCON.2019.02.011.

Verberne, J. (2016). *Building circularity indicators an approach for measuring circularity of a building*. Eindhoven University of Technology.

WBCSD. (2018). *A joint report on the current landscape of circular metrics use and recommendations for a common measurement framework Circular Metrics Landscape Analysis Executive summary*.

Zhai, J. (2020). *BIM-based Building Circularity Assessment from the Early Design Stages A BIM-based framework for automating the building circularity assessment from different levels of a building's composition and providing the decision-making support on the design of circular building from the early design stages*.

Zhang, N., Han, Q., & de Vries, B. (2021). Building circularity assessment in the architecture, engineering, and construction industry: A new framework. *Sustainability (Switzerland)*, *13*(22). https://doi.org/10.3390/su132212466

Zhang, N., Nl, Z., Han, Q., Nl, H., & Zhai, J. (2021). A BIM-based Building Circularity Assessment tool for the early design stage. *Proc. of the Conference CIB W78 2021, 11-15 October 2021, Luxembourg*.

#27: Toward zero-carbon HVAC for temperate regions: Cooling using Thermoelectric Heat Exchanger

An Experimental Study

M. Hasan SHARIQ[1], Ben HUGHES[2]

[1] University of Hull, United Kingdom, h.shariq@hull.ac.uk
[2] University of Hull, United Kingdom, b.r.hughes@hull.ac.uk

Abstract: As buildings contribute up to 40% of greenhouse gas emissions, exploring eco-friendly and sustainable HVAC and heat recovery solutions is vital. This experimental study presents a novel integration for passive wind towers that use thermoelectric heat exchangers to cool or heat fresh air as it enters a room. The proposed method utilises thermoelectric modules (TEM) also known as Peltier devices or thermoelectric coolers (TECs) to regulate the surface temperature of heat pipes within a wind tower. The TECs are capable of cooling as well as heating based on the current polarity. This paper focuses on investigating the cooling potential of this system through a range of experimental and CFD analyses.

The primary experimental setup consisted of heat pipe(s), TEC module, heatsink and fans for heat dissipation. Water-filled aluminium heat pipes allow effective and consistent temperature distribution across their length (1m). Preliminary results show a reduction of pipe surface temperatures by up to 11.8ºC using 40.8W of power at natural convection (indoor). Despite the rated voltage of 12V, experimental results showed 7.5V of input voltage delivers an optimal temperature drop (10.1ºC) to power consumption (13.5W) ratio. Convection tests showed reduced temperature drop with higher wind velocities, however, an addition of a volume control damper (at 30° opening) before the heat pipes was proposed as a solution to restore optimum cooling. The CFD model of a wind tower mounted on top of a closed room having two rows of heat pipes was used for simulations. A total of 35 heat pipes were modelled to reflect steady state temperatures from the experimental data, which showed temperature reductions below the pipes of 0.9ºC with no damper and 3.5ºC with damper at 1m/s supply wind velocity and of 3.7ºC with no damper and 6.6ºC with damper at 0.5m/s supply wind velocity.

The preliminary results showed a viable opportunity for a solar-powered thermoelectric heat exchanger system on passive wind towers. The proposed TEC-based cooling offers a low-maintenance, sustainable and environmentally friendly solution to meet the heating and cooling demands of buildings in temperate regions. Further design optimisation and improvements are recommended to maximise the cooling performance whilst ensuring ventilation requirements.

Keywords: Thermoelectric Cooling, HVAC, Heat pipes, Peltier heat recovery, Buildings

1. INTRODUCTION

With the increasing emphasis on global CO_2 reduction, building energy usage has been under scrutiny as it consumes around 40% of the overall CO_2 consumption (Shariq & Hughes, 2020). This paper proposes and investigates a thermoelectric-driven heat exchanger system for wind towers that has the potential to significantly reduce space cooling demands and contribute towards global CO_2 reduction efforts.

Wind towers (also known as wind catchers) offer a passive ventilation solution that works by utilising pressure differences created by wind forces (Calautit et al., 2014). Various studies have emerged in recent years to utilise wind towers for space cooling and heating applications through the use of heat pipes to reduce or eliminate energy demands (Calautit et al., 2016; Liu et al., 2022; Mahon et al., 2022). However, existing methods typically rely on capturing the temperatures from the exhaust stream of air and transferring it to the incoming stream. This preheating (or precooling) fresh air approach is limited by the range of exhaust temperatures from within the room.

This paper investigates a thermoelectric-driven active cooling of heat pipes as a retrofit to those existing methods. A thermoelectric cooler (TEC) is a solid-state heat pump that converts electrical energy into a temperature difference across its sides. TECs typically have low efficiencies (Gołębiowska & Widomski, 2022), however, thanks to the low power consumption of these devices, solar-powered cooling of heat pipes for the purpose of convective heat transfer can benefit from the massive temperature gradients that they can provide. Although the potential for this method includes both cooling and heating by reversing the polarity of the TECs, the scope of this paper is limited to cooling only.

2. METHODS

2.1. Thermoelectric Coolers

A thermoelectric cooler (TEC), also known as Peltier device is made up of two different semiconductor materials (N and P type) that is sandwiched between two ceramic plates as shown in Figure 1. These semi-conductors that are arranged in parallel work with a reversed Seebeck effect, i.e., when an electric current is applied, it pumps heat from one to the other creating one side hot and the other side cold. The hot side requires active and efficient heat dissipation to prevent heat from translating to the cold side internally. Hence, TECs are often used with a heatsink and a fan for active heat removal.

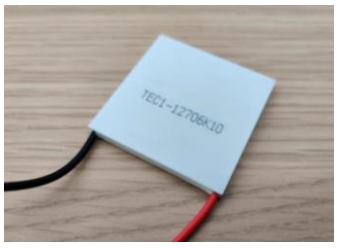

Figure 1 Peltier module

In this study, a TEC1-12706 Peltier device is used that has a rated voltage of 12V and maximum current consumption of 6A. As these TEC work using Peltier effect, the change of polarity can effectively switch the hot and cold side.

2.2. Heat Pipe Assembly

Heat pipes have a much higher thermal conductivity than regular solid pipes as it uses phase change with capillary action to translate heat. The pipe is sealed with a working fluid (such as water) at partial pressure inside. As one end of the pipe is heated, the working fluid vaporises and moves along the cavity to the colder end where it condenses thanks to the porous wick that surrounds the inner walls of the pipe. This releases thermal energy to the cold end and as the fluid moves back to the hot end the cycle repeats and provides an effective heat transfer across the length of the pipe. This process is illustrated in Figure 2.

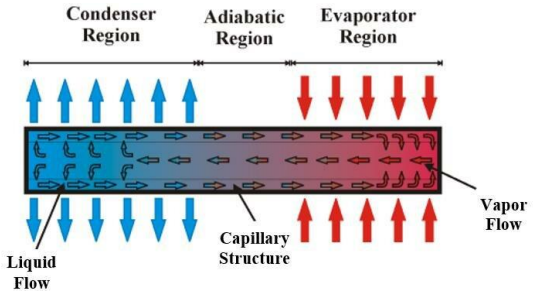

Figure 2 Operation of a heat pipe (Krambeck et al., 2019)

This paper utilises the thermal cycle of heat pipe however in reverse. Instead of heating, a small region of the pipe is to be actively cooled, which forces the working fluid of the other (warmer) end to translate the heat to the actively cooled section. This provides a rapid cooling effect on the heat pipe. The idea is to use one TEC per pipe to cool the entire surface of the heat pipe to allow the exchange of heat as the wind passes through. The heat pipe cooling unit is shown in Figure 3 and the arrangement of these heat pipes inside a wind tower is presented in the next subsection.

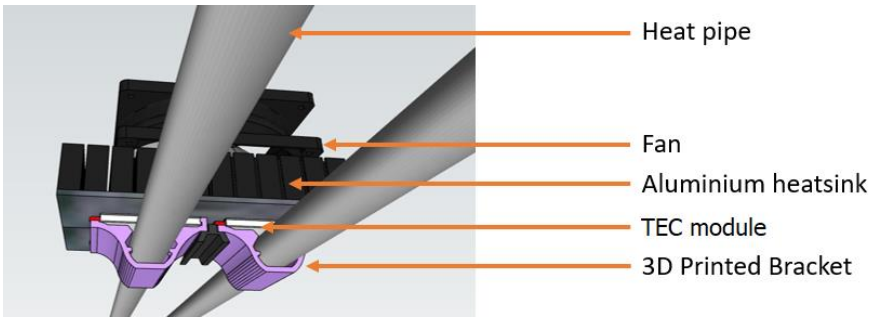

Figure 3 Heat pipe cooling assembly using TEC module

2.3. Wind Tower Integration

A CAD model of a Wind Tower from the study of (Calautit & Hughes, 2014) was used for the analysis with our TEC based heat exchanger (cooling) unit. A total of 35 heat pipes are to be placed at the bottom of the wind tower. These pipes are arranged in two layers separated by 50mm horizontally and 35mm vertically. The overall CAD model (that will be used in CFD simulations later) is shown in Figure 4.

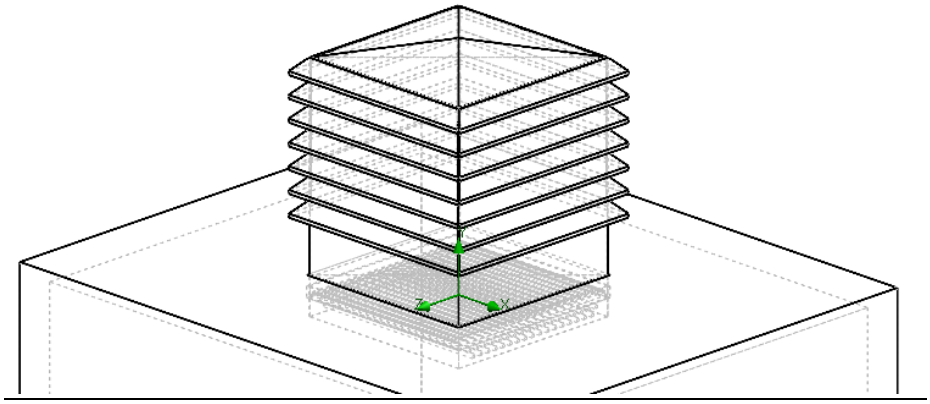

Figure 4 CAD model showing wind tower and heat pipes

3. EXPERIMENTATION AND PRELIMINARY RESULTS

As a prototype of the proposed system, a single TEC and up to 2 heat pipes were experimentally tested to inspect the cooling potential and performance with various physical variables/conditions as detailed in this section. Furthermore, a CFD model was simulated using the steady state (cooled) pipe surface temperatures as a complete assembly installed in a CAD model of a passive wind tower. The CFD modelling and results are also presented in this section.

3.1. Experimental Setup and Results

The aim is to cool the water-filled aluminium heat pipes through conduction with the cold side of a TEC. To ensure optimum performance, heat must be actively dissipated from the hot side of the TEC. For this, heat sinks with fans are essential to be integrated into the system. The initial experimental setup for (1) proof of concept using TEC-heatpipe conduction, (2) performance test against ambient temperatures and power input, and (3) forced convection to study the heat transfer at different wind velocities.

Proof of Concept

Water-filled aluminium heat pipes are used to observe the thermal conductivity by actively cooling from one end. Two heat pipes are cooled simultaneously using a single TEC1-12706 device using 12V power. The experimental setup is shown in Figure 5.

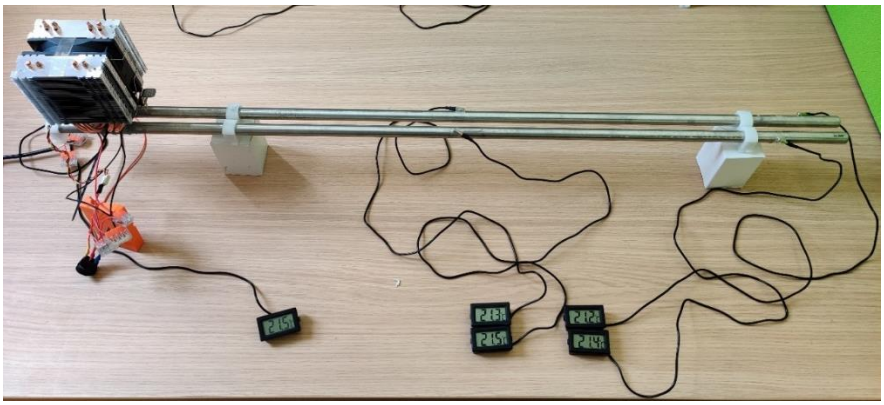

Figure 5 TEC-driven cooling of heat pipe set up

The preliminary results present a proof-of-concept of Peltier-based cooling of heat pipes as 48W of power through the TEC mounted on two heat pipes cooled the cold side of the TEC to -5°C and the heat pipes consistently across their length to an average of 11.5°C.

It is observed that the temperature is consistently distributed across the length of each heat pipe. This allows for simplification in modelling the heat pipe for CFD simulation. A constant surface heat flux should reflect the energy delivered to this system which is translating into a steady state constant temperature of the pipe surface. Alternatively, since the time constant to reach a steady state is up to 20 minutes, a constant surface temperature can also be modelled to visualise the steady-state heat transfer.

Note: All future experimentations and simulations will have the TEC device mounted in the centre of the pipe for quicker and more efficient heat transfer (across the length of the pipe) and recovery against ambient conditions. The experimental setup shown in Figure 6 consists of two heat pipes cooled via Peltier modules consuming 6V and 2A each. Three temperature sensors are attached at different locations (both ends and one at the centre) on each heat pipe.

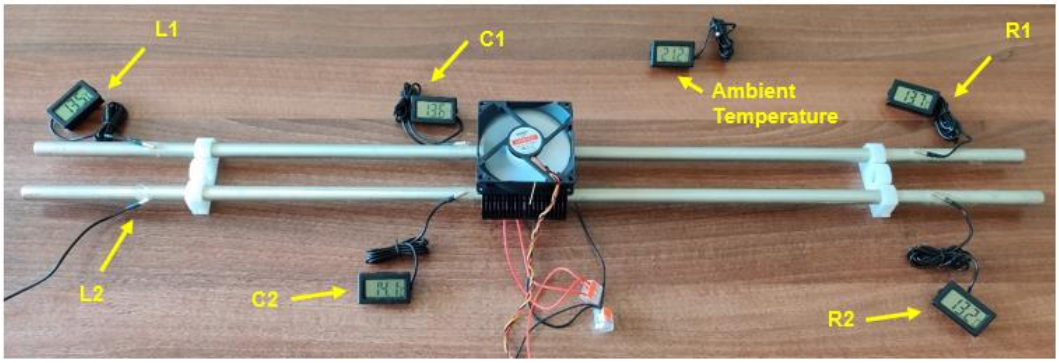

Figure 6 Experimental setup for two pipe arrangement with 6 temperature probes

Figure 7 shows the temperature data of pipes' surface recorded in the first 20 minutes of turning the TEC on. The ambient temperature and the initial temperature of the heat pipes were at 22°C. (L, C and R refers to Left, Centre and Right temperature probes for both Pipe1 and Pipe2)

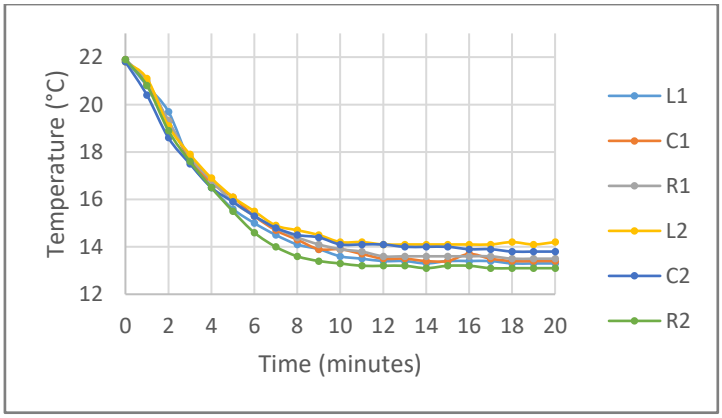

Figure 7 Heat pipes surface temperatures vs time at 22°C ambient temperature

The above results confirm the following:

a. Despite the cooling source being in the center, the temperatures remain even across the whole length of the heat pipes. (Hence, for future experiments, an 'average temperature' (T_{avg}) will be used when referring to the temperature of each heat pipe)
b. The change in temperature occurs during the first 10 to 15 minutes, after which the temperatures reach a steady state. This steady state slightly varies with ambient temperature as studied in the section 3.1.2)
c. Approximately 8°C of change in temperature (ΔT) was observed on both pipes.

Performance inspection

As the system is highly dependent on efficient heat dissipation to optimise the coefficient of performance (COP) and attain a larger temperature difference across the TEC, it is important to study the performance (i.e. cooling capacity) of the heat pipes under increasing ambient temperatures as well as power input. Hence, the experiment is now repeated at different ambient temperatures, i.e. to observe the rate of change and maximum cooling performance (ΔT) at various different ambient temperatures. Figure 8 shows the transient response of five independent experiments at ambient temperatures of 22°C, 25.3°C, 28°C, 31°C, and 33.8°C represented as the average temperatures of heat pipes for each experiment.

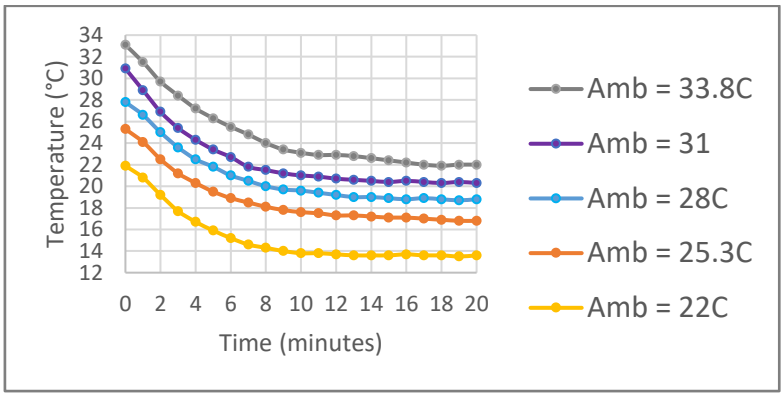

Figure 11 Heat pipe surface temperature drop at various ambient temperatures

The results show a common trend in the rate of drop in temperatures with time, which also maintains a similar time taken (12-15 minutes) to reach the steady state temperature irrespective of the ambient temperature. However, to assess the cooling performance at different ambient temperatures, a graph of ΔT is plotted against each experiment's starting temperature as shown in Figure 9.

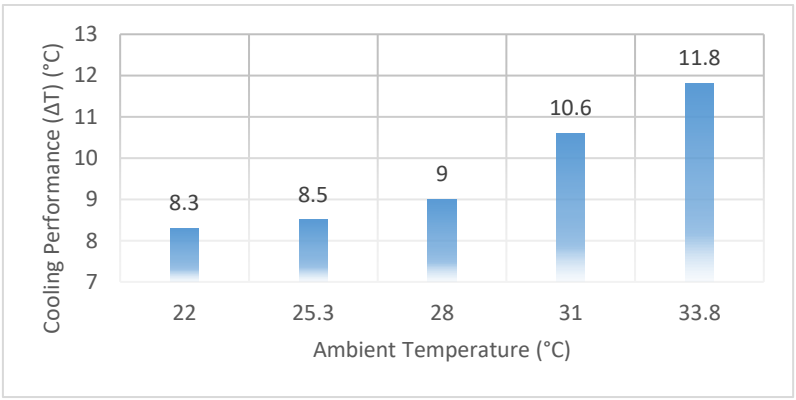

Figure 9 Summary of steady-state temperature drop vs ambient temperature

This shows that at higher (ambient) temperatures, the cooling performance improves accordingly, i.e. from ΔT of 8°C at 22°C of ambient temperature, the TEC modules are capable of dropping the temperatures of all heat pipes by up to 12°C when the ambient temperature climbs up to 34°C. However, since the power input is unchanged during the experiments, the increased temperature difference is only a result of the increasing efficiency of the system with higher ambient temperatures. The higher cooling efficiency (with the same power input), as ambient temperatures rise, is presumably due to a combination of (1) increased COP of TEC due to the higher temperature difference between hot and cold ends, (2) better relative heat dissipation from the heat sink and fan, and (3) improved heat pipe operational conditions with a more efficient heat transport leveraging the phase change of its working fluid. This increase in efficiency is highly beneficial in the application of space cooling in hotter climates.

The next set of experiments measures the performance of the same system by varying the power input while maintaining the same ambient temperatures (and other conditions). Table 1 shows the summary of these five experiments with current consumption, power input and a ratio of temperature drop to power input.

Table 2: Summary of experimental results for power consumptions

Input Voltage	T_{amb}	ΔT_{avg}	I (A)	P_i (W)
5V	21.5	7.9	1.4	7.0
6V	21.6	8.3	1.5	9.0
7.5V	22.7	10.1	1.8	13.5
9V	22.0	10.6	2.3	20.7
12V	22.8	10.7	3.4	40.8

This shows the as more power is consumed, higher the temperature drop. However, the performance is not linear. As the proposed system is to be solar-powered, it is essential to identify the optimum value of power requirements. Figure 10 shows 7.5V as the desired input voltage with highest efficiency. Voltage input above 7.5V induces saturation as minimal change in temperature is observed with a much higher power consumption.

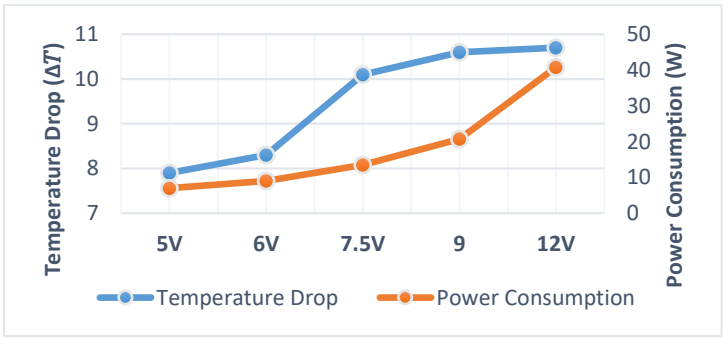

Figure 10 Temperature drop (°C) and Power consumption (W) against voltage input

Forced convection test

The above experiments were performed as a proof of concept under natural convection. In a real-world scenario, especially inside a wind tower, the heat pipes will be subjected to varying wind speeds that are expected to impact the steady-state temperatures (as the pipes would then be exposed to a quicker heat transfer rate of ambient temperatures). To precisely measure this, an experimental setup for forced convection was prepared with an array of four 12V DC fans replicating wind, a wind speed sensor, and contact sensors to measure the pipe surface temperatures. The voltage of the fans was regulated to vary the wind speeds. This setup is shown in Figure 11.

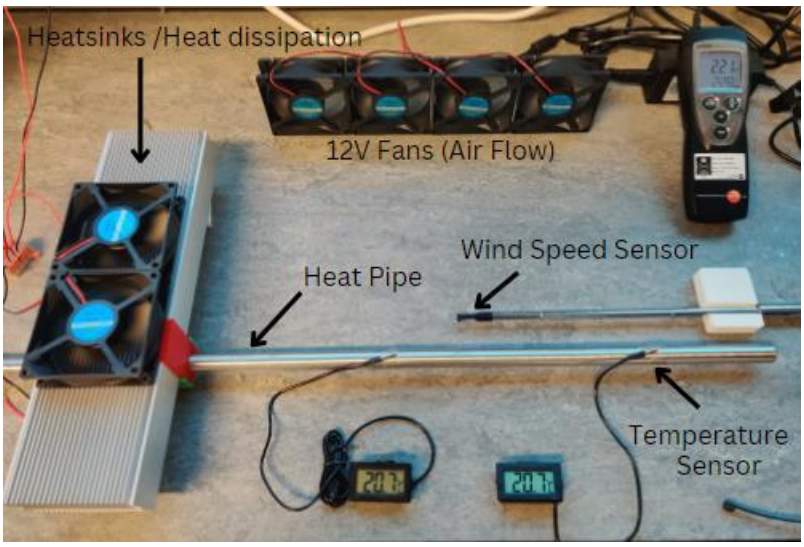

Figure 11 Experimental setup for forced convection

The results from the above experiment is shown in Figure 12 that shows the steady state temperatures of the heat pipe surface subjected to wind/airs speeds from 0.1m/s to 3m/s. This data helps in modelling a more realistic steady state temperature heat source as detailed in the next section.

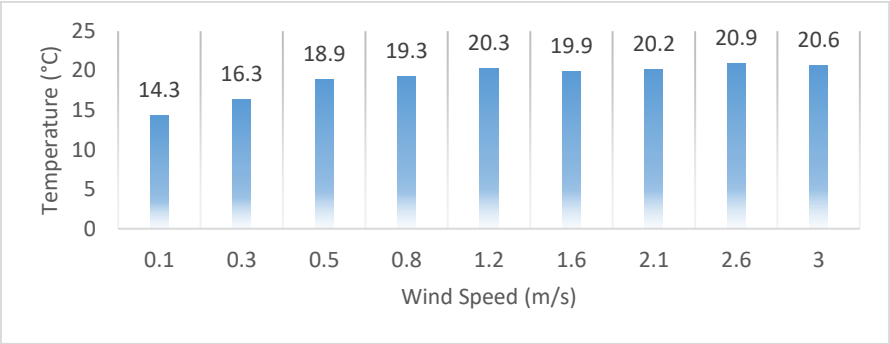

Figure 12 Experimental results of forced convection tests

3.2 CFD Modelling and Results

To study the impact of TEC-driven cooling through heat pipes within a wind tower, CFD modelling and comparisons help visualise the flow, turbulence and temperature gradients of air within the wind tower as it passes through the heat exchanger (i.e. arrays of heat pipes). Solidworks 2022 Flow Simulation is used for CAD, CFD modelling and simulation.

CFD Model

A 2D cross-section of mesh used in CFD for the wind tower is shown in Figure 13.

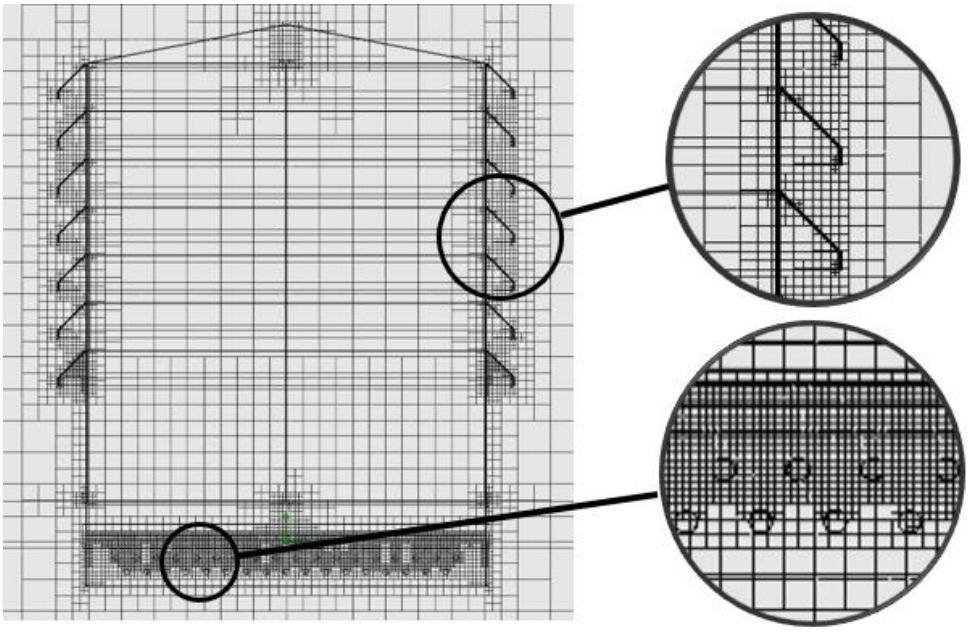

Figure 13 CFD Mesh of Wind Tower

The measurement probes that are used for CFD analysis for velocity and temperature (fluid) are placed at the inlet quadrant (i.e. the East quadrant). The velocity probe is 60mm above the pipes that help ensure the steady state temperature of pipes according to the results of experimental data for forced convection (Figure 12). The temperature probe is located 30mm after the pipes.

As the experimental results of forced convection showed higher temperature drop with lower velocities, in this study, another configuration is compared side by side which includes a damper below the pipes. This damper has a 30° louvre angle that helps regulate the wind flow (especially lowering the high wind speeds) to ensure increased residence time with the pipes and allow more heat exchange to occur before the wind enters the room.

Figure 14 shows the cross-section of the end of the wind tower (towards the inlet quadrant) labeled with the two measurement probes and damper arrangement.

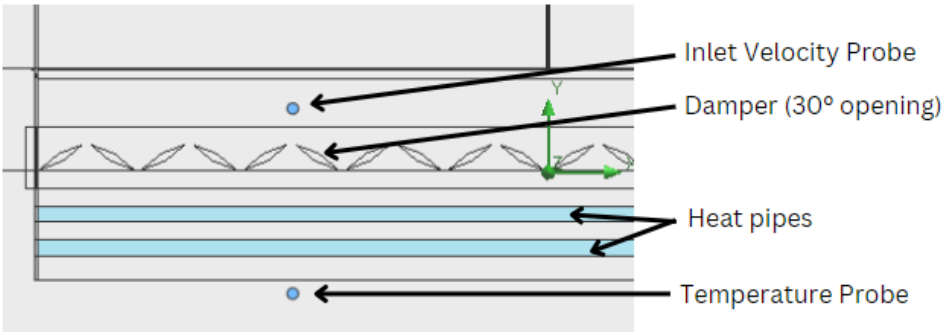

Figure 14 Arrangement of damper and measurement probes

CFD Results

Preliminary CFD simulations were performed using an ambient temperature of 30ºC at 1m/s wind speed to compare cooling capacity in both configurations, i.e., without a damper and with a damper before the pipes.

Figure 15 shows the CFD results of the velocity contour plot at steady-state with 1m/s inlet wind velocities for both configurations: with and without damper. The addition of dampers reduces the wind speeds before the heat pipes.

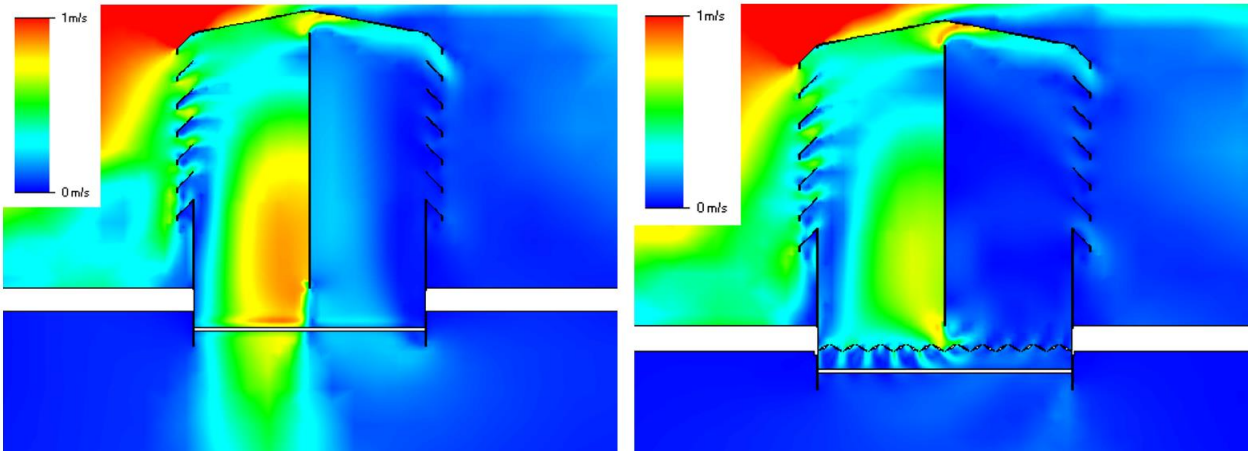

Figure 15 Velocity contour plots with (right) and without damper (left)

Figure 16 shows the turbulence contour plot at steady state of CFD results with 1m/s inlet wind velocities for both configurations: with and without damper. As observed, massive turbulence occurs around the heat pipes causing a better heat transfer to take place before wind enters the room.

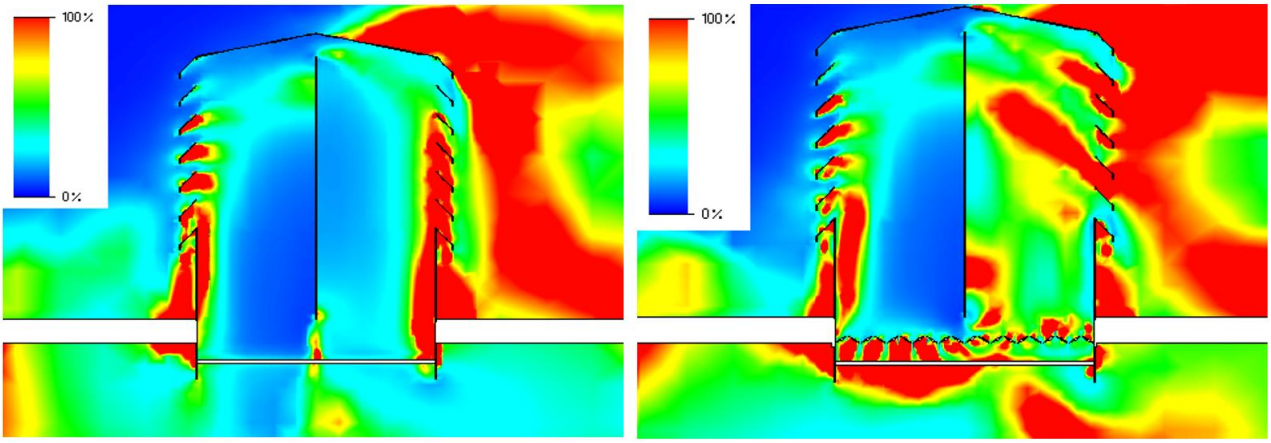

Figure 12 Turbulence contour plot with (right) and without damper (left)

Figure 17 shows the temperature contour plot at steady state of CFD results with 1m/s inlet wind velocities for both configurations: with and without damper. The temperature on the right side is colder as the exhaust room temperature

proceeds to exit the wind tower which further cools the air. An envelope of concentrated cold region forms at the exhaust region of the heat pipes especially at the damper configuration as seen in Figure 17 (right). This colder air gradually descends into the room contributing to the overall cooling effect.

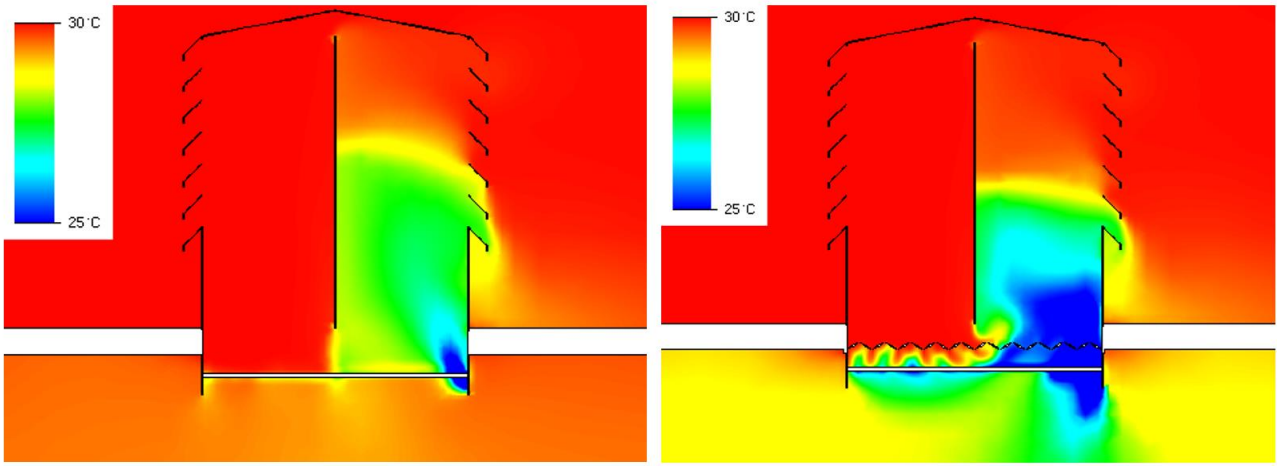

Figure 17 Fluid temperature contour plot with (right) and without damper (left)

The summary of results that shows the temperature drop across the temperature probe (after the pipes) with and without the damper are shown in Table 2.

Table 2: Summary of CFD results

	No Damper	Damper (30°)	No Damper	Damper (30°)
Wind Velocity (m/s)	1	1	0.5	0.5
Inlet Velocity (m/s)	0.65	0.64	0.21	0.18
Steady State Time (min)	30	45	30	45
Temperature Drop (°C)	0.9	3.5	3.7	6.6

4. CONCLUSION AND FUTURE SCOPE

The aim of this experimental study was to investigate the potential of a thermoelectric-driven heat exchanger for a four-quadrant wind tower. A Peltier device was used to cool a heat pipe by up to 11.8°C using 40.8W of electrical power. It was observed that higher ambient temperatures improved heat pipes performance and better cooling efficiencies were achieved. Among the various voltage input tested against the resulting temperature drops, 7.5V showed optimum performance. The steady-state pipe surface temperatures were measured experimentally against wind speeds through forced convection tests. The experimental results of steady-state temperatures helped model a larger-scale CFD model with 35 heat pipes placed at the bottom of a wind tower mounted on top of a closed room. A wind speed of 1m/s was supplied to measure the inlet velocities (before the pipes) and the temperatures below the pipe. Two configurations were examined, i.e., with and without a damper before the pipes. The CFD results showed a massive improvement in temperature drop (i.e., from 0.9°C to 3.5°C @ 1m/s and 3.7°C to 6.6°C @ 0.5m/s) with the damper configuration as it helped reduce the wind speeds and increase turbulence, improving the effective heat transfer. However, this may impact the ventilation rates that need addressing.

The following future recommendations are currently being addressed by the authors:

1. Integrating an array of fans below the heat pipes to regulate ventilation and along with cooling requirements.
2. Addition of another layer of heat pipes to improve the cooling capacity.
3. Conduct a full-scale experimental test using 35 pipes and validate the CFD model with the same setup to obtain a more precise representation of temperature drop after the pipes and examine the impact on room temperatures.

To conclude, the TEC-cooling method provides a massive opportunity towards retrofitting solar-powered TEC-driven cooling/heating systems for wind towers. The proposed approach and recommendations show a feasible potential to replace conventional mechanical cooling/heating systems in temperate regions and help reduce the cooling/heating demands in tropical or equatorial regions.

5. ACKNOWLEDGEMENT

The work is a part of the FREECOOL+ project funded by InnovateUK (Project number: 79459) in collaboration with Free Running Buildings (Ltd).

6. REFERENCES

Calautit, J. K., & Hughes, B. R. (2014). Wind tunnel and CFD study of the natural ventilation performance of a commercial multi-directional wind tower. Building and Environment, 80, 71–83. https://doi.org/10.1016/J.BUILDENV.2014.05.022

Calautit, J. K., O'Connor, D., & Hughes, B. R. (2014). Determining the optimum spacing and arrangement for commercial wind towers for ventilation performance. Building and Environment, 82, 274–287. https://doi.org/10.1016/J.BUILDENV.2014.08.024

Calautit, J. K., O'Connor, D., & Hughes, B. R. (2016). A natural ventilation wind tower with heat pipe heat recovery for cold climates. Renewable Energy, 87, 1088–1104. https://doi.org/10.1016/J.RENENE.2015.08.026

Gołębiowska, J., & Widomski, M. K. (2022). Numerical Assessment of the Experimental Thermoelectric Cooling System Effectiveness. Journal of Ecological Engineering, 23(12), 99–110. https://doi.org/10.12911/22998993/154845

Krambeck, L., Baptista Nishida, F., Marrone De Aguiar, V., Dias Dos Santos, P. H., & Antonini Alves, T. (2019). Thermal performance evaluation of different passive devices for electronics cooling. Thermal Science, 23(2), 1151–1160. https://doi.org/10.2298/TSCI170610300K

Liu, M., Jimenez-Bescos, C., & Calautit, J. (2022). CFD investigation of a natural ventilation wind tower system with solid tube banks heat recovery for mild-cold climate. Journal of Building Engineering, 45, 103570. https://doi.org/10.1016/J.JOBE.2021.103570

Mahon, H., Friedrich, D., & Hughes, B. (2022). Wind tunnel test and numerical study of a multi-sided wind tower with horizontal heat pipes. Energy, 260, 125118. https://doi.org/10.1016/J.ENERGY.2022.125118

Shariq, M. H., & Hughes, B. R. (2020). Revolutionising building inspection techniques to meet large-scale energy demands: A review of the state-of-the-art. Renewable and Sustainable Energy Reviews, 130, 109979. https://doi.org/10.1016/J.RSER.2020.109979

#30: A field study on occupants' thermal sensation vote in a test room equipped with trombe wall

Erfan Malekian NOBARANI [1], Murat OZDENEFE [2], Seyedeh Zahra SHAHABI [3]

[1] *Department of Mechanical Engineering, Eastern Mediterranean University, G. Magosa, TRNC Mersin 10, Turkey, erfan.nobarani@emu.edu.tr*
[2] *Department of Mechanical Engineering, Eastern Mediterranean University, G. Magosa, TRNC Mersin 10, Turkey, murat.ozdenefe@emu.edu.tr*
[3] *Department of Architecture, Eastern Mediterranean University, G. Magosa, TRNC Mersin 10, Turkey, 19600149@emu.edu.tr*

Abstract: Trombe walls have emerged as energy-efficient and sustainable solutions for providing thermal comfort. They make use of solar energy to passively deliver heat, reducing the need for traditional heating systems that rely on non-renewable energy sources, and contributing to the mitigation of carbon emissions.

During the day, a Trombe wall absorbs solar radiation and heats the air that lies between the glass cover and the wall. Heated air rises and circulates through the vents positioned at the top and bottom of the wall supplying predominantly convective heat to the occupied space. In contrast, during the night, the vents are closed to prevent heat loss, enabling the wall to gradually release the stored energy into the occupied space, thereby providing mostly radiant heat .

In addition to sustainability and energy efficiency, Trombe walls may offer better thermal comfort than traditional heating systems, thanks to low air speeds and radiant heat. To evaluate their performance in terms of thermal comfort, it is essential to assess the Predicted Mean Vote (PMV) and Predicted Percentage of Dissatisfied (PPD) indices, which quantitatively measure human thermal comfort by taking into account several factors, including air temperature, radiant temperature, air velocity, humidity, and clothing insulation. Although PMV and PPD are widely used for assessing comfort, real occupant votes would be more reliable.

This study aims to evaluate a Trombe wall-installed test room's thermal comfort performance located in Cyprus through real occupant votes during daytime use. Indoor and outdoor environmental conditions were monitored to determine the correlation between comfort levels reported by the occupants and the recorded conditions. Participants completed a survey on their thermal sensation, which was converted into a 7-point scale using the Fanger model for quantitative and qualitative analysis. Although the mean value of the occupants' votes did not entirely fall within the acceptable PMV and PPD range suggested by the standards, the deviation was not significantly high. The thermal sensation votes indicated that the conditions were slightly warm.

Keywords: Trombe wall, solar energy, Thermal comfort, thermal sensation vote, Radiant heating

1. INTRODUCTION

Anthropogenic greenhouse gas emissions are increasing year by year. For instance, CO_2 emissions by heating demand of buildings had a new high for the year 2021 according to the data published by the international energy agency. The role of efficient and low-carbon heating technologies continues to grow, but fossil fuels still meet over 60% of the heating energy demand (IEA, 2022). Radiant heating and cooling systems have shown a good contribution to easing this problem by providing energy efficiency together with thermal comfort conditions for people (Rhee and Kim, 2015). Trombe walls as a passive radiant heating technology, have attracted significant attention in recent years as a sustainable, low-carbon approach for improving indoor thermal comfort which is significant for occupants' wellbeing. Trombe walls function by absorbing and storing solar radiation during the day and releasing it into the indoor space at night, thereby reducing the need for conventional heating systems that rely on non-renewable energy sources (Duffie and Beckman, 2013).

In the literature, there are various studies on Trombe walls ranging from their energy performance to sizing, and from their construction methods to different operation arrangements. In a review study, Sonrek et al. (2023) examined the experimental and numerical investigations conducted on Trombe wall solutions encompassing conventional Trombe walls, Trombe walls integrated with phase change materials and photovoltaic cells as well as solar chimneys. The authors found that in most of the studies, Trombe walls show potentials in energy conservation and reduction of carbon emissions. Also, it has been seen that these advantages can be achieved while maintaining thermal comfort (Sornek et al., 2023). In another review study (Hu et al. (2017) examined prominent works on Trombe walls that had been realized in the last 15 years. Many studies focused on sizing Trombe walls and found that increasing the wall area can significantly enhance the heat output. The recommended Trombe wall-to-other-wall ratio is 37%. The storage capacity of the wall material has also received considerable attention, and it has been found that lightweight materials with lower volumes have superior performance. Environmental factors, such as solar radiation and wind pressure, were analysed in several studies, which revealed that Trombe walls are more efficient in locations with higher solar radiation and low air speeds. The impact of these factors on heat loss coefficients was also noted (Hu et al., 2017).

While the current findings hold value, further research is required to comprehensively assess the thermal comfort conditions offered by Trombe walls. Although there are studies examining thermal comfort in spaces with Trombe walls, many of them focus on the hybrid Trombe walls incorporating phase change materials (PCM) rather than conventional ones (Li et al., 2022; Lin et al., 2021; Xiong et al., 2022). Moreover, the prevalent methodology employed for such thermal comfort assessments existing in the literature primarily rely on numerical and mathematical modelling rather than actual measurements or occupants' subjective thermal sensation assessments. Only a few studies do employ experimental approaches to measure environmental parameters, including air temperature, humidity, and wall temperatures, aiming to evaluate thermal comfort indices based on achieved set point temperatures within the room.

For instance, In a parametric study considering energy and economic aspects, Trombe wall sizing is evaluated along with comfort parameters such as room temperature, relative humidity, and CO_2 concentration (Özdenefe et al., 2018). The study utilized the Energy Plus simulation tool to do energy calculations. Also, savings-to-investment ratios have been calculated for different wall areas in existing and new buildings. Thermal comfort analysis included assessments of zone mean air temperature, humidity, and CO_2 concentration, as well as graphical methods using psychometric charts to determine comfort zones. Findings indicate that increasing the wall area improves the economic feasibility of Trombe walls, but larger areas may occasionally lead to room temperatures exceeding comfort thresholds. Overall, constructing a Trombe wall is economically viable in thermally insulated new buildings with limited winter occupancy, while in non-insulated buildings, a minimum area of 9 m^2 is required for feasibility.

In a numerical study utilizing CFD simulations, the distribution of air temperature and air circulation as thermal comfort indicators within a room were investigated for different types of Trombe wall constructions (Błotny and Nemś, 2019). The findings revealed that during the heating seasons, a Trombe wall with triple glazing filled with argon gas resulted in an average air temperature increase of 1.52 ℃. In contrast, when the Trombe wall construction was changed from concrete to brick, the average air temperature increase was only 0.4℃, indicating a lower capability for temperature enhancement. Regarding air circulation, the study demonstrated that in both cases, the air velocity within the room, assisted by air circulation from the Trombe wall cavity, remained within an acceptable range for comfort, measuring 0.013 m/s and 0.02 m/s for the argon-filled glazing and substituted material cases, respectively. There are few studies considering more exclusive thermal comfort indices, like PMV and PPD, not to mention that most of the approaches are based on simulation and mathematical modelling (Xiao et al., 2022, 2023).

It is obvious that there is need for investigating the thermal comfort in Trombe wall installed buildings through real votes of the occupants. Hence the objective of this work is to assess the thermal comfort in a test room which is installed with Trombe wall via the thermal sensation votes of real occupants. This work also aims to assess the local comfort of the occupants at their head and feet regions again through their votes which have not been studied before. The work is intended for the winter operation of the Trombe wall specifically focusing the morning use. Most existing studies in literature primarily concentrate on the use of stored energy by the Trombe wall during the evening hours which there is no solar radiation. This aspect sets the current study apart and contributes to the existing body of knowledge.

2. METHODOLOGY

2.1. Test room specifications

The test room is located in Famagusta, Northern Cyprus. The Trombe wall is located on the south-facing wall of the room. The floor area of the room is 11 m^2 and its height is 3.13 m. The Trombe wall construction is made up from three layers; 16 cm reinforced concrete wall, glass cover of the wall and an air layer of 14 cm which lies between the concrete wall and the glass cover. The reinforced concrete wall has four vents on it as shown in Figure 1. The vents are for letting air in and out of the living space and each can be opened and closed individually for obtaining different arrangements. Figure 1 also presents the dimensions of the cover system.

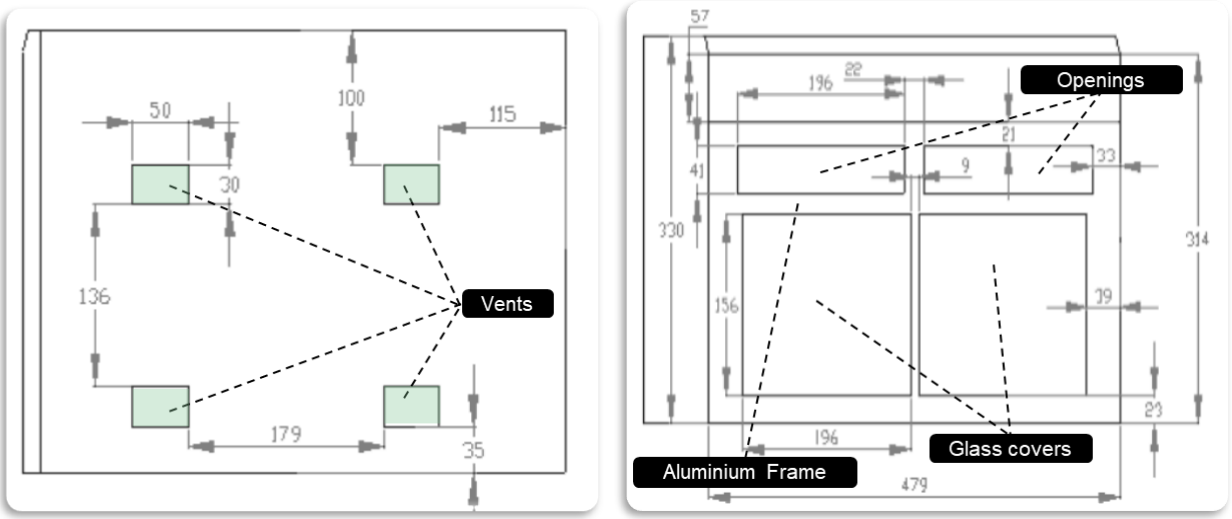

Figure 1 Trombe wall cover dimensions (on the left), Internal view of TW and location of vents (on the right)).

The current study focuses on evaluating the performance of a Trombe wall for heating during the daytime when all the vents are open. Air movement and heating occurs through buoyancy effect and natural convection within the cavity which is driven by absorbed solar radiation by the reinforced concrete wall. With this arrangement the heated air in the cavity is introduced into the room through upper vents and cool air from the room flows into the cavity. In addition the wall that stores solar radiation begins to gradually release radiant heat into the room during afternoon hours. Figure 2 illustrates the daytime operation of the Trombe wall.

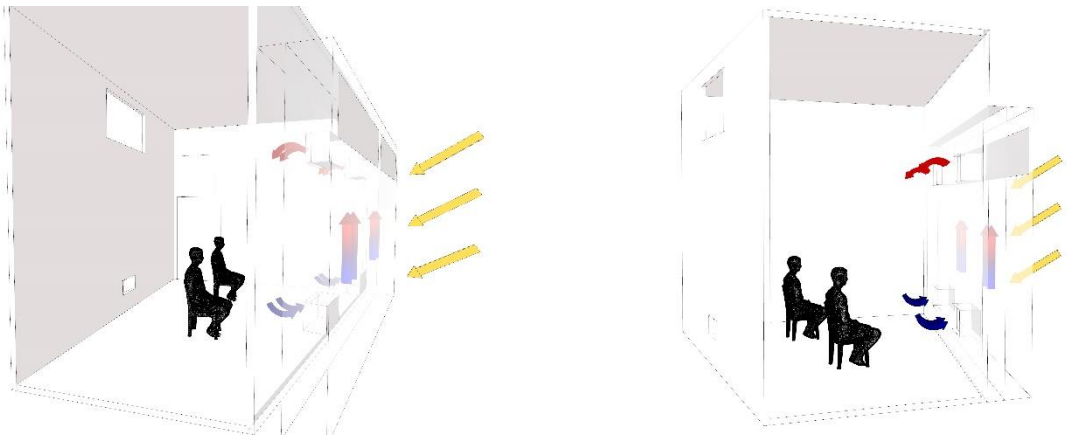

Figure 2 Wall and vents airflow

2.2. Evaluation method

To evaluate the thermal comfort performance of the Trombe wall under the specified configuration, real occupants' votes were utilized through a survey. The survey took place on February 7, 2023, during daytime hours. Inside and outside air and Trombe wall surface temperatures were monitored during the test. The test room accommodated a total of 2 occupants simultaneously, resulting in an occupancy density of 0.18 persons per square meter. The survey included 6 participants in total who provided their feelings regarding their general thermal sensation, local thermal sensation, and general satisfaction

level, by answering the questions given in Table 1. The participants selected one of the answers that are given in Table 2. Each pair of occupants spent 20 minutes at seated position in the room corresponding to a metabolic rate of 0.9 met and casted their votes two times, one after 10 minutes and the other after 20 minutes they get into the room. Subsequently they leave the room and a new pair of occupants come. The occupants were given instructions to wear a suitable combination of clothes which led to insulation level of 1 clo. In Figure 3, shows the arrangement of the occupants during the survey.

Table 1: Survey questions

#	Question	Remarks
1	How do you feel overall temperature in the room?	For general thermal sensation
2	How do you feel temperature at your head region?	For local thermal sensation
3	How do you feel temperature at your feet region?	For local thermal sensation
4	How do you generally find the thermal comfort condition in the room?	For general sensation/satisfaction

Table 2: Answers and corresponding points to occupants' votes on the survey

Answers for question 1, 2 and 3	Corresponding point	Answers for question 4	Corresponding point
Cold	-3	Comfortable	0
Cool	-2	Slightly comfortable	0.5
Slightly cool	-1	Not comfortable	1
Neutral	0		
Slightly warm	+1		
Warm	+2		
Hot	+3		

Figure 3 Arrangement of Occupants in the test room during the survey

The survey results for revealing the general satisfaction level, have been indicated in the results in terms of predicted dissatisfied (PD). This is done by taking the average of each two votes which has been recorded in every voting instant. Moreover, the predicted percentage of dissatisfied (PPD) which is a function of predicted mean vote (PMV) is calculated by using the following equation (Equation1) (Butcher and Craig, 2015). PMV is an index for estimating occupants' votes on a 7-point scale from cold to hot. It should be noted that if real occupant votes would not be sought PMV can be calculated from environmental parameters' measurements using the Fanger model (Fanger, 1970) which relates PMV to metabolic rate, the ratio of the clothed to the unclothed area of the human body, air temperature, operative temperature, surface temperature of the clothing, partial water vapor pressure, and convective heat transfer coefficient. In this work the real votes are collected (referred as TSV) hence real votes were substituted for PMV in Equation 1.

Equation 1: PPD estimation from PMV

$$PPD = 100 - 95\exp[-(0.03353\,PMV^4 + 0.2179\,PMV^2)]$$

Where:

- PPD = Predicted percentage dissatisfied (%)
- PMV = Predicted mean vote

The assessment of thermal comfort includes the analysis of Predicted Dissatisfied (PD) and its comparison with the Predicted Percentage of Dissatisfied (PPD). Finally, the Thermal Sensation Vote (TSV), PD, and PPD are assessed to determine whether they fall within the acceptable range defined by ASHRAE standards.

3. RESULTS AND DISCUSSION

3.1. Environmental conditions

Inside and outside air and Trombe wall temperatures were monitored during the experiment. Figure 4 illustrates the variation of the recorded temperatures throughout the survey. The figure suggests that the variation in the inside air and wall temperatures were minor, thereby indicating close to steady state conditions. The mean values of the recorded temperatures and their corresponding standard deviations are evaluated and presented in Table 3. The mean outside temperature throughout the experiment was 12 ℃ which is a typical daytime temperature for the coldest months in Cyprus.

Table 3: Environmental parameters averages with their standard deviation

Property	Outside air temp. ℃	Outside wall temp. ℃	Inside air temp. ℃	Inside wall temp. ℃
Measurements	12.07±1.45	39.30±2.62	23.53±0.88	32.33±0.76

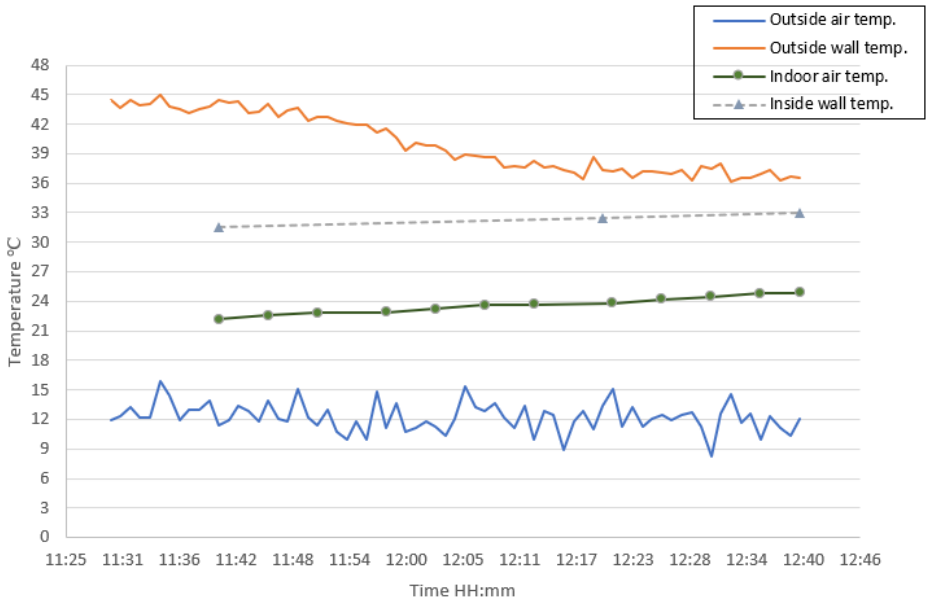

Figure 4 Variation of environmental parameters during the test

3.2. General thermal sensation

The results of the questionnaire administered to the occupants on the 7th of February during the daytime have been presented through the subsequent figures. Figure 5 illustrates the general thermal sensation of the participants during their occupation of the test room, plotted against time. This graph shows the distribution of the votes over time and at each time there are two votes since there were 2 occupants simultaneously in the room during the survey. The mean value of TSV and its corresponding standard deviation have been calculated as 1.08±0.79.

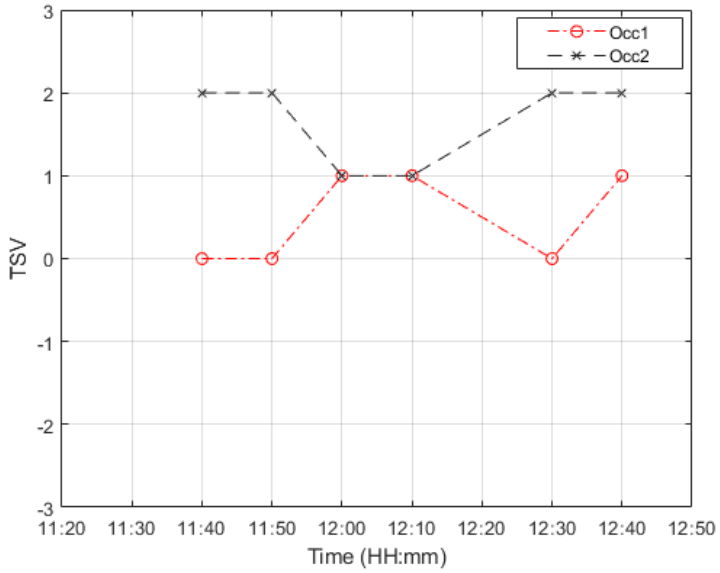

Figure 5 General thermal sensation votes by the occupants

Figure 6 depicts the percentage of occurrence of each vote. The results reveal that the majority of the votes were concentrated in the warm region of the thermal sensation scale. Specifically, the highest percentage of votes, amounting about 42 per cent, was for conditions characterized by slightly warm thermal sensation.

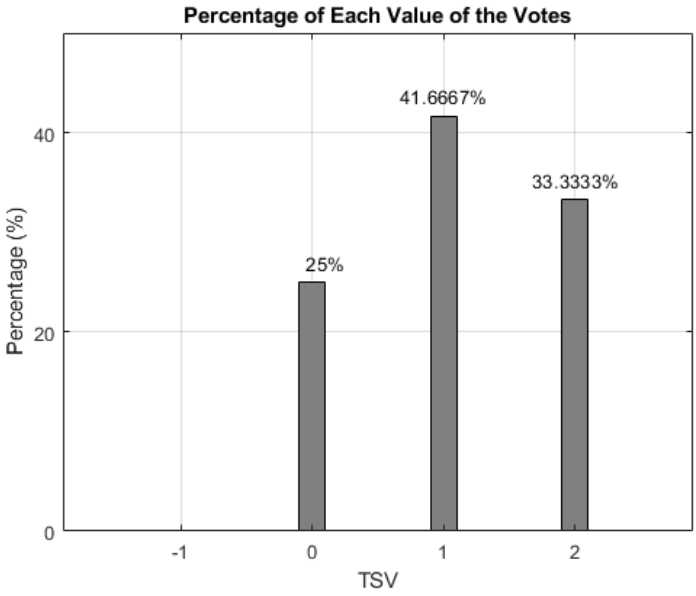

Figure 6 Percentage share of each vote

3.3. Local thermal sensation

General thermal sensation plot versus local thermal sensation at the head and feet regions is shown in Figure 7. The graph represents the correlation between the occupants' general thermal sensation and the thermal sensation of their head and feet regions. The results indicate a moderate positive correlation between the general thermal sensation and the thermal sensation of the head region, with a correlation coefficient of 0.57. In contrast, a strong positive correlation was observed between the general thermal sensation and the thermal sensation of the feet region, with a correlation coefficient of 0.79. Figure6 reveals that the correlation between the occupants' thermal sensation and their dissatisfaction levels are different for different body regions. The findings suggest that the occupants' overall thermal comfort perception is more related to the thermal conditions experienced at their feet region than the thermal conditions experienced at their head region.

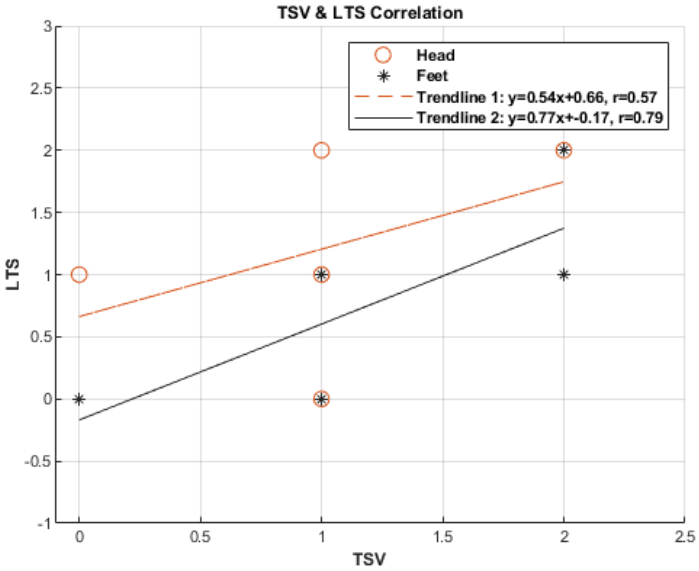

Figure 7 Correlation between TSV and LTS

Distribution of the votes at the head and feet region is presented in a bar chart in Figure 8 where it is observed that 50% of the votes at the feet region is allocated to the neutral feeling, while at head region only 16.7 % of the occupants felt neutral. Most of the votes at the head region (around 84 per cent) lie within the warm thermal condition (sightly warm and warm votes corresponding to the points 1 and 2). On the other hand, at the feet region, only 16.7 % felt warm (corresponds to 2) while this number is 41.7 in the head region, and 33% felt slightly warm on their feet.

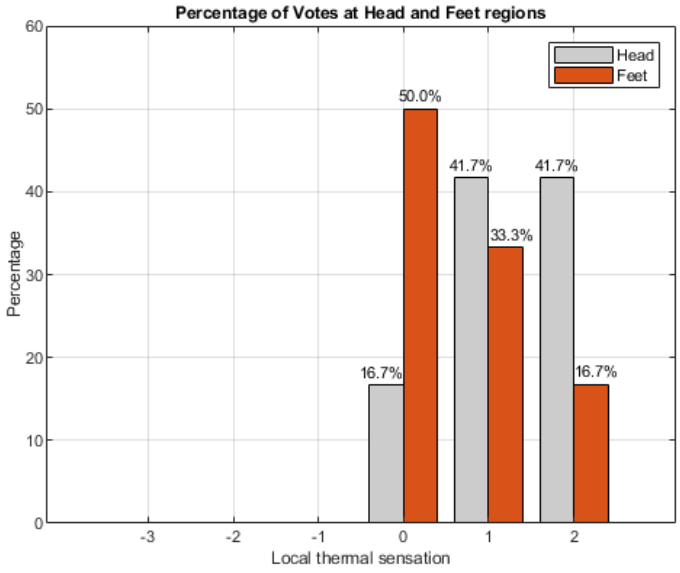

Figure 8 Percentage of each point on the thermal sensation scale at Head and Feet regions

3.4. Level of general satisfaction

The calculation of percentage of dissatisfied (PD) is based on the direct votes given by the survey attendees to question 4. In Figure 9, the votes for PD cast by the two occupants during each reading time are illustrated, together with the Predicted Percentage of Dissatisfied (PPD) that is estimated from the average of the thermal sensation votes submitted by the two occupants.

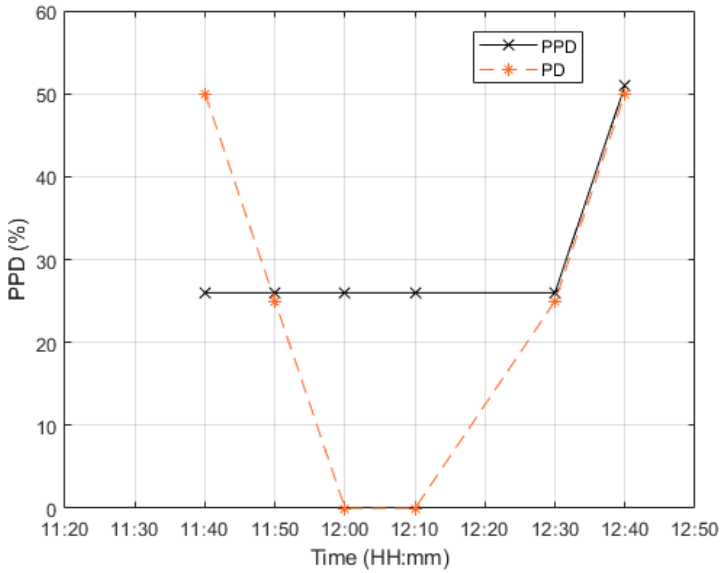

Figure 9 Percentage dissatisfied (PD) and predicted percentage dissatisfied (PPD) (Averaged over every 2 votes)

As PD and PPD are determined based on the percentage of dissatisfied individuals, the computed values reflect the overall dissatisfaction rate of the occupants with the thermal environment. The mean values of PD and PPD can be seen in Table 4 where we can notice a high standard deviation in votes for the PD and for PPD. This can be due to different sensitivities and perceptions of the thermal comfort of people. Furthermore, we should consider that the standard deviation is influenced by the sample size, and a smaller sample size will tend to result in a larger standard deviation. In our study, we have only six data points, which may contribute to the high standard deviation. This is because of the size of the test room (Almost 11 m^2) which is merely suitable for the instantaneous use of 2 people. This shows the challenges attributed to the evaluation of the thermal comfort criterion inside the room using real occupants' votes. It can be suggested to do more tests and investigations to mitigate this problem, although, for the current study, we may use the standard error of the mean (SEM) to have better anticipation of the quality of the mean of the population of our data. Hence the SEM for PD and PPD have been calculated as 9.13% and 4.13%, respectively.

It is noteworthy to mention that, considering individual votes without considering averages of 2 votes every 10 minutes (total 12 votes), exactly 50% of the votes were slightly comfortable and 50% comfortable.

Table 4: Mean values of PD and PPD and their standard deviation

Occ.Votes	PD	PPD
Occ1 & 2	50	26.12
Occ1 & 2	25	26.12
Occ3 & 4	0	26.12
Occ3 & 4	0	26.12
Occ5 & 6	25	26.12
Occ5 & 6	50	50.90
Mean ± Std.Dev.	25±22.36	30.25±10.12

3.5. Evaluation of comfort level according to standards

The assessment of comfort levels is typically accomplished by comparing study results with established standards, such as those developed by the American Society of Heating, Refrigerating, and Air-Conditioning Engineers (ASHRAE). ASHRAE recommends a generally acceptable range of ±0.5 on a 7-point scale for the Predicted Mean Vote (PMV) when environmental measurements are used to predict thermal comfort. However, this range only applies to the time when PMV is calculated. In contrast, when assessing thermal comfort based on occupants' actual sensation, as reflected in the survey details presented in Table 1 and Table 2, ASHRAE recommends an acceptable range of Thermal Sensation Vote (TSV) between -2 and 2. It is important to note that this range only applies when the available options for thermal sensation vote are integer numbers (ASHRAE, 2017). Figure 10 highlights the acceptable range, which all the votes fall within. Furthermore, all the votes are positive numbers, indicating a slightly warm, warm, or hot sensation of the space. Overall, the results suggest that the specific arrangement of the Trombe wall tested can provide acceptable thermal comfort for the test room's internal space.

On the other side, the evaluation of thermal comfort can be done by considering the average of the total votes. In this case, TSV explicitly can be considered as PMV. From the results, the average of TSV corresponds to PMV = 1.08 which has a deviation of 0.58 from the generally acceptable range of ±0.5.

Evaluation of the satisfaction level of the occupants can be done by the PPD index. A Predicted Mean Vote (PMV) range of ±0.5 predicts that 90% of the population will be satisfied, resulting in a PPD of 10%. However, in most buildings, a satisfaction rate of 90% is rarely achieved, with the maximum satisfaction rate typically around 80%. This discrepancy is attributed to the discomfort that is felt in localized parts of the body. As the results of this study show, PD and PPD are slightly deviating from 20% by of 5 and 10.25 points respectively.

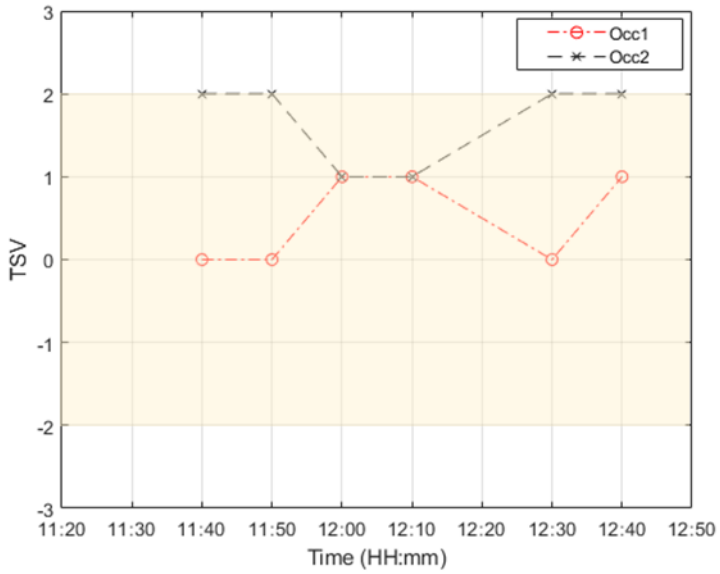

Figure 10 TSVs cast and the acceptable comfort range

4. CONCLUSION

In conclusion, this study aimed to assess the thermal comfort in a test room which has Trombe wall for heating under North Cyprus weather conditions. It was identified that there are limited studies examining the thermal comfort of spaces utilizing conventional Trombe walls and to the knowledge of the authors there is no study focusing on the real votes of the occupants for comfort evaluation of Trombe wall installed buildings. Therefore, this study filled that research gap by employing a survey of actual occupants to evaluate the thermal comfort.

The methodology involved monitoring environmental variables, such as inside and outside air and Trombe wall temperatures. The survey included six participants who provided their selections on general thermal sensation, local thermal sensation, and satisfaction level. The results showed that the fluctuations in the environmental factors were negligible, indicating a steady-state condition in the test room.

The analysis of thermal comfort conditions revealed that the majority of the votes for general thermal sensation were concentrated in the warm region of the thermal sensation scale, with slightly warm thermal sensations being the most common. The correlation between general thermal sensation and thermal sensation at the head and feet regions indicated a moderate positive correlation for the head region and a strong positive correlation for the feet region. This suggests that occupants' overall thermal comfort perception is more bounded by the thermal conditions experienced at their feet region.

The calculation of the percentage of dissatisfied (PD) based on direct votes cast by the occupants showed a high standard deviation, indicating different sensitivities and perceptions of thermal comfort. The predicted percentage of dissatisfied (PPD) was estimated based on the thermal sensation votes and showed consistency with PD.

Overall, this study provided valuable insights into the thermal comfort conditions offered by a Trombe wall in the specific test room under North Cyprus climate conditions. The findings contribute to the understanding of the performance and potential benefits of Trombe walls in terms of thermal comfort. However, due to the limited sample size in this study, further research with a larger sample size is recommended to obtain more robust and representative results. Additionally, future studies could explore the impact of other parameters, such as clothing insulation and air velocity, on thermal comfort in spaces utilizing Trombe walls.

5. REFERENCES

ASHRAE (2017): Standard 55, Thermal Environmental Conditions for Human Occupancy, Atlanta.

Błotny, J. and Nemś, M. (2019) 'Analysis of the Impact of the Construction of a Trombe Wall on the Thermal Comfort in a Building Located in Wrocław, Poland', Atmosphere, vol. 10, no. 12, p. 761 [Online]. DOI: 10.3390/atmos10120761.

Butcher, K. and Craig, B. (2015) Environmental design: CIBSE guide A/editors: Ken Butcher, Bonnie Craig, London, Chartered Institution of Building Services Engineers.

Duffie, J. A. and Beckman, W. A. (2013) Solar engineering of thermal processes, Hoboken, New Jersey, Wiley.

Fanger, P. O. (1970) 'Thermal comfort. Analysis and applications in environmental engineering, Thermal comfort. Analysis and applications in environmental engineering.

Hu, Z., He, W., Ji, J. and Zhang, S. (2017) 'A review on the application of Trombe wall system in buildings', Renewable and Sustainable Energy Reviews, vol. 70, pp. 976–987 [Online]. DOI: 10.1016/j.rser.2016.12.003.

IEA (2022) Heating – Analysis - IEA [Online]. Available at https://www.iea.org/reports/heating.

Li, J., Zhang, Y., Zhu, Z., Zhu, J., Luo, J., Peng, F. and Sun, X. (2022) 'Thermal comfort in a building with Trombe wall integrated with phase change materials in hot summer and cold winter region without air conditioning', Energy and Built Environment [Online]. DOI: 10.1016/j.enbenv.2022.07.007.

Lin, Y., Zhong, S., Yang, W., Hao, X. and Li, C.-Q. (2021) 'Multi-objective design optimization on building integrated photovoltaic with Trombe wall and phase change material based on life cycle cost and thermal comfort', Sustainable Energy Technologies and Assessments, vol. 46, p. 101277 [Online]. DOI: 10.1016/j.seta.2021.101277.

Özdenefe, M., Atikol, U. and Rezaei, M. (2018) 'Trombe wall size-determination based on economic and thermal comfort viability', Solar Energy, vol. 174, pp. 359–372 [Online]. DOI: 10.1016/j.solener.2018.09.033.

Rhee, K.-N. and Kim, K. W. (2015) 'A 50 year review of basic and applied research in radiant heating and cooling systems for the built environment', Building and Environment, vol. 91, pp. 166–190 [Online]. DOI: 10.1016/j.buildenv.2015.03.040.

Sornek, K., Papis-Frączek, K., Calise, F., Cappiello, F. L. and Vicidomini, M. (2023) 'A Review of Experimental and Numerical Analyses of Solar Thermal Walls', Energies, vol. 16, no. 7, p. 3102 [Online]. DOI: 10.3390/en16073102.

Xiao, L., Qin, L.-L. and Wu, S.-Y. (2022) 'Proposal and application of comprehensive thermal comfort evaluation model in heating seasons for buildings with solar Trombe wall', Applied Thermal Engineering, vol. 213, p. 118774 [Online]. DOI: 10.1016/j.applthermaleng.2022.118774.

Xiao, L., Qin, L.-L. and Wu, S.-Y. (2023) 'Effect of PV-Trombe wall in the multi-storey building on standard effective temperature (SET)-based indoor thermal comfort', Energy, vol. 263, p. 125702 [Online]. DOI: 10.1016/j.energy.2022.125702.

Xiong, Q., Alshehri, H. M., Monfaredi, R., Tayebi, T., Majdoub, F., Hajjar, A., Delpisheh, M. and Izadi, M. (2022) 'Application of phase change material in improving trombe wall efficiency: An up-to-date and comprehensive overview', Energy and Buildings, vol. 258, p. 111824 [Online]. DOI: 10.1016/j.enbuild.2021.111824.

#31: Minimizing the performance gap using longitudinal monitoring of environmental measurements: a case of a residential building

An Empirical Study of a Residential Building

Shireen ALQADI[1], Amira ELNOKALY[2]

[1] Birzeit University, Birzeit, Ramallah, Palestine, shalqade@birzeit.edu
[2] University of Lincoln, Brayford Pool, Lincoln LN6 7TS, UK, aelnokaly@lincoln.ac.uk

Abstract: Energy consumption is steadily rising globally, especially in buildings. When moving towards a greener approach in constructing new buildings, it is essential to target the existing building stock through retrofitting. Dynamic Building Energy Simulation (DBES) modelling helps designers and professionals estimate the potential amount of energy saving in buildings. Although DBES plays a major role in quantifying energy demand, a performance gap, defined as the discrepancy between calculated and actual energy savings, remains a concern for professionals. To overcome this performance gap, calibrating DBES models is a prerequisite before using the model to estimate energy savings through specific measures. The commonly used calibration method is a statistical one that depends on indices related to energy bills. As the energy crisis worsens, users are shifting towards cheaper energy sources and using a combination of energy sources to meet their needs. Hence, these statistical indices that depend on energy bills are not easily applied in many cases, especially in countries where a combination of fuels is sometimes used for heating, cooking, and heating water. In this paper, the heating load in an apartment in Hebron, Palestine, was modelled as an internal gain. Subsequently, the model was calibrated using internal environment measurements (internal temperature) taken during two monitoring phases for an apartment in Hebron, Palestine. A validation method for an apartment was presented using internal temperature data from the monitoring phases. The results demonstrate that the model was calibrated and is a reliable tool for optimisation.

Keywords: (DBPS) models; Calibration; performance gap; statistical indices; energy saving

1. INTRODUCTION

Energy consumption worldwide had shown great increase recently (Ahmadian et al, 2022; Cao et al., 2016; Lombard et al., 2007). The International Energy Agency has reported that the energy consumption has increased with an annual average of 1.8% to 2% between the years of 1984 to 2004, forming an increase of energy consumption by 49% and an increase in CO2 emissions by 43% during the reported period (Lombard et al., 2007; Ahmadian et al., 2023). This is accelerated in developing countries where they face several additional challenges in terms of energy like poor infrastructure, waste management and fuel poverty (Oyedele et al., 2013; Alqadi et al, 2017; Alqadi et al, 2023). These challenges are more urgent in areas with political instability. In addition, urban growth and higher standards of living have raised the per capita energy consumption by 8.6% between 2007 and 2014 (PCBS, 2017). This was coupled with the absence of sustainable consumption of energy (Alqadi et al., 2018). One of the main reasons behind the lack of sustainable consumption in the housing sector is the poor quality of housing in terms of thermal insulation and performance (Ahmadian, 2021; Alqadi et al, 2022). The combination of these challenges has several implications for Palestinians. Lack of access to safe and affordable energy in the housing sector affects users' health, safety, wellbeing and decreases the chances of achieving thermal comfort (Alqadi et al., 2017; Alqadi et al., 2018).

Using renewable energy can help the less privileged to have access to safe, secured, and affordable source of energy (Alqadi and Alrjoub, 2011). Energy retrofit of the existing building stock can play a major role in optimizing the energy consumed on the national level (Elnokaly and Elseragy, 2013; Lazzeroni, 2017). Shifting towards renewable energy should be proceeded by optimizing the energy consumed in buildings which can be performed using Dynamic Building Performance Simulation (DBPS) (Clarke, 2015). To decrease the discrepancy between the real building and the simulated model, a calibration process is needed (Cacabelos et al., 2017; Mahaya et al., 2022). In this paper, an apartment is calibrated opposite to actual monitored temperature in Hebron, Palestine.

2. PERFORMANCE GAP

The term "Performance gap" defines the difference between the predicted and the actual energy consumption in buildings (Norford et al., 1994; de Wilde, 2014; van Dronkelaar et al., 2016; Khoury et al., 2017; Aly et al., 2017; Menezes et al., 2012; Bordass et al., 2001). Research has shown that performance gap can vary 6-140% (Johnston et al., 2015; Powell et al., 2015; Aly et al., 2017). The gap was spotted in new and retrofitted buildings (Sunikka-Blank et al., 2012; Loucari et al., 2016; Benzar et al., 2020; Alqadi et al., 2020). The causes behind the performance gap vary and can go back to different stages of the building life (Powell et al., 2015; Motuzienė et al., 2021). Unlike the synergetic design process, the traditional linear design process starting from the architect, followed by the engineer (Civil, mechanical and electrical) neglects the interdependent relation between the different roles in this process, especially in terms of energy consumption (Cantin et al., 2012; Alqadi et al., 2019). In many cases architects make significant assumption due to insufficient data during the design and energy simulation phase (Ayoub and Elseragy, 2018; Chong et al., 2021; Ahmed et al., 2016; Zhan et al., 2022).

As the physical qualities and performance of the building materials in the lab is different from the site, energy performance may also vary from what is expected (Burman et al., 2014). In other cases, building materials can be substituted while construction with others with different specifications due to the complex and specific procurement processes which can cause discrepancy between actual and theoretical performance (Burman et al., 2014). Therefore, the mal construction of the building and not following the specification can largely affect the buildings' performance (Newsham et al., 2009). Occupants' behaviour effect on the energy performance of buildings has been addressed extensively in the literature (Kobach et al., 2022; Neu et al., 2015; Martincigh et al., 2016). The behaviour of the occupants has substantial impacts on the energy performance of buildings; however, its precise impact is not determined (Niu et al., 2015). Adding to this, falling to predict the energy savings due to energy efficiency measurements a term that describes a phenomenon of increasing the energy efficiency leads to more energy consumption which is known by the "prebound effect' (Sunikka-Blank et al., 2012). Finally, buildings are constructed to stay for decades, and under the climate change scenarios it is hard to predict how to model the thermal performance of the buildings in the future (Alqadi, et al., 2017; Elnokaly, et al., 2019; Alqadi et al., 2023).

3. CALIBRATION AND VALIDATION OF THE SIMULATION MODELS

Several studies (Karlsson et al., 2007; Scofield, 2009) have reported discrepancies of up to 100% differences between DBPS model-predicted and the actual monitored data. To improve the accuracy of the DBPS model results to determine meaningful energy conservation measures, calibration is needed (Coakley et al., 2015; Alqadi et al., 2022). The main goal is to approximate the DBPS model results to the real data as closely as possible (Raftery et al., 2011). Since uncertainty is unavoidable in (BDES) models, uncertainty management is essential (Chong et al., 2018). Four main categories of calibration methodologies were presented by Reddy et al. (2007). These are manual calibration, graphical-based calibration, Calibration based on special tests and Automated calibration. Global organizations such as ASHRAE, IPMVP, and FEMP have set their own standards for two of the previous measures of the baseline model, which are as follows for the hourly criteria (%) in Table 1.

Table 3: Protocol for calibration of DBPS models

Standard	MBE%	CV(RMSE)%	Source
ASHRAE Guideline 14	10	30	(ASHREA.2002)
IPMVP	5	20	(EVO,2007)
FEMP	10	30	(US DOE,2008)

4. THE BUILDING'S CHARACTERISTICS AND SYSTEMS USED

The case study of the floor plan depicted in Figure 1 is a flat that has a floor area of 120m2 and a ceiling height of 2.8m. It is occupied by a couple. The building is seven years old and consist of eight floors, including storage on the ground floor. Each floor contains five flats of different sizes. The flat in question is on the fourth floor and comprises two bedrooms, a living room, and a salon, a kitchen, one bathroom, one WC in addition to a balcony. It is oriented to the north-west. The external walls are made from concrete, concrete hollow blocks and stone, but there is no insulation. The windows have aluminium profiles and are single-glazed. Most of the windows are 1.6*1.2 m2. All the windows have external shutters and internal curtains. The apartment is naturally ventilated all day during summer. During winter, it is naturally ventilated for certain hours during the day and occupied spaces are heated during the day. A combination of energy sources is used to heat the house i.e., electricity and LPG.

5. METHODOLOGY

The research depends on a mixed method approach: quantitative data (environmental measurements) and qualitative data, the data was collected using a combination of method which are:

5.1. Semi-structured interview with the household

To understand the users' behaviour, extensive interviews were performed, concerning the behaviour of the household. The questions concentrated on the occupancy schedule, the adaptive measures that the users' used such as opening and closing windows, the patterns of using heating and cooling systems. The collected data was used to determine the occupancy and the macro flow profiles.

5.2. Environmental measurement and longitudinal monitoring

Longitudinal monitoring was used to collect two sets of data to evaluate the performance of the building. Two calibrated Extech RH10 loggers (±0.1°C) were used as part of the monitoring phase, one and one outside the building (Extech, 2018). The data loggers encompassed a sensor part and a record system that saves the readings. The Extech RH10 loggers recorded the indoor air temperatures and relative humidity (RH) in the living rooms, as well as outdoor air temperature and (RH). The data loggers collected the data every 5 minutes to increase the resolution of the data to be used for calibration later. The longitudinal approach in this kind of research is highly recommended to spread the data across time (Azizi et al., 2015; Bros-Williamson et al., 2016). The longitudinal covered two periods, the first reading set was collected between 12th October and 1st November 2017, and the second set was collected between 28th January and 24th February 2018. After each monitoring period, the data loggers were collected, and the monitored data downloaded into an Excel sheet.

5.3. Developing a weather file for Hebron using metrological data

Weather files are essential for (DBPS) to predict the energy demand (Jentsch et al., 2008). Weather files are defined as samples of real weather data taken from a certain period that have similar average weather parameters to the actual, but it is not the average of weather parameters over a certain period (Tiwari, 2000). The simulation weather files can be sourced from various places like Weather-shift, CIBSE 2016 Weather Files, Meteonorm, Australia Weather Files, Agrément South Africa or EnergyPlus Weather Files (EPW) (IESVE, 2018). The weather files that are available are specific for certain cities. The closest available weather file to Hebron was Jerusalem. However, the weather in Jerusalem slightly differs than in Hebron. Hence, it was important to create a weather file that is specific for Hebron. The weather file that represents the exact weather conditions of the context is needed and will decrease the gap that occurs due to the variation between the weather between the two cities. Accordingly, weather data for the period between March 2017 and February 2018 was obtained for Hebron from the Palestinian Metrological Department on the 20th/March/2018 (Palestine Meteorological Deportment, 2018). The main goal was to create a weather file based on formal measured data representing the actual weather in the context during the monitoring periods that cover the two periods of monitoring.

6. CREATING DYNAMIC BUILDING PERFORMANCE SIMULATION (DBPS) MODEL

For this research, an IESVE model was developed. The modelling process includes creating the building geometry and embedding the physical characteristics of the building envelope. Then the profiles of heating, cooling, lighting and appliances was added. The occupancy profiles of the users were set based on the data gathered through the interviews. The same was done for the opening and closing of the windows (Macroflow).

6.1. Creating the geometric model

Using the Revit software, the buildings' geometry was considered in relation to the surrounding buildings, as seen in Figure 2. The model was then exported in gbXML (Green Building XML) format to IESVE. Internal spaces were defined as rooms with all the physical elements of the building were defined such as the shading devices. Since the urban context has a major impact on the buildings' energy performance, surrounding buildings were also modelled to reflect a more accurate performance of the building. The model was assigned to the actual location of the building in Hebron with a latitude longitude coordinate of 31°31'45.66"N, 35°5'37.68"E. The developed weather file was allocated for the model so that it performs under the same climatic conditions of the real world.

Figure 1 Plan of the apartment

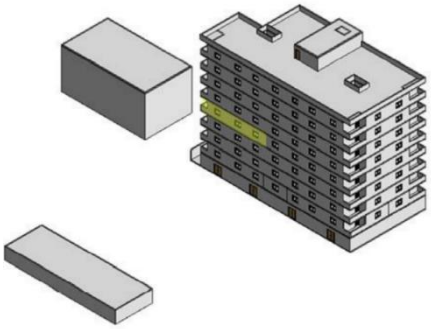

Figure 2 Building geometry in Revit

6.2 Assigning building materials to the model

Depending on the data from the site visits and the interviews, the building materials of the building envelope were assigned. The materials' characteristics were assigned based on the interviews and local materials specifications in the Building Energy Efficiency Code (Ministry of Local Government,2004). Since there were no guidelines before 2004 and no specifications were available, the most compatible guidelines with the modelled building were used. The thermal characteristics of the materials that were used in the modelling process are illustrated in Table 2.

Table 2: Building's components specifications

Building component	Configuration (cm)	U value (W/m^2k)	Thermal mass ($Kg/m^2. K$)
External walls	Stone 7, concrete 15, concrete hollow blocks 7, plaster 1.5	2	143.8
Ground	Reinforced concrete20, concrete baking8, sand 5, mortar 2, concrete tile 2	1.5	175.7
Roof	Waterproof membrane 0.3, concrete baking 8, bricks and ribs 17, plaster 1.5	1.7	108.4
Ceiling	Concrete tiles 2.5, mortar2.0, sand 2.0, concrete baking 8, bricks and ribs 12, cement plaster 1.5	2.4	146.7
Internal walls	Plaster1.5, concrete hollow blocks 7, plaster1.5	2.7	74.6
External doors	Iron 0.5, cavity 1.5, iron 0.5	5.7	---
Glazing (g) value 0.5, transmittance (T) 0.7	Single glazing		

6.3 Assigning the heating and cooling systems

In the IESVE the ApacheSim is a dynamic thermal simulation program that applied energy physics and mathematical modelling (IESVE, 2015). For this modelling process, assigning the thermal conditions for the ApacheSim in the IESVE includes defining the heating and cooling systems, internal gains and air changes ratios. Since there is a discrepancy between occupancy and the (HC) profiles of the rooms, a separate thermal condition was defined for each of them. When defining the rooms' conditions, it was not possible to assign the individual heaters and fans used by the households in the

IESVE models. After consulting the IESVE support team, they advised to add the heating systems as internal gains and the cooling load as a heat loss instead (IESVE, 2018). For this research, the (HC) loads were termed miscellaneous gains. The (HC) loads were calculated based on the voltage of systems and usage period. In addition, other internal loads were assigned for each room based on data from the physical survey and the semi-structured interviews. These internal gains included the lighting, people and appliances. At steady-state conditions, and based on the conservation of energy principle, the total heat output is equal to the total power input (Evren et al., 2016). Although the case here are not in steady-state conditions, the researchers assumed that the input energy is equal to the output. Moreover, the efficiency of the system is beyond the scope of this research and hence the output was defined based on watt-hour calculations. These were obtained from the system's manuals and the duration of usage as expressed by the households. The air exchange rate that was assumed by this study was the infiltration of 3.5 ach since the air exchange due to natural ventilation was assigned in the Macro-flow section. This value was assigned following consultation with the IESVE support team (IESVE, 2018).

6.4 Modelling users' behaviour

The occupancy patterns are generally affected by the number of users and the lifestyles which defines the time a person wakes up in the morning, the time spent at home and the time the person goes to bed (Ren et al., 2013) and the way that occupants use the different systems, opening and closing windows, and other energy related behaviour (Ren et al., 2013). According to Aerts et al. (2014), there are three realistic possible occupancy states: (1) at home and awake (active); (2) sleeping (non-active); or (3) absent. Based on that, Figure 3 illustrates the pattern of using the building. Depending on the data gathered through the interviews the typical day occupancy profile was developed as seen in Figure 3. The apartment is typically unoccupied during the day as the occupants are at work. The household spends the evening in the kitchen and the living room, and at night one bedroom is occupied. The daily profile of each of these rooms is shown in Figure 4.

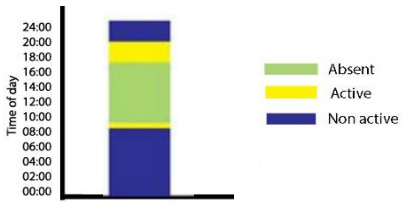

Figure 3 Occupancy profiles in the building

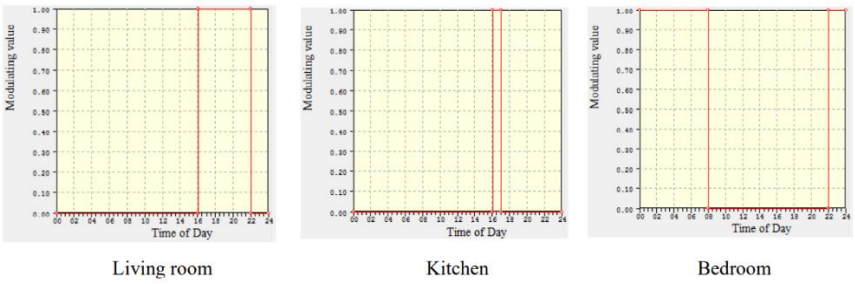

Figure 4 The occupancy profiles for the rooms

6.5 Assigning the heating, cooling, and internal gains profiles

The heating and cooling systems were assigned based on the interviews. The heaters were on during between the (15th November-30th April) and were off during the rest of the year. The heating systems specification were assigned according to the producer's manual. For cooling, fan is used, and the cooling pattern was assigned as a cooling profile as the fan worked for two hours between (15th June-15th August) and was off during the rest of the year. Internal gains were specified according to actual pattern of use, while the maximum sensible gain from the users was assigned as 90W/person and the minimum latent gain is 60W/person.

6.6 Assigning the window opening profiles (Macroflow)

There were different daily patterns for opening the different types of the windows, which were driven by certain reasons which are: thermal adaptation, privacy, and for preventing pollution. Typically, most window openings occur in the morning during summer and winter. In summer, most of the windows are opened 24 hours a day, facilitating cross-ventilation in both cases while light curtains are used to enhance privacy. In winter, while cooking in the kitchen during afternoon, the number of open windows is the highest to increase the cross ventilation, then decreases in the afternoon. To Prevent heat loss all windows are closed during evening and night. The windows opening and closing profiles were assigned in the IESVE using the Macroflow reflecting the variation of usage between summer and winter.

6.7 Weather file validation

To validate the weather file that was developed earlier, annual weather files for Hebron were downloaded from https://www.wunderground.com/wundermap. The two annual weather files covered the years 2017-18. The weather file developed earlier used data from 1st March 2017-31st December 2017 and from 1stJanuary to 28th February 2018. The developed weather file was examined against the downloaded weather file for the compatible periods and was very close to the downloaded weather files.

7. CALIBRATION

Since more than one energy source is used for heating, it was not useful to collect the energy bills (Alqadi et al., 2017). No energy meter readings were involved so the calibration of the models was based on the internal monitored temperature. This approach was used in other similar research where energy readings were not available (Paliouras et al., 2015; Saleh et al., 2018). There are no specific standards for calibration using the measured temperature. Research-based on calibrating buildings' temperature behaviour relies on the same energy validation protocols, rather than on specific temperature ones (Saleh et al., 2018). The uncertainty in the DBPS models was classified into four main sources by de Wit and Augenbroe (2002): (i) specification uncertainty, (ii) modelling uncertainty (simplification of complex physical processes), (iii) numerical uncertainty (errors during simulation process) and (iv) scenario uncertainty (related to external conditions). As the researcher has no control over the modelling and numerical uncertainties, the goal was to decrease the first and the fourth effect on the simulation results. During the interviews, the household described their typical day in both summer and winter. Using the obtained data, the heating and cooling loads, occupancy profiles, heating and cooling and natural ventilation and the other system profiles were developed and input. In addition, local weather parameters were collected from Hebron weather station and a weather file was developed to reflect the actual climatic conditions that affected the building performance during the monitoring phase. Hence, this source of uncertainty was minimized.

The other source of uncertainty was the specification uncertainty. Regarding the external input data (i.e., assigned by the user and not embedded in the software), Macdonald (2002) suggested three distinct methods that can be used for calibration: changing one parameter at a time; changing one set of parameters at a time; or changing all the parameters at the same time. The last method is known as the Monte Carlo method (Macdonald, 2002). The manual calibration approach was adopted, and one parameter was changed at a time, which is simple and valid for calibration (Kheiri, 2018; Saleh et al., 2018). For calibrating the models, the U value of the external walls and the infiltration rate was used to calibrate the models. Although there are a lot of other factors that can affect the simulation results like the solar radiation, U and g values of the glazing, the colour of the envelope. Three rounds of calibration were performed for the apartment, based on the monitored internal temperature readings in the two monitoring periods (12th Oct-1st Nov and 28th Jan-10th Feb). The building material values were inputted using the local Energy Efficient Building Code (Ministry of Local Government, 2004). In the first round, all schedules are as expressed by the users or observed by the researcher. In the second round, the envelope (external walls U-value) was increased, by increasing the conductivity rate, using the maximum value limits presented in the local Energy Efficient Building Code (Ministry of Local Government, 2004). Table 3 shows the external walls' conductivity and the thermal transmittance (U value) parameters that were changed in the second round of simulation. In the third round, the infiltration rate was increased from 3.5 to 3.7 ach. Figures 5 and 6 illustrate the three simulation rounds vs. the monitored temperature during the two monitored periods. The calibration metrics are presented in Table 4.

Table 3: The external wall thermal characteristics used in calibration

		Stone	Concrete	Concrete blocks	Plaster
Conductivity	Old value	1.3	1.0	0.7	0.25
	New value	2.2	1.2	1.0	0.75
U value (W/m^2. k)	Old value	1.53			
	New value	2.01			
Thermal mass (J/K)	Old value	790			
	New value	812			

Table 4: Characteristics of the three calibration rounds including NMBE, RMSE and CVRMSE

		Calibration characteristics		
		Round 1 (red)	*Round 2 (green)*	*Round 3 (blue)*
		HL 1.6 kWh *CL 0.014 kWh* *U value 1.53* *Infiltration rate 3.5 ach*	*HL 1.6 kWh* *CL 0.014 kWh* *U value 2.01* *Infiltration rate 3.5 ach*	*HL 1.6 kWh* *CL 0.014 kWh* *U value 2.01* *Infiltration rate 3.7 ach*
Guestroom (n= 4030)	*NMBE*	1.215821	-3.38083	-3.20197
	RMSE	2.01907	2.387962	2.299965
	CV(RMS)	15.59174	18.44041	17.76087
Guestroom (n= 2894)	*NMBE*	4.230516	0.219816	0.18785
	RMSE	1.439116	2.236973	1.911669
	CV(RMS)	7.607527	11.8252	10.10556
Weighted	*NMBE*	2.475863	-1.87588	-1.78514
	RMSE	0.601857	2.324854	2.13767
	CV(RMSE)	12.25461	15.67547	14.56121

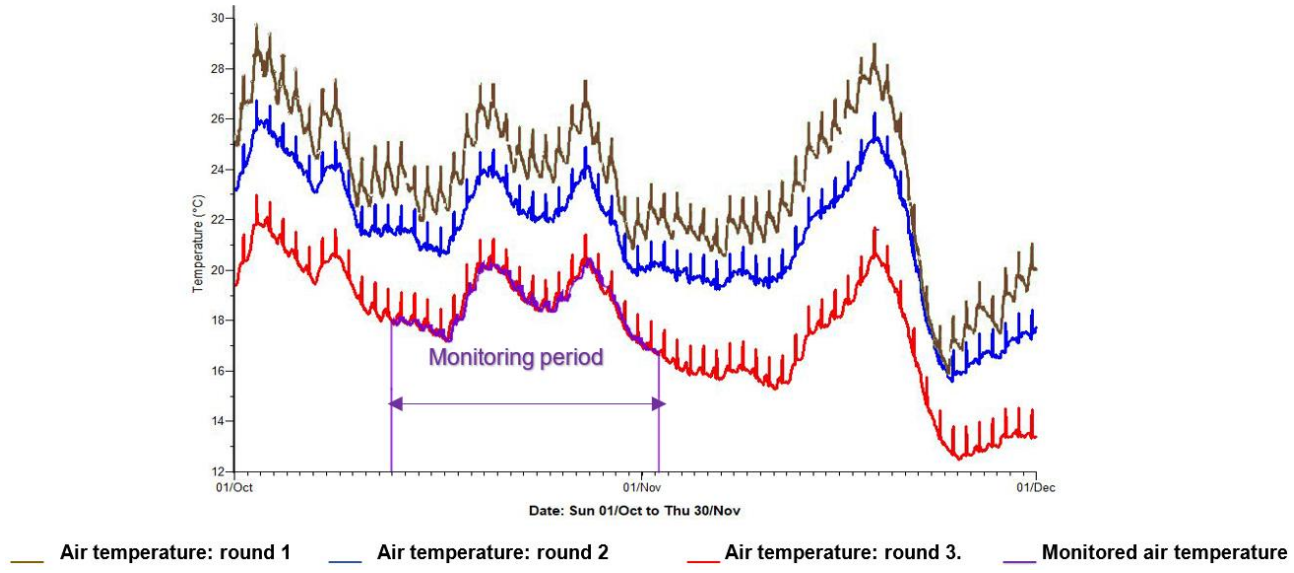

Figure 5 Simulation results of the three rounds and the monitored temperature in the guestroom for the period 12th October-1st November/2017

In the first round, simulated temperature was higher during the two periods of monitoring. In round two, the U-value of the external walls was increased from 1.53 to 2.01. Figures 5 and 6 show that the second the temperature simulation was lower and closer to the monitored data. In the third round, the infiltration rate increased from 3.5 to 3.7 ach; the simulated temperature in the guestroom shown good statistical values; and the number of matching values increased. The weighted metrics of the two rooms are within acceptable ranges: 14.56% for CVRMSE and -1.78% for NMBE, so the model can be considered calibrated. Figures 7 and 8 illustrate the third-round results with the monitored.

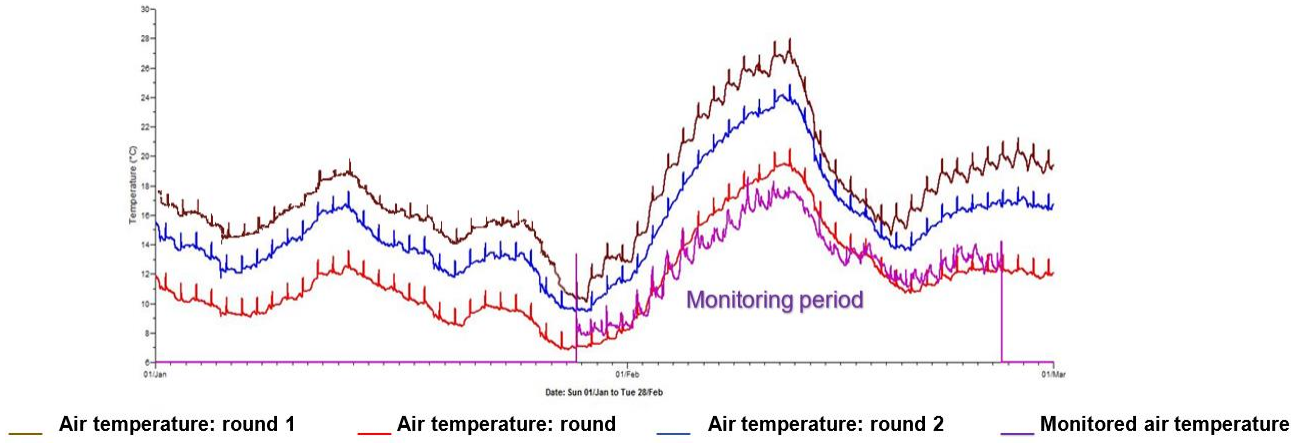

Figure 6 Simulation results of the three rounds and the monitored temperature in the guestroom for the period 28th January-24th February/2017

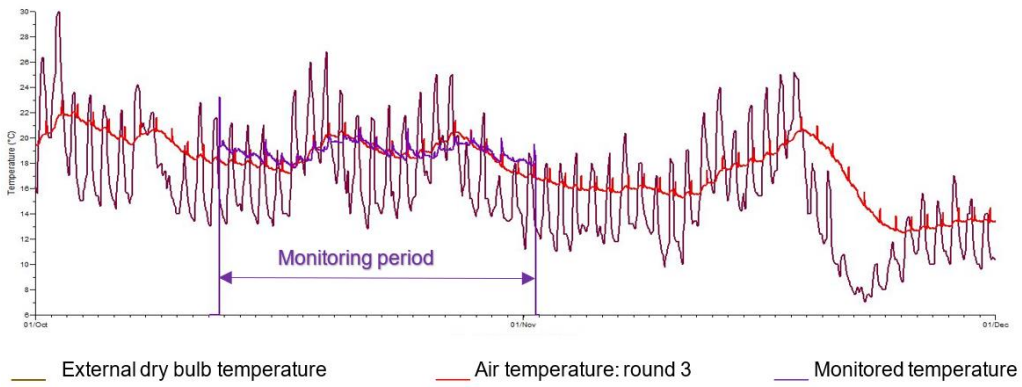

Figure 7 Simulation results of the third round, the monitored temperature in the guestroom and the external dry bulb temperature between 12th October- 1st November 2017

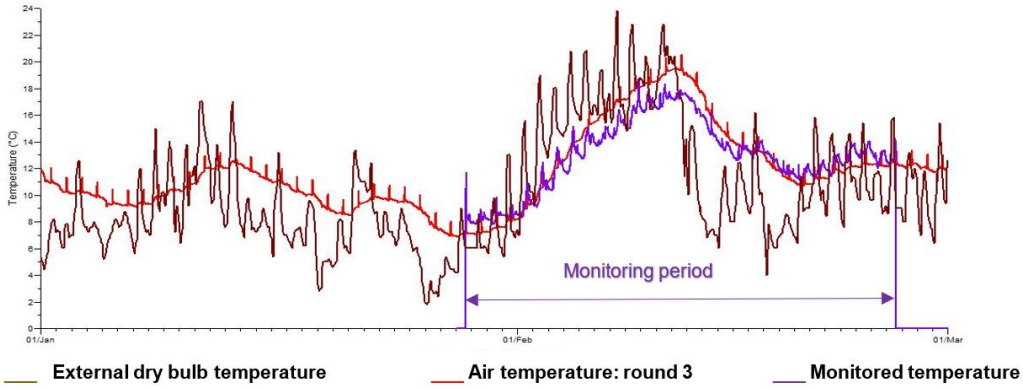

Figure 8 Simulation results of the third round, the monitored temperature in the guestroom and the external dry bulb temperature between 28th January-24th February

The temperature was considerably lower than some of the night dry bulb values. Between the 10th and the 19th of February, the temperature was considerably higher than the dry bulb temperature and the simulated temperature, whereas between the 20th and the 27th of February, the monitored temperature was higher than the simulated and external dry bulb temperature. In both monitoring periods, peak simulated temperatures were higher than the monitored values. Figures 7 and 8 illustrate the third-round results with the monitored.

8. CONCLUSION

The optimisation of energy consumption in the existing building stock is a crucial objective at the national level, and Data-Based Predictive Simulation (DBPS) models play a vital role in predicting energy demand post retrofit. However, these models often encounter the challenge of a performance gap. The study presented in this paper emphasised that calibrating DBPS models is essential to enhance the accuracy of estimated energy savings. Existing standardised statistical indices, typically reliant on energy bills, serve as international reference criteria for validating calibrated models. However, in specific contexts where a mix of fuels is utilized, and submetering systems are absent, calibrating models based on energy bills becomes impractical. In this study, a validation method was presented for a typical apartment design in Palestine, reflecting the prototype standard prevalent in the region. The investigation focused on internal temperature and incorporating users' behavioural aspects during model development.

The results demonstrated successful model calibration, establishing its potential for optimisation in subsequent stages and thereby mitigating the performance gap. The contribution of this paper to the field lies in providing a calibrated model tailored to this region, addressing a significant research gap. To generalise and extend the applicability of this method to various locations, further cases must undergo calibration utilizing internal environment measurements. Additionally, it is imperative to develop statistical indices tailored for DBPS models based on internal environment measurements, enabling their utilisation in scenarios where energy bill calibration is not viable. Lastly, future research should encompass the potential performance gap resulting from climate change and its effects on building performance, shaping policy and regulations to account for these evolving dynamics."

9. REFERENCES

Ahmadian, E., Bingham, C., Elnokaly, A., Sodagar, B. and Verhaert, I. (2022) Impact of Climate Change and Technological Innovation on the Energy Performance and Built form of Future Cities. Energies, 15 (22). ISSN 1996-1073

Ahmadian, E., Elnokaly, A., Sodagar, B. and Verhaert, I. (2023) Impact of Climate on Building Energy Performance, Urban Built Form and Urban Geometry. In: Sustainability in Energy and Buildings 2022. SEB 2022. Smart Innovation, Systems and Technologies. Smart Innovation, Systems and Technologies, 336. Springer, Singapore, pp. 1-11. ISBN 9789811987687, 9789811987694

Ahmadian, E., Sodagar, B., Bingham, C., Elnokaly, A. and Mills, G. (2021) Effect of urban built form and density on building energy performance in temperate climates. Energy and Buildings, 236. p. 110762. ISSN 0378-7788

Alqadi, S. and Alrjoub, M. The Economics of Solar Energy, Solar Energy in the Palestinian Schools. (2011), In: The 4th International Energy Conference, Engineers Association – Jerusalem Center. Ramallah: Engineers Association Jerusalem Branch

Alqadi, S. B., Elnokaly, A. and Sodagar, B., Predicting the energy performance of buildings under present and future climate scenarios: lessons learnt, (2017) In: First International Conference on Climate Change (ICCCP), 5-8 May 2017, Palestine.

Alqadi, S., Sodagar, B. and Elnokaly, A. (2018) Estimating the heating energy consumption of the residential buildings in Hebron, Palestine. Journal of Cleaner Production, 196. pp. 1292-1305. ISSN 0959-6526

Alqadi, S., Elnokaly, A. and Sodagar, B. (2019) The role of the benchmarking tools in increasing the collective awareness of energy consumption at the domestic sector. In: The Second International Conference on Civil Engineering (2nd ICCE-P) is organized by the Engineers Association - Jerusalem Center, Palestine (EA-JCP)., 25-26 November 2019, Bethlehem, Palestine.

Alqadi, S., Elnokaly, A. and Sodagar, B. (2020) Personalised Thermal Comfort to Reduce the Performance Gap in Residential Buildings: A Method Developed in a Mediterranean Climate. In: Proceedings of the 35th International Conference on Passive and Low Energy Architecture, 1-3 September 2020, Spain, University of A Coruña.

Alqadi, S., Elnokaly, A. and Sodagar, B. (2022) Calibrating Building Thermal Simulation Model Using Indoor Environmental Measurements. In: Zero Energy Mass Custom Home 2021 International Conference (ZEMCH 2021), 26th - 28th October 2021.

Alqadi, S., Elnokaly, A., Abureesh, N., Rjoub, S.; and Alnatsheh, Z. (2023) Energy demand reduction in two case studies based on the same residential studio: Mediterranean and Hot Climates. WILL CITIES SURVIVE? The future of sustainable buildings and urbanism in the age of emergency. BOOK OF PROCEEDINGS VOL 2 PLEA 2023, 2. pp. 802-806. ISSN 9789561430693

Aly, A., Elnokaly, A. and Mills, G. (2017) Mind the gap: Methodology discussion of the extraction and analysis of pilot phase data to generate multi-configuration household behavioural profiles. Proceedings of 33rd PLEA International Conference Design to Thrive. Volume I, 1. pp. 353-360.

ASHRAE, ASHRAE Guideline 14-2002: Measurement of Energy Demand and Savings, (2002) Atlanta, GA: ASHRAE.

Ayoub, M. and Elseragy, A. (2018) Parameterization of traditional domed-roofs insolation in hot-arid climates in Aswan, Egypt. Energy & Environment, 29 (1). pp. 109-130. ISSN 0958-305X

Azizi, N., Wilkinson, S. and Fassman, E., Do occupants in green buildings practice better energy saving behaviour in computer usage than occupants in conventional buildings? (2015), Journal of Green Building, 10(4) 178-193.

Benzar, B.-E., Park, M., Lee, H.-S., Yoon, I., & Cho, J. Determining retrofit technologies for building energy performance, (2020). Journal of Asian Architecture and Building Engineering, 19(4), 367–383. https://doi.org/10.1080/13467581.2020.1748037

Bordass, B., Cohen, M. Standeven, R., A. Leaman, Assessing building performance in use 3: Energy performance of the probe buildings, (2001), Building Research & Information, vol. 29, no. 2, pp. 114–128, Mar.

Bros-Williamson, J., Garnier, C. and Currie, J. A longitudinal building fabric and energy performance analysis of two homes built to different energy principles, (2016), Energy and Buildings, 130, 578-591.

Burman, E., Mumovic, D., & Kimpian, J. Towards measurement and verification of energy performance under the framework of the European directive for energy performance of buildings. (2014), Energy, 77, 153–163. https://doi.org/10.1016/j.energy.2014.05.102

Cacabelos, A., Eguía, P., Febrero, L. and Granada, E., (2017) Development of a new multi-stage building energy model calibration methodology and validation in a public library, Energy and Buildings, 146, 182-199.

Cantin, R., Kindinis, A., & Michel, P., New approaches for overcoming the complexity of future buildings impacted by new energy constraints. (2012), Futures, 44(8), 735–745. https://doi.org/10.1016/j.futures.2012.05.001

Chong, A., & Menberg, K. (2018) Guidelines for the Bayesian calibration of building energy models. (2018), Energy and Buildings, 174, 527–547. https://doi.org/10.1016/j.enbuild.2018.06.028

Chong, A., Augenbroe, G., & Yan, D., (2021) Occupancy data at different spatial resolutions: Building energy performance and model calibration., (2021). Applied Energy, 286, 116492. https://doi.org/10.1016/j.apenergy.2021.116492

Cimbala, J., Basic Statistics, Penn State University, (2011) Available from https://www.mne.psu.edu/cimbala/me345web_Fall_2014/Lectures/Basic_Statistic s.pdf [accessed 19 October 2018].

Clarke, J., A vision for building performance simulation: a position paper prepared on behalf of the IBPSA Board., (2015), Journal of Building Performance Simulation, 8(2) 39-43.

Coakley, D., Raftery, P., & Keane, M. (2014). A review of methods to match building energy simulation models to measured data. Renewable and sustainable energy reviews, 37, 123-141.

Johnston, D., Miles-Shenton, D. and Farmer, D. (2015) Quantifying the domestic building fabric performance gap ‘, Building services Engineering research and Technology, vol. 36, no. 5, pp. 614–627, Feb.

de Wilde, P., (2014) The gap between predicted and measured energy performance of buildings: A framework for investigation, Automation in Construction, vol. 41, pp. 40– 49, May.

de Wit, S. and Augenbroe, G., (2002) Analysis of uncertainty in building design evaluations and its implications Energy and Buildings, 34(9) 951-958.

Elnokaly, Amira and Elseragy, Ahmed (2013) Sustainable heritage development: learning from urban conservation of heritage projects in non-western contexts. European Journal of Sustainable Development, 2 (1). pp. 31-56. ISSN 2239-5938

Elnokaly, Amira, Ayoub, Mohamed and Elseragy, Ahmed (2019) Parametric Investigation of Traditional Vaulted Roofs in Hot-Arid Climates. Renewable Energy, 138. pp. 250-262. ISSN 0960-1481

IESVE (2018) About IES | Integrated Environmental Solutions. Available from http://www.iesve.com/about [accessed 15 October 2018].

Jentsch, M., Bahaj, A. and James, P., Climate change future proofing of buildings—Generation and assessment of building simulation weather files. (2008), Energy and Buildings, 40(12) 2148-2168.

Norford, K., Socolow, R. H., Hsieh, E. S. and Spadaro, G. V. (1994) "Two-to-one discrepancy between measured and predicted performance of a low-energy 'office building: Insights from a reconciliation based on the DOE-2 model,", 1994., Energy and Buildings, vol. 21, no. 2, pp. 121–131, Jan.

Karlsson, F., Rohdin, P. and Persson, M. Measured and predicted energy demand of a low energy building: important aspects when using Building Energy Simulation. (2007), Building Services Engineering Research and Technology, 28(3) 223- 235.

Kheiri, F., A review on optimisation methods applied in energy-efficient building geometry and envelope design. (2018), Renewable and Sustainable Energy Reviews, 92, 897-920.

Khoury, J., Hollmuller, pierre LACHAL, B. M. "Energy performance gap in building retrofit: characterization and effect on the energy saving potential," in 19. Status- Seminar «Forschen für den Bau im Kontext von Energie und Umwelt, 2016. [Online]. Available: http://archive-ouverte.unige.ch/unige:86086 .

Lazzeroni, P., Olivero, S., Stirano, F., Micono, C., Montaldo, P., Zanzottera, G., ... & Repetto, M. Energy efficiency measures for buildings in Hebron city and their expected impacts in the distribution grid. (2017). Energy Procedia, 134, 121-130.

Loucari, C., Taylor, J., Raslan, R., Oikonomou, E., Mavrogianni, A., Retrofit solutions for solid wall dwellings in England: The impact of uncertainty upon the energy performance gap, (2016) Building Services Engineering Research and Technology, vol. 37, no. 5, pp. 614–634, May 2016.

Macdonald, I. (2002) Quantifying the effect of Uncertainty in building simulation. PhD

Mahaya, C., Zemmouria, N., Benharra, H. and Elnokaly, A. (2022) Solar Access Assessment in Semi-Arid Urban Context: An Application Study for Ten Urban Forms of Existing Apartment Buildings Districts in Batna City, Algeria. Sustainable Cities and Society, 83 (103909). ISSN 2210-6707

Martincigh, L., Bianchi, F., Di Guida, M., & Perrucci, G., The occupants 'perspective as catalyst for less energy intensive buildings. (2016), Energy and Buildings, 115, 94–101. https://doi.org/10.1016/j.enbuild.2015.04.018

Menezes, A. C., Cripps, A., Bouchlaghem, D. and Buswell, R., Predicted vs. Actual energy performance of non- domestic buildings: Using post-occupancy evaluation data to reduce the performance gap, (2012) Applied Energy, vol. 97, pp. 355–364, Sep.

Motuzienė, V., Lapinskienė, V., ynkun, G., & Bielskus, J., Energy Performance Gap nalysis in Energy Efficient Residential Buildings in Lithuania. (2021). Environmental and Climate Technologies, 25(1), 610–620. https://doi.org/10.2478/rtuect-2021-0045

Newsham, G. R., Mancini, S., & Birt, B. J., Do LEED-certified buildings save energy? Yes, but. (2009). Energy and Buildings, 41(8), 897–905. https://doi.org/10.1016/j.enbuild.2009.03.014

Niu, S., Pan, W., & Zhao, Y., A Virtual Reality Supported Approach to Occupancy Engagement in Building Energy Design for Closing the Energy Performance Gap. (2015), Procedia Engineering, 118, 573–580. https://doi.org/10.1016/j.proeng.2015.08.487

Oyedele, L., Regan, M., Meding, J. von, Ahmed, A., Ebohon, O. John and Elnokaly, A. (2013) Reducing waste to landfill in the UK: identifying impediments and critical solutions. World Journal of Science, Technology and Sustainable Development, 10 (2). pp. 131-142. ISSN 2042-5945

Palestine Meteorological Deportment, (2018). Hebron Historic weather data [email]. Sent to S. Alqadi, 20th/March/2018

Paliouras, P., Matzaflaras, N., Peuhkuri, R. and Kolarik, J., Using Measured Indoor Environment Parameters for Calibration of Building Simulation Model- A Passive House Case Study. (2015), Energy Procedia, 78, 1227-1232

PEA, P., Palestinian Green Buildings Guidelines. Ramallah. (2013) Available from https://www.researchgate.net/publication/262915250_Palestinian_Green_Buildings_Guidelines [accessed 21 January 2019].

Raftery, P., Keane, M. and Costa, A., Calibrating whole building energy models: Detailed case study using hourly measured data. (2011), Energy and Buildings, 43(12) 3666-3679.

Reddy, T., Maor, I. and Panjapornpon, C. (2007). Calibrating Detailed Building Energy Simulation Programs with Measured Data—Part II: Application to Three Case Study Office Buildings, (RP-1051). HVAC&R Research, 13(2) 243-265.

Ren, Z., Foliente, G., Chan, W., Chen, D., Ambrose, M. and Paevere, P., A model for predicting household end-use energy consumption and greenhouse gas emissions in Australia. (2013), International Journal of Sustainable Building Technology and Urban Development, 4(3) 210-228.

Saleh, P., Schiano-Phan, R. and Gleeson, C. (2018), Heavy Weight Thermal Calibration and Validation Methodologies: from Modelling to Full Scale Built Test Cells in Lebanon. (In: 4th Building Simulation and Optimisation Conference, Cambridge, UK

Scofield, J. (2009) Do LEED-certified buildings save energy? Not really. Energy and Buildings, 41(12) 1386-1390.

Sunikka-Blank, M., Chen, J., Britnell, J., & Dantsiou, D., Improving Energy Efficiency of Social Housing areas: Case study of a retrofit chieving an ǁ Energy Performance rating in the UK. (2012), European Planning Studies, 20(1), 131–145. https://doi.org/10.1080/09654313.2011.638494

Tiwari, P., Architectural, Demographic, and Economic Causes of Electricity Consumption in Bombay (2000). Journal of Policy Modelling, 22(1)81-98.

US DOE (2008) M&V guidelines: measurement and verification for federal energy projects version 3.0. US Department of Energy

van Dronkelaar, M. Dowson, C. Spataru, and D. Mumovic, A review of the regulatory energy performance gap and its underlying causes in non-domestic buildings, (2016), Frontiers in Mechanical Engineering, vol. 1, Jan.

Wainer, G. and Qi Liu, Tools for Graphical Specification and Visualization of DEVS Models, (2009) SIMULATION, 85(3) 131-158.

Y. Lyu, Y. Pan, T. Yang, Y. Li, Z. Huang, R. Kosonen, an automated process to calibrate building energy model based on schedule tuning and signed directed graph method, (2021), Buildings and Engineering, 35, Article 102058, 10.1016/j.jobe.2020.102058

Yu, C., Du, J., & Pan, W. Improving accuracy in building energy simulation via evaluating occupant behaviours: A case study in Hong Kong. (2019), Energy and Buildings, 202, 109373. https://doi.org/10.1016/j.enbuild.2019.109373

Zhan, S., Wichern, G., Laughman, C., Chong, A., & Chakrabarty, A. (2022). Calibrating building simulation models using multi-source datasets and meta-learned Bayesian optimization. Energy and

#33: The intermittency and flexibility of heating systems with different terminal types in buildings

Baoping XU[1, 2], Qiangang LI[2], Yanzhe DOU[2], Yuying YAN[1]

1 University of Nottingham, Nottingham NG7 2RD, United Kingdom, Yuying.Yan@nottingham.ac.uk
2 North China Electric Power University, Beijing 102206, China, Baoping.Xu@nottingham.ac.uk

Abstract: The electrification of building heating is an effective way to meet the global carbon target. As a clean and sustainable electrified heating technology, air-source heat pumps (ASHPs) are widely used in areas lacking central heating. As a major component of heating systems, heating terminals have great effect on both intermittency and flexibility of the system.

In this study, an integrated dynamic model was developed by considering the interaction of thermal processes among building envelopes, terminals, and heat pumps. The radiant heat transfer ratio of the heating terminal, which was introduced in the dynamic thermal balance equations, was a key parameter to describe the characteristic of heat transfer between the terminal and the building. Field tests demonstrated that the simulated results were closer to the tested values when considering the proposed ratio. An intermittent heating control strategy as well as demand response operation were applied to heat pump heating systems respectively. The effect of different terminals on room temperature response speed, energy saving rate, load shifting rate and load shifting efficiency was analysed.

The results indicated that heat pumps under intermittent heating were more efficient in buildings with convective heating terminals. Specifically, fan-coil heating systems could use 16.48% less energy, while radiant floor heating systems consumed more energy under intermittent heating. For buildings with convective terminals (such as fan coils), the warm-up time was 0.09 h to 0.33 h, and for those with convective-radiative terminals (such as radiators), the warm-up time was 0.23 h to 4 h under daily intermittent heating, while there was nearly no need to preheat in buildings with radiative terminals (such as radiant floors). On the other hand, the buildings with radiative heating terminals had better flexibility potential. By adopting the model predictive control strategy, the load shifting ratio of radiator heating systems was about 2.9 times that of fan coil heating systems. Finally, an idea of a novel radiation-adjustable heating terminal was proposed in order to achieve both intermittency and flexibility.

Keywords: Heating terminal; Radiant heat transfer ratio; Intermittent heating; Demand response; Load shifting ratio

1. INTRODUCTION

Since the Chinese government proposes that CO_2 emissions peak around 2030 and that CO_2 emissions are neutralized around 2060 (Zhang et al.,2019), the measures to stimulate energy efficiency and unlock flexibility are both important.

Intermittent heating has been considered to have a high energy saving rate compared with continuous heating (Wang, Lin and Zhu, 2015). The possibility exists that intermittent heating, when compared to continuous heating, can provide: significant energy savings; about the same; or have higher energy consumption. One of the factors that affect the efficacy of intermittent heating, is the radiative heat transfer coefficient of the terminal (Wang, Lin and Zhu, 2015; Xu, Zhou and Hu, 2017; Hu, Xu and Meng, 2022). Meanwhile, the heating terminal types has significant influence on the load flexibility of the system, which is rarely discussed and needs further comprehensive analysis.

Most models or experiments in previous studies can display information for parts of a heating system, but there is a lack of research taking account of combinations of different heating terminals, building thermal processes, and the heating supply system's operation characteristics, all of which are necessary to analyze a system's thermal properties and energy performance in its entirety.

The main purpose of this study is to build a systematic simulation platform for evaluating the intermittency and flexibility of heat pump heating systems for multizone buildings with different terminals. The evaluation is based on a dynamic model (integrating the multi-zone building thermal model, the terminal model, and the ASHP model), combined with different control strategies (MPC for intermittent heating, and demand response operation respectively). The comparison is made with respect to the room temperature response time, the energy saving rate, and the flexibility indicators. Finally, an idea of achieving both intermittency and flexibility is discussed.

2. MODELING APPROACH

The integrated model consists of three parts: a multi-zone building thermal model, a terminal model and a heat pump model. The integrated model systematically describes the dynamic thermal processes of an entire heating system, by considering the influencing mechanisms of different heating terminals on the multi-zone indoor thermal environment, and the operating characteristics of ASHPs.

Three typical heating terminals (radiator, radiant floor, and fan coil), are chosen as the research objects. The COP of the ASHP is expressed as a function of supply temperature and outdoor temperature, which is built by the parameter identification, based on the product sample data of the ASHP.

2.1. Framework of an integrated model

The models of the multi-zone building, terminals and the heat pump are not independent. As shown in Figure 1, the variables in one model always interact with those in the other models.

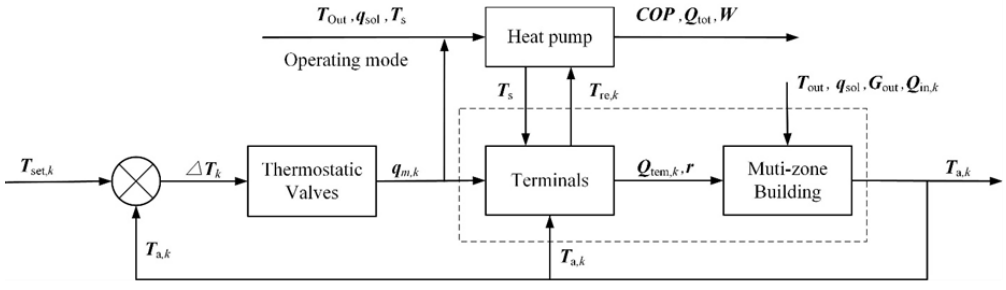

Figure 13 Diagram of the integrated model

The integrated model takes weather parameters, supply water temperature, indoor casual heat gains, and the characteristic value of each component as input parameters. For each step in the calculation, the terminal flow rate, outlet water temperature, heating power, and air temperature for each room can be obtained. Then, the time series response of total water flow and return temperature in the building can be calculated according to the mass and heat quantity conservation. Finally, the dynamic electricity consumption of the ASHP can be obtained.

2.2. Innovation of the model

The innovation of this model lies in that: it systematically describes the dynamic thermal processes of heat pumps, building envelopes and heating terminals; it reveals the influencing mechanisms of different types of heating terminals on a multi-zone indoor environment; and incorporates the operating characteristics of heat pumps and terminals.

Accounting for the convection and radiation-heat of terminals is very important for an accurate analysis of the thermal performance of buildings. Radiators emit heat by convection and radiation, while fan coils affect the temperature of indoor air by convective heat transfer, and radiant floors emit heat mainly by radiation. Therefore, a definition of the radiant ratio (r) of heat emitted from terminals is proposed and introduced in the following thermal-balance equation for indoor air.

Equation 1: thermal-balance equation for indoor air.

$$C_{p,a}\rho_a V_a \frac{dT_a(t)}{dt} = \sum_{i=1}^{n} h_i f_i (T_i(t) - T_a(t)) + C_{p,a}\rho_a G_{out}(t)(T_{out}(t) - T_a(t)) + \sum_j C_{p,a}\rho_a G_{adj}(t)(T_j(t) - T_a(t)) + Q_{in,1}(t) + (1-r)Q_{term}(t)$$

Where:

- $C_{p,a}\rho_a V_a$ = total heat capacity of indoor air (J/K)
- T_a = indoor air temperature (ºC)
- h_i = convective heat transfer coefficient between the interior surface i and the air (W/(m^2·ºC))
- f_i = area of the interior surface i (m^2)
- T_i = temperature of surface i (ºC)
- G_{out} = air exchange rate between the room and the outdoors (m^3/s)
- G_{adj} = air exchange rate between the room and adjacent rooms (m^3/s)
- T_{out} = outdoor air temperature (ºC)
- T_j = air temperature in the adjacent room j (ºC)
- $Q_{in,1}$ = convective portion of the internal disturbance, calculated by the calorific value of each person, lighting equipment and computer equipment (W)
- Q_{term} = heat power from terminals (W)
- r = proportion of radiant heat to total heat emitted from terminals
- t = time (s)

The difference approach of setting up the dynamic thermal model for systems with different terminals, results in the difference of thermal disturbance incidence matrix B in Equation 2, which describes the thermal processes within a building by state space method (Hong and Jiang, 1997).

Equation 2: thermal process within a building.

$$C \cdot \dot{\theta}(t) = A \cdot \theta(t) + B \cdot H(t)$$

Where:

- θ = *N*-dimensional column vector describing the temperature of all nodes in the state space
- $\dot{\theta}$ = derivative of θ with respect to time
- C = a diagonal matrix describing the thermal capacity of all nodes
- A = an *N*×*N* symmetric matrix describing heat conduction, heat convection and long wave heat radiation among all nodes
- B = an *N*×*M* matrix describing the impact of the *M* heat disturbances on the node temperatures
- H = an *M*-dimensional column vector standing for the *M* heat disturbances, including outdoor temperature, solar radiation, indoor casual gains, heat input from terminals, heat disturbance from adjacent rooms and infiltration or ventilation through openings

3. SIMULTED SYSTEM

For case studies and analysis, a simulated system was built for a multi-zone building adopting heat pumps with specific terminals. The model together with typical control strategies (intermittent heating strategy and demand response strategy respectively) is applied to simulate the thermal behaviour of heat pump heating systems for buildings under various conditions.

3.1. Building and heating system

The simulated building is located in Beijing. The geometry of the building is shown in Figure 2. The heat transfer coefficients of envelopes are given in Table 1, which was confirmed in accordance with Design Standard for Energy Efficiency of Public Buildings (China Academy of Building Research, 2015).

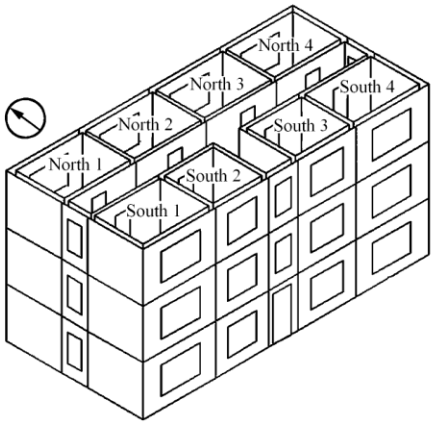

Figure 2 Diagram of the simulated building

Table 1: Physical thermal parameters of building envelopes.

Type of envelope	Thickness /mm	Density /(kg/m^3)	Specific heat /(J/(kg·K))	Heat transfer coefficient /(W/(m^2·K))
Exterior walls	340	589	1218	0.37
Interior walls	170	706	1319	1.19
Roof	300	300	1800	879
Ground	1200	1930	1010	-
Windows	4	2500	837	1.80

According to the thermal characteristics of different heating terminals, and experimental results (Zhang et al., 1994), the ratios of convection heat and radiation heat over total heat emitted by typical terminals are set as listed in Table 2. In addition, different design supply/return water temperatures are considered for different heating terminals under continuous heating and intermittent heating. By adopting intermittent heating, the reheating process requires a higher supply temperature to perform quickly when the buildings are reheated to increase the indoor temperature and secure the expected comfort (Benakopoulos et al., 2022)

Table 2: Terminal heating device parameters.

Type of terminals	Ratios of convection heat and radiation heat over total heat	Supply/return temp. under intermittent heating /°C	Supply/return temp. under continuous heating /°C
Fan-coil	1: 0	55/40	45/30
Radiator	0.6: 0.4	60/45	50/35
Radiant floor	0.32: 0.68	45/35	40/30

The COP of the ASHP can be expressed as a function of supply temperature and outdoor temperature, as follows:

Equation 3: COP of the ASHP.

$$COP(t) = f(T_s(t), T_{out}(t))$$

Where:

- T_s = *supply water temperature of the heat pump* (°C)
- T_{out} = *outdoor air temperature* (°C)

The specific functional relationship in Equation 3 can be built by the parameter identification, based on the product sample data of the ASHP, as shown in Figure 3.

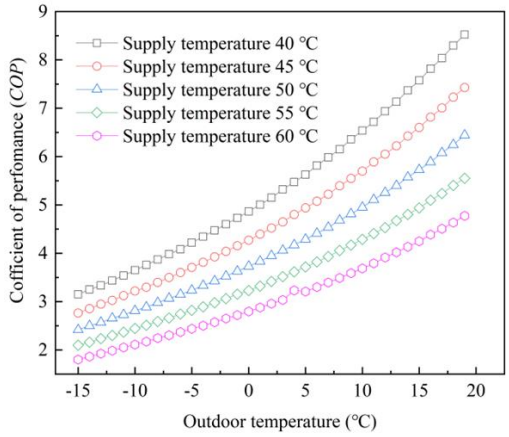

Figure 3 COP of the ASHP under different operating conditions

3.2. Intermittent heating strategy

As shown in Figure 4, the goal of using an intermittent heating control strategy is to reduce the runtime of the system while maintaining a comfortable room temperature during working hours. The key factor for an intermittent heating strategy is the optimal start time of the heating system for each working day, which is predicted by an iterative method (Xu, Zhou and Hu, 2017).

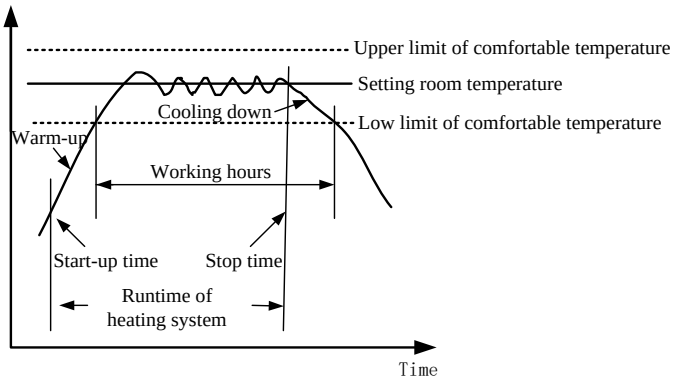

Figure 4 Room temperature variations under intermittent heating operation

3.3. Demand response strategy

A MPC (model predictive control) strategy of heat pump heating systems for demand response operation is proposed. By using a deep learning algorithm and the big data obtained from the integrated simulation platform, a neural network model for room temperature prediction of the thermostatic controller can be built, as indicated in Figure 5.

The objective of the optimization problem is to ensure indoor thermal comfort with minimal electric cost of the system, by searching an optimal opening degree sequence for thermostatic valves, as described in Equation 4.

$$\min \quad J = \sum_1^j \left(\frac{P(\tau_j)\times Q(\tau_j)}{3600COP}\right) + \sum_1^j \left(P(\tau_j) \times W(\tau_j)\right) + a \times \sum_1^j \sum_{i=1}^n \left(T_i(\tau_j) - T_s\right)^2$$

Equation 4: The objective equation.

- j = *calculation time steps*
- P = electricity prices, as listed in Table 3 (RMB/kWh)
- Q = the total heat consumption of the building during the calculation timestep (kJ)
- W = electricity consumption of the transmission system, e.g., circulating water pump, fan (kWh)
- T_s = the limit value of the comfortable temperature range, when T_i > 22°C, T_s=22°C; when T_i <18°C, T_s=18°C; when T_i is in the range of 18°C-22°C, T_i-T_s=0 (ºC)
- a = *regulation coefficient, which is taken as 100 in this study*

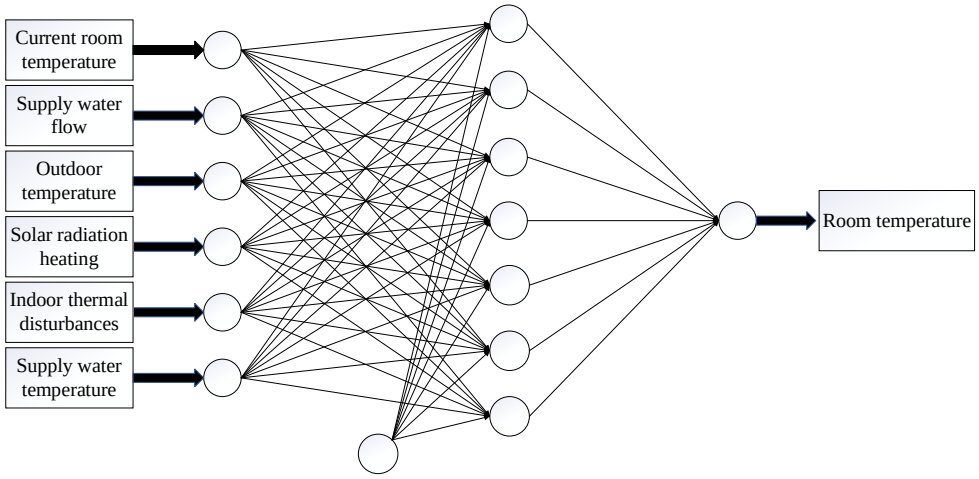

Figure 514 Neural network model of room temperature prediction for thermostatic controller

Table 3: Electricity prices in Beijing.

Type	Voltage level	Electricity prices (RMB/kWh)		
		Peak periods	Flat periods	Valley periods
		10:00-15:00, 18:00-21:00	Other hours	23:00-24:00, 0:00-7:00
General commercial electricity consumption	<1kV	1.3104	0.7847	0.3113

Combined the neural network model with an annealing algorithm, the optimization problem can be resolved, and the results of load shape changes by applying MPC strategy is obtained. Several indexes including load shifting ratio and demand response duration are defined to qualify the flexibility of the heating system.

For comparison the effect of MPC strategy, the traditional proportional control (PC) strategy and the Rule-Based control (RBC) strategy are also considered and applied to the simulated system separately.

4. RESULTS AND DISCUSSIONS

To test the integrated model, two district heating systems, one in Beijing and another in Tianjin, were investigated (Xu, Fu, and Di, 2008). There was good agreement between the measured and simulated values for the room temperature, return water temperature, and flow rate of the terminals.

4.1. Model validation

In this study, the neural network models for control prediction were trained by using Neural Net Fitting in MATLAB. The training set occupies 70% of the entire samples, meanwhile the validation and the test set occupy 15% of the entire samples separately. In order to verify the accuracy of the prediction results, the simulated results of the neural network model are compared with those of the integrated physical model. As shown in Figure 6, the simulated results are fit well.

4.2. Effects of different terminals on intermittency

Figure 7 shows the simulated results of room temperature variations during a typical week under daily intermittent heating. Room temperatures fluctuated the most for fan coil heating terminals. When a radiant floor is used as the heating terminal, the room temperature fluctuation is the least. That is, the larger the radiant heat ratio of terminals, the slower the thermal response speed of the system, and the smaller the temperature fluctuation during intermittent heating.

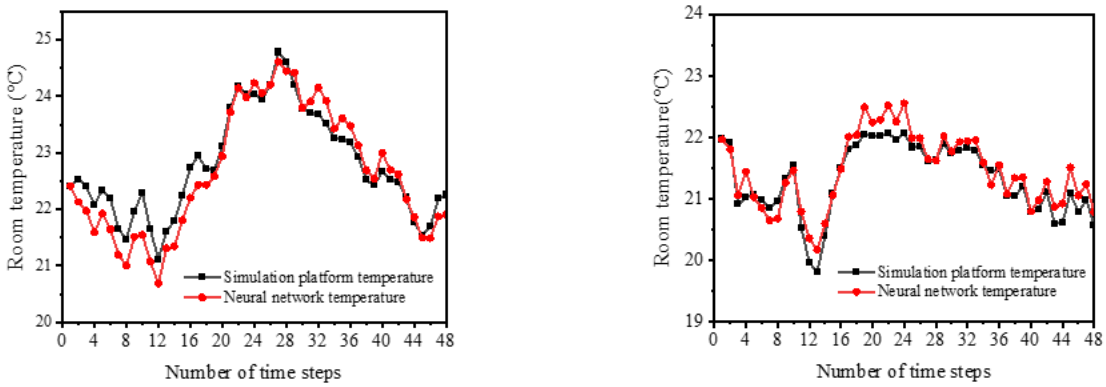

(a) Typical southern room *(b) Typical northern room*

Figure 6 Comparison of room temperature simulated by neural network model and physical integrated model

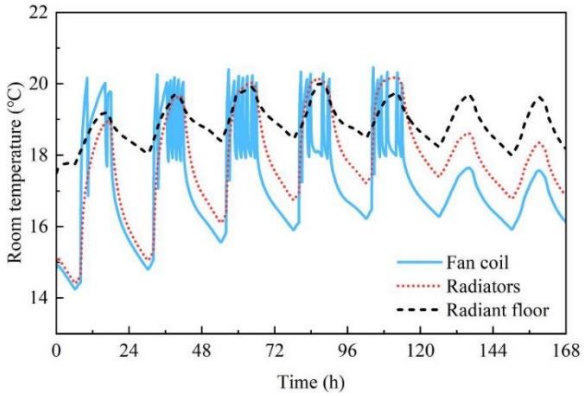

Figure 7 Variation in room temperature for different terminals during a typical week under daily intermittent heating

Table 4 lists the room temperature response parameters under daily intermittent heating during a typical week (from Jan 1 to Jan 7). The warm-up time for radiator heating systems is obviously longer than that for fan-coil heating systems, and the time needed on Monday morning is much longer than that needed on Tuesday to Friday mornings. Due to the large thermal inertia of radiant floor heating systems, the room temperature variation is minimal, and there is almost no need to preheat during the daily intermittent heating process.

Table 4: Room temperature response parameters for different terminals under daily intermittent heating

		Fan coils	Radiators	Radiant floor
Monday	Warm-up time /h	0.33	4	0
	Temperature increasing rate /(°C/h)	10.79	0.86	-
Tuesday-Friday	Warm-up time /h	0.09-0.20	0.23-1.83	0
	Temperature increasing rate /(°C/h)	14.72-16.62	1.47-2.51	-

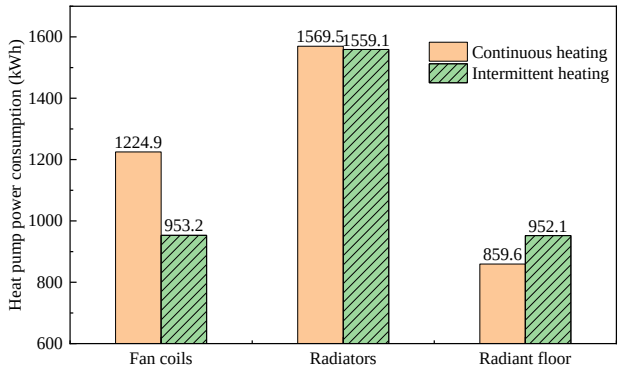

Figure 8 Heat pump power consumption with different heating terminals under intermittent heating versus continuous heating

The power consumptions of heat pumps for buildings with different kinds of terminals in the first month of heating season, are compared in Figure 8. The results of the calculation show that, compared with the power consumption of the heat pump under continuous heating, the power consumption of the heat pump under intermittent heating may be lower, similar or even higher, depending on the terminal type. Specifically, under intermittent heating, fan-coil heating systems can significantly achieve energy savings (with an energy saving rate of 16.48%), while radiant floor heating systems consume more energy.

4.3. Effects of different terminals on flexibility

In order to analyse the effect of control strategies for demand response, three indicators are defined to qualifiy the flexibility of the heating system: heating load shifting ratio, heating load shifting efficiency and the demand response duration, as described in Equations (5)– (7).

Equation 5: Heating load shifting ratio.

$$\alpha = (\int_{t1}^{t0} P_{\text{def}} dt - \int_{t1}^{t0} P dt) \Big/ \int_{t1}^{t0} P_{\text{def}} dt$$

Equation 63: Heating load shifting efficiency.

$$\phi = Q_{\text{xf}} / Q_{\text{tg}} = \int_{t1}^{t0} (P_{\text{def}} - P) dt \Big/ \int_{t0}^{t2} (P - P_{\text{def}}) dt$$

Equation 7: Demand response duration.

$$t_{\text{DR}} = t_{\text{m}} - t_{\text{n}}$$

Where:

- P= Electric power of heat pump when adopting demand response control strategy (kW)
- P_{def}= Electric power of heat pump without considering demand response control strategy (kW)
- Q_{xf}= Total quantity of *peak power shaving at peak usage periods* (kWh)
- Q_{tg}= Total quantity of *valley power filling at valley usage periods* (kWh)
- t_1= Start time of the peak period (h)
- t_0= Time when the peak ends and the valley begins (h)
- t_2= End time of the valley period (h)
- t_m= End time of demand response period when the room temperature decreases from upper limit to lower limit (h)
- t_n= Start time of demand response period when the heating stopped (h)

Figure 9 shows the results of the heating load shape changes by applying different strategies on a typical day during the coldest stage of heating season. The time of a day is divided into different periods according to local policy on time-of-use electricity price, and the heating load can be shifted from peak and flat period to valley period by MPC strategy.

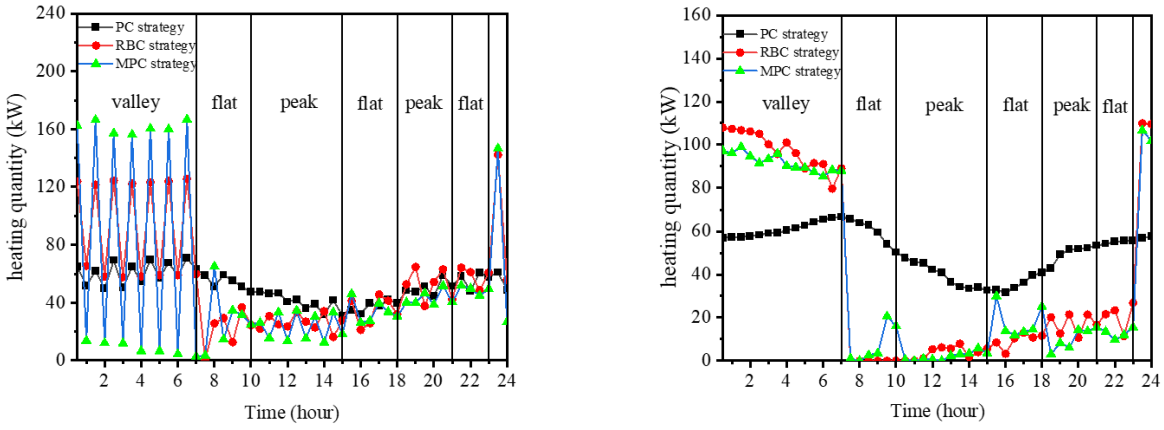

(a) Fan coil heating system

(b) Radiator heating system

Figure 9 Heating load shape variations under different control strategies on a typical day

Compared with fan coil heating system, radiator heating systems have better flexibility potential, as indicated in Table 5 and Table 6. For example, the load shifting ratio of radiator heating systems is about 2.9 times that of fan coil heating systems, and the load shifting coefficient of radiator heating systems is 2.2 times that of fan coil heating system.

Table 5: Flexibility indexes for heating system with different terminals during coldest stage of heating season

Terminal types	Total quantity of *peak power shaving at peak periods* (kWh)	Total quantity of *valley power filling at valley periods* (kWh)	heating load shifting coefficient	Heating load shifting ratio
Radiator heating system	453.0	264.2	1.71	83.2%
Fan coil heating system	157.0	198.2	0.79	28.8%

Table 6: Demand response duration for heating systems with different terminals

Heating periods	Average outdoor temperature (°C)	Demand response duration for radiator heating system (h)	Demand response duration for fan coil heating system (h)
the beginning or ending stage of the heating season	7.58	16	12
The middle stage of the heating season	2.24	10.5	4
The coldest stage of the heating season	-6.65	5	0.5

4.4. An idea of achieving both intermittency and flexibility

The type of terminals is a very important factor that influences the thermal inertia and the flexibility of the system. It can be found that, the system with radiative terminals is beneficial to support load shift, while the system with convective terminals has faster thermal response which is more appropriate for intermittent heating. In order to achieve both intermittency and flexibility, a new type of terminal with an adjustable radiant ratio might be the solution.

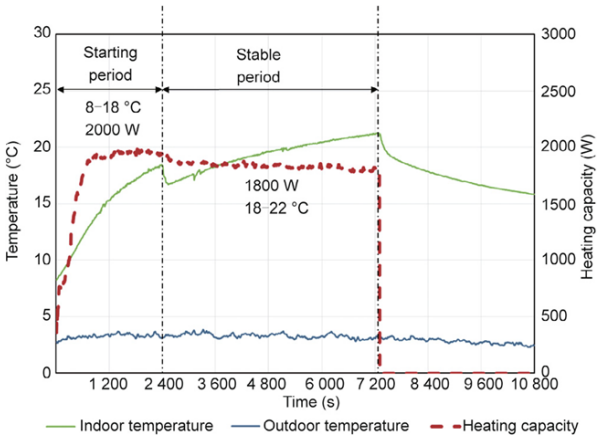

Figure 10 A phased operation strategy for achieving both intermittency and flexibility

Tsinghua Terminal Lab (Wu et al., 2023) proposed a novel terminal integrated with flat-heat-pipe and cross flow fan. The experimental results indicate that the radiation heat transfer ratio declined gradually with increasing forced convection wind speed, and the radiation ratio could be adjusted from 10.1% to 30.9%. Further study is necessary to improve the regulation capacity.

Then, a phased operation strategy could be applied for the novel terminal. As shown in Figure 10, the heating process can be mainly divided into two periods: the initial starting period and subsequent stable period. During the initial heating period, the novel terminal uses forced convection to achieve its maximum heating capacity quickly, and thus achieves a fast thermal response. During the stable period a high radiation heat transfer ratio is provided to maintain flexibility.

5. CONCLUSION

A dynamic integrated model for simulating the thermal process of buildings with heat-pump heating systems was proposed. The proposed model was implemented to simulate the thermal performance of heat pump heating systems for office buildings, under intermittent heating and also under demand response operation mode. The effect of different terminals (fan coil, radiator and radiant floor) on intermittency and flexibility of heating systems was analysed. The main conclusions are:

(1) Field tests demonstrated that the simulated results are closer to the tested values when introducing the proposed radiant heat ratio of terminals in the dynamic thermal balance equations of the integrated model.

(2) The heating system with convective terminals has faster thermal response and is more energy efficient, which can achieve an energy saving rate of 16.48% in the simulated intermittent heating scenario. However, the heating system with radiative terminals has greater flexibility potential. The load shifting ratio of radiator heating system is about 2.9 times that of fan coil heating system, and the load shifting efficiency of radiator heating system is 2.2 times that of fan coil heating system, when applying demand response strategy.

(3) The development of a novel radiation-adjustable heating terminal would be a promising solution to achieve both intermittency and flexibility of heating systems. Further study is necessary to improve the regulation capacity of the radiant heat of the terminal.

6. REFERENCES

Benakopoulos, T., Vergo, W., Tunzi, M. et al. (2022) 'Energy and cost savings with continuous low temperature heating versus intermittent heating of an office building with district heating', *Energy*, 252(8), 124071. Available at: https://doi.org/10.1016/j.energy.2022.124071

China Academy of Building Research (2015) *Design standard for energy efficiency of public buildings (GB 50189-2015)*, Beijing.

Hong, T., Jiang, Y. (1997) 'A new multizone model for the simulation of building thermal performance', Building and Environment, 32(2), pp.123-128. Available at: https://doi.org/10.1016/S0360-1323(96)00045-5

Hu, C., Xu, R., and Meng, X. (2022) 'A systemic review to improve the intermittent operation efficiency of air-conditioning and heating system', *Journal of Building Engineering*, 60(11), 105136. Available at: https://doi.org/10.1016/j.jobe.2022.105136

Wang, Z., Lin, B., and Zhu, Y. (2015) 'Modeling and measurement study on an intermittent heating system of a residence in Cambridgeshire', *Building and Environment*, 92(5), pp.380-386. Available at: http://dx.doi.org/10.1016/j.buildenv.2015.05.014

Wu, Y., Sun, H., Duan, M. et al. (2023) 'Novel radiation-adjustable heating terminal based on flat heat pipe combined with air source heat pump', *Engineering*, 20 (1), pp. 192-207. Available at: https://doi.org/10.1016/j.eng.2021.09.019

Xu, B., Zhou, S., and Hu, W. (2017) 'An intermittent heating strategy by predicting warm-up time for office buildings in Beijing', *Energy and Buildings*, 155(8), pp.35-42. Available at: http://dx.doi.org/10.1016/j.enbuild.2017.08.062

Xu, B., Fu, L., and Di, H. (2008) 'Dynamic simulation of space heating systems with radiators controlled by TRVs in buildings', Energy and Buildings, 40(3), pp.1755-1764. Available at: http://dx.doi.org/10.1016/j.enbuild.2008.03.004

Xu, B., Zhou, S., and Hu, W. (2017) 'An intermittent heating strategy by predicting warm-up time for office buildings in Beijing', *Energy and Building*, 55(8), pp.35-42. Available at: http://dx.doi.org/10.1016/j.enbuild.2017.08.062

Zhang, X., Chen, W., Yu, W. et al. (1994) 'Experimental study on the proportion between the convection heat and radiation heat for commonly used radiators', *Heating Ventilation and Air Conditioning*, 24(6), pp.13-15.

Zhang, Y., Yan, D., Hu, S. et al. (2019) 'Modelling of energy consumption and carbon emission from the building construction sector in China, a process-based LCA approach', *Energy Policy*, 134, 110949. Available at: https://doi.org/10.1016/j.enpol.2019.110949

#34: Investigation on heat transfer and flow organization characteristics of porous medium in quick freezer based on entransy analysis model

A New Entransy Analysis Model

Yong YANG[1*], Baojun CHEN[2*], Guangfu LI[2], Shuai ZHANG[2], Zhao ZHANG[3], Hong LIU[1], Shengqiang SHEN[1]

[1]School of Energy and Power Engineering, Dalian University of Technology, Dalian, China, yangyong@dlut.edu.cn
[2]Dalian Bingshan Lingshe Quick Frozen Equipment Co. Ltd, Dalian, China, chenbaojun@bingshan.com
[3]Department of Engineering Mechanics, Dalian University of Technology, Dalian, China, zhangz@dlut.edu.cn

Abstract: In the paper, a new Entransy analysis model of heat transfer process in porous medium is built, in which utilization efficiency of entransy is ideal Carnot efficiency and the field function characteristics of entransy are considered. Based on the cooling curve, surface temperature of cooling corns stacked in porous medium and convective heat transfer coefficient along quick freezer are predicted for the first time. Based on entransy theory, the coupling mechanism of conduction, convection and radiation in heat transfer process is quantitatively evaluated. The investigations of internal temperature gradient distribution in monomer and airflow organization efficiency in porous medium present field synergy characteristics of heat transfer process. It is found that convective heat transfer coefficients of the upper part of corn surface and the lower part in porous medium zone for the top layer stacked corns are significantly different. It is confirmed that radiation heat transfer could inhibit convective heat transfer under certain conditions. The surface heat transfer coefficient modified by radiation is used to predict cooling trend of central temperature and different cooling curves match well with measured values. The cooling curve of convex, concave and approximate straight line can be simulated by using the along convective heat transfer coefficient with high accuracy for different types of cooling process. It is found that developing of heat transfer process of conduction in corn or convection and radiation on the surface of the corn is a wavy distribution. Temperature gradient and airflow organization efficacy can reflect field synergy characteristics to a considerable extent. And the enhanced heat transfer characteristics of porous medium are found, which provides inspiration for the optimization design and performance evaluation in porous medium.

Keywords: Entransy; Entransy Efficiency; Along Heat Transfer Coefficient; Field Synergy Principle; Temperature Gradient

1. INTRODUCTION

Worldwide, one-third of all food produced for human consumption is lost or wasted, equating to approximately 1.3 billion tons per year. This inevitably also means that huge amounts of the resources in food productions are used in vain, and that the greenhouse gas emissions caused by production of food that gets lost or wasted are also emissions in vain (Shahla, 2018; Gustavsson, 2011). In particular, the convenience food market is becoming more popular globally. However, some researchers have indicated that a highly industrialized and centralized modern food system can cause more energy consumption and also more waste generation (Ju, 2017). The 2011 Roadmap to a Resource Efficient Europe pointed out that “reduced food waste could contribute to improving resource efficiency and food security at a global level” and set a milestone target for halving edible food waste in the EU by 2020 (EC, 2011). Later, in 2015, as part of the 2030 Sustainable Development Goals, the United Nations General Assembly adopted the target of halving per capita food waste at the retail and consumer level – an objective subsequently taken up in the EU Action Plan for the Circular Economy (EC, 2015). These political goals draw on the work of wide range of organizations that put effort into describing, analysing and understanding the assessment of Food Loss and Waste (FLW) (Redlingshöfer, 2017).

To improve the efficiency of food system, product and process optimization design and development are typical activities to perform. Nowadays quick freezing has become one of the most important unit operations in food processing and preservation, which can keep the sensory and nutritional properties of food farthest to meet the wonderful pursuit of green, convenient, and healthy food of people. Different means of cooling are available for food industry, including force-air cooling, vacuum cooling, room cooling, hydro cooling or contact freezing, immersion freezing. With the industry cooling or quick-freezing systems extending from small scale to large industrial scale, the limited understanding of the complex multiscale cooling process and systems often results in the design of inefficient cooling systems, lowering product quality and increasing energy wastage (Ajani, 2021). The major technical requirements in food cooling or freezing technologies is to improve the refrigeration efficiency, freezing quality, energy consumption, carbon emission intensity, production capacity, etc. The factors influencing refrigeration utilisation or performance of the cooling or freezing equipment include performance coefficient of the refrigeration system, homogenization of heat and mass transfer process in the equipment, airflow organisation, insulation performance of the body, and so on. For the force-air cooling or freezing equipment, the homogenization and airflow organization are most important characteristics, especially in the process of large industrial scale equipment design.

Optimization of the airflow can efficiently enhance cooling efficiency and reduce energy consumption, so the uniform performance of airflow organisation is critical to cooling or freezing quality. When airflow blockage and guide technologies are adopted, the production capacity and energy utilisation efficiency can be increased by 28.3% with airflow organisation improved from 51.4% to 65.9% (Huan,2003). And modification of package design in the force-air cooling can have significant influence on the aerodynamic and thermodynamic performance, heat transfer coefficient increases with airflow and distribution follows the air flowing profile. The entransy and exergy analyses show that the entransy-dissipation-based thermal resistance can be used to evaluate the airflow organization, and results show that with air mixing process improved, the entransy-dissipation-based thermal resistance and exergy loss both decrease, and energy consumption decreases correspondingly. The minimum entransy-dissipation-based thermal resistance occurs at the same time with the optimal heat load, while the minimum exergy loss per unit cooling capacity does not correspond to the largest heat load sometimes, which shows that the entransy analysis method is more accurate (Qian, 2015).

Non-homogeneous flow of the cooling air inside stack may cause uneven cooling and product quality. Hence refrigerated food bulks, packaged or not, usually arranged in stacks inside cooling or freezing equipment to form porous medium to enhance heat transfer and improve the homogenization, which can increase the local velocity and turbulence intensity (Ambaw,2013; Verboven,2006). It is found that for stacked foods, heat transfer coefficient without liners is higher 74% in average than that with plastic liners (Ambaw, 2017). And even for same monomer, heat transfer coefficients in the tunnel of freezer is significantly different located in porous medium or not, the heat transfer coefficient facing evaporator is only about 60% of the part on the porous sole in average (Amarante,2005). As the high-velocity flows in porous media lead to turbulence within the pores and highly chaotic structures develop when pore-Reynolds number $Re > 300$. And it’s well known that the Nusselt number Nu can increase by 25% when turbulence rises from 1% to 7% (Alvarez, 2003; Comings, 1948). For bins filled with spheres, the velocity maps show that a strong turbulence intensity, up to 50%, is generated by vortices in the wake of spheres and perforated inlet wall (Alvarez,1999). Based on the second law of thermodynamics, Guo developed the uniformity principle for optimizing heat exchangers. It states: “The more uniform the temperature difference field, the higher the effectiveness of heat exchanger for a given number of heat transfer unit and heat capacity rate ratio” (Guo, 1994; Li, 1995). Based on which, the Field Synergy Principle and Entransy theory have been put forward. The main content is that when the degree of field synergy of the heat and flow filed is improved, the process of heat transfer will be optimized and improved, meanwhile the maximum of entransy dissipation achieves with the highest heat flux following the principle of minimum entransy dissipation in temperature representation, which is also the principle of energy conservation (Guo, 1998; Cheng, 2004).

The heat transfer in stacked foods in cooling or freezing equipment includes conduction, convection and radiation, and the three heat transfer mechanisms generally occur simultaneously. It is found that radiation represents an important contribution to the heat transfer through the packed porous media, and there is a similarity in the probability density

distributions of dimensionless heat flows among particles under different temperatures, indicating that the packing structure is a dominant factor in controlling the distribution whereas the mean heat flow between particles mainly depends on temperature and related material properties (Cheng, 2013). Based on the superposition principle of heat transfer, the contributions of radiation and conduction can be separated to allow a better understanding of the underlying phenomena and characteristics of the resultant heat transfer, and it is found the near-wall effects have a notable influence on the effective heat transfer which is a function of the macro temperature gradient, and with a high porosity, the radiation heat transfer increases with high porosity (Beer, 2017). While for combined heat transfer of conduction, convection and radiation, porous medium has very significant impact, the enhance ratio of convective heat transfer coefficient is nearly a constant value in average with same porosity characteristics (Amarante, 2005).

It is very important to predict the surface temperature of products in porous medium to analyse and optimize the heat transfer process in cooling or freezing equipment. But, at present, theoretical calculation methods for surface temperature prediction in porous medium have not yet emerged. Researchers mainly use CFD numerical simulation methods and manufacturers mainly use measurement methods to monitor the surface temperature, heat flux or heat transfer coefficient in porous medium. In the paper, an entransy analysis model of heat transfer process in porous medium is built, and a new utilization efficiency of entransy is proposed. Based on the model, depending on the cooling curve of corns in quick freezer, the surface temperature of frozen products in porous medium zone and the convective heat transfer coefficient along quick freezing device can be predicted. The entransy dissipation mechanism in heat transfer process is analysed, meanwhile the coupling mechanism of conduction, convection and radiation is quantitatively evaluated, which provides inspiration for the optimization design and performance evaluation in porous medium, for example choosing the appropriate cooling air temperature or heat transfer temperature difference, optimizing the length of cooling or freezing device, improving the airflow organisation and homogenization, adapting to the development requirements of large industrial scale food processing and preservation plants.

2. ENTRANSY ANALYSIS MODEL IN POROUS MEDIUM

2.1. Physical model

Figure 1 shows the structure of tunnel type quick freezer, in which the frozen corns enter the body on conveyor belt for continuous cooling. The refrigeration system is located at the side of conveyor belt, and centrifugal blower under the refrigeration system, the cooling air being drained through pressure stabilizing box and guide plate to achieve vertically blown to the stacked porous medium zone of corns. The conveyor belt speed can be adjusted to adapt for different freezing times.

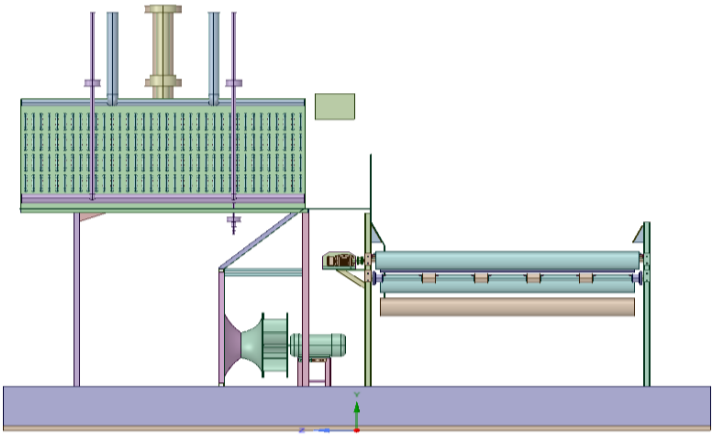

Figure 1 Structure of tunnel type quick freezer

The heat transfer model of porous medium zone is shown in Figure 2, assuming that the corn is a cylinder with radius of R_1. During the cooling process, the central area is the internal heat transfer core (in red) with a uniformly distributed temperature T_c, which gradually decreases combined with a radius of R_2 that varies with cooling process. The inner core area and the out boundary of corn form a heat conduction zone (white cirque), and surface temperature of corn is T_w, decreasing with cooling process. The periphery of corn is low-temperature cooling air, which conducts resultant convective heat transfer with corn at temperature of T_a, combined with radiation with surface temperature of corn. The cooling air is continuously circulated and refrigerated by the blower and evaporator. During the heat transfer process, it is assumed that the inlet temperature of cooling air remains constant, and after heat exchange, it enters the evaporator again. The corns are stacked in form of porous medium zone with porosity of ε。

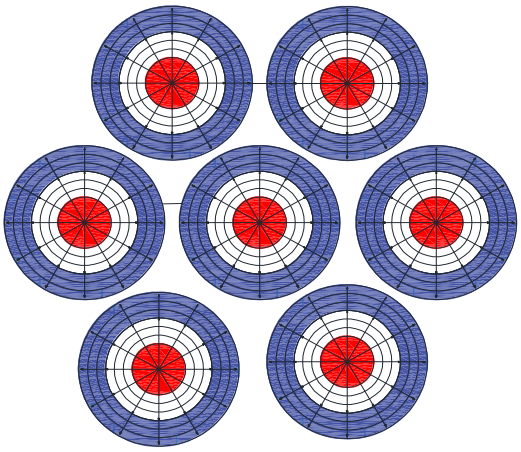

Figure 2 Heat transfer model of stacked porous medium zone of corns

2.2. Mathematical model

Assuming that the central temperature *Tc* of corns in porous medium zone is equal, and the porous medium zone is a uniform heat transfer zone, then the temperature field and radiation field in the analysis unit are in superposition state with unified field strength. Inside of a single corn, the internal temperature field and temperature gradient are internal properties, with surface of corn as heat transfer boundary.

The entransy is considered as field function in porous medium. Based on its thermal potential energy characteristics, it follows the first law of thermodynamic, and it is conserved on the heat transfer boundary, with surface temperature *Tw* as thermal boundary, which satisfies the boundary condition for radiation.

$$\dot{G}_H = \dot{G}_C + \dot{G}_R \tag{1}$$

$$\dot{G}_H = \dot{G}_h + \dot{G}_{FR} = \dot{G}_C + \dot{G}_R \tag{2}$$

$$\dot{G}_h = \dot{G}_C + \dot{G}_{Fr} \tag{3}$$

Where:

- $\dot{G}_H$ = total entransy strength((k • J)/m^3)
- $\dot{G}_C$ = convection entransy strength ((k • J)/m^3)
- $\dot{G}_R$ = radiation entransy strength ((k • J)/m^3)
- $\dot{G}_h$ = entransy strength without surface radiation ((k • J)/m^3)
- $\dot{G}_{FR}$ = surface radiation entransy strength ((k • J)/m^3)
- $\dot{G}_{Fr}$ =entransy strength caused by electromagnetic effect of internal temperature difference between centre and surface ((k • J)/m^3)

Equation (3) can be calculated as following,

$$\frac{G_h}{V_{pm}} = \frac{G_C}{V_a} + \dot{G}_{Fr} \tag{4}$$

$$G_h = \int_0^{R_1} \frac{1}{2} M_{cr} C_{Vcr} (T_{cr}^2 - T_w^2) \tag{5}$$

$$G_C = \frac{1}{2} M_a C_{Va} (T_w^2 - T_a^2) \tag{6}$$

Where:

- G_h = entransy of hot side (k • J)
- G_C =entransy of cold side by convection heat transfer (k • J)
- T_{cr} = resultant temperature of the center Tw and cirque Tr (K)
- M_{cr} = resultant quality of the center and cirque (kg)
- $C_{V\,cr}$ = resultant specific heat of corn (kJ/(kg • K))
- M_a = quality of the cooling air flow through the porous medium (kg)
- $C_{V\,a}$ = specific heat of cooling air (kJ/(kg·K))
- V_{pm} =volume of the porous medium (m^3)
- V_a =volume of the cooling air (m^3)

Assuming the entransy from the hot side caused an increase of work ability of fluid with convection and flow, the utilization efficiency η is identically equal to Carnot cycle,

$$\eta = 1 - \frac{T_a}{T_c} \tag{7}$$

$$\eta \dot{G}_h = \dot{G}_C \tag{8}$$

Based on the superposition principle of heat transfer, the individual analysis for conduction and convection as following,

$$-k_{cr} A \left.\frac{dT}{dR}\right|_{R=R1} + \dot{q}_{Fr} + \dot{q}_{FR} = hA(T_w - T_a) + \dot{q}_R \tag{9}$$

$$-k_{cr} A \left.\frac{dT}{dR}\right|_{R=R1} \cong hA(T_w - T_a) \tag{10}$$

Where:

- k_{cr} = thermal conductivity of corn (W/(m·K))
- *h*=convective heat transfer coefficient in porous medium (W/(m^2·K))
- *A*=surface area of corn (m^2)

The internal conduction of corn at any radius *R* can be calculated as following,

$$-k_{cr} A_R \left.\frac{dT}{dR}\right|_{R=R2}^{R=R1} = -k_{cr} A \left.\frac{dT}{dR}\right|_{R=R1} \tag{11}$$

The cooling and freezing process of corn can be calculated by lumped capacity method as following,

$$hA(T_w - T_a) = \rho C_P V \frac{dT_c}{dt} \tag{12}$$

Where:

- *t*= time (s)
- ρ =density of corn (kg/m^3)
- *V*=volume of corn (m^3)

The cooling rate of corn adopts the long cylindrical food model with Bi≤4 as following, in which T_0 is the initial center temperature,

$$t = 0.3565 \frac{\rho C_p}{k_{cr}} R_1 \left(R_1 + \frac{3.16 k_{cr}}{h}\right) \left(lg \frac{T_0 - T_a}{T_c - T_a}\right) \tag{13}$$

The convective heat transfer coefficient of cooling air can be calculated by the model of Alvarez (Alvarez, 1999),

$$Nu=2+3.78Re_t^{0.44}Tu^{0.33}Pr^{0.33} \tag{14}$$

$$\sigma_u=\sqrt{\frac{\sum_{i=1}^{n}\left(u_i-\bar{u}\right)^2}{n}} \tag{15}$$

$$Tu=\frac{\sigma_u}{\bar{u}} \tag{16}$$

Where:

- Nu= Nusselt number in porous medium
- Pr=Prandtl number in porous medium
- Re_t=Reynolds number in porous medium
- Tu= relative turbulence intensity in porous medium
- σ_u =standard deviation of fluctuation of instantaneous local air velocity (m/s)
- $\bar{u}$ = averaged local air velocity (m/s)

As a heat transfer enhancement technology, porous medium has been widely used in the field of food cooling and freezing, but the evaluation for airflow organization in porous medium is still relatively rare. So, the airflow organization efficiency proposed by Huan (Huan,2003) is modified in the paper, stripping off the energy efficiency evaluation for evaporator, and changing evaporation temperature to outlet temperature of cooling air from the evaporator. So, the airflow organization efficiency is targeted evaluation for porous medium, as following,

$$\eta_f=\frac{h(\bar{T}_a-T_w)}{h_0(T_{a0}-T_w)} \tag{17}$$

$$Nu_0=0.0266Re_0^{0.805}Pr_0^{1/3} \tag{18}$$

Where:

- η_f = airflow organization efficiency
- $\bar{T}_a$ =average temperature of cooling air (K)
- T_{a0} = outlet temperature of cooling air from the evaporator (K)
- h_0 =convective heat transfer coefficient calculated by velocity of blower outlet (W/(m^2 • K))
- Nu_0= Nusselt number of initial properties
- Pr_0= Prandtl number of initial properties
- Re_0=Reynolds number of initial properties

3. THEORETICAL PREDICTION AND RESULT ANALYSIS OF ENTRANSY MODEL

3.1. Heat transfer process analysis in porous medium based on entransy model

The model was validated depending on to temperature cooling curve of the corn centre measured in the precooling tunnel of quick freezer, in which the German Detu Testo 105 thermometer records the real time measurement temperature. The boundary conditions of corn porous medium zone are shown in Table 1.

Table 1: The boundary conditions of the corn Porous medium zone

Parameters	Inlet temperature of cooling air ℃	Outlet temperature of cooling air ℃	layers of corn	Length of precooling tunnel m
quick freezer1	-2.4	-0.4	4	About 7.5
quick freezer 2	-1.75	0.15	4	About 7.5

Porosity of porous medium ε=0.4, and the thermal conductivity of corn k_{cr}=0.5116 W/(m·K) is calculated depending on the moisture content of corn, and the specific heat capacity of corn before freezing is C_P=C_V=3.53 kJ/(kg·K).

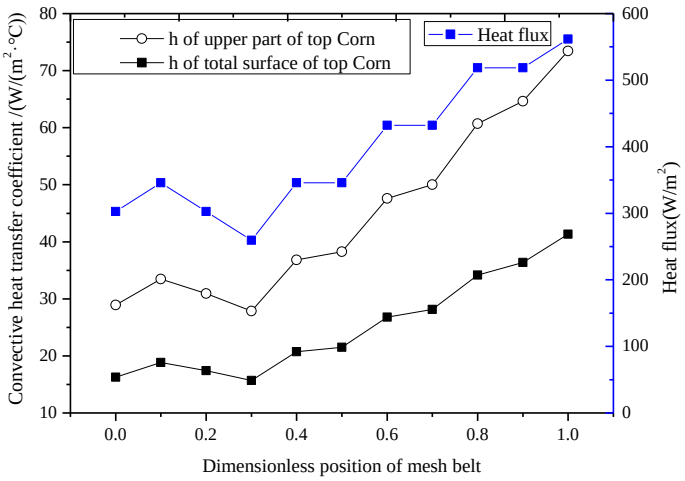

Figure 3 Comparison of surface heat flux and convective heat transfer coefficient

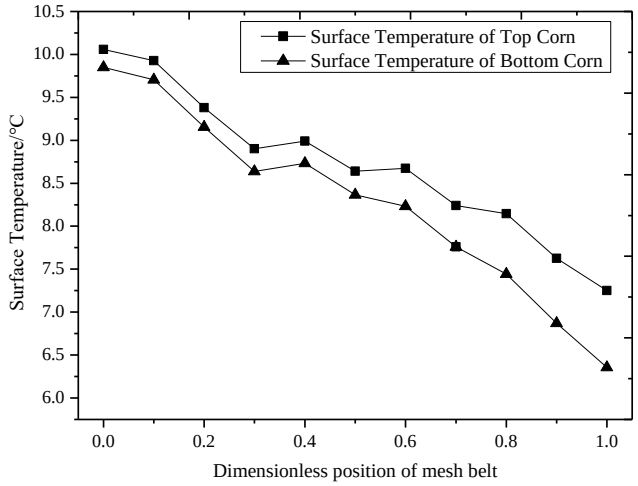

Figure 4 Prediction of surface temperature of corn

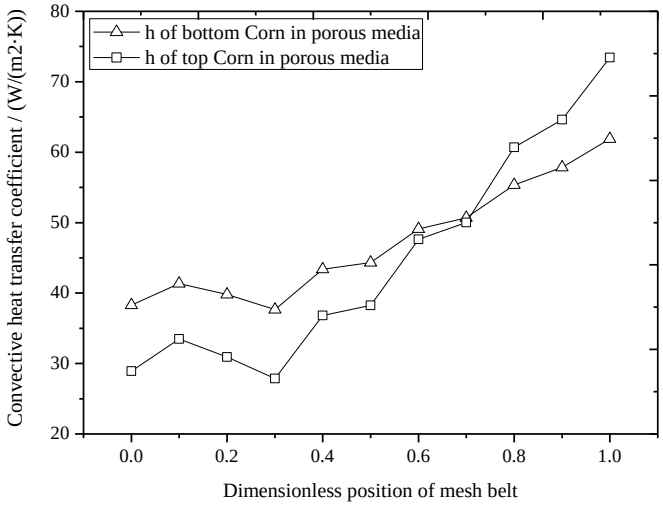

Figure 5 Prediction of convective heat transfer coefficient along the quick-freezing device

Figures 3 and 4 show the variation trend of convective heat transfer coefficient and surface temperature of corn predicted by the entransy analysis model. The overall distribution trend of convective heat transfer coefficient and heat flux in the precooling tunnel of quick freeze is same with Amarante's experimental results (Amarante,2005). As shown in Figure 3, the heat flux on corn surface obtained depending on the measured centre temperature generally shows an increasing trend along the quick freezer, where it decreases between 0.1-0.3 at the dimensionless position and remains constant between 0.4-0.5, 0.6-0.7 and 0.8-0.9. The predicted convective heat transfer coefficient also shows increasing trend overall, and the deceasing trend between 0.1-0.3 is the same with the variation trend of heat flux. The results indicate that, the convective heat transfer coefficient is positively related to the heat flux in general, but the correlation will be weakened under certain circumstances. The surface temperature of corn generally shows decreasing trend, but slightly increases at 0.3-0.4 and 0.5-0.6, where heat flux significantly increases. Indicating that, if the increasing of convective heat transfer coefficient is insufficient, surface temperature will slightly increase. When convective heat transfer coefficient is large enough, such as between 0.7-0.8, surface temperature will also decrease where heat flux increases. When heat flux keeps constant, convective heat transfer coefficient will increase with the decreasing of surface temperature and temperature difference between cooling air and the corn.

According to Amarante's experimental results, convective heat transfer coefficients on the surface facing the air side and the side close to the bottom porous medium zone are different (Amarante,2005). For a single corn on the top layer, the down part is located in porous medium zone, with higher heat transfer intensity combined with higher convective heat transfer coefficient. As shown in Figure 3, combined with the relative turbulence intensity obtained from CFD simulation, the correction coefficient Φ is calculated based on the convective heat transfer correlation of (14) obtained by Alvarez (Alvarez, 1999), and the value of $\Phi=0.563$, which is roughly equivalent to the proportion coefficient obtained from Amarante's experimental of about 0.6.

Due to air temperature on the surface of top layer corn being -0.4℃, the temperature difference is approximately consistent with surface temperature of corn as shown in Figure 4. The surface temperatures of top and bottom corns are different, surface temperature of top corn is higher than the bottom, at the end of the precooling tunnel the distinction growing to about 1℃ with cooling air temperature about -2.4℃. As shown in Figure 5, in the front part of precooling tunnel, convective heat transfer coefficient of bottom corn in porous medium is higher than the top corn, but in the rear part of precooling tunnel, convective heat transfer coefficient of bottom corn is lower than the top corn. Considering heat transfer temperature difference of bottom corn is higher than the top corn, the results show that heat transfer in the quick freezer has good uniformity overall.

Based on the field synergy principle, when flow is normal to temperature gradient, the increasing of velocity of flow doesn't make any contribution to the heat transfer occurring in the temperature gradient direction (Ma, 2007). For convective heat transfer in porous medium, the field synergy principle is also suitable. As shown in Figure 4 and 5, when the flow is general normal to temperature gradient, the convective heat transfer coefficient is generally increasing with the decreasing of temperature different. According to this principle, the field synergy degree based on the intersection angle between fluid velocity and temperature gradient is the fundamental mechanism for enhancing convective heat transfer, and for the chaotic flow in porous media with fluid velocity general normal to temperature gradient on the surface of corn, when temperature difference matches well with velocity, the field synergy degree increases which means the thickness of thermal boundary layer reduces at the same time, and convective heat transfer is enhanced. In the front part of precooling tunnel, temperature difference is much higher, the bottom corn owns higher convective heat transfer coefficient with higher fluid velocity. But in the rear part, the top corn in porous medium owns higher convective heat transfer coefficient with smaller temperature difference. And generally, for similar flowing characteristics, convective heat transfer coefficient generally increases with the field synergy degree increasing combined with temperature difference decreasing on the surface of corn.

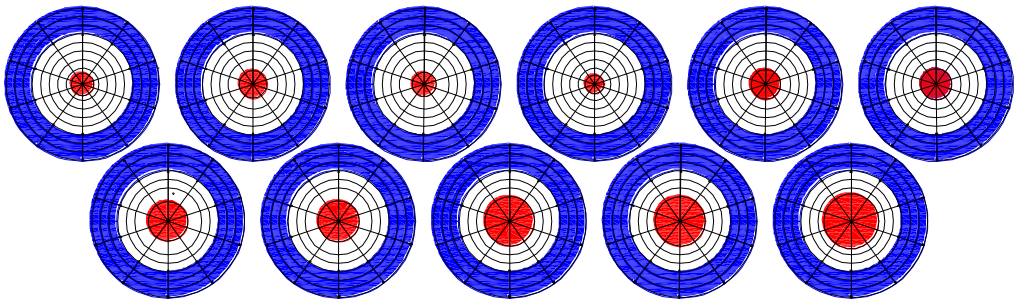

Figure 6 Phenomenological characteristics of the development of internal heat transfer core in corn

To identify the unsteady mechanism of heat transfer process along quick freezer, Figure 6 shows the development of internal equivalent heat transfer core R_2 of corn. As shown in Figure 6, the developing process of R_2 is significantly consistent with the trend of convective heat transfer coefficient. When the volume of heat transfer core is small, the

convective heat transfer is relatively low, and convective heat transfer coefficient increases combined with heat flux increasing with the volume of heat transfer core grows. The mechanism is that the changing of internal temperature gradient with heat flux and the changing of central and surface temperature.

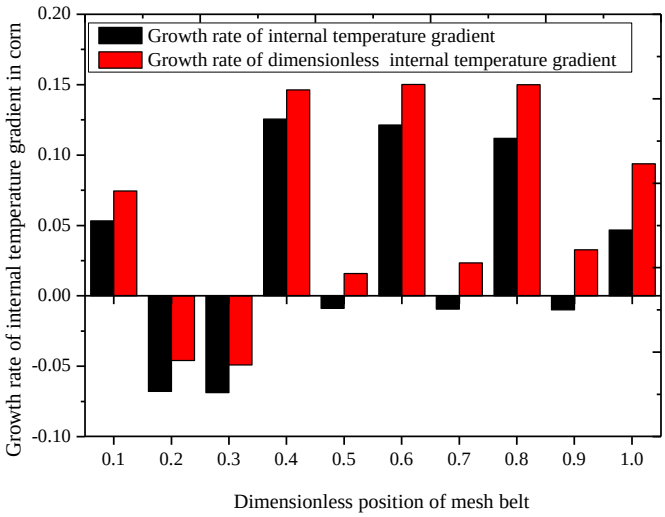

Figure 7 Growth rate of internal temperature gradient in top corn

To research the distribution of temperature gradient in corn, the dimensional temperature gradients Λ_t and dimensionless temperature gradients Λ in corn is defined as (19) and (20),

$$\Lambda_t = \frac{T_c - T_w}{R_1 - R_2} \tag{19}$$

$$\Lambda = \frac{(T_c - T_w)/T_c}{(R_1 - R_2)/R_1} \tag{20}$$

Figure 7 shows the developing trend of growth rate for internal temperature gradient of corn during the cooling process in quick freezer. As shown in the figure, growth rate of internal temperature gradient of corn has a significant decline at 0.1-0.3, and growth rate is negative, where heat flux and convective heat transfer coefficient drops correspondingly. Within the region with higher growth rate of temperature gradient, convective heat transfer coefficient has significant increase. From the comparison in Figure 7, it can be found that the dimensionless temperature gradient can better characterize the heat transfer process. The growth rate is positive at the location where convective heat transfer coefficient increases, while the growth rate of dimensional temperature gradient appears negative locally, where heat flux remains constant. In the region where the growth rate of temperature gradient is significantly reduced, growth rate of convective heat transfer coefficient and heat flux drops correspondingly. An interesting phenomenon is found that the distribution of growth rate of internal temperature gradient during the cooling process is wavy distribution, which indicates that the conduction heat transfer in the corn is thermal wave.

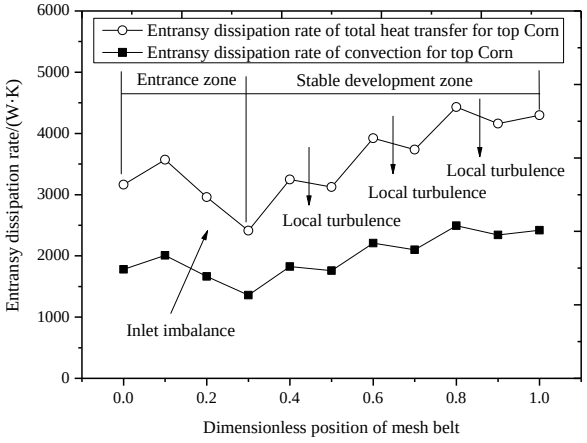

Figure 8 Entransy dissipation rate of surface corn based on effection analysis of radiation on convection

Figure 8 shows the distribution of entransy dissipation during cooling process of the top corn along quick freezer. It can be found that the entransy dissipation is also wavy distribution which shows the mechanism of combined heat transfer process of conduction, convection and radiation. The entransy dissipation rate of convection for the top corn is only part of total heat transfer process, which shows radiation affects the heat transfer process on the surface of corn significantly. On one side, radiation occupies a certain part of entransy dissipation rate, which means convective heat transfer can be weaken for the top layer corns which facing the evaporator and large radiation space. On the other side, the entransy dissipation caused by convection and radiation decreases or increases at the same time, the overall heat transfer can be enhanced synchronously.

Based on the entransy theory, the entransy dissipation rate represents heat transfer ability. For same heat transfer temperature difference or similar condition, the entransy dissipation achieves maximum when heat flux reaches peak and heat transfer can be enhanced. As shown in Figures 8 and 3, the heat flux and convective heat transfer coefficient is generally increasing in the cooling process along quick freezer, and the entransy dissipation rate achieves maximum at the outlet of precooling tunnel, which shows that the heat transfer process is overall enhanced with decreasing of heat transfer temperature difference. And based on the principle of extreme entransy dissipation, for the given heat flux, heat transfer process develops toward minimum entransy dissipation in temperature representation, which is also the principle of energy conservation. As shown in Figures 3, 4 and 8, when heat flux is constant during 0.4-0.5, 0.6-0.7 and 0.8-0.9, following the turbulence flow, the entransy dissipation rate reduces significantly with decreasing of surface temperature and heat transfer difference on the corn. While during 0.1-0.3, when the field synergy degree is relatively low with high temperature difference and slow velocity of fluid in porous medium, the entransy dissipation rate reduces significantly to push the heat transfer into small temperature difference heat transfer process with surface temperature dropping significantly combined with heat transfer difference decreasing dramatically, where the growth rate of temperature gradient is negative. The results show that the convective heat transfer process can be evaluate by convective heat transfer coefficient or entransy dissipation respectively, and the phenomenological characteristics is different.

Figures 9 and 10 respectively show the predicted cooling curve of centre temperature of corn in quick freezer 1 and 2 (Φ= *0.635*) based on the along heat transfer coefficient calculated by the entransy analysis model. As shown in Figure 9, for the convex cooling curve, the prediction by along heat transfer coefficient is more accurate with actual measurement than the average heat transfer coefficient. For the cooling curve in approximate straight line (or slightly concave), the prediction by along heat transfer coefficient and average heat transfer coefficient has similar accuracy. The results show that the correction coefficient $\Phi \approx 0.6$ is suitable for the corn with half part located in porous medium. And the result matches well with the experiment by Amarante (Amarante,2005).

However, it is worth noting that the maximum heat transfer coefficient reached in porous medium zone in precooling tunnel is 73.44 W/(m^2·K) for quick freezer 1 and 67.31 W/(m^2·K) for quick freezer 2, and the maximum convective heat transfer coefficient for top corn is 41.32 W/(m^2·K) and 42.72 W/(m^2·K) respectively, which shows little difference between two quick freezers. But the average convective heat transfer coefficient for top corn is 25.2 W/(m^2·K) and 34.43 W/(m^2·K) respectively, which indicates the difference is obvious. The results is significant for the optimization design, performance evaluation and improvement of the cooling and freezing machine.

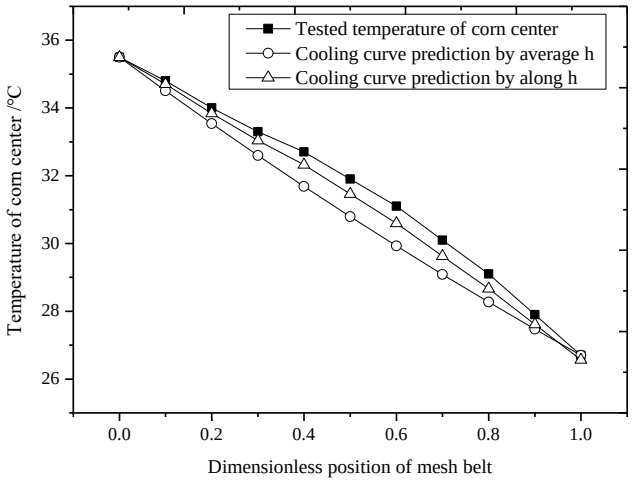

Figure 9 Prediction of cooling curve in convex shape for corn centre (quick freezer1)

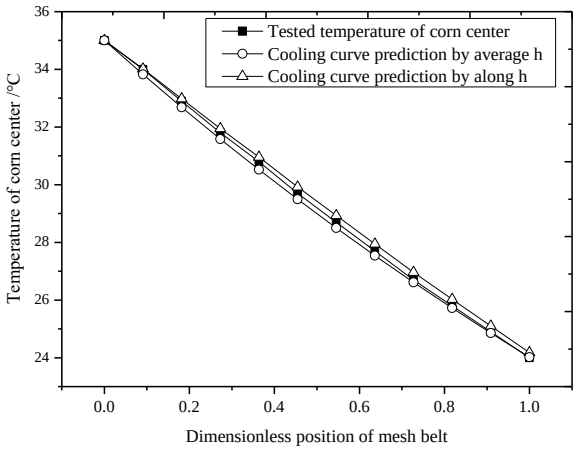

Figure 10 Prediction of cooling curve in approximate straight line for corn centre (quick freezer 2)

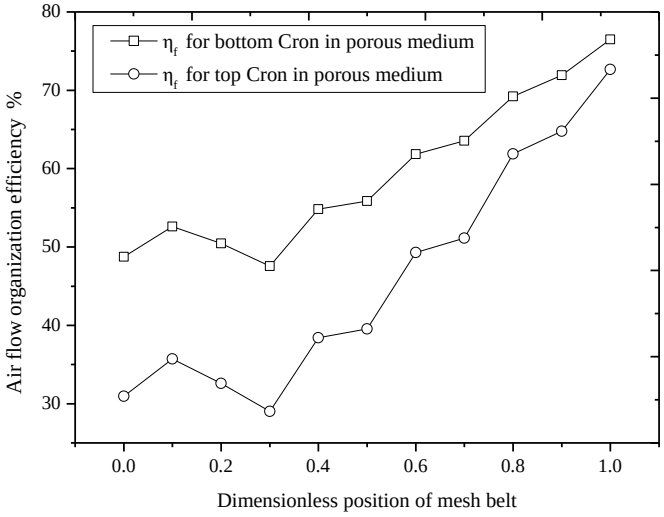

Figure 11 Air flow organization efficiency along the quick freezer

Figure 11 shows the airflow organization efficiency in porous medium zone of quick freezer and its trend is consistent with convective heat transfer coefficient but with some different characteristics. Generally, the airflow organization efficiency increases with convective heat transfer coefficient and drops down when convective heat transfer coefficient decreases. But the airflow organization efficiency is also consistent with velocity of fluid, the value of bottom corn in porous medium is always higher than the top corn, as the air flow enters porous medium form the bottom corn. But based on the field synergy principle, when flow is general normal to temperature gradient, the contribution of increasing of velocity of flow is fading or even dissipating. The mechanism of convective heat transfer coefficient is affected by temperature gradient as shown in Figure 7, which is also influenced by field synergy degree. As shown in Figure 5 and 11, at the rear part of precooling tunnel, the airflow organization efficiency for bottom corn is higher than the top corn, but convective heat transfer coefficient is lower than the later. As heat transfer temperature difference on the surface of top corn is smaller, which show that the synergy degree of temperature difference or temperature gradient with velocity is the key mechanism which influence the convective heat transfer process. Based on the second law of thermodynamics, the minimum heat transfer temperature difference corresponds to the minimum thermodynamic loss. The results show that optimized temperature difference is very important for design of cooling or freezing process in quick freezer. However, the airflow organization efficiency proposed in the paper can reflect the field synergy characteristics of heat transfer in a considerable extent.

4. CONCLUSION

In the paper, a new entransy analysis model of heat transfer process in porous medium is built, and a new utilization efficiency of entransy is proposed, meanwhile the field function characteristics of entransy are found. Based on this model, depending on the cooling curve, surface temperature of cooling corns in porous medium and convective heat transfer

coefficient along the quick freezer are predicted for the first time. Based on entransy theory, the coupling mechanism of conduction, convection and radiation in the heat transfer process is quantitatively evaluated. Based on the investigation of internal temperature gradient distribution in corn and the airflow organization efficiency in porous medium, field synergy characteristics of heat transfer process are researched. The main conclusions are as followings:

1) Based on the entransy analysis model of heat transfer process in porous medium, in which utilization efficiency of entransy is ideal Carnot efficiency, surface temperature of corn and along convective heat transfer coefficient in the precooling tunnel of quick freezer can be predicted, and simulation for the cooling curve indicates the entransy analysis model has accepted accuracy. The convex, straight or concave style cooling curve can be predicted by along heat transfer coefficient.
2) Internal temperature gradient distribution in corn affects the distribution of heat flux and heat transfer coefficient on surface of corn, and conduction, convection and radiation in heat transfer process has coupling mechanism. The simulation results show that scaling factor of heat transfer coefficient within and without porous medium is about 0.6, which matches well with the experiment by Amarante.
3) An interesting phenomenon is found that developing of heat transfer process of conduction in the corn or convection and radiation on the surface of corn is wavy distribution, which indicates that heat transfer is thermal wave.
4) The research results show that convective heat transfer process can be evaluate by convective heat transfer coefficient or entransy dissipation respectively, and phenomenological characteristics is different.
5) Temperature gradient and airflow organization efficacy can reflect field synergy characteristics to a considerable extent.

5. REFERENCES

Ajani CK, Zhu ZW, Sun DW, 2021. Recent advances in multiscale CFD modelling of cooling processes and systems for the agrifood industry. *Critical Reviews in Food Science and Nutrition*, 61(15), 2455-2470.

Alvarez G, Bournet PE, Flick D, 2003. Two-dimensional simulation of turbulent flow and transfer through stacked spheres. *International Journal of Heat and Mass Transfer*,46, 2459–2469.

Alvarez G, Flick D,1999. Analysis of heterogeneous cooling of agricultural products inside bins Part I: aerodynamic study. *Journal of Food Engineering*, 39,227–237.

Amarante A, Lanoisellé JL, 2005. Heat transfer coefficients measurement in industrial freezing equipment by using heat flux sensors.Journal of Food Engineering, 66(3), 377-386.

Ambaw A, Delele MA, Defraeye T, Ho QT, Opara LU, Nicolaï BM, Verboven P, 2013. The use of CFD to characterize and design post-harvest storage facilities: Past, present and future. *Computers and Electronics in Agriculture*, 93, 84-194.

Ambaw A, Mukama M, Opara UL, 2017. Analysis of the effects of package design on the rate and uniformity of cooling of stacked pomegranates: Numerical and experimental studies. *Computers and Electronics in Agriculture,* 136, 13-24.

Beer MD, Toit CGD, Rousseau PG, 2017. A methodology to investigate the contribution of conduction and radiation heat transfer to the effective thermal conductivity of packed graphite pebble beds, including the wall effect. *Nuclear Engineering and Design*, 314, 67-81.

Cheng GJ, Yu AB, 2013. Particle Scale Evaluation of the Effective Thermal Conductivity from the Structure of a Packed Bed: Radiation Heat Transfer. *Industrial & Engineering Chemical Research*, 52(34), 12202-12211.

Cheng XG, 2004. Entranspy and its application in heat transfer optimization. Beijing: Tsinghua University.

Comings EW, Clapp JT, Taylor JF, 1948. Air turbulence and transfer process. *Industrial & Engineering Chemistry*, 40(6), 1076–1082.

European Commission, 2011. Roadmap to a Resource Efficient Europe. Brussels, Belgium.

European Commission,2015. An EU Action Plan for the Circular Economy. Brussels, Belgium.

Guo ZY, Hu WL, Li ZX, Zhou SQ, Xiong DX, 1994, The effects of uniformity of temperature difference field on thermal performance of heat exchangers. International heat transfer conference 10, Brighton, UK,381-389,.

Guo ZY, Li DY, Wang BX, 1998. A novel concept for convective heat transfer enhancement. *International Journal of Heat and Mass Transfer*,41(14), 2221–2225.

Gustavsson J, Cederberg C, Sonesson Ulf, 2011. Global food losses and food waste-extent, causes and prevention. Food and Agriculture Organization (FAO) of the United Nations, Rome.

Huan ZJ, 2003. Performance evaluation indexes for quick-freezers. *International Journal of Refrigeration*,26, 817–822.

Ju M, Osako M, Harashina S, 2017. Food loss rate in food supply chain using material flow analysis. *Waste Management*, 61,443-454.

Li ZX, Xiong DX, Zhou SQ, 1995. Analytical and numerical study on the uniformity of temperature difference field in heat exchangers. *Journal of Thermal Science*, 4 (2), 104–108.

Liangdong Ma, Zengyao Li, Wenquan Tao, 2007. Experimental verification of the field synergy principle. *International Communications in Heat and Mass Transfer*, 34, 269–276.

Qian XD, Li Z, Li ZX, 2015. Entransy and exergy analyses of airflow organization in data centers. *International Journal of Heat and Mass Transfer*, 81, 252-259.

Redlingshöfer B, Coudurier B, Georget M, 2017. Quantifying food loss during primary production and processing in France. *Journal of Cleaner Production*, 164, 703-714.

Shahla MW, Natalie MM, 2018.Conserving natural resources through food loss reduction: Production and consumption stages of the food supply chain. *International Soil and Water Conservation Research*,6, 331-339.

Verboven P, Flick D, Nicolaï BM, Alvarez G, 2006. Modelling transport phenomena in refrigerated food bulks, packages and stacks: basics and advances. *International Journal of Refrigeration*, 29, 985-997.

#35: A novel hybrid multi-layer CdTe based PV ventilated window system integrated with phase change material: concept, construction and experimental investigation

Wei KE[1], Jie JI[2], Chengyan ZHANG[3], Hao XIE[4]

[1] Department of Thermal Science and Energy Engineering, University of Science and Technology of China, Hefei, Anhui, China, kewei@mail.ustc.edu.cn
[2] Department of Thermal Science and Energy Engineering, University of Science and Technology of China, Hefei, Anhui, China, jijie@.ustc.edu.cn
[3] Department of Thermal Science and Energy Engineering, University of Science and Technology of China, Hefei, Anhui, China, zcy19013@mail.ustc.edu.cn
[4] Department of Thermal Science and Energy Engineering, University of Science and Technology of China, Hefei, Anhui, China, xh1140@mail.ustc.edu.cn

Abstract: Aim to expand the functions of traditional building envelope windows and improve its thermal performance, a novel hybrid multi-layer CdTe based PV ventilated window system integrated with phase change material (abbreviated as CdTe-PCMVW) was proposed, constructed and experimentally investigated in this current work. Detailed fabrication process of the key component, the hybrid PV glass module integrated PCM (abbreviated as PCMG) was provided. Functions of electrical power generation, indoor passive space heating, heat preservation and ventilation cooling are integrated for this novel system, which can be realized by switching the operating modes. Different operating modes were established according to the ambient conditions and indoor thermal demands. Experiment platform was constructed and the PCMVW system was installed on it for experimental test. Two groups of continuous full-day experiments were conducted under the heating and non-heating season days. Main conclusions of the current study are: (1) Daily total electricity generation and average electrical efficiency were respectively 0.419 kWh, 0.423 kWh and 7.42 %, 7.40 % for the heating season days and 0.156 kWh, 0.159 kWh and 6.20 %, 6.33 % for the non-heating season days. (2) Utilization of PCM has realized thermal management of the PV glass, with the decrease and delay of peak temperature of PV glass. Thermal comfort rates (TCR) of the experimental room and reference room were respectively 25.51 %, 6.25 % and 37.45 %, 17.74 % for the two groups of experiment. (3) Effective lighting rates (ELR) of the novel system during the working time under the two groups of experiment were respectively 99.91 % and 98.52 %. The indoor daylighting performance of the PCMVW system was able to meet the demands of indoor daily work and life activities under the sunny days of both heating and non-heating season.

Keywords: Solar energy; BIPV/T; Ventilated window; Phase change material; Experimental test; Performance analysis.

1. INTRODUCTION

With the rapid development of urbanization and improvement of people's living standards for the indoor thermal comfort, urban residential buildings have gradually become one of the important sources of a country's total annual energy consumption and carbon emissions. According to the 2022 research report of China building energy consumption and carbon emissions released by China association of building energy efficiency (CABEE), in 2020, the energy consumption in building and construction was 2.27 billion tons of standard coal (tce), accounting for 45.5 % of the country's total energy consumption. The carbon emissions caused by the building and construction were 5.08 billion tce of carbon dioxide, accounting for 50.9 % of the country's total carbon emissions. Among them, the carbon emissions caused during the building operation were 2.16 billion tons of carbon dioxide, which has a proportion of 21.7 %. To reduce the building energy consumption and carbon emissions, it's significant to increase the utilization ratio of the renewable energy in buildings. Solar energy, due to its clean, pollution-free and renewable characteristics, makes its combination with building envelopes have great potential for building energy saving and carbon emissions reduction.

The technology of building integrated with photovoltaic/ thermal (BIPV/T) is a mature and efficient technique to take advantage of solar energy through the building envelope components, like wall, window and roof. In contrast to traditional rooftop solar modules, the PV modules in BIPV/T are built as part of the building body, which improves the buildings' integrity and aesthetics. As the least energy-efficient part of the building envelope, plenty of research have been focused on the performance enhancement and function diversification of building windows. Different types of PV cells have been utilized and investigated on the PV windows in the past several years. Generally, the PV cells applied on the window can be classified as the two main categories: crystalline silicon (c-Si) PV cells and thin-film PV cells. Chen et al. (2019) proposed a c-Si PV window system and installed it on the building room. Comparative experimental study was performed and the heat transfer, optical and electrical model was validated in southwest China. Research indicated that a maximum energy saving could be achieved with a PV coverage ratio of 0.87 and air gap of 9 mm. Peng et al. (2019) designed and fabricated a novel c-Si based semi-transparent BIPV laminate and investigated its energy performance. The solar heat gain coefficient of the combined BIPV laminate and insulated glass unit was 0.25. Tang et al (2022) proposed a novel reversible radiative sky cooling CdTe PV (RRC-PV) window system. Take the electricity generation into consideration, the annual comprehensive energy saving potential was 264.23 MJ/m2 over the common clear glazing window under the hot summer and warm winter climate of Shenzhen, China. According to the above literature review, the research on the development and optimization of novel PV window system has been an important approach to improve the thermal performance and expand the functions of traditional windows.

Recently, to enhance the poor thermal performance of the traditional single-layer building window, phase change material (PCM) has been combined and utilized in the novel smart window systems, due to its characteristic of large latent heat during phase change process, which can effectively decrease the indoor temperature fluctuation and improve the indoor thermal comfort. Zhong et al (2015) installed the PCM-filled glass window (PCMW) on a building and experimental results showed the thermal insulation and peaking cooling load shifting effects were remarkable. The optimal melting temperature of PCM recommended by the simulated results was 25 °C ~ 31 °C. Li et al (2018) investigated the effect of nanoparticle volume fraction and particle diameter of Nano-PCM on the temperature difference between the interior surface of the double glass unit containing PCM and indoor environment. Results indicated the minimal energy consumption can be achieved with nanoparticle concentration of 1% and diameter of 100 nm for all seasons. A PCM enhanced ventilated window (PCMVW) for ventilation preheating/ precooling purposes was proposed by Hu et al (2020) and experimental and numerical research have been performed. The building energy saving was up to 62.3% and 9.4% under the developed control strategies. Zhang et al (2022) proposed a novel reversible multiple-glazing roof integrated with two PCM, silica aerogel and low-e glass. Simulated results indicated that the new PCM-glazed roof could achieve an energy saving rate of 14.08% in summer and 33.74% in winter compared to the traditional roof. According to the existed research, the transparent glazing building envelope combined with the phase change energy storage technology has a promising potential to improve indoor thermal comfort and reduce energy consumption during the building's annual operation.

However, according to the above literature review, none research has been conducted on the combination of PCM and multi-layer PV ventilation window system which utilized the semi-transparent thin-film PV cells. In this current work, we proposed a novel CdTe based multi-layer PV ventilated window system with a middle PCM layer (abbreviated as CdTe-PCMVW), which integrated with the following functions: electrical power generation, passive space heating, heat preservation and ventilation cooling. Compared with the traditional CdTe PV window, power generation performance can be enhanced by the PCMVW due to the cooling management on the PV glass by PCM. Besides, the utilization of PCM can improve the indoor thermal comfort as well. While the electrical and thermal performance of the window system were enhanced, the indoor lighting can still satisfy the demand of indoor daily work and life. Different operating modes were defined according to the ambient condition and corresponding indoor thermal demands. An outdoor experimental platform was constructed in Hefei and two groups of seasonal experiments were conducted. Electrical, thermal and indoor lighting performance of the novel system were analysed and discussed in this present work.

2. SYSTEM DESCRIPTIONS AND WORKING PRINCIPLES

In this section, system structure of the novel CdTe-PCMVW system was introduced and detailed fabrication process of the key component (PCMG) was provided. Specific working principles of the system under different operating modes were explained.

2.1. Fabrication of the PCMG module

As shown in Figure 1, the main key components of the CdTe-PCMVW include the outermost CdTe PV glass, middle PCM layer, outer clear glass and inner clear glass from the outside to the inside. The middle PCM layer is sandwiched by the CdTe PV glass and the outer clear glass. The novel CdTe-PCMG module was designed and fabricated by the author. An air channel is established by the outer and inner clear glass and airflow enters the air channel through the lower air inlet and leaves through the upper air outlet. Hence, the natural air ventilation circulation between the indoor room air and air channel is established. The figure also shows the diagram of the installation of the CdTe-PCMVW on the south wall of the experimental building room. Two vents were left at the upper and lower ends of both indoor and outdoor sides, and eight ventilation baffles were set up for the switching of different operating modes, which will be introduced in detail in the following section.

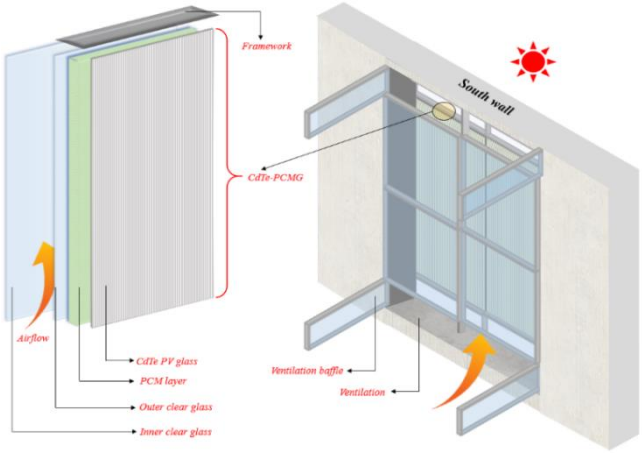

Figure 1 Structural composition and installation diagram of the CdTe-PCMVW system

For the fabrication process of the CdTe-PCMG module, the detailed flow chart is shown in Figure 2. Firstly, the CdTe PV glass and clear glass are glued together with glass glue, leaving a 2 cm hollow interlayer in the middle, which was left for the PCM. The middle PCM layer is sandwiched by the outermost PV glass and innermost clear glass and the four sides are wrapped by the acrylic sheets and stainless steel. The acrylic sheet has a thickness of 0.45 cm and was laser cut into strips with a dimension of 60 cm long and 3 cm wide to serve as the internal frame. Thickness of the inner clear glass is 0.32 cm. On the periphery of the acrylic frame, a stainless steel frame is used for edging to ensure the rigidity and strength of the composite PV glass module. After combining the CdTe PV glass and clear glass, we melt the PCM in the resistance furnace and inject it into the hollow interlayer after complete melting. Then, a layer of waterproof glue is applied on the outside of each acrylic sheet and glass joint to ensure the sealing of the module and prevent the PCM from leaking out when it is in liquid state. Finally, after all these were done, the top side was also encapsulated by acrylic sheet and stainless steel. Particularly, the bottom four corners need to be strictly leak-proof. The main component of the utilized PCM in this current study is n-octadecane with a concentration of over 99%. Melting temperature of the PCM is around 28 °C and latent heat is around 250 J/g. When the PCM is completely melted and in the liquid state, it's a kind of colourless, transparent liquid and has a good transmittance to light. Therefore, combining the PCM with the transparent CdTe PV glass can realize the effects of improving the indoor thermal comfort, reducing the PV glass temperature fluctuation without affecting the lighting (in the liquid state during the daytime) and improving the PV electrical output of the PV cells.

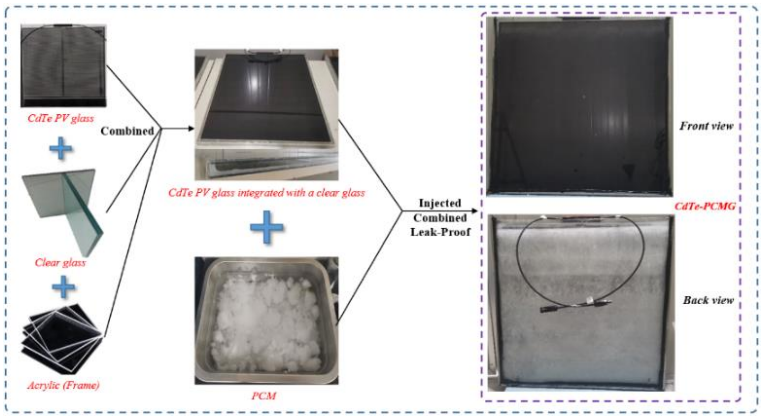

Figure 2 Detailed fabrication process of the CdTe-PCMG module

2.2. Experiment platform of the PCMVW system

Two comparable hot-box type room were built on the rooftop of a building in the campus of University of Science and Technology of China Hefei (32° N, 117° E), China, for the comparative experimental tests. The CdTe-PCMVW is installed on the south wall of a hot-box type room, and the rest one is used as the blank reference room. The two rooms are completely identical except for the novel window system is installed on the south wall of the experimental room. The structure diagrams of the two rooms and installation position of the CdTe-PCMVW are shown in the following Figure 3 (a). The internal geometry dimensions of the two rooms are both 3m long, 3m width and 2.6m height. Thickness of the envelope wall is 10 cm. The envelope wall is a kind of light insulation wall. In order to reduce the influence of the ambient environment on the other walls of the room (east wall, west wall, north wall and roof), and then affect the indoor thermal environment, a layer of wall is added on the periphery of the hot box room. The width of the corridor mezzanine is 60cm, and each room has two doors. Specific dimensions and room structures can be seen in the following diagram. The actual photos of the experimental and reference room are shown in Figure 3 (b). The outdoor views of the reference room and experimental room are displayed.

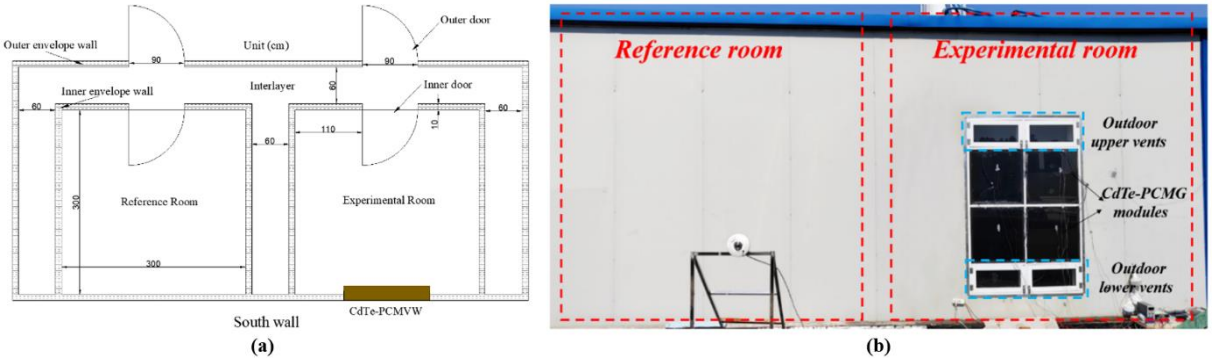

Figure 3 (a) Structure diagram of the two comparable hot-box type rooms; (b) Actual photos of the outdoor views of the experimental and reference room

2.3. Working principles

When the solar radiation is projected on the outermost PV glass, part of the radiation is converted into electrical energy output, and the other part is absorbed by the PV glass, which caused the temperature rise. Heat is transferred from the outside to the inside along the thickness direction, eventually entering the room. According to the ambient weather conditions and practical indoor thermal comfort demands, the operating modes of the novel proposed CdTe-PCMVW are mainly divided into two parts: operating modes in the heating season and non-heating season.

For the heating season, due to the lower ambient temperature for the whole day, the space heating and heat preservation are necessary. During the daytime, vents a ~b are kept closed while vents c ~d are kept opened and the space heating (SH) mode is run, as shown in Figure4 (a). The indoor cool air enters the air channel through vent d and heated by convection heat transfer between the internal surface of the PCMG. Under the impacts of thermosiphon effect, the airflow climbs upward and finally re-enters the indoor room through vent c. In this way, the internal air circulation between room air and air channel is established and room air is heated by repeated cycles. When the solar radiation is reduced to close to 0, the PCM turns from heat sink to heat source, releasing the latent heat stored during daytime to the inner clear glass,

so as to avoid the temperature of the inner glass falling too low. During the nighttime, all the vents are kept closed to reduce the heat loss of indoor room as much as possible and the heat preservation (HP) mode is run, as shown in Figure4 (b). The closed air channel and middle PCM layer can both enhance the heat preservation capacity of the window system. Functions of the system in the heating season mode mainly include: electrical power generation, passive space heating and heat preservation.

For the non-heating season, due to the relatively higher ambient temperature, ventilation cooling is necessary for the whole day. Therefore, both for the daytime and nighttime of the non-heating season days, vents a ~b are kept opened and vents c ~d are kept closed. The ventilation cooling (VC) mode is run, as shown in Figure 4 (c). The ambient air enters the air channel through vent b and takes away the heat of PCM and internal clear glass to decrease the indoor cooling load. The external air circulation between the ambient air and airflow is established. Functions of the system in the heating season mode mainly include: electrical power generation, thermal insulation and ventilation cooling.

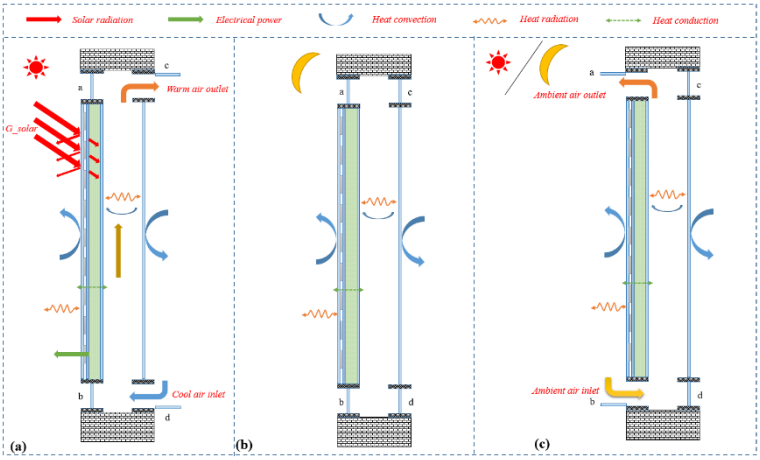

Figure 4 Schematic diagrams of different operating modes and corresponding energy flows of the system

3. PERFORMANCE EVALUATION PARAMETERS

For the electrical performance evaluation, electrical efficiency (η_e) is introduced to evaluate the photoelectrical conversion efficiency and is defined as:

Equation 1: Electrical efficiency (η_e)

$$\eta_e = \frac{E_{PV}}{G_{solar}\xi A_{pg}}$$

Where:

- E_{PV} = instantaneous electrical output power (W)
- G_{solar} = solar radiation intensity on the vertical south façade (W/m^2)
- ξ = PV coverage
- A_{pg}= area of the PV glass surface (m^2)

For the indoor thermal performance evaluation, thermal comfort rate (TCR) is introduced. It represents the rate of the time length that the room air temperature is in the comfortable temperature range occupied the total time length. The indoor comfortable temperature range for the human body in this study is set as 18 °C~ 25 °C in this current work. It's defined as:

Equation 2: Thermal comfort rate (TCR)

$$TCR = \frac{\Delta\tau_{comfort}}{\tau_{total}}$$

Where:

- $\Delta\tau_{comfort}$= time length when the room air was in the comfortable range (18 °C~ 25 °C) (min)
- τ_{total} = total experimental period length (min)

For the indoor lighting performance evaluation, the effective lighting rate (ELR) is introduced, which represents the rate of the effective lighting (100 lux ~ 2000 lux) among the investigated experimental period. It's defined as:

Equation 3: Effective lighting rate (ELR)

$$ELR = \frac{\Delta\tau_{effective}}{\tau_{total}}$$

Where:

- $\Delta\tau_{comfort}$= time length when the indoor illuminance was in the effective range (100 lux ~ 2000 lux) (min)
- τ_{total} = total experimental period length (min)

4. RESULTS AND DISCUSSIONS

Based on the established operating modes, two groups of continuous full-day experiments were respectively conducted in February and May in 2023, which both lasted for 48 hours. For the first group of experiment, it was conducted from 0:00 on 26th to 24:00 on 27th in February. The ambient condition is shown in Figure 5 (a). The ambient temperature was in the range of 2 °C to 16 °C and the daily total solar radiation received by the outer PV glass was respectively 25.85 MJ and 26.23 MJ. The two days were typical cold and sunny days in the heating season of Hefei. The SH mode was run during the daytime and HP mode was run for the rest time. For the second group of experiment, it was conducted from 0:00 on 14th to 24:00 on 15th in May. The ambient condition is shown in Figure 5 (b). The ambient temperature was in the range of 20 °C to 36 °C and the daily total solar radiation was respectively 11.49 MJ and 11.40 MJ. The amount of total received solar radiation was lower than the first group, which was caused by the higher solar altitude angle in the summer of Hefei. The two days were typical hot and sunny days in the non-heating season of Hefei. The VC mode was run for the total experimental period.

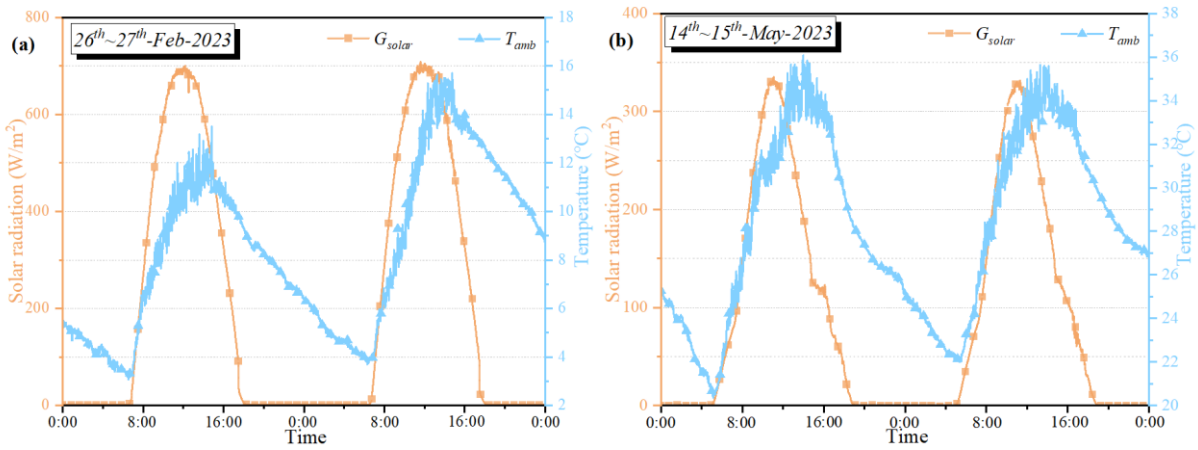

Figure 5 Ambient conditions of the two groups of experiment test: (a) 26th~ 27th, February, 2023; (b) 14th ~ 15th, May, 2023

4.1. Electrical performance

For the PV window system, electrical power generation is one of the most significant functions. The electrical power (E_{PV}) and electrical efficiency (η_e) of the PCMVW system under the two operating modes are shown in the following Figure6 (a) ~ (f). For the first group of experiment in the heating season, as shown in Figure 6 (a) ~ (c), the daily total E_{PV} of the window system was respectively 0.419 kWh and 0.423 kWh and daily average η_e was 7.42 % and 7.40 % for the two days. The maximum E_{PV} and η_e for the two days were respectively 59.42 W, 61.10 W and 8.21 %, 8.51 %. For the second group of experiment in the non-heating season, as shown in Figure6 (d) ~ (f), the daily total E_{PV} of the window system was respectively 0.156 kWh and 0.159 kWh and daily average η_e was 6.20 % and 6.33 % for the two days. The maximum E_{PV} and η_e for the two days were respectively 26.65 W, 24.75 W and 8.22 %, 7.93 %. Compared with the non-heating season days experiment, the system has achieved a better electrical performance in the heating season, due to the lower solar altitude angle. Besides, the utilization of the middle PCM layer can realize the cooling management of the PV glass, by absorbing the heat of PV glass and storing as latent heat, which can enhance the electrical output of the PV module. The cooling effect will be analysed in the next section.

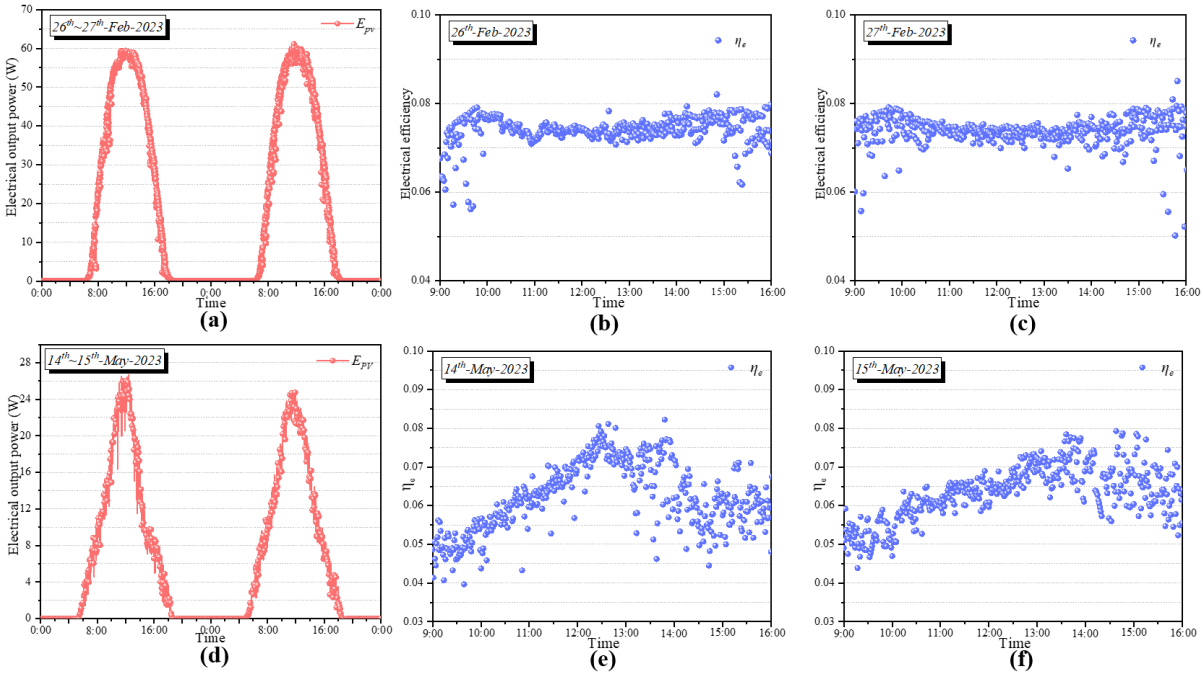

Figure 6 Electrical performance of the novel system during the two experiment tests

4.2. Thermal performance

For the thermal performance, temperature of the outermost PV glass, PCM layer, outer and inner clear glass, exterior and internal wall surface, air inlet, air outlet and indoor room air were all measured and displayed in the following Figure 7 (a) ~ (h). For the first group of experiment in the heating season, compared with the PV glass for reference, the maximum temperature of PV glass was respectively reduced by 3.67 °C, 5.46 °C and delayed by 13 min and 18 min. The utilization of PCM has played an effective role in cooling the PV glass. Besides, for the cold days, due to the existence of PCM layer, the PV glass has maintained a higher temperature during nighttime, which can prevent the indoor room air temperature from dropping too low. The wall surface temperature was shown in Figure 7 (b). The internal surface temperature of the reference room was always lower than the experimental room, which was caused by the effective space heating performance of the PCMVW system. The only heat source of the indoor room air of the reference room was the convection heat transfer with the internal wall surface. Temperature of the air inlet and outlet was shown in Figure 7 (c). As the figure shows, the outlet temperature was higher than the inlet for most time, which proves the effective heating function of the PCMG module on the airflow. The maximum temperature difference was 5.67 °C and 5.59 °C for the two days. For the room air temperature, the experimental room (in the range of 5.35 °C ~ 25.91 °C) was always higher than the reference room (in the range of 4.37 °C ~19.02 °C). The temperature difference was in the range of 0.88 °C ~ 8.11 °C. The system has achieved effective functions of space heating during daytime and heat preservation during nighttime. The TCR of the experimental room and reference room was respectively 25.51 % and 6.25 %, with an increase ratio of 308.16 %. Compared with the reference room, the utilization of the PCMVW system has greatly improved the indoor thermal comfort.

For the second group of experiment in the non-heating season, compared with the PV glass for reference, the maximum temperature of PV glass was respectively reduced by 2.25 °C, 2.43 °C and delayed by 43 min and 54 min. The PCM has also played a role in cooling PV glass during in the non-heating season days, which was beneficial for the improvement of photoelectric conversion efficiency. The internal south wall surface of the reference room was higher than other internal surfaces of the experimental room. For the airflow, the air outlet temperature was also higher than the air inlet in most time, with a temperature difference in the range of -1.51 °C ~ 2.20 °C. For the indoor room air temperature, as shown in Figure 7 (h), the experimental room (in the range of 21.16 °C ~34.15 °C) was always lower than the reference room (in the range of 23.32 °C ~ 36.96 °C). The temperature difference was in the range of -4.25 °C ~ -1.22 °C. The TCR of the experimental room and reference room was respectively 37.45 % and 17.74 %, with an increase ratio of 111.10 %. Results indicated that the PCMVW system achieved an effective function of ventilation cooling under the VC mode in the non-heating season days. On the whole, the novel system was more effective in providing indoor space heating and heat preservation functions in the colder days during the heating season.

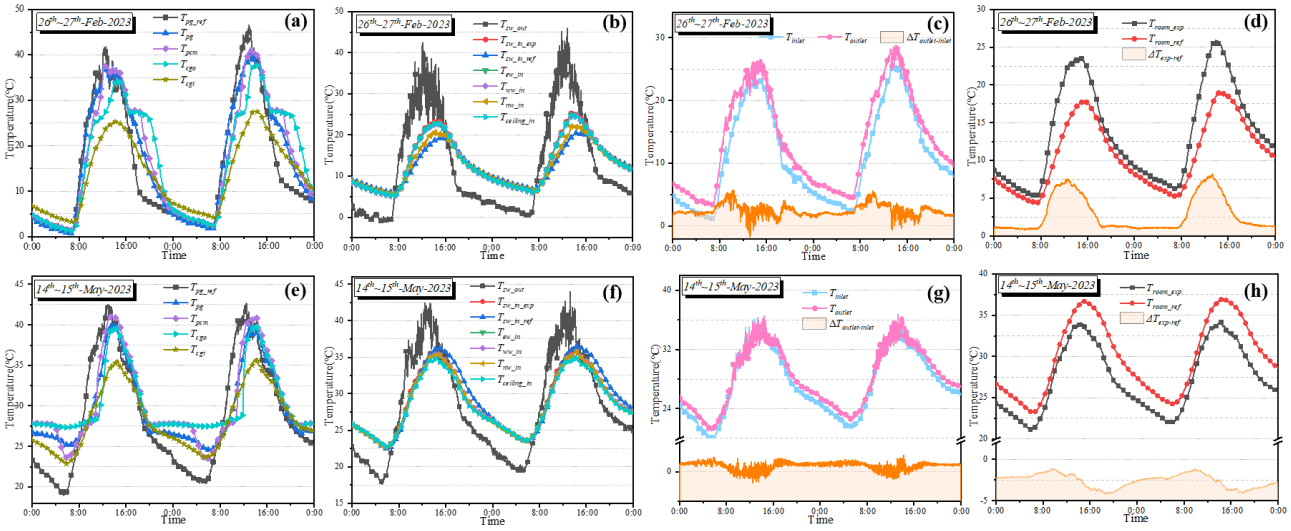

Figure 7 Thermal performance of the novel system during the two experiment tests

4.3. Indoor lighting performance

For a window system, indoor lighting is one of its most basic and significant functions. For this novel hybrid window system, the outdoor light can mainly reach the indoor through the following two paths to satisfy the indoor lighting demands: one is through the indoor upper and lower vents; the other path is through the PCMG modules. Therefore, for the indoor room installed with the CdTe-PCMVW, the indoor lighting performance would be affected by the solar radiation and the melting state of PCM. As shown in the following Figure 8, when the PCM begins to melt, it has little effect on the indoor lighting due to the PCM's transparent characteristic. After the PCM was in the complete melted stats (pure liquid), it has no influence on the indoor lighting. On the contrary, the semi-transparent characteristic of the CdTe PV glass can effectively reduce the possibility of indoor dazzle phenomenon in the sunny days.

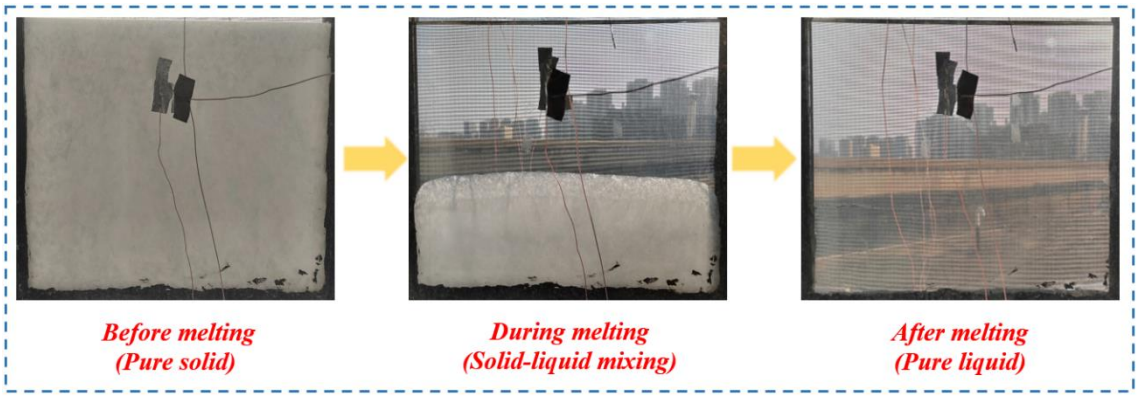

Figure 8 Melting state of the PCM and corresponding indoor view of the novel window system

To quantitatively evaluate the indoor lighting performance, the illuminometer was placed in the experimental room to test the indoor illuminance. The illuminometer was placed one meter away from the window (inner clear glass) and 76cm above the ground (usually the height of the desktop in the office). Figure 9 shows the indoor illuminance during the whole experimental period for the two groups of experiments under the heating and non-heating season days. For the Group I in the heating season, as shown in Figure 9 (left), during the daytime, the indoor illuminance can achieve a maximum value of 575 lux, and the ELR during the working time (from 8:00 to 17:00) was 99.91 %. For the Group II in the non-heating season, as shown in Figure 9 (right), during the daytime, the indoor illuminance can achieve a maximum value of 323 lux, and the ELR during the working time was 98.52 %. In conclusion, both for the sunny days of heating and non-heating season, the indoor daylighting performance of the PCMVW system was able to meet the demands of indoor daily work and life activities.

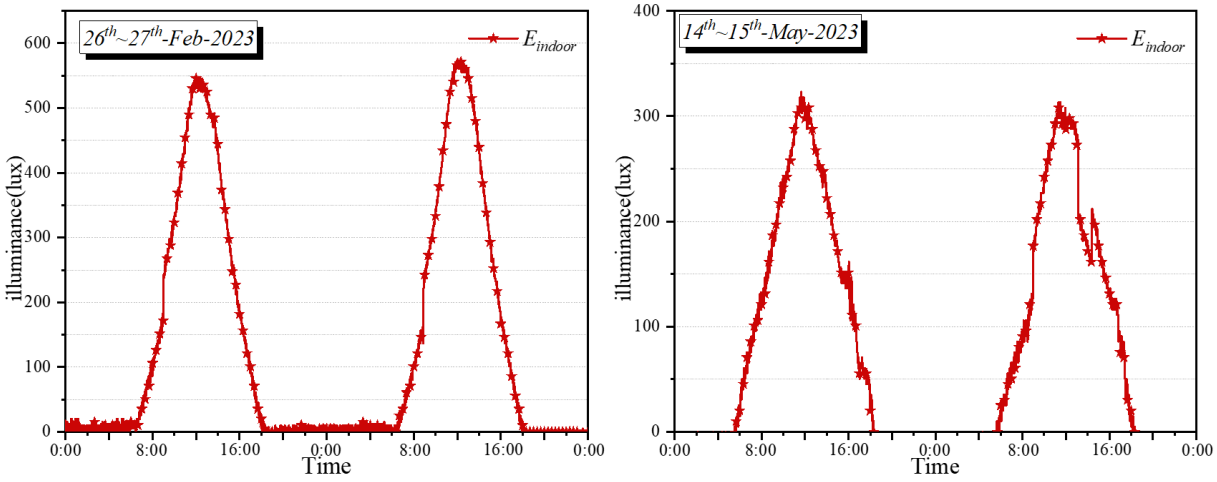

Figure 9 Indoor illuminance of the experimental room

5. CONCLUSION

In this current work, a novel hybrid CdTe based multi-layer PV ventilated window system integrated with PCM (abbreviated as CdTe-PCMVW) is proposed and constructed. According to the ambient conditions and corresponding indoor thermal demands, different operating modes were established and corresponding continuous full-day experiment tests were conducted in two comparable hot-box room test platforms to evaluate the system's comprehensive electrical, thermal and lighting performance. TCR is utilized to analyse the indoor thermal comfort and ELR is introduced to evaluate the indoor lighting performance. Main conclusions of this current experimental study are shown as the follow:

- For the electrical performance, the daily total electricity generation and average electrical efficiency were respectively 0.419 kWh, 0.423 kWh and 7.42 %, 7.40 % for the heating season days experiment and 0.156 kWh, 0.159 kWh and 6.20 %, 6.33 % for the non-heating season days experiment. The system has achieved better electrical performance in the heating season days for the lower solar altitude angle.
- For the thermal performance, the utilization of PCM has realized cooling management of the PV glass, with the decrease and delay of peak temperature of PV glass. Besides, the system has also achieved effective functions of space heating, heat preservation for the heating season mode and ventilation cooling for the non-heating mode. The TCR of the experimental room and reference room were respectively 25.51 %, 6.25 % and 37.45 %, 17.74 % for the two groups of experiment. The utilization of the novel PCMVW system has greatly improved the indoor thermal comfort, compared with the reference room.
- For the indoor lighting performance, the ELR of the novel system during the working time under the two groups of experiment were respectively 99.91 % and 98.52 %. The indoor daylighting capacity of the PCMVW system was able to meet the demands of indoor daily work and life activities under the sunny days of both heating and non-heating seasons.

Nevertheless, several problems might be faced in the practical application of the novel CdTe-PCMVW system. Firstly, although PCM is colourless and transparent after complete melting, for some cloudy, overcast or rainy days, the radiation intensity is low and PCM cannot be completely melted. In this case, the indoor lighting demand might be affected to some extent. Secondly, for some extreme days in summer (too hot) and winter (too cold), the PCM might always be in the liquid or solid days, thus the effects of thermal management on the PV glass and thermal regulation of indoor room air would be weakened. Besides, the total cost of this complete system is another disadvantage, especially reflected by the prices of the PV glass and PCM material. In the future, with the advancement of manufacturing processes and the reduction of costs, the cost of this system might be reduced, which is beneficial for the practical application. Anyhow, this newly proposed system still provides an effective way of organic combination of phase change energy storage technology and the translucent building envelope based on the comprehensive PV/T utilization of solar energy.

6. REFERENCES

Chen M et al. (2019) Experimental and numerical evaluation of the crystalline silicon PV window under the climatic conditions in southwest China, Energy,183:584-98.

Hu Y et al. (2020) Performance and control strategy development of a PCM enhanced ventilated window system by a combined experimental and numerical study. Renewable Energy, 155:134-52.

Li D et al. (2018) Energy investigation of glazed windows containing Nano-PCM in different seasons. Energy Conversion and Management,172:119-28.

Peng J et al. (2019) Study on the overall energy performance of a novel c-Si based semitransparent solar photovoltaic window. Applied Energy, 242:854-72.

Tang H et al. (2022) Experimental and numerical study of a reversible radiative sky cooling PV window. Solar Energy, 247:441-52.

Zhang S et al. (2022) Thermal performance of a reversible multiple-glazing roof filled with two PCM. Renewable Energy, 182:1080-93.

Zhong K et al. (2015) Simulation study on dynamic heat transfer performance of PCM-filled glass window with different thermophysical parameters of phase change material. Energy and Buildings,106:87-95.

#39: Evaluation of photovoltaic/thermal radiative cooling (PVT-RC) system for closed-loop hydronic cooling of PV panels in the hot and arid region

Hazim DIRAWI[1], Mingke HU[2], Michele BOTTARELLI[3], Yuehong SU[4]

[1]Department of Mechanical Engineering, University of Nottingham, Nottingham NG7 2RD, UK, alyhd5@nottingham.ac.uk
[2]Department of Mechanical Engineering, National University of Singapore, Singapore, mingke.hu@nus.edu.sg
[3] Department of Architecture, University of Ferrara, via Quartieri 8, 44121 Ferrara, Italy, michele.bottarelli@unife.it
[4]Department of Architecture and Built Environment, University of Nottingham, Nottingham NG7 2RD, UK, yuehong.su@nottingham.ac.uk

Abstract: Photovoltaics/thermal radiative cooling (PVT-RC) system generates both electricity and thermal energy from solar radiation. However, the performance of PV panels can be limited by high operating temperatures, leading to reduced power output and decreased efficiency. To address this issue for hot and arid climates, a closed-loop hydronic cooling system is proposed to enhance the performance of PV systems. The system consists of a PV collector mounted on the cooling panel of a closed-loop hydronic system, which includes a water tank as a thermal buffer for diurnal heat/cold storage. This study focuses on analysing the design of the closed-loop hydronic cooling system, encompassing the heat transfer fluid, tubing, and evaluating the system's performance by investigating the effects of various parameters on its design and operation. The study analysed various parameters, such as the size of water storage tank and different tank shapes of the same capacity. A 3D CFD simulation was employed to assess the effects of these parameters, aiming to determine the optimal system design and operation. The primary design parameter of the proposed system is the total water amount, with larger tank capacities proving beneficial. Modifying the shape of the storage tank further enhances photovoltaic efficiency. According to the comprehensive evaluation, the suggested system is appropriate for dry and hot regions with significant diurnal temperature variations. This study found that eliminating the PE cover and insulation from PVT-RC modules can substantially enhance power production by up to 20% compared to conventional designs and 14% compared to PVT-RC design with PE and cover, respectively. The results of this study offer valuable insights into the design and performance of closed-loop hydronic PV cooling systems and the optimal selection of parameters to improve overall efficiency.

Keywords: PV cooling; Closed-loop hydronic system; Radiative cooling; COMSOL modelling.

1. INTRODUCTION

The global concern about developing sustainable energy sources has grown rapidly day by day, owing to the importance of meeting worldwide energy shortages as well as mitigating the effects of climate change. Solar cell technology is regarded as an important player in the sustainable power landscape across these sources. Photovoltaic (PV) systems immediately convert solar energy into electrical power by harvesting sunlight, potentially providing a sustainable and environmentally friendly solution (Hasanuzzaman et al., 2015). On the other hand, just a portion of the incident energy can be transformed into useful electrical power, with the rest constituting wasteful thermal energy that accumulates inside the solar cell, producing a rise in solar cell temperature (Dubey and Tiwari, 2009; Teo et al., 2012). The conversion efficiency of PV is observed to decline by 0.5% for each degree increase in PV temperature (Skoplaki and Palyvos, 2009; Soliman et al., 2019). As a result, PV efficiency represents strongly influenced by cells operating temperature. Numerous approaches have been devised and investigated to maintain the PV module at an ideal operating temperature and ensure its optimal functionality. The choice of these approaches is influenced by factors such as the type of PV cell, prevailing climate conditions, and utilizing the generated heat for temperature regulation within the PV unit. Research indicates that the implementation of an appropriate cooling method has the potential to extend the lifespan of a PV module from 25 to 48 years (Royo et al., 2016; Soliman and Hassan, 2018). Both active and passive cooling techniques are utilized for controlling the temperature of the PV panel, each with its own set of advantages and disadvantages.

Numerous studies have extensively examined active cooling techniques that employ energy-driven devices like pumps or fans, including channel and spray cooling. According to Bahaidarah et al.(2013) active water cooling of PV module cans results in a 20% drop in cell temperature, about 9% improvement in efficiency, and higher power production efficiency. A number of researchers have developed new PV cooling techniques, such as photovoltaic and thermal (PV/T) panels. Balochet al.(2015) investigated the use of a converged channel in PV module to produce more uniform temperature. Seven angles were simulated and evaluated, with the best results achieved at a 2° converged angle. Thermal studies revealed that during a real hot June day and cold December day, PV module temperature could be decreased by about 26 °C and 12 °C, respectively. Aside from thermal assessment, the uncooled and cooled units were economically evaluated. The cooling technology reduced the net energy price of electricity from 1.95 (€/kWh) to 1.57 (€/kWh). Therefore, the continual cooling process with air leads, even in different percentages, to decreasing the solar system temperature and improving its efficiency. Passive cooling techniques are preferred in certain situations due to their ease of use (Qu et al., 2018), cost-effectiveness, and ability to conserve materials (Soliman and Hassan, 2019). These techniques, however, have drawbacks in that they lack control and have a limited capacity for managing heat, thereby falling short of meeting some requirements of PV devices. Passive cooling techniques include phase change material (PCM), air, liquid and radiative-based approaches. Thus, PCMs are explored as a way to decrease PV cells surface temperature during sunlight hours to improve the cells electrical efficiency (Waqas and Jie, 2018). One of the most significant findings of their study is a 10% increase in cell efficiency due to a 30°C drop in cell temperature. Moreover, they observed that PCMs cooling is more effective when having at least temperature differential of 10-12°C between their melting point and lowest ambient temperature especially during the hottest months of summer.

A balanced solution that can offer the thermal loads of the PV system while competing the weaknesses in other cooling methods, was proposed as the hybrid system. This system effectively integrates active and passive methods, resulting in a new regulated thermal load-controlled technique with minimum cost and energy ability to store which could be applied in multiple kinds of as-needed applications. The choice of system will depend on the size of the PV array, the climate, and the desired level of efficiency. (Browne et al., 2016) studied an outdoor experiment to investigate the impact of utilising PCM materials on the electrical efficiency of a PV/T hybrid module. A thermosyphon closed-loop flow technique was used to circulate water via the heat exchanger incorporated in PV/T module. Moreover, the data confirmed that coupling PCM with PV/T system reduced PV temperature by about 5 °C when compared to a PV/T module without PCM. Hu et al. (2018)proposed a new PV/RC idea based on a selective plate. This effect, unfortunately, cannot lower panel temperature below 5.2 C in diurnal due to the high solar irradiation, restricting the efficiency improvement (Zhu et al., 2015). Hu et al. (2020) and Zhao et al. (2019a) have demonstrated that the nocturnal temperature decrease of a standard PV system could reach as high as 11°C under ambient temperature with no changes on top cover. Later, (Zhao et al., 2019b) refined the radiative cooling concept design by using water circulation as a secondary cooling method. Thus, if the nocturnal cooling of PV unit is utilized for cooling water, and a significant amount of cold water could be gathered and used for PV unit cooling throughout the day, the total performance of the system's harvested energy will be considerably boosted (Yoon et al., 2022).

In this study, we proposed a design for a closed-loop hydronic PV cooling system and evaluated its performance through a simulation study. We developed a validated 3D time-dependent CFD model to conduct a comprehensive analysis of heat exchange for each layer in the PV panel, considering a closed-loop system that utilizes water as a coolant for both day and night operation. The cooling water is contained within an insulated tank connected to the PV system through pipelines. The numerical analysis for this 3D system is a rare approach for such a large-scale system, providing critical insights and information to better understand the heat transfer process. Various modelling cases, including different tank sizes and shapes within control strategies, were investigated and simulated to identify the optimal system design. This study contributes to further research in cooling systems, aiming to find the best designs tailored to specific applications and ambient conditions. Finally, the proposed PVT-RC cooling system offers a sustainable and cost-effective solution to enhance the performance of PV modules, especially when removing the PE cover with insulation. This approach is particularly effective in hot and dry climate regions.

2. DESCRIPTION OF SYSTEM AND MODELLING

In comparison to a common flat PV panel (Figure 1), the proposed closed-loop hydronic PV cooling system adopts a PVT-RC module which applies radiative cooling design and consists of several layers, as shown in Figure 2. The collector is comprised of a polyethene (PE) cover, a PV plate, an absorber plate, a tube, working fluid, and insulation. There is one air gap between the cover and PV plate and seven copper water tubes are joined to the absorber's bottom side, as shown in Figure 3.

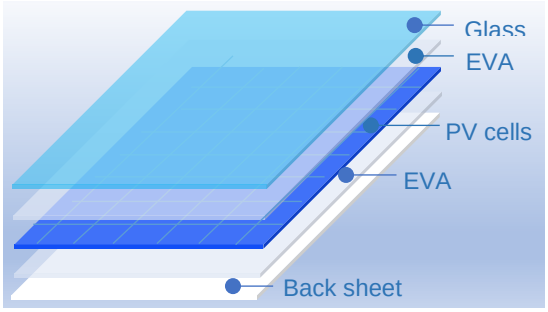

Figure 1 Common flat PV panel components.

The PV-RC panel's efficient area for gathering radiation is 0.964 x 1.964 m^2, while the area occupied by the cells is 1.12 m^2. The PV panel is made up of 72 individual cells, and the remaining surface of the absorber plate is coated with black paint. A mono-crystalline silicon cell with 13.5% theoretical conversion efficiency is chosen, as is standard in this type of system. The glass cover often used in PV is an inadequate windscreen for RC devices. Because of its excellent transmissivity in most bands, polyethene film is used to cover the PVT-RC panel (Zeyghami et al., 2018).

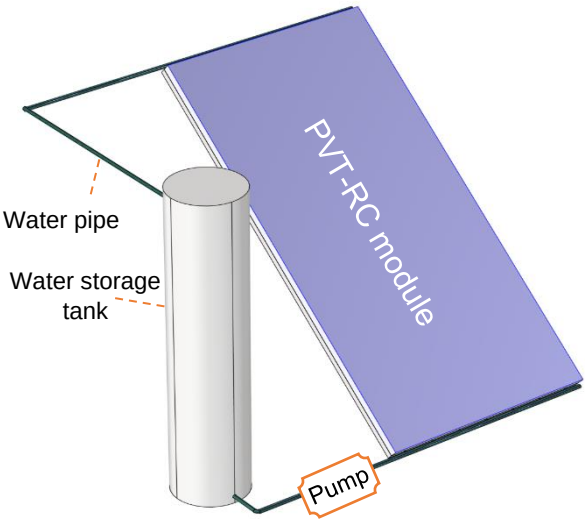

Figure 2 Schematic view for a closed-loop hydronic PVT-RC system.

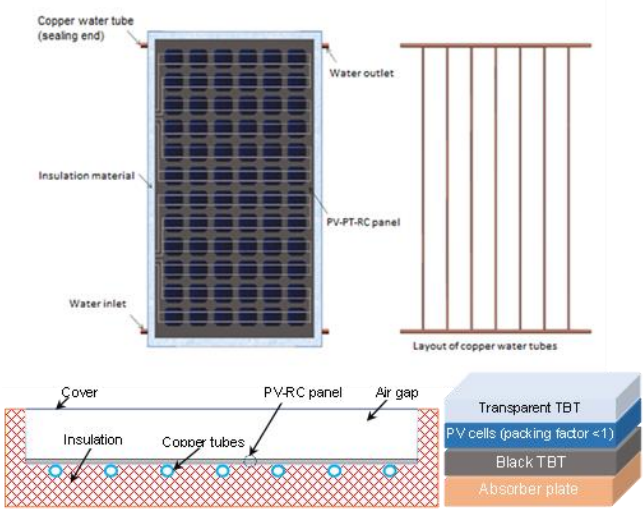

Figure 3 Layout of PVT-RC panel (a) top views of the panel with a water tube (b) Cross-section view of the panel.

3. MATHEMATICAL MODEL OF PVT-RC SYSTEM

A mathematical model of PV module has been developed to evaluate PV performance by operating the energy equations in dynamic-state conditions, considering the energy influx rate and energy outflux rate within each layer of the PV system. The scheme of energy exchange of the main components of the PV collector is represented in Figure 4Figure .

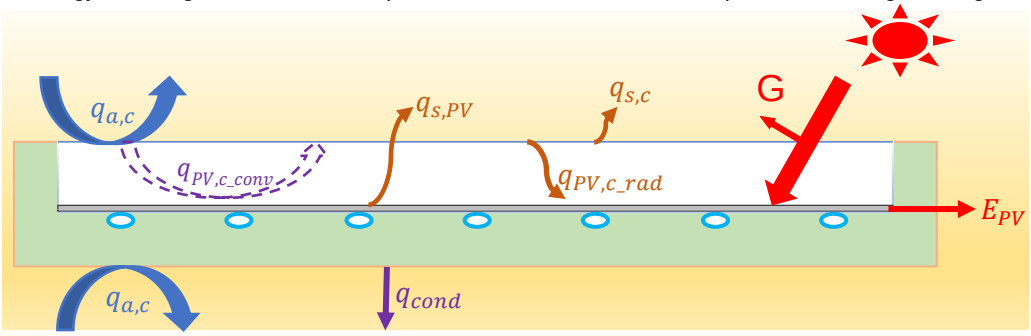

Figure 4 Illustration of heat transfer balance at PVT-RC collector.

A time-dependent study is performed on the simulation model in the COMSOL Multiphysics programme to determine the temperature of the collector layers and storage tank. The heat transfer equations for the various layers of the PV collector have been built using the normal energy equation for that layer, enabling a detailed and extensive analysis. The mass and momentum balance equations, coupled with heat transfer equations, are numerically solved for the modelling of temperature profiles by employing the FEM (finite element method) developed using COMSOL Multiphysics® software. Therefore, the governing equations of fluid flow are given in equations (1-3):

Equation 1: The conjugate heat transfer for the fluid flow

$$\rho\, C \frac{\partial T}{\partial t} + \rho\, C\, u.\nabla T = \nabla.\left(k\nabla T\right)$$

- ρ=density of fluid (kg/m^3).
- C = specific heat capacity of fluid (kJ/kg.ºC).
- t= time (s).
- T= fluid temperature (K).
- u = velocity of fluid (m/s).
- k= conductivity of fluid (W·m^{-1}·K^{-1}).

Equation 2: The momentum conservation

$$\rho \frac{\partial u}{\partial t} + \rho u.\nabla(u) = -\nabla p + \nabla.(\mu(\nabla u + \nabla u^T))$$

- p=pressure of fluid (Pa).
- μ = viscosity of fluid (Pa.s).

Equation 3: The continuity

$$\frac{\partial \rho}{\partial t} = \nabla.(\rho u)$$

In addition, the longwave radiation as heat losses from PV module to outer space within atmospheric window (8:13 μm) is calculated from Equation 4 below:

Equation 4: The longwave radiation heat losses

$$q_{lw} = \varepsilon \cdot \sigma \left(T_{pv}^4 - T_s^4\right)$$

- ε = emissivity of PV.
- σ = the Stefan-Boltzmann constant (5.67x10^{-8} W·m^{-2}·K^{-4}).
- T_{pv}= PV temperature (K).
- T_s = sky temperature (K).

In order to determine the electrical efficacy of PV collector, the initial step, calculate solar irradiance, that has been transformed into electrical energy.

Equation 5: The electrical energy of PV

$$E_{pv} = G\, \tau_c\, \eta_{ref}\, [1 - \beta_r \left(T_{pv} - T_{ref}\right)]$$

- τ_c= transmissivity of cover.
- η_{ref} = referenced efficiency of PV cells.
- β_r =temperature coefficient for PV cells.
- T_{pv} = solar cells temperature.
- T_{ref} = referenced temperature (25 ºC).
- β_r =temperature coefficient for PV cells.

At every iteration in the simulation, the solar cell efficiency is calculated from Equation 6.

Equation 6: Electrical efficiency

$$\eta_{pv} = \frac{E_{pv}}{G}$$

The thermal efficiency for PV module could be calculated by the entire solar radiation absorbed by PV panel and the thermal energy extracted by the working fluid, water, that is given by Equation 7:

Equation 7: The thermal efficiency of PV cooling system

$$\eta_{th} = \frac{E_{th}}{E_{in}} = \frac{\dot{m}\, C_w \,(T_{out} - T_{in})}{G \cdot A_p}$$

- $\mathrm{E_{th}}$= thermal energy absorbed by coolant water during the daytime(W).
- $\mathrm{E_{in}}$= the total amount of solar energy (W).
- A_p = area of panel (m²).
- $\dot{m}$= mass flow rate (kg/s).
- C_w = specific heat capacity of water (kJ/kg.ºC).
- T_{out}= temperature of water outlet (ºC).
- T_{in} = temperature of water inlet (ºC).

The immediate cooling power is expressed in Equation 8:

Equation 8: The cooling power during the nighttime

$$P_{cool} = \frac{\dot{m}\, C_w \,(T_{in} - T_{out})}{A_p}$$

The equations for the relative error and the mean relative error are employed to quantify the difference between the simulation and experimental results:

Equation 9: Relative error (RE)

$$RE = \left| \frac{X_{exp} - X_{sim}}{X_{exp}} \right|$$

Equation 10: Mean relative error (MRE)

$$MRE = \frac{1}{N} \sum_{i=1}^{i=N} |RE_i|$$

- X_{exp} = the experimental results
- X_{sim} = the simulation results

3.1. Model validation

This study employs computational fluid dynamics (CFD) simulations utilizing the COMSOL platform to validate the model against the experimental results. For numerical computation, the PVT-RC module was meshed using COMSOL's built-in physics-controlled mesh setting with 240247 domain elements after making the mesh dependency study. At each boundary, the number of mesh elements increases to accurately resolve the heat transfer and flow fields. To validate the simulation, experiment data performed by Hu et al. (2020) was compared with simulation data. The PVT-RC is 1.964 m in length and 0.964 m in width and the panel is inclined with the tilt angle of 32°. The applied PVT-RC module is consisting of several layers with their specifications summarised in Table 1Table 1. There are also two air gaps, one of them between the cover and PV plate, the other between absorber and back insulation, and seven copper water tubes are joined to the absorber's bottom side. The solar PVT-RC experiment was conducted in Hefei, China. The electrical power of PV panel and temperature of water tank, and the water temperature in each inlet and outlet of the model were simulated and compared with the experimental data. After several attempts to get a comparable result to the validated case study, finally, the closest result can be drawn. In this study, the RE of some critical parameters were taken to assess the accuracy rating of the mathematical model.

Table 1: Design parameters of PVT-RC collector.

Components	Thickness(m)	Density(kg/m³)	Specific heat(J/kg)	Conductivity (W/m·K)	Transmissivity	Absorptivity	Emissivity
Cover	0.000006	920	2260	0.33	0.9	0.05	0.05
PV plate	0.0006	600	700	149	-	0.95	0.95
Absorber	0.0004	2702	917	238	-	-	0.1
Tubes (small)	di=0.01, do=0.008	8933	385	401	-	-	0.1
Insulation	0.03	30	670	0.046	-	-	0.2

The daytime mode Validation

The theoretical model's accuracy for estimating the daytime working mode was confirmed. The simulation used experimental data (such as temperatures, solar irradiation, and water flow rate). Figures 4-5 show the comparative results of the current numerical model with experimental results. Figure 5(a) displays the comparison of COMSOL model results with the experiment during daytime for electric power. The good consistency between the experimental and simulated electrical powers is illustrated in Figure 5(a). In the initial and final stages, the simulated electrical outputs were slightly higher than the experimental ones. In overall terms, the MRE for electrical power was only 6.06%. The experimental and numerical results of water temperature in the storage tank during the daytime working mode are plotted in Figure 5(b). The estimated and experimental temperatures show a very high agreement. The MRE of the water temperature in the storage tank was 1.56%.

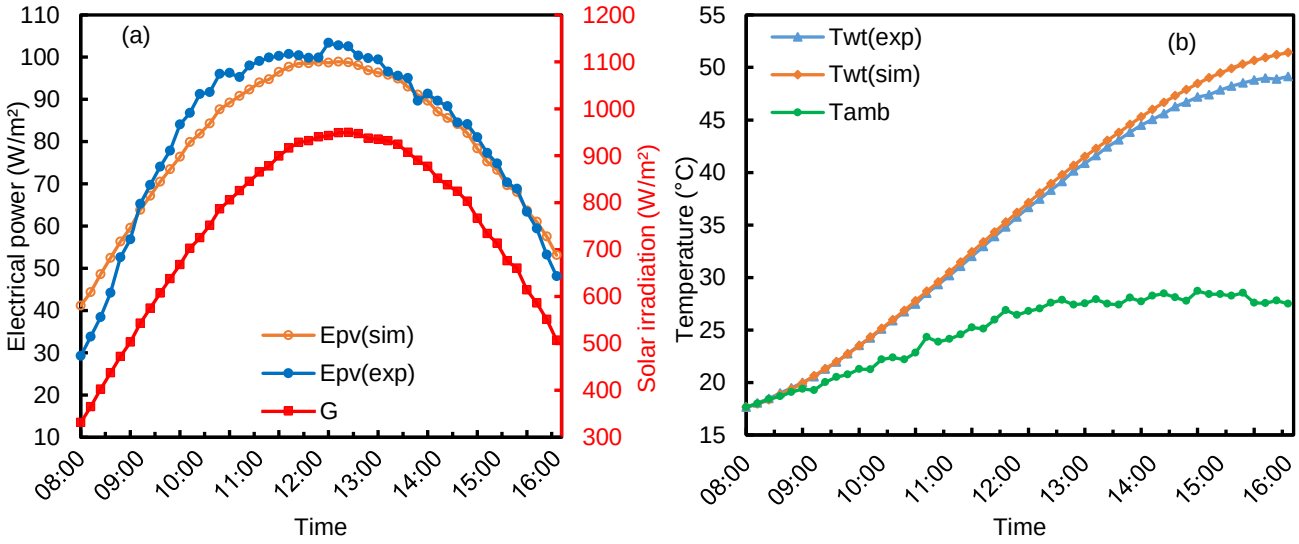

Figure 5 Experimental and simulation (a) electrical power and (b) temperatures of water in tank (day-time working mode).

The nighttime mode Validation

The simulation with experiment results for water temperature inside heat storage tank through night-time illustrated in Figure 6 (a). The MRE for water temperature inside storage tank was 1.29%, indicating that both the numerical and experimental results are reliable. Figure 6 (b) shows that the simulation and experimental cooling powers have also been highly reliable in the nighttime working mode. In the beginning, the estimated cooling capacity was considerably less than the calculated. Nonetheless, by 19:00, the experimental and simulated cooling powers were nearly similar. During the working period, MRE accounted for 5.79% of the overall cooling power. Figures 5-6 show how the developed computational system can evaluate the efficiency of the PV-RC device during both day and night modes.

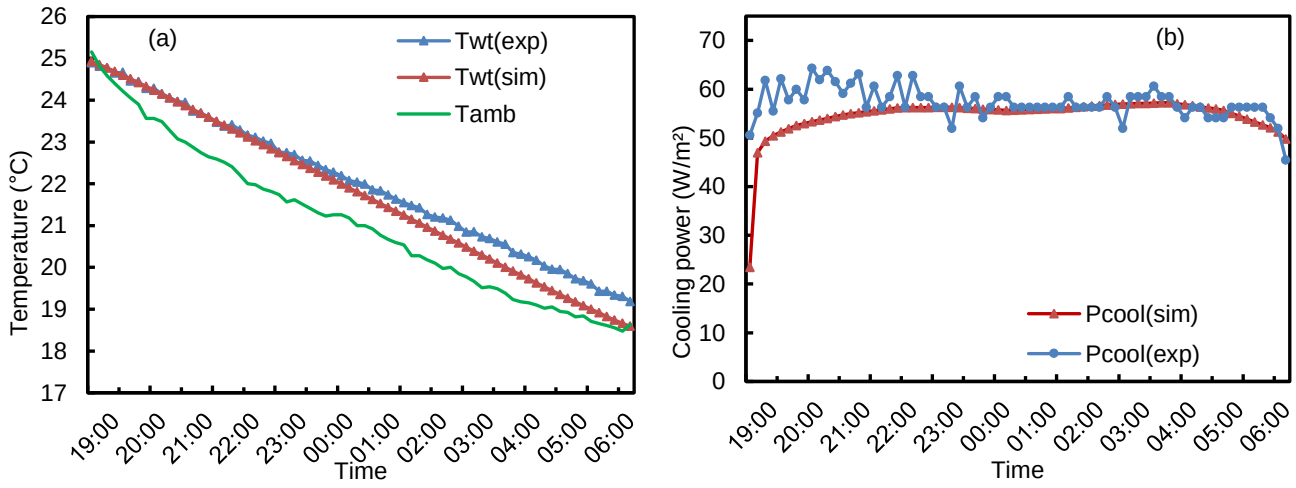

Figure 6 Experimental and simulation (a) temperatures of the water in tank and (b) cooling power (night-time working mode).

4. RESULTS AND DISCUSSION

By applying the verified system, the performance for the closed-loop hydronic PV cooling system is investigated under different working modes: daytime and nighttime. A thorough layer-by-layer mathematical model for this PV cooling system has been established in COMSOL Multiphysics with a time-dependent study. A 3D numerical analysis for the system is performed to investigate heat transfer for each layer in PV panel, the thermal absorber employed with water as a coolant and finally, the heat storage tank. Weather data from Hu et al. (2020) were utilized for this analysis. The model simulates a 24-hour period to assess the system's daytime performance, focusing on the electrical and solar thermal aspects, corresponding to the charging heat period. In contrast, the model predicts the discharging of heat energy during nighttime, when the working fluid in the storage tank and panel is cooled for subsequent daytime usage.

4.1. Dynamic behaviour of the PVT-RC closed-loop hydronic PV cooling system

Examining the operation principle of the proposed PV collector, we assume h_a =(2.8+3*Va) W/m².K. The preliminary volume of water in the storage tank is applied to Vt = 170L (i.e., the storage tank inner diameter is 30cm), and the storage tank wall is designed with Wt = 0.085m. The hourly thermal behaviours of the PV module system are investigated to find out deeper about it. Importantly, the water channels underneath the PV panel collect cold energy throughout the night and actively cool the PV panel over the day, leading to Twt to fluctuate during the day. The hourly outlet panel water temperature and the water of storage tank are depicted in Figure 7. It is good to note that the night-time period of summer is relatively shorter, and the diurnal temperature difference is lower, despite the night cooling effect, which still allows the temperature of the water tank to gradually decrease by the end of the night. Furthermore, Figure 7 illustrates the reduction in temperature difference between Tout and Twt as the night progresses.

Figure 8 compares PV temperature of the proposed and conventional systems throughout the entire day. It is evident that the PV conventional panel experiences significant temperature fluctuations mainly due to intense solar absorption in the daytime as well as the effect of radiative cooling at night. At night, the conventional PV temperature declines by approximately 0.002°C to 0.17°C below the ambient temperature. In contrast, the proposed system makes use of the natural temperature drop which happens in the nighttime without needing any modifications for the conventional. The proposed system exhibits a considerable reduction in temperature fluctuations, which can be attributed to the thermal capacity of storage tank water. During the night, cold energy is saved within circulating water, and this stored energy is then actively employed to cool PV panel over the day, effectively suppressing the abrupt temperature increase during daytime. For storage tank size of 170L, the proposed system reduces PV panel temperature by 10°C, compared to the conventional PV. In fact, with the proposed PV system, the temperature can be maintained below 57°C for the 170L tank size.

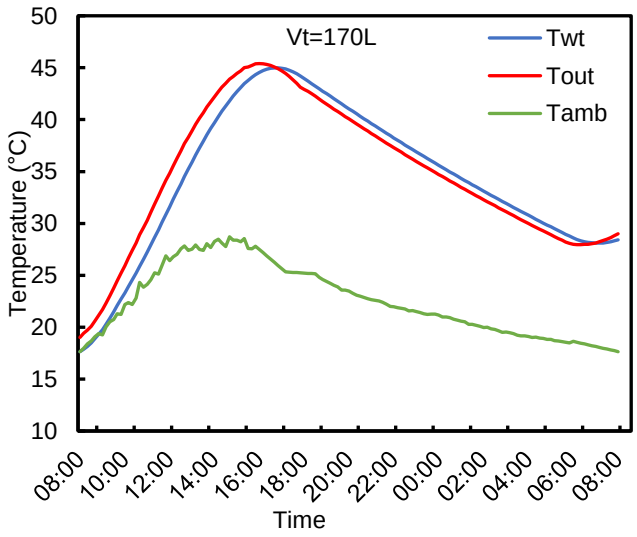

Figure 7 Channel outlet temperature (Tout) and tank water temperature (Twt) of the proposed closed-loop hydronic PV cooling system.

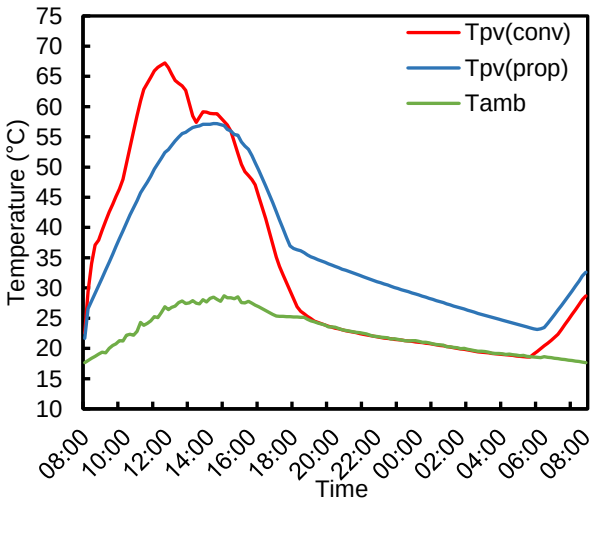

Figure 8 PV panel temperature comparison between common flat PV and proposed closed-loop hydronic PV cooling system.

4.2. Effect of Different Storage Tank Sizes (water mass).

In this study, the impact of tank volume (Vt) (for storage tank sizes of 100L, 120L and 170L) on the efficiency of a proposed PVT-RC system is investigated. Compared to the conventional system, the proposed system is presented in Figure 9(a), which shows that the temperature fluctuation for Tpv of the conventional system is higher than that of the proposed system as the storage tank size increases. This temperature fluctuation of Tpv in PV conventional is mainly because the radiative cooling in the glass at nighttime and a lack of daytime cooling. Conversely, the Tpv of PV module has a relatively high

temperature during night due to the circulating water absorption for cold energy from the PV collector and stores it in the storage tank. During daylight hours, the proposed PV system is capable of effectively mitigating fluctuations in temperature

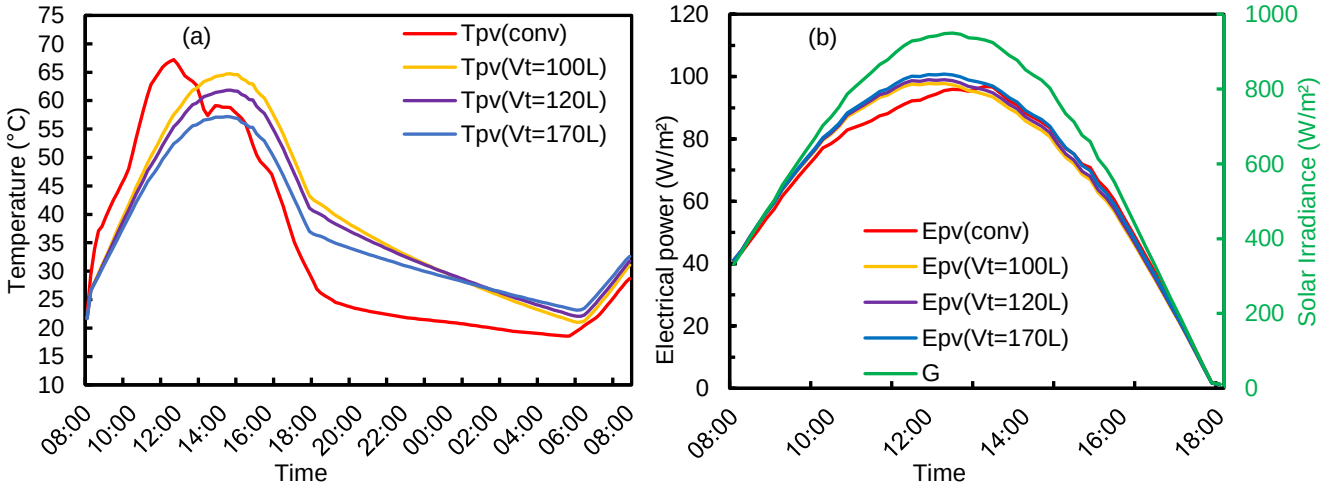

Figure 9 Effect of water tank volume (Vt) on (a) PV temperature (Tpv) and (b) electrical power Epv.

(Tpv) through the circulation of water. However, the Tpv of the proposed PV module may exceed that of the conventional system, particularly towards the end of the day, thereby resulting in a phenomenon known as "temperature inversion". This temperature inversion hinders the proposed system's capacity to produce more energy, particularly when Vt is small. On the other hand, with a larger Vt, the temperature increase during the day is relatively minimal with temperature inversion takes place for a shorter duration. It has been observed that greater storage capacity of tanks can lead to enhancement of operational efficiency such as the electrical power (Epv) as shown in Figure 9(b).

4.3. Effect of storage tank shapes.

The effect of the water tank geometries on the PVT-RC proposed performance is the focus of this analysis. Specifically, the study assesses three distinguishable tank shapes, namely cylindrical, rectangular, and cubic, all having a fixed tank capacity of 170 L. The computational models were executed utilizing a mass flow rate of 0.038 kg/s. The simulated distribution of water temperature on the water tank at distinct time levels of 16:00 (considering the peak point of temperature during daytime) is illustrated in Figure 10(a). The results indicate that the tank with a rectangular shape, identified as case 3, sustains an almost shape-optimized structure with a lower outlet temperature from the PV module as shown in Figure 10(b). This modification of temperature and energy absorbed by water provides a better cooling effect for the PV module in comparison to the other tank shapes.

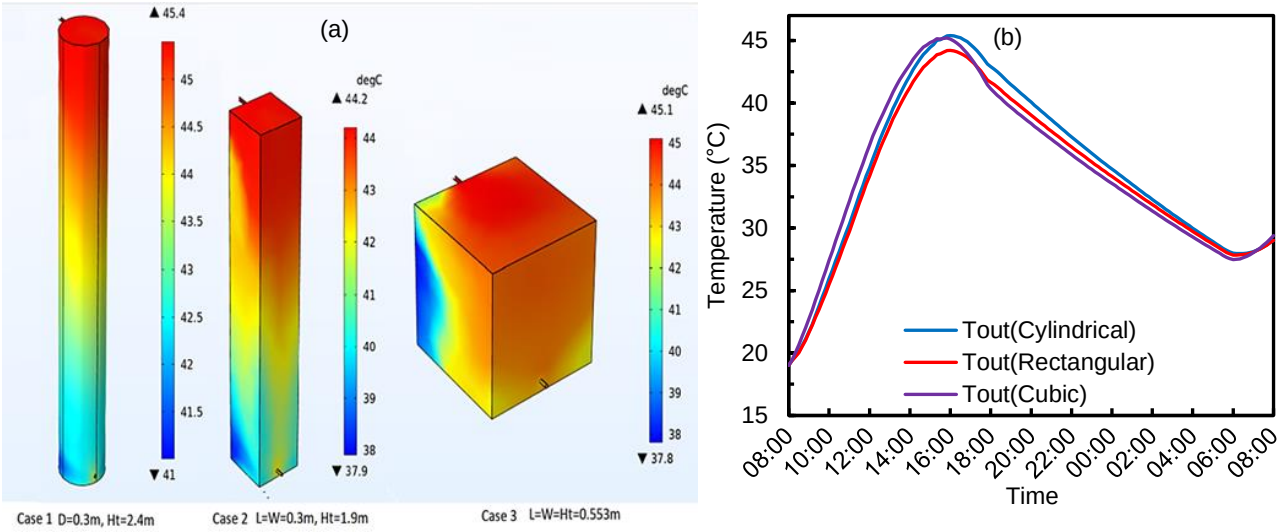

Figure 10 Comparison of temperature for different cases: (a) along storage tank height at 16:00 and (b) panel outlet temperature.

4.4. Analysing the Impact of PE Cover and Insulation

The removal of the PE cover and insulation from PV collector can result in several performance advantages. The maximum temperature of the PV module without PE and insulation system is significantly lower, up to 24°C lower than the conventional system and 14°C lower than the PVT-RC system as shown in Figure 11(a). This temperature variation is

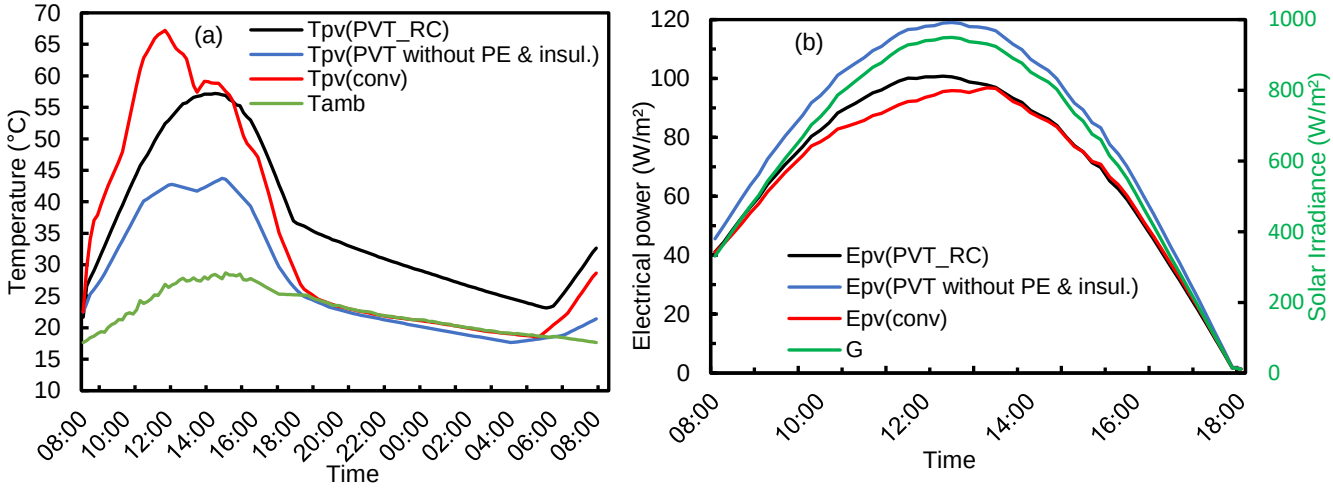

Figure 11 Illustration of a comparison PVT-RC, conventional PV and PVT without PE cover and insulation (a) PV temperature and (b) electrical power

associated with an increase in power output, as illustrated in Figure 11(b). This noteworthy temperature difference can have a substantial positive impact on the power output of the PVT module without PE & insulation design, potentially resulting in a significant increase in energy production of up to 20% and 14% when compared to conventional PV and PVT-RC systems. These findings suggest that the absence of a PE cover and insulation in this system contributes to better thermal management, potentially benefiting PV panel efficiency and lifespan.

5. CONCLUSION

A PVT-RC system for closed-loop hydronic PV cooling system was introduced in this study, comprising a standard PV module for power generation and cold energy capture, a water heat storage tank and a pump for active cooling circulation. The system operates on the principle of utilizing PV collector as radiative cooling surface at night to extract and store the cold energy via the water passing beneath it. This stored cold water is utilised during the day to efficiently cool the panel over the daytime, with no system modifications required.

To investigate the estimated performance of the proposed system, a dynamic thermal model was developed. The findings revealed that storing cold water effectively reduces temperature fluctuations in the PV module, thereby maintaining a relatively low temperature and increasing net power output, especially when a larger storage tank is used. However, it was discovered that temperature inversion hinders power generation improvement, particularly when using a relatively small storage tank. Furthermore, adopting the rectangular shape for the tank was found to be preferable as it provides an additional heat dissipation path through the tank. Moreover, removing the insulation can enhance heat dissipation, further lowering PV panel temperatures. These performance enhancements can translate into increased energy production by up to 20% compared to conventional PV systems and reduced electricity costs over the lifespan of the PV system.

In conclusion, the proposed PVT-RC closed-loop hydronic PV cooling system demonstrates its efficiency in regions characterized by significant diurnal temperature variations, which are prevalent in hot and arid climate zones. This suggested PVT-RC cooling system provides a sustainable and cost-effective solution for enhancing PV module performance, particularly when removing PE and insulation. The findings of this research have important implications for the development of sustainable energy technologies and efficient energy production.

6. ACKNOWLEDGEMENT

The first author would like to acknowledge The Higher Committee of Education Development in Iraq (HCED) for funding the PhD scholarship to carry out research.

7. REFERENCES

Bahaidarah, H., Subhan, A., Gandhidasan, P. and Rehman, S. 2013. Performance evaluation of a PV (photovoltaic) module by back surface water cooling for hot climatic conditions. *Energy*. 59, pp.445–453.

Baloch, A.A.B., Bahaidarah, H.M.S., Gandhidasan, P. and Al-Sulaiman, F.A. 2015. Experimental and numerical performance analysis of a converging channel heat exchanger for PV cooling. *Energy Conversion and Management*. 103, pp.14–27.

Browne, M.C., Norton, B. and McCormack, S.J. 2016. Heat retention of a photovoltaic/thermal collector with PCM. *Solar Energy*. 133, pp.533–548.

Dubey, S. and Tiwari, G.N. 2009. Analysis of PV/T flat plate water collectors connected in series. *Solar Energy*. 83(9), pp.1485–1498.

Hasanuzzaman, M., Al-Amin, A.Q., Khanam, S. and Hosenuzzaman, M. 2015. Photovoltaic power generation and its economic and environmental future in Bangladesh. *Journal of renewable and sustainable energy*. 7(1).

Hu, M., Zhao, B., Ao, X., Ren, X., Cao, J., Wang, Q., Su, Y. and Pei, G. 2020. Performance assessment of a trifunctional system integrating solar PV, solar thermal, and radiative sky cooling. *Applied Energy*. 260.

Hu, M., Zhao, B., Ao, X., Zhao, P., Su, Y. and Pei, G. 2018. Field investigation of a hybrid photovoltaic-photothermic-radiative cooling system. *Applied Energy*. 231, pp.288–300.

Qu, Z.G., Chen, G., Zhou, L. and Miao, J.Y. 2018. Numerical study on the operating characteristics of cryogenic loop heat pipes based on a one-dimensional heat leak model. *Energy Conversion and Management*. 172, pp.485–496.

Royo, P., Ferreira, V.J., López-Sabirón, A.M. and Ferreira, G. 2016. Hybrid diagnosis to characterise the energy and environmental enhancement of photovoltaic modules using smart materials. *Energy*. 101, pp.174–189.

Skoplaki, E. and Palyvos, J.A. 2009. On the temperature dependence of photovoltaic module electrical performance: A review of efficiency/power correlations. *Solar Energy*. 83(5), pp.614–624.

Soliman, A.M.A. and Hassan, H. 2018. 3D study on the performance of cooling technique composed of heat spreader and microchannels for cooling the solar cells. *Energy Conversion and Management*. 170, pp.1–18.

Soliman, A.M.A. and Hassan, H. 2019. Effect of heat spreader size, microchannel configuration and nanoparticles on the performance of PV-heat spreader-microchannels system. *Solar Energy*. 182, pp.286–297.

Soliman, A.M.A., Hassan, H. and Ookawara, S. 2019. An experimental study of the performance of the solar cell with heat sink cooling system. *Energy Procedia*. 162, pp.127–135.

Teo, H.G., Lee, P.S. and Hawlader, M.N.A. 2012. An active cooling system for photovoltaic modules. *Applied Energy*. 90(1), pp.309–315.

Waqas, A. and Jie, J. 2018. Effectiveness of Phase Change Material for Cooling of Photovoltaic Panel for Hot Climate. *Journal of Solar Energy Engineering, Transactions of the ASME*. 140(4).

Yoon, S., Seo, J., Choi, M. and Lee, B.J. 2022. Enhanced photovoltaic efficiency through radiative cooling augmented by a thermosyphon effect. *Energy Conversion and Management*. 268.

Zeyghami, M., Goswami, D.Y. and Stefanakos, E. 2018. A review of clear sky radiative cooling developments and applications in renewable power systems and passive building cooling. *Solar Energy Materials and Solar Cells*. 178, pp.115–128.

Zhao, B., Hu, M., Ao, X., Chen, N., Xuan, Q., Jiao, D. and Pei, G. 2019. Performance analysis of a hybrid system combining photovoltaic and nighttime radiative cooling. *Applied Energy*. 252.

Zhao, B., Hu, M., Ao, X., Huang, X., Ren, X. and Pei, G. 2019. Conventional photovoltaic panel for nocturnal radiative cooling and preliminary performance analysis. *Energy*. 175, pp.677–686.

Zhu, L., Raman, A.P. and Fan, S. 2015. Radiative cooling of solar absorbers using a visibly transparent photonic crystal thermal blackbody. *Proceedings of the National Academy of Sciences - PNAS*. 112(40), pp.12282–12287.

#42: Comparison of spray characteristics for diesel and its blends with diethyl ether: an experimental study

Utkarsha SONAWANE[1], Avinash Kumar AGARWAL[2]

[1, 2] *Engine Research Laboratory, Department of Mechanical Engineering*
Indian Institute of Technology Kanpur, Kanpur-208016, India, akag@iitk.ac.in

Abstract: Compression ignition (CI) engines have wide applications and are explored for alternative fuels as the sources of fossil fuels are anticipated to be exhausted within a few decades. Using alternative fuels that are cheaper and more sustainable to replace conventional fossil fuels has captured the attention of researchers. Diethyl ether (DEE) is explored in the present study for partial replacement of diesel. Fuel spray development starts with liquid fuel being injected into an environment at high pressure and temperature. After fuel injection, the spray approaches the cylinder liner, while it interacts with the hot ambient air leading to the fuel vaporization and followed by combustion. Spray atomization has a great effect on the spray's local mixture formation, which influences spray penetration and structure. The present study investigates the spray characteristics of diesel and its blends with DEE under various fuel injection pressure (FIP) and ambient pressure (Pamb). The spray parameters like liquid axial penetration, radial penetration, spray area, and droplet diameter were investigated experimentally. Macroscopic results revealed lower axial penetration and spray area for DEE40 due to its lower viscosity, density, and surface tension. However, radial penetration was higher for DEE40 due to more dispersion of finer droplets in the radial direction. A higher FIP of 1200 bar showed longer axial and shorter radial penetration compared to 700 bar. This is due to the formation of finer droplets at higher FIP, which are losing their momentum in an axial direction and getting dispersed due to air entrainment in a radial direction. The atomization of diesel spray was improved by the introduction of DEE. The droplets with the addition of DEE spray showed a smaller diameter, reducing the spray inertia and thus resulting in a lower liquid penetration. The higher FIP of 1200 bar and/or DEE40 spray showed lower chances of droplet coalescence with increasing Pamb from 10 to 30 bar. This study strongly suggests the blending of DEE in conventional diesel for improving the atomization and evaporation properties of the fuel spray.

Keywords: Renewable fuels, Diesel, Spray, Diethyl Ether, Energy

1. INTRODUCTION

Compression ignition (CI) engines are widely accepted in the transportation sector owing to their high combustion efficiency and reliable output performance (Reitz et al., 2020). Various alternative fuels have been proposed to meet the upcoming stringent emission norms and further improve the potential advantages of CI engines (Plamondon and Seers, 2019). Alternative fuels play a significant role in the reduction of engine emissions and engine noise. Using alternative fuels in CI engines helps meet the growing demand for fossil fuels. Various types of oxygenated and renewable alternative fuels have been explored by researchers for CI engine applications such as biodiesel, alcohols, ether, etc. The depleposef fossil reserves poses a complex problem for every country to secure its future energy requirement. Though electrification of the transport industry looks like a solution at present; however, life cycle (LCA) and total cost analysis (TCO) have shown otherwise. The more practical solution is to use the biomass available in abundance to make our future transport energy secure and independent. Production and usage of renewable alternative fuels is one pathway to a sustainable energy future. The use of renewable fuels may also reduce their contribution to global climate change. Ethanol produced from biomass shows promising future fuel. Ethanol can be easily converted to diethyl ether (DEE) through the dehydration process. The production of ether and alcohols from biomass can convert municipal, industrial, agricultural, and forestry wastes into energy at a low cost. The fuel spray development and atomization characteristics have a vital role in superior combustion and emissions as they affect fuel-air mixture formation. Hence, it is important to study the spray characteristics of various fuels to lower tailpipe emissions and increase the efficiency of the CI engine (Kim, Park and Lee, 2010).

DEE is a renewable and oxygenated alternative fuel having similar fuel characteristics to conventional diesel. The DEE-fuelled engine emits lower emissions than diesel. Therefore, DEE has become an emerging alternative fuel for research in recent years. However, there are some differences in physical properties between DEE and diesel. Therefore, it is necessary to study the spray characteristics of DEE concerning its implementation in CI engines. While the influence of ether has been reviewed (Hua, 2023), few studies have been done with a diesel engine (Lee and Kim, 2017) (Ibrahim, 2016) (Rakopoulos et al., 2012). As this paper addresses the influence of the addition of DEE blended in conventional diesel. DEE has suitable fuel properties for CI engines, such as higher cetane number (CN), comparable energy density, fuel-bound oxygen content, lower auto-ignition temperature, prolonged flammability, etc. It was found that DEE significantly reduces viscosity, density, and surface tension and improves the low-temperature properties of fuels (Górski, Smigins and Longwic, 2020). DEE is more likely to result in an even better atomization and mixture formation process due to the high vapor pressure of DEE. Zhan et al. (Zhan et al., 2020) showed that the addition of DEE formed a greater fraction of smaller droplets, indicating a better atomization process. Apart from this, the latent heat of evaporation for DEE is higher than diesel, reducing the combustion temperature and NOx emissions. The fuel-bound oxygen in DEE lowers the formation and improved the oxidation of soot. The presence of DEE in the blended fuels will remarkably accelerate the auto-ignition process. The addition of 20% DEE decreases smoke opacity emission compared to the diesel fuelled engine (Górski, Smigins and Longwic, 2020). DEE blended fuel spray resulted in longer vapor penetration, larger spray angle, and lower liquid cross-sectional area, enhancing vaporization with DEE addition (Zhan et al., 2020). The liquid penetration of diesel spray was higher than ether fuels because of the high viscosity, surface tension, and density of diesel. Ether fuels exhibited low Ohnesorge numbers and high Reynolds numbers, showing improved atomization than diesel (Mohan et al., 2017). Despite of specified advantages of DEE, both the advanced engine and fundamental spray research on the basic physical and chemical effects due to DEE addition is still quite inadequate.

Fuel spray characterization can be classified into two types: macroscopic and microscopic. Macroscopic characterization includes spray penetration, spray area, and cone angle that can be measured by direct high-speed imaging method. Microscopic characteristics such as droplet velocity, droplet diameter, and diameter distribution can be measured by particle image velocimetry (PIV), phase Doppler particle analyzer (PDPA), or laser diffraction particle analyzer (LDPA). As described in the above research studies, while spray characteristics of conventional diesel have been well studied, almost no attention has been paid to scaling the spray characteristics for oxygenated and renewable alternative fuels. Optimization of spray atomization and combustion phenomenon for CI engines is one of the effective tools to meet the upcoming stringent regulation for lower tailpipe emissions. However, spray characterization of diesel-DEE blends was not explored widely. Such kind of fundamental studies helps in the implementation of new alternative fuels for partial or full replacement of conventional fuels. This study is therefore aimed to study spray characteristics of different blends of diesel and DEE. The blends of DEE and diesel (20% and 40% DEE in diesel, v/v) are investigated and compared with baseline diesel. Apart from the influence of fuel properties, the effect of fuel injection pressure (FIP) and ambient pressure (P_{amb}) on spray characterization is explored.

2. EXPERIMENTAL SETUP

A Bosch injector having 7 nozzles with a diameter of 137 µm was used for the present investigation. An injector cap was employed to cut out 6 nozzles as only one plume was used for experimentations. Whereas the other six spray plumes flow through a bypass passage in the injector cap. The fuels tested were pure diesel and its blends with DEE (20 and 40% v/v). The properties of test fuels are given in Table 1. In the text, pure diesel will be referred to as D100 and corresponding blends with diesel will be noted as DEE20 and DEE40. All these test fuels were at room temperature at the time of measurement.

Table 1: Properties of DEE and Diesel

	Diesel	**DEE**
Density @ 25°C (kg/m^3)	822	713.4
Kinematic Viscosity (cSt @ 40 ^{o}C)	2.15	0.23
Surface Tension @ 25°C (N/m)	0.020	0.017
Vapor pressure @ 25°C (Pa)	58660	1280
Flashpoint (^{o}C)	49	-40
Boiling point (^{o}C)	180–330	34.6
Self-ignition temperature (^{o}C)	210	160
Oxygen content (% w/w)	0.03	21.6
Cetane number	53	>125
Calorific value (MJ/kg)	43.2	33.9
Latent heat of vaporization (kJ/kg)	250	355

The FIP was varied to 700 and 1200 bar by using a pneumatics high-pressure pump. The P_{amb} was measured by a pressure gauge and was adjusted manually by closing and opening the intake and exhaust valves. The total injection quantity of 20 mg/cycle is injected through the injector, which replicates the medium load and speed conditions of the CI engine. The injector calibration was performed to calculate the injection duration for various test fuels and FIPs.

Table 2: Test matrix for experimentation

Test conditions	
Test fuels	DEE20, DEE40, and Diesel
Ambient pressure (bar)	40
Total injection quantity (mg)	20
Injection Pressures (bar)	700, 1200
Injector Specifications	
Number of nozzles	7
Nozzle diameter (µm)	137
Spray included angle	154^o

Table 2 shows the details of the test conditions investigated in the present study. Stand Alone Direct Injection (SADI) was used to operate the injector for a particular injection duration. TTL signal was sent to trigger the camera and the Phase Doppler Interferometry (PDI) processor so the instrument can record data only after the start of injection. This synchronization was done between SADI and PDI or high-speed camera.

2.1. High-Speed Imaging

Macroscopic spray characteristics were measured using a constant-volume spray chamber. Macroscopic transient spray evolution was recorded by a high-speed CMOS camera (Photron, SA-1). white light sources were used to illuminate the fuel spray to capture the spray images. The images were captured at a rate of 10000 frames per second (Sonawane, Kalwar and Agarwal, 2020). A schematic of the constant volume spray chamber (CVSC) experimental setup is shown in Figure 2. The chamber was maintained at ambient pressure of 40 bar. A MATLAB code was developed for measuring the macroscopic spray characteristics: axial and radial spray penetration and spray projected area. The images taken were converted into binary for subtraction to remove background noise. These images were processed for further analysis and calculation of the spray penetration and spray area.

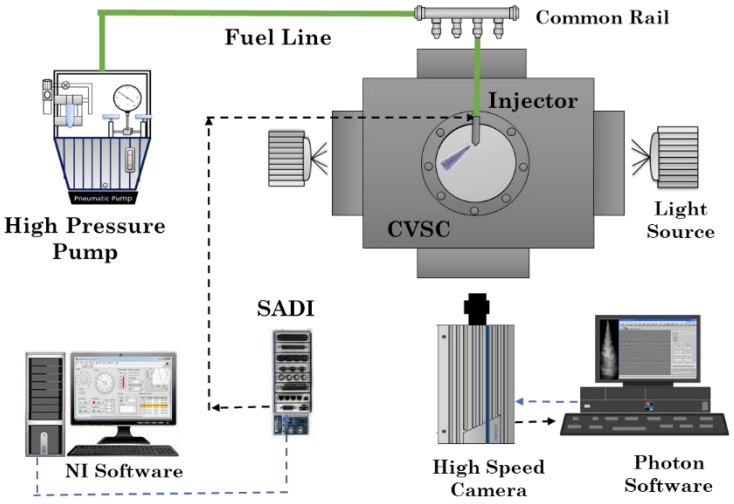

Figure 1 Experimental setup for macroscopic spray characterization

2.2. Phase Doppler Interferometry (PDI)

Microscopic spray characteristics were evaluated by PDI, which consists of 2 transmitters and 1 receiver. Transmitter 1 has two green and two blue laser beams. Whereas transmitter 2 has a pair of yellow laser beams. All six laser beams intersect at a single point, known as 'probe volume,' which is moved to the measurement point across the spray (Kong and Bae, 2012). The measurement point was on the spray plume, ~30 mm downstream of the nozzle along the axial direction (Wang et al., 2017). The measurement point distance from the injector nozzle was kept constant for all measurements. In the present study, transmitter 1 was used for the measurement of diameters and velocities. Whereas transmitter 2 measures velocity only. The ambient pressure was maintained at 10 and 30 bar.

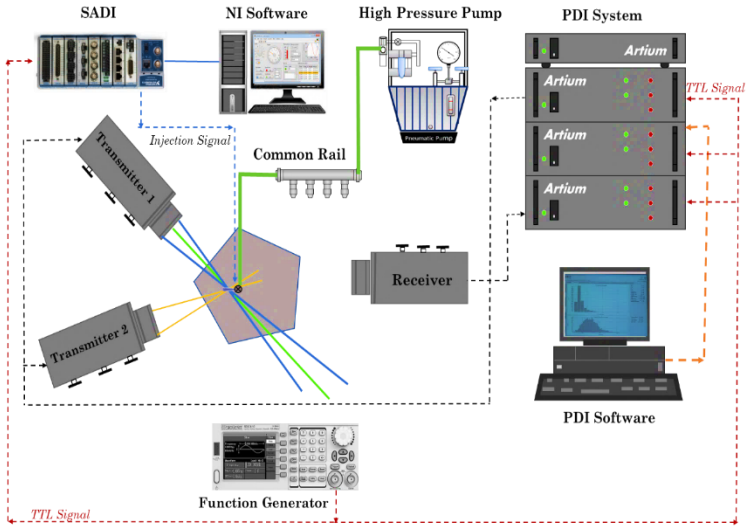

Figure 2 Schematic of microscopic spray experiments

3. RESULTS AND DISCUSSION

Fuel is injected from the injector into the high-pressure and temperature ambient gas during the compression stroke, and the interaction between the spray and the ambient air leads to spray droplet breakup. Macro and microscopic spray parameters are influenced by the fuel's physical properties. Fuel viscosity and surface tension were found to greatly affect spray stability and atomization (Zhu et al., 2013). Hence, it is required to characterize the influence of the fuel properties on the spray morphology and atomization. Figure 3 shows the liquid penetration length variation after the start of injection. The macroscopic spray images taken by a high-speed camera were used to investigate the influence of the FIP and various test fuels on the spray development process. Higher FIP advances the combustion because of better atomization which forms a superior air-fuel mixture. However, shorter liquid penetration may form an improper mixture and poor air utilization, leading to higher engine emissions. Thus, spray penetration length is a critical parameter for lowering exhaust emissions. Longer penetration length with a high swirl ratio results in superior combustion.

The liquid penetration increased with time and the increment was higher in the initial stage, which get retarded afterward. The ambient air drag was applied continuously on the fuel spray, which reduces the momentum of the spray and cause the droplet breakup. As soon as the droplet breakup starts, the kinetic energy of the spray gets dissipated in the breakup process and the spray losses its momentum. At the initial stage, the higher momentum of the liquid jet contributed to the higher rate of penetration. However, the formation of finer droplets due to atomization resulted in a slower penetration rate. It was found that a higher FIP of 1200 bar (solid line) showed longer liquid penetration compared to 700 bar (dash line). The rate of penetration was higher for higher FIP than lower FIP, showing higher spray momentum at 1200 bar FIP. The higher liquid penetration of spray indicates the better reach of fuel droplets inside the combustion chamber, improving air-fuel mixture formation. Higher initial injection momentum promotes the spray spatial dispersion. However, there is a limit on increasing the liquid penetration with increasing the FIP. After a certain FIP, the spray gets atomized well and forms finer droplets, lowering the droplet momentum. The liquid penetration is achieved as the overall effect of higher spray momentum due to higher FIP and lower spray momentum due to finer droplets. Too short liquid penetration limits the fuel spray reach and forms a locally rich mixture inside the chamber. Therefore, optimum penetration length is suggested for better and dispersed air-fuel mixture formation.

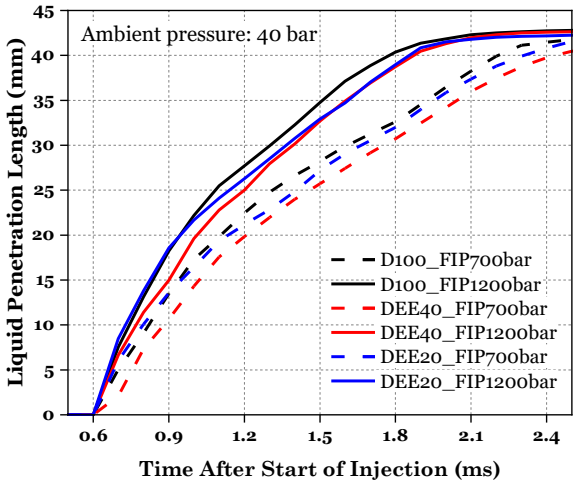

Figure 3 Liquid penetration length for diesel and its blends with DEE

The fuel viscosity and surface tension greatly influence the rate of penetration length through the droplet breakup and atomization and this process slows down the evolution of the spray penetration. The addition of DEE to diesel showed a reduction in liquid penetration length. This is due lower viscosity, density, and surface tension of blended fuels. These changes in properties support the breakup of droplets, resulting in a decrease in spray droplet size (Figure 7) and a loss in spray momentum which ultimately slow down the penetration. DEE40 showed the lowest liquid penetration among all test fuels. However, the reduction in penetration was not that significant to affect the mixture formation negatively.

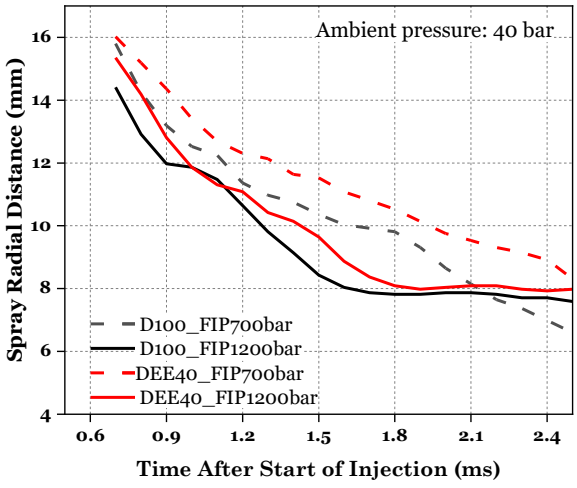

Figure 4 Spray radial distance for diesel and its blends with DEE

Figure 4 shows the radial distance variation after the time of the start of injection for diesel and DEE40. The radial distance was higher initially, which reduced drastically with further spray development. A lower FIP of 700 bar showed more spray radial distance than 1200 bar. The chances of spray spreading in a radial direction were more for lower FIP. However, the spray penetrates more in an axial direction with increasing FIP. More radial dispersion is necessary for better air entrainment and mixture formation. The air utilization would be superior for the more dispersed spray of lower FIP. The addition of DEE in diesel exhibited a higher spray radial distance than pure diesel, indicating better air utilization and

mixture formation. The finer droplets formed for DEE40 due to its fuel properties get deviated from their axial path and follow air vortices. Air entrainment at the spray periphery dispersed finer droplets in the radial direction. The coarser droplets formed for diesel spray have higher momentum and follow the axial path. Coarser droplets have less chance of getting along the vortices and spreading in the radial direction. Therefore, diesel spay showed more axial and lower radial penetration compared to DEE40.

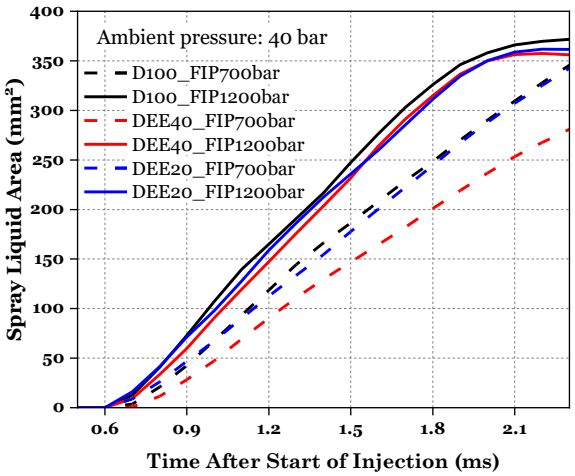

Figure 5 Projected spray area distance for diesel and its blends with DEE

The projected area indicates the diffusion range of the fuel spray. The spray cone angle can reflect the projected area of the spray approximately. However, it is still not an implicit and correct way to measure the projected area, as it is believed that the spray shape is the triangle in the calculation of the spray cone angle. Whereas, the actual spray is asymmetrical. Therefore, it is essential to measure the projected spray area directly from experiments. Figure 5 shows a comparison of the liquid spray area of all test fuels for both FIPs. The spray area is an overall parameter, representing the distribution of fuel inside the spray chamber. It considers both axial and radial penetration of fuel spray. The fuel spray reach inside the chamber is best represented by the spray area compared to penetration lengths. The spray area increased after the start of injection and get almost steady due to the end of optical access. Generally, the spray area increases to achieve maximum value and starts reducing after the end of the injection. The spray area was higher for 1200 bar compared to 700 bar, showing similar trends as axial penetration length (Figure 3). This shows that the major contribution of axial penetration in spray area than radial penetration. In the present study, the spray area results showed similar trends like liquid penetration length. Higher FIP delivers the fuel faster than lower FIP and caused the sprays to reach a steady state sooner. It can be concluded that fuel properties showed less influence at higher FIP. The addition of DEE in the diesel reduced the spray liquid area, indicating better evaporation (Zhan et al., 2020).

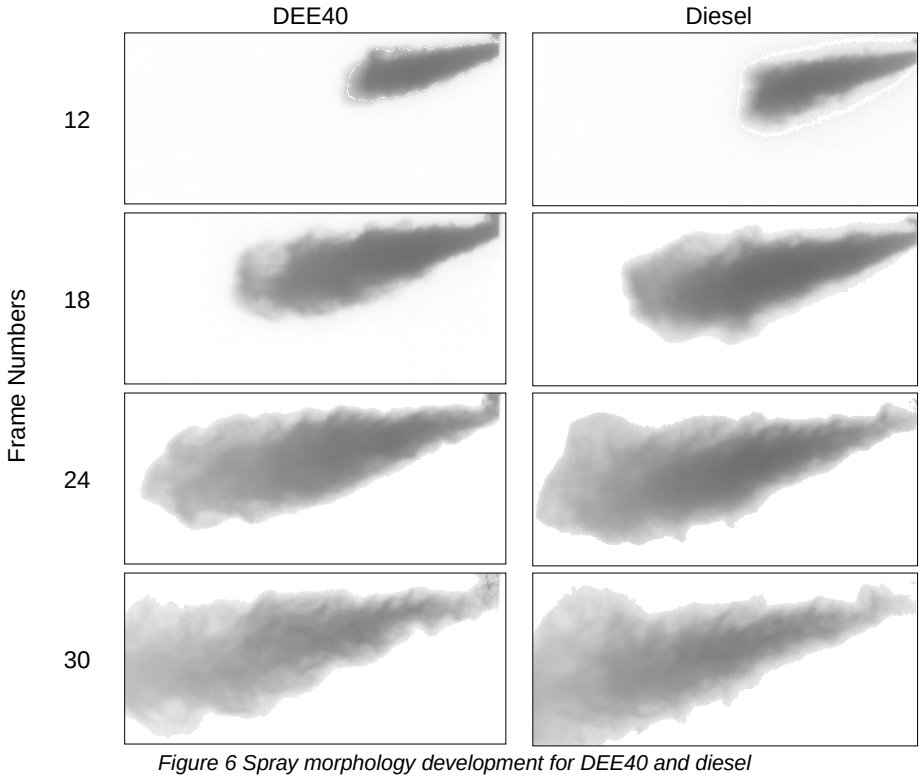

Figure 6 Spray morphology development for DEE40 and diesel

The spray images captured using the high-speed camera show the transient morphology of sprays after the start of injection. These images are presented in Figure 6 for DEE40 and diesel at a FIP of 700 bar. It can be observed from the images that diesel spray showed a longer penetration length, spray area, and hence, the largest spray volume. The higher liquid penetration rate of diesel spray under higher FIP makes the penetration and interaction of the spray with air faster and stronger. The addition of DEE lower viscosity and surface tension, leading to easier droplet breakup. The better atomization reduces droplet diameter and losses spray momentum which ultimately slows down the penetration.

Figure 7 shows the droplet diameter distribution and overall AMD of the fuel spray. With increasing FIP, the number of smaller diameter droplets improved. For both ambient pressures, the diameter probability density (PDF) peak shifted toward the lower diameter range (Figure 7a). This indicates better atomization of fuel spray with increasing FIP. However, reverse trends were observed with increasing P_{amb} from 10 to 30 bar. The formation of coarser droplets was found with increasing P_{amb}, showing the occurrence of droplet coalescence. The same things can be interpreted from overall AMD (Figure 7c). The coarse the spray droplets possess higher momentum and hence, the smaller the resistance due to air drag.

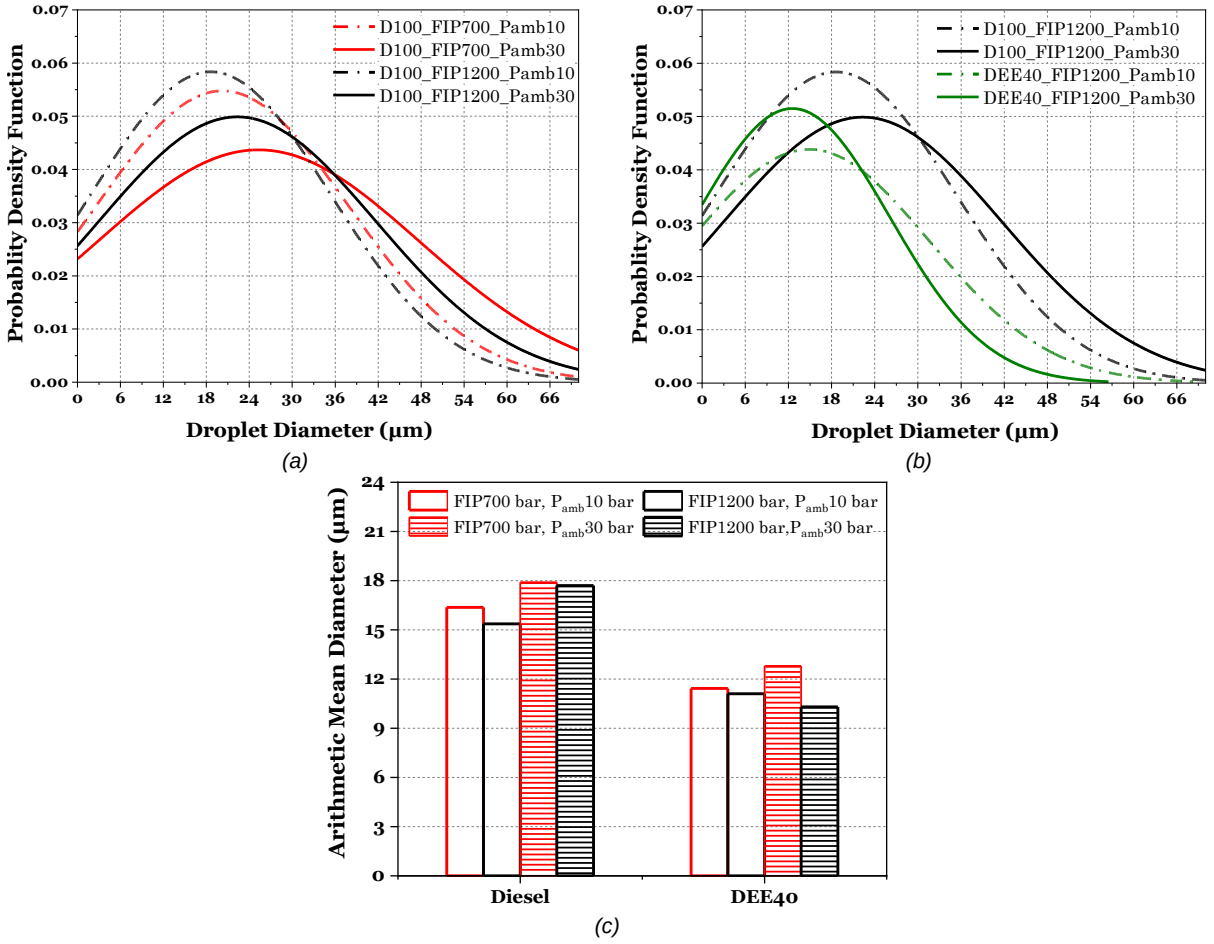

Figure 7 Droplet diameter distribution for single injection at different fuel injection and ambient pressure

The microscopic spray characteristics showed strong influences of fuel properties on the droplet diameter distribution. DEE addition remarkably improves atomization because of the lower viscosity, density, and surface tension of DEE. A higher fuel viscosity results in a lower spray velocity, leading to coarse droplet formation. Higher surface tension makes the droplet breakup inferior. Increasing the amount of DEE in the blend produced smaller and smaller droplets. This is due to more active atomization with the addition of DEE. Whereas higher viscosity, density, and larger surface tension of diesel inhibit the droplet breakup process. It can be concluded that the atomization characteristic of diesel was improved with the blending of DEE. The spray droplets of diesel DEE blends showed a statistically smaller droplet diameter, reducing the spray inertia and consequently decreasing liquid penetration (Figure 3). The lower the viscosity and surface tension of DEE indicates it is easier for the fuel droplets to overcome the molecular viscous force and droplet surface tension, breaking into finer droplets. It is believed that DEE is susceptible to droplet breakup and forms a better mixture due to the higher vapor pressure of DEE. The AMD result indicates that higher FIP promoted spray atomization and reduced the effect of change in fuel properties. Increasing FIP is an effective way of reducing droplet size. At higher FIP, finer droplets distribute in a narrower range and have less variation in their sizes. The higher FIP of 1200 bar for DEE40 spray showed lower chances of droplet coalescence with increasing P_{amb} from 10 to 30 bar.

4. CONCLUSION

The present study aims to investigate the spray characteristics of diesel and its blends with DEE under various FIP and P_{amb}. The spray parameters like liquid axial penetration, radial penetration, spray area, and droplet diameter were investigated experimentally. This study strongly suggests the blending of DEE in conventional diesel for improving the atomization and evaporation properties of the fuel spray. The maximum replacement of 40% (on a volume basis) is possible. Further increment in DEE addition may cause the problem of vapor lock in the fuel injection system. The major findings were listed below,

- Macroscopic results revealed lower axial penetration and spray area for DEE40 due to its lower viscosity, density, and surface tension. However, radial penetration was higher for DEE40 due to more dispersion of finer droplets in a radial direction.
- A higher FIP of 1200 bar showed longer axial and shorter radial penetration compared to 700 bar. This is due to the formation of finer droplets at higher FIP, which are losing their momentum in the axial direction and getting dispersed by vortices in the radial direction.
- The atomization characteristic of diesel was improved by the blending of DEE in the diesel. Blended fuel showed the formation of finer droplets in fuel spray, reducing the spray inertia and ultimately decreasing liquid penetration. Microscopic results showed the formation of finer droplets for higher FIP of 1200 bar and DEE40.
- The higher FIP of 1200 bar for DEE40 spray showed lower chances of droplet coalescence with increasing P_{amb} from 10 to 30 bar.

5. REFERENCES

Górski, K., Smigins, R. and Longwic, R. (2020) 'Research on physico-chemical properties of diethyl ether/linseed oil blends for the use as fuel in diesel engines', Energies, 13(24), p. 6564. Available at: https://doi.org/10.3390/en13246564.

Hua, Y. (2023) 'Ethers and esters as alternative fuels for internal combustion engine: A review', International Journal of Engine Research, 24(1), pp. 178–216. Available at: https://doi.org/10.1177/14680874211046480.

Ibrahim, A. (2016) 'Investigating the effect of using diethyl ether as a fuel additive on diesel engine performance and combustion', Applied Thermal Engineering, 107, pp. 853–862. Available at: https://doi.org/10.1016/j.applthermaleng.2016.07.061.

Kim, H.J., Park, S.H. and Lee, C.S. (2010) 'A study on the macroscopic spray behavior and atomization characteristics of biodiesel and dimethyl ether sprays under increased ambient pressure', Fuel Processing Technology, 91(3), pp. 354–363. Available at: https://doi.org/10.1016/j.fuproc.2009.11.007.

Kong, J. and Bae, C. (2012) 'EFFECT OF NOZZLE HOLE GEOMETRY ON NON-EVAPORATING DIESEL SPRAY CHARACTERISTICS AT HIGH-PRESSURE INJECTION', Atomization and Sprays, 22(1), pp. 1–21. Available at: https://doi.org/10.1615/AtomizSpr.2012003630.

Lee, S. and Kim, T.Y. (2017) 'Performance and emission characteristics of a DI diesel engine operated with diesel/DEE blended fuel', Applied Thermal Engineering, 121, pp. 454–461. Available at: https://doi.org/10.1016/j.applthermaleng.2017.04.112.

Mohan, B. et al. (2017) 'Numerical analysis of spray characteristics of dimethyl ether and diethyl ether fuel', Applied Energy, 185, pp. 1403–1410. Available at: https://doi.org/10.1016/j.apenergy.2016.01.128.

Plamondon, E. and Seers, P. (2019) 'Parametric study of pilot–main injection strategies on the performance of a light-duty diesel engine fueled with diesel or a WCO biodiesel–diesel blend', Fuel, 236, pp. 1273–1281. Available at: https://doi.org/10.1016/j.fuel.2018.09.111.

Rakopoulos, D.C. et al. (2012) 'Characteristics of performance and emissions in high-speed direct injection diesel engine fueled with diethyl ether/diesel fuel blends', Energy, 43(1), pp. 214–224. Available at: https://doi.org/10.1016/j.energy.2012.04.039.

Reitz, R.D. et al. (2020) 'IJER editorial: The future of the internal combustion engine', International Journal of Engine Research, 21(1), pp. 3–10. Available at: https://doi.org/10.1177/1468087419877990.

Sonawane, U., Kalwar, A. and Agarwal, A.K. (2020) 'Microscopic and Macroscopic Spray Characteristics of Gasohols Using a Port Fuel Injection System', in. Available at: https://doi.org/10.4271/2020-01-0324.

Wang, Z. et al. (2017) 'The influence of flash boiling conditions on spray characteristics with closely coupled split injection strategy', Applied Energy, 187, pp. 523–533. Available at: https://doi.org/10.1016/j.apenergy.2016.11.089.

Zhan, C. et al. (2020) ‘The spray vaporization characteristics of gasoline/diethyl ether blends at sub-and super-critical conditions’, Applied Thermal Engineering, 164, p. 114453. Available at: https://doi.org/10.1016/j.applthermaleng.2019.114453.

Zhu, H. et al. (2013) ‘Defeat of the Soot/NOx Trade-off Using Biodiesel-Ethanol in a Moderate Exhaust Gas Recirculation Premixed Low-Temperature Combustion Mode’, Journal of Engineering for Gas Turbines and Power, 135(9). Available at: https://doi.org/10.1115/1.4024380.

#43: Concept of net-zero-ready residential buildings in hot-humid region

Lessons learned from the Arabian Gulf vernacular architecture

Mosad ALHAWAS[1], Rabah BOUKHANOUF[2]

[1]The University of Nottingham, UK, Nottingham, NG23BE, Mosad.Alhawas@nottingham.ac.uk
[2] The University of Nottingham, UK, Nottingham, NG7 2RD, Rabah.Boukhanouf@nottingham.ac.uk

Abstract: This paper investigates the energy performance and feasible energy efficient measures to achieve a Net-Zero-Ready House stage for the eastern Arabian Gulf peninsula considering the local vernacular architecture and passive cooling techniques, regional hot and humid climate conditions, and architectural context. The Net-Zero-Ready stage is when it's reasonable to start installing the solar panels, and usually, the building consumes around 50% less than the regional EUI. This study can help enhance residential building energy consumption by producing a new housing construction trend of low energy, less carbon footprint. Even though the Gulf residential buildings' electricity consumption is almost double that of their international counterparts, most of the NZEH in hot-humid climates have reached the zero-energy stage through active and passive measures. Usually, after applying the passive measures, the building achieved a low energy consumption level at this stage, with an average of 70 kWh/m2 /year for all investigated studies of a typical residential building in the hot-humid regions. Using computer software simulation (IES), a base case building model energy performance was evaluated by introducing passive cooling techniques and applying energy-efficient measures. The result showed that the total energy consumption could be reduced by around 11% by utilizing ancient building construction methods, including natural ventilation strategies, through a wind catcher, wind scooping, and a courtyard. Those techniques are established in Arabian Gulf traditional and vernacular architecture to cope sustainably with the harsh condition of the desert's hot-arid-humid climate. Furthermore, additional energy efficiency measures helped reduce energy consumption by 30%, making the home perform at a low energy consumption level and reach the Net-Zero-Ready stage. It was found that the most effective measures to reduce energy consumption are enhancing the envelope specification and increasing the mechanical air conditioning efficiency with an energy reduction of 8 % and 24% respectively.

Keywords: Net-Zero, passive-cooling, energy-conservation, Passivhaus, Natural-Ventilation

1. INTRODUCTION

The abundance of oil resources allowed Gulf Council Countries (GCC) to use revenues from oil sales to construct new modern cities and associated infrastructure, with a huge environmental impact on energy demand and carbon emissions (Alyousef and Stevens, 2011). The oil wealth also has been reflected in considerable changes in lifestyle patterns and standards of living. It was found that lifestyle, individual consumer behavior, and other socio-cultural factors influence energy use in individuals' dwellings (Picard et al, 2020), which has listed the Arabian Gulf Countries among the top ten countries of electricity consumption and CO2 emission per capita (The World Bank, 2011). Furthermore, with oil prices fluctuating in unstable conditions, and since 80% of our electricity generation is driven by oil as the primary energy source, the necessity to diversify our energy resources is becoming vital (eia, 2013). In fact, in late 2014, the Saudi government hiked the price of household energy bills by 60% due to low oil prices, putting pressure on many ordinary families to take more notice of their daily living expenses (Blanchard,2014).

Consequently, to contribute to domestic energy needs and long-term environmental sustainability, the GCC countries must immediately consider the many benefits of promoting Zero Energy Homes (ZEHs) for the regional residential market. ZEHs can be a feasible solution to reduce the dependence on fossil fuels for energy production by promoting sustainable and renewable approaches in the residential sector (Feng, 2019). However, in this harsh climate region, our ancestors in the Arabian Gulf region had a critical issue coping with living in this environment. Nevertheless, they have adapted to the complex condition by utilizing some techniques extracted from their ambient environment (Hawker, 2008). Those techniques (passive approaches) interact in harmony with nature rather than in conflict with it (Bhamare, 2019), which results in moving the Indore environment to reach the thermal comfort stage without the need for any artificial source of energy (Khalili and Amindeldar, 2014).

Even though the Gulf residential buildings' electricity consumption is almost double that of their international counterparts (Krart, Aldubyan and Williams,2020), most of the NZEHs prototypes in hot and humid climates have reached the zero-energy stage through active and passive measures (Cabeza and Chàfer, 2020), (Thomas and Duffy, 2013). Most cases began the design stage by enhancing the building envelope quality, then applying passive measures and EEMs. The building reaches a low energy consumption level at this stage, which was for most case studies, on average of 70 kWh/m2 /year (Feng, 2011), (Al-khateeb and Abu-hijleh, 2019), (Shin et al, 2019), (Casini, 2020), (Eshraghi et al, 2014),(Alfaris, Juaidi and Manzano, 2017),(Lan, Wood and Yuen, 2019),(Kristiansen, MA and Wang, 2019). After the building reaches the low energy combustion stage, the active measures become feasible to utilize in order to reach the NZE stage. In most cases, active measures have proven to be more useful in reducing energy demand than passive measures. For instance, in the Al-khateeb & Abu-Hijleh case (2019), the passive parameters reduced electricity consumption by 14.7%, while active measures reduced electricity demand by 63.2%.

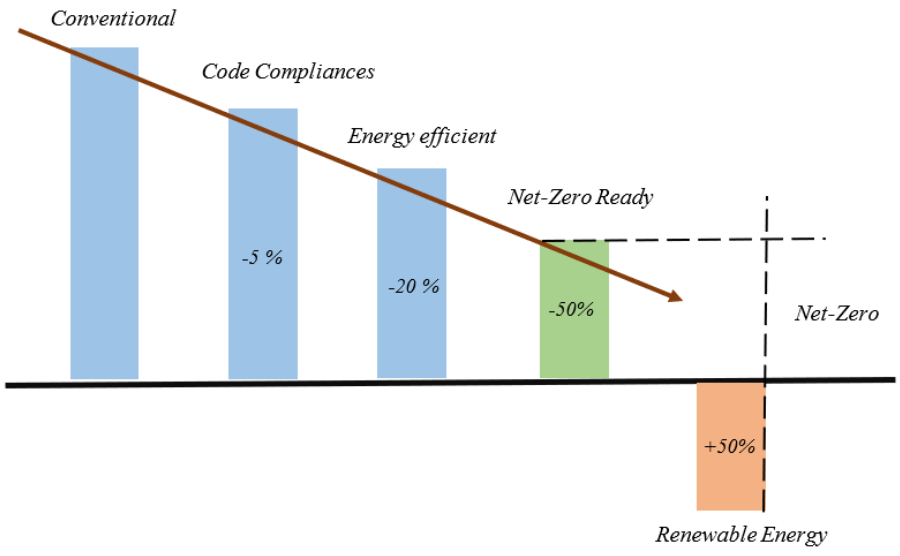

Figure 1 Trend to Net Zero Energy Buildings

Figure 1 shows a general trend of energy reduction stages to achieving zero energy building. It is shown that more than compliance with construction codes and energy efficiency measures are needed to achieve a net zero energy building level, and energy generation from renewables is the crucial factor toward reaching a net zero level. (Maclay, 2014).

1.1. Arabian Gulf's Vernacular Passive Cooling Techniques

Passive cooling refers to any technologies or design features utilized to reduce the temperature of buildings without the need for power consumption. The passive design responds to the local climate and ambient environment to ensure the comfort and well-being of building users while conserving energy use (Bhamare, Banerjee and Rathod. 2019). The core of designing a passive building is to utilize the best advantage of the local climate (Taleb and Hanan, 2014). Both building systems and passive design parameters have been proven to be an essential key to reach an NZEB goal, Combined and integrated based on local climatic conditions and ambient environment (Feng, 2011). A study showed that passive cooling techniques could sustain the indoor temperature within the comfort range while reducing the required building cooling load and energy consumption (Al-khateeb and Abu-hijleh, 2019).

By utilizing the surrounding ambient environment, the ancient builder "Banna" utilized so many environmental phenomena through observation and perception (Hawker, 2008). Such as, Stack Effect through wind-catchers, Thermal Mass in the use of massive walls, Cross Ventilation through Wind Scoops (Sakiyama, Frick, Garrecht and Carlo,2020), Underground Temperature in the use of the basement, and The Swing in Temperature Between Day and Night through courtyards. (Khalili and Amindeldar, 2014). Likewise, by understanding the material's physical characteristics, the ancient builder decided which materials to use in summer or winter. For instance, coral stone is preferred in the summer because it has a low thermal conductivity due to its high porosity. Conversely, mud bricks to use in the winter to utilize their high thermal capacity (Friess & Rakhshan, 2017). Nevertheless, locally available construction materials were widespread until the industrialized revolution, which marked the increased use of modern techniques and standardized building materials. Modern architecture has given emergence to a universal aesthetic architecture that looks alike and is highly dependent on energy consumption (United Nations Environment Programme, 2021).

The lessons we are given by traditional and vernacular architecture in the harsh condition of deserts' hot-arid-humid zones make us respect our ancestors' imagination and creativity (Hawker, 2008). (See Table 1). Nowadays, the modern builder has mimicked and evoked some modern technologies and measures by following our ancestor's ancient methods, such as adobe walls, wind scops, finish materials, and a wide variety of shading devices to improve climatic comfort in the internal and semi-internal building surrounding (Kroll et al, 2019). Architects can attain climatic comfort by skillfully manipulating architectural design parameters and using nature abundantly wisely. Therefore, like how our ancestors managed to live in the Arabian Gulf's harsh climate, we should design our homes in harmony with the ambient environment and climatic change by offering a more flexible design and a wised selection of materials that suit our environments.

Table 1: Summary of the passive cooling Techniques, which were matched with their own environmental characteristics to apply to the base case (Hawker, 2008), (Khalili and Amindeldar, 2014), (Sakiyama, Frick, Garrecht, and Carlo,2020) and (Tamimi and Alibaba. 2017).

Passive cooling Techniques		Technique Description	Advantages	Disvanteges
1-Wind Tower		Collect the prevailing summer wind by its opening then guide the air down and circulate it through the building.	✓ Increasing air ventilation. ✓ Works even with the absence of wind. ✓ Collecting wind from all directions. ✓ Focused on the designated desirable area.	• Large openings cumulate dust inside the area. • Tower discharger serves only one designated container.
2-Massive Wall		Using adobe walls made of mud bricks or coral stone in order to utilize the thermal mass characteristic.	✓ has high thermal capacity. ✓ Has a low heat conductivity. ✓ Absorb the heat during the day and radiate it at night.	• cannot be laid when it rains heavily or when temperatures fall below freezing. • Massive wall thickness consumes space from the designed area.
3-Courtyard		A private cooled area that opens to the sky is usually surrounded by house rooms and located in the center of the house.	✓ helps ventilation and filters dust and noise. ✓ The ground and envelope work as a massive wall. ✓ Provides rooms with daylight.	• Hard to maintain during sandstorm seasons. • During the day, must provide shading element.
4-Wind Scoop		Sunken niche on the external wall creates wind scoops which make the air penetrates through the building rooms.	✓ Encourage air ventilation inside the room. ✓ Provide privacy more than windows. ✓ Easy to control during winter.	• Usually, the niche is blocked by bards' nests. • Doesn't provide any view. • Limited sunlight access
5- Ivan		Traditional Iranian architecture works as a semi-open space (Arcade) with access to the courtyard from one side.	✓ creating thermal comfort conditions in adjacent indoor spaces. ✓ linking the spaces and taking advantage of the sky view.	• Can't control at cold night • It's hard to control during sandstorm seasons.

1.2. Hot-humid climate's Energy-efficient measures

The path towards NZEH begins with enhancing the building construction materials and design quality to reduce energy consumption, which depends on involving some energy efficiency measures that contribute to the whole building categories (Cabeza and Chàfer, 2020). In contrast with how our ancestors interacted with their environment in harmony, especially in designing their shelters, most buildings in the Gulf Region are designed with no response to the local climate. Preferably, they rely on active systems to surmount the impact of uncomfortable climatic conditions, making them notable contributors to high energy consumption and carbon emissions. Therefore, much of the obligation to reduce buildings' environmental impact relies on architects, developers, and engineers. Building construction should be responsive and adaptive to local climatic conditions and ambient environment as our ancestor way of design (Hawker, 2008). Architects and developers should consider utilizing passive cooling techniques and energy efficiency measures in their design, which can reduce the energy need for cooling, heating, and lighting to a figure close to zero as the building becomes an energy generator (Feng, 2019). Feasible planning and integration during the building envelope's design process is the solution to produce energy-efficient buildings since arrangements made at different stages of the building envelope's design can influence overall building energy consumption and performance (Cabeza and Chàfer, 2020).

Selecting the most effective energy strategies will require an integrated evaluation of all energy-efficient measures as a package. For instance, the interaction between shading, glazing, and interior artificial lighting elements can together influence the cooling load reduction. For example, shading devices can prevent direct solar heat gains. Simultaneity allows indirect daylighting to penetrate the building, reducing artificial lighting use by dimming or switching in response to daylight intensity. When parameters like this are evaluated as a combination, they have higher efficiency regarding energy conservation and materials cost feasibility (Al-khateeb and Abu-hijleh, 2019).

Energy efficiency in buildings can be obtained through a set of measures that vary in their ability to influence the cooling load demand. For instance, HVAC systems with a higher Energy Efficiency Ratio significantly impact reducing the building cooling load (Vakiloroaya et al, 2014) (Pérez et al, 2011). (See Table 2). On the other hand, some measures have a minimal effect on reducing energy consumption. As multiple studies have shown, green roofs are not a feasible measure to utilize in a hot climate because it has a minimal impact on reducing building cooling load, need a previous structural calculation and must be irrigated during the year (Fantozzi et al, 2021) (Andric, Kamal and AL-Ghamdi, 2020). So, selecting the most compatible energy-efficient measures combination, in terms of feasibility & efficiency, is the key toward energy conservation including reaching the stage of NZE – ready.

Table 2: Summary of energy-efficient measures that is suitable for hot-humid climate with some suggestions and limitations and applied to the Base case (Saudi Building Code, 2018) (Kristiansen, and Wang, 2019) (Al-khateeb and Abu-hijleh, 2019) (Bhamare, 2019) (Ghisi and Tinker, 2005) (Vakiloroaya et al, 2014).

Energy Efficient Measure		Technique Description	Suggestions	limitations
1-Building Shape and Orientation	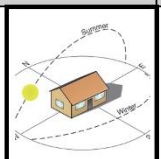	Arrangements about fundamental building design (shape & orientation) At the initial stage of the architectural scheme in the meaning of minimizing summer heat gain.	- In the Gulf region, Rooms with higher internal gains can be located on the north side of the building. - Avoiding uninsulated exterior surfaces exposed to the sun which results in heat gain, and places greater cooling demands.	- It can't be applied as retrofitting strategy. - It can't be applied when the site location restricts the building's orientation.
2-Wall and Roof Insulation		Layers made by low thermal conductivity materials which reduce unwanted heat loss or gain and minimize the energy demands of heating and cooling systems.	- For the Gulf Region, R-value for insulation should not be less than 2.38 m^2* k \ w for roofs and 1.34 m^2* k \ w for walls. - insulation with a thickness of 2 cm could save energy up to 22%.	-Thicker external wall insulations are not financially feasible. - Limitations to be applied as retrofitting strategies.
3-Window Shading and Glazing Type		Shading fenestrations by vertical or horizontal elements (fins or overhangs) in the sake of prevents direct solar heat gain and allows daylighting.	- Glazing should not exceed 25% of the total wall area -The infiltration rate in windows should not surpass 1.5 L/s, and SHGC should be between 0.25 - 0.35.	-About 45-60% of the building cooling load generates by heat gain throw windows in cases where windows cover 20–30% of the walls.
4-Natural Ventilation		Natural driving forces are either the stack effect, due to the temperature variation, or the crosswind effect, due to the difference in air pressure.	- A high air velocity is required in hot and humid climates to ensure reaching the thermal comfort situation due to the humidity. - Combining driven forces is a helpful strategy for better thermal comfort.	- It is vital to avoid any possible adverse effects of forces combination. - Not feasible at high outdoor temp.

5-Day lighting		In the initial design stage, utilizing daylighting and minimizing artificial light reliance for the sake of decreasing buildings' energy consumption.	- Diffused daylight is considerably lower in heat gain than direct light. Thus, it is favoured in reaching thermal comfort. - Rooms whose width is greater than their depth have higher daylight levels.	-More daylight in the building may result in added heat gain. - Climatic factors such as sky conditions influence the room's illuminance.
6- Thermostat Setback		Balancing the actual indoor temperature with an objective temperature setpoint to control the HVAC equipment's performance status results in cooling demand reduction.	- Users have reported that a reasonable thermostat program brings a range of 10% to 30% reduction to their electrical energy bills. -Several studies showed its recommended setting the Thermostat to 25 ºC.	- Studies have reported that 90% of users seldom adjust the thermostat to set a holiday or weekday program.
7- HVAC System Efficiency		Install HVAC systems with a higher Energy Efficiency Ratio (EER) and (SEER), to influence a reduction in the buildings' cooling demand.	- Recommended buying Air conditioners with an energy efficiency ratio of 13 EER and above to ensure energy efficiency in hot, humid climates. - The EER increase when the outdoor temperature is lower than the indoor.	- Unfeasible to be applied as retrofitting strategies - HVAC systems with higher efficiency usually have higher initial costs.

2. THE BASE CASE

The base case was designed in the eastern region of Arabian Gulf. Key aspects and developing features for the Dammam city conventional base case were carried out from the Dammam city residential building case studies and the residential building survey that has been distributed and analyzed. Moreover, the Saudi building code that has been established since 2018 has been examined and included in designing the essential aspects. Also, previous models from other researchers were reviewed and compared to identify the Dammam city base case (see Figure 3).

The designing process was compatible with All the base case main design parameters, including the building geometry and functional spaces, Construction materials, Heating, ventilation, air-conditioning system (HVAC), and electrical system, including lighting. Each designing parameter contains secondary key aspects that were examined in detail to ensure that all base case aspects are covered (see Table 3). After performing the simulation on the IES energy simulation program, the base case energy consumption was 126 kWh/m2 /year (see Figure 4). The average EUI value for the housing stock in KSA is around 149.6 kWh/m2 /year (Krarti, Aldubyan and Williams, 2020) (Alalouch, Saleh and Al-saadi, 2016).

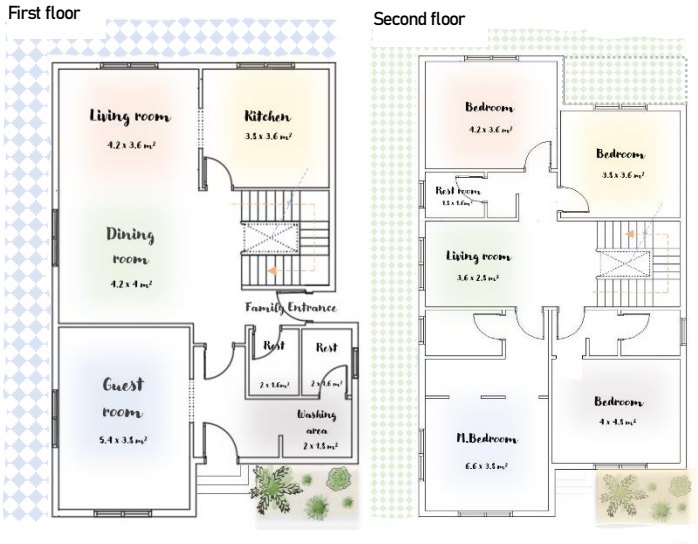

Figure 3 2D layouts of the designed base case first and second-floor plan

Table 3: The base case construction specifications which have been simulated in IES

External Wall U-Value (W/M²K)	Double-Glazed Window System U-Value (W/M²K)	Window-To-Wall Ratio (wwr)	Roof U-Value (W/M²K)
25mm Stucco+250mm Sandwich Concrete Block Eps Filled Core +25mm Stucco (0.41 W/M²K)	Openable double-glass windows (6mm/ gap/6mm) (1.25 W /m²K)	8 % of the gross wall area (31 m²)	25mm terrazzo tiles+25mm mortar+ 4mm bitumen layer+ EPS 50 mm +150 mm cast concrete +25mm stucco (0.43 W/m²K).
HVAC System	Infiltration Rate (ACH)	Simulation Set-Point (Heating & Cooling)	Equipment & Lighting Power Density
Mini-Split Unit EER 2.5 & SEER 3.6	0.25 ACH	23ºC-24ºC for Cooling, 21ºC-18ºC for Heating	Lighting: 1.6 W/m², Refrigerating: 1.8W/m², cooking: 12Wm², misc.: 4W/m² People: 90W/person

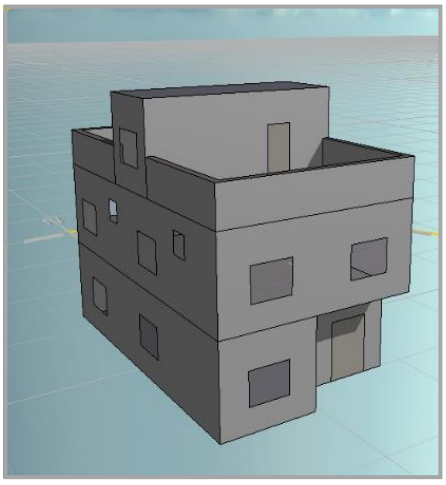

Figure 4 The base case 3D model simulated in the IES energy simulation tool

3. METHODOLOGY

The paper methodology is divided into three stages to meet the main gap aims and objectives. Each step will require a specific and different conducting tool to answer a particular question and fulfil the specified purposes. **Stage one** begins with enriching the background by understanding specific topics about the gap area, including how our ancestors managed to survive in the Arabian Gulf's harsh climate by utilizing only passive cooling approaches. Also Highlighting some of the EEM & techniques which are suitable for our climate conditions toward reaching the NZE-ready stage. **Stage two** consists of investigating the actual construction practices in the region and establishing a base case to be a reference point toward NZE. As it is known, The Individuals in Saudi and the Gulf have a unique community that is traditional in culture and centred around religious practices and legislations as a focal element that shaped our lifestyle, including the building design criteria such as privacy level and energy consumption behaviour. Therefore, it is vital to identify the parameters influencing building design criteria and energy consumption in the domestic sector. This approach requires a public survey analysis which was done for this purpose. Moreover, it is necessary to pursue a different path and identify the physical and practical factors influencing energy consumption in the domestic sector by analysing a base case based on the climatic conditions in Dammam city. **Stage three,** an NZE-ready prototype, is built by utilizing some of the data gathered in phase one, including the passive cooling techniques, EEM, and enhancing building envelope. Therefore, it is necessary to validate the framework and answer the final gap questions by conducting an additional approach employing simulation tools to identify the extent to which the NZE-ready in general can be achieved in Dammam city and the Arabian Gulf. In the end, final recommendations and remarks are set including the NZE- ready proposed prototype which is designed and validated using IES energy simulation tool.

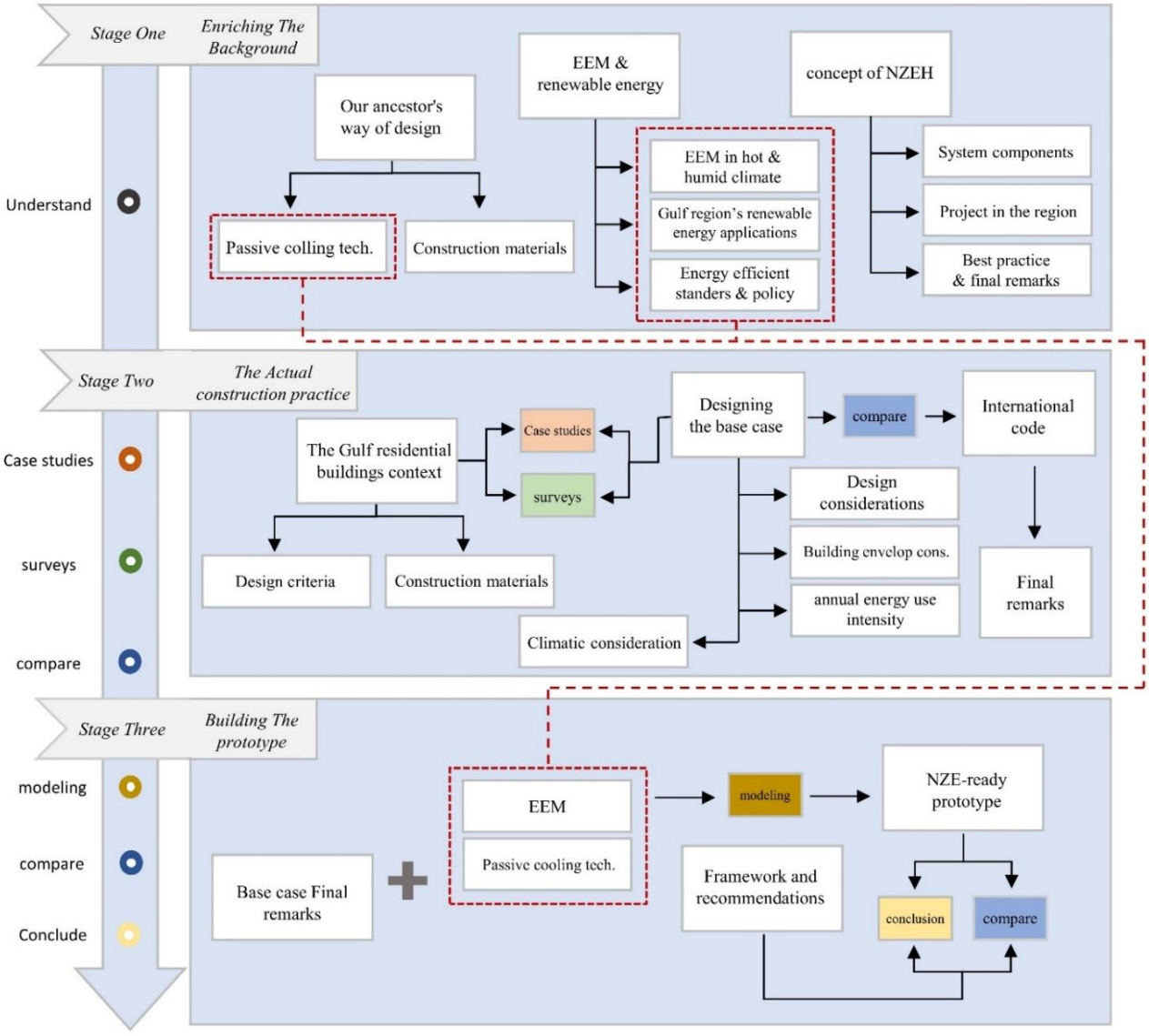

Figure 5 Methodology diagram, which is divided into three main stages to meet the main gap aims and objectives. Each step will require a specific and different conducting tool to answer a particular question and fulfil a specified purpose

4. APPLING PASSIVE COOLING DESIGN

In this step, natural ventilation will be introduced to the home through a wind catcher, wind scopes and an operable door centred inside a courtyard. The base case main geometry design has been developed to re-engage the passive cooling strategies in the home. Natural ventilation developed techniques will work only if the room temperature is higher or equal to the outside air temperate (room temp. ≥ outside air temp.). The idea behind the design is to utilize the staircase area to make it work as a wind catcher, which simultaneously serves as a central area to distribute the air throughout the home spaces and allow hot air to escape the building (see Figure 6). Hawker (2008) describes that the wind tower has two ends and a shaft. One rises via the roof as the upper part with a maximum of four openings, and the other reaches the end of the cellar, which could “discharge opening.” The base case wind catcher has been designed considering Sanji’s (2015) recommendations with a 2.6 x 2.6x 3.6 m diminution. Moreover, a discharger opening on each floor allows air distribution throughout the building. The wind catcher has four openings with an area of 1.2 x 2.2 m and five discharge openings with the same designed area. All home openings are linked to sensors to control the wind catcher’s operation.

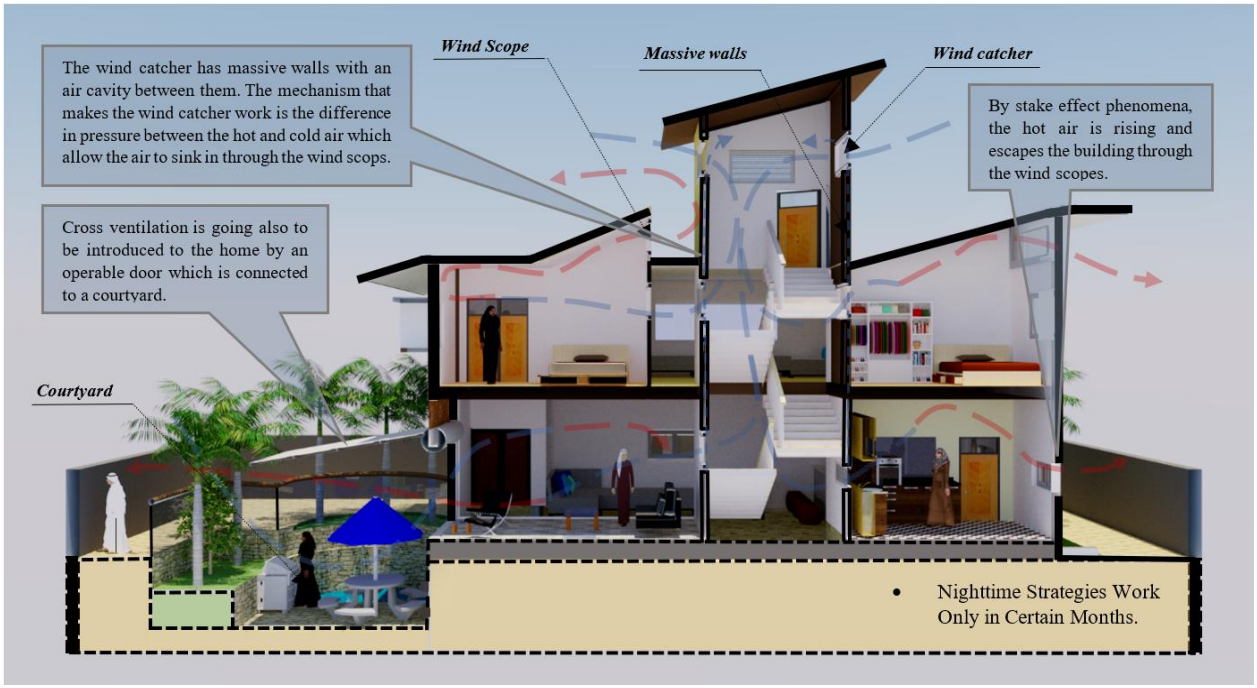

Figure 6 the Base Case has been redesigned by applying a wind catcher, an operable door that is centred on a courtyard and wind scopes to introduce cross ventilation to the building

The wind tower mechanism functions by differentiating the temperature and density between the outside of the home and the inside. Since the temperature outside is higher than inside, the air density outside is lower, making the light air around the tower sink inside the shaft. So, the differentiation in the temperature and density makes the tower work even with the absence of wind by the concept of stack effect phenomena. On the other hand, Windcatcher inside the house is linked to the main spaces inside the home like a (majlis) and serves more than one floor. To utilize the ultimate benefit of the wind catcher, discharge openings should always serve a container to make it works as a cool lake or reservoir. The natural ventilation geometry has been developed and analysed through the Microflow feature in the IES energy simulation program (see Figure 7). The Microflow feature calculates the average airflow the building can receive throughout the year. The airflow volume that the building gets determines the total heat loss throughout the ventilation process, which then the energy conservation can be estimated (see Figure 8). Also, the building’s space cooling consumption and the CO2 concentrations can be estimated through IES to estimate the improvements.

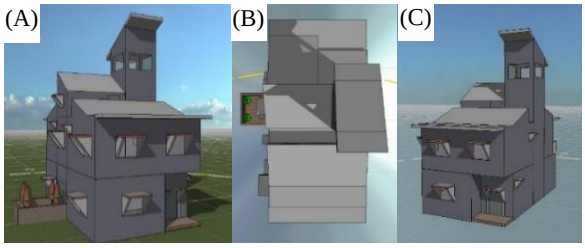

Figure 7 The base case geometry on the IES energy simulation program, shows the natural ventilation measures

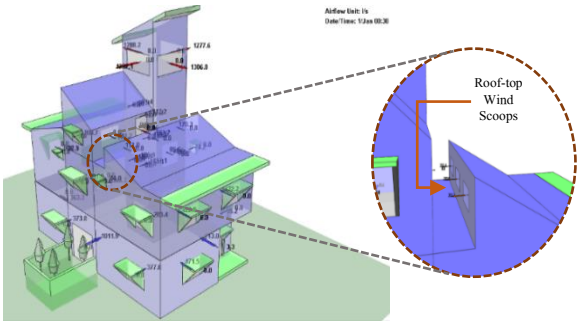

Figure 8 IES Microflow analysis feature shows the base case natural airflow movement through the prototype openings

After performing the simulation through the microflow feature, the result showed that, in the summer, the home wouldn't receive any natural ventilation, except the ACH., for the months of (Jun, Jul, Aug, and Sep) since the natural ventilation will stop if the external temperature is more elevated than the room temperature. On the other hand, in certain winter months, the total natural ventilation the building can receive exceeds 20000 l/s. Furthermore, the average natural ventilation throughout the year (volume flow) the house receives from all geometry inlets is around 4239 l/s (see Figure 9). On the other hand, regarding building CO2 concentrations, During the day, the outside temperature is more elevated than the inside, preventing natural ventilation. Hence, the high CO2 concentrations are connected directly to the absence of ventilation during noon. In fact, during noon, the CO2 consecration exceeds 1000 ppm, which might associate with complaints of drowsiness and poor air quality. Nevertheless, natural ventilation helped reduce home carbon emissions (kgCO2/h) by 9.8% (see Figure 10). Also, regarding home energy consumption in general, natural ventilation helped reduce the building's space cooling consumption (MWh) by 17% And reduce the building's total electricity consumption (MWh) by approximately 10%.

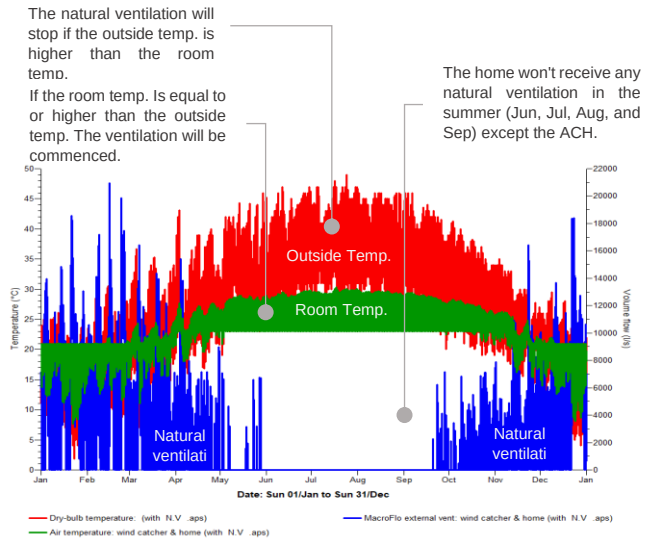

Figure 9 IES Graph shows the relationship between base case outside temperature, room temperature and ventilation

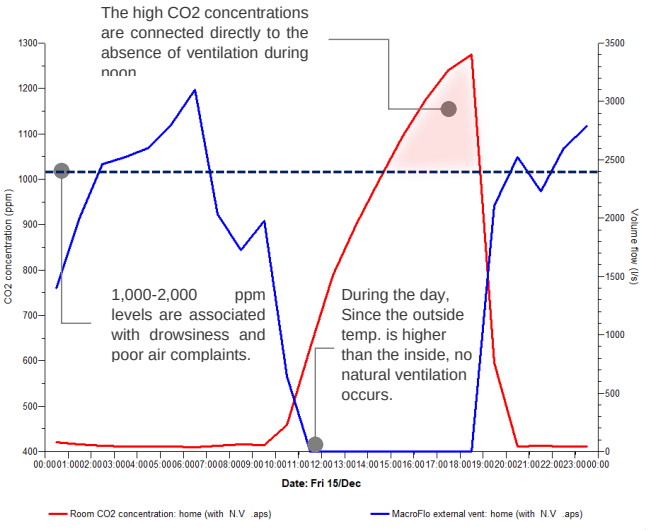

Figure 10 IES Graph shows the relation between CO2 concentration and introducing natural ventilation in the base case on the 15th of December

5. APPLING ENERGY EFFICIENT MEASURES

In this step, the base case energy consumption efficiency will be enhanced by applying some efficient and sustainable measures, which will be selected depending on the analysis of the Dammam city survey and the previous data review in this paper. Each measure will be applied individually to measure the actual effect of each enhancement. On the other hand, some of the selected criteria might be eliminated in the final design depending on the energy-saving efficiency of each tested technique. The measures that have been set, which are suitable for hot-humid climates, include window shading, building shape and orientation, daylighting, HVAC system efficiency and thermostat setback point. The Base Case building envelope u- value for the roof and wall has been enhanced by 50% more to reach around 0.25 w/m²k for the wall and 0.21 w/m²k for the roof. In this investigation, increasing the wall efficiency by more than 50% from the base case scenario led to several obstacles, such as increasing the wall thickness by 40cm and the cost of expanding the wall insulations. The envelope windows have been changed from Double-glazed to a triple system with a u-vale of 0.82 w/m²k (glass only). On the other hand, the base case HVAC efficiency has been increasing 50% more to reach a SEER of 5.4, and the HVAC set point is to be increased to 24°c-25°c for cooling (see Table 4).

Table 4 The improved base case construction specifications &EEMs that have been simulated in the IES tool.

Home			
External Wall U-Value (W/M²K)	Double-Glazed Window System U-Value (W/M²K)	Window-To-Wall Ratio (wwr)	Roof U-Value (W/M²K)
25mm stucco,150mm L.W concrete block, EPS. 50mm, 150mm L.W concrete block,25mm stucco (0.25W /m ²K)	Openable triple Low-E glass windows filled with Argon. (6mm/gap/6mm/gap/6mm) (0.82 W /m ²K)	8 % of the gross wall area (31 m²)	12.5 mm terrazzo tiles+12.5 mm mortar+ 4mm bitumen layer+ EPS 100 mm +150 mm cast L.W concrete +25mm stucco (0.21 W /m ²K)
HVAC System	Infiltration Rate (ACH)	Simulation Set-Point (Heating & Cooling)	Equipment & Lighting Power Density
Mini-Split Unit EER 3.75 & SEER 5.4	0.25 ACH	24°C-25°C for Cooling, 18°C-21°C for Heating	Lighting: 1.6 W/m², Refrigerating: 1.8W/m², cooking: 12Wm², misc.: 4W/m² People: 90W/person

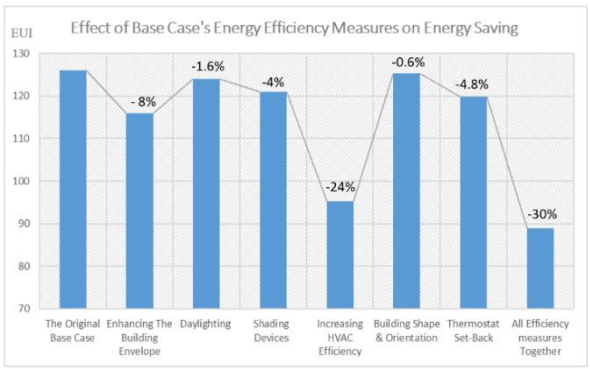

Figure 11 shows the Effect of the Base Case's Energy Efficiency Measures on Energy Saving

After performing the modified model in the IES energy simulation program, the result showed that enhancing the home envelope u-value by 50% helped decrease the total home energy consumption by 8%. Moreover, installing a shading device on the home openings has shown an energy consumption reduction of 4%. Furthermore, depending on daylighting during the day by minimising the reliance on artificial lighting helped to decrease energy consumption by 1.6%. On the other hand, the most effective measure was increasing the Base case HVAC system efficiency by 50%, showing a significant energy consumption reduction of 24% and adjusting the thermostat set-back point to 24°c-25°c for cooling has decreased the total energy consumption by 4.8 % (see Figure 11). The key to achieving the NZE stage is to combine multiple parameters, including passive cooling techniques and EEMs, and enhance the building efficiency, then utilise renewable energy (See Figure 13). Moreover, as a combination, the whole set of previous measures helped reduce the total energy consumption to reach the NZE-ready stage by up to 40%. (See Figure 12).

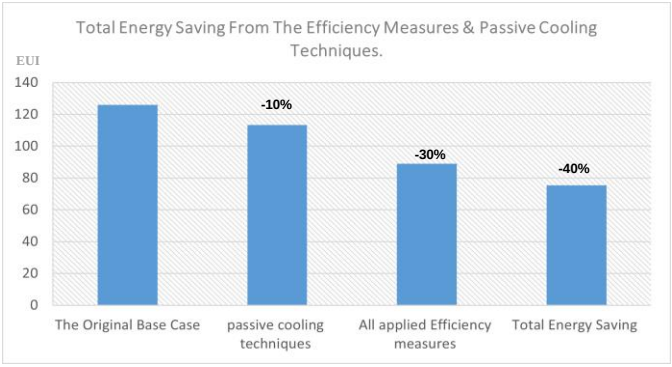

Figure 12 Total Energy Saving from The Efficiency Measures & Passive Cooling Techniques

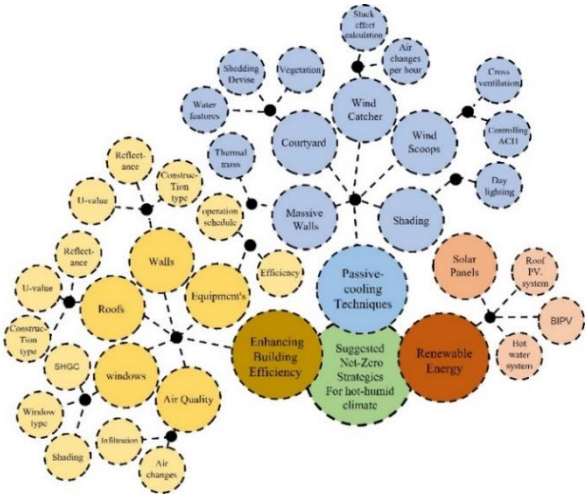

Figure 13 Synthesis diagram showed suggestions for hot-humid climate Net-Zero strategies

6. CONCLUSION

The harsh desert climatic conditions of the Arabian Peninsula pose critical living conditions due to high seasonal temperatures. Nevertheless, the region's ancient inhabitants have adapted to the ambient environment by utilizing low-energy approaches for thermal comfort in buildings. This paper showed that by incorporating passive cooling techniques into conventional residential buildings, such as natural ventilation through a wind catcher, wind scoops, and an operable door centred inside a courtyard, a home's total energy consumption is reduced by 10%. Moreover, the building's space cooling consumption is reduced by 17%. Regarding emissions, Natural ventilation reduced residences' carbon emissions by 9.8%. On the other hand, applying EEMs to the home has helped reduce the home's energy consumption by 30%. The most effective measure was increasing the HVAC system efficiency, which reduced total energy consumption by 24%. Moreover, enhancing the wall u-value by 50% has reduced energy consumption by 8%. To have feasible planning and design, the path towards applying the concept of NZEH begins with reducing home energy consumption before applying renewable energy strategies. Thus, reaching the stage of NZE-ready is essential before applying renewable. The key to achieving the NZE stage is to combine multiple parameters, including passive cooling techniques and EEMs, and enhance the building efficiency, then utilize renewable energy to avoid any unfeasible oversizing for the building systems.

7. REFERENCES

Alfaris, F., Juaidi, A. & Manzano-Agugliaro, F. 2017. Intelligent home technologies to optimize the energy performance for the net zero energy home. Energy and Buildings, 153, 262-274.

Alkhateeb, E. & Abu-Hijleh, B. 2019. Potential for retrofitting a federal building in the UAE to net zero electricity building (nZEB). Heliyon, 5, e01971.

Alyousef, Y. & Stevens, P. 2011. The cost of domestic energy prices to Saudi Arabia. Energy Policy, 39, 6900-6905.

Andric, I., Kamal, A. & Al-Ghamdi, S. G. 2020. Efficiency of green roofs and green walls as climate change mitigation measures in extremely hot and dry climate: Case study of Qatar. Energy Reports, 6, 2476-2489.

Bank, T. W. 2011. CO2 emissions (metric tons per capita) [Online].: The World bank Available: https://data.worldbank.org/indicator/EN.ATM.CO2E.PC [Accessed 2011].

Blanchard, A. A. 2014. Seven Questions About The Recent Oil Price Slump. Available from: https://www.imf.org/en/Blogs/Articles/2014/12/22/seven-questions-about-the-recent-oil-price-slump.

Cabeza, L. F. & Chàfer, M. 2020. Technological options and strategies towards zero energy buildings contributing to climate change mitigation: A systematic review. Energy and Buildings, 219.

Casini, M. 2020. A positive energy building for the Middle East climate: ReStart4Smart Solar House at Solar Decathlon Middle East 2018. Renewable Energy, 159, 1269-1296.

Committee-Sbcnc, S. B. C. N. 2018. Saudi Building Code (SBC). In: (SBCNC), T. S. B. C. N. C. (ed.) Saudi Building Code National

Dehghani-Sanij, A. R., Soltani, M. & Raahemifar, K. 2015. A new design of wind tower for passive ventilation in buildings to reduce energy consumption in windy regions. Renewable and Sustainable Energy Reviews, 42, 182-195.

Dnyandip K. Bhamare, M. K. R. & , J. B. 2019. Passive cooling techniques for building and their applicability indifferent climatic zones—The state of ar. Energy & Buildings.

Eshraghi, J., Narjabadifam, N., Mirkhani, N., Sadoughi Khosroshahi, S. & Ashjaee, M. 2014. A comprehensive feasibility study of applying solar energy to design a zero-energy building for a typical home in Tehran. Energy and Buildings, 72, 329-339.

Fantozzi, F., Bibbiani, C., Gargari, C., Rugani, R. & Salvadori, G. 2021. Do green roofs really provide significant energy saving in a Mediterranean climate? Critical evaluation based on different case studies. Frontiers of Architectural Research, 10, 447-465.

Feng, W., Zhang, Q., Ji, H., Wang, R., Zhou, N., Ye, Q., Hao, B., Li, Y., Luo, D. & Lau, S. S. Y. 2019. A review of net zero energy buildings in hot and humid climates: Experience learned from 34 case study buildings. Renewable and Sustainable Energy Reviews, 114.For Buildings And Constructio.

Friess, W. A. & Rakhshan, K. 2017. A review of passive envelope measures for improved building energy efficiency in the UAE. Renewable and Sustainable Energy Reviews, 72, 485-496.

Ghisi, E. & Tinker, J. A. 2005. An Ideal Window Area concept for energy efficient integration of daylight and artificial light in buildings. Building and Environment, 40, 51-61.

Hawker, R. W. 2008. Building on desert tides: traditional architecture of the Arabian Gulf UK, Southampton.

Khalili, M. & Amindeldar, S. 2014. Traditional solutions in low energy buildings of hot-arid regions of Iran. Sustainable Cities and Society, 13, 171-181.

Krarti, M., Aldubyan, M. & Williams, E. 2020. Residential building stock model for evaluating energy retrofit programs in Saudi Arabia. Energy, 195.

Kristiansen, A. B., Ma, T. & Wang, R. Z. 2019. Perspectives on industrialized transportable solar powered zero energy buildings. Renewable and Sustainable Energy Reviews, 108, 112-124.

Kroll, D., Breen Lovett, S., Jimenez-Bescos, C., Chisnall, P. & Aitchison, M. 2019. Passive house vs. passive design: sociotechnical issues in a practice-based design research project for a low-energy house. Architectural

Lan, L., Wood, K. L. & Yuen, C. 2019. A holistic design approach for residential net-zero energy buildings: A case study in Singapore. Sustainable Cities and Society, 50.

Maclay, B. 2014. The New Net Zero: Leading-Edge Design and Construction of Homes and Buildings for a Renewable Energy Future, USA, Chelsea Green Publishing Co.

Pérez-Lombard, L., Ortiz, J., Coronel, J. F. & Maestre, I. R. 2011. A review of HVAC systems requirements in building energy regulations. Energy and Buildings, 43, 255-268.

Picard, T., Hong, T., Luo, N., Lee, S. H. & Sun, K. 2020. Robustness of energy performance of Zero-Net-Energy (ZNE) homes. Energy and Buildings, 224.

Sakiyama, N. R. M., Carlo, J. C., Frick, J. & Garrecht, H. 2020. Perspectives of naturally ventilated buildings: A review. Renewable and Sustainable Energy Reviews, 130.

Shin, M., Baltazar, J.-C., Haberl, J. S., Frazier, E. & Lynn, B. 2019. Evaluation of the energy performance of a net zero energy building in a hot and humid climate. Energy and Buildings, 204.

Taleb, H. M. 2014. Using passive cooling strategies to improve thermal performance and reduce energy consumption of residential buildings in U.A.E. buildings. Frontiers of Architectural Research, 3, 154-165.

Thomas, W. D. & Duffy, J. J. 2013. Energy performance of net-zero and near net-zero energy homes in New England. Energy and Buildings, 67, 551-558.

United Nations Environment Programme 2021. 2021 Global Status Report

Vakiloroaya, V. S., Bijan & Fakhar, Ahmad & Pishghadam, Kambiz. 2014. A review of different strategies for HVAC energy saving. Energy Conversion and Management.

#44: Exploring vernacular courtyard strategies to improve thermal performance of modern housing in Dhaka

Shayeeka ALAM[1], Lucelia RODRIGUES[2], Lorna KIAMBA[3]

[1] University College London, London, UK, Shayeeka.alam.22@ucl.ac.uk
[2] University of Nottingham, Nottingham, UK, Lucelia.Rodrigues@nottingham.ac.uk
[3] University of Nottingham, Nottingham, UK, l.kiamba@nottingham.ac.uk

Abstract: The present Dhaka, a rapidly growing unban centre of Bangladesh, is experiencing a major shift in the last three decades, exhibiting a mixed and complex set of characteristics. This study aimed to investigate the thermal effect of the age-old courtyard strategy of Bengal architecture by integrating them with the modern housing. Through an extensive literature study, three vernacular case studies were selected to represent different building styles. Generic models based on typical modern housing styles were also generated for studies. The thermal performance of courtyard in the vernacular buildings was analysed followed by a comparative study between the modern conventional and courtyard buildings. Each study was comprehensively analysed to observe the efficiency of courtyard throughout the year. The final outcomes of this research were based on experiments conducted through building performance simulations software (IES-VE). The investigation revealed that the courtyard helped the vernacular buildings to remain within the thermal comfort temperature range up to 10%. The incorporation of the courtyard in the modern housing in the hot humid temperature resulted in 3% lesser indoor temperature than the conventional houses. The analysis also reviewed that the courtyards support to provide additional solar radiation to increase the comfortable indoor temperature by 10.5% in the winter season.

Keywords: Dhaka, Tropical climate, Courtyard, Thermal comfort, Vernacular strategy, Thermal simulations.

1. INTRODUCTION

Courtyards are one of the oldest vernacular passive design strategies for housing, spanning over 5000 years and creating a distinctive architectural appearance in many regions of the world (Edwards, 2006). In Dhaka, the capital of Bangladesh, courtyards were a prominent architectural feature in residential buildings, which evolved from the indigenous rural houses. Most of the houses contained courtyards either single or multiple in number to epitomize the traditional demand, in addition to improve the thermal and microclimatic conditions of the surrounding spaces providing space for transition, religious purpose and entertainment (Mridha, 2002).

Courtyard had been used in Bengali houses for hundreds of years. By creating a stack effect within a building, courtyards build a significant microclimate inducing air changes in the adjoining rooms and spaces (Mallick, 1994). Courtyards are well-established design strategy for build forms in tropical areas, where both air temperature and humidity are high (Koenigsberger, 1975; Hyde, 2000). In Bengali vernacular houses, courtyard was the focal point for different household and socio-cultural activities defining the spatial arrangement of the buildings (Haque, 1997).

Recently identified as one of the fastest growing megacities of South Asia (Ahsan, 2009), Dhaka is experiencing more pressure than ever for housing solutions, because of the expeditious urbanization factor. Due to the business employment, educational and opportunities it offers as the capital city, Dhaka attracts people from other urban and rural areas in Bangladesh. Both spontaneous and planned developments are taking place in Dhaka in order to accommodate the increasing population (Hafiz,2004; Khan, 2009). According to Raja and Neema (Raja, 2013), the wetlands of Dhaka city decreased by 53.7% while the vegetation decreased by 16.5% from the year 1989-2010; while the built-up area has increased abruptly by 118.7%. If this trend persists further in the future, the built-up area is estimated to be increased up to 49% and 57% of the total city area by the year 2019 and 2029 respectively (Raja, 2013). According to studies by Ahmed (Ahmed, 2013), the annual average temperature of Dhaka in the last two decades has increased by 0.5°C from 1950 to 2000. This trend would result in 56% and 87% temperature rise above 30°C by 2019 and 2029 respectively (Raja, 2013), which needs immediate awareness and appropriate measurements.

Plot sizes have successively become smaller in Dhaka, while the buildings became taller to accommodate more housing units on a given plot, resulting in the extinction of courtyards (Raja, 2013). Despite having a powerful impact on the microclimate of the buildings, courtyards are becoming rare in the modern built environment; although many modern architects are incorporating the vernacular courtyard strategies to mitigate the increasing global temperature and energy consumption in recent days (Aldawoud, 2008; Yaşa, 2014). The rapid urbanization of modern Dhaka city is leading to severe environmental deterioration, unhealthy living conditions, shortage of energy and increased natural calamities (Mridha, 2002). Apparently, the modern apartment buildings in Dhaka are mostly dependent on artificial lighting and ventilation, resulting in the high consumption of energy (Ahsan, 2009). Moreover, the energy consumption is increasing in a dramatic way due to the improved living standard (Ahsan, 2009). To minimise the increasing temperature trend and energy consumption of Dhaka city, including courtyard in modern building design, can be an effective passive method.

A few studies were done on Bengali house forms with courtyards (Mridha, 2002), but none of them evaluated the environmental performance of the vernacular courtyards. Developed by an age-old trial and error process, the courtyards can be an important design element for the tropical countries. This vernacular strategy deserves more attention and study, especially its potential benefits for modern buildings.

2. METHODS

The courtyard is an effective passive way to control the microclimate in the hot and humid region. By ventilating the air of the building through the open space, courtyard helps to keep the internal temperature lower than the outside (Zamani, 2018). A fraction of heat can be stored within the thermal mass of the courtyard in the daytime (Figure 1), which can be released in the nighttime. The remaining heat transfers through conduction and natural ventilation (Yang, 2012).

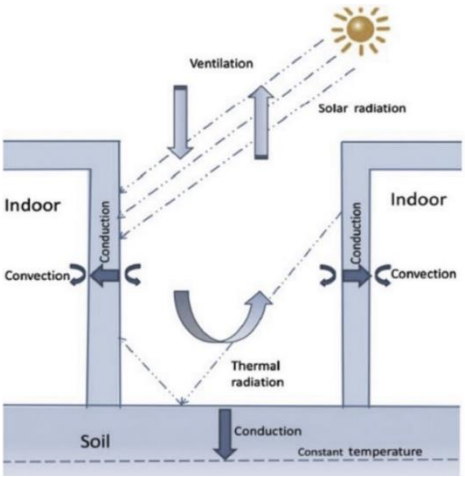

Figure 1 Ventilation and heat exchange in the courtyard (Source: (Yang & Yang, 2012, p.581), adapted by author)

The principal aim of this research was to study and analyse the vernacular courtyard strategies in residential houses in Dhaka and their effect on the thermal performance of the surrounding rooms. Extracted from the vernacular buildings through an extensive literature review, the strategies (Figure 2) were applied to the typical modern housing in Dhaka, to observe the impact of courtyards to enhance the thermal quality of the modern buildings.

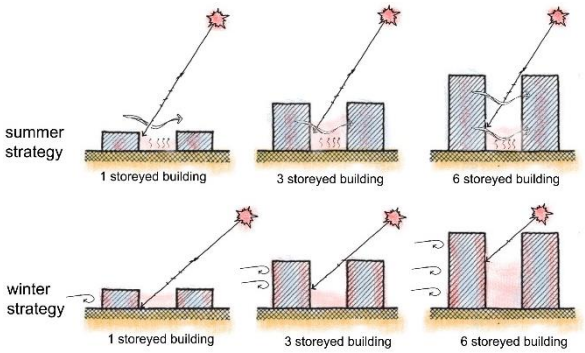

Figure 2 Courtyard strategies

Three vernacular case studies were selected from the detailed literature studies, each representing a dominant style from the mid ninetieth-century historical timeline: the Ruplal house was a famous mansion (Case study 1), the Bashanta Babu's house (Case study 2) was a typical square planned residential building with two courtyards and the House of Prashanna Babu (Case study 3) was a representative of the typical linear shaped building with multiple courtyards (Figure 3).

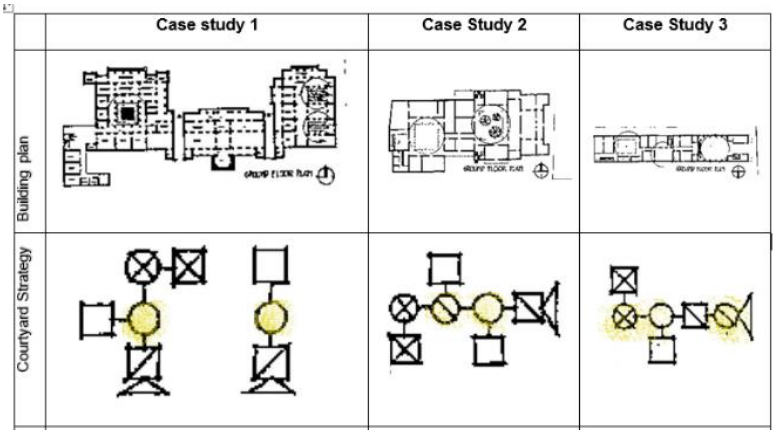

Figure 3 Vernacular case study strategies

It was concluded from the literature review that there was no exact typical dwelling type in the modern housing in Dhaka (Ahsan, 2009). However, from general guidelines, a typical typology was inferred, with 100m^2 of built area and six storeys, and this was used for the thermal analysis (Figure 4). According to the National Building Codes of Dhaka, the width of the plot may be maximum 3.25 times of its depth (Ahmed, 2013); hence, the ratio of depth and width of the built area was kept within 3.25. Moreover, it was seen in the analysis that the vernacular buildings of Dhaka were mostly square and linear in the plan, so both square and rectangular plans were analysed.

The first set A was base case 1, starting from A-1 to A-6 (Figure 4). It was the square plan (10m x 10m) without any courtyard from one storey to six storeys. The second set, B was the square plan (10.5m x 10.5m) with a 3m x 3m courtyard. Starting from B-1, which was the single storey building mass, it went up to B-6 with six storeys as well (Figure 4), The built area was same as base case 1, with a courtyard in the middle.

The third set, C: base case 2 was the linear plan having an exact same built area (20m x 5m) as base case 1. This set was solid plan having east-west elongation, no courtyard was considered. This set started from C-1 and gradually became C-6 with six storeys. Finally, the fourth set D was the linear plan (19m x 6m) with courtyards (6m x 1.5m) in the middle. This set also had six plans from D-1 to D-6.

For the studies, building simulation program named Integrated Environmental Solutions-Virtual Environment (IES-VE), version 2017 was used. As inferred by Sousa (Sousa, 2012), IES-VE is considered one of the most effective and reliable building simulation programs. Each study was comprehensively analysed considering the following assumptions (Table 1):

The external surfaces of the simulated forms were assumed to be opaque. No openings, i.e. windows or doors were considered to avoid the impact of glazed surfaces on the thermal performance of the building. No casual heat gain or

mechanical ventilation was considered so that all the thermal factors involved could be similar. As a result, the heat gain in the building mass is expected to be the result of only solar radiation through the courtyards.

Table 1: Assumptions for simulations

Weather data	Energy plus (.epw) formatted file calibrated with the meteorological data of Dhaka (the year of 2015)
Calendar	Summer (1 March to 31 May) Winter (1 Dec. to 28 February)
Systems	No HVAC or DHW system
Air exchange	Natural ventilation: 1 ACH, Infiltration: 0.25 ACH
Opening type	Pivoted window with 100% openable area

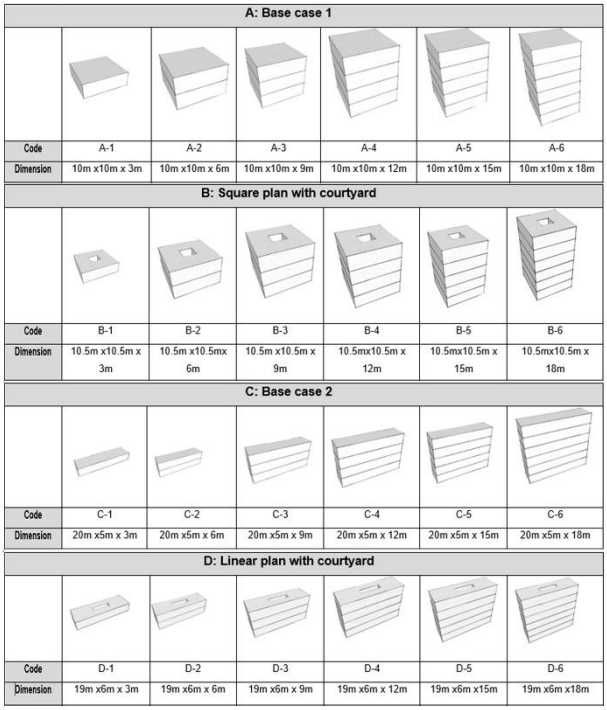

Figure 4 Parameters of modern building simulation cases

3. RESULTS

The thermal impact of the courtyard was significant in the simulated vernacular case studies. The difference of temperature between the buildings with courtyard and without courtyard was maximum 10%. In addition to providing light and shade, courtyard allows ventilating the surrounding rooms, resulting in a lower mean radiant temperature.

In this paper, the thermal performance of courtyard buildings was analysed using generic models for Dhaka climate. Interesting results were found when courtyard was integrated within the conventionally built forms.

The internal air temperature changed with seasons with the incorporation of the courtyard in the building masses. In summer (March-April-May), the internal dry bulb temperature was lower for the courtyard buildings for both square and linear plan. The mean radiant temperature was always higher than the dry bulb temperature, similar to the findings from Duan (Duan, 2012). Since courtyards create more exposed external walls to the solar radiation, the solar gain, as well as conduction gain, remain higher in courtyard buildings in comparison to non-courtyard buildings. It was observed (Figure 5) that the courtyard buildings received more conduction gain than the buildings without a courtyard. It is the cross-ventilation within the courtyard buildings that keep the internal air temperature lower.

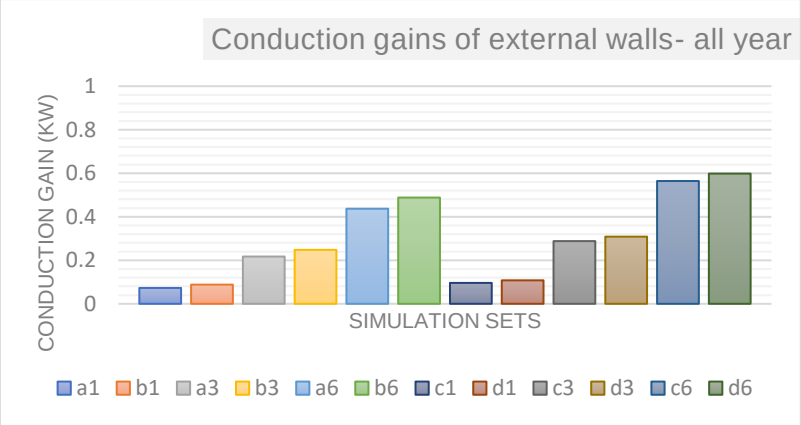

Figure 5 Conduction gain of the external walls- All year

The investigation also revealed that the vernacular buildings maintained 3-10% lower indoor temperature with the presence of courtyards in them (Figure 6). The incorporation of the courtyard in the modern housing resulted in 3% lesser indoor temperature than the conventional houses (Figure 7), confirming average 20.1% more comfortable temperature (within 24°C-32°C) (Mallick, 1994) in the summer season.

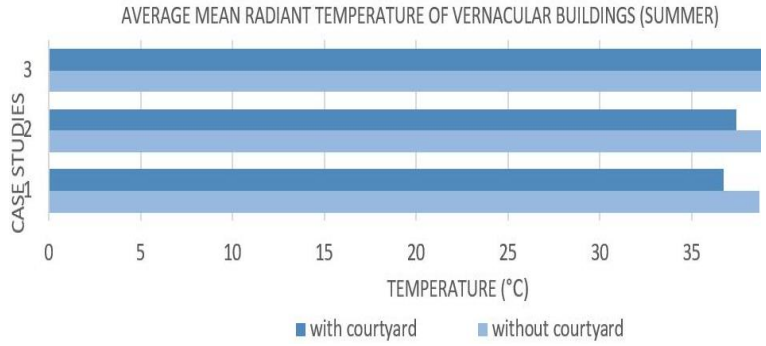

Figure 6 Average mean radiant temperature of vernacular buildings with and without courtyards

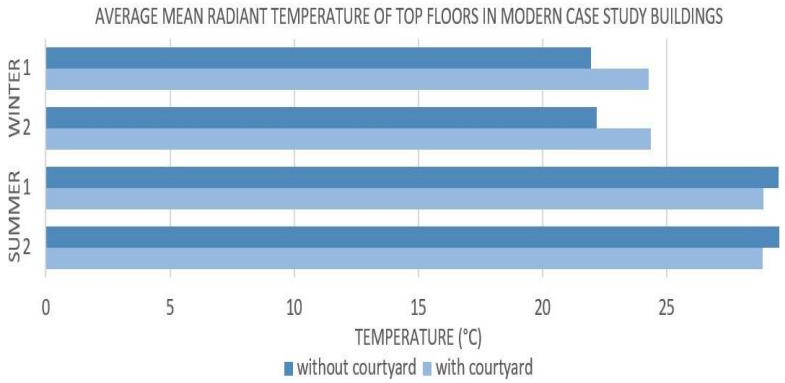

Figure 7 Average mean radiant temperature of modern buildings with and without courtyards

The analysis also reviewed that the courtyards provided additional solar gain to increase the comfortable indoor temperature by 10.5% in the winter season. Average 19.4% more temperature was within the comfort range (within 24°C-32°C) (Mallick, 1994) for the buildings with courtyards throughout the year (Figure 4).

The parametric studies showed that, in the summer season, the square courtyard buildings remained in comfort zone for average 98.45% time, while linear courtyard buildings got 98.2% comfort range (24°C-32°C). On the other hand, in the winter season, square plans received 75.38% comfort range while linear plans received 75.96%. It was observed that the linear plans had a more consistent temperature in all the floors than square plans. It can be concluded that the square plan could achieve a lower maximum temperature in significant floors, but linear plans provided persistent temperature all over the buildings. These findings complied with the studies of Duan (Duan, 2012) and Muhaisen (Muhaisen, 2006).

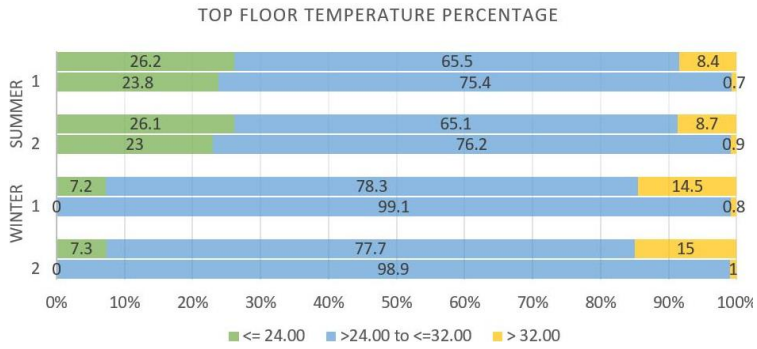

Figure 8 Mean Radiant Temperature percentage within comfort range of Dhaka

4. CONCLUSION

The courtyard building form is considered as a successful vernacular strategy that developed through a long trial and error process to mitigate the extreme climate all over the world (Muhaisen, 2006). Courtyards can be found in many climatic regions in different shape and forms. Due to continuous pressure on the land to give accommodation for the increasing population load, courtyards are diminishing form the modern building forms. The objective of this research was to investigate the concept of the courtyard as a design parameter to improve the microclimate, hence its relationship with the thermal comfort with respect to the climate of Dhaka.

The elaborate literature studies on the climate of Dhaka showed that the overall temperature is increasing over the last few decades. Dhaka is experiencing a rapid urban growth, as a result the necessity of additional housing is even more demanding now (Ahsan, 2009). While accommodating the elevating population, the buildings are losing their own vernacular identity and authentic design features, one of which was the courtyard. While courtyard was an integral design feature of vernacular Bengal houses, they are hardly found in modern day residential buildings.

This research attempted to evaluate the thermal performance of courtyards in the vernacular buildings. Extracting the strategies from case studies, they were implemented on the generic models of modern residential buildings. Computer simulated models were made in the software IES-VE, to achieve precise results of the thermal performances. From the literature study, the summer and winter season was chosen as academic calendar as they would give a clear idea of the courtyard mechanism.

In Bengali vernacular houses, courtyard was the focal point for different household and socio-cultural activities defining the spatial arrangement of the buildings. In addition to providing light and shade, courtyard ventilated the surrounding rooms, resulting in a lower mean radiant temperature. Total 48 sets of simulations were run, both in the summer and the winter season to observe the effect of courtyard in various conditions. The results showed that the buildings with courtyards had better thermal performance than the building without courtyard. The Average Dry Bulb Temperature was 0.1°C -0.25°C lower than the respective Average Mean Radiant Temperature during summer season, as the buildings gain soar radiation through the courtyard walls as well. In the winter season, the difference was 0.07°C-0.2°C. By incorporating a courtyard in a building mass, cross ventilation became active in the buildings. As the courtyards create a stack effect within the building, the hot airs can ventilate easily. The square plans (Code A and B) gained the lowest minimum temperature, but the rectangular building (Code C and D) had an overall lower temperature. The top floors always had the maximum temperature as they were directly exposed to the solar radiation. With the courtyard inserted in the built area, there was 3% less indoor air temperature in the summer season. Average 19.4% more temperature was within the comfort range in summer for the buildings with courtyards.

In winter, the buildings with courtyard gained more temperature than the non-courtyard buildings. With the integration of courtyards, the buildings become more exposed to the solar radiation. Using the solar radiation, buildings could have a better thermal performance. Average 10.2% more temperature was within the comfort range in the winter season for the buildings with courtyards.

The findings of this study can provide design guidelines for the contemporary architects and planners to evaluate the courtyard strategy and the wisdom of the age-old design features in vernacular buildings, to be integrated into the modern architectural features to achieve better thermal performance in modern housing in Dhaka.

The developed generic model was simplified to concentrate only on the thermal performance. This helped to understand the effect of the courtyard in similar building masses. However, more detailed thermal studies can be added to study other variables. A large number of factors influence the thermal performance of a building. For example, wind direction, the velocity of the winds could be changed to see the result of ventilation. As demonstrated, ventilation is required for tropical climates, it can lead to significant heat loss resulting in less energy usage. Each of the analysed parameter could be studied to more extend to achieve more specific understanding. Additionally, the infiltration rate could be analysed in more detailed manner.

The results showed that the buildings with courtyards had better thermal performance than the building without courtyard. This study was at the primary phase to analyse the effect of courtyard on the thermal performances of modern buildings, further studies can provide more specific design features that could be directly implemented in the modern housings in Dhaka. This vernacular strategy deserves more attention and study, to investigate its effect on the modern buildings as well.

5. REFERENCES

Aldawoud, A. and Clark, R., 2008. Comparative analysis of energy performance between courtyard and atrium in buildings. Energy and Buildings, 40(3), pp.209-214.

Ahmed, B., Kamruzzaman, M., Zhu, X., Rahman, M.S. and Choi, K., (2013). Simulating land cover changes and their impacts on land surface temperature in Dhaka, Bangladesh. Remote Sensing, 5(11), pp.5969-5998.

Ahsan, T., (2009). Passive design features for energy-efficient residential buildings in tropical climates: the context of Dhaka. Bangladesh, KTH Architecture and the Built Environment, Master's Thesis in Environmental Strategies Research, Stockholm.

Duan, Z., 2012. The environmental performance of vernacular skywell dwellings in south-eastern China (Doctoral dissertation, University of Nottingham).

Edwards, B., Sibley, M., Land, P. and Hakmi, M. eds., (2006). Courtyard housing: past, present and future. Taylor & Francis.

Hafiz, R., 2004. The Urban Frontiers of Dhaka: Creating Space above the Water. Urbanization in Bangladesh: Emerging Challenges; Jahan, S., Zaman, M., Eds.

Haque, F.A., 1997, 'Multi-court house of old Dhaka, a study of Form and Context', Thesis, Department of Architecture, Bangladesh University of Engineering and Technology.

Hyde, R., 2000. Climate responsive design. Routledge.

Khan, N. and Nilufar, F., 2009. Spatial Logic of Morphological Transformation. In Proceedings of the 7th International Space Syntax Symposium, Stockholm [Online].

Koenigsberger, O.H., 1975. Manual of tropical housing & building. Orient Black swan.

Mallick, F.H., 1994. Thermal comfort for urban housing in Bangladesh (Doctoral dissertation, unpublished) Environment and Energy Studies Programme, Architectural association, London.

Mridha, A.M.M.H., (2002). A study of thermal performance of operable roof insulation, with special reference to Dhaka. M. Arch Thesis (Unpublished), Department of Architecture, BUET.

Muhaisen, A.S. and Gadi, M.B., 2006. Effect of courtyard proportions on solar heat gain and energy requirement in the temperate climate of Rome. Building and Environment, 41(3), pp.245-253.

Raja, D.R. and Neema, M.N., (2013), June. Impact of urban development and vegetation on land surface temperature of Dhaka city. In International Conference on Computational Science and Its Applications (pp. 351-367). Springer, Berlin, Heidelberg.

Sousa, J., 2012, September. Energy simulation software for buildings: review and comparison. In International Workshop on Information Technology for Energy Applicatons-IT4Energy, Lisabon.

Yang, X., Li, Y. and Yang, L., 2012. Predicting and understanding temporal 3D exterior surface temperature distribution in an ideal courtyard. Building and Environment, 57, pp.38-48

Yaşa, E. and Ok, V., 2014. Evaluation of the effects of courtyard building shapes on solar heat gains and energy efficiency according to different climatic regions. Energy and Buildings, 73, pp.192-199.

Zamani, Z., Heidari, S. and Hanachi, P., 2018. Reviewing the thermal and microclimatic function of courtyards. Renewable and Sustainable Energy Reviews, 93, pp.580-595.

#47: Machine learning applications in data centre cooling performance optimisation and forecasting: A review

Zhichu WANG[1], Cheng ZENG[1], Zishang ZHU[1], Xiaoli MA[1], Xudong ZHAO[1]

[1] School of Engineering, University of Hull, Hull, HU6 7RX, zhichu.wang-2021@hull.ac.uk

Abstract: The demand for data centres (DCs) is surging due to the explosive growth of cloud services and social media. In 2022, DCs accounted for 1% of global electricity consumption, while in the United Kingdom, this figure further increases to 2.5%. Even though the IT system attributes primarily (around 56%) to a DC's total power consumption, depending on different cooling techniques (air, liquid, and free cooling), the cooling system alone can make up to 30% to 40% of the energy demand. As a subset of free cooling, dew-point evaporative cooling (DPC) can achieve a Coefficient of Performance (COP) of up to 52.5, compared to the COP of 2 to 4 of most wildly applied traditional mechanical vapour compression cooling. Therefore, applying DPC to DC can achieve significate energy saving and carbon reduction.

To meet the cooling demand of DCs without sacrificing thermal safety, preliminary modelling is required during the designing stage. While due to the dynamics natural of DCs cooling system, it often results in inadequate optimisation and inaccurate forecasting of cooling performance which require hand-tuning for specific devices. In this case, machine learning (ML) technique fundamentally outperform conventional modelling as it only learns and derives from the massive data collected from the desired system. Combining ML technique with DCs cooling can achieve energy saving for up to 26.6%, 15%, and 72% of air, liquid and dew-point cooling respectively under diverse climate conditions, which makes integrating ML into DC cooling systems, especially DPC, a promising research area.

This review paper focuses on the development of ML techniques in DCs' control strategy optimisation and long-term performance forecasting from 2000 to 2022. Existing literatures are categorized based on seven elements, while five ML based optimisation strategies and six forecasting methods are firstly introduced, followed by jointly optimizing approaches with IT system. Based on above analysis, existing research gaps in DC cooling optimisation and forecasting are identified, and associated recommendations are offered from the standpoint of the authors. The findings of this review can act as a steppingstone for scholars, researchers and policy makers in related fields, therefore contribute to the advancement of the SET agenda.

Keywords: Data centre cooling, Machine learning, Control optimisation, Performance forecasting, Energy saving

1. INTRODUCTION

Data centres (DCs) are physical infrastructures utilized by organizations to house their computing applications and data (National Grid ESO, 2022). Over the past decade, the DCs have evolved into a critical infrastructure that underpins the daily lives of individuals, facilitating remote data services for diverse needs including cloud services, social media, and various other requirements (Wen et al., 2014, Hu et al., 2014). With their compact infrastructure, DCs effectively tackle the intricate task of simultaneously managing large-scale data processing and storage for a substantial user base. Consequently, the power consumption of DCs has garnered considerable attention in the realm of energy efficiency and environmental sustainability.

In 2022, DCs accounted for 1% of global electricity consumption (IEA, 2022), while in the United Kingdom, this figure further increases to 2.5% (National Grid ESO, 2022). Even though the IT system attributes primarily (around 56%) to a DC's total power consumption, depending on different cooling techniques (air, liquid, and free cooling), the cooling system alone can make up to 30% to 40% of the energy demand (Wan et al., 2018, Alkharabsheh et al., 2015). As a subset of free cooling, dew-point evaporative cooling (DPC) can achieve a Coefficient of Performance (COP) of up to 52.5 (Xu et al., 2017), compared to the COP of 2 to 4 of most wildly applied traditional mechanical vapour compression cooling (Mahmood et al., 2021). Therefore, applying DPC to DC can achieve significate energy saving and carbon reduction.

To meet the cooling demand of DCs without sacrificing thermal safety, preliminary modelling is required during the designing stage (Zhang et al., 2021). While due to the dynamics natural of DCs cooling system, it often results in inadequate optimisation and inaccurate forecasting of cooling performance which require hand-tuning for specific devices (Ran et al., 2019). In this case, machine learning technique fundamentally outperform conventional modelling as it either interacts with the system directly or learns and derives from the massive data collected from the desired system. Combining machine learning technique with DCs cooling can achieve energy saving for up to 26.6% (Wang et al., 2022), 15% (Li et al., 2020), and 72% (Golizadeh Akhlaghi et al., 2021) of air, liquid and dew-point cooling respectively under diverse climate conditions, which makes integrating machine learning into DC cooling systems, especially DPC, a promising research area.

2. METHODOLOGY

This review paper focuses on the development of machine learning techniques in DCs' control strategy optimisation and long-term performance forecasting from 2000 to 2022. Existing high-cited literatures are categorized based on seven elements, cooling system type, learning method, energy type, input data parameter, target, target variable and time scale, while five machine learning based optimisation strategies (Deep Q-Network(DQN), Parameterized Deep Q-Network(PADQN), Deep Deterministic Policy Gradient(DDPG), Model Predictive Control(MPC), Temporal-Difference (TD)) and six forecasting methods (Multilayer Perceptron (MLP), Random Forest (RF), Extreme Gradient Boosting(XGBoost), Long-Short-Term Memory(LSTM), Multiple Linear Regression(MLR), Artificial Neural Network(ANN)) are introduced, followed by jointly optimizing approaches with IT system. Based on above analysis, existing research gaps in DCs' cooling optimisation and forecasting are identified, and associated recommendations are offered from the standpoint of the authors.

3. DATA CENTRE COOLING SYSTEMS

3.1. Air-Cooling Systems

In most air-cooling systems, server racks are positioned face-to-face and back-to-back to create channels for cold and warm air flows, which makes the adjacent racks cold and warm aisles. The configuration is schematically presented in Figure 1.

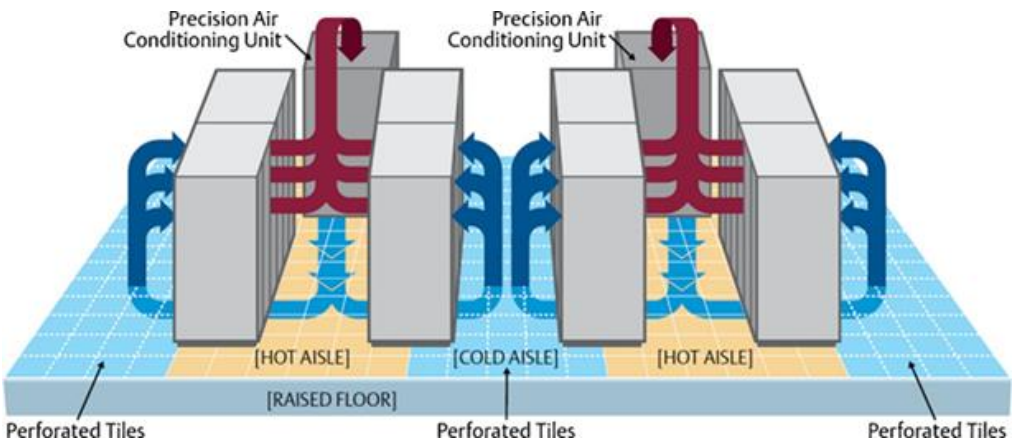

Figure 1 Hot/cold- aisle configuration (Emerson Network Power, 2011)

The cooling process has been illustrated as the following: chilled air produced by CRAC (Computer Room Air Conditioning) units is driven into cold aisles. After passing through the server racks and performing cooling, the chilled air comes out from the back of the server racks as warm air stream, then it is captured and returned as (part of) the intake air of CRAC. The heat is then absorbed by water through a chiller or cooling tower loop for ultimate dissipation to ambient. Depending on where the airflow paths are, the configuration can be further divided into room-level cooling (Taniguchi et al., 2017), row level cooling (overhead cooling) (Wang et al., 2017), and rack-level cooling (Dunlap and Rasmussen, 2012). However, even with elaborate designs, the intermixing of cold inlet air and warm returned air may still affect cooling efficiency, such as hot air recirculation (HAR) (Tang et al., 2007) and cold air bypass (CAB) (Wan et al., 2018, Zhang et al., 2017).

To alleviate or possibly eliminate the problems, many researchers have proposed different methods in airflow management aspect, like Air Containment System (CAS) (Bob Sullivan et al., 2018), Hot Aisle Containment System (HACS) (Sahini et al., 2016), and Cold Aisle Containment System (CACS) (Chu et al., 2020).

3.2. Liquid-Cooling Systems

While air-cooling systems are more commonly used in DCs, liquid-cooling systems are more efficient, due to the better thermal properties of liquid compared to air, such as thermal conductivity, specific heat, and density. Schematic system comparison is presented in Figure 2. Depending on how the liquid coolant and heat source contacts, liquid-cooling can be classified to indirect and direct liquid-cooling (Capozzoli and Primiceri, 2015). For indirect liquid-cooling systems, chilled coolant flows into the Coolant Distributor (CD), which delivers it to the heat source, while hot liquid flows back to the CD to be cooled by the chiller, a loop connecting cold and heat sources is formed (Ellsworth et al., 2012). In regard to different Mechanical Refrigeration Sub-System (MRSS), indirect liquid-cooling systems can be classified into three types, single-phase (Lee et al., 2015), two-phase (Salamon et al., 2017), and heat-pipe liquid-cooling (McGlen et al., 2004). For direct liquid-cooling, with dielectric fluid provides electrical insulation, liquid coolant can make direct contact with electronic devices like server blades (Bar-Cohen et al., 2006), which also makes it possible for higher performance of the servers as all server components are cooled simultaneously (Tuma, 2010). Depending on the form of the liquid coolant as it makes contact with heat source, direct liquid-cooling can be classified into two types, pool-boiling (Liang and Mudawar, 2019) and spray-boiling cooling (Kim, 2007). Nevertheless, the presence of liquid within electronic equipment gives rise to apprehensions regarding potential leaks and the potential for irreparable damage if direct contact with ICT equipment occurs.

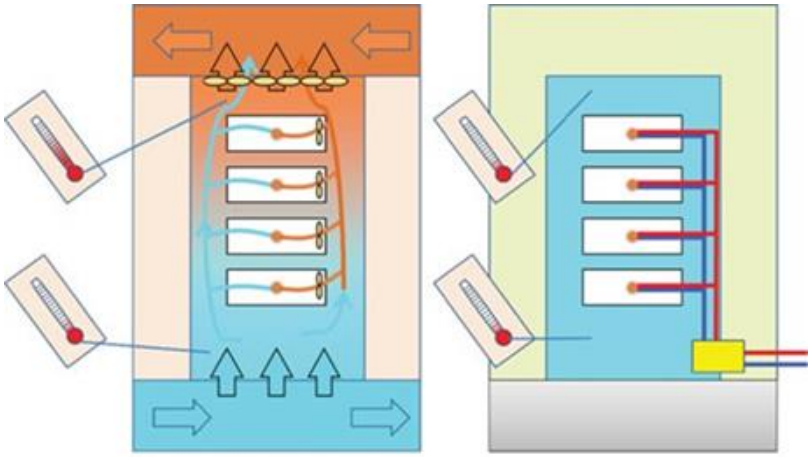

(a) Air-cooling *(b)Liquid-cooling*

Figure 2 Air-cooling and liquid-cooling system comparison (Ellsworth et al.,2012)

3.3. Free-Cooling Systems

Free cooling is also known as economizer cycle, which makes use of natural climate (cold air or water) as the cooling source to help absorb the heat dissipated by DC servers. Depending on the outdoor weather condition, free cooling systems can either be the main cooling source of data, or a supplement to the existing cooling source of DCs, either way, there are many studies have already proven the advantages of applying free cooling to DCs (Zhang et al., 2014). While there are two types of systems of the most applied air-side free cooling, direct and indirect free cooling system. The difference of these two is made by an air-to-air heat-exchanger, which is built for the full separation of outside cooling air and inside working air, leading to higher stability and longer lifespan for ICT equipment (Breen et al., 2011). Schematic direct and indirect air-side free-cooling system is shown in Figure 3.

3.4. Dew-Point Cooling Systems

Utilizing the latent heat of water to cool air, evaporative cooling represents a cooling technology that exhibits higher energy efficiency. The dew point cooling technology is a type of indirect evaporative cooling technology as shown in Figure 4(a). The product air for air supply is cooled by the water evaporation effect of the adjacent wet channel, which reduces the product air temperature without changing the moisture content (Glanville, Kozlov and Maisotsenko, 2011). Meanwhile the working air of the wet channel becomes humid and leaves the system. The minimum product air temperature in theory of this configuration is the wet-bulb temperature of the working air. To maximise the temperature reduction effect, a dew point cooling principle has been proposed as shown in Figure 4(b), where a part of the product air is extracted to the entrance of

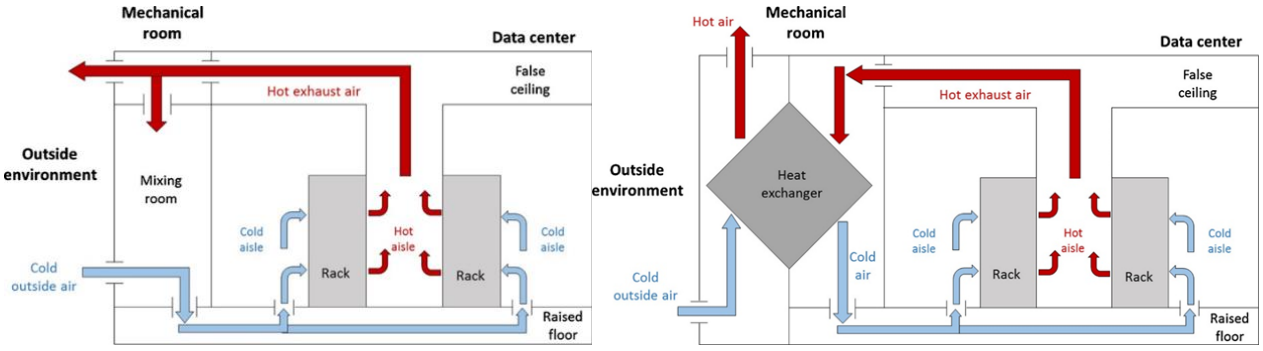

(a) Direct air-side free-cooling *(b) Indirect air-side free-cooling*

Figure 3 DC air-side free-cooling systems schematic configuration (Nadjahi et al., 2018)

the wet channel as the working air. The partial extraction, water evaporation, and air flow sensibly cools the working air before it enters the wet channel. Under ideal conditions, the product air can be cooled to the dew point of the incoming ambient. Through the utilization of a super-performance wet material layer, complex HMX, and an intermittent water supply scheme, Xu et al. (2017) have developed a highly efficient dew-point cooler. This innovative design achieves a remarkable wet-bulb cooling effectiveness of 114% and a dew-point cooling effectiveness of 75%, resulting in a substantially high coefficient of performance (COP) value of 52.5. Despite limited exploration in the realm of DC cooling, this technology presents a promising avenue for future research.

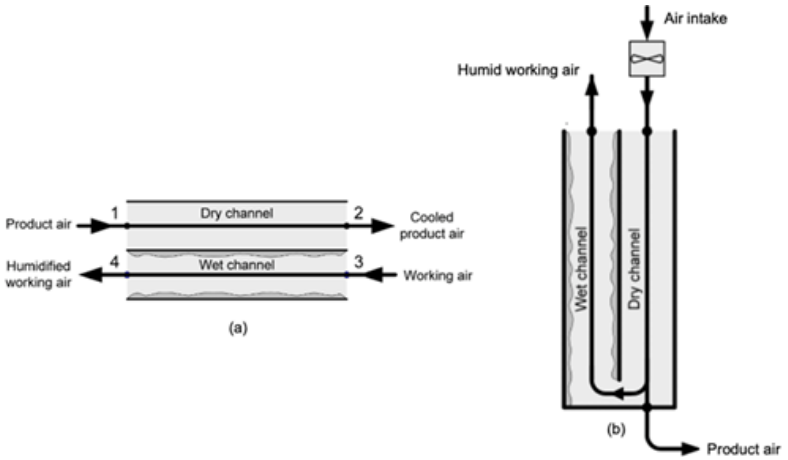

Figure 4 The air flow arrangements: (a) indirect evaporative cooling, (b) dew point

Nevertheless, the intricate interplay among various non-linear mechanical and electrical systems in both cooling and ICT systems necessitates manual adjustments in the aforementioned approaches to accommodate specific equipment architectures, layouts, and configurations. To address these challenges, numerous researchers have embraced machine learning-based techniques.

4. MACHINE LEARNING APPLICATIONS IN DATA CENTRE

Moore et al. (2006) first presented an approach based on Artificial Neural Networks (ANN) to precisely forecast heat distribution in DCs based on workload distribution and cooling configuration. This work eliminates the necessity for static and manual configuration of thermal load management systems.

Chen et al. (2011) have proposed a spatially aware workload and thermal management system (SPAWM) for DCs, utilizing a Temporal-Difference (TD) reinforcement learning approach. By employing thermally aware workload placement, SPAWM aims to achieve a uniform thermal distribution within the rack. The results demonstrate a reduction of 2-3°C in the maximum rack inlet temperature and a cooling energy reduction of up to 18%.

Wang et al. (2011) have introduced an approach for predicting the thermal impact of workloads on DCs. The findings suggest that machine learning techniques can effectively forecast the thermal effects of workloads in a prompt manner, making them highly suitable for real-time scenarios.

Gao J. (2014) has created an Artificial Neural Network (ANN) framework that utilizes real operational data to model plant performance and forecast Power Usage Effectiveness (PUE) for Google DCs. The research demonstrates that employing a comprehensive DC efficiency model holds the potential to lower PUE and enables operators to simulate various operating configurations without the need for physical alterations.

Shoukourian et al. (2017) have introduced Infrastructure Data Analyser (IDA), a prediction model based on Long Short-Term Memory (LSTM), specifically designed for a hot water-cooling DC. IDA effectively captures the intricate interactions among different factors that impact the overall power and energy efficiency of the cooling infrastructure. Additionally, the research findings contribute to the quantification of interdependencies among various components within the cooling circuit.

Lazic et al. (2018) have devised a Model-Predictive Control (MPC) model that relies on non-exploratory data. The outcomes of their research showcase that this controller, which utilizes a coarse-grained linear dynamics model, can effectively, safely, and cost-efficiently regulate conditions within a large-scale commercial DC, even when only a few hours of data exploration are available.

Ran et al. (2019) have introduced the Parameterized action space based Deep Q-Network (PADQN) algorithm to address the challenge of hybrid action space. The algorithm simultaneously optimizes the job scheduling for the ICT system and adjusts the airflow rate for the cooling system. By employing this approach, a more favourable balance can be achieved between energy savings and ensuring service quality.

Van Le et al. (2019) have introduced a hybrid model based on Deep Q-Network (DQN), which overcomes the challenges faced by air free-cooled DCs in tropical regions. They employ psychrometric and Multilayer Perceptron (MLP) models to characterize the supply air temperature, relative humidity (RH), and non-IT power consumption. These models are then used to drive the offline trained Deep Reinforcement Learning (DRL) agent. Once the training is completed, the DRL agent is deployed online to control an actual free-cooled DC located in tropical areas. The performance of the DRL agent surpasses that of hysteresis-based and model-predictive control approaches.

Zhang et al. (2019) have proposed an approach based on model-based reinforcement learning, comprising three main components. Firstly, the system dynamics are learned using Long Short-Term Memory (LSTM) by interacting directly with the system. Secondly, the acquired system dynamics are utilized in Model Predictive Control (MPC) using a random-sampling shooting method. Lastly, the model is evaluated using EnergyPlus simulation of a two-zone DC. To address challenges associated with system distribution shift, such as variations in outside temperature and IT equipment load schedules, an on-policy data aggregation process has been implemented. The results demonstrate that this approach enhances sample efficiency by a factor of 10, while achieving a significant reduction in total energy consumption of up to 21.8%.

Li, Y. et al. (2020) have introduced an offline deep deterministic policy gradient (DDPG) based algorithm for end-to-end Cooling Control Algorithm (CCA). In contrast to existing Two-Stage optimization methods, the proposed CCA enables direct optimization of a policy network using historical data and generates optimized control settings for any given state. Evaluation results obtained from a real-trace DC demonstrate the potential of the proposed approach to achieve up to 15% energy savings in cooling without compromising thermal safety.

Chi et al. (2020) have developed an approach named MACEEC, which utilizes Deep Deterministic Policy Gradient (DDPG) as a model-free Multi-Agent joint optimization technique for both ICT and cooling systems in DCs. This approach effectively addresses the synchronization issue by employing an asynchronous control optimization algorithm, enabling the asynchronous generation of scheduling and cooling decisions. Experimental evaluations conducted using real-world trace data demonstrate that the proposed approach shows promise in enhancing overall energy efficiency in DCs, while simultaneously ensuring temperature constraints and service quality compared with existing joint optimization approaches in these aspects.

Golizadeh Akhlaghi et al. (2021) have made significant advancements by introducing an explainable and interpretable Deep Neural Network (DNN) model for a Guideless Irregular Dew Point Cooler (GIDPC). The study also pioneers the application of two Evolutionary Optimization methods, namely the Slime Mould Algorithm (SMA) and Particle Swarm Optimization (PSO), in the DC sector. The results indicate that the predicted cooling power savings achieved from 2020 to 2050 can reach a remarkable 72%.

Wan et al. (2021) have implemented a model-free and fully online control algorithm based on Deep Q-Networks (DQN) for a DC utilizing a raised-floor design and Active Ventilation Tiles (AVTs) architecture. Upon applying this algorithm to an

operational DC, the findings demonstrate that the solution significantly improves the distribution of server rack inlet temperatures.

MirhoseiniNejad et al. (2021) have created a DC thermal model employing a time series forecasting technique known as Nonlinear Auto-Regressive Network with Exogenous Input (NARX). The outcomes obtained from this model were subsequently utilized in the development of a Holistic Data Centre Infrastructure Control (HDIC) framework. By employing the MATLAB fmincon tool, HDIC effectively addresses the heterogeneous optimization challenges associated with cooling and server units. This approach demonstrates the potential for significant power savings through workload scheduling and optimization of operational cooling parameters.

Le et al. (2021) have devised a hybrid model that merges a Multilayer Perceptron (MLP) based prediction model with a Deep Q-Network (DQN) based optimization model. This hybrid model is utilized for regulating the supply air temperature and relative humidity (RH) in an air free-cooled tropical DC, ensuring they remain below specific thresholds. Through comprehensive evaluations performed on an enhanced constrained Deep Reinforcement Learning (DRL) solution, the hybrid model exhibited superior performance compared to two other baseline methods.

Wang et al. (2022) have introduced a safety-aware reinforcement learning framework, Safari, which designed to prioritize the reduction of DC energy consumption while considering the thermal safety constraints of IT equipment. By applying Safari to two operational DCs in varying climate conditions, the research outcomes exhibited substantial potential for energy savings ranging from 22.7% to 26.6% compared to conventional control methods and further mitigated safety violations by 94.5% to 99% compared to reward shaping techniques.

Misaghian et al. (2023) have implemented three distinct machine learning algorithms, Random Forest (RF), XGBoost, Multiple Linear Regression (MLR), for forecasting DC energy consumption, yielding remarkable accuracies of up to 98.1%. Subsequently, these trained models are seamlessly integrated into an operational DC power system scheduling framework, resulting in a notable reduction of carbon emissions by up to 6.5%.

Table 1 in Appendix categorizes the above literatures based on seven elements, cooling system type, learning method, energy type, input data parameter, target, target variable and time scale.

5. DISCUSSION AND CONCLUSION

Amidst a range of optimization and forecasting methods, the adoption of efficient model-based data-driven approaches has gained significant attention in the field of DC control and energy performance prediction due to their capacity to swiftly deliver accurate interventions and results. This paper provides a comprehensive review of recent highly cited literatures in this domain, outlining the key highlights and findings discovered as below.

- Despite the availability of various cooling systems, air-cooling remains the predominant choice in DCs owing to its cost-effectiveness and reliability. However, similar to other cooling systems, the performance of air-cooling is significantly influenced by the IT load. In the context of optimization and forecasting, incorporating both cooling and ICT systems in the analysis has the potential to capture the dynamics of the entire system, leading to improved energy efficiency and enabling the transferability of the model to other systems.
- There is currently a lack of comprehensive investigation into the application of machine learning in dew-point DC cooling systems for both optimization and forecasting purposes. While a few researchers have proposed integrating dew-point cooling technology into operational DCs, only one study has explored the application of machine learning in this context, demonstrating substantial energy savings. This indicates that further research in this field holds great promise.
- The energy consumption of free cooling and evaporative cooling methods, such as dew-point cooling, is strongly influenced by outdoor climate conditions. In contrast, the impact of outdoor climate conditions on air- and liquid-cooling systems is relatively insignificant. When adjusting the weights of various parameters, it is crucial to consider both the learning algorithm's preference and the sensitivity of cooling and ICT systems in DCs.
- In optimization applications, power consumption is frequently examined in conjunction with temperature as target variables. This is particularly evident in RL and DRL approaches, where achieving highly accurate energy efficiency optimization often necessitates direct interaction with operational DCs. However, it should be noted that this trial-and-error process can potentially jeopardize the thermal constraints of ICT systems.
- When employing Reinforcement Learning (RL) algorithms for system optimization, Model-free approaches such as Off-policy DQN and DDPG demand a substantial volume of labelled data to attain high accuracy. These algorithms offer advantages in terms of speed and flexibility, but their sample efficiency is relatively low. Conversely, Model-based algorithms eliminate the need for importance sampling, resulting in higher sample efficiency, consistency, and stability. However, they may require more time to converge and can become trapped in local minima. The selection of appropriate algorithms should consider the specific system dynamics under particular conditions. Combining diverse algorithms, such as neural networks, can be beneficial in mitigating the limitations associated with these approaches.

6. REFERENCES

Alkharabsheh, S. et al. (2015) 'A brief overview of recent developments in thermal management in data centers', Journal of Electronic Packaging, 137(4).

Bar-Cohen, A., Arik, M. and Ohadi, M. (2006) 'Direct liquid cooling of high flux micro and Nano Electronic Components', Proceedings of the IEEE, 94(8), pp. 1549–1570.

Bob Sullivan, R., Li, G. and Zhang, X. (2018) 'Cold aisle or hot aisle containment - is one better than the other?', 2018 IEEE International Telecommunications Energy Conference (INTELEC) [Preprint].

Breen, T.J. et al. (2011) 'From chip to Cooling Tower Data Center modeling: Influence of server inlet temperature and temperature rise across Cabinet', Journal of Electronic Packaging, 133(1).

Capozzoli, A. and Primiceri, G. (2015) 'Cooling Systems in data centers: State of Art and Emerging Technologies', Energy Procedia, 83, pp. 484–493.

Chen, H. et al. (2011) 'Spatially-aware optimization of energy consumption in Consolidated Data Center Systems', ASME 2011 Pacific Rim Technical Conference and Exhibition on Packaging and Integration of Electronic and Photonic Systems, MEMS and NEMS: Volume 2 [Preprint].

Chi, C. et al. (2020) 'Jointly optimizing the IT and cooling systems for data center energy efficiency based on multi-agent deep reinforcement learning', Proceedings of the Eleventh ACM International Conference on Future Energy Systems [Preprint].

Chu, W.-X. et al. (2020) 'Assessment on rack intake flowrate uniformity of data center with cold aisle containment configuration', Journal of Building Engineering, 30, p. 101331.

Dunlap, K. and Rasmussen, N. (2012) Choosing between room, row, and rack-based cooling for data centers: APC by Schneider Electric, White. Available at: https://www.apc.com/us/en/download/document/SPD_VAVR-6J5VYJ_EN/ (Accessed: 07 April 2023).

Ellsworth, M.J. et al. (2012) 'An overview of the IBM Power 775 supercomputer Water Cooling System', Journal of Electronic Packaging, 134(2).

Emerson Network Power (2011) Five strategies for Cutting Data Center Energy Costs. Available at: https://issuu.com/enpliebertproducts/docs/five_strategies_for_cutting_data_center_energy_cos (Accessed: 07 April 2023).

Gao, J. (2014) Machine learning applications for data center optimization. Available at: https://research.google.com/pubs/archive/42542.pdf (Accessed: 07 April 2023).

Glanville, P., Kozlov, A. and Maisotsenko, V. (2011) 'Dew Point Evaporative Cooling: Technology Review and Fundamentals', ASHRAE Transactions. Golizadeh Akhlaghi, Y. et al. (2021) 'Hourly performance forecast of a dew point cooler using explainable artificial intelligence and evolutionary optimisations by 2050', Applied Energy, 281, p. 116062.

Hu, H. et al. (2014) 'Toward scalable systems for Big Data Analytics: A technology tutorial', IEEE Access, 2, pp. 652–687.

IEA (2022) Data Centres and Data Transmission Networks. Available at: https://www.iea.org/reports/data-centres-and-data-transmission-networks (Accessed: 17 March 2023)

Kim, J. (2007) 'Spray cooling heat transfer: The state of the art', International Journal of Heat and Fluid Flow, 28(4), pp. 753–767.

Lazic, N et al. (2018) Data Center cooling using model-predictive control: Proceedings of the 32nd International Conference on Neural Information Processing Systems, Guide Proceedings. Available at: https://dl.acm.org/doi/10.5555/3327144.3327297 (Accessed: 07 April 2023)

Le, D.V. et al. (2021) 'Deep reinforcement learning for tropical air free-cooled data center control', ACM Transactions on Sensor Networks, 17(3), pp. 1–28.

Lee, Y.J., Singh, P.K. and Lee, P.S. (2015) 'Fluid flow and heat transfer investigations on enhanced microchannel heat sink using oblique fins with parametric study', International Journal of Heat and Mass Transfer, 81, pp. 325–336.

Li, Y. et al. (2020) 'Transforming cooling optimization for Green Data Center via deep reinforcement learning', IEEE Transactions on Cybernetics, 50(5), pp. 2002–2013.

Liang, G. and Mudawar, I. (2019) 'Review of pool boiling enhancement by surface modification', International Journal of Heat and Mass Transfer, 128, pp. 892–933.

Mahmood, R.A. et al. (2021) ‘Review of Mechanical Vapour Compression Refrigeration System Part 2: Performance challenge’, International Journal of Applied Mechanics and Engineering, 26(3), pp. 119–130.

McGlen, R.J., Jachuck, R. and Lin, S. (2004) ‘Integrated Thermal Management Techniques for high power electronic devices’, Applied Thermal Engineering, 24(8–9), pp. 1143–1156.

MirhoseiniNejad, S., Badawy, G. and Down, D.G. (2021) ‘Holistic thermal-aware workload management and infrastructure control for heterogeneous data centers using machine learning’, Future Generation Computer Systems, 118, pp. 208–218.

Misaghian, M.S. et al. (2023) ‘Assessment of carbon-aware flexibility measures from data centres using machine learning’, IEEE Transactions on Industry Applications, 59(1), pp. 70–80.

Moore, J., Chase, J.S. and Ranganathan, P. (2006) ‘Weatherman: Automated, online and Predictive Thermal Mapping and management for Data Centers’, 2006 IEEE International Conference on Autonomic Computing [Preprint].

Nadjahi, C., Louahlia, H. and Lemasson, S. (2018) ‘A review of thermal management and innovative cooling strategies for Data Center’, Sustainable Computing: Informatics and Systems, 19, pp. 14–28.

National Grid ESO (2022) Data Centres. Available at: https://www.nationalgrideso.com/document/246446/download (Accessed: 21 March 2023)

Ran, Y. et al. (2019) ‘DeepEE: Joint optimization of Job Scheduling and cooling control for data center energy efficiency using Deep Reinforcement Learning’, 2019 IEEE 39th International Conference on Distributed Computing Systems (ICDCS).

Sahini, M. et al. (2016) ‘Study of air flow energy within data center room and sizing of hot aisle containment for an active vs passive cooling design’, 2016 15th IEEE Intersociety Conference on Thermal and Thermomechanical Phenomena in Electronic Systems (ITherm) [Preprint].

Salamon, T. et al. (2017) ‘Two-phase liquid cooling system for electronics, part 1: Pump-driven loop’, 2017 16th IEEE Intersociety Conference on Thermal and Thermomechanical Phenomena in Electronic Systems (ITherm) [Preprint].

Shoukourian, H. et al. (2017) ‘Using machine learning for data center cooling infrastructure efficiency prediction’, 2017 IEEE International Parallel and Distributed Processing Symposium Workshops (IPDPSW) [Preprint].

Tang, Q., Gupta, S.K. and Varsamopoulos, G. (2007) ‘Thermal-aware task scheduling for data centers through minimizing heat recirculation’, 2007 IEEE International Conference on Cluster Computing [Preprint].

Taniguchi, Y. et al. (2017) ‘Tandem equipment arranged architecture with exhaust heat reuse system for software-defined data center infrastructure’, IEEE Transactions on Cloud Computing, 5(2), pp. 182–192.

Tuma, P.E. (2010) ‘The merits of open bath immersion cooling of Datacom Equipment’, 2010 26th Annual IEEE Semiconductor Thermal Measurement and Management Symposium (SEMI-THERM) [Preprint].

Van Le, D. et al. (2019) ‘Control of air free-cooled data centers in tropics via deep reinforcement learning’, Proceedings of the 6th ACM International Conference on Systems for Energy-Efficient Buildings, Cities, and Transportation [Preprint].

Wan, J. et al. (2018) ‘Air flow measurement and management for improving cooling and energy efficiency in raised-floor data centers: A survey’, IEEE Access, 6, pp. 48867–48901.

Wan, J., Zhou, J. and Gui, X. (2021) ‘Intelligent rack-level cooling management in data centers with active ventilation tiles: A deep reinforcement learning approach’, IEEE Intelligent Systems, 36(6), pp. 42–52.

Wang, C.-H., Tsui, Y.-Y. and Wang, C.-C. (2017) ‘Airflow management on the efficiency index of a container data center having overhead air supply’, Journal of Electronic Packaging, 139(4).

Wang, L. et al. (2011) ‘Task scheduling with ann-based temperature prediction in a data center: A simulation-based study’, Engineering with Computers, 27(4), pp. 381–391.

Wang, R. et al. (2022) ‘Toward physics-guided safe deep reinforcement learning for Green Data Center Cooling Control’, 2022 ACM/IEEE 13th International Conference on Cyber-Physical Systems (ICCPS).

Wen, Y. et al. (2014) ‘Cloud Mobile media: Reflections and outlook’, IEEE Transactions on Multimedia, 16(4), pp. 885–902.

Xu, P. et al. (2017) ‘Experimental investigation of a super performance dew point air cooler’, Applied Energy, 203, pp. 761–777.

Zhang, C. et al. (2019) 'Building HVAC scheduling using Reinforcement Learning via neural network based model approximation', Proceedings of the 6th ACM International Conference on Systems for Energy-Efficient Buildings, Cities, and Transportation [Preprint].

Zhang, H. et al. (2014) 'Free cooling of data centers: A Review', Renewable and Sustainable Energy Reviews, 35, pp. 171–182.

Zhang, Q. et al. (2021) 'A survey on Data Center Cooling Systems: Technology, Power Consumption Modeling and control strategy optimization', Journal of Systems Architecture, 119, p. 102253.

Zhang, X. et al. (2017) 'Cooling Energy Consumption Investigation of data center IT room with vertical placed server', Energy Procedia, 105, pp. 2047–2052.

7. APPENDIX

Table 1 Categorized of machine learning applications in data centre cooling based on seven study criteria

Year	Authors	Cooling type				Learning method								
		Air cooling	Liquid cooling	Free cooling	Dew-point cooling	MPC	TD	DDPG	DQN	PADQN	NARX	LSTM	ANN	MLP
2023	Misaghian *et al.*	●												
2022	Wang *et al.*	●						●						
2021	Golizadeh Akhlaghi et al.				●									
2021	Le *et al.*			●					●					
2021	MirhoseiniNejad *et al.*	●									●			
2021	Wan *et al.*	●							●					
2020	Chi *et al.*	●						●					●	
2020	Li, Y. *et al.*	●						●				●		
2019	Zhang *et al.*	●				●						●		
2019	Van Le *et al.*			●					●					●
2019	Ran *et al.*	●								●				
2018	Lazic *et al.*	●				●								
2017	Shoukourian *et al.*		●									●		
2014	Gao J.	●										●		
2011	Wang *et al.*	●											●	
2011	Chen *et al.*	●					●							
2006	Moore *et al.*	●											●	

Table 1 Categorized of machine learning applications in data centre cooling based on seven study criteria (continued)

Learning method					Energy type		Input parameter				Target variable		
RF	XGBoost	MLR	SMA	PSO	Cooling System	ICT	Indoor air/water conditions	Outdoor air conditions	ICT load	DC design parameters	Temperature	Relative humidity	Air flow rate
●	●	●			●	●			●		●		
					●	●	●	●	●	●	●		
			●	●	●		●	●					
		●			●		●	●			●	●	
					●	●	●		●	●	●		
							●		●	●	●		
					●	●	●		●	●	●		
					●	●	●		●		●		
					●	●	●	●	●				
					●		●	●		●	●	●	
					●	●	●		●				●
							●		●		●		●

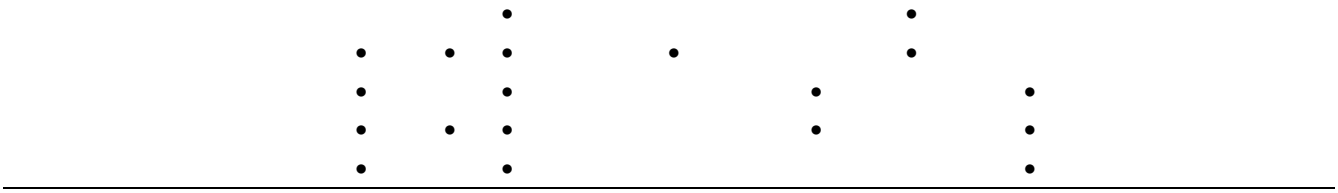

Table 1 Categorized of machine learning applications in data centre cooling based on seven study criteria (continued)

Target variable			Target		Time scale				
Power consumption	COP	PUE	Optimisation	Forecasting	Annual	Monthly	Daily	Hourly	Sub-hourly
●			●	●			●	●	
●			●				●		
●	●		●	●	●	●		●	
●			●	●		●	●		
●			●	●					●
			●						●
●			●						●
		●	●						●
●			●				●	●	
●			●					●	●
		●	●						●
			●					●	
	●					●			
		●		●					●
●				●				●	
●			●						●
●	●			●					

#48: Rapid evaluation of buildings thermal performance using infrared thermography and artificial intelligence

Arijit SEN[1], Amin AL-HABAIBEH[2]

[1] Research Fellow, Product Innovation Centre, Nottingham Trent University, Email: arijit.sen@ntu.ac.uk
[2] Director of Product Innovation Centre, Nottingham Trent University, Email: amin.al-habaibeh@ntu.ac.uk

Abstract: Domestic energy consumption significantly contributes to the UK's overall energy usage. Space and water heating are responsible for most households' energy consumption. Any price hike, such as the current energy price situation, would seriously affect the budget of many households living in poorly insulated buildings. Improving insulation by deep retrofitting of existing buildings is expected to be a reasonable solution for reducing the domestic heating energy demands for those households. However, the level of insulation is a key issue, as retrofitting with excess insulation will incur higher cost and result in longer payback periods, especially in countries with moderate temperatures such as the UK. Therefore, it is necessary to estimate the thermal performance of existing building stock at the planning stage of retrofitting. Such evaluation of thermal performance requires, in most cases, prolonged monitoring of buildings using sensors installed for data analysis leading to significant time and cost issues. To address this knowledge gap and provide rapid evaluation of expected energy savings of retrofitting, this paper presents a novel technology with a case study to estimate energy savings between insulated and uninsulated residential buildings using Infrared Thermography and Artificial Intelligence. The results prove that the suggested AI technology, combined with infrared thermography, can provide rapid evaluation of heat losses through the building envelop and estimate the potential energy savings due to the enhancement of wall insulation by retrofitting.

Keywords: Retrofitting; Infrared thermography; Artificial Intelligence; Neural Networks; Insulation; Insulation.

1. INTRODUCTION

The increase in market economy activities, particularly during the post-COVID era, has resulted in a surge in energy demand in 2021, which is still growing but at a slower rate (Ritchie, Roser and Rosado, 2022). The recent global situation has affected household energy prices, increasing them globally by 112.9% (Guan *et al.*, 2023). Despite the growth of renewable energy, fossil fuels still dominate energy production (BP PLC, 2021). Buildings contribute significantly to greenhouse gas emissions (UN Environment Programme, 2020), with heating responsible for around 80% of domestic energy consumption in the UK (Department for Business Energy & Industrial Strategy, 2023). Although a case study has proven that newly built houses in England and Wales have lower energy demand (The National Energy Efficiency Network, 2019), a significant number of English dwellings fall into the category of poor energy efficiency in existing housing stock, with 75% of houses being pre-1990 constructions (Piddington *et al.*, 2020). The UK Government is considering strategies to reduce energy consumption in buildings, such as improving insulation and energy efficiency, to meet their goal of net-zero emissions by 2050 (Government Property Agency, 2022).

Wall insulation plays a crucial role in improving energy efficiency, but its effectiveness depends on various factors, such as local weather, insulation materials, level of insulation (U-value), and occupants' behaviour, including working from home (Al-Habaibeh et al., 2021) or opening of windows (Salim and Al-Habaibeh, 2023). A wide variety of insulation materials are commercially available in today's market, which are classified as organic materials, inorganic materials, combined materials, and new technology materials (Papadopoulos, 2005;Sadineni, Madala and Boehm, 2011). Understanding how these different types of insulation materials impact energy savings is important. Tabrizi, Hill and Aitchison, (2017) conducted a study to investigate the impact of different insulation materials and thicknesses on energy consumption in a multi-story residential building in Sydney. The authors tested six types of insulation materials at three different thicknesses (30mm, 60mm, and 90mm). The study found a significant range variation in heating energy consumption. The most effective insulation material for saving heating energy was extruded polystyrene. Therefore, selecting the right insulation material is crucial for optimizing energy savings, as well as considering other factors such as environmental impact, resistance to sound, moisture, and fire. However, cost of materials and installation will need to be taken into consideration. Insulation can be applied to both internal and external surfaces of a building's wall, known as internal and external insulation, respectively. Theoretically, the effectiveness of insulation depends on its layer's thickness rather than its placement. However, in reality, the thermal performance of walls after retrofitting with improved insulation varies based on whether they are internally or externally insulated and the building's location and climate (Kossecka and Kosny, 2002). Several studies have explored the energy performance of externally and internally insulated walls and the changes in energy performance due to retrofitting in different climates. Some studies found external wall insulation to be more effective (Kim and Moon, 2009;Kolaitis *et al.*, 2013), while others favoured internal wall insulation (Reilly and Kinnane, 2017;Wang *et al.*, 2016). Internally insulated buildings consume less energy but have reduced available indoor space, leading to a trade-off between space requirements and energy demand reduction (Reilly and Kinnane, 2017). On the other hand, buildings with external insulation have better thermal stability (Wang *et al.*, 2016); but the appearance, for example, of heritage buildings in such situations will not be preserved.

Infrared thermography is a quick and effective way of evaluating the post-retrofit effectiveness of wall insulation. Infrared radiation from objects make infrared thermography, following suitable calibrations, a useful tool for non-contact measurement of walls surface temperature (Marino, Muñoz and Thomas, 2017). It is also useful for estimating the thermal transmittance in a non-invasive way, such as through a building's windows (Baldinelli and Bianchi, 2014), heat loss through door openings (Al-Habaibeh, Medjdoub and Pidduck, 2012), and characterizing the thermal performance of building facade (Bienvenido-Huertas *et al.*, 2019). Several researchers have demonstrated the successful use of this technology, for example, the estimation of heat flow rate through a thermal bridge (O'Grady, Lechowska and Harte, 2017), estimation of time shift values of temperature in building elements, and investigation of transient temperature response behaviour over time (Xie *et al.*, 2019). Moreover, infrared thermography can be used to calculate thermal power and heat losses through a building's walls (Albatici and Tonelli, 2010; Albatici, Tonelli and Chiogna, 2015; Nardi, Sfarra and Ambrosini, 2014).

Artificial intelligence has been significantly used in many research studies to predict energy consumption in buildings. Among them, Artificial Neural Networks (ANNs) have been most widely used due to their suitability over conventional statistical methods (Wang and Srinivasan, 2017; Deb *et al.*, 2017). These studies have tested various types of ANNs, including feedforward and recurrent neural networks, and have used different input variables. The feedforward neural network is suitable for regression, classification, and pattern recognition tasks (Gori, 2018). On the other hand, recurrent neural networks can be successfully applied to time series problems. However, they have a limitation in terms of vanishing gradients (Haykin, 2000). To overcome this limitation, Hochreiter and Schmidhuber (1997) developed a special type of recurrent neural network called Long Short-Term Memory (LSTM) network. The LSTM network is equipped with memory blocks that process information through different gates, such as forget gate, peephole, input gate, and output gate. These gates allow the memory blocks to selectively remember or forget information, allowing the LSTM network to overcome the vanishing gradient problem (Witten *et al.*, 2017). ANNs can achieve high accuracy in predicting energy consumption and can outperform other methods, such as energy simulation software (Naji *et al.*, 2016; Martellotta *et al.*, 2017; Wang, Lee and Yuen, 2018). Retrofitting with enhanced insulation can improve the energy efficiency of existing buildings (Al-Habaibeh *et al.*, 2022), but estimating energy savings prior to retrofit and the payback period of investments is a challenging task.

Previous research shows that by combining infrared thermography and ANN, it is possible to predict future heat losses through buildings' walls from midterm (around 8 years) historical climate data with reasonable accuracy (Al-Habaibeh, Sen, and Chilton, 2021). However, the study does not estimate energy savings. In the current paper, we use infrared thermography and ANN to estimate energy savings due to retrofitting.

2. METHODOLOGY

The steps involved in the heat loss prediction and energy savings estimations by combining infrared thermography and ANN is presented in Figure 1. To calculate the heat loss per square meter of a building's wall, we use the thermal power approach developed by Albatici and Tonelli (2010), as shown in Equation 1.

Equation 1: *Thermal power* $$P = 5.67\varepsilon_{tot}\left(\left(\frac{T_s}{100}\right)^4 - \left(\frac{T_{ext}}{100}\right)^4\right) + 3.8054v(T_s - T_{ext})$$

Where:

- T_{ext} = outdoor temperature
- v = wind speed
- Ts = external wall surface temperature
- ε_{tot} = emissivity

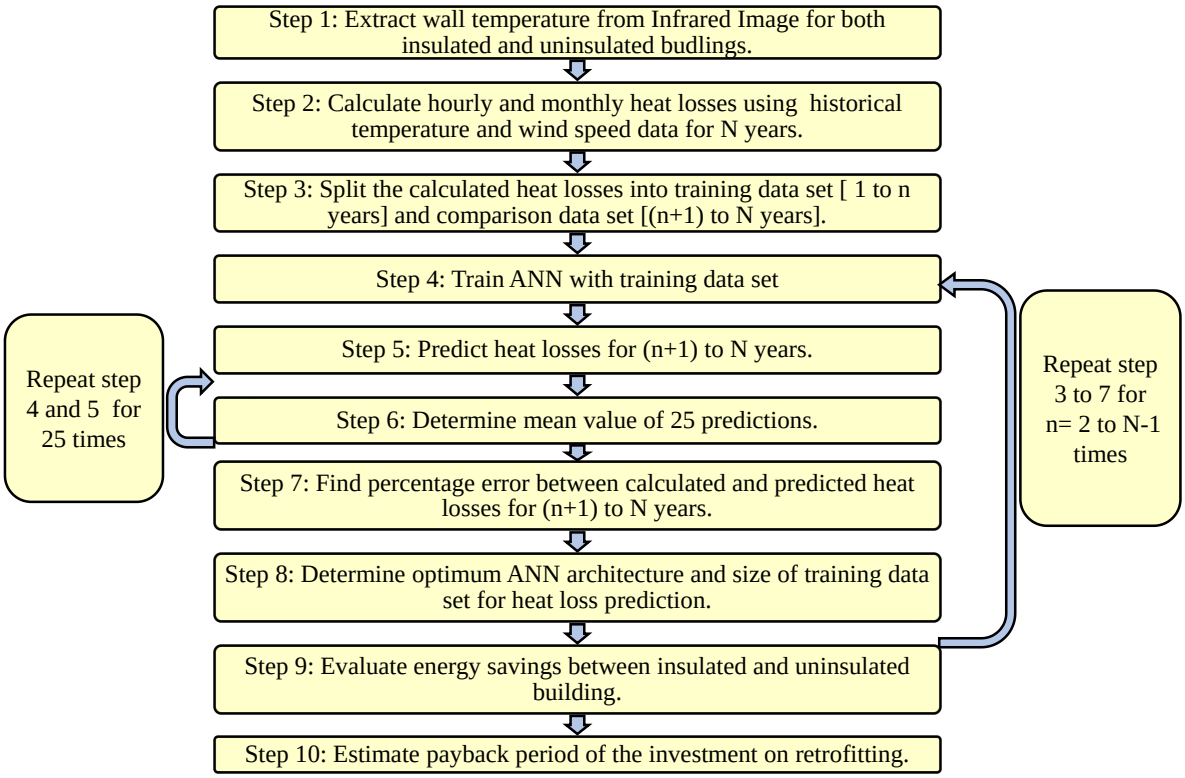

Figure 1 A schematic representation of the research methodology; adopted from Al-Habaibeh, Sen, and Chilton (2021)

By taking into account the external wall surface temperature in relation to the respective outdoor temperature at the moment when the infrared image is captured as an initial point; and 20°C as the secondary point, a linear curve can be generated. Such linear curves are used for the case study in this paper are illustrated in Figure 2. The external wall surface temperatures necessary for calculating heat loss using Equation 1; and are extracted from this linear curve at different outdoor temperatures. For plastered brick walls, the emissivity is considered to be 0.93 (CIBSE, 2006). If 1 W/m^2 of heat is radiated for one hour, it will be equivalent to 1 Wh/m^2 of heat energy transfer. Therefore, the value of P for each hour, calculated from equation 1, can be considered as the hourly heating energy loss per square meter of the building's wall. Equation 2 expresses the average heat loss in any given hour i in a given month j through per square meter of a wall, P_{ij}. The heat loss P_i is obtained using equation 1. Likewise, equation 3 expresses the total heat loss in each calendar month in a year as the summation of hourly heat losses in that month.

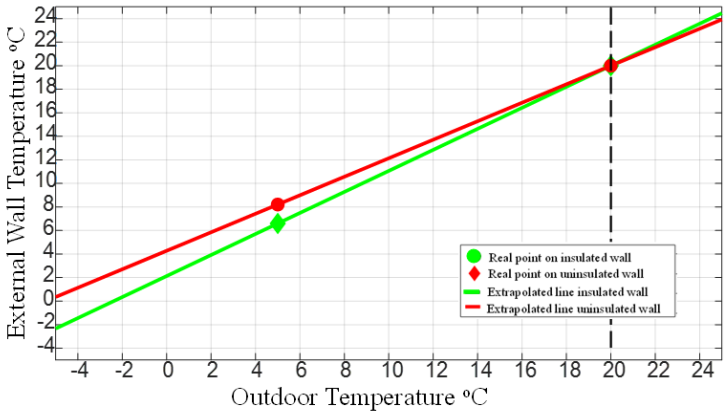

Figure 2 The assumed relationship between outdoor temperature and external wall temperature

Equation 2: Heat loss at i^{th} hour of each day in j^{th} month $P_{ij} = \frac{1}{n}\sum_{n=1}^{D} P_i$

Where:

- i= 00:00 to 23.00.
- j = January to December.
- D = the number of days in j[th] month of a given year

Equation 3: Total heat loss through a building's wall in a calendar month $P_m = \sum_{1}^{D}\sum_{1}^{24} P$

Where:

- D = number of days in that month and
- P = hourly heat loss obtained using equation 1.

Using historical local weather data, the hourly average heat loss and the monthly total heat loss for N years are calculated. These values are then divided into training and test data sets for neural network analysis. Different combinations of training and test data sets are formed, ranging from 2 years to N-1 years. The training data set is used to train the neural network, and the test data set is used to evaluate its performance. Performance evaluation is conducted considering percentage errors, which are calculated using equations 4 and 5, respectively.

Equation 4: Error $e = \sum_{i=1}^{n}(Y_i - P_i)$

Where:

- Y = ANN predicted heat loss and
- P = calculated heat loss from equation 2 for hourly averaged heat loss and the same from equation 3 for monthly total heat loss, respectively.
- n = 288 (24×12) in case of hourly average heat loss and 12 in case of monthly total heat loss

Equation 5: Percentage error $e_p = \frac{|e|}{\sum_{i=1}^{n} P_i} \times 100$

Where:

- e = error calculated using equation 4.
- P = calculated heat loss from equation 2 for hourly averaged heat loss and the same from equation 3 for monthly total heat loss, respectively.
- n = 288 (24×12) in case of hourly average heat loss and 12 in case of monthly total heat loss

3. CASE STUDY

A case study was conducted in two buildings located in Nottingham, England: an externally insulated mid-terraced building and an uninsulated end-terraced building. Figure 3 displays an infrared image of the adjacent buildings taken on February

12th at around 8:30 pm using a FLIR T640 thermal camera during a thermographic survey. The ambient temperature during the survey was 5°C. The Thermacam Quick Report software from FLIR was utilized to extract the pixelwise temperature values from the infrared image of the buildings.

3.1. Analysis of infrared image

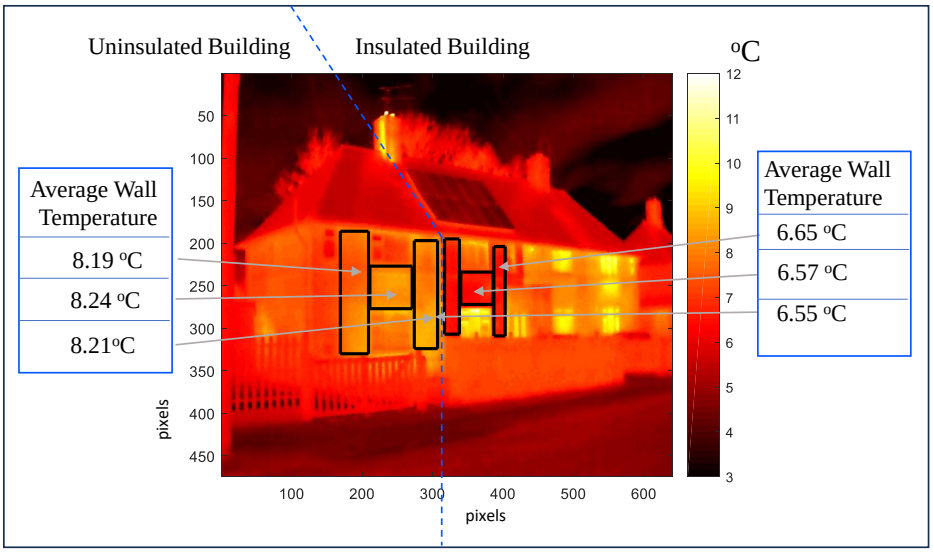

Figure 3 An infrared image of the insulated and the uninsulated house

In Figure 3, the average wall surface temperature is marked for different sections of both the insulated and uninsulated buildings. The average wall surface temperature for various sections of the uninsulated building ranges from 8.19°C to 8.24°C. In contrast, the wall surface temperature for different sections of the insulated building ranges from 6.55°C to 6.65°C. Additionally, Figure 3 shows that the insulated building has photovoltaic solar cells on its roof to enhance its energy efficiency. The temperature difference in the average wall surface temperature between the two buildings is approximately 1.6°C. Figure 4 displays the temperature profile along line ABCD in the infrared image, where the wall surface temperature values along AB represent the uninsulated building, BC represents the insulated building, and CD represents another uninsulated building adjacent to the insulated one.

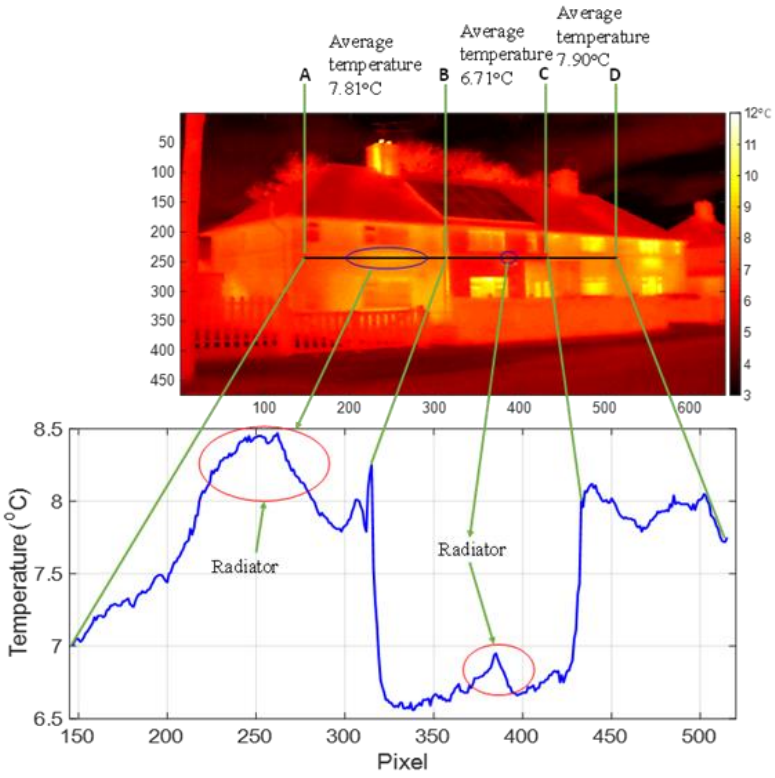

Figure 4 Temperature profiles generated from the infrared image

3.2. Heat loss calculations

Equation 1 is utilized to calculate the heat transfer through the building's wall in W/m^2 for both case studies, which is then multiplied by 1 to convert it into heat energy loss in Wh/m^2. The wall surface temperature Ts is first extracted from the infrared image and then interpolated against the external temperature to estimate the historical heat loss. The outdoor ambient temperature T_{ext} and wind speed v are obtained from weather station observations. The hourly average and monthly total heat losses are calculated by extracting the historical hourly ambient temperature and hourly wind speed between 2004 and 2019 from the Met Office database (2019) for the location of the case studies. The hourly average heat loss is determined by calculating the average heat loss for all days for a given hour in a particular month. For example, the hourly average heat loss at 1:00 am in January 2004 will be the average of the heat loss values calculated using equation 1 for 1:00 am each day from January 1st to January 31st, 2004. Similarly, the monthly total heat loss is the sum of the hourly heat loss for each hour and each day. The historical hourly average heat losses in Wh/m^2 and monthly total heat losses in kWh/m^2 are calculated for both insulated and uninsulated buildings. The historical heat loss values for a building, calculated using equations 2 and 3, represent the characteristics of heat loss for that building, which can be learned by ANN to predict future heat losses. Although heat loss is dependent on external temperature and wind speed according to equation 1, predicting heat loss over temperature and wind speed simplifies and speeds up the prediction process by reducing the number of parameters to be forecasted and the uncertainty related to the prediction of temperature and wind speed.

3.3. ANN prediction

The literature review indicates the successful use of feed-forward neural networks and different recurrent neural networks, such as NARnet, NARxnet, and LSTM neural networks, for predicting energy demand in buildings. Therefore, these four neural networks are considered for ANN analysis using the hourly average and monthly total heat loss data. The historical heat loss data from 2004 to 2019 are divided into training and test datasets, with different combinations ranging from 2 to 15 years. For example, if the training dataset includes data from 2004 and 2005, the test dataset will contain data from 2006 to 2019. Fourteen different combinations of training and test datasets are evaluated using the above-mentioned neural networks for both hourly and monthly heat loss prediction. In each case, the neural networks are used to predict the heat loss for the same length of data in the test dataset and compared against the test data to evaluate the performance of the neural network. In the training process of the hourly average heat loss prediction using a feed-forward neural network, the hour, month, and year are the three parameters considered as inputs, and the hourly average heat loss obtained from equation 2 is the output. In the case of monthly heat loss prediction using a feed-forward neural network, the month and year are the two input parameters, and the monthly heat loss obtained from equation 3 is the output for the network.

The recurrent neural network works differently than the feed-forward neural network, where the output of the previous time step is considered an additional input for the next time step. The training process of the recurrent neural network involves sequential training, and the time step is one of the default inputs for these networks. In the case of hourly average heat loss prediction, the hourly average heat loss obtained from equation 2 for the previous time step is chosen as the other input. For monthly heat loss prediction, the monthly total heat loss obtained from equation 3 is chosen as the second input instead of the hourly average heat loss. However, the NARxnet accepts additional inputs. Therefore, hour, month, and years are chosen as the additional inputs in the case of hourly average heat loss prediction, and month and year are chosen as the additional inputs in the case of monthly total heat loss analysis for NARxnet. The heat loss at the current time step is chosen as the output for all recurrent neural networks. For hourly average heat loss prediction, it will be the heat loss value obtained from equation 2, and for monthly total heat loss prediction, it will be the heat loss value obtained from equation 3.

4. RESULT AND DISCUSSION

To determine the best architecture for the artificial neural network (ANN), a sensitivity analysis is performed based on the number of layers and neurons in each layer. The training data set consists of the first four years of the entire data set (2004-2007), while the next four years (2008-2011) are used as the test data set. Heat loss data for insulated and uninsulated walls are included, and the average percentage error (APE) is used to measure performance. The feed-forward neural network can have multiple hidden layers with multiple neurons in each layer, so both the number of hidden layers and the number of neurons in each hidden layer are evaluated. Recurrent neural networks typically have one hidden layer with multiple neurons, so only one hidden layer is used for the NARnet, NARxnet, and LSTM networks in this study. The sensitivity analysis includes the number of neurons in the hidden layer for hourly average and monthly total heat loss predictions. Finally, the optimal ANN is used to predict heat loss for both insulated and uninsulated walls, and the energy savings are calculated based on the difference between the predicted heat loss for the two types of walls.

4.1. Sensitivity analysis

The sensitivity analysis for hourly average and monthly total heat loss predictions is presented in Figures 5 and 6, respectively. Figure 5-a shows the sensitivity of the number of hidden layers, while Figure 5-b shows the sensitivity of the number of neurons in each hidden layer for the feed-forward neural network. The sensitivity of the number of neurons in the hidden layer for recurrent neural networks is presented in Figure 5-c. From Figure 5-a, it is found that the average percentage error decreases as the number of hidden layers increases from two to six and then slightly increases with seven hidden layers. Figure 5-b shows that the minimum average percentage error is obtained with three neurons in each hidden layer. Therefore, the best network architecture for hourly heat loss analysis with the feed-forward neural network is composed of six hidden layers and three neurons in each hidden layer. From Figure 5-c, it is found that the NARnet and NARxnet networks show the lowest APE with 20 neurons in the hidden layer, while for the LSTM network, the minimum average percentage error is found with 40 and 140 LSTM cells in the hidden layer. However, the performances of all three recurrent neural networks are poor compared to the performance of the feed-forward network, possibly due to the small sample size of the training data set. Therefore, NARnet and NARxnet with 20 neurons in the hidden layer are selected for hourly heat loss prediction, while the LSTM network with 100 cells in the hidden layer is selected for hourly heat loss analysis due to previous research showing that 100 cells in the hidden layer provide the best performance without significantly increasing computing time.

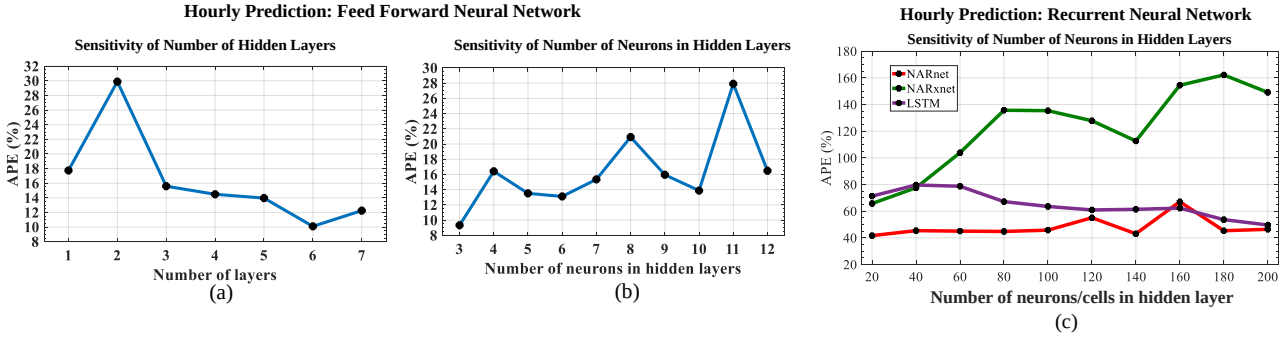

Figure 5 Results of sensitivity analysis for hourly heat loss

Figure 6 presents the sensitivity analysis for monthly predictions. From Figure 6-a and 6-b, it is found that the APE decreases with the increase in the number of hidden layers and increases with the increase in the number of neurons in a hidden layer. However, the APE reaches the minimum and remains stable between 10 to 12 hidden layers. Therefore, 11 hidden layers are selected as it is in the mid of the stable range. For the sensitivity of the number of neurons in a hidden layer, the minimum APE is obtained with two neurons in each hidden layer. Thus, the feed-forward network configuration with 11 hidden layers and two neurons in each hidden layer is selected for monthly heat loss prediction. Figure 6-c shows the sensitivity analysis results for NARnet and NARxnet networks and the LSTM neural network regarding the number of neurons/cells in the hidden layer. Again, the APE of the LSTM neural network is much lower than the APE of NARnet and NARxnet, as found in the first case study. The minimum APE for NARnet and NARxnet is found to be 60% with 12 neurons in the hidden layer, indicating poor prediction accuracy. However, these two networks are further considered to evaluate their performance with the full data set for monthly heat loss prediction. The APE of the LSTM neural network remains stable and below 10% with all different combinations of LSTM cells in the hidden layer. Therefore, the LSTM neural network with 12 cells in the hidden layer is selected for the current case study, as the same configuration showed excellent prediction accuracy in the first case study. Moreover, keeping the number of cells in the hidden layer as low as possible facilitates faster calculation in a shorter time.

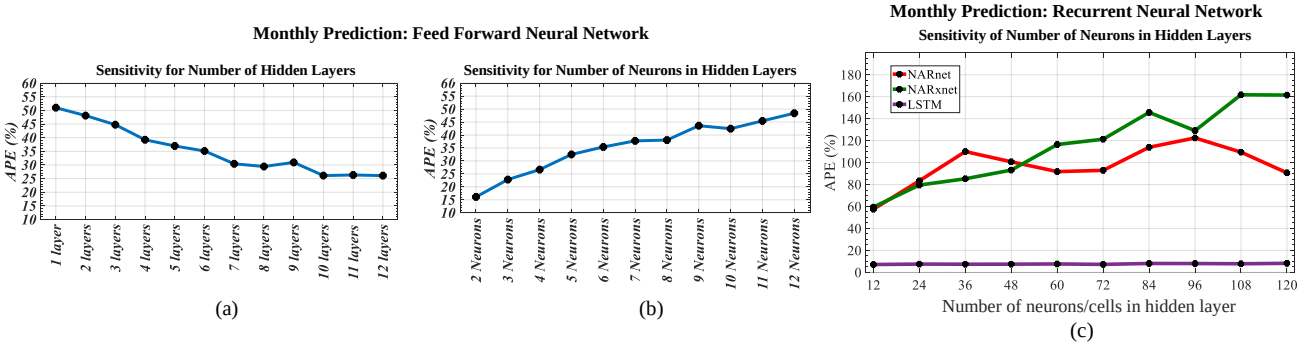

Figure 6 Results of sensitivity analysis for Monthly heat loss

4.2. Heat loss prediction

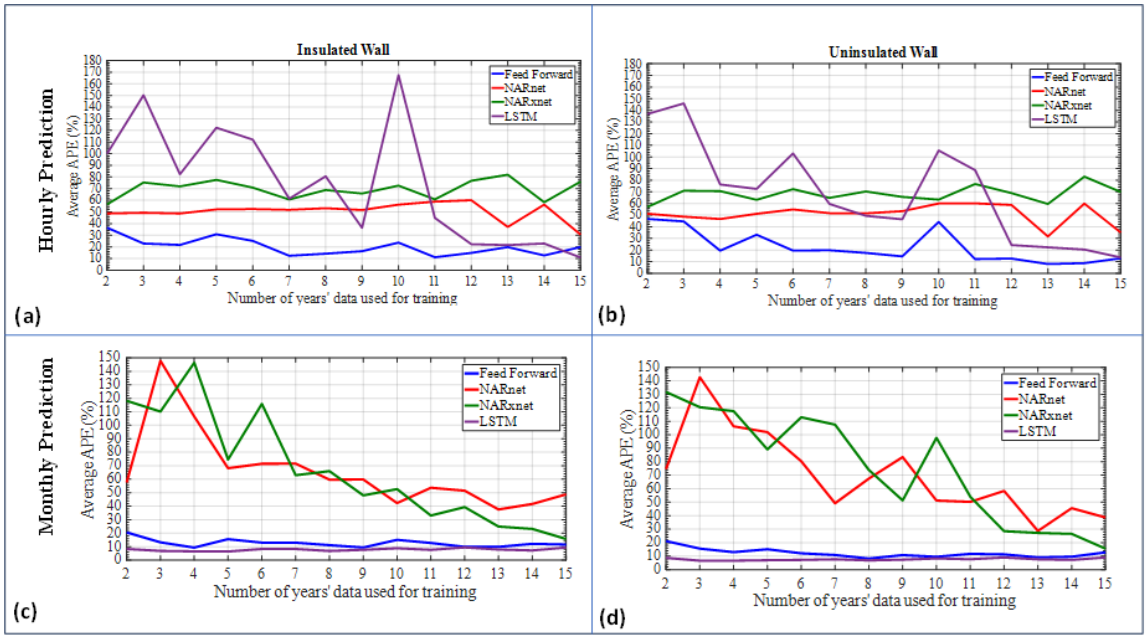

Figure 7 The comparison of performance among feed forward, NARnet, NARXnet and LSTM neural network

Figure 7 presents the average percentage errors (APE) in heat loss prediction for the feed-forward, NARnet, NARxnet, and LSTM neural networks trained using two to fifteen years of heat loss data. Among all four neural networks, the feed-forward neural network shows the lowest APE for the insulated wall in all cases, except when trained with 15 years of heat loss data (shown in Figure 7-a). The APE reaches around 10% when the feed-forward network is trained with 7 to 11 years of heat loss data. For the uninsulated wall, the APE of the feed-forward neural network is the lowest throughout all training cases (shown in Figure 7-b). The APE stays below 20% for both walls when the feed-forward network is trained with 7 years or more of heat loss data, except with 10 years of training. When the feed-forward network is trained with 10 years of heat loss data, the APE slightly goes over 20% for the insulated wall, while for the uninsulated wall, it jumps to around 40%. Despite this aberration in the uninsulated wall, the feed-forward network achieves 80% accuracy in all cases when trained with 7 years or more of heat loss data. The APE of NARnet and NARxnet mostly stays above 50%, except for NARnet, which shows below 40% APE when trained with 13 and 15 years of heat loss data, respectively. The LSTM neural network shows close to 20% APE when trained with 12 years or more of heat loss data, with the lowest APE achieved by the network trained with 15 years of heat loss data. Figures 7-c and 7-d show the mean percentage errors in monthly heat loss prediction for the insulated and uninsulated walls for different networks trained with 2 to 15 years of heat loss data. It is found from these two figures that the LSTM neural network shows the best performance in predicting monthly heat loss, with the APE remaining around 10% throughout. In comparing the feed forward neural network and the LSTM network, the APE of the former remains slightly higher, ranging between 10% and 20%. However, there are cases where the APE is the same for both networks, such as when the network is trained with 9 or 12 years of heat loss data for an insulated wall. Similar results are observed for an uninsulated wall when trained with 8 years and 10 years of heat loss data. The NARnet and NARxnet perform poorly compared to the LSTM and feed forward networks, with only NARxnet showing below 20% APE when trained with 15 years of heat loss data. The feed forward neural network is suitable for predicting hourly average heat loss with over 80% accuracy when trained between 7 and 9 years of heat loss data, while the LSTM network is 90% accurate for predicting monthly heat loss when trained with 8 years of data. Hence, for prediction of future heat loss for both hourly and monthly cases, the feed forward neural network is chosen for hourly heat loss prediction, and the LSTM network is chosen for monthly heat loss prediction. These predictions are made using 8 years of training data (2004 to 2007) to forecast the next 8 years (2012 to 2019) of heat loss. The predicted heat loss from these two ANNs is used in energy savings estimation. However, the NARnet and NARxnet are not recommended for hourly and monthly total heat loss prediction due to their high APE.

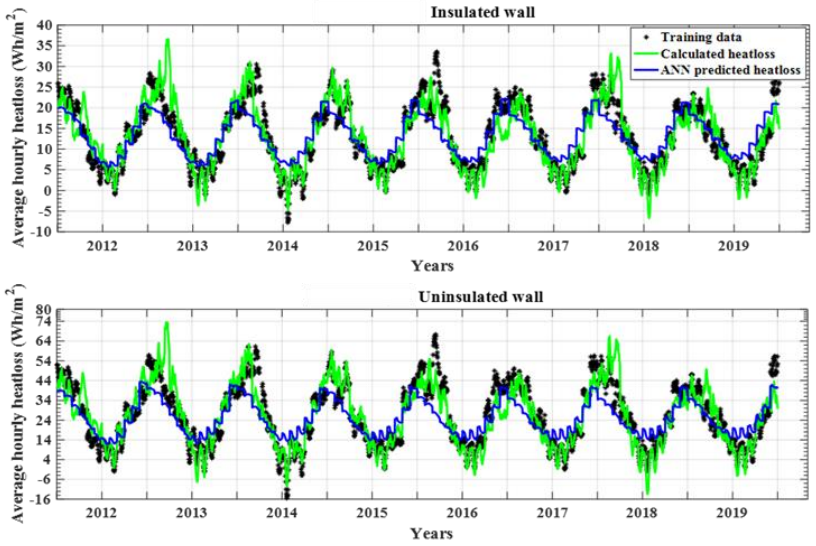

Figure 8 The comparison between the calculated and the ANN (feed forward) predicted hourly heat loss for the years 2012 to 2019

In Figure 8, the predicted heat loss curve of the feed forward neural network is compared to the calculated heat loss curve for both insulated and uninsulated walls from 2012-2019. Overall, the ANN predicted heat losses are very close to the calculated heat loss, with few exceptions. For example, the calculated heat loss is significantly higher in February and March of 2013 and 2018.

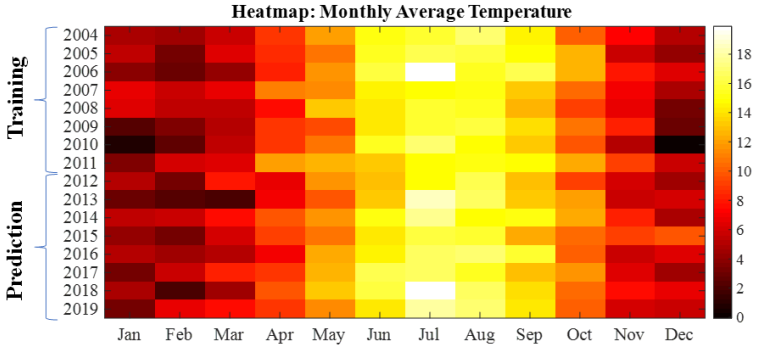

Figure 9 A heatmap representation of average temperature in each month from 2004 to 2019 in Nottingham

The heatmap of average temperature in Figure 9 shows that these months were cooler than in other years. Conversely, the calculated heat loss is far less than the ANN predicted heat loss for July 2013 and 2018, which were exceptionally warmer than in other years. The calculated heat loss curves also show negative heat loss or heat gain due to solar irradiation during the summer. This is not captured by the ANN prediction algorithm, which is designed to predict heat loss. However, this is sensible as heat gain during daytime summer does not contribute to heating energy savings, which is a key factor in estimating the payback period for retrofitting a building with improved insulation. In Figure 10, the calculated heat loss is compared to the LSTM neural network predicted heat loss for both insulated and uninsulated walls. It is observed that both the actual and ANN predicted heat loss curves have an identical trend, with some deviations noted. For example, the higher calculated heat loss in February-March of 2013 and 2018 can be attributed to extreme weather, as discussed in the hourly heat loss predictions.

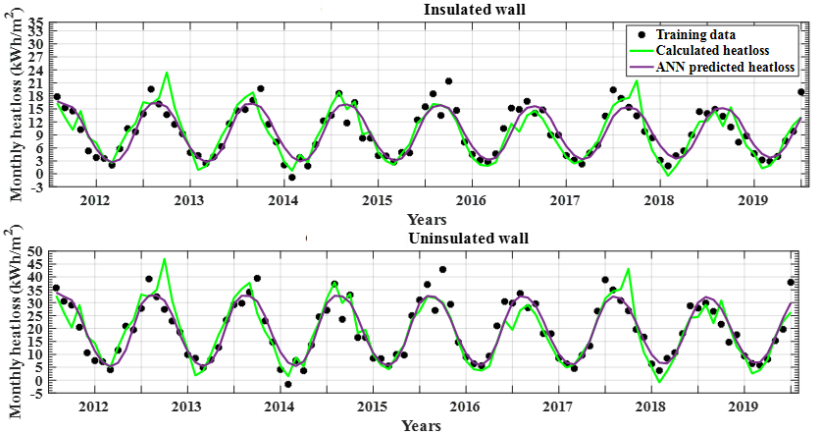

Figure 10 The comparison between the calculated and the ANN (LSTM) predicted monthly heat loss for the years 2012 to 2019

4.3. Energy savings

The case study presented in this paper demonstrates that the feed forward neural network is suitable for predicting hourly average heat loss, while the LSTM neural network is suitable for monthly total heat loss prediction with significant accuracy when trained with more than 8 years of heat loss data. However, it is also important to consider the estimated energy savings using ANN predicted heat losses. Figure 11 shows the estimated energy savings if an uninsulated building were retrofitted with improved insulation to match the level of an insulated building. The hourly average heat loss predicted by the feed forward network and the monthly total heat loss predicted by the LSTM neural networks are used for energy savings estimation, with all networks trained with 8 years of heat loss data. Energy savings are represented by the difference in yearly total heat loss between insulated and uninsulated buildings, calculated for the years 2012 to 2019. The calculated heat loss for both buildings in these years is compared to the ANN results. It is found that the difference between ANN predicted energy savings and calculated energy savings remains within ±15 kWh/m^2 (±10%) for all years except 2013, where the deviation is ±22 kWh/m^2 (±16%). Upon examining the heat map in Figure 9, it is observed that the winter in 2013 was cooler than any other year in the heat map, while the summer was warmer than any other year in the heat map. Therefore, extreme weather conditions in 2013 are responsible for the high deviation in ANN energy savings. The case studies confirm that the ANN can guarantee 84% accuracy in estimating energy savings, despite the influence of extreme weather conditions. It is highly unlikely to regularly experience extreme winters and summers like in 2013, and therefore, the ANN is expected to achieve 90% prediction accuracy in estimating energy savings in the majority of cases.

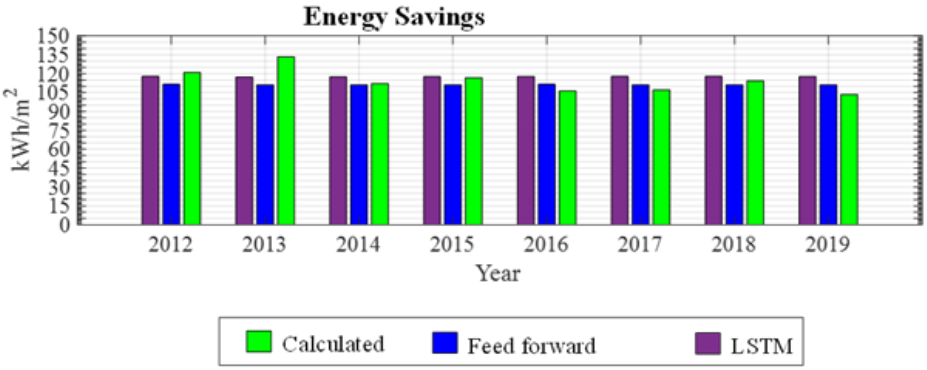

Figure 11 The comparison of energy savings for calculated heat loss and ANN predicted heat loss

5. CONCLUSION

Although monitoring of a building for years is a common practice for estimating energy savings, it is not always an accurate method due to the complex and variable nature of environmental parameters and human behaviour. However, this study presents a simplified novel approach that can provide sufficient information on future energy savings with reasonable accuracy by utilising AI and infrared thermography; combined with some reasonable assumptions. The use of AI in simple experimental work can allow for reasonable estimation of heat losses or energy savings, with ANN demonstrating an 84% accuracy rate in estimating energy savings according to the case studies. The LSTM neural network is suitable for monthly heat loss prediction, while the feed forward neural network is appropriate for hourly heat loss prediction. Both ANNs can accurately estimate heat loss with just 8 years of historic weather training data. The current study did not account for the impact of occupants' behaviour on energy savings. Future research will aim to include this factor to improve the estimation of energy savings.

6. REFERENCES

Al-Habaibeh, A., Medjdoub, B. and Pidduck, A., 2012. 'Investigating The Influence of Door Design on The Energy Consumption of Buildings Using Infrared Thermography', in *4th. JIIRCRAC 2012, Amman-Jordan, Sept. 10th – 12th 2012*.

Al-Habaibeh, A., Sen, A. And Chilton, J., 2021. Evaluation tool for the thermal performance of retrofitted buildings using an integrated approach of deep learning artificial neural networks and infrared thermography. Energy and Built Environment. ISSN 2666-1233.

Al-Habaibeh, A., Hawas, A., Hamadeh, L., Medjdoub, B., Marsh, J. and Sen, A., 2022. 'Enhancing the sustainability and energy conservation in heritage buildings: The case of Nottingham Playhouse', *Frontiers of Architectural Research*, 11(1), pp. 142–160. doi:10.1016/j.foar.2021.09.001.

AL-HABAIBEH, A., WATKINS, M., WARIED, K. and BATHAEI JAVARESHK, M., 2021. Challenges and opportunities of remotely working from home during Covid-19 pandemic. Global Transitions Proceedings. ISSN 2666-285X

Albatici, R. and Tonelli, A.M., 2010. 'Infrared thermovision technique for the assessment of thermal transmittance value of opaque building elements on site', *Energy and Buildings*, 42(11), pp. 2177–2183. doi:10.1016/j.enbuild.2010.07.010.

Albatici, R., Tonelli, A.M. and Chiogna, M., 2015. 'A comprehensive experimental approach for the validation of quantitative infrared thermography in the evaluation of building thermal transmittance', *Applied Energy*, 141, pp. 218–228. doi:10.1016/j.apenergy.2014.12.035.

Bienvenido-Huertas, D. *et al.,* 2019. 'Influence of ICHTC correlations on the thermal characterization of façades using the quantitative internal infrared thermography method', *Building and Environment*, 149, pp. 512–525. doi:10.1016/j.buildenv.2018.12.056.

BP PLC, 2021. *bp Statistical Review of World Energy*. Available at: https://www.bp.com/content/dam/bp/business-sites/en/global/corporate/pdfs/energy-economics/statistical-review/bp-stats-review-2022-full-report.pdf (Accessed: 10 August 2023).

Deb, C. *et al.,* 2017. 'A review on time series forecasting techniques for building energy consumption', *Renewable and Sustainable Energy Reviews*, 74, pp. 902–924. doi:10.1016/J.RSER.2017.02.085.

Department for Business Energy & Industrial Strategy, 2023. *ENERGY CONSUMPTION IN THE UK*. London. Available at: https://www.gov.uk/government/collections/energy-consumption-in-the-uk).

Gori, M., 2018. 'Deep Architectures', in *Machine Learning*. Elsevier, pp. 236–338. doi:10.1016/B978-0-08-100659-7.00005-1.

Government Property Agency, 2022. *NET ZERO PROGRAMME: Looking beyond carbon emissions*. Available at: https://www.gov.uk/government/case-studies/net-zero-programme-looking-beyond-carbon-emissions (Accessed: 10 August 2023).

Guan, Y. *et al.,* 2023. 'Burden of the global energy price crisis on households', *Nature Energy*, 8(3), pp. 304–316. doi:10.1038/s41560-023-01209-8.

Hochreiter, S. and Schmidhuber, J., 1997. 'Long Short-Term Memory', *Neural Computation*, 9(8), pp. 1735–1780. doi:10.1162/neco.1997.9.8.1735.

Kim, J. and Moon, J.W., 2009. 'Impact of Insulation on Building Energy Consumption', *Building Simulation 2009*, pp. 674–680. Available at: http://citeseerx.ist.psu.edu/viewdoc/summary?doi=10.1.1.172.4791.

Kolaitis, D.I. *et al.,* 2013. 'Comparative assessment of internal and external thermal insulation systems for energy efficient retrofitting of residential buildings', *Energy and Buildings*, 64, pp. 123–131. doi:10.1016/j.enbuild.2013.04.004.

Kossecka, E. and Kosny, J., 2002. 'Influence of insulation configuration on heating and cooling loads in a continuously used building', *Energy and Buildings*, 34(4), pp. 321–331. doi:10.1016/S0378-7788(01)00121-9.

Marino, B.M., Muñoz, N. and Thomas, L.P., 2017. 'Estimation of the surface thermal resistances and heat loss by conduction using thermography', *Applied Thermal Engineering*, 114, pp. 1213–1221. doi:10.1016/j.applthermaleng.2016.12.033.

Martellotta, F. *et al.,* 2017. 'On the use of artificial neural networks to model household energy consumptions', *Energy Procedia*, 126, pp. 250–257. doi:10.1016/j.egypro.2017.08.149.

Naji, S. *et al.,* 2016. 'Application of adaptive neuro-fuzzy methodology for estimating building energy consumption', *Renewable and Sustainable Energy Reviews*, 53, pp. 1520–1528. doi:10.1016/J.RSER.2015.09.062.

Nardi, I., Sfarra, S. and Ambrosini, D., 2014. 'Quantitative thermography for the estimation of the U-value: state of the art and a case study', *Journal of Physics: Conference Series*, 547, pp. 1–8. doi:10.1088/1742-6596/547/1/012016.

O'Grady, M., Lechowska, A.A. and Harte, A.M., 2017. 'Infrared thermography technique as an in-situ method of assessing heat loss through thermal bridging', *Energy and Buildings*, 135, pp. 20–32. doi:10.1016/j.enbuild.2016.11.039.

Papadopoulos, A.M., 2005. 'State of the art in thermal insulation materials and aims for future developments', *Energy and Buildings*, 37(1), pp. 77–86. doi:10.1016/j.enbuild.2004.05.006.

Piddington, J. *et al.,* 2020. *The Housing Stock of The United Kingdom*. Available at: https://files.bregroup.com/bretrust/The-Housing-Stock-of-the-United-Kingdom_Report_BRE-Trust.pdf (Accessed: 6 October 2020).

Reilly, A. and Kinnane, O., 2017. 'The impact of thermal mass on building energy consumption', *Applied Energy*, 198, pp. 108–121. doi:10.1016/j.apenergy.2017.04.024.

Ritchie, H., Roser, M. and Rosado, P., 2022. *Energy Production and Consumption*, *Published online at*

OurWorldInData.org. Available at: https://ourworldindata.org/energy-production-consumption (Accessed: 10 August 2023).

Sadineni, S.B., Madala, S. and Boehm, R.F., 2011. 'Passive building energy savings: A review of building envelope components', *Renewable and Sustainable Energy Reviews*, 15(8), pp. 3617–3631. doi:10.1016/j.rser.2011.07.014.

SALIM, S. and AL-HABAIBEH, A., 2023. Exploring windows opening behaviour of occupants of residential buildings using artificial intelligence. Energy and sustainable futures: proceedings of the 3rd ICESF, 2022. Cham: Springer, pp. 311-321. ISBN 9783031309595

Tabrizi, T.B., Hill, G. and Aitchison, M., 2017. 'The Impact of Different Insulation Options on the Life Cycle Energy Demands of a Hypothetical Residential Building', *Procedia Engineering*, 180, pp. 128–135. doi:10.1016/j.proeng.2017.04.172.

The National Energy Efficiency Network, 2019. *Energy consumption in new domestic buildings 2015 – 2017 (England and Wales)*. Available at: https://assets.publishing.service.gov.uk/government/uploads/system/uploads/attachment_data/file/853067/energy-consumption-new-domestic-buildings-2015-2017-england-wales.pdf (Accessed: 10 August 2023).

UN Environment Programme, 2020. *Building sector emissions hit record high, but low-carbon pandemic recovery can help transform sector – UN report*. Available at: https://www.unep.org/news-and-stories/press-release/building-sector-emissions-hit-record-high-low-carbon-pandemic (Accessed: 10 August 2023).

Wang, D. *et al.,* 2016. 'The influence of thermal insulation position in building exterior walls on indoor thermal comfort and energy consumption of residential buildings in Chongqing', *IOP Conference Series: Earth and Environmental Science*, 40, p. 012081. doi:10.1088/1755-1315/40/1/012081.

Wang, L., Lee, E.W.M. and Yuen, R.K.K., 2018. 'Novel dynamic forecasting model for building cooling loads combining an artificial neural network and an ensemble approach', *Applied Energy*, 228, pp. 1740–1753. doi:10.1016/j.apenergy.2018.07.085.

Wang, Z. and Srinivasan, R.S., 2017. 'A review of artificial intelligence based building energy use prediction: Contrasting the capabilities of single and ensemble prediction models', *Renewable and Sustainable Energy Reviews*, 75, pp. 796–808. doi:10.1016/J.RSER.2016.10.079.

Witten, I.H. *et al.,* 2017. 'Deep learning', in *Data Mining*. Elsevier, pp. 417–466. doi:10.1016/B978-0-12-804291-5.00010-6.

Xie, B. *et al.,* 2019. 'Evaluation of stearic acid/coconut shell charcoal composite phase change thermal energy storage materials for tankless solar water heater', *Energy and Built Environment* [Preprint]. doi:10.1016/j.enbenv.2019.08.003.

#51: Electricity Distribution Networks for Multi-Technology Residential Communities: A Sufficiency Assessment

Abdullah DIK[1], Cagri KUTLU, Siddig OMER, Rabah BOUKHANOUF, Hao SUN, John Kaiser CALAUTIT

[1] Department of Architecture and Built Environment, Faculty of Engineering, The University of Nottingham, Nottingham, NG7 2RD, UK, abdullah.dik@nottingham.ac.uk

Abstract: Climate change is becoming an increasing concern all around the world. The fossil-based sources of electricity generation are one of the primary factors of climate change. In many countries, the transition to low-carbon technology has already begun toward achieving zero-carbon targets. Electric vehicles (EVs) and heat pumps (HPs) are promising technologies to help tackle the source of carbon emissions. However, the uncontrolled application of these technologies could potentially result in unintended outcomes and damage the distribution networks. This research paper examines the hourly based electrical demand in a residential community using advanced multistage stochastic modelling methods. Moreover, this study investigates the sufficiency of the existing distribution networks in the UK for full EV and HP adaptations. The study also discusses the requirements for future grid systems to provide uninterrupted and safe electricity to end users.

Keywords: Electric Vehicle (EV); Vehicle-to-Grid (V2G); Renewable Energy Source (RES); Heat Pump (HP), Energy Storage

1. INTRODUCTION

Nowadays, developed countries started to change their energy market. Instead of fossil fuels commonly used for electricity generation, renewable energy sources (RESs) are now encouraged to be integrated into the grid. The United Kingdom (UK) significantly succeeded in reducing carbon emissions by lowering 40% within the last three decades. (BEIS, 2021). Additionally, low-carbon technologies such as electric vehicles (EVs) and heat pumps (HPs) are effective technologies that can be used for grid decarbonisation. Therefore, the government supported adopting these technologies in the UK. As a result of these incentives, the number of EVs and HPs is expected to increase significantly. However, the electricity demand for these technologies is one of the biggest concerns for future distribution systems. Both technologies can add an extra electricity load on the grid, especially when the demand is high (Liang et al., 2022, Dik et al., 2022). Therefore, the distribution system might face much electricity demand above the maximum capacity. For this reason, these technologies' hourly base charging demand under high penetration rate should be detailly analysed, and the most effective penetration techniques should be discussed.

The study aims to examine the energy demands of residential communities using various technologies such as electric vehicles and heat pumps. A multi-stage stochastic model is utilised to address the uncertainties and randomness of electricity use. Additionally, this research aims to evaluate whether the existing electricity distribution networks are sufficient to meet the electricity demand of the simulated community under the high penetration rate of EV and HP scenarios.

2. METHODOLOGY

2.1. Conventional Power Consumptions of the Buildings

The energy consumption in houses, excluding heating and EV charging, is called here as conventional energy demand. The Energy Saving Trust (Owen and Foreman, 2012) analysed the energy consumption habits of 26 British residents and published an in-depth report. The report calculated the UK household's average conventional energy load as 3,638 kWh per year. This study uses the 24-hour energy demand profile given in the Energy Trust report was used as conventional load demand data.

2.2. Heating Requirements of the Buildings

A case study is carried out using IESVE software for a house at the University of Nottingham. A heating load of the building is simulated using actual fabrics of the house and assumed user profiles. The house is a two-story building with a total interior floor area of 124.82 m^2 (62.41 m^2 for each floor), as shown in Figure 1. The software uses measured Nottingham's weather data for one year. It is assumed that a family of four people is living in the house. The main construction elements and their U-values are Roof (0.19 W/(m^2K)), external wall (0.22 W/(m^2K)), floor (0.2 W/(m^2K)), windows (1.8 W/(m^2K)) and doors (2.2 W/(m^2K)).

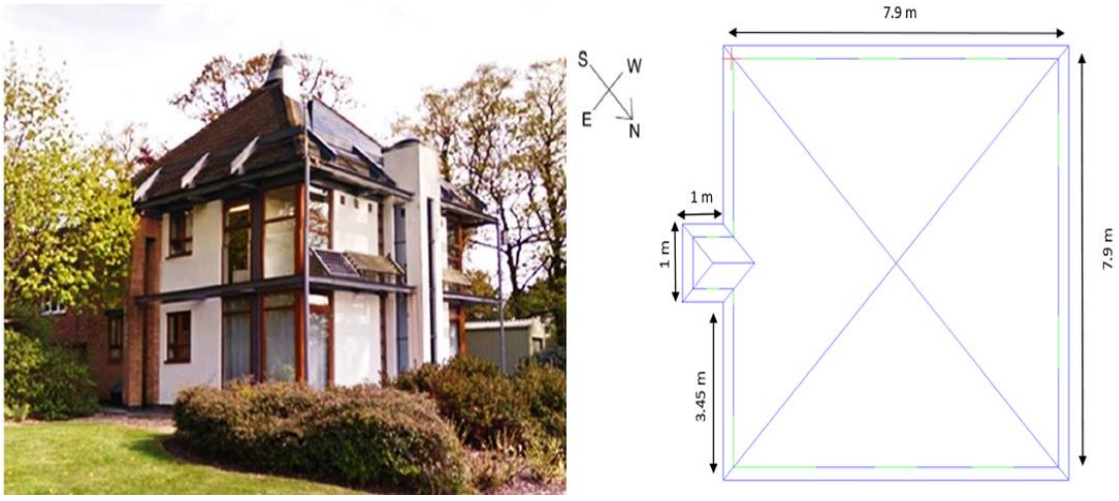

Figure 1 Examined Eco-house (left) and floor layout (right)

The user profile is given as follows: On weekdays, the house is empty from 07:30 am to 18:00, while at the weekends, all the family members are home all day. Heat gain from people, lighting, appliances, and heat loss due to ventilation and leakage are estimated according to reference (Kutlu et al., 2022). Rooms temperature set point is 18 ℃ from 22:00 to 05:30 am. This is based on the CIBSE guide (Butcher and Craig, 2016), which sets bedrooms' winter day operating conditions as 17-19 ℃. During the daytime, when the building is unoccupied, the temperature is set at 15 ℃. In the remaining times, the set temperature for the kitchen, hall, bedrooms and living rooms is set at 21℃ (Butcher and Craig, 2016).

2.3. Electric Vehicle Charging Demand

Typically, the produced electricity is transferred to high-voltage transmission networks controlled by the National Grid. This system distributes electricity through long distances at high voltages, including 275 kV and 400 kV in England. After that, the power joins the distribution network under the control of Distribution Network Operators (DNOs), where it is sent to various end-users, including households and businesses (2015).

The generated power passes through 33/11 kV substations with two 11 MVA transformers in the UK power network. The 11 kV substation separates six feeders, and each feeder supplies power to eight 11/0433 kV substations. In the last stage, these substations transmit power to 384 homes (Ingram et al., 2003). Similar to (Han et al., 2022), this investigation assumes that the efficiency and power factors are 100% and 1, respectively. Therefore, the maximum power capacity is set as 500 kW in the simulated distribution mechanism.

The present study uses the UK's National Travel Survey to calculate the total number of EVs (2022b). Survey results claimed the average number of cars per house in the UK is 1.2. Considering 384 residences in the simulated community, the total number of EVs is 461 units. The hourly charging demand for EVs is directly related to three key factors: battery capacity, the power output of chargers, and arrival and departure times. For more realistic results, all trends in the UK's EV market and the uncertainties in the demand calculation are considered in this paper.

The variety of EVs and, therefore, the storage capacities of their batteries have been considered in this study by analysing the most used EVs in the UK. Table 1 illustrates the ten most popular Battery Electric Vehicles (BEVs) on the UK's roads for the third quarter of 2022, as provided by the Department for Transport (DfT) (2022a). For every 461 vehicles in the simulated community, the model randomly assigns one of the cars shown in the table, considering the popular vehicles' usage frequency in the UK. The characteristics listed in Table 1, such as battery capacity and consumption rate, were gathered from Electric Vehicle Database (EV-Database).

Table 1: The most popular EVs used in the UK

Popularity Rank	Vehicles	Type	Capacity [kWh]	Consumption Rate [kWh/mile]
1	TESLA MODEL 3	BEV	60	0.232
2	NISSAN LEAF	BEV	40	0.269
3	KIA NIRO	BEV	64.8	0.27
4	RENAULT ZOE	BEV	52	0.274
5	VOLKSWAGEN ID3	BEV	58	0.264
6	JAGUAR I-PACE	BEV	84.7	0.36
7	TESLA MODEL Y	BEV	60	0.267
8	AUDI E-TRON	BEV	85	0.34
9	BMW I3	BEV	42.2	0.261
10	HYUNDAI KONA	BEV	67.5	0.261

The different charger units' power outputs have also been modelled in this paper. The variety of the chargers is a crucial factor because it can affect the hourly charge demand, the power capacity of the distribution network and the energy management in the grid. Zap-Map (Zap-Map, 2023) announced that the number of public EV chargers in the UK reached 42,566 EV charging units at 24,909 locations at the end of April 2023. However, it should be noted that this data is just related to public chargers and do not include the estimated 400,000+ possible chargers in homes and businesses. Nonetheless, the Domestic Electric ChargePoint Analysis from the Department for Transport (DfT) (DfT, 2018) declared that the power ratings for domestic chargers are generally rated as 3kW or 7kW. Therefore, in the present study, only 3kW and 7kW chargers are modelled, and the model selects a random charger in each charging operation.

EV availability is the final factor that affects the charging demand predictions of EVs. Modelling EVs' arrival and departure times is essential as this data can impact the hourly charging loads by EVs on the grid. Additionally, the hour-based charging needs of EVs are vital in efficiently planning and managing energy infrastructure. Unanticipated energy load on the grid can result in overloads and potential power outages. In this study, the analysis results of the 2009 National Household Travel Survey (NHTS) by Ahmadian et al. (Ahmadian et al., 2015) are used for EVs' arrival and departure times. NHTS (Santos et al., 2011), conducted by the US Federal Highway Administration (FHWA), is a survey that examines the travel behaviour of approximately 150,000 households and 300,000 people. In this survey, travel-related data such as modes of transportation, travel times, distances and purposes are collected and then analysed. At this stage, the vehicle percentages for arrival and departure time slots were obtained from (Ahmadian et al., 2015) and normalised. Then, the arrival and departure times were generated stochastically for the EVs in the community based on empirical distributions using the inverse transform sampling method. The two-sample Kolmogorov-Smirnov (K-S) test was conducted to assess the similarity between the generated and original samples statistically. The original distribution of the EV availability period is shown in Figure 2.

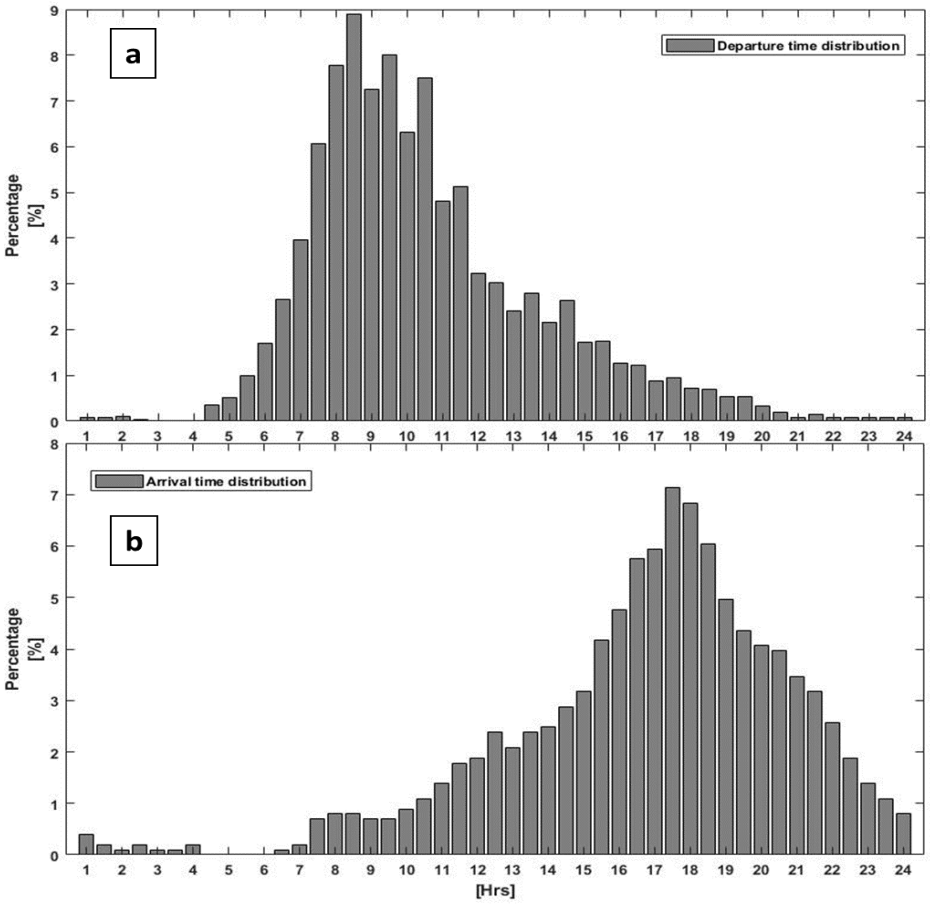

Figure 2 Distribution of Departure and Arrival Times of the Vehicle

This study analyses daily EV usage habits and mileage of vehicles to calculate the demand for EV charging. According to a travel report published by DfT (DfT,2022b), EVs in the UK travel 5,200 miles per year; thus, the average daily travel is roughly 15 miles. In order to create a more realistic model for the mileage distribution, the annual travel ranges and percentages of vehicles taken from the DfT's National Travel Survey (NTS) (DfT, 2022a) were used to create random samples. Two methods, Weighted Random Sampling (WRS) and Uniform Random Sampling (URS), were used to generate random samples. WRS was utilised as a first step to assign probability weights based on the raw data mileage ranges. Subsequently, URS was conducted to generate specific mileage values within these ranges. As an accuracy check step, a Chi-Square goodness-of-fit test was performed as a control step. This test determines how well the generated data matches the original distribution. It is worth mentioning that Plug-in Hybrid Electric Vehicles (PHEVs) are not considered in this study due to their reliance on traditional fuel sources for daily travel. The Monte Carlo Simulation (MCS) is utilised to calculate the hourly demands of EVs. Each uncertainty mentioned earlier is inputted into the MCS model, and then an optimised 24-hour load profile is taken as output. It is important to note that for this MCS model, the number of iterations and charging efficiency is set as 1,000 and 90%, respectively.

3. RESULTS

3.1. Heating Demand of the Buildings

Figure 3a shows weather data for the designed day which will be used for system performance analysis. The 1st of February was chosen as the design day due to the moderate heating load in this period. The heating demand profile of the building is calculated and given in Figure 3b using given assumptions, building fabrics and user profiles. The heating of the building is needed in the morning to maintain the set temperature. After the occupants leave, the set temperature decreases, and no heating is required. When people return home, the heating need increases until reaching the set temperature again. These two heating periods match well with the peak grid periods; thus, it is important to have an efficient heating unit such as, solar assisted heat pump which will be investigated in the following sections.

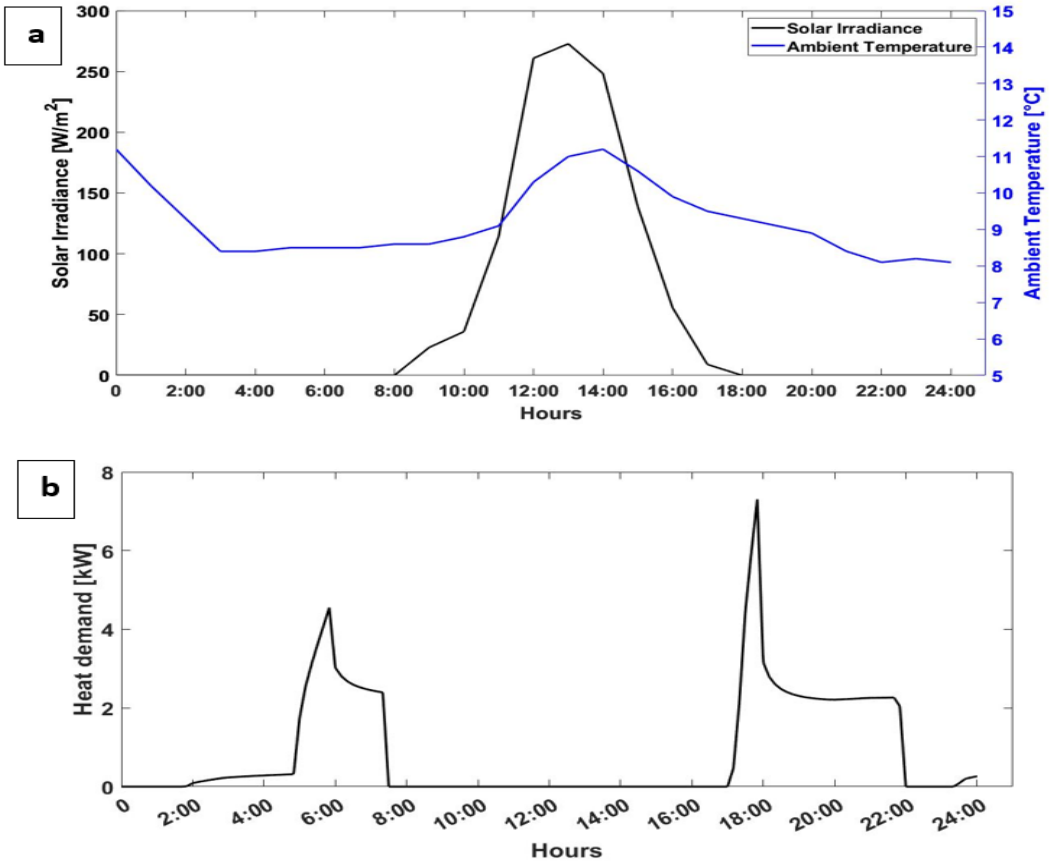

Figure 3 Weather data and heating profiles, a) Solar radiation and ambient temperature b) The heating demand profile of the building

The advantage of the solar-assisted heat pump unit is the higher coefficient of performance (COP) since the heat pump uses stored solar energy during the day in the buffer tank, which has a higher temperature than ambient air. However, one of the drawbacks of the solar-assisted heat pump unit is that it requires a large buffer tank size in order to operate even at night. Thus, in this section, air-sourced heat pump and solar-assisted heat pump performances are compared considering the same building demand profile.

3.2. Analysis of the Heat Pumps

Figure 4a shows the buffer tank temperature and the ambient temperature variation during the day based on the initial design specifications. Depending on the heating requirements, heat is taken from the tank two times a day, and the tank is charged in the daytime by the solar collectors. Therefore, the temperature in the buffer tank depends on the heating requirements and the available solar energy during the day. As a design condition, the heat pump condenser temperature was fixed at 70 ℃. The COP of the solar-assisted HP unit depends on buffer tank temperature, but the air source HP performance changes with ambient temperature. Since the heating periods are only from 5:00 am to 7:30 am and 17:00 to 22:00, the buffer tank temperature decreases during these periods because the HP uses the stored heat in the tank. However, buffer tank temperature increases during solar hours, from 8:00 am to 18:00. The collected thermal energy by solar collectors is stored in the tank regardless of heat pump operation. Since the higher heat source temperature means higher heat pump COP, the heat pump performance is better in the afternoon. Figure 4b shows the COP variation of air and solar-assisted HPs. The COP of the air-sourced HP unit is quite stable as the ambient temperature varies less than 5 ℃ as shown in Figure 3a. However, the COP of the solar-assisted HP varies during the day as the buffer temperature is not constant. When the compressor energy consumption and the heating provided by the condenser are considered for all the day, the COP of the air source heat pump reaches 2.67, and the COP of solar-assisted HP reaches 4.04.

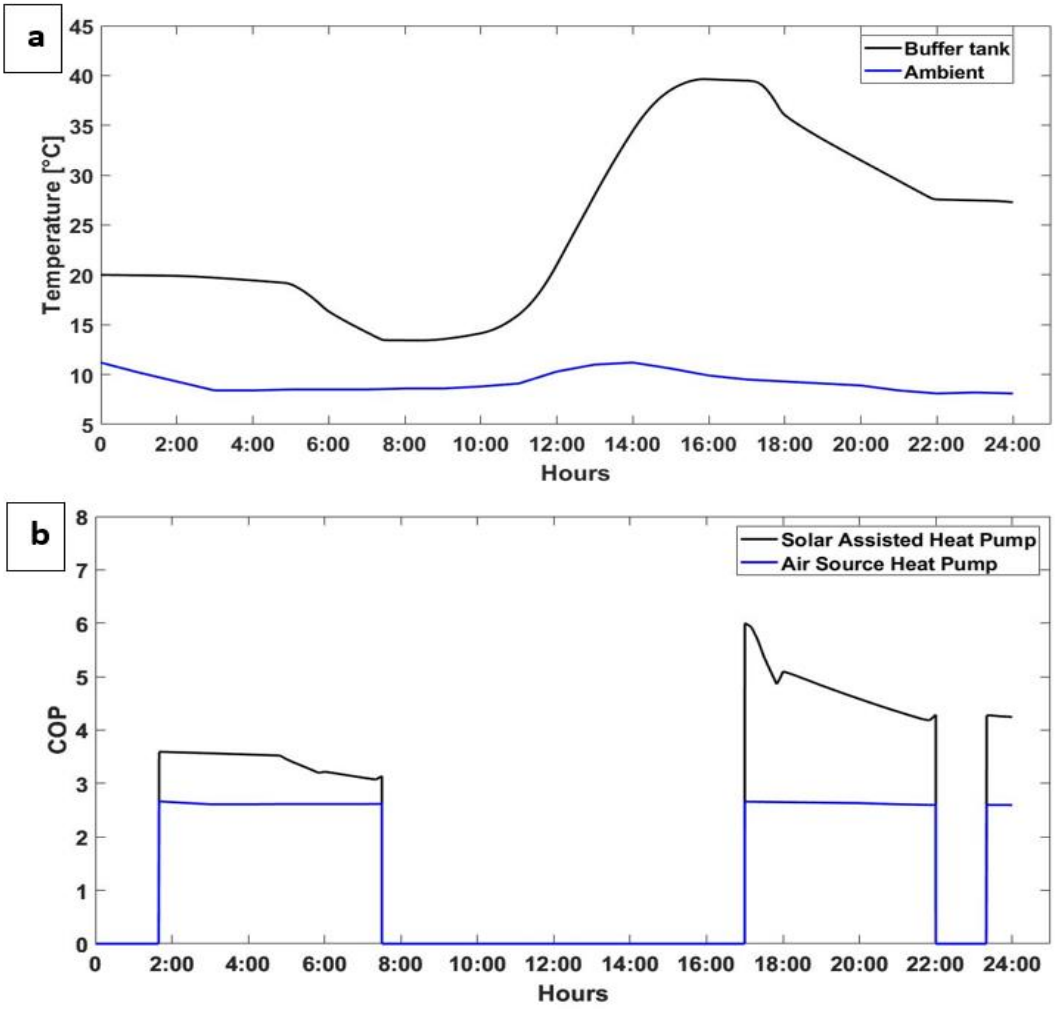

Figure 4 Temperature variation of the buffer tank and COP values of the solar assisted heat pump and air source heat pump for a collector area: 50 m2, and a buffer tank volume of 800 Litre

In order to find out the overall electricity requirement of the building, the electricity consumption of heat pumps is considered. Transient electricity consumption profiles of the heat pumps are given in Figure 5. The same trend can be seen in both profiles as they are dependent on the heating profile, but solar-assisted HP significantly reduces the electricity requirement for heating. For the studied 24-hour analysis, the air-source HP consumes 7.9 kWh of electricity, while the solar-assisted HP needs only 5.14 kWh.

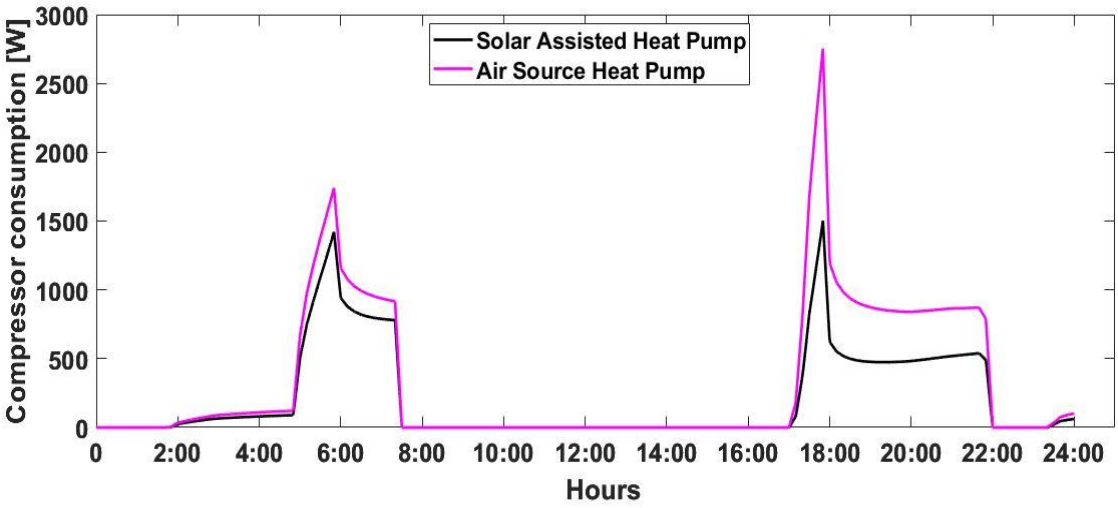

Figure 5 Electricity consumption profiles of solar assisted and air source HPs

3.3. Analysis of the Electric Vehicles

The first set of analyses examined the availability of EVs in the community. Figure 6 presents the results obtained from the inverse transform sampling method and gives a distinct pattern of the EV drivers' daily travel habits. It can be seen that the most significant population of EV owners leave the house in the early morning for commuting and return around 5-6 pm. When the US-based survey (Santos et al., 2011) was used for the analysis, the graph illustrated a correlation between EV travel patterns and the typical UK working hours.

A K-S test was applied to determine if the developed time series pattern followed the actual time series figure. It is calculated that p-value is 0.8912 for both the arrival and departure times. Using a significance level (α) of 0.05, this result shows that it failed to reject the null hypothesis that states two samples have the same distribution, for both departure and arrival times.

The daily distance travelled by these EVs was considered to calculate the charging load of the vehicles in the community. The annual vehicle utilisation levels, on the mile-basis, provided by DfT were modelled for EVs in the community using WRS and URS methods. The obtained distribution from the analysis is shown in Figure 7. The findings indicate that vehicles are primarily driven between 10 and 20 miles per day. This aligns very well with the average daily driving distance of 15 miles reported by DfT (DfT, 2022b) in 2023. The samples generated using WRS and URS were designed to follow the distribution that is already specified, but still, as a validation tool, the Chi-Square test was conducted in the model. The test result calculated the p-value as 0.4644. This means that it failed to reject the null hypothesis considering α of 0.05, that is, the differences between the original and empirical distributions were not considered statistically significant.

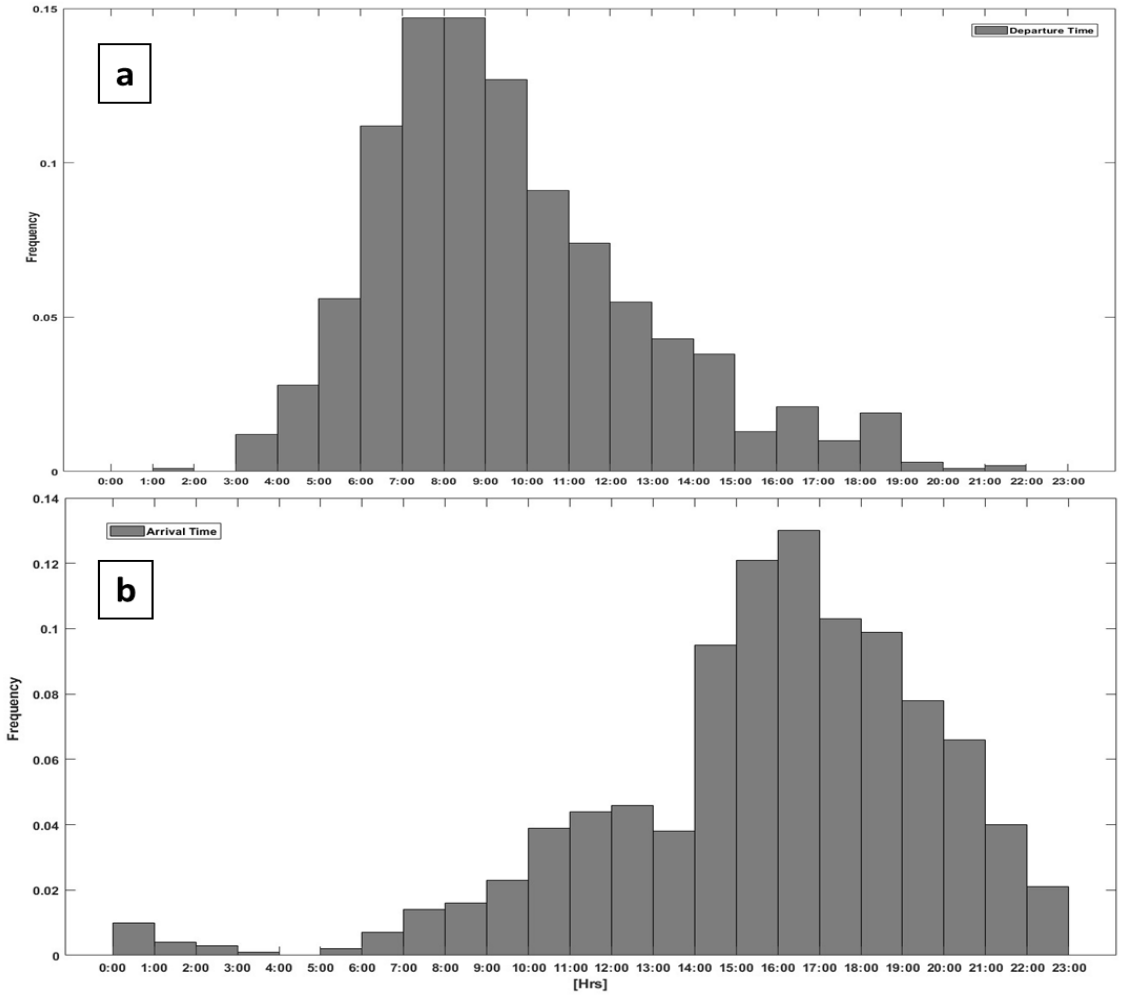

Figure 6 The generated arrival and departure times

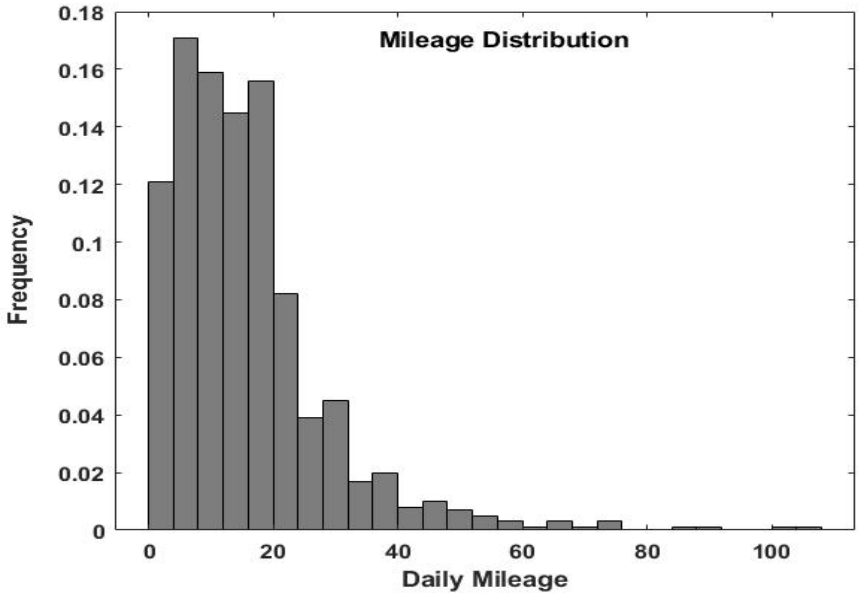

Figure 7 Distribution of the daily travel mileage of the vehicles

MCS is the final step in calculating the charging demand for EVs in the community. MCS, which considers many uncertainties, such as different EV models, a range of battery capacities and chargers, vehicle availability, and usage trends in the UK, is modelled for 461 vehicles in this study. The charge load created by these 461 vehicles at the day times is shown in Figure 8. No charge management strategy is applied in the model, and it is assumed that the vehicles are directly plugged into the charger when they arrived. This approach is valid for observing the problems created by EVs in the network in possible future uncontrolled charging situations.

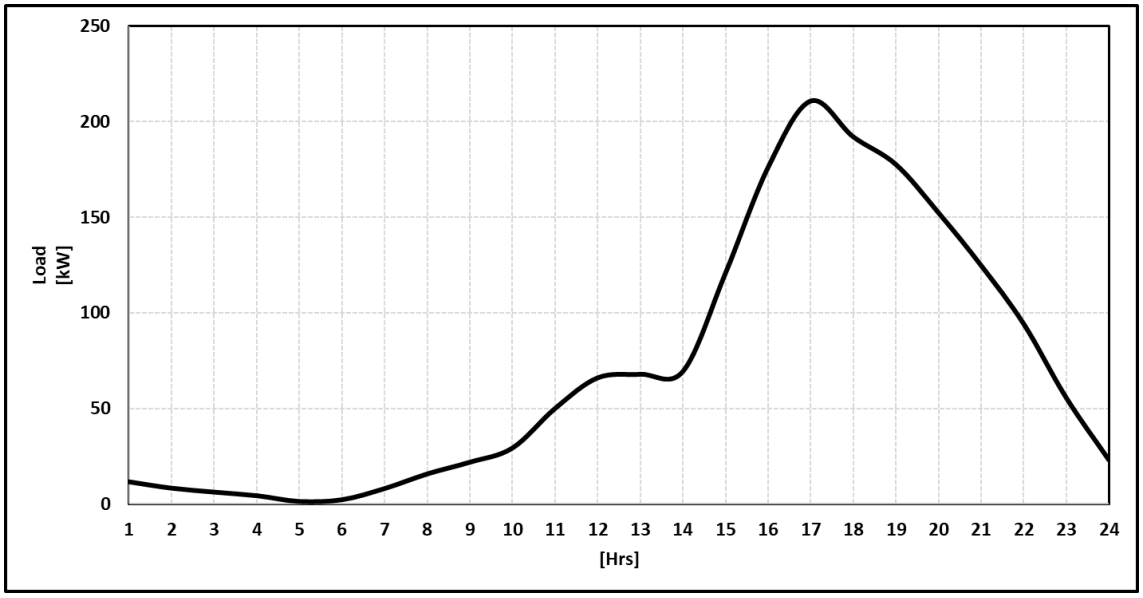

Figure 8 The hourly EV charging demand

As expected from the arrival and departure times of EVs, there is a peak charge demand between 5 pm and 6 pm. MCS results show that EVs in the simulated community generate approximately 1.7 MWh of charging demand per day. Additionally, from Figure 8, it is seen that there is a lower charge demand in the community at night (between 00.00 - 06.00 am) and this demand starts to increase in the morning hours (after 06.00 am). Then, the charging demand increases throughout the day. It is also observed that the lowest demand value is 1.2 kWh after midnight, while the highest demand value is 210.8 kWh after 5 pm.

3.4. Analysis of the Community Network

After calculating the conventional load, EV charging and HP electricity demands, the peak and operational capacity of the network are examined. As stated before, the network peak capacity is 500 kW. Similar to (Han et al., 2022), the capacity reserve margin for the distribution network has been taken as 20%, thus the operational power capacity is 400kW.

The results vary based on the HP types used in the community. As seen in Figure 9, there are changes in the peak demand depending on air-source HP usage (Total_ASHP) and solar-assisted HP (Total_SAHP) usage.

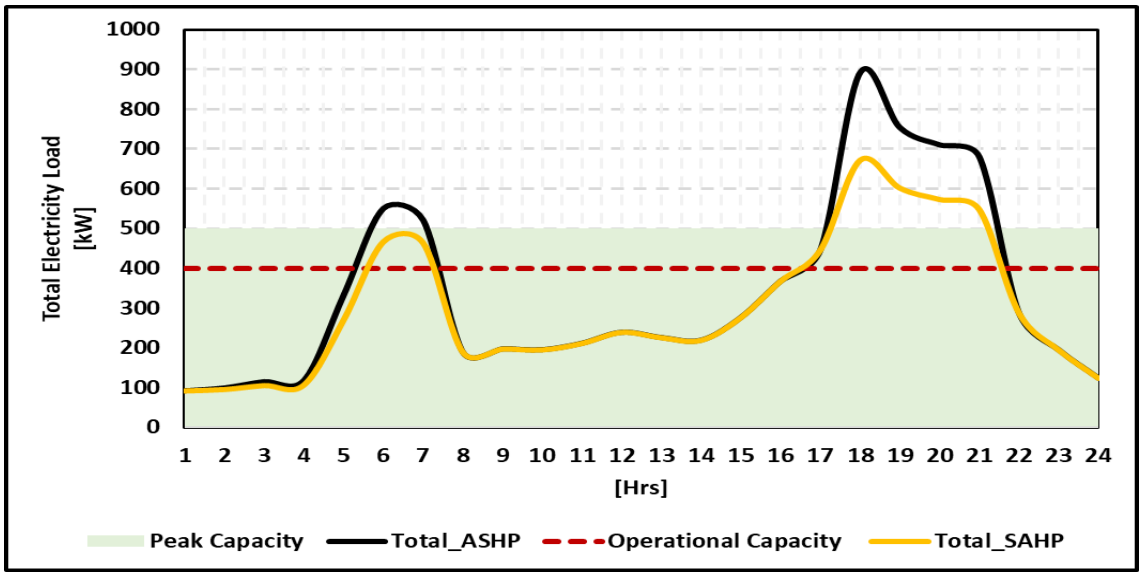

Figure 9 Total hourly electricity demand of the simulated community

In the simulated community, if the vehicles are fully electrified and the heating needs are completely provided by air-source HPs, it has been observed that the operational capacity excess in the network is 1751.3 kWh. Operational capacity is an important parameter to consider in energy management, as it usually represents the amount of energy that can be regularly supplied in the system. Additionally, it has been observed that the sum of the peak capacity exceedance in this scenario is 1105.7 kWh. Peak capacity means the amount of energy that can be supplied at peak electricity demand. Therefore, the findings indicated that the power supply capability of the distribution network is not sufficient to meet the demands of the simulated community. Furthermore, in this scenario, the peak hours for operational overcapacity are typically 6:00 am, 7:00 am, 17:00, 18:00, 19:00, 20:00, and 21:00. The times for peak overcapacity are generally established as 5:00 am, 6:00 am, 7:00 am, 18:00, 19:00, 20:00, and 21:00. This is an indication that we need to adjust our energy management strategies to these peak demand periods and maybe consider various storage systems, demand management and smart charging systems. Otherwise, it is seen that additional investment costs and capacity increases are inevitable during peak capacity exceeding hours. As an additional result, the energy storage capacity required to meet the peak capacity exceedances has been determined as 1105.7 kWh for this scenario.

On the other hand, another scenario under consideration includes installing fully EVs and solar-assisted HPs in the community. In this scenario, the analysis pointed out that solar energy support can reduce the operational and peak capacity exceedances to 968.2 and 392.6 kWh, respectively. Although solar-assisted HPs cause a decrease in the electricity demand, there is no change in the hours when the operational capacity threshold exceeds. However, the peak capacity exceeding does not occur in the morning hours, and it appears only at 6 pm, 7 pm, 8 pm and 9 pm. In this scenario, it has been calculated that the capacity of a possible storage system to be designed decreased by approximately 65% compared to the air-source HP scenario. As a result, while the use of solar-assisted HPs significantly mitigates the stress on the grid, it seems that energy management strategies are still necessary.

4. CONCLUSION

This study examines the effects of EV and HP usage on the distribution network and investigates how suitable the existing network systems are for 100% EV and HP adaptation. The most apparent findings from this study are summarised as follows: ① It has been observed that the heating demands are high when the electricity usage is high in the community. Matching heating and electrical loads showed that heat pumps would increase the peak demand in the network. Therefore, solar-assisted HPs should be considered in communities over air-source HPs due to their lower energy consumption. ② Considering the performance of heat pumps, solar-assisted HPs can operate almost twice as efficient as air-source HPs with a COP of 4.04 under the given conditions. Also, end-of-day energy analyses have shown that the daily amount of energy consumed by solar-assisted and air-source HPs is 5.14kWh and 7.9 kWh, respectively. ③ Examining the EV charging demands, the daily charging load in the community is 1.7 MWh, and the peak charging demand is 210.8 kWh, and occurs between 5pm and 6 pm. Similar to HPs, the most common charging time matches the network's peak demand time, which puts more stress on the distribution network. ④ Considering the total charging demands of the community, it seems that the existing distribution networks are not ready for 100% EV and HP penetrations. In air-source and solar-assisted scenarios, morning and evening peak demands exceed the network's maximum capacity.

5. ACKNOWLEDGEMENT

The authors would like to acknowledge the Republic of Türkiye for the support of this research.

6. REFERENCES

Current and Upcoming Electric Vehicles [Online]. Electric Vehicle Database. Available: https://ev-database.org/ [Accessed [02.06.2023].

2015. Connecting Community Energy: A guide to getting a network connection. ENA (Energy Network Assiciation).

2022a. Licensed ultra low emission vehicles (ULEVs) at the end of the quarter by body type and fuel type, including breakdown of generic models: Great Britain and United Kingdom (VEH0133).

2022b. National Travel Survey 2021: Household car availability and trends in car trips. Department for Transport (DfT).

Ahmadian, A., Sedghi, M. & Aliakbar-Golkar, M. Stochastic modeling of plug-in electric vehicles load demand in residential grids considering nonlinear battery charge characteristic. 2015 20th Conference on Electrical Power Distribution Networks Conference (EPDC), 2015. IEEE, 22-26.

Beis 2021. Net Zero Strategy: Build Back Greener. Department for Business, Energy & Industrial Strategy (BEIS).

Butcher, K. & Craig, B. 2016. *CIBSE guide: A Environmental design*, Cibse.

DFT 2018. Electric ChargePoint Analysis 2017: Domestics. Department for Transport (DfT).

DFT 2022a. Annual mileage band of cars, England: 2002 onwards (NTS0904). Department for Transport (DfT).

DFT. 2022b. *NTS0901: Annual mileage of cars by ownership and trip purpose: England, since 2002* [Online]. Department for Transport (DfT). Available: https://www.gov.uk/government/statistical-data-sets/nts09-vehicle-mileage-and-occupancy [Accessed 07.07.2023].

Dik, A., Omer, S. & Boukhanouf, R. 2022. Electric Vehicles: V2G for Rapid, Safe, and Green EV Penetration. *Energies,* 15**,** 803.

EV-Database. *Current and Upcoming Electric Vehicles* [Online]. Available: https://ev-database.org/ [Accessed [10.02.2023].

Han, M.-E., Alston, M. & Gillott, M. 2022. A multi-vector community energy system integrating a heating network, electricity grid and PV production to manage an electrified community. *Energy and Buildings,* 266**,** 112105.

Ingram, S., Probert, S. & Jackson, K. 2003. The impact of small scale embedded generation on the operating parameters of distribution networks. *PB Power, Department of Trade and Industry (DTI)*.

Kutlu, C., Tapia-Brito, E., Agbonaye, O., Su, Y., Smith, S. T., Hughes, B. & Riffat, S. 2022. Incorporation of controllable supercooled phase change material heat storage with a solar assisted heat pump: Testing of crystallization triggering and heating demand-based modelling study. *Journal of Energy Storage,* 55**,** 105744.

Liang, J., QIU, Y. L. & XING, B. 2022. Impacts of electric-driven heat pumps on residential electricity consumption: an empirical analysis from Arizona, USA. *Cleaner and Responsible Consumption,* 4**,** 100045.

Owen, P. & Foreman, R. 2012. Powering the nation: Household electricity using habits revealed. *Energy Saving Trust/DECC/DEFRA, London*.

Santos, A., Mcguckin, N., Nakamoto, H. Y., Gray, D. & Liss, S. 2011. Summary of travel trends: 2009 national household travel survey. United States. Federal Highway Administration.

ZAP-MAP. 2023. *EV Charging Statistics 2023* [Online]. Zap-Map. Available: https://www.zap-map.com/ev-stats/how-many-charging-points/ [Accessed [04.06.2023].

#53: A novel modelling approach for performance analysis of a concentrated radiative cooling system using the compound parabolic concentrator

Ya DAN[1], Mingke HU[2,*], Yuehong SU[3,*], Saffa RIFFAT[4]

[1] Department of Architecture and Built Environment, University of Nottingham, University Park, Nottingham, NG7 2RD, UK, ya.dan@nottingham.ac.uk
[2] Department of Architecture and Built Environment, University of Nottingham, University Park, Nottingham, NG7 2RD, UK, mingke.hu@nottingham.ac.uk
[3] Department of Architecture and Built Environment, University of Nottingham, University Park, Nottingham, NG7 2RD, UK, yuehong.su@nottingham.ac.uk
[4] Department of Architecture and Built Environment, University of Nottingham, University Park, Nottingham, NG7 2RD, UK, saffa.riffat@nottingham.ac.uk

Abstract: Radiative sky cooling (RC), a passive cooling strategy, can emit the waste heat from the earth into outer space to cool itself or practical objects. Despite it has great potential for energy saving and environmental protection, the low energy density of RC technology and its dependence on atmospheric conditions have limited its practical application. To enhance the cooling capacity of the RC system, concentrated RC systems have been developed. In this study, a compound parabolic concentrator (CPC) is put forward as the concentrator for the concentrated RC system, and a modelling approach to investigate its cooling performance is developed. Previous outdoor experiments have demonstrated the CPC can block a portion of daylight and undesirable external radiation, while effectively concentrating the thermal radiation emitted by the emitter, thereby enhancing the RC performance. Building upon these findings, the amount of light emitted from the RC emitter reaching different annular intervals is simulated using the optical software Photopia. The equivalent sky emissivity can be calculated by the simulated light ratio, and the net cooling power of various models is further deduced. Through the investigation of relevant parameters in the mathematical model, the key factors influencing the cooling power of the RC systems are analysed and determined, providing further evidence of the cooling advantages offered by the CPC-RC system.

Keywords: concentrated radiative cooling system, equivalent sky emissivity, net cooling power, Photopia.

1. INTRODUCTION

Radiative sky cooling (RC), as a passive cooling strategy, is widely employed in various areas such as buildings (Chen and Lu 2020; Liu et al. 2022), solar cells (B. Zhao et al. 2022) and personal thermal management(Li et al. 2022; Gu et al. 2023), promising to reduce energy consumption due to increased cooling demand(Suhendri et al. 2022). RC emitters achieve cooling power without any energy input by dissipating excess heat into outer space through the "atmospheric window", spanning from 8 to 13 μm (D. Zhao et al. 2019). Hence, it is imperative for RC emitters to demonstrate a high spectral emissivity within this "atmospheric window" while simultaneously maintaining low spectral absorptivity outside the "atmospheric window". Nevertheless, commonly available materials that possess high infrared emissivity often exhibit significant absorptivity in the solar spectrum (Mouhib et al. 2009), presenting substantial challenges in realizing daytime RC. Fortunately, continuous advancements in materials science have yielded the development of RC materials with near-optimal spectral selectivity(Zhou et al. 2019; Zhai et al. 2017), making the realization of all-day RC possible. Despite the advancements in material spectroscopic enhancing RC capacity, practical implementation of RC technology still faces numerous challenges. One of the most significant challenges is the low energy density of RC systems. Under clear nighttime conditions, RC systems typically provide an average net cooling power ranging from 40 to 80 W/m^2 (Eicker and Dalibard 2011). The low energy density is attributed to the fact that the cooling power (P_{cooling}) is not exclusively determined by the outward thermal radiation (P_{surf}) emitted by the surface of the RC emitter when it is horizontally oriented and exposed to the surrounding environment. It also needs to account for the solar irradiation (P_{sol}) and atmospheric radiation (P_{sky}) absorbed by the emitter. Furthermore, if the RC emitter is placed obliquely or vertically, the heat exchange with the surrounding objects (P_{sur}) becomes a crucial consideration. Consequently, in practical applications, the RC power can easily be reduced by half or even more (Tso, Chan, and Chao 2017). Therefore, it is essential to explore innovative and reliable RC systems that enhance P_{rad} while minimizing the absorption of downward thermal radiation ((P_{sol}, P_{sky}, P_{sur}) by the emitter to enhance RC performance.

Recently, there has been a proposal for concentrated radiative cooling (RC) systems to enhance cooling performance (Peoples et al. 2022; Voorthuysen and Roes 2014; Zhou et al. 2021). Concentrated RC systems employ concentrators to focus the hemispherical thermal radiation emitted by the emitters, directing it towards deep space through the most transparent region of the atmosphere, near the zenith angle (Dong et al. 2022). Additionally, the height difference between the concentrators and the emitters serves as a shading mechanism, obstructing a portion of the downward radiation from large incidence angles entering the concentrators. Inspired by the concept of concentrated RC systems, we have developed and investigated the cooling performance of a compound parabolic concentrator (CPC) as the concentrator for a concentrated RC system (referred to as the CPC-RC system). The experimental findings conducted during nighttime reveal that the CPC-RC system achieves an average emitter temperature 5.83 °C lower than the average ambient temperature, indicating exceptional cooling performance. Moreover, the RC performance exhibited a notable enhancement of 30% when compared to a flat-RC system without concentrator. Alongside elucidating the cooling advantages offered by the CPC-RC system, we delved into the potential of this system to address the challenges associated with integrating RC systems into sloping roofs of buildings. Through a tilted systems experiment, the results demonstrated that when the CPC-based RC system tilted 30° facing north, it not only achieves sub-ambient temperatures during the daytime but also outperforms the flat-RC system in terms of cooling performance at night.

However, our previous analysis of CPC-RC systems has predominantly focused on practical experiments, with limited development of relevant theories and mathematical models. Hence, this study employs the ray tracing software Photopia(Photopia Optical Design Software' n.d.) to simulate the light propagation emitted by the emitter in various RC systems. Subsequently, it quantifies the light distribution within each 1° interval to determine the proportion of in different angular directions. Simulated RC models including the CPC-RC model, the flat-CPC model, as well as another common concentrated RC model - the trapezoid-RC model. This simulation allows us to determine the number of light distributions in different angles, further, calculate the equivalent atmospheric emissivity of different RC models. Finally, we can establish a mathematical model to analyse the net cooling power of the RC models. Through these investigations, we aim to explore the advantages and potential of the CPC-RC system more comprehensively.

2. SIMULATION MODEL

Photopia is a fast and accurate optical design program widely utilized for evaluating complex non-imaging optical systems (Wittkopf et al. 2010; Tian and Su 2018). During the simulation process, a diffuse flat lamp is utilized to emulate the emitter of the RC system, emitting light uniformly in all directions. A hemisphere is created to represent the sky dome to receive the emitted light. In the case of the CPC-RC model, a CPC with a reflectivity of 0.95 and a concentration ratio of 2× is incorporated on both sides of the emitter. Similarly, for the trapezoid-RC model, a trapezoidal concentrator with geometric parameters consistent with the CPC is integrated. The results of the light ratio in the CPC-RC model, flat-RC model, and Trapezoid-RC model are illustrated in Figure 1. The simulation divides the hemisphere from the zenith direction to 90° (parallel to the horizon direction) into 90 annular intervals, each spanning 1°. Subsequently, the number of rays reaching each interval is determined. A total of 100,000 rays were simulated, yielding the light distribution ratio for each interval. In the flat-RC model, where the emitter directly faces the unobstructed sky, an equal number of rays are distributed within each 1° interval, accounting for 1.11% of the total. In contrast, both the CPC-RC model and Trapezoid-RC model exhibit

variations in ray distribution across different annular intervals due to the presence of concentrators. The overall trends of both models exhibit similar patterns, characterized by a steep increase from the zenith direction, reaching a peak at 25°, followed by a gradual decline. The CPC-RC model achieves a peak light ratio of approximately 2.5%. After 28°, the light ratio starts to decline slowly due to surpassing the maximum half-acceptance angle range of the CPC, and finally, negligible light reaches 90°. On the other hand, the peak of the Trapezoid-RC model is slightly smaller, around 2.1%, but it maintains a consistent light ratio of 2% within the range of 25° to 35°. However, the light ratio starts to decrease after reaching 38°.

By simulating the light distribution at zenith angle from 0° to 90° to obtain the proportion of light of each 1° interval, the equivalent sky emissivity of different systems can be calculated, and the sky radiation power can be determined. (Percentage per degree)

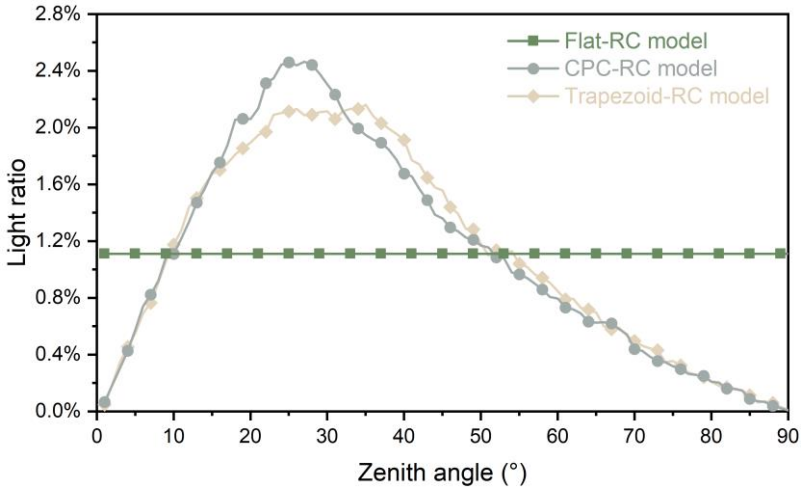

Figure 1 The light ratio of three different models in 0° - 90°

3. MATHEMATICAL MODEL

In this study, a mathematical model is developed to quantitatively assess the net cooling power of three RC systems: the CPC-RC system, trapezoid-RC system, and flat-RC system. The numerical study is conducted with certain assumptions to establish the equations that describe the heat transfer of the RC system in the surrounding air:

1. The RC system incorporates an automated control heater that automatically adjusts the emitter temperature to match the ambient temperature.
2. The uniform temperature distribution across the entire surface of the emitter.
3. The environment around the RC system is unobstructed, allowing us to disregard the effect of surrounding radiation (P_{sur}).
4. Sky emissivity is equal in every 1° interval.

3.1 Fundamentals Of Radiative Sky Cooling

The suitability of Earth's surface temperature for human habitation is attributed to the interaction between environmental radiation and the Earth's atmosphere. Environmental radiation encompasses solar irradiation and the infrared radiation emitted from the Earth's surface ((Bergman and Incropera 2011)). Solar irradiation is mainly concentrated in the short wavelength region (0.3-2.5 μm), which undergoes processes of absorption, reflection, or scattering by air molecules or clouds as it traverses the atmosphere. The longer the path of sunlight and the more atmospheric layers it passes through, the more attenuation occurs. In contrast, the infrared radiation emitted from the Earth's surface predominantly falls within the wavelength range of 2.5 to 50 μm ((D. Zhao et al. 2019)). Like solar irradiation, a fraction of this infrared radiation is absorbed or scattered by the atmosphere as it propagates outward. The absorbed thermal radiation is subsequently re-emitted and propagates downwards, giving rise to atmospheric radiation. In addition to heat radiation, non-radiative heat transfer processes from the surroundings (such as convection and conduction) also need to be considered. In addition to the process of radiative heat transfer, there is additional non-radiative heat transfer. These modes encompass convection and conduction and occur between objects situated on earth and their surrounding environment(D. Zhao et al. 2019). It is imperative to consider these non-radiative heat transfer mechanisms when analyzing RC power. Consequently, the cooling power of an RC model incident on a horizontally oriented surface facing the sky is determined by utilizing the provided Equation 1.

Equation 1: The cooling power of RC model

$$P_{\text{cooling}} = P_{\text{surf}} - P_{\text{sol}} - P_{\text{sky}} - P_{\text{non-radiative}}$$

Where:

- P_{surf} is the thermal radiation power emitted by the emitter surface.
- P_{sol} is the solar irradiation absorbed by the emitter surface.
- P_{sky} is the atmospheric radiation power absorbed by the emitter surface.
- $P_{\text{non-radiative}}$ is the non-radiative heat transfer processes from the surrounding, such as convection and conduction. However, in the following mathematical model, since it is assumed that the temperature of T_{surf} is always consistent with that of T_{amb}, its influence can be ignored.

3.2 Sky Radiation Power Absorbed By The RC Surface

Before calculating the atmospheric emissivity, it is necessary to assume that the sky exhibits characteristics similar to a blackbody or to assume that the sky behaves as a grey body, distinguished by an apparent emissivity ((Maghrabi and Clay 2011). This assumption allows us to express the radiative effects associated with the atmosphere using Equation 2.

Equation 2: Sky radiation power

$$P_{\text{sky}} = \alpha_{\text{surf}}\, \varepsilon_{\text{sky}}\, \sigma\, T_{\text{amb}}^4$$

Where:

- α_{surf} is the total weighted average absorptivity in 0-25 μm of the emitter surface.
- ε_{sky} is the emissivity of the sky.
- σ is the Stefan-Boltzmann constant, equal to $5.67*10^{-8}$ W/m²·K⁴.
- T_{amb} is the ambient temperature, K.

The total, directional emissivity can be calculated using Equation 3, representing a weighted average of all possible wavelengths in the ambient temperature.

Equation 3:Total, directional emissivity

$$\varepsilon_{\text{sky}}\ (\theta) = \frac{\int_0^{25} \varepsilon_{\text{sky}}(\theta,\lambda) E_{\lambda,b}(\lambda,T_{amb})\, d\lambda}{E_b(T_{amb})}$$

Where:

- $\varepsilon_{\text{sky}}(\theta,\lambda)$ is the sky emissivity in different angles with 0-25 μm, can be calculated by a “box model” ((Granqvist and Hjortsberg 1981). The equation is $\varepsilon_{\text{sky}}(\theta,\lambda) = 1 - [1 - \varepsilon_{\text{sky}}\,(0,\lambda)]^{1/cos\theta}$
- $E_{\lambda,b}(\lambda, T_{amb})$ is the spectral emissive power of the blackbody.

After the total, directional emissivity $\varepsilon_{\text{sky}}(\theta)$ is calculated, the equivalent sky emissivity of different models can be calculated by using the simulated light ratio k of different models.

Equation 4: Equivalent sky emissivity of flat-RC system

$$\varepsilon_{sky(flat-RC)} = \int_0^{90} \varepsilon_{\text{sky}}(\theta)\, k_{\text{flat-RC}}(\theta) d\theta$$

Equation 5: Equivalent sky emissivity of CPC-RC system

$$\varepsilon_{sky(CPC-RC)} = \int_0^{90} \varepsilon_{\text{sky}}(\theta)\, k_{\text{CPC-RC}}(\theta) d\theta$$

Equation 6: Equivalent sky emissivity of flat-RC system

$$\varepsilon_{\text{sky(trapezoid-RC)}} = \int_0^{90} \varepsilon_{\text{sky}}(\theta)\, k_{\text{Trap-RC}}(\theta) d\theta$$

Where:

- $k_{\text{flat-RC}}$ is the light ratio of the flat-RC model.
- $k_{\text{CPC-RC}}$ is the light ratio of the CPC-RC model.
- $k_{\text{Trap-RC}}$ is the light ratio of the Trapezoid-RC model.

3.3 Thermal Radiation From The Sky-Facing RC Surface

The sky-facing RC surface is constantly exposed to the atmosphere. Therefore, the thermal radiation power emitted by the surface is an important parameter determining the cooling performance of the RC, can be described by Equation 7 (Evangelisti, Guattari, and Asdrubali 2019).

Equation 7: The thermal radiation power

$$P_{\text{surf}} = \varepsilon_{\text{surf}}\, \sigma\, (T_{\text{surf}}^4)$$

Where:

- $\varepsilon_{\text{surf}}$ is the weighted average emissivity of the emitter surface in the infrared region.
- T_{surf} is the emitter surface temperature, K.

3.4 Solar irradiation absorbed by the RC surface

To achieve the RC effect during the daytime, besides sky radiation power, downward solar irradiation is another important factor affecting RC cooling power. The solar irradiation absorbed by the RC surface can be calculated using Equation 8.

Equation 8: The solar irradiation

$$P_{\text{sol}} = C\,\eta\,\alpha_{\text{surf}}\,G$$

Where:

- C is the concentration ratio of the concentrator
- η is the optical efficiency of the concentrator.
- α_{surf} is the weighted average absorptivity of the emitter surface in the solar spectrum.
- G is the total incident solar energy, W/m^2.

4. RESULTS AND DISCUSSION

4.1 Equivalent Sky Emissivity Of Three Different Models

The spectral emissivity of the atmosphere is influenced by atmosphere composition and climatic conditions, rendering the calculation of atmospheric emissivity a complex task. Thanks to the various models developed by previous researchers, such as LOWTRAN(E. Shettle et.al, 1976) or MODTRAN('MODTRAN®' n.d.), estimating the emissivity of the atmosphere in the zenith direction is achieved.

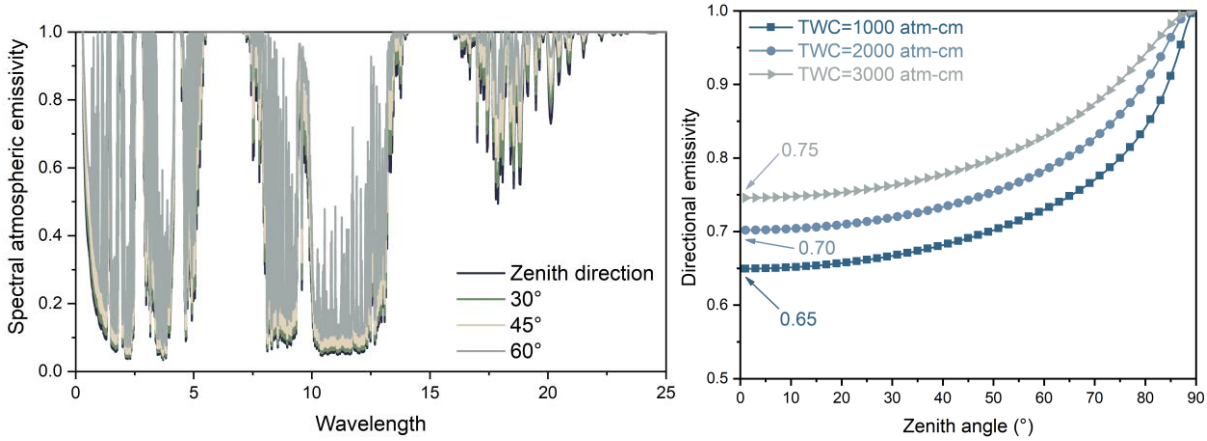

Figure 2 (a) The atmospheric emissivity of four zenith angle in 0 - 25 μm. (b) Variation of directional emissivity at 0-90° zenith angle for three total water vapor columns.

Figure 2(a) illustrates the variation of atmospheric emissivity with spectral wavelength at four different zenith angles under the condition of total water vapor column (TWC) is 1000 atm-cm. The zenith direction spectral emissivity $\varepsilon_{sky}(0, \lambda)$ is obtained from MODTRAN (2018) ('MODTRAN®' n.d.), other angles are calculated by the "box model". It can be observed that the atmospheric emissivity in the zenith direction remains consistently lower compared to other zenith angles, particularly within the "atmospheric window" region. Under clear sky conditions, the spectral, directional transmittance of the atmosphere, $\tau_{sky}(\theta, \lambda)$, can be approximately considered equal to $\left[1 - \varepsilon_{sky}(\theta, \lambda)\right]$, (D. Zhao et al. 2019). Consequently, the zenith direction exhibits the highest $\tau_{sky}\,(\lambda)$, facilitating the thermal radiation through the atmosphere to outer space. Conversely, as the zenith angle increases, the atmospheric emissivity also increases, impacting the propagation of radiation.

Once the spectral emissivity of the zenith direction is determined, the total, directional emissivity can be calculated using Equation 3. Figure 2(b) shows the influence of varying zenith angles on total, directional emissivity for three different TWC conditions. The figure demonstrates that for the zenith direction, three TWC values (1000, 2000, 3000) result in different spectral emissivity, namely 0.65, 0.70, and 0.75, respectively. This suggests that an increase in TWC leads to an elevated total, directional emissivity, consequently exacerbating the adverse impact on RC performance. The overall trends of the three curves are similar. The emissivity gradually rises before the zenith angle reaches 60°. However, after 60°, the emissivity exhibits a significant increase. At 90°, the directional emissivity reaches 1.

Table 1: The equivalent sky emissivity of three models in different total water vapor column

	Flat-RC model	CPC-RC model	Trapezoid-RC model
ε_{sky} (1000)	0.73	0.68	0.69
ε_{sky} (2000)	0.78	0.73	0.74
ε_{sky} (3000)	0.82	0.78	0.79

To obtain the equivalent sky emissivity for the three different RC models, it is necessary to multiply the light ratio at various zenith angles obtained from the previous simulation by the corresponding angle's total， directional emissivity and sum them together. Table 1 presents the calculated values of equivalent sky emissivity for the three models using Equations 4, 5, and 6.

At a TWC of 1000 atm-cm, the CPC-RC model exhibits the lowest equivalent sky emissivity of 0.68 among the three models. This is attributed to the CPC's function to concentrate most of the thermal radiation near the zenith. The Trapezoid-RC model closely follows the CPC-RC model, with an equivalent sky emissivity value of 0.69. In contrast, the flat-RC model, lacking a concentrator, emits thermal radiation in all directions, resulting in a higher equivalent sky emissivity of 0.73. When the TWC is set to 3000 atm-cm, the equivalent sky emissivity for the three models is less desirable. The CPC-RC model still maintains the lowest value at 0.78, while the flat-RC model exceeds 0.82. These values are considerably higher than the equivalent sky emissivity at 1000 atm-cm. This finding suggests that RC technology is more suitable for dry regions. In areas with higher water vapor column in the atmosphere, the atmospheric emissivity is higher, resulting in greater sky radiation power and reduced RC cooling power.

4.2 Effect of different meteorological parameters on RC cooling power

In Section 4.1, the equivalent sky emissivity of different RC models can be determined, allowing for the calculation of the sky radiation power absorbed by these models using Equation 2. However, Equation 2 shows that, in addition to the equivalent sky emissivity, the ambient temperature, as a variable parameter, will influence the sky radiated power. On the other hand, in assumption 1, we assume that the ambient temperature is consistent with the surface temperature of the emitter. According to Equation 7, this means that the ambient temperature also affects the thermal radiation power emitted by the emitter surface. Therefore, the ambient temperature becomes a crucial meteorological parameter for investigating RC cooling power. During daytime RC, solar irradiation is another significant meteorological parameter. It directly affects the absorbed solar irradiation by the emitter and has a profound impact on the cooling performance of the RC system. This section investigates the effect of varying solar irradiation and ambient temperature on cooling power while maintaining the spectral characteristics of the emitter surface (with a weighted averaged emissivity of 0.05 under the solar spectrum and 0.95 outside the solar spectrum).

Figure 3(a) illustrates the varying of the cooling power for the three models within the solar radiation range of 0-1000 W/m^2. In this modelling, the ambient temperature is maintained at 20 °C. When the solar irradiation is 0, indicating no solar radiation absorbed by the emitter, the flat-RC model exhibits the lowest cooling power among the three models at only 109.3 W/m^2. In contrast, the CPC-RC model and the Trapezoid-RC model achieve higher cooling powers of 126.35 and 124.12 W/m^2, respectively, indicating superior cooling performance of concentrated-RC model compared to the flat-RC model in the nighttime. The cooling power of all models gradually decreases as solar irradiation increases. However, the CPC-RC model and the Trapezoid-RC model are more significantly affected by solar irradiation due to the concentrating effect of the concentrator, resulting in a steeper downward trend. At 375 W/m^2, the decline curves of the Trapezoid-RC model intersect with the curves of the flat-RC model. This means when the solar irradiation exceeds 375 W/m^2, the cooling power of the flat-RC model surpasses that of the Trapezoid-RC model. After 425 W/m^2, the cooling power obtained by the flat-RC model is larger than that of the CPC-RC model. When the solar irradiation reaches 1000 W/m^2, the Trapezoid-RC model achieves the lowest cooling power at only 34.12 W/m^2, while the CPC-RC model reaches 36.36 W/m^2. In contrast, the flat-RC model achieves the highest cooling power in this scenario, at 59.03 W/m^2. These results illustrate that an increase in solar irradiation has a greater impact on the RC models with a concentrator. Specifically, from 0 to 1000 W/m^2 of solar irradiation, the cooling power of the CPC-RC model and the Trapezoid-RC model decreases by 90 W/m^2, respectively, whereas the flat-RC model only experiences a decrease of 50 W/m^2. This emphasizes the suppressive role of the concentrator in achieving daytime RC. However, when solar irradiation is below 375 W/m^2, the RC system with a concentrator can achieve higher cooling power.

Figure 3(b) illustrates the changes in cooling power for the three models when the ambient temperature is modified, while maintaining a solar irradiance value of 600 W/m^2. It is evident that the cooling power trend differs significantly from that shown in Figure 3(a) after adjusting the ambient temperature, displaying an upward trend. This indicates that the cooling power of the three models exhibits a gradual increase with rising ambient temperature. Among the three models, the two concentrated-models exhibit similar trends of increase, while the flat-RC model demonstrates a slower change. At an ambient temperature of 10 °C, the flat-RC model attains the highest cooling power, measuring 64.90 W/m$^{2.}$ In comparison, the CPC-RC model and the Trapezoid-RC model achieve lower cooling powers of 55.97 W/m^2 and 54.03 W/m^2, respectively. However, when the ambient temperature arrives at 30°, the flat-RC model still demonstrates the highest cooling power. This is because, as shown in Figure 3(a), when the solar irradiation surpasses 375 W/m^2 and 425 W/m^2, the cooling power of the flat-RC model surpasses that of the concentrated-RC models. Therefore, these findings are

considered reasonable under the assumed constant solar irradiation of 600. At an ambient temperature of 30 °C, the cooling power of the flat-RC model is 94.69 W/m^2, followed by the CPC-RC model and Trapezoid-RC model at 90.50 W/m^{2}and 87.95 W/m^2, respectively. But it is worth noting that the cooling power of the CPC-RC model and Trapezoid-RC model currently is 34 W/m^2 higher than that at 10 °C, which is significantly greater than the 30 W/m^2 increment of the flat-RC model. The results indicate that variations in the ambient temperature exert a relatively minor influence on the flat-RC model compared to the concentrated-RC model. However, when compared to solar radiation, varying ambient temperatures have a negligible impact on the cooling power trends of the three models. This can be attributed to the fact that varying in ambient temperature will simultaneously alter the emitted thermal radiation and the absorbed sky radiation power by the emitter's surface.

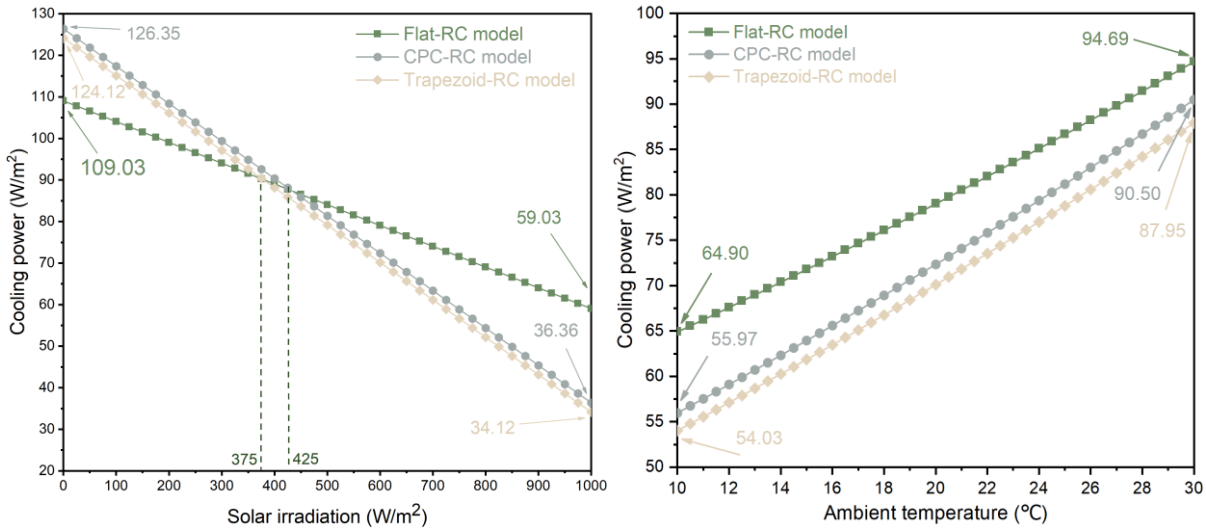

Figure 3 (a)The effect of solar irradiation on the cooling power of the models. (b)The effect of ambient temperature on the cooling power of the models

4.3 Effect Of Different Spectral Characteristics of The Emitter On RC Cooling Power

Section 4.2 examines the effect of meteorological parameters on the cooling power of different RC models with identical spectral characteristics. The findings reveal the significant impact of solar irradiation on cooling power. However, controlling solar irradiation is beyond human capability. Fortunately, modifying the spectral characteristics of the emitter material provides an effective approach to reduce solar irradiation absorption and enhance cooling power. This section investigates the effect of modifying the spectral selectivity of the emitter on the cooling power of the models under constant solar irradiation and ambient temperature conditions (600 W/m^2 and 20 °C), as depicted in Figure 4.

Figure 4(a) demonstrates the impact of increasing the weighted average emissivity of the emitter in the solar spectrum on cooling power. As the weighted average emissivity increases, there is a rapid decrease in the cooling power of all three models. Specifically, when the weighted average emissivity rises to 0.117, the cooling power of the two RC models with concentrators reaches 0 W/m². After 0.117, RC becomes unfeasible. This significant decline in cooling power for the concentrated-RC models can be attributed to the combined effects of the concentrator's concentrating capability and the increased absorption of solar irradiation by the emitter. In contrast, the flat-RC model, lacking a concentrator, exhibits a smaller decrease in cooling power compared to the previous two models. It is observed that the RC effect cannot be achieved when the weighted average emissivity of the emitter in the solar spectrum exceeds 0.182. These findings underscore the critical role of the weighted average emissivity of the emitter in the solar spectrum in achieving daytime RC. Therefore, achieving daytime RC is only possible when the weighted average emissivity of the emitter in the solar spectrum is less than 0.11.

Conversely, the weighted average emissivity outside the solar spectrum has minimal effect on the change in cooling power, as depicted in Figure 4(b). The cooling power of all three models decreases by approximately 22 W/m² when the weighted emissivity is decreased from 0.95 to 0.85, with no noticeable change in the trend.

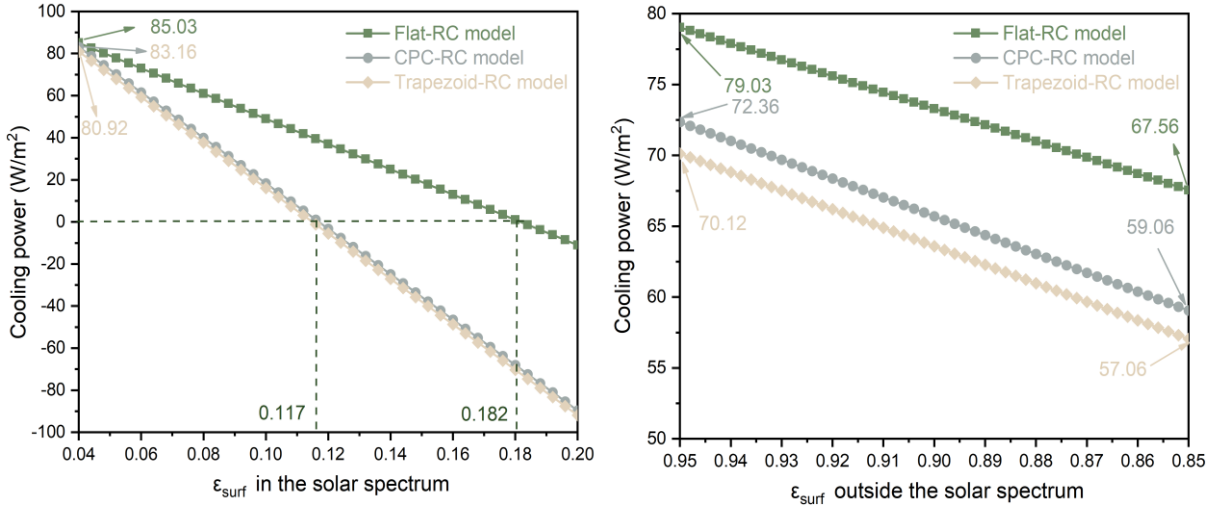

Figure 4 (a)The effect of weighted average emissivity in the solar spectrum on the cooling power of the models. (b) The effect of weighted average emissivity outside the solar spectrum on the cooling power of the models.

5. CONCLUSION

In this study, we propose a novel modelling approach to analyse the performance of various RC models. The mathematical model is utilized to calculate the net cooling power of the CPC-RC model, flat-RC model, and Trapezoid-RC model. Furthermore, we investigate the impact of varying parameters on the cooling power of the concentrated-RC models and flat-RC model.

1. Simulation is conducted to determine the light ratio of the different RC models, which can be used to calculate their equivalent sky emissivity. The results indicated that the CPC-RC model exhibited the lowest equivalent sky emissivity, resulting in the smallest sky radiation power absorbed by the emitter, obtained excellent cooling power at night.

2. Solar irradiation and ambient temperature are identified as significant meteorological parameters affecting the cooling power. The RC model with concentrators is found to be more dependent on solar irradiation. When the solar irradiation exceeded 375 W/m^2 at typical ambient temperature, the promotion effect of the concentrator on RC will transition into an inhibitory effect, leading to a lower cooling power compared to the flat-RC model.

3. The impact of ambient temperature on the concentrated-RC models are more pronounced than the flat-RC model. The cooling power of all three models increasing as the ambient temperature rose.

4. Maintaining other parameters constant, the spectral characteristics of the emitter are identified as crucial for achieving daytime RC. A weighted average emissivity within the solar spectrum has a significant impact on cooling power, particularly for RC models with concentrators. Once the weighted average emissivity within the solar spectrum exceeded 0.117, the cooling power dropped to 0 W/m^2. Conversely, modifying the weighted average emissivity outside the solar spectrum has minimal effect on cooling power.

In future, the research will be focused on further studying and refining the modelling approach. The influence of additional relevant parameters such as concentrating ratio of concentrators and the model tilted angle on cooling power will be investigated. Furthermore, the accuracy of the model will be validated through comparison with field experiments.

6. ACKNOWLEDGEMENT

The authors would like to acknowledge the Engineering and Physical Sciences Research Council (Horizon Europe Guarantee grant number: EP/Y016645/1) for the financial support to this research.

7. REFERENCES

Bergman, T. L., and Frank P. Incropera, eds. 2011. *Fundamentals of Heat and Mass Transfer*. 7th ed. Hoboken, NJ: Wiley.

Chen, Jianheng, and Lin Lu. 2020. 'Development of Radiative Cooling and Its Integration with Buildings: A Comprehensive Review'. *Solar Energy* 212 (December): 125–51. https://doi.org/10.1016/j.solener.2020.10.013.

Dong, Minghao, Linxiao Zhu, Bo Jiang, Shanhui Fan, and Zhen Chen. 2022. 'Concentrated Radiative Cooling and Its Constraint from Reciprocity'. *Optics Express* 30 (1): 275. https://doi.org/10.1364/OE.445544.

Eicker, Ursula, and Antoine Dalibard. 2011. 'Photovoltaic–Thermal Collectors for Night Radiative Cooling of Buildings'. *Solar Energy* 85 (7): 1322–35. https://doi.org/10.1016/j.solener.2011.03.015.

Evangelisti, Luca, Claudia Guattari, and Francesco Asdrubali. 2019. 'On the Sky Temperature Models and Their Influence on Buildings Energy Performance: A Critical Review'. *Energy and Buildings* 183 (January): 607–25. https://doi.org/10.1016/j.enbuild.2018.11.037.

Granqvist, C. G., and A. Hjortsberg. 1981. 'Radiative Cooling to Low Temperatures: General Considerations and Application to Selectively Emitting SiO Films'. *Journal of Applied Physics* 52 (6): 4205–20. https://doi.org/10.1063/1.329270.

Gu, Bin, Fan Fan, Qihao Xu, Dahua Shou, and Dongliang Zhao. 2023. 'A Nano-Structured Bilayer Asymmetric Wettability Textile for Efficient Personal Thermal and Moisture Management in High-Temperature Environments'. *Chemical Engineering Journal* 461 (April): 141919. https://doi.org/10.1016/j.cej.2023.141919.

Li, Yiping, Zhimin An, Xinchao Liu, and Rubing Zhang. 2022. 'A Radiative Cooling Paper Based on Ceramic Fiber for Thermal Management of Human Head'. *Solar Energy Materials and Solar Cells* 246 (October): 111918. https://doi.org/10.1016/j.solmat.2022.111918.

Liu, Jie, Chengfeng Xu, Xianze Ao, Kegui Lu, Bin Zhao, and Gang Pei. 2022. 'A Dual-Layer Polymer-Based Film for All-Day Sub-Ambient Radiative Sky Cooling'. *Energy* 254 (September): 124350. https://doi.org/10.1016/j.energy.2022.124350.

Maghrabi, A., and R. Clay. 2011. 'Nocturnal Infrared Clear Sky Temperatures Correlated with Screen Temperatures and GPS-Derived PWV in Southern Australia'. *Energy Conversion and Management* 52 (8–9): 2925–36. https://doi.org/10.1016/j.enconman.2011.02.027.

'MODTRAN®'. n.d. Accessed 23 June 2023. http://modtran.spectral.com/.

Mouhib, T., A. Mouhsen, E.M. Oualim, M. Harmouchi, J.P. Vigneron, and P. Defrance. 2009. 'Stainless Steel/Tin/Glass Coating as Spectrally Selective Material for Passive Radiative Cooling Applications'. *Optical Materials* 31 (4): 673–77. https://doi.org/10.1016/j.optmat.2008.07.010.

'Optical Design Software | Photopia | Photopia Optical Design Software'. n.d. Accessed 31 January 2023. https://www.ltioptics.com/en/optical-design-software-photopia.html.

Peoples, Joseph, Yu-Wei Hung, Xiangyu Li, Daniel Gallagher, Nathan Fruehe, Mason Pottschmidt, Cole Breseman, et al. 2022. 'Concentrated Radiative Cooling'. *Applied Energy* 310 (March): 118368. https://doi.org/10.1016/j.apenergy.2021.118368.

Suhendri, Suhendri, Mingke Hu, Yuehong Su, Jo Darkwa, and Saffa Riffat. 2022. 'Performance Evaluation of Combined Solar Chimney and Radiative Cooling Ventilation'. *Building and Environment* 209 (February): 108686. https://doi.org/10.1016/j.buildenv.2021.108686.

Tian, Meng, and Yuehong Su. 2018. 'Multiple Nonlinear Regression Model for Predicting the Optical Performances of Dielectric Crossed Compound Parabolic Concentrator (DCCPC)'. *Solar Energy* 159 (January): 212–25. https://doi.org/10.1016/j.solener.2017.10.090.

Tso, C. Y., K. C. Chan, and Christopher Y. H. Chao. 2017. 'A Field Investigation of Passive Radiative Cooling under Hong Kong's Climate'. *Renewable Energy* 106 (June): 52–61. https://doi.org/10.1016/j.renene.2017.01.018.

Voorthuysen, E. du Marchie van, and R. Roes. 2014. 'Blue Sky Cooling for Parabolic Trough Plants'. *Energy Procedia* 49: 71–79. https://doi.org/10.1016/j.egypro.2014.03.008.

Wittkopf, Stephen, Lars Oliver Grobe, David Geisler-Moroder, Raphaël Compagnon, Jérôme Kämpf, Friedrich Linhart, and Jean-Louis Scartezzini. 2010. 'Ray Tracing Study for Non-Imaging Daylight Collectors'. *Solar Energy* 84 (6): 986–96. https://doi.org/10.1016/j.solener.2010.03.008.

Zhai, Yao, Yaoguang Ma, Sabrina N. David, Dongliang Zhao, Runnan Lou, Gang Tan, Ronggui Yang, and Xiaobo Yin. 2017. 'Scalable-Manufactured Randomized Glass-Polymer Hybrid Metamaterial for Daytime Radiative Cooling'. *Science* 355 (6329): 1062–66. https://doi.org/10.1126/science.aai7899.

Zhao, Bin, Kegui Lu, Mingke Hu, Jie Liu, Lijun Wu, Chengfeng Xu, Qingdong Xuan, and Gang Pei. 2022. 'Radiative Cooling of Solar Cells with Micro-Grating Photonic Cooler'. *Renewable Energy* 191 (May): 662–68. https://doi.org/10.1016/j.renene.2022.04.063.

Zhao, Dongliang, Ablimit Aili, Yao Zhai, Shaoyu Xu, Gang Tan, Xiaobo Yin, and Ronggui Yang. 2019. 'Radiative Sky Cooling: Fundamental Principles, Materials, and Applications'. *Applied Physics Reviews* 6 (2): 021306. https://doi.org/10.1063/1.5087281.

Zhou, Lyu, Haomin Song, Jianwei Liang, Matthew Singer, Ming Zhou, Edgars Stegenburgs, Nan Zhang, et al. 2019. 'A Polydimethylsiloxane-Coated Metal Structure for All-Day Radiative Cooling'. *Nature Sustainability* 2 (8): 718–24. https://doi.org/10.1038/s41893-019-0348-5.

Zhou, Lyu, Haomin Song, Nan Zhang, Jacob Rada, Matthew Singer, Huafan Zhang, Boon S. Ooi, Zongfu Yu, and Qiaoqiang Gan. 2021. 'Hybrid Concentrated Radiative Cooling and Solar Heating in a Single System'. *Cell Reports Physical Science* 2 (2): 100338. https://doi.org/10.1016/j.xcrp.2021.100338.

#54: Simulation of thermal performance and thermal interference of horizontal slinky-loop ground heat exchangers

Man LUO, Guohui GAN, Lingze LIN

1 Department of Architecture and Built Environment, the University of Nottingham, University Park, Nottingham, NG7 2RD, UK, laxml24@exmail.nottingham.ac.uk
2 Department of Architecture and Built Environment, the University of Nottingham, University Park, Nottingham, NG7 2RD, UK, lazgg@exmail.nottingham.ac.uk
3 Department of Architecture and Built Environment, the University of Nottingham, University Park, Nottingham, NG7 2RD, UK, ezxll2@exmail.nottingham.ac.uk

Abstract: The thermal performance of a horizontal slinky ground heat exchanger has been investigated using a validated transient 3D model for different trench separations, initial soil temperature profiles and soil properties. The effect of trench separation on the thermal interference was analysed for a range of centre-to-centre distances between parallel trenches from 1.5 m to 11 m. The initial soil temperature was found to have a significant effect on the predicted thermal performance. The predicted heat extraction using a varying and more realistic initial soil temperature for a heating season would decrease with the increasing depth of installation whereas using a uniform initial temperature would lead to increasing heat extraction with installation depth. It has also been found that soil with a high thermal conductivity would exacerbate the thermal interference between trenches with a small separation as a results of heat depletion in the ground.

Keywords: Ground source heat pump; Horizontal slinky-loop heat exchanger; Thermal interference; Trench separation.

1. INTRODUCTION

Nearly a quarter of the United Kingdom's carbon emissions come from heating buildings (Department for Energy Security and Net Zero, 2023). Therefore, all heat generation in buildings must be decarbonized to achieve net zero targets. The electrification of heat is considered as a crucial move in decreasing emissions from homes, since the majority of emissions are connected with boilers now running on natural gas, as part of UK Government initiatives to reduce emissions from buildings over the coming decades. Global gas price increases have resulted in a considerable increase in the energy price cap (+96% or +£1223 yearly costs for the average household by October 2022, compared to October 2021) (Calvillo et al., 2023). Affordability is a growing concern and a significant public policy challenge with the wider cost-of-living crisis. To replace the Domestic Renewable Heat Incentive (RHI), the UK government has introduced the Boiler Upgrade Scheme (2022), which provides subsidies of £5,000 and £6,000 for air source and ground source heat pumps, respectively. The report from Department for Business (2021) pointed out that the Boiler Upgrade Scheme will play an important part in ensuring that all newly installed heating systems are low carbon by the year 2035. By 2028, the government hopes to have installed 600,000 new homes annually (House of Commons Committee, 2022).

The installation method classifies ground heat exchangers (GHEs) into two categories: vertical boreholes and horizontal loops (Banks, 2012). Typically, the installation depth of vertical GHE ranges from 70 to 130 metres, resulting in a relatively smaller land field requirement. However, the application of vertical GHE requires specialised drilling equipment, which raises the initial cost of installation. In contrast, the installation depth of horizontal GHE ranges from 1 to 3 metres. Therefore, the initial cost of installation is reduced, but a larger land area is required to achieve the same heat transfer amount. Consequently, numerous researchers have investigated horizontal GHEs using experimental methods, analytical approaches, semi-analytical solutions, or numerical methodology to calculate and/or predict the system's overall thermal performance.

There is still a lack of reliable numerical investigation on the energy output efficiency from HGHEs for the whole heating season, in particular with varied trench separations under diverse circumstances. This work aims to study the thermal performance of slinky HGHEs and its surrounding soil temperature at different trench separations between parallel heat exchanger pipes considering initial soil temperature profile, installation depths, and soil properties.

2. DESCRIPTION OF THE NUMERICAL MODEL

The numerical model of slinky HGHEs was developed using the commercial CFD software package ANSYS FLUENT (2022). Assuming negligible natural convection and radiation or moisture transfer, the heat transfer in soil surrounding a heat exchanger is defined by the following conduction Equation 1:

Equation 1: Heat transfer in surrounding soil.

$$\rho C_p \frac{\partial T}{\partial t} + \nabla(k \nabla T) = H$$

Where:

- ρ = Density of the soil (kg/m^3)
- C_p = Specific heat of soil (kJ/kg K)
- T = Soil temperature (K)
- t = Time (s)
- k = Thermal conductivity of soil (W/m K)
- H = Heat generation or extraction (W/m^3)

The thermal properties for three representative types of soil (loamy, clayey and sandy) in the UK as shown in Table 1 were used in the simulation based on the data recommended for the determination of thermal properties for horizontal ground collector loops (Busby *et al*., 2015).

Table 1: Soil properties for simulation.

Soil type	Density (kg/m^3)	Specific Heat (kJ/kgK)	Thermal conductivity (W/mK)	Diffusivity ($\times 10^{-6} m^2/s$)	Location
Loamy	1470	1.039	1.5	0.9842	Coventry
Clayey	1520	1.014	0.62	0.4002	Mylnefield
Sandy	1250	1.398	2.79	1.7971	Wellesbourne

The main part of the horizontal heat exchanger consisted of a DN40 (i.e., 40mm) circular HDPE pipe. The installation depth (Z_1) of 1.2 meters under soil surface in loamy soil was selected as a base case. The impact of thermal interference was simulated for different distances (separations) between adjacent trenches (defined as the distance between centers of two trenches) ranging from 1.5 m to 11m and for different initial soil temperature profiles, soil types and installation depths. Figure 1 shows the slinky-loop heat exchanger model and solution domain. The total depth Z_d (= Z_1+Z_2) of the

computational domain was 10m. The simulations were conducted for the heating season in the UK from 1st September to 31st March. The simulation results are presented in terms of monthly or seasonally total heat transfer in kWh and the variation of surrounding soil temperature profile.

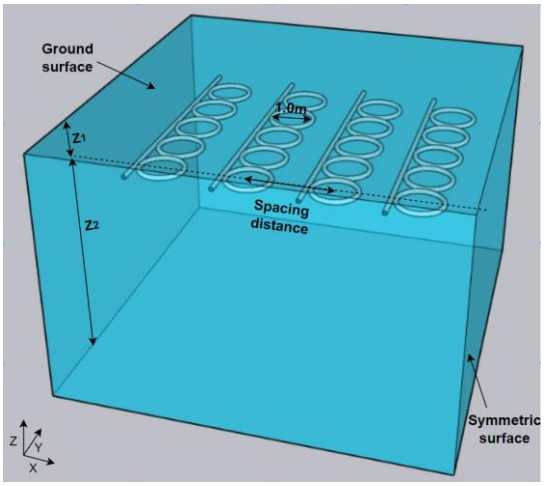

Figure 1 Computational domain for soil with slinky-coil ground heat exchanger

2.1. Initial and Boundary Conditions

Since the top surface of soil interacts with the ambient, the boundary conditions at the topsoil surface were assumed to vary monthly with a monthly average ambient air temperature and a monthly average wind speed. The vertical boundary was defined as symmetrical surfaces, assuming the domain was part of a larger volume of the soil buried with the same configuration of HE loops. The temperature of bottom boundary was set as constant 10°C – the annual mean temperature of the deep soil in the UK (Chong et al., 2013). During operation times, water-ethylene glycol (30% by weight) mixture with a constant inlet temperature of 1°C was assumed to circulate through the heat exchanger at a fluid velocity of $0.4 m/s$. The initial soil temperature is another essential set of data for simulation and design optimization of GSHPs. The initial soil temperature at depth Z (m) for simulation at the start of heating season was calculated with the following empirical Equation 2 for soil with homogeneous properties (Gan, 2018).

Equation 2: The initial soil temperature.

$$T = T_a + T_{amp} e^{-Z/D} \sin\left((t - t_0)\frac{2\pi}{365} - \frac{Z}{D} - \frac{\pi}{2}\right)$$

Where:

- T = Initial soil temperature ($°C$)
- T_a = Yearly average temperature of soil ($°C$)
- T_{amp} = Yearly amplitude of surface temperature ($°C$)
- t_0 = Time lag from a beginning date to the day with the lowest temperature in a year (day)
- t = Time (day)
- D = Annual fluctuation damping depth (m)

2.2. Validation of numerical model

The present simulation model was validated against the published experimental data measured by Wu *et al*. (2010). For the validation, the measured climatic data and topsoil temperature at 00:00 on November 7, 2009, were set as the initial conditions. Figure 2 shows that the predicted soil temperature at 08:00 on November 7, 2009, which agrees very well with experimental results.

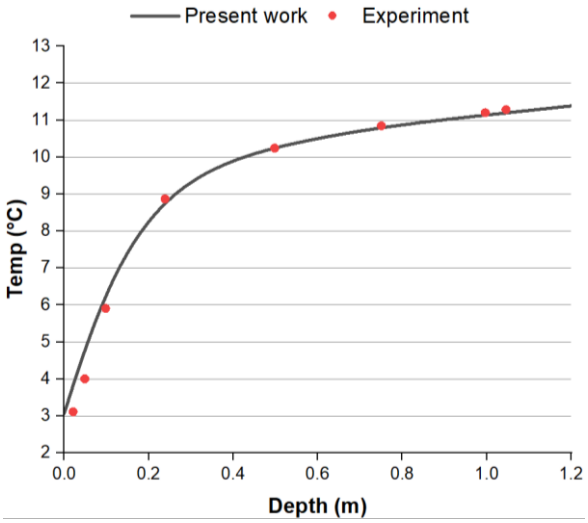

Figure 2 Comparison of the soil temperature at 08:00 between the numerical modelling and the experimental results of Wu et al. (2010).

3. RESULTS AND DISCUSSION

Thermal interference among adjacent parallel pipes has a large impact on overall thermal performance and the variation of surrounding soil temperature. Simulation was conducted to determine the interference in terms of the effect of spacing distance between adjacent loops on heat exchange. The numerical simulation of the heat exchanger performance was investigated for the effects of initial soil temperature, soil type and loop trench spacing distance. The results are presented as the amount of heat transfer per meter length of trench for a given period (in kWh/m) and surrounding soil temperature distribution.

3.1. The Effect of the Interference of Different Slinky Loops for a Base Case

The thermal interference in terms of the effect of spacing between adjacent loops on heat exchange was first simulated under the same boundary conditions with loamy soil. The centre-to-centre distances of 1.5m, 2.0m, 2.5m, 3.5m, 4.5m, 6.0m, 8.5m and 11.0m were considered. The base case was mentioned in the model description section with the heat exchanger 1.2 m deep from the top surface. Figure 3 presents typical temperature distributions from simulations for the slinky ground heat exchangers and the surrounding soil domain. It can be seen that as the separation distance decreases the area of low temperature surrounding each heat exchanger and between adjacent parallel heat exchangers increases. The soil temperature at the installation depth is close to the pipe surface temperature due to heat extraction from surrounding soil. This indicates that thermal interference among short separation distances is more significant. However, this interaction impact becomes much less when the distance is over 6 m. This indicates that thermal interference between adjacent pipes decreases as the separation distance increases. Figure 4(a) illustrates the predicted soil temperature distribution in vertical direction at the slinky loop centre. The soil temperature lines are getting closer for distances over 6m. However, the difference between various separation distances at the centre of adjacent trenches in vertical direction is still large as shown in Figure 4(b). This is another way to shows the influence of spacing distance on the soil temperature or thermal interference between the adjacent trenches.

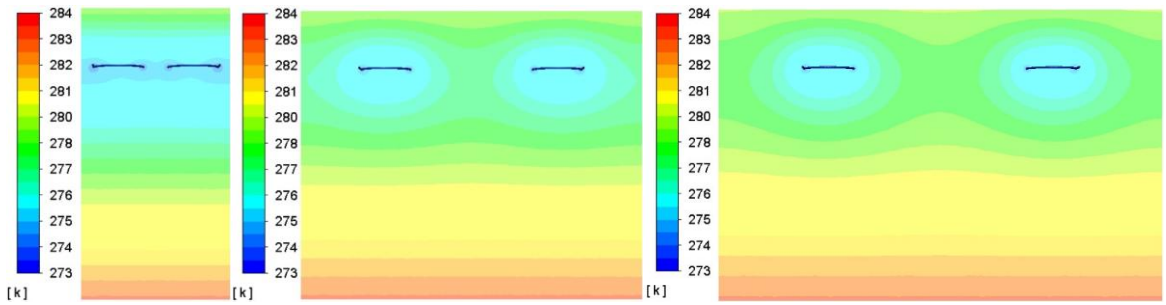

(a) Spacing distance of 1.5 m *(b) Spacing distance of 3.5 m* *(c) Spacing distance of 4.5 m*

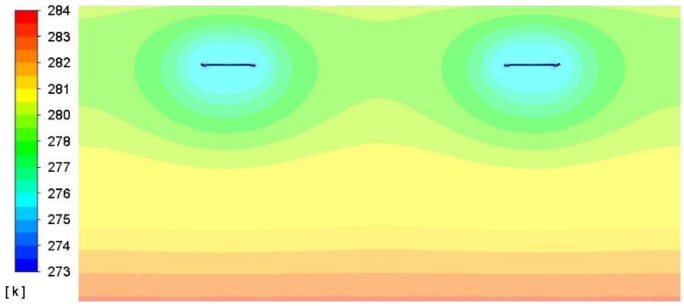

(d) Spacing distance of 6 m

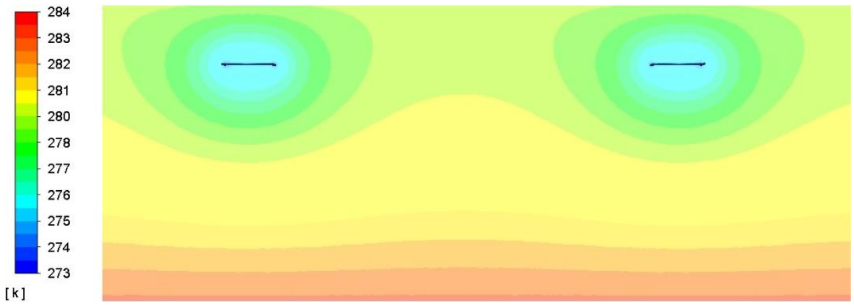

(e) Spacing distance of 8.5 m

Figure 3 Soil temperature distribution (K) on a vertical section located at the centre of the slinky loops at the end of heating season for different spacing distances.

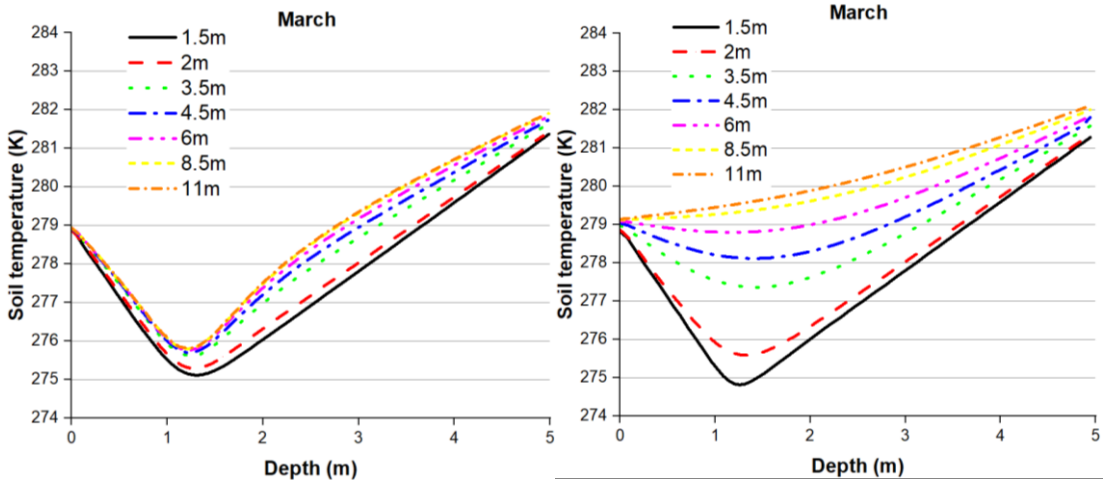

(a) At the centre of slinky loop *(b) At the centre of adjacent trench*

Figure 4 Effect of spacing distance on variations in soil temperature through the slinky-loop heat exchanger (at the end of March)

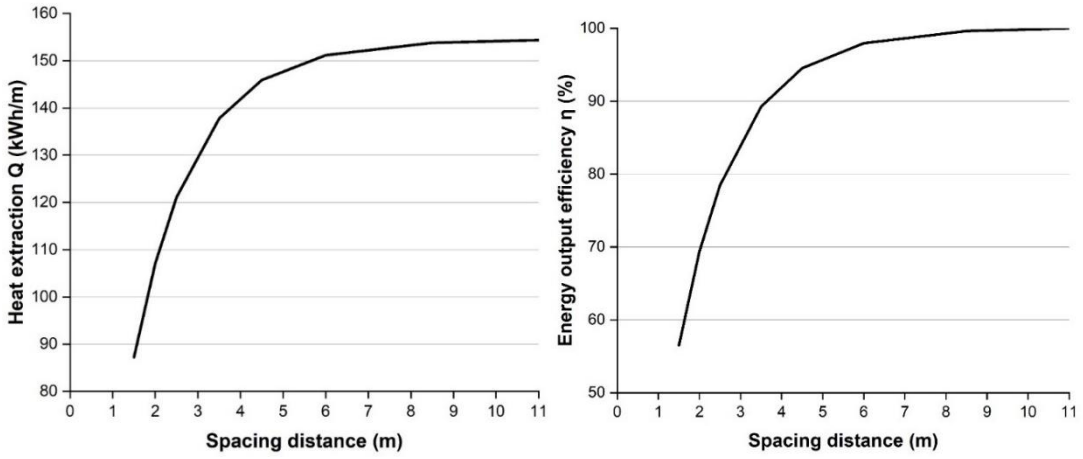

(a) *(b)*

Figure 5 Effect of spacing distance between adjacent trenches on heat extraction through the slinky heat exchanger (Base case)

The total amount of heat extraction for the heating season per unit length of trench from the slinky loop is compared for different spacing distances in Figure 5 (a). Figure 5(b) shows the corresponding energy output efficiency η which is calculated based on the 7-months heat extraction values for the slinky GHE using the following equation:

Equation 3: Energy output efficiency.

$$\eta = \frac{Q_d}{Q_s} \text{ x } 100\%$$

Where:

η = energy output efficiency (%)

Q_d = heat extraction from one of the loops of slinky GHE under different trench separation distances

Q_S = heat extraction from a single loop slinky GHE without considering multiple trench loop thermal interaction

Figure 5 (b) shows that by increasing the distance between slinky GHEs trenches to over 8m, annual energy output approaches the single loop operation, i.e., no thermal interference. From above figure, a nearly perfect polynomial correlation Equation 4 can be obtained between the energy output efficiency and spacing distance.

Equation 4: Energy output efficiency.

$$\eta = -0.03L^4 + 1.01L^3 - 11.17L^2 + 54.68L - 3.28$$

Where L is the distance of trench separation (m)

This correlation could be used to estimate the thermal performance of other different spacing distance. The thermal performance is greatly enhanced when the distance is increased to 3.5 m. Further improvement is seen at 4.5m spacing, while the benefit of increasing spacing beyond 6 m becomes negligible. As a result, considering the practical construction of the HGHE, the spacing distance between 5-6m is suggested compared with ideal (no interference) conditions, since further increasing the distance leads to less improvement of heat extraction rate but with less trench numbers and total energy output for a given land area. Considering the limit of land area, if the spacing distance is not more than 5m, the following simpler quadratic Equation 5 can be used with a loss of accuracy of less than 3%:

Equation 5: Energy output efficiency.

$$\eta = -3.69L^2 + 34.75L + 13.68$$

Figure 8 shows the variation in monthly heat extraction per metre length of the trench occupied by heat exchangers at various short loop spacing distances. The interference between parallel pipe loops decreased overall thermal performance (for each loop). The heat extraction amount decreased from September to February, and then increased during March. When the spacing distance between heat exchanger is at 1.5m, 2.5m and 4.5m, the heat transfer amount in September is 28.54 kWh/m, 37.31 kWh/m and 41.12 kWh/m, respectively, and decreased to 8.71 kWh/m, 12.06 kWh/m and14.56 kWh/m in March. The difference between the spacing distance of 1.5m and 6m was 31% in September, and then increased to 42% in March. This is because the thermal interference in 7-month continuous operation is accumulated as a results of heat depletion in the ground.

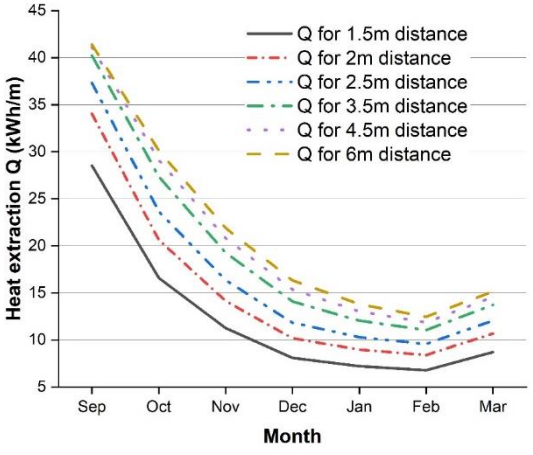

Figure 6 Monthly heat extraction under different spacing distances

3.2. The Effect of Initial Soil Temperature

Figure 7 depicts the simulation results of heat transfer amount through the slinky-loop heat exchanger at the depth of 1.2m in loamy soil, with two types of initial soil temperature - uniform soil temperature of 10°C and varying temperature with the depth at the beginning of heating season. For comparison purposes, the centre-to-centre distance of 11m was considered with negligible thermal interference. The calculated initial temperature at 1.2 m deep, for instance, was 14.3 °C instead of

the constant value of 10 °C and the resulting discrepancy in soil temperature would have a significant impact on the heat transfer rate in the first few heating months. The difference for the first month was 16%, and then decreases to 6% and 2% at the end of the second and third month, respectively. The effect of initial soil temperature decreased further and became negligible at the end of the heating season. This difference reduction can be explained by Figure 8(a), which illustrates the vertical soil temperature distribution at the centre of the slinky loop from ground surface to 5 m below the surface. At the end of September, there are significant differences in the soil temperature from 1.2 m depth to 5 m depth between the two types of initial soil temperature. This variation in the soil temperature decreases gradually at the end of October and November, and by the end of December these two predicted soil temperature lines are nearly overlapped. It can be observed from Figure 8(b), the simulated soil temperature with initial uniform profile from ground surface to 1.2 m below the surface is lower than that calculated using Equation 2. The largest difference occurs at the first hour, and then the trend of two simulated lines becomes similar from the first day to the 10th day within two meters depth. It can be concluded that the initial soil temperature condition has a negligible impact on the soil temperature after three months of operation.

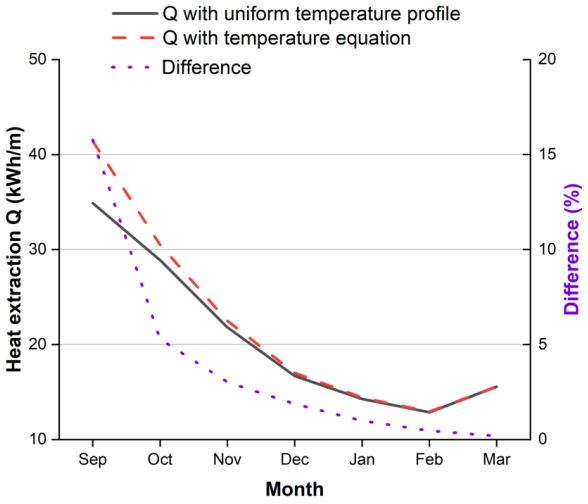

Figure 7 Effect of initial soil temperature on the predicted heat extraction through the heat exchanger

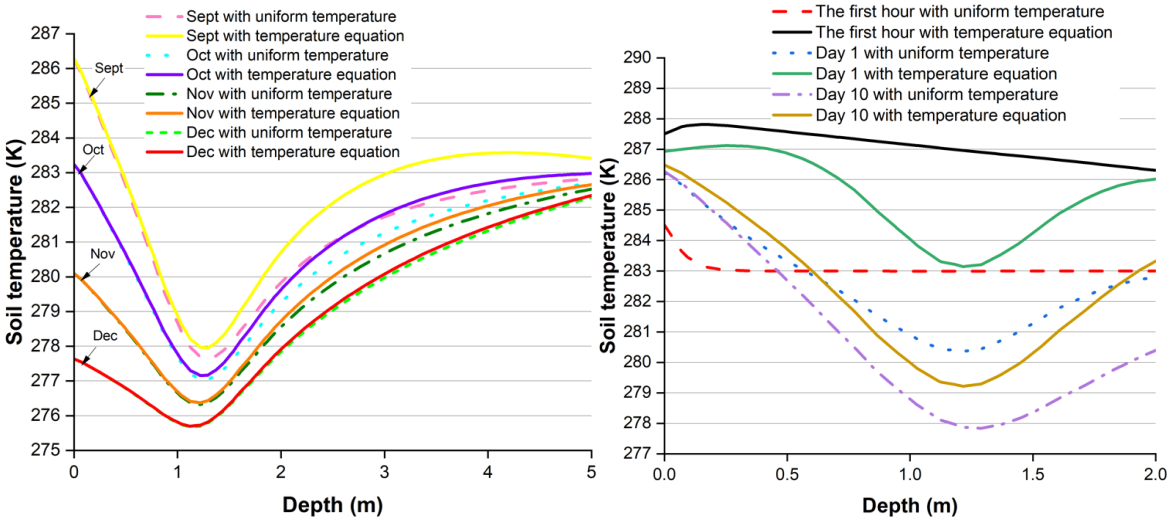

(a) First 4 months *(b) First 10 days*

Figure 8 Effect of initial soil temperature on the predicted variation of soil temperature at various times

3.3. The Effect of the Soil Thermal Conductivity on the Interference of Different Slinky Loops

To investigate the impact of trench spacing distance and soil texture on the thermal performance of the slinky ground heat exchanger, further simulation was carried out using three types of soil with different thermal conductivities 0.62 W/mK, 1.5 W/mK and 2.79 W/mK as well as other thermophysical properties as shown in Table 1. The centre-to-centre distance of adjacent loops of 1.5m and at the installation depth of 1.2m for simulation is presented here as an example. The soil temperature patterns with three types soil are similar. The cooler soil temperature around the heat exchanger covers a wider area in the sandy soil shown in Figure 9 (a) than that in the clayey soil (lower thermal conductivity of 0.62 W/mK) shown in Figure 9 (c).

Figure 10 show the predicted vertical soil temperature distributions along the centre of the heat exchanger loop at three selected times. At the end of September, the soil temperature at a distance of 1m below the heat exchanger in vertical direction was approximately 281.02K for soil thermal conductivity of 0.62 W/mK, but decreased to around 278.74K and 277.80K for soil thermal conductivities of 1.5 and 2.79 W/mK, respectively. At the same time and same position, the soil temperature decreased with increasing thermal conductivity. The decrease in the predicted soil temperature is accelerated by heat extraction (relative to the initial temperature profile). The extent of temperature decrease increases with the increasing of soil thermal conductivity at the beginning of the heating season. Thus, the heat exchanger installed in soil with a higher thermal conductivity had a higher heat transfer amount. However, the difference between three types of soil deceased with the operation time. At the same position, the temperature of clayey soil and loamy soil is getting close in the end of December and almost become the same at the end of March. This is due to a lack of heat recovery in short trench separation distance after a long period of continuous operation, and heat transfer rates in different soil types all drop to a low value, leading to a negligible difference in the surrounding soil temperature at the end of heating season.

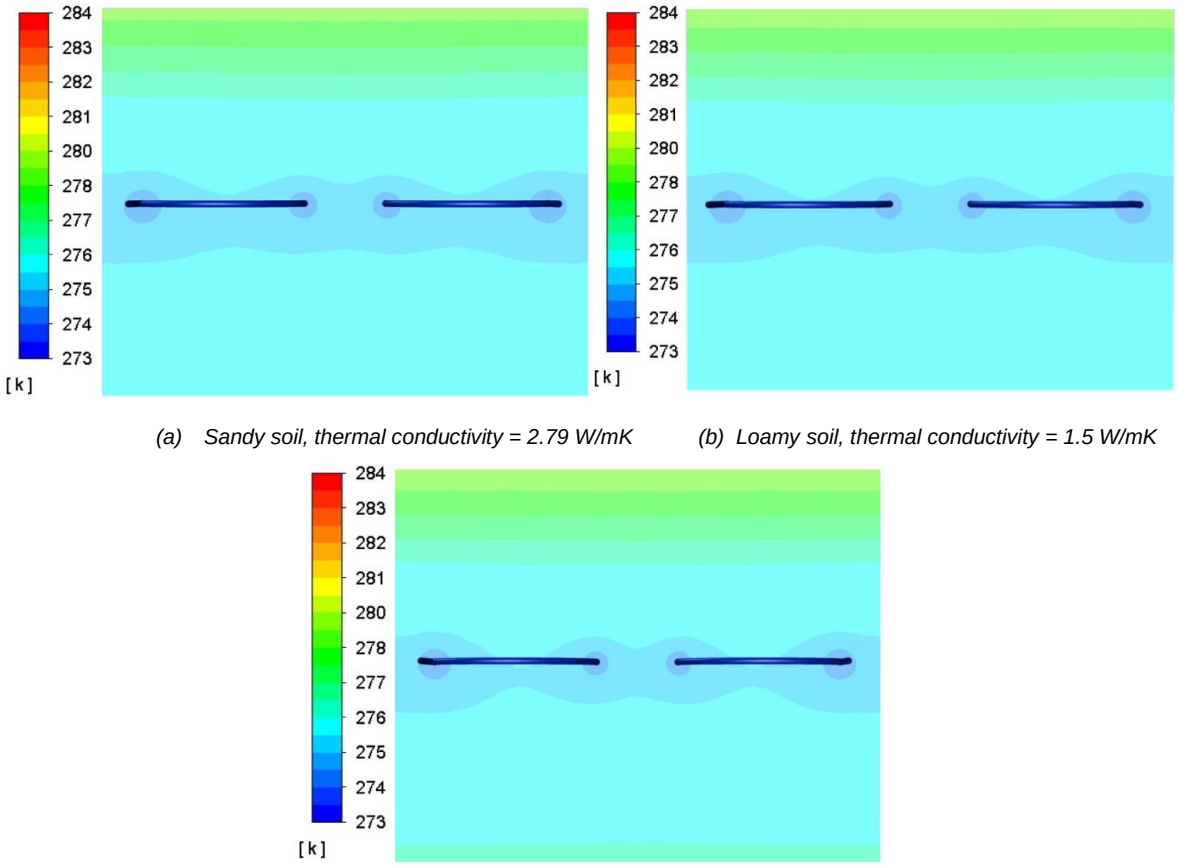

(a) Sandy soil, thermal conductivity = 2.79 W/mK *(b) Loamy soil, thermal conductivity = 1.5 W/mK*

(c) Clayey soil, thermal conductivity = 0.62 W/mK

Figure 9 Temperature distribution on vertical section with three soil types for the separation distance of 1.5 m slinky heat exchanger at the end of heating season (March)

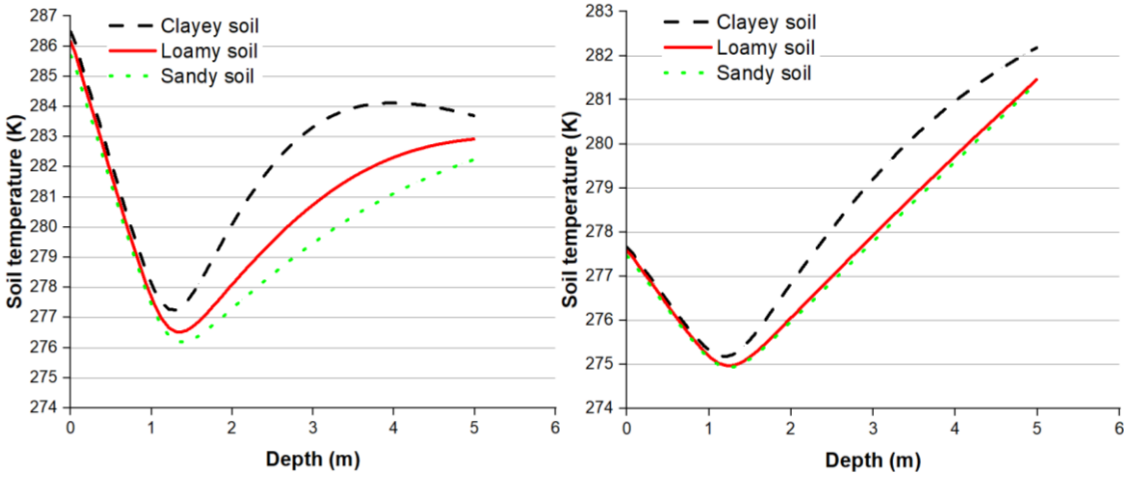

(a) At the end of September *(b) At the end of December*

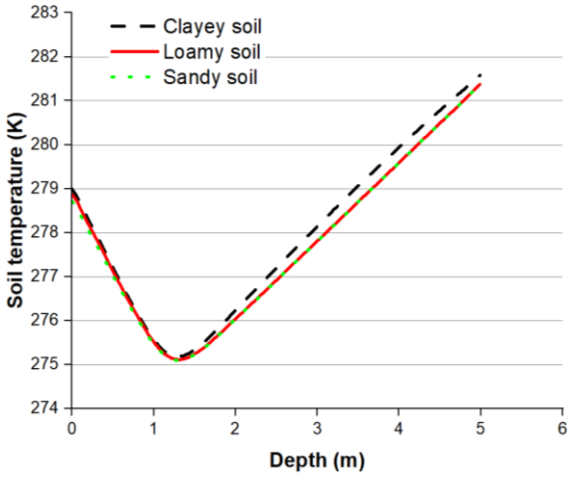

(c) At the end of March

Figure 10 Predicted variation of soil temperature with depth, at different times for different soil thermal conductivities

4. CONCLUSION

A 3D numerical model has been developed for dynamic thermal performance simulation of the horizontal slinky-loop ground heat exchangers with different trench separations for different initial soil temperature profiles and soil properties. The effect of trench separation was analysed for separation distances from 1.5 to 11 m. The numerical model was validated with the experiment data from literature. The simulation shows that heat transfer between parallel pipes would interfere with each other, resulting in a reduction in overall thermal performance if the separation distance is too short. Correlations have been developed from the numerical simulation to estimate the thermal performance of different spacing distances. It is suggested that the centre-to-centre trench separation distance should be between 5-6m to achieve good thermal performance while making use of the available land. Soil temperature between the adjacent trenches is also affected by the variation of the spacing distance.

The thermal performance of a slinky-loop heat exchanger was predicted with two types of initial soil temperature – uniform and varying with depth. The discrepancy in predicted heat transfer through a 1.2 m deep heat exchanger in loamy soil using a uniform temperature profile compared with that with varying temperature would be up to 16% at the end of the first month's operation, and then drops to 6% and 2% in the second and third months, respectively. The soil temperature difference for the first month would be far greater for a heat exchanger placed at shallower depths because of a larger temperature difference between the uniform value and varying profile. It is found that the initial soil temperature condition has a negligible impact on the soil temperature after three months of operation.

The increase in soil thermal conductivity would greatly improve the overall heat extraction amount. However, soil with a higher thermal conductivity will exacerbate the phenomenon of thermal interference between parallel pipes with a shorter separation distance. The lack of heat recovery after long time continuous operation with short trench separation distances reduces the heat transfer rate to a low value for all soil types at the end of heating season.

5. REFERENCES

Ansys. (2022) Ansys *Fluent Fluid Simulation Software.* Available at: https://www.ansys.com/products/fluids/ansys-fluent (Accessed: 11 July 2023).

Banks, D. (2012) "Horizontal Closed-Loop Systems," in An introduction to thermogeology: Ground source heating and cooling. Hoboken, NJ: John Wiley & Sons, Ltd. pp. 325-352.

Busby, J.P. (2015). 'Determination of Thermal Properties for Horizontal Ground Collector Loops', Proceedings *World Geothermal Congress 2015* Melbourne, Australia, 19-25 April 2015

C. F. Calvillo, A. Katris, O. Alabi, J. Stewart, L. Zhou, and K. Turner. (2023) 'Technology pathways, efficiency gains and price implications of decarbonising residential heat in the UK', *Energy Strategy Reviews*, 48, p. 101113. doi:10.1016/j.esr.2023.101113.

C. S. A. Chong, G. Gan, A. Verhoef, R. G. Garcia, and P. L. Vidale. (2013) 'Simulation of thermal performance of horizontal slinky-loop heat exchangers for ground source heat pumps', *Applied Energy*, 104, pp. 603–610. doi:10.1016/j.apenergy.2012.11.069.

Department for Business, E.& I.S. (2021) *Plans unveiled to decarbonise UK Power System by 2035*, *GOV.UK*. Available at: https://www.gov.uk/government/news/plans-unveiled-to-decarbonise-uk-power-system-by-2035 (Accessed: 11 July 2023).

Department for Energy Security and Net Zero (2023) *Heat and buildings strategy*, *GOV.UK*. Available at: https://www.gov.uk/government/publications/heat-and-buildings-strategy (Accessed: 11 July 2023).

Gan, G. (2018) 'Dynamic thermal performance of horizontal ground source heat pumps – the impact of coupled heat and moisture transfer', *Energy*, 152, pp. 877–887. doi:10.1016/j.energy.2018.04.008.

House of Commons Committee. (2022) *Decarbonising heat in homes - business, Energy and Industrial Strategy ...* Available at: https://publications.parliament.uk/pa/cm5802/cmselect/cmbeis/1038/report.html (Accessed: 11 July 2023).

Housing and local services.(2022)*Boiler upgrade scheme*. *GOV.UK*. Available at: https://www.find-government-grants.service.gov.uk/grants/boiler-upgrade-scheme (Accessed: 11 July 2023).

Weather history in Coventry United Kingdom (2022) *Coventry 2022 Past Weather (United Kingdom) - Weather Spark*. Available at: https://weatherspark.com/h/y/41841/2022/Historical-Weather-during-2022-in-Coventry-United-Kingdom (Accessed: 11 July 2023).

Y. Wu, G. Gan, A. Verhoef, P. L. Vidale, and R. G. Gonzalez. (2010) 'Experimental measurement and numerical simulation of horizontal-coupled slinky ground source heat exchangers', *Applied Thermal Engineering*, 30(16), pp. 2574–2583. doi:10.1016/j.applthermaleng.2010.07.008.

#55: A novel PCM cooling system for building applications

Tianhong ZHENG[1], Hasila JARIMI[2], Saffa RIFFAT[3]

[1] Department of Architecture and Built Environment, Faculty of Engineering, University of Nottingham, University Park, NG7 2RD, UK, tianhong.zheng@nottingham.ac.uk
[2] Solar Energy Research Institute (SERI), Universiti Kebangsaan Malaysia (UKM), 43600 Bangi, Selangor, Malaysia, hasila.jarimi@ukm.edu.my
[3] Department of Architecture and Built Environment, Faculty of Engineering, University of Nottingham, University Park, NG7 2RD, UK, saffa.riffat@nottingham.ac.uk

Abstract: In Malaysia, addressing heat stress-related issues and providing sustainable long-term affordable energy is crucial. Malaysia has great potential for solar energy as it is located near the equator, with the estimated potential for solar generation reaching up to 6500 MW. To utilize abundant solar energy resources and alleviate living issues in Malaysia, a novel solar PV power cooling system has been proposed. The system combines a radiant cooling ceiling with a PV-driven vapour-compression system and stores phase change material (PCM) in a water tank. The experimental setup consists of mini-DC refrigeration, a water tank containing PCM material, a circulation pump connected to the chiller unit, and a second pump connected to the radiant ceiling. The system effectively cools the PCM water tank, supplying cold water to the radiant ceiling. This significant temperature difference highlights the potential for energy savings in relation to the ambient temperature. Besides, the field measurement was conducted in Malaysia. The findings carry significant implications for the citizens of Malaysia as it allows for the investigation of the cooling performance of this system in a tropical climate setting, where the need for cooling is particularly acute.

Keywords: phase change materials; PV-vapour compressor system, radiant cooling, thermal energy storage

1. INTRODUCTION

Nowadays, buildings contribute to approximately 40% of global energy consumption and greenhouse gas emissions, significantly impacting global warming, primarily due to the extensive use of fossil fuels for heating and cooling systems (Yang, Yan et al. 2014). In fact, cooling and heating systems alone account for 60% of total energy consumption, and it is projected that energy consumption for cooling will increase substantially by 2050 (Cuce and Riffat 2016). Recent studies predict an annual growth rate of 1.8% in the impact of cooling and heating systems until 2050. Consequently, researchers have focused their investigations on various strategies to mitigate the environmental impact of building heating and cooling processes (Gielen, Boshell et al. 2019). Cooling and heating systems in buildings consume substantial amounts of energy to maintain acceptable human thermal comfort levels (Manzano-Agugliaro, Montoya et al. 2015). Cooling systems, although effective in enhancing indoor ambient temperatures, account for a significant portion of building energy consumption (Chua, Chou et al. 2013).

Over the past few decades, numerous Asian countries, particularly those in the Southeast region, have witnessed rapid economic growth and urbanisation (Zhao, Peng et al. 2006). Unquestionably, this has had a profound impact on energy consumption rates, particularly in urban areas (Wang, Fang et al. 2014). Many cities in these regions experience hot-humid climates throughout the year. Consequently, there is a high demand for passive cooling techniques to counterbalance the escalating need for conventional air-conditioning systems (Beccali, Strazzeri et al. 2018). In Malaysia, for example, buildings contribute to 48% of the country's electricity demand, primarily driven by space cooling requirements and appliance usage (Hassan, Zin et al. 2014). The number of households equipped with air-conditioners in Malaysia has surged significantly, from 13,000 households in 1970 to 229,000 households in 1990 and 775,000 households in 2000, primarily due to increased household incomes (Kubota, Chyee et al. 2009). Cooling is not only crucial for providing human comfort in Malaysia but also for addressing heat-related issues faced by its residents, such as physiological stress, increased health risks, and elevated mortality rates resulting from excessive heat exposure (Armstrong, Casa et al. 2007). In addition, sustainable economic growth in the future hinges on the ability to provide long-term access to affordable energy, with a particular focus on low-carbon technologies.

Malaysia possesses a high potential for solar energy utilisation, given its strategic location near the equator, with an estimated solar generation capacity of up to 6500 MW (Ahmad, Ab Kadir et al. 2011). To harness the abundant solar energy resources and alleviate challenges associated with living in a hot climate, a new concept called "PCM Cool", which revolves a radiant cooling storage system with a solar PV-driven vapor-compression cooling system, is proposed. The radiant cooling systems have gained popularity in recent years, finding common applications in commercial buildings, apartments, and airports (Hu and Niu 2012). Studies evaluating energy performance have demonstrated that radiant cooling systems offer energy savings by reducing fan energy consumption and increasing chiller efficiency, among other benefits (Stetiu 1999) (Szabó and Kalmár 2019). Radiant cooling/heating systems have garnered increased attention as they are considered more efficient compared to traditional air conditioning systems, providing enhanced indoor human thermal comfort (Memon, Chirarattananon et al. 2008). Additionally, these systems can be coupled with renewable energy sources for operation and integrated with other systems to meet the desired thermal comfort requirements (Yin, Yang et al. 2020). Besides, research on radiant cooling systems has shown that users perceive a higher level of thermal comfort and increased satisfaction compared to conventional AC systems (Teufl, Schuss et al. 2021). However, it is worth noting the limitation that while radiant cooling systems effectively handle indoor sensible heat loads, separate dehumidification systems are necessary to manage indoor moisture loads (Fong, Chow et al. 2011). Therefore, controlling indoor humidity becomes crucial when implementing radiant cooling systems to prevent condensation on radiant surfaces. Studies have primarily focused on developing strategies to minimize water vapor development and control condensation on radiant panels (Zarrella, De Carli et al. 2014).

This study proposed a novel system focuses on integrating a radiant cooling ceiling with a PV-driven vapour-compression system, incorporating phase change material (PCM) stored in a water cylinder to enhance system performance. The operation of the system involves the circulation of refrigerant through various components, driven by a compressor. Initially, the low-pressure vapour from the evaporator is compressed by the compressor, resulting in the generation of high-pressure superheated vapour. Subsequently, the vapour is directed to the condenser where it undergoes a phase change, transitioning from a vapour to a liquid state. This condensation process occurs as the vapour releases its latent heat to the surroundings. The high-pressure liquid refrigerant then passes through the expansion valve, which causes a substantial pressure drop, leading to a reduction in both pressure and temperature. The heat exchanger plays a critical role in the system, facilitating the evaporation of the refrigerant. It serves as the interface between the fluid medium and the refrigerant, enabling efficient heat transfer. During the evaporation process, the refrigerant extracts heat from the fluid medium, resulting in the cooling of the surrounding environment. The chilled fluid, now in a gaseous state, is then circulated back to the evaporator unit to continue the cooling cycle. Meanwhile, the liquid refrigerant is pumped through the water storage tank, which contains PCM material. The PCM material stores thermal energy during the charging phase, allowing for the storage of excess cooling capacity. This stored energy is subsequently utilised during the cooling process, enhancing the overall efficiency of the system. The water storage cylinder is designed with two closed loops. The first loop is connected to the refrigerant system, enabling the transfer of thermal energy between the refrigerant and the PCM material. This interaction ensures efficient charging and discharging of the PCM. The second loop is linked to the radiant cooling panel, which serves as the primary mechanism for delivering cooling to the indoor space. The chilled fluid from the water tank is circulated through the radiant cooling panel, effectively cooling the surrounding environment through radiant heat exchange.

By integrating a radiant cooling ceiling with a PV-driven vapour-compression system and incorporating PCM material, this proposed system offers several advantages. It allows for efficient utilisation of renewable energy through the PV panels,

minimising the reliance on conventional energy sources. The incorporation of PCM material enhances the system's thermal energy storage capacity of the system, enabling the system to provide cooling even during periods of low solar radiation or limited PV power generation. The integration of the radiant cooling panel ensures effective heat exchange and distribution, resulting in improved indoor thermal comfort.

2. SYSTEM DESCRIPTION AND EXPERIMENTAL SETUP

The proposed project aligns with the initiatives of the Malaysian government to foster the establishment of innovative, environmentally friendly, and sustainable energy technologies within the business sector. Upon the successful culmination of the project, the consortium aims to introduce PCM-Cool to the wider commercial market in Malaysia as well as other developing countries. The outcomes of the project will facilitate expedited access to comfortable cooling solutions for households in these developing regions. Beyond the confines of the consortium, PCM-Cool systems present an enticing prospect for meeting sustainable energy development targets with relative ease. Substantial economic opportunities arise in terms of financing and installation services to meet to the demands of the PCM-Cool systems enabled energy market. Therefore, an innovative system will be developed and proposed in this study.

2.1. PCM-cooling roof system description

Radiant cooling systems present numerous advantages when compared to conventional all-air systems. One of their key benefits is the ability to provide a distributed air temperature gradient, effectively eliminating cold draughts that may occur with forced air systems (Feustel and Stetiu 1995). Furthermore, radiant cooling systems offer aesthetic appeal, require less space for installation, and operate silently, making them ideal for various architectural and design applications (Hassan and Abdelaziz 2020). Additionally, these systems excel in maintaining thermal comfort even in environments with higher ambient temperatures, resulting in energy savings and reduced primary energy consumption. In a radiant cooling system, heat transfer occurs through both radiation and convection (Stetiu 1999). Radiant panels, which can be installed on ceilings (Kitagawa, Komoda et al. 1999), floors (Zhao, Liu et al. 2016), and walls (Tang, Liu et al. 2016), utilise cold water as the heat transfer fluid. The panels efficiently exchange heat with the surrounding space, ensuring even and consistent cooling performance throughout the area (Saber, Tham et al. 2016). However, there are certain limitations to consider. One such limitation is the potential for uneven heat distribution and condensation. Condensation can occur when the temperature of the radiant panel falls below the dew point temperature of the air, leading to moisture transformation and water droplet formation on the panel surface. Researchers have focused on addressing this issue by exploring methods such as uniform arrangement of cold-water pipes within the radiant cooling system (Xing, Li et al. 2021). To further enhance the performance and effectiveness of radiant cooling systems, various control strategies have been implemented. For instance, the utilisation of desiccant dehumidification systems has proven effective, as it prevents overcooling of the air while maintaining thermal comfort temperatures and reducing overall energy consumption (Fong, Chow et al. 2011). Other approaches, such as the implementation of membranes and assisted ventilation systems, have also been explored to address challenges related to hot and humid climates (Binghooth and Zainal 2012). In terms of system design, a compact layout is essential to optimise efficiency and overcome space limitations (Tye-Gingras and Gosselin 2011).

Furthermore, the vapour compression unit will operate as a conventional cooling/refrigeration unit that uses efficient and compact heat exchangers and a compressor unit. The compressor plays a crucial role in circulating the refrigerant within the system. Upon exiting the evaporator, the low-pressure vapour is compressed, resulting in a high-pressure superheated vapour. Subsequently, the vapour undergoes condensation in the condenser, transitioning into a liquid state. The high-pressure liquid refrigerant is then directed to the expansion valve, where it undergoes expansion, leading to a decrease in both pressure and temperature. This transformation generates a low-pressure, low-temperature refrigerant, which is then ready for further cooling. In addition, the water cylinder acts as a storage medium for PCM material, allowing for efficient heat transfer between the refrigerant circuit and the radiant cooling ceiling. The water tank is equipped with two closed loops: one connected to the refrigerant circuit and the other to the radiant. The system components are presented in Figure 1.

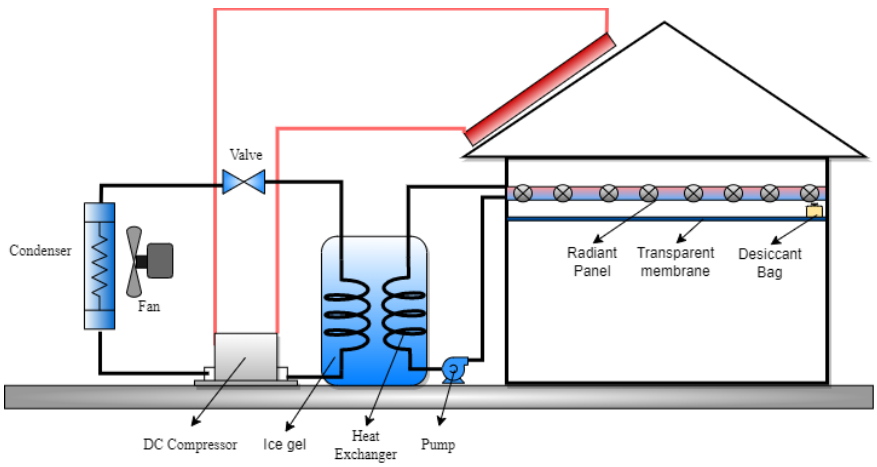

Figure 1 Schematic of the novel PCM cooling system

The incorporation of a secondary loop within the refrigeration system serves the purpose of integrating energy storage capabilities, thereby enhancing the cooling capacity while alleviating reducing the workload on the primary refrigeration system, particularly during periods of high demand. Extensive research investigations have indicated that the utilisation of a two-phase ice fluid as the latent heat storage medium results in an amplified energy storage capacity, owing to the more efficient solid-liquid phase change process compared to sensible heat storage in a solitary liquid phase (Zhang, Ma et al. 2010). Consequently, the selection of an appropriate working fluid for the water cylinder assumes critical importance in such a system, as it significantly influences the cooling performance of the heat transfer fluid (HTF). The subsequent circulation of the chilled HTF emanating from the water cylinder involves its directed flow into the radiant ceiling, thereby facilitating effective space cooling. Additionally, to mitigate potential condensation issues, desiccant dehumidification is proposed, which involving the strategic placement of a transparent membrane between the radiant ceiling and the room. This membrane allows for concurrent heat transfer and humidity absorption, as depicted in Figure 2.

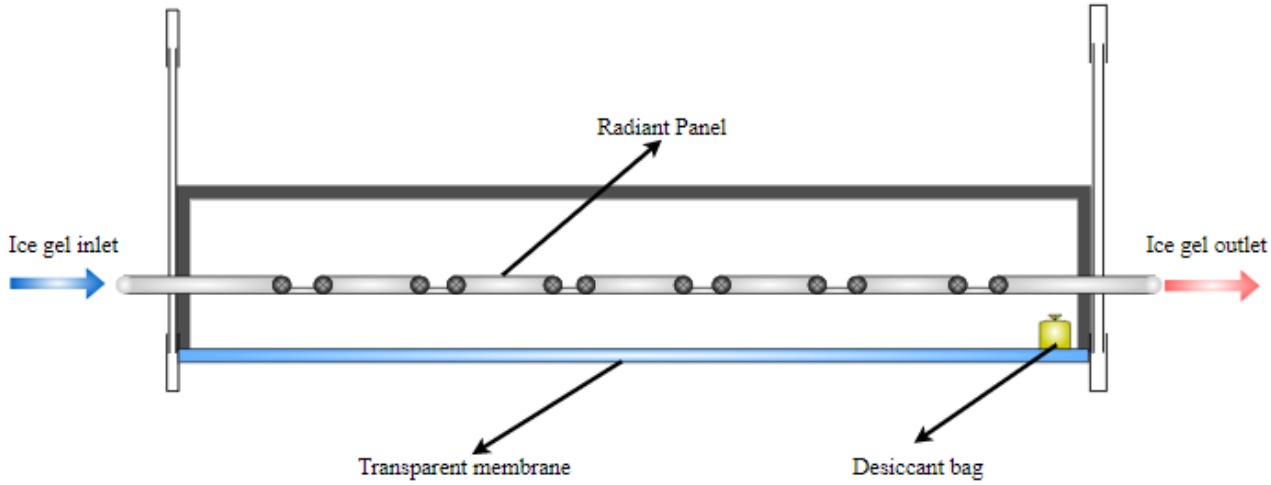

Figure 2 Detail schematic of PCM radiant ceiling

2.2. Phase change materials selection

PCMs are characterised by their ability to store and release thermal energy through the utilisation of "latent" heat. This phenomenon arises from the rearrangement of chemical bonds within the material during a phase transition, specifically when transitioning from a solid to a liquid state or vice versa. Such transitions are commonly referred to as changes in state or phase (Tyagi and Buddhi 2007). There exist multiple options for the utilisation of PCM to fulfil cooling requirements. These options encompass the integration of PCM within the building's envelope, such as walls, roofs, and floors, thus augmenting the thermal mass. Within this context, numerous paraffin and non-paraffin organic materials have been proved that they have a high potential y in cooling storage applications (Oró, de Gracia et al. 2012) (Osterman, Tyagi et al. 2012). These materials, when combined with chilled water, offer an attractive solution that enables high-energy storage density and efficient cooling (Oró, Miró et al. 2013). In addition to the commercially available PCMs, considerable attention has been directed towards studying binary mixtures with varying concentrations. Notably, the sodium chloride solution (NaCl-H_2O) has emerged as one of the extensively studied salt solutions in this domain (Oró, de Gracia et al. 2012).

In general, there are four kinds of two-phase HTF, which can potentially be used as the secondary refrigerant: (1) phase change materials that are encapsulated and protected from the carrying medium, (2) stabilised slurries, (3) ice slurries (4) hydrate slurries (Fournaison, Delahaye et al. 2004). Among the various fluids considered, ice slurry has garnered significant attention in extensive research efforts and emerges as a compelling candidate for the secondary refrigeration loop (Zhang, Ma et al. 2010),which refers to a homogenous mixture of small ice particles and carry medium (Kauffeld, Wang et al. 2010).

In the tropical regions, Malaysia for example, the water has been the ideal HTF as coolant owing to its low cost, high specific heat, low viscosity and hence lower pumping power, etc. However, the main disadvantage of water is the high freezing point (0°C), which is a risk that the frozen water can lead to expansion and potential damage to the cooling system components. Therefore, alcohol has been extensively employed as a coolant in engine cooling systems (Aprea, Greco et al. 2019) (Soltanimehr and Afrand 2016) due to the lower freezing point of the mixture than pure water (Rebsdat and Mayer 2000) (Takamuku, Saisho et al. 2005). However, the disadvantage of the glycol is the toxicity concerns (Bove 1966). In this context, serval researches conducted to investigate the ice gel mixture of water-glycerine-ethanol for achieving a stable amorphous state (Akilu, Baheta et al. 2018), (Namburu, Kulkarni et al. 2007). In addition, glycerol is virtually nontoxic, non-hazardous fluid. Adding glycerol to the mixture can provide lower freezing point, higher heat transfer, increased viscosity, lubricating system, and corrosion prevention (Akilu, Baheta et al. 2018).

Four different percentage of ice gel HTFs have been chosen: (a) Glycerine (7.5%) + Water (92.5%), (b) Glycerine (7.5%) + 2-Propanol (1%) + Water (92.5%), (c) 2-Propanol (15%) + Water (85%), (d) Glycerine (7.5%) +2-Propanol (15%) + Water (85%). All the HTFs are frozen in -10℃ condition, in order to measure the working temperature and cooling capacity. The phase change process have been shown in Figure 3.

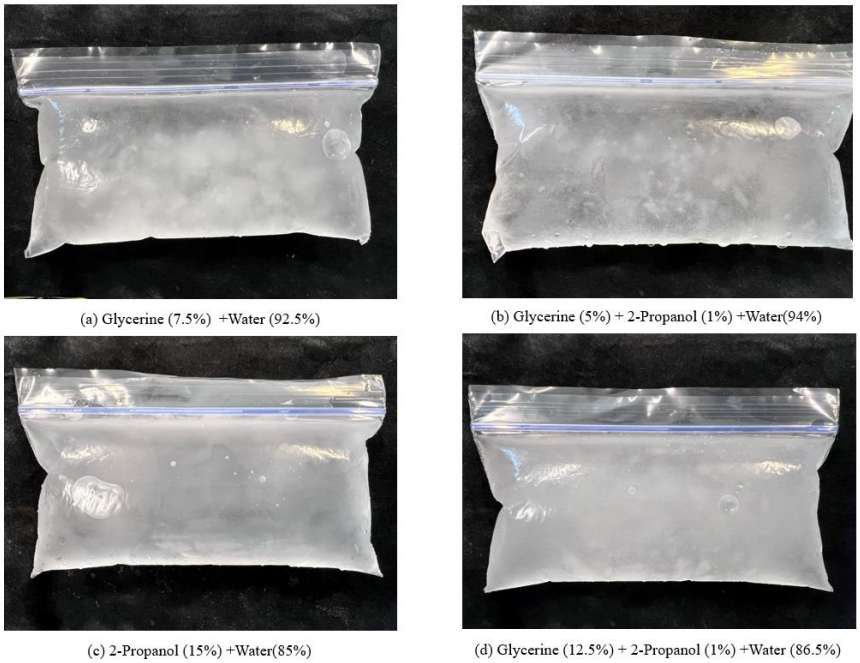

Figure 3 The phase change process of chosen HTFs in 3 hours freezing (ice gel solution)

The temperature of the HTFs has been thoroughly examined and the results are presented in Table 1, as depicted below. It should be noted that HTFs (c) and (d) exhibit closely similar temperatures and possess excellent cooling capacities, rendering them the ideal HTFs selected for this experimental study.

Table 1: The temperature changing for HTFs

HTFs	3 hours (℃)	12 hours (℃)	24 hours (℃)
(a)	-1.2℃	-7.4℃	-9.5
(b)	-1.4℃	-6.9℃	-10.1
(c)	-3.9℃	-9.3℃	-13.5
(d)	-4.2℃	-10.1℃	-14.2

2.3. Experimental setup

The primary aim of this investigation is to evaluate the cooling performance of the PCM-cooling system under varying temperature and humidity conditions, specifically to assess its effectiveness for applications in the Malaysian climate. Experimental testing was conducted at The University of Nottingham, within the Department of Architecture and Built Environment, using an Environmental Climatic Chamber.

The experimental setup included a DC- vapour compressor for refrigeration purposes (Model FS-RX1907), patriating with the voltage of 24VDC. The working environment ranged from -20℃ to 50℃, with humidity levels varying from 30% to 90%. In additional, a water cylinder is used to store the PCM material. The setup also incorporated a circulation pump connected to the compressor, ensuring proper movement of the refrigerant within the system. Additionally, a second pump was employed to circulate coolant through the radiant ceiling, facilitating effective heat transfer to the surrounding space. The system rig is shown as below.

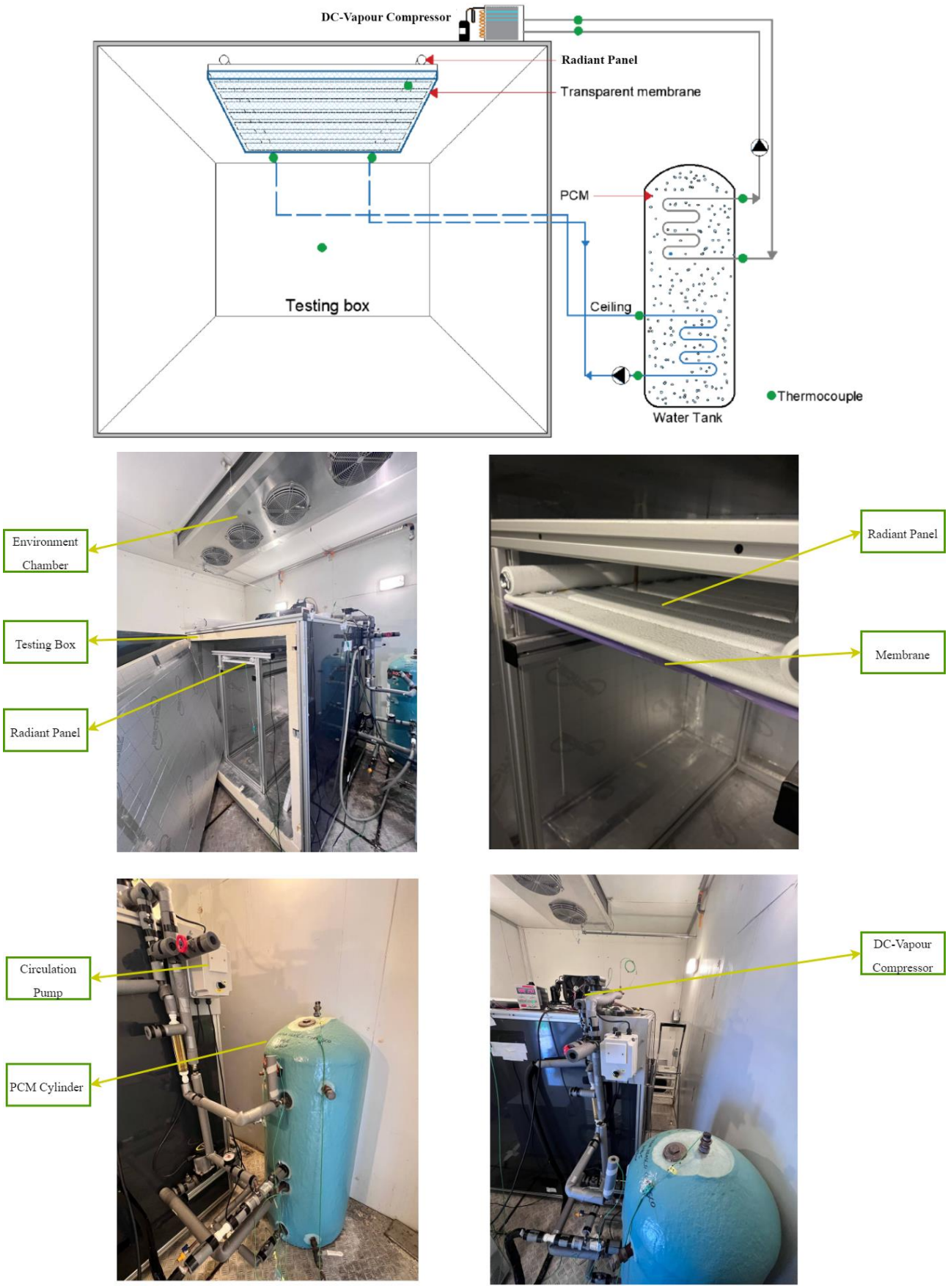

Figure 4 Experimental diagram of system and the components of the system inside the environment chamber.

3. EXPERIMENTAL OPERATION

This study aims to conduct a comprehensive assessment of the thermal behaviour exhibited by a radiant cooling system. Additionally, the thermal performance evaluation of a PCM water cylinder, including the charging and discharging processes, is undertaken (Cabeza, Ibáñez et al. 2006). Notably, the investigation emphasises the application of a PCM water cylinder, focusing specifically on the charging process whereby the fluid undergoes solidification, facilitating the storage of thermal energy in the form of latent heat (Kurnia, Sasmito et al. 2013).

During the charging process, the primary objective is to achieve cooling by harnessing both latent and sensible heat. In the present investigation, the ice gel material serves as the PCM, and the completion of the cooling process is contingent upon the PCM temperature reaching 1.9 °C (for the PCM tank) or the outlet water temperature from the tank attaining 1.9 °C (in relation to the radiant ceiling). A meticulous analysis of this stage assumes pivotal significance, as it ensures the successful implementation of the system, while providing valuable insights into the temporal dynamics of material charging and the requisite energy consumption for cooling 100 litres of the ice gel solution.

Subsequently, the study encompasses an evaluation of space cooling, whereby the cooling demands are met through the employment of a radiant panel and the thermal energy storage (TES) mechanism of the ice gel. This phase encompasses an assessment of the radiant panel's effectiveness in controlling the indoor temperature of the testing box, thereby yielding important findings concerning the overall system performance during the charging phase.

To facilitate the aforementioned research proposes, a thermal box, characterised by a volume of 1 m^3 and equipped with 10 cm of insulating material (Recticel Eurothane GP insulation and thermal conductivity is 0.022W/mK), is employed. The thermal box is positioned within an environmental chamber, thereby enabling the monitoring of temperature differentials between ambient air and the radiant panel surfaces. The measurement parameters encompass the ambient temperature both within and outside the testing box, in addition to the temperature of the solution inlets and outlets originating from the PCM water tank. The acquisition of these measurements is accomplished through the utilisation of K-type thermocouples. Data logging is performed utilising a data logger (DT85), with a standard deviation of ±0.3°C.

In Malaysia, the average daytime temperature is approximately 30℃, while the nighttime temperature averages around 25℃, and relative humidity in the region typically reaches around 80% (data 2023). To accurately replicate the Malaysian weather conditions, the environmental chamber was configured to simulate the actual annual average temperature and humidity profiles. This included a daytime condition of 30℃ and 80% humidity, as well as a nighttime condition of 25℃ and 70% humidity.

4. EXPERIMENTAL RESULTS AND DISCUSSION

The proposed PCM cool system experiment was conducted at The University of Nottingham, within the Department of Architecture and Built Environment. The research was conducted utilising an Environmental Climatic Chamber, which provided controlled environmental conditions for the experiment. The primary objective of this experiment was to assess the performance potential of the PCM cooling system under the specific weather conditions prevalent in Malaysia. The rationale behind this evaluation was to explore the viability and effectiveness of the system in addressing space cooling requirements in regions characterised by hot and humid weather. The ultimate goal is to promote the adoption and implementation of this innovative cooling system in other countries that experience similar weather conditions.

By conducting the experiment within the controlled environment of the Environmental Climatic Chamber, the researchers aimed to simulate the Malaysian climate accurately and replicate the real-world scenarios experienced in hot and humid regions. This approach ensured that the performance evaluation of the PCM cooling system was reliable and relevant to the target application, thus enabling robust conclusions and recommendations for its potential deployment in similar weather conditions worldwide.

4.1. The system operation

The HTF (c) (d) have been used to analyse the stable operability of the PCM cooling roof system, the time step have been set as 24hours, the ambient temperature (chamber temperature) is set as 30℃, and the humility is 80%. Figure 8 presents the experimental evaluation focusing on the DC-vapor compressor capacity to cool the ice gel. During the experimental evaluation, the temperature is constantly dropping throughout.

The investigation on HTF (c) revealed a notable maximum temperature difference of 15.57 °C in the testing box, with temperatures ranging from 29.27℃ to 13.7℃. Correspondingly, the radiant panel demonstrated a substantial maximum temperature difference of 16.26°C, oscillating between 28.85℃ and 12.59℃ during the cooling process. The average temperature difference between the radiant panel and the testing box was measured at 2.19 °C, signifying the efficient cooling performance of the radiant cooling system. Additionally, the average temperature difference between ambient conditions and the testing box was determined to be 15.69℃.

In the case of HTF (d), the testing box exhibited a maximum temperature difference of 14.23 °C, ranging from 29.17℃ to 12.94℃ during the cooling cycle. Simultaneously, the radiant panel demonstrated a significant maximum temperature difference of 14.9 °C, with temperatures varying from 28.84℃ to 11.94℃. The average temperature difference between the radiant panel and the testing box was found to be 1.94 °C, underscoring the effective cooling capabilities of HTF (d). Moreover, the average temperature difference between ambient conditions and the testing box was recorded as 16.9 °C.

Throughout the continuous 24-hour operational period, the proposed system exhibited exceptional stability and consistently delivered space cooling without any interruptions, reaffirming its reliability and efficacy in prolonged cooling applications. These findings contribute valuable insights into the performance evaluation of the PCM cooling system with different HTFs, offering potential implications for sustainable cooling strategies in buildings under hot and humid climatic condition.

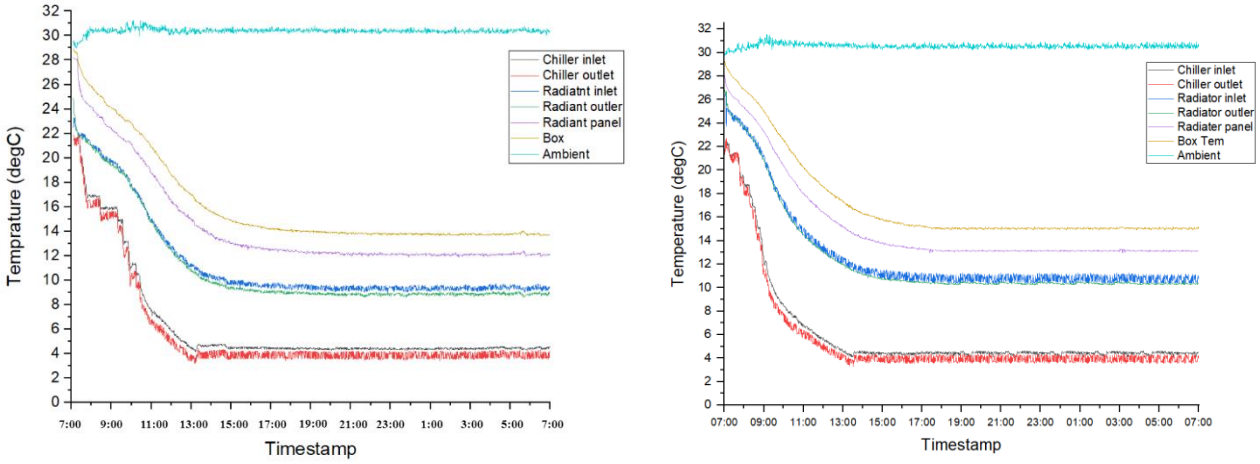

Figure 5 The stable operability of the system during the 24 hours experiment.

4.2. Diurnal and nocturnal periods experiment

To ensure the experiment accurately represents the real weather conditions in Malaysia, and to incorporate the use of renewable energy through PV panels, the system operated continuously during both the diurnal and nocturnal periods, accounting for the natural variations caused by sunrise and sunset.

During the diurnal period, the PV panels captured solar radiation and converted it into electrical power. This power was then supplied to the DC-compressor, which functioned to chill the HTF. The HTF circulated through the system, absorbing heat from the environment and transferred it to the chilled fluid. This process allowed for the cooling of the desired space or component. As the nocturnal period approached, the PV panels received reduced solar radiation, leading to a decrease in power generation. Consequently, the power supplied to the DC-compressor diminished, ultimately causing the compressor to stop operating. This cessation of compressor operation during the nocturnal period aligns with the natural decrease in available sunlight and ensures the experiment accurately reflects real-world conditions. By encompassing both the diurnal and nocturnal periods, the experiment accounts for the cyclical nature of sunlight availability and the corresponding fluctuations in renewable energy generation. This approach allows for a comprehensive assessment of the performance if the system and the reliance on renewable energy sources in different timeframes throughout the day.

During the nocturnal period (from 19:00 to 7:00), the temperature behaviour of the experimental setup with HTF (c) and HTF (d) exhibited notable trends. For HTF (c), the initial temperature inside the box was 14.31℃ at 19:00, and it gradually increased to 19.77℃ by 7:00 the next morning. Simultaneously, the temperature of the radiant panel began at 12.29℃ and rose to 19.14℃ during the same nocturnal period. Similarly, when HTF (d) was employed, the initial temperature inside the box was 13.27℃ at 19:00 and experienced a gradual increase to reach 18.35℃ by 7:00. Concomitantly, the temperature of the radiant panel started at 11.68℃ and rose to 17.71℃ throughout the nocturnal period. These observations indicate that both HTF (c) and HTF (d) effectively contributed to space cooling during the diurnal period. Remarkably, they continued to provide cooling effects during the nocturnal period without necessitating the operation of the compressor. This feature holds substantial significance in terms of energy conservation and highlights the potential of this PCM cooling system to offer continuous cooling during daily cycles without the need for active refrigeration during the nocturnal period.

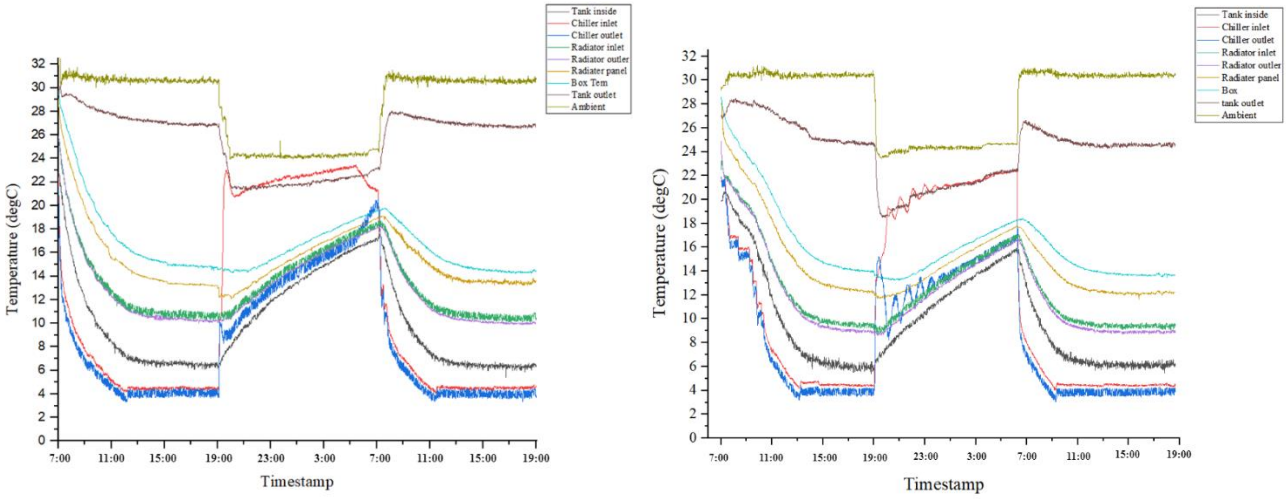

Figure 6 System operation during both the diurnal and nocturnal periods

5. CONCLUSION

This study focuses on the application of a PV-driven vapour-compressor system coupled with a PCM radiant ceiling. The system proposes a novel radiant panel coupled with a membrane to promote the utilisation of a radiant ceiling cooling system in a hot and humid climate condition and address the condensation concerns. This innovative system has supported the application of this technology to assist with the cooling performance under hot and humid environments. Radiant cooling can be considered as a low carbon technology that promotes energy saving and at the same time assisting indoor thermal comfort in buildings.

However, despite the numerous advantages, radiant cooling technology faces challenges associated with condensation, limiting its broader adoptions. In response to this issue, the inclusion of a membrane has been introduced as an effective measure to mitigate condensation concerns, while minimising any adverse impact on the temperature exchange within the testing unit. This membrane solution ensures the continuous operation of the radiant cooling system even in high-humidity environments, making it a practical and viable option for various building applications.

The successful application of the PV-driven vapour compressor further contributes to the effectiveness of the system. It has demonstrated its capability to cool the PCM within the water cylinder efficiently, enabling continuous space cooling throughout the daily life cycle. This aspect highlights the system's potential for achieving sustainable cooling solutions with reduced energy consumption and environmental impact.

6. REFERENCES

Ahmad, S., M. Z. A. Ab Kadir and S. Shafie (2011). "Current perspective of the renewable energy development in Malaysia." Renewable and sustainable energy reviews 15(2): 897-904.

Akilu, S., A. T. Baheta, M. A. M.Said, A. A. Minea and K. V. Sharma (2018). "Properties of glycerol and ethylene glycol mixture based SiO2-CuO/C hybrid nanofluid for enhanced solar energy transport." Solar Energy Materials and Solar Cells 179: 118-128.

Aprea, C., A. Greco, A. Maiorino and C. Masselli (2019) "Enhancing the Heat Transfer in an Active Barocaloric Cooling System Using Ethylene-Glycol Based Nanofluids as Secondary Medium." Energies 12 DOI: 10.3390/en12152902.

Armstrong, L. E., D. J. Casa, M. Millard-Stafford, D. S. Moran, S. W. Pyne and W. O. Roberts (2007). "Exertional heat illness during training and competition." Medicine & Science in Sports & Exercise 39(3): 556-572.

Beccali, M., V. Strazzeri, M. L. Germanà, V. Melluso and A. Galatioto (2018). "Vernacular and bioclimatic architecture and indoor thermal comfort implications in hot-humid climates: An overview." Renewable and Sustainable Energy Reviews 82: 1726-1736.

Binghooth, A. S. and Z. A. Zainal (2012). "Performance of desiccant dehumidification with hydronic radiant cooling system in hot humid climates." Energy and Buildings 51: 1-5.

Bove, K. E. (1966). "Ethylene glycol toxicity." American journal of clinical pathology 45(1): 46-50.

Cabeza, L. F., M. Ibáñez, C. Solé, J. Roca and M. Nogués (2006). "Experimentation with a water tank including a PCM module." Solar Energy Materials and Solar Cells 90(9): 1273-1282.

Chua, K. J., S. K. Chou, W. M. Yang and J. Yan (2013). "Achieving better energy-efficient air conditioning – A review of technologies and strategies." Applied Energy 104: 87-104.

Cuce, P. M. and S. Riffat (2016). "A state of the art review of evaporative cooling systems for building applications." Renewable and Sustainable Energy Reviews 54: 1240-1249.

Feustel, H. E. and C. Stetiu (1995). "Hydronic radiant cooling — preliminary assessment." Energy and Buildings 22(3): 193-205.

Fong, K. F., T. T. Chow, C. K. Lee, Z. Lin and L. S. Chan (2011). "Solar hybrid cooling system for high-tech offices in subtropical climate–Radiant cooling by absorption refrigeration and desiccant dehumidification." Energy Conversion and Management 52(8-9): 2883-2894.

Fong, K. F., T. T. Chow, C. K. Lee, Z. Lin and L. S. Chan (2011). "Solar hybrid cooling system for high-tech offices in subtropical climate – Radiant cooling by absorption refrigeration and desiccant dehumidification." Energy Conversion and Management 52(8): 2883-2894.

Fournaison, L., A. Delahaye, I. Chatti and J.-P. Petitet (2004). "CO2 Hydrates in Refrigeration Processes." Industrial & Engineering Chemistry Research 43(20): 6521-6526.

Gielen, D., F. Boshell, D. Saygin, M. D. Bazilian, N. Wagner and R. Gorini (2019). "The role of renewable energy in the global energy transformation." Energy Strategy Reviews 24: 38-50.

Hassan, J. S., R. M. Zin, M. Z. A. Majid, S. Balubaid and M. R. Hainin (2014). "Building energy consumption in Malaysia: An overview." Jurnal Teknologi 70(7): 33-38.

Hassan, M. A. and O. Abdelaziz (2020). "Best practices and recent advances in hydronic radiant cooling systems – Part II: Simulation, control, and integration." Energy and Buildings 224: 110263.

Hu, R. and J. L. Niu (2012). "A review of the application of radiant cooling & heating systems in Mainland China." Energy and Buildings 52: 11-19.

Kauffeld, M., M. J. Wang, V. Goldstein and K. E. Kasza (2010). "Ice slurry applications." International Journal of Refrigeration 33(8): 1491-1505.

Kitagawa, K., N. Komoda, H. Hayano and S.-i. Tanabe (1999). "Effect of humidity and small air movement on thermal comfort under a radiant cooling ceiling by subjective experiments." Energy and Buildings 30(2): 185-193.

Kubota, T., D. T. H. Chyee and S. Ahmad (2009). "The effects of night ventilation technique on indoor thermal environment for residential buildings in hot-humid climate of Malaysia." Energy and Buildings 41(8): 829-839.

Kurnia, J. C., A. P. Sasmito, S. V. Jangam and A. S. Mujumdar (2013). "Improved design for heat transfer performance of a novel phase change material (PCM) thermal energy storage (TES)." Applied Thermal Engineering 50(1): 896-907.

Manzano-Agugliaro, F., F. G. Montoya, A. Sabio-Ortega and A. García-Cruz (2015). "Review of bioclimatic architecture strategies for achieving thermal comfort." Renewable and Sustainable Energy Reviews 49: 736-755.

Memon, R. A., S. Chirarattananon and P. Vangtook (2008). "Thermal comfort assessment and application of radiant cooling: a case study." Building and environment 43(7): 1185-1196.

Namburu, P. K., D. P. Kulkarni, D. Misra and D. K. Das (2007). "Viscosity of copper oxide nanoparticles dispersed in ethylene glycol and water mixture." Experimental Thermal and Fluid Science 32(2): 397-402.

Oró, E., A. de Gracia, A. Castell, M. M. Farid and L. F. Cabeza (2012). "Review on phase change materials (PCMs) for cold thermal energy storage applications." Applied Energy 99: 513-533.

Oró, E., L. Miró, C. Barreneche, I. Martorell, M. M. Farid and L. F. Cabeza (2013). "Corrosion of metal and polymer containers for use in PCM cold storage." Applied Energy 109: 449-453.

Osterman, E., V. V. Tyagi, V. Butala, N. A. Rahim and U. Stritih (2012). "Review of PCM based cooling technologies for buildings." Energy and Buildings 49: 37-49.

Rebsdat, S. and D. Mayer (2000). Ethylene Glycol. Ullmann's Encyclopedia of Industrial Chemistry.

Saber, E. M., K. W. Tham and H. Leibundgut (2016). "A review of high temperature cooling systems in tropical buildings." Building and Environment 96: 237-249.

Soltanimehr, M. and M. Afrand (2016). "Thermal conductivity enhancement of COOH-functionalized MWCNTs/ethylene glycol–water nanofluid for application in heating and cooling systems." Applied Thermal Engineering 105: 716-723.

Stetiu, C. (1999). "Energy and peak power savings potential of radiant cooling systems in US commercial buildings." Energy and Buildings 30(2): 127-138.

Szabó, G. L. and F. Kalmár (2019). "Investigation of energy and exergy performances of radiant cooling systems in buildings–A design approach." Energy 185: 449-462.

Takamuku, T., K. Saisho, S. Nozawa and T. Yamaguchi (2005). "X-ray diffraction studies on methanol–water, ethanol–water, and 2-propanol–water mixtures at low temperatures." Journal of Molecular Liquids 119(1): 133-146.

Tang, H., X.-H. Liu and Y. Jiang (2016). "Theoretical and experimental study of condensation rates on radiant cooling surfaces in humid air." Building and Environment 97: 1-10.

Teufl, H., M. Schuss and A. Mahdavi (2021). "Potential and challenges of a user-centric radiant cooling approach." Energy and Buildings 246: 111104.

Tyagi, V. V. and D. Buddhi (2007). "PCM thermal storage in buildings: A state of art." Renewable and Sustainable Energy Reviews 11(6): 1146-1166.

Tye-Gingras, M. and L. Gosselin (2011). "Investigation on heat transfer modeling assumptions for radiant panels with serpentine layout." Energy and Buildings 43(7): 1598-1608.

Wang, S., C. Fang, X. Guan, B. Pang and H. Ma (2014). "Urbanisation, energy consumption, and carbon dioxide emissions in China: A panel data analysis of China’s provinces." Applied Energy 136: 738-749.

Xing, D., N. Li, C. Zhang and P. Heiselberg (2021). "A critical review of passive condensation prevention for radiant cooling." Building and Environment 205: 108230.

Yang, L., H. Yan and J. C. Lam (2014). "Thermal comfort and building energy consumption implications – A review." Applied Energy 115: 164-173.

Yin, X., R. Yang, G. Tan and S. Fan (2020). "Terrestrial radiative cooling: Using the cold universe as a renewable and sustainable energy source." Science 370(6518): 786-791.

Zarrella, A., M. De Carli and C. Peretti (2014). "Radiant floor cooling coupled with dehumidification systems in residential buildings: A simulation-based analysis." Energy Conversion and Management 85: 254-263.

Zhang, P., Z. W. Ma and R. Z. Wang (2010). "An overview of phase change material slurries: MPCS and CHS." Renewable and Sustainable Energy Reviews 14(2): 598-614.

Zhao, K., X.-H. Liu and Y. Jiang (2016). "Application of radiant floor cooling in large space buildings–A review." Renewable and Sustainable Energy Reviews 55: 1083-1096.

Zhao, S., C. Peng, H. Jiang, D. Tian, X. Lei and X. Zhou (2006). "Land use change in Asia and the ecological consequences." Ecological Research 21(6): 890-896.

#56: Performance of CO_2 air-to-water heat pumps for small domestic buildings in the UK

Usman QAYYUM[1], Savvas TASSOU[1], Debarati TORRENS[1]

[1]College of Engineering, Design and Physical Sciences, Brunel University London, UB83PH, 1843385@brunel.ac.uk

Abstract: The current study presents the performance analysis of a domestic high-temperature CO2 air-to-water heat pump (AWHP) coupled with a thermal energy storage system for a 2-bedroom house in the UK. TRNSYS simulation model incorporating the heat pump with the house and storage tank was developed to investigate their interactions. Data collected from experiments carried out on a commercially available 4.5 kW transcritical CO2 AWHP was used to build the heat pump model. Single storage tank of varying capacity under the same operating conditions were implemented on the model to assess their impact on the performance of the heat pump. Simulation results indicated that a tank size of 300 L was the most suitable one for a 2-bedroom house in the UK with heat load of around 7797 kWh. Environmental effect and cost analysis were undertaken by calculating the carbon emissions and annual fuel expenses for both the heat pump and natural gas boiler, simulated under the same working boundaries. While the utilisation of heat pump showed a reduction of CO2 emission by 44% compared to gas boiler, and the operating cost at present tariffs was higher for heat pumps by 38%.

Keywords: CO_2 air-to-water heat pump; CO_2 emission; Domestic hot water; Hot water storage tank; Space heating

1. INTRODUCTION

The United Kingdom (UK) and other major economies around the world have legally binding goals of net zero CO_2 emissions by the year 2050 (Fankhauser et al., 2022). One-third of all greenhouse gas emissions come from the building sector, half of which is attributed to space heating and hot-water provision (IEA, 2021). Currently, fossil fuel technologies dominate domestic heating systems in many countries. For example, gas boilers are installed in more than 85% of homes in the UK (BEIS, 2021). Boilers run on fossil fuels which leads to greenhouse gas emissions. Therefore, conventional gas boilers should be gradually replaced, and the use of heat pumps (HPs) is one of the ways of achieving this (Adamson et al., 2022). The heat pump is a renewable heating technology that transfers heat from external air or ground to heat the indoor air or water circulating in the heat emitters. Heat pumps also offer higher energy performance than combustion systems (Carroll et al., 2020). Space heating and hot water for domestic buildings account for about 40% of the UK's total energy demand and 20% of the total greenhouse gas emissions. Although nearly all homes would need to be low-carbon by 2050. However, only about 2% of the buildings are presently heated with low-carbon sources, and the energy efficiency in the housing stock is the lowest in European Union (EU) (Gillich et al., 2019). The boiler and radiator (~89%) are the most prevalent form of household heating in the UK (BEIS, 2021). This is also very common in EU countries such as France, Austria and Germany. When it comes to home heating in the UK, a radiator is always employed for the terminal unit of the user, which is served by the design supply/return water temperature of 70/50 °C.

The working fluid for heat pumps, known as refrigerant, has a significant impact on its performance. Thus, choosing the right refrigerant according to system design and temperature requirements is crucial (Yıldız & Yıldırım, 2021). In recent years, R410A refrigerant is being used in the UK, which has a high global warming potential (GWP= 2088). There has also been an uptick in the consumption of R134a (GWP=1300) and R32 (GWP=675) (BEIS, 2021). In contrast, natural refrigerants, such as CO_2, NH_3 and hydrocarbons (HCs) have zero or very close to zero GWP and good thermophysical properties. Among these CO_2 (R744) has the advantages of non-flammability, non-toxicity, high thermal conductivity, low dynamic viscosity, large thermal capacity and low cost. Also, it has a low critical temperature (31.3 °C) and high critical pressure (7.37 MPa). These characteristics enable operation with higher delivery temperatures compared to other refrigerants. At low temperatures, CO_2 as a working fluid in a transcritical cycle has a higher coefficient of performance (COP) than conventional refrigerants (Wang et al., 2020). Furthermore, conventional single-stage AWHPs that use R134a or R410A are not capable of producing an outlet water temperature high enough to satisfy the heat demand of the radiator serving as the terminal unit without compromising efficiency. To address this issue, AWHP employing CO_2 as a refrigerant is a promising alternative technology for commercial and residential heat pump systems (Dai et al., 2019), which can also deliver water at temperature of up to 70 °C, for the space heating system using radiator as a terminal unit (Rony et al., 2019).

The primary issue with AWHPs is that their heating capacity and COP decrease at low ambient temperatures (Liu et al., 2017), which is in contradiction to the increased heating load. Enhancing AWHPs' heating performance at low ambient temperatures is crucial. Numerous options exist for enhancing the AWHP heating system's efficiency with regard to energy consumption. Many efforts are invested in enhancing the efficiency of the heat pump cycle, by improving the performance of compressors (Du et al., 2021), evaporators (Wang et al., 2018), and other components, developing multistage cycles (Bertsch & Groll, 2008), exploring new safe and green refrigerants (Chen et al., 2018) and so on. The COP of the AWHP can be improved using these techniques. However, AWHP's ability to save energy for heating by optimising the refrigeration cycle is constrained by the Carnot cycle's low efficiency. According to Li et al. (2020) and Deng et al. (2019), the decrease in the heating capacity and COP of an AWHP operating at low ambient temperatures is the main challenge in utilizing an AWHP for heating. Many studies have focused on integrating a water storage tank (or thermal energy storage) with an AWHP unit in order to increase the COP and operating conditions of the heating system (Wu et al., 2020).

Osterman & Stritih's (2021) assessment of heat pump systems with thermal energy storage for heating and cooling concludes that the AWHP heating system benefits from the energy storage tank because of its increased efficiency and lower operating costs. Le et al. (2019) examined the techno-economics of an AWHP coupled with a water storage tank installed in a retrofitted UK mid-terrace home. Field experiments and simulations indicate that CO_2 emissions were 14% to 57% lower than those of a gas boiler and a high-efficiency oil boiler. Masip et al. (2019) investigated the energy and techno-economic performance of various coupled AWHPs and the storage tank for the production of hot water. The double-walled condenser case coupling between the heat exchanger and thermal storage tank was optimal, according to him. Compared to an immersion electric heater, this coupling option offers the utmost efficiency and cost-effectiveness, as well as the lowest CO_2 emissions. Kelly et al. (2014) demonstrated that a 1000 L hot water tank or a 500 L PCM storage tank was necessary to shift the heat pump's operation to off-peak hours without compromising indoor thermal comfort. Shah et al. (2018) compared a gas boiler with a heat pump system operating at 75 °C, and they found that a COP of approximately 2 led to a 12% reduction in CO_2 emissions. Primary energy savings of 12% to 56% were demonstrated by Carella & D'Orazio (2021) when they replaced conventional energy systems with heat pumps while retaining the radiators. Their findings suggest that, compared to a traditional boiler system, a high-temperature AWHP can reduce primary energy demand by up to 54% in Milan and up to 60% in Salerno, Italy. In addition, a number of studies have reported that the AWHP has frequent start-up and shut-down issues due to fluctuations in ambient temperature and building heat demand (Li et al., 2021). The reliability of a heating system can be improved with the help of buffer water tanks or hot water storage tanks in real-world applications (Dannemand et al., 2019). In order to reduce the impact of start-stop operation on the energy

efficacy of the AWHP, an energy storage tank is typically combined with the heat pump. According to the experimental findings of (Meng et al., 2021), the number of start-stop times for the AWHP decreases from 31 to 7 when using the energy storage tank, in comparison to the non-energy storage technique.

However, the studies related to transcritical CO_2 heat pumps integrated with water storage tanks for space heating and domestic hot water are very limited. Therefore, the main objective of the present work is to analyse the performance of a transcritical CO_2 heat pump integrated with a water storage tank to provide the heating demand for space heating and hot water for a single-family house. The whole system was modelled which included the building, rooms, heat pump, thermal storage tank, radiators, valves and controllers. The building modelled in this study was a 2-bedroom semi-detached house with 4 occupants. The system was evaluated for a 4.5 kW heat pump and different capacities of space heating thermal storage tank to investigate the required size of the system. Finally, the selected system was compared with the conventional boiler system based on the annual CO_2 production and operating bill cost according to the current tariffs. This paper provides guidelines on the deployment of CO_2 heat pump for domestic applications which is necessary for heat electrification in buildings and probably toward net-zero emission goals.

2. METHODOLOGY

The research aims to integrate the air-to-water heat pump (AWHP) system into a typical semi-detached house and to investigate the seasonal energy performance and indoor comfort condition of different thermal energy storage tanks when coupled with AWHP. A dynamic simulation model was required to determine the building's thermal load as well as the energy demand for space heating and domestic hot water. The building considered in this study was a single-family home located in London, UK; the heating system was composed of an inverter-driven air-to-water heat pump with two-pipe radiators as terminal units. Results from four simulations carried out for varying tank capacity are presented in this paper.

3. ENERGY MODELLING OF A 2-BEDROOM SEMI-DETACHED HOUSE

The building modelled in this study is a 2- bedroom semi-detached single-family house, with a total heated floor area of 78 m^2. It is a typical UK single-family house construction. The building has two floors and an unheated attic. It was assumed that 4 people were living in this house. Figure 1(a) shows the planning layout of the proposed building including the schematic of the proposed house and the floor plans. Figure 1(b) displays the building geometry which was created in Sketchup 2022/TRNSYS 3d plug-in. The wall with no windows represents the shared wall with the adjacent semi-detached house, which was assumed to be adiabatic. The building comprises 8 thermal zones. Both air volume and thermal capacitance vary between zones. The thermal zones are naturally ventilated. The temperature is maintained at 20 °C all year round in each zone that is heated. The assessment of building heating load was the first step to be carried out in a detailed building energy simulation analysis. For each building's thermal zone, the calculation procedure starts with the analysis of the related heat flows. These flows were determined by heat conduction through the walls, convection and radiation both internally and externally, radiation from the sun entering through the windows, and heat loss due to infiltration and ventilation (Antonopoulos & Koronaki, 2001). In order to determine the building's energy balance, dynamic modelling techniques often calculate the envelope's heat loss and gain.

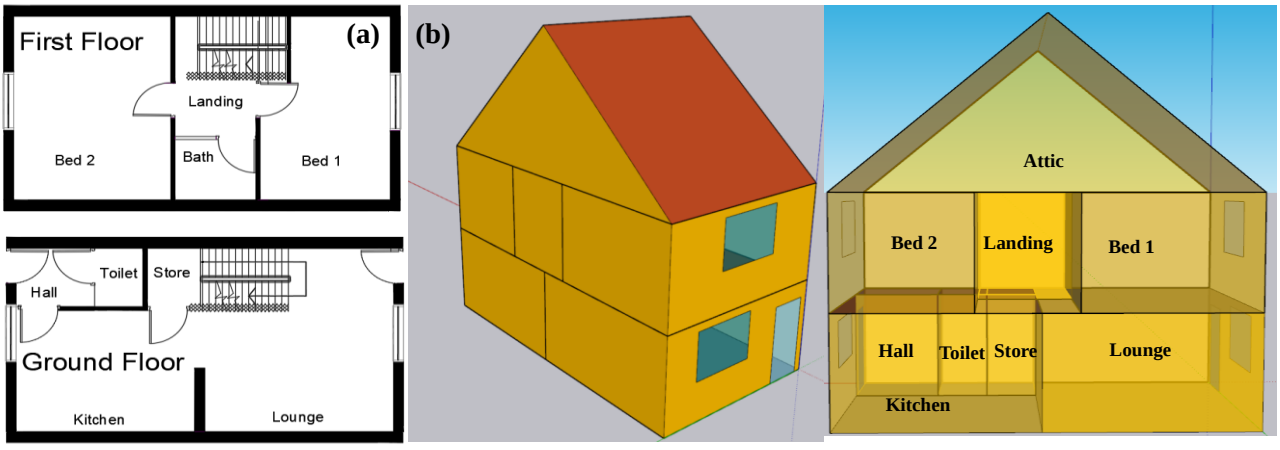

Figure 1 (a) layout of the studied semi-detached 2 bed-room house, (b) the schematic of the studied semi-detached 2-bedroom house

TRNSYS is a graphical simulation environment for transient systems. The objective of the TRNSYS building project was to assess the thermal energy demand and calculate the thermal peak loads of buildings. TRNSYS 18, a popular dynamic simulation programme, was used to create the model of this system (Burke & Stephens, 2017). The tool is highly precise and reliable for assessing the energy demand of buildings (Calise et al., 2020) and the scientific community considers it a standard tool for validating in-house building simulation models (Buonomano et al., 2019). TRNSYS 18's extensive library of components can properly replicate the energy performance of the building-plant system's components. The types within

the TRNSYS environment are regarded as reliable and have been verified (Klein, 1988). In the energy model designed here, the house is assumed to be located in the center of London. Therefore, the weather station located in London central (Latitude: 51.51 - Longitude: -0.09) is selected in TRNSYS with the data obtained from the Meteonorm database (Remund et al., 2010).

3.1. Thermal construction of the building

The construction details employed in the studied building were selected from the CIBSE guide A – Part F: Environmental Design (Chapter 3-Thermal properties of building structures) (CIBSE Guide A, 2019). The constructions were presented in the CIBSE guide based on the Government's Standard Assessment Procedure for Energy Rating of Dwellings (SAP 10). Table 1 presents the details of the construction material. The properties of all the employed materials were obtained from the CIBSE guide including density, thermal conductivity and specific heat. It should be noted that among many different types of construction as the typical wall construction in the CIBSE guide (Appendix 3. A8); the most insulated constructions (lowest u-value) were selected due to being closer to the future standards of the building.

Table 1: Details of the construction in different parts of the building.

Unit	Description	U-value (W/m^2K)
External walls (Brick/lightweight aggregate concrete block cavity walls)	105 mm brick, 100 mm blown fibre insulation, 100 mm lightweight aggregate concrete block, 13 mm dense plaster	0.30
Internal wall (Party wall)	12 mm plasterboard, 22 mm airspace/battens, 100 mm lightweight aggregate concrete block, 75 mm airspace, 100 mm lightweight aggregate concrete block, 22 mm airspace/battens, 12.5 mm plasterboard	0.56
Pitched roof (insulated at ceiling level)	Waterproof roof covering, 100 mm polyurethane insulation, vapour control layer, 19 mm timber decking, unventilated airspace, 12.5 mm plasterboard	0.17
Ground floor	10 mm carpet/underlay, 19 mm timber or chipboard on 100 mm joists, ventilated underfloor cavity	0.76
Internal floor/Ceiling	19 mm timber flooring or chipboard on 100 mm joists, 12.5 mm plasterboard ceiling	1.64
Semi-exposed ceiling	12 mm plasterboard, airspace, 150 mm mineral wool quilt on 100 mm joists, 19 mm timber flooring or chipboard	0.2
Door	52 mm Hardwood	2.18

According to Part L1A of current Building Regulations, a domestic window installation should achieve a U-value of no higher than 1.4 W/m²K based on the current 2013 part L standard. The windows for the proposed building were selected from CIBSE guide A, part F (chapter 3-Table 3.30) as a triple-glazed window with a 16 mm air gap with wood or PVC frame considering 30% window frame fraction presented with details in Table 2.

Table 2: Details of the glazing units used in the proposed building

Unit	type	Air layer thickness	U-value (W/m^2K)
External windows	Triple glazed (air filled-Low emissivity)	16 mm	1.4

3.2. Infiltration and natural ventilation

Infiltration and natural ventilation are the other important parameters that affect the heating load of the building noticeably. The equation from Building Research Establishment (BRE) (BRE, 2012) was used to calculate the air changes per hour by both fabric (infiltration) and deliberate ventilation as follow.

$$L_{sub} = (L_{fab} + L_{DV}) \times Sh_E \times Sh_D \times V_{wind}/4 \quad (1)$$

where L_{fab} is the infiltration rate of building fabric (ACH-air changes per hour), L_{DV} is the deliberate ventilation (ACH), Sh_E is the site exposure factor, is the dwelling exposure factor and V_{wind} is the wind speed. The value of Sh_E is considered 0.95 as the proposed building is placed in the average exposure category which includes partially sheltered urban and rural sites where there is some geographical reduction in local wind speed. Sh_D is so considered 0.925 as the proposed building based on the local shielding class of the building. L_{fab} is determined area-weighted average of different building components. For the filled cavity wall, L_{fab} is 0.3 ACH. As most of the exposed building structure is the walls, the value of 0.3 is considered as the mean value. Natural ventilation is considered due to openable windows, flow through cracks or vents due to wind and buoyancy pressure. To model this, an open flue is considered for the main rooms including the lounge, kitchen, toilet, bathroom and bedrooms which the airflow is 20 m^3/hour according to BRE report (BRE, 2012). The L_{DV} is then calculated by dividing the amount of airflow by the volume of the room.

The average wind speed in London placed in the south-east of England is 4.04 m/s according to BREDEM and thus the average infiltration rate from the fabric according to Equation (1) is 0.27 ACH. Based on CIBSE guide A (Environmental design, Chapter 4: Ventilation and air infiltration), the empirical value for air infiltration for rooms in buildings on normally exposed sites in winter for dwellings with 2 floors is 0.25 for new dwellings considering the air permeability of 5 m^3/m^2h at 50 Pa showing a good agreement with the calculated data from BREDEM method

4. CO_2 HEAT PUMP MODEL

The standard TRNSYS 18 library includes performance-map models and thermodynamic models for heat pumps. In the first scenario, heat pump performance was determined by interpolating a series of experimental data acquired from a limited number of laboratory experiments, whereas in the second scenario, the heat pump model was based on the modelling of all components of the refrigeration cycle. In order to evaluate the dynamic behaviour of a heat pump system, the performance map of commercially available CO_2 AWHP was developed at Brunel University (CSEF laboratory) by executing a series of experiments at steady state conditions as shown in Figure 2. The nominal heating capacity and coefficient of performance (COP) were 4.5 kW and 2.5, respectively. TRNSYS was used to simulate the AWHP (Type 941) using the performance map that included heating capacity and power consumption data, which were functions of the ambient temperature and inlet water temperature in the gas cooler. The heat pump supplied water to the radiators at a temperature of 62 °C.

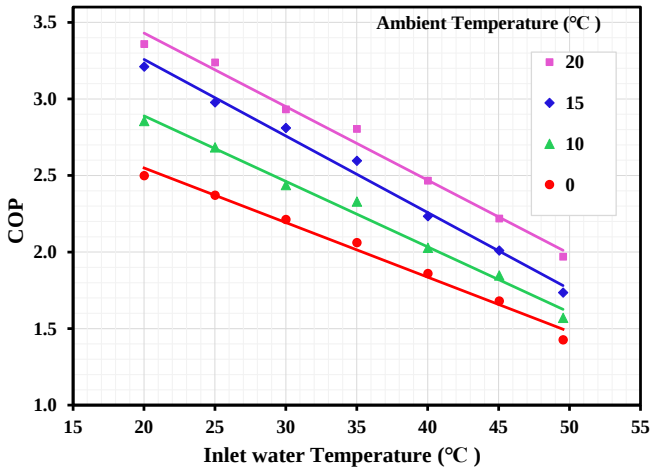

Figure 2 Performance map of CO_2 AWHP

4.1. Other components model and system control strategies

The loss coefficient of the water tank (Type 534) was determined to be 0.85 W/(m^2•K) and its volume was set at 300 L. It was divided into a single node with the outlet water temperature of the CO_2 AWHP unit set at 62 °C. Two water circulating pumps (Type 114) were installed, with a supply flow rate of 0.4 kg/sec and a return flow rate of 0.06 kg/sec, to transfer hot water from the storage tank to the radiators and the heat pump. To regulate the system, two On/Off differential temperature controllers (Type 1502 and Type 106) were used. The temperature in the room was monitored by one controller (Type 1502), while the hot water load temperature was tracked by a second controller (Type 106). When the water temperature in the water tank reaches the pre-set temperature of 62 °C, the water pump 1 and CO_2 AWHP unit will shut off and restart when the temperature drops by 5 °C. Additionally, the upper dead band and the lower dead band were both set to 1 °C, and the room temperature was maintained at 20 °C. When the temperature in the room was between 20 ± 1 °C, water pump 2 was switched off; when the temperature dropped 1 °C below the setting room temperature, the pump was turned back on. In order to assure the simulation's stability and convergence, a time step of 4 minutes was employed in this study. All these simulation parameters are emulated from original experiments.

In the simulation, a hot-water radiator heating system (Type 1231) was evaluated for the central heating system. In the system, the heat was generated in AWHP (Type 941) and distributed via heated water (heat carrier) to the radiators. Rooms were heated by radiators. A continuously operating pump circulates the heated water. Hot water passes through a bypass line if the valves are closed. As a general rule, the radiators were positioned next to the cold surfaces of the envelope. They have a major impact on thermal comfort.

5. SPACE HEATING AND DOMESTIC HOT WATER DEMAND

The space heating (SH) demand was based on the temperature of the internal space of the house and was scheduled in a way that the temperature of 20 ± 1 °C was maintained from 5:00 to 9:00 and 15:00 to 23:00 in the building. Figure 3(a)

displays the schedule for the space heating plan during the day. SH was provided by a thermostat that activates the heating system when the internal space temperature falls below 19 °C and turns it off when it rises above 21 °C.

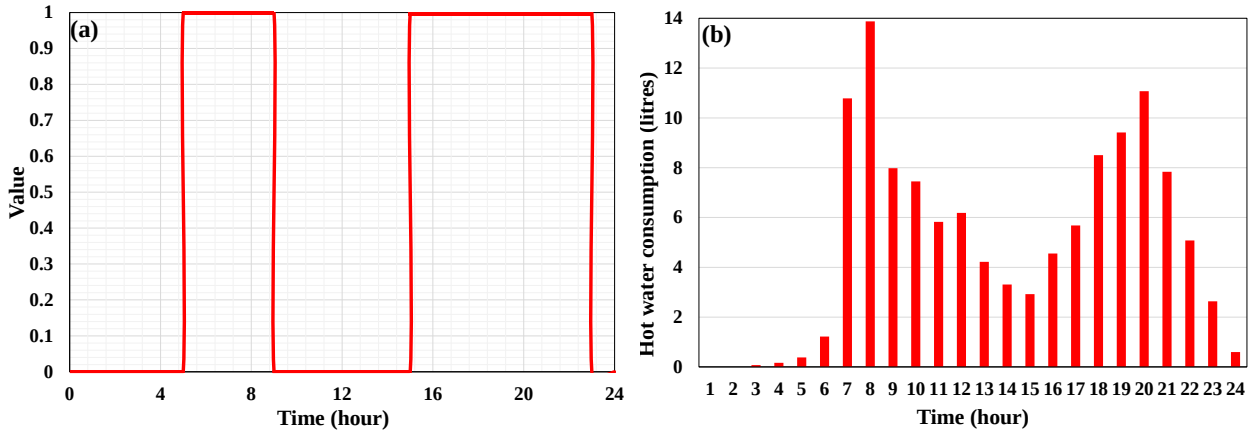

Figure 3(a) Schedule for space heating plan during the day (b) Average hourly hot water demand profiles derived from 12 months of measured data in LEEDR for 24 hours

To calculate the hot water demand of the proposed building with 4 occupants, first, the hot water consumption profile was gathered from the LEEDR project home energy dataset 24/04/18 which includes the measurement data for hot water consumption profiles for different types of buildings in the UK (Buswell et al.2018). According to the measured data, Figure 3 (b) the average volume of hot water consumed daily is 119.7 litres. This profile in Figure 3(b) was used in the TRNSYS simulation to calculate the amount of required heat for domestic hot water demand in the proposed building. The supply temperature of domestic hot water (DHW) is 45 °C, which is in the typical range for baths, showers and most other domestic hot-water applications. When water at a higher temperature is available, it is supposed to be mixed with mains water at 10 °C.

5.1. Working principle of the system

Figure 4 displays a schematic diagram of the whole system including the CO_2 heat pump, one water storage tank, building, radiators, valves, hot water system (shower and tabs). It consists of three different loops: The supply loop connects the CO_2 heat pump to the storage tanks through a gas cooler that exchanges heat between CO_2 and water delivered to the storage tanks. For the demands' loops, at the junction one supply line connects the DHW to the taps for hot water usage and the other one connects the SH to the radiators inside the building for space heating purposes.

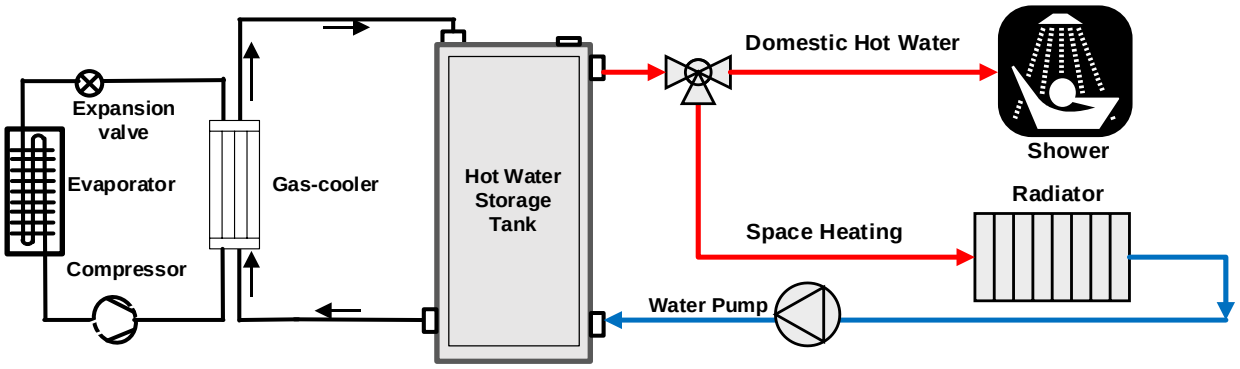

Figure 4 The schematic of the whole system

Figure 5 displays the TRNSYS model to calculate the required heating load demand for both space heating and hot water. It includes different components for space heating and hot water demands and also controllers and equations to control the system as well as printers and plotters to present the results.

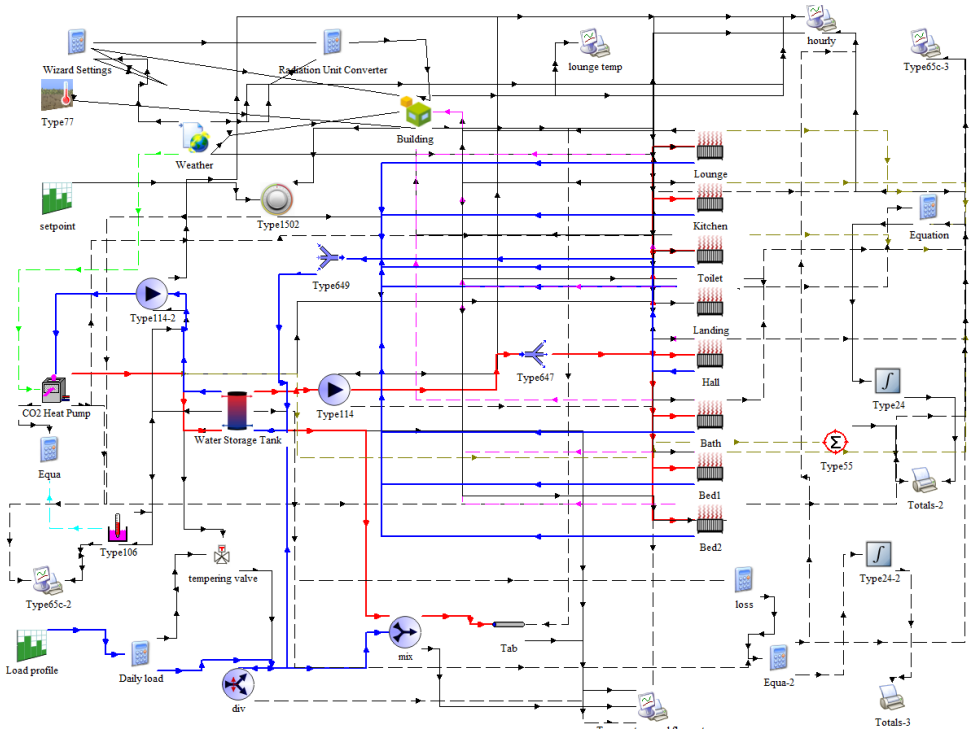

Figure 5 TRNSYS model of the proposed system

6. RESULTS AND DISCUSSION

The developed model was used to analyse the behaviour of the system. Results were presented for the annual usage of the 4.5 kW heat pump with a water storage tank capacity of 300 L. Further simulations were carried out to study the effects of HP capacity with different volumes of storage tanks.

6.1. The influence of the storage volume

Figure 6(a) presents the yearly values for the heat pump-generated heat, heat loss for the tank (SH and DHW), and the energy delivered from the HP to the tank. By increasing the capacity of the storage tank, the required energy for the DHW was not changed. Expectedly, when the volume of the tank increases, the increased tank thermal losses increase from 425.23 kWh for the tank of 150 L to 751.09 kWh for the tank of 300 L. By increasing the capacity of the storage tank, more heat was required to provide the temperature of 62 ℃ in the thermal storage tank. The heat required in the thermal storage tank was changed from 7317.73 kWh in a year for the system with a 150 L tank to 7797.43 kWh for a 300 L tank and this increment difference is about 6%.

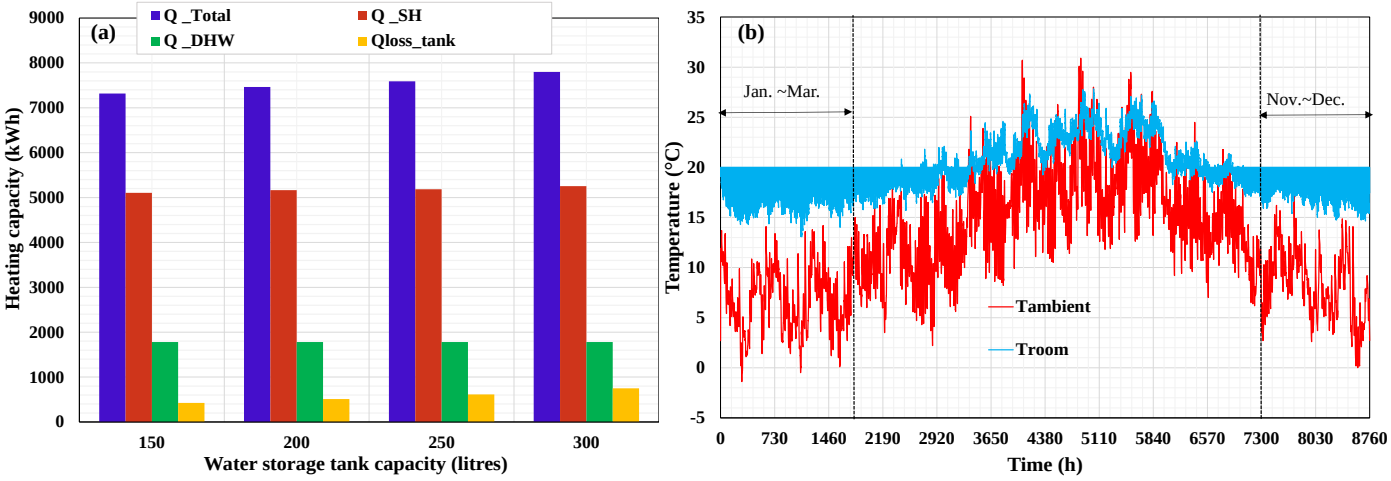

Figure 6 (a) The total annual heat generated by the AWHP (SH & DHW) and the heat loss in the storage tanks for different storage tank volumes (b) The annual variation of the lounge's temperature with ambient temperature

Figure 7(a) depicts the supply/return water temperature variations of the CO_2 heat pump for different water storage tanks on 15th January (24 hours) during the heating period. The maximum and minimum water temperatures were 62 °C and 52 °C for the 300 L storage tank. The supply and return water temperatures for a volume of 250 L were 60 °C and 49 °C, respectively. Similarly, 200 L and 150 L tank capacity results indicated the same supply and return water temperature which were 57 °C and 47 °C respectively. This happened due to the decrease in ambient temperature reduced the evaporation temperature of the AWHP, resulting in a decrease in the heating capacity and a drop in the supply water temperature for all the storage tanks (250 L, 200 L and 150 L) except the 300 L tank. Due to higher storage capacity, the 300 L tank contains higher thermal energy and its operation was quite stable. In addition, frost may be accumulated on the surface of the outdoor heat exchanger which increased the heat transfer resistance between the outdoor air and heat exchanger, so the CO_2 heat pump unit needs to use a periodic frost-defrost cycle, which further increased this phenomenon (Off and on cycling of the compressor).

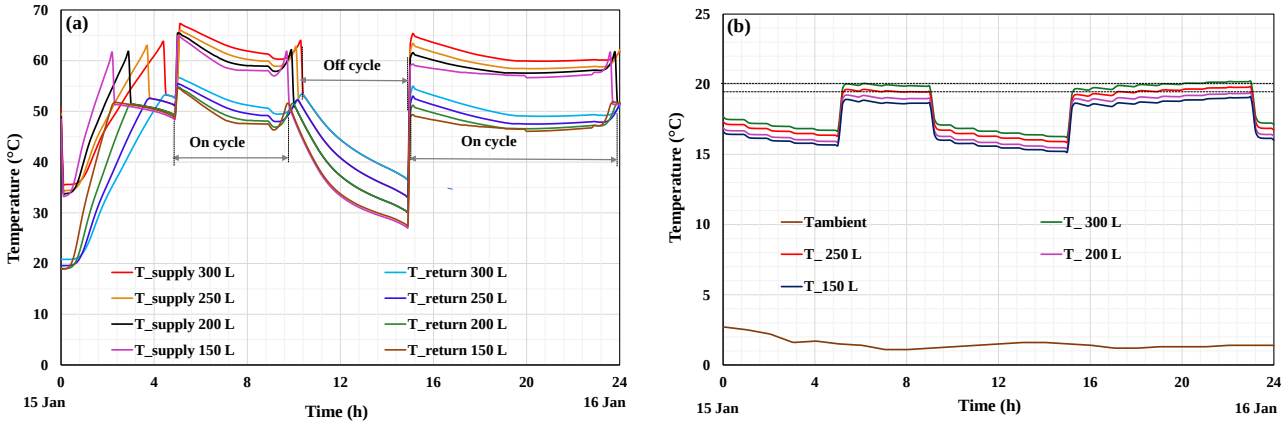

Figure 7 (a) Supply and return water temperature profile in on-off AWHP, (b) the variation of lounge's temperature for different storage tank

To find out if the system was capable of providing thermal comfort inside the building, the variation of the ambient temperature in the lounge was considered as the selection criteria for a period of 24 hours from the 15th of January to the 16th of January (start from 336 hours to 360 hours). The average temperature over 24 hours was shown in Figure 7(b), which was the coldest time of the year. It displays the variation of the lounge's temperature during this period for various volumes of the thermal storage tank using the 4.5 kW heat pump. It was observed that the 300 L storage tank was capable of maintaining the lounge's temperature at 20 °C during one complete cycle (24 hours). On the other hand, a 250 L tank steadily reached 19 °C throughout the whole time. The other storage tanks (200 L and 150 L) found it challenging to maintain the lounge's temperature even at 19 °C, indicating that these systems were incapable of maintaining the required thermal comfort temperature within the building. This was a result of the lower outdoor temperature and higher heating demands of the house on 15th January during the heating time, resulting in a decrease in the supply water temperature (see Figure 7(a)), and consequently overall drop in the indoor temperature for thermal comfort (Figure 7(b)). It should be noted that the 300 L storage tank, always maintained the lounge's temperature at 20 °C during the coldest time, but it would be oversized for other heating periods. For all other cases, thermal storage sizes increase have a slight positive effect on the indoor comfort temperature. Additionally, it was observed that a larger storage capacity increases operational flexibility because it stores the largest heat for space heating demand. Thus, a storage tank of 250 L appears to be the optimum size for the building considered in this paper.

6.2. Yearly evaluation of the system

The heat loss of the building was estimated using the design's outdoor temperature and with no internal heat gains. The heating season was assumed to begin on November 1 (7296 hr) and end on March 31 (2136 hr) with an indoor set-point temperature of 20 °C. The peak design heat loss was 7.5 kW. Figure 6(b) illustrates the temperature in the lounge room compared with the ambient temperature during the whole year. As mentioned, during the pre-defined hours for the heating system, the room's temperature was maintained between 19 °C and 21 °C. During the unheated hours, it dropped to lower temperatures during winter. Changes in the outdoor air temperature, solar heat gains, and internal heat gains all contributed to fluctuations in the indoor air temperature. As shown in Figure 6(b), the minimum temperature inside the room was 13 °C. During the summer, when the ambient temperature was higher than the pre-defined temperatures as the thermal comfort temperature, the maximum room temperature was around 27 °C. Table 3 shows the annual heating demand for different rooms of the building, hot water demand, the energy input from the heat pump to the thermal storage tank, and the heat loss from the storage tank. There was a difference between the heat pump energy input and the sum of heat loss and the heat required for the radiators. This can be accounted for as the stored heat in the tank.

Table 3: Annual heating demand for different rooms of the building and domestic hot water.

Room	Annual heating load (kWh)
Lounge	1413.07
Kitchen	1170.78
Toilet	210.07
Hall	255.34
Bed 1	1188.09
Bed 2	1149.09
Bath	297.61
Landing	240.68
Total heat required in the radiators	5253.77
Hot water demand	1780.11
Heat lost from the tank	751.09
Heat pump energy to the tank	7797.43

Table 4 presents the total heat produced by the heat pump, heat pump power, compressor power, maximum and average COP of the heat pump. The maximum COP of the system was 2.80 while the average annual COP, which was calculated by dividing the total generated heat by the heat pump power was 1.80.

Table 4: Annual thermal energy and power as well as maximum and mean COP of the heat pump

	Value (kWh)
Total generated heat	7797.43
Compressor power	4004.91
Heat pump power	4329.74
COP (maximum)	2.80
COP (average)	1.80

6.3. CO_2 emission and operating cost analysis

The electricity required to operate the heat pump was provided from national grid. According to the UK government report on greenhouse gas emission, the CO_2 emissions for domestic energy usage in 2023 are 0.205 kg of CO_2e per kWh of electricity and 0.183 kg of CO_2e per kWh of gas (Bramwell et al., 2023). Therefore, considering the current carbon footprint of electricity generation, Table 5 presents a comparison of the heat pump employed in this study and a conventional boiler as the heat source. It should be noted that to provide 7797.43 kWh thermal energy by a conventional boiler with an efficiency of even 90%, 8663.81 kWh energy should be provided. As shown, in Table 5, the CO_2 emission produced by the heat pump system is around 44 % less than that produced by the conventional boiler system, it should be noted that the net CO_2 emission factor for electricity generation using 100% renewable energy is zero which can be a possibility in the future.

Table 5: Annual CO_2 emission of the proposed CO_2 heat pump compared with a conventional boiler system

	Required energy (kWh)	CO_2 emission (kg)	Annual operating cost (£)
CO_2 heat pump	4329.74 (electricity)	887.59	1437.47
Boiler	8663.81 (gas)	1585.48	892.37

Table 5 also presents the annual operating cost for the CO_2 heat pump compared with the conventional boiler system based on the current tariffs in the UK. The average net selling value of gas and electricity for the domestic sector in the UK in 2023 is 10.3 pence/kWh and 33.2 pence/kWh, respectively (Bramwell et al., 2023). According to the current tariffs, the annual operating cost of the CO_2 heat pump is £545 higher than that of the conventional gas boiler.

7. CONCLUSION

In this study, a transcritical CO_2 AWHP was investigated and integrated with a thermal storage tank to provide the heating demand for both space heating and hot water in a 2-bedroom house with 4 occupants. The whole system was modelled using TRNSYS 18 software on a daily and yearly basis, comprehensively. The following results were the key outcomes of this study: (a) Comparing different volumes of thermal heating storage tanks with the heat pump capacity of 4.5 kW it was observed that a 250 L storage tank was capable of meeting the heating demand and comfort temperature required inside the house. (b) The annual thermal energies required for space heating and domestic hot water demands were 5253 and 1780 kWh, respectively, while the energy obtained from the 4.5 kW heat pump with 300 L tank was 7797 kWh and the heat loss from the tank was 751 kWh (less than 10%). (c) The heat pump required electrical power of 4329 kWh and the maximum and mean COP obtained were 2.80 and 1.80 respectively. (d) Compared with a boiler system with an efficiency of 0.9 and based on the current tariffs for the CO_2 emission and operating cost; the heat pump system produced around 44 % less CO_2e annually; however, the operating cost of the heat pump system was £545 per year higher than that for the boiler system. (e) The performance evaluation presented in this study for an integrated CO_2 heat pump with thermal storage might help towards heat electrification in the near future as the main pathway for different countries to achieve heat decarbonization and thereby net-zero goals.

8. REFERENCES

Adamson, K. M., Walmsley, T. G., Carson, J. K., Chen, Q., Schlosser, F., Kong, L., & Cleland, D. J. (2022). High-temperature and transcritical heat pump cycles and advancements: A review. Renewable and Sustainable Energy Reviews, 167(April), 112798. https://doi.org/10.1016/j.rser.2022.112798

BEIS. (2021). Annual Fuel Poverty Statistics Report, 2021 (2019 data) (Vol. 2020, Issue March). https://assets.publishing.service.gov.uk/government/uploads/system/uploads/attachment_data/file/882404/annual-fuel-poverty-statistics-report-2020-2018-data.pdf

Bertsch, S. S., & Groll, E. A. (2008). Two-stage air-source heat pump for residential heating and cooling applications in northern U.S. climates. International Journal of Refrigeration, 31(7), 1282–1292. https://doi.org/10.1016/j.ijrefrig.2008.01.006

Bramwell, R., Brown, P., Galatioto, F., Ingledew, D., Karagianni, E., Maccarthy, J., Mullen, P., Walker, C., Willis, D., Wong, J., Energy, R., & Harris, B. (2023). 2023 Government Greenhouse Gas Conversion Factors for Company Reporting Methodology Paper for Conversion Factors Final Report 2. www.nationalarchives.gov.uk/doc/open-government-licence/

Bre, S. A. P. (2012). The government's standard assessment procedure for energy rating of dwellings. Building Research Establishment, Watford, UK.

Buonomano, A., Calise, F., Palombo, A., & Vicidomini, M. (2019). Transient analysis, exergy and thermo-economic modelling of façade integrated photovoltaic/thermal solar collectors. Renewable Energy, 109–126. https://doi.org/10.1016/j.renene.2017.11.060

Burke, M. J., & Stephens, J. C. (2017). Energy democracy: Goals and policy instruments for sociotechnical transitions. Energy Research and Social Science, 33, 35–48. https://doi.org/10.1016/j.erss.2017.09.024

Calise, F., Cappiello, F. L., Dentice d'Accadia, M., & Vicidomini, M. (2020). Dynamic simulation, energy and economic comparison between BIPV and BIPVT collectors coupled with micro-wind turbines. Energy, 191. https://doi.org/10.1016/j.energy.2019.116439

Carella, A., & D'Orazio, A. (2021). The heat pumps for better urban air quality☆. Sustainable Cities and Society, 75. https://doi.org/10.1016/j.scs.2021.103314

Carroll, P., Chesser, M., & Lyons, P. (2020). Air Source Heat Pumps field studies: A systematic literature review. Renewable and Sustainable Energy Reviews, 134(July), 110275. https://doi.org/10.1016/j.rser.2020.110275

Chen, X., Liu, C., Yang, J., & Chen, J. (2018). Experimental study on R-22, R-427A, R-161 and R-290 in air-source heat pump for space heating at low ambient temperatures. International Journal of Refrigeration, 96, 147–154. https://doi.org/10.1016/j.ijrefrig.2018.08.021

CIBSE. (2019). Guide A: Environmental design (2019). In Design History: A Students' Handbook (Issue May). https://www.cibse.org/knowledge/knowledge-items/detail?id=a0q20000008I79JAAS

Dai, B., Qi, H., Liu, S., Zhong, Z., Li, H., Song, M., Ma, M., & Sun, Z. (2019). Environmental and economical analyses of transcritical CO2 heat pump combined with direct dedicated mechanical subcooling (DMS) for space heating in China. Energy Conversion and Management, 198. https://doi.org/10.1016/j.enconman.2019.01.119

Dannemand, M., Perers, B., & Furbo, S. (2019). Performance of a demonstration solar PVT assisted heat pump system with cold buffer storage and domestic hot water storage tanks. Energy and Buildings, 188–189, 46–57. https://doi.org/10.1016/j.enbuild.2018.12.042

Deng, J., Wei, Q., Liang, M., He, S., & Zhang, H. (2019). Does heat pumps perform energy efficiently as we expected: Field tests and evaluations on various kinds of heat pump systems for space heating. Energy and Buildings, 182, 172–186. https://doi.org/10.1016/j.enbuild.2018.10.014

Du, Y., Wu, J., & Wang, C. (2021). Research on control method of a R290 ASHP under low-temperature heating condition. International Journal of Refrigeration, 129, 60–68. https://doi.org/10.1016/j.ijrefrig.2021.04.026

Fankhauser, S., Smith, S. M., Allen, M., Axelsson, K., Hale, T., Hepburn, C., Kendall, J. M., Khosla, R., Lezaun, J., Mitchell-Larson, E., Obersteiner, M., Rajamani, L., Rickaby, R., Seddon, N., & Wetzer, T. (2022). The meaning of net zero and how to get it right. In Nature Climate Change (Vol. 12, Issue 1, pp. 15–21). Nature Research. https://doi.org/10.1038/s41558-021-01245-w

Gillich, A., Saber, E. M., & Mohareb, E. (2019). Limits and uncertainty for energy efficiency in the UK housing stock. Energy Policy, 133. https://doi.org/10.1016/j.enpol.2019.110889

IEA. (2021). Net Zero by 2050 A Roadmap for the. https://iea.blob.core.windows.net/assets/deebef5d-0c34-4539-9d0c-10b13d840027/NetZeroby2050-ARoadmapfortheGlobalEnergySector_CORR.pdf

Kelly, N. J., Tuohy, P. G., & Hawkes, A. D. (2014). Performance assessment of tariff-based air source heat pump load shifting in a UK detached dwelling featuring phase change-enhanced buffering. Applied Thermal Engineering, 71(2), 809–820. https://doi.org/10.1016/j.applthermaleng.2013.12.019

Klein, S. A. (1988). TRNSYS-A transient system simulation program. University of Wisconsin-Madison, Engineering Experiment Station Report, 12–38.

Le, K. X., Huang, M. J., Shah, N. N., Wilson, C., Artain, P. Mac, Byrne, R., & Hewitt, N. J. (2019). Techno-economic assessment of cascade air-to-water heat pump retrofitted into residential buildings using experimentally validated simulations. Applied Energy, 250, 633–652. https://doi.org/10.1016/j.apenergy.2019.05.041

Li, H., Yang, Q., Xu, Z., Shao, S., Wang, Z., Sun, X., Wang, Y., Xu, C., & Zhao, W. (2021). Impact of water volume on the energy saving potential of air source heat pump systems. International Journal of Refrigeration, 130, 128–139. https://doi.org/10.1016/j.ijrefrig.2021.06.025

Liu, F., Zhu, W., Zhao, J., Ren, J., Groll, E. A., & Cai, Y. (2017). A new method for optimal control of a dual-mode CO2 heat pump with thermal storage. Applied Thermal Engineering, 125, 1123–1132. https://doi.org/10.1016/j.applthermaleng.2017.07.068

Li, Y., Zhang, N., & Ding, Z. (2020). Investigation on the energy performance of using air-source heat pump to charge PCM storage tank. Journal of Energy Storage, 28. https://doi.org/10.1016/j.est.2020.101270

Masip, X., Cazorla-Marín, A., Montagud-Montalvá, C., Marchante, J., Barceló, F., & Corberán, J. M. (2019). Energy and techno-economic assessment of the effect of the coupling between an air source heat pump and the storage tank for sanitary hot water production. Applied Thermal Engineering, 159. https://doi.org/10.1016/j.applthermaleng.2019.113853

Meng, Q., Ren, X., Wang, W., Xiong, C., Li, Y., Xi, Y., & Yang, L. (2021). Reduction in on-off operations of an air source heat pump with active thermal storage and demand response: An experimental case study. Journal of Energy Storage, 36. https://doi.org/10.1016/j.est.2021.102401

Osterman, E., & Stritih, U. (2021). Review on compression heat pump systems with thermal energy storage for heating and cooling of buildings. In Journal of Energy Storage (Vol. 39). Elsevier Ltd. https://doi.org/10.1016/j.est.2021.102569

Remund, J., Müller, S., Kunz, S., & Schilter, C. (2010). Meteonorm handbook part I: software. Retrieved From.

Rony, R. U., Yang, H., Krishnan, S., & Song, J. (2019). Recent advances in transcritical CO 2 (R744) heat pump system: A review. Energies, 12(3), 1–35. https://doi.org/10.3390/en12030457

Shah, N. N., Wilson, C., Huang, M. J., & Hewitt, N. J. (2018). Analysis on field trial of high temperature heat pump integrated with thermal energy storage in domestic retrofit installation. Applied Thermal Engineering, 143, 650–659. https://doi.org/10.1016/j.applthermaleng.2018.07.135

Wang, Z., Li, G., Wang, F., Liu, Z., & Wang, M. (2020). Performance analysis and operation optimization of air-to-water CO2 heat pump with phase change thermal storage. Energy and Buildings, 209. https://doi.org/10.1016/j.enbuild.2019.109738

Wang, Z., Song, M., Wang, F., Ma, Z., & Lin, Q. (2018). Experimental investigation and seasonal performance assessment of a frost-free ASHP system with radiant floor heating. Energy and Buildings, 179, 200–212. https://doi.org/10.1016/j.enbuild.2018.09.019

Wu, P., Wang, Z., Li, X., Xu, Z., Yang, Y., & Yang, Q. (2020). Energy-saving analysis of air source heat pump integrated with a water storage tank for heating applications. Building and Environment, 180. https://doi.org/10.1016/j.buildenv.2020.107029

Yıldız, A., & Yıldırım, R. (2021). Investigation of using R134a, R1234yf and R513A as refrigerant in a heat pump. International Journal of Environmental Science and Technology, 18(5), 1201–1210. https://doi.org/10.1007/s13762-020-02857-z

#57: Design, production and thermodynamic analysis of solar energy supported, nanofluid integrated thermoelectric vaccine cabinet

Pınar Mert CUCE[1*], Erdem CUCE[2], Tamer GUCLU[3]

1 Recep Tayyip Erdogan University, Engineering and Architecture Faculty, Architecture, 53100 Rize, Turkiye, mertcuce@gmail.com*
2 Recep Tayyip Erdogan University, Engineering and Architecture Faculty, Mechanical Engineering, 53100 Rize, Turkiye, erdemcuce@gmail.com
3 Bayburt University, Engineering Faculty, Mechanical Engineering, 69000 Bayburt, Turkiye, tamerguclu@bayburt.edu.tr

Abstract: Thermoelectric coolers (TECs) are becoming the focus of attention of researchers on a global scale due to their various advantages such as quiet and vibration-free operation and the absence of moving parts, as well as being energy efficient and compact. It is frequently preferred especially for portable cooler applications. This study is about the design, fabrication, and thermodynamic analysis of a solar-assisted nanofluid integrated thermoelectric vaccine cabinet. It is aimed to investigate the effects of using nanofluids as refrigerants in portable thermoelectric vaccine cabinet applications on basic performance parameters. For this purpose, it is planned to design and manufacture a cooling cabinet. Then, the Peltier assembly, with a water-cooled block integrated on its hot surface, will be placed from the cooling cabinet, and a water-to-air heat exchanger will be used to transfer the heat taken from the hot surface of the Peltier to the environment with the help of the refrigerant. Hybrid nanofluids will be used as refrigerants in the system. PV panels will be placed on the upper surface of the cooling cabinet in order to benefit from solar energy. In order to store the electrical power obtained from the PV panel, a battery will be located at the bottom of the cabinet. Cooled cabin temperatures will be observed with experimental studies, and the results will be compared with the situation where no nanofluid is used as the reference situation.

Keywords: Thermoelectric cooling, nanofluids, cooling of vaccines, electrical efficiency

1. INTRODUCTION

Thermoelectric coolers work silently and vibration-free, do not contain any stationary parts, suitable for automation, have a long life and have a compact structure. Thanks to these advantages, they have a wide range of uses, from in-car refrigerators to organ and drug transport boxes (Guclu, 2019). It consists of P-type and N-type semiconductors placed between two ceramic plates. These semiconductors are connected electrically in series and thermally in parallel to form a circuit, and if current is applied to this circuit, one of the ceramic plate surfaces begins to cool and the other begins to heat up. This phenomenon is called the Peltier effect, and thermoelectric coolers are also specifically called Peltier. The appearance of a typical thermoelectric cooler is as in Figure 1 (Enescu, 2014).

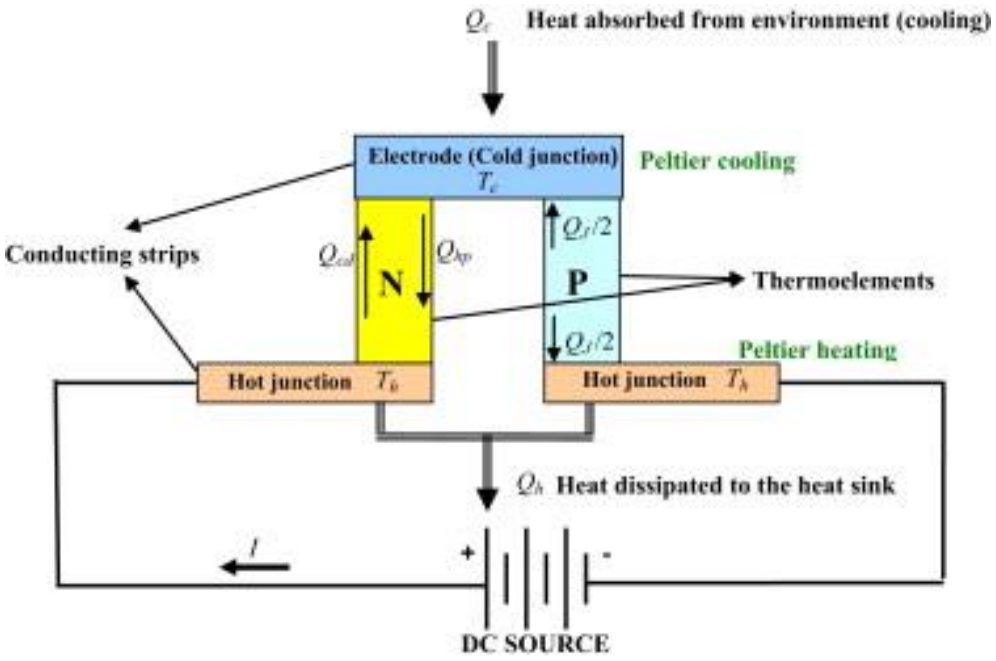

Figure 1 Schematic description of thermoelectric cooler (Enescu, 2014)

The most important advantage of thermoelectric coolers compared to conventional cooling systems is that they do not contain large, space-consuming, and noisy parts. However, the coefficient of efficiency (COP) values of thermoelectric coolers is low (Sadighi Dizaji, 2016). This situation limits the usage areas of thermoelectric cooling applications (Sadighi Dizaji, 2016). Therefore, especially in recent years, various new designs are implemented, such as circulating a refrigerant to sweep more heat from the hot surface of the Peltier (Sohel, 2014). Thus, the cold surface can drop to lower temperatures earlier [6]. With this method, the efficiency of thermoelectric coolers can be increased significantly. As another method, Cuce et al. (Cuce, 2020) showed that by using various nanofluids in various mass mixing ratios instead of base liquid as refrigerant, their efficiency can be increased up to 55% compared to cooling with base fluid. Another study is Cuce et al. (Cuce, 2022) showed that the use of hybrid nanofluids is a more efficient method as it will accelerate the heat transfer.

Cold chain is the special storage conditions created during the storage, transportation and presentation stages in order to ensure that the products that are sensitive to temperature are kept in the temperature range determined by the manufacturer for the healthy preservation of the product from the production stage until they are packaged and delivered to the end user. There are many products in a wide range from the food industry to health products subject to cold chain application. It is extremely important that the chain continues undisturbed until the final consumer, since health products will lose their effectiveness and food products will lose their freshness and deteriorate if the cold chain ring is broken during storage, transportation and distribution of these products (Küçüktürkmen, 2018). One of the most important products subject to the cold chain is vaccines. Especially with the new-type coronavirus disease, it has been revealed that the storage, transportation and delivery of the vaccines at the determined temperatures is extremely important for the effectiveness of the vaccine (Çoban, 2022). A well-planned transportation route needs to be planned for vaccines in different conditions and with different shelf lives (Ay, 2022). In this regard, delivery of vaccines from health institutions, especially to the elderly, bedridden, or incapable of access to a health institution, creates significant problems, and in this process, problems such as deterioration or decreased effectiveness of vaccines may occur.

2. MATERIAL AND METHODS

First, a cooling cabinet of 20 cm width, 30 cm length and 20 cm depth was produced by using 6 mm thick XPS insulation material. In determining the cabinet dimensions, it was taken into account that the cabinet was designed for portable

applications. The designed and manufactured cooling cabinet consists of four sections: injector section, ampoule for injection section, battery and inverter section, and circulation pump and fan section. The system is designed to have a capacity of 100 ampoule for injection and 100 injectors. The appearance of the vaccine cabinet is shown in Figure 2.

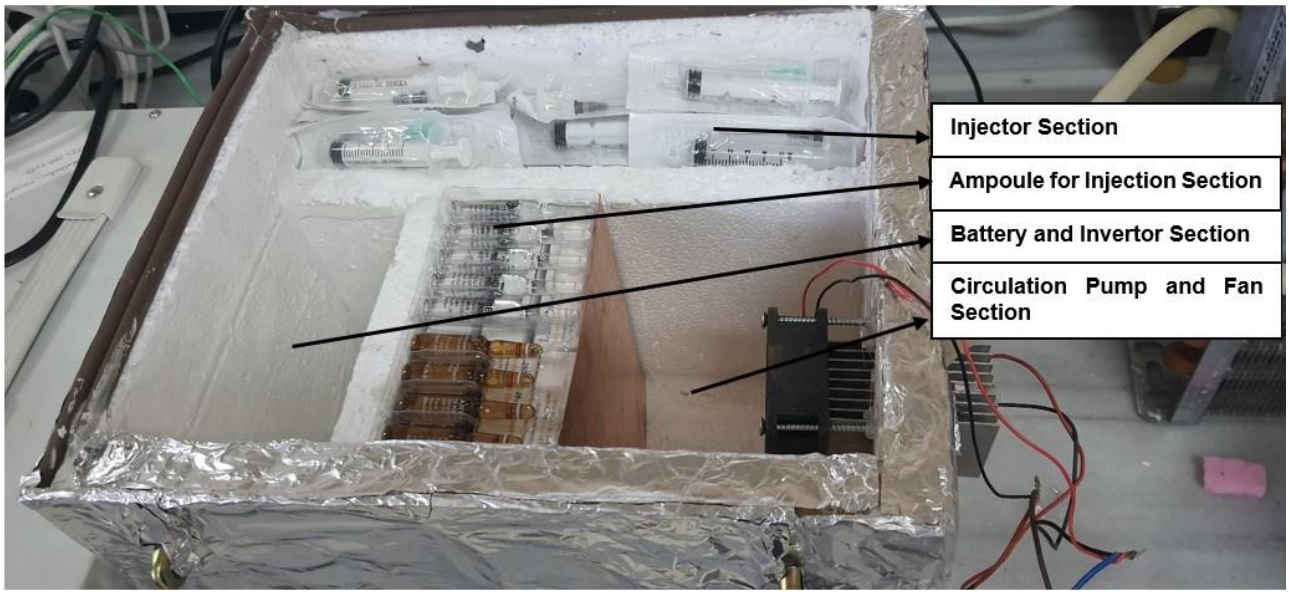

Figure 2 Schematic description of vaccine cabinet

A PV panel is placed on the upper surface of the vaccine cabinet in order to benefit from solar energy. Thus, a part of the electrical energy required by the vaccine cabinet is met from solar energy, thus ensuring energy efficiency. In order to store the electrical power obtained from the PV panel, a battery is located at the bottom of the cabinet. Aluminium heatsink and a fan are used on the cold side of the Peltier placed from the side surface of the vaccine cabinet. A liquid-cooled block is used on the hot side of the Peltier and an aluminium heatsink is used on the other surface of this block to further accelerate the heat dissipation. A small circulation pump is located under the Peltier section to circulate the refrigerant. 2% by mass of Al_2O_3-TiO_2-SiO_2-Water nanofluid was used as the refrigerant in the system. During the experimental studies, vaccine cabinet temperature, cold and hot heatsink temperatures, outdoor temperature and refrigerant temperature were observed. The schematic representation of the experimental setup is as in Figure 3. During the experiment, a voltage of 9 volts was applied to the system by means of a regulated power supply, and it was observed that the system drew 7 amps of current.

Figure 3 Schematic description experimental setup

3. RESULTS

During the experiments, the time when the cabin temperature converged to 4 °C, which is the refrigerator cabinet temperature, was taken into account as the test period. After about an hour, it was observed that the indoor temperature reached equilibrium around 4 °C. At the end of this period, the cold heatsink temperature was observed to be in the range of 1-2 °C, and the hot heatsink temperature was approximately 22 °C. Obtained results are shown in Figure 4.

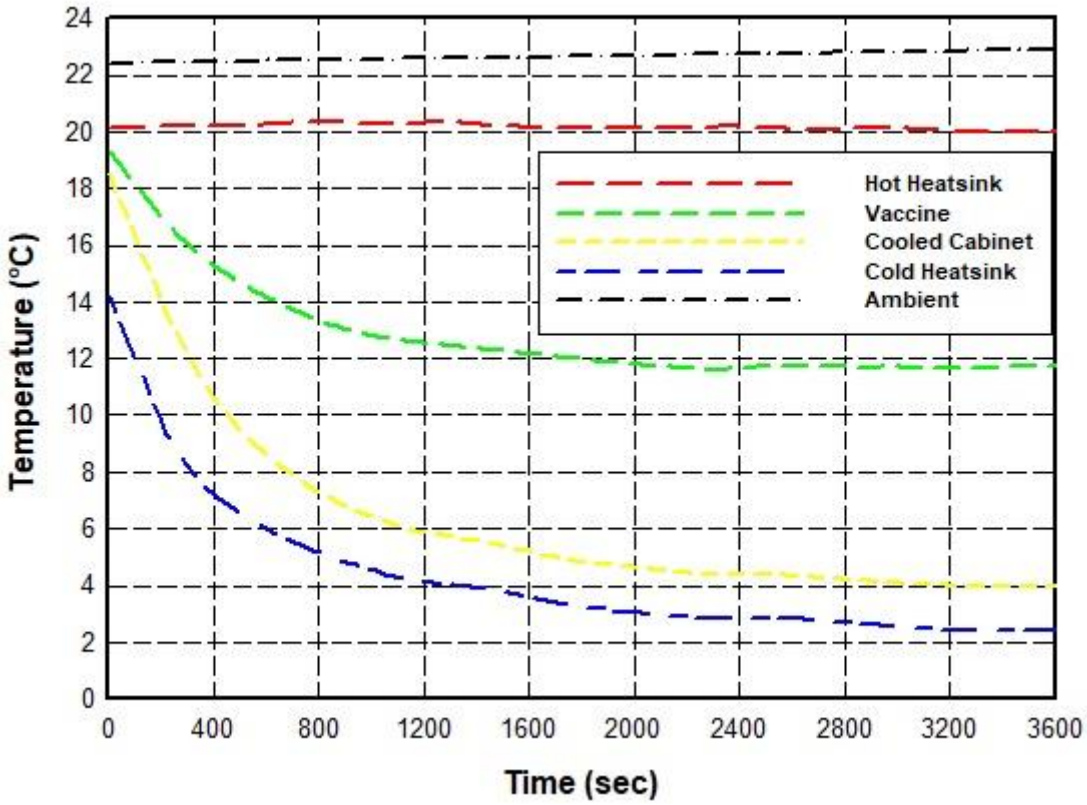

Figure 4 Experimental results

The average COP value of the system was calculated as 0.51 and shown in Figure 5.

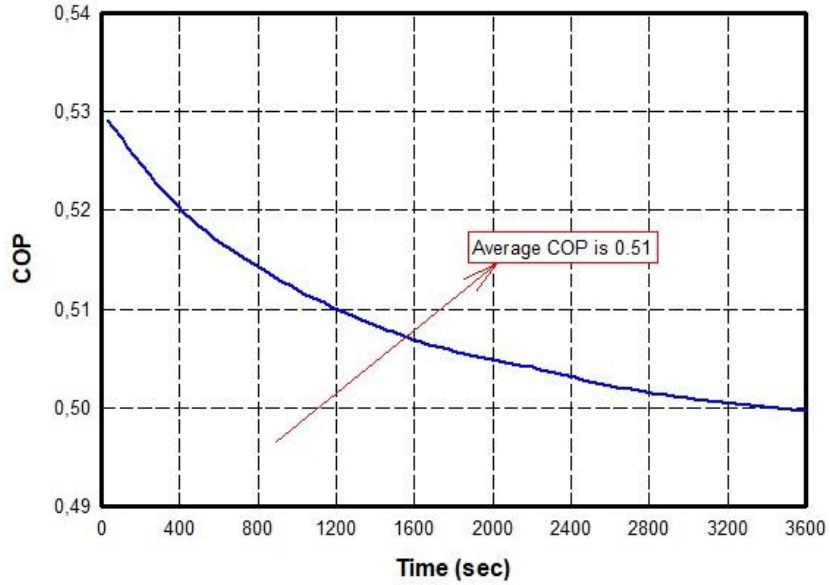

Figure 5 COP values of the system

4. CONCLUSION

In this study, a new type of solar powered, nanofluid integrated thermoelectric vaccine cabinet is presented to develop a solution to the stated problem. Thus, it is aimed to produce a thermoelectric vaccine cabinet that contributes to the reduction of carbon emissions with the use of renewable energy sources, in a fast, easy, practical and economically efficient way, without spoiling and losing the effectiveness of the vaccines to the users living in rural areas.

5. REFERENCES

M. Ay, B. Akdoğan, E. Morrice Fidan, and L. Özbakır, “A two-echelon model for the location-routing problem: distribution of Covid-19 vaccines,” Pamukkale Univ. J. Eng. Sci., vol. 28, no. 4, pp. 559–568, 2022, doi: 10.5505/pajes.2022.23316.

P. M. Cuce, T. Guclu, and E. Cuce, “The Effect of Nanofluid Usage on Electricity Consumption in Thermoelectric Refrigeration Application: An Experimental Study,” GAZİ J. Eng. Sci., vol. 8, pp. 228–236, 2022, doi: 10.30855/gmbd.0705006.

E. Cuce, T. Guclu, and P. M. Cuce, “Improving thermal performance of thermoelectric coolers (TECs) through a nanofluid driven water to air heat exchanger design: An experimental research,” Energy Convers. Manag., vol. 214, no. April, p. 112893, 2020, doi: 10.1016/j.enconman.2020.112893.

E. Çoban et al., “Covid-19 AşisiÇizelgelemeProblemi: TermalNakliyeKonteynerleri Uygulamasi Covid-19 Vaccine Scheduling Problem: an Application of Thermal Shipping Containers,” J. Ind. Eng., vol. 33, no. 1, pp. 177–193, 2022, [Online]. Available: https://orcid.org/0000-0002-3818-1957.

T. Guclu and E. Cuce, “Thermoelectric Coolers (TECs): From Theory to Practice,” J. Electron. Mater., vol. 48, no. 1, pp. 211–230, 2019, doi: 10.1007/s11664-018-6753-0.

D. Enescu and E. O. Virjoghe, “A review on thermoelectric cooling parameters and performance,” Renew. Sustain. Energy Rev., vol. 38, pp. 903–916, 2014, doi: 10.1016/j.rser.2014.07.045.

B. Küçüktürkmen and A. Bozkir, “Drugs subject to special storage conditions or cold chain and evaluation in terms of applications,” Turk Hij. ve Deney. Biyol. Derg., vol. 75, no. 3, pp. 305–322, 2018, doi: 10.5505/TurkHijyen.2018.67674.

P. Mert, E. Cuce, T. Guclu, S. Shaik, and S. Alshahrani, “Effect of using hybrid nanofluids as a coolant on the thermal performance of portable thermoelectric refrigerators,” Sustain. Energy Technol. Assessments, vol. 53, no. PC, p. 102685, 2022, doi: 10.1016/j.seta.2022.102685.

H. Sadighi Dizaji, S. Jafarmadar, S. Khalilarya, and A. Moosavi, “An exhaustive experimental study of a novel air-water based thermoelectric cooling unit,” Appl. Energy, vol. 181, pp. 357–366, 2016, doi: 10.1016/j.apenergy.2016.08.074.

M. R. Sohel, S. S. Khaleduzzaman, R. Saidur, A. Hepbasli, M. F. M. Sabri, and I. M. Mahbubul, “An experimental investigation of heat transfer enhancement of a minichannel heat sink using Al2O3-H2O nanofluid,” Int. J. Heat Mass Transf., vol. 74, pp. 164–172, 2014, doi: 10.1016/j.ijheatmasstransfer.2014.03.010.

#58: Design, production, and performance analysis of a pyramid-type solar desalination system: an experimental study

Pınar Mert CUCE[1*], Erdem CUCE[2], Tamer GUCLU[3]

1 Recep Tayyip Erdogan University, Engineering and Architecture Faculty, Architecture, 53100 Rize, Turkiye, mertcuce@gmail.com*
2 Recep Tayyip Erdogan University, Engineering and Architecture Faculty, Mechanical Engineering, 53100 Rize, Turkiye, erdemcuce@gmail.com
3 Bayburt University, Engineering Faculty, Mechanical Engineering, 69000 Bayburt, Turkiye, tamerguclu@bayburt.edu.tr

Abstract: With the rapid increase in the world population and the rapid decrease in clean water resources, access to clean water is rapidly progressing to become a worldwide problem. Moreover, global warming, especially caused by fossil fuel-based energy production, triggers the rapid depletion of water resources. In addition to being a basic nutrient, water is a basic need in almost every sector. The increase in the rate of industrialization and population density also stands out as important factors in the rapid depletion of clean water resources. According to international research, by 2030, almost half of the world's population will have problems in accessing clean water. For this reason, obtaining clean water, especially by using renewable energy sources, is of global importance. In this context, solar desalination systems come to the fore. Solar-assisted desalination systems attract attention as an environmentally friendly technology as well as being economical and sustainable. Especially in rural areas where access to traditional energy sources such as electricity grids, batteries or fossil fuel energy sources is limited, solar-assisted desalination systems can meet the average freshwater requirement of a family. Although solar-assisted desalination systems are economically feasible, the water production cost is around $/L 0.03 and still needs improvement compared to large-scale production systems. For this reason, even minor improvements in the efficiency of these systems are important. In this study, the design, production, and performance analysis of a pyramid-type solar desalination system will be made. With the tests to be performed at different radiation values, the daily production amounts of the produced system will be observed.

Keywords: Solar desalination, solar still, water productivity, fresh water

1. INTRODUCTION

The rapid depletion of energy resources around the world and fossil fuels that are insufficient to respond to the increasing energy demand have pushed scientists to search for new energy sources (P. M. Cuce et al. 2021). Environmental disasters caused by fossil-based energy sources is another important issue that causes the importance of clean, renewable energy sources to increase. In this respect, the use of renewable and environmentally friendly energy sources such as solar, wind and geothermal has become widespread, especially in recent decades (E. Cuce, Cuce, Guclu, et al. 2020). Among these renewable energy sources, solar energy is one of the most widely used sources worldwide. It has a wide range of uses from heating-air conditioning applications to drying-cooking applications. Another application where solar energy is widely used is solar water treatment systems (Bait and Si-Ameur 2018). Because meeting the need for clean water is the most important condition for the continuation of life on Earth. However, desalination processes are especially important, since salty water sources constitute a very large part of the water resources worldwide (Jani and Modi 2018). According to the report of the United Nations, clean water resources are insufficient to meet the demand worldwide and water scarcity is expected soon. On the other hand, it is important to obtain clean water with renewable energy sources in order not to accelerate the consumption of other energy sources while obtaining clean water. Solar-powered desalination systems come to the fore in this regard (Darawsheh, Islam, and Banat 2019).

Desalination is one of the oldest methods used for water purification purposes. In its most general terms, it is the process of removing minerals from water (Panchal 2016). Solar distillation systems are simple and efficient setups. Water placed in a reservoir is evaporated by solar energy and collected on a glass surface. The water collected on the surface starts to condense and the condensed water is collected in another chamber (Al-Hayeka and Badran 2004). Thus, microorganisms and heavy metals in the water are separated. However, since the beneficial minerals in the water decompose currently, it is necessary to add minerals again. Solar distillation systems are easy and economical to install. They do not require much maintenance and can be produced in sizes to suit the needs (El-Sebaii and El-Bialy 2015).

Solar distillation systems are divided into two categories, as shown in Figure 1, direct and indirect, depending on the working principle (Sharon and Reddy 2015). Indirect systems consist of two different subsystems. Systems, where evaporation and condensation occur on the same mechanism, are called direct systems and are ideal for low usage requirements. The number of slopes of the glass surface used can be produced in various types depending on the installation method (M. and Yadav 2017).

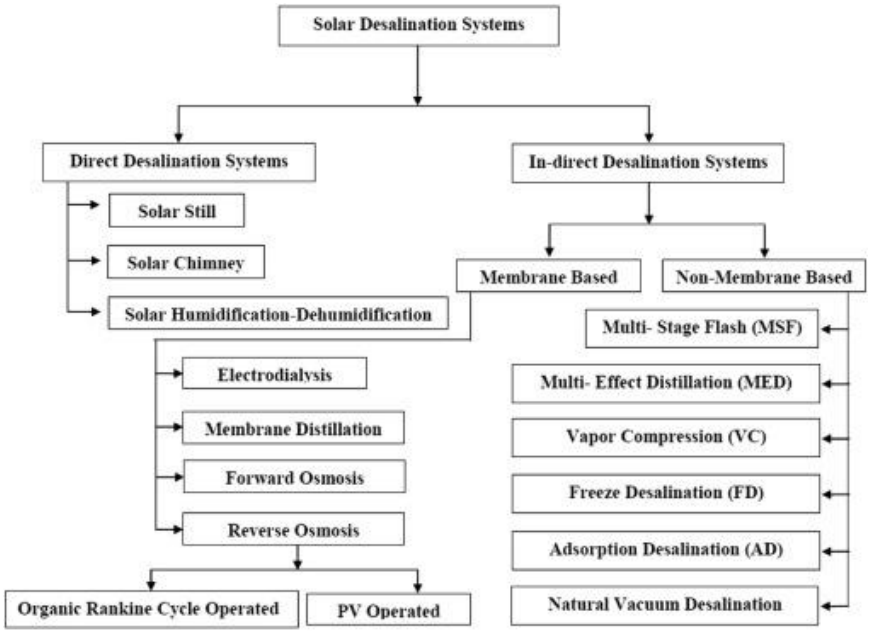

Figure 1 Characterization of solar desalination systems (Sharon and Reddy 2015)

The applications of direct solar desalination systems are frequently mentioned in the literature. Researchers are especially designing to increase the efficiency of these methods. In this respect, performance-enhancing methods such as inclination angle, thermal storage material, and phase change material integration are emphasized. Cuce et al. (E. Cuce, Cuce, Saxena, et al. 2020) experimentally investigated water distillation performance by designing and manufacturing a solar water distillation system with sensible energy storage and passive reflective support. A cooling mechanism on the glass surface and insulation around the chamber was not used in the system. In the tests carried out on sunny days in July, they managed to obtain an average of 2200 ml of distilled water per day. In the second phase of the study, Cuce et al. (P. M. Cuce, Cuce, and Tonyali 2021) observed the performance of the system as a result of the improvements they made on

the experimental setup. In this context, the chamber is insulated, and a spray cooling mechanism is used on the glass surface. As a result of the experiments carried out in similar climatic conditions, it was observed that the efficiency increased up to 110% compared to the previous system.

2. MATERIAL AND METHODS

Firstly, a 60X60 cm and 20 cm deep chamber was produced by using 1 mm thick iron sheet plate. A water discharge channel is formed from the lower corner of the chamber. The chamber surface and bottom are painted with black matte paint in order to absorb heat more. In order to accelerate the evaporation time by minimizing the heat losses from the body, the chamber is insulated from all surfaces except the glass surface. XPS insulation element is used on the bottom surface and glass wool is used on the side surfaces as insulation material. The pyramid-type was chosen as the glass surface. In this preference, it is aimed to increase the evaporation rate by increasing the surface area. Glass surfaces are formed by joining four triangular glass plates with a height of 30 cm and a floor area of 50 cm. Thanks to the inclined channel formed at the bottom of the glass surfaces, the water condensed on the surface is collected and reached the discharge channel. Silicone is used in joining the glass surfaces to each other and joining the glass surface and the chamber. Thus, air tightness is ensured, and evaporation is prevented from slowing down. The general view of the experimental setup is shown in Figure 2. The experimental setup consists of an insulated chamber, pyramid-type glass surface, data logger, pyranometer, temperature sensors and a computer, as shown in Figure 2.

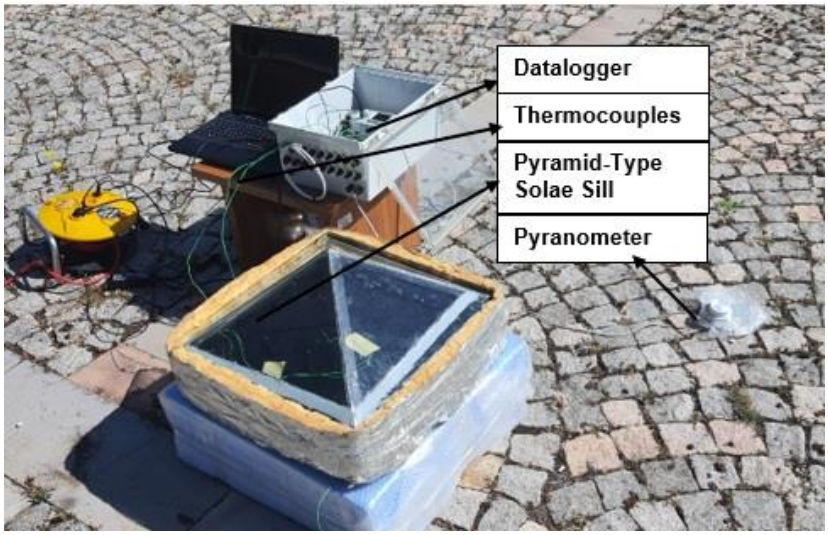

Figure 2 Schematic description of experimental setup

The experimental setup was established at the Recep Tayyip Erdoğan University Low/Zero Carbon Energy Technologies Laboratory. Experiments were carried out in Bayburt University Faculty of Engineering in August. In the outdoor tests, days with sunny and clear weather conditions were preferred. During the experiments, outdoor temperature, chamber bottom temperature, chamber temperature, glass outer surface temperature and radiation amount with the help of pyranometer were observed using K-type thermocouples. The distilled water was collected and measured in an insulated container. The condensation on the glass surface and the inclined channel design that allows the condensed water to reach the discharge channel and the distilled water are shown in Figure 3.

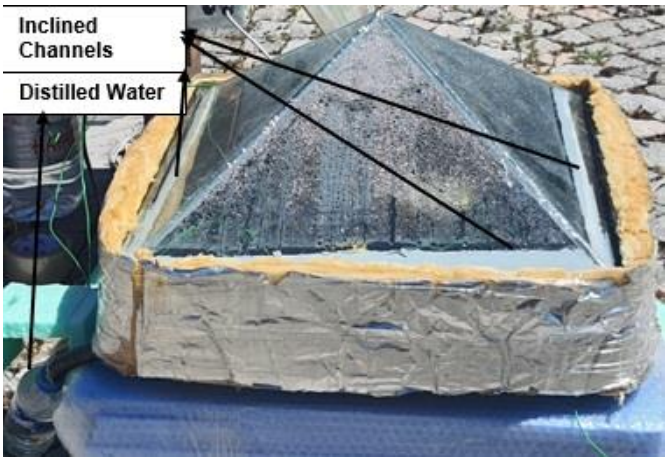

Figure 3 Inclined channel design

3. RESULTS

The period from 9:30 to 18:00 in the morning was taken into account as the experimental period. During this period, the outside temperature, glass outer surface temperature, basin temperature, water temperature in the basin and the amount of radiation were observed. Specified temperature and radiation values are shown in Figure 4. At the end of the experiment, it was observed that 1085 ml of distilled water was obtained from the system.

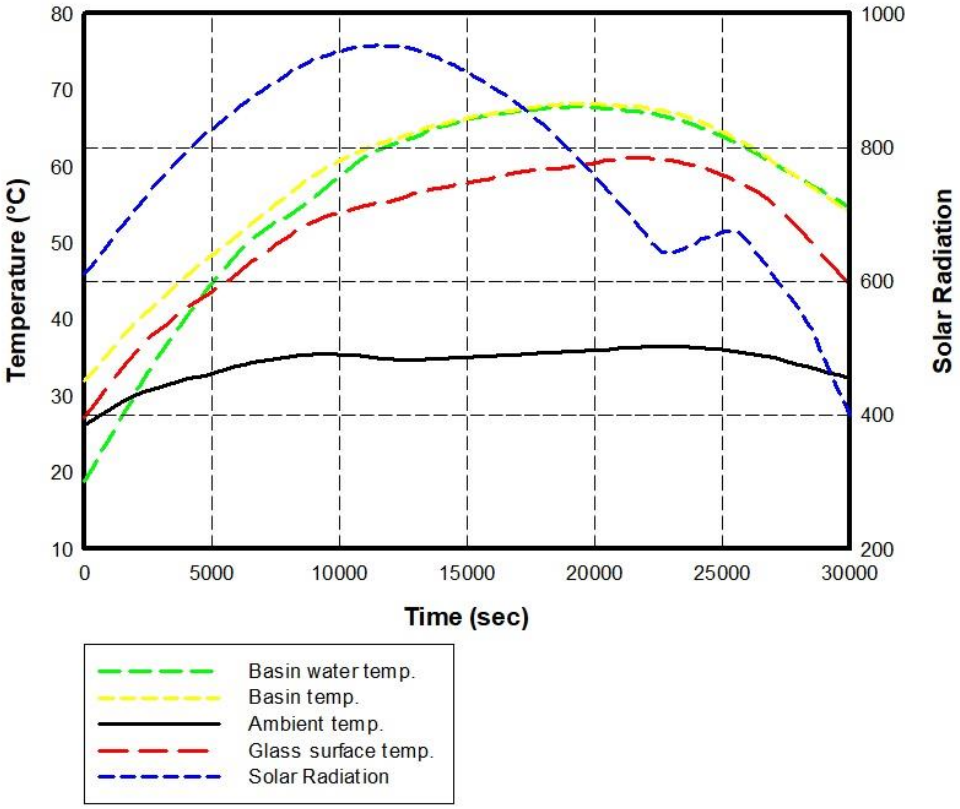

Figure 4 Measurements of performance parameters

4. CONCLUSION

In this study, the design and production of solar water distillation system was carried out and its experimental efficiency was investigated. For this purpose, a pyramid-type solar distillation system was designed, manufactured and experimentally tested. According to the experimental results it was observed that 1085 ml of distilled water was obtained from the system.

5. REFERENCES

Al-Hayeka, Imad, and Omar O. Badran. 2004. “The Effect of Using Different Designs of Solar Stills on Water Distillation.” *Desalination* 169(2): 121–27.

Bait, Omar, and Mohamed Si-Ameur. 2018. “Enhanced Heat and Mass Transfer in Solar Stills Using Nanofluids: A Review.” *Solar Energy* 170(March): 694–722. https://doi.org/10.1016/j.solener.2018.06.020.

Cuce, Erdem, Pinar Mert Cuce, Abhishek Saxena, et al. 2020. “Performance Analysis of a Novel Solar Desalination System – Part 1: The Unit with Sensible Energy Storage and Booster Reflector without Thermal Insulation and Cooling System.” *Sustainable Energy Technologies and Assessments* 37(September 2019): 100566.

Cuce, Erdem, Pinar Mert Cuce, Tamer Guclu, and Ahmet Burhaneddin Besir. 2020. “On the Use of Nanofluids in Solar Energy Applications.” *Journal of Thermal Science* 29(3): 513–34.

Cuce, Pinar Mert, Erdem Cuce, Tamer Guclu, and Veysel Demirci. 2021. “Energy Saving Aspects of Green Facades: Current Applications and Challenges.” *Green Building & Construction Economics*: 1–11.

Cuce, Pinar Mert, Erdem Cuce, and Abdulkadir Tonyali. 2021. “Performance Analysis of a Novel Solar Desalination System – Part 2: The Unit with Sensible Energy Storage with Thermal Insulation and Cooling System.” *Sustainable Energy*

Technologies and Assessments 48(October): 101674.

Darawsheh, I., M. D. Islam, and F. Banat. 2019. “Experimental Characterization of a Solar Powered MSF Desalination Process Performance.” *Thermal Science and Engineering Progress* 10(January): 154–62.

El-Sebaii, A. A., and E. El-Bialy. 2015. “Advanced Designs of Solar Desalination Systems: A Review.” *Renewable and Sustainable Energy Reviews* 49: 1198–1212.

Jani, Hardik K., and Kalpesh V. Modi. 2018. “A Review on Numerous Means of Enhancing Heat Transfer Rate in Solar-Thermal Based Desalination Devices.” *Renewable and Sustainable Energy Reviews* 93(May): 302–17.

M., Chandrashekara, and Avadhesh Yadav. 2017. “Water Desalination System Using Solar Heat: A Review.” *Renewable and Sustainable Energy Reviews* 67: 1308–30.

Panchal, Hitesh N. 2016. “Use of Thermal Energy Storage Materials for Enhancement in Distillate Output of Solar Still: A Review.” *Renewable and Sustainable Energy Reviews* 61: 86–96.

Sharon, H., and K. S. Reddy. 2015. “A Review of Solar Energy Driven Desalination Technologies.” *Renewable and Sustainable Energy Reviews* 41: 1080–1118.

#62: Experimental researches on the operation modes for a water source heat pump system to expand heating operation range

Gilbong LEE[1], Sun Ik NA[2], Kibong KIM[3], Kichang CHANG[4], Eunseok WANG[5], Junhyun CHO[6], Bongsoo CHOI[7], Bong Seong OH[8], Jaehyeok HEO[9]

[1]Korea Institute of Energy Research, 152 Gajeong-ro, Yuseong-gu, Daejeon, Republic of Korea, giblee@kier.re.kr
[2]Korea Institute of Energy Research, 152 Gajeong-ro, Yuseong-gu, Daejeon, Republic of Korea, happy8earth@kier.re.kr
[3]Korea Institute of Energy Research, 152 Gajeong-ro, Yuseong-gu, Daejeon, Republic of Korea, kimkibong@kier.re.kr
[4]Korea Institute of Energy Research, 152 Gajeong-ro, Yuseong-gu, Daejeon, Republic of Korea, kcchang@kier.re.kr
[5]Korea Institute of Energy Research, 152 Gajeong-ro, Yuseong-gu, Daejeon, Republic of Korea, eswang@kier.re.kr
[6]Korea Institute of Energy Research, 152 Gajeong-ro, Yuseong-gu, Daejeon, Republic of Korea, jhcho@kier.re.kr
[7]Korea Institute of Energy Research, 152 Gajeong-ro, Yuseong-gu, Daejeon, Republic of Korea, cbs@kier.re.kr
[8]Korea Institute of Energy Research, 152 Gajeong-ro, Yuseong-gu, Daejeon, Republic of Korea, bongseongoh@kier.re.kr
[9]Korea Institute of Energy Research, 152 Gajeong-ro, Yuseong-gu, Daejeon, Republic of Korea, jhheo@kier.re.kr

Abstract: Recently, since water heat energy was included in renewable energy in Korea, interest in water source heat pumps for space cooling and heating has increased. Since the temperature of the water is lower than the ambient temperature in summer and higher in winter, a water source heat pump has an advantage in COP over an air source system. However, when the water temperature drops in winter, the operation of a water source heat pump becomes limited due to the risk of freezing in heat exchangers. In this study, we analyse the heating operation characteristics according to the change in the temperature of the water and propose operation modes to overcome the drawbacks in heating operation. A test loop of 20 kWth was constructed. As operation modes for utilizing low-temperature water sources, reverse cycle operation, heat storage tank-associated operation, and heat source compensation operation were derived. Among them, test results and operation characteristics analysis for heat source compensation operation are presented. These results tested in the laboratory can be used to design the optimal operation modes for water source heat pumps when applied to actual buildings in the future.

Keywords: water source, heat pump, heating operation

1. INTRODUCTION

As a heat source for heat pump system, water source has higher heat capacity and smaller temperature change than air heat, thus providing more stable operation. In summer, the temperature of the water source is lower than the outside air temperature. This makes the cooling COP of water source heat pump higher than that of air source one. In addition, free cooling is possible by just using water heat during the winter seasons. Therefore, water source certainly has an advantage in COP over air source in cooling operation. In the case of heating operation in winter, water source part is located in the evaporator and undergoes temperature decrease. If the inlet water temperature falls below a certain level, freezing could occur in the evaporator heat exchanger. In general, when operating a heating operation with a water source heat pump, the minimum water temperature is set around 5 to 10 °C to limit operation. However, in Korea, the water temperature in the winter drops below 5 °C. If the heat pump operation should be stopped due to the risk of freezing, the heating cannot be supplied by heat pump only. Therefore, additional heating equipment is required. Therefore, in order for a water source heat pump to respond sufficiently to both cooling and heating, it is necessary to develop robust operation method for heating operation at low water temperatures.

2. OPERATION METHODS FOR HEATING AT LOW WATER TEMPERATURE

When the evaporator temperature drops below freezing, frost or ice forms on the surface of the heat exchanger. In the case of an air source heat pump, frost is removed through a reverse cycle operation or a hot gas bypass operation. Various operation logics related to defrost of air source heat pump have been developed. However, in the case of water source, little research on de-icing operation has been conducted. Water source system is more suitable for central, high-capacity heat pumps that cover air conditioning for the entire the building since considerable amount of investment is required to build infrastructure for water intake. Since heat storage systems are generally equipped in building air conditioning systems, the heating operation methods were developed including heat storage systems. In the case of reverse cycle operation, in the case of large-capacity systems, the water circuit switching method is generally used. So only the water circuit switching method was considered in this study. The below table shows several operation methods to extend the heating operation in case of low water source temperature. In addition to the reverse cycle, if the temperature of the evaporator heat source water is heated with other heat source, freezing can be delayed. In this study, this heat source compensation method was adopted to experimentally test the effect of improving low temperature heating of water source heat pump.

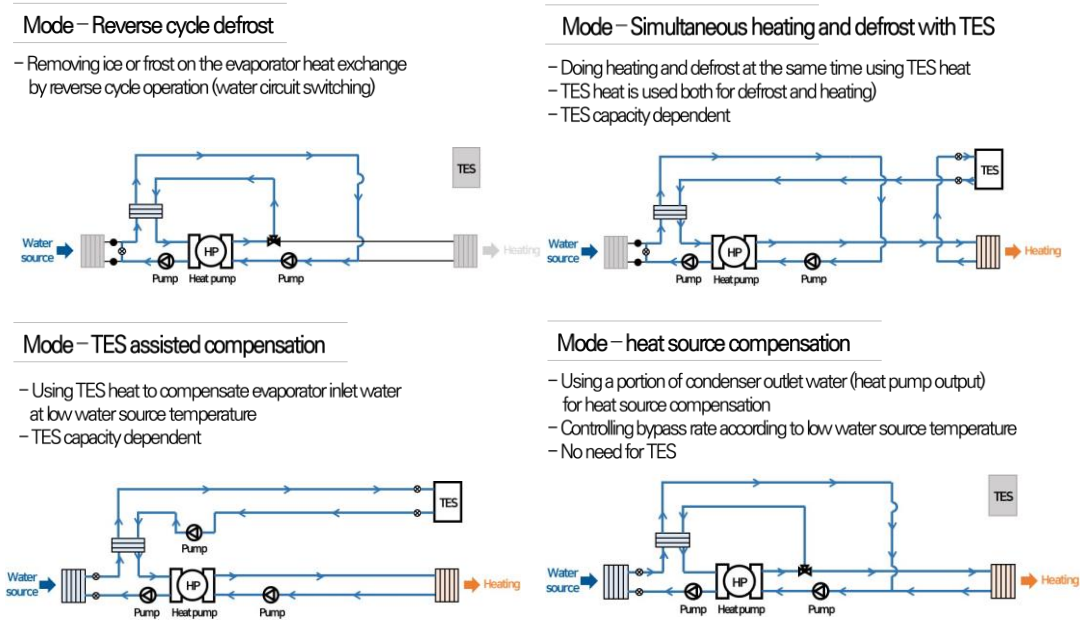

Figure 1 Various operation modes for the enhancement of heating at low water source temperature

3. LAYOUT OF TEST APPARATUS

A test loop was constructed to evaluate heating performance of water source heat pump system at low water temperature conditions in the winter (Figure 2). As shown in figure 2, the test loop consists of a heat source part which simulates river water, operation control part which has automatic valves and heat pump to change operation modes and thermal load part which stores hot and cold water and simulates the heating load at the place of interests. The heat source part has a heat storage tank (about 2 m^3), a cleaning device to prevent fouling, and a heat exchanger which transfers water source heat to the heat pump. The operation control unit consists of a heat pump to produce hot water, six 3-way valves that can automatically change the operation modes and correspond water switching method, and two control valves. The refrigerant was R-410A. On the thermal load part, two heat storage tanks (about 1.5 m^3) that store hot and cold water were installed,

and a partition wall was installed inside the heat storage tank to create temperature stratification in both the inlet and outlet part of the heat storage tank. In addition, FCU (Fan Coil Unit) was installed to simulate the load side. Figure 2(b) shows a river water heat pump experimental device installed to test the performance of a heat pump. The design capacity was 20 kW. Each operation mode in this test loop is shown in Figure 3. Figure 3(a) and (b) show the valve location and flow path for cooling and heating operation. The heat source compensation operation, which is one of the methods to utilize low-temperature water source in winter, is shown in Figure 3(d), and the bypass valve is automatically controlled by the water outlet temperature of the evaporator.

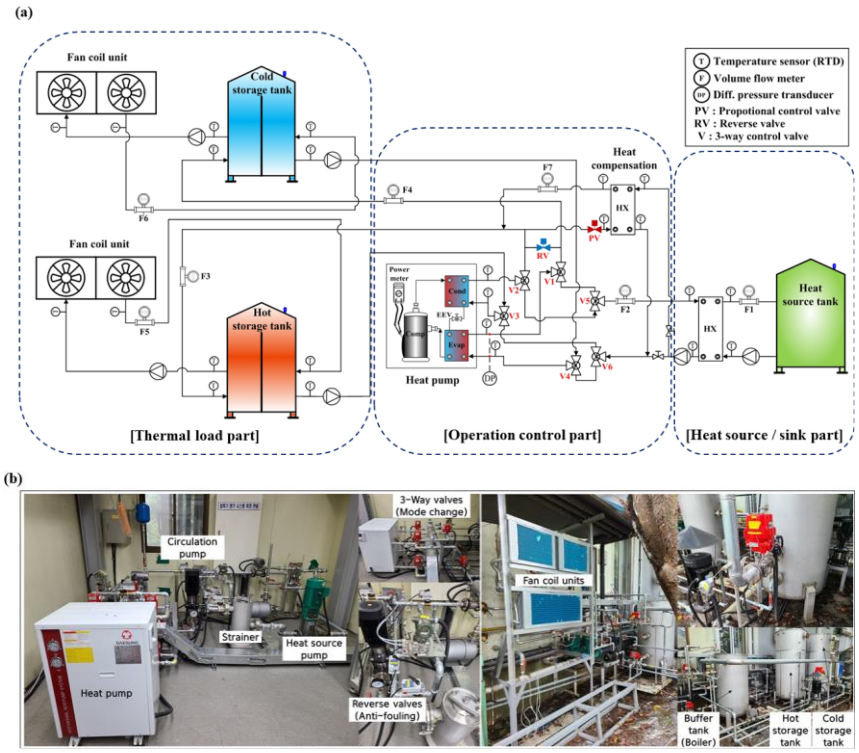

Figure 2 Experimental set-up for water-circuit type water heat source heat pump: (a) schematic of experimental set-up, (b) experimental equipment of 20kW scale water heat source heat pump.

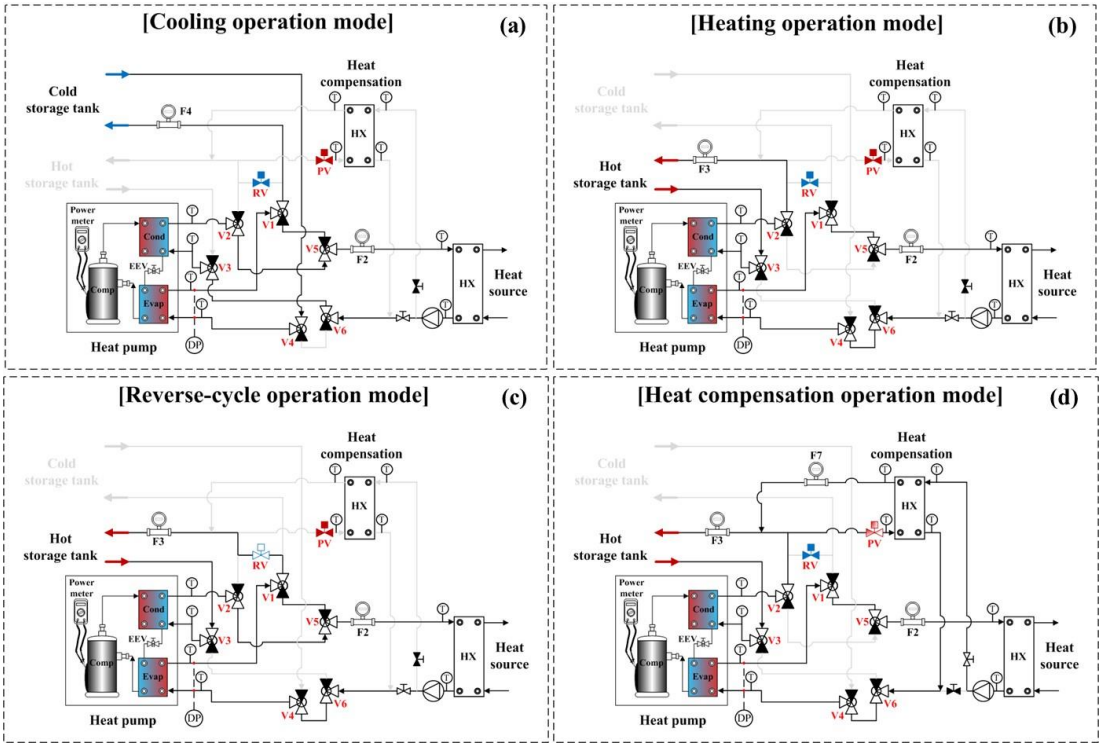

Figure 3 Water-circuit type by each mode: (a) cooling operation mode, (b) heating operation mode, (c) reverse-cycle operation mode, (d) heat compensation operation mode.

4. TEST RESULTS OF HEAT SOURCE COMPENSATION OPERATION

As the first step of the heat source compensation operation test for low-temperature water utilization, an experiment was conducted to find operation characteristics when freezing occurred. By observing the outlet temperature and operation stability of the evaporator, the water source temperature was decreased while keeping the compressor operation constant. The figure below is a graph of changes in operating conditions at water source temperature of 3.8°C. At this point, the water outlet temperature of the evaporator became -1°C and freezing occurred for the first time. The ice formation showed a rapid change rather than a slow progress, and when the ice occurred, the flow rate decreased rapidly and the differential pressure temporarily decreased, followed by a rapid increase due to the pressure of the pump. When the evaporator was frozen, hot gas of the compressor discharge was sent to melt it, and then test was repeated. The operation time before 2nd time icing was shortened. It took about 20 minutes until the 1st icing occurred, but the 2nd icing occurred about 15 minutes and the 3rd icing about 10 minutes after each restart.

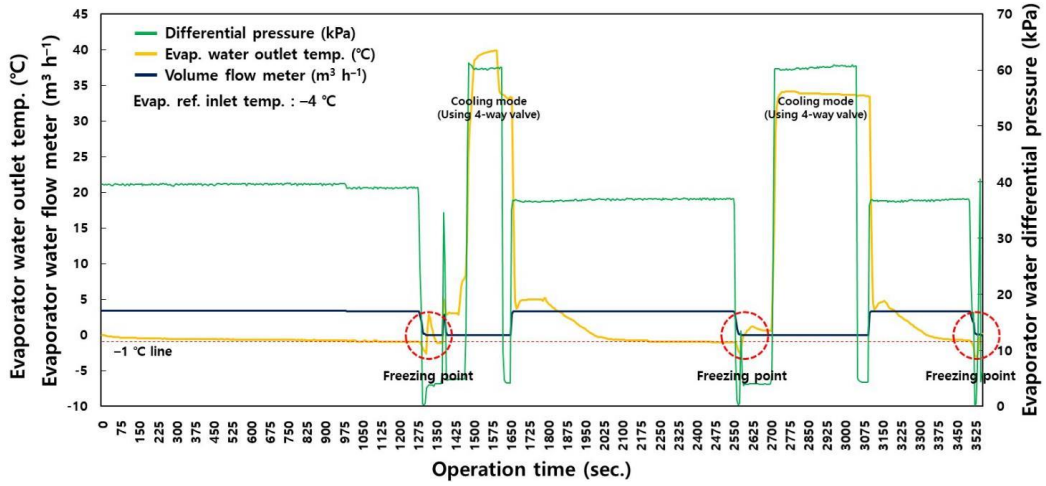

Figure 4 Water source operation trend when freezing occurs in the evaporator

Since freezing occurred at the evaporator water outlet temperature of -1°C (heat source temperature of 3.8°C), the heat source compensation operation was designed as maintaining the evaporator water outlet temperature at -0.8°C. Then heating operation tests were conducted by lowering the heat source temperature from 5°C to 1.4°C. By compensating the inlet of the evaporator with the bypass heat of condenser outlet, even if the water source temperature fell below 3.8°C, icing did not occur and heating operation was maintained. The table below summarizes the performance test results under the counter-current condition at the heat source temperature of 3.5°C and 2°C. The COP decreased from 3.45 to 2.82 showing a performance degradation rate of 18%. With parallel flow configuration in the evaporator, the COP dropped to 2.24 at 2°C water source, and the performance difference between counter flow and parallel flow was more than 20%.

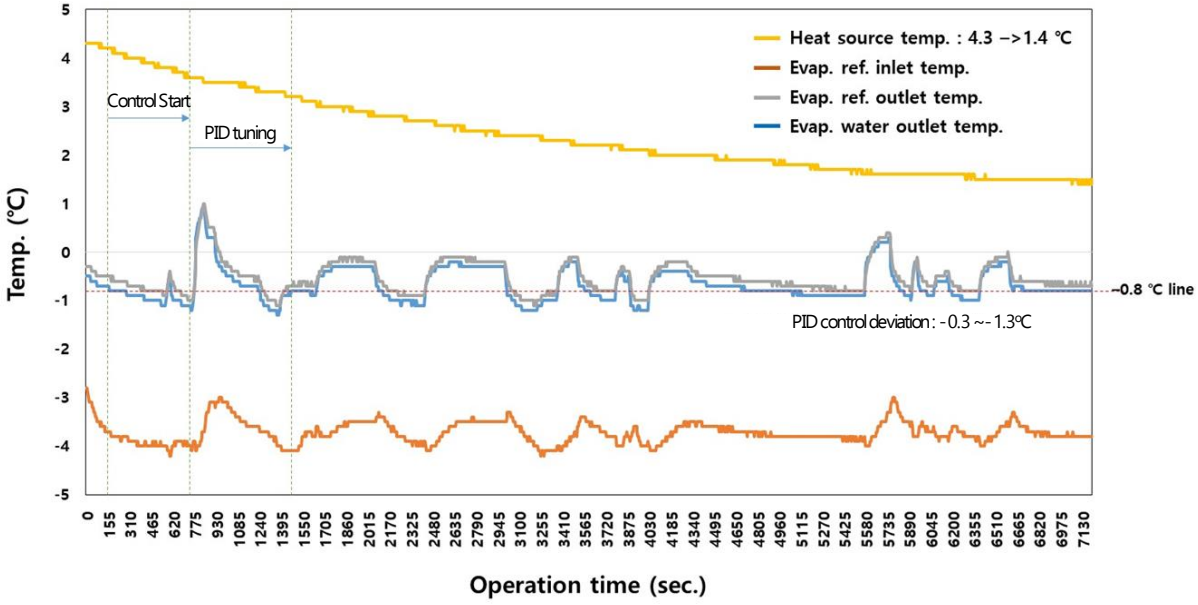

Figure 5 Heat source compensation control logic test when water source temperature gradually changes from 4.3°C to 1.4°C

Table 1: Performance results under the counter-current condition at heat source compensation mode.

Water source temperature	3.5℃	2℃
Compensation target temperature	- 0.8℃	- 0.8℃
Q_{cond}	17 kW	17 kW
$Q_{compensation}$	0.58 kW	3.58 kW
W_{comp}	4.75 kW	4.75 kW
COP	3.45	2.82

5. COMPARISION BETWEEN WATER SOUCE AND AIR SOURCE

To compare the performance of water source and air source heat pumps, the efficiency of water source heat pumps to temperature was assumed as follows. Operation was divided into two modes; normal heating operation and heat source compensation operation. Since, in the experiment, the evaporator freezing occurred at water source temperature of 3.8°C, it was assumed that heat source compensation operation was started with water source temperature of 4°C or below. Based on the previously performed heating experiment data, the efficiency in each operation mode was assumed to be linear to water temperature. The comparison was conducted with the parallel flow configuration of the evaporator because the performance degradation of the parallel flow was more than the counter flow. For the efficiency of the air source, heating efficiency was assumed based on KC C 9306. The correlations for the fixed speed compressor case were adopted and defrost operation was ignored. For the water temperature and outdoor temperature values, measured data in the Paldang area in 2018 were used. The annual trend of temperatures is shown in the figure below.

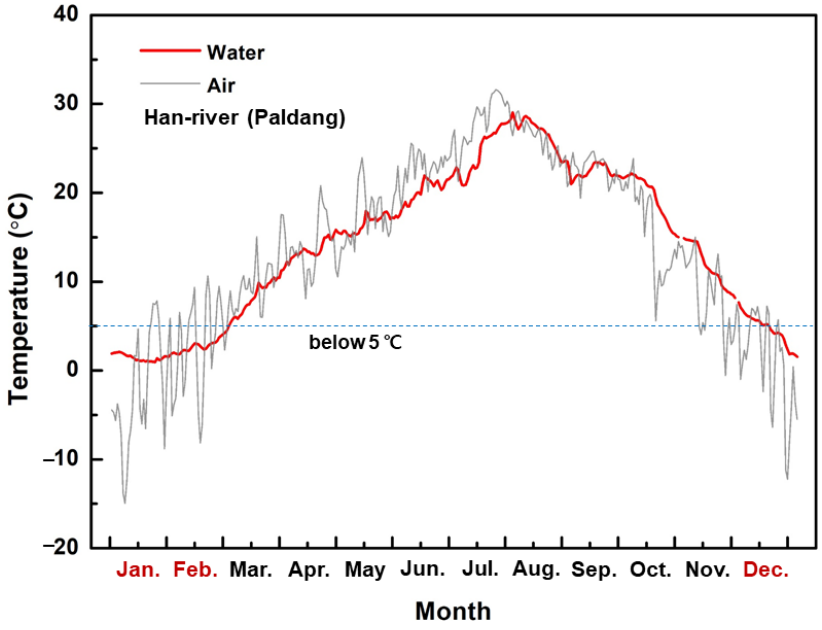

Figure 6 Temperature measurements of river water in Paldang and air in Seoul in 2018

The COP value of air source case at the 7°C outdoor temperature was set to be equal to the COP value of water source heat pump at the 5°C water temperature. Then, the COPs of the water source and air source heat pump were calculated for the heating operation from November to February based on the reference climate data. Figure 7 shows the calculation results. Heat pump operation using water source was restricted when the heat source temperature was 4°C or below due to the risk of freezing. In the reference climate data, most of the winter period (more than 68 days) was below 4°C, and the heat source compensation operation mode dominated most of the heating operation time. The minimum temperature of the outdoor air was -14.9°C, and at this point, the COP was predicted to be 2.1. The minimum temperature of the water source was 1°C, and the COP was about 1.3 with heat source compensation mode.

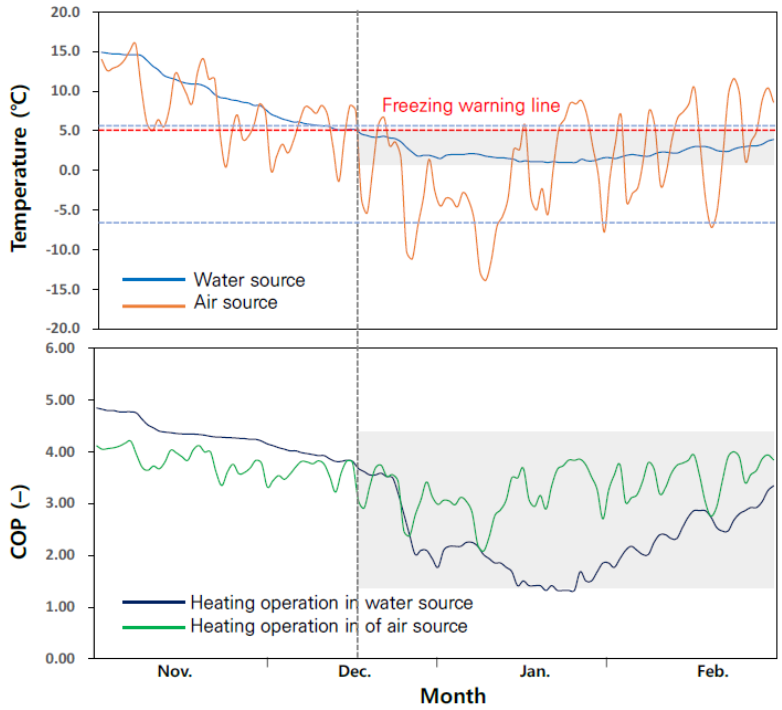

Figure 7 Water and air source temperatures and COP predictions for each corresponding heat pump system

The low water temperature had the greatest effect on the poor performance of water source heat pump compared to air source. Similar comparisons were conducted by increasing the minimum water source temperature. The results is in Figure 8 and in this figure water source heat pump seemed to generate competitive efficiency to air source when the minimum water temperature increased from 1°C to 3°C.

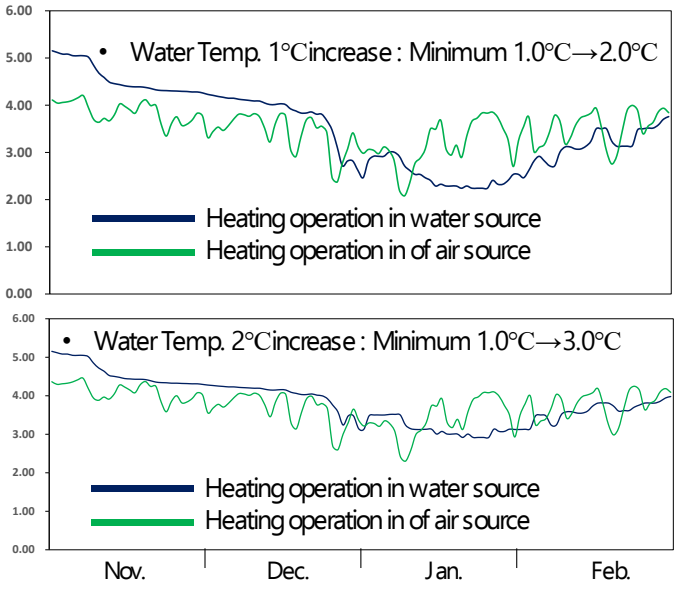

Figure 8 Effect of minimum water source temperature to the heating COP of water source heat pump system

Considering the fact that water source system generally has larger capacity and use turbo compressor, which is more efficient than displacement type compressor, COPs of water source heat pump was increased by 20%. (Figure 9) However, just increasing the COP only could not overcome the performance degradation due to low water temperature. Even in this higher efficiency case, the minimum water temperature should be over 2°C for the water source to be competitive to air source.

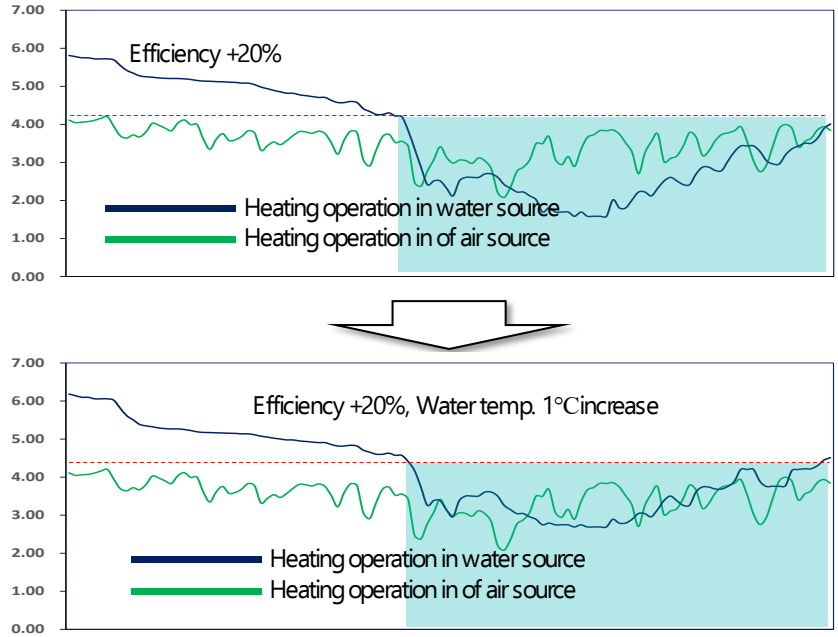

Figure 9 Effect of efficiency increase to the heating COP of water source heat pump system

The key underlining fact for these operation characteristics is higher heat capacity of water than air. Below graph provides temperature distributions in the winter season. Since water temperature is less sensitive to outdoor air temperature, the lower temperature part occupies the most portion in the distribution graph. However, since air source fluctuates more, the mid or upper part occupies the most portion for the air temperature case. Therefore, minimum water source temperature has the highest effect on the efficiency.

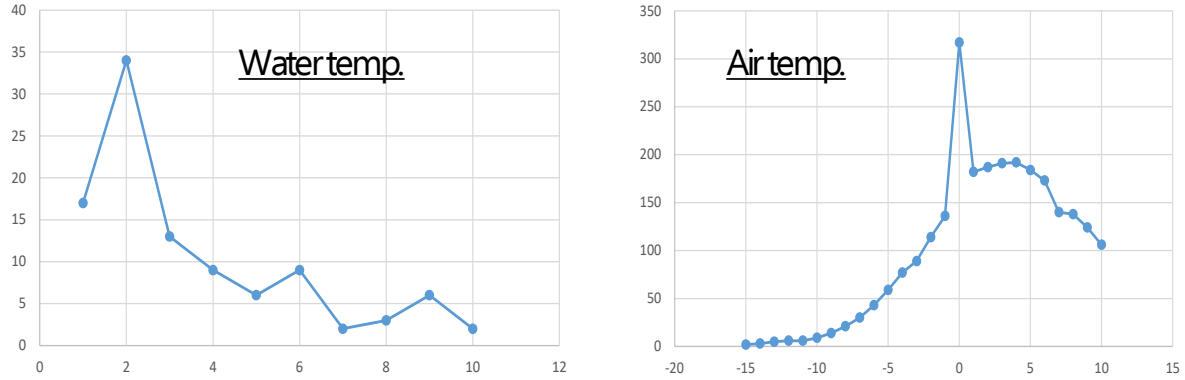

Figure 10 Temperature distribution of water (river water) and outdoor air in the winter

6. CONCLUSION

In this study, the low-temperature operation characteristics of water source heat pumps and methods to improve the operation performance were conducted. In the test, evaporator freezing occurred at water source temperature of 3.8°C and an evaporator water outlet temperature of -1°C. Heat source compensation operation method was selected as the low temperature heating mode. In the heat source compensation operation, the condenser water outlet bypass valve was controlled so that the evaporator water outlet temperature was maintained at -0.8°C. In the experiment, it was found that the heating operation became possible without freezing even at a low water temperature of down to 1.5°C. In the counter flow evaporator, the COP was 3.45 at 3.5°C and 2.82 at 2°C. In the parallel flow, the efficiency was reduced to 2.24 at 2°C. This shows that the freezing and compensation characteristics were different depending on the heat exchanger configuration. Then, a simple comparison of the efficiency characteristics with air source was performed. Based on the experimental data, the COP values of water source heat pump according to water temperature was assumed. For the COP of the air source, KS C 9306 appendix was used and the defrosting was ignored. The heat pump efficiencies according to reference climate data was compared. The results showed that the effect of the lowest water temperature had the greatest effect on the performance. The heat source compensation control method presented in this study would change depending on the individual systems. Nevertheless, the procedures presented here could be applied to secure the maximum heating operation of water source heat pump.

7. ACKOWLEDGEMENT

This work was supported by the Korea Institute of Energy Technology Evaluation and Planning (KETEP) and the Ministry of Trade, Industry & Energy(MOTIE) of the Republic of Korea (No. 20208901010010, No. 20212020800070)

8. REFERENCES

Korean Agency for Technology and Standards, KS C 9306:2017, Air Conditioner.

Park, C. Y., Lee, H., Nam, Y., Cho, H., Shin, Y. and Moon, H., 2020, "The Analysis on the Hydrothermal Energy Capacity and Survey on Possible Application Sites," K-Water

#63: Sustainable cooling solutions for rural communities: solar PV-driven DC vapour compression with low cost PCM storage

Hasila JARIMI[1], TIANHONG ZHENG[2], Saffa RIFFAT[3]

[1] *Solar Energy Research Institute, National University of Malaysia 43800 Selangor, Malaysia, hasila.jarimi@ukm.edu.my*
[2] *University of Nottingham, University Park, NG7 2RD, Tianhong.Zheng@nottingham.ac.uk*
[3] *University of Nottingham, University Park, NG7 2RD, saffa.riffat@nottingham.ac.uk*

Abstract: This paper presents a solar photovoltaic (PV) driven DC vapor compression system with low-cost phase change material (PCM) storage for cooling. Its primary objective is to provide an affordable and sustainable cooling solution in rural areas of Malaysia. The system operates by utilizing PV panels to power the compressor during the day, delivering cooling to the space, and storing excess electricity as cooling energy for later use. The system's key performance was assessed in two operational modes: Mode 1 (off-grid) and Mode 2 (grid). The results reveal that the grid mode exhibits a higher average COP, approximately 4-5% higher compared to the off-grid mode, attributed to consistent grid power. However, the off-grid mode outperforms in terms of COPpv and SPFpv due to PV integration. Despite lower COP values in Mode 1, a 10-year life cycle cost savings analysis unveils significant advantages for the fully off-grid system, primarily due to the exorbitant cost of electricity for air conditioning. Moreover, the low-cost PCM storage unit significantly contributes to reducing the system's overall cost, hence, it is more affordable for low-income communities. The system holds substantial potential for general use in rural areas and stop centres located in low-income regions, offering much-needed daytime cooling to individuals. In conclusion, the solar PV-driven DC vapor compression system with low-cost PCM storage represents an affordable and sustainable cooling solution for low-income communities. The findings of this study can offer valuable insights for designing and implementing similar systems in other low-income communities, thereby contributing to the sustainable development of such areas.

Keywords: PV cooling, PCM storage, off-grid

1. INTRODUCTION

Solar cooling technologies converts solar energy into cooling via two key mechanisms namely, solar photoelectric conversion cooling and solar photothermal conversion cooling (Gao et al., 2018). In photoelectric conversion cooling, photovoltaic (PV) cells are used to transform solar energy into electric energy, which is then used to power conventional vapor-compression chillers. This vapour compression chillers can either be DC or AC powered. On the other hand, solar photothermal conversion cooling relies on solar collectors to turn solar energy into thermal energy, which is used to drive absorption chillers. Among the photothermal conversion methods, solar absorption cooling is generally considered the most cost-effective (Gao et al., 2018). Compared with the solar absorption refrigeration system, the solar PV refrigeration system is simpler in structure and easier to maintain (Gao et al., 2021).

Moreover, in recent years, some studies have shown that the economic performance of PV cooling systems can be better than that of solar photothermal conversion cooling systems in certain areas due to the drop in the PV panel cost (Ayadi & Al-Dahidi, 2019). Although promising, the directly PV powered compressors cannot operate during nighttime, and during time of low to zero solar irradiance. This justifies the need of energy storage device. In an off-grid PV cooling system, it often uses batteries to store energy, but this increases both the cost and the accident risk. As a result, some researchers are exploring ways to reduce the use of batteries in such systems (Gao et al., 2021). In addition, for larger PV refrigeration systems, battery costs remain high, and frequent replacement of batteries due to degradation issues increases the overall investment and operating cost with potential environmental issues during its end of lifetime. Therefore, in recent years, as summarised in Table 1 ice thermal storage integrated with PV powered vapour compression system has been actively investigated by researchers such as in (Xu et al., (2017), (Liang et al., 2022) and (Varvagiannis et al., 2021).

Although promising, there are still several research areas that require attention namely; the dynamic relationship between PCM storage and the availability of solar irradiance, particularly in the context of fully off grid/solar driven system, and research has not been conducted on exploring the potential applications in rural areas for complete off-grid systems, especially in hot and humid climates. Addressing these gaps will enhance our understanding and improve the practical implementation of solar PV-driven DC vapor compression systems with PCM cold energy storage. These systems are intended for use in rural areas, specifically for commercial buildings operating from 8 a.m. to 5 p.m., which is a typical office hour schedule in Malaysia. This paper will investigate two main configurations of DC vapor compression systems with PCM cold energy storage and propose the most promising configuration for utilization in rural areas, particularly in general practices facilities.

2. METHODOLOGY

We initially conducted experimental investigations on two different operational approaches, namely: Mode 1, which is the PV-powered DC vapor compression system with an optimized low-cost phase change material (PCM) thermal storage (PV-PCM), and Mode 2, which is the grid-electricity powered DC vapor compression system with PCM (GRID-PCM). To facilitate this study, we established a proof-of-concept prototype, as illustrated in Figure 1, under real-world conditions in Malaysia at the Solar Energy Research Institute, National University of Malaysia. To compare the performance between these two approaches, we considered the following key parameters: COPsystem, COPpv, and the key performance indicator known as SFPV, which correspond to Equation 1 through Equation 3, respectively. We employed the COP value to estimate the performance of the off-grid systems under various configurations.

The solar DC vapor compression system, operating directly using distributed photovoltaic (PV) arrays, comprises three primary subsystems: distributed photovoltaic energy, a DC compressor with variable refrigerant flow (VRF), and a thermal storage tank with low-cost phase change materials (PCM). In this setup, the distributed photovoltaic energy system converts solar energy into electricity and supplies DC current to power the compressor unit. As depicted in Figure 1, during periods of available solar irradiance (i.e., when the power supply ranges from 410 W to 1920 W), the evaporator installed in the thermal storage tank absorbs heat from the cooling coil. Simultaneously, if there is still a temperature difference between the evaporator and the thermal storage tank, the refrigerant will also absorb heat from the thermal storage tank, gradually reducing its temperature towards the solidification point of the PCM. During this process, any remaining cooling capacity from the evaporator (excess from the cooling coil) is stored in the PCM tank. In this study, the size of the PCM storage was limited to 200 Liters with the maximum possible thermal storage of 76.5 kJ/h. The summary of the design parameters associated with the experiment is as in Table 1.

Table 1: The summary of the design parameters.

Component	Parameters
Solar DC driven vapour compression unit	DC power input range (410Watt- 1970Watt), R32 refrigerant
Solar panel	6 x 330 Wp
Test area	2.7 m x 2.7 m x 2.7 m
Phase Change Material Storage	Low cost-phase change materials (PCM) at 200 litres capacity
Fan coil unit	Mass flow rate: 0.05 kg/s

Equation 1: Coefficient of performance of the system COPs

$$COP_{system} = {Q_{useful}}/{P_{in}}$$

Equation 2: Coefficient of performance of the system based on the PV power supply COPpv

$$COP_{PV} = {Q_{useful}}/{P_{PV}}$$

Equation 3: Performance quality factor of the PV-HP system SFPV

$$SPFPV = SPF\ (1 + (PR\ \times SCR\ \times SFPV))$$

Where:

- SPF is the performance quality of the heat pump given by the COP_{system};
- PR is the Performance Ratio for evaluating the performance of the PV generator.
- SCR self-consumption ratio
- And SFPV is a PV Solar Fraction which is the fraction of the heat pump powered by the available power produced by PV panel, which is equal to 0.8 for PV-PCM, and 0 for grid mode

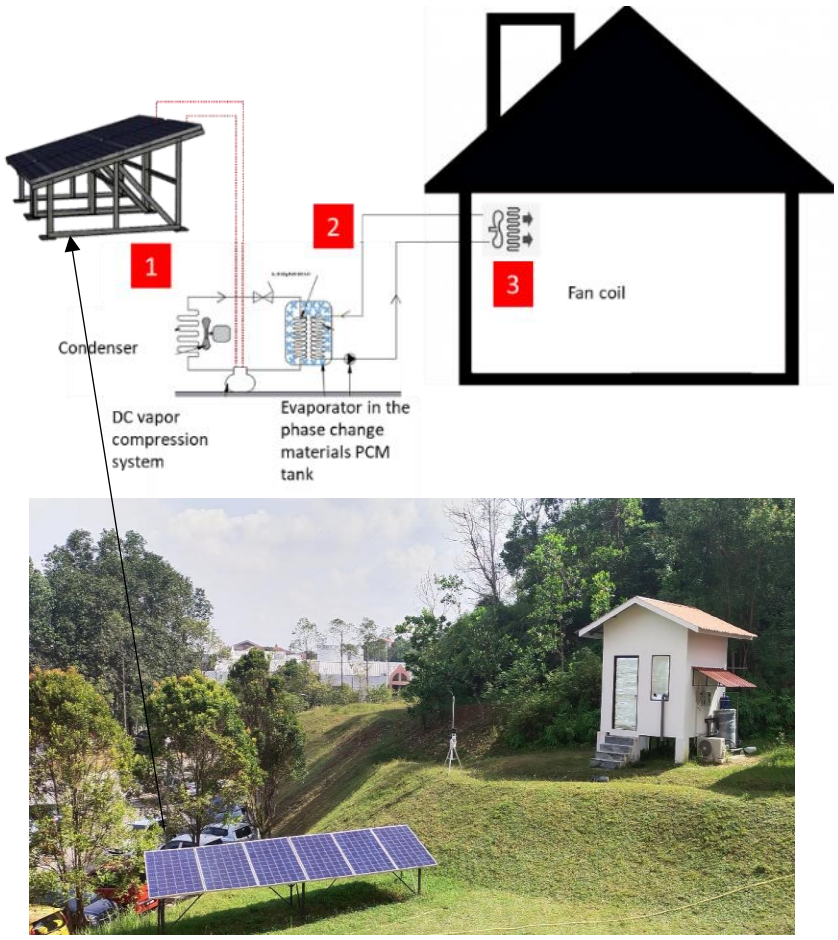

Figure 1 Top: Schematics of the experimental setup. Bottom: The proof-of-concept prototype installed under real conditions

3. RESULTS AND DISCUSSION

3.1. Experiment

Mode 1: PV-PCM: The variable refrigerant flow (VRF) DC compressor operates directly using power generated by the PV arrays during the daytime, without the need for battery storage. Any excess cooling generated by the evaporator is stored in a phase change material storage tank when the chilled water line has reached its target temperature. In instances where there is insufficient solar irradiance, the chilled water line is cooled by transferring its heat to a cooling storage tank. As illustrated in Figure 2, the average evaporator temperature $T_{evaporator}$ clearly varies with the availability in solar irradiance. This is expected since the compressor power varies with the available amount of maximum power supply available from

the PV panel which varies throughout the day and affect the overall temperature of the liquid refrigerant into the evaporator. This, as a result affect the overall average temperature of the PCM tank T_{tank} however, without affecting the overall cooled space temperature which was maintained between 26 to 27.5 ° C and at relative humidity *RH* of 60-70% inline thermal comfort level as outlined in ASHRAE Standard 55. This is due to the available cooling from the PCM storage that has been stored during the available solar irradiance of which, even without the reliance of electrical battery storage the system can still be operated and provide cooling. From Figure 2, the lowest average evaporator temperature achieved was approximately -40. 5 ° C and this was observed at maximum average power available by the PV panel. Also, it is worth noting that at Pmax lower than 410 Watt, the DC compressor will not be in operation, hence explain the increase in the average temperature of the evaporator and hence reducing the cooling capacity of the cooling system.

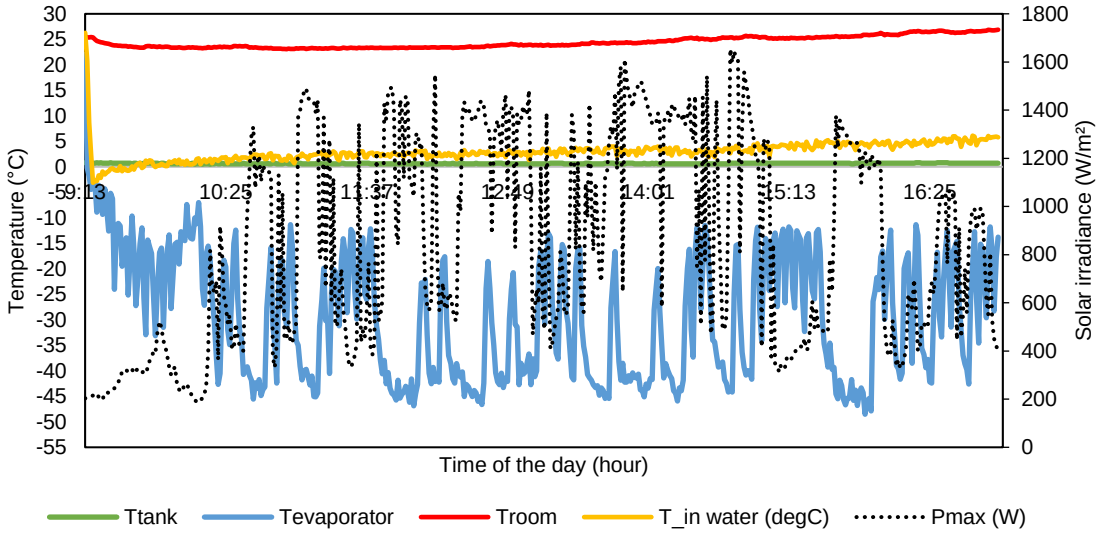

Figure 2 Characteristic curves for Mode1 (PV+PCM)

Mode 2: Grid-PCM: Figure 3 illustrates some of the temperature parameters when the system is fully operated by the grid. According to the specifications, the maximum power that can be delivered to the compressor is 1920 watts. The system, in general, is independent of available solar irradiance, so the average evaporator temperature is unaffected by both the available solar irradiance and the maximum power of the PV panel. Due to a consistent power supply throughout the day, the average temperature in the storage tank could reach approximately -5°C. However, it's important to emphasize that the temperature variation in the room is quite similar to Mode 1. This is because the cooling capacity provided by the vapor compression unit to the chilled line in Mode 1 remains unaffected by the unavailability of solar irradiance, due to the cooling storage by the PCM.

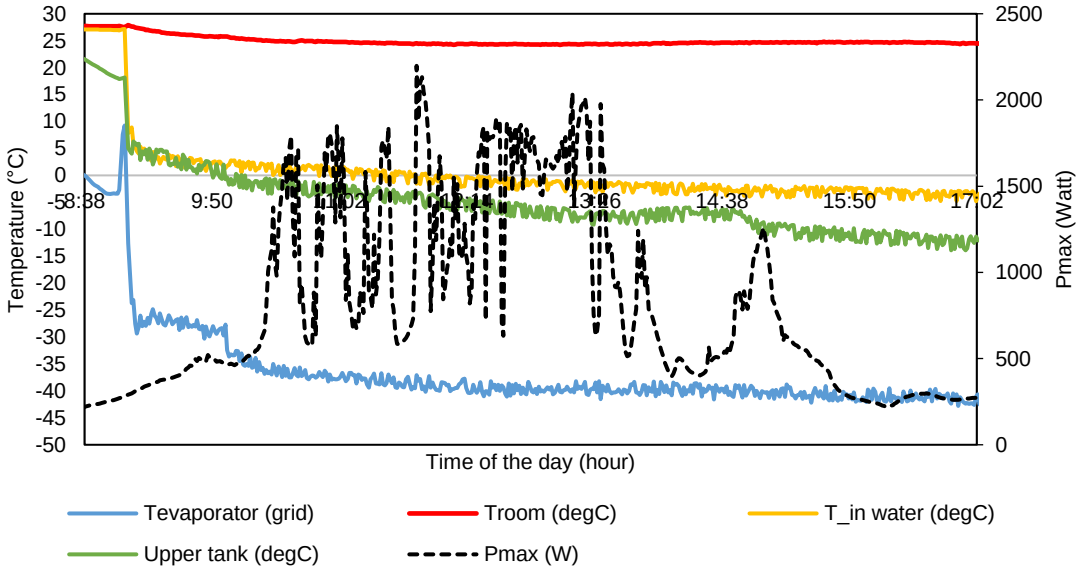

Figure 3 Characteristic curves for Mode 2 (Grid+PCM)

3.2. Performance analysis

The experimental performance of Mode 1 and Mode 2 is illustrated in Figure 4. Experimental results show that the average COP of the system (COPs), when operated by the power grid, is approximately 4-5% higher than when the system is operated off-grid via solar photovoltaic panels. However, when compared based on the COPpv, the system operated by the power grid has a value of zero. Moreover, when comparing the key performance indicator using SPFpv, the performance of the system in Mode 1 is higher. This can be attributed to the fraction of the PV power integrated into the system. For Mode 2, since there is no contribution of PV power, the COP of the system solely determines the SPF. It is worth emphasizing that, despite the lower COPs, the life cycle cost savings analysis over a 10-year period shows a significant advantage of using the fully off-grid. This advantage is due to the inflated cost of fuel associated with electricity usage for air conditioning. As illustrated in Figure 4, the life cycle cost savings analysis results in -$6,283.94 for the system when it is grid-connected. Meanwhile, for the off-grid system, the savings are as high as $5,289.22, with a payback period of 4 years. Please note that all costs associated with the subcomponents of the system have been considered in the calculation.

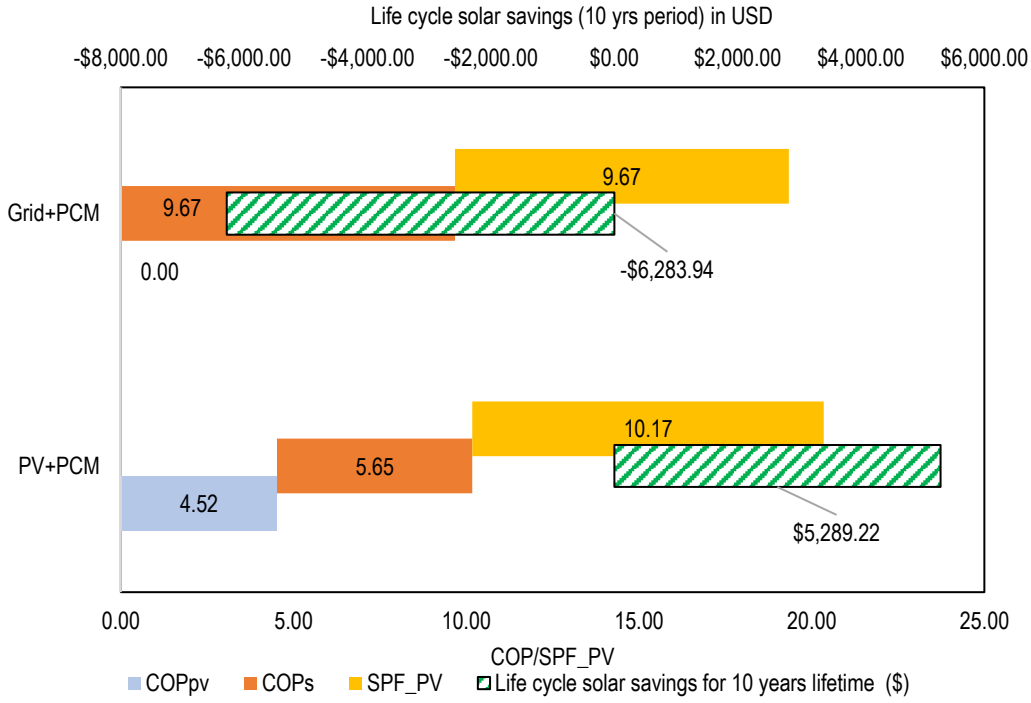

Figure 4 Life Life cycle solar savings (10 yrs period) in USD

4. POTENTIAL APPLICATION IN RURAL AREA IN MALAYSIA

In Malaysia, access to electricity, measured as the percentage of the population with access, reached 100% in 2021. However, it's essential to emphasize that this achievement was made possible through the Rural Electricity Supply (BELB) Program, which extends electricity coverage to areas not served by local authorities. The primary objective of the BELB program is to provide electricity to traditional villages located beyond the jurisdiction of local authorities (PBT) across the country, including remote longhouses in Sabah and Sarawak, indigenous communities in Peninsular Malaysia, island villages, and small estates smaller than 400 hectares (approximately 1,000 acres).The BELB Program employs two distinct methods for implementation. The first method involves connecting these areas to the grid lines provided by the State Electricity Authority (PBEN), which includes Tenaga Nasional Berhad (TNB) for Peninsular Malaysia, Sabah Electricity Sdn. Bhd (SESB) for Sabah, and Sarawak Electricity Supply Corporation (SESCo) for Sarawak. For rural areas, generating electricity with an off-grid system, such as solar panels, can be more cost-effective than relying on grid power, especially if the cost of extending grid infrastructure to remote areas is prohibitive. Over time, the savings on electricity bills can offset the initial investment in the off-grid system.

There is a substantial body of literature addressing the utilization of this technology for rural electrification, which mainly focuses on the economic feasibility of off-grid solar energy and explores its potential benefits and challenges. For instance, a study by Roche and Blanchard (2017) investigated the affordability and reliability of electricity access for rural populations in Kenya, revealing that extending the grid is prohibitively expensive. Therefore, off-grid solar systems appear as a sustainable and cost-effective solution to enhance energy accessibility in such areas. Warnecke and Houndonougbo (2016) further reinforce the advantages of off-grid solar systems, highlighting their ability to provide direct access to clean

energy. This aligns with Sustainable Development Goal number 7, which promotes clean and affordable access to electricity.

To analyse the potential of the proposed off-grid solar DC cooling system for rural areas in Malaysia, a location in rural Sarawak, Malaysia, has been considered. Using weather data from that area, the maximum PV power generation of the proposed system has been estimated by considering three key configurations: Configuration A with 4 x 550-Watt solar panels, Configuration B with 6 x 550-Watt solar panels, and Configuration C with 8 x 550-Watt solar panels. As shown in Table 2, The analysis revealed that the more PV panels used to drive the system, the greater the power available to run the DC compressor at its full capacity, which, in turn, increases the amount of available useful cooling.

Table 2 The summary of estimated cooling potential at rural areas with different configurations

	Configuration A	Configuration B	Configuration C
Average useful PV (kWh/day)	8	11	14
Qload (kWh/day)	36.16	49.72	63.28
Estimated size of the cooling space (with poor insulation) sqm	25	36	49

5. CONCLUSION

In this study, we have experimentally investigated two different approach of space cooling using a variable refrigerant flow (VRF) DC type compressor operation. To compare the performance between two approaches, the following key parameters have been taken into consideration namely, COPsystem, COPpv, and key performance indicator known as SFPV which are Equation 1 to Equation 3 respectively. Using the COP value, the performance of the off-grid systems under various configurations were estimated accordingly. In Mode 1, which combines photovoltaic (PV) power and phase change material (PCM) for cooling, the variable refrigerant flow (VRF) DC compressor operates directly using power generated by the PV arrays during the daytime. There's no need for battery storage. Excess cooling generated by the evaporator is stored in a PCM storage tank or transferred to a cooling storage tank when there's insufficient solar irradiance. The average evaporator temperature varies with solar irradiance because the compressor's power depends on available PV panel output. However, the room's temperature remains consistent due to cooling from PCM storage. In Mode 2, the system is fully operated by the grid. The system is independent of solar irradiance, and the average evaporator temperature is unaffected by solar conditions. The cooling capacity is maintained through PCM storage, similar to Mode. 1.

- Comparing Mode 1 (PV-PCM) and Mode 2 (Grid+PCM), Mode 2 shows a higher average COP, about 4-5% higher, attributed by the grid power. However, Mode 1 outperformed in terms of COPpv and SPFpv due to PV integration.
- Despite lower COP values in Mode 1, a 10-year life cycle cost savings analysis revealed significant advantages for the fully off-grid system. This was primarily due to the excessive cost of electricity for air conditioning.
- In rural settings, off-grid solutions such as solar panels prove to be economically advantageous when compared to the expenses associated with expanding traditional grid infrastructure. Therefore, the suggested cooling system not only offers potential cost savings on electricity bills, but over time, these savings can offset the initial setup costs.

6. ACKNOWLEDGEMENT

We would like to acknowledge Royal Society (ICA\R1\201236) for the financial support to this research. Besides, we would like to acknowledge Universiti Kebangsaan Malaysia (RS 2020-006) for the corporation to this research.

7. REFERENCES

Ayadi, O., & Al-Dahidi, S. (2019). Comparison of solar thermal and solar electric space heating and cooling systems for buildings in different climatic regions. *Solar Energy*, *188*, 545–560. https://doi.org/10.1016/j.solener.2019.06.033

El-Bahloul, A. A. M., Ali, A. H. H., & Ookawara, S. (2015). Performance and Sizing of Solar Driven dc Motor Vapor Compression Refrigerator with Thermal Storage in Hot Arid Remote Areas. *Energy Procedia*, *70*, 634–643. https://doi.org/10.1016/j.egypro.2015.02.171

Gao, Y., Ji, J., Guo, Z., & Su, P. (2018). Comparison of the solar PV cooling system and other cooling systems. *International Journal of Low-Carbon Technologies*, *13*(4), 353–363. https://doi.org/10.1093/ijlct/cty035

Gao, Y., Ji, J., Han, K., & Zhang, F. (2021). Comparative analysis on performance of PV direct-driven refrigeration system under two control methods. *International Journal of Refrigeration*, *127*, 21–33. https://doi.org/10.1016/j.ijrefrig.2021.03.003

Han, K., Ji, J., Cai, J., Gao, Y., Zhang, F., Uddin, M. M., & Song, Z. (2021). Experimental and numerical investigation on a novel photovoltaic direct-driven ice storage air-conditioning system. *Renewable Energy*, *172*, 514–528. https://doi.org/10.1016/j.renene.2021.03.053

Liang, J., Du, W., Wang, D., Yuan, X., Liu, M., & Niu, K. (2022). Analysis of the Refrigeration Performance of the Refrigerated Warehouse with Ice Thermal Energy Storage Driven Directly by Variable Photovoltaic Capacity. *International Journal of Photoenergy*, *2022*. https://doi.org/10.1155/2022/3441926

Roche, O. and Blanchard, R. (2018). Design of a solar energy centre for providing lighting and income-generating activities for off-grid rural communities in Kenya. Renewable Energy, [online] 118, pp.685-694. Available at: https://doi.org/10.1016/j.renene.2017.11.053

Tonia Warnecke & Ahiteme N. Houndonougbo (2016) Let There Be Light: Social Enterprise, Solar Power, and Sustainable Development, Journal of Economic Issues, 50:2, 362-372, DOI: 10.1080/00213624.2016.1176479

Tobin, P., Schmidt, N. M., Tosun, J., & Burns, C. (2018). Mapping states' Paris climate pledges: Analysing targets and groups at COP 21. *Global Environmental Change*, *48*, 11–21. https://doi.org/10.1016/J.GLOENVCHA.2017.11.002

Varvagiannis, E., Charalampidis, A., Zsembinszki, G., Karellas, S., & Cabeza, L. F. (2021). Energy assessment based on semi-dynamic modelling of a photovoltaic driven vapour compression chiller using phase change materials for cold energy storage. *Renewable Energy*, *163*, 198–212. https://doi.org/10.1016/j.renene.2020.08.034

Xu, Y., & Li, M. (2022). Impact of instantaneous solar irradiance on refrigeration characteristics of household PCM storage air conditioning directly driven by distributed photovoltaic energy. *Energy Science and Engineering*, *10*(3), 752–771. https://doi.org/10.1002/ese3.1050

Xu, Y., Ma, X., Hassanien, R. H. E., Luo, X., Li, G., & Li, M. (2017). Performance analysis of static ice refrigeration air conditioning system driven by household distributed photovoltaic energy system. *Solar Energy*, *158*, 147–160. https://doi.org/10.1016/J.SOLENER.2017.09.002

#66: Assessing the economic viability of a proposed DSM program utilizing heat pump driven thermochemical heat storage

Marzieh REZAEI[1], Devrim AYDIN[2], Yuehong SU[3], Saffa RIFFAT[3]

[1]Department of Architecture and Built Environment, University of Nottingham, University Park, Nottingham, NG7 2RD, UK
[2]Department of Mechatronics Engineering, Near East University, Nicosia, TRNC Mersin 10, Turkey
[3]Department of Mechanical Engineering, Eastern Mediterranean University, G. Magosa, TRNC Mersin 10, Turkey

Abstract: Nowadays, thermal energy storage systems are of particular interest for balancing the mismatch between renewable electricity production and the peak demand hours. Using thermal storage technologies to provide heat during the peak demand hours enables alleviating the need for electricity usage, which is attractive for both customers and the utilities. Due to its high energy storage density and long-term storage capability, thermochemical heat storage (TCHS) compromises the opportunity of reducing space heating costs of buildings. The current study investigates the viability of implementing a demand-side management (DSM) strategy aimed at utilizing the stored energy of TCHS systems during peak hours, thereby providing economic benefits for electric utility. With this purpose, initially, annual heating load of the living room of a hypothetical building under the United Kingdom (UK) climate conditions is simulated by employing DesignBuilder software. Later, sizing of TCHS unit is completed by considering the obtained energy storage density in a previous experimental work. In the study, vermiculite-calcium chloride (V-CaCl2) is selected as the TCHS material due to its proven performance data available in the literature. Based on the obtained results, economic feasibility of the proposed DSM program is evaluated by using net present value (NPV) and saving to investment ratio (SIR) method. Potential strategies and approaches for improving economic viability of TCHS-HP systems are also discussed.

Keywords: Thermochemical Heat Storage, Demand Side Management, Economic Feasibility Analysis, DesignBuilder Simulation, Heat Storage Density

1. INTRODUCTION

Decarbonisation and electrification are two key pillars in the global effort to mitigate climate change and transition towards a sustainable energy future. The combination of decarbonisation and electrification holds immense potential for significantly reducing greenhouse gas emissions. It requires coordinated efforts from governments, businesses, and individuals to invest in renewable energy infrastructure, develop efficient electric technologies, and embrace sustainable lifestyles.

The United Kingdom (UK) serves as a prime example of a nation committed to decarbonisation and electrification. Additionally, the UK has been actively promoting the electrification of heating systems, encouraging the use of heat pumps as a low-carbon alternative to traditional gas boilers. The government has introduced financial incentives such as grants and subsidies to support homeowners and businesses in the installation of heat pump systems. However, the widespread adoption of heat pumps in the UK also brings attention to the potential challenges associated with the increased demand for electricity. As more households and buildings move from gas boilers to heat pumps, there could be a significant shift in electricity consumption patterns, leading to potential peak demand challenges.

Proposing integration of energy storage to thermal energy systems for heating purpose in domestic section goes back to decades ago (Packer and Glicksman., 1979). However, it was found that integrating energy storage into the existing systems (heat pumps) is not economically viable. Lately, researchers verified that thermal energy can be stored during off peak hours when the electricity prices are in the lowest range and discharged during on peak hours while electricity prices are high through a transformation chain (Katulic et al., 2014). Thermochemical energy storage (TCES) technology is a promising component in energy system, energy balance and demand. It typically involves using materials that can undergo reversible chemical reactions and store energy in the form of chemical bonds. The absorption and release of heat during the chemical reactions can be used for various applications, such as space heating, industrial processes, and power generation. Chen et al. (2021) investigated the characterization of an ettringite-based thermochemical energy storage material in an open-mode reactor. In this study, the average energy releasing power estimated as 33.3 W/kg. Thermochemical materials have a major challenge which is the difficulty of recharging them. This process can be time-consuming and energy-intensive, and therefore poses a significant challenge to the practical implementation of TCES systems. Research is ongoing to develop more efficient and cost-effective methods for charging thermochemical materials, including the use of catalysts and alternative heating sources such as solar energy. Kant and Pitchumani (2022) studied on an optimized TCES design, which simultaneously reduces storage cost and maximizes energy storage density resulted in a total energy storage density of 142.75 kWh/m^3 and a levelized storage cost of $3.64/kWh. Li et al. (2020) characterise salt-hydrate based composite sorbent for low-grade TCES. The study determined that the sorbent has an active energy of 2.58 x 109 s-1 and a pre-exponential factor of 59.5 kJ/mol. Through simulations, the storage unit achieved a thermal power of 123 W and a thermal efficiency of 83.6%, providing further evidence that the composite sorbent is a viable option for low-grade heat storage. Zeng et al. (2019) investigated a three-phase thermochemical reactor through an experimentally validated numerical modelling. Researchers suggested that the numerical calculations can be significantly influenced by reference diffusivity, heterogeneity factor, and initial water uptake. Therefore, the parameters must be adjusted appropriately to ensure accurate and reliable results. Reynolds et al. (2023) developed $CaCl_2$ impregnated expanded graphite/alginate polymer composites for TCES applications. SrBr2/expanded vermiculite and LiCl/expanded vermiculite composites were synthesized by Ding et al. (2021) and Brancato et al. (2019) respectively. A cascade TCES system using cement/$SrCl_2$ is proposed by Clark and Farid (2022). Energy density in the range of 108–138 kWh/m^3 is obtained for the charging temperatures between 50 ^{o}C and 130 ^{o}C. Aydin et al. (2018) performed numerical and experimental analysis of a novel heat pump driven TCES system (Figure 1). Based on the findings, the system's coefficient of performance (COP) exhibited a range of 1 to 2 during short-term operation (where t < 240 min).

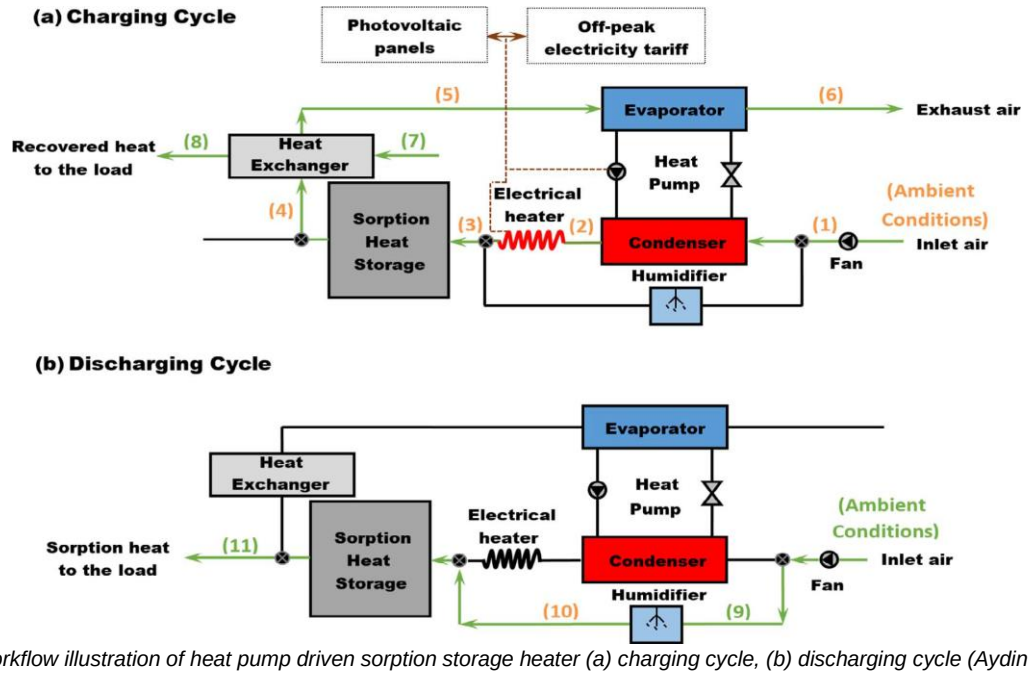

Figure 1 Workflow illustration of heat pump driven sorption storage heater (a) charging cycle, (b) discharging cycle (Aydin et al., 2018)

While the heating capabilities of TCES are widely recognized, its implementation in domestic settings has not been commonly adopted. One potential factor contributing to this is the concerns surrounding the complex and costly charging process. Given that the adoption of TCES has the potential to alleviate morning and evening peaks and consequently enable utilities to avoid relying on peak generators, it is recommended to explore the use of DSM as a means to promote TCES in buildings. To accomplish this, it is crucial to conduct an economic feasibility analysis of promoting TCES implementation using utility resources. The system studied by Aydin et al. (2018), which is depicted in Figure 1, has the potential to promote the adoption of TCES, facilitate peak shifting, and aligns with the energy policy goals of the UK. Although numerous studies have focused on evaluating the performance and economic aspects of TCES systems, the authors have not come across any existing literature that specifically investigates the economic feasibility of promoting TCES through DSM.

2. METHODOLOGY

In several countries where smart grid infrastructure is not yet in place, the implementation of the six strategies of DSM can be accomplished through the introduction of rebate programs or the adoption of multi-tariff electricity pricing (see Figure 2). In this study, we explore the potential of promoting a novel heat pump driven sorption as a strategy to align the usage of renewable electricity with the demand for space heating. Furthermore, this approach has the potential to assist the utility in cost reduction. The suggestion put forth is for the utility not only to generate electricity to meet the demand but also to implement a rebate program that financially supports the installation of such systems in residential properties. This approach aims to shift peak demand, thereby enhancing the profitability of the utility's operations. Normally, maximum peak generators are only utilized for a few weeks throughout the year. Therefore, it is highly preferable to avoid investing in these generators due to the uncertainty surrounding their economic viability. In the suggested approach, the desired reduction in peak demand is determined as a starting point. It would be reasonable to consider this reduction as equivalent to a deferred power unit with a known capacity and cost. The promotion of the novel heat pump in residential properties aims to encourage end-users to refrain from using electric heating devices during peak hours. Figure 3 demonstrates a simplified setup of the DSM approach utilized in the present study.

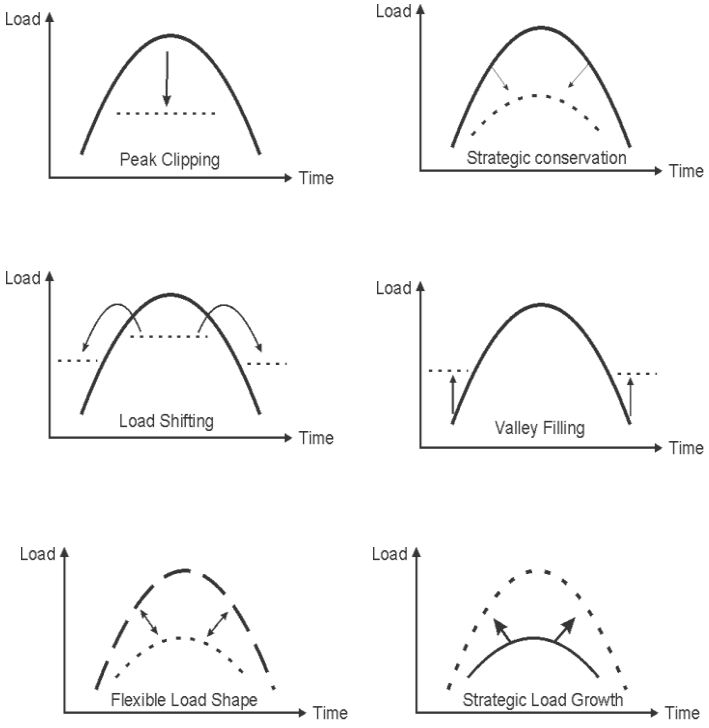

Figure 2 Six techniques of DSM. Adapted from Gellings (1985)

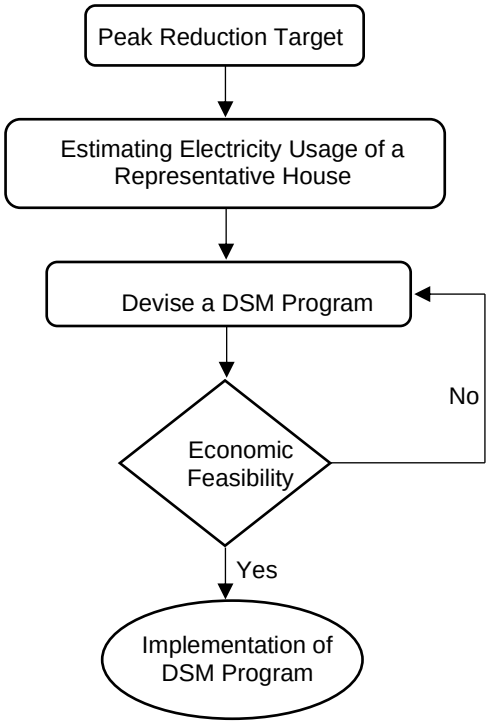

Figure 3 Proposed approach for enhancing the economic feasibility of TCHS in residences

The primary objective of the proposed DSM program is to minimize electricity consumption during peak hours by utilizing the heating capabilities of the innovative heat pump driven TCES. This TCES will be charged with renewable energies or during off-peak hours (load shifting) by using the heat pump system.

2.1. Mathematical Model

DesignBuilder software is applied for simulating the building heat load variation. The accuracy of the simulation is investigated by Ozdenefe et al. (2018). The annual heating load of the living room of the hypothetical building is estimated and utilized in the economic analysis of the proposed DSM program. The required size of the heat pump for charging process, daily heating load of the living room on the coldest day of the winter is considered.

2.2. Economic Feasibility Calculations

The economic viability of the program is assessed by comparing the net present savings with the net present investments, as well as the lost net income from electricity sales. Typically, if the savings outweigh the losses over the lifespan of the DSM program, then the program is considered economically feasible from the utility's perspective.

The net present savings (NPS) can be evaluated as follows (Rezaei., et al 2020):

Equation 1: Net present savings

$$NPS = C_{PP} + C_{Fuel} + C_{(O\&M)}$$

Where:

- C_{PP}= cost of the avoided power plant
- C_{Fuel}=total cost of the avoided fuel consumption
- $C_{O\&M}$ =operation and maintenance cost during the lifetime of the DSM program

The operation and maintenance costs encompass both fixed and variable expenses. $C_{O\&M,PP(variable)}$ include production-related cost which depends on electrical generation and $C_{O\&M,PP(fixed)}$ incurred at a power plant which is not related to generation.

The net present investments (NPI) for a DSM program can be expressed as:

Equation 2: Net present investment

$$NPI = C_{DSM} + C_{DS}$$

where:

- C_{DSM}= cost of the DSM program
- C_{DS}= cost of decreased sales that may take place during the implementation of the program

Typically, C_{DSM} includes the incentive provided to participants and any other services obtained specifically for the DSM program.

The feasibility of any proposed DSM program can be assessed by using indicators such as Net Present Value (NPV) and Savings-to-Investment Ratio (SIR), which provide valuable insights into the program's viability throughout its life cycle, such that:

Equation 3: Net Present Value

$$NPV = NPS - NPI$$

Equation 4: Savings-to-Investment Ratio

$$SIR = NPS/NPI$$

Equation 5: Present value of cash flow at different time

$$Present\ Value\ of\ Cash\ Flow = \frac{Cash\ flow\ in\ year\ zero}{(1 + discount\ rate)^n}$$

Where:

- n= number of years taken for economic lifetime of the project

This is a widely accepted method and has been utilized in many studies (Agboola et al., 2015).

NPV should be greater than zero and SIR should be more than one at the end of the project period for achieving economic feasibility.

3. RESULTS AND DISCUSSIONS

Building performance simulation results and the feasibility evaluation of the proposed DSM strategy are provided in this section.

3.1. Building Features and Energy Simulation

In this study a two storey hypothetical building is considered for energy simulation. The virtual two storey residential building has 280 m^2 floor area with a 35 m^2 floor area living room. Figure 4 demonstrates the three dimensional view of the building. It is notable to mention that the minimum U values for new builds in UK are considered in the simulation parameters (insulation4less.co.uk, 2023). Figure 5 demonstrates the indoor temperature profile of the living room for one of the coldest days of the winter (December 27). The air conditioning system is set to provide heating from November 1 to May 1 once the living room temperature falls below 22 °C. In addition, the time schedules for occupancy and air conditioning system working during weekdays and weekend are set to be from 7 to 11 am and 17 to 21 pm (peak hours). The ratio of required total heating load to floor area for the whole heating season and for the selected day are 38.31 kWh/m^2 and 0.46 kWh/m^2, respectively. By considering the COP of 2.75, the total electricity consumption per floor area is13.93 and 0.17 kWh/m^2 for the whole heating season and selected coldest day, respectively. It is anticipated that the implementation of the proposed DSM program will result in a reduction and shift of the peak load to the off-peak hours. This will be accomplished by charging the TCHS materials using the novel heat pump during off-peak hours to release the heat (discharging) during peak hours.

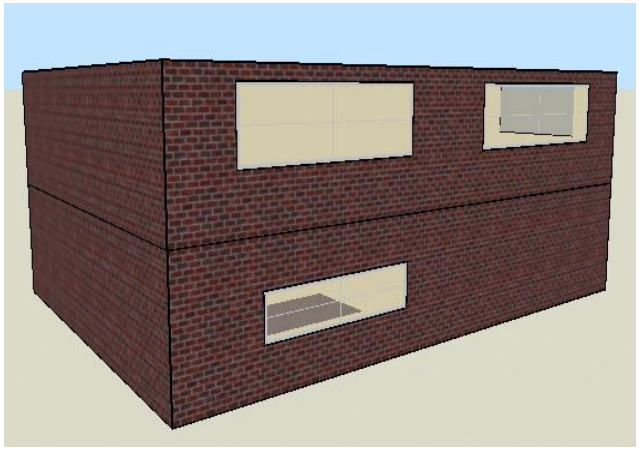

Figure 4 Two storey hypothetical building

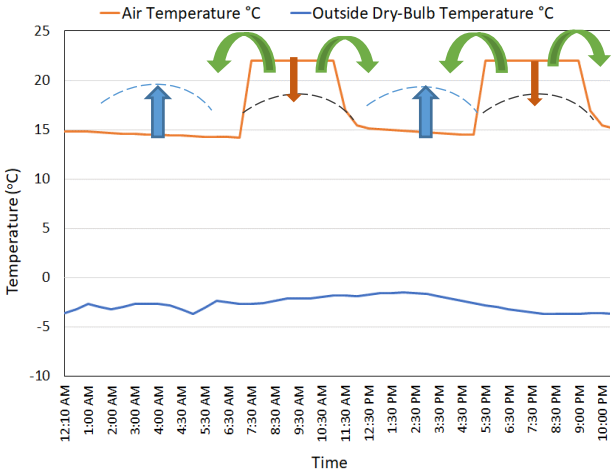

Figure 5 Profile indoor temperature of the living room

3.2. Economic Justification of Promoting TCHS through DSM

This study examines the economic viability of implementing a DSM program that promotes the adoption of novel heat pumps in residential settings, with the objective of avoiding the use of peak power generation units during the winter season in the UK. It is customary to consider that the capacity of the peak generators is equal to the reduction achieved through the implementation of the proposed DSM program. The smallest capacity thermal power units assumed in this case are peak generators with a capacity of 17.5 MW. In the current study, it is typical to install heat pumps with a heating capacity of 24,000 Btu/h (7.032 kW) in rooms of the size being considered. With a coefficient of performance (COP) of 2.75, the power demand for such a heat pump would be approximately 2.56 kW. The objective is to avoid heat pump operations during peak hours by replacing the heating system with TCHS system through proposed DSM program (see Figure 6).

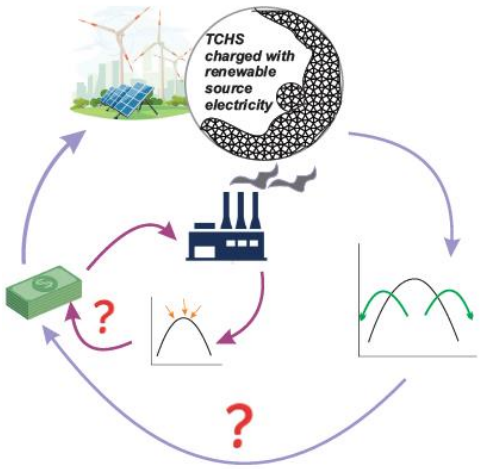

Figure 6 The simplified schematic of proposed DSM program

To achieve a reduction of 17.5 MW from the peak, approximately 6,842 houses would be required. The suggestion is to incorporate consumers into the DSM program who are willing to install an astronomic relay that restricts the operation of heat pumps during peak hours in the winter season. Table 1 shows the total cost of the proposed DSM program. The cost breakdown of the TCHS system is presented in Table 2.

Table 1: Costs taken into account for DSM program (Rezaei et al., 2020; Aydin et al., 2018)

Item	Cost (EUR)
Heat pump	3200
Astronomic relay timer	100
TCHS material	13.8
TCHS system	389.7

Table 2: Costs taken into account for manufacturing TCHS system

Item	Unit	Number of Unit	Price (EUR)	Reference
Aluminium Sheet	2*1 (m)	3	85.3	Metalswarehouse, 2023
Wire Mesh	3*0.5	1	12.87	Amazon, 2023
PIR Insulation Board	2.4*1.2	3	28.92	Insulation super store, 2023
Humidifier	-	1	34.17	Probreeze, 2023

The utilized assumptions in DSM analysis are provided in Table 3. It is assumed that the DSM program will take three years to be completed. The economic analysis period is 20 years.

Table 3: Assumptions utilized in DSM analysis in UK

Discount Rate (%)	2
Analysis period (years)	20
DSM program completion period (years)	3
Winter peak hours (weekdays and weekend)	7:00-11:00 & 17:00-21:00
Power reduction anticipated (MW)	17.5
Occupied zone floor area (m^2)	35

The fuel used in the power plant is natural gas. It is noticeable to mention that $C_{O\&M}$ involves two different cost of variable and fixed which are presented in Table 4. There will be cash flows due to savings in fuel consumption, O&M, and decreased sales of electricity which should be discounted each year due to time value of money and can be calculated from Equation 5. In the present study, the average cost of natural gas delivered to power plant is assumed to be 0.08091 EUR/kWh (Trading economics, 2023).

Table 4: Expenditures associated with power production (Rezaei et al., 2020)

C_{PP}	1140.7	Eur/kW
$C_{O\&M,PP(variable)}$	0.0049725	Eur/kWh
$C_{O\&M,PP(fixed)}$	5.865	Eur/kW-yr

Table 5 demonstrates the economic analysis of proposed DSM program. Results are calculated by employing Equations 1-5.There are two different options considered for the SIR calculation. The values of SIR are calculated 2.14 and 1.01 for option 1 and 2, respectively. As it can be seen from Table 5, if the DSM program considers those houses with fixed rate (option 1) electricity payment, the value of SIR is higher than when houses with dynamic tariff (option 2) participate in the DSM program. This is due to the higher lost income that utility is faced. Since utility is not able to sell electricity during peak hours (expensive rate) and instead sells during off peak hours (cheap rate). Although both proposed DSM program are feasible and have the value of SIR higher than 1, option 2 is risky and requires to be devised.

Table 5: Results of the DSM program analysis located in UK

	Option 1	Option 2
Description of rebate program	Rebate program for the participant houses with fixed rate electricity payment	Rebate program for the participant houses with dynamic tariff electricity payment
NPV (EUR)	50,606,488	227,971
SIR	2.14	1.01

4. CONCLUSION

In this study, a DSM strategy is suggested to achieve the goal of shifting morning and evening peak hours. The peak shifting is achieved by the utilization of a novel heat pump driven TCHS system, which can be charged during off peak hours. In the proposed DSM program, an astronomic relay in participating houses is installed ensuring that the air conditioners are kept off during the peak hours. The assumption is made that each house utilizes a 24,000 BTU/h (7.034 kW) air conditioner in the occupied room. By not operating these air conditioners during the peak hours of winter, a

reduction of 17.5 MW from the maximum peak can be attained by involving 6842 houses in the program. The total cost of DSM program for each house is calculated as 3703.50 EUR. After conducting energy and economic calculations and making appropriate assumptions, it has been determined that the proposed DSM program is feasible for both options. The SIR values for option 1 and option 2 are obtained as 2.14 and 1.01, respectively. However, if the DSM program is implemented specifically for participants who benefit from dynamic electricity tariffs (option 2), it becomes more challenging and requires careful planning. In such cases, it is recommended that utilities take advantage of government grants to enhance the feasibility of the program. Another potential solution is to explore the possibility of homeowners participating in the cost of the DSM program, which would require further investigation and study. Moreover, conducting a comprehensive sensitivity analysis is regarded as a crucial area for further study.

5. ACKNOWLEDGEMENT

This work is funded by the Engineering and Physical Sciences Research Council (United Kingdom) [grant number: EP/T021233/1].

6. REFERENCES

Agboola, O.P., Atikol, U., Assefi, H. (2015) 'Feasibility assessment of basin solar stills', *Int. J. Green Energy*, 12, pp. 139–147.

Brancato, V., et al. (2019) 'Experimental characterization of the LiCl/vermiculite composite for sorption heat storage applications', *International Journal of Refrigeration*, 105, pp. 92–100

Chen, B., Johannes, K., Horgnies, M., Morin, V., Kuznik F. (2021) 'Characterization of an ettringite-based thermochemical energy storage material in an open-mode reactor', *Journal of Energy Storage*, 33, pp. 102159.

Clark, R.J. and Farid, M. (2022) 'Experimental investigation into cascade thermochemical energy storage system using SrCl2-cement and zeolite-13X materials', *Applied Energy*, 316, pp. 119145.

Zeng, C., Liu S., Yang L., Han X., Song M., Shukla A. (2019) 'Investigation of a three-phase thermochemical reactor through an experimentally validated numerical modelling', Applied Thermal Engineering, 162, pp. 114223.

Aydin, D., Casey, S. P., Chen, X., Riffat S., (2018) 'Numerical and experimental analysis of a novel heat pump driven sorption storage heater', *Applied Energy,* 211, pp. 954–974.

Ding, B. et al. (2021) 'Study on long-term thermochemical thermal storage performance based on SrBr2-expanded vermiculite composite materials', *Journal of Energy Storage*, 42, pp. 103081.

https://www.amazon.co.uk, (June 2023)

Insulation 4 less, https://insulation4less.co.uk/blogs/guides-and-news/building-regs-u-values

Insulation super store (June 2023), Retrieved from https://www.insulationsuperstore.co.uk

Kant, K. and Pitchumani, R. (2022) 'Analysis of a novel constructal fin tree embedded thermochemical energy storage for buildings applications', *Energy Conversion and Management*, 258, pp. 115542.

Katulic, S., Cehil, M., Bogdan, Z. (2014) 'A novel method for finding the optimal heat storage tank capacity for a cogeneration power plant', *Applied Thermal Engineering*, 65, pp. 530-538.

Li, W., Klemes, J. J., Wang, Q., Zeng, M., (2020) 'Development and characteristics analysis of salt-hydrate based composite sorbent for low-grade thermochemical energy storage', *Renewable Energy*, 157, pp. 920-940.

Metalswarehouse (June 2023), Retrieved from https://www.metalswarehouse.co.uk/product/2-0mm-aluminium-sheet

Ozdenefe, M., Atikol, U., Rezaei, M, (2018) 'Trombe wall size-determination based on economic and thermal comfort viability', *Solar Energy*, 174, pp. 359-372.

Packer M.B., Glicksman, L.R. (1979) 'An assessment of thermal energy storage in conjunction with heat pumps for residential heating and cooling', *Energy*, 4, pp. 393-399.

Probreeze (June 2023), Retrieved from https://probreeze.com/products/3-8-litre-ultrasonic-cool-mist-humidifier-with-aroma-diffuser

Reynolds, J. et al. (2023) 'Development and characterisation of an alginate and expanded graphite based composite for ther-mochemical heat storage', *Journal of Materials Science*, 58, pp. 5610–5624.

Rezaei, M., Atikol, U. and Ozdenefe, (2020) 'M. Promotion of Trombe wall through demand-side management', *Solar Energy*, 206, pp. 216–227.

Trading economics (June 2023). Retrieved from tradingeconomics.com/commodity/uk-natural-gas

#67: Graph neural network-based spatio-temporal methodology for hydraulic-thermal modelling of district cooling systems

Jing ZHANG[1], Hanbei ZHANG[2], Fu XIAO[3]

1 Department of Building Environment and Energy Engineering, The Hong Kong Polytechnic University, Hong Kong, China, jing-amber.zhang@connect.polyu.hk
2 Department of Building Environment and Energy Engineering, The Hong Kong Polytechnic University, Hong Kong, China, hanbei.zhang@connect.polyu.hk
3 Department of Building Environment and Energy Engineering and Research Institute for Smart Energy, The Hong Kong Polytechnic University, Hong Kong, China, linda.xiao@polyu.edu.hk

Abstract: Hydraulic-thermal modelling plays a crucial role in effective management of district cooling systems, enabling fault detection and diagnosis and pump speed control to achieve energy savings. The development of traditional detailed physical hydraulic models is time consuming and labour intensive, and the models developed need to be calibrated several times during the operational stage. Data-driven modelling has made significant strides in capturing temporal relationships using advanced machine learning algorithms. However, existing data-driven modelling methods often make simplistic assumptions about water distribution and generally overlook structural relationships, such as the topology of cooling water pipes and pumps. To address this issue, this study presents a novel spatio-temporal data-driven methodology for representing district cooling systems as graphs and modelling the hydraulic system. A case study of a district cooling system based on real cooling load simulation is carried out to evaluate the efficacy of the proposed methodology. Graph neural network-based models that consist of a graph layer and a recurrent layer were developed to capture the structural and temporal relationships separately. The graph layer utilizes graph convolutional network (GCN) and graph attention network (GAT) to learn the structural relationships from the input graphs. The recurrent layer utilizes Long Short-Term Memory (LSTM) to learn the temporal relationships from massive historical operational data. The developed models generated better prediction performance than conventional deep learning models. This methodology provides a new approach to analyzing hydraulic systems that can facilitate effective management of district cooling systems. By incorporating both the structural and temporal relationships in the data-driven modelling process, the methodology offers a more comprehensive understanding of the hydraulic system and can provide valuable insights for optimizing the system's energy efficiency and fault detection. It has the potential to be widely applied in the field of district cooling systems and other related hydraulic systems.

Keywords: Hydraulic model; Graph; District cooling system; Spatio-temporal modelling

1. INTRODUCTION

The building sector accounts for about 30% of global energy consumption and 27% of energy-related greenhouse gas emissions (IEA, 2022), making it a key area for achieving climate objectives. District cooling systems (DCS) have gained substantial attention due to their superior energy efficiency and cost-effectiveness in comparison to conventional cooling systems (Inayat & Raza, 2019).

Hydraulic modelling is essential for efficient district cooling system management, as it facilitates fault detection and diagnosis and enables optimal control to achieve energy savings and enhance operational efficiency (Brown et al., 2022). Two types of models were developed, the while-box model and the black-box (also known as data-driven) models.

White-box models are developed based on physical principles and detailed system information, which are usually accurate but time-consuming in both development and application. Del Hoyo Arce et al. developed detailed distribution pipe network models in Modelica and reduced mathematical models in Simulink to simulate system dynamics (Del Hoyo Arce et al., 2018). Van der Heijde et al. developed a thermo-hydraulic network model in Modelica to cope with highly variable mass flow and temperature profiles (Van Der Heijde et al., 2017). Hirsch and Nicolai developed a detailed thermo-hydraulic network model considering flow regime for heat loss calculation and demonstrated the model on a real-world 5GDHC network (Hirsch & Nicolai, 2022).

Data-driven models using machine learning attract increasing attention in the pervasive big data revolution AI. Compared with conventional physics-based methods, which are mainly based on engineering methods and dedicated building energy simulation tools, data-driven methods require less information and understanding of buildings and their energy systems. Guo et al. developed a data-driven hydraulic-thermal dynamic model for fast calculation using backpropagation (BP) neural network (Guo et al., 2023). Cui et al. proposed a data-driven framework including parameter estimation and initialization for solving hydraulic equations (Cui et al., 2020).

However, existing data-driven modelling methods rely on time-series data and tend to neglect the inclusion of spatial information. This oversight overlooks important structural relationships like the topology of cooling water pipes and pumps. Consequently, these data-driven models can only capture temporal correlations between variables, limiting their effectiveness to dynamic modelling alone.

Substantial research in other fields proved that using both spatial and temporal attributes of the data, i.e. spatio-temporal data, are very helpful in engineering tasks of prediction, detection, classification, inference, etc (Wang et al., 2022), e.g., traffic prediction (Ermagun & Levinson, 2018) and weather forecasting (Chattopadhyay et al., 2020; Karevan & Suykens, 2018). Graph neural networks (GNNs) exhibit their powerful potential in making use of spatial-temporal data (Wu et al., 2021). Sanchez-Gonzalez et al. proposed a recurrent GNN-based method for simulating complex physics, in which physical states were represented by nodes and dynamic interactions by the edge in graphs (Sanchez-Gonzalez et al., 2020). Hu et al. developed a spatial-temporal graph convolutional network (ST-GCN) for time series energy consumption prediction of multiple neighbouring buildings, in which buildings were represented by nodes and their dynamic solar impacts by edges (Hu et al., 2022).

This study proposes a spatio-temporal data-driven methodology to represent district cooling systems as graphs and model the hydraulic system. The proposed methodology utilizes graphs to represent the hydraulic system, incorporating both spatial and temporal information. A stacked GNN-RNN model architecture is employed for hydraulic modelling to effectively capture the spatial and temporal dependencies among input features. To validate the effectiveness of the proposed methodology, a case study is conducted using real cooling load simulation data from a district cooling system.

2. METHODOLOGY

This study proposed a generic graph representation for district cooling system, which integrates the related spatial (e.g., system topology, etc.) and temporal (e.g., system operational data, etc.) information. The nodes represent different physical entities, and the graph structure (i.e., connection between nodes) is designed based on physical connection. A stacked GNN-RNN model architecture is adopted for spatio-temporal hydraulic-thermal modelling of district cooling system. The graph generated will be used as the model input. The graph layer and recurrent layer are capable of capturing the spatial dependency and temporal dependency among input features, respectively.

2.1. Graph-based data structure

Graph is recognized as one of the most generic, natural, informative and interpretable formats for data representation (Fan et al., 2019). A graph $\boldsymbol{G}$ can be represented as Equation 1.

Equation 1: A graph.

$$\boldsymbol{G} = (\boldsymbol{V}, \boldsymbol{E}, \boldsymbol{A})$$

Where:

- $\boldsymbol{G}$ = A graph.
- $\boldsymbol{V}$ = Set of nodes. Here, $v_i \in \boldsymbol{V}$ denote a node.
- $\boldsymbol{E}$ = Set of edges. Here, $e_{ij} = (v_i, v_j) \in \boldsymbol{E}$ denotes an edge which connects node v_i and node v_j.
- $\boldsymbol{A}$ = Adjacency matrix.

The graph structure is usually described by the adjacency matrix and the node attributes are described by the feature matrix. For an undirected and connected graph with *N* nodes, the adjacency matrix $\boldsymbol{A} = [a_{ij}] \in \mathbb{R}^{N\times N}$ can be represented as Equation 2.

Equation 2: Adjacency matrix.

$$a_{ij} = \begin{cases} 1, e_{ij} \in \boldsymbol{E} \\ 0, e_{ij} \notin \boldsymbol{E} \end{cases}$$

For a graph with *M*-dimensional nodes with time sequence *T*, the feature matrix $\boldsymbol{X} = [x_{i,m}^t] \in \mathbb{R}^{N\times M\times T}$ stores the node attributes.

Figure 1 shows a comparison between a conventional tabular structure for temporal data only and a graph-based data structure for spatio-temporal data. Typically, building operational data (e.g., time, energy consumption data, operating variables, environmental parameters, etc.) are stored in a two-dimensional tabular form, where each column represents a variable and each row stores the measurements or signals at the same time step, as is shown in Figure 1 (a). However, spatial information, like the topology of the system, cannot be considered in the tabular data structure. Graphs are more informative and suitable for spatio-temporal data, which consists of nodes representing physical entities (like pumps, etc.) and edges representing the relationship of the entities, as shown in Figure 1 (b).

Variables

Time	1	2	3	4	5	6	7	8
t	V_1^t	V_2^t	V_3^t	V_4^t	V_5^t	V_6^t	V_7^t	V_8^t
t+1	V_1^{t+1}	V_2^{t+1}	V_3^{t+1}	V_4^{t+1}	V_5^{t+1}	V_6^{t+1}	V_7^{t+1}	V_8^{t+1}
t+2	V_1^{t+2}	V_2^{t+2}	V_3^{t+2}	V_4^{t+2}	V_5^{t+2}	V_6^{t+2}	V_7^{t+2}	V_8^{t+2}
t+3	V_1^{t+3}	V_2^{t+3}	V_3^{t+3}	V_4^{t+3}	V_5^{t+3}	V_6^{t+3}	V_7^{t+3}	V_8^{t+3}
…	…	…	…	…	…	…	…	…

Note: for V_i^t, *i* is node number and *t* is time instant

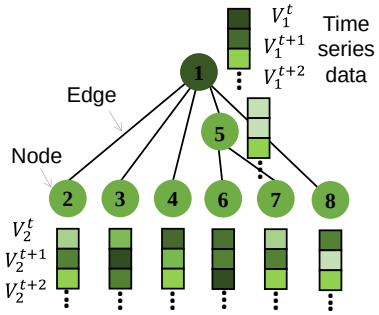

a) Conventional tabular data structure *b) Graph-based data structure*

Figure 1 Comparison of conventional tabular data structure and graph-based data structure

2.2. Graph representation of district cooling systems

The spatial and temporal information can be embedded in the graph structure, adjacency matrix, and feature matrix.

Nodes. The nodes can represent the physical entities of target system, e.g., pumps, air handling unit (AHU), etc. These nodes can be homogeneous or heterogeneous.

Edges. The graph structure corresponds to physical configuration of the target system. Nodes connected in the water distribution network are set to be connected in the graph representation.

Adjacency matrix. The adjacency matrix indicates whether there is an edge between two nodes. In this study, a Boolean matrix is used to represent the connections between nodes.

Feature matrix. Feature matrix stores operational data of district cooling system, e.g., flow rate, pressure, etc.

Figure 2 provides a graph representation example of a simple district cooling system. The nodes represent the physical entities of the system, and the node connections (graph structure) are determined based on physical connections. The temporal information (i.e., system operation data) is encoded in the feature matrix and the spatial information (i.e., the edges) can be encoded in the adjacency matrix. In this way, the spatio-temporal data can be integrated into a graph representation.

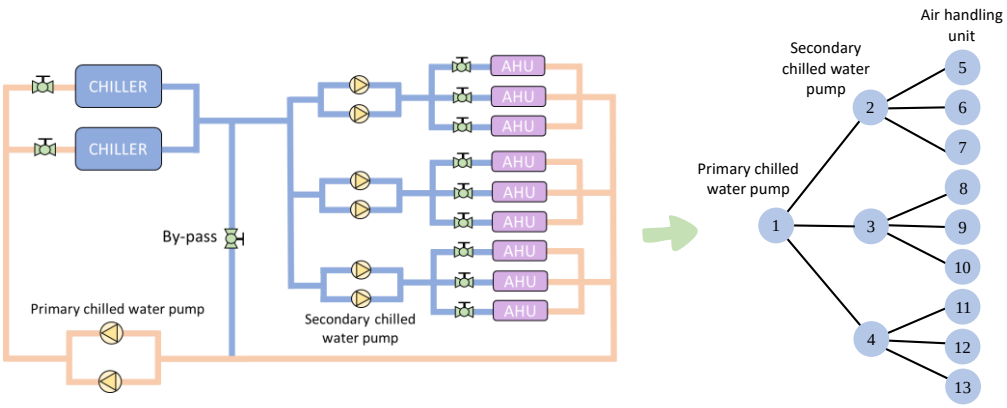

Figure 2 Proposed graph representation of a simple district cooling system

2.3. Spatio-temporal modelling of district cooling system

A stacked GNN-RNN model architecture is adopted for hydraulic modelling of the district cooling system. The graph generated in Section 2.2 will be used as the model input.

As shown in Figure 3, a stacked GNN-RNN architecture is adopted for the spatio-temporal modelling of district cooling system. The developed GNN-RNN model consists of a graph layer, a recurrent layer, and a fully connected layer. The graph layer is responsible for capturing the spatial relationship within the system, while the recurrent layer is responsible for handling the temporal relationship.

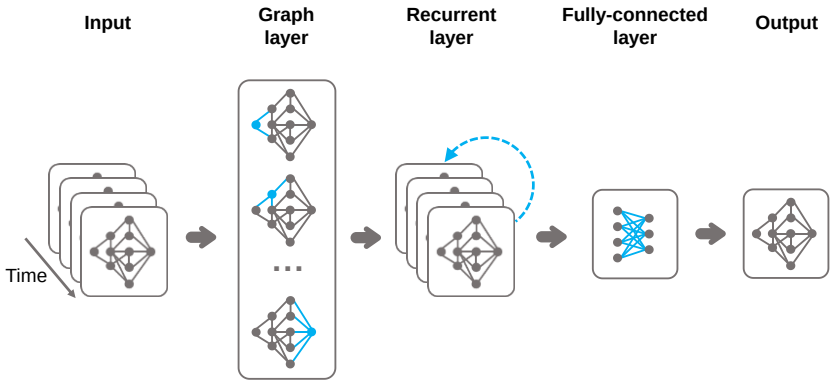

Figure 3 Spatio-temporal model for district cooling system

Graph neural network (GNN). The earliest motivation for GNNs can be rooted in the 1990's owing to graph analysis and graph representation learning (Sperduti & Starita, 1997), while the recent re-advancement of GNNs is mainly attributed to the success of deep neural networks, particularly convolutional neural networks (CNN) (Lecun et al., 1998). A GNN (Scarselli et al., 2009) can be regarded as an extension of a CNN architecture, and provides an effective method to capture spatial dependencies among graph-structured inputs. The adjacency matrix representing the graph structure can assist the message propagation within neural layers in the GNNs. Based on the connection information provided by the adjacency matrix, GNNs can efficiently capture graphs' structural dependencies via message propagation between the nodes by aggregating information only from connected nodes (Battaglia et al., 2018). Depending on the information aggregation method (Wu et al., 2021), GNNs can be further classified into several types, e.g., chebyshev neural network (ChebNet) (Defferrard et al., 2016), graph convolution networks (GCNs) (Kipf & Welling, 2017), adaptive graph convolution network (AGCN) (R. Li et al., 2018), graph attention networks (GATs) (Veličković et al., 2018), etc. Among them, GCNs play a crucial role in capturing structural dependencies, while networks in other categories partially rely on GCNs in building blocks (Xiao & Fan, 2022). GCNs accomplish convolutional feature extraction through neighbourhood aggregation. This propagation rule can be motivated via a first-order approximation of localized spectral filters on graphs. The graph attention networks (GATs) are created by incorporating the attention mechanism into the propagation stage. The attention mechanism enables the neural networks to pay attention to how different inputs influence outputs at each step of inference. In general, the most widely used types of GNNs nowadays are GCNs and GATs.

Recurrent neural network (RNN). Recurrent neural network (RNN) has been an important focus of research during the 1990's, which is developed for analysing time-series data (Medsker & Jain, 1999). RNNs can learn temporal relationships or dynamics from a sequence. The capability of RNNs in capturing long-term temporal dependencies can be limited due to vanishing or exploding gradient problem. To overcome this problem, the two special types of RNN called long short-term memory (LSTM) (Hochreiter & Schmidhuber, 1997) and gated recurrent units (GRU) (Chung et al., 2014) were created by introducing the concept of gates to control the flow of information and learn the important information in the memory unit, which can pass the information in long sequences. LSTM enables the reinjection of past information later by calculating what percentage will the past information be allowed to affect the present information, thus contributing to dealing with the problem of vanishing or exploding gradients. On the other hand, GRU is a simplified and efficient alternative to the LSTM, which uses only an update gate and a reset gate. In this study, the LSTM is used as the RNN layer.

3. CASE STUDY

A case study is conducted on a district cooling system simulation platform developed by physical equations based on real cooling load.

3.1. Introduction of the target district cooling system and the simulation platform

Figure 4 shows the district cooling system designed for the Hong Kong Polytechnic University Campus. A primary-secondary pumping system with 3 secondary loops was chosen to provide cooling capacity for the whole campus. The

dimensions of the pipeline, including its length and diameter, have been carefully determined to align with the actual conditions on-site. Figure 5 shows the detailed chiller water distribution system.

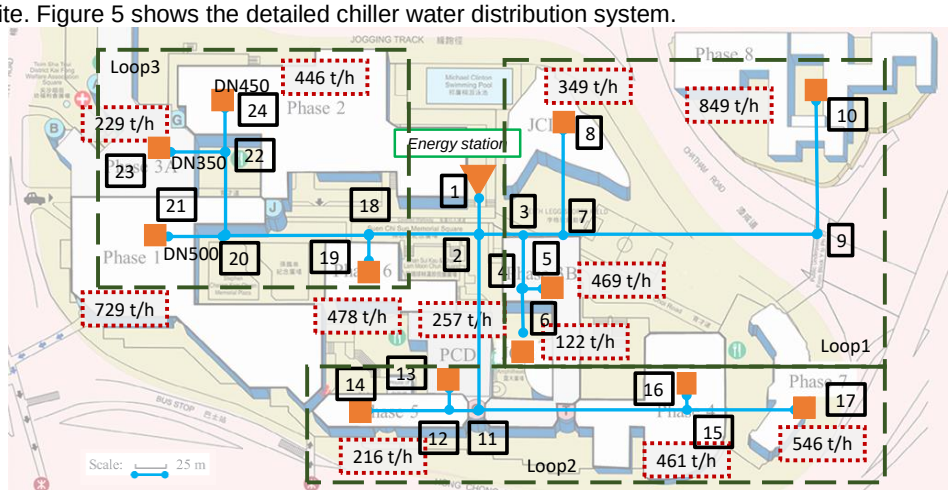

Figure 4 District cooling system designed for the campus

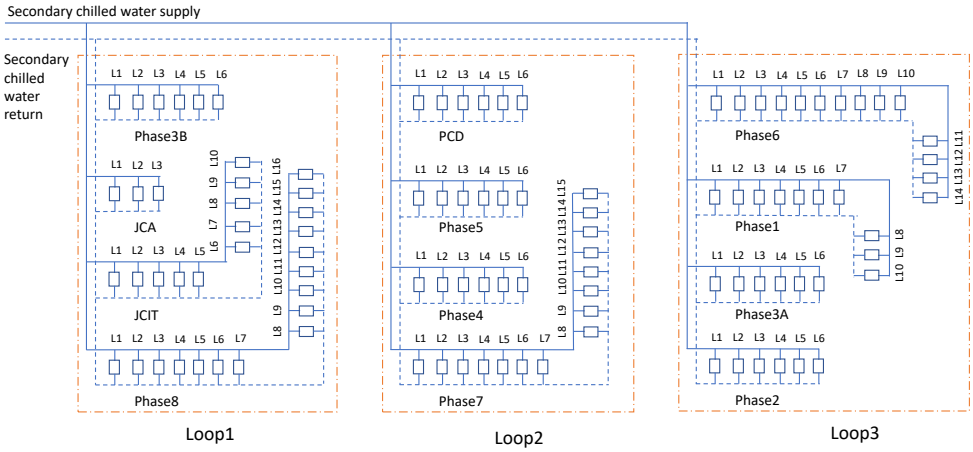

Figure 5 Detailed chilled water distribution system

To simulate the operation of the district cooling system that has been designed, the actual hourly cooling load data from February 10th, 2015 to November 30th, 2015 have been utilized. The hydraulic simulation is based on fundamental equations from Equation 3 to Equation 5 (Kang et al., 2019).

Equation 3: Mass conservation equation of water.

$$A_k \cdot Q = Q_q$$

Equation 4: Pressure drop of a loop.

$$B_f \cdot \Delta P = 0$$

Equation 5: Pressure drop of a pipe segment.

$$\Delta P = S \cdot |Q| \cdot Q - DP$$

Where:

- A_k = Basic incidence matrix.
- Q = Fluid flow rates (t/h). Here, $Q = [Q_1, Q_{2,\dots}, Q_n]^{\mathrm{T}}$ indicate fluid flow rates from each pipe.
- Q_q = leakage flow rate (t/h). Here, $Q_q = [Q_{q,1}, Q_{q,2,\dots}, Q_{q,n}]^{\mathrm{T}}$ indicate leakage flow rates from each node.
- B_f = Independent loop matrix.
- ΔP = Pressure drop (kPa). Here, $\Delta P = [\Delta P_1, \Delta P_{2,\dots}, \Delta P_n]^{\mathrm{T}}$ indicate pressure drop from each pipe.
- S = Resistance coefficient. Here, $S = diag\{s_1, s_2, \dots s_n\}$ indicate resistance coefficients of each pipe.
- DP = Pump head of pipe segment (kPa). Here, $DP = [DP_1, DP_{2,\dots}, DP_n]^{\mathrm{T}}$ indicate the pump head of each pipe segment.

3.2. Development of spatio-temporal hydraulic-thermal models

As shown in Figure 6, each graph contains 108 nodes (i.e., *N*=108) including 1 primary chilled water pump (PCWP) node, 3 secondary chilled water pump (SCWP) nodes, and 104 air handling unit (AHU) nodes with 2-dimensional vector of attribute values (i.e., *M*=2).

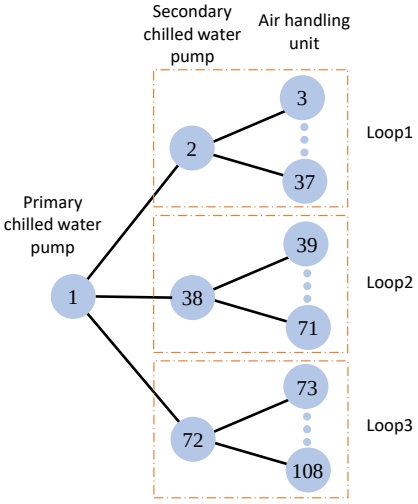

Figure 6 Graph representation in the case study

The feature matrix is constructed using Figure 6

$$X = [x_F^t, x_{\Delta P}^t]$$

Equation 6: Feature matrix in the case study.

Where:

- x_F^t = Flow rate of timestep *t* (t/h).
- $x_{\Delta P}^t$ = Pressure drop of timestep *t* (kPa).

The hydraulic modelling of the target district cooling system aims to predict the pressure drops for the next timestep based on operational data of previous 3 timestep (i.e., *T*=3). The whole dataset (containing 3124 observations) is transformed into sub-sequences via a sliding-window manner. Data preprocessing is performed to enhance data quality. The missing values are filled in using the moving average method, while the outliers are identified with domain expertise. Min-max normalization is adopted to transform the data into a suitable scale for further analysis. The historical data are randomly divided into training dataset and testing dataset. The training dataset and testing dataset account for 80% and 20% of the total data, respectively.

3.3. Prediction results of spatio-temporal models and analysis

For the proposed GNN-RNN neural architecture, three widely-used graph layers are tested, including graph convolutional layer (i.e., GCN-RNN) (Kipf & Welling, 2017), diffusion convolution layer (i.e., DC-RNN) (Y. Li et al., 2018), and graph attention layer (i.e., GAT-RNN) (Veličković et al., 2018). For comparison, two conventional deep learning model architectures, i.e. CNN-RNN and Dense-RNN, are tested, which replace the graph layer with a convolutional layer and fully-connected layer. For the recurrent layer, long short-term memory (LSTM) is chosen in all models.

All the models and methods are tested using Python programming language, as well as Keras (CNN and RNN), Spektral (GNN) packages. The hyperparameters are identified based on a grid search. To prevent overfitting, an early-stopping training scheme is adopted, i.e., terminating the model training process when the resulting accuracy in validation data stops increasing after a specified number of iterations. Each combination of model architectures is tested 20 times.

In this study, five model architectures are tested and compared. The prediction accuracy of the models on testing dataset is shown in Table 1 and Figure7.

Table 1: Model prediction accuracy (RMSE: kPa)

	CNN-RNN	Dense-RNN	GAT-RNN	GCN-RNN	DC-RNN
RMSE (kPa)	7.3 ± 0.4	7.4 ± 0.7	6.8 ± 0.2	6.9 ± 0.3	7.0 ± 0.3

As the results suggest, GNN-RNN models (i.e., GAT-RNN, GCN-RNN, DC-RNN) achieve better prediction performance than the conventional deep learning models (i.e., CNN-RNN, Dense-RNN). GAT-RNN achieves the best prediction performance with an RMSE of 6.8 ± 0.2, which shows a 8.9% improvement over the Dense-RNN architecture.

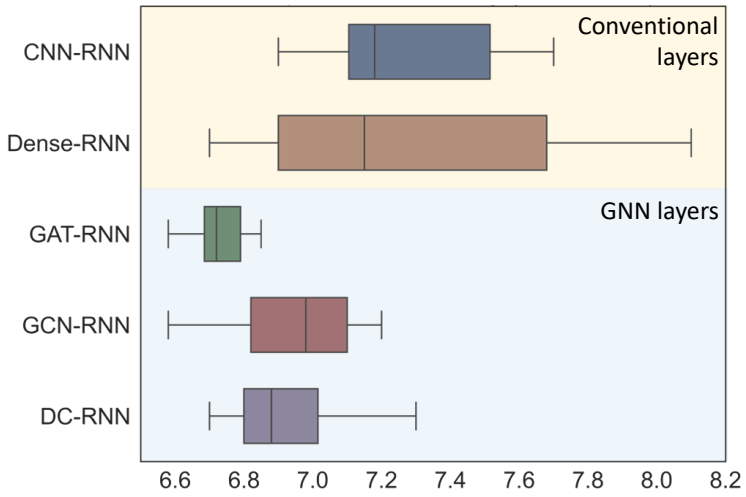

Figure 7 Model prediction accuracy (*(RMSE: kPa)*

The Dense-RNN model performed poorly in comparison to the other models tested. This result is likely since connecting unrelated nodes can interfere with the model's inference mechanism. Additionally, the increased number of model parameters makes the training process more complicated. CNN-RNN model with a random input order also performed worse than the GNN-RNN models. This indicates that utilizing conventional data-driven modelling techniques without arranging the data according to the physical system structure can result in the loss of a substantial amount of crucial structural information, leading to a decrease in model accuracy.

Among all graph layers, the GAT layer performs better. The attention mechanism is incorporated into the propagation step, enabling neural networks to focus on how different inputs influence outputs at each step of inference in the model development process. This allows the model to assign varying importance to different nodes, leading to further improvements in performance.

The node connection, which defines the flow of information between different nodes, plays a crucial role in the performance of neural networks. The results demonstrate that node connections can be designed based on prior information of physical connection (i.e., system topology) between the physical entities, to alleviate the interference of unnecessary information between irrelevant nodes and ease the complexity of model training. Compared with a graph with pairwise connections between nodes, the graph structure designed in this study removes the association between many irrelevant nodes. This can significantly reduce the difficulty for the model to learn the complex correlations between multiple physical entities by aggregating information only from adjacent nodes.

4. CONCLUSION

This study has developed a novel spatio-temporal data-driven methodology for hydraulic-thermal modelling of district cooling systems. The study integrates multi-source spatio-temporal data in a graph structure instead of a traditional tabular format. This approach provides a graph-based perspective to symbolize, analyze, and model the district cooling systems based on their physical configuration, representing a significant step towards leveraging spatio-temporal data. Graph neural network-based spatio-temporal models are then developed for hydraulic prediction, considering both structural and temporal relationships. Using the developed modelling method, the building design information and operational data can be effectively integrated and utilized. Additionally, this study provides a valuable methodology for incorporating the physical knowledge, particularly the design information, into machine learning modelling. It demonstrates an ideal synergy between machine learning and domain expertise.

5. ACKNOWLEDGEMENT

The authors gratefully acknowledge the support of this research by National Key R&D Program of China (2021YFE0107400), Innovation and Technology Fund (ITP/002/22LP) and the Research Grants Council (C5018-20GF; 15220323) of the Hong Kong SAR, China.

6. REFERENCES

Battaglia, P. W., Hamrick, J. B., Bapst, V., Sanchez-Gonzalez, A., Zambaldi, V., Malinowski, M., Tacchetti, A., Raposo, D., Santoro, A., Faulkner, R., Gulcehre, C., Song, F., Ballard, A., Gilmer, J., Dahl, G., Vaswani, A., Allen, K., Nash, C., Langston, V., … Pascanu, R. (2018). Relational inductive biases, deep learning, and graph networks (arXiv:1806.01261). arXiv. http://arxiv.org/abs/1806.01261

Brown, A., Foley, A., Laverty, D., McLoone, S., & Keatley, P. (2022). Heating and cooling networks: A comprehensive review of modelling approaches to map future directions. Energy, 261, 125060. https://doi.org/10.1016/j.energy.2022.125060

Chattopadhyay, A., Hassanzadeh, P., & Pasha, S. (2020). A test case for application of convolutional neural networks to spatio-temporal climate data: Re-identifying clustered weather patterns. Scientific Reports, 10(1), 1317. https://doi.org/10.1038/s41598-020-57897-9

Chung, J., Gulcehre, C., Cho, K., & Bengio, Y. (2014). Empirical Evaluation of Gated Recurrent Neural Networks on Sequence Modeling (arXiv:1412.3555). arXiv. https://doi.org/10.48550/arXiv.1412.3555

Cui, G., Jia, Q.-S., Guan, X., & Liu, Q. (2020). Data-driven computation of natural gas pipeline network hydraulics. Results in Control and Optimization, 1, 100004. https://doi.org/10.1016/j.rico.2020.100004

Defferrard, M., Bresson, X., & Vandergheynst, P. (2016). Convolutional Neural Networks on Graphs with Fast Localized Spectral Filtering. Advances in Neural Information Processing Systems, 29. https://proceedings.neurips.cc/paper/2016/hash/04df4d434d481c5bb723be1b6df1ee65-Abstract.html

Del Hoyo Arce, I., Herrero López, S., López Perez, S., Rämä, M., Klobut, K., & Febres, J. A. (2018). Models for fast modelling of district heating and cooling networks. Renewable and Sustainable Energy Reviews, 82, 1863–1873. https://doi.org/10.1016/j.rser.2017.06.109

Ermagun, A., & Levinson, D. (2018). Spatiotemporal traffic forecasting: Review and proposed directions. Transport Reviews, 38(6), 786–814. https://doi.org/10.1080/01441647.2018.1442887

Fan, C., Xiao, F., Song, M., & Wang, J. (2019). A graph mining-based methodology for discovering and visualizing high-level knowledge for building energy management. Applied Energy, 251, 113395. https://doi.org/10.1016/j.apenergy.2019.113395

Guo, S., Ji, W., Wang, C., Song, T., & Wang, J. (2023). Hydraulic-thermal coupling dynamic models based on mechanism and data-driven methods of the heating networks in integrated energy systems. Energy Conversion and Management, 292, 117353. https://doi.org/10.1016/j.enconman.2023.117353

Hirsch, H., & Nicolai, A. (2022). An efficient numerical solution method for detailed modelling of large 5th generation district heating and cooling networks. Energy, 255, 124485. https://doi.org/10.1016/j.energy.2022.124485

Hochreiter, S., & Schmidhuber, J. (1997). Long Short-Term Memory. Neural Computation, 9(8), 1735–1780. https://doi.org/10.1162/neco.1997.9.8.1735

Hu, Y., Cheng, X., Wang, S., Chen, J., Zhao, T., & Dai, E. (2022). Times series forecasting for urban building energy consumption based on graph convolutional network. Applied Energy, 307, 118231. https://doi.org/10.1016/j.apenergy.2021.118231

IEA. (2022). Buildings. IEA. https://www.iea.org/reports/buildings

Inayat, A., & Raza, M. (2019). District cooling system via renewable energy sources: A review. Renewable and Sustainable Energy Reviews, 107, 360–373. https://doi.org/10.1016/j.rser.2019.03.023

Kang, J., Wang, S., & Yan, C. (2019). A new distributed energy system configuration for cooling dominated districts and the performance assessment based on real site measurements. Renewable Energy, 131, 390–403. https://doi.org/10.1016/j.renene.2018.07.052

Karevan, Z., & Suykens, J. A. K. (2018). Spatio-temporal Stacked LSTM for Temperature Prediction in Weather Forecasting (arXiv:1811.06341). arXiv. https://doi.org/10.48550/arXiv.1811.06341

Kipf, T. N., & Welling, M. (2017). Semi-Supervised Classification with Graph Convolutional Networks (arXiv:1609.02907). arXiv. https://doi.org/10.48550/arXiv.1609.02907

Lecun, Y., Bottou, L., Bengio, Y., & Haffner, P. (1998). Gradient-based learning applied to document recognition. Proceedings of the IEEE, 86(11), 2278–2324. https://doi.org/10.1109/5.726791

Li, R., Wang, S., Zhu, F., & Huang, J. (2018). Adaptive Graph Convolutional Neural Networks. Proceedings of the AAAI Conference on Artificial Intelligence, 32(1), Article 1. https://doi.org/10.1609/aaai.v32i1.11691

Li, Y., Yu, R., Shahabi, C., & Liu, Y. (2018). Diffusion Convolutional Recurrent Neural Network: Data-Driven Traffic Forecasting (arXiv:1707.01926). arXiv. http://arxiv.org/abs/1707.01926

Medsker, L., & Jain, L. C. (1999). Recurrent Neural Networks: Design and Applications. CRC Press.

Sanchez-Gonzalez, A., Godwin, J., Pfaff, T., Ying, R., Leskovec, J., & Battaglia, P. (2020). Learning to Simulate Complex Physics with Graph Networks. Proceedings of the 37th International Conference on Machine Learning, 8459–8468. https://proceedings.mlr.press/v119/sanchez-gonzalez20a.html

Scarselli, F., Gori, M., Tsoi, A. C., Hagenbuchner, M., & Monfardini, G. (2009). The Graph Neural Network Model. IEEE Transactions on Neural Networks, 20(1), 61–80. https://doi.org/10.1109/TNN.2008.2005605

Sperduti, A., & Starita, A. (1997). Supervised neural networks for the classification of structures. IEEE Transactions on Neural Networks, 8(3), 714–735. https://doi.org/10.1109/72.572108

Van Der Heijde, B., Fuchs, M., Ribas Tugores, C., Schweiger, G., Sartor, K., Basciotti, D., Müller, D., Nytsch-Geusen, C., Wetter, M., & Helsen, L. (2017). Dynamic equation-based thermo-hydraulic pipe model for district heating and cooling systems. Energy Conversion and Management, 151, 158–169. https://doi.org/10.1016/j.enconman.2017.08.072

Veličković, P., Cucurull, G., Casanova, A., Romero, A., Liò, P., & Bengio, Y. (2018). Graph Attention Networks (arXiv:1710.10903). arXiv. https://doi.org/10.48550/arXiv.1710.10903

Wang, S., Cao, J., & Yu, P. S. (2022). Deep Learning for Spatio-Temporal Data Mining: A Survey. IEEE Transactions on Knowledge and Data Engineering, 34(8), 3681–3700. https://doi.org/10.1109/TKDE.2020.3025580

Wu, Z., Pan, S., Chen, F., Long, G., Zhang, C., & Yu, P. S. (2021). A Comprehensive Survey on Graph Neural Networks. IEEE Transactions on Neural Networks and Learning Systems, 32(1), 4–24. https://doi.org/10.1109/TNNLS.2020.2978386

Xiao, F., & Fan, C. (2022). Building information modeling and building automation systems data integration and big data analytics for building energy management. Research Companion to Building Information Modeling, 525–549.

#68: Rotary desiccant wheel systems: a review

Erdem CUCE[1*], Pınar Mert CUCE[2], Yusuf Nadir YILMAZ[3]

1 Recep Tayyip Erdogan University, Engineering and Architecture Faculty, Mechanical Engineering, 53100 Rize, Turkiye, erdemcuce@gmail.com*
2 Recep Tayyip Erdogan University, Engineering and Architecture Faculty, Architecture, 53100 Rize, Turkiye, mertcuce@gmail.com
3 Recep Tayyip University, Engineering and Architecture Faculty, Mechanical Engineering, 53100 Rize, Turkiye, yusufnadir_yilmaz22@erdogan.edu.tr

Abstract: Rotary desiccant wheel systems work according to the principle of dehumidification. These systems use salt such as silica gel for dehumidifying the process air. Desiccant cooling is adopted as an alternative option against traditional cooling systems owing to its outstanding advantages. Regeneration is of vital importance in the overall performance assessment of rotary desiccant wheel systems. In terms of regeneration technique, these systems can be split into two types which are natural and electrical regeneration. Natural regeneration systems usually have solar air collectors. On the other hand, electrical regeneration systems use typical fossil fuel-powered heaters. There are many design-oriented factors that affect the performance of rotary desiccant wheel systems. At the same time, operating conditions have a notable influence on system performance. This article aims to provide information about recent studies on rotary desiccant wheel systems, and cost-effective and eco-friendly strategies to enhance system performance characteristics. COP, cost, payback period, dehumidification effectiveness, and moisture reduction rate are taken into consideration in the comparative performance assessment analyses.

Keywords: Rotary desiccant wheel, cooling, dehumidifiers

1. INTRODUCTION

Fossil fuel consumption and emission of gases utilised in HVAC systems, which are among the contributions to be increment of climate change in recent years, play of vital critical role (Tian, Su and Geng 2022). Among these factors, traditionally used air-conditioning (AC) units are of great value. In addition, the working principle of conventional AC units shown in Figure 1 cools the air at 100% relative humidity (RH), which is entirely called rotten air (Guzelel et al., 2022). This rotten air can even harm human health in buildings with insufficient ventilation.

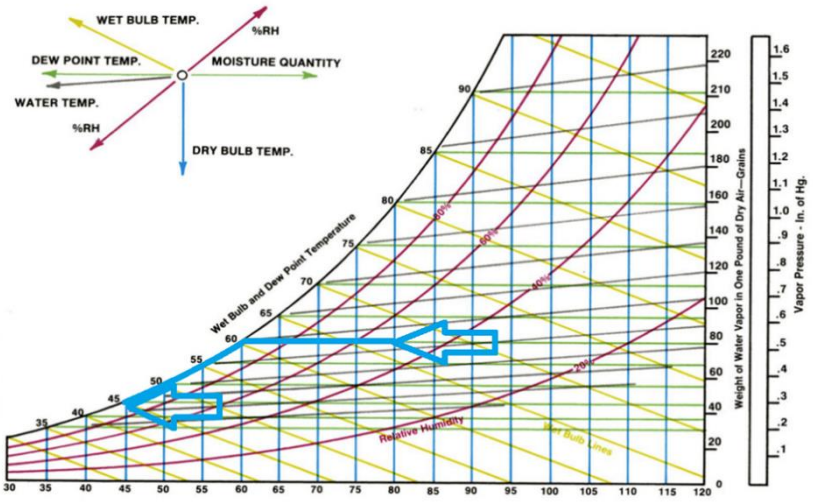

Figure 1 Representation of the working principle of traditional AC units on the psychometric diagram

Global warming with rising fossil fuel consumption has also enhanced with vapour compression AC. Hence, efforts to improve existing AC systems and solid dryer-based AC as alternative AC systems have increased in system performance significantly recently (Tsai and Wu, 2022).

Following these studies, it can be said that Rotary Desiccant Wheel (RDW) systems are the highest alternative to conventional air conditioners. In RDW systems, silica gel (SG)-based desiccant salts are used. RDW systems generally consist of two compartments which are the process and regenerative compartments. Whilst the ambient air is taken indoors in the process chamber, thanks to the salts, including SG, it is largely purified from moisture. In the regenerative chamber, the moisture collected in the SG-based salts is heated and purged. Finally, it is thrown into the environment. Thus, the life of SG-based salts is extended. Hence, there are many studies about RDW systems.

Different features of RDW systems made in this review are compared. As a result of these comparisons, it has been taken into account what kind of differences occur in the systems.

2. RESEARCH ON RDW SYSTEMS

2.1 Comparisons according to RDW systems operating conditions

Panaras et al. (2010) have investigated the performance of a desiccant rotary wheel system with a comparison of theoretical and experimental. RDW dimension, 360mm diameter-200mm thickness made by SG. In addition, the evaporative cooler used for pre-cooling is of the evaporative cooling pad type with a 60cmx60cm useful surface and 30cm pad thickness. For different states of desiccant wheel operation conditions, at 1000 m^3/h airflow, the measurement condition ranges applied daily in stable state conditions are as shown in Table 1 airflow.

Table 1: Measuring range conditions (Panaras et al., 2010).

	t_1(C)	$\omega_1(g/kg)$	t_2(C)		$\omega_2(g/kg)$
MIN	24	4	50		3
MAX	40	14	80		15
Flow rate (m3/h)		600	1000		1200

Considering the operating conditions of the impeller, although the temperature values are compatible, the humidity values are higher than expected. The reason for the humidity difference is that the dryer's ability to absorb moisture in regeneration after the initial dehumidification decreases each time after each cycle. If this reduction is due to product irritation or if the humidity is 80% when the dryer first dehumidifies when there is 5% humidity, it is almost impossible to reduce it back to 5% after regeneration. After regeneration, the permanent (within the existing natural cycle) moisture content will certainly have increased, even to a small extent, in the desiccant (Panaras et al., 2010). Ge et al. (2009) have developed an

experimental study on a two-stage rotary desiccant cooling (TSRDC) system in buildings, as can be represented at Figure 2.

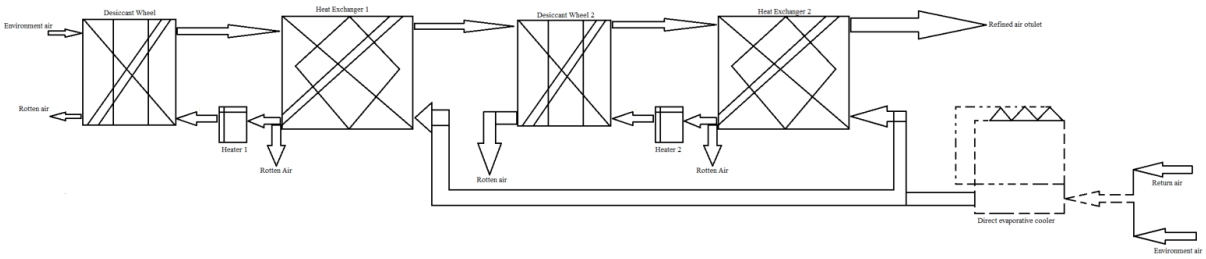

Figure 2 Schematic illustration of experimental study on a TSRDC system in buildings

A 65% efficient evaporator is placed at the regeneration air (RA) inlet to lower the temperature of the RA and increase the COP. In order to gain the heat of the RA back and to reduce the system thermal consumption, 5600 channels and an aluminium heat exchanger with a pressure loss of less than 120Pa with an efficiency of about 60% are used. The RDW is made of SG-haloid composite desiccant ceramic surface material with honeycomb, 0.003m flow channel half height and width, 0.26m diameter and 0.1m width, 8 r/h rotation speed, with low regeneration temperature (RT) and high dehumidification capacity. The RT of the single-stage system is extremely high in accordance with the TSRDC system. The humidity and temperature values obtain for three weather conditions at the recommended RTs (65-80 °C, 65-75 °C and 80-90 °C) are shown in Table 2 (Ge et al., 2009).

Table 2: The humidity and temperature values obtain for three weather conditions (Ge et al., 2009).

Condition	Process Air (PA) Inlet Condition (Ambient Air)		Return Air Condition (Indoor Air)		RA Inlet Condition	
	Dry bulb (°C)	Humidity ratio (%)	Dry bulb (°C)	Humidity ratio (%)	Dry bulb (°C)	Humidity ratio (%)
ARI summer	35.0	14.3	26.7	11.1	23.5	14.5
ARI humid	30.0	16.2	26.7	11.1	22.5	16.0
Shangai (August)	35.0	23.2	27	13.5	26.5	19.5

Ge et al. (2008) have designed a single rotor two-stage dehumidifier system. In addition to other designs, a single rotor operation consisting of a total of four parts, two regenerations and two processes, has been added to the newly designed dehumidification system as shown comparative Figure 3.

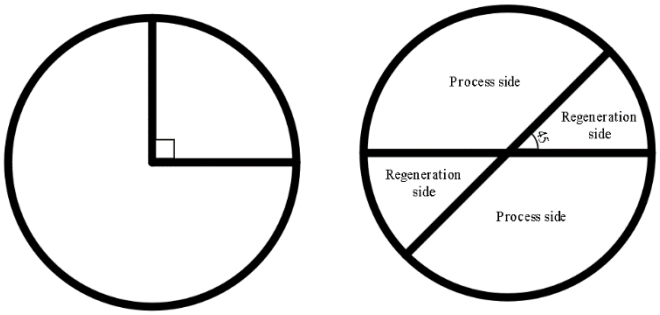

Figure 3 Sections of conventional and engineered RDWs

The values found for weather conditions are shown in Table 3. Increment performance over thickness it is found to be more performant than other systems.

Table 3: Weather conditions of the study (Ge et al., 2008)

Operation Parameters	Baseline Values
PA inlet temperature (ARI SUMMER)	$35\ °C$
PA air inlet humidity ratio (ARI SUMMER)	$14.3\ g/kg$
PA air inlet temperature (ARI HUMID)	$30\ °C$
PA inlet humidity ratio (ARI HUMID)	$19.2\ g/kg$
Return air (indoor air) temperature (summer & humid)	$26.7\ °C$
Return air humidity ratio	$11.1\ g/kg$
Enthalpy air flux	$55.2\ kJ/kg$
PA flux	$360\ m^3/h$
RA flux in desiccant wheel (M_9/M_{13})	$135\ m^3/h$
RA flux in heat exchanger (M_7/M_{11})	$360\ m^3/h$
RT (T_9/T_{13})	$50-90\ °C$

The two-stage dehumidification process with a single swivel wheel is approximately 4.5% more than other systems with a rotation speed of 4-8 rpm and is half the size of other systems (Ge et al., 2008).

2.1. Comparison of RDW systems by structure and design differences

O'Connor, Calautit and Hughes (2016) have developed a novel RDW for inactive aeration implementations in buildings, following the Figure 4.

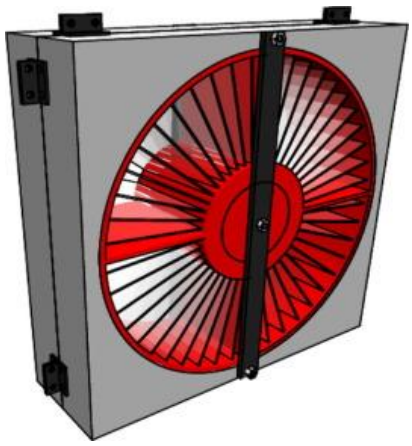

Figure 4 Illustration of the working principle of the RDW (O'Connor, Calautit and Hughes, 2016).

Since the surface area is of vital importance in rotary wheel dehumidifiers, the drying materials have been collocated in a honeycomb structure that will provide a minimum pressure reduction against the rotary wheel. The designed wheel is aimed to sustain pressure mitigation of approximately 2 Pa been necessary for adequate ventilation. The SG porosity is 66.1%, which is considerably less than the 90% porosity size in honeycomb wheels. During a testing process of 600 s, the dehumidification effectiveness of the rotary wheel dehumidifier is investigated for various inlet temperatures and RH of incoming air. For the regeneration purpose, source air with the temperature of 48 ℃ and velocity of 0.8 m/s has been utilised. In addition to the experimental works, performance parameters of the novel RDW design have been analysed by ANSYS-based CFD simulations. Additionally, the performance parameters of the new dryer rotary wheel design are analysed, and the experimental results are compared with ANSYS-based CFD simulations, as shown in Table 4. CFD results have been in well accordance with the empirical datum. By the results, the dehumidification effectiveness of the novel rotary wheel ventilation system has been found to be 65%, which is noteworthy. The aforesaid moisture reduction has been achieved with an increase in air temperature of only 9.6 ℃ after regeneration (O'Connor, Calautit and Hughes, 2016).

Table 4: Comparison of CFD and experimental studies (O'Connor, Calautit and Hughes, 2016).

		Temperature (℃)		RH (%)	
		Before Wheel	After Wheel	Before Wheel	After Wheel
Adsorption	CFD	20	27.14	90.7	33.14
	Experiment	20.11	27.46	91.28	27.46
	Error (%)	0.55	1.17	0.64	-20.68
Desorption	CFD	48	45.54	7.32	11.45
	Experiment	49.68	45.29	6.60	10.23
	Error (%)	3.38	-0.55	-10.91	-11.93

Jia et al. (2007) have designed a composite dryer wheel, as shown in Figure 5 to boost RDW cooling system performance. The new wheel they designed consists of a honeycomb main matrix made of SG and a double layer of lithium chloride impregnated into the pores of the honeycomb structure. Honeycomb structure has a pore surface area of the 194 m^2 and a pore diameter of 3.98 m.

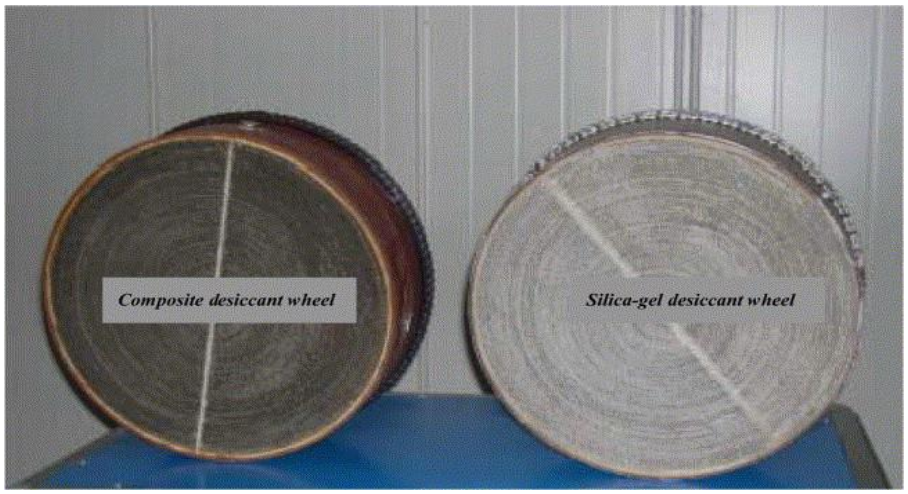

Figure 5 Pictures of the developed composite and SG-based RDW (Jia et al., 2007).

The newly designed dryer wheel is able to reduce water molecules further. It has removed about 25% more moisture from the air compared to SG. The system COP is 1.28, 35% higher than SG. The conditioner air can be set to 20°C (Jia et al., 2007). Zhang et al. (2006) have checked against the hygroscopicity of SG, calcium chloride and compound desiccant. Hygroscopic properties of individual formations of wheels are tested at 25°C and 70% RH weather conditions. Also, SG appears to absorb water faster than SG-$CaCl_2$. Wheel diameters and thicknesses are the same, the diameter is 40cm, and the thickness is 20cm. For stable and unstable states, PA flow, temperature and RH are 790m^3/h, 27-35°C, and 40-63%, respectively, at 263m^3/h flow rate at 70-120°C different RTs. In this comparative experimental test study, it is observed that composite dryers reach equilibrium faster than SG dryers and are sufficient for drying wheel application with their water absorption feature (Zhang et al., 2006).

2.2. Pre-cooling and comparisons by rotational speed

Su et al. (2021) have developed a dehumidification system integrated with precooling and recirculated regenerative RDW. The diameter of the rotary drying wheel is 260mm, in addition, the processing area of the drying wheel is three times the regeneration area. While the proposed system uses conventional cooling conditions, the PA temperature, the RH of the PA, the flow rate of the PA, the temperature of the RA and the pre-cooling temperature is approximately respectively 35°C, 75%, 225m^3/h, 135°C, 22°C. While the process RH of the developed system increases from 60% to 90%, there is a 7.8% diminish in the dehumidification capacity and a rise of 1.3% in the dehumidification capacity when the PA temperature is increased by 4°C. The improved dehumidification system integrates with the developed pre-cooling and recirculating regenerative, rotary dryer impeller removes approximately 30% more moisture than conventional systems. Even though the RA flow rate is about 10 to 18%, the sensible heat rate decreases as this rate increases. The dehumidification performance coefficient varies between 0.36 and 4.32 according to the sensible heat ratio (0.23-4.62) (Su et al., 2021). Angrisani, Roselli and Sasso (2013) have tested the effects of rotational speed on the RDW. As a result of these tests, it is observed that the adsorption rate of the drying wheel is gradually increased when it is at a low PA input temperature. The temperature and humidity of the environment are 32°C and 15g/kg, respectively. The ideal speed to keep the dehumidification rate high depends on the operating conditions. Alteration according to these conditions; 7 to 10 RPM when inlet process humidity rises from 8 to 11 g/kg, 6-10 RPM when RT rises from 45°C to 65°C, and the ratio between when regeneration and PA flow rates ascend from 0.5 to 1.1 5-9 RPM. It also decreases from 8 RPM to 6 RPM when the inlet process temperature rises from 25°C to 34°C. The highest dehumidification efficiency is obtained at 0.5-0.6 with low inlet process humidity and temperature, as well as high RT and flow rate. Optimum rotation speed, according to DCOP does not interfere with operating conditions. It achieves high DCOP with a low RT, flow rate, and high entry process humidity and temperature. The sensible energy proportion increases with low RT and flow rate, with high input process humidity and temperature compared to the rotational ratio of the dryer wheel. That is, whilst sensible energy proportion and DCOP increase in direct proportion, they are inversely proportional to the dehumidification rate (Angrisani, Roselli and Sasso, 2013).

2.3. Solar Energy integrated RDW

Ahmed, Kattab and Fouad (2005) have designed the rotary dryer wheel system with a solar heater regeneration process is as shown in Figure 6 a). The schematic illustration of the principle of working is observed as indicated from Figure 6 b).

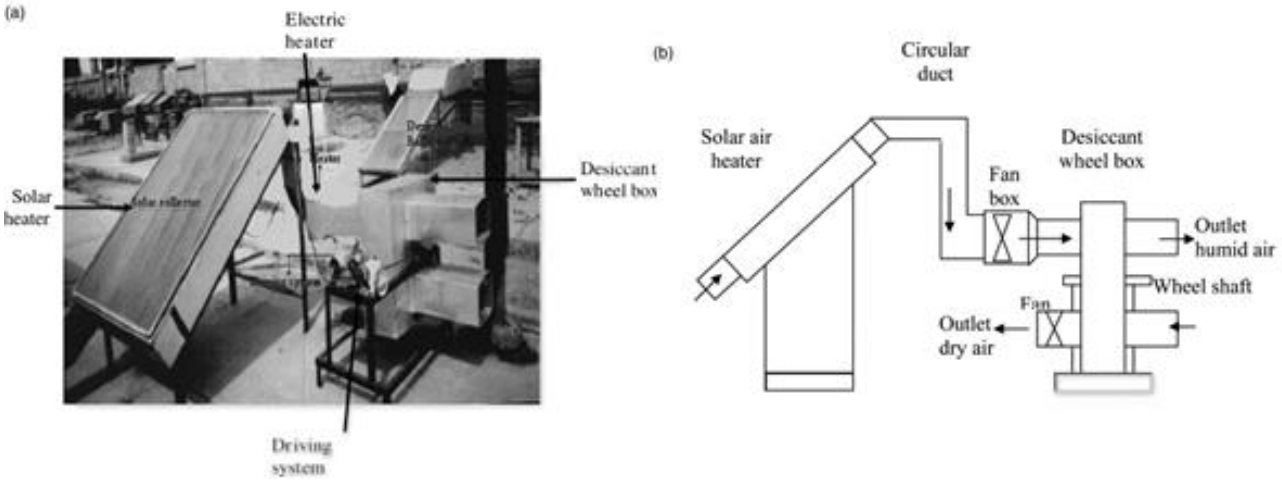

Figure 6. a) The designed system and b) the schematic representation of the designed system (Ahmed, Kattab and Fouad, 2005).

The system mainly takes place of a solar collector of $2m^2$, a rotating dryer wheel made of galvanised iron with 30kg of SG, with 0.7m diameter and a thickness of 0.2m separate from two equal parts for the temperature of regeneration between 60-90°C, the tire thickness is found to be between 0.26 and 0.18m. The influential airflow rate is figured out to have 1-5kg/min for 60-90°C and 15-60 RPM. It can be assumed that the wheel may be projected with a mean refurbishment portion of 0.8 and 0.3 at regenerating temperatures of 60-90°C, separately and the more appropriate pore spacing is ranging from 0.4 to 0.7 depending on the temperature of regeneration and airflow. The perforated plate solar heater with an area of $2m^2$ transfers an average of 72.8% of the overall regeneration energy been necessary at an airflow rate of 1.9kg/min and a regenerating temperature of 60°C. It decreases to an average of 13.7% during the flow rate of 72.8%, 9.4kg/min and the regenerating temperature of 90°C (Ahmed, Kattab and Fouad, 2005).

3. CONCLUSION

According to the literature studies above, many design and construction-oriented factors affect the performance of RDW systems. At the same time, operating conditions have a remarkable impact on system output. This article provides information on the fundamental studies on rotary dryer wheel systems and a strategy for both a cost reduction and a green approach to improving system performance characteristics.

4. REFERENCES

Ahmed, M. H., Kattab, N. M., and Fouad, M., 2005. Evaluation and optimization of solar desiccant wheel performance. Renewable Energy, 30(3), 305-325.

Angrisani, G., Roselli, C., and Sasso, M., 2013. Effect of rotational speed on the performances of a desiccant wheel. Applied Energy, 104, 268-275.

Ge, T. S., Dai, Y. J., Wang, R. Z., and Li, Y., 2008. Experimental investigation on a one-rotor two-stage rotary desiccant cooling system. Energy, 33(12), 1807-1815.

Ge, T. S., Li, Y., Wang, R. Z., and Dai, Y. J., 2009. Experimental study on a two-stage rotary desiccant cooling system. International Journal of Refrigeration, 32(3), 498-508.

Güzelel, Y. E., Olmuş, U., Çerçi, K. N., Büyükalaca, O., 2022. New multiple regression and machine learning models of rotary desiccant wheel for unbalanced flow conditions. International Communications in Heat and Mass Transfer, 134, 106006.

Jia, C. X., Dai, Y. J., Wu, J. Y., and Wang, R. Z., 2007. Use of compound desiccant to develop high performance desiccant cooling system. International journal of refrigeration, 30(2), 345-353.

O'Connor, D., Calautit, J. K., and Hughes, B. R., 2016. A novel design of a desiccant rotary wheel for passive ventilation applications. Applied Energy, 179, 99-109.

Panaras, G., Mathioulakis, E., Belessiotis, V., and Kyriakis, N., 2010. Experimental validation of a simplified approach for a desiccant wheel model. Energy and Buildings, 42(10), 1719-1725.

Su, M., Han, X., Chong, D., Wang, J., Liu, J., and Yan, J., 2021. Experimental study on the performance of an improved dehumidification system integrated with precooling and recirculated regenerative rotary desiccant wheel. Applied Thermal Engineering, 199, 117608.

Tian, S., Su, X., and Geng, Y., 2022. Review on heat pump coupled desiccant wheel dehumidification and air conditioning systems in buildings. Journal of Building Engineering, 54, 104655.

Tsai, H. Y., and Wu, C. T., 2022. Optimization of a rotary desiccant wheel for enthalpy recovery of air-conditioning in a humid hospitality environment. Heliyon, 8(10).

Zhang, X. J., Sumathy, K., Dai, Y. J., and Wang, R. Z., 2006. Dynamic hygroscopic effect of the composite material used in desiccant rotary wheel. Solar energy, 80(8), 1058-1061.

#69: Thermal insulation performance assessment of UK dwellings through co-heating test methodology: A critical review

Erdem CUCE[1*], Pınar Mert CUCE[2], Emre ALVUR[3]

1 Recep Tayyip Erdogan University, Engineering and Architecture Faculty, Mechanical Engineering, 53100 Rize, Turkiye, erdemcuce@gmail.com*
2 Recep Tayyip Erdogan University, Engineering and Architecture Faculty, Architecture, 53100 Rize, Turkiye, mertcuce@gmail.com
3 Recep Tayyip Erdogan University, Engineering and Architecture Faculty, Mechanical Engineering, 53100 Rize, Turkiye, emre.alvur@erdogan.edu.tr

Abstract: Several studies show that the designed performance value of buildings may be dissimilar to the actual energy performance value. A large part of this performance criterion is due to the thermal resistance of the elements in the building envelope. The most frequently utilised technique for calculating the thermal performance of a real building is the co-heating test. It is an experimental method used to specify the heat loss coefficient (HLC) of an as-built of building. This determination emerges by determining and plotting the daily heat input against the indoor and outdoor temperature difference of the building. Also, it is a quasi-steady state method that can be calculated correctly for the whole dwelling HLC. This article covers the evaluation of the thermal insulation performance of residential buildings in the UK by using the co-heating test method. The aim of this study is to describe improvements in U-values of building envelopes at pre- and post-retrofit cases in the UK dwellings. The assessments are done over a wide range of building types with different structural and constructional features.

Keywords: Co-heating test, Energy performance, Envelope performance, Performance gap, Heat loss

1. INTRODUCTION

Energy has such a very crucial place for every living thing on earth. Energy and its consumption are immediately to affect the life of the living thing (Riffat and Cuce, 2011). Hence, if there are energy-related problems, attempts to solve these problems are so valuable (Cuce and Cuce, 2013). With the increase in the world population, there is a rapid increment in global energy consumption due to the rise in the demand, for instance, for the construction sector, and due to this growth, environmental problems, including ozone sheet exhausting, climate change and global warming will arise (Cuce and Riffat, 2016). Developed and developing countries are following a series of policies to reduce energy consumption against this increasing threat. One of them is the Paris Agreement, which was signed in 2015 with the aim of trying to hold the global temperature increment below 2°C as per the pre-industrial era (Sutter and Berlinger, 2015). Total energy consumption in buildings accounts for more than a third (about 40%) in the UK. According to the law drafted by the United Kingdom in June 2019, it is the leading country to succeed in the net zero carbon emissions target by 2050 (Gupta and Gregg, 2021). Thanks to the efforts to raise the cognisance of the sector on the utilisation of low/zero carbon energy technologies in buildings and to increase energy efficiency, it can be ensured that the increment in energy costs can be prevented by reducing the greenhouse gas effect and minimising heat losses (Kim et al., 2022). With the rise in mission awareness in countries, the carbon emission rate of buildings in the UK has been observed to be mitigated by around 30% between 2009 and 2019. Additionally, in December 2020, the mean yearly decrease in UK emissions is decided that it should be at least 21 MtCO2e in order to attain the net zero goal according to the UK Climate Change Act report (Gupta and Gregg, 2021). It can be either with an environmentally friendly new house equipped with advanced technologies or by reinforcing an existing building with low-cost, eco-friendly technologies and high energy efficiency in order to meet the requirement of buildings with net zero carbon emissions (Cuce, Besir and Cuce, 2018). Air leakage and thermal bridges are among the things that should not be forgotten when reinforcing a building since it has been recorded that approximately 20-30% of the total heat losses are due to thermal bridges and about 50% due to air leakage (Enhanced Construction Details: Thermal Bridging and Airtightness, 2009).

2. STUDIES IN THE LITERATURE ABOUT THE CO-HEATING TEST IN THE UK

The co-heating test is one of the most popular known ways to find out the heat loss coefficient (HLC) of a building. It is a practical test technique that reveals the HLC of a building that is reliable and still easily usage nowadays, which is calculated by dividing the power of the electrical heater in a room belonging to the specified dwelling by the difference between the inlet temperature of the room and the outside temperature. The electric heater and fan used during the co-heating test are necessary tools to keep each point of the interior temperature of the room to be tested homogeneously at approximately 25°C (Deb et al., 2021). It is recommended to keep the temperature difference at an average of at least 10°C along the wall layers where heat transfer takes place (Jack et al., 2018). There are some restrictions to do the co-heating test. Some of these are examples of some limitations, such as the fact that it is more convenient to be done in the winter state to retain the temperature difference constant (Johnston, Wingfield and Miles-Shenton, 2010), the test period takes so long time in order to make the test even more confident (Alzetto et al., 2018), and it has a case that no one is in the room through the trial (Johnston et al., 2013). Therefore, many researchers have done a series of studies to uncover the HLC in W/K of a building by co-heating test method, which can be done under actual dynamic conditions, and thus for retrofitting existing building layers in the dwelling as a next step. It has been implemented a dynamic co-heating test methodology to assess the alteration in the thermal transmittance (U-value) of the hermetic window sill. The study is executed at a UK Nottingham residence. In accordance with the results of the study, whilst the total U-value of a casual window sash is 2.67 W/m^{2}K, a value of 1.79 W/m^{2}K is obtained for the window used in this study. Consequently, there is a practically 33% mitigation in heat loss relative to the other. The data obtained as a result of the test are shown in Figure 1 graphically (Cuce, 2017).

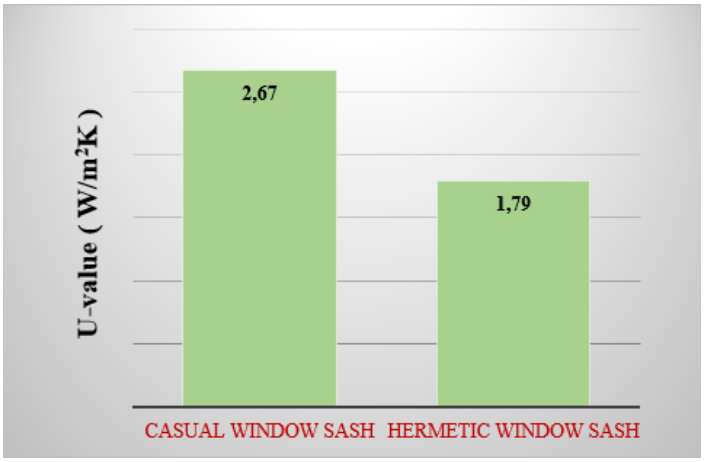

Figure 1 Comparison of the data obtained from the study

It has been utilised 20 mm thick fibre-silica opaque aerogel thermal superinsulation materials to the interior of a 1930s dwelling, and the heat loss and thermal bridge effects effect of the house are looked for using the co-heating test method. In accordance with the study, it has emerged that only interior reinforcements are not a direct solution to mitigate heat losses that may arise from dwellings unless due care is given to buildings that do not have insulation. Additionally, the purpose of the study is to peruse the impact of heat flow on the partition wall before and after insulation from the inside of the dwelling. Accordingly, the heat loss passing through the separation wall before retrofitting is 0.66 W/m^2. On the other hand, this situation is recorded as 5.86 W/m^2 after retrofitting. This result has shown that excellent insulation is obtained even with thin thermal superinsulation (Cuce and Cuce, 2016). Alexander and Jenkins (2015) and Parker et al. (2019) have provided the expected and actual thermal performance analysis of the test houses, where they have determined before retrofitting and after retrofitting with the standards of 1990, 2010, and 2012 by using the co-heating method. According to the results, the heat loss has decreased due to the materials used in each facade of the house as the year progressed. In a study by Gupta and Kotopouleas (2018) covering 188 buildings in the United Kingdom, they have used the co-heating test, which is a standardised method anymore, to examine the heat loss inherent in each of the dwellings. Alzetto et al. (2018) have introduced the co-heating test method for analysing thermal yield pre and post-enhancing, which they have represented in a test room for the performance of energy development in the UK. They have monitored the behaviour under the experimental method by reinforcing the wall of the intact archetype from 1919 and then gradually removing it. After the test methodology is utilised, the HLC value of the relevant areas interested in the test is created in Table 1.

Table 1: HLC values of the test house at each retrofit step taken while performing the co-heating test (Alzetto et al., 2018)

Test stage	HLC (W/K)
Full retrofitting	69.7 ± 2.9
Full retrofitting without floor insulation	82.7 ± 2.8
Solid wall insulation	101.2 ± 2.8
Glazing	174.2 ± 3.2

Whilst the HLC value of full reinforcement without floor insulation is 82.7 W/K, the value of the fully reinforced area is 69.7 W/K. Even though the floor is uninsulated and the remaining area is insulated, a 20% higher value is obtained in accordance with in the fully insulated area. Jack et al. (2018) have ensured robust proof, clearly indicating for the first time the credibility of the co-heating test in Watford, UK. Stamp, Lowe and Altamirano (2013) have utilised a co-heating test to take the HLC onto two types of building envelopes with heavy (brick-insulation-block) and light (cladding-insulation-plaster) structures and to determine which one is the more stable structure, according to the 2010 UK Building Code enforcement. Through with the test, it has been observed that the light design gives more exact and confident results than the other.

3. CONCLUSION

The co-heating test method is among the most prevalent techniques that it is surveyed for the performance thermally of an existing building. The co-heating test must have a particular temperature difference between indoor and outdoor environments. In order to make this temperature difference easier and the test to be more reliable, the winter season is preferred. An electrical heater is needed to increase the temperature of the indoor environment, the purpose of raising the inlet medium temperature is to create a temperature difference readily. The value obtained from this test is figured out by dividing the thermal power required to bring the indoor environment to a certain temperature difference by the temperature difference. This critical review describes the work done in the UK to reduce heat loss from residential buildings to align with low / zero carbon technologies and how these efforts have been achieved by testing the co-heating.

4. REFERENCES

Alexander, D. K., and Jenkins, H. G., 2015. The validity and reliability of co-heating tests made on highly insulated dwellings. Energy Procedia, 78, 1732-1737.

Alzetto, F., Farmer, D., Fitton, R., Hughes, T., and Swan, W., 2018. Comparison of whole house heat loss test methods under controlled conditions in six distinct retrofit scenarios. Energy and Buildings, 168, 35-41.

Cuce, E., Besir, A. B., and Cuce, P. M., 2018. Low/Zero-Carbon Buildings for a Sustainable Future. In Low Carbon Transition-Technical, Economic and Policy Assessment. IntechOpen. Available at: 10.5772/intechopen.74540 (Accessed: 10 July 2023).

Cuce, E., 2017. Role of airtightness in energy loss from windows: Experimental results from in-situ tests. Energy and Buildings, 139, 449-455.

Cuce, E., and Riffat, S. B., 2016. A comprehensive assessment of sectoral energy consumption in the UK: past, present and future. International Journal of Low-Carbon Technologies, 11(3), 424-430.

Cuce, E., and Cuce, P. M., 2016. The impact of internal aerogel retrofitting on the thermal bridges of residential buildings: An experimental and statistical research. Energy and Buildings, 116, 449-454.

Cuce, E., and Cuce, P. M., 2013. A comprehensive review on solar cookers. Applied Energy, 102, 1399-1421.

Deb, C., Gelder, L. V., Spiekman, M., Pandraud, G., Jack, R., and Fitton, R., 2021. Measuring the heat transfer coefficient (HTC) in buildings: A stakeholder's survey. Renewable and Sustainable Energy Reviews, 144, 111008.

Energy Saving Trust. Enhanced Construction Details: Thermal Bridging and Airtightness 2009. Available at: https://www.energysavingtrust.org.uk/sites/default/files/reports/CE302%20-%20ECD_thermal%20bridging%20and%20airtightness.pdf (Accessed: 10 July 2023).

Gupta, R., and Gregg, M., 2021. Integrated testing of building fabric thermal performance for calibration of energy models of three low-energy dwellings in the UK. Sustainability, 13(5), 2784.

Gupta, R., and Kotopouleas, A., 2018. Magnitude and extent of building fabric thermal performance gap in UK low energy housing. Applied Energy, 222, 673-686.

Jack, R., Loveday, D., Allinson, D., and Lomas, K., 2018. First evidence for the reliability of building co-heating tests. Building Research & Information, 46(4), 383-401.

Johnston, D., Miles-Shenton, D., Farmer, D., and Wingfield, J., 2013. Whole house heat loss test method (Coheating). Leeds Metropolitan University: Leeds, UK.

Johnston, D., Wingfield, J., and Miles-Shenton, D., 2010, September. Measuring the fabric performance of UK dwellings. In Proceedings of the Association of Researchers in Construction Management (ARCOM) Twenty-Sixth Annual Conference vol. 2, pp. 1371-1380.

Kim, S., Seo, J., Jeong, H., and Kim, J., 2022. In situ measurement of the heat loss coefficient of thermal bridges in a building envelope. Energy and Buildings, 256, 111627.

Parker, J., Farmer, D., Johnston, D., Fletcher, M., Thomas, F., Gorse, C., and Stenlund, S., 2019. Measuring and modelling retrofit fabric performance in solid wall conjoined dwellings. Energy and Buildings, 185, 49-65.

Riffat, S. B., and Cuce, E., 2011. A review on hybrid photovoltaic/thermal collectors and systems. International Journal of Low-Carbon Technologies, 6(3), 212-241.

Stamp, S., Lowe, R., and Altamirano-Medina, H., 2013. An investigation into the role of thermal mass on the accuracy of co-heating tests through simulations & field results.

Sutter, J. D., and Berlinger, J., 2015. Final draft of climate deal formally accepted in Paris. CNN. Cable News Network, 3, 3

#72: Experimental and numerical analysis of a wind tower with run around heat exchanger

Harry MAHON[1], Daniel FRIEDRICH[2], Ben HUGHES[3]

[1] School of Engineering, University of Edinburgh, Edinburgh, EH9 3DW, United Kingdom, a.h.mahon@sms.ed.ac.uk
[2] School of Engineering, University of Edinburgh, Edinburgh, EH9 3DW, United Kingdom, d.friedrich@ed.ac.uk
[3] Department of Engineering, University of Hull, Hull, HU6 7RX, Yorkshire, United Kingdom, b.r.hughes@hull.ac.uk

Abstract: This study proposes the integration of a run around heat exchanger within a passive ventilation wind tower to provide heating, cooling, and thermal energy recovery on a seasonal basis. A field trial of the system was conducted at a test site in Sheffield, UK, with the results recorded through experimental testing used to validate a numerical model. The numerical model was developed through the commercial computational fluid dynamics program ANSYS and was used to investigate the performance of the proposed system under a range of boundary conditions.

The minimum volumetric flow rate through the wind tower was 0.09 m3/s at an inlet velocity of 1 m/s for a heat exchanger model featuring three rows of pipes. Fresh air temperature was increased by 4.14 °C and reduced by 4.36 °C when the temperature difference between the fresh air and water flowing through the heat exchanger was 27 °C. The difference in water temperature between the inlet and outlet of the heat exchanger was 6.15 °C for both heating and cooling simulations at the same temperature difference, equivalent to 2 kW of thermal energy recovery.

Keywords: Passive ventilation, wind tower, heat recovery, computational fluid dynamics

1. INTRODUCTION

Buildings account for approximately 40% of global energy consumption (Amasyali & El-Gohary, 2018), with Heating, Ventilation, and Air Conditioning (HVAC) systems responsible for up to 70% of total building energy consumption depending upon the local climate (Qian et al., 2020; Vakiloroaya et al., 2014). In response, the EU-wide 2030 climate and energy framework aims to reduce greenhouse gas emissions by at least 40% from 1990 levels whilst improving energy efficiency to 32.5% (European Commission, 2020; European Council, 2014). Consequently, the decarbonisation of Heating, Ventilation, and Air Conditioning (HVAC) systems is highly desirable to reduce end user energy consumption within buildings, with the simultaneous recovery of waste thermal energy crucial in improving buildings energy efficiency.

Wind towers were first developed for use throughout the Middle East but have since been adapted for use in a wide range of climates with varying designs (Alwetaishi & Gadi, 2020; Hughes et al., 2012; Saadatian et al., 2012), sustaining a flow of fresh air through a combination of regional pressure differences and the stack effect (Figure 1). Although capable of providing ventilation with zero energy demand, passive ventilation systems such as wind towers are often closed throughout the winter to prevent the introduction of unconditioned fresh air from outside into the indoor environment.

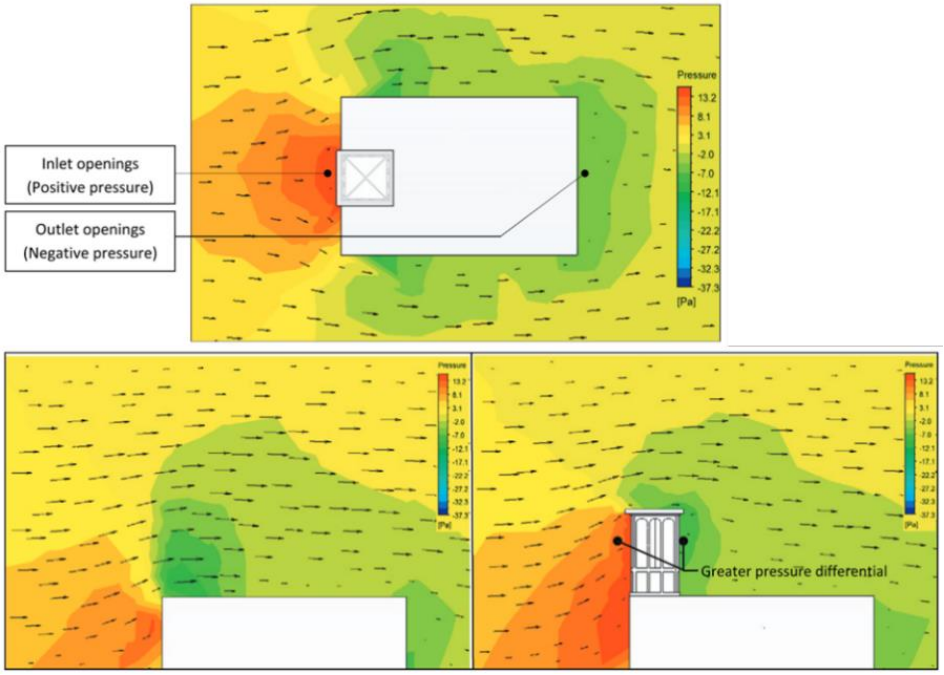

Figure 1 Analysis showing positive pressure on the windward building's façade and negative pressure on the leeward side (Hughes, Calautit and Ghani, 2012)

Heat recovery devices such as run arounds can be used to recover waste thermal energy from exhaust to inlet air streams. Run arounds are comprised of two individual heat exchangers linked via a fluid system to transfer thermal energy between them (Jouhara et al., 2018; Vali et al., 2009). They are beneficial in that they can transfer heat over long distances, don't require any mixing of the respective source and sink, and can easily transfer thermal energy between different mediums (Mardiana-Idayu & Riffat, 2012; O'connor et al., 2016).

Hviid and Svenson (2011) developed a run around system connecting two air-to-liquid heat exchangers for use within passive ventilation. The total heat recovery efficiency was between 64.5 – 75.4% while the pressure drop over the heat exchanger was as low as 0.37 Pa. Flaga-Maryanczyk et al (2014) installed a run around system within a passive house ventilation system, using a ground source heat exchanger to increase air temperature throughout the winter. An average of 15% of the heating demand was met for the tested period by pre-heating the fresh air prior to mixing throughout the house. Despite their effectiveness, run arounds are limited by the necessity of a constant supply of heat or cool to operate effectively.

Thermal energy storage can be used to address the mismatch between supply and demand of renewable energy resources and can be deployed to reduce the impact of environmental changes on system performance. Seasonal Thermal Energy Storage (STES) technologies such as aquifer, borehole, tank, and pit STES are all capable of storing waste thermal energy for periods up to six months which can be used to provide heating or cooling in the winter and summer respectively.

This study seeks to determine the potential for a Run Around Heat Exchanger (RAHE) installed within a passive ventilation wind tower to provide heating and cooling to fresh air whilst also quantifying the recovery of waste heat and cold in the summer and winter respectively for storage using STES. The impact of air velocity and temperature through the wind tower

as well as the temperature and velocity of the water through the RAHE on the level of pre-heating, pre-cooling, and thermal energy recovery are explored.

2. METHODOLOGY

To evaluate the performance of the proposed system a field trial was conducted at a test site in Sheffield, UK. Testing was carried out in the summer, evaluating the cooling potential of the RAHE. Experimental results were then used to validate a numerical model built using the commercial Computation Fluid Dynamics (CFD) program ANSYS. Subsequently a number of simulations were conducted to evaluate the performance of the RAHE under a range of boundary conditions.

2.1. SYSTEM DECRIPTION

The proposed system aims to combine a wind tower and RAHE to create a system capable of providing heating and cooling to fresh air passing through the wind tower inlet whilst recovering waste thermal energy. Throughout summer the system is used to pre-cool fresh air. Cold water is pumped through a series of copper pipes installed through the base of the wind tower that constitute the heat exchanger. As warm fresh air passes over the heat exchanger heat is transferred from the air to the water via convective and conductive heat transfer, decreasing and increasing the air and water temperatures respectively. Fresh air is discharged into the room where it can be cooled further using conventional cooling systems and the water is discharged to a form of STES. In the winter, the stored heat can be used to provide heating through the same process, in turn lowering the water temperature which can then be stored and used to provide cooling in the subsequent summer.

The effectiveness of the heat exchange system is dependent upon the ambient air temperature, the air velocity over the heat exchanger, and the velocity and temperature of the water through the RAHE. In recovering and storing waste thermal energy the energy demand of the system is kept low, although a heat pump may be required. In this case, an insulated water tank with separate submersible chiller and water pump were used to provide water to the RAHE system at a near constant temperature.

2.2. EXPERIMENT DESIGN

An office site in Sheffield, UK, was used to conduct a field test of the combined wind tower and RAHE system (Figure 2).

Figure 2 Field trial location and surrounding buildings and topography provided through Google Earth with red dot indicating placement of the wind tower in the roof (Google, 2023)

The wind tower was installed through the pitched roof of an unused office space with an internal volume of 61.5 m^3. A weather station was mounted to the side of the wind tower reporting values for wind speed, direction, and ambient temperature at five-minute intervals (Figure 3). The commercial wind tower design measured 1 x 1 x 2.5 m (width x depth x height), featuring an internal x-frame that divides the wind tower into four equal quadrants. The heat exchanger of the run around is installed through the base of the wind tower ducting with the pipes running perpendicular to the direction of flow. The transversal pitch, outer diameter and wall thickness are 0.05, 0.016, and 0.001 m respectively. Water was

circulated through the RAHE using a submersible water pump with the flow rate recorded using a digital flow meter. Dampers are installed at the base of the ducting to control the flow of air into the room, however for the purposes of this experiment are left fully open.

Figure 3 Wind tower installation

A wind rose was produced using the wind velocity and direction provided by the weather station (Figure 4). Due to the surrounding buildings and shape of the roof, the incident wind direction onto the wind tower is largely constrained to a westerly direction. The wind velocity is typically also low, falling between 0 - 0.5 m/s approximately 56% of the time.

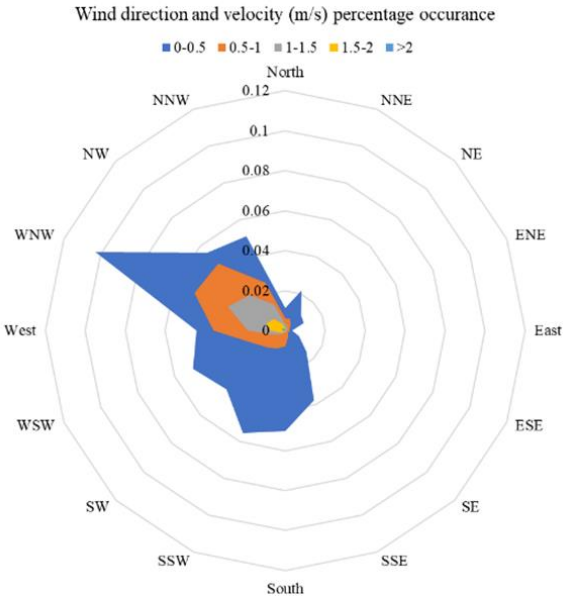

Figure 4 Wind rose produced using data recorded between 06 – 08/22 at the trial site

Temperature measurements were taken throughout the wind tower and RAHE using k-type thermocouples. As the wind direction is predominantly westerly several sensors were placed in the corresponding quadrant as the primary inlet. The average decrease in fresh air temperature over the heat exchanger is found by averaging the values at points 2 and 3 against the value at point 1 due to variation in velocity through the inlet quadrant (Figure 5)

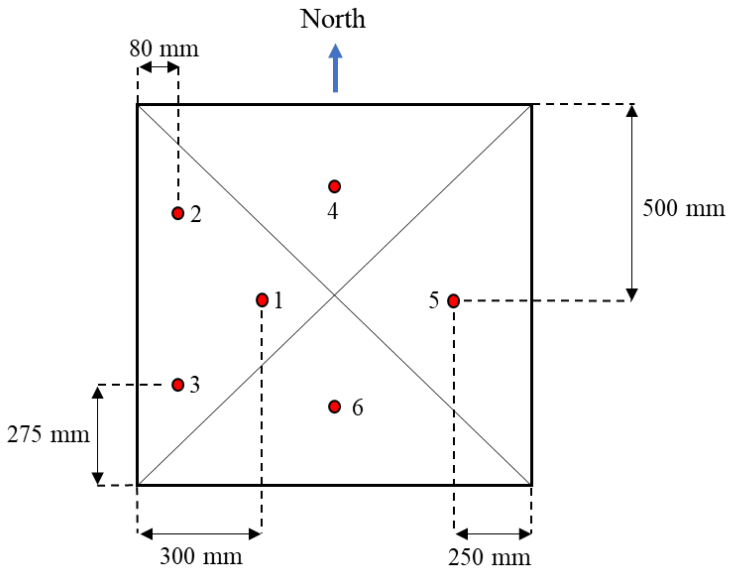

Figure 5 Temperature sensor location within wind tower

Although external wind speed is measured by the weather system installed on the wind tower, velocity measurements were not recorded as the reference velocity was highly variable and the reporting period too infrequent to provide any consistent measurements.

2.3. Numerical modelling

ANSYS Fluent is used to design and simulate a numerical model replicating the physical experiment. ANSYS uses the Finite Volume Method (FVM) with the Semi Implicit Method for Pressure Linked Equations (SIMPLE) velocity-pressure coupled solver. The standard k-epsilon turbulence model with standard wall functions is applied to resolve the turbulent elements of the air flow (Hosseinnia et al., 2013). Monitor points were placed throughout the computational domain to record temperature and velocity values at each iteration with the result considered converged once the values at each monitor remained constant for several hundred iterations. The governing equations used to calculate values throughout the computational domain are detailed in the ANSYS User Guide (Ansys, 2020).

Geometry and meshing

A three-dimensional model was created replicating the experimental design using Computer Aided Design (CAD) software. The wind tower, ducting, and RAHE reflect the physical system used for the field trial. The fluid region within the confines of the test room was extracted accounting for large objects that remained within the room throughout testing. The fluid region representing the ambient air was created using the boundaries of the building and surroundings to limit the size of the domain (Figure 6). Although not accounting for the leading edge of the building in the flow has been shown to result in an over estimation of the mass flow rate through a wind tower, given the complexity of the surrounding buildings the velocity distribution of the atmospheric boundary layer is difficult to predict. As a result, a uniform inlet velocity profile is applied with the understanding that the calculated volumetric flow rate through the wind tower may be a slight overestimation. Additional CAD models featuring heat exchangers with two and three rows of pipes featuring 35 and 52 pipes respectively were also created where the longitudinal pitch between rows of pipes was 0.35 m.

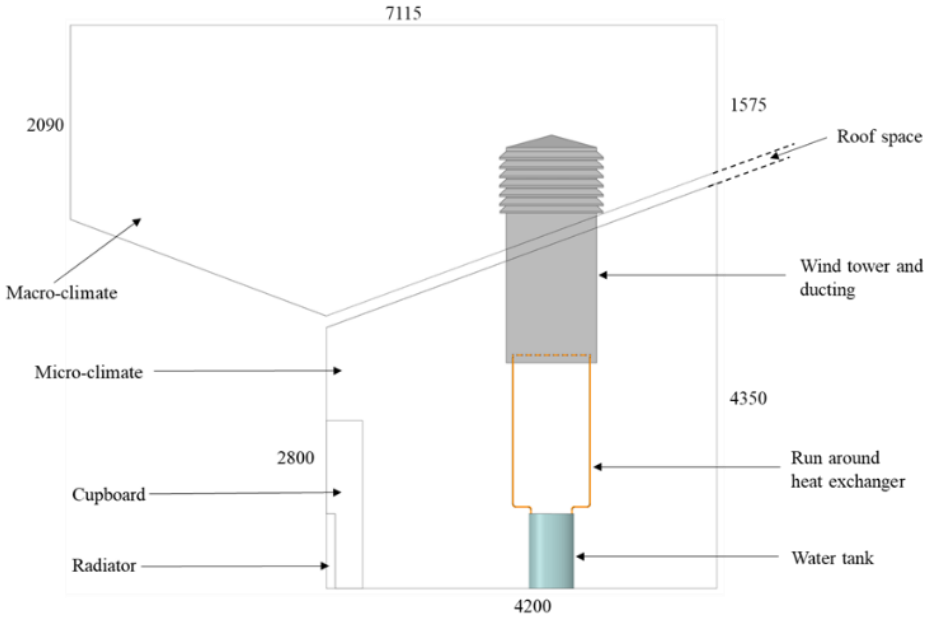

Figure 6 CAD model replicating experimental design

The CAD geometry was then discretised, splitting the bodies of the geometry into many smaller volumes that together constitute the mesh. An unstructured tetrahedral mesh featuring 11,804,286 cells was created, with size functions used throughout the domain to control the size of the cells around the wind tower louvres, the regions of air above and below the heat exchanger, and the RAHE itself. The tetrahedral cells were then converted to polyhedral, reducing the total cell count to 10,799,507. Converting tetrahedral to polyhedral cells has been shown to improve the accuracy of the results whilst reducing cell count and calculation time (Kim & Chung, 2015).

Boundary conditions

To validate the model a transient simulation was conducted over twenty-six, five-minute long timesteps using boundary conditions derived from the experimental conditions at each timestep and comparing the temperature below the heat exchanger through the wind tower inlet and at the outlet of the heat exchanger (Table 1). Wind speed is resolved into the horizontal X and Z components to replicate the incident wind angle onto the wind tower where the computational domain is oriented so that the positive X direction is due west, and the positive Z direction is due north.

Table 1: Transient boundary conditions for numerical model validation

Time	Timestep No.	Air inlet temp (°C)	Air X velocity (m/s)	Air Z velocity (m/s)	Inlet water temp (°C)	Water velocity (m/s)
12:04	1	300.84	-1.41	-1.41	286.72	0.56
12:09	2	300.96	-0.85	-0.85	286.73	0.56
12:14	3	300.21	-0.99	-0.99	286.81	0.56
12:19	4	299.84	-1.48	-0.61	286.80	0.56
12:24	5	300.53	-1.66	-0.69	286.79	0.56
12:29	6	300.53	-2.30	0.00	286.82	0.56
12:34	7	300.65	-1.11	0.46	286.93	0.56
12:39	8	300.40	-1.63	1.63	286.95	0.56
12:44	9	301.59	-1.34	-1.34	286.97	0.56
12:49	10	300.28	-1.48	0.61	287.03	0.56
12:54	11	300.46	-1.94	0.80	287.03	0.56
12:59	12	301.78	-1.02	0.42	287.05	0.56
13:04	13	301.21	-0.96	-2.31	287.17	0.56
13:09	14	300.28	-1.29	-0.54	287.20	0.56
13:14	15	301.15	-1.85	0.77	287.28	0.56
13:19	16	301.15	-1.94	-0.80	287.32	0.56
13:24	17	301.90	-0.85	-0.85	287.27	0.56
13:29	18	302.46	-1.39	-0.57	287.33	0.56
13:34	19	301.78	-1.60	0.00	287.41	0.56
13:39	20	301.71	-2.03	-0.84	287.45	0.56
13:44	21	301.46	-1.94	-0.80	287.59	0.56
13:49	22	302.59	-0.92	-0.92	287.57	0.56
13:54	23	302.34	-1.76	-0.73	287.57	0.56
13:59	24	302.34	0.88	-2.12	287.69	0.56
14:04	25	302.34	-0.84	-2.03	287.68	0.56
14:09	26	302.53	-1.27	-1.27	287.76	0.56

Following validation simulations were conducted under steady state conditions to evaluate the performance of the wind tower and RAHE under a range of boundary conditions (Table 2).

Table 2: Summary of boundary conditions for field trial numerical model

Discretisation scheme	Second order upwind
Algorithm	SIMPLE
Time scheme	Steady stae
Viscous model	k-epsilon
Wall functions	Standard
Air velocity (m/s)	1 - 5 m/s
Air temperature °C	0 - 30
Water temperature °C	8 - 30

3. VALIDATION

To validate the numerical model the results of the transient simulation are compared with the results recorded during physical testing. Figure 7 shows the average air temperature below the heat exchanger relative to the inlet air temperature for each timestep.

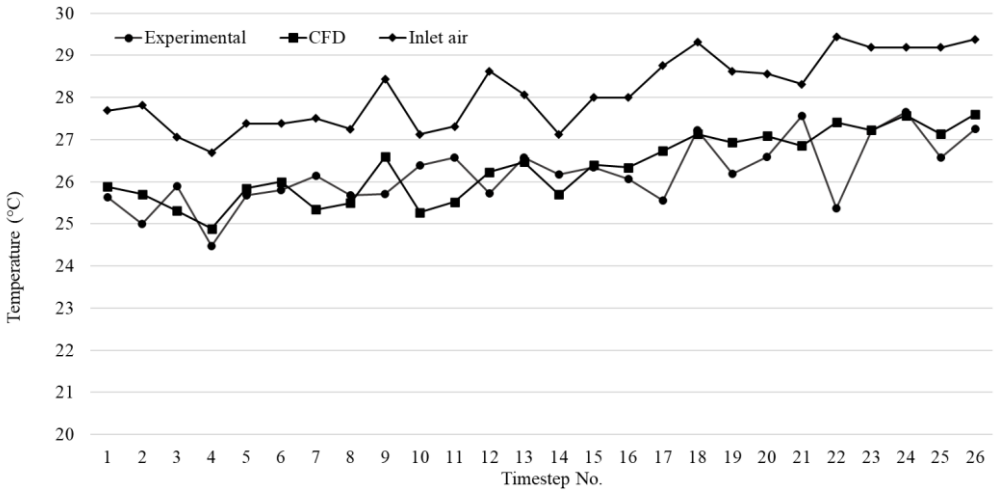

Figure 7 Experimental vs CFD results for cooling of fresh air

The average error between the two datasets is found to be 2.1%, where the CFD results are much more dependent upon the inlet air temperature relative to the experimental results. This discrepancy may occur due to changes in the wind velocity after the reading is provided by the weather station. Air temperature, wind speed and direction are provided as a value at the start of each five-minute interval by the weather station, however each parameter is not constant throughout the interval until the next reading. The numerical model assumes these boundary conditions are constant throughout each timestep and therefore for some timesteps there is a greater difference between the experimental and numerical results.

Further comparisons were made between the water temperature recorded at the outlet of the RAHE because of heat gained from the air passing over the surface of the copper pipes. Figure 8 shows a comparison between the experimental and CFD outlet temperature vs the inlet temperature.

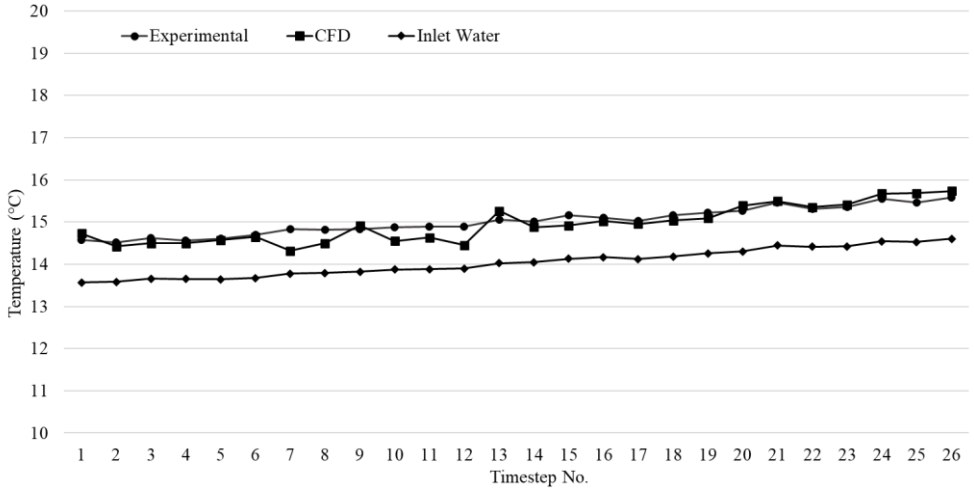

Figure 8 Experimental vs CFD results for run around outlet temperature

The average error across the timesteps is 1.1%. The experimental results show a very consistent temperature increase of around 1 °C between the inlet and outlet of the heat exchanger whereas the CFD results fluctuate recording a minimum temperature increase of 0.54 °C and a maximum of 1.24 °C. Errors relating to passive ventilation simulations are often higher given the low driving forces through the system and therefore trends are evaluated as well as making direct comparisons between the experimental and numerical results (Chen & Srebric, 2002; Connor et al., 2019; Hughes & Mak, 2011).

4. RESULTS AND DISCUSSION

4.1. Volumetric flow rate

Figure 9 shows the inlet mass flow rate versus the inlet velocity for models with heat exchangers comprised of one to three rows of pipes.

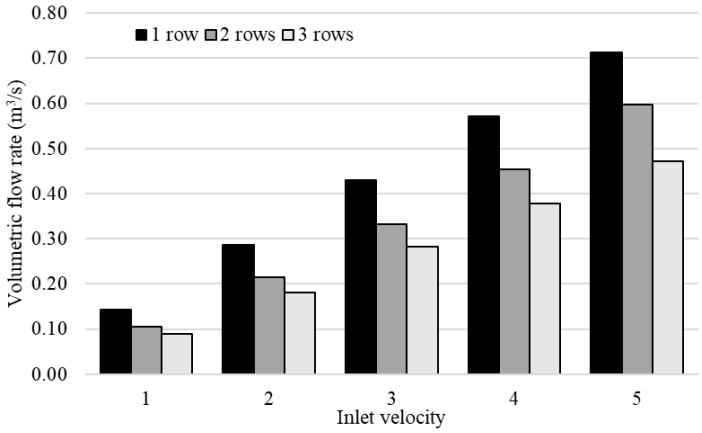

Figure 9 Volumetric flow rate through wind tower inlet with increasing inlet velocity

Volumetric flow rate increases linearly with increasing inlet velocity but non-linearly with an increasing number of pipes constituting the heat exchanger. This results from the staggered arrangement of the pipes, where the blockage of the inlet channel increases by much more between 1 and 2 rows than from 2 to 3 rows. Comparing the results with previous studies shows that the increased ducting length below the wind tower results in a marginally lower volumetric flow rate as the driving pressure dissipates through the length of channel (Mahon et al., 2022).

4.2. Pre-heating and cooling

Figure 10 shows the performance of a heat exchanger with three rows of pipes for heating and cooling. For the cooling simulations air temperature was increased from 20 to 35 °C in increments of 3 °C while water temperature remained constant at 8 °C. For the heating simulations air temperature was increased from 0 to 15 °C while water temperature remained at 30 °C. Air and water inlet velocities were 3 and 0.5 m/s respectively under a wind angle of zero degrees ensuring one quadrant behaved as an inlet and the remaining three as outlets. The relative increase or decrease in air temperature over the heat exchanger is plotted against the difference in temperature between the air passing through the wind tower and the water running through the RAHE.

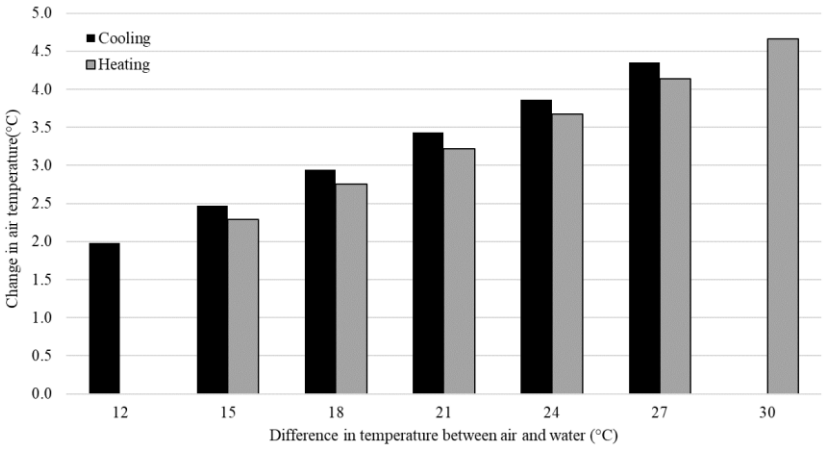

Figure 10 Pre-cooling of fresh air versus the temperature difference between the air and water

At a temperature difference of 27 °C the air temperature is increased by 4.14 °C when heating and reduced by 4.36 °C when cooling. Although only a small difference this is consistent throughout the corresponding heating and cooling simulations, likely due to the minor differences in air density arising from the differences in temperature between the simulations. Figure 11 shows a temperature contour through the wind tower inlet when the inlet air and water temperatures are 35 and 8 °C respectively. A greater amount of cooling occurs towards the outer edges of the quadrant as the air velocity is lower here than through the center. Some short circuiting occurs whereby fresh air exits directly through the adjacent wind tower quadrants without mixing throughout the room.

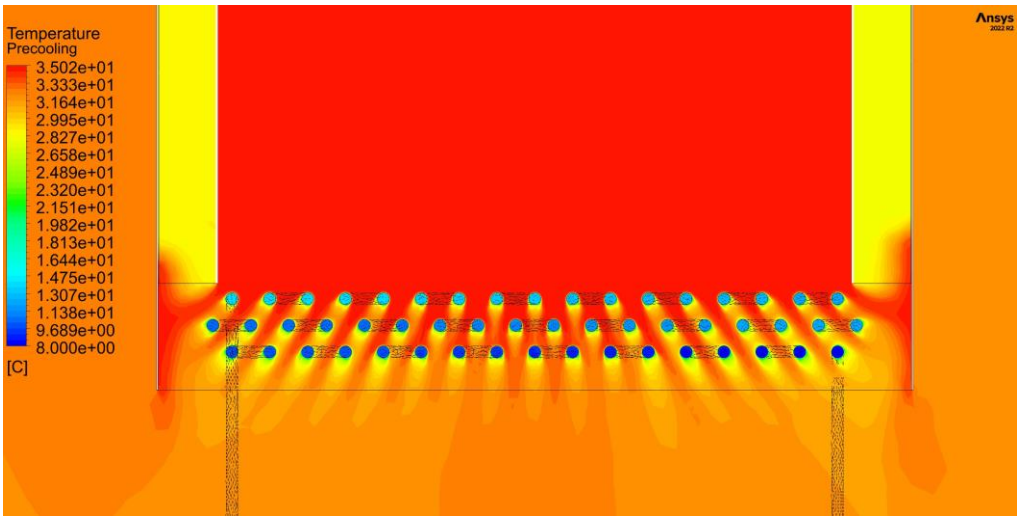

Figure 11 Pre-cooling of fresh air over heat exchanger

Figure 12 shows the difference in water temperature between the inlet and outlet of the RAHE. Under the same inlet conditions, at a temperature difference of 27 °C the water temperature was increased by 6.15 °C for both heating and cooling simulations, in contrast to the difference in air temperature recorded. As three quadrants are behaving as outlets and only one as an inlet the temperature change of the water is more dependent on the air outlet temperature than the inlet temperature creating a more consistent result between both sets of simulations.

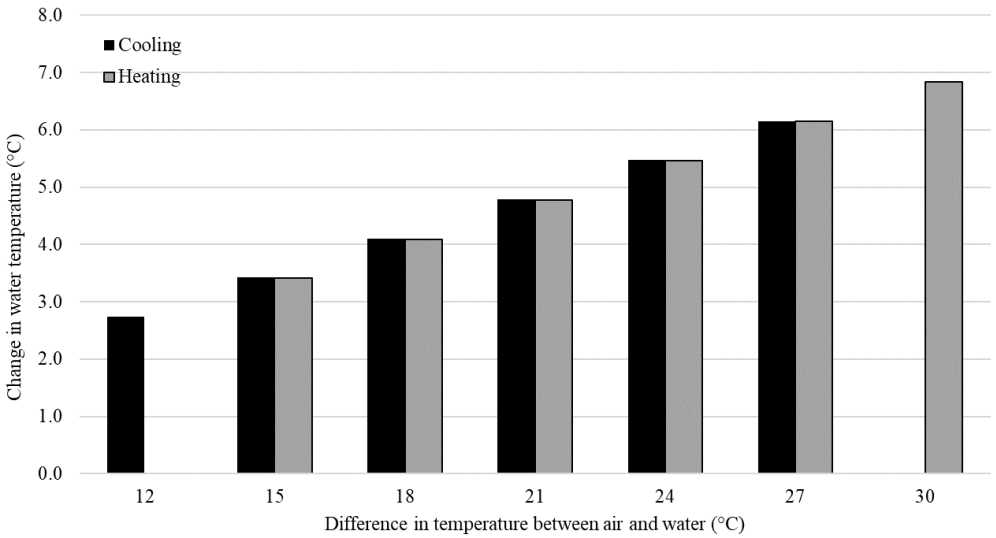

Figure 12 Temperature increase of water through RAHE with increasing number of pipes

Table 3 indicates the thermal energy recovered as a result of the increase in water temperature through the RAHE. The thermal energy recovered Q_H is calculated according to $Q_H = Q_v \rho C_p dT$ where Q_v is the volumetric flow rate, ρ is the density, C_p is the specific heat capacity, and dT is the difference in water temperature between the inlet and outlet.

Table 3: Thermal energy recovery through heat exchanger

	Cooling		Heating	
dT Air/Water (°C)	T change (°C)	Energy (kW)	T change (°C)	Energy (kW)
12	2.74	0.88		
15	3.42	1.10	3.41	1.09
18	4.10	1.32	4.09	1.31
21	4.79	1.55	4.77	1.53
24	5.47	1.77	5.47	1.75
27	6.15	1.98	6.15	1.97
30			6.84	2.19

Given the widespread use of HVAC systems towards creating thermally comfortable environments, it would be anticipated that the exhaust temperature through the wind tower would be higher or lower than the fresh air delivery temperature from the wind tower in the winter and summer respectively. As the change in water temperature is also dependent upon the outlet temperature through the wind tower this would result in a smaller measurable temperature difference between the inlet and outlet of the heat exchanger and less thermal energy recovered in a single pass. In this case imposing a system control whereby water was recirculated until it reached a certain temperature would ensure the maximum amount of thermal energy was extracted from the air.

5. CONCLUSION & FUTURE WORK

A combination of experimental testing and numerical modelling is used to predict the performance of a wind tower with integrated RAHE. The study focused on the performance of the heat exchanger under a range of boundary conditions that could reasonably be expected to be experienced in the summer and winter of a mild-cold climate such as the UK. The numerical model was validated using a transient simulation, replicating the boundary conditions and results produced through experimental testing showing good agreement between the two. The results of further simulation results showed the ability of the system to provide fresh air at 0.09 m^3/s when the inlet velocity was as low as 1 m/s. Under summer conditions the heat exchanger reduced the fresh air temperature by up to 4.36 °C, recovering 2 kW in the process. In the winter the fresh air temperature increased by 4.14 °C at the same temperature difference between the fresh air and water through the run around. The thermal energy recovered through the RAHE has been shown to be significant enough to consider storage using STES to provide heating and cooling from thermal energy recovered in the opposing seasons. Further analysis will evaluate a full wind tower, run-around heat exchanger, and seasonal thermal energy storage system using TRNSYS, evaluating system performance over the course of a year through concurrent heating and cooling seasons to predict total system performance.

6. REFERENCES

Alwetaishi, M., & Gadi, M. (2020). New and Innovative Wind Catcher Designs to Improve Indoor Air Quality in Buildings. *Energy and Built Environment*. https://doi.org/10.1016/j.enbenv.2020.06.009

Amasyali, K., & El-Gohary, N. M. (2018). A review of data-driven building energy consumption prediction studies. *Renewable and Sustainable Energy Reviews*, *81*(September 2017), 1192–1205. https://doi.org/10.1016/j.rser.2017.04.095

Ansys. (2020). *ANSYS FLUENT Theory Guide*. *January*.

Chen, Q., & Srebric, J. (2002). A procedure for verification, validation, and reporting of indoor environment CFD analyses. *HVAC and R Research*, *8*(2), 201–216. https://doi.org/10.1080/10789669.2002.10391437

Connor, D. O., Calautit, J. K., Calautit, K., Shazad, S., Hughes, B. R., & Pantua, C. (2019). Analysis of a rotary passive heat recovery device for natural ventilation windcatcher. *IOP Conference Series: Materials Science and Engineering*, *556*(1). https://doi.org/10.1088/1757-899X/556/1/012001

European Commission. (2020). *Stepping up Europe's 2030 climate ambition*.

European Council. (2014). *European Council 23-24 October 2014 - Conclusions*.

Flaga-Maryanczyk, A., Schnotale, J., Radon, J., & Was, K. (2014). Experimental measurements and CFD simulation of a ground source heat exchanger operating at a cold climate for a passive house ventilation system. *Energy and Buildings*, *68*(PARTA), 562–570. https://doi.org/10.1016/j.enbuild.2013.09.008

Google. (2023, July 16). *Google Earth*.

Hosseinnia, S. M., Saffari, H., & Abdous, M. A. (2013). Effects of different internal designs of traditional wind towers on their thermal behavior. *Energy and Buildings*, *62*, 51–58. https://doi.org/10.1016/j.enbuild.2012.10.058

Hughes, B. R., Calautit, J. K., & Ghani, S. A. (2012). The development of commercial wind towers for natural ventilation: A review. In *Applied Energy*. https://doi.org/10.1016/j.apenergy.2011.11.066

Hughes, B. R., & Mak, C. M. (2011). A study of wind and buoyancy driven flows through commercial wind towers. *Energy and Buildings*, *43*(7), 1784–1791. https://doi.org/10.1016/j.enbuild.2011.03.022

Hviid, C. A., & Svendsen, S. (2011). Analytical and experimental analysis of a low-pressure heat exchanger suitable for passive ventilation. *Energy and Buildings*, *43*(2–3), 275–284. https://doi.org/10.1016/j.enbuild.2010.08.003

Jouhara, H., Khordehgah, N., Almahmoud, S., Delpech, B., Chauhan, A., & Tassou, S. A. (2018). Waste heat recovery technologies and applications. *Thermal Science and Engineering Progress*, *6*(January), 268–289. https://doi.org/10.1016/j.tsep.2018.04.017

Kim, J., & Chung, J. (2015). Untangling polygonal and polyhedral meshes via mesh optimization. *Engineering with Computers*, *31*(3), 617–629. https://doi.org/10.1007/s00366-014-0379-5

Mahon, H., Friedrich, D., & Hughes, B. (2022). Wind tunnel test and numerical study of a multi-sided wind tower with horizontal heat pipes. *Energy*, *260*. https://doi.org/10.1016/j.energy.2022.125118

Mardiana-Idayu, A., & Riffat, S. B. (2012). Review on heat recovery technologies for building applications. *Renewable and Sustainable Energy Reviews*, *16*(2), 1241–1255. https://doi.org/10.1016/j.rser.2011.09.026

O'connor, D., Calautit, J. K. S., & Hughes, B. R. (2016). A review of heat recovery technology for passive ventilation applications. *Renewable and Sustainable Energy Reviews*, *54*, 1481–1493. https://doi.org/10.1016/j.rser.2015.10.039

Qian, F., Gao, W., Yang, Y., & Yu, D. (2020). Potential analysis of the transfer learning model in short and medium-term forecasting of building HVAC energy consumption. *Energy*, *193*, 116724. https://doi.org/10.1016/j.energy.2019.116724

Saadatian, O., Haw, L. C., Sopian, K., & Sulaiman, M. Y. (2012). Review of windcatcher technologies. *Renewable and Sustainable Energy Reviews*, *16*(3), 1477–1495. https://doi.org/10.1016/j.rser.2011.11.037

Vakiloroaya, V., Samali, B., Fakhar, A., & Pishghadam, K. (2014). A review of different strategies for HVAC energy saving. *Energy Conversion and Management*, *77*, 738–754. https://doi.org/10.1016/j.enconman.2013.10.023

Vali, A., Simonson, C. J., Besant, R. W., & Mahmood, G. (2009). Numerical model and effectiveness correlations for a run-around heat recovery system with combined counter and cross flow exchangers. *International Journal of Heat and Mass Transfer*. https://doi.org/10.1016/j.ijheatmasstransfer.2009.07.020

#73: Rural energy accessibility profiling to enable effective energy decarbonisation research

Samir SOARES[1], Mark GILLOTT[2], Gavin WALKER[3]

[1] University of Nottingham, United Kingdom, samir.soares@nottingham.ac.uk
[2] University of Nottingham, United Kingdom, mark.gillott@nottingham.ac.uk
[3] University of Nottingham, United Kingdom, gavin.walker@nottingham.ac.uk

Abstract: Accessing energy is a key challenge to rural users of energy. The forms of energy required and available to rural energy users is much more varied in addition to electricity and grid gas such as oil, LPG gas, coal and wood.

This splintering of the forms of energy used inefficiencies and therefore increases cost, resulting domestically in high rates of fuel poverty and health and safety implications from greater exposure and risk from more toxic and 7greater polluting fuels. This varies from urban energy systems where typically only gas and electricity from the grid are used in relatively higher, safer and cleaner energy efficient devices and buildings.

With the broader societal goal to decarbonise the energy we consume in all walks and aspects of life, understanding on a local level the current conditions is key to best develop archetypes of typical rural energy users that will be different from urban energy users to better develop decarbonised energy systems in these places.

This work begins to develop archetypes of rural energy user, informed by surveys carried out to rural residents and broader collating of figures. It is key to do this as rural dwellings are much more varied in age, quality, technology and climate compared to urban dwellings which increases the difficulty of developing an archetypal representative rural dwelling. Developing archetypal dwellings is important in developing a base common model of a dwelling to enable more effective research in rural energy decarbonisation with technologies and measures such as hydrogen, heat pumps and insulation. Particularly rural off grid homes, which can be difficult to characterise and develop effective research or policy.

Keywords: Rural, decarbonisation, study, heating, fuels

1. INTRODUCTION

If you live in rural UK, how energy is consumed and what types of energy that is consumed varies greatly on where you live, the survey described in this report aims to build some archetypal descriptions of a rural UK homes energy systems and habits from this. Producing archetypal descriptions of different homes and their energy access/technologies covering most possible combinations.

In the United Kingdom a minority of the population lives in rural regions. With 18% of the UK population living in rural areas, encompassing 91% of UK land area. The decarbonisation of homes and communities' energy and fuel consumption is key to achieving a societal shift to a low carbon society. Progress has been made towards this in decarbonising power with government funded research and investment to develop renewable electricity production through wind and solar resulting in some of the largest offshore wind farms in the world located in the UK. Work decarbonising and modernising end use energy consumption is ongoing. A greater and complex challenge is decarbonising heat.

Heating in the UK consumes 44% of annual energy consumption (BEIS 2018) and produces 23% of all emissions (Government 2021). In the UK over 70% of buildings are heated using natural gas from a national gas grid with users heating their own buildings with individual boilers in each building. Shifting from the current reliance of majority natural gas heating to a low carbon alternative is much undecided in its early stages of research, policy and investment.

In researching domestic energy consumption it is key to not only understand the energy consumption figures and trends, but also to understand the composition and fabric of the buildings in question. Such as the fuels (e.g. electricity and gas), energy conversion devices (e.g. boilers, radiators) and the level and composition of insulation of a building. This provides a sufficient level of detail to research the costs and challenges of energy decarbonisation on a local level and provide a more informed understanding of what is required to achieve this.

There is no one standard "typical" home, with factors such as building age, fabric and location all contributing towards the energy system setup and energy demands, as well as the composition of people living within the building.

A more appropriate breakdown of types of homes can be made, producing a series of archetypes of UK homes that encompasses the diversity of UK homes and energy fuels/technologies used to heat and power homes. This paper develops a series of rural energy user profiles based on a series of factors such as location, current energy fuels used and building characteristics. The primary underlying data to develop these rural energy user profiles is a self-developed online survey distributed to parish councils across multiple districts in the United Kingdom.

1.1. Objectives

Rural energy is the focus here as there is little understanding on a local level of the current state of energy accessibility, particularly when looking towards decarbonising rural energy usage. There is a greater diversity in how energy is accessed rurally than urban, making higher level characterisations of how energy is access broad and unrepresentative of any significant minority that is trying to be represented.

Below listed are the key overall objectives of the survey:

- Who lives rurally?
- What do respondents think about sustainability?
- What infrastructure is in the home?
- What fuels are used?

This work attempts to break down this diverse group of rural homes that may have varying levels of energy access into roughly analogous groups that can enable further research of these groups in terms of the built environment and energy.

2. SURVEY METHODOLOGY

The primary dataset used in this analysis are results of an online survey on the topic of rural energy accessibility. Consisting of 26 primarily multiple-choice questions on the topics of; respondents demographics, location, attitude towards sustainability, the respondents home and the forms and methods of energy consumption in the home.

This survey was distributed online to over 500 parish councils or equivalent lowest level of local government across the UK, Isle of Man, Jersey and Republic of Ireland. There are over 10,000 parish councils in England alone (National Association of Local Councils), selecting appropriately what councils to target and ask to distribute the survey within the parish council and their wider community was based on the district councils the parishes are located within and the corresponding counties the district council is found within.

First identified were counties that should be targeted to distribute the survey. Counties selected were those that have notable and substantial rural area or also have certain geography that would be beneficial to have responses from. Such

as the English Peak District and Scottish Highlands where there are notable for their remote and rugged geography where energy access may be limited.

Once these counties were identified (such as Derbyshire, Lincolnshire and Highland), identifying the constituent district/borough councils (or equivalent) that make up the county was selected, based on the same criteria in selecting counties to target. Each district council is often made up of tens of parishes, contact details for these parishes were found on the local district council website. Often the contact person for a parish council is the clerk, sometimes others were the points of contact.

The contact email sent out included a brief description of the rural energy access project and asking the recipient to fill out the survey linked in the email and to distribute the survey among their council and wider community. Attached also in the delivered email is a letter further describing the background of the project and the purposes of this survey. Due to the nature of this project involving outreach to the general public, this project and survey was approved by the University of Nottingham, Faculty of Engineering, Ethics Committee.

2.1. The questions asked

The content of the survey sent to respondents consisted of a 26 question, mostly multiple-choice Google Form, making it accessible to both computer and mobile phone users to respond to, and the ability to quickly and simply export the survey results into Excel for data processing.

The first 11 questions asked are generally demographic questions to find out *who* the respondent is and what kind of household do they live in. Asking questions such as age, gender, employment status and the degree of working from home there is had. Also asked in this first section are questions such as what kind of building and geography the respondent considers themselves to live in. This first set of questions are key to developing the background of *who* is responding and *where* do they live, to better understand and develop more effective engineering solutions.

Questions 12 to 16 are a series of multiple-choice questions that asks the respondents attitudes towards the environment, sustainability and the cost of energy. These questions are asked to understand the attitudes of the respondents towards these issues, which often are motivations to adopting low carbon energy systems. This set of questions also helps respondents begin thinking about the related topics in anticipation of the subsequent questions asked.

The final section of questions 17-27 are a series of technical questions asking the respondent to report key factors of their energy consumption such as the types of devices used in the home, what fuels are used for what application (power, heat, cooking or transport), how the fuels used is transported to their building and what sort of temperature is their thermostat set to throughout the year. These technical questions help build a profile of the archetypal homes that is later identified.

3. SURVEY RESULTS

The survey returned 229 responses, primarily from the Midland and Highland regions of the UK. Geographic identification of respondents is limited to only the outward section of a UK postcode (e.g. SE16 or L7) often consisting of two to four alphanumeric characters. Providing a general area-based location that would make identifying individual respondents locations not possible yest still be able to provide a reasonable sized area where one geography is consistent throughout, helping in identifying the type of energy access challenges had in the postcode area.

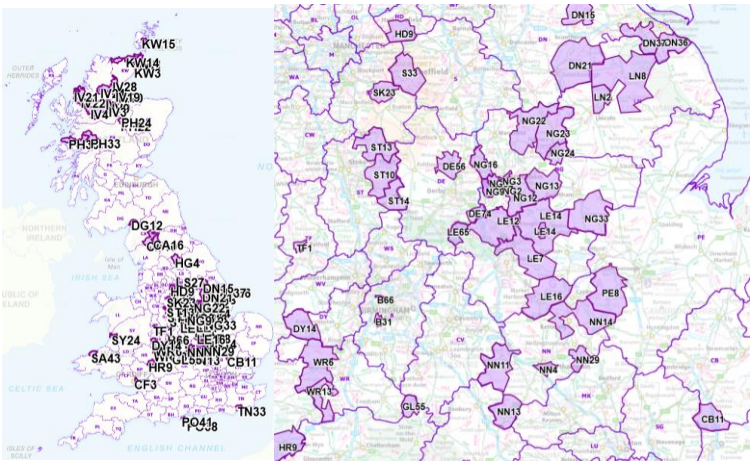

Figure 1 Map of Great Britain (left) and the English Midlands (right) with postcode areas of survey respondents

3.1. Overall survey results

First looking at overall figures and results from the survey without filtering any results. Who has responded to the survey and who lives rurally? Approximately 55% of respondents are male (45% female), 59% of occupants in respondents' homes are over the age of 44 and 78% of respondents live in a rural setting (village or smaller).

Looking overall trends of energy infrastructure in the home, over 85% of respondents report having some form of insulation, double glazing and energy efficient lighting, whereas 44% of respondents have a smart meter. 35% of respondents do not store energy in their residence, those who do store energy report having a wood pile and/or hot water cylinder at over 40% each.

A key result from this survey which is important to understand the fuels used in respondents day to day life, Figure 2 shows the response of what heating fuels are used by respondents. Finding that 56% of respondents use wood as a heating fuel closely followed by mains gas and electricity.

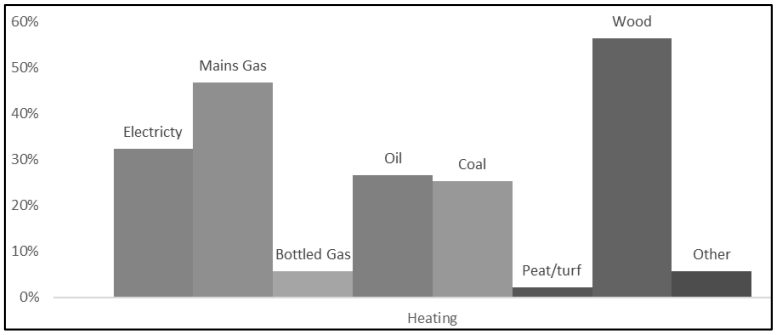

Figure 2 Multiple choice response of what fuels are used for heating

3.2. Overall survey discussion

The overall results of the survey build an overall picture of who has responded to this survey, where they live, what energy infrastructure is in their home and what fuels they use in their home. To validate the use of the results of this survey, comparing key figures from the survey to external sources such as the Statistical Digest of Rural England (Statistical Digest of Rural England 2022) derived from the 2011 Census will help validate how representative the results of the survey are in a national and rural context.

Looking at population by age nationally over 50% of rural residents are above the age of 44, the survey results find the figure for this age racket to be 59%. A comparable figure highlighting the general trend of the majority of rural residents being older in age.

Comparing the building types reported in the survey to (Statistical Digest of Rural England 2022) finds that those reporting live in detached homes as a majority followed by semi-detached and terraced homes in both datasets as seen in Table 1. The survey results output more building types than (Statistical Digest of Rural England 2022) such as bungalow, farmhouse and other, these additional building categories could be integrated into the four DEFRA building category types, which could change the composition of building types present. This has not been done as the survey wants to specifically focus on the varied building types found rurally.

Table 1: Comparing residential building types from (Statistical Digest of Rural England 2022) *and from the total survey results.*

Building Type	DEFRA (Statistical Digest of Rural England 2022)	Survey
Flat	**7%**	**5%**
Bungalow		7%
Terrace	**17%**	**13%**
Semi detached	**31%**	**20%**
Detached	**45%**	**44%**
Farmhouse		7%
Other		5%

A key metric in understanding energy efficiency of homes and the possible measures to improve energy efficiency is the energy performance certificate (EPC), which incorporates factors such as running costs, building insulation, heating

technology and heating fuel to determine how energy efficient a home is. 45% of survey respondents do not know what the EPC rating of their home is, highlighting the challenge of public awareness of such ratings that are key to improving the energy efficiency of housing stock. Especially as there is there is upcoming UK government legislation requiring new rental properties to have a minimum EPC rating of C by 2028 (Advice for landlords | Westminster City Council).

Of the respondents that do know the EPC rating of their home if present a 46% minority of respondents have an EPC rating of C or better, in line with research finding that 40% of English homes have an EPC rating of C or better (2022: 40% of homes in England have an EPC rating of 'C' or above | Open Property Group).

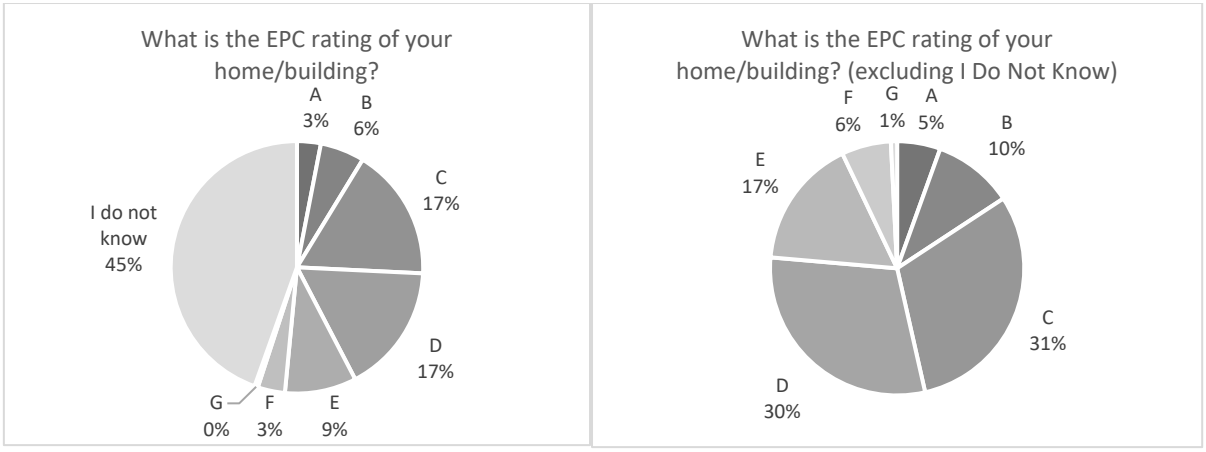

Figure 3 EPC rating of survey respondents homes (left) and excluding "I Do Not Know" (right)

Understanding the overall data collected from the rural energy survey is key, particularly as the sample size of results is small, validation of the data is required to provide confidence that the data collected can be further analysed to develop archetypal rural users for future research. Validating this dataset by comparing key figures found in the survey data to comparable figures from other sources. This has been achieved by looking at survey results for respondents age, building type and EPC rating of their homes. Comparing the results for these three categories have provided similar results, enough to assume that the data collected has captured a representative portion of the public, particularly rural residents.

4. DEVELOPING ARCHETYPES

To encompass the spread of different types of rural domestic energy user, developing a series of user archetypes of different energy users is key. Enabling future energy research to be streamlined and work from a common basis. Five archetypal user groups have been derived from the results of the rural energy survey as seen below in Table 2. These five groups have been selected primarily based on geography, access to the national grid and EPC rating. This criterion was used to select the archetypes as they are key and clear distinguishing factors that separate each group which a layperson can understand.

The first two archetypes are complementary of each other focusing on rural village residents, where the majority of respondents originated from, with group P01 being village residents connected to the national gas grid and P02 conversely being village residents not connected to the national gas grid. The third archetype P03 looks at off gas grid respondents from sparse geographies, those who report to live communities smaller than a village (hamlet, farmhouse or other) not connected to the national gas grid.

The fourth and fifth archetypes are complimentary of each other also as "Modern rural" P04 and "Old rural" P05. Where P04 focused on respondents whom report having an EPC rating of C or greater and report having some energy saving measures installed such as heat pumps electric vehicle (EV) chargers and smart meters. Conversely P05 looks at those reporting EPC less than C and excludes those with heat pumps or EV chargers. A key exclusion of both P04 and P05 is the exclusion of those who report that they do not know their EPC rating of their dwelling, which encompasses a majority of survey respondents.

Table 2: List of five archetypal rural energy users based on the survey results that use geography, connection to the national gas grid and reported EPC level as key filters.

Number	Key attributes	Key exclusions
P01	Village gas (On gas grid, village only)	City, town, suburb, hamlet, farm, other
P02	Village off gas (Off gas grid, village only)	City, town, suburb, hamlet, farm, other
P03	Sparse off gas (Off gas grid, sparse only)	City, town, suburb, village
P04	Modern rural (Village or sparse, EPC >= C, Insultation, energy efficient lighting, smart meter, heat pump or EV charging reported)	Excludes "I do not know my EPC", City, town, suburb
P05	Old rural (Village or sparse, EPC < C)	Excludes "I do not know my EPC", Heat pump, EV charger, City, town, suburb

4.1. Five archetypes overview

Key results of each developed archetype will be presented here with the complete list of survey responses for each archetype will be presented in the appendix.

Group P01 comprises of a 60% majority of two person households and 56% are over the age of 54, 43% are retired. Over 60% live in detached buildings and the largest reported EPC rating is C. Regarding attitudes to the cost of energy 12% have no concern whereas 50% are sometimes concerned, however almost 75% of respondents sometimes take measures to reduce energy consumption and only 3% take no energy consumption measures. All of group P01 report having a connection to the national gas grid, only 90% use gas for heating and 44% use gas for cooking. Other fuels used for heating and cooking are electricity, wood and coal. It can be inferred that a majority of P01 store energy at home in some form with Wood piles (46%), hot water cylinders (35%), coal stores (12%) and electric batteries (6%), whereas 41% do not store energy on site.

Group P02 has a slight female majority (53%) in contrast to P01 and the overall survey results with 57% of this group over the age of 54 where 45% are retired. 49% lie in detached buildings where the largest reported group of EPC rating is C. 6% are not concerned with the cost of energy whereas 51% are sometimes concerned, only 8% of respondents in P02 have no interest in installing sustainable technologies in their residences. Fuels used in heating by P02 include wood (80%), oil (53%), electricity (43%) and coal (43%). The most common device used to provide hot water to the residence is an oil boiler (53%). Only 14% do not store energy in some form on site, of those who do the most common energy stores are wood pile, hot water cylinder and heating oil tank. There is a more varied methods of heating homes in P02 compared to P01 with only 53% using central heating in P02 whereas 84% use central heating in P01 compared to other methods such as electricity and fireplaces.

Group P03 has a slight female majority (51%) and 54% of the group are over the age of 54. A majority of this group consider themselves to live in a hamlet (42%) followed by a single dwelling (29%) and farm (22%), where 39% of P03 live in detached homes and 24% in farmhouses. EPC D is the most prevalent reported EPC rating (18%) followed by EPC E (11%). 40% of P03 do not work from home for any proportion of their work, only 15% exclusively work from home. The major fuels reported for heating are wood (84%), oil (62%), electricity (33%) and coal (29%). Central heating is used by 56% of P03 as the principal method of heating. The primary stores of energy onsite are wood pile (69%), hot water cylinder (55%) and heating oil tank (53%), 11% report not having any form of energy storage on site.

Group P04 “modern rural” encompasses any response with an energy saving measure installed up to and including heat pumps and EV chargers AND if their EPC is greater or equal to C, the government ambition of the minimum EPC rating for housing. This group comprises of a male majority (59%), largely of two person households (69%) and where 51% are above the age of 54, 46% are retired. Almost all respondents in P04 live in villages (90%) followed by hamlets (8%) and farms (2%), where detached homes are the most popular at 62%. EPC C is most common (74%) followed by B (18%) and A (8%). Of the energy efficiency measures reported almost all respondents had some form of double glazing (100%), insulation (100%) and energy efficient lighting (97%), the uptake of heat pumps (21%) and EV chargers (10%) are relatively very low. The main heating fuels reported are wood (67%), electricity (49%), mains gas (49%), coal (26%) and oil (21%). The major heating devices reported is a gas boiler (51%), followed by oil boiler (21%) and heat pump (21%).

Group P05 covers rural residences who have a EPC less than C and do not have a heat pump or EV charger. 42% are over the age of 54, where the majority live in a village (61%). EPC D is most prevalent (46%) followed by E (40%). The energy fuels used for heating are roughly similar in uptake to each over other than wood as seen in Figure 4. Similarly the main heating devices reported are the gas and oil boilers.

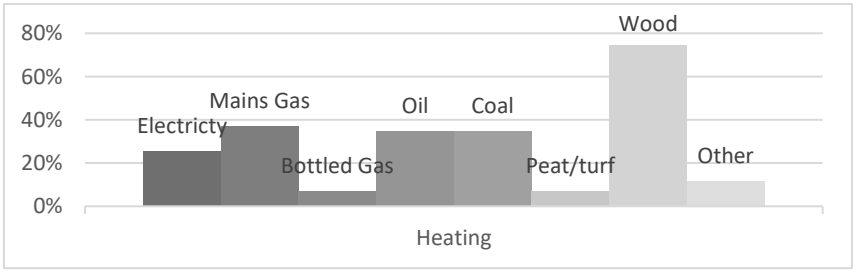

Figure 4: Heating fuels used by archetype P05

4.2. Five archetypes discussion

Looking at the overview of the archetypes selected, with an overview of key figures for each of the defined archetypes. A key overall observation was the prevalence of wood across all archetypes, suggesting wood being a popular secondary heating fuel in fireplaces. Secondary as across all archetypes question 20 asks the typical device used to provide heat/hot water is not a wood fuelled device, typically being gas, oil or electricity fuelled. This suggests a greater usage of secondary

heating systems to meet demand. Each of the identified groups are quite diverse in terms of fuels used, with generally positive attitudes and interest in addressing sustainability and installing sustainable technologies. This helps define a general final profile of each archetype by interpreting the top trends of each archetype area defined, such as;

- P01 consists of mostly 2 person households over the age of 54 with an EPC of C. Mostly using natural gas to heat. Mostly using grid natural gas to heat their homes using either gas or electricity to cook and have some form of energy storage typically most usefully in a hot water cylinder.
- P02 typically consists of people aged over 54 in detached buildings with an EPC of C. the primary heating fuel used is oil with over half using an oil boiler with a large proportion of homes having a working fireplace for secondary heating with often wood.
- P03 mostly lives in a hamlets where a significant minority lives in detached homes followed by farmhouses. EPC ratings of D and E are common, where oil is the most common primary heating fuel.
- P04 are almost all in villages with a majority being 2 person households at a typical EPC of C. All have basic energy efficiency measures of double glazing, insulation and energy efficient lighting, very few have heat pumps or EV chargers. The primary heating fuels are equally either electricity or grid gas.
- P05 finds the majority living in a village with a typical EPC of D and E, with no outright most common primary heating fuel across grid gas and oil when considering reported fuels used and reported heating devices used.

The overall data collected by this survey has been validated by comparing key statistics from authoritative sources, subsequently defining five key archetypal groups that generally encompass most types of different resident. The methodology could be improved as there are some questions asked that overlap asking similar topics and returns slightly different results for example what fuel is used and what heating device is used. Another example is not asking explicitly if any secondary or tertiary heating systems and fuels are used, this can be inferred from the data collected however this is not an ideal means of finding this data.

The results from this survey and the identified archetypes will be useful for future work towards rural energy decarbonisation, particularly in terms of the built environment, infrastructure, demographic and social elements.

And of course, with any survey-based research, more responses will improve the quality of data received.

5. CONCLUSION

This research has provided a comprehensive examination of rural energy accessibility in the United Kingdom, with a specific focus on profiling diverse user archetypes to inform and streamline future energy decarbonisation efforts. The study's in-depth survey methodology, targeting a range of geographical areas and encompassing detailed demographic, infrastructural, and energy consumption data, has yielded significant insights into the diverse energy access and usage patterns in rural settings. The creation of five distinct archetypal groups based on this data – namely Village gas, Village off gas, Sparse off gas, Modern rural, and Old rural – each characterised by specific energy consumption patterns, infrastructure, and attitudes towards sustainability, represents a pivotal step in understanding and addressing the challenges of energy decarbonisation in rural areas.

Key findings indicate a notable prevalence of wood as a secondary heating fuel across all archetypes, reflecting a reliance on a mix of traditional and modern energy sources. The demographic profiles, notably older residents in detached homes with varied energy performance ratings, highlight the complexity of tailoring energy solutions to diverse rural contexts. The insights into residents' attitudes towards energy costs and sustainability further underscore the need for inclusive, context-sensitive approaches in decarbonisation policies and interventions.

Importantly, the research also identifies areas for methodological refinement, such as the need for clearer delineation in survey questions related to secondary or tertiary heating systems and fuels. Such refinements are crucial for capturing the nuanced realities of rural energy consumption and ensuring that future research and policy initiatives are grounded in accurate, comprehensive data.

In conclusion, this study lays a foundational framework for future research and policy-making in rural energy decarbonisation. By providing a nuanced understanding of the different archetypes of rural energy users, the research not only contributes to academic discourse but also offers practical insights for developing targeted, effective strategies for energy transition in rural communities. This is particularly pertinent in the context of global efforts towards sustainable, low-carbon societies, where understanding and addressing the unique challenges of rural energy access and decarbonisation is critical.

6. REFERENCES

2022: 40% of homes in England have an EPC rating of 'C' or above | Open Property Group. [cited 2023 Jun 29]. Available from: https://www.openpropertygroup.com/landlord-hub/2022-epc-ratings/

Advice for landlords | Westminster City Council. [cited 2023 Jun 29]. Available from: https://www.westminster.gov.uk/tackling-climate-change-westminster/changes-at-home/advice-landlords

BEIS. Clean Growth - Transforming Heating - Overview of Current Evidence. 2018;

Government H. Heat and Buildings Strategy. 2021;

National Association of Local Councils. [cited 2023 Jun 5]. Available from: https://www.nalc.gov.uk/

Statistical Digest of Rural England. 2022 [cited 2023 May 25]; Available from: www.nationalarchives.gov.uk/doc/open-government-licence/version/3/oremailPSI@nationalarchives.gsi.gov.uk

7. APPENDIX

Rural energy survey archetypes		Overall	P01	P02	P03	P04	P05
4. What is your gender?	Male	54%	54%	47%	45%	59%	37%
	Female	45%	46%	53%	51%	38%	63%
	Prefer not to say	1%	0%	0%	4%	3%	0%
	Other	0%	0%	0%	0%	0%	0%
5. how many occupants live in your home?	1	13%	12%	16%	5%	8%	7%
	2	56%	63%	59%	58%	69%	58%
	3	14%	13%	14%	13%	10%	12%
	4	11%	9%	6%	18%	10%	19%
	5+	4%	3%	4%	6%	3%	5%
6. What is the age range of the occupants [Tick all that apply]	Under 18	9%	6%	6%	9%	9%	9%
	18-24	10%	12%	3%	12%	3%	8%
	25-34	12%	9%	9%	7%	16%	11%
	35-44	9%	10%	6%	9%	10%	13%
	45-54	12%	8%	18%	11%	10%	19%
	55-64	18%	21%	18%	22%	17%	15%
	65-74	20%	23%	29%	21%	22%	18%
	75+	9%	12%	10%	11%	12%	9%
7. Where do you consider yourself primarily to live?	City	5%	0%	0%	0%	0%	0%
	Town	12%	0%	0%	0%	0%	0%
	Suburb	5%	0%	0%	0%	0%	0%
	Village	51%	100%	100%	0%	90%	60%
	Hamlet	12%	0%	0%	42%	8%	16%
	Single Dwelling	8%	0%	0%	29%	0%	16%
	Farm	5%	0%	0%	22%	3%	2%
	Other	2%	0%	0%	7%	0%	5%
8. What kind of home/building do you reside in?	Flat, purpose built	3%	0%	2%	0%	3%	0%
	Flat, converted	2%	0%	2%	0%	0%	0%
	Bungalow	7%	4%	10%	13%	10%	12%
	Terrace	13%	7%	8%	2%	5%	2%
	Semi detached	20%	19%	24%	16%	15%	30%
	Detached	44%	62%	49%	36%	62%	47%
	Farmhouse	7%	3%	0%	24%	0%	5%
	Other	5%	4%	4%	9%	5%	5%
9. What is the EPC rating of your home/building?	A	3%	0%	4%	2%	8%	0%
	B	6%	7%	2%	5%	18%	0%
	C	17%	25%	20%	7%	74%	0%
	D	17%	15%	16%	18%	0%	47%
	E	9%	9%	10%	11%	0%	40%
	F	3%	1%	6%	5%	0%	12%
	G	0%	0%	2%	0%	0%	2%
	I do not know	45%	43%	39%	51%	0%	0%
10. What is your employment status?	Employed	34%	32%	24%	36%	33%	40%
	Self Employed	9%	7%	12%	15%	15%	9%
	Not Employed	1%	1%	0%	2%	3%	0%
	Student	14%	6%	2%	11%	0%	5%
	Retired	32%	43%	45%	31%	46%	26%
	Part time	8%	9%	16%	4%	0%	21%
	Prefer not to say	1%	1%	0%	2%	3%	0%

11. Do you work from home?	0% of the time - I do not work from home	38%	41%	35%	40%	33%	33%
	25% of the time - Sometimes	23%	29%	16%	13%	33%	21%
	50% of the time	7%	3%	10%	7%	10%	7%
	75% of the time - Often	15%	12%	12%	25%	5%	23%
	100% of the time - I always work from home	17%	15%	27%	15%	18%	16%
12. To what extent do you consider yourself aware of environmental issues?	Extremely	27%	22%	22%	38%	36%	14%
	Very	46%	56%	47%	44%	44%	63%
	Moderately	25%	22%	27%	16%	21%	21%
	Slightly	2%	0%	4%	2%	0%	2%
	Not at all	0%	0%	0%	0%	0%	0%
13. How interested are you in sustainability?	Extremely	31%	28%	24%	42%	38%	26%
	Very	50%	51%	57%	44%	41%	58%
	Moderately	17%	18%	16%	15%	18%	16%
	Slightly	1%	1%	2%	0%	3%	0%
	Not at all	0%	1%	0%	0%	0%	0%
14. Are you interested in installing your own sustainable low emissions technologies at home?	Definitley Definitely	39%	35%	45%	42%	54%	30%
	Probably	28%	32%	20%	29%	21%	37%
	Possibly	24%	25%	27%	22%	23%	28%
	Probably not	7%	6%	6%	7%	3%	2%
	Definitley not Definitely not	3%	1%	2%	0%	0%	2%
15. How concerned are you about your cost of energy?	No concern. I have no concern regarding affording energy	8%	12%	6%	11%	13%	12%
	Occasionally concerned	17%	21%	27%	13%	18%	26%
	Sometimes concerned	53%	50%	51%	53%	51%	49%
	Regularly concerned. It is often difficult to afford to pay my energy bills	18%	18%	16%	15%	15%	12%
	Yes, always concerned. I cannot afford to pay for my energy	3%	0%	0%	9%	3%	2%
16. Do you actively take measures to reduce your energy consumption?	No. I do not take active measures	2%	3%	0%	4%	0%	2%
	Sometimes. When I am able	25%	24%	27%	20%	21%	16%
	Yes. I actively take measures to reduce energy consumption	72%	74%	73%	76%	79%	81%
17. Does your building include any of the following features?	Double/triple Glazing	86%	85%	88%	91%	100%	86%
	Insulation	87%	91%	96%	87%	100%	93%
	electric vehicle charging point	8%	7%	12%	7%	10%	0%
	Heat pump	9%	3%	16%	16%	21%	0%
	Smart meter	44%	56%	45%	22%	69%	42%
	Energy efficient lighting	89%	90%	98%	89%	97%	91%
18.a. What rough temperature do you usually set your thermostat or equivalent throughout the year? [Less than 10 degrees]	Winter	1%	0%	0%	0%	0%	0%
	Spring	9%	7%	6%	16%	13%	12%
	Summer	30%	29%	33%	42%	38%	35%
	Autumn	5%	6%	2%	9%	8%	5%
18.a. What rough temperature do you usually set your thermostat or equivalent throughout the year? [10 - 15 degrees]	Winter	3%	3%	4%	4%	0%	5%
	Spring	15%	15%	20%	15%	21%	16%
	Summer	10%	13%	14%	7%	13%	9%
	Autumn	9%	9%	10%	13%	8%	14%
18.a. What rough temperature do you usually set your thermostat or equivalent throughout the year? [16 - 20 degrees]	Winter	44%	46%	53%	51%	64%	56%
	Spring	34%	40%	41%	33%	49%	42%
	Summer	19%	16%	29%	16%	28%	23%
	Autumn	37%	46%	43%	36%	46%	44%
18.a. What rough temperature do you usually set your thermostat or equivalent throughout the year? [21- 25 degrees]	Winter	19%	24%	20%	16%	23%	14%
	Spring	6%	9%	6%	5%	10%	2%
	Summer	3%	4%	2%	2%	5%	0%
	Autumn	7%	12%	6%	5%	18%	2%
18.a. What rough temperature do you usually set your thermostat or equivalent throughout the year? [26 - 30 degrees]	Winter	0%	1%	0%	0%	3%	0%
	Spring	0%	0%	0%	0%	0%	0%
	Summer	0%	1%	0%	0%	3%	0%
	Autumn	0%	0%	0%	0%	0%	0%
	Winter	0%	0%	0%	0%	0%	0%

18.a. What rough temperature do you usually set your thermostat or equivalent throughout the year? [30+ degrees]	Spring	0%	0%	0%	0%	0%	0%
	Summer	0%	0%	0%	0%	0%	0%
	Autumn	0%	0%	0%	0%	0%	0%
18.a. What rough temperature do you usually set your thermostat or equivalent throughout the year? [I do not have temperature control]	Winter	11%	9%	18%	9%	3%	9%
	Spring	11%	38%	53%	47%	67%	60%
	Summer	12%	41%	57%	51%	72%	65%
	Autumn	10%	35%	49%	44%	62%	56%
18.c. Is that in Celsius or Fahrenheit?	Celsius	84%	85%	84%	82%	90%	88%
	Farenheit Fahrenheit	1%	3%	2%	0%	3%	0%
19. What energy fuels do you use? [Electricity]	Heating	32%	31%	43%	33%	49%	26%
	Power	93%	96%	90%	89%	97%	93%
	Cooking	79%	84%	90%	78%	82%	88%
	Transport	7%	7%	10%	4%	10%	0%
	I do not use	0%	0%	0%	2%	0%	0%
19. What energy fuels do you use? [Mains Gas]	Heating	47%	90%	2%	0%	49%	37%
	Power	1%	3%	0%	0%	3%	0%
	Cooking	26%	44%	2%	0%	26%	16%
	Transport	0%	0%	0%	0%	0%	0%
	I do not use	51%	6%	98%	100%	46%	63%
19. What energy fuels do you use? [Bottled Gas]	Heating	6%	3%	6%	13%	3%	7%
	Power	0%	0%	0%	0%	0%	0%
	Cooking	15%	1%	27%	31%	10%	19%
	Transport	0%	0%	0%	0%	0%	0%
	I do not use	82%	97%	69%	60%	90%	77%
19. What energy fuels do you use? [Oil]	Heating	27%	0%	53%	62%	21%	35%
	Power	0%	0%	0%	0%	0%	0%
	Cooking	4%	0%	0%	15%	0%	2%
	Transport	1%	3%	0%	0%	3%	2%
	I do not use	71%	97%	47%	35%	77%	63%
19. What energy fuels do you use? [Coal]	Heating	25%	22%	43%	29%	26%	35%
	Power	0%	0%	0%	0%	0%	0%
	Cooking	0%	0%	2%	0%	0%	0%
	Transport	1%	0%	2%	2%	0%	0%
	I do not use	73%	78%	53%	69%	74%	65%
19. What energy fuels do you use? [Diesel]	Heating	1%	1%	0%	2%	3%	2%
	Power	1%	0%	2%	2%	0%	0%
	Cooking	0%	0%	0%	0%	0%	0%
	Transport	61%	54%	57%	95%	59%	81%
	I do not use	37%	44%	41%	2%	38%	16%
19. What energy fuels do you use? [Petrol]	Heating	0%	0%	0%	2%	0%	2%
	Power	0%	0%	0%	2%	0%	0%
	Cooking	0%	0%	0%	0%	0%	0%
	Transport	60%	69%	61%	55%	62%	56%
	I do not use	39%	31%	39%	44%	38%	42%
19. What energy fuels do you use? [Peat/turf]	Heating	2%	0%	2%	5%	0%	7%
	Power	0%	0%	0%	0%	0%	0%
	Cooking	0%	0%	0%	0%	0%	0%
	Transport	1%	0%	2%	2%	0%	0%
	I do not use	97%	100%	96%	95%	100%	93%
19. What energy fuels do you use? [Wood]	Heating	56%	53%	80%	84%	67%	74%
	Power	0%	0%	0%	0%	0%	0%
	Cooking	3%	4%	4%	4%	0%	7%
	Transport	0%	0%	0%	0%	0%	0%
	I do not use	44%	49%	18%	16%	33%	26%
20. Heat/hot water supply. How do you get your heat/hot water?	Gas boiler	52%	93%	8%	11%	51%	47%
	Oil boiler	26%	0%	53%	58%	21%	35%
	Electric boiler	7%	4%	8%	7%	5%	0%
	Biomass boiler	2%	0%	6%	2%	3%	5%
	Heat pump	7%	3%	12%	15%	21%	0%
	Electric heater	15%	10%	20%	20%	13%	16%
	(District) Heat network	0%	0%	0%	0%	0%	0%
	Solar thermal	7%	7%	14%	7%	10%	7%
	Other	12%	9%	16%	20%	10%	16%
21. How is your building typically heated?	Central heating	71%	84%	53%	56%	74%	60%
	Electric	3%	0%	8%	0%	3%	2%
	Fireplace	17%	13%	24%	27%	15%	26%
	Other	8%	3%	14%	16%	8%	12%
22. Storage. Do you store energy on site? [Please select all that apply]	Electric battery	5%	6%	6%	7%	10%	2%
	Hot water cylinder	41%	35%	53%	55%	46%	40%

	Heating oil tank	21%	0%	37%	53%	18%	33%
	Gas tank	4%	0%	4%	9%	0%	5%
	Gas bottles	10%	1%	20%	18%	13%	9%
	Wood pile	46%	46%	61%	69%	56%	60%
	Coal store	14%	12%	27%	16%	15%	21%
	Other	3%	1%	4%	5%	3%	5%
	No	35%	41%	14%	11%	28%	21%
23. How do you get electricity to your building? [Please select all that apply]	National grid	100%	100%	100%	98%	100%	100%
	On site generator	3%	1%	0%	7%	5%	0%
	On site wind turbine	0%	0%	0%	0%	0%	0%
	On site solar panel	20%	18%	24%	33%	36%	19%
	Other	0%	0%	2%	0%	0%	2%
	I do not use	0%	0%	0%	0%	0%	0%
24. How do you get natural gas to your building? [Please select all that apply]	The gas grid	51%	100%	0%	0%	56%	35%
	Bottled gas brought in yourself	4%	0%	6%	9%	5%	5%
	Bottled gas delivered	7%	0%	12%	18%	0%	12%
	Delivered by tanker	4%	0%	4%	11%	0%	7%
	Other	0%	0%	0%	0%	0%	0%
	I do not use	34%	0%	78%	62%	38%	44%
25. How do you get heating fuel oil to your building? [Please select all that apply]	Bottle (brought in yourself)	0%	0%	0%	0%	0%	0%
	Bottle (delivered)	0%	0%	0%	0%	0%	0%
	Delivered by tanker	28%	0%	55%	67%	21%	35%
	Other	0%	0%	0%	0%	0%	0%
	I do not use	72%	100%	45%	33%	79%	65%
26. How do you get Coal to your building? [Please select all that apply]	Delivered	10%	10%	20%	5%	8%	9%
	Brought in by yourself	11%	7%	20%	16%	13%	19%
	Other	0%	1%	0%	0%	3%	0%
	I do not use	80%	82%	61%	78%	79%	72%

#74: A BIM-based conceptual framework for embodied carbon assessment

James HUNT[1], Carlos A. OSORIO-SANDOVAL[2]

[1] Department of Civil Engineering, The University of Nottingham
[2] Department of Civil Engineering, The University of Nottingham, carlos.osorio@nottingham.ac.uk

Abstract: Understanding the integration of BIM as an enabling factor in embodied carbon (EC) assessment is becoming exponentially vital as the global climate crisis accelerates. This paper introduces a BIM-based conceptual framework to quantify the EC of a building, enabling informed design decisions early into a project's development. A comprehensive review of existing literature on EC assessment techniques was conducted to identify current gaps. Based on this review and the background theory, a conceptual framework was proposed for EC assessment within a BIM environment. The framework was developed using the design science research (DSR) approach, focusing on the first three stages: problem identification, contextualising the problem within existing body of knowledge and proposing a solution to address the problem domain. The framework lays the groundwork for the development of tools that integrate EC assessment into BIM workflows, which has the potential to provide quick assessment at the design stage where key decisions are made.

Keywords: embodied carbon; building information modelling; embodied carbon assessment; design science research

1. INTRODUCTION

The significance of embodied carbon (EC) and greenhouse gases (GHG) is increasingly prevalent as society continues to develop. EC encapsulates all carbon associated with the construction of a structure, the extraction, fabrication, refinement, transportation and installation of materials and the disposal of old matter. Essentially, "embodied carbon is built into the fabric of the building" (Tasker, Purslow and Boland, 2022). With populations expanding, advancements in economies and the resultant demand for construction materials, the building operations and construction sector now accounts for almost 40% of global emissions (Bowles, Cheslak and Edelson, 2022). Thus far, despite the pressing need for mitigation measures, global stakeholders have offered minimal support to counter this substantial issue, with much of the initial emphasis on GHGs the construction industry focusing on reducing the operational costs. However, more recently there has been a notable shift towards more energy efficient structures utilising decarbonised energy resources, moving EC to the focal point of a structures life cycle assessment (LCA). Consequently, numerous research initiatives are underway with the objective to mitigate EC and achieve Net Zero Carbon buildings (Tirelli and Besana, 2023).

Incorporating EC assessment early into a project's design process plays a significant part in determining its suitability (IStructE, 2011). By including EC assessment at an early stage, stakeholders can make more informed decisions tailored to the EC assessment where applicable, whereas changes made later on may be restricted by other model properties, such as the structural layout. Figure 1 illustrates the importance of integrating EC assessment early on in the design process, emphasising how it can impact the final outcome of a project.

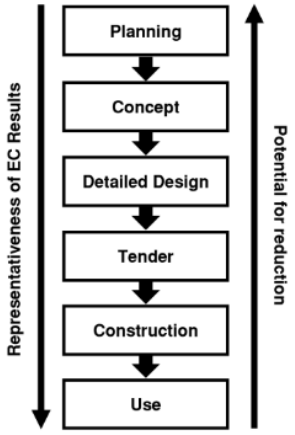

Figure 1 Importance of incorporating EC assessment early into the development of a project (IStructE, 2011)

Building Information Modelling (BIM) is a digital tool extensively utilised in engineering to effectively design, construct, and operate structures. It provides significant opportunities for advancements in the field of EC assessment, primarily due to its capabilities as a data repository. It enables informed decision-making regarding material selection based on their environmental impact, while also serving as a powerful visualisation tool that can present 2D/3D geometry project geometry with relevant data. Whilst several approaches have been developed to facilitate EC assessment within BIM, it is important to acknowledge that these approaches are still limited and have yet to fully utilise capabilities of BIM as an enabling factor in EC assessment.

2. RELATED WORK

EC assessment is often categorised in the wider context of life cycle assessment (LCA), which envelopes all environmental impacts of a building throughout its life cycle, from the extraction of raw materials to its final disposal. The focus of this paper is the integration of EC assessment into BIM workflows, which can be achieved under one of three classified flows of data exchange (Teng et al., 2022):

- Type I – This approach involves the extraction of BIM data and combining it with carbon emission factors obtained from a selected EC database, typically in a spreadsheet format. This method is executed outside of the BIM environment.
- Type II - In this approach, carbon emission factors are directly integrated into BIM tools by employing plug-ins and APIs, utilising BIM potential as a comprehensive data repository and visualisation platform.
- Type III – This approach entails importing BIM information into a dedicated LCA software tool, where the assessment is conducted directly by the specialized tool. This process occurs outside the BIM environment, utilising the BIM data as input for the LCA software.

Several examples for each of these data exchange methods for an EC assessment have been identified in the literature, each with their own inherent limitations that have hindered effectively incorporating them in a BIM workflow. For instance, the Structural Carbon Tool (Wood, 2022), classified under Type I, utilises data obtained from a BIM model quantity take-off and estimates the EC of different elements using carbon factors from the Inventory of Carbon and Energy (ICE) (Jones and Hammond, 2008), an open and freely available inventory of carbon emissions factors providing cradle to gate information assembled from a substantial repository of published information and life cycle assessment. A drawback of this type of tool is the assessment is executed outside of the BIM environment, meaning it lacks that ability to visualise the EC results within a BIM model and any changes to the design require to repeat the assessment process again.

Tools that adopt the Type II approach, integrate EC assessment directly within a BIM workflow through plugins and other API tools. An example of this is the Revit add on, Beacon, proposed by Tomasetti (2020), where carbon factors are inputted directly into the developed tool and EC assessment is carried out within the BIM environment. This approach is advantageous over Type I tools, as any changes to the model are directly reflected on the EC assessment, thereby increasing the time efficiency for revaluations. However, such a tools effectiveness is directly proportional to accuracy of information assigned between EC coefficients and the BIM material parameters. In the past, Type II tools have been limited due to having a disconnect between this data mapping but as more standards have been developed to support them, the matching of data has become more effective. Moreover, these carbon factors need to be continuously monitored and updated as more accurate data becomes available. For instance, adjustments may be necessary to account for emissions during transportation, construction, operation, and end of life processes that are outside the scope of most carbon inventories that gather data from cradle to gate (Lockie, 2012), effectively modifying the boundary conditions of the factors. Other tools such as One Click LCA's integration within Trimble Tekla, take further advantage by using BIM's visualisation capabilities to highlight potential carbon emission hotspots within a 3D BIM model. However, their utilisation of BIM's visualisation capacity can be argued to be limited, by having a fixed colour scale for all elements, that is restricted to identifying the most onerous elements but not always the elements that can be improved.

The Type III EC assessment method involves importing BIM data into a dedicated EC analysis software, taking advantage of its reliability as a dedicated software for EC assessment with a comprehensive store of up-to-date carbon coefficients. A recent example of this approach was seen in a study by Xu et al. (2022), which incorporated EC assessment within the wider context of life cycle assessment (LCA). The study aimed to address the recognised issues of this approaches, such as the data interoperability between BIM and LCA tools, manual data capture, and the absence of spatial-level methods for evaluating carbon emissions. Nevertheless, the effectiveness of employing such a tool within a BIM framework could be constrained by limited budgets faced by project stakeholders and limiting access to a commercial dedicated EC assessment software. Hence restricting their capacity to perform comprehensive EC assessment, having a significant impact, particularly during the initial concept design phase.

It is worth noting that despite numerous research efforts to streamline the incorporation of EC assessment, its widespread implementation in the construction sector has not been fully realised. Consequently, initiatives have been developed to urge stakeholders to establish carbon targets and reduce the carbon footprints of their buildings. These initiatives offer ways to qualitatively assess the suitability of a design. The commonly applied approach is to quantify the EC (kg CO_2e) relative to a projects gross internal area (GIA)(m^2). This provides a quantifiable output in terms of mass per unit area (kg $CO2_e/m^2$), which can be assigned a relative score based on a defined EC rating scheme. For instance, the Structural Carbon Rating Scheme (SCORS), developed by the Institute of Structural Engineers is used to 'contextualise both the carbon impact of our work and the progress that must be made in the coming decade' (Arnold et al., 2020). This scheme assesses the carbon emissions of a building project from cradle to completion and assigns a rating from A+ to G. It enables stakeholders (including engineers, architects, clients, and planners) to understand the environmental impact of a structure in relation to other industry practices, as the range and gradation of ratings was informed on a review of 326 projects shared by Arup, Price & Myers, and Thornton Tomasetti. The scheme aims for 'typical designs achieving an A rating by the year 2030' and provide a roadmap towards achieving net zero emissions by 2050. This and other schemes are critical during the design stage as it provides a quantifiable standard for projects to meet and holds the industry accountable for its actions to meet these targets.

In this paper, a conceptual framework is constructed based on this literature, that takes forward the strengths of each data transfer method, and its respective integrations in tools. The framework presents a roadmap intended to use at an early stage to conduct rapid EC assessment of structural models, by giving designers insight into make informed design decision by identifying potential hot spots and areas for optimisation.

3. METHODOLOGY

The underlying research strategy adopted for this project is based on the design science research (DSR) methodology (Henver et al., 2004) on the basis that it is particularly suited for the development and evaluation of new artefacts use to solve practical problems. This research project is tasked with creating a new conceptual framework and provide a route for a solution in the problem domain of EC assessment within BIM. In this study, the problem statement is further refined by claiming that at present the full potential of BIM as an enabling factor for EC assessment has not been fully utilised to streamline early-stage assessment for designers and stakeholders alike. As part of suggesting as solution, the BIM

integration types were evaluated against developed criteria with the outcome indicating BIM type II assessment provides the most suitable roadmap for the development. Therefore, this paper introduces a novel conceptual framework for assessing the EC of structural models through application of the underlying theory. This DSR approach is illustrated in Figure 2, adopted from Schimanski et al. (2021). Notably, this research focuses on DSR activities one to four of Figure 2, highlighted in yellow as at present, the integration of the conceptual framework into a prototype tool, its demonstration and verification of its applicability is a topic of further research.

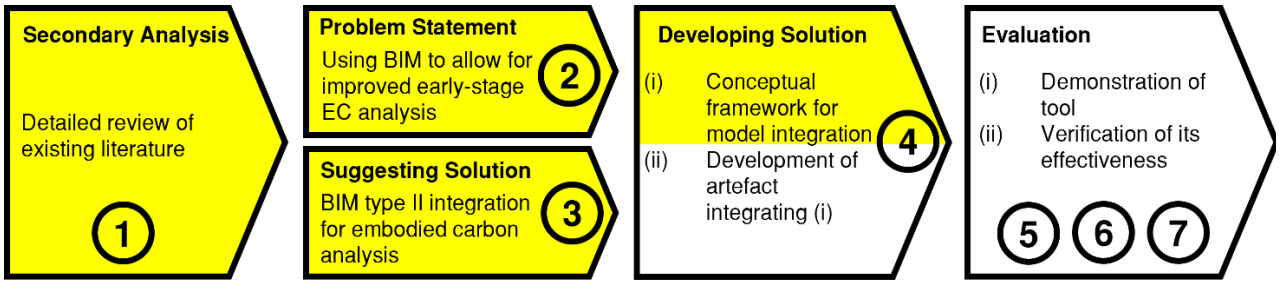

Figure 2 DSR strategy

4. PROPOSED FRAMEWORK

The primary motivation behind developing the conceptual framework was to propose a roadmap for seamlessly integrating the process of EC assessment within a BIM workflow. In accordance with the methodology outlined above, a framework was built upon the type II BIM and EC assessment integration approach. The purpose of this framework is to represent the DSR artifact that will serve as a solution to the identified problem. The initial phase of development focussed on the formulation of a comprehensive list of functional requirements to develop an artifact for BIM-based EC assessment, alongside a breakdown of the underlying background theory. Next, a detailed overview of the conceptual framework is presented, highlighting its integral elements.

4.1. Functional requirements

The proposed framework represents an artifact that should meet the following functional requirements:

- The artifact shall calculate the EC of each relevant BIM element within a model (i.e., a structural beam). This process involves identifying an elements type, identifying the elements material breakdown, obtaining its mass and volume data, and retrieving its corresponding EC factor. All these factors should allow an EC calculation to be performed.
- The artifact shall calculate the total EC of a structure by taking into account the EC of all the models' constituent elements and adding them together.
- The artifact shall calculate an EC score for the model by dividing the total EC by its GIA.
- The artifact shall provide an appropriate rating for the structure based on established rating schemes using the calculated EC score.
- The artifact shall relay this information back into the model by visually displaying the EC distribution of each element within the model through a colour code system. This feature highlights potential EC hotspots through a newly established dynamic colour code range based on a elements category.

4.2. Background theory

Without an adequate understanding of the factors involved in EC calculation, this research could not be conducted. This subsection looks to briefly shed light on these different factors. Within a BIM model, volumetric information is accessible for each individual element by looking at its parametric data. In combination with the appropriate material density data for that element, the mass of an element can be calculated using the formula:

Equation 1: Mass of element.

$$m = \rho V$$

Where:

- m = mass of element (kg)
- r = density of material (kg/m^3)
- V = volume of element (m^3)

EC can be calculated by multiplying the mass of the element by its corresponding EC factor, taking into account all the carbon emissions from "Cradle to Gate".

Equation 2: EC of element.

$$m_{EC} = mEC_f$$

Where:

- m_{EC} = EC of element (kg CO_2e)
- m = mass of element (kg)
- EC_f = EC factor (kg CO_2e/kg)

As outlined in the literature, to be able to evaluate buildings of different temporal magnitudes on the same scale they needed to be quantified with respect to their gross internal area (GIA). A structure's EC rating can be calculated by finding the sum of EC elements and dividing by the GIA, to get an EC mass per unit area.

Equation 3: EC score structure

$$EC_{score} = \frac{\sum m_{EC}}{GIA}$$

Where:

- EC_{score} = EC score of structure (kg CO_2e/ m^2)
- m_{EC} = EC of element (kg CO_2e)
- GIA = gross internal area (m^2)

4.3. Overview of the framework

The proposed framework used to implement the fundamental principles in Section 4.1 and the background theory in Section 4.2 can be seen in Figure 3. The framework can be divided into two main components, firstly, the calculation of EC and identification of hotspots. Secondly, calculating the EC score of a structure and assigning and applicable scoring system. The framework has two key inputs:

- BIM Model – used to provide parametric data for EC assessment (materials, volume etc) and to relay assessment back into (colour code 3D visualisation).
- Input Data Repository – used to provide input of material densities and EC factors.

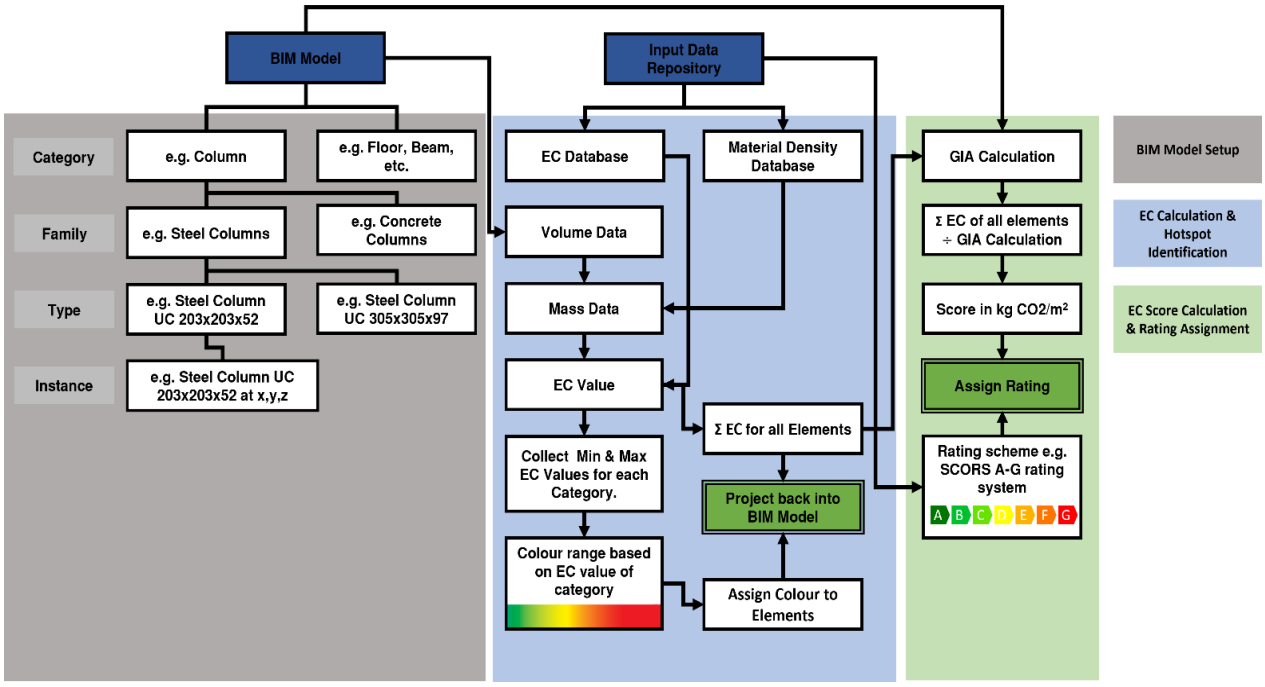

Figure 3 Conceptual framework

4.4. Features of conceptual framework

There are several sections of the conceptual framework which should be noted, along with the reasons behind their inclusion.

Element EC Calculation

Expanding on Figure 3, for an example RC column element, the process for EC assessment can be broken down further, as a RC column (compound element) consists of concrete and steel, each having their own respective carbon factors. Figure 4 shows the process by which applying the background theory within the conceptual framework, the EC of the two constituent materials can be calculated and used to find the resultant EC for a compound element. The premise for an isotropic material is the same but just with one material.

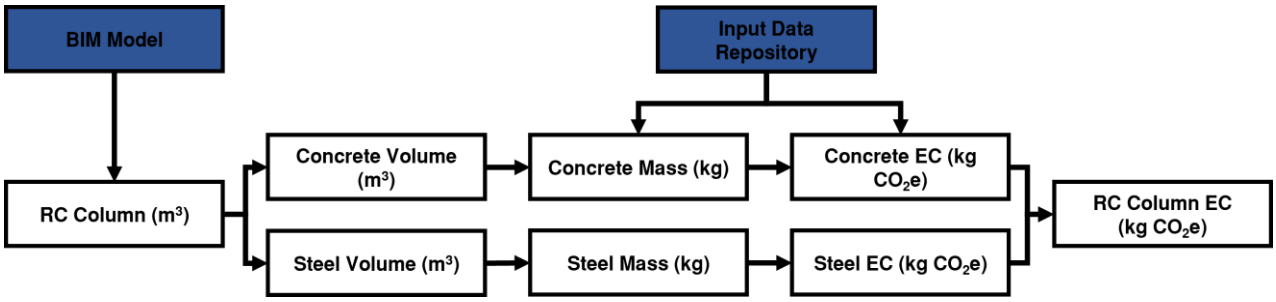

Figure 4 Conceptual framework application for example RC column EC calculation

Colour range assignment

During the comprehensive review of existing literature, it was understood that existing colour coding schemes use a universal scheme applied to all elements across the entire model (Bowles et al., 2022). This method was evaluated to be fairly limited, as the coding would favour certain elements with a significant EC footprint due to their size and mass, e.g., floor systems. However, this universal colour scheme fails to highlight elements, that although have a comparatively lower EC value in relation to other elements within the model, relative to other elements of their category, may have significant EC and require further examination. This research instead looked to use a separate colour range for each category e.g., beams, columns, floors, etc. by applying appropriate scales for said category. This method highlights the different "hotspots" within each category and is proposed to be more effective in improving the EC of a structure. Additionally, existing schemes use fixed scales that are constrained by predetermined boundaries, which may limit their effectiveness. With this type of scale, elements may potentially all have a good EC colour assignment "green colour" however may not identify that there might still be room for further improvement. This project instead makes use of a newly devised dynamic scheme to assign colours within each category, based on the position of an element in relation to the maximum and minimum EC of that category, meaning there will always be a most and least onerous element and hence always identify an area for further improvement if it's feasible to do so. The colour range assigned will use a red-to-green scale, as outlined in Figure 5 for an example category (columns), is based on the widely acknowledged colour theory that green is associated with good whilst red is linked to bad (Pravossoudovitch et al., 2014).

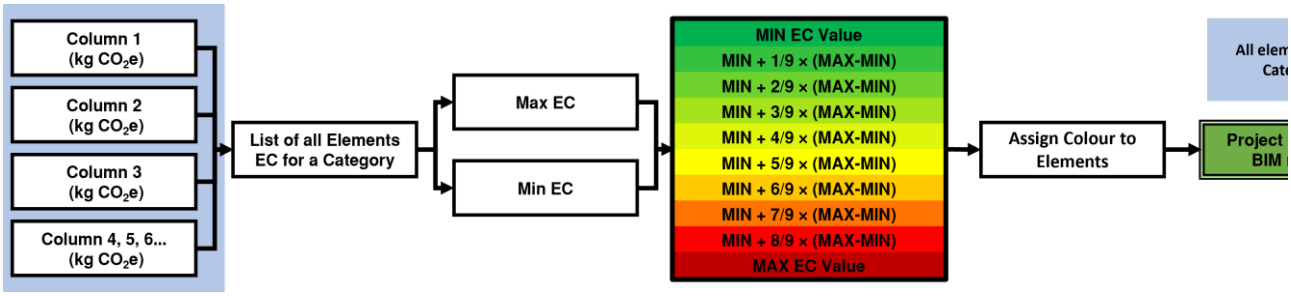

Figure 5 Application of dynamic colour code system within the conceptual framework

EC score & rating assignment

The review of literature highlighted that there was no universally adopted rating system in use by the industry, however, they all followed the same premise of equating a mass per unit area to a rating. By following this framework, it allows for a buildings EC score to be quantifiable against a given rating scheme and allows for appropriate action to be undertaken with respect to the result. Figure 6 illustrates this process, where the calculated EC score of a model is equated to a rating scheme provided within the input data repository. In this instance, the SCORS (Arnold et al., 2022) rating scheme has been implemented however by including the rating scheme within the repository it can be readily updated or changed to the most applicable scheme.

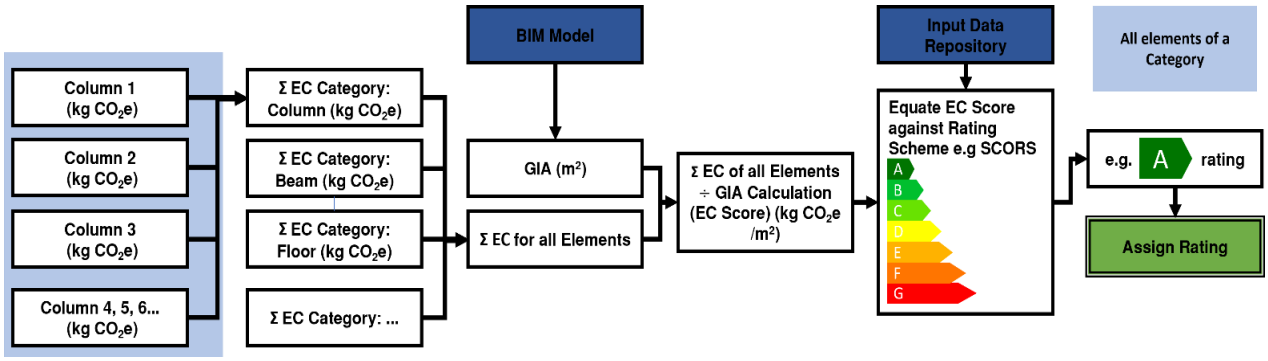

Figure 6 EC score calculation and application of rating scheme within the conceptual framework

5. CONCLUSION

The main contribution of this research is the proposal of the framework that facilitates the integration of EC assessment within a BIM workflow. By utilising BIM capabilities as a powerful visualisation tool and data repository, the framework paves the way to developing tools to incorporate EC assessment at an early stage of project development. This integration has the potential to enable designers to make early on informed decisions and strive towards minimising the carbon footprint of their structures. The framework offers a systematic approach to isolate the most onerous elements within a model, indicating the key areas for improvement. This proposed approach holds significant potential to drive advancement in sustainability practices, providing a solid platform for the development of BIM tools and contribute to the global efforts in combating climate change.

The study has implemented the first 4 steps of DSR, suggesting a solution to the identified problem in the form of a conceptual framework. The next steps are to develop such solution into an actual tool that implements the proposed framework, with the aim of demonstrating its functionality to provide a solution in the problem domain of EC assessment. Additionally, at this stage, the conceptual framework allows for substantial flexibility and adaptability, as the framework can be implemented and refined in many different software solutions.

One identified limitation of this study is that the scope of this research was limited to EC assessment, not considering other significant sustainability metrics such as operational carbon or LCA. However, by expanding the developed artefact to include these other sustainability metrics, a more comprehensive evaluation of structures can be achieved. Future work involves integrating the conceptual framework within a BIM workflow by constructing a prototype tool, as developed, and presented in Hunt and Osorio-Sandoval (2023), utilising Revit and Dynamo (a visual programming language). Furthermore, the subsequent steps involve the testing of this prototype tool in an actual project, thereby verifying its effectiveness and applicability.

6. REFERENCES

Arnold, W. et al. (2020) 'Setting carbon targets: An introduction to the proposed Scors Rating Scheme, The Structural Engineer, 28(1), pp. 8–12. Available at: https://doi.org/10.17863/CAM.63446

Bowles, W., Cheslak, K., and Edelson, J. (2022) Lifecycle GHG impacts in building codes. Available at: https://newbuildings.org/wp-content/uploads/2022/04/LifecycleGHGImpactsinBuildingCodes.pdf (Accessed: 06 February 2023).

Hevner, A.R. et al. (2004) 'Design Science in Information Systems Research', MIS Quarterly, 28(1), pp. 75–105. Available at: https://doi.org/10.2307/25148625.

Hunt, J. and Osorio-Sandoval, C.A. (2023) 'Assessing Embodied Carbon in Structural Models: A Building Information Modelling-Based Approach', Buildings, 13(7), pp. 1679. Available at: https://doi.org/10.3390/buildings13071679

IStructE (2011) A short guide to embodied carbon in building structures. London: Institution of Structural Engineers.

Jones, C., and Hammond, G. (2008) 'Embodied energy and carbon in construction materials', Proceedings of The Ice – Energy, 161, pp. 87-98. Available at: http://dx.doi.org/10.1680/ener.2008.161.2.87

Lockie, S. and Berebecki, P. (2012) Methodology to calculate embodied carbon of materials. Coventry: RICS, RICS information paper.

Schimanski, C.P. et al. (2021) 'Integrating bim with lean construction approach: Functional requirements and production management software', Automation in Construction, 132, pp. 103969. Available at: https://doi.org/10.1016/j.autcon.2021.103969

Tasker, A., Purslow, K., and Boland, C. (2022) Embodied Carbon: What it is and how to tackle it. Available at: https://www.rpsgroup.com/services/environment/sustainability-and-climate-resilience/expertise/what-is-embodied-carbon/ (Accessed: 06 February 2023).

Teng, Y. et al. (2022) 'A systematic review of the integration of building information modeling into Life Cycle Assessment', Building and Environment, 221, pp. 109260. Available at: https://doi.org/10.1016/j.buildenv.2022.109260

Tirelli, D. and Besana, D. (2023) 'Moving toward net zero carbon buildings to face Global Warming: A narrative review', Buildings, 13(3), pp. 684. Available at: https://doi.org/10.3390/buildings13030684

Tomasetti, T. (2020) Beacon – An Embodied Carbon feedback tool for Structural Engineers. Available at: https://core-studio.gitbook.io/beacon (Accessed: 29 May 2023).

Pravossoudovitch, K. et al. (2014) 'Is red the colour of danger? testing an implicit red–danger association', Ergonomics, 57(4), pp. 503-510. Available at: http://dx.doi.org/10.1080/00140139.2014.889220

Wood, E. (2022) The structural carbon tool version 2. Available at: https://www.istructe.org/resources/guidance/the-structural-carbon-tool/ (Accessed: 29 May 2023).

Xu, J. et al. (2022) 'BIM-integrated LCA to automate embodied carbon assessment of prefabricated buildings', Journal of Cleaner Production, 374, pp. 133894. Available at: https://doi.org/10.1016/j.jclepro.2022.133894

#75: Forecasting PV generation for a community energy scheme

Mitchell SEARJEANT[1], Mark GILLOTT[1], Lucelia RODRIGUES[1], Rabah BOUKHANOUF[1]

[1] University of Nottingham, University Park NG7 2RD, mitchell.searjeant@nottingham.ac.uk
[2] University of Nottingham, University Park NG7 2RD, mark.gillott@nottingham.ac.uk
[3] University of Nottingham, University Park NG7 2RD, lucelia.rodrigues@nottingham.ac.uk
[4] University of Nottingham, University Park NG7 2RD, rabah.boukhanouf@nottingham.ac.uk

Abstract: In 2022, the domestic sector accounted for 38% of UK electricity demand at 109 TWh, exhibiting a larger percentage share of electricity demand than the industrial sector. With the push towards net-zero goals, grid stress is only going to be exacerbated by the electrification of heat and EVs. Community energy schemes aim to directly address growing concerns surrounding peak grid demand stress by maximising the usage of on-site micro-generation and simultaneously decarbonising the community. In the case of utilising community PV alongside energy storage technologies, understanding site-specific future PV generation is a key challenge in implementing an energy management strategy.

This work outlines a linear regression model that relates the measured on-site global solar irradiance and community PV array generation. The model is used to generate a 5-day PV generation forecast using forecast solar irradiance data via a weather API whilst using observational data to continually retrain the model to improve specificity and accuracy. This data will then be used to optimise a community energy management system in determining the available on-site generation and how this interacts with community electricity demand loads, storage and grid imports/exports.

The model has demonstrated an average forecasting accuracy of 88% ± 9%, thus providing an effective forecast tool for on-site PV generation. Over time, the linear regression fit has changed by over 36% when compared with the initial training set fit, demonstrating a clear improvement in model performance over a 5-month period. This flexibility is an important characteristic in making the model specific to the community site and resilient to change. Further work will involve improving forecast resolution and implementing this as part of a wider community energy management system.

Keywords: Community Energy, PV, Energy Storage, Optimisation

1. INTRODUCTION

The push towards net-zero goals in the UK demands radical change in order to reach these targets. In 2022, the domestic sector accounted for 38% of electricity demand in the UK at 109 TWh, demonstrating a sizeable portion of the energy sector to address in decarbonisation (BEIS, 2022). The move towards electrification in the form of heat pumps and electric vehicles (EVs) as a means of decarbonisation will exacerbate the increase in domestic electricity demand, particularly around peak periods. This is already being seen, with the electricity sector increasing from 15% in 2000 to 19% in 2017 in the global energy consumption mix, showing the fastest growth rate in final energy consumption (IEA, 2018). Ensuring the decarbonisation of the domestic electric sector is thus a crucial part in reducing carbon emissions, particularly as electricity demand continues to increase.

Community energy presents a means of addressing the energy demands of the domestic sector (Rodrigues, 2020). This can be achieved by optimising the use of household renewable generation such as solar photovoltaics (PV) to simultaneously reduce grid reliance and the associated carbon intensity with electricity consumption. This optimisation hinges on the use of energy storage to leverage excess local renewable generation. The Trent Basin community energy demonstrator in Nottingham utilises a 2.1 MWh Tesla battery coupled with a 67 kWp roof-mounted PV array as a means of ongoing research for the application and optimisation of community energy (Shipman, 2019). Energy storage of this scale opens possibilities for additional revenue streams by facilitating the means for electricity arbitrage as well as the participation in grid services (Rodrigues, 2020). This is a crucial component in improving the financial viability of such community energy schemes while providing opportunities to enhance carbon savings.

Understanding the on-site PV generation is a fundamental component of such a community energy scheme as this informs the availability of power and energy available to the community before grid imports. In this paper, the author outlines the development of a 5-day forecast of site-specific PV generation for the Trent Basin project. The data from this forecast is crucial in understanding the interaction between the PV generation and the community demand load, storage and grid imports/exports and forming a holistic energy management strategy based on these data inputs.

2. OBJECTIVES

The primary objective of this research was to develop a PV forecasting tool specific to the 67 kWp community PV array at the Trent Basin site. A key requirement of this tool was to have minimal data inputs to reduce the need for excessive on-site monitoring equipment such that the methodology could be equally applied to other sites. With this in mind, it was necessary to employ a learning approach to improve the tool's accuracy over time while also allowing for adaptation to any potential changes in the PV array capacity resulting from fault or maintenance. The irregularity in the orientation of a roof-mounted PV array across a community inherently introduces complications regarding forecasting, heightening the need for a learning approach in the presence of minimal monitoring equipment. Finally, the tool needs to have sufficient accuracy in predicting the volume of PV energy coming into the community such that it can reliably inform the energy management strategy.

3. METHODOLOGY

The PV forecasting tool was developed using the scikit-learn package in the Python programming language (Pedregosa, 2011). A linear regression model was chosen to correlate forecast solar irradiance with on-site PV array generation as a means of forecasting 5-day-ahead PV generation for the site. This model was chosen due to its simplicity to reduce the number of data inputs and its ability to be continuously retrained with observed data over time. Forecast solar irradiance data was obtained via the Visual Crossing weather API which provided regional hourly data for solar irradiation in Wm^{-2}. This metric is expedites the need for a solar irradiance forecast model based on general weather metrics (Visual Crossing, 2023; Antonanzas, 2016). PV generation data in kW for the Trent Basin site was available via the University of Nottingham SCENe API down to a 5-minute resolution, deliberately choosing an hourly resolution to match the input for solar irradiance (Shipman, 2019). Using this approach allows for the model to develop and improve over time in the absence of any historical data sets, with the only ongoing on-site data required being the power/energy of the PV array. This is important because while historical weather data is typically readily accessible from many sources, obtaining historical forecast data is far more difficult. Thus, by employing a learning approach, this allows for present day weather forecasts to be used to retrain the model with observational PV data, circumventing the need for historical forecast data.

Initially, 2 years of on-site measured solar irradiance data via the aforementioned SCENe API was used to train the linear regression in the absence of weather forecast data as shown in Figure 1 (Shipman, 2019). However, training the model on this data inherently introduced a lack of specificity as the intention is to use forecast solar irradiance data for both predictions and further retraining of the model. As can be seen in Figure 1, there is clear erroneous data associated with discrepancies in the measurements of the on-site PV generation (kW) and solar irradiance (Wm^{-2}). Despite these pitfalls, this initial model is only intended to act as a starting point to build via the retraining with forecast solar irradiance from the Visual Crossing weather API (Visual Crossing, 2023).

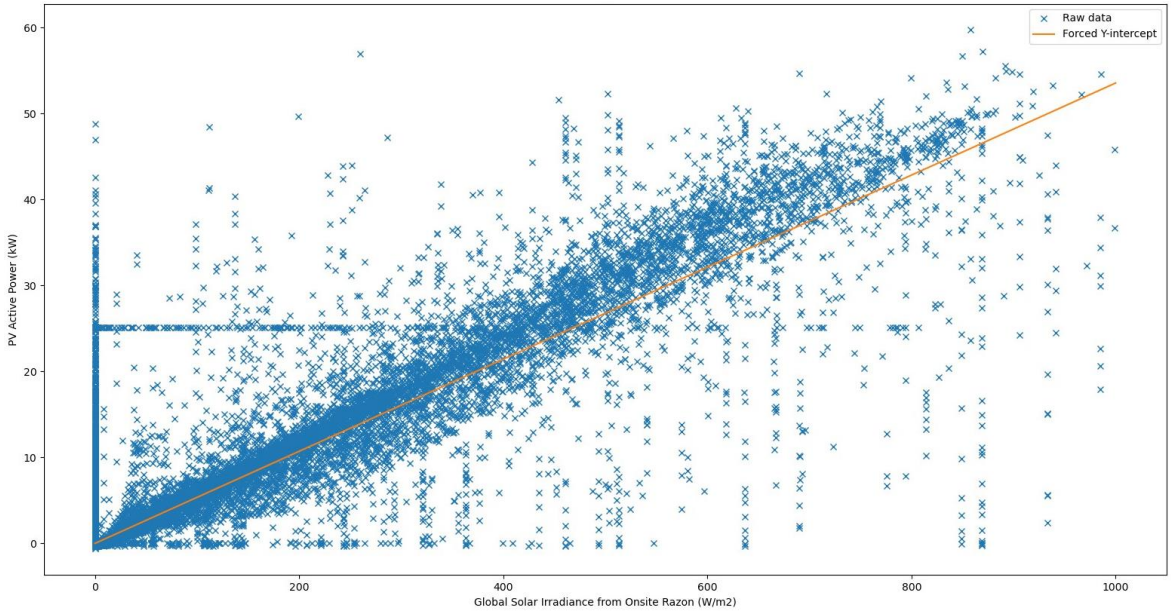

Figure 1 Plot of PV generation data against measured global solar irradiance with initial linear regression fit at the Trent Basin site in Nottingham

The initial predictions using this model are shown in Figure 2, which demonstrates clear overprediction of the PV generation, likely resulting from the non-specific training data. Figure 2 also shows an autoregression approach to forecasting PV generation that was trialled during the development of this work. This was ultimately ruled out due to it showing more drastic overprediction when compared to the linear regression. To overcome this overprediction, the model was continuously retrained with forecast solar irradiance and observed PV array generation from the site with the intention of improving model accuracy. This acts as a learning strategy for the model and fulfils the necessary objective of adapting to potential changes in the PV array capacity. Moreover, Figure 1 shows that the initial model had a forced value of 0 kW for the intercept. For ongoing retraining of the model, the intercept was changed to a free parameter to account for any potential parasitics in the on-site PV generation.

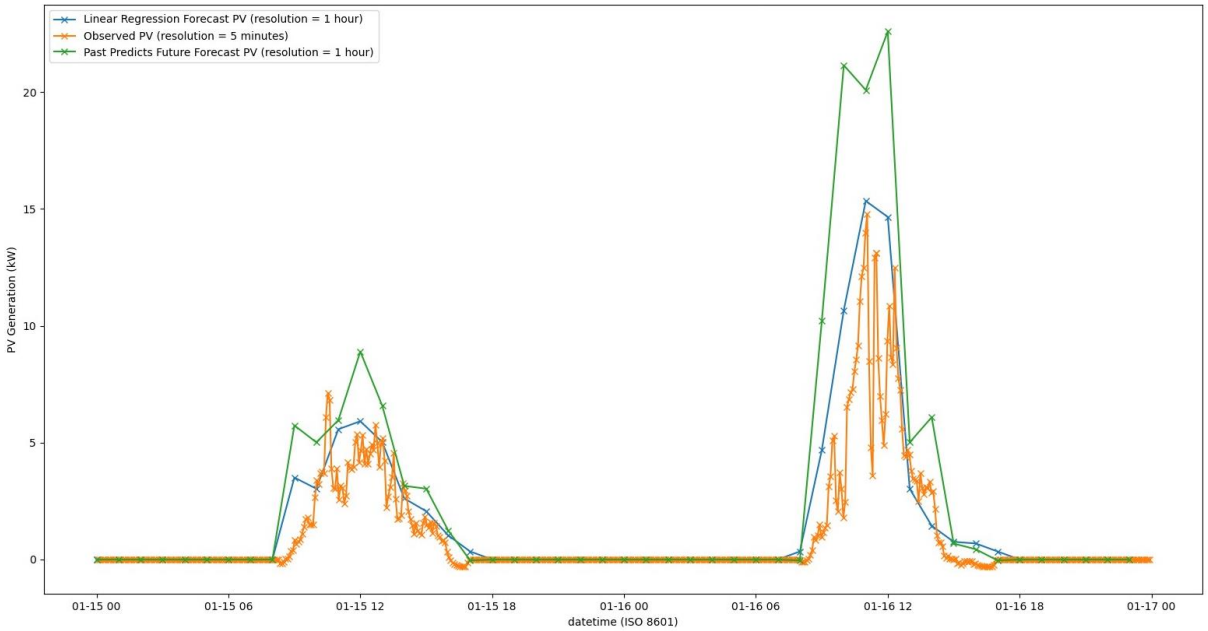

Figure 2 Initial forecast and observed PV generation at the Trent Basin site for January 2023 using linear regression and autoregression models

4. RESULTS

The model was used to generate 43 separate 5-day forecasts of PV array generation for the Trent Basin site over the course of 5 months in 2023 between March and July. Across this period, the observed data combined with the forecast solar irradiance from the Visual Crossing weather API was used to retrain the model. Figures 3 and 4 show example 5-day PV forecasts for March and April respectively. The 5-day forecast for March shown in Figure 3 demonstrated an accuracy of 85% for the total PV energy generated during the period with a mean absolute error (MAE) for power prediction of

± 2.4 kW. The 5-day forecast in April shown in Figure 4 demonstrated and accuracy of 99% for the total PV energy generated during the period with a MAE for predicted power of ± 2.7 kW.

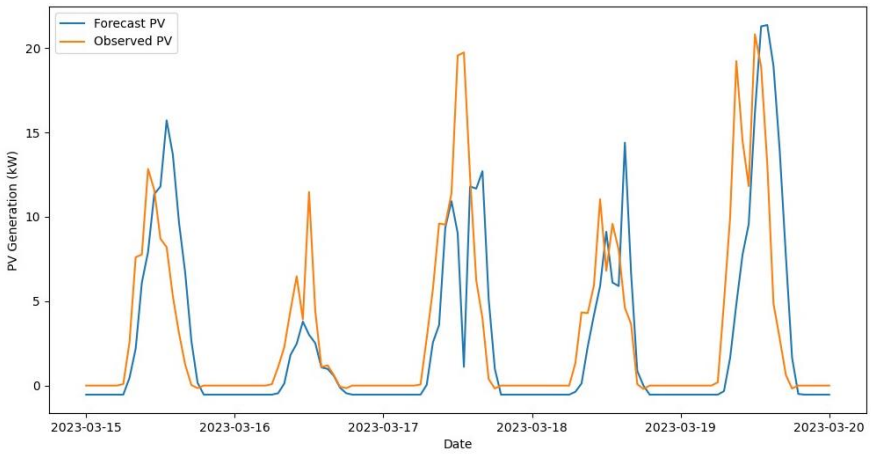

Figure 3 Forecast and observed hourly PV generation for the Trent Basin site using linear regression model for March 2023. Total energy generated during the period was forecast at 330 kWh and observed at 388 kWh

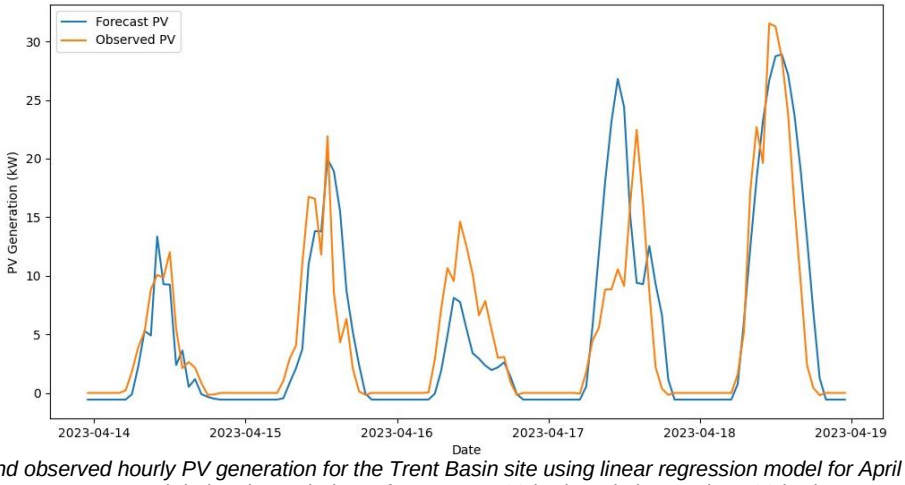

Figure 4 Forecast and observed hourly PV generation for the Trent Basin site using linear regression model for April 2023. Total energy generated during the period was forecast at 592 kWh and observed at 590 kWh

The average model accuracy for the forecast PV energy across the 43 forecasts is shown in Figure 5, broken down by both total accuracy and day of forecast. It is observed that the average accuracy declines by day-ahead of forecast with the exception of 5 days ahead. The average accuracy for generated PV energy across the entire 5-day period was observed to be 88% ± 9% overall, as is seen in Figure 5. This forecast energy accuracy is observed to be 84% ± 15% and 86% ± 12% when treated as 3 and 4 day PV forecasts respectively.

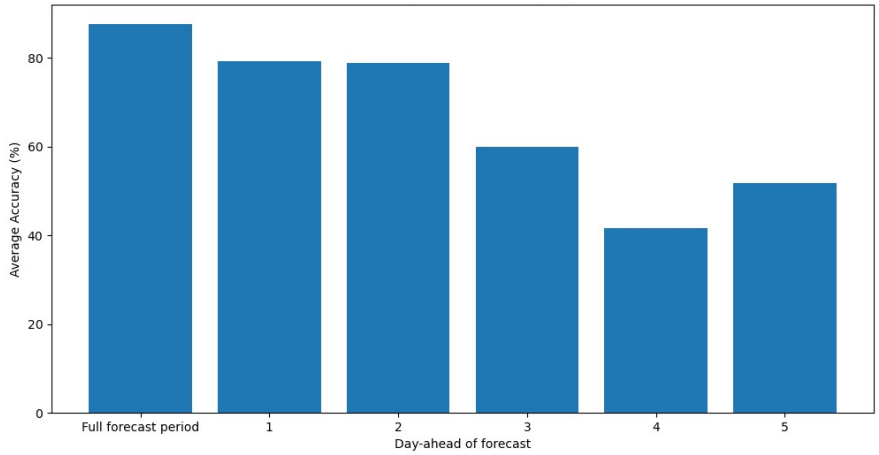

Figure 5 Average accuracy of forecast PV generation energy by day for the Trent Basin site using linear regression model between March and July of 2023

The MAE for the PV forecast power across the 43 forecasts is communicated in Figure 6, similarly broken down by both day of forecast and total forecast period. The MAE is seen to increase with the day of forecast between 1 and 5 days ahead, with the overall MAE for the 5 day period being ± 3.3 kW.

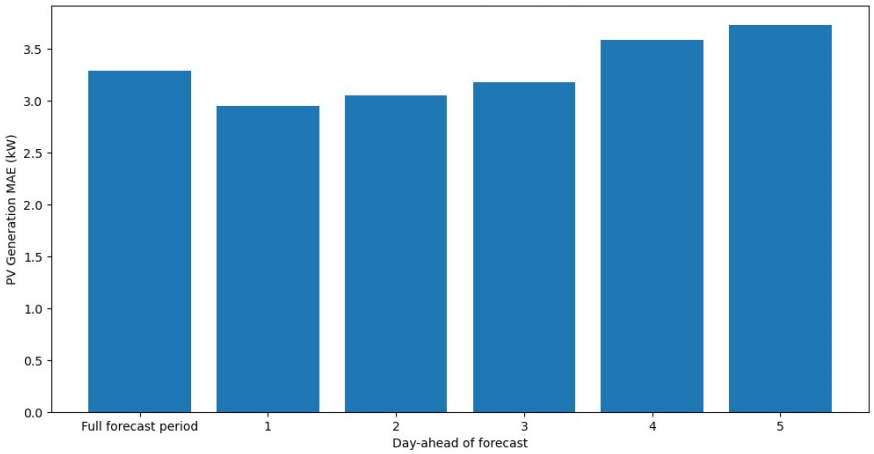

Figure 6 Mean absolute error of forecast PV generation power by day for the Trent Basin site using linear regression model between March and July of 2023.

The coefficient of fit for the linear regression model changed by 36% over the 5 month period for which the model was ran, as shown in Figure 7. This occurred via the iterative retraining of the model over the course of the 43 forecasts as the model adapted to the forecast solar irradiance data set. Moreover, this adaptation occurred in response to a phasic change in the size of the community PV array at the Trent Basin site from 67 kWp to 49 kWp between January and April of 2023, thus inherently changing the relationship between solar irradiance and the total PV array generation.

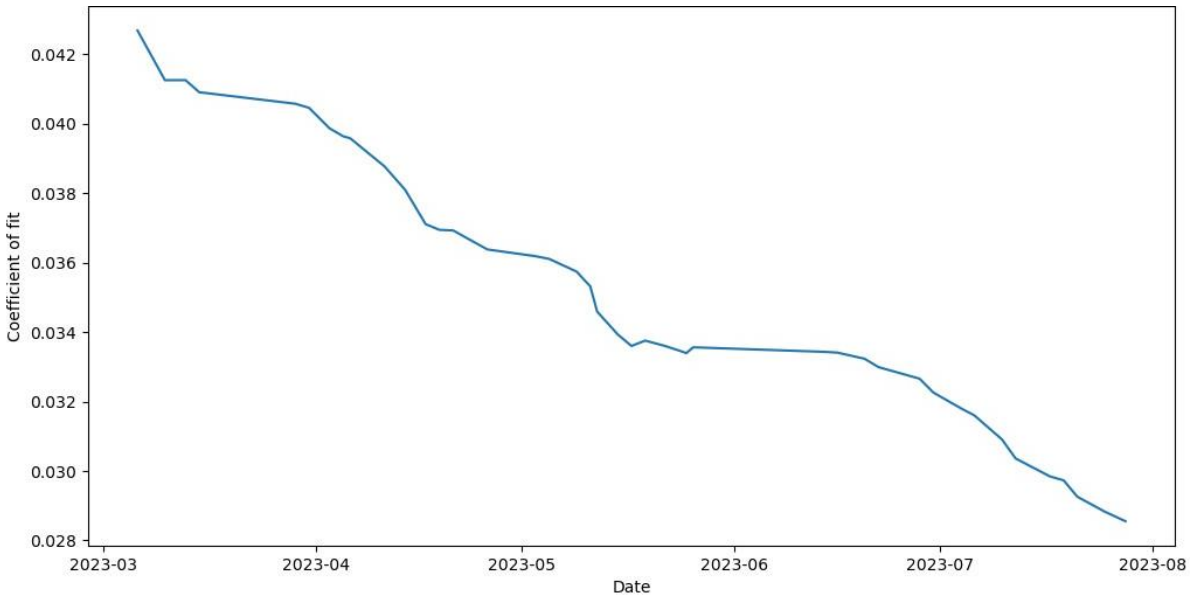

Figure 7 Coefficient of fit for linear regression model forecasting PV generation over time at the Trent Basin site between March and July of 2023.

5. DISCUSSIONS

The forecasting accuracy of 88% ± 9%, as shown in Figure 5, for generated PV energy across a 5-day forecast demonstrates a reliable method of forecasting available PV energy for the purpose of a community energy management strategy. Moreover, the accuracy of individual days in the forecast is seen to be within acceptable means. The accuracy is observed to be greater for multi-day forecasts due to the smoothing out of random error over longer total forecast periods. In practice, the 3-day forecast is more applicable to the energy management strategy due to the shorter time horizon being better matched to other variables such as energy pricing and carbon intensity. Although, this comes at the expense of lower energy forecast accuracy and variance at 84% ± 15%. The MAE for the forecast power, at ± 3.3 kW for the full 5-day forecast and ± 2.9 kW for the 1-day-ahead forecast as shown in Figure 6, is to be expected due to the greater room for error by being assessed per prediction. Having a reliable forecast for PV power is important for instantaneous management of the community energy scheme and understanding when additional imports will be required. However, for optimisation of the system on a macro-scale, accuracy of PV forecast with respect to energy is of primary interest.

Ultimately, the inaccuracies in the forecasts produced by the model are fundamentally limited by the accuracy of the weather forecasting data available via the API. Weather forecasts in the UK are generally considered to be 85% accurate for 24-hour forecasts and dropping off thereafter, although this is likely an overestimate in practice and is dependent on the forecast metric of interest (Thornes, 1996). The model presented in this work utilises forecast solar irradiance which is

intrinsically related to cloud cover, which is stochastic by nature. Therefore, the accuracies achieved here by the PV forecast model are well within expectations.

Furthermore, the change of the coefficient of fit by 36% shown in Figure 7 represents both adaptation to initial training set over-predictions as well as the aforementioned change in community PV array size. This behaviour thus expedites the need for a training set such as that shown in Figure 1 as the model exhibits capacity to adjust and become specific to the relevant PV array of interest. This, combined with robust forecast performance, makes the model a suitable fit for generating PV forecasts as a data input for a community energy management strategy.

6. CONCLUSION

In conclusion, the PV forecasting tool was successfully developed with sufficient accuracy and application for further use within a wider community energy management system at the Trent Basin project in Nottingham. The model importantly demonstrated a reliable ability to adapt through the use of forecast solar irradiance data available via the Visual Crossing weather API, making it an appropriate tool for potential use at other sites in the future (Visual Crossing, 2023).

Future work will centre around tying this PV forecasting tool in with a holistic energy management strategy and utilising this data as a means of optimising the financial viability and carbon intensity of the Trent Basin community energy scheme. Moreover, efforts will be directed towards increasing the PV forecast resolution. Improving the resolution to 30 minutes from 1 hour would be invaluable as it would have better synergy with other components of the energy management strategy such as energy demand and variable electricity price markets.

7. REFERENCES

Antonanzas, J., Osorio, N., Escobar, R., Urraca, R., Martinez-de-Pison, F.J. and Antonanzas-Torres, F., 2016. Review of photovoltaic power forecasting. *Solar energy*, *136*, pp.78-111.

IEA (2018). *World Energy Outlook 2018 – Analysis - IEA*. [online] IEA. Available at: https://www.iea.org/reports/world-energy-outlook-2018.

Pedregosa, F., Varoquaux, G., Gramfort, A., Michel, V., Thirion, B., Grisel, O., Blondel, M., Prettenhofer, P., Weiss, R., Dubourg, V. and Vanderplas, J., 2011. Scikit-learn: Machine learning in Python. *the Journal of machine Learning research*, *12*, pp.2825-2830.

Rodrigues, L., Gillott, M., Waldron, J., Cameron, L., Tubelo, R., Shipman, R., Ebbs, N. and Bradshaw-Smith, C., 2020. User engagement in community energy schemes: A case study at the Trent Basin in Nottingham, UK. *Sustainable Cities and Society*, *61*, p.102187.

Shipman, R. and Gillott, M., 2019. SCENe things: IoT-based monitoring of a community energy scheme. *Future Cities and Environment*, *5*(1).

The Department for Business, Energy and Industrial Strategy, 2022. UK Energy in Brief 2022. *The Department for Business, Energy and Industrial Strategy, UK.*

Thornes, J.E., 1996. The quality and accuracy of a sample of public and commercial weather forecasts in the UK. *Meteorological Applications*, *3*(1), pp.63-74.

Visual Crossing Corporation, 2023. Visual Crossing Weather (2022-2023). Available at https://www.visualcrossing.com/

#83: Feasibility study of machine learning in solar energy storage systems optimisation

Yanan ZHANG[1], Ziwei CHEN[2], Yong ZHANG[3], Cagri KUTLU[4], Yuehong SU[5], Saffa RIFFAT[6], Xiao LI[7]

[1] University of Nottingham, Nottingham, NG7 2RD, UK, yanan.zhang1@nottingham.ac.uk
[2] University of Nottingham, Nottingham, NG7 2RD, UK, ziwei.chen@nottingham.ac.uk
[3] University of Nottingham, Nottingham, NG7 2RD, UK, ezxyz9@nottingham.ac.uk
[4] University of Nottingham, Nottingham, NG7 2RD, UK, cagri.kutlu2@nottingham.ac.uk
[5] University of Nottingham, Nottingham, NG7 2RD, UK, yuehong.su@nottingham.ac.uk
[6] University of Nottingham, Nottingham, NG7 2RD, UK, saffa.riffat@nottingham.ac.uk
[7] University of Aberdeen, Aberdeen, AB24 3FX, UK, xiao.li@abdn.ac.uk

Abstract: The rapid expansion of renewable energy sources such as solar and wind power is crucial to meet the increasing global demand for clean and sustainable power generation. However, the inherent intermittency and volatility of these energy sources bring forth challenges in maintaining the operation and stability of energy systems. Efficiently storing surplus energy during periods of peak generation and releasing it during peak demand is vital for ensuring a stable and reliable energy supply. While traditional methods of forecasting and optimizing renewable energy systems have their merits, they often fall short when it comes to handling the complexity and uncertainty of renewable energy generation and utilization processes. Machine learning techniques emerge as a potent solution, enabling the development of accurate predictive models and optimization strategies derived from extensive historical data analysis. This study focuses on applying machine learning to optimize solar and renewable energy systems, aiming to boost power generation, enhance grid stability, and ensure seamless integration with conventional power sources.

In our comprehensive review of recent research utilizing learning-based methods in the renewable energy domain, we pay special attention to deep learning and machine learning algorithms. We conducted a feasibility study to evaluate the effectiveness of machine learning techniques in tackling the challenges associated with solar and renewable energy system optimisation and energy storage. Our findings indicate that hybrid learning techniques, which integrate machine learning and deep learning with other optimization methods, show great promise in enhancing the development and optimization of these systems. We propose that future endeavours in solving energy production challenges adopt blended learning techniques, leveraging the strengths of multiple approaches to achieve more accurate predictions and efficient energy utilisation.

Keywords: energy storage, grid connection, smart control, artificial-intelligence, deep learning

1. INTRODUCTION

The global energy panorama is undergoing a significant shift, motivated by the urgent need to progress towards a more sustainable and eco-friendly mode of energy production. Traditional energy sources, such as fossil fuels and nuclear energy, have primarily fuelled our energy systems for decades, contributing substantially to environmental harm and climate alterations. As a reaction to the urgent call for cleaner and renewable substitutes, an extraordinary increase in the adoption of renewable energy technologies, particularly solar and wind energy, has been observed (Best and Burke, 2018) (Kumar et al., 2016) . Renewable energy technologies, predominantly solar and wind energy, have seen a significant worldwide expansion due to the growing demand for cleaner and more sustainable energy production (Hussain et al., 2017). The shift towards renewables is influenced by their potential to address key issues including improving energy security, reducing greenhouse gas emissions, and enhancing air quality (Abolhosseini et al., 2014). Various sectors - governments, industries, academia, and private corporations - appreciate the tremendous potential of these modern energy technologies, stimulating the research and deployment of renewable energy systems (Majid, 2020).

Within the renewable energy system, solar and wind methodologies have gained substantial interest as practical replacements for conventional nuclear and fossil fuel energy systems, in light of escalating environmental concerns (Lund, 2014). The appeal of solar and wind renewable systems resides in their environmental benefits, diminished carbon emissions, cost-effectiveness, energy source diversification, and potential for energy autonomy (Bagherian and Mehranzamir, 2020). However, the efficient exploitation of renewable energy brings about multifaceted challenges. As solar and wind energy become prominent figures in the renewable energy arena, emphasis on optimizing their use becomes essential. Nonetheless, the sporadic and variable nature of these energy sources presents unique obstacles for their incorporation into existing energy systems. A paramount challenge is the effective storage of energy, which is vital for containing excess energy generated during peak times and dispensing it during periods of high demand, thereby ensuring a stable and reliable energy supply (Semadeni, 2003). The inherent unpredictability and intermittence of renewable energy sources create hurdles for precise forecasting, prompting the need for efficient energy storage solutions (Gawusu et al., 2022). Addressing issues of power quality, resource location, cost, and availability is vital to fully exploit the potential of renewable energy systems (Oyekale et al., 2020).

Against this backdrop, this paper focuses on the viability of employing machine learning strategies to optimise solar energy and renewable energy systems equipped with energy storage. Through leveraging machine learning capabilities, this study endeavours to navigate the complexities and uncertainties inherent to renewable energy generation and usage. Machine learning paves the way for the creation of accurate predictive models and optimisation strategies derived from patterns and trends distilled from voluminous historical data (Adi et al., 2020). A thorough review of recent research utilising machine learning and deep learning technologies in renewable energy storage systems is provided, with particular attention given to applications in solar energy. The intention is to highlight key concepts that have fascinated researchers and consolidate their significant contributions for the benefit of future readers. The selected studies are grouped into two principal categories: solar energy systems that employ machine learning and deep learning techniques. In addition, critical advancements in this field are discussed, and potential research directions are proposed to guide further inquiries.

This exploration of the feasibility of machine learning in the optimisation of solar energy and renewable energy systems with energy storage contributes crucial insights towards enhancing the incorporation of clean and sustainable energy sources into global energy systems. The deployment of machine learning methods promises improvements in renewable energy production, grid stability, and overall energy efficiency, laying the groundwork for a more sustainable and resilient energy future.

2. CHALLENGES IN SOLAR ENERGY STORAGE SYSTEMS

Solar energy storage systems face multiple challenges in their deployment and operation. This section addresses these obstacles, including the intermittency of solar energy, the limitations of current energy storage techniques, and the challenges associated with forecasting and optimization.

2.1. Intermittency of Solar Energy

Solar energy generation is inherently variable, influenced significantly by several environmental factors. This variability is principally due to the sun's irradiance, which fluctuates throughout the day and is affected by weather patterns and seasonal shifts (Engeland et al., 2017). For instance, solar energy production can dramatically decrease during night-time hours, or under cloudy or rainy weather conditions, leading to imbalances between energy supply and demand. This unpredictability and intermittency pose challenges to the reliability and stability of solar energy systems. Historically, these fluctuations were mitigated by operating on an immediate supply-consumption model, in which energy was generated and instantly supplied to consumers (Strielkowski, 2019). This model, however, presents difficulties when integrating solar energy into existing energy systems, as sudden peaks and troughs in output could lead to power disruptions.

With solar energy increasingly contributing to the global energy mix, forecasting fluctuations in total energy supply has become more complex (Hong et al., 2016). The intermittent nature of solar power, characterized by variations in sun exposure due to weather changes, seasonal shifts, and the contrast between day and night, presents considerable challenges to consistent energy generation (Yin et al., 2020). As solar energy continues its upward trajectory, the scale of this fluctuation becomes increasingly critical, leading to potential threats to the stability of energy systems. The shift towards solar energy also brings about the complexity of managing decentralized, small-capacity energy units. Solar photovoltaic (PV) systems, ranging from large-scale solar farms to residential rooftop installations, are often spread across various locations. This decentralization adds another layer of complexity to managing and optimizing the integration of solar energy into existing energy systems.

Energy storage plays an integral role in addressing the intermittent nature of solar energy, promoting a more balanced and stable energy supply (Dunn et al., 2011). It introduces a time dimension to energy supply, uncoupling the direct relationship between energy generation and consumption, a concept that resonates strongly within the realm of solar energy. As illustrated in Figure 1, energy storage mechanisms become exceedingly important during periods of abundant solar generation, where the energy produced exceeds immediate grid demand. These instances provide an opportunity to capture excess solar energy, storing it for later usage. This ability to bank solar energy for future use is particularly beneficial during times when solar generation is not possible or is reduced, such as at night or during overcast weather conditions.

Energy storage acts as a buffer, enabling energy providers to optimize their production cycles in accordance with the cost of generation. It allows for the strategic production of electricity, specifically during periods when generation costs are at their lowest. In the context of solar energy, this signifies that storage systems can accumulate and conserve energy when solar irradiance is high, reducing the need for solar energy generation during less optimal periods. In essence, energy storage systems serve as a vital component in solar energy systems, providing a solution to the inherent intermittency issue by allowing efficient storage of surplus energy during peak solar production for later use when solar generation is low or absent.

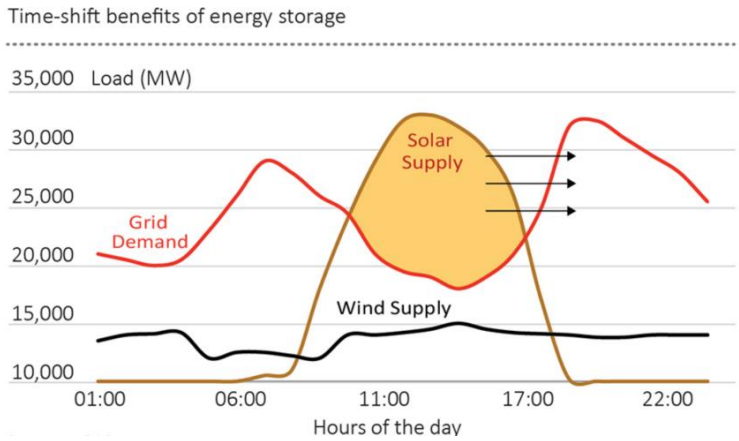

Figure 1 The benefit of energy storage of saving excess energy for later use.

2.2. Energy Storage Techniques: Limitations and Challenges

Effective energy storage systems are essential in mitigating the intermittency issues intrinsic to solar energy. The dominant storage methods for solar energy consist of battery storage technologies (particularly lithium-ion batteries), thermal storage, and pumped hydro storage. Despite their importance, each of these storage techniques contends with a unique set of challenges.

Battery Storage Technologies: The use of battery storage, specifically lithium-ion batteries, has increased significantly due to their high energy density and declining costs, which have seen approximately an 85% reduction over the past decade (Li et al., 2017). Notwithstanding their benefits, these technologies are associated with certain constraints. For instance, lithium-ion batteries undergo degradation over time, with a loss of approximately 20% of their storage capacity following 1000 charge cycles. The limited life cycle, typically spanning 5-15 years depending on use and maintenance, necessitates regular replacements, adding to the long-term expenditure (Liu et al., 2022). Furthermore, the disposal of exhausted batteries raises environmental concerns due to the hazardous materials involved, while the current recycling rates hover at a meagre 5% (Roy and Ragunath, 2018).

Thermal Storage Systems: These systems, capable of storing surplus solar energy as heat for subsequent usage, are also subject to certain limitations. They require substantial space and significant insulation to avoid energy loss. To illustrate, a molten salt thermal storage system deployed in a concentrated solar power plant could necessitate tanks measuring up to 30 meters in diameter and 14 meters in height (Khan et al., 2022). The large scale of these storage systems often restricts their implementation in densely populated or geographically constrained areas.

Pumped Hydro Storage Systems: Pumped hydro storage systems store energy as the gravitational potential energy of water, boasting high energy storage potential and the ability to supply power over lengthy periods. However, they incur high initial costs, typically over $1,000 per installed kilowatt, and their deployment is restricted to locales with suitable topography and water sources (Botterud et al., 2014).

The economic and technical complexities linked with storing surplus solar energy during periods of low production amplify the difficulties in the energy storage landscape. Storing excess solar energy calls for considerable investment in storage capacity. Efficiently managing this storage while minimizing losses demands intricate control systems. For example, the expense of storing electricity in lithium-ion batteries can range from $187 to $298 per MWh, contributing to escalated overall energy costs (Al-Alawi and Bradley, 2013). While these energy storage techniques are crucial in countering the intermittent nature of solar energy, they pose several limitations and challenges that need to be addressed. Understanding these challenges is of paramount importance when investigating the feasibility of machine learning in optimizing solar renewable energy storage systems. In the forthcoming sections, this study delves into how machine learning techniques could potentially address these constraints and enhance the efficiency of solar energy systems.

2.3. Forecasting and Optimisation Challenges in Solar Energy Storage Systems

The effective operation of solar energy storage systems relies heavily on the accurate forecasting of solar power generation and energy demand. This, however, presents a significant challenge due to the inherent variability of solar energy production and the complexities associated with energy demand patterns. Forecasting models for solar energy production traditionally draw from historical irradiance data and weather forecasts (Law et al., 2014). However, such methods may not fully account for sudden, unforeseen changes in weather conditions, such as unexpected cloud cover or atmospheric particulate levels, which can drastically affect solar power output. For instance, errors in irradiance forecast models can range up to 30%, contributing to inaccurate solar power predictions (Kostylev and Pavlovski, 2011).

Energy demand forecasting, too, comes with its own set of complications. Predicting energy usage patterns involves considering a plethora of factors including seasonal trends, daily routines, economic activities, and even sudden events such as heatwaves or power outages (Board et al., 2016). Models built on historical demand data might fail to adapt quickly to these abrupt changes, causing discrepancies between the forecasted and actual demand. This inaccuracy can lead to either an excess of stored energy that could potentially be wasted or a shortage that fails to meet the energy demand (Larcher and Tarascon, 2015).

Optimizing the operation of solar energy storage systems also introduces an additional layer of complexity. It necessitates a delicate balance between storing energy for future use, particularly during non-generating periods, and using or selling the energy immediately to meet current demand or take advantage of favourable market prices (Fikru et al., 2018). These decisions are influenced by a multitude of ever-changing factors, including the present and future states of the energy market, the current capacity of the storage system, and the forecasted weather conditions. Such a multifaceted decision-making process, coupled with the uncertainties associated with these factors, makes the task of optimization significantly challenging for solar energy storage systems. These issues underline the necessity for more sophisticated techniques, such as machine learning, to improve the precision of solar power and demand forecasts and to effectively manage the operation of solar energy storage systems (Alkabbani et al., 2021).

The challenges related to the intermittency of solar energy, limitations and drawbacks of storage techniques, and complexities in forecasting and optimization, signify the need for sophisticated tools and strategies to enhance the efficiency and reliability of solar energy storage systems. Machine learning, with its ability to learn from data and make predictions, presents promising approach to tackle these issues, as will be discussed in the subsequent sections of this paper.

3. APPLICATION OF MACHINE LEARNING IN SOLAR ENERGY STORAGE SYSTEMS

Machine Learning (ML) has increasingly been applied to various facets of Solar Energy Storage Systems (SESS), revealing its immense potential to revolutionize this sector (Senthil Kumar et al., 2022). At the heart of SESS is the effective utilization and management of solar energy, a resource that is inherently variable due to environmental and weather conditions. ML algorithms, through their learning and predictive capabilities, can be used to forecast solar irradiance with greater accuracy (Ağbulut et al., 2021). These forecasts can, in turn, be used to optimize energy storage and release schedules, ensuring the most efficient use of stored solar energy and minimizing waste. ML also plays a pivotal role in predictive maintenance within SESS. Sophisticated ML algorithms can identify irregularities and anticipate faults in solar panels or in the energy production process. This early detection allows for proactive maintenance, reducing downtime and overall system costs (Afridi et al., 2022, Çınar et al., 2020). Moreover, ML can assist in managing the integration of SESS with other energy systems, such as the power grid (Carrasco et al., 2006). Machine learning algorithms can be used to model and predict the behaviour of these complex, interconnected systems, leading to improved grid stability and reliability.

Machine learning has found a myriad of applications within the sphere of solar energy, significantly enhancing forecasting accuracy, fault detection, and energy storage optimization, thereby improving the efficiency and reliability of solar energy

systems (Mai et al., 2022). As technology and research continue to progress, the role of ML in SESS will likely become even more central and impactful.

3.1. Enhancing Solar Irradiance Forecasting with Machine Learning

Machine learning models possess the enhanced capability to surpass conventional methods in accurately predicting solar irradiance. This predictive prowess plays a crucial role in the efficient management of energy loads. It aids in minimizing reliance on cost-intensive and pollutant-emitting peak power plants, while also optimizing the utilization of energy storage systems. Forecasting stands out as a crucial machine-learning application within solar energy. Using historical data and weather forecasts, machine learning models can accurately predict future solar energy production (Sharma et al., 2011) (Anuradha et al., 2021). Yu et al. (Yu et al., 2019) used LSTM to forecast one-hour-ahead solar irradiance in Atlanta, New York, and Hawaii, considering inputs like clear sky index, relative humidity, cloud type, and others. They utilized 2013-2017 data from NSRDB and reported an RMSE between 45.84 W/m^2 and 41.37 W/m^2 for these locations. Qing and Niu (Qing and Niu, 2018) utilized LSTM to predict the next day's hourly solar irradiance using parameters like month, hour, day of the month, and others. They trained their model on 2.5 years of data (March 2011-August 2012, January 2013-December 2013) from a Santiago, Cape Verde solar plant. Their model showed superior accuracy with an RMSE of 76.245 W/m^2 and excellent agreement between actual and predicted solar irradiance, as indicated by Figure 3. In 2019, Mishra and Palanisamy (Mishra and Palanisamy, 2019) created an LSTM model to predict solar irradiance for various forecast periods, demonstrating a 71.5% improvement over conventional machine learning models. In 2020, Jeon and Kim (Jeon and Kim, 2020) employed LSTM to predict next-day hourly solar irradiance, using inputs like temperature, humidity, sky cover, wind speed, and precipitation from the Korea Meteorological Administration. The model demonstrated substantial accuracy, with an RMSE of 30 W/m^2 , using data from various locations within the target region. Justin and his team introduced a variant of LSTM, the stacked LSTM integrated with PCA, for solar irradiance prediction (de Guia et al., 2020). The model, with R^2 value of 0.953 and MAE value 41.738 W/m^2, displayed better accuracy compared to other deep learning models like CNN and Bidirectional-LSTM.

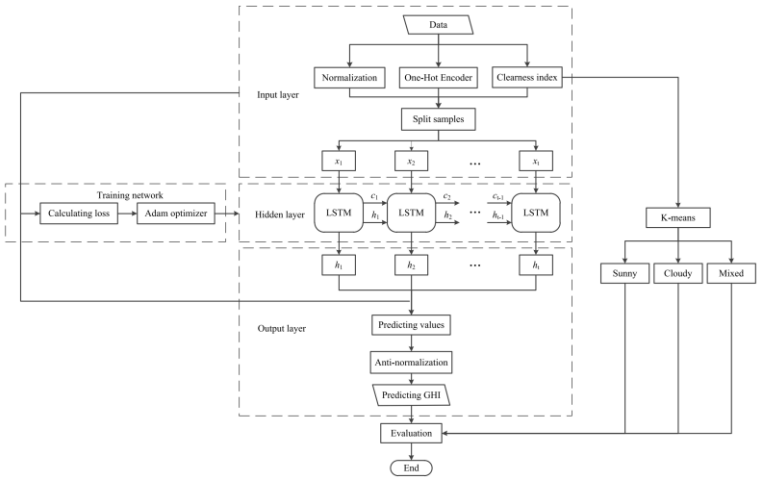

Figure 2 LSTM-based GHI prediction framework. (Yu et al., 2019)

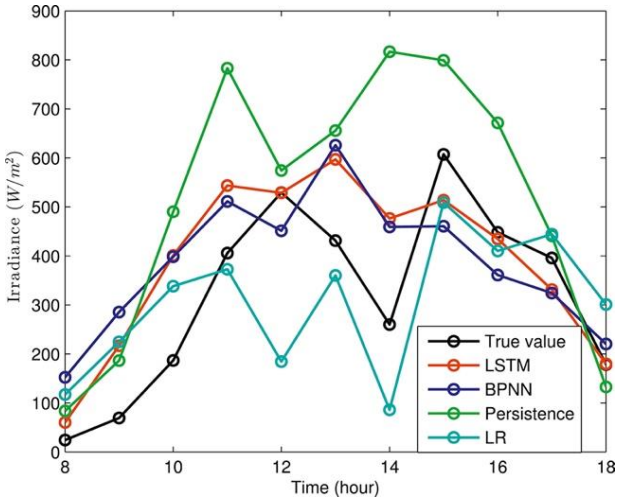

Figure 3 A comparison of actual irradiance and predicted irradiance. (Qing and Niu, 2018)

3.2. Machine Learning in Predictive Maintenance for SESS

When it comes to identifying errors within solar energy systems, machine learning takes on a crucial role. Sophisticated algorithms have the ability to detect irregularities and forecast malfunctions in solar panels or the energy generation process. The research conducted by Wang et al. introduces a novel concept of an Integrated Energy System using Machine Learning technology (IES-ML) (Wang et al., 2021). This approach carries significant practical and strategic implications for the development of energy systems. Key components in the fault detection of regional heating systems are the Regional Internet Research (RIR) and Development In Energy (DIE). The IES-ML, when compared to traditional power delivery systems, bolsters economic efficiency and authenticates the protection, reliability, stability, and strength of multi-energy coupling. RIR and AIE are deployed to substantially reduce the environmental demand from the district heating energy system. With an impressive accuracy of 98.67%, the IES-ML demonstrates exceptional performance in fault detection and control within the Integrated Energy System. Memon et al. introduce a smart model designed to identify faults in photovoltaic (PV) panels (Memon et al., 2022). Their proposed model employs a Convolutional Neural Network (CNN), trained using historical data. This data set, which included various parameters like current, voltage, temperature, and irradiance across five distinct classes, underwent preprocessing prior to being input into the CNN. Simulation results demonstrated that the proposed CNN model reached a training accuracy of 97.64% and a testing accuracy of 95.20%, significantly surpassing the performance of previous studies conducted using this dataset.

Another study introduces an SVM-based fault diagnosis algorithm for photovoltaic (PV) arrays, leveraging the hot-decking method to mend missing fault data (Wang et al., 2023). This leads to an average error rate of 1.45% between real and repaired values and a reduction in mixing ratios of fault data to below 4.55% through normalization. Parameter optimization for the algorithm employs grid search and k-fold cross-validation, enhancing accuracy and generalization. The algorithm, independent of extra equipment, doesn't escalate diagnosis costs and can detect real-time PV array faults using historical data. The trained and test accuracy rates are 98.72% and 97% respectively, outperforming the BP neural network-based algorithm.

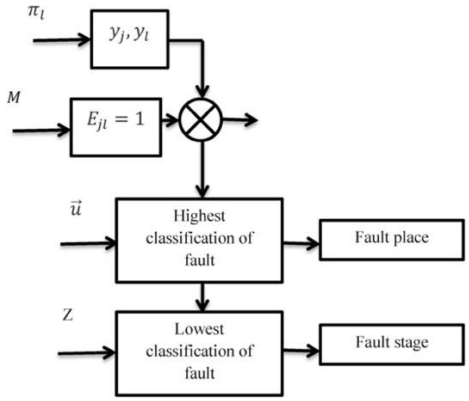

Figure 4 Fault detection in the energy system. (Wang et al., 2021)

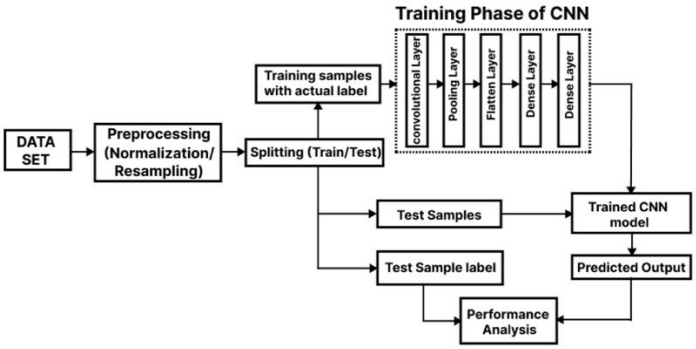

Figure 5 The system architecture for fault diagnosis. (Memon et al., 2022)

Machine learning has emerged as a vital tool in the domain of solar energy systems, particularly in identifying system errors and irregularities. This assertion is supported by a multitude of studies that showcase the practical application and effectiveness of machine learning in this context. These studies indicate not only the capability of machine learning algorithms to accurately predict and diagnose faults but also their potential to improve overall system efficiency. As such, the incorporation of machine learning in solar energy systems research is not only plausible but also holds significant promise for future advancements in the field.

3.3. Application of machine learning in energy efficiency management of solar energy storage systems

The innovative application of optimization techniques in solar energy storage and management has significantly enhanced the performance and efficiency of various energy systems, as evidenced by numerous studies across different settings and scenarios. Kneiske et al. (Kneiske and Braun, 2017) developed a robust optimization method for thermoelectric storage systems, ensuring optimal performance even when faced with inaccurate weather and load forecasts, setting it apart from conventional control methods. Their approach highlights the vital role of integrated thermal and electrical storage systems in maintaining system flexibility and efficiency. Wang et al. (Wang et al., 2019) and Ren et al. (Ren et al., 2010) explored integrated power systems, utilizing a diverse range of energy sources and optimization algorithms to improve operational efficiency. Berardi et al. (Berardi et al., 2020) focused on achieving efficient fuel use and minimizing logistics in a system that integrates renewable energy, storage, and waste heat recovery. Luo et al. (Luo et al., 2018) proposed a dual-level optimization strategy for a desalination system and an independent CCHP system located on a remote island. Jing et al. (Jing et al., 2012) provided a life-cycle perspective assessment of a photovoltaic-based distributed system, while Weeratunge et al. (Weeratunge et al., 2018) aimed for maximum efficiency in ground source heat pump systems utilizing solar and geothermal energy. Zhou et al. (Zhou et al., 2013) introduced a two-level stochastic programming model to aid in developing a more efficient distributed energy system for a hotel (see Figure 6). The approach systematically handles demand and supply uncertainties, providing enhanced efficiency and detailed results when compared to deterministic models.

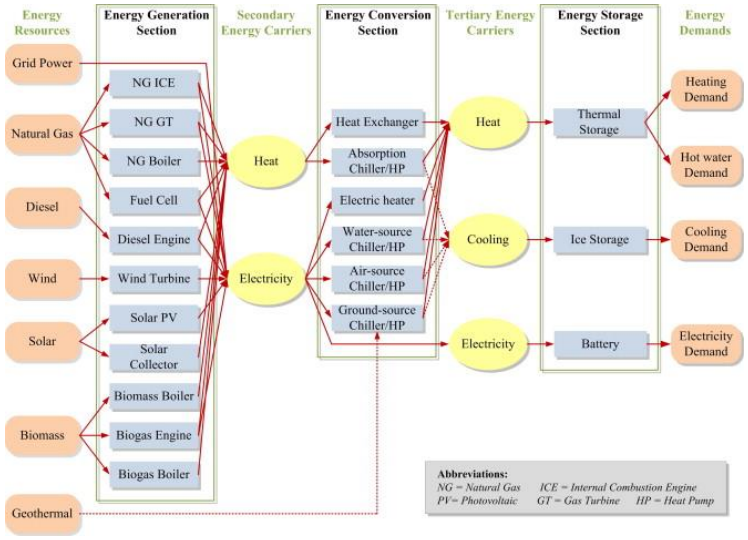

Figure 6 The superstructure representation of a distributed energy system. (Zhou et al., 2013)

Ren et al. (Ren and Gao, 2010) and Luo et al. (Luo et al., 2019) crafted optimization models for distributed energy systems and a multigenerational energy setup on a distant island, highlighting the importance of societal costs over individual expenses. These studies collectively highlight the transformative impact of optimization and machine learning in improving solar energy storage and distribution, leading to more sustainable and efficient energy solutions. These techniques enhance system performance, ensure optimal use of solar energy, and increase reliability by proactively predicting and addressing potential issues. The efficiency of energy storage and distribution is significantly improved, contributing to a steady and reliable energy supply. In sustainable development, these advancements play a crucial role in reducing reliance on fossil fuels and facilitating the transition towards a cleaner, greener energy future, marking a significant step forward in addressing the challenges of energy security and climate change.

4. FUTURE DIRECTIONS AND RESEARCH OPPORTUNITIES

Building upon the existing advancements in solar energy storage systems, there is an exciting avenue of opportunities for integrating machine learning to further optimize their performance and efficiency. Beyond the realm of solar energy, machine learning has demonstrated its versatility and effectiveness in a plethora of domains, including HVAC systems management in medical facilities, showcasing the extensive potential of these technologies. A remarkable stride has been made in the domain of predictive maintenance, especially pertaining to HVAC systems, where machine learning algorithms play a pivotal role. A noteworthy example is the data-driven predictive maintenance framework introduced by Cheng et al. which utilizes machine learning to forecast the future conditions of chillers within HVAC systems (Cheng et al., 2020). This innovative framework, drawing upon data from various sources including Building Information Modelling (BIM), Facility Management (FM) systems, and Internet of Things (IoT) technologies, opens up new possibilities for long-term forecasting. Building upon this, a promising avenue for future research lies in expanding the applicability of this framework to

encompass a broader spectrum of HVAC systems. This includes delving into machine learning algorithms capable of making both short-term and long-term predictions about the system's conditions. Such advancements could play a crucial role in enhancing the efficiency and reliability of these systems.

Another pivotal area of research is the integration of Building Management System (BMS) sensor data with Computerized Maintenance Management System (CMMS) databases, particularly for predictive maintenance in hospital HVAC systems. This is of paramount importance in components such as Air Handling Units (AHUs), where the implementation of machine learning models holds the potential to not only reduce maintenance costs significantly but also improve system efficiency and uphold indoor air quality (IAQ) standards. Drawing parallels with solar energy storage systems, these insights and research directions underscore the potential of machine learning in transforming the landscape of energy storage and optimization. Future research endeavours in this domain could lead to groundbreaking innovations, ensuring that solar energy storage systems operate at peak efficiency, adapt seamlessly to changing conditions, and contribute to the broader goal of sustainable and resilient energy networks.

5. CONCLUSION

In this paper, we have extensively explored the global shift towards sustainable and eco-friendly energy solutions, emphasizing the swift adoption of solar and wind technologies in response to the pressing demand for sustainable energy alternatives. The paper highlighted the potential of machine learning strategies in optimizing solar and renewable energy systems, along with their integration with energy storage solutions, addressing the challenges posed by their inherent unpredictability and variability. We have provided a thorough review of recent advancements in machine learning and deep learning technologies in this field, categorizing existing studies, and discussing critical developments. Drawing from the content of the paper, we can conclude the following:

1) Rapid Development and Integration of Solar and Renewable Energy: The global transition towards sustainable and eco-friendly energy solutions is well underway, with solar and wind technologies being rapidly adopted. This not only contributes to enhanced energy security, reduced emissions, and improved air quality but also underscores the urgency of addressing the intermittency and variability associated with these renewable energy sources.
2) Challenges in Solar Energy Storage Systems: Despite their potential benefits, solar and renewable energy systems pose significant challenges, particularly in terms of energy storage and integration into existing energy infrastructures. These challenges are multifaceted, stemming from the intermittent nature of solar energy production, limitations of current energy storage technologies, and the complexities involved in forecasting and optimization.
3) Application of Machine Learning in Optimizing Solar Energy Storage Systems: Machine learning strategies offer a viable solution to optimize the operation of solar and renewable energy systems, addressing challenges arising from their unpredictability and variability. Machine learning enables more accurate solar irradiance forecasting, fault detection and predictive maintenance in solar energy systems, as well as improved energy management in solar energy storage systems.
4) Future Research Directions: The paper proposes future research directions, aiming to improve the efficiency, reliability, and sustainability of global energy systems through the integration of renewable energy and advanced machine learning techniques.

The application of machine learning in solar energy storage systems has shown immense potential in enhancing system efficiency and reliability. As technology and research continue to advance, machine learning is poised to play a more central and impactful role in optimizing solar and renewable energy systems. These advancements are crucial in facilitating the transition towards a cleaner, greener energy future and mark significant strides in addressing the challenges of energy security and climate change.

6. REFERENCES

Abolhosseini, S., Heshmati, A. & Altmann, J. 2014. A review of renewable energy supply and energy efficiency technologies.

Adi, E., Anwar, A., Baig, Z. & Zeadally, S. 2020. Machine learning and data analytics for the IoT. *Neural computing and applications,* 32**,** 16205-16233.

Afridi, Y. S., Ahmad, K. & Hassan, L. 2022. Artificial intelligence based prognostic maintenance of renewable energy systems: A review of techniques, challenges, and future research directions. *International Journal of Energy Research,* 46**,** 21619-21642.

Ağbulut, Ü., Gürel, A. E. & Biçen, Y. 2021. Prediction of daily global solar radiation using different machine learning algorithms: Evaluation and comparison. *Renewable and Sustainable Energy Reviews,* 135**,** 110114.

Al-Alawi, B. M. & Bradley, T. H. 2013. Total cost of ownership, payback, and consumer preference modeling of plug-in hybrid electric vehicles. *Applied Energy,* 103**,** 488-506.

Alkabbani, H., Ahmadian, A., Zhu, Q. & Elkamel, A. 2021. Machine learning and metaheuristic methods for renewable power forecasting: a recent review. *Frontiers in Chemical Engineering,* 3**,** 665415.

Anuradha, K., Erlapally, D., Karuna, G., Srilakshmi, V. & Adilakshmi, K. Analysis of solar power generation forecasting using machine learning techniques. E3S Web of Conferences, 2021. EDP Sciences, 01163.

Bagherian, M. A. & Mehranzamir, K. 2020. A comprehensive review on renewable energy integration for combined heat and power production. *Energy Conversion and Management,* 224**,** 113454.

Berardi, U., Tomassoni, E. & Khaled, K. 2020. A smart hybrid energy system grid for energy efficiency in remote areas for the army. *Energies,* 13**,** 2279.

Best, R. & Burke, P. J. 2018. Adoption of solar and wind energy: The roles of carbon pricing and aggregate policy support. *Energy Policy,* 118**,** 404-417.

Board, O. S., National Academies Of Sciences, E. & Medicine 2016. *Next generation earth system prediction: strategies for subseasonal to seasonal forecasts*, National Academies Press.

Botterud, A., Levin, T. & Koritarov, V. 2014. Pumped storage hydropower: benefits for grid reliability and integration of variable renewable energy. Argonne National Lab.(ANL), Argonne, IL (United States).

Carrasco, J. M., Franquelo, L. G., Bialasiewicz, J. T., Galván, E., Portilloguisado, R. C., Prats, M. M., León, J. I. & Moreno-Alfonso, N. 2006. Power-electronic systems for the grid integration of renewable energy sources: A survey. *IEEE Transactions on industrial electronics,* 53**,** 1002-1016.

Cheng, J. C., Chen, W., Chen, K. & Wang, Q. 2020. Data-driven predictive maintenance planning framework for MEP components based on BIM and IoT using machine learning algorithms. *Automation in Construction,* 112**,** 103087.

Çinar, Z. M., Abdussalam Nuhu, A., Zeeshan, Q., Korhan, O., Asmael, M. & Safaei, B. 2020. Machine learning in predictive maintenance towards sustainable smart manufacturing in industry 4.0. *Sustainability,* 12**,** 8211.

De Guia, J. D., Concepcion, R. S., Calinao, H. A., Alejandrino, J., Dadios, E. P. & Sybingco, E. Using stacked long short term memory with principal component analysis for short term prediction of solar irradiance based on weather patterns. 2020 IEEE REGION 10 CONFERENCE (TENCON), 2020. IEEE, 946-951.

Dunn, R. I., Hearps, P. J. & Wright, M. N. 2011. Molten-salt power towers: newly commercial concentrating solar storage. *Proceedings of the IEEE,* 100**,** 504-515.

Engeland, K., Borga, M., Creutin, J.-D., François, B., Ramos, M.-H. & Vidal, J.-P. 2017. Space-time variability of climate variables and intermittent renewable electricity production–A review. *Renewable and Sustainable Energy Reviews,* 79**,** 600-617.

Fikru, M. G., Gelles, G., Ichim, A.-M., Kimball, J. W., Smith, J. D. & Zawodniok, M. J. 2018. An economic model for residential energy consumption, generation, storage and reliance on cleaner energy. *Renewable energy,* 119**,** 429-438.

Gawusu, S., Zhang, X., Ahmed, A., Jamatutu, S. A., Miensah, E. D., Amadu, A. A. & Osei, F. A. J. 2022. Renewable energy sources from the perspective of blockchain integration: From theory to application. *Sustainable Energy Technologies and Assessments,* 52**,** 102108.

Hong, T., Pinson, P., Fan, S., Zareipour, H., Troccoli, A. & Hyndman, R. J. 2016. Probabilistic energy forecasting: Global energy forecasting competition 2014 and beyond. Elsevier.

Hussain, A., Arif, S. M. & Aslam, M. 2017. Emerging renewable and sustainable energy technologies: State of the art. *Renewable and sustainable energy reviews,* 71**,** 12-28.

Jeon, B.-K. & Kim, E.-J. 2020. Next-day prediction of hourly solar irradiance using local weather forecasts and LSTM trained with non-local data. *Energies,* 13**,** 5258.

Jing, Y., Bai, H. & Zhang, J. Multi-objective optimization design and operation strategy analysis of a solar combined cooling heating and power system. Zhongguo Dianji Gongcheng Xuebao(Proceedings of the Chinese Society of Electrical Engineering), 2012. Chinese Society for Electrical Engineering, 82-87.

Khan, M. I., Asfand, F. & Al-Ghamdi, S. G. 2022. Progress in research and technological advancements of thermal energy storage systems for concentrated solar power. *Journal of Energy Storage,* 55**,** 105860.

Kneiske, T. M. & Braun, M. 2017. Flexibility potentials of a combined use of heat storages and batteries in PV-CHP hybrid systems. *Energy Procedia,* 135**,** 482-495.

Kostylev, V. & Pavlovski, A. Solar power forecasting performance–towards industry standards. 1st international workshop on the integration of solar power into power systems, Aarhus, Denmark, 2011. Energynautics GmbH Mühlstraße Langen, Germany, 1-8.

Kumar, Y., Ringenberg, J., Depuru, S. S., Devabhaktuni, V. K., Lee, J. W., Nikolaidis, E., Andersen, B. & Afjeh, A. 2016. Wind energy: Trends and enabling technologies. *Renewable and Sustainable Energy Reviews,* 53**,** 209-224.

Larcher, D. & Tarascon, J.-M. 2015. Towards greener and more sustainable batteries for electrical energy storage. *Nature chemistry,* 7**,** 19-29.

Law, E. W., Prasad, A. A., Kay, M. & Taylor, R. A. 2014. Direct normal irradiance forecasting and its application to concentrated solar thermal output forecasting–A review. *Solar Energy,* 108**,** 287-307.

Li, J., Du, Z., Ruther, R. E., An, S. J., David, L. A., Hays, K., Wood, M., Phillip, N. D., Sheng, Y. & Mao, C. 2017. Toward low-cost, high-energy density, and high-power density lithium-ion batteries. *Jom,* 69**,** 1484-1496.

Liu, K., Wang, Y. & Lai, X. 2022. *Data science-based full-lifespan management of lithium-ion battery: manufacturing, operation and reutilization*, Springer Nature.

Lund, H. 2014. *Renewable energy systems: a smart energy systems approach to the choice and modeling of 100% renewable solutions*, Academic Press.

Luo, X., Liu, J., Liu, Y. & Liu, X. 2019. Bi-level optimization of design, operation, and subsidies for standalone solar/diesel multi-generation energy systems. *Sustainable Cities and Society,* 48**,** 101592.

Luo, X., Zhu, Y., Liu, J. & Liu, Y. 2018. Design and analysis of a combined desalination and standalone CCHP (combined cooling heating and power) system integrating solar energy based on a bi-level optimization model. *Sustainable Cities and Society,* 43**,** 166-175.

Mai, H., Le, T. C., Chen, D., Winkler, D. A. & Caruso, R. A. 2022. Machine learning for electrocatalyst and photocatalyst design and discovery. *Chemical Reviews,* 122**,** 13478-13515.

Majid, M. 2020. Renewable energy for sustainable development in India: current status, future prospects, challenges, employment, and investment opportunities. *Energy, Sustainability and Society,* 10**,** 1-36.

Memon, S. A., Javed, Q., Kim, W.-G., Mahmood, Z., Khan, U. & Shahzad, M. 2022. A machine-learning-based robust classification method for PV panel faults. *Sensors,* 22**,** 8515.

Mishra, S. & Palanisamy, P. 2019. An integrated multi-time-scale modeling for solar irradiance forecasting using deep learning. *arXiv preprint arXiv:1905.02616*.

Oyekale, J., Petrollese, M., Tola, V. & Cau, G. 2020. Impacts of renewable energy resources on effectiveness of grid-integrated systems: Succinct review of current challenges and potential solution strategies. *Energies,* 13**,** 4856.

Qing, X. & Niu, Y. 2018. Hourly day-ahead solar irradiance prediction using weather forecasts by LSTM. *Energy,* 148**,** 461-468.

Ren, H. & Gao, W. 2010. A MILP model for integrated plan and evaluation of distributed energy systems. *Applied energy,* 87**,** 1001-1014.

Ren, H., Zhou, W., Nakagami, K. I., Gao, W. & Wu, Q. 2010. Multi-objective optimization for the operation of distributed energy systems considering economic and environmental aspects. *Applied Energy,* 87**,** 3642-3651.

Roy, S. & Ragunath, S. 2018. Emerging membrane technologies for water and energy sustainability: Future prospects, constraints and challenges. *Energies,* 11**,** 2997.

Semadeni, M. 2003. Energy storage as an essential part of sustainable energy systems: a review on applied energy storage technologies. *CEPE Working Paper,* 24.

Senthil Kumar, R., Saravanan, S., Pandiyan, P., Suresh, K. & Leninpugalhanthi, P. 2022. Green Energy Using Machine and Deep Learning. *Machine Learning Algorithms for Signal and Image Processing***,** 429-444.

Sharma, N., Sharma, P., Irwin, D. & Shenoy, P. Predicting solar generation from weather forecasts using machine learning. 2011 IEEE international conference on smart grid communications (SmartGridComm), 2011. IEEE, 528-533.

Strielkowski, W. 2019. *Social impacts of smart grids: The future of smart grids and energy market design*, Elsevier.

Wang, J., Gao, D., Zhu, S., Wang, S. & Liu, H. 2023. Fault diagnosis method of photovoltaic array based on support vector machine. *Energy sources, part a: recovery, utilization, and environmental effects,* 45**,** 5380-5395.

Wang, P., Poovendran, P. & Manokaran, K. B. 2021. Fault detection and control in integrated energy system using machine learning. *Sustainable Energy Technologies and Assessments,* 47**,** 101366.

Wang, Z., Yang, X., Wang, Y. & Weng, S. 2019. Strategic analysis and optimal design of a multi-energy coupling combined cooling, heating and power system. Therm. *Energy Power Eng,* 34**,** 9-14.

Weeratunge, H., Narsilio, G., De Hoog, J., Dunstall, S. & Halgamuge, S. 2018. Model predictive control for a solar assisted ground source heat pump system. *Energy,* 152**,** 974-984.

Yin, J., Molini, A. & Porporato, A. 2020. Impacts of solar intermittency on future photovoltaic reliability. *Nature communications,* 11**,** 4781.

Yu, Y., Cao, J. & Zhu, J. 2019. An LSTM short-term solar irradiance forecasting under complicated weather conditions. *IEEE Access,* 7**,** 145651-145666.

Zhou, Z., Zhang, J., Liu, P., Li, Z., Georgiadis, M. C. & Pistikopoulos, E. N. 2013. A two-stage stochastic programming model for the optimal design of distributed energy systems. *Applied Energy,* 103**,** 135-144.

#86: Enhancing energy efficiency in hospital buildings

A comprehensive diagnosis strategy for chiller plant fault detection

Xi BAI[1], Caihua LIANG[2], Qi TANG[3], Yubo MAO[4], Junjie HUANG[5]

1 School of Energy and Environment, Southeast University, 2 Sipailou Road, Nanjing, PR China, 230179380@seu.edu.cn
2 School of Energy and Environment, Southeast University, 2 Sipailou Road, Nanjing, PR China, caihualiang@seu.edu.cn
3 School of Energy and Environment, Southeast University, 2 Sipailou Road, Nanjing, PR China, tqszbd@gmail.com
4 School of Energy and Environment, Southeast University, 2 Sipailou Road, Nanjing, PR China, maoyubo1998@foxmail.com
5 School of Energy and Environment, Southeast University, 2 Sipailou Road, Nanjing, PR China, hjj739882962@163.com

Abstract: Due to the lack of process and easy-to-learn system-level diagnosis methods for a chiller plant. The authors of this article presented an energy-saving diagnosis strategy for chiller plants to detect faults early and achieve sustainable built environments. This strategy analyses common weaknesses in building chilled water systems from maintenance, design, and operation perspectives. It comprises four steps: macroscopic energy efficiency index judgment, system troubleshooting, design diagnosis, and operation diagnosis. The authors applied the strategy to a typical hospital building in a hot and cold region of China. They found that partial-load conditions were a significant problem, reducing cooling efficiency and excess cooling in unoccupied rooms. The overall yearly energy efficiency (COP_{plant}) was 3.27, and the useless energy consumption caused by this operation in 2021 is as high as 510327 kWh. A specific solution was proposed, including replacing the check valve, cleaning the condenser, and avoiding multiple water pumps with a small number of hosts. The authors also recommended developing a frequency conversion control strategy for the water pump under partial load and creating a chiller opening strategy at different load intervals of the building.

Keywords: Energy-saving, Fault detection, Chiller plant, Sustainability, Building Efficiency

1. INTRODUCTION

The cold source system consisting of chillers, circulating pumps, cooling towers, and piping networks is the main component of the energy system of large buildings, and its energy consumption accounts for more than 50% of the whole building system (Saidur, 2009). Malfunctioned HVAC systems lead to significant energy waste, about 30%(Brambley et al., 1998, Chen et al., 2022). Even though personal equipment has met the relevant standards, energy wastage in centralized air conditioning systems is still common. It is due to poor design selection, inadequate commissioning, and absent operational management. A study of 10 buildings lasting 12 years found that, on average, annual energy savings in heating or cooling would decay by 25% after 3-5 years if no follow-up measures were taken to maintain savings(Lin and Claridge, 2015).

According to the scale of the diagnosis object, the study is divided into two categories: equipment-level fault diagnosis and system-level diagnosis. At the equipment level, the fault diagnosis of the chiller is a research hotspot(Yao et al., 2022, Han et al., 2022, Li et al., 2021, Zhu et al., 2021). In addition, it also includes the diagnosis of fan coil units(Ranade et al., 2020), Air-Handling Units(Rosato et al., 2022, Torabi et al., 2022), variable air volume terminals (Gunay et al., 2022, Wei et al., 2022, Wang et al., 2021), and other components. At the system level, Lu et al.(Lu et al., 2021)developed a Modelica-based medium office virtual testbed to analyse the impact and robustness of multiple failures. The work is remarkable, but there is a lack of actual architectural inspection. Lin et al.(Lin and Claridge, 2015)introduced a temperature-based approach – the Days Exceeding Threshold-Toa (DET-Toa) method to detect a slight increase or decrease in typical building energy consumption. Sun et al.(Sun et al., 2014)proposed a plan combining SPC, Kalman filter, and system analysis for diagnosing HVAC system-level faults. The above system-level fault diagnosis mainly focuses on symptom description without analysing the cause and source of the defect, so it isn't easy to obtain information that can guide new buildings.

Although there are different types of evaluation methods for the performance degradation problem of existing buildings, they either do not consider the design goal, or their research objects are independent devices and ignore the synergy between devices. These studies do not focus on systematic summary to describe the potential causes of performance problems. There is a lack of process and easy-to-learn system-level diagnosis methods for a chiller plant. Therefore, this paper puts forward an energy-saving diagnosis strategy at the level of the cold source system. The authors used a hospital building in a hot summer and cold winter region of China as an example, analyse the operation data of the building for two years, and they verified that the proposed strategy can identify the performance problems. Finally, they gave suggestions for improving energy efficiency.

2. OVERALL STRATEGY

In this paper, the authors proposed a system-level chiller plant diagnosis process based on actual measurement data and makes a comprehensive diagnosis analysis from three perspectives of maintenance, design and operation. This process diagnosis method is divided into four steps: 1. based on the preliminary judgment of the energy efficiency index; 2. the troubleshooting of the chiller and pipe network system; 3. the design diagnosis to evaluate the matching degree between equipment selection and actual building; 4. the operation diagnosis to save energy as the goal. On the basis of determining the macroscopic diagnostic index, the authors established a diagnosis process based on fault tree analysis, as shown in Figure 1. There are thirteen species of diagnostic results, where the dashed boxes indicate human-caused performance degradation and the solid boxes show improper selection. Table 1 lists all bottom events and there corresponding solution. All events can be divided into performance failures, design defects, and malfunctions, see Table 2.

Table 1: Failure of the chiller plants and the corresponding measures

	Name	Measures
X1	The pump operation efficiency was low	Replace with a new pump
X2	Excess flow pumps were selected during the design phase	Reduce pump frequency
X3	Excess pumps turned on due to mis operation	Turn off additional pumps
X4	End pipe network hydraulic imbalance	Regulate the end hydraulic balance
X5	Chiller failure	Maintenance
X6	Cooling tower performance decayed	Replace cooling tower packing
X7	Excess capacity chillers were selected during the run phase	Optimization of chillers
X8	The pump operating frequency was too low	Increase pump frequency
X9	Insufficient flow rate pumps were selected in the design phase	Replace with a new pump
X10	Under-designed pipe diameter	Maintenance
X11	Valve blockage	Maintenance
X12	Valve sticking or malfunction	Maintenance
X13	The Kv Factor of a value is too small	Replace with a new valve

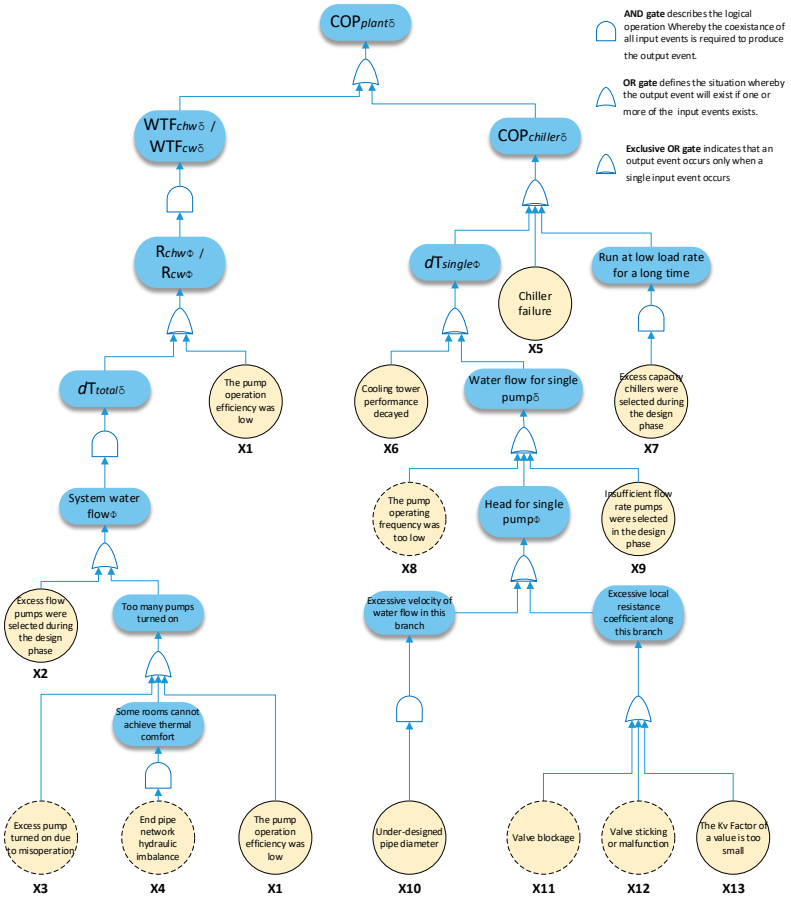

Figure 1 Chiller diagnosis strategy based on fault tree

Table 2: Classification of faults

	The fault numbers					
Performance failure	X1	X5	X6	X11	X12	X13
Reversible design defects	X2	X7				
Irreversible design defects	X9	X10				
mis operation	X3	X8				

Step 1： Macroscopic evaluation of chiller plant

The collected data are first pre-processed, including culling, filtering, calibration, etc. Then, the authors calculated the macroscopic diagnostic indicators of the chiller plant based on the measured data. According to the previous research, we selected the following parameters as the macro indicators for the preliminary system diagnosis. Total energy efficiency ratio(COP_{plant}), an energy efficiency ratio of a single chiller($COP_{chiller}$), chilled water pump delivery coefficient(WTF_{chw}), cooling water pump delivery coefficient(WTF_{cw}), energy consumption ratio of equipment($R_{chiller}$, R_{chw}, R_{cw}), total chilled water temperature difference(dT_{ch}), total cooling water temperature difference(dT_c), cooling tower cooling amplitude(dT_{tower}).

Equation 1: Total energy efficiency ratio

$$COP_{plant} = Qe/W_{plant}$$

Equation 2: energy efficiency ratio of a single chiller

$$COP_{chiller} = Qe/W_{chiller}$$

Equation 3: chilled water pump delivery coefficient

$$WTF_{chw} = Qe/W_{chpump}$$

Equation 4: cooling water pump delivery coefficient

$$WTF_{cw} = Qc/W_{cpump}$$

Equation 5: energy consumption ratio of chillers

$$R_{chiller} = W_{chiller}/W_{plant}$$

Equation 6: energy consumption ratio of chilled water pumps $$R_{chw} = W_{chpump}/W_{plant}$$

Equation 7: energy consumption ratio of cooling water pumps $$R_{cw} = W_{cpump}/W_{plant}$$

Where:

- Qe = instantaneous cooling capacity of the chiller(kW)
- W = power consumption of the equipment(kW)

Step 2： Fault diagnosis

Fault detection and diagnosis of the system from three dimensions: the chiller, the chilled water circuit, and the cooling water circuit. The faults discussed in this paper are mainly soft faults that can cause energy wastage and system performance degradation. (Hard failures often bring down the system and are easy to detect and beyond this paper's scope.) The failure of the chiller contains heat exchanger scaling, unreasonable refrigerant charge, and the presence of non-condensable gas. The authors have given a specific troubleshooting process in previous work(Bai et al., 2022). Pipeline failures include improper pressure distribution, stuck or blocked valves, and decaying pump performance. This corresponds to the “performance failure” in Table 2.

Step 3： Design Diagnosis

Determine whether the equipment in the current system can be well adapted to the actual building while troubleshooting. Specifically, assess whether the capacity selection of chillers and pumps is reasonable, whether the liquid flow rate in the pipeline is reasonable, and whether the pipe diameter design is practical. This corresponds to the “design defects” in Table 2. In general, it is often possible to improve the energy efficiency of redundant capacity equipment through operation adjustment, but the lack of capacity equipment needs to be replaced to meet the demand.

Step 4： Operation Diagnosis

For the system operation diagnosis problem combined with the chiller model, we used the modelling approach from the literature(Huang et al., 2019). Based on summarizing the current operation pattern and determining the operation target, the operation diagnosis has two objectives: firstly, to determine whether the design defects found in the previous step can be compensated by operation, and secondly, to determine whether there is room for further optimization of the current operation pattern. This corresponds to the “Reversible design defects” and “mis operation” in Table 2.

3. PROJECT OVERVIEW

3.1 System description

The project is located in the hot summer and cold winter region of China (Nanjing, Jiangsu Province). It is a hospital complex including an outpatient building, inpatient department, and operation theatre. The construction area of this project is 225,191 square meters, consisting of two underground floors, fourteen main floors of the main building, five feet of the south side podium, and six floors of the north side podium. The project is designed according to the ice storage air-conditioning fractional ice storage mode, and Figure 2 shows the schematic diagram of the cooling source system. The air conditioning system is equipped with two dual-condition screw units, and the evaporative side of the circulating solution is a glycol solution. The units can operate under two working conditions: air conditioning and ice production. In order to meet the demand of night load and daytime cooling requirements, three base load centrifugal chillers and one base load screw chiller are also equipped.

The cooling water pumps have a one-to-one correspondence with the host; each pump is connected in series with the host and then in parallel. The air-conditioning water system is a closed-cycle, primary pump variable volume system. There are six chilled water circulation pumps in the system, among which 1-4# pumps correspond to the host one by one and are connected in series with the host and then in parallel. 5 and 6# chilled water pumps are water-side circulation pumps of the ice storage and cooling plate heat exchanger. 5 and 6# pumps are connected in parallel and then in series with the plate heat exchanger and then in parallel with other branches. The plate heat exchanger isolates the glycol circuit of the ice storage system from the air conditioning system circuit. The import and export temperature of the water side of the plate heat exchanger is 11/7℃. The import and export temperature of the glycol side is 5/13℃, and two plate heat exchangers with a heat exchange capacity of 3800kW are selected; Table 3 lists the specific parameters of the cold source equipment.

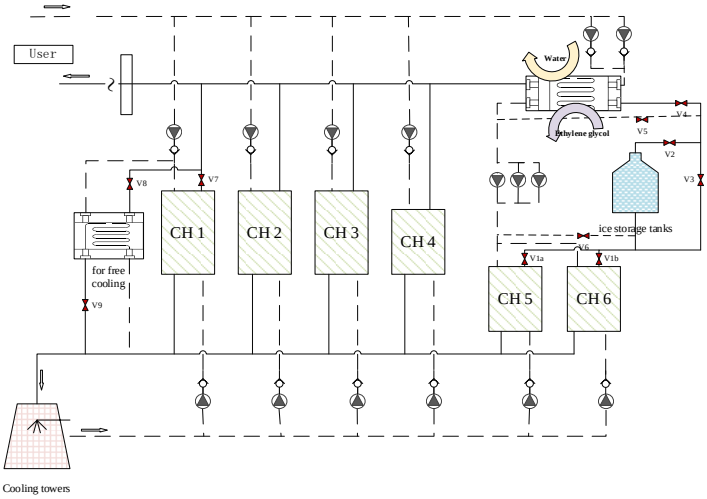

Figure 2 The schematic diagram of the cooling source system with ice storage

Table 3: The equipment parameters

	Chillers	Rated cooling capacity (kW)	Refrigerant	Rated power (kW)	Quantity
1-3#	centrifugal chillers	4147	R134a	770	3
4#	screw chiller	1406	R22	270	1
5、6#	Screw duplex chillers	1688	R22	312	2
	Pumps	**Rated flow(m3/h)**	**Rated head(m)**	**Rated power (kW)**	**Quantity**
1-3#	1-3#Cooling water pumps	870	33	110	3
4#	4#Cooling water pump	350	52	55	1
5、6#	5、6#Cooling water pump	400	30	55	2
1-3#	1-3#Chilled water pump	610	41	110	3
4#	4#Chilled water pump	230	41	45	1
5、6#	5、6#Chilled water pump	470	41	75	2
	Glycol circulation pumps	265	32	75	3
	Cooling tower	**Rated Air Flow(m3/h)**		**Rated power (kW)**	**Quantity**
	1-22#Cooling tower	5318		7.5	22

3.2 data description

In this paper, the hospital's cooling system analysis is based on operational data, both long-term data obtained from the testing system and short-term data obtained from field measurements. The imbalance rate is used to verify the energy balance of the collected data orderly. The field testing of the refrigeration system included testing the pressure distribution in the transmission and distribution lines of the cold source system and testing the performance parameters. Figure 3 shows the distribution of measurement points for the pressure test of the single-branch chilled water distribution system.

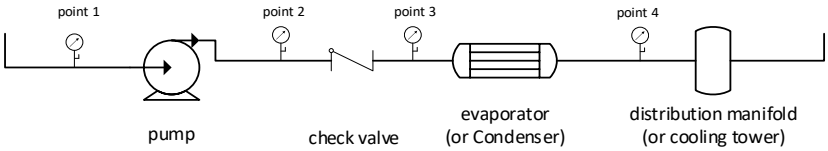

Figure 3 Distribution of measurement points for pressure testing of single-branch fluid piping network

The primary test data for the performance testing of the refrigeration system are water temperature, air temperature, humidity, refrigerant temperature, refrigerant pressure, pump power, flow rate, pump inlet, outlet pressure, unit power, etc. The measuring equipment includes parameter measuring elements, power meters, flow meters, etc. All measuring instruments are calibrated and within the effective use period. The measuring parameters are listed in Table 4.

Table 4: Measurement parameters

Measured parameters	Way	Measured parameters	Way	Measured parameters	Way
Air dry bulb temperature	Field test	Temperature of the water entering the evaporator	Filed read	Water pump power	Long-term monitoring
Air wet bulb temperature	Field test	Temperature of the water leaving the evaporator	Filed read	Chiller power	Long-term monitoring
Cooling water flow	Field test	Temperature of the water entering the condenser	Filed read	Power for the fan of the cooling tower	Long-term monitoring
Power of cooling tower fan	Field test	Temperature of the water leaving the condenser	Filed read	Chilled water flow	Long-term monitoring
Water pressure into the pump	Field test	Compressor suction temperature	Filed read	Temperature of the chilled water main entering the end	Long-term monitoring
Water pressure leaving the pump	Field test	Compressor discharge temperature	Filed read	Temperature of the chilled water main leaving the end	Long-term monitoring
Water pressure into the chiller	Field test	Condensing pressure	Filed read		
Water collector pressure	Field test	Evaporation pressure	Filed read		
Water distributor pressure	Field test	Part load of the chiller	Filed read		
		Water pump frequency	Filed read		

3.3 Cooling capacity analysis

The hour-by-hour cooling capacity of chillers are generally obtained by the equation Q = CMT, where m is the chilled water mass flow rate, and T is the absolute temperature difference, which is used as an approximate representation of the building's load. The gap between the two comes from the following three points: 1. Due to inadequate insulation or other factors leading to an inevitable loss of chilled water in the transmission and distribution process, the actual amount of cooling obtained by the building is less than that provided by the cold source system; 2. there is a gap between the building demand for cooling and the amount of cooling provided by the cold source system. When part of the end branch valve, which is not in use, is not closed, the amount of cooling provided by the cold source may be greater than the actual demand of the building; 3. Similarly, the cooling source may not be able to meet the user's request, and some end-users initiate complaints at this time.

In this project, no user complaints occurred to ensure the hospital operation's stability. The cooling capacity of the cooling source >= the building load. Figure 4 shows the cooling capacity distribution for two-cycle years after August 14th, 2020. The blue curve is from 8.14.2020 to 2021.8.14(Year b); The orange curve is from 2021.8.14 to 2022.8.14 (Year b). The hourly peak of the cooling capacity is 17,776.8 kW, which occurs at 11:00 a.m. on August 18th, 2020. The hospital has cooling load demand throughout the year, with relatively low cooling loads outside of the cooling season.

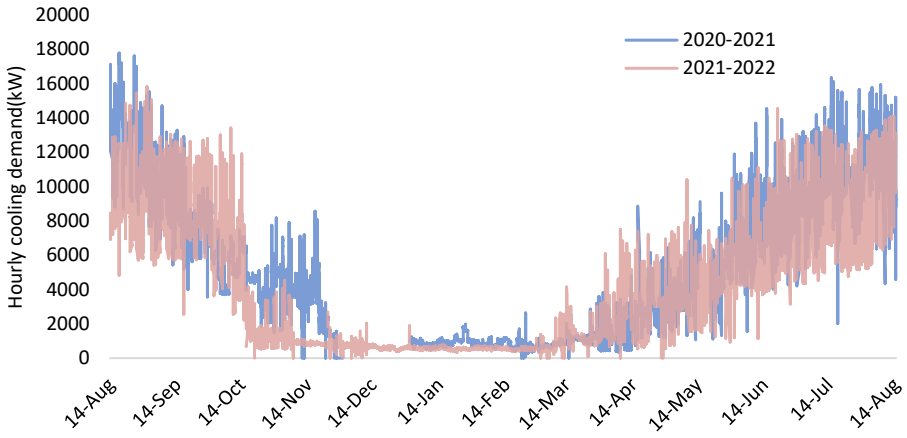

Figure 4 Annual building hour-by-hour cold load for two-cycle years beginning August 2020

3.4 Part load analysis

Define PLR = current cooling capacity/maximum cooling capacity. Figure 5 shows the cumulative hours at different PLRs for two years, A and B. The cooling distribution is pyramidal. In year A, the PLR is below 20-43% of the time. In year B, the PLR is below 20-55% of the time. It is concentrated in the winter and transition seasons. There were very few times when the partial load was more significant than 80%, with 3% in year A and only 15 hours in year B.

Figure 6 shows the PLR distribution for summer 2021 and 2022 (from *June 1st* to *September 30th*). Cooling capacity in 2022 was lower than in 2021. 54% of the time in summer 2021, the PLR is concentrated in the 40-60% range. 2022 PLR in the range of 20-40% occupies 46% of the time in summer. It is worth noting that the cooling capacity in 2022 in the case of persistent high temperatures in July-August in Nanjing is still lower compared to 2021, as shown in Table 5. It is due to the staff's strict implementation of the timely shutdown of the idle air conditioning since 2022. the cumulative cooling capacity in July-August 2021 was 15.88 million kWh, and in 2022 was 13.07 million kWh, a 17.7% reduction in cooling capacity, for a total of 2.81 million kWh. Thus, the hospital's energy loss due to untimely regulation is significant.

Table 5: Comparison of the cooling capacity of the hottest month in years A and B

Low-temperature average ~ High-temperature average	2021	2022
July	25℃~31℃	27℃~35℃
August	24℃~31℃	28℃~36℃
Accumulated cooling capacity from July to August	15.88 million kwh	13.07 million kwh

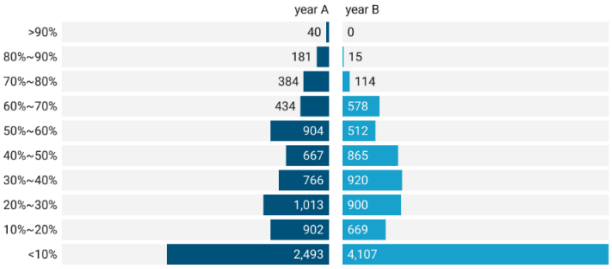

Figure 5 The cumulative hours at different PLR for two years

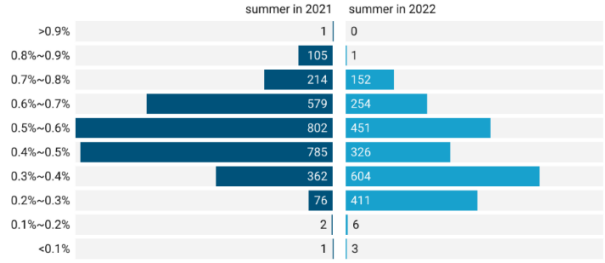

Figure 6 The cumulative hours at different PLRs for summer (6.1-9.30) *of two years*

4. CASE STUDY

HVAC systems were controlled by staff based on experience:

1) Ice making at night, ice melting during the day. Additional screw chillers or centrifugal chillers to suit the load size. All chillers are at a constant speed.
2) Variable speed pumps run at 50Hz all year round.
3) When the chillers are not all working, the pumps without cooling branches still run. It is to ensure the environmental comfort of the most disadvantaged end users.

4.1 Macroscopic evaluation of chiller plant

The diagnostic table shown in Figure 7 was developed for the target system based on the energy efficiency evaluation method for the chiller plant in the literature (Hartman, 2001, Li and Li, 2018). For the year 2021, data from the summer season were selected for calculation. The reason is to exclude the effect of free cooling in winter. Note that the calculation of the *COPchiller* average does not include Screw duplex chillers.

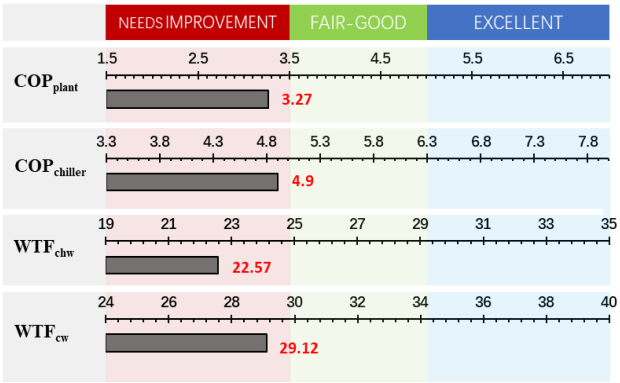

Figure 7 Average summer chiller plant efficiency in kW/ kW (COP). Input energy includes chillers, pumps, and tower fans.

The chilled water temperature difference for a single chiller was 5-6.5°C, while the total chilled water temperature difference averaged 3.89 in the summer. The cooling water temperature difference for a single chiller ranged from 4-6.5°°C, and the total cooling water temperature difference averaged 3.48 in the summer.

The reasons for the low-COP plant chiller are the excessive proportion of energy consumption of the pump and the insufficient water flow of the chiller. The system turned on too many pumps to meet the environmental demands of the most disadvantaged end users, which created an additional problem: heavy blending. When the number of working pumps exceeds the chiller, mixing high-temperature and low-temperature chilled water occurs in the main tube. For example, when turning on a chiller and two chilled water pumps, the chilled water of 7℃ and 13℃ is mixed, and the final water temperature is 10℃. Increasing the chilled water's temperature loses part of the dehumidification capacity. It also cannot meet the needs of some rooms' dehumidification.

4.2 Fault diagnosis

Chillers Fault diagnosis

It is found that the chilled water flow rate is less than the rated flow rate for all branches, with a non-significant reduction for branch 2 and a 16% reduction for the other branches.The cooling water flow rate in branch 2 was only 48% of the rated value, and the other branches reduced by about 8%.Insufficient water flow is the leading cause of heat exchanger performance degradation. The pressure drop of the condenser of the 1#chiller is too large(127kpa), and the condenser's heat transfer temperature difference is the highest of all chillers, exceeding 2K. 1# chiller has a "condenser fouling" fault.

Fault diagnosis for the fluid piping network

Figure 3 shows the distribution of measurement points for pressure testing of a single-branch fluid piping network. There are abnormal resistance pieces in the transmission and distribution network, and the pressure drop of the slow-closing check valve at the pump outlet is too large. Take 1# chilled water pipeline, for example, pump head 430 kPa, check valve pressure drop 264kpa is 61% of the head. There is only one resistance component from the pump outlet to the evaporator inlet, the check valve. The pressure drop between the pump inlet and the evaporator outlet is 116kPa, which is the actual power provided by the pump to the end. The same problem exists in the cooling water pipeline. Figure 8 shows the pressure variation of 1, 2, and 3# water lines.

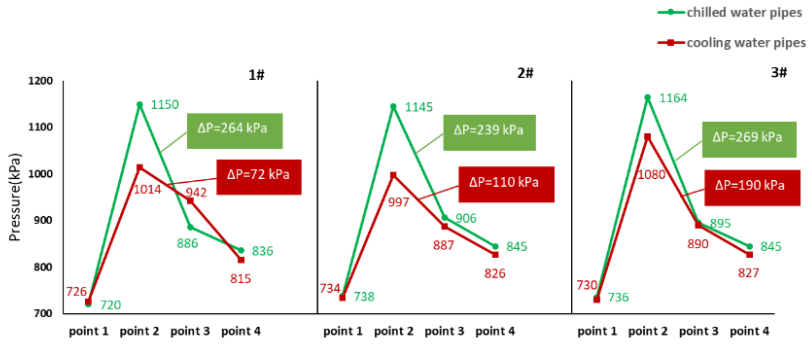

Figure 8 Pressure drop of water pipe of 1-3# branch

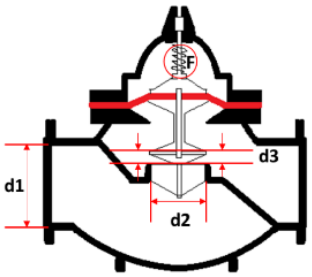

Figure 9 Schematic of the internal structure of the check valve.

The structure of the check valve is shown in Figure 9, which is more complex than the swing check valve. It is to reduce the noise when the valve is closed.

Cv is used to characterize the flow capacity of the valve:

Equation 8: Flow coefficient

$$Cv = \mathrm{Q} * \sqrt{\rho / \Delta P}$$

Where:

- ΔP = pressure drop (PSI)
- Q = volume flow rate (US gal/min)
- ρ = density of the fluid(g/cm^3)

According to the investigation, the valve is not stuck or blocked. Taking the 1# chilled water pump check valve as an example, calculated by the Equation 8, Cv equals 350 when the flow rate is 500 m^3/h. The Cv of the swing check valve is usually greater than 1000 under the same working condition.

4.3 Design diagnosis

Replace the check valve with the swing type, the local pressure drop of the valve is reduced from 269kPa to 15kPa (3# branch), and the fault point is eliminated. The pipeline characteristic curve has changed. In the original system, due to the

check valve pressure drop being too large, the pump head is high (434kPa), the flow is small (500m3/h), and after the transformation, the pump head is reduced (290kPa), the flow is increased (890m3 /h).After the pipe network fault is eliminated, the flow rate of the water pump is too large, especially when the chiller runs under partial load, and the energy consumption of the water pump is too high. It does not match the system well.

4.4 Operation Diagnosis

Control strategy for chillers

In the whole summer of 2021, the time of opening 2-3 chillers is the largest. The ordinate of Figure 10 (a) represents the number of open chillers, and the negative value represents the number of opened screw duplex chillers for cold storage at night.The minimum load in summer is 2020kw, and at least one centrifugal chiller should be started. As the load increases, a centrifugal chiller cannot meet the cooling capacity demand of the building. In this case, the alternative scheme is 1. Supplement opens a screw machine 2. Use the ice storage system's melting or combined cooling mode 3. Use the ice storage system's melting or combined cooling mode while opening a screw machine; 4. Start one more centrifugal chiller.When the cooling load of the building cannot be met after the two centrifugal chillers are started, the options are the same as the above four points. After starting three centrifugal chillers, the options are the same as 1.2.3 above. Without considering ice making at night, there are 12 operating modes in the full load section of the cooling season.

In a certain load interval, there are a variety of strategies to meet the cooling demand of the building. However, there is no standardized operation strategy for the system at present. It can be seen from the statistical results of the cooling season in 2021 that there is great randomness in the opening strategy of the chiller under different loads, which inevitably leads to a certain degree of energy consumption waste.

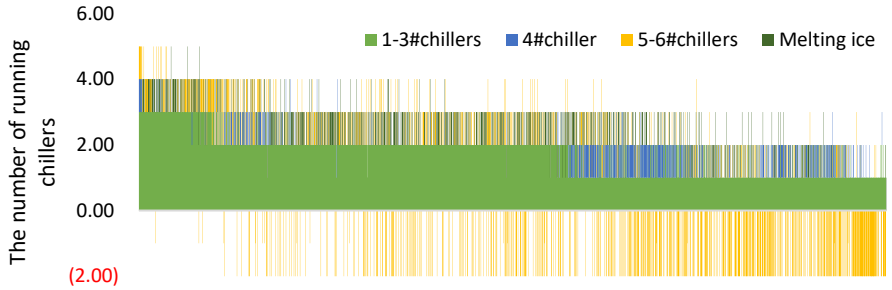

(a)

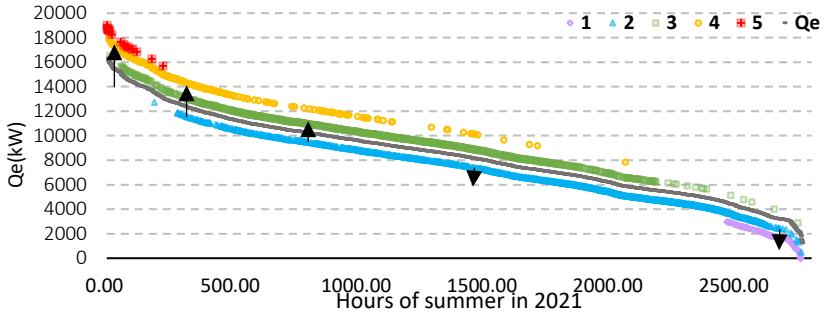

(b)

Figure 10 Number of chillers started per hour in descending order of cooling capacity. The melting mode is also considered a chiller

Control strategy for pumps

The relationship between the number of chiller pumps and chillers started in 2021 was analysed. Only 27% of the time, the number of working chillers and water pumps is consistent, and this time is concentrated from June to August when the building load is heavy. 73% of the time, the working pumps are more than the working chillers. One or more pumps worked 57% of the time, and two or more pumps started 16% of the time. Table 6 shows the energy consumption of over open pump in 2021. The energy consumption caused by this operation is as high as 510327 kWh.

Table 6: Extra opened pump energy consumption in 2021

	1#~3#Centrifugal chillers are closed		One centrifugal chiller is opened		Two centrifugal chillers are opened	4#Screw chiller is closed
	One more pump	Two more pump	One more pump	Two more pump	One more pump	4#pump is opened
Number of hours(h)	647	330	1216	165	940	1414
Extra opened pump energy consumption(kWh)	60996	61918	115836.5	29962.67	177984	63630

The recommendation and solution

- Excessive check valve pressure drop is the source of a vicious cycle. The water pump's high energy consumption, the chiller's low energy efficiency, and the high temperature of cold water are all caused by it. It is the first thing that should be eliminated in the transformation. The scheme of replacing it with a swing type is put forward and tested in the 3# chilled water branch. After replacement, the chilled water flow is increased, and the energy efficiency of the host is improved.
- There is a scaling fault in the chiller. Clean the condensers in all chillers, especially the 1# chiller.
- The pump selection does not match the system, and the pump's flow is too large at 50Hz. However, this design defect can be remedied by implementing frequency conversion adjustments. Next, the chiller and water pump simulation model will be used to work out the frequency conversion control strategy of the water pump under a partial load of the chiller, aiming at the lowest total energy consumption of equipment.
- The current system lacks scientific management measures. There is neither a strategy for the opening sequence of chillers nor a process for partial load distribution. Next, multiple chiller models should be established to work out the opening strategy of the chiller in different load intervals of the building, aiming at the highest total energy efficiency of the chiller system.
- Strictly avoid the situation of multiple pumps with a few hosts.
- Ice storage and free cooling technology have played a good role in improving the system's economy. However, there is still room for further energy consumption reduction through a unique optimization control design.

5. CONCLUSION

In this paper, the authors proposed an energy-saving diagnosis strategy for chiller plants based on measured data, which includes four steps: calculation of macroscopic energy efficiency index, fault diagnosis, design diagnosis, and operation diagnosis. Fault diagnosis aims to find the root cause of system performance degradation, design diagnosis seeks to evaluate the matching degree between existing equipment selection and actual demand, and operation diagnosis is used to assess the repairability of existing defects. A case study of a typical hospital building in a hot and cold winter region in China is conducted. The main conclusions are as follows:

1) Partial-load conditions are a critical problem in the hospital building. The time for which the PLR is less than 20% occupies more than 43% in year A and is even as much as 55% in year B. The time of the peak load is less than 3%. Cooling capacity in the summer of 2022 was lower than in 2021. 54% of the time in the summer of 2021, the PLR is concentrated in 40-60% range, and the range of 20-40% occupies 46% of the time in 2022. In the hottest months, the excess cooling in the rooms of absent users is as high as 1.4 million kWh/ month.
2) It was found that the check valve pressure drop at the pump outlet was too significant, which resulted in insufficient water flow, high pump energy consumption, low chiller efficiency, and increased water supply temperature. The rated COP of the chiller is 5.9, and the average value of the actual test is only 4.9. Scaling of the condenser is one of the reasons for the substandard performance of the chiller. After troubleshooting, the selection of the water pump is too large. If no frequency conversion measures are taken, the water pump will run on the performance curve's right side of the rated operating point. The operation of the system relies on workers' experience and lacks coordination, resulting in a high energy waste of 510,327 kWh for the extra opening of the water pump.
3) A specific solution to this case is proposed. First, the check valve should be replaced with the swing type, the condenser should be cleaned, and the situation of multiple water pumps with a small number of hosts should be strictly avoided. Secondly, the frequency conversion control strategy of the water pump under a partial load of a chiller will be formulated based on the model, aiming at the lowest total energy consumption of equipment. The chiller opening strategy at different load intervals of the building will be developed, aiming at the highest total energy efficiency of the chiller system.

6. REFERENCES

bai, X., Zhang, M. X., Jin, Z. H., You, Y. L. & Liang, C. H. 2022. Fault detection and diagnosis for chiller based on feature-recognition model and Kernel Discriminant Analysis. *Sustainable Cities and Society,* 79.

Brambley, M., Pratt, R., Chassin, D., Katipamula, S. & Hatley, D. 1998. Diagnostics for outdoor air ventilation and economizers. *Ashrae Journal-American Society of Heating Refrigerating and Air-Conditioning Engineers,* 40**,** 49-+.

Chen, J. L., Zhang, L., Li, Y. F., Shi, Y. F., Gao, X. H. & Hu, Y. Q. 2022. A review of computing-based automated fault detection and diagnosis of heating, ventilation and air conditioning systems. *Renewable & Sustainable Energy Reviews,* 161.

Gunay, B., Bursill, J., Huchuk, B. & Shillinglaw, S. 2022. Inverse model-based detection of programming logic faults in multiple zone VAV AHU systems. *Building and Environment,* 211.

Han, S. Y., Shao, H. D., Huo, Z. Q., Yang, X. K. & Cheng, J. S. 2022. End-to-end chiller fault diagnosis using fused attention mechanism and dynamic cross-entropy under imbalanced datasets. *Building and Environment,* 212.

Hartman, T. 2001. All-variable speed centrifugal chiller plants. *Ashrae Journal,* 43**,** 43-+.

Huang, T., Liang, C., Bai, X., Feng, Z. & Wang, F. 2019. Study on the feature-recognition-based modeling approach of chillers. *International Journal of Refrigeration-Revue Internationale Du Froid,* 100**,** 326-334.

Li, G. N., Yao, Q., Fan, C., Zhou, C. L., Wu, G. H., Zhou, Z. X. & Fang, X. 2021. An explainable one-dimensional convolutional neural networks based fault diagnosis method for building heating, ventilation and air conditioning systems. *Building and Environment,* 203.

Li, H. R. & Li, X. F. 2018. Benchmarking energy performance for cooling in large commercial buildings. *Energy and Buildings,* 176**,** 179-193.

Lin, G. J. & Claridge, D. E. 2015. A temperature-based approach to detect abnormal building energy consumption. *Energy and Buildings,* 93**,** 110-118.

Lu, X., Fu, Y., O'neill, Z. & Wen, J. 2021. A holistic fault impact analysis of the high-performance sequences of operation for HVAC systems: Modelica-based case study in a medium-office building. *Energy and Buildings,* 252.

Ranade, A., Provan, G., Mady, A. E. D. & O'sullivan, D. 2020. A computationally efficient method for fault diagnosis of fan-coil unit terminals in building Heating Ventilation and Air Conditioning systems. *Journal of Building Engineering,* 27.

Rosato, A., Guarino, F., El Youssef, M., Capozzoli, A., Masullo, M. & Maffei, L. 2022. Faulty Operation of Coils' and Humidifier Valves in a Typical Air-Handling Unit: Experimental Impact Assessment of Indoor Comfort and Patterns of Operating Parameters under Mediterranean Climatic Conditions. *Energies,* 15.

Saidur, R. 2009. Energy consumption, energy savings, and emission analysis in Malaysian office buildings. *Energy Policy,* 37**,** 4104-4113.

Sun, B. A., Luh, P. B., Jia, Q. S., O'neill, Z. & Song, F. T. 2014. Building Energy Doctors: An SPC and Kalman Filter-Based Method for System-Level Fault Detection in HVAC Systems. *Ieee Transactions on Automation Science and Engineering,* 11**,** 215-229.

Torabi, N., Gunay, H. B., O'brien, W. & Barton, T. 2022. Common human errors in design, installation, and operation of VAV AHU control systems-A review and a practitioner interview. *Building and Environment,* 221.

Wang, H. T., Feng, D. G. & Liu, K. 2021. Fault detection and diagnosis for multiple faults of VAV terminals using self-adaptive model and layered random forest. *Building and Environment,* 193.

Wei, D., Feng, H. D., Han, Q. & Jia, K. 2022. Fault detection and diagnosis for variable-air-volume systems using combined residual, qualitative and quantitative techniques. *Energy and Buildings,* 254.

Yao, W. L., Li, D. H. & Gao, L. 2022. Fault detection and diagnosis using tree-based ensemble learning methods and multivariate control charts for centrifugal chillers. *Journal of Building Engineering,* 51.

Zhu, X., Chen, K., Anduv, B., Jin, X. Q. & Du, Z. M. 2021. Transfer learning based methodology for migration and application of fault detection and diagnosis between building chillers for improving energy efficiency. *Building and Environment,* 200.

#93: Splitting the exergy destruction into avoidable and unavoidable parts for integrated biomethane liquefaction process and liquid air energy storage system

Ali REHMAN[1], Bo ZHANG[1,2]*, Xiangji GUO[1,2], Muhammad Abdul QYYUM[3], Fatima ZAKIR[4], Salman IJAZ[5], Ahmad NAQUASH[6]

1Ningbo Institute of Dalian University of Technology, Ningbo, 315200, Zhejiang, China
*2School of Energy and Power, Dalian University of Technology, Key Laboratory of Complex Energy Conversion and Utilization of Liaoning, Dalian, China. *Corresponding author: Bo Zhang zhangbo@dlut.edu.cn*
3Petroleum and Chemical Engineering Department, College of Engineering, Sultan Qaboos University, Muscat, Oman
4Donlinks School of Economics & Management, University of Science and Technology Beijing, Beijing, China
5Key Laboratory of More Electric Aircraft, School of Aerospace, University of Nottingham, Ningbo, China
6School of Chemical Engineering, Yeungnam University, Gyeongsan, Gyeongbuk, 38541, Republic of Korea

Abstract: Regarding bioenergy alternatives, biomethane (BM) emerges as a highly competitive option with the potential to reduce the world's dependency on fossil fuels. Among the various forms of BM, liquefied biomethane (LBM) stands out as the most suitable for both storage and transportation to remote regions across the globe. However, it's worth noting that the process of liquefying BM is both costly and energy-intensive. This is mainly due to the significant electricity consumption associated with the compressors used in the BM liquefaction process, similar to those used in natural gas processing. Furthermore, unlike conventional natural gas, which is generated under high pressure, biomethane is produced at atmospheric pressure. Consequently, the liquefaction of BM demands more energy because the pressure at which BM is produced is substantially lower than its critical pressure counterpart. To address these challenges and create a cost-effective, energy-efficient system, we propose the integration of a biomethane liquefaction process with a liquid air energy storage (LAES) system discharge end. Notably, the thermal exergy of a compressed mixed refrigerant (MR) contributes to the expansion stage of liquid air, adding another layer of advantage to the system. In this research paper, we assess the impact of this innovative integration of LBM and LAES through both conventional and advanced exergy analyses.The outcomes of the conventional exergy analysis highlight that compressors and heat exchangers are the primary sources of irreversibility, accounting for 16.5% and 39.6% of the total, respectively. However, the integration of these two energy systems has yielded promising results. It has been observed that the exergy efficiency of the process has increased to 53%, in contrast to the conventional SMR LBM process, which maintains an exergy efficiency of 35.5%. Advanced exergy analysis showed that 50% of the overall destruction of exergy in the modified process could be avoided. Compressors and turbines had the most potential for improvement and could avoid 54% and 94% of exergy destruction, respectively. However, cryogenic heat exchangers and coolers had the highest percentage of unavoidable exergy destruction, 62% and 83%, respectively. A rigorous comparison was performed among multiple cases like conventional LBM process, LBM-LAES integrated process and optimized LBM-LAES process in terms of avoidable exergy destruction and maximum exergy saving potential was observed in the third case.

Keywords: Liquid biomethane; Liquid air energy system; Renewable energy; Advanced exergy analysis; Improvement potential

1. INTRODUCTION

Energy is essential for every aspect of life, but our current overconsumption of fossil fuels is causing a destabilization of the energy-environment balance globally, leading to issues such as climate change (SHELL LNG OUTLOOK 2019). To meet the needs of energy demand and address the challenges of climate change, the development of green and clean energy sources has been increased. 196 countries have demonstrated their Acknowledgement of the seriousness of climate change by signing the Paris Climate Agreement in 2015 (Paris Agreement 2016). Though the use of fossil fuels has contributed significantly to climate change, renewable energy and biofuels provide a viable solution. Reducing and mitigating greenhouse gas emissions can be obtained by using various biofuels like bioethanol, biomethane and biodiesel (Abdul et al. 2021). Biomethane is an environmentally friendly fuel source which is produced from biogas via upgrading techniques after organic biomass is fermented anaerobically (Pellegrini, De Guido, and Langé 2018)(Ali et al. 2023). This gas mixture is mainly composed of methane (95–97 mol%), and is able to replace natural gas for electricity production, transportation, domestic expenditure and space expeditions (Pellegrini, De Guido, and Langé 2018).

Typically, gas transmission pipelines (GTP) are utilized for transferring biomethane or natural gas to end-users. When GTP is not cost-effective, liquefied biomethane (LBM) is often employed to transport fuel to far-off regions. LBM, also considered as the LBG, is a cryogenic energy storage medium with a high energy density that is also eco-friendly. Biomethane is compressed six hundred times to a liquid form at atmospheric pressure and -160 degrees Celsius (Capra, Magli, and Gatti 2019). Its energy density of 21 MJ/L is comparable to that of liquefied natural gas (LNG), making LBM a viable option for transporting fuel to remote areas of the globe (Capra, Magli, and Gatti 2019)(Zakir et al. 2020). Compressors for LBM require significantly more energy than compressors for LNG. Natural gas is drawn out at of 46.5 bar pressure, whereas biomethane is obtained at atmospheric pressure, making the production of LBM more costly and energy-intensive. To liquefy biomethane, it is necessary to remove a significant quantity of condensation's latent heat. The amount of energy required to transform 1 kg BM into LBM is estimated to be 1188 kilojoules (Qyyum et al. 2019).

To reduce the substantial consumption of energy associated with gas liquefaction processes, it is common practice to combine various energy storage systems to exchange additional hot or cold exergy. The liquid air energy storage system (LAES) charging phase is frequently incorporated with the LNG regasification phase (Penga et al. 2019)(Zhang et al. 2018). The LNG cold exergy is used to facilitate the process of air liquefaction (Wang and Zhang 2017) (She et al. 2018). Additionally, A. Rehman et. al developed an energy-efficient mechanism in which the cold-exergy of LAES at regasification mode helps the pre-cooling phase of mixed refrigerant (MR) for the NG liquefaction (Ali; Rehman et al. 2020). The liquid air cold exergy during its discharge stage aids in cooling down the MR that is used for liquefying natural gas, thus decreasing the specific energy consumption (SEC). That type of novel approach of integration provides twofold benefits by enhancing the performance of the LAES discharging stage and the MR pre-cooling stage of the liquefaction process. Nevertheless, the components used for one process can impact the performance of the components used for the other process and also the same process. To compute the total exergy destruction of a process, conventional exergy analysis can be used (Ali Rehman, Qyyum, Zakir, et al. 2020)(Tirandazi et al. 2011). This method considers the transfer of energy to the surroundings as a sign of an inadequate system, whereas exergy analysis also consider the irreversibility of the system (Bejan, A., Tsatsaronis, G., Moran 1996). When analysing the entire energy system, conventional exergy analysis has limitations, such as its incapacity of detecting interactions among components (Mehrpooya;, Kalhorzadeh;, and Chahartaghi 2015). Consequently, advanced exergetic analysis (AEA) is used to identify the interactions among equipment of the process according to thermodynamic parameters. Avoidable (AV-ED) and unavoidable (UN-ED) exergy destructions are the two primary categories of exergy destruction in AEA. With regard to technological and economical limitations, it is unachievable to eradicate the unavoidable portion of exergy destruction. (Ali Rehman, Qyyum, Ahmad, et al. 2020); however, the avoidable portion of exergy destruction might be reduced by means of operational optimization techniques. Rehman et al. employed advanced exergy analysis to the SMR LNG operation and then utilized optimization approach to improve the efficiency. Using the multivariate Coggins optimization (MCO) method, an SEC value of 0.35 kWh/kg-LNG was calculated and it was found that 66% of the exergy destruction was avoidable (Ali Rehman et al. 2021). Yang et al. employed advanced exergetic analysis in the retorting process of oil shale and carried out optimal results for the mentioned process of the plant. Under the optimal conditions, their results revealed a 5.7% decrease in the altogether product-cost/exergy-unit and an increase in the exergetic efficiency from 35% to 37% (Yang et al. 2016). H. Ansarinasab used AEA to investigate a innovative approach to produce LNG using the process scheme of absorption-refrigeration (Ansarinasab and Mehrpooya 2017). In this paper, AV-ED and UN-ED parts of exergy destructions were extracted from the stand-alone BM liquefaction process (case-I), integrated processes of BM liquefaction and discharging mode of LAES (case-II); and case-III, where the modified coordinate descent (MCD) algorithm was employed to enhance the optimization of the integrated process, aiming to realize the utmost potential advantages of this proposed integration (Ali Rehman et al. 2019). The AEA was used to identify the sources of irreversibility and potential improvements; and corresponding comparison was executed among mentioned cases. Calculations were done to determine the unavoidable and avoidable portions of exergy destruction of each equipment of the processes. The findings of AV exergy destruction values determine the potential for future developments.

2. PROCESS DESCRIPTION

The following section describes the conventional single mixed refrigerant (SMR) BM liquefaction process (case-I), as shown in Figure 1. In this process, multistage compressors (K1-4) with a fixed efficiency of 80% are used to compress the mixed refrigerant (MR). Interstage water-coolers (E1-4) are incorporated into the system to assist in cooling the MR. These water coolers function as shell-and-tube heat exchangers, where cold water (CW) enters from the shell-inlet, cools the MR as it flows through, and exits as hot water (HW) with an elevated temperature at the shell-outlet. The coolers maintain a constant temperature of 40°C after each compressor stage. Water is used as the coolant in these interconnected coolers, and its temperature is assumed to be 20°C, dependent on the environmental conditions. The MR used in this process is a conventional mixture consisting of nitrogen, methane, ethane, and propane. Biomethane from stream-13 is introduced into the primary cryogenic heat exchanger (CHX-1), where it undergoes sub-cooling. It then passes through a Joule-Thomson (JT) valve (VLV-1) and expands, resulting in the production of liquefied biomethane (LBM) at a cryogenic temperature of -159°C. This LBM is ultimately stored in a dedicated tank. The estimated capacity of this continuous operational LBM plant is 157 metric tons per annum (MTPA).

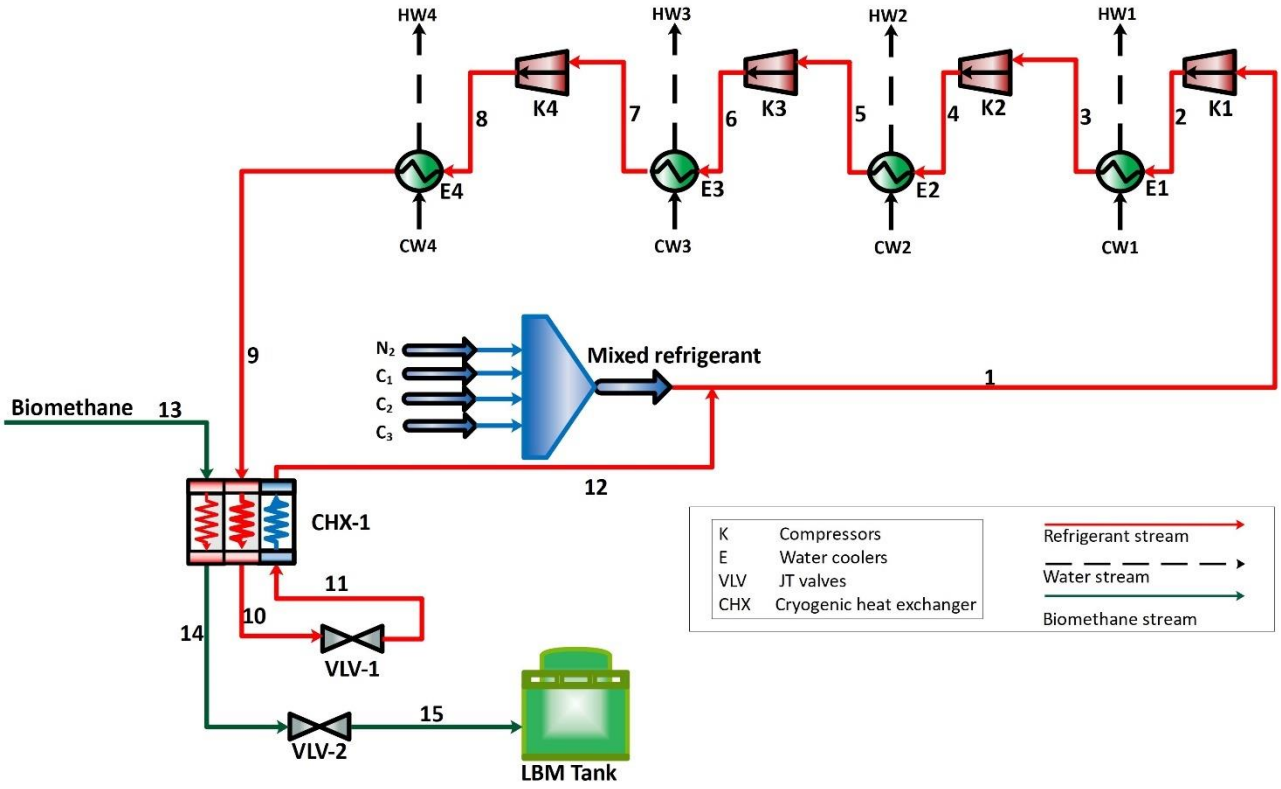

Figure 1 Flow diagram of the conventional LBM process (Ali et al. 2023)

The Figure 2 configuration is designed to take full advantage of the synergistic potential between the BM liquefaction and the regasification phase of LAES. This system increases energy efficiency and reduces operating costs by using cold-exergy produced during the discharging phase to help with the BM liquefaction process, and hot-exergy from the compressed mixed refrigerant to assist in the liquid air regasification process. The LNG heat exchanger (CHX-1) cools the input BM having feed conditions of 4.0 bar and 30°C to the value of -144 °C, and the heat exchanger (CHX-2) then sub-cools the stream-15 to the value of -154 °C and liquefies it. The pressure of mixed refrigerant stream-12 is reduced further to 1.2 bar by utilizing the JT valve (VLV-2) to acquire additional cooling of the liquefied biomethane. This study focuses on the generation of electric power from the third stage of the LAES system for the compression units of LBM plants. Furthermore, a considerable cold exergy resulted in the process, which can be used to boost the efficiency of biomethane liquefaction. Stream-19's LA is pressurized to 25.0 bar. Partially liquefied BM stream-15 is cooled with the cold exergy of the LA when it passes via CHX-2. The cold energy from the LA is then divided between MR and BM at CHX-1, reducing the stream-22 temperature to the value of 36°C. For additional increase in the air temperature and to improve the pre-cooling stage of mixed refrigerant, air passes through the heat exchanger (RHE-1), meaning no external heat source is needed to regasify the LA at the stream-23 having temperature of 89°C; thus, reducing the overall energy consumption for the given process. The hot exergy from the turbine's outlet (TG) is used at the heat exchanger (RHE-2) to maximize efficiency. The chamber of combustion is used to enhance the temperature of stream-25 to 1300°C, driving the turboexpander and producing power. Compression and cooling are done through four inter-connected compressors (K1-

4) and four watercoolers (E1-4). At the RHE-1 stream-8 is pre-cooled to 104.0°C having discharge pressure value of of 52.0 bar. E4 and LA cold-exergy are then utilized to take on the stream-9, before it passes through CHX-1, reducing the temperature of mixed refrigerant stream-11 to the -144°C. The expansion at the valve (VLV-1) containing Joule–Thomson effect allows the MR duty to reduce and gives the highest synergistic effect at CHX-1. The temperature of s tream-13 is increased to the value of 36°C at the end of the cycle. The process yields LBM having mass flow rate of 5.0 kg/s and the cryogenic temperature of -159°C. The discharging phase of the LAES process produces 4529 kW electrical power, decreasing the reliance on external power resources. This electric power can then be used by the LBM facilities for their compression units. In addition, the cold exergy acquired from the LAES system can enhance the efficiency of biomethane liquefaction.

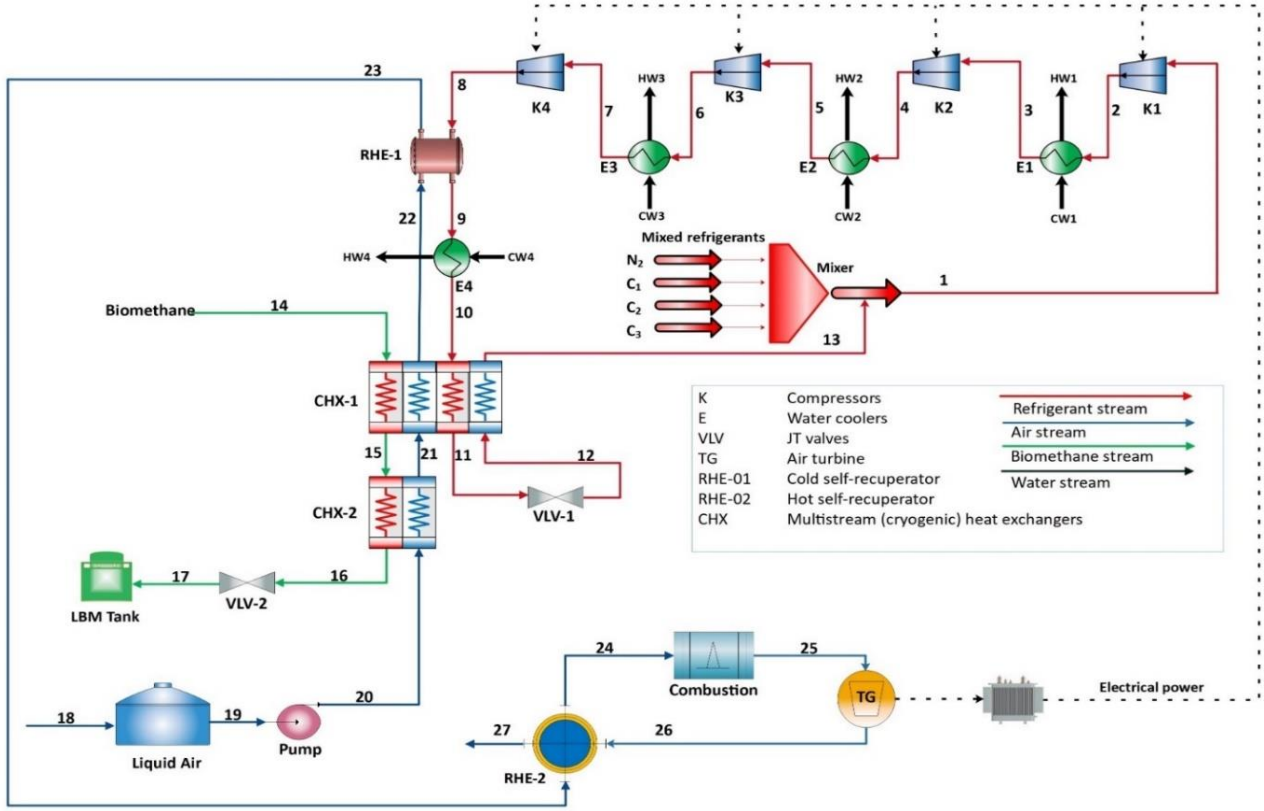

Figure 2 Process flow diagram of the LBM-LAES integrated systems (Ali; Rehman et al. 2020)

The LBM-LAES procedure was simulated utilizing Aspen Hysysys® V12 software. The Peng-Robinson state equations with the Lee-Kesler enthalpy model was used, as research has shown it to be the most reliable for gases, especially at elevated pressures (Lee and Kesler 1975). The Lee-Kesler model was selected to determine enthalpy and entropy using the Peng-Robinson equation (Peng and Robinson 1976). Feed conditions and compositions of integrated process are given in the Table 1.

Table 1: Compositions and feed conditions for biomethane and liquid air

Feed	Air	Biomethane
Temperature (°C)	−194.0	30.0
Pressure (bar)	1.5	4.0
Mass flow rate (kg/s)	5.33	5.0
Composition	mass fraction (%)	
Methane	−	100.0
Nitrogen	78.09	–
Oxygen	20.95	–
Argon	0.91	
Carbon dioxide	0.03	
Other gases	0.02	

3. RESULTS AND DISCUSSION

3.1. Conventional exergy analysis

Exergy analysis is used to estimate the destruction of exergy associated to equipment of the liquefaction system (Remeljej CW 2006). Exergy balance equation for all process components is provided in Equation 1 to calculate the values of the exergy destruction:

$$\dot{E}_F = \dot{E}_D + \dot{E}_P. \quad (1)$$

Here, the rate of product exergy, fuel exergy and exergy destruction are corresponded by $\dot{E}_P$, $\dot{E}_F$, and $\dot{E}_D$, respectively. The ratio of $\dot{E}_P$ and $\dot{E}_F$ is the exergy efficiency of each component of the process and presented in Equation 2 as:

$$\varepsilon = \frac{\dot{E}_P}{\dot{E}_F} \quad or \quad \varepsilon = 1 - \frac{\dot{E}_D}{\dot{E}_F}. \quad (2)$$

Figure 3 details the values of exergy destruction for all equipment for case-I, case-II and case-III processes. It can be observed that exergy destruction is decreased significantly for case-II and case-III as compared to case-I. Figure 4 provides the information of exergy destruction of each involved components with its corresponding exergy efficiency for the integrated LBM-LAES process (Case-II). As a result of the combination of the two energy systems, the process exergy efficiency is observed to have increased to 53%, in comparison with conventional SMR process which has an exergy efficiency of 35.5%. Figure 5 displays the portion of exergy destruction attributed to each component involved in the process, which is seen to be led by compressors and heat exchangers at 16.5% and 39.6% respectively (case-II). This difference is the primary reason of the decrease in efficiency of the liquefaction process. Integrating LBM and LAES has resulted in an overall decrease of exergy destruction by 15.70%, having additional electrical power generation of 4529 kW (case-II).

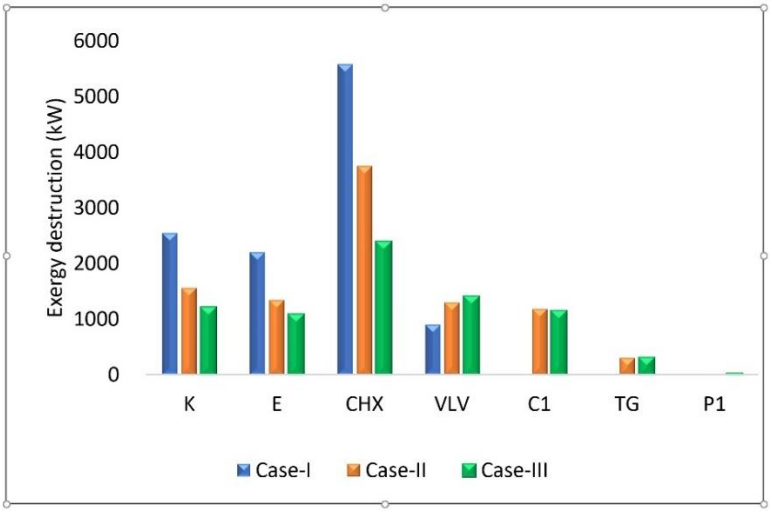

Figure 3 Exergy destruction of equipment involved in the processes in all cases

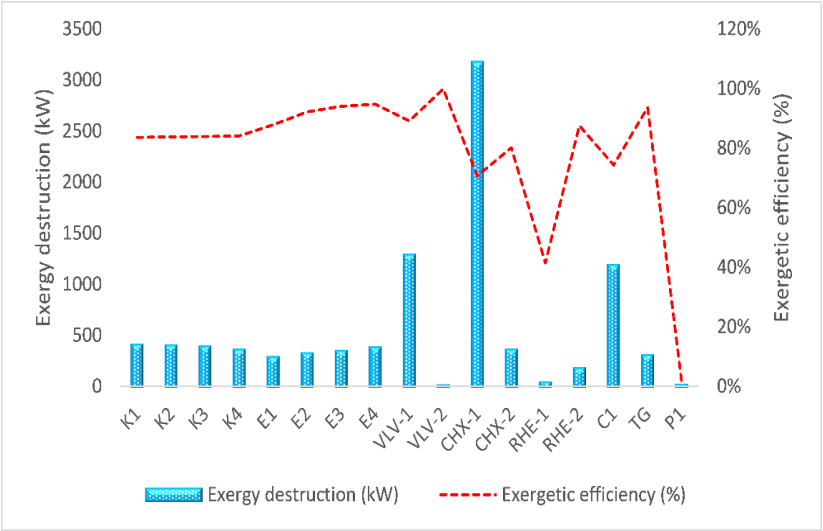

Figure 4 Exergy destruction of components with its corresponding exergy efficiency for integrated LBM-LAES process (Case-II)

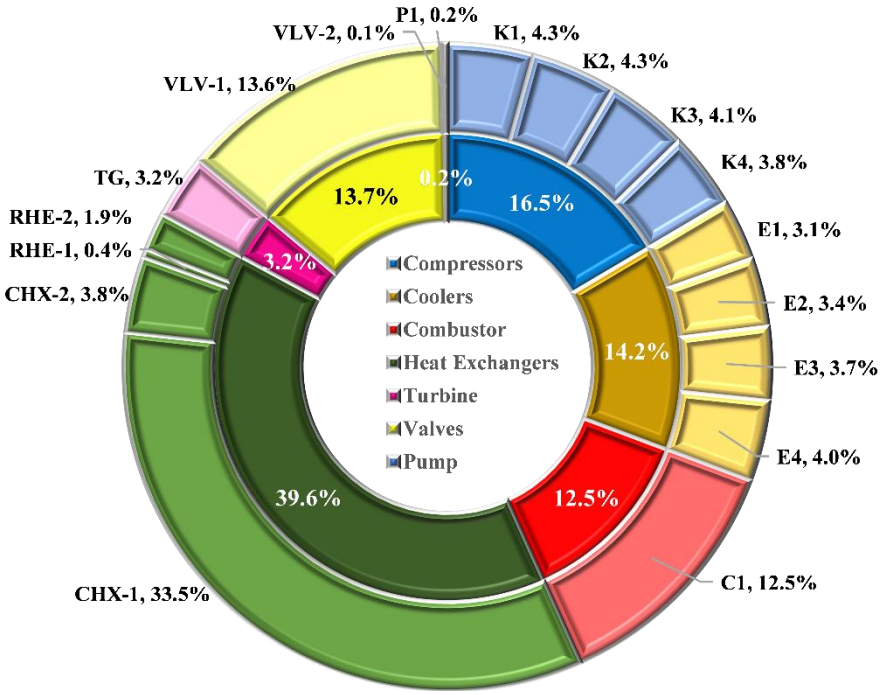

Figure 5 Detailed exergy destruction share of all equipment of integrated process

3.2. Advanced exergy analysis

The importance of advanced exergy analysis (AEA) is evident that it can detect sources of irreversibility which conventional exergy analysis cannot detect (Açikkalp, Aras, and Hepbasli 2014). It is further used to gauge the real improvement potential related to exergy destruction for the equipment of the liquefaction process (Morosuk and Tsatsaronis 2011). Moreover, AEA can classify exergy destruction in all the equipment of the entire process. Additionally, AV-ED and UN-ED can be linked using Equation 3 as stated below:

$$\dot{E}_{D,k} = \dot{E}_{D,k}^{AV} + \dot{E}_{D,k}^{UN} \quad (3)$$

The terms $\dot{E}_{D,k}^{AV}$ and $\dot{E}_{D,k}^{UN}$ describe the AV-ED and UN-ED of the k_{th} component, respectively. Despite technological limitations, the AV-ED can be minimized through the implementation of suitable technical advancements in the equipment (Mehrpooya et al. 2018). It is essential to be aware that certain components of UN-ED are contingent on unavoidable factors. To lower the AV-ED, design and operational optimization techniques can be employed. The AV-ED and UN-ED can be determined using Equation 4 and Equation 5, respectively (Morosuk and Tsatsaronis 2011).

$$\dot{E}_{D,k}^{UN} = \dot{E}_{P,k} \left(\frac{\dot{E}_{D,k}}{\dot{E}_{P,k}} \right)^{UN} \quad (4)$$

$$\dot{E}_{D,k}^{AV} = \dot{E}_{D,k} - \dot{E}_{D,k}^{UN} \quad (5)$$

Figure 6 describes the avoidable and unavoidable portions of exergy destruction with corresponding avoidable exergy saving potential for case-II. The values of avoidable exergy destruction (AV-ED) is used to measure the improvement potential of a process. Figure 6 also reveals that there is a large potential to increase the thermodynamic efficiency of power-consuming equipment such as compressors, pumps, and turbines by reducing the AV-ED. Results show that the cryogenic heat exchangers (CHX_{1-4}) are the major source of irreversibilities in the whole process; especially CHX-1 contains 78% of unavoidable exergy destruction; while pump contains the maximum potential to reduce exergy destruction. On the other hand, Figure 7 demonstrates the rigorous comparison among mutual components used in the case-I, case-II and case-III; and provides the exergy saving potential in case-II and case-III as compared to case-I. Hence, innovative integration of LBM and LAES processes in reduces the AV-ED and increases the exergy saving potential while case-III provides additional exergy saving potential for the integrated process.

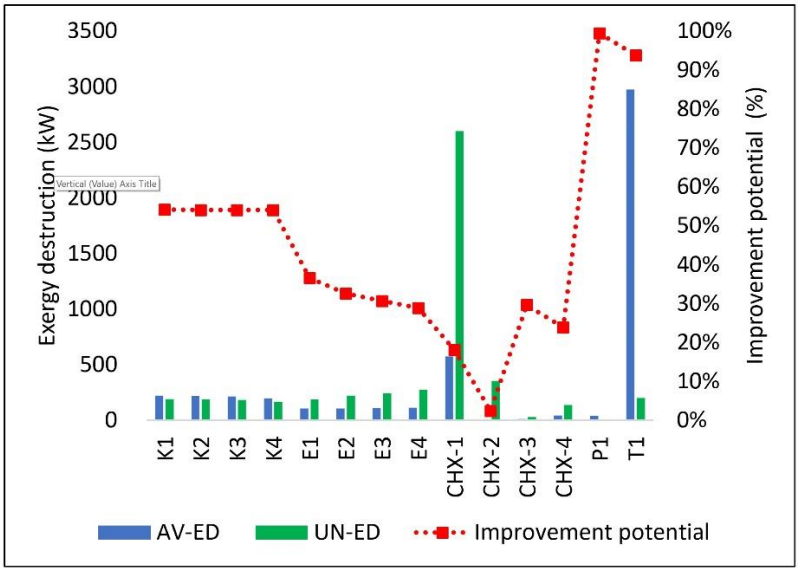

Figure 6 Avoidable and unavoidable parts of exergy destruction with corresponding improvement potential

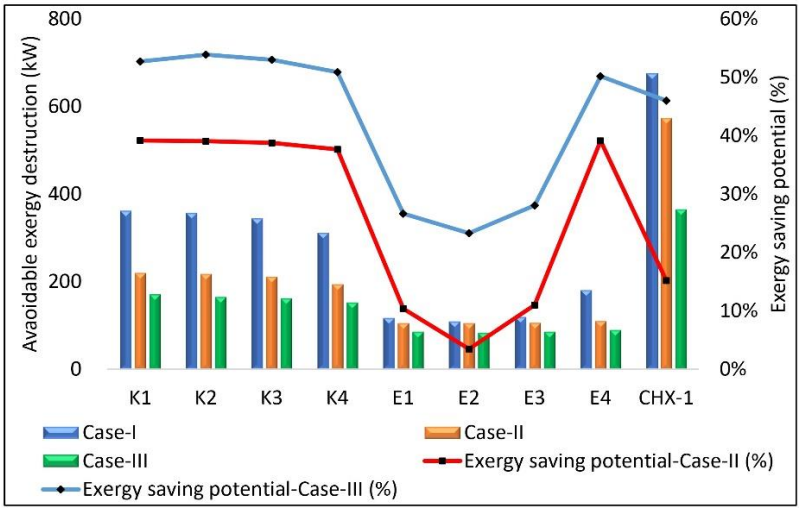

Figure 7 Avoidable parts of exergy destruction with corresponding exergy saving potentials for case-II and case-III as compared to case-I

4. CONCLUSION

In this research, the SMR process for liquefying biomethane was modified by combining the discharging mode of LAES. This combination created a synergistic effect by leveraging the hot- and cold-exergy of the LBM and LAES systems, respectively. The compressed mixed refrigerant hot-exergy of SMR LBM system was used to enhance the LAES regasification phase, while the cold-exergy of LAES aided the BM liquefaction process. To analyse the multiple aspects of this new integration, advanced exergetic analysis was employed due to the reason that conventional exergy analysis would not have been able to pinpoint the sources of entropy generation for the given process. The results of the conventional exergetic analysis showed a 15.9% drop in destruction of exergy and an additional 4529kW power produced by the gas turbine. Additionally, the process exergy efficiency was increased to 53%, compared to the 35.5% efficiency of the conventional process. The advanced exergy analysis resulted that 50% of the total exergy destruction in the modified process could be avoided. Compressors and turbine contain maximum potential to improve having avoidable exergy destruction of 54% and 94%, respectively; while cryogenic heat exchangers and coolers have major portions of unavoidable exergy destruction of 62% and 83%, respectively. A rigorous comparison was observed among case-I, case-II and case-III in terms of avoidable exergy destruction and maximum exergy saving potential was observed in case-III.

5. REFERENCES

Abdul, Muhammad et al. 2021. “Weed Colonization-Based Performance Improvement Opportunities in Dual-Mixed Refrigerant Natural Gas Liquefaction Process.” (November 2020): 297–312.

Açikkalp, Emin, Haydar Aras, and Arif Hepbasli. 2014. “Advanced Exergy Analysis of an Electricity-Generating Facility Using Natural Gas.” *Energy Conversion and Management* 82: 146–53.

Ali, Rehman et al. 2023. “Improvement Potential Detection of Integrated Biomethane Liquefaction and Liquid Air Energy Storage System.” *Journal of Energy Storage*.

Ansarinasab, Hojat, and Mehdi Mehrpooya. 2017. “Advanced Exergoeconomic Analysis of a Novel Process for Production of LNG by Using a Single Effect Absorption Refrigeration Cycle.” *Applied Thermal Engineering* 114: 719–32. http://dx.doi.org/10.1016/j.applthermaleng.2016.12.003.

Bejan, A., Tsatsaronis, G., Moran, M. 1996. *Thermal Design and Optimization*.

Capra, Federico, Francesco Magli, and Manuele Gatti. 2019. “Biomethane Liquefaction: A Systematic Comparative Analysis of Refrigeration Technologies.” *Applied Thermal Engineering* 158(May): 113815. https://doi.org/10.1016/j.applthermaleng.2019.113815.

Lee, Byung Ik, and Michael G Kesler. 1975. “A Generalized Thermodynamic Correlation Based on Three-Parameter Corresponding States.” *AIChE Journal* 21(3): 510–27.

Mehrpooya;, Mehdi, Masoud Kalhorzadeh;, and Mahmood Chahartaghi. 2015. “Investigation of Novel Integrated Air Separation Processes, Cold Energy Recovery of Liquefied Natural Gas and Carbon Dioxide Power Cycle.” *Journal of Cleaner Production* 113: 411–25.

Mehrpooya, Mehdi, Mohammad Mehdi Moftakhari Sharifzadeh, Masoud Jalali Zonouz, and Marc A Rosen. 2018. “Cost and Economic Potential Analysis of a Cascading Power Cycle with Liquefied Natural Gas Regasification.” *Energy Conversion and Management* 156: 68–83.

Morosuk, T., and G. Tsatsaronis. 2011. “Comparative Evaluation of LNG - Based Cogeneration Systems Using Advanced Exergetic Analysis.” *Energy* 36(6): 3771–78. http://dx.doi.org/10.1016/j.energy.2010.07.035.

“Paris Agreement.” 2016. *United Nations Treaty Collection. 8 July 2016. Archived*. https://treaties.un.org/pages/ViewDetails.aspx?src=TREATY&mtdsg_no=XXVII-7-d&chapter=27&clang=_en.

Pellegrini, Laura Annamaria, Giorgia De Guido, and Stefano Langé. 2018. “Biogas to Liquefied Biomethane via Cryogenic Upgrading Technologies.” *Renewable Energy* 124: 75–83.

Peng, Ding-Yu, and Donald B Robinson. 1976. “A New Two-Constant Equation of State.” *Industrial & Engineering Chemistry Fundamentals* 15(1): 59–64.

Penga, Xiaodong et al. 2019. “Liquid Air Energy Storage Flexibly Coupled with LNG Regasification for Improving Air Liquefaction.” *Applied Energy* 250(May): 1190–1201. https://doi.org/10.1016/j.apenergy.2019.05.040.

Qyyum, Muhammad Abdul et al. 2019. “Nitrogen Self-Recuperation Expansion-Based Process for Offshore Coproduction of Liquefied Natural Gas, Liquefied Petroleum Gas, and Pentane Plus.” *Applied Energy* 235(August 2018): 247–57. https://doi.org/10.1016/j.apenergy.2018.10.127.

Rehman, Ali; et al. 2020. “Integrated Biomethane Liquefaction Using Exergy from the Discharging End of a Liquid Air Energy Storage System.” *Applied Energy* 260: 114260. https://doi.org/10.1016/j.apenergy.2019.114260.

Rehman, Ali et al. 2019. “Integrated Biomethane Liquefaction Using Exergy from the Discharging End of a Liquid Air Energy Storage System.” *Applied Energy*.

Rehman, Ali, Muhammad Abdul Qyyum, Fatima Zakir, et al. 2020. “Investigation of Improvement Potential of Modified Single Mixed Refrigerant (MSMR) LNG Process in Terms of Avoidable and Unavoidable Exergy Destruction.” *2020 3rd International Conference on Computing, Mathematics and Engineering Technologies (iCoMET)*.

Rehman, Ali, Muhammad Abdul Qyyum, Ashfaq Ahmad, et al. 2020. “Performance Enhancement of Nitrogen Dual Expander and Single Mixed Refrigerant LNG Processes Using Jaya Optimization Approach.” *Energies* 13(12).

Rehman, Ali et al. 2021. “Single Mixed Refrigerant LNG Process: Investigation of Improvement Potential, Operational Optimization, and Real Potential for Further Improvements.” *Journal of Cleaner Production* 284: 125379. https://doi.org/10.1016/j.jclepro.2020.125379.

Remeljej CW, Hoadley AFA. 2006. “An Exergy Analysis of Small-Scale Liquefied Natural Gas (LNG) Liquefaction Processes.” *Energy* 31: 2005–19.

She, Xiaohui et al. 2018. “Preliminary Study of Liquid Air Energy Storage Integrated with LNG Cold Recovery.” *Energy Procedia* 158: 4903–8. https://doi.org/10.1016/j.egypro.2019.01.702.

“SHELL LNG OUTLOOK.” 2019. https://www.shell.com/energy-and-innovation/natural-gas/liquefied-natural-gas-lng.

Tirandazi, Behnam, Mehdi Mehrpooya, Ali Vatani, and S. M.Ali Moosavian. 2011. “Exergy Analysis of C2+ Recovery Plants Refrigeration Cycles.” *Chemical Engineering Research and Design* 89(6): 676–89.

Wang, Guan Bang, and Xin Rong Zhang. 2017. “Thermodynamic Analysis of a Novel Pumped Thermal Energy Storage System Utilizing Ambient Thermal Energy and LNG Cold Energy.” *Energy Conversion and Management* 148: 1248–64. http://dx.doi.org/10.1016/j.enconman.2017.06.044.

Yang, Qingchun et al. 2016. “Framework for Advanced Exergoeconomic Performance Analysis and Optimization of an Oil Shale Retorting Process.” *Energy* 109: 62–76. http://dx.doi.org/10.1016/j.energy.2016.04.076.

Zakir, Fatima et al. 2020. “LNG Supply Chain: Challenges, Opportunities and Future Prospects.” *2020 3rd International Conference on Computing, Mathematics and Engineering Technologies: Idea to Innovation for Building the Knowledge Economy, iCoMET 2020*.

Zhang, Tong et al. 2018. “Thermodynamic Analysis of a Novel Hybrid Liquid Air Energy Storage System Based on the Utilization of LNG Cold Energy.” *Energy* 155: 641–50. https://doi.org/10.1016/j.energy.2018.05.041.

#96: A comparison of photovoltaic sun tracking methods

Fariba MOGHADDAM[1], Parham QANAAT[2], Mohsen SALIMI-KHANGAH[3]

1 University of Applied Sciences Western Switzerland, Sion - Switzerland, fariba.moghaddam@hevs.ch
2 University of Kurdistan, Sanandaj - Iran, parham.qanaat@uok.ac.ir
3 Amirkabir University of Technology, Tehran - Iran, mohsen.salimi@aut.ac.ir

Abstract: Solar energy is one of the most sustainable sources of energy that many countries are investing in. Photovoltaic technologies are becoming increasingly popular due to their renewable energy perspective and low environmental impact. However, the efficiency of commercial fixed photovoltaic panels is under 27% as a reduced amount of solar radiation can be captured during the day. Solar tracking systems are gaining ground as they propose to optimize the angle of incidence of the sun's rays on photovoltaic panels to address the low efficiency issue of fixed PV panels.

This study compares the different methods of solar tracking systems with single-axis movable PV panels to quantify the increase in energy production versus fixed PV panels. A simple sun tracking method based on the sun-path diagram is compared with more advanced approaches using the incident angle of the sun ray, measured by a sun position sensor. The electric output power produced by the photovoltaic system is also used to track the sun's position with a high degree of accuracy. Additionally, other hybrid strategies combining different sun tracking algorithms are proposed to improve the low PV efficiency during cloudy days.

The performance of the solar tracking system is evaluated by measuring the power output of the PV panels in both static and dynamic positions. A test bench of several single-axis movable PV panels is used to compare the performance of the different sun trackers simultaneously, under the same weather conditions. Key parameters such as solar radiation, sun position in the sky and generated output voltage and current are considered to evaluate the effectiveness of the various sun tracking methods. The experimental results demonstrate significant benefits of sun tracking control strategies by improving the efficiency of PV panel systems up to 16%.

Keywords: Photovoltaic Technology, Sun Tracking System, Sun Sensor, Single-axis movable PV Panel

1. INTRODUCTION

Photovoltaic energy systems are currently the world's most broadly employed renewable energy technologies. Although some experimental solar systems have achieved efficiencies of close to 50%, the efficiency of photovoltaic panels using Crystalline Silicon technology has reached nearby 27% (Al-Ezzi and Ansari, 2022). As the inherent limitations of fixed PV panels result in suboptimal energy conversion, sun tracking technology may be addressed as a promising solution by dynamically adjusting the position of the solar panel to track the sun's movement. The photovoltaic panel is headed towards the sun to optimize the angle of incidence (the angle at which the sun hits a solar panel). A single-axis sun tracker tilts on a singular axis to follow the sun from east to west as it moves throughout the course of each day to increase the electric power and improve the poor efficiency of the photovoltaic panel.

This study compares different methods of solar position tracking systems using single-axis movable PV panels to quantify the increase in energy production versus fixed PV panels. A simple sun tracking method based on the sun-path diagram is compared with more advanced approaches using the incident angle of the sun ray, measured by a sun position sensor. Additionally, the electric output power of the photovoltaic system itself is used to serve as an indicator to track the sun's position with a commendable level of accuracy. Furthermore, during cloudy days when solar panel efficiency drops off by 10% to 25%, a hybrid sun tracker combining different types of algorithms is proposed to improve the photovoltaic energy output. The study provides a better understanding of the effectiveness, benefits and limitations of the different single-axis sun tracking approaches. Moreover, some original tactics are suggested to improve the different sun tracking methods.

2. TEST BENCH

A real-time embedded controller (CompactRIO of National Instruments) and a Web-based monitoring platform are developed to carry out this study (*Moghaddam and Forestal, 2023*). A test bench of 6 single-axis movable PV panels is used to facilitate the comparison of the different sun tracking methods, simultaneously under the same weather conditions. Measurements such as solar radiation, sun position in the sky, output voltage and current generated are considered to evaluate the different sun tracking methods.

As shown in Figure 1, the infrastructure used for the tests is composed of:

- A pool of 6 movable Single-axis movable PV panels fully equipped with different sensors such as sun position, output voltage, current, PV temperature as well as solar radiation.
- Two real-time embedded controllers of National Instruments with FPGA and CPU modules, IO modules and Ethernet connection allowing remote data monitoring. Each controller is connected to 3 PV panels.
- A common gateway interface with standard telecommunication protocols (WebSocket) for secure data transmission between the local infrastructure and the remote Web-based interface.
- A Web-based Interface offering an online monitoring panel which connects the users/programmers to the remote infrastructure. The Web interface proposes a user-friendly interface with live video streaming of the test site and data visualisation as well as different data logging features.

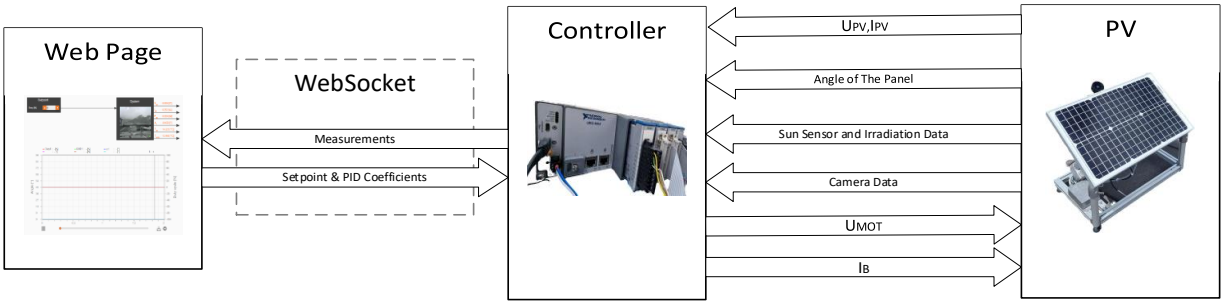

Figure 1 Infrastructure composed of movable single-axis movable PV panels, local controller, bidirectional data transfer and Web-based interface with remote monitoring tools.

3. SOLAR POSITION

In order to track the sun as the earth rotates, the sun’s position in the sky by means of solar angles is needed. We start by defining the solar altitude, zenith and azimuth angles required for following the sun across the sky. Depending on the level of accuracy and complexity required, the solar angles can be calculated by using a variety of analytical, empirical or experimental methods. Once the sun's position in the sky is determined, it becomes crucial to calculate the optimal tilt angle of the PV panel. The tilt angle is determined to maximize the power output of the panel by ensuring the most efficient alignment with the sun's rays.

3.1. Solar angles definition

The solar angles refer to the position of the sun in the sky relative to a particular location on the Earth's surface. The solar angles are defined with two parameters: the azimuth angle and the altitude angle. The azimuth angle describes the horizontal position of the sun in the sky and changes throughout the day as the sun moves across the sky from east to west. The altitude angle describes the vertical position of the sun in the sky and changes throughout the day as the sun rises and sets, with a maximum angle at noon. Figure 2 shows that the azimuth and altitude angles can be used to calculate the direction in which the sun's rays are striking a particular location on the Earth's surface, which is important for determining the optimal orientation and the tilt angle for single-axis movable PV panels (Zhang *et al.,* 2021).

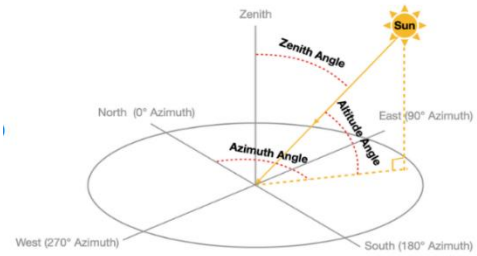

Figure 2 Solar angles.

3.2. Solar angles calculation

The solar angles can be calculated using a variety of methods, depending on the level of accuracy and complexity required. The three common methods are:

- Analytical methods: These methods employ mathematical equations to calculate the solar angles using inputs such as latitude, longitude, date, and time. The SPA (Solar Position Algorithm) is a widely used analytical method that provides accurate estimation of solar angles for any location on Earth. Other analytical methods include the NREL (National Renewable Energy Laboratory) Solar Position Algorithm and the ISES (International Solar Energy Society) Solar Radiation Data Manual.
- Empirical methods: These methods use statistical analysis of historical data to estimate the solar angles for a particular location. These methods are less accurate than analytical methods, but can still provide useful estimates for practical applications. One example of an empirical method is the use of lookup tables based on historical solar radiation data.
- Experimental methods: Experimental methods use sensors or instruments to directly measure the solar angles in real time. For example, a sun tracker equipped with a photodiode sensor can be used to measure the azimuth and altitude angles of the sun and adjust the orientation of the solar panel accordingly.

In general, the most accurate method for calculating solar angles is an analytical method, but this requires access to accurate data on the location, date, and time. In this study, we use analytical methods for sun tracking based on open-loop strategy and experimental methods with real-time measurements for sun tracking based on closed-loop strategy.

3.3. Analytical method

We use several mathematical relations to reach an algorithm for finding the sun's azimuth and altitude angles before calculating the optimal tilt angle of the PV panel (Duffie and Beckman, 2013).

The zenith angle is an important solar angle which is used to describe the solar position in the sky. It can be calculated by the following equation:

Equation 1: The zenith angle of the sun.

$$cos\,\theta_z = cos\,\varphi\,cos\,\delta\,cos\,\omega + sin\,\varphi\,sin\,\delta$$

Where:

- θ_z = Zenith angle of the sun (º)
- φ = Latitude of the PV location (º)
- δ = Angle of the declination (º)
- ω = Hour angle (º)

As for the angle of declination, it can be calculated as follows:

Equation 2: Angle of declination.

$$\delta = 23.45° \, sin\left[\frac{2\pi(N-81)}{365}\right]$$

Where N is the day number defined as the number of days elapsed in a given year up to a particular date (e.g., the 2nd of February corresponds to 33).

The hour angle, ω, is the angular displacement of the Sun from the focal point and it is given by (Khatib and Elmenreich, 2016):

Equation 3: Hour angle. $$\omega = 15^{\circ}(AST - 12h)$$

Where AST is apparent or true solar time and is given by the daily apparent motion of the true or observed sun. It is based on the apparent solar day, which is the interval between two successive returns of the sun to the local meridian. Apparent solar time is given by (Khatib and Elmenreich, 2016):

Equation 4: Apparent solar time. $$AST = LMT + EoT \pm \frac{4^{\circ}}{LSMT - LOD}$$

The LMT is the local meridian time, LOD is the longitude, LSMT is the local standard meridian time, and EoT is the equation of time.

The LSMT is a reference meridian used for a particular time zone and is similar to the prime meridian, used for Greenwich Mean Time.

Equation 5: Local standard meridian time. $$LSMT = 15^{\circ}(T_{GMT})$$

The EoT is the difference between apparent and mean solar times, both taken at a given longitude at the same real instant of time.

Equation 6: Equation of time. $$EoT = 9.87\,sin(2B) - 7.53cosB - 1.5sinB$$

Equation 7: Parameter B. $$B = \frac{2\pi(N-81)}{365}$$

The solar altitude angle (α_s) is the complement of the zenith angle:

Equation 8: The solar altitude angle. $$\alpha_s = 90^{\circ} - \theta_z$$

Finally, the solar azimuth angle (γ_s) is equal to the angular displacement from south of the projection of beam radiation on the horizontal plane (Duffie and Beckman, 2013). It should be noted that the displacements east of south are negative and west of south are positive.

Equation 9: The azimuth angle of the sun. $$\gamma_s = sign\,(\omega)\left|cos^{-1}\left(\frac{cos\,\theta_z\,sin\,\varphi - sin\,\delta}{sin\,\theta_z\,cos\,\varphi}\right)\right|$$

After calculating the position of the sun in the sky with its altitude, zenith and azimuth angles, it is necessary to calculate the optimal tilt angle of the PV panel. The optimal tilt angle refers to the angle at which the panel should be tilted to maximize its power output, as shown in figure 3. This angle is influenced by various factors, including the latitude of the location, the time of year, and the panel's orientation. The equation 10 is used to calculate the tilt angle based on the altitude and azimuth angles of the sun, as well as the observer's latitude.

Equation 10: Tilt angle calculation of single-axis PV. $$\beta_{Tilt} = tan^{-1}(tan\theta_z|cos(\gamma - \gamma_s)|)$$

Surface azimuth angle (γ) is the deviation of the projection on a horizontal plane of the normal to the surface from the local meridian, with zero due south, east negative, and west positive. The surface azimuth angle γ will be 180◦ or −180◦ depending on the sign of the solar azimuth angle:

Equation 11: Surface azimuth angle. $$\gamma = \begin{cases} 180^{\circ} & if \quad \gamma_s > 0 \\ -180^{\circ} & if \quad \gamma_s \leq 0 \end{cases}$$

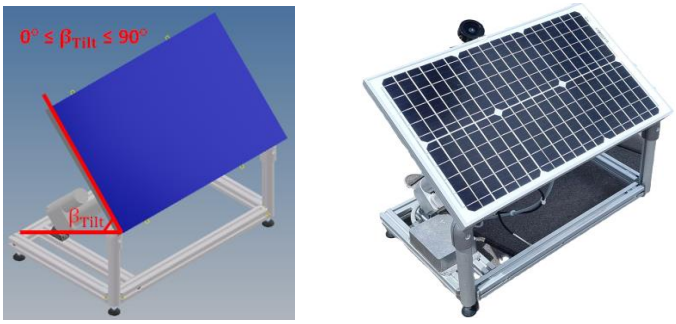

Figure 3 Mechanical structure of movable single-axis PV panel with its tilt angle.

3.4. Experimental method

For experimental method, we use a sun sensor to measure the incident angle of the sun ray in orthogonal axes (Solar MEMS). The incidence angle of the sun ray in orthogonal axes is measured by a 4 quadrants photodetectors device. The sunlight is guided to the detector through a window above the sensor. Depending on the angle of incidence, the sunlight induces photocurrents in the four quadrants of the detector. Angle X and Angle Y specify the angular position of the incident sun ray inside the field of view of the chosen sun sensor, as shown in Figure 4.

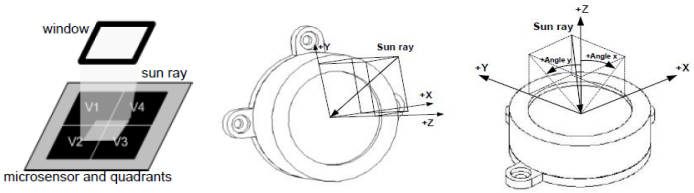

Figure 4 Sun sensor based on a 4 quadrants photodetectors device and angles X and Y of the incident ray on the solar sensor.

Angles X and Y of the incident ray can be obtained with a simple set of equations involving the four photodiode voltages generated by the sun sensor. The accuracy of the sensor increases when receiving radiation perpendicular to the sensor, close to zero degrees in X and Y. This is an outstanding feature that makes it suitable for tracking applications.

4. SUN TRACKING STRATEGIES

This chapter presents the different sun tracking strategies by highlighting the advantages and limitations of each approach. A simple open-loop control strategy based on the sun-path diagram is compared to two different closed-loop strategies based on feedback measurements such as sun position and electric power. The state of the art refers to many hybrid strategies combining different types of algorithms to show how the photovoltaic energy output can be boosted under different weather conditions (Gutierrez *et al.,* 2020), (Karafil, *et al.,* 2015). We propose a hybrid control using a switching mechanism based on the radiation level to switch between the different control strategies depending on the weather conditions.

4.1. Open-loop control strategy

The open-loop control strategy for solar tracking relies on calculating the position of the sun in the sky described in chapter 3.3 to adjust the tilt angle of the single-axis movable PV panel. Two different methods have been implemented. The first method uses the equations 1 to 9 for calculating the position of the sun as well as the equations 10 and 11 for calculating the PV tilt angle. These equations can be simply implemented, for example as a block diagram in LabVIEW.

The second method uses the Ephem Python package (Rhodes, B.C., 2011) to calculate the sun's position in the sky, based on the date, time and location of the PV panel. Ephem is a powerful astronomy package that allows us to determine the precise position of celestial objects with high accuracy. Based on this library, a Python code has been developed to give the sun's position as a function of time and PV location. All the data saved in a database in CSV format is called in LabVIEW every 5 minutes to calculate the PV tilt angle setpoint, as shown in Figure 5. This method takes advantage of both LabVIEW and Python, allowing to exploit the easy-to-use LabVIEW graphical programming environment and the powerful mathematical and data processing capabilities of Python.

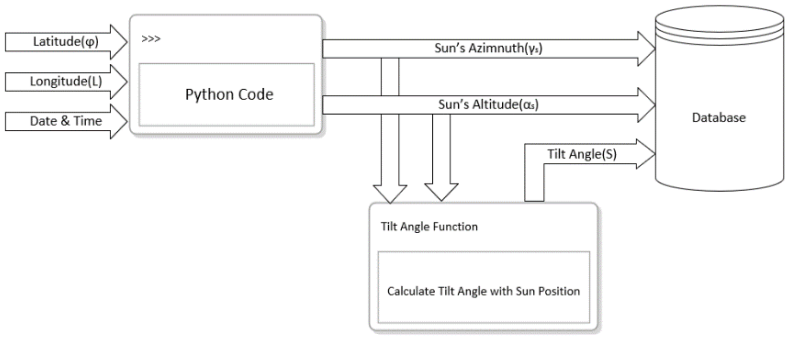

Figure 5 Block diagram for calculating the solar position via Ephem Python library and a Database.

Upon analyzing the database, we discovered that the sun's movement along its path within a duration of less than 5 minutes has a negligible impact on the tilt angle of the panels. Hence, a 5-minutes waiting time for each iteration has been defined as shown in the flowchart of Figure 6.

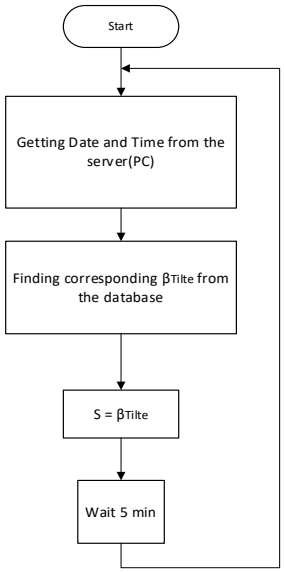

Figure 6 Flowchart for sun tracking based on open-loop control strategy.

4.2. Closed-loop control strategy based on solar sensor

A LabVIEW program has been developed to calculate the angles X and Y of the incident ray through the 4 quadrants photodetectors output signals. Considering the use of a horizontal single-axis movable PV panel and the requirement to track the sun's movement from west to east, only the Y angle was utilized. Through the sensor calibration process, the optimal Y angle of 15° was determined to achieve maximum output power at the PV panel location. As a result, an algorithm has been developed to calculate the optimal tilt angle to reach the maximum amount of power from the sunlight, as seen in the flowchart of Figure 7. Furthermore, the algorithm incorporates a 30-seconds waiting time for each iteration, which has been determined through extensive experimentation and analysis of the system's outputs and the time impact.

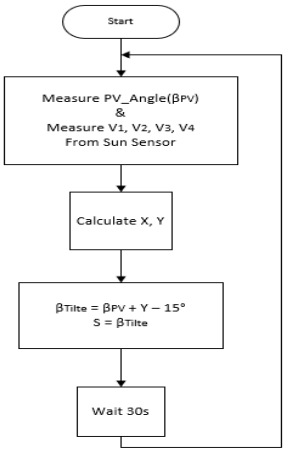

Figure 7 Flowchart for sun tracking based on a closed-loop control strategy with a solar sensor.

4.3. Closed-loop control strategy based on measured electric power

This method uses the measured electric output power produced by the photovoltaic system to track the sun's position with a good degree of accuracy. Figure 8 shows how the optimal tilt angle of the PV panel can be calculated in order to maximize its power output.

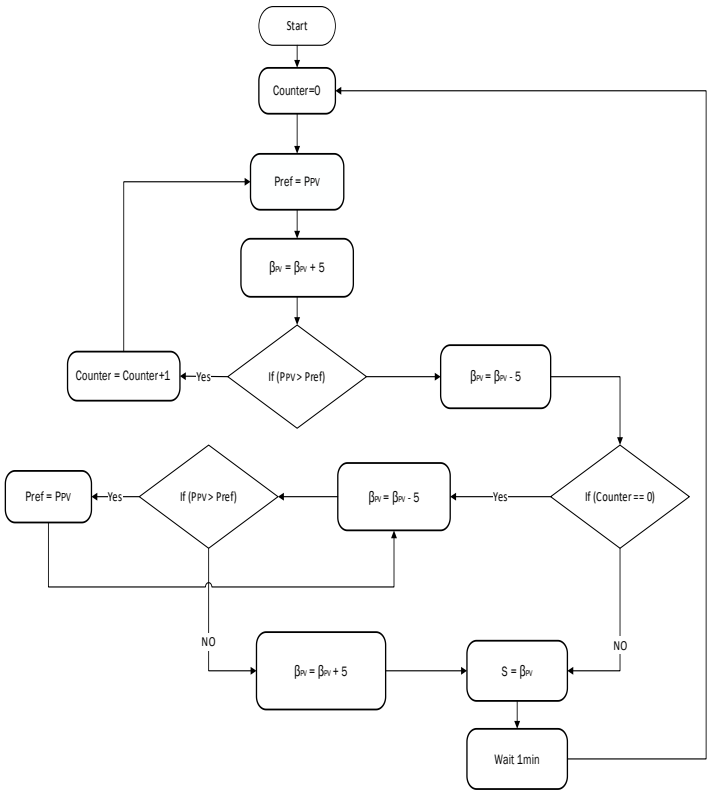

Figure 8 Flowchart for sun tracking based on measured electric power.

The algorithm starts by setting the actual measured electric power of the PV panel as a reference. To begin calculating the optimal PV angle, 5 degrees are added to the actual PV angle. If the power of the PV panel increases, after being compared to the previous power reference, it will be updated to the new value, and another 5 degrees are added to the PV angle. This process continues while the power reference is smaller than the actual PV power. However, when the power of the PV panel does not increase in the first step, 5 degrees are subtracted from the PV angle, and the power is checked again. This iterative process continues by updating the power reference and subtracting 5 degrees from the PV angle until the power reference becomes greater than the actual PV power. Once the power reference exceeds the actual PV power, the algorithm determines the optimal tilt angle setpoint and sends it for further action. In this algorithm, a 1-minute waiting time has been set through a series of experiments conducted under various conditions, considering the movement of the sun and the execution time requirement.

4.4. Hybrid control strategy

Hybrid control is a control strategy that combines two or more different control techniques to achieve better performance in a system. In a hybrid control system, the different control techniques are integrated in a coordinated way, taking advantage of each technique. The system switches between the different control techniques based on certain conditions or events to optimize the system's overall performance. Hybrid control is often used in complex systems where a single control strategy may not be sufficient to achieve the desired performance. In PV solar tracking systems, hybrid control can combine open-loop and closed-loop control strategies to maximize the amount of solar energy captured by the PV panel, for example by adapting possible changes in weather conditions and sun position.

In this section, we discuss the design and implementation of a hybrid control system for the solar tracking system that combines open-loop strategy described in chapter 4.1 and closed-loop control strategy described in chapter 4.2. The hybrid control system uses a switching mechanism based on the radiation level measured by a pyranometer to switch between the two control strategies depending on the current weather conditions. The hybrid control system is designed to operate in real time, to adjust continuously the orientation of the panel to maximize the amount of sunlight captured by the panel. Figure 9 shows the flowchart of the hybrid control strategy, combing the open-loop strategy and the closed-loop strategy using a pyranometer. The key element for switching decision is the amount of radiation (E_{solar}) which varies with the weather condition.

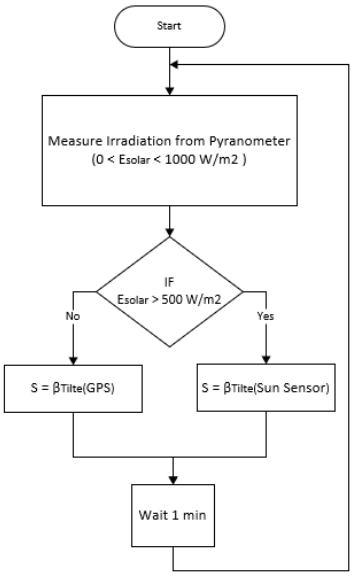

Figure 9 Flowchart of the hybrid controller using a pyranometer for switching mechanism.

5. EXPERIMENTATION RESULTS

The performance of the different sun tracking controllers described in chapter 4 has been evaluated based on the generated electric power and has been compared with the power produced by a fixed inclined PV panel, without considering the energy consumption of the controller or the electric motor. The fixed inclined PV panel was oriented to the geographical south with an optimum annual tilt. All the experiments have been conducted on the roof of the Campus “Energypolis” at University of Applied Sciences Western Switzerland in Sion.

In Figure 10, the power generated by the fixed PV panel on a sunny day in May 2023 is compared to the power output of the PV sun tracker with an open-loop controller, as well as the PV sun tracker with closed-loop controllers based on a sun sensor and measured electric power. During the experimentation time while the fixed PV panel showed an average power of 14.59W, the open-loop controller achieved an average output power of 16.35W, while the closed-loop controller based on measured electric power reached an average output power of 16.77W and the closed-loop controller based on a sun sensor performed an average output power of 16.93W. These results indicate that the open-loop controller increased the output power by 12.06%. The closed-loop controllers, based on measured electric power and sun sensor feedback, exhibited similar performance, increasing the output power by 14.94% and 16.03% respectively. Additionally, during the time interval from 10:51 am to 11:15 am, the angles of the three sun trackers closely matched that of the fixed panel, resulting in similar output power. Notably, at 10:03 am, there was a significant instantaneous increase in output power of up to 35.1% for the open-loop controller and up to 41% for the closed-loop controllers compared to the fixed panel.

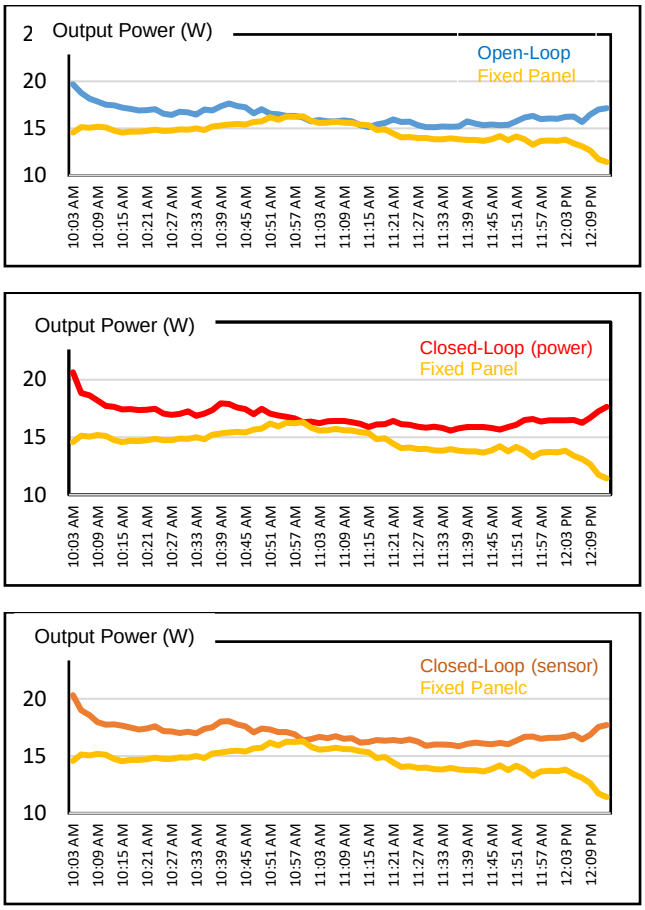

Figure 10 Output electric power of the PV sun trackers with different open-loop and closed-loop controllers.

Figure 11 shows the power generated by a hybrid control system during a partly cloudy day in May 2023. During the sunny time intervals, where a higher amount of radiation is recorded, the controller switched to closed-loop mode by using the sun sensor feedback. When the irradiation dropped with cloudy sky, the controller switched to open-loop mode to ensure the sun's path tracking. We have observed even when the cloud cover was thick and the sun sensor failed to detect the sun's rays, the controller could maintain the correct path. During the time interval "overlap of angle", the angle of the hybrid controller closely matched that of the fixed panel with similar output power. For the tests of Figure 11, the hybrid controller recorded an overall increase of 6% in average output power, compared to the fixed panel.

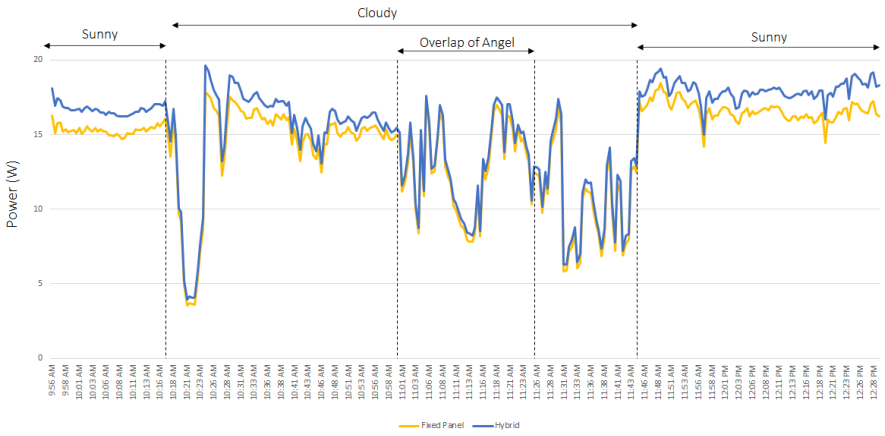

Figure 11 Output power of the PV sun tracker with hybrid controller switching between open-loop and closed-loop controllers.

6. CONCLUSION

The experimental results in this study demonstrate some significant benefits of implementing sun tracking control strategies by improving the performance of PV panel systems up to 16%. Both open-loop and closed-loop control techniques proved to be effective in optimizing the output power of the single-axis movable PV panel compared to a fixed panel configuration, especially during the sunny days.

The hybrid control, combining the advantages of both open-loop and closed-loop control approaches, demonstrates its adaptability and improved performance, particularly during variable weather conditions. In fact, the hybrid control strategy provides better performance compared to either open-loop or closed-loop control separately. By combining the strengths of both control strategies, the system is adapted to different weather conditions and to changes in the sun's position more effectively for a better solar energy capture. In addition, the hybrid control strategy helps to increase the efficiency of the system by reducing the amount of energy required to track the sun. By switching between open-loop and closed-loop modes based on weather conditions, the system enhances energy production when conditions are less favorable. In this way, the hybrid system is more robust to weather disturbances and uncertainties.

Regarding the disadvantages of sun tracking control strategies, it is important to acknowledge the additional complexity they introduce to the system. Implementing sun tracking requires additional sensors, hardware, and advanced control algorithms, as well as the inclusion of switching mechanisms. This increases the cost of the system in design and development, as well as in maintenance. Particularly, the hybrid control strategy requires careful design and testing to ensure that the switching mechanism works correctly with desired performance. Another drawback of the sun trackers is the energy consumption of the movable parts (motors and actuators) as well as the used sensors. For evaluating the output power performance of the sun trackers, we have neglected the energy consumption of the different elements.

Finally, these findings highlight the importance of sun tracking control strategies in maximizing the efficiency and output power of PV panel systems, making them a valuable consideration for solar energy applications. Further research and development in this field can lead to even more efficient control techniques, for example through biaxial PV panels, contributing to the widespread adoption and utilization of solar energy in various settings.

7. ACKNOWLEDGEMENT

The work presented in this paper is carried out by two Iranian students during their master exchange stay of 3 months in Switzerland. The project is co-funded by the “Swissuniversities” Development and Cooperation network (SUDAC) program and the Swiss program for international research of Swiss National Science Foundation (SNSF). These programs seek targeted support for collaboration between the various types of Swiss higher education institutions and their partners from the Global South to achieve an excellent standard of education and research on global challenges.

8. REFERENCES

Al-Ezzi, A.S. and Ansari, M. (2022). 'Photovoltaic Solar Cells: A Review', Applied System Innovation, MDPI Open Access, 2022

Moghaddam, F. and Forestal, M. (2023). 'Remote real-time research platform for control engineering', REV2023 20th International Conference on Remote Engineering and Virtual Instrumentation, 2023.

Zhang, Y., Wijeratne, L.O., Talebi, S. and Lary, D.J. (2021). 'Machine learning for light sensor calibration', Sensors 21, 2021.

Duffie, J.A. and Beckman, W.A. (2013). 'Solar engineering of thermal processes', John Wiley & Sons, 2013.

Khatib, T. and Elmenreich, W. (2016). 'Modeling of photovoltaic systems using Matlab', John Wiley & Sons, 2016.

Rhodes, B.C. (2011). 'PyEphem: astronomical ephemeris for Python', Astrophysics Source Code Library, 2011.

Gutierrez, S., Rodrigo, P.M., Alvarez, J., Acero, A. and Montoya, A. (2020). 'Development and testing of a single-axis photovoltaic sun tracker through the Internet of Things', Energies 13, 2020.

Karafil, A., Ozbay, H., Kesler, M. and Parmaksiz, H. (2015). 'Calculation of optimum fixed tilt angle of PV panels depending on solar angles and comparison of the results with experimental study conducted in summer in Bilecik, Turkey in 2015', 9th International Conference on Electrical and Electronics Engineering (ELECO), 2015.

#97: Study on the effect of inter-cellular gaps on the thermal profile of solar photovoltaic systems

Shubham KUMAR[1], PMV SUBBARAO[1]

1 Dept. of Mech. Eng., Indian Institute of Technology Delhi, Hauz Khas, New Delhi, 110016, Delhi, India.

Abstract: Solar photovoltaics (PV) is a leading means of renewable power generation. One of the biggest challenges PV systems faces is the increase in cell temperature in the real field which leads to a reduction in its efficiency and lifetime. To propose a viable cooling method, it is imperative to study the thermal behaviour of PV systems using CFD modelling. Most of the researchers have modelled a PV module as a single or multi-layered cuboidal body, ignoring its internal geometrical complexities. This study implements an improved geometric model of a PV module that rightfully considers PV cells as different individual domains with encapsulant-filled intercellular gaps and investigates its effect in the obtained temperature profile vis a vis a conventional geometrical model. Conjugate heat transfer analysis is performed using an experimentally validated CFD model under three different wind speeds. K-ω SST and Surface to surface were used as turbulence and radiation models, respectively. The results reveal that the improved geometrical model consistently predicts higher cell temperature than the conventional model. For a PV module of 88% packing fraction and at a wind speed of 1m/s, the maximum and mean differences are 3.52^{O}C (or 6.52%) and 2.42^{O}C (or 4.65%), respectively. The values of these percentage differences remain approximately constant even at higher wind speeds. The incorporation of intercellular gaps also impacts the nature of the thermal profile by producing a greater difference of 3.35^{O}C (or 6.18%) in the prediction of the temperature of hotter cells compared to only 1.15^{O}C (or 2.31%) in the case of colder cells. This study suggests that the encapsulant-filled poorly conducting intercellular gaps have a considerable effect on the thermal characteristics of a PV system at all wind speeds and hence, should be incorporated into the geometry for more accurate and reliable results.

Keywords: Solar PV Module, Heat Transfer, Cell Temperature, CFD Analysis, Thermal Profile.

1. INTRODUCTION

Solar photovoltaic (PV) systems are being readily used to convert solar energy directly into electrical power. The efficiency of PV devices has also increased exponentially in the last two decades leading to its remarkable growth. However, solar PV systems have some challenges in the real field which diminish their final returns. Low solar irradiation, dust deposits, and an increase in PV temperature are some of those challenges (Sharaf *et al.* 2022). Due to these factors, solar PV systems very rarely are able to produce the same output power that is claimed by the manufacturers. The increase in cell temperature causes two problems in a PV system. Firstly, the real field PV efficiency diminishes at a significant rate which depends on the cell material. For instance, a crystalline silicon PV module loses 0.45% of relative PV efficiency for each $^{\circ}$C increase in the cell temperature(Dupré *et al.* 2015, 2016). Secondly, an increase in cell temperature decreases the lifespan of the PV systems. It has been estimated that a 6°C increase in cell temperature can shorten the lifespan of a PV system by up to 85% (Sun *et al.* 2017). To tackle these problems, it is important to study the thermal behaviour of solar PV systems and design suitable cooling methods. Many researchers have used various tools to analyse the thermal behaviour of solar PV systems in different irradiance and wind conditions.

Computational Fluid Dynamics (CFD) has been used by several researchers for the thermal analysis of a solar PV system placed in a given surroundings. CFD enables us to obtain the thermal profile of the system, visualize the fluid flow around the system and accordingly suggest possible ways of cooling. However, these CFD-based simulations can give accurate results only if we provide accurate inputs about the system, for instance, the thermal properties, emissivity, optical losses, etc. How the geometry of a solar PV system has been modelled for running CFD simulations can significantly affect the accuracy of the obtained results as well as the computational cost. A solar PV module is a complex appliance and has several notable geometrical complexities. It typically consists of 5 different layers. Apart from a top glass layer and a bottom Tedlar layer, there are two layers of encapsulants (usually EVA) in the middle of which PV cells are placed at a very small gap from each other. Thus, the cell layer is actually not continuous. It is actually a group of several individual cells placed at a small gap with each other and floating between the two encapsulant layers. During the lamination of all layers, the encapsulant material melts and fills these intercellular gaps.

Several researchers have assumed a PV module as a simple cuboidal body filled with a uniform and homogenous material (Jubayer *et al.* 2016, Jaszczur *et al.* 2018, Dabaghzadeh and Eslami 2019). This oversimplification leads to the assumption of uniform heat generation throughout the module. This is an inaccurate assumption since the majority of the heat is generated in the PV cells only. besides the whole module is assumed to have uniform thermal conductivity and specific heat capacity. This would mean that heat can be diffused at a uniform rate throughout the module which is again a very inappropriate assumption. In an actual system, the thermal conductivity (k) of glass, EVA and tedlar are only 1 $Wm^{-1}K^{-1}$, 0.3 $Wm^{-1}K^{-1}$, and 0.2 $Wm^{-1}K^{-1}$ which are very low compared to that of silicon (k=150 $Wm^{-1}K^{-1}$) (Mahdi *et al.* 2021).

A few researchers have assumed a PV module as a multi-layered cuboidal domain (Nižetić *et al.* 2016, Marinić-Kragić *et al.* 2018). This geometrical model assumes a continuous cell layer comprising all PV cells with one front layer consisting of glass and EVA at top and one back layer consisting of EVA and tedlar at the bottom. This multi-layered model may be considered as an upgradation over the single-layered geometrical model as it enables assuming all heat generation in the cell layer only and distinguishes the thermal properties of cells from other layers. However, it still ignores the effects of poor thermal conductance of EVA-filled intercellular gaps. Thus, the obtained thermal profile can be substantially different from that of an actual PV module. Moreover, the total area of all PV cells is less than the area of the PV module. This will affect the calculation of the heat source per unit volume. Apparently, these conventional single-layered and multi-layered geometrical models are a very simplified version of an actual module and can produce errors in the final result. As CFD is a costly tool, it is expected to provide as accurate results as possible. Improving the geometrical model of a PV module and incorporating the effects of the intercellular gaps may help in improving the accuracy and reliability of the results obtained by CFD modelling. On the other hand, if incorporating the intercellular gaps has a negligible effect on the final results then, the conventional geometrical models can be preferable for their simplicity and lower computational cost. Any such conclusion can be drawn only by comparing the results obtained using the geometrical models with and without the intercellular gaps. This study aims to perform this comparison and draw out conclusions regarding the magnitude of effect of intercellular gaps on the thermal profile of PV systems and whether those should be incorporated in the CFD modelling or not.

2. METHODOLOGY

CFD analysis of solar PV systems involves the conduction occurring inside the system as well as the fluid flow occurring around the system leading to convective heat transfer. Radiation heat transfer between the PV system and surroundings also needs to be considered properly. The following subsections provide a brief summary of the different steps of CFD modelling.

2.1. Geometry

Two different geometries of a PV module have been created for the present analysis. The first geometry has assumed 12 individual silicon cells (13cm x 20cm each) at a gap of 5mm from each other while the second conventional geometry replaces these all cells with a single continuous silicon layer having no intercellular gaps. Both geometries include one front domain representing glass and top EVA layer, and one back domain representing back EVA and Tedlar layers. The intercellular gap in the novel geometry is assumed to be filled with the same material as the back domain. The Aluminium

frame has not been incorporated in both geometries because of the very high thermal conductivity of Aluminium (Mahdi *et al.* 2021) and the very low surface area of frames compared to the module (Kant *et al.* 2016). The PV module (55cm x 65cm x 0.45cm) is kept at the centre of a cuboid-shaped fluid domain, as shown in Figure 1. The view of the novel module geometry, seen along its normal, is also depicted. The wind has been assumed to be at angle α with X-axis and parallel to X-Z plane.

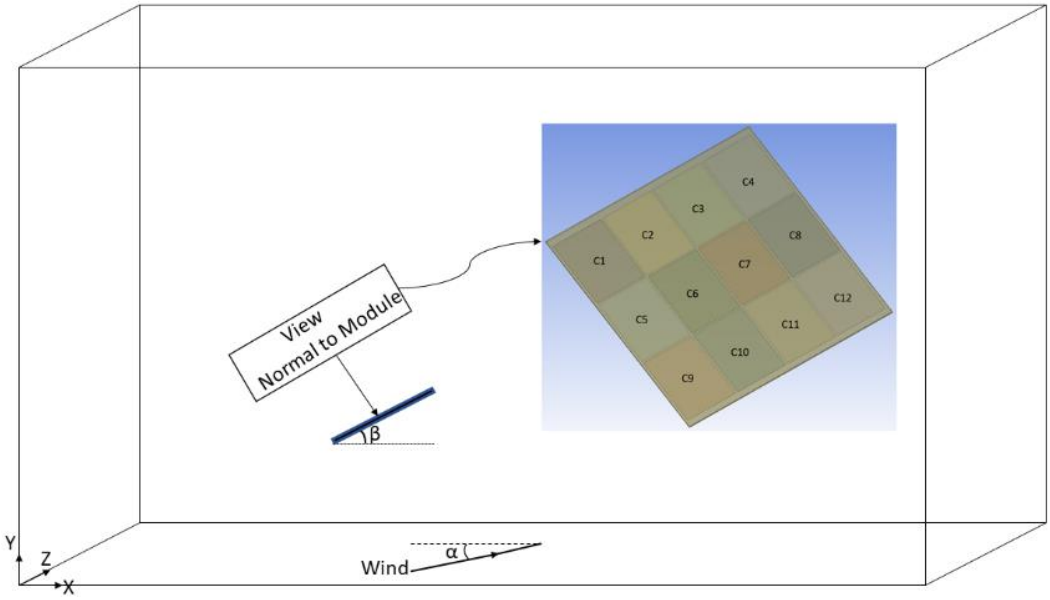

Figure 1 Diagram showing the position of module, direction of wind and geometry of module when seen along its normal.

2.2. Meshing

Ansys ICEM software has been used to perform structured meshing in the whole fluid and solid domain, as shown in Figure 2(a) and Figure 2(b) respectively. To get accurate gradients near the solid surface and obtain the boundary layer growth properly, the element size near the PV module has been kept very fine starting from 10^{-5}m, as shown in Figure 2(c). The growth rate of the cells near the module is lower than 1.3 in all directions. A similar mesh has been created for the conventional geometry.

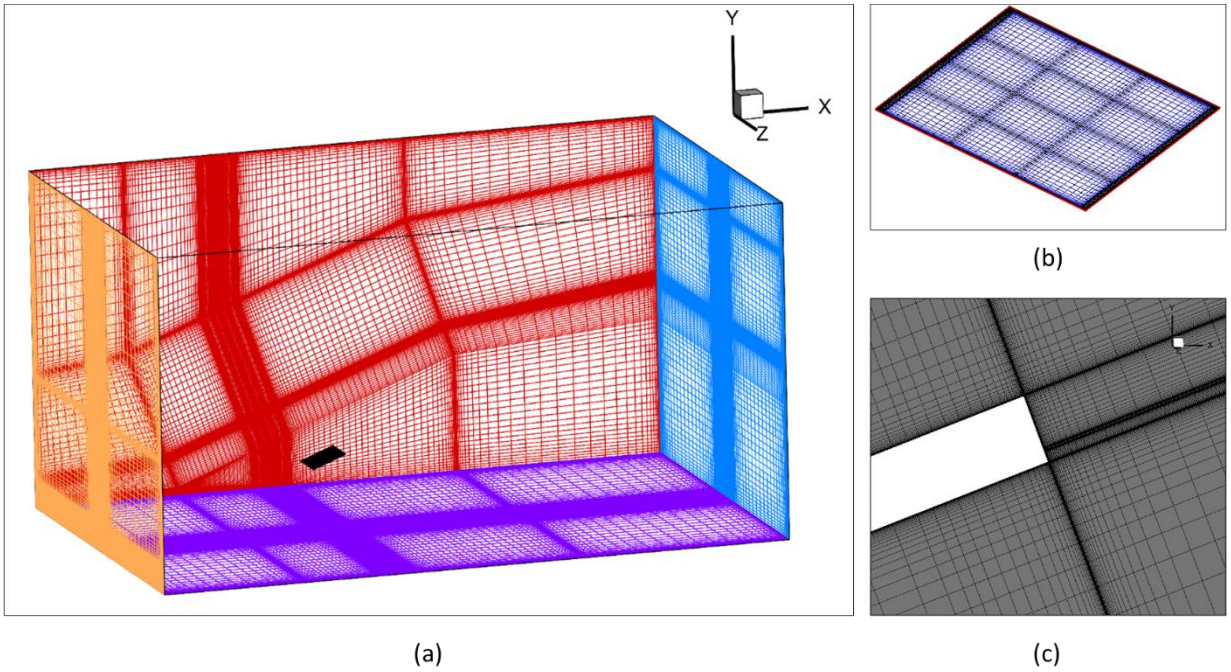

Figure 2 Structured meshing in (a) whole fluid domain (b) solid domain (c) near the PV module

2.3. Governing Equations and Heat Source Calculations

The described model along with continuity, momentum (Navier-Stokes) and energy equations has been solved by a finite volume method based commercial software Ansys Fluent 2021R1 with a pressure-based solver in steady-state conditions. k-ω SST has been used as the viscous model because of its accuracy in simulating turbulent flow and predicting flow separation occurring due to any bluff body (PV module in the present case). Besides k-ω SST model is accepted to be accurate for both low Reynolds number (Re) and high Re flows as it resembles the k-ω standard model in the inner boundary layer and gradually switches to k-ε model in regions away from the walls. Surface to surface model has been used for radiation heat transfer modelling and view factor calculations.

As efficiency and heat generation rate depends on the operating cell temperature, a temperature-dependent heat source has been assumed for the cell domain. The parasitic heat absorption by glass, EVA and tedlar layers has been ignored, as recommended by (Kumar and Subbarao 2023). In the case of conventional geometry, the rate of heat generation per unit volume (Q') is calculated using Equation 1 and dividing it by cell thickness.

Equation 1: Rate of heat generation per unit area in the single cell domain of the conventional geometry.

$$Q' = \tau a I - P = I(\tau a - \eta)$$

Where: 'τ' is the transmittance, 'a' is the absorptance, 'I' is the incident solar intensity, and P is the electric power produced. η denotes the electric efficiency of the PV module, as given by Equation 2.

Equation 2: PV efficiency as a function of cell temperature

$$\eta = \eta_{STC}(1 + \beta(T - T_{STC})$$

Where: η_{STC} is the PV efficiency in standard testing conditions (STC), T_{STC} is the reference temperature of 25°C, T is the operating cell temperature and β is the temperature coefficient.

On the other hand, in the case of the novel geometrical model, the total area of cell domains is less than the area of module (or single cell domain of the conventional geometry). Hence, in order to accommodate the same amount of heat, Q' is calculated using Equation 3.

Equation 3: Rate of heat generation per unit volume in each cell domain in the novel geometry.

$$Q' = \frac{I(\tau a - \eta)}{\mathrm{f}}$$

Where: 'f' is the packing density of the PV module defined as the total area of all cells divided by the area of the module.

2.4. Boundary Conditions and Solver Setup

The windward and leeward faces of the fluid domain have been given boundary conditions of velocity inlet of given wind velocity (V) and pressure outlet of zero gauge pressure, respectively. Ground has been assumed to be a no-slip wall and all remaining faces of the fluid domain are assumed as walls with free slip to simulate the faraway atmosphere. The emissivity of front and back surfaces has been taken as 0.85. The temperature of the sky and ground have been calculated using Equation 4 and Equation 5, respectively (Kumar and Subbarao 2023).

Equation 4: Temperature of the sky in terms of ambient temperature

$$T_s = 0.0552\ \mathrm{T_o^{1.5}}$$

Equation 5: Temperature of ground in terms of ambient temperature

$$T_g = T_o + a_r I$$

Where T_s, T_g and T_o denote sky, ground and ambient temperature respectively. $'a_r'$ denotes the absorption coefficient of the ground and depends on the material of the ground. It has been assumed to be zero in the present study.

Pressure velocity coupled equations have been solved using the SIMPLE method, the gradients have been discretized using the least squares cell method and all other quantities have been discretized using the second-order upwind method. For better convergence, under-relaxation factors of 0.3, 0.6 and 0.6 have been used for momentum, k and ω, respectively. For convergence, the residual for the energy equation has been kept as 10^{-6} and the residual for all other equations, including the continuity equation, has been kept as 10^{-5}.

2.5. Grid Independence Test

The maximum cell temperature for V = 1.5ms, α = 45° and I = 837W/m^2 was obtained using different mesh sizes. The results for the case of the novel geometrical model have been plotted in Figure 3. After 10 million elements, there is negligible change in the results. Based on this, the mesh having 11.8 million elements has been chosen as the optimum mesh for further analysis. A similar grid independence test has been performed in the case of the conventional geometrical model and a mesh with 9 million elements was found to be optimum in that case.

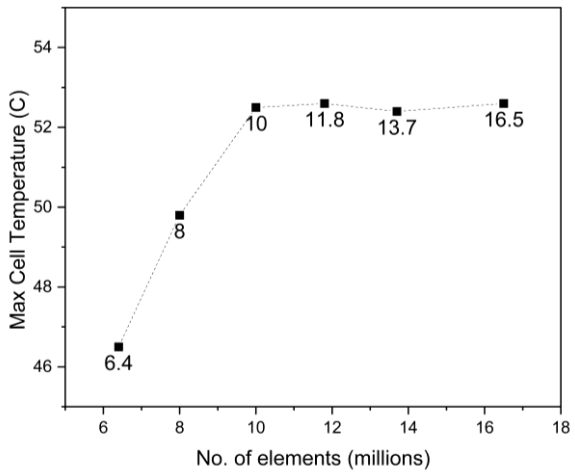

Figure 3 Grid Independence test depicting maximum cell temperature for different mesh sizes.

3. RESULTS

3.1. Validation of CFD Model

(Nižetić *et al.* 2016) had performed an experimental and CFD study which measured the cell temperature at 4 locations of a c-Si PV module tilted at 20^o with horizontal in real field conditions. The numerical results obtained using the present CFD analysis have been compared with the experimental as well as numerical results published by those authors. The values of all relevant parameters such as reference efficiency, emissivity of front and back surfaces, optical loss factor, etc. have been taken the same as those reported in the same study. For the case of V = 2.7 m/s, α = 0^o and I = 837 W/m^2, the results have been plotted in Figure 4. The present CFD model is able to predict the experimental values of temperatures of sensors 1-4 with an accuracy of 7.3%, 1.1%, 1.1% and 9.6%, respectively. As the present CFD model is able to predict each local temperature with an error of less than 10%, the model is considered to be validated and usable for further analysis. The main reasons of these errors should be instrumental errors, uncertainty in the value of optical losses and emissivity, neglecting the mounting structure in the CFD modelling, etc.

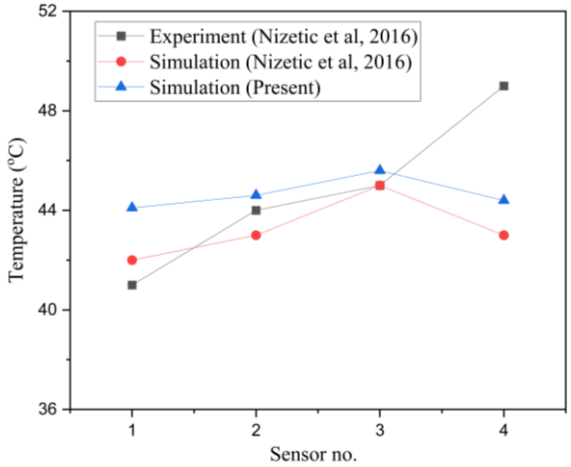

Figure 4 Comparison of CFD simulation results with experimental results

3.2. Comparison of thermal profiles obtained using the novel and conventional geometries.

Figure 5 (a) and Figure 5 (b) depict the thermal profiles of the cell layer of the PV module at V=3m/s, α=0^o, and I=850W/m^2 for the novel geometry and the conventional geometry, respectively. Figure 6 shows the same result in the form of a radar chart using temperatures obtained at 12 points located at the centre of all cell domains. Apparently, both thermal profiles have similarities in the patterns and predict the hottest and coldest temperatures at similar locations. For instance, both geometric models predict cell 6 to be the hottest and cells 4 and 12 to be the coldest.

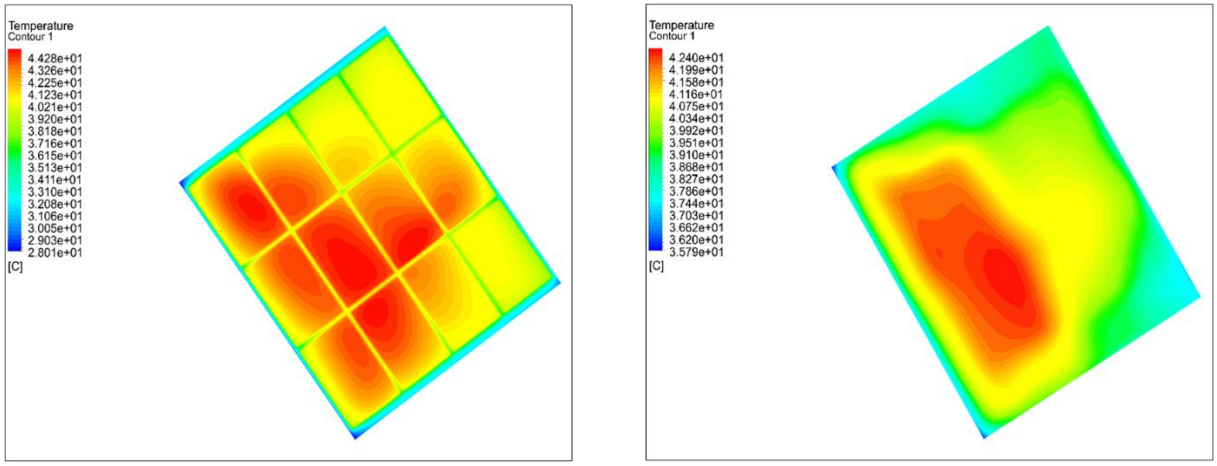

(a) (b)

Figure 5 Temperature contours of PV module obtained using (a) novel geometrical model and (b) conventional geometrical model

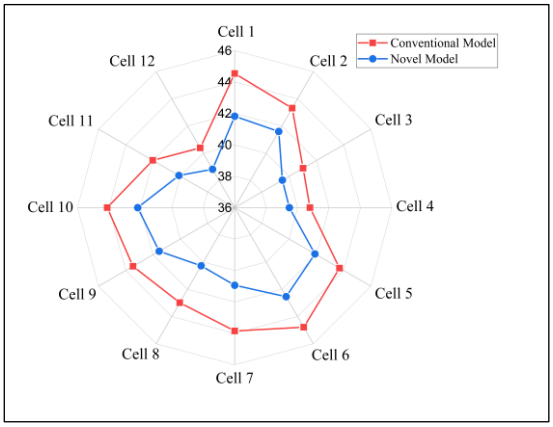

Figure 6 Comparison of temperature at all cell centre locations obtained using both geometrical models at V=3m/s

Similar observations can be made in the radar charts drawn corresponding to V=1m/s and V=5m/s in Figure 7(a) and Figure 7(b), respectively. However, in all cases, the novel geometry consistently predicts higher temperatures than the conventional model for all cell domains. Table 1 shows that the maximum difference between the cell temperature predicted using these two geometrical models can be as high as 3.52°C for V=1m/s. The mean temperature difference is also significant viz. 2.42°C at V=1m/s and decreases to 2.02°C and 1.82°C at higher wind speeds of 3m/s and 5m/s, respectively.

Table 1: Comparison between cell temperature predicted using novel and conventional geometrical models.

Wind speed (V)	Max Temp Diff	Mean Temp Diff
1 m/s	3.52°C (6.52%)	2.42°C (4.65%)
3 m/s	2.91°C (6.64%)	2.02°C (4.71%)
5 m/s	2.89°C (7.01%)	1.82°C (4.64%)

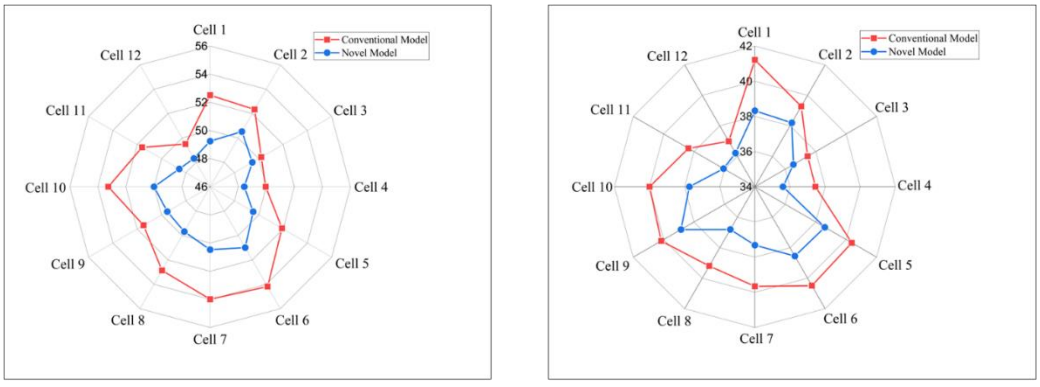

(a) (b)

Figure 7 Comparison of temperature at all cell centre locations obtained using both geometrical models at (a) V=1m/s and (b)V=5m/s.

3.3. Discussions

The prediction of higher cell temperature in the novel geometrical model compared to the conventional model can be mainly attributed to two factors. Firstly, as explained in Section 2.3, due to less than 100% packing fraction of a PV module, the rate of heat generation per unit volume calculated in the case of the present geometry is higher than that in a conventional geometry. This will lead to a higher value of heat generation per unit volume within cell domains leading to higher cell temperature. In reality, the heat generated in EVA filling the intercellular gaps and module's borders is non-zero but still very small compared to the heat generated in the PV cells (Hanifi *et al.* 2018)**.** Hence, the present geometrical model, though more complex, represents a more accurate description of the actual thermal characteristics of a PV module.

Secondly, in a conventional geometry having a continuous cell layer of high thermal conductivity, all of the heat generated gets very readily diffused to the whole layer giving comparatively a more uniform thermal profile. However, in reality, EVA is almost 500 times less thermally conducting than Silicon and consequently, the heat generated in a particular cell will not be so readily diffused to the non-cell domains due to the high thermal resistance of intercellular gaps. This would consequently mean that the cell domains themselves will have to absorb a higher amount of heat leading to higher temperatures. These arguments also explain why the temperature of intercellular gaps and module borders are considerably lower than cells in Figure 5(a). The present novel geometrical correctly incorporates the effect of low thermal conductivity of EVA-filled intercellular gaps and hence, arguably provides a more accurate thermal profile of PV modules than a simplified conventional geometry.

It can also be observed from the results that the difference between the mean cell temperature obtained using both geometrical models remains significant at all wind speeds. This means that consideration of intercellular gaps in the geometrical model remains important at low as well as high wind speeds. However, the PV performance and lifetime depend on the absolute value of cell temperature and hence, the absolute difference in the prediction of the cell temperature becomes more crucial. As reported in Table 1, the absolute value of both mean and maximum temperature differences continue to decrease at higher wind speeds. Conversely, this indicates that at low wind speed, CFD modelling using a conventional geometry is liable to underpredict the cell temperature by an even greater margin. In such low convection cases, the need to consider the intercellular gaps in the geometry becomes more important. Moreover, as apparent from Figure 5, the thermal profile obtained using the present geometry is visually more appealing and easier to analyse. Distinguishing each cell separately enables a more precise and scientific study of the problem at hand which is a good advantage to have in CFD analysis and post-processing.

The overall analysis leads to an understanding that the novel geometrical model proposed in this paper is a closer and more accurate manifestation of an actual PV module. The inclusion of the intercellular gaps in the CFD simulations enhances the understanding of the involved thermal physics. Ignoring these geometrical complexities and implementing a simplified conventional geometrical model significantly underpredicts the cell temperature and can give wrong conclusions about the performance and lifetime of a PV system. The degree of underprediction becomes starker at low wind speeds as well as for modules with low packing fractions. Due to more complex geometry and bigger mesh, the simulation using the presented geometrical model becomes more costly. Nonetheless, the present novel geometry should be preferred for analysing the thermal behaviour of a solar PV system.

4. CONCLUSION

This study presents an experimentally validated CFD analysis of a solar PV module by using a geometrical model which is very close to an actual PV module and incorporates the gap between different individual PV cells. The results are compared with those using a conventional geometry used by most of the past researchers which assumes all cells as a single continuous layer with no gaps. Since the material filling the intercellular gaps has very low thermal conductivity than the cell material, the presented geometrical model is able to capture the actual thermal characteristics of a PV module more accurately and vividly. Compared to the novel geometrical model, a conventional geometrical model consistently and considerably underpredicts the cell temperature in real operating conditions. For a PV module of a packing fraction of 88% at solar intensity of 850W/m^2 and wind speed of 1m/s, the maximum and mean temperature differences resulting from both geometrical models are noted to be 3.52°C (or 6.52%) and 2.42°C (or 4.65%), respectively. The magnitude of underprediction remains significant at all wind speeds. For instance, the maximum and mean temperature differences are 2.89°C (or 7.01%) and 1.82°C (or 4.64%) for a wind speed of 5m/s. However, since the absolute value of underprediction is more crucial in predicting PV performance, the incorporation of intercellular gaps becomes even more important at lower wind speeds. The study recommends that using a conventional geometrical model and ignoring the complexities of an actual PV module will underpredict the cell temperature which may lead to erroneous prediction of its real field performance and lifetime. On the other hand, incorporating the intercellular gaps and considering individual PV cells as distinct domains improves the accuracy of CFD modelling of a solar PV system and helps in capturing the actual thermal physics of the system with greater precision. The proposed improvements in the geometrical model should yield more accurate clues and stronger motivation for finding viable cooling methods for the heating problem of solar PV systems and enhancing their real field power output and lifetime.

In future work, a similar study can be performed to find out if the wind direction influences the percentage difference in mean and maximum cell temperatures obtained using the novel and conventional geometrical models. The corresponding results may probably provide a simple mathematical process to modify the cell temperature obtained using a conventional geometry and make it more accurate for further usage while saving computational resources.

5. REFERENCES

Dabaghzadeh, N. and Eslami, M., 2019. Temperature distribution in a photovoltaic module at various mounting and wind conditions: A complete CFD modeling. *Journal of Renewable and Sustainable Energy*, 11 (5).

Dupré, O., Vaillon, R., and Green, M.A., 2015. Physics of the temperature coefficients of solar cells. *Solar Energy Materials and Solar Cells*, 140, 92–100.

Dupré, O., Vaillon, R., and Green, M.A., 2016. A full thermal model for photovoltaic devices. *Solar Energy*, 140, 73–82.

Hanifi, H., Pfau, C., Turek, M., and Schneider, J., 2018. A practical optical and electrical model to estimate the power losses and quantification of different heat sources in silicon based PV modules. *Renewable Energy*, 127, 602–612.

Jaszczur, M., Hassan, Q., Szubel, M., and Majewska, E., 2018. Fluid flow and heat transfer analysis of a photovoltaic module under varying environmental conditions. *In*: *Journal of Physics: Conference Series*. Institute of Physics Publishing.

Jubayer, C.M., Siddiqui, K., and Hangan, H., 2016. CFD analysis of convective heat transfer from ground mounted solar panels. *Solar Energy*, 133, 556–566.

Kant, K., Shukla, A., Sharma, A., and Biwole, P.H., 2016. Thermal response of poly-crystalline silicon photovoltaic panels: Numerical simulation and experimental study. *Solar Energy*, 134, 147–155.

Kaplani, E. and Kaplanis, S., 2020. Dynamic electro-thermal PV temperature and power output prediction model for any PV geometries in free-standing and BIPV systems operating under any environmental conditions. *Energies*, 13 (18).

Kumar, S. and Subbarao, P.M.V., 2023. An improved numerical model to predict the operating temperature and efficiency of solar photovoltaic systems. *Environmental Science and Pollution Research*, 1–14.

Mahdi, J.M., Pal Singh, R., Taqi Al-Najjar, H.M., Singh, S., and Nsofor, E.C., 2021. Efficient thermal management of the photovoltaic/phase change material system with innovative exterior metal-foam layer. *Solar Energy*, 216, 411–427.

Marinić-Kragić, I., Nižetić, S., Grubišić-Čabo, F., and Papadopoulos, A.M., 2018. Analysis of flow separation effect in the case of the free-standing photovoltaic panel exposed to various operating conditions. *Journal of Cleaner Production*, 174, 53–64.

Nižetić, S., Grubišić- Čabo, F., Marinić-Kragić, I., and Papadopoulos, A.M., 2016. Experimental and numerical investigation of a backside convective cooling mechanism on photovoltaic panels. *Energy*, 111, 211–225.

Peng, Z., Herfatmanesh, M.R., and Liu, Y., 2017. Cooled solar PV panels for output energy efficiency optimisation. *Energy Conversion and Management*, 150, 949–955.

Sharaf, M., Yousef, M.S., and Huzayyin, A.S., 2022. Review of cooling techniques used to enhance the efficiency of photovoltaic power systems. *Environmental Science and Pollution Research*.

Sun, X., Silverman, T.J., Zhou, Z., Khan, M.R., Bermel, P., and Alam, M.A., 2017. Optics-Based Approach to Thermal Management of Photovoltaics: Selective-Spectral and Radiative Cooling. *IEEE Journal of Photovoltaics*, 7 (2), 566–574.

Wu, Y.Y., Wu, S.Y., and Xiao, L., 2017. Numerical study on convection heat transfer from inclined PV panel under windy environment. *Solar Energy*, 149, 1–12.

#98: Exploring the relationship between investor profiles and sustainable investment drivers: a systematic review

Kumar MANASWI[1], Archana SINGH[2], Vikas GUPTA[3]

1 Delhi Technological University, Shahbad Daulatpur, Main Bawana Road, Delhi-110042, India, manaswiblog.kumar@gmail.com
2 Delhi Technological University, Shahbad Daulatpur, Main Bawana Road, Delhi-110042, archanasingh@dtu.ac.in
3 Delhi Technological University, Shahbad Daulatpur, Main Bawana Road, Delhi-110042, vikasguptadtu@gmail.com

Abstract: The purpose of the present study is, firstly, to systematically review research papers on sustainable investments (SI); secondly, to identify and classify investors engaged in SI; thirdly, to map out linkages between investor classifications and drivers of SI; and lastly, to provide future research directions in the domain. To undertake the present study, the PRISMA protocol was used to choose 81 publications that were published between 2015 and 2023 from the Web of Science database. These publications were then analysed using VOSviewer software. A thematic analysis was conducted to assess various themes in the field of sustainable investments (SI). Further, a mapping exercise was conducted by the authors to assess the linkages between types of investors and SI drivers. This exercise can help identify opportunities for collaboration among investors, policymakers, corporations, and NGOs to achieve common sustainability goals. The study revealed that the number of published research papers on sustainable investments has exponentially grown in the last eight years. A total of three clusters emerged from the analysis that was conducted on the selected set of research papers. The study identified a total of seven drivers and eight types of investors for sustainable investments. Policymakers can draw inferences from this study and investigate the different barriers, ways to get around them, and opportunities that come with successfully implementing sustainability practices. Future researchers and scholars can conduct a comparative study of developed and developing economies regarding the integration of sustainability practices like environment, social, and governance (ESG) in investor decisions in order to get a comprehensive outlook.

Keywords: Sustainable Investments, Environment, Social, and Governance (ESG), VOSviewer, Thematic Mapping

1. INTRODUCTION

Recent years have witnessed a remarkable surge in sustainable investments (SI) (Collinson, 2020). This upsurge can be attributed to the growing interest of investors in environmental, social, and governance (ESG) considerations and the rising preference for investments that yield financial returns while positively impacting society and the environment (Stobierski, 2021; Ren, Hao and Wu, 2021). Investors are increasingly incorporating ESG factors into their investment decisions, recognising the crucial role of companies and investors in promoting sustainable development. The different stakeholders in society are increasingly becoming conscious of issues such as climate change, pollution, resource depletion, diversity, human rights, and social justice, leading them to seek out companies that align with their values to mitigate the risks associated with these challenges. In the changed scenario, investors are more likely to back businesses that place an emphasis on ESG concerns while also looking for long-term financial rewards.

When it comes to making sustainable investments, it's important to address that investors exhibit a wide array of motivations and priorities in such investments. For some investors, their primary driving force lies in the pursuit of maximising their returns and accumulating wealth, others are driven by a strong sense of social and environmental responsibility. Such investors place great importance on the impact, their investments can have on society and the planet. The motivations behind these investment choices are as diverse as the investors themselves. For instance, some are propelled by a deep sense of responsibility towards future generations. Other may view sustainable investments as a means to align their financial portfolios with their ethical values (Li et al., 2021). To gain a comprehensive understanding of this evolving landscape, further research is needed, including comparative studies across different cultural and economic contexts, which can provide more insightful results (Garg et al., 2022).

In the present study, the authors aim to scrutinise the linkages between investor profiles and sustainable investment drivers. By analysing existing literature, this study seeks to provide insights into the factors that motivate different types of investors to participate in sustainable investments besides financial returns (Beisenbina et al., 2022; Serafeim, 2020). The findings of this study would assist investors and investment managers in better understanding the preferences and motivations of various investor profiles and in developing better strategies for sustainable investments. The research questions of the study aim to (1) systematically review research papers on different types of SI; (2) identify and classify the types of investors in SI; (3) outline the connections between the classification of investors in SI and drivers for SI; and (4) provide recommendations for future research in the field of SI.

Section 2 of the paper deals with the methodology used for paper selection and analysis. In Section 3, the results of the systematic analysis have been presented. In Section 4, investor classifications in SI are identified and discussed. Section 5 deals with the mapping exercise based on investor classification in SI and drivers of SI. The summary and conclusion of the study are given in Section 6. The implications and future research directions related to the present study have been presented in sections 7 and 8, respectively.

2. METHODOLOGY

A three-step process has been followed in the present study to provide a clear and precise analysis. Firstly, using the PRISMA protocol, a set of eighty-one papers was constructed from 2015–2023. The PRISMA protocol enables researchers and practitioners to improve the quality of systematic reviews and meta-analyses, which would prove to be better and more reliable sources of information. Figure 1 shows a list of factors included and excluded in the overall process of the PRISMA protocol. In the second step, using VOSviewer, a systematic analysis was performed on the selected set of research papers in order to identify and analyse emerging themes in the field of sustainable investments. VOSviewer is a piece of software that facilitates the visualisation and comprehension of intricate bibliometric data. Users are able to gain significant insights about the relationships between clusters, themes, and study subjects through this software. In the last step, the authors conducted a mapping exercise based on the classifications of investors in SI and the drivers for SI. Further, the research included articles from the Web of Science database that were published between 2015 and 2023. Users have access to some of the most prestigious academic journals, books, and conference materials from all around the world through the Web of Science. It is inclusive of a vast range of academic disciplines, some of which are the sciences, management, and economics, amongst others.

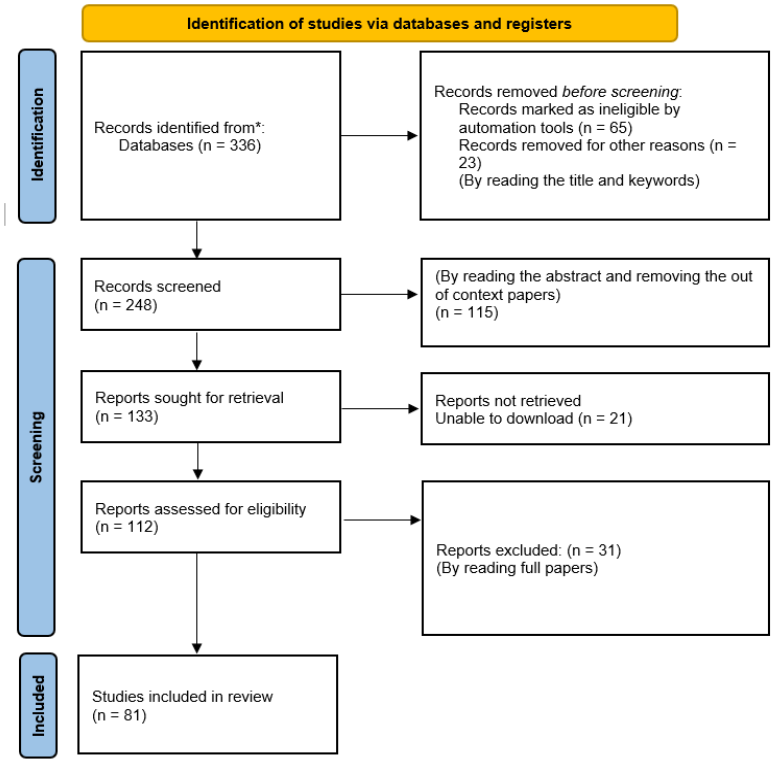

Figure 1 PRISMA Protocol

3. CLUSTER ANALYSIS

The authors have made an effort in this section to identify main themes or clusters by basing their analysis on the co-occurrence of keywords. The results of cluster analysis can lead to novel conclusions and a more in-depth comprehension of the topic at hand because it enables the discovery of patterns and connections between various concepts and subjects covered in the study (Aggarwal and Manaswi, 2022).

3.1. Cluster 1-Red: Sustainable Investments and Investment Performance

Recent studies on sustainable investments have yielded valuable insights into their performance and impact. Notably, sustainable investment funds have demonstrated the potential to outperform their conventional counterparts, frequently delivering financial returns comparable to or exceeding traditional funds (US SIF, n.d.). The Morningstar US Sustainability Index experienced a modest decline of 18.9% during the year 2022. Surprisingly, this decline was slightly lower than the 19.5% experienced by the renowned Morningstar US Large-Mid Cap Index. Further, the widely recognised S&P 500 witnessed a decline of 19.4% in parallel (US SIF, n.d.; Norton, 2023). Morgan Stanley, in a comprehensive analysis of 3,000 US mutual funds and exchange-traded funds (ETFs), published a report that underscored the significance of ESG considerations in investment portfolios during a period marked by heightened market volatility and an economic downturn (Morgan Stanley, 2021). The study revealed that portfolios neglecting ESG factors underperformed in comparison to those incorporating them, encompassing both equity and bond investments. Remarkably, sustainable equity funds demonstrated a noteworthy median total return in 2020, outperforming their non-ESG counterparts by an impressive margin of 4.3 percentage points. Similarly, sustainable taxable bond funds exhibited a median total return that surpassed competing funds by 0.9% during the same period. These positive trends of superior performance extended further back to 2019, with both sustainable equity funds and sustainable taxable bond funds outshining their traditional peer funds. Further, compelling findings from Morgan Stanley's study highlight the enduring advantages and financial rewards associated with integrating ESG considerations into investment strategies. Cunha et al. (2019) conducted a study suggesting that the effectiveness of sustainable investments varies based on the geographical location of the investment. It has also been observed that green portfolios tend to outperform the market during financial crises, indicating a growing awareness of the significance of sustainability among investors. Notably, developing economies like India are showing a heightened interest in corporations' green initiatives, which can stimulate demand for their shares (Kaur and Chaudhary, 2022). Jain, Sharma, and Srivastava (2019) affirm that businesses that prioritise eco-friendly practices and invest in green initiatives tend to generate substantial returns, creating better financial value and attracting proactive stakeholders concerned with environmental conservation. However, it is worth noting that several studies suggest no significant difference in performance between sustainable and traditional investments. Therefore, it is crucial to consider various factors such as

risk tolerance, investment objectives, and personal values alongside the investment performance of sustainable investments when making investment decisions (Talan and Sharma, 2019).

Some studies have found a positive relationship between sustainable investments and investment performance, while others have found no significant difference (Jain, Sharma, & Srivastava, 2019). The investment performance of sustainable investments should not, however, be the sole factor that investors consider when making investment decisions. Other factors, including risk tolerance, investment goals, and personal values, should also be considered (Talan and Sharma, 2019).

3.2. Cluster 2-Blue: Drivers of Sustainable Investments

According to Rücker (2021), there are three crucial factors that drive sustainable investments. Firstly, companies that prioritise ESG practices tend to achieve greater economic prosperity and generate more risk-adjusted returns in financial markets. Secondly, advances in technology and social media have brought about increased awareness regarding environmental conservation, action against climate change, and the need to exercise social responsibility. This shift in values has influenced investment decisions, with investors desiring to put their money into companies that align with their beliefs and values. Thirdly, regulatory measures are emerging as key drivers of sustainable investments, with businesses coming under increasing pressure to become more environmentally conscious and responsible. This trend is set to persist as the world strives to achieve collective political goals such as the Paris Agreement or the Sustainable Development Goals outlined by the United Nations. For instance, the European Union's efforts in sustainable finance and classification serve as a case in point (Lopes et al., 2022). Investors exhibit varying degrees of motivation driven by both higher risk-adjusted returns and values, considering different age groups. To illustrate, a notable 42% of investors aged 25–34 anticipate superior risk-adjusted returns from investments based on ESG, compared to a mere 16% of investors aged 55–64. Furthermore, across all age brackets, a significant 47% of investors express a desire to engage in ESG investments, either to manifest their personal values or to support companies actively contributing to positive societal and environmental impacts. This indicates that both financial considerations and ethical convictions play influential roles in shaping investor attitudes towards ESG investing across different age cohorts (Boffo and Patalano, 2020; Neufeld, 2021). Chatzitheodorou et al. (2019) identified seven types of motivation for investors engaged in socially responsible investing. Their analysis of motivations was based on the triple bottom line. The identified motivations were environmentally profit-seeking, environmentally conscious, socially profit-seeking, socially conscious, socio-environmentally profit-seeking, and value-based investing. This highlights the growing relevance of investment drivers and their significance for investor classification.

3.3. Cluster 3-Green: Investment opportunities based on Socially Responsible Investing

Socially responsible investing (SRI) provides investment opportunities that align financial goals with ethical values. Key opportunities include investing in renewable energy, sustainable agriculture, socially responsible companies, sustainable infrastructure, and social impact projects. These investments contribute to addressing climate change, promoting responsible farming, supporting social justice, enhancing urban development, and empowering underserved communities (Talan and Sharma, 2019). By capitalising on these opportunities, investors can generate financial returns while making a positive impact on society and the environment, contributing to a more sustainable and inclusive future. Socially responsible investments (SRI) have garnered considerable attention, particularly regarding their impact on financial performance. However, the absence of reliable instruments like ESG ratings has led to confusion surrounding the true representation of social responsibility (Chen, 2019; Boffo and Patalano, 2020). While veteran investors have been at the forefront of sustainable investments, individual participation has been relatively low over the past three decades (Meunier and Ohadi, 2022). Extensive comparisons between sustainable investments (SI) and traditional investments have sought to identify various determinants and intentions of investing through behavioural models (Avram, 2022). However, there is a dearth of studies investigating the linkages between investor classifications and drivers of sustainable investments. For instance, Thanki et al. (2022) conducted a cross-sectional analysis of 449 individual investors and found that collectivism, SI awareness, environmental concerns, and financial performance had significant positive effects on attitudes towards SI, subsequently influencing SI investment intentions. Additionally, research by Morgan Stanley revealed that sustainable mutual funds outperformed traditional mutual funds in the US over a ten-year period, while MSCI's study demonstrated that corporations with high ESG scores exhibited better risk-adjusted returns compared to their competitors. SRI has the potential to guide investors in aligning their investments with their values and beliefs while providing valuable insights into investor classifications. To further expand the understanding of sustainable investments and their ever evolving drivers, more in depth studies are warranted in order to provide a more comprehensive outlook (Peterdy, 2023).

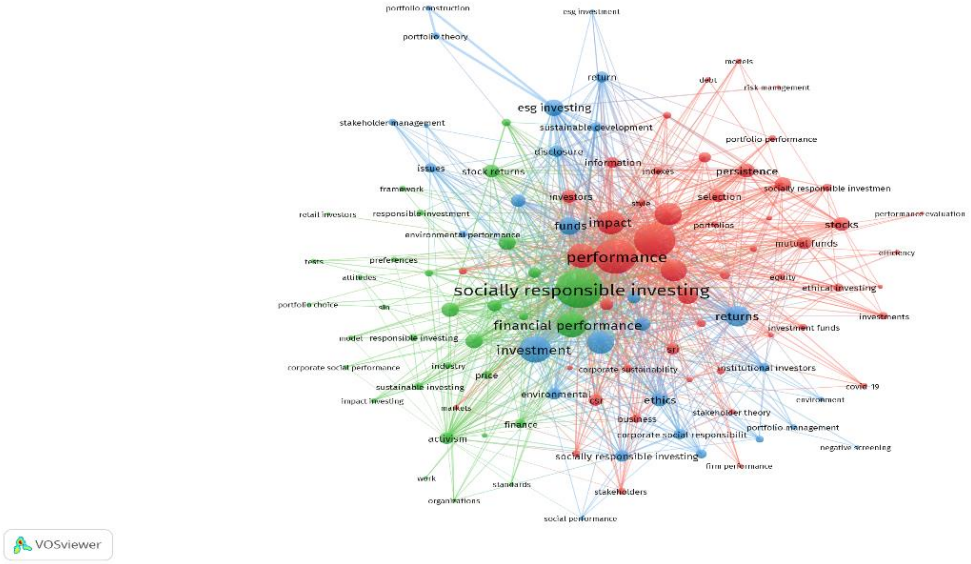

Figure 2 Cluster Analysis

4. INVESTOR CLASSIFICATIONS

In this section, the authors identified and categorised investors who engage in sustainable businesses to learn more about what drives and motivates them. This analysis is a continuation of the three different clusters that were discussed above. Each cluster presents a distinct perspective on sustainable investments. In Cluster 1, the authors looked at studies on how well sustainable investments did. This helped in understanding the risks as well as potential returns that come with these types of investments. In Cluster 2, the authors have attempted to provide insights into the motivations and preferences of investors as well as the larger social and economic contexts that shape sustainable investment decisions. In Cluster 3, assisted in the assessment and identification of socially conscious investors, as SRI mainly focuses on those investors. Overall, these three clusters contribute to a comprehensive analysis of investor classifications, offering insights into investment opportunities, driving forces, and performance outcomes in the context of sustainable investments. To better comprehend the motivations behind sustainable investments, it is essential to address two key questions: (a) which categories of investors are the most active in sustainable investments? and (b) what are the motivations for such investments? In Figure 3 the authors present a comprehensive synopsis of the different classifications of investors. In the figure, a total of four dimensions are presented: environment (top), social (left), corporate governance (right), and the economic dimension at the core which depicts traditional investments that prioritise financial gain over ESG considerations.

Environmental Domain

Existing literature suggests two fundamental categories of investors in this domain. The first group consists of environmentally conscious investors who prioritise environmental protection and preservation over financial gain. They base their investment decisions on the environmental impact of the companies they choose to invest in. On the other hand, the second group comprises investors primarily driven by financial returns but who also consider the environmental impact of their investments. They aim to avoid environmental risks while pursuing profits (Bergek, Mignon, and Sundberg, 2013). To illustrate this distinction, Figure 3 depicts environmentally conscious investors in area E1 and environmentally profit-seeking and risk-averse investors in area E2. By analysing these different investor categories, researchers gain valuable insights into the preferences and priorities of investors within the environmental domain.

Social Domain

The social domain encompasses investors who are driven by social motivations and seek to invest in initiatives that promote the common good and improve community living standards. Extensive literature exploration revealed two distinct types of investors within the social realm, each with different incentives and levels of emphasis on sustainability. The first group, represented as “S1” in Figure 3, consists of socially conscious investors who conscientiously refrain from investing in industries considered “dirty,” such as tobacco, alcohol, gambling, or armaments, due to their ethical principles. These investors willingly forgo potentially lucrative opportunities, prioritising their principles over financial gains. The second category comprises investors primarily motivated by profit maximisation or risk mitigation with minimal concern for social issues (Jain, Sharma, and Srivastava, 2019). They engage in social investment to explore untapped profit potential or safeguard their investments from potential negative societal repercussions. Referred to as “socially profit-seeking and risk-

averse investors," this group is symbolised as area S2 in Figure 3. According to Collinson (2020), ethical investments sometimes attract conventional investors who are expecting better returns than conventional investments.

Socio-Environmental Domain

The socio-environmental domain of investment is witnessing remarkable growth as more investors seek to align their financial goals with their personal values and make a positive impact on the world (Garg et al., 2022). Within this domain, two distinct categories of investors emerge after a thorough analysis of the literature. The first category consists of investors who primarily consider a company's socio-environmental performance and its societal impact when making investment decisions. They favour businesses that operate sustainably and responsibly (SE1 in Figure 3). The second category includes socio-environmentally profit-seeking and risk-averse investors who believe that investing in companies committed to social and environmental responsibility can generate higher long-term returns (SE2 in Figure 3). These investors recognise the growing significance of socio-environmental considerations and their potential to drive financial success.

Governance Domain

The governance domain focuses on investing in companies that demonstrate a firm commitment to ethical business conduct and effective governance procedures (G1 in Figure 3). Investors in this domain are driven by diverse and intricate motivations, which encompass factors such as transparency, social accountability, risk mitigation, and overall financial success (Shank, Paul Hill, and Stang, 2013). By prioritising strong governance practices, investors aim to benefit from increased transparency, enhanced accountability, and reduced risk. This domain plays a vital role in aligning investment decisions with ethical and responsible business practices.

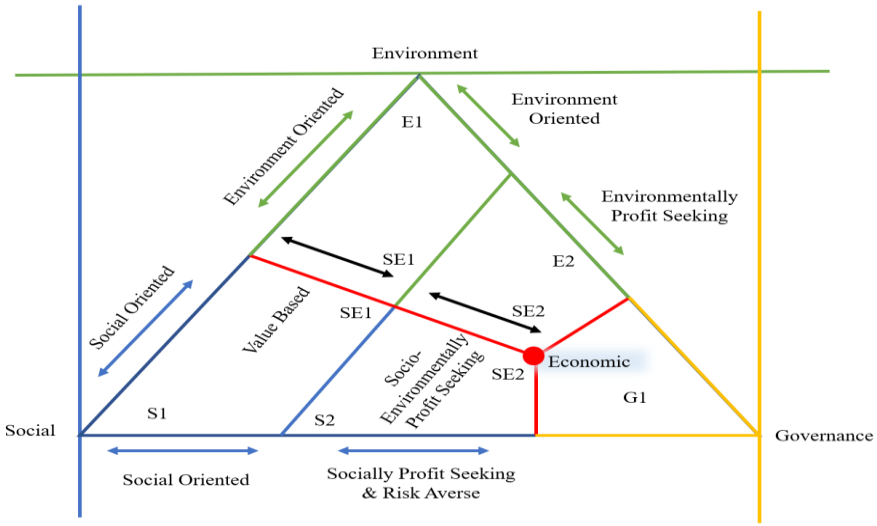

Figure 3 Investor Classification

5. MAPPING INVESTOR CLASSIFICATIONS AND DRIVERS OF SUSTAINABLE INVESTMENTS

The proposed mapping exercise aims to consolidate the fragmented literature on sustainable investments (SI) and enhance scholars' and academicians' understanding of this field, particularly in the absence of a standard definition. By mapping the relationships between investor classifications and drivers of sustainable investments, several objectives can be achieved. Firstly, this mapping would bring clarity to investors' interest in SI by highlighting the most influential drivers and distinguishing them from less critical factors. Secondly, a better comprehension of these linkages would stimulate greater investor participation in sustainable investments, directing capital towards socially and environmentally responsible projects. Thirdly, policymakers can develop targeted policies to promote sustainable investment when equipped with a comprehensive understanding of these interconnections, thereby fostering long-term investments. Lastly, the construction of a diagram illustrating the connections between different investor types and driving factors would help in identifying areas that require further investigation, prompting academics and industry professionals to disseminate relevant data to the investment community.

Table 1: Mapping Investor Classifications with Drivers of SI

Investor Types	ESG Focus	Investor Motivation		Potential Investors	Drivers of SI	Mapping Drivers
		Value Based	Profit Seeking & Risk Averse			
Climate-conscious investors	Environment	✓		NPOs, Green MFs	Climate change awareness, Environmental stewardship, Sustainable future	E1
Environmentally Profit Seeking & Risk Averse	Environment		✓	Conventional Investors, institutional investors, NGOs, NPOs, charities	Financial returns, Environmental preservation, Risk management, Resource efficiency, Sustainable business models	E2
Ethical Investors	Social, Governance	✓		Social Investors, Charities, Foundations	Values alignment, Ethical considerations, social impact, Responsible investing, Alignment with values and beliefs	S1, G1
Socially Profit Seeking and Risk Averse	Social		✓	Conventional Investors	Financial gains, social impact, Risk management, Responsible business practices, Sustainable growth	S2
Socially Responsible Investors	Socio-Environment	✓		Institutional investors, pension funds, charities	Environmental preservation, social responsibility, Ethical governance, Impactful investing, Sustainable development	SE2
Socio-Environmentally Profit Seeking & Risk Averse	Socio-Environment		✓	Individual investors, institutional investors, NGOs, NPOs, charities	Sustainable development, social progress, Environmental responsibility, Balanced risk exposure	SE1
Governance focused	Governance		✓	Institutional investors, pension funds, sovereign wealth funds	Corporate transparency, Strong governance practices, Shareholder rights, Board accountability, Board diversity	G1
ESG Investors	Environment Social Governance	✓	✓	Institutional investors, pension funds, sovereign wealth funds, charities	Environmental awareness, social responsibility, Governance considerations, Long-term value creation	SE1, SE2

The Table 1 maps eight different types of sustainable investors and their investment drivers. The first column lists the investor types, namely: climate-conscious investors, environmentally profit-seeking and risk-averse investors, ethical investors, socially profit-seeking and risk-averse investors, socially responsible investors, socio-environmentally profit-seeking and risk-averse investors, governance-focused investors, and ESG investors. The second column focuses on ESG criteria, including environmental, social, governance, and socio-environmental factors, respectively. The third and fourth columns show investor motivations, i.e., value-based and profit-seeking investors, respectively. The fifth column highlights potential investors, including institutional investors, high net-worth individuals, retail investors, pension funds, NPOs, and charities and NGOs. The sixth column shows potential drivers for those investors, and the last column maps these characteristics with investor classifications identified in Section 4 (Figure 3).

The purpose of the mapping exercise that is presented in the table is significant to the overall study because it illustrates the linkages that exist between the different types of sustainable investors and the investment motivations that are associated with them. For instance, environmental concerns drive climate-conscious investors to prioritise environmental factors in their investment decisions (Cunha et al., 2019). These investors may prioritise the reduction of carbon emissions or the promotion of renewable energy projects. On the other hand, investors who are concerned about the environment but are also interested in making a profit place a primary emphasis on financial returns while also taking environmental considerations into account (Boffo and Patalano 2020). Through this exercise, scholars would gain a better understanding of how various categories of investors match certain ESG criteria and motives. The fact that this activity is able to shed light on the various viewpoints and priorities of sustainable investors is the primary reason why it is relevant. The table offers valuable insights into the complex environment of sustainable investments by mapping the different categories of investors to specific ESG criteria, motivations, potential investors, and drivers. In Table 1, ethical investors emphasise the significance of social and governance elements alongside their investing decisions. Additionally, they take values and ethical considerations into account while selecting portfolios. According to Garg et al. (2022), Collinson (2020), and Derwall, Koedijk, and Ter Horst (2011), these investors may include social investors, non-profit organisations (NPOs), charities, or non-government organisations (NGOs). This demonstrates their commitment to having a positive impact on society. Chatzitheodorou et al., (2019) also conducted a similar study wherein they only looked at SRIs and identified additional investor classifications, giving readers a comprehensive understanding of the sustainable investment landscape. Finally, COVID-19's influence on environmentally responsible spending is not to be discounted. Many investors have been forced to revise their investment strategies because of the economic slowdown caused by the pandemic. Additionally, it has emphasised the significance of making sustainable investments in resilience-building and tackling global crises.

6. CONCLUSION

Sustainable investments (SI) are increasingly gaining attention for their ability to blend financial viability with social responsibility, making them a powerful force that fosters positive returns and fuels long-term economic growth. A meticulous systematic review by the authors unveiled three emerging themes in the field of SI: 'sustainable investments and investment performance,' 'drivers of sustainable investments,' and 'investment opportunities based on socially responsible investments (SRI)' (as shown in Figure 2). These themes provide invaluable insights into the emerging frontiers of SI. After the thematic analysis, the authors then identified and classified investors engaged in SI based on their different drivers and motivations. This comprehensive investigation yielded a total of seven distinctive classifications, as demonstrated in Figure 3. The authors in this study also conducted a mapping exercise, examining the intricate linkages between investor classifications and the driving forces behind sustainable investments (Table 1). This exercise provides a profound framework, enabling researchers and practitioners alike to navigate the diverse landscape of sustainable investors, drawing out similarities and highlighting their unique differentiating factors. Socially responsible investors consider both environmental and social factors when making investment decisions, attracting retail investors and pension funds seeking to align their investments with their values and societal impact goals. Further, the exercise highlights the alignment between investor characteristics and the identified investor classifications from Section 4 and Figure 3 of the study. This correlation further validates and strengthens the understanding of investor behaviour in the context of sustainable investments. For instance, governance-focused investors prioritise good governance practices in the companies they invest in, primarily attracting pension funds that emphasise responsible corporate practices and transparency. By mapping the investor types, ESG criteria, motivations, potential investors, and drivers, researchers can identify patterns, trends, and interconnections within the sustainable investment landscape. This knowledge not only enhances our understanding of sustainable investing but also informs policymakers, practitioners, and stakeholders about the potential avenues for promoting and advancing sustainable practices. Therefore, as the understanding of sustainable investments continues to evolve, policymakers can leverage this knowledge to develop policies that foster long-term investments and support sustainable practices.

7. IMPLICATIONS

The present study has important implications for asset managers, enabling them to better engage with the businesses in which they have invested. By integrating human rights and environmental concerns into business strategies and corporate governance, ethical and sustainable business practices can be promoted. Additionally, fund managers and investors can benefit from this study by gaining a deeper understanding of which activities are sustainable and which are not, empowering them to make more informed investment decisions.

Exploring investor classification within sustainable investments holds significant potential for shaping the trajectory of sustainable finance and driving investments towards responsible and sustainable practices. The present study comprehensively identified and categorised investors based on their preferences, motivations, and engagement with sustainable investments. Such understanding would lay the groundwork for informed strategies and initiatives that foster positive environmental and social impacts within the financial landscape.

Further, policymakers can leverage the findings of this study to design targeted initiatives and regulations that encourage greater investment in sustainable practices. For instance, tax incentives or subsidies can be provided to make certain types of sustainable investments more attractive to investors. Policymakers can also focus on improving transparency and standardisation of sustainable investment products, facilitating investor understanding and comparison of different options. In addition, the analysis of investor classification assists policymakers in evaluating the impact of sustainable investments on various stakeholders, such as businesses, communities, and the environment.

8. FUTURE RESEARCH DIRECTIONS

Table 2: Future Research Directions

Clusters	Particulars
Cluster 1 'Red': Sustainable Investments and Investment Performance	❖ The landscape of sustainable investments is ever changing due to financial innovations like impact investing, green bonds, ETFs, among others. Future studies assessing the impact of these new financial products on sustainable investment performance and their potential to drive positive social and environmental outcomes can be insightful (Quatrosi, 2022). ❖ Sustainable investments can provide benefits beyond social and environmental dimensions i.e., portfolio diversification. Future studies focusing on potential benefits of integrating sustainable investments into portfolio management, particularly in terms of risk reduction and long-term performance can yield interesting results.
Cluster 2 'Green': Drivers of Sustainable Investments	✓ Assessing sustainable investments through a multicultural lens, researchers can gain deeper insights into how economic and cultural factors shape investors' overall behaviour and attitudes. Such a comparative analysis can shed light on the nuances and variations in sustainable investment practices worldwide, enhancing our understanding of the complex interplay between culture, economics, and sustainable finance (Garg et al., 2022). ✓ Advances in technology are enabling new ways of investing in sustainability, such as impact investing and blockchain-based platforms. Future research could examine how technology is changing the landscape of sustainable investing and how it is influencing investor behaviour (Li et al., 2022).
Cluster 3 'Blue': Investment Opportunities based on Socially Responsible Investments	○ Sustainable business practices are becoming the norm, and investors are increasingly looking for possibilities based on ESG factors. The impact of the indicated sustainability metrics on investment outcomes needs more investigation (Koenigsmarck and Geissdoerfer, 2023). ○ Since the UN introduced ESG in 2004, academic research has favoured it over CSR. Studies have mostly focused on developed nations when it comes to the impact analysis of SIs. Further research on developing nations can be insightful to get a comparative and comprehensive outlook.

9. REFRENCES

Aggarwal, P. and Manaswi, K. (2022). Role of Circular Economy, Industry 4.0 and Supply Chain Management for Tribal Economy: A Systematic Review. *Journal of the Anthropological Survey of India*, p.12. doi:https://doi.org/10.1177/2277436x221125914.

Avram, C.B. (2022). Bibliometric analysis of sustainable business performance: where are we going? A science map of the field. *Economic Research-Ekonomska Istraživanja*, p.25. doi:https://doi.org/10.1080/1331677x.2022.2096094.

Beisenbina, M., Fabregat-Aibar, L., Barberà-Mariné, M. and Sorrosal-Forradellas, M. (2022). The burgeoning field of sustainable investment: Past, present and future. *Sustainable Development*, p.9. doi:https://doi.org/10.1002/sd.2422.

Bergek, A., Mignon, I. and Sundberg, G. (2013). Who invests in renewable electricity production? Empirical evidence and suggestions for further research. *Energy Policy*, 56, p.13. doi:https://doi.org/10.1016/j.enpol.2013.01.038.

Boffo, R. and Patalano, R. (2020). *ESG Investing: Practices, Progress and Challenges - OECD*. [online] *oecd.org*, p.31. Available at: https://www.oecd.org/finance/ESG-Investing-Practices-Progress-Challenges.pdf.

Chatzitheodorou, K., Skouloudis, A., Evangelinos, K. and Nikolaou, I. (2019). Exploring socially responsible investment perspectives: A literature mapping and an investor classification. *Sustainable Production and Consumption*, 19, p.9. doi:https://doi.org/10.1016/j.spc.2019.03.006.

Chen, J. (2019). *Socially Responsible Investment (SRI)*. [online] Investopedia. Available at: https://www.investopedia.com/terms/s/sri.asp.

Collinson, P. (2020). *Ethical investments are outperforming traditional funds*. [online] The Guardian. Available at: https://www.theguardian.com/money/2020/jun/13/ethical-investments-are-outperforming-traditional-funds.

Cunha, F.A.F. de S., Oliveira, E.M., Orsato, R.J., Klotzle, M.C., Cyrino Oliveira, F.L. and Caiado, R.G.G. (2019). Can sustainable investments outperform traditional benchmarks? Evidence from global stock markets. *Business Strategy and the Environment*, 29(2), p.15. doi:https://doi.org/10.1002/bse.2397.

Derwall, J., Koedijk, K. and Ter Horst, J. (2011). A tale of values-driven and profit-seeking social investors. *Journal of Banking & Finance*, 35(8), p.6. doi:https://doi.org/10.1016/j.jbankfin.2011.01.009.

Garg, A., Goel, P., Sharma, A. and Rana, N.P. (2022). As you sow, so shall you reap: Assessing drivers of socially responsible investment attitude and intention. *Technological Forecasting and Social Change*, 184, p.9. doi:https://doi.org/10.1016/j.techfore.2022.122030.

Jain, M., Sharma, G.D. and Srivastava, M. (2019). Can Sustainable Investment Yield Better Financial Returns: A Comparative Study of ESG Indices and MSCI Indices. *Risks*, [online] 7(1), p.3. doi:https://doi.org/10.3390/risks7010015.

Kaur, J. and Chaudhary, R. (2022). Relationship between macroeconomic variables and sustainable stock market index: an empirical analysis. *Journal of Sustainable Finance & Investment*, p.12. doi:https://doi.org/10.1080/20430795.2022.2073957.

Koenigsmarck, M. and Geissdoerfer, M. (2023). Shifting the Focus to Measurement: A Review of Socially Responsible Investing and Sustainability Indicators. *Sustainability*, 15(2), p.5. doi:https://doi.org/10.3390/su15020984.

Li, T.-T., Wang, K., Sueyoshi, T. and Wang, D.D. (2021). ESG: Research Progress and Future Prospects. *Sustainability*, [online] 13(21), p.6. doi:https://doi.org/10.3390/su132111663.

Lopes, J.M., Gomes, S., Pacheco, R., Monteiro, E. and Santos, C. (2022). Drivers of Sustainable Innovation Strategies for Increased Competition among Companies. *Sustainability*, 14(9), p.7. doi:https://doi.org/10.3390/su14095471.

Meunier, L. and Ohadi, S. (2022). Misconceptions about socially responsible investments. *Journal of Cleaner Production*, 373, p.4. doi:https://doi.org/10.1016/j.jclepro.2022.133868.

Morgan Stanley (2021). *Sustainable Funds Beat Peers in 2020*. [online] Morgan Stanley. Available at: https://www.morganstanley.com/ideas/esg-funds-outperform-peers-coronavirus.

Neufeld, D. (2021). *ESG Investing: The Top 5 Drivers*. [online] Advisor Channel. Available at: https://advisor.visualcapitalist.com/esg-investing-the-top-5-drivers/.

Norton, L. (2023). *ESG Investing Keeps Pace With Conventional Investing in 2022*. [online] Morningstar, Inc. Available at: https://www.morningstar.com/articles/1132007/esg-investing-keeps-pace-with-conventional-investing-in-2022.

Peterdy, K. (2023). *Sustainable Investing*. [online] Corporate Finance Institute. Available at: https://corporatefinanceinstitute.com/resources/esg/sustainable-investing/.

Quatrosi, M. (2022). Financial Innovations for Sustainable Finance: An Exploratory Research. *SSRN Electronic Journal*, p.7. doi:https://doi.org/10.2139/ssrn.4155960.

Rücker, N. and Jordan, N. (2021). *Three main drivers of responsible investing*. [online] Julius Baer. Available at: https://www.juliusbaer.com/en/insights/sustainability/three-main-drivers-of-responsible-investing/.

Serafeim, G. (2020). *Social-Impact Efforts That Create Real Value*. [online] Harvard Business Review. Available at: https://hbr.org/2020/09/social-impact-efforts-that-create-real-value.

Shank, T., Paul Hill, R. and Stang, J. (2013). Do investors benefit from good corporate governance? *Corporate Governance: The international journal of business in society*, 13(4), p.11. doi:https://doi.org/10.1108/cg-03-2010-0027.

Stobierski, T. (2021). *What Is Sustainable Investing?* [online] Business Insights - Blog. Available at: https://online.hbs.edu/blog/post/sustainable-investing.

Talan, G. and Sharma, G. (2019). Doing Well by Doing Good: A Systematic Review and Research Agenda for Sustainable Investment. *Sustainability*, 11(2), p.2. doi:https://doi.org/10.3390/su11020353.

Thanki, H., Shah, S., Rathod, H.S., Oza, A.D. and Burduhos-Nergis, D.D. (2022). I Am Ready to Invest in Socially Responsible Investments (SRI) Options Only If the Returns Are Not Compromised: Individual Investors' Intentions toward SRI. *Sustainability*, [online] 14(18), p.9. doi:https://doi.org/10.3390/su141811377.

US SIF (n.d.). *The Forum for Sustainable and Responsible Investment*. [online] www.ussif.org. Available at: https://www.ussif.org/performance#:~:text=A%20growing%20body%20of%20research.